Defects in Semiconductors
ICDS-19
Part 1



Editors:

Gordon Davies and
Maria Helena Nazaré

DISTRIBUTION STATEMENT A
Approved for public release;
Distribution Unlimited

ttp TRANS TECH PUBLICATIONS

Materials Science Forum

ISSN 0255-5476

As of January 1992 combined with Crystal Properties and Preparation

Editors:

G.E. Murch
University of Newcastle
Department of Mechanical Engineering
NSW 2308, Australia
Fax +61 (49) 60 22 28
e-mail CGGEM@cc.newcastle.edu.au

Fred H. Wöhlbier
Trans Tech Publications Ltd
Brandrain 6
CH-8707 Uetikon-Zuerich, Switzerland
Fax +41 (1) 922 10 33
e-mail woehlbier@ttp.ch

Editorial Board:

F. Benière (Rennes), C.R.A. Catlow (London), L.T. Chadderton (Melbourne), M. Doyama (Tokyo), P. Kofstad (Oslo), R. Krishnan (Trombay), C. Moynihan (Troy), J. Nowotny (Lucas Heights), W. Schilling (Jülich), J.B. Wagner (Tempe), H. Wollenberger (Berlin)

Advisory Board:

Australia
D.P. Dunne (Wollongong)
P.G. McCormick (Nedlands)
P.L. Rossiter (Clayton)

Belgium
J.P. Issi (Louvain-la-Neuve)
J. van Humbeeck (Heverlee-Leuven)

Canada
H.W. King (Victoria)
R.W. Smith (Kingston)

Czech Republic
P. Lukac (Praha)

Denmark
M.M. Eldrup (Roskilde)

Finland
P. Kettunen (Tampere)
R.M. Nieminen (Espoo)

France
C. Boulesteix (Marseille)
A. Charlier (Metz)
L.P. Kubin (Chatillon)
V. Pontikis (Palaiseau)
R. Streiff (Marseille)
D. Stievenard (Lille)

Germany
G.H. Bauer (Oldenburg)
K.-H. Bennemann (Berlin)
D. Bimberg (Berlin)
E. Bucher (Konstanz)
H. Foell (Kiel)
B. Ittermann (Marburg)
U. Köster (Dortmund)
E. Macherauch (Karlsruhe)
W. Moench (Duisburg)
H. Mughrabi (Erlangen)
H. Neuhäuser (Braunschweig)
J. Pollmann (Münster)
H.-E. Schaefer (Stuttgart)
J.-B. Suck (Chemnitz)
W. Schüle (Frankfurt/Main)
H. Zabel (Bochum)

Hungary
D.L. Beke (Debrecen)
A. Roosz (Miskolc)

India
D.C. Agrawal (Kanpur)
H.D. Banerjee (Kharagpur)
A.K. Bhatnagar (Hyderabad)
A.H. Chokshi (Bangalore)
P. C. Jain (Delhi)
P.C. Mathur (New Delhi)
D. Pandey (Varanasi)
I.K. Varma (New Delhi)

Ireland
M. Buggy (Limerick)

Israel
A. Voronel (Tel-Aviv)

Italy
G. Artioli (Modena)
F. Belluci (Naples)
E. Bonetti (Bologna)
R. Cantelli (Roma)
E. Evangelista (Ancona)
M. Magini (Roma)

Japan
M. Miki (Himeji)
Y. Murakami (Fukuoka-shi)
S. Nitta (Gifu)
T. Shimizu (Kanazawa-shi)
P.H. Shingu (Kyoto)
H. Tamaki (Niigata)
K. Yokogawa (Kure-shi)

Korea
Y.-H. Jeong (Pohang)
D. Kwon (Seoul)
J.-S. Lee (Ansan)
K. Yong Lee (Seoul)
I.-H. Moon (Seoul)

Pakistan
Z. Iqbal (Islamabad)

Poland
J. Jedlinski (Krakow)
L.B. Magalas (Krakow)
D. Oleszak (Warszawa)
H. Stachowiak (Wroclaw)

Portugal
R.P. Martins (Lisboa)

Rumania
M. Petrescu (Bucharest)

Slovakia
M. Turna (Bratislava)

South Africa
P. de V. du Plessis (Johannesburg)

Spain
F. Agulló-Lopez (Madrid)
E. Calleja (Madrid)
N. Clavaguera (Barcelona Catalonia)
C. Conde (Sevilla)
R. Navarro Linares (Zaragoza)

Sweden
H.G. Grimmeiss (Lund)

Switzerland
R. Car (Geneva)

The Netherlands
C.A.J. Ammerlaan (Amsterdam)
J.T. de Hosson (Groningen)
E.J. Mittemeijer (Delft)

UK
R.J. Cernik (Warrington)
R.G. Faulkner (Loughborough)
C.M. Friend (Swindon)
G.W. Lorimer (Manchester)
W.J. Plumbridge (Milton)
B. Ralph (Uxbridge)
D.K. Ross (Salford)
B. Wilshire (Swansea)
A.S. Wronski (Bradford)

USA
B.L. Adams (Pittsburgh)
I. Baker (Hanover)
R.G. Bautista (Reno)
G.C. Farrington (Philadelphia)
T.B. Flanagan (Burlington)
Y.C. Jean (Kansas City)
T.G. Langdon (Los Angeles)
R.B. McLellan (Houston)
A.K. Mukherjee (Davis)
G.F. Neumark (New York)
S.Pearton (Gainesville)
D.N. Seidman (Evanston)
G.B. Stingfellow (Salt Lake City)
W. Yen (Athens)

See back inside cover for scope and subscription information

REPORT DOCUMENTATION PAGE

Form Approved OMB No. 0704-0188

Public reporting burden for this collection of information is estimated to average 1 hour per response, including the time for reviewing instructions, searching existing data sources, gathering and maintaining the data needed, and completing and reviewing the collection of information. Send comments regarding this burden estimate or any other aspect of this collection of information, including suggestions for reducing this burden to Washington Headquarters Services, Directorate for Information Operations and Reports, 1215 Jefferson Davis Highway, Suite 1204, Arlington, VA 22202-4302, and to the Office of Management and Budget, Paperwork Reduction Project (0704-0188), Washington, DC 20503.

1. AGENCY USE ONLY (Leave blank)	2. REPORT DATE	3. REPORT TYPE AND DATES COVERED
	23 January 1998	Conference Proceedings

4. TITLE AND SUBTITLE

Nineteenth International Conference of Defects in Semiconductors

5. FUNDING NUMBERS

F6170897W0091

6. AUTHOR(S)

Conference Committee

7. PERFORMING ORGANIZATION NAME(S) AND ADDRESS(ES)

Aviero University
3810 Aveiro
Aveiro
Portugal

8. PERFORMING ORGANIZATION REPORT NUMBER

N/A

9. SPONSORING/MONITORING AGENCY NAME(S) AND ADDRESS(ES)

EOARD
PSC 802 BOX 14
FPO 09499-0200

10. SPONSORING/MONITORING AGENCY REPORT NUMBER

CSP 97-1035

11. SUPPLEMENTARY NOTES

Three volumes.

12a. DISTRIBUTION/AVAILABILITY STATEMENT

Approved for public release; distribution is unlimited.

12b. DISTRIBUTION CODE

A

13. ABSTRACT (Maximum 200 words)

The Final Proceedings for International Conference of Defects in Semiconductors, 21 July 1997 - 25 July 1997

Emphasis will be given on the properties of wide-bandgap materials, including quantum enhancement of effective band-gaps, semiconductors (silicon and III-V materials), plus radiation effects on detector materials. Topics will also include: GaN, Nanostructures, Large bandgap materials, defects in Epitaxial growth, self-organizing rare earth, metastable defects, pairs and complexes, defect reactions, radiation effects on detector material.

14. SUBJECT TERMS

Semiconductors, Electronic Devices

15. NUMBER OF PAGES

1864

16. PRICE CODE

N/A

17. SECURITY CLASSIFICATION OF REPORT	18. SECURITY CLASSIFICATION OF THIS PAGE	19. SECURITY CLASSIFICATION OF ABSTRACT	20. LIMITATION OF ABSTRACT
UNCLASSIFIED	UNCLASSIFIED	UNCLASSIFIED	UL

Defects in Semiconductors
ICDS-19
Part 1

19980715 015

Defects in Semiconductors
ICDS-19

Part 1

Proceedings of the 19th International Conference on Defects in Semiconductors, Aveiro, Portugal, July 1997

Editors:

Gordon Davies and Maria Helena Nazaré

TRANS TECH PUBLICATIONS LTD
Switzerland • Germany • UK • USA

Copyright © 1997 Trans Tech Publications Ltd, Switzerland

ISBN 0-87849-786-2 (3-Vol. Set)
0-87849-787-0 (Part 1)
0-87849-788-9 (Part 2)
0-87849-789-7 (Part 3)

Volumes 258-263 of
Materials Science Forum
ISSN 0255-5476

***Distributed** in the Americas by*

Trans Tech Publications Ltd
PO Box 699, May Street
Enfield, New Hampshire 03748
USA
Phone: (603) 632-7377
Fax: (603) 632-5611
e-mail: ttp@ttp.net
Web: http://www.ttp.net

and worldwide by

Trans Tech Publications Ltd
Brandrain 6
CH-8707 Uetikon-Zuerich
Switzerland
Fax: +41 (1) 922 10 33
e-mail: ttp@ttp.ch
Web: http://www.ttp.ch

Printed in the United Kingdom
by Hobbs the Printers Ltd,
Totton, Hampshire SO40 3WX

Organising committees
of the
19th International Conference on Defects in Semiconductors

The Local Organising Committee:

Chairs: M.H. Nazaré and G. Davies

Members:

M.C. do Carmo	M.F. Thomaz	A. Neves
C. Boemare	T. Gasche	F. Duarte
	S. Amarante	

The Programme Committee:

C.A.J. Ammerlaan	B. Clerjaud	V.V. Emtsev
A. Fazzio	M.O. Henry	T. Kennedy
W. Jantsch	Z. Iqbal	C. Herrero
H. Katayama Yoshida	H. Kukimoto	E. Pereira
J.-M. Spaeth	M. Stavola	A.M. Stoneham
J. Vanhellemont	E.R. Weber	

The International Advisory Committee:

C.A.J. Ammerlaan	M.J. Caldas	J. Chadi
G.G. DeLeo	W. Jantsch	H. Kanda
L.C. Kimerling	H. Kukimoto	J.M. Langer
B. Monemar	R.C. Newman	J.-M. Spaeth
M. Stavola	K. Sumino	M.L.W. Thewalt
C.G. Van de Walle	G.D. Watkins	E.R. Weber
	J. Weber	

The Steering Committee:

G. Davies	G.G. DeLeo	W. Jantsch
M.H. Nazaré	M. Stavola	K. Sumino

Acknowledgements

ICDS-19 was held in the elegant new Cultural and Congress Centre in Aveiro, Portugal. Here 263 delegates presented new data on defects in semiconductors, surveyed current knowlege in reviews and hopefully started to map out the future of this active research area. The scientific work is presented here in the 301 papers in these volumes.

To mount a meeting like this requires a huge input of time and energy from many people. We want to thank, first, Celeste do Carmo for the unlimited energy she gave to the organisation and for allowing so many members of the Physics Department of Aveiro University to give their skills and time to the meeting. Members of the Department processed electronic and paper submissions into abstract books and programmes, they set up the computing facilities at the meeting, they helped in the smooth running of the sessions, and they organised the conference excursions. Without all this input the meeting could not have taken place.

As well as the scientific programme, a meeting like ICDS involves much background organisation: of transport, of accomodation, of providing advice on a wide range of matters to delegates. We thank Dr$^{a.}$ Maria de Jesus Galaricha and her staff of the Fundação João Jacinto de Magalhães for the excellent support they provided. We are particularly indebted to Sandra Amarante for her input at the meeting in solving the hundreds of problems which were brought to her during the week. An abundance of beautiful food and drink was provided by the staff of the University of Aveiro. Many delegates have commented on the Portuguese hospitality shown during the meeting, and we record here the thanks of everyone to all these support staff. We also thank the innocent bystanders who became caught up in the meeting — the spouces, daughters and friends — for their contributions.

All the papers in these proceedings were refereed, mainly during the meeting itself. We thank all the referees for their anonymous but valued work which not only ensures the standard of work presented, but also gives the opportunity for referees to help colleagues with the peculiarities of the English language. The editors also thank the invaluable assistance provided by Carol Booth and Tracey Glasspool.

A major input to a conference comes, of course, from the Session Chairs. For their work in this capacity we thank:

Rob Ammerlaan	Marília Caldas	William Carlos
Weimin Chen	Bernaud Clerjaud	Vadim Emtsev
Alberto Fazzio	Haflidi Gislason	Eugene Haller
Martin Henry	Lionel Kimerling	Mats Kleverman
Jerzy Langer	Arne Nylandsted Larsen	Kurt Laßmann
Bruno Meyer	Bo Monemar	Pat Mooney
Ron Newman	Brian Bech Nielsen	Tony Peaker
Estela Pereira	Bhushan Sopori	Martin Spaeth
Michael Stavola	Klaus Thonke	Jan Vanhellemont
Eicke Weber	Jörg Weber	

Finally we thank the financial sponsors of the meeting for their essential contributions. They are listed on the following page.

Helena Nazaré **Gordon Davies**

Sponsors

The organisers of ICDS-19 wish to thank the following for their generous contribution to the success of this conference:

European Union DG XII Science, Research and Development
Fundação Calouste Gulbenkian
Junta Nacional de Investigação Cientifica e Tecnológica
United States Army Research Office
Trans Tech Publications Ltd
United States Office of Naval Research grant number N00014-97-1-0546

For hosting delegates during the conference excursions we thank:

Câmara Municipal de Aveiro
Câmara Municipal de Águeda
Direcção Regional de Agricultura da Beira Litoral
Reitoria da Universidade de Coimbra
Comissão de Turismo Rota da Luz
Caves São João
Caves Aliança

We also acknowledge the support in the form of staff time and facilities given to the conference by the University of Aveiro and by King's College London.

Organisations presenting displays and advertising were:

Biótica
CRIOLAB
Decada Espectral
Elnor
MT Brandão
Sula Technologies
World Scientific

The James W. Corbett Prize

The Corbett Prize, awarded in memory of one of the founders of the fields of defects in semiconductors, was first awarded in 1995 at the Sendai meeting. The prize is awarded to the best paper presented at the meeting by a young investigator. At ICDS-19 the votes of the International Advisory Committee were equal votes for three delegates.

The joint winners of the Corbett Prize for 1997 were:

Joanne E. Gower, King's College London, for her presentation
The I centre: a hydrogen related defect in silicon

Thomas Hallberg, Linköping University, for his presentation
The oxygen dimer in silicon: some experimental observations

and **Tomi Mattila**, Helsinki University of Technology, for his presentation
Ab-initio studies of atomic-scale defects in GaN and AlN

The Corbett Prizes awarded at ICDS-19 were financed by Trans Tech Publications Ltd.

ICDS-20, Berkeley, California

The next meeting of ICDS will be held during the second half of July 1999 in Berkeley, California. The organisers are:

Chairman: E.E. Haller,
UC Berkeley (UCB) and Lawrence Berkeley National Laboratory (LBNL).
Fax. +1 510 486 5530, e-mail: eehaller@lbl.gov

Program chairman: N. Johnson,
Xerox Palo Alto Research Center (PARC)

Proceedings: W. Walukiewicz (LBNL) and C.G. van de Walle (PARC)

Finances: E.R. Weber (UCB & LBNL)

Treasurer: P.Y. Yu (UCB & LBNL)

Secretary: J.W. Ager III (LBNL)

Members: M. Giles (Intel Corp.) and K.M. Yu (LBNL).

In addition to the committees directly involved with organising each meeting, the ICDS series has two international committees. The International Advisory Committee decides the venues of the Defect Conferences from proposals submitted to it, and has the responsibility for the defining the primary areas of interest for the Conferences. Members of the International Advisory Committee also pass on to the Steering Committee information about other conferences which may overlap the topics covered by the ICDS series. Elected members are chosen for a period of four years by a ballot, held during each ICDS conference, of the International Advisory Committee.

The members of the **International Advisory Committee** are:

a. Elected for 1995-1999:

Dr. James Chadi
NEC Research Institute
Fax: +1 (609) 951 2496
e-mail: chadi@research.nj.nec.com

Prof. Lionel C. Kimerling
Massachusetts Institute of Technology
Fax. (617) 253 6782
e-mail: lck@kim.mit.edu

Prof. Hiroshi Kukimoto
Tokyo Institute Of Technology
Fax: +81-3-3831-3896
e-mail: hiroshi.kukimoto@toppan.co.jp

Prof. Bo Monemar
Linköping University
Fax: +46 13-14 23 37
e-mail: bom@ifm.liu.se

Prof. J.M. Spaeth
Universitat Paderborn
Fax: +49 (5251) 60- 3247 (or: 3216)
e-mail: sp_tacke@physik.uni-paderborn.de

b. Elected for 1997-2001

Prof. Jerzy Langer
Polish Academy of Sciences
fax: +48 22 430926
e-mail: langer@ifpan.edu.pl

Prof. Ron Newman
Imperial College London
fax: +44 71 581 3817
e-mail: r.newman@ic.ac.uk

Prof. Michael Stavola
Lehigh University
Fax. +1 610 758-5730
e-mail: mjsa@lehigh.edu

Prof. George D. Watkins
Lehigh University
fax: +1 215 758 4561
e-mail: gdw0@ns.cc.lehigh.edu

Dr. Jörg Weber
Max-Planck-Institut für Festkörperforschung
Fax. +49 711 689 1010
e-mail: weber@vaxff1.mpi-stuttgart.mpg.de

Five additional members will be appointed by the chairman of the ICDS-20, Prof. E.E. Haller, for the two-year period 1997-1999.

The second committee is the Steering Committee, whose rôle is to ensure continuity of the ICDS conferences. The members are previous conference chairs and the chairman designate of the next ICDS. The members of the **International Steering Committee** are therefore:

Chairman, 1997-99:
Prof. Wolfgang Jantsch
Johannes Kepler Universität
Fax. +43 732 2468 9696 or 650
e-mail: wolfgang.jantsch@jk.uni-linz.ac.at

Secretary, 1997-99:
Prof. Koji Sumino
Nippon Steel
Fax: +81 439 80 2769
e-mail: sumino@kikaku.re.nsc.co.jp

Prof. Gordon Davies (chair ICDS-19)
King's College London
Fax. +44 171 8732423
e-mail: g.davies@kcl.ac.uk

Prof. Eugene.E. Haller (chair ICDS-20)
Lawrence Berkeley Lab, MS2-200
Fax. +1 510 486 5530
e-mail: eehaller@lbl.gov

Prof[a]. M.H. Nazaré (chair ICDS-19)
Universidade de Aveiro
Fax +351 34 24965
e-mail: mhnazare@ideiafix.fis.ua.pt

ICDS-21, July 2001

The Operational Guidelines under which the ICDS series operates currently require proposals for future conferences to be sent to the Secretary of the Steering Committee by the 1 March preceding a conference. The International Advisory Committee meets during the ICDS and chooses one of the proposals for the conference four years ahead. Following these Guidelines, at the Aveiro meeting the IAC considered presentations for ICDS-21.

The 21st International Conference on Defects in Semiconductors is planned to be held in Giessen, Germany in July 2001.

The co-chairs will be Prof. Dr. B.K. Meyer, University of Giessen, and Prof. Dr. J.-M. Spaeth, University of Paderborn.

Contents - Survey

PART 1

Section 1. Plenary sessions 1
Section 2. Germanium 35
Section 3. Alloys of Si, Ge and C 83
Section 4. Silicon: hydrogen 171
Section 5. Silicon: oxygen 341
Section 6. Silicon: metals 411
Section 7. Silicon: radiation damage 503

PART 2

Section 8. Silicon carbide 677
Section 9. Diamond 745
Section 10. Indium phosphide 805
Section 11. Gallium arsenide: Impurities 849
Section 12. Antisite defects and EL2 945
Section 13. Gallium arsenide: radiation damage 1021
Section 14. Gallium phosphide 1063
Section 15. Gallium nitride 1081
Section 16. Other III-V compounds 1211

PART 3

Section 17. Aluminium gallium arsenide 1293
Section 18. II-VI compound semiconductors 1321
Section 19. Cadmium fluoride 1431
Section 20. Chalcopyrites and other host lattices 1455
Section 21. Erbium 1485
Section 22. Low dimensional structures 1607
Section 23. Surfaces and interfaces 1731
Section 24. Diffusion 1761

Author Index 1845
Keyword Index 1859

Table of Contents

Organising Committees of ICDS-19 v
Acknowledgements vii
Sponsors viii
The James W. Corbett Prize ix
ICDS-20, Berkeley, California x
ICDS-21, July 2001 xii

PART 1

Section 1. Plenary sessions

Recent developments and theory relating to impurity induced LVMs in GaP and GaAs. (Invited)
R.C. Newman, E.G. Grosche, M.J. Ashwin, B.R. Davidson, D.A. Robbie, R.S. Leigh and M.J.L. Sangster 1

Optically-induced defects in Si-H nanoparticles. (Invited)
M.J. Caldas, B.J. Baierle, E. Molinari and S. Ossicini 11

Defects and doping in III-V nitrides. (Invited)
C.G. Van de Walle and J. Neugebauer 19

A programme for the future? (Invited)
A.M. Stoneham 27

Section 2. Germanium

The hydrogen-saturated self-interstitial in silicon and germanium
M. Budde, B. Bech Nielsen, P. Leary, J. Goss, R. Jones, P.R. Briddon, S. Öberg and S.J. Breuer 35

Matrix-induced isotope shift of a vibrational mode of interstitial oxygen in germanium
B. Pajot, E. Artacho, L.I. Khirunenko, K. Itoh and E.E. Haller 41

Isotopic shifts of the rotational states of interstitial oxygen in germanium
N. Aichele, U. Gommel, K. Laßmann, F. Maier, F. Zeller, E.E. Haller, K.M. Itoh, L.I. Khirunenko, V.I. Shakhovtsov, B. Pajot, E. Fogarassy and H. Müssig 47

DLTS combined with perturbed angular correlation (PAC) or radioactive ^{111}In atoms in Ge
Ch. Zistl, R. Sielemann, H. Hässlein, S. Gall, D. Bräunig, J. Bollmann 53

Microscopic study of the vacancy and self-interstitial in germanium by PAC
H. Hässlein, R. Sielemann and Ch. Zistl 59

Localization of nondegenerate electrons at random potential of charged impurities
M.S. Kagan, E.G. Landsberg and N.G. Zhdanova 65

Resonance acceptor states and THz generation in uniaxially strained p-Ge
I.V. Altukhov, E.G. Chirkova, M.S. Kagan, K.A. Korolev, V.P. Sinis, K. Schmalz, M.A. Odnoblyudov and I.N. Yassievich 71

Ionized impurity scattering in isotopically engineered, compensated Ge:Ga, As
K.M. Itoh, T. Kinoshita, W. Walukiewicz, J.W. Beeman, E.E. Haller, J. Muto, J.W. Farmer and V.I. Ozhogin 77

Section 3. Alloys of Si, Ge and C

Defects in SiGe. (Invited)
A. Nylansted Larsen 83

Acceptor states in boron doped SiGe quantum wells
K. Schmalz, M.S. Kagan, I.V. Altukhov, K.A. Korolev, D.V. Orlov, V.P. Sinis, S.G. Tomas, K.L. Wang and I.N. Yassievich 91

Substitutional carbon in Ge and $Si_{1-x}Ge_x$
L. Hoffmann, J.C. Bach, J. Lundsgaard Hansen, A. Nylandsted Larsen, B. Bech Nielsen, P. Leary, R. Jones and S. Öberg 97

Ge content dependence of the infrared spectrum of interstitial oxygen in crystalline Si-Ge
D. Wauters and P. Clauws 103

Optical investigation of Ge-rich $Ge_{1-x}Si_x$ ($0 \leq x \leq 0.1$) alloys
M. Franz, K. Pressel, K.F. Dombrowski, H. Rücker, A. Barz, P. Dold and K.W. Benz 109

Electrical characterization of electron beam induced defects in epitaxially grown $Si_{1-x}Ge_x$
M. Mamor, F.D. Auret, S.A. Goodman, G. Myburg, P.N.K. Deenapanray and W.E. Meyer 115

Lattice defects in $Si_{1-x}Ge_x$ epitaxial diodes induced by 20-MeV alpha rays
H. Ohyama, J. Vanhellemont, E. Simoen, C. Claeys, Y. Takami, K. Hayama, H. Sunaga, J. Poortmans and M. Caymax 121

Positron annihilation study of electron-irradiated silicon-germanium bulk alloys
A. Kawasuso, S. Okada, I. Yonenaga, T. Honda and M. Suezawa 127

Electronic properties of defects introduced in n- and p-type $Si_{1-x}Ge_x$ during ion etching
S.A. Goodman, F.D. Auret, M. Mamor, P.N.K. Deenapanray and W.E. Meyer 133

The role of non-radiative defects in thermal quenching of luminescence in SiGe/Si structures grown by molecular beam epitaxy
I.A. Buyanova, W.M. Chen, G. Pozina, B. Monemar, W.X. Ni and G.V. Hansson 139

Gold-related levels in relaxed $Si_{1-x}Ge_x$ alloy layers: a study of the pinning effect
A. Mesli, P. Kringhøj and A. Nylandsted Larsen 145

Dislocation-related electronic states in strain-relaxed $Si_{1-x}Ge_x$/Si epitaxial layers grown at low temperature. (Invited)
P.M. Mooney and Kai Shum 151

Dislocation activities in bulk GeSi crystals
I. Yonenaga and K. Sumino 159

Schottky diodes on $Si_{1-x-y}Ge_xC_y$ alloys: measurement of band off-set by DLTS
M. Serpentini, G. Brémond and F. Meyer 165

Section 4. Silicon: hydrogen

Molecular-dynamics simulations of microscopic defects in silicon. (Invited)
S.K. Estreicher and P.A. Fedders 171

Comparison of muonium (hydrogen) dynamics in germanium and silicon
R.L. Lichti, K.H. Chow, S.F.J. Cox, T.L. Estle, B. Hitti and C. Schwab 179

Hydrogenation and passivation of B in Si by boiling in water pressurized up to 10 atm
Y. Ohmura, K. Abe, M. Ohtaka, A. Kimoto and M. Yamaura 185

Low temperature hydrogen diffusion in silicon: influence of substrate quality and the surface damage
M.I. Symko, B.L. Sopori, R. Reedy and K.M. Jones 191

Mechanism of ultrasonic enhanced hydrogenation in poly-Si thin films using ultrasound treatment
S. Ostapenko 197

Hydrogen molecules in crystalline silicon. (Invited)
M. Kitajima, K. Ishioka, K.G. Nakamura, N. Fukata, K. Murakami, J. Kikuchi and S. Fujimura 203

Thermal stability of hydrogen molecule in crystalline silicon
N. Fukata, K. Murakami, K. Ishioka, K.G. Nakamura, M. Kitajima, S. Fujimura, J. Kikuchi and H. Haneda 211

Emission and capture kinetics for a hydrogen-related negative-U center in silicon: evidence for metastable neutral charge state
V.P. Markevich, L.I. Murin, T. Sekiguchi and M. Suezawa 217

IR studies of Si-H bond-bending vibrational modes in Si
S.Zh. Tokmoldin and B.N. Mukashev 223

Optical absorption due to hydrogen bound to interstitial Si in Si crystal grown in hydrogen atmosphere
M. Suezawa 229

Trapping site of hydrogen molecule in crystalline silicon
K. Ishioka, K.G. Nakamura, M. Kitajima, N. Fukata, K. Murakami, S. Fujimura and J. Kikuchi 235

Formation and structure of hydrogen molecules in crystalline Si
A.W.R. Leitch, V. Alex and J. Weber 241

Structure and charge-state-dependent instability of a hydrogen-carbon complex in silicon
Y. Kamiura, N. Ishiga, S. Ohyama and Y. Yamashita 247

The trapping of hydrogen at carbon defects in silicon
A. Mainwood 253

The M-line (760.8 meV) luminescence system associated with the carbon-hydrogen acceptor centre in silicon
A.N. Safonov and E.C. Lightowlers 259

Interstitial carbon-hydrogen defects in silicon
P. Leary, S. Öberg, P.R. Briddon and R. Jones 265

Low-temperature migration of hydrogen and interaction with oxygen
K. Bonde Nielsen, B. Bech Nielsen and J. Hansen 271

Anomalous shift of the 1075 cm^{-1} oxygen-hydrogen defect in silicon
B. Hourahine, R. Jones, S. Öberg and P.R. Briddon 277

Vibrational absorption from oxygen-hydrogen (O_i-H_2) complexes in hydrogenated CZ silicon
R.E. Pritchard, M.J. Ashwin, R.C. Newman, J.H. Tucker, E.C. Lightowlers, M.J. Binns, R. Falster and S.A. McQuaid 283

The I centre: a hydrogen related defect in silicon
J.E. Gower, G. Davies, E.C. Lightowlers and A.N. Safanov 289

Theory of gold-hydrogen complexes in silicon
A. Resende, J. Goss, P.R. Briddon, S. Öberg and R. Jones 295

Electrically active silver-hydrogen complexes in silicon
N. Yarykin, J.-U. Sachse, J. Weber and H. Lemke 301

Palladium-hydrogen related complexes in silicon
J.-U. Sachse, J. Weber and H. Lemke 307

Effects of hydrogen plasma on dislocation motion in silicon
Y. Yamashita, F. Jyobe, Y. Kamiura and K. Maeda 313

Hydrogenation of copper related deep states in n-type Si containing extended defects
J. Kaniewski, M. Kaniewska, L. Ornoch, T. Sekiguchi and K. Sumino 319

Hydrogenation of deep defect states in n-type Si containing extended defects and transition metal (Ni or Fe)
M. Kaniewska, J. Kaniewski, L. Ornoch, T. Sekiguchi and K. Sumino 325

Metastable defects and recombination in hydrogenated amorphous silicon
E. Morgado and R.T. Henriques 331

Tracing diffusion by Laplace deep-level spectroscopy
K. Bonde Nielsen and L. Dobaczewski 337

Section 5. Silicon: oxygen

Defects in as-grown silicon and their evolution during heat treatments
J. Vanhellemont, E. Dornberger, J. Esfandyari, G. Kissinger, M.-A. Trauwaert, H. Bender, D. Gräf, U. Lambert and W. von Ammon 341

An investigation of the possibility that oxygen diffusion in Czochralski silicon is catalyzed during clustering. (Invited)
S.A. McQuaid, B.K. Johnson, R. Falster and K.F. Kelton 347

Temperature-dependent widths of infrared and far-infrared absorption lines of oxygen in silicon
H. Yamada-Kaneta 355

The oxygen dimer in silicon: some experimental observations
T. Hallberg, J.L. Lindström, L.I. Murin and V.P. Markevich 361

Formation of oxygen dimers in silicon during electron-irradiation above 250 °C
J.L. Lindström, T. Hallberg, D. Åberg, B.G. Svensson, L.I. Murin and V.P. Markevich 367

High-field EPR spectroscopy of thermal donors in silicon
R. Dirksen, F. Berg Rasmussen, T. Gregorkiewicz and C.A.J. Ammerlaan 373

Shallow thermal donors in annealed CZ silicon and links to the NL10 EPR spectrum: the relevance of H, Al and N impurities
R.C. Newman, M.J. Ashwin, R.E Pritchard, J.H. Tucker, E.C. Lightowlers, T. Gregorkiewicz, I.S. Zevenbergen, C.A.J. Ammerlaan, R. Falster and M.J. Binns 379

Formation of ultra shallow donors in silicon by long-term-annealing at 470 °C
D. Åberg, T. Hallberg, B.G. Svensson, J.L. Lindström and M. Kleverman 385

Local vibrational modes of a weakly bound O-H complexes in Si. (Invited)
B. Bech Nielsen, K. Tanderup, M. Budde, K. Bonde Nielsen, J.L. Lindström, R. Jones, S. Öberg, B. Hourahine and P. Briddon 391

Phonon scattering in heat-treated CZ-silicon
F. Zeller, C. Wurster, K. Laßmann and W. Eisenmenger 399

Determination of stoichiometry and oxygen content in platelike and octahedral oxygen precipitates in silicon with FT-IT spectroscopy
O. De Gryse, P. Clauws, J. Vanhellemont and C. Claeys 405

Section 6. Silicon: metals

Influence of the Li concentration in the photoluminescence spectra of neutron-irradiated silicon: passivation of radiation induced centers
F. Rodriguez, G. Davies and E.C. Lightowlers 411

Electric-dipole spin resonance of Be-doped silicon
H. Schroth, K. Laßmann, Chr. Borgmann and H. Bracht 417

Cadmium-related defects in silicon: electron-paramagnetic resonance identification
W. Gehlhoff, A. Näser, M. Lang and G. Pensl 423

Iron in p-type silicon: A comprehensive model. (Invited)
S. Zhao, A.L. Smith, S.H. Ahn, G.J. Norga, M.T. Platero, H. Nakashima, L.V.C. Assali, J. Michel and L.C. Kimerling 429

Mossbauer spectroscopy of Fe in silicon with the novel laser-ionized $^{57}Mn^{+}$ ion beam at ISOLDE
G. Weyer, S. Degroote, M. Fanciulli, V.N. Fedoseyev, G. Langouche, V.I. Mishin, A.-M. Van Bavel, A. Vantomme and the ISOLDE Collaboration 437

Recombination-enhanced Fe atom jump of Fe-acceptor pairs in Si
T. Takahashi and M. Suezawa 443

Precipitation of iron in FZ and CZ silicon
H. Hieslmair, A.A. Istratov, S.A. McHugo, C. Flink and E.R. Weber 449

The orthorhombic FeIn complex in silicon
P. Tidlund and M. Kleverman 455

Copper in silicon: quantitative analysis of internal and proximity gettering
S.A. McHugo, T. Heiser, H. Hieslmair, C. Flink, E.R. Weber, S.M. Myers and G.A. Petersen 461

A study of the copper-pair related centers in silicon
A.A. Istratov, T. Heiser, H. Hieslmair, C. Flink, J. Krüger, and E.R. Weber 467

The photoluminescence of Pt-implanted silicon
E. Alves, J. Bollmann, M. Deicher, M.C. Carmo, M.O. Henry, M.H.A. Knopf, J.P. Leitão, R. Magerle and C.J. McDonagh 473

The identification of the Si:Au and Si:Pt $1S_{3/2}$ (Γ_8) + Γ phonon-assisted Fano resonance
M. Kleverman, J. Olajos and P. Tidlund 479

Silver-related donor defect in silicon
M.-X. Zhu, G. Davies, M.Z. Iqbal and E.C. Lightowlers 485

Isolated substitutional silver and silver-induced defects in silicon: an electron paramagnetic resonance investigation
P.N. Hai, T. Gregorkiewicz, C.A.J. Ammerlaan and D.T. Don 491

Pseudo or deep donor excitation spectra in silicon
M. Kleverman 497

Section 7. Silicon: radiation damage

Vacancies and interstitial atoms in electron-irradiated silicon
H. Zillgen and P. Ehrhart 503

Vacancy aggregates in silicon
J.L. Hastings, S.K. Estreicher and P.A. Fedders 509

Identification of VH in silicon by EPR
P. Johannesen, J.R. Byberg, B. Bech Nielsen, P. Stallinga and K. Bonde Nielsen 515

Novel luminescent centres in cadmium doped silicon
C.A. Frehill, M.O. Henry, E. McGlynn, S.E. Daly, M. Deicher, R. Magerle, K.G. McGuigan, A.N. Safanov and E.C. Lightowlers 521

Defect clusters in silicon: impact on the performance of large-area devices
B.L. Sopori. (Invited) 527

Modeling of self-interstitial clusters and their formation mechanism in Si
S. Takeda, N. Arai, and J. Yamasaki 535

Self-interstitials in irradiated silicon
B.N. Mukashev, K.A. Abdullin and Yu.V. Gorelkinskii 541

High resolution EELS study of extended defects in silicon
H. Kohno, N. Arai, T. Mabuchi, M. Hirata, S. Takeda, M. Kohyama, M. Terauchi and M. Tanaka 547

Electron irradiation effects in silicon thin foils under ultra-high vacuum environment
S. Takeda, K. Koto, M. Hirata, T. Kuno, S. Iijima and T. Ichihashi 553

Application of spin dependent recombination for investigation of point defects in irradiated silicon
M.M. Afanasjev, R. Laiho, L.S. Vlasenko and M.P. Vlasenko 559

Electrical and optical characterisation of defects induced in epitaxially grown n-Si during 1 keV noble gas ion bombardment
P.N.K. Deenapanray, F.D. Auret, G. Myburg, W.E. Meyer and S.A. Goodman 565

Fano resonances in a vibronic sideband in silicon
J.E. Gower, G. Davies and E.C. Lightowlers 571

Frenkel pairs and impurity-defect interactions in p-type silicon irradiated with fast electrons and gamma-rays at low temperatures
V.V. Emtsev, U. Dedek, P. Ehrhart, P.D. Kervalishvili, M.A. Margaryan, D.S. Poloskin and H. Zillgen 575

Impurity-vacancy complexes formed by electron irradiation of Czochralski silicon
V. Avalos and S. Dannefaer 581

Luminescence centers in high-energy ion-implanted silicon
K. Terashima, T. Ikarashi, M. Watanabe and T. Kitano 587

Performance degradation of microcrystalline and amorphous silicon-based p-i-n detectors upon He^4 irradiation
R. Schwarz, M. Vieira, A. Maçarico, S. Koynov, S. Cardoso and J.C. Soares 593

Persistent excited conductivity induced by proton irradiation in a-Si:H
H. Amekura, N. Kishimoto and K. Kono 599

Photoluminescence centres associated with noble-gas impurities in silicon
S.K. Estreicher and J. Weber 605

Implantation of reactive and unreactive ions in silicon
J.R. Brucato, G.A. Baratta, G. Compagnini and G. Strazzulla 611

Photoluminescence vibrational spectroscopy of defects containing the light impurities carbon and oxygen in silicon
E.C. Lightowlers and A.N. Safonov 617

Raman scattering measurements in neutron-irradiated silicon
M. Coeck, C. Laermans, R. Provoost and R.E. Silverans 623

Recombination centers in electron irradiated Si and GaAs
J.C. Bourgoin, M. Zazoui and M.A. Zaidi 629

Study of a Li- and C-related center formed at high annealing temperatures in neutron-irradiated FZ silicon doped with Li
F. Rodriguez, G. Davies and E.C. Lightowlers 635

The influence of accumulated defects on the lateral spread of implanted ions
S.T. Nakagawa 641

Structural change and relaxation processes of tetrahedral point defects
El-Maghraby Mohamed and Y. Shinozuka 647

The Jahn-Teller effect and the structure of monovacancies in Si, SiC and C
A. Zywietz, J. Furthmüller and F. Bechstedt 653

Transient lattice vibration induced by successive carrier captures at a deep-level defect and the effect on defect reactions
Y. Shinozuka and T. Karatsu 659

Characterisation of recombination centres in solar cells by DLTS
T. Markvart 665

Defect-engineering RAD-HARD detectors for the CERN LHC
B. MacEvoy, K. Gill and G. Hall 671

PART 2

Section 8. Silicon carbide

Theory of 3d transition metal defects in 3C-SiC. (Invited)
H. Overhof 677

A deep photoluminescence band in 4H SiC related to the silicon vacancy
E. Sörman, N.T. Son, W.M. Chen, C. Hallin, J.L. Lindström and E. Janzén 685

Thermal activation energies for the three inequivalent lattice sites for the B_{Si} acceptor in 6H-SiC
A.O. Evwaraye, S.R. Smith, W.C. Mitchel, H.McD. Hobgood, G. Augustine and V. Balakrishna 691

Optical absorption and Zeeman study of the 6H SiC:Cr
A. Dörnen, B. Kaufmann, J. Baur, M. Kunzer, U. Kaufmann and P.G. Baranov 697

High-frequency EPR studies of shallow and deep boron acceptors in 6H-SiC. (Invited)
J. Schmidt, T. Matsumoto, O.G. Poluektov, A. Arnold, T. Ikoma, P.G. Baranov and E.N. Mokhov 703

Gas and heat treatment effects on the defect structure of a-SiC:H films
T. Friessnegg, M. Boudreau, P. Mascher, P.J. Simpson and W. Puff 709

Capacitance spectroscopy of deep centres in SiC
A.A. Lebedev and N.A. Sobolev 715

Native and electron irradiation induced defects in 6H-SiC
T. Friessnegg and S. Dannefaer 721

Raman scattering analysis of defects in 6H-SiC induced by ion implantation
A. Pérez-Rodríguez, O. González-Varona, L. Calvo-Barrio, J.R. Morante, H. Wirth, D. Panknin and W. Skorupa 727

Vacancy-type defects in proton-irradiated SiC
W. Puff, P. Mascher, A.G. Balogh and H. Baumann 733

Theoretical studies on defects in SiC
P. Deák, A. Gali, J. Miró, R. Guiterrez, A. Sieck and Th. Frauenheim 739

Section 9. Diamond

Formation and relaxation of hydrogen-related defects in the subsurface region of diamond films
K. Hayashi, T. Sekiguchi and H. Okushi 745

Hydrogen and hydrogen-like defects in diamond
S.H. Connell, J.P.F Sellschop, R.D. Maclear, B.P. Doyle, I.Z. Machi, R.W.N. Nilen, J.E. Butler and K. Bharuth-Ram 751

Fine structure of the boron bound exciton in diamond
H. Sternschulte, S. Wahl, K. Thonke, R. Sauer, T. Ruf, M. Cardona and T.R. Anthony 757

Investigation of ion-implanted boron in diamond
K. Bharuth-Ram, B. Ittermann, H. Metzner, M. Füllgrabe, M. Heemeier, F. Kroll, F. Mai, K. Marbach, P. Meier, D. Peters, H. Thiess, H. Ackermann, J.P.F. Sellschop, H.-J. Stockmann, K.P. Lieb and M. Uhrmacher 763

Isotopic shifts of the N3 optical transition in diamond
G. Davies, I. Kiflawi, G. Sittas and H. Kanda 769

Breakdown of the vacancy model for impurity-vacancy defects in diamond
J.P. Goss, R. Jones, P.R. Briddon and S. Öberg 775

A first principles study of interstitial Si in diamond
J.P. Goss, R. Jones, S.J. Breuer, P.R. Briddon and S. Öberg 781

Radiation damage of diamond and silicon by high energy neutrons, protons and α particles
A. Mainwood, J. Cunningham and D. Usher 787

Study of defects in diamond films by electrical measurements
L. Pereira, E. Pereira and H. Gomes 793

Valence controls and codoping in low resistivity n-type diamond by ab-initio molecular-dynamics simulation
T. Nishimatsu, H. Katayama-Yoshida and N. Orita 799

Section 10. Indium phosphide

Intrinsic modulation doping in InP-based heterostructures. (Invited)
W.M. Chen, I.A. Buyanova, W.G. Bi and C.W. Tu 805

Pressure dependent two-dimensional electron transport in defect doped InGaAs/InP heterostructures
D. Wasik, L. Dmowski, J. Mikucki, J. Lusakowski, L. Hsu, W. Walukiewicz, W.G. Bi and C.W. Tu 813

Study of iron-related defects in SI-InP by positron annihilation spectroscopy
B. Marí, F.J. Navarro, M.A. Hernández and J.L. Ferrero 819

Homogeneity of Fe-doped InP wafers using optical microprobes
L.F. Sanz, M.A. Gonzalez, M. Avella, A. Alvarez, J. Jimenez and R. Fornari 825

Osmium related deep levels in p-InP and their interaction with alpha radiation
S. Parveen, A. Khan, U.S. Qurashi, N. Zafar, M.Z. Iqbal, L. Köhne, A. Dadgar and D. Bimberg 831

A sharp defect-annealing stage below room temperature in irradiated n-type indium phosphide
A. Canimoglu and D.W. Palmer 837

Alpha radiation-induced deep levels in p-InP
A. Khan, U.S. Qurashi, N. Zafar, M.Z. Iqbal, A. Dadgar and D. Bimberg 843

Section 11. Gallium arsenide: Impurities

Site stability, diffusion and charge dynamics for muonium in GaAs
T.L. Estle, K.H. Chow, S.F.J. Cox, E.A. Davis, B. Hitti, R.F. Kiefl, R.L. Lichti and C. Schwab 849

Structure and reorientation of the Si_{As}-H and Zn_{Ga}-H complexes in gallium arsenide
A.A. Bonapasta, P. Giannozzi and M. Capizzi 855

Ab-initio study of the C_{As} local oscillator in gallium arsenide
K. Petzke, C. Göbel, C. Schrepel and U. Scherz 861

Spectroscopy of nitrogen-related centers in gallium arsenide
H.Ch. Alt, B. Wiedemann and K. Bethge 867

Atomic configuration of oxygen negative-U center in GaAs
A. Taguchi and H. Kageshima 873

Ga vacancies as compensating centers in homogeneously or δ-doped GaAs(Si) layers
T. Laine, K. Saarinen, P. Hautojärvi, C. Corbel, L.N. Pfeiffer, P.H. Citrin, M.J. Ashwin and R.C. Newman 879

Positron annihilation and scanning tunneling microscopy used to characterise defects in highly Si-doped GaAs. (Invited)
J. Gebauer, R. Krause-Rehberg, C. Domke, Ph. Ebert and K. Urban 885

Chemical trends in electronic properties of arsenic vacancy-3d transition metal pairs in GaAs
E.J. França and L.V.C. Assali 893

Perturbed angular correlation measurements and lattice site location of Br in GaAs
M. Wehner, M. Risse, R. Vianden, M. Dalmer, H. Hofsäss, M.C. Ridgway, M. Petravic and the ISOLDE Collaboration 899

Equilibrium vacancies in Te-doped GaAs studied by positron annihilation
J. Gebauer, R. Krause-Rehberg, M. Lausmann and G. Lippold 905

Spectroscopic investigation of neutral niobium in GaAs
D. Ammerlahn, B. Clerjaud, D. Côte, L. Köhne, M. Krause and D. Bimberg 911

Yb luminescence centres in MBE-grown and ion-implanted GaAs
A.A. Gippius, V.M. Konnov, N.N. Loyko, V.V. Ushakov, T.V. Larikova, I.P. Kazakov, V.A. Dravin and N.A. Sobolev 917

Arsenic interstitial pairs in GaAs
P. Papoulias, C.G. Morgan, J.T. Schick, J.I. Landman and N. Rahhal-Orabi 923

Electrical properties of low temperature grown GaAs
M. Stellmacher, J. Nagle, K. Khirouni and J.C. Bourgoin 929

Traps found in GaAs MESFETS: properties, location and detection
B.K. Jones and M.A. Iqbal 933

Influence of dopant species on electron mobility in heavily doped semiconductors
G. Kaiblinger-Grujin, H. Kosina, Ch. Köpf and S. Selberherr 939

Section 12. Antisite defects and EL2

Creation of Ga_{As} antisites in GaAs by transmutation of radioactive $^{71}As_{As}$ to stable $^{71}Ga_{As}$
R. Magerle, A. Burchard, D. Forkel-Wirth, M. Deicher and the ISOLDE Collaboration 945

Defect control in As-rich GaAs
P. Specht, S. Jeong, H. Sohn, M. Luysberg, A. Prasad, J. Gebauer, R. Krausse-Rehberg and E.R. Weber 951

As antisite-related defects detected by spin dependent recombination in delta-doped (Si) GaAs grown by MBE at low temperature
K. Krambrock, M.V.B. Pinheiro and S.M. Madeiros 957

Electrically detected magnetic resonance at different microwave frequencies
M.S. Brandt, M.W. Bayerl, N.M. Reinacher, T. Wimbauer and M. Stutzmann 963

Metastable antisite pair in GaAs
S. Pöykkö, M.J. Puska and R.M. Nieminen 969

Theoretical study of antistructure defects in GaAs
A. Janotti, A. Fazzio, P. Piquini and R. Mota 975

Study of plastically deformed semiconductors by means of positron annihilation
H.S. Leipner, C.G. Hübner, J. Krüger and R. Krause-Rehberg 981

The micro structure of the EL2 defect in GaAs - a different look to former spin-resonance data
F. Wirbeleit and J.R. Niklas 987

Detection and identification of the EL2 metastable state in GaAs
J.C. Bourgoin 993

Defects in thick epitaxial GaAs layers
H. Samic and J.C. Bourgoin 997

Effects of copper diffusion on the native defect EL2 in GaAs
D. Seghier and H.P. Gislason 1003

EL2 induced enhancement of donor-acceptor pair luminescence in GaAs
V. Alex and J. Weber 1009

Observation of persistent electron capture in n-type gallium arsenide studied by optically detected magnetic resonance
K. Krambrock, M.V.B. Pinheiro, K.-H. Wietzke and J.-M. Spaeth 1015

Section 13. Gallium arsenide: radiation damage

ODMR investigation of proton irradiated GaAs
S.A. Goodman, F.K. Koschnick, Ch. Weber, J.-M. Spaeth and F.D. Auret 1021

Uniaxial-stress symmetry studies on the E1, E2 and E3 irradiation-induced defects in gallium arsenide
S.J. Hartnett and D.W. Palmer 1027

Magnetic resonance and positron annihilation of intrinsic acceptors in ITC-treated GaAs
K. Krambrock, C. Corbel and J.-M. Spaeth 1033

Defects in neutron-irradiated LEC semi-insulating-GaAs
B.K. Jones, J.M. Santana and T. Sloan 1039

Electrical characterization of defects introduced during plasma-based processing of GaAs
F.D. Auret, S.A. Goodman, G. Myburg, W.E. Meyer, P.N.K. Deenapanray, M. Murtagh, S.-R. Ye, H.J. Masterson, J.T. Beechinor and G.M. Crean 1045

Metastable charge recovery in plasma-irradiated n-GaAs
K. Wada and H. Nakanishi 1051

Metastable amorphous structure in ion implanted GaAs
I.D. Desnica-Franković, U.V. Desnica, M. Ivanda, D. Gracin and T.E. Haynes 1057

Section 14. Gallium phosphide

Theory of nitrogen-hydrogen complexes in GaP
V.J.B. Torres, S. Öberg and R. Jones 1063

Photoluminescence, optical absorption, and EPR studies of the Co^{2+}-Sp pair defect in GaP
R. Göser, J. Kreissl, K. Thonke and W. Ulrici 1069

Resonance-mode phonon replica in the optical spectra of transition-metal impurities in GaP
C. Schrepel, U. Scherz, W. Ulrici and K. Thonke 1075

Section 15. Gallium nitride

GaN grown using trimethylgallium and triethylgallium
A. Saxler, P. Kung, X. Zhang, D. Walker, J. Solomon, W.C. Mitchel and M. Razeghi 1081

ODMR studies of As-grown and electron-irradiated GaN and AlN
G.D. Watkins, M. Linde, P.W. Mason, H. Przybylinska, C. Bozdog, S.J. Uftring, V. Härle, F. Scholz, W.J. Choyke and G.A. Slack 1087

Electrical and optical characterization of defects in GaN generated by ion implantation
D. Haase, M. Burkard, M. Schmid, A. Dörnen, H. Schweizer, H. Bolay and F. Scholz 1093

Implantation doping and hydrogen passivation of GaN
A. Burchard, M. Deicher, D. Forkel-Wirth, E.E. Haller, R. Magerle, A. Prospero, A. Stötzler and the ISOLDE Collaboration 1099

Electrically and optically detected magnetic resonance in GaN based LEDs. (Invited)
W.E. Carlos 1105

Donor acceptor pair transitions in GaN
K. Kornitzer, M. Mayer, M. Mundbrod, K. Thonke, A. Pelzmann, M. Kamp and R. Sauer 1113

Ab-initio studies of atomic-scale defects in GaN and AlN
T. Mattila and R.M. Nieminen 1119

Photoluminescence dynamics in the near bandgap region of homoepitaxial GaN layers
K.P. Korona, J.P. Bergman, B. Monemar, J.M. Baranowski, K. Pakula, I. Grzegory and S. Porowski 1125

Zeeman study of the 0.94 eV emission in AlN and GaN
P. Thurian, I. Loa, P. Maxim, K. Pressel, A. Hoffmann and C. Thomsen 1131

A first-principles study of Mg-related defects in GaN
K.J. Chang and S.-G. Lee 1137

Impact of radiation-induced defects on the yellow luminescence in MOCVD GaN
V.V. Emtsev, V.Yu. Davydov, I.N. Goncharuk, E.V. Kalinina, V.V. Kozlovskii, D.S. Poloskin, A.V. Sakharov, N.M. Shmidt, A.N. Smirnov and A.S. Usikov 1143

On the origin of yellow donor-acceptor pair emission in GaN
M. Godlewski, V.Yu. Ivanov, A. Kamińska, H.Y.Zuo, E.M. Goldys, T.L.Tansley, A. Barski, U. Rossner, J.L. Rouvicre, M. Arlery, I. Grzegory, T. Suski, S. Porowski, J.P. Bergman and B. Monemar 1149

Blue emission in Mg doped GaN studied by time-resolved spectroscopy
R. Seitz, C. Gaspar, T. Monteiro, E. Pereira, M. Leroux, B. Beaumont and P. Gibart 1155

GaN doped with sulphur
A. Saxler, P. Kung, X. Zhang, D. Walker, J. Solomon, M. Ahoujja, W.C. Mitchel, H.R. Vydyanath and M. Razeghi 1161

Identification of iron transition group trace impurities in GaN bulk crystals by electron paramagnetic resonance
P.G. Baranov, I.V. Ilyin and E.N. Mokhov 1167

Local vibrational modes at transition metal impurities in hexagonal AlN and GaN crystals
C. Göbel, C. Schrepel, U. Scherz, P. Thurian, G. Kaczmarczyk and A. Hoffmann 1173

Local vibrational modes at As_N in cubic GaN: comparing ab initio calculations to a semi-empirical model
K. Petzke, C. Göbel, C. Schrepel, P. Thurian and U. Scherz 1179

A codoping method in GaN proposed by ab initio electronic-structure calculations
T. Yamamoto and H. Katayama-Yoshida 1185

Photoluminescence of donor acceptor pair transitions in hexagonal and cubic MBE-grown GaN
J. Krüger, D. Corlatan, C. Kisielowski, Y. Kim, R. Klockenbrink, G.S. Sudhir, M. Rubin and E. R. Weber 1191

Raman scattering from defects in GaN
H. Siegle, A. Kaschner, I. Loa, P. Thurian, A. Hoffmann, I. Broser and C. Thomsen 1197

Structural and electrical properties of threading dislocations in GaN
J. Elsner, R. Jones, P.K. Sitch, Th. Frauenheim, M.I. Heggie, S. Öberg and P.R. Briddon 1203

Section 16. Other III-V compounds

Defects analysis in strained InAlAs and InGaAs films grown on (111)B InP substrates
N. Bécourt, J.C. Ferrer, F. Peiró, A. Cornet, J.R. Morante, P. Gorostiza, G. Halkias, K. Michelakis and A. Georgakilas 1211

Irradiation induced lattice defects in $In_{0.53}Ga_{0.47}As$ PIN photodiodes
T. Kudou, H. Ohyama, J. Vanhellemont, E. Simoen, C. Claeys, Y. Takami, A. Fujii and H. Sunaga 1217

Acceptor-hydrogen interaction in InAs
A. Burchard, J.G. Correia, M. Deicher, D. Forkel-Wirth, R. Magerle, A. Prospero, A. Stötzler and the ISOLDE Collaboration 1223

Electroluminescence of III-nitride double heterostructure light emitting diodes with silicon and magnesium doped InGaN
A. Saxler, K.S. Kim, D. Walker, P. Kung, X. Zhang, G.J. Brown, W.C. Mitchel and M. Razeghi 1229

Effect of neutron irradiation on Ga-based semiconductors
L.C. Damonte, F.J. Navarro, J.L. Ferrero, A. Segura and V. Muñoz 1235

Polaron coupling for sulphur impurity in GaSb
P. Kaczor, A. Zakrzewski, L. Dobaczewski, Z. Kalinski, A.M. Gerrits and J. Perenboom 1241

Resonant interaction between local vibrational modes and extended lattice phonons in AlSb
M.D. McCluskey, E.E. Haller, W. Walukiewicz and P. Becla 1247

Defect reactions in low temperature electron irradiated AlAs investigated by measurements of the lattice parameter
A. Gaber, H. Zillgen, P. Ehrhart, P. Partyka and R.S. Averback 1253

Transition from tunneling to Poole-Frenkel type transport in aluminium-nitride
R. Schwarz, J.J. Sun, R. Rocha, E. Morgado, and P.P. Freitas 1259

Growth surface dependence of cathodoluminescence of cubic boron nitride
H. Kanda, A. Ono, Y. Suda and K. Era 1265

N-vacancy defects in c-BN and w-BN
R. Mota, P. Piquini, V. Torres and A. Fazzio 1275

Multiphonon-assisted tunnel ionisation of deep impurities in high-frequency electric field
I.N. Yassievich and V.I. Perel 1281

Long-range lattice relaxation for donor centers in supercell method
S. Bednarek and J. Adamowski 1287

PART 3

Section 17. Aluminium gallium arsenide

Decay kinetics of growth-induced alignment of the first neighbor shell of C_{As} in $Al_xGa_{1-x}As$
J.A. Zhou, C.Y. Song , J.-F. Zheng, M. Stavola, C.R. Abernathy and S.J. Pearton 1293

A plausible evidence of the existence of deep acceptors in Si δ-doped AlGaAs
K. Takarabe, N. Okada, K. Ohmura and H. Ohkura 1299

Magneto-optical and magnetic resonance investigations of intrinsic defects in electron-irradiated n-type $Al_xGa_{1-x}As$
K.-H. Wietzke, M.V.B. Pinheiro, F.K. Koschnick, K. Krambrock and J.-M. Spaeth 1303

Gallium interstitials in GaAs/AlGaAs heterostructures investigated by optically and electrically detected magnetic resonance
T. Wimbauer, M.S. Brandt, M.W. Bayerl, M. Stutzmann, D.M. Hofmann, Y. Mochizuki and M. Mizuta 1309

ODMR investigations of Ge acceptors in p-type $Al_{0.4}Ga_{0.6}As$
M.V.B. Pinheiro, K. Krambrock, A.S. Chaves, K.-H. Wietzke, F.K. Koschnick and J.-M. Spaeth 1315

Section 18. II-VI compound semiconductors

Inverted charge states of anion and caton-site vacancies in zinc blende semiconductors: theory. (Invited)
D.J. Chadi 1321

Degradation of II-VI laser diodes. (Invited)
K. Nakano and A. Ishibashi 1329

Defect characterization of II-VI compound semiconductors using positron lifetime spectroscopy
G. Tessaro and P. Mascher 1335

Defect structures in heavily In-doped II-VI semiconductors
V. Ostheimer, T. Filz, J. Hamann, St. Lauer, D. Weber, H. Wolf and Th. Wichert 1341

The role of cation vacancy in compensation of II-VI compounds by fast diffusors - example of Cu in CdS
U.V. Desnica, I.D. Desnica-Franković, R. Magerle, A. Burchard and M. Deicher 1347

Experimental evidence for the two-electron nature of In-related DX states in CdTe
C. Skierbiszewski, P. Wisniewski, A. Wilamowski, W. Jantsch and G. Karczewski 1353

Nature of dislocation-related deep levels in CdS
A.A. Istratov and O.F. Vyvenko 1359

NMR study of carrier states and trapping complexes in the transparent conductor ZnO: M_{III}
W.W. Warren Jr, N. Roberts, R.-P. Wang and W. Sleight 1365

Cathodoluminescence study on the hydrogenation of ZnO luminescence
T. Sekiguchi, N. Ohashi and Y. Terada 1371

Observation of Frenkel pairs on both sublattices of electron irradiated ZnSe
H. Zillgen and P. Ehrhart 1377

Interface defects and their effect on the electrical properties of ZnSe/GaAs heterojunctions grown by MBE
D. Seghier, I.S. Hauksson, H.P. Gislason, K.A. Prior and B.C. Cavenett 1383

Donor doping of ZnSe: lattice location and annealing behaviour of implanted boron
B. Ittermann, G. Welker, F. Kroll, F. Mai, K. Marbach, H. Ackermann, H.-J. Stöckmann, E. Oldekop and W.-D. Zeitz 1389

Determination of the lattice site of nitrogen after implantation into ZnSe
K. Marbach, B. Ittermann, M. Füllgrabe, M. Heemeier, F. Kroll, F. Mai, P. Meier, D. Peters, H. Thieß, H. Ackermann, H.-J. Stöckmann, W.-D. Zeitz, H. Wenisch, D. Hommel and G. Landwehr 1395

Charge-transfer at Ti ions in ZnTe
H.R. Selber, P. Peka, H.J. Schulz, U.W. Pohl, J. Kreissl, B. Kaufmann and A. Dörnen 1401

Bistable centers in CdMnTeSe: In crystals studied by light-induced gratings
B. Koziarska-Glinka, M. Ponder, A. Suchocki, T. Wojtowicz and I. Miotkowski 1407

Deep levels in $Cd_{0.99}Mn_{0.01}Te$: Ga
J. Szatkowski, E. Placzek-Popko, K. Sieranski, P. Fijalkowski, A. Hajdusianek, and B. Bieg 1413

Vacancy-type defects in electron and proton irradiated II-VI compounds
S. Brunner, W. Puff, P. Mascher, A.G. Balogh and H. Baumann 1419

UV enhanced and solar blind photodetectors based on large-band-gap materials
A. Malik and R. Martins 1425

Section 19. Cadmium fluoride

Lattice relaxation of In donors in CdF_2
A. Suchocki, J. Rauluszkiewicz, J.M. Langer, B. Koziarska-Glinka 1431

Shallow electron centres in CdF_2:M^{3+} and silver halides
C.-R. Fu and K.S. Song 1437

EPR investigation of metastable donor states in CdF_2: In, Ga
Z. Wilamowski, J. Dmochowski and W. Jantsch 1443

Photoinduced magnetism in CdF_2 with bistable donors: the clue for negative U ?
J.M. Langer, A. Suchocki, R. Szymczak and M. Baran 1449

Section 20. Chalcopyrites and other host lattices

Evidence of metastable deep acceptors in $AgGaS_2$ from time-resolved emission
I.-H. Choi and P.Y. Yu 1455

A positron lifetime study of lattice defects in chalcopyrite semiconductors
M.S. Al-Kotb, W. Puff and G. Bischof 1461

Magneto-optical characterisation of $CuIn(Ga)Se_2$
B.K. Meyer, Mt. Wagner, I. Dirnstorfer, D.M. Hofmann and F. Karg 1467

Defects spectroscopy in β-Ga_2O_3
B.K. Meyer, U. Leib, A. Hofstaetter, C. Krummel and D. Kohl 1473

Bistability of oxygen vacancy in silicon dioxide
A. Oshiyama 1479

Section 21. Erbium

Energy transfer processes at erbium ions in silicon
J. Michel, J. Palm, T. Chen, X. Duan, E. Oullette, S.H. Ahn, S.F. Nelson and L.C. Kimerling 1485

Energy transfer rate between erbium 4f shell and Si host
A. Taguchi, K. Takahei, M. Matsuoka and S. Tohno 1491

Photoluminescence study of erbium in silicon with a free-electron laser
I. Tsimperidis, T. Gregorkiewicz, H.P.Th. Bekman, C.J.G.M. Langerak and C.A.J. Ammerlaan 1497

Direct evidence for stability of tetrahedral interstitial Er in Si up to 900 ^{o}C
U. Wahl, J.G. Correia, G. Langouche, J.G. Marques, A. Vantomme and the ISOLDE collaboration 1503

Photo- and electro-luminescence of erbium-doped silicon
S. Lanzerstorfer, M. Stepikhova, J. Hartung, C. Skierbiszewski and W. Jantsch 1509

Donor centers in Er-implanted silicon
V.V. Emtsev, B.A. Andreev, D.S. Poloskin, N.A. Sobolev and E.I. Shek 1515

Structural defects and photoluminescence in dislocation-rich erbium-doped silicon
V.I. Vdovin, N.A. Sobolev, E.M. Emel'yov, E.I. Shek and T.G. Yugova 1521

Influence of fabrication conditions on properties of Si:Er light-emitting structures
N.A. Sobolev, A.M. Emel'yanov, Yu.A. Nikolaev, K.F. Shtel'makh, Yu.A. Kudryavstev, V.I. Sakharov, I.T. Serenkov, M.I. Makovijchuk and E.O. Parshin 1527

High temperature luminescence due to Er in porous Si
M. Strepikhova, W. Jantsch, G. Kosher, M. Schoisswohl, J.P. Cantin and H.J. von Bardeleben 1533

Electron paramagnetic resonance of erbium in bulk silicon carbide crystals
P.G. Baranov, I.V. Ilyin and E.N. Mokhov 1539

1.54 mm photoluminescence of Er and Er + O implanted 6H SiC
A. Kozanecki, W. Jantsch, S. Lanzerstorfer, B.J. Sealy and S. Jackson 1545

Erbium-related defects in gallium arsenide. (Invited)
A.R. Peaker, F. Coppinger, H. Efeoglu, J.H. Evans-Freeman, D.K. Maude, J.-C. Portal, P. Rutter, K.E. Sionger, A. Scholes and A.C. Wright 1551

Electron spin resonance of Er-oxygen complexes in GaAs
T. Ishiyama, E. Katajama, K. Takahei, A. Taguchi and K. Murakami 1559

Er centers in GaAs: Er, O studied by optical spectroscopy under hydrostatic pressure
R.A. Hogg, A. Taguchi and K. Takahei 1565

EXAFS measurement on local structure around erbium atoms doped in GaAs with oxygen co-doping
M. Tabuchi, H. Ofuchi, T. Kubo, K. Takahei and Y. Takeda 1571

Luminescence and annealing studies of Er-implanted GaN with and without oxygen co-doping
E. Silkowski, Y.K. Yeo, R.L. Hengehold and L.R. Everitt 1577

Er-luminescence in MBE-grown AlGaAs
O.B. Gusev, E.K. Lindmark, J.P. Prineas, M.S. Bresler, G. Khitrova, H.M. Gibbs, I.N. Yassievich, B.P. Zakharchenya and V.F. Masterov 1583

Crystal-field transitions of Nd^{3+} and Er^{3+} in Perovskite-type crystals
M. Dietrich, P. Thurian, I. Loa, S. Gronemeyer, A.P. Litvinchuk and C. Thomsen 1589

Excitation and de-excitation of erbium ions in semiconductor matrices
I.N. Yassievich, M.S. Bresler, O.B. Gusev and G. Khitrova 1595

Mechanism of generation of f-f radiation in semiconductor heterostructures
G.G. Zegrya and V.F. Masterov 1601

Section 22. Low dimensional structures

Infrared induced emission from silicon quantum wires
N.T. Bagraev, E.I. Chaikina, W. Gelhoff, L.E. Klyachkin, I.I. Markov and A.M. Malyarenko 1607

Acceptor states in boron doped SiGe quantum wells
K. Schmalz, M.S. Kagan, I.V. Altukhov, K.A. Korolev, D.V. Orlov, V.P. Sinis, S.G. Tomas, K.L. Wang and I.N. Yassievich 1613

Coulomb interaction between carriers localized in InAs/GaAs quantum dots and on point defects
M.M. Sobolev, A.R. Kovsh, V.M. Ustinov, A.Yu. Egorov, A.E. Zhukov, M.V. Maximov and N.N. Ledentsov 1619

Influence of the erbium doping on structure and optical properties of the InGaAs/GaAs superlattices
L.G. Gerchikov, V.F. Masterov, T.R. Stepanova, H.M. Gibbs, G. Khitrova and N.N. Faleev 1625

Defect formation during laser induced intermixing of GaAs/AlGaAs multiple-quantum-well structures
N.H. Ky 1631

Localized epitaxy for vertical cavity surface emitting laser applications
M. Erdtmann, S. Kim and M. Razeghi 1637

The long wavelength luminescence observation from the self-organised InGaAs quantum dots grown on (100) GaAs substrate by metalorganic chemical vapor deposition
K.S. Kim, M. Erdtmann and M. Razeghi 1643

Deep hole traps in Be-doped $Al_{0.5}Ga_{0.5}As$ MBE layers
J. Szatkowski, E. Placzek-Popko, K. Sieranski and O.P. Hansen 1653

Nanotubes and pinholes in GaN and their formation mechanism
Z. Liliental-Weber, Y. Chen, S. Ruminov and J. Washburn 1659

Defect related recombination processes in low-dimensional structures of ZnCdSe/ZnSe, CdTe/CdMnTe and GaAs/AlGaAs
M. Godlewski, D. Hommel, T. Wojtowicz, G. Karczewski, J. Kossut, K. Reginski, M. Bugajski, J.P. Bergman and B. Monemar 1665

Study of hole traps in p-type ZnSe and ZnSSe epilayers by DLTS and admittance spectroscopy
I.J. Hauksson, D. Seghier, H.P. Gislason, K.A. Prior and B.C. Cavenett 1671

Auger type nonradiative recombination processes in bulk and quantum well structures of II-VI semiconductors containing transition metal ions
M. Godlewski, M. Surma, A.J. Zakrewski, T. Wojtowicz, G. Karczewski, J. Kossut, J.P. Bergman and B. Monemar 1677

Spin-dependent processes in self-assembly impurity quantum wires
N.T. Bagraev, W. Gelhoff, L.E. Klyachkin, A.M. Malyarenko and A. Näser 1683

Comparison between as-grown and annealed quantum dots morphology
J.C. Ferrer, F. Peiró, A. Cornet, J.R. Morante, T. Utzmeier, G. Armelles and F. Briones 1689

EPR studies of magnetic superlattices
Z. Wilamowski, V. Svrcek, G. Springhoz and W. Jantsch 1695

Er diffusion and Er-induced Ga-Al interdiffusion in GaAs/AlGaAs quantum structures
M.S. Bresler, B.Ya. Ber, O.B. Gusev, E.K. Lindmark, J.P. Prineas, H.M. Gibbs, G. Khitrova, V.F. Masterov, I.N. Yassievich and B.P. Zakharchenya 1701

Ground and excited states of D- centres in semiconductor quantum dots
B. Szafran, J. Adamowski and B. Stébé 1707

Section 23. Surfaces and interfaces

Electron spin resonance features of the Pb_1 interface defect in thermal (100)Si / SiO_2
A. Stesmans and V.V. Afanas'ev 1713

Silicon surface defects: the roles of passivation and surface contamination
A.J. Reddy, T.A. Burr, J.K. Chan, G.J. Norga, J. Michel and L.C. Kimerling 1719

Heat-treatment induced modifications of porous silicon
S. Dannefaer, C. Wiebe and D. Kerr 1725

Luminescence due to electron-hole condensation in silicon-on-insulator and its application to defect and interface characterization
M.Tajima, S. Ibuka and M. Warashina 1731

Deep electronic states at the inverted AlAs/GaAs interface under different growth modes
P. Krispin, R. Hey, H. Kostial and K.H. Ploog 1737

TEM-study of Frank partial dislocations in ZnSe/GaAs (001) caused by substrate preparation
H. Preis, T. Frey, T. Reisinger and W. Gebhardt 1743

Defect formation and electronic transport at AlGaN/GaN interfaces
L. Hsu, W. Walukiewicz and E.E. Haller 1749

Characterization of the relaxation by misfit dislocations confined at the interface of GaN/Al_2O_3(0001) studied by TEM
S. Kaiser, H. Preis, O. Ambacher and W. Gebhardt 1755

Section 24. Diffusion

Formation kinetics of the Al-related shallow thermal donors: a probe for oxygen diffusion in silicon
P. Kaczor, L. Dobaczewski, T. Gregorkiewicz and C.A.J. Ammerlaan 1761

Diffusion and precipitation of oxygen in silicon doped with germanium
L.I. Khirunenko, V.I. Shakhovtsov and V.V. Shumov 1767

The influence of isovalent doping on diffusion of interstitial oxygen in silicon
L.I. Khirunenko, Yu.V. Pomozov, V.I. Shakhovtsov and V.V. Shumov 1773

EPR evidence of hydrogen-enhanced diffusion of aluminum in silicon
Yu.V. Gorelkinskii, B.N. Mukashev and Kh.A. Abdullin 1777

Segregation of gold at dislocations confirmed by gold diffusion into highly dislocated silicon
H. Bracht, A. Rodriguez Schachtrup and I.Yonenaga 1783

Annealing of low-temperature substitutional gold in silicon: ring-diffusion of substitutional gold in silicon
M. Morooka 1789

Rate limiting mechanism of transition metal gettering in multicrystalline silicon
S.A. McHugo, A.C. Thompson, M. Imaizumi, H. Hieslmair and E.R. Weber 1795

Intrinsic point defect engineering in silicon high-voltage power device technology
N.A. Sobolev 1801

Influence of the dislocation loops on the anomalous diffusion of Fe implanted into InP
C. Frigeri, A. Carnera, B. Fraboni, A. Gasparotto, F. Priolo, A. Camporese and G. Rossetto 1807

Lithium induced vacancy formation and its effect on the diffusivity of lithium in gallium arsenide. (Invited)
H.P. Gislason, K. Leosson, H. Svavarsson, K. Saarinen and A. Mari 1813

Ab-initio investigations on diffusion of halogen atoms in GaAs
T. Ohno, T. Sasaki and A. Taguchi 1821

Low temperature intrinsic diffusion coefficient of lithium in GaAs
K. Leosson and H.P. Gislason 1827

Low temperature impurity diffusion into large-band-gap semiconductors
N.T. Bagraev, A.A. Gippius, L.E. Klyachkin and A.M. Malyarenko 1833

Background doping effects on Zn diffusion in GaAs/AlGaAs multiple-quantum-well structures
N.H. Ky 1839

Author Index 1845

Keyword Index 1859

Materials Science Forum Vols. 258-263 (1997) pp. 1-10
© 1997 Trans Tech Publications, Switzerland

RECENT MEASUREMENTS AND THEORY RELATING TO IMPURITY-INDUCED LVMS IN GaP AND GaAs

R C Newman[1], E G Grosche[1], M J Ashwin[1], [1]B R Davidson, D A Robbie[2], R S Leigh[2] and M J L Sangster[2]

[1]Interdisciplinary Research Centre for Semiconductor Materials, The Blackett Laboratory, Imperial College, Prince Consort Road, London SW7 2BZ, UK

[2]J J Thomson Physical Laboratory, University of Reading, Whiteknights, P O Box 220, Reading RG6 6AF, UK

Keywords: LVMs, gap modes, line widths, force constants, impurities, GaP, GaAs.

Abstract

We review some recent infrared (IR) and Raman scattering measurements and related results from theory, making use of *ab initio* methods, of localised vibrational modes resulting from the presence of impurities in GaAs and GaP. We discuss linewidths, host lattice isotopic fine structure for isolated impurities and changes of local force constants for these impurities and for impurity complexes. Specifically, we outline results for C, B, Si and S impurities and also S-Cu and Si-Cu impurity pairs in GaAs and GaP.

Introduction

Localised vibrational mode (LVM) spectroscopy provides detailed information about the identity and the lattice location of both isolated and complexed impurity atoms in semiconductor crystals. The physics of the technique is basically simple. If the presence of the impurity leads to the existence of a mode with a frequency that falls outside the bands for the perfect lattice modes, the new mode cannot propagate. For a compound such as GaAs for which the component atoms have similar masses (^{69}Ga, 60% abundant: ^{71}Ga, 40%: ^{75}As, 100%), an LVM can occur only at frequencies greater than the maximum lattice frequency. Other compounds, including GaP (^{31}P, 100%), have a gap in the phonon spectrum between the acoustic and optic bands. We shall call a localised mode in this spectral region a *gap mode*. Light impurity atoms substituting for the heavy lattice atom may give rise to both an LVM and a gap mode but a heavy atom substituting for the light lattice atom can produce only a gap mode [see Refs. 1-4]. In the former case, the orthogonality of mode eigenvectors leads to differences in the displacement patterns for the two modes: displacements of the impurity will be dominant in the LVM and relatively unimportant in the gap mode [4,5].

Isotopic substitution of the impurity (e.g. ^{10}B, 20%: ^{11}B, 80%) and/or the near neighbours will produce changes in the mode frequency that can often be resolved in cryogenic (~ 10 K) Fourier transform infrared (FTIR) absorption spectra, provided the full width half-maximum linewidths (Δ) of the components of fine structure are not too great. Sources of line broadening are inhomogeneities, random strain [6] and the limited lifetime of the excited state of the mode due to decay into the underlying 2-phonon density of lattice modes [2]. Recently, perfect lattice frequencies and eigenvectors have been calculated by *ab initio* methods for III-V compounds (including GaAs and GaP) [7,8]. Excellent agreement with the measured phonon dispersion is obtained and, since the mode frequencies and the eigenvectors are produced together, this provides confidence in the eigenvectors and the perfect lattice Green's functions calculated from them. Green's

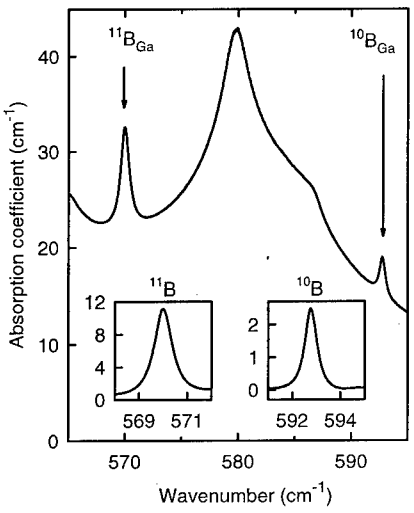


Fig.1. *IR absorption (resolution = 0.02 cm^{-1}) due to $^{11}B_{Ga}$ and $^{10}B_{Ga}$ LVMs in GaP: broad underlying features are due to intrinsic 2-phonon absorption. Note that Δ = 0.9 cm^{-1} for $^{11}B_{Ga}$ and Δ = 0.6 cm^{-1} for $^{10}B_{Ga}$ [12].*

functions for the defective lattice containing the impurity are determined by standard procedures [1], taking account of the change of mass and local changes of the force constants[9]. The LVM and gap mode frequencies are then found from poles in these functions. We shall discuss the results of such calculations for GaAs and GaP, and also local density functional (LDF) *ab initio* calculations relating to the geometry of impurity centres and the associated LVM frequencies for GaAs.

Local Modes

Isotopic fine structure: The five line fine structure of the C_{As} LVM in GaAs (582 cm^{-1}, ^{12}C: 561 cm^{-1}, ^{13}C) is easily resolved by FTIR [10]. Cluster calculations [11] show that the vibrational displacements of the C_{As} atom are large (consistent with a large shift of 21 cm^{-1} for the two isotopes), those of the 4 Ga nearest neighbours (NN) are quite small, while those of more distant neighbours are negligible. The NN combinations give rise to two triplets ($^{69}Ga_4$ and $^{71}Ga_4$), two doublets and five singlets: grouping of the transitions leads to the observations of five nearly equally spaced lines, the inner three of which correspond to singlet transitions. This fine structure is also fully resolved in GaAs for the LVMs of the B_{As} double acceptor (628 cm^{-1}, ^{10}B: 601 cm^{-1}, ^{11}B) [6]. These two modes occur above the 2 phonon cut-off at ~ 590 cm^{-1} (4.2 K) [6], while the C_{As} modes lie just below this limit. However, fine structure for the $^{28}Si_{As}$ LVM (399 cm^{-1}) is not fully resolved (see later Fig. 3) and it has not been reported for P_{As} (334 cm^{-1},^{31}P).

The linewidths of the LVMs from $^{10}B_{Ga}$ (Δ = 0.35 cm^{-1} for GaAs: Δ = 0.6 cm^{-1} for GaP) are smaller than those for $^{11}B_{Ga}$ (Δ = 0.85 cm^{-1} for GaAs: Δ = 0.9 cm^{-1} for GaP) in both GaAs and GaP. The ratio of the measured widths (1.5) for the two isotopes in GaP (Fig. 1) is close to that shown in Fig.2 (1.9) for the ratio of the 2-phonon densities at the relevant LVM frequencies [12]: there is a similar correspondence for GaAs:B_{Ga}. The 2-phonon densities were obtained as convolutions (with no selection rules applied) of the 1-phonon densities, from *ab initio* calculations (see introduction). This procedure ignores any modifications to the lattice modes resulting from the presence of the defects and variations in the coupling to these modes for different impurities. Nevertheless, it is clear that the mode lifetime limits the minimum linewidth for B_{Ga} in both hosts, and this will also occur for the LVMs of other impurities.

The LVM of 606 cm^{-1} from the $^{12}C_P$ acceptor in GaP shows only poorly resolved NN fine structure and it has always been assumed that there are large strains in liquid encapsulated Czochralski (LEC) crystals. However, the profile can be synthesised from the expected 9 component lines, each with a linewidth of 0.34 cm^{-1}, to give an overall spread of 0.46 cm^{-1} [13]. The component linewidth is only 38% of that of the $^{11}B_{Ga}$ LVM, although it is much larger than that of ~ 0.05 cm^{-1} for GaAs:C_{As}. It follows that the lack of observed fully resolved fine structure is due to the limited lifetime of the LVM excited state, rather than inhomogeneities or random strains in the crystals.

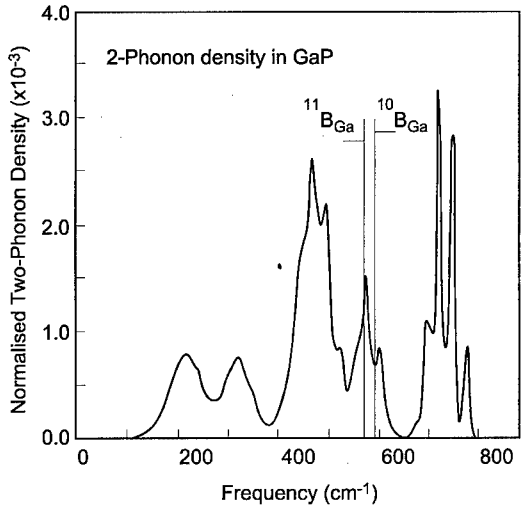


Fig. 2. *2 -phonon density for GaP obtained as a convolution (no selection rules applied) of the 1-phonon density determined from ab initio calculations [12].*

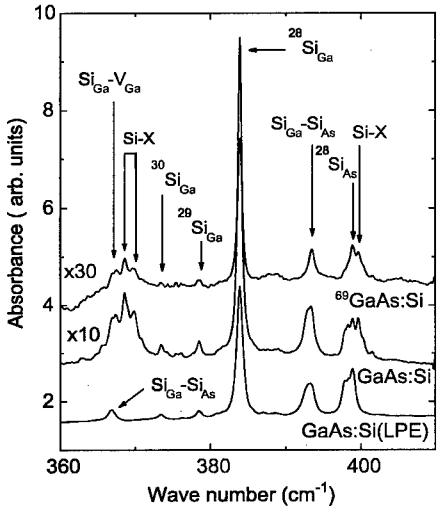


Fig.3. *IR absorption from MBE GaAs:Si ($3x10^{19}$ cm^{-3}) after subtraction of 2-phonon intrinsic absorption. A new line at 399.6 cm^{-1} is identified for the first time for the Si-X defect using ^{69}GaAs:Si [15].*

We complete this section by discussing GaAs heavily doped with Si that shows modes from Si_{Ga}, Si_{As}, Si_{Ga}-Si_{As} pairs, Si_{Ga}-V_{Ga} (Ga vacancy) pairs and a defect labelled Si-X (Fig. 3) [6,14]. Progress in making an assignment for Si-X was limited because it was unclear whether overlapping lines near 367 cm^{-1} were due to Ga isotopic structure or to distinct modes of the Si-X complex. New measurements made on Si doped epitaxial layers of GaAs grown by molecular beam epitaxy (MBE) using a single isotope ^{69}Ga source [15] show (a) that the second possibility (above) is correct and (b) that there is a previously unrecognised satellite LVM at 399.6 cm^{-1} on the high energy side of the now relatively "sharp" Si_{As} LVM (Δ = 0.7 cm^{-1}) that is correlated with the part of the structure close to 367 cm^{-1} due to Si-X. It is evident that Si-X incorporates a single Si_{Ga} atom and the disposition of the 3 modes at 368.4, 370.0 and 399.6 cm^{-1} is similar to that observed for the second neighbour Si_{Ga}-V_{Ga} pair (366.8, 367.5 and 397.8 cm^{-1}) [15]: there is also broad agreement with values calculated by LDF theory [16]. Thus, Si-X is attributed to a Si_{Ga}-V_{Ga} defect that is slightly perturbed, perhaps by a nearby interstitial Si atom. Alternatively, Si-X could be the Si_{Ga}-V_{Ga} pair and the lines previously attributed to this defect may relate to the perturbed centre. There is an outstanding need to relate the IR measurements to the results of recent scanning tunnelling microscopy and positron annihilation measurements [17,18], since comparisons of common samples have not been made and references to the IR studies have not been quoted.

Force Constants

Cluster calculations have been used to determine nearest neighbour Keating bond stretching (α') and bending (β') force constants that lead to agreement between calculated and measured LVM frequencies for a range of impurities in various host crystals [19]. Values of α' and β' may then be compared with α and β for the perfect lattice. For isoelectronic impurities, the changes $\Delta\alpha$ and $\Delta\beta$ are always small: for group IV donors

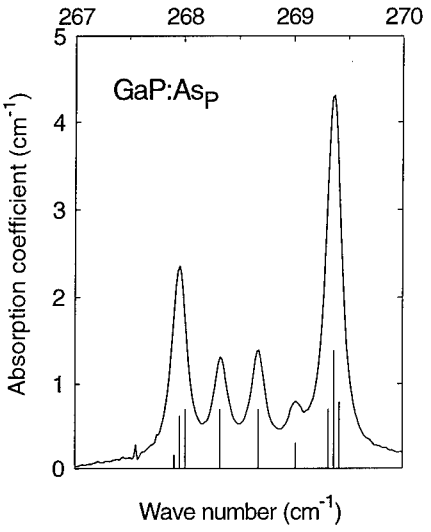


Fig. 4. *IR absorption from the $^{75}As_P$ gap mode in GaP showing five line fine structure due to the mixed nearest neighbour Ga isotopes. The overall width is 1.4 cm^{-1} [5].*

occupying group III sites and group IV acceptors occupying group V sites, α' is larger than α by up to ~ 25%: for group VI donors occupying group V sites and group II acceptors occupying group III sites, α is reduced by a similar percentage. Comparisons with *ab initio* calculations indicate that these numerical percentages may not be too reliable but they serve as a general guide. Thus in GaAs, the order of the LVM sequence for $^{24}Mg_{Ga}$ (331 cm^{-1}), $^{27}Al_{Ga}$ (362 cm^{-1}) and $^{28}Si_{Ga}$ (384 cm^{-1}) is the opposite of that expected from increases in the masses [6].

It is proposed that the changes are due to the partial ionicity of the compound, i.e. III$^+$-V$^-$. In GaAs or GaP, a donor D_{Ga}^+ attracts and shortens the NN covalent bond leading to the increase in α: conversely, an acceptor A_{Ga}^- will lead to a reduction in α. These interactions are also expected for shallow donors or acceptors in their neutral charge states since the electron (hole) density associated with the ground state wavefunction is located mainly outside the region of the impurity and its NNs. Thus the LVMs of the ionised and neutral species are expected to have essentially the same frequency, as found for GaAs:C_{As} [20]. Measurable shifts can occur however if the electron density is highly localised around the impurity, as for the O_i-V centre (electron trap) in Si, or for the O_{As} centre in GaAs [6]. These concepts are important in relation to the interpretation of a gap mode found in GaP:S, to be discussed later.

Gap Modes in GaP

GaP:As. Green's function analysis predicted that, for appropriate defects, gap modes will show NN isotopic fine structure, comparable with that for LVMs but with a larger spread of frequencies [9]. Subsequently, we observed this structure for the As_P gap mode in GaP (Fig. 4) [5] (the gap extends from 255 to 326 cm^{-1}). Calculated component frequencies, allowing only for the mass change were all smaller by 4.5 cm^{-1} than the measured values of 267.95, 268.34, 268.68, 269.02 and 269.37 cm^{-1}. These values were reproduced exactly when the local force constants were increased with $\Delta\alpha$ = 2.227 Nm^{-1} and $\Delta\beta$ = 4.717 Nm^{-1} [19] (changes to other force constants were not taken into account): for comparison, typical values for the host are α ~ 40 Nm^{-1} and β ~ 5 Nm^{-1}. The component linewidths of 0.15 cm^{-1} and the overall spread of the structure of 1.42 cm^{-1} are smaller and larger respectively than the corresponding measurements for the GaP:C_P LVM. Calculations for a fictitious As atom with a mass of 76 amu (an increase of 1 amu) lead to a reduction in the gap mode frequency of $^{75}As_P$ by ~ 1 cm^{-1}, indicating that the presence of impurities with more than one isotope may give rise to overlapping fine structure patterns.

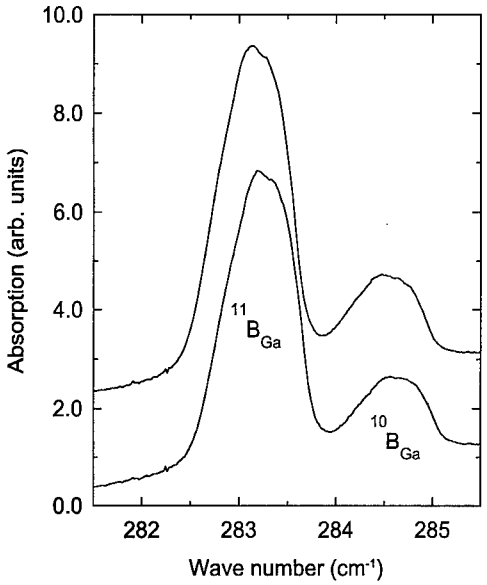


Fig. 5. *IR absorption from B_{Ga} gap modes in two GaP samples cut from different ingots. The unusual asymmetric line shape of the $^{11}B_{Ga}$ line is due to mixed ^{69}Ga and ^{71}Ga second neighbours and can be simulated by theory (see Fig. 6) [12].*

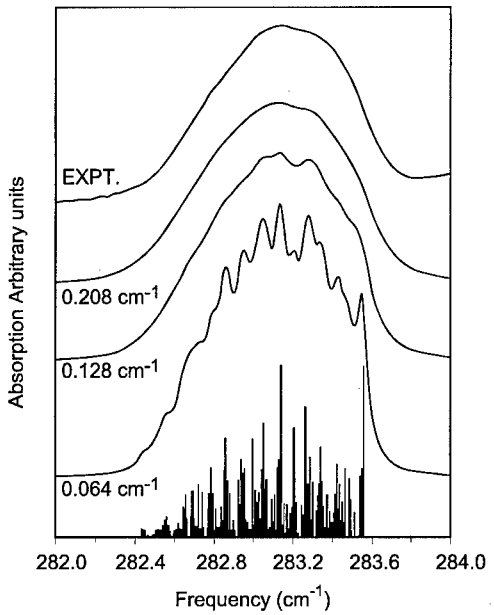


Fig.6 *Simulation of the line shape for the $^{11}B_{Ga}$:GaP gap mode using a model with $\delta\alpha$ = -8.3 Nm^{-1} and a physically unrealistic value of $\delta\beta$ = 21.3 Nm^{-1}, implying that second neighbour force constants should be modified [12].*

GaP:B. In addition to the LVMs discussed above for GaP:B_{Ga}, a gap mode had been reported as an asymmetric peak at 283 cm^{-1} that was deconvoluted into two components with a separation of 1.5 cm^{-1} and a strength ratio of 1:4 to correspond to gap modes of $^{10}B_{Ga}$ and $^{11}B_{Ga}$. The two modes have now been fully resolved with a separation of 1.4 cm^{-1} (Fig. 5) [12]. The lines have an unusual asymmetric shape and their widths (Δ = 0.9 cm^{-1}) are significantly greater than the component widths of the As_p gap mode (Δ = 0.15 cm^{-1}). There are also small features (dips) near the peaks that were reproduced for several samples cut from different ingots. The displacements of the B atoms must be small because of the small isotopic shifts in the frequencies, as expected from the orthogonality with the LVM eigenvector, but there is nevertheless strong gap mode absorption (about 50% of the boron LVM absorption). Appreciable displacements of the 12 second NN ^{69}Ga and ^{71}Ga atoms are expected and are taken into account in obtaining the histogram of frequencies shown in Fig. 6. Broadening the $3x2^{12}$ components with Lorentzian profiles with Δ = 0.21 cm^{-1} leads to an overall linewidth of 0.9 cm^{-1}, in agreement with the measurements, and the dip feature is also reproduced. Thus, we have been able to see the effects of second NNs for the first time. There is, however, a surprisingly high sensitivity of the line shape to the choice of local force constants [12].

GaP:S. Sulphur and selenium donors (S_P and Se_P) in GaP have ground states at (E_c-107 meV) and (E_c-105 meV) respectively. As-grown samples with a doping level of ~ 10^{18} cm^{-3} show complete carrier freeze-out so that IR spectra can be obtained at 10 K for samples containing either neutral or ionised donors [13,21]. GaP:Se shows no gap modes from Se_P with dominant isotopes ^{78}Se (23%) and ^{80}Se (49.8%). This is not surprising since mode

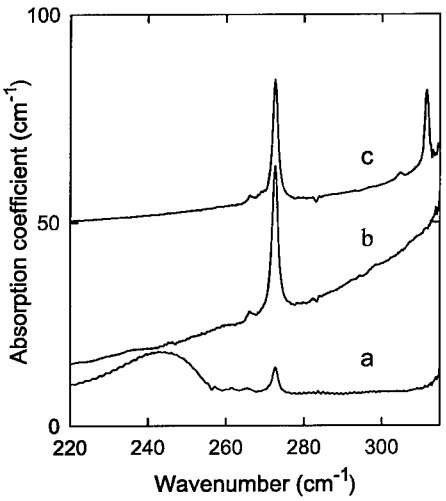


Fig.7. *Gap modes in GaP:S_P: a) as-grown, b) after complete compensation by 2MeV e-irradiation and c) after Cu in-diffusion. Note the broad absorption at the top of the acoustic band: the $^{32}S_P$ mode in (a): the very weak $^{34}S_P$ mode in (b) and (c) and modes from S_P-Cu_{Ga} pairs in (c).*

frequencies, calculated by ignoring force constant changes, are only 5 cm^{-1} above the top of the acoustic band and reduced force constants (α') are expected. As-grown GaP:S shows a weak mode at 272.5 cm^{-1} with a width of 1.6 cm^{-1} but no resolved fine structure (Fig. 7). Progressive electrical compensation of a sample by 2 MeV e$^-$-irradiation at 300 K led to decreases in the strength of the photo-excitation spectrum and increases in the strength of the gap mode by a factor of ~ 10. Its assignment to $^{32}S_P$ (95%) is certain since a second new mode is then detected at 266.2 cm^{-1} due to $^{34}S_P$ (4.6%). Broad absorption at the top of the band of lattice modes induced by neutral S^o (Fig. 7 Trace (a)), Se^o or Te^o [21] has been observed but will not be discussed here.

Reproduction of the $^{32}S_P$ mode requires setting $\delta\alpha$ = -19.3 Nm^{-1}[21]. This corresponds to a very large reduction in the stretch force constant of ~ 50% but the predicted isotopic shift of $^{34}S_P$ to 266.14 cm^{-1} agrees with the measurements. There is no reason to believe that the grown-in donors are complexed with a native defect such as a V_{Ga} as the normal photo-excitation spectrum is observed and similar samples show the electron paramagnetic resonance (EPR) spectrum from neutral sulphur donors with T_d symmetry. A consequence of the weak bonding is that the neighbours have relatively small vibrational displacements so that the calculated overall spread of frequencies for the gap mode components of 0.46 cm^{-1} is only ~ 30% of that for the $^{75}As_p$ mode. The implied large width of the fine structure components is explained by anharmonic coupling of the S_P mode to the *modified* modes of the GaP crystal. Calculations lead to an estimate of the component width of 1.95 cm^{-1}, whereas the corresponding estimate for $^{75}As_p$ is only 0.13 cm^{-1}: both values are in essential agreement with the measurements [21].

Compensation of grown-in S_P donors was alternatively effected by Cu in-diffusion. Similar in-diffusion has been used previously to compensate Si_{Ga} donors in GaP (Fig. 8) and GaAs [14]. For both hosts, there is formation of *second* neighbour $Si_{Ga}^{+} - Cu_{Ga}^{2-}$ pairs, involving an estimated 50% of the Si donor concentration [14,22] and the other Si atoms remain as isolated donors. Since the Cu_{Ga} atom is expected to be a double acceptor, the Si_{Ga}-Cu_{Ga} pair centres should be single acceptors that compensate the isolated Si_{Ga} donors, leading to an explanation of the observations. Similar pairing of S_P donors was expected in both GaP and GaAs so that *nearest* neighbour $S_P^{+} - Cu_{Ga}^{2-}$ pairs should form. Cu diffusion into our GaP:S samples at 900°C led to a large increase in the strength of the S_P gap mode (Fig. 7) [13]. In addition, new gap modes occur at higher frequencies of 311.5 cm^{-1} ($^{34}S_P$) and 304.7 cm^{-1} ($^{32}S_P$) that we attribute to the transverse Γ_3 vibrations of the pairs. A local mode is also produced at 408.1 cm^{-1} that we attribute to the longitudinal Γ_1 mode. This mode is in a sense pushed through the reststrahl band as a result of increasing the strength of the S - Cu stretch force constant compared with the S - Ga force constant. Similarly,

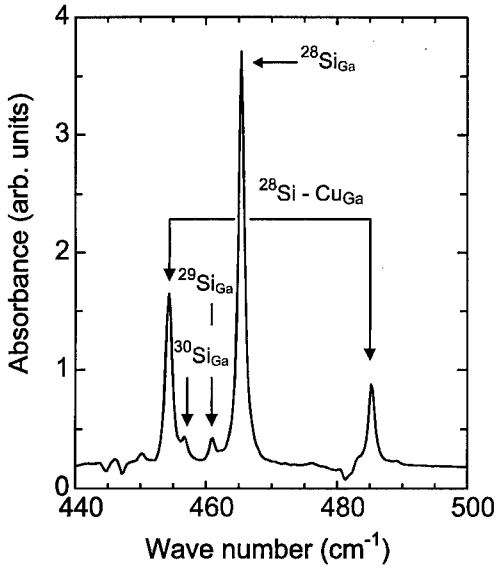


Fig. 8 *IR spectrum showing LVMs from Si_{Ga}-Cu_{Ga} second neighbour pairs in GaP with the lines straddling the LVM from isolated Si_{Ga}. By analogy with the spectrum from the same pairs in GaAs [14], the line at 453.8 cm^{-1} is an unresolved doublet.*

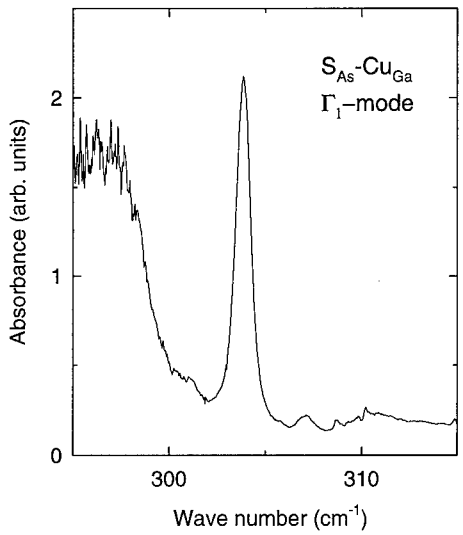


Fig. 9. *The longitudinal LVM due to $^{32}S_{As}$-Cu_{Ga} nearest neighbour pairs formed in GaAs:S after in-diffusion of Cu at 900°C for 16h. The mode is close to the reststrahl band which prevents observation of the weak $^{34}S_{As}$-Cu_{Ga} pair line.*

formation of S_{As}^{+}-Cu_{Ga}^{2-} pairs in GaAs also leads to an LVM at 303 cm^{-1} (Fig. 9). The important conclusion from these observations is that the strength of the isolated S_P gap mode increases as a result of compensation of the donors effected either by Cu diffusion or by 2 MeV electron irradiation.

The outstanding problem is to understand why there is no significant contribution to the absorption from S_p^0: absorption from S_P^+ would occur in as-grown material due to the presence of C_P acceptors and possibly O_P impurities. Only a small proportion of the wavefunction for the extra bound electron lies inside a region bounded by the nearest neighbours, according to an effective mass calculation, implying that the local force constants should be insensitive to the charge state of the impurity [21], as discussed above. It has been proposed that the dipole moment associated with the mode for S_P^+ is, to a large extent, screened by the bound electron of the neutral donor S_p^0. An essential condition for this interpretation to be valid is that the region of the crystal in which appreciable displacements of atoms occur in the localised mode must be small compared with that in which there is an appreciable fraction of the wavefunction of the bound electron. In addition, the vibrational frequency (272.5 cm^{-1}) of the donor atom must be much smaller than the threshold frequency for electronic transitions (somewhat below 850 cm^{-1}). S_p^0 in GaP seems to be an unusual case in which these conditions apply. Further analysis is in progress.

High Doping Levels and Complexes

So far, only samples relatively "lightly" doped with active donors or acceptors have been discussed. At much higher concentrations ($\geq 10^{19}$ cm^{-3}), the electronic levels form bands and there is intense free-carrier absorption that increases towards low wave numbers. The

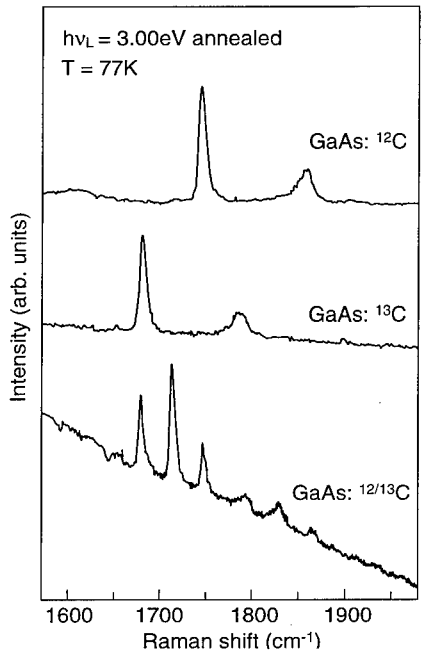
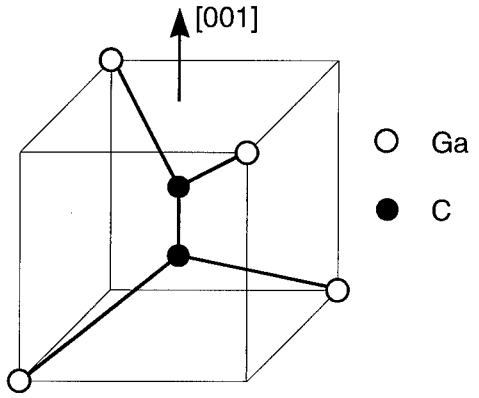


Fig. 10 *Raman spectra from GaAs:^{12}C, GaAs:^{13}C and GaAs containing nearly equal concentrations of ^{12}C and ^{13}C, (total [C_{As}] ~ 10^{20} cm^{-3}) following anneals at 850°C for up to 4h (Kr^{+} ion laser source (3.00 eV) line and a sample temperature of ~ 77 K [26]).*

energies of the vibrational and electronic states are then degenerate at the LVM frequency of the dopant and mixing of the states occurs. This leads to features in spectra that appear as Fano profiles (derivative-shaped for GaAs:C_{As} [23] or a dip for GaAs:Si_{As} [14]) superposed on the background continuum absorption. These features are always quite broad and all fine structure from mixed host isotopes is lost, although changes in the impurity isotope are usually resolved.

There is often an advantage in using the Raman scattering technique to reveal the impurity LVMs since the probing light penetrates only a short distance into the host crystal (for photons with an energy of 3.0 eV, this depth is ~ 10 nm in GaAs). For example, the spectrum of the Raman shift for GaAs highly doped with Si shows all the features that can only be observed clearly by IR absorption if samples are first compensated by electron irradiation. For p-type Si doped MBE or LPE GaAs, Fano dips due to Si_{As} observed in IR spectra appear as "normal" symmetrical Raman scattering profiles. We note that the symmetry of the defect can also be determined by Raman scattering without the need to apply uniaxial stress, as demonstrated for GaP:B_{Ga} [25]. A disadvantage of the technique is its limited resolution of ~ 1 cm^{-1} so that fine structure is not detected.

The process of hydrogen in-diffusion may be used to reduce the carrier concentration in thin epitaxial layers but this results in the formation of close hydrogen - impurity pairs so that many additional LVMs may occur (e.g. for H-C_{As} in GaAs) [23]. Sometimes the hydrogen is introduced during the growth of layers by metal organic vapour phase epitaxy or chemical beam epitaxy. A different problem may arise if this hydrogen is out-diffused at an elevated temperature (T > 600°C) since impurity atoms may change their lattice locations. It has been demonstrated that there is a loss of C_{As} atoms during this process and the formation of bonded C-C split-interstitial defects [26]. It is implied that C_{As} atoms move to interstitial sites and that they then migrate and are captured by remaining C_{As} atoms. The C-C pairs cannot be observed by IR absorption because of their D_{2d} symmetry (no dipole moment) but they are Raman active. Examination of samples containing equal concentrations of ^{12}C and ^{13}C then show scattering from ^{12}C - ^{12}C, ^{12}C - ^{13}C and ^{13}C - ^{13}C pairs at 1742, 1708 and 1674 cm^{-1} that demonstrates the pair structure unambiguously (Figs. 10 and 11). These defects, predicted to be deep donors, were first predicted by *ab initio* theory for AlAs [27], and subsequent calculated frequencies are close to those observed for the Triplet (1) structure found in GaAs [26]. Recent calculations for ^{12}C-^{12}C pairs indicate frequencies of 1764 and 1793 cm^{-1} for GaAs and AlAs respectively. New measurements of the defect in MOVPE AlAs show lines at 1755.8 (Triplet (1)) and 1856.3 cm^{-1} (Triplet (2)) [28]. The origin of Triplet (2) is still not understood [26].



(C-C) Defect	Frequencies (cm^{-1}) $^{12}C_2$	^{12}C-^{13}C	$^{13}C_2$
Expt. : Triplet (1)	1742	1708	1674
Expt : Triplet (2)	1859	1824	1788
LDF $(C\text{-}C)^+$[100]	1798	1764	1728

Fig.11 *Model for the di-carbon split interstitial defect in heavily C doped GaAs following a high temperature anneal. Tabulated frequencies are given for the Triplet (1) (lower frequencies) and Triplet (2) lines together with frequencies calculated from LDF theory [26].*

Conclusions

Several mechanisms for broadening component lines in LVM spectra have been considered. The large widths of the resolved $^{10}B_{Ga}$ and $^{11}B_{Ga}$ gap modes in GaP are explained by the distributions of ^{69}Ga and ^{71}Ga isotopes which occupy the 12 second nearest neighbours (NN) to the impurity. Correlations between linewidths and underlying two-phonon densities of states have been pointed out and the importance of the modifications to these densities due to changes in force constants around the impurity is highlighted in a comparison between the resolved fine structure for As_P in GaP and the broad structureless lines for $^{34}S_P$ and $^{32}S_P$ in the same host. The gap modes for isolated $^{32}S_P$ and $^{34}S_P$ have much greater strengths for the ionised donors than the neutral impurities. A difference in frequency for the two charge states of the impurity is not expected and it is proposed that the dipole moment may be largely screened by the bound electron in the relatively deep ground state. The use of GaAs heavily doped with Si grown with a single isotope source (^{69}Ga) has led to a reassessment of the Si-X defect that is now shown to be a Si_{Ga}-V_{Ga} second neighbour pair, possibly perturbed by another Si atom or vacancy in a nearby site. At high doping levels information about impurity-induced LVMs can be obtained by Raman scattering without the prior need to compensate the crystal by electron irradiation or the in-diffusion of a counter dopant. Use of this technique has led to the observation of di-carbon split interstitial centres previously predicted to be present in annealed heavily C doped AlAs and GaAs.

There are some further general comments. IR absorption studies parallel to those described here have revealed isotopic fine structure for both LVMs and gap modes from various isolectronic impurities in CdTe, ZnTe, ZnS and hexagonal CdS: comparisons were also made with the results of cluster calculations [29]. A range of other crystal structures (e.g. GaN) could in principle be studied by LVM spectroscopy. The use of Raman scattering could also prove valuable, as indicated by the study of InP:C [30], although significantly more work is required to obtain an unambiguous assignment for this particular system.

Acknowledgments

We thank Drs. R.Jones, C.Latham and J.Wagner for allowing us to quote their unpublished results. The Engineering and Physical Sciences Research Council is thanked by R.C.Newman, E.G.Grosche, M.J.Ashwin and B.R.Davidson for financial support (contract GR/K96977) and by D.A.Robbie for the provision of a research studentship.

References

1. A.A.Maradudin, E.W.Montroll, G.H.Weiss and I.P.Ipatova, in Solid State Physics, edited by H.Ehrenreich, F.Seitz and D.Turnbull (New York:Academic Press), 2nd Ed. Suppl. 3 (1971).
2. P.G.Dawber and R.J.Elliott, Proc. Roy. Soc.A, **273**, 222 (1963):Proc. Phys. Soc. **81**, 453 (1963).
3. R.C.Newman, Adv.Phys. **18**, 545 (1969): Infrared Studies of Crystal Defects (London, Taylor & Francis) (1973).
4. A.S.Barker, Jr. and A.J.Sievers, Rev. Mod. Phys. **47**, Suppl. No.2 (1975).
5. E.G.Grosche, M.J.Ashwin, R.C.Newman, D.A.Robbie, M.J.L.Sangster, T.Pletl, P.Pavone and D.Strauch, Phys. Rev. B **51**, 14758 (1995).
6. R.C.Newman, in Imperfections in III/V Materials, Edited by E.R.Weber, Semiconductors and Semimetals (San Diego, Academic) **38**, 117 (1993).
7. P.Giannozzi, S. de Gironcoli, P.Pavone and S.Baroni, Phys.Rev. B **43**, 7231 (1993).
8. T. Pletl, P. Pavone and D. Strauch, unpublished (1996).
9. D.A.Robbie, M.J.L.Sangster and P.Pavone, Phys. Rev.B **51**, 10489 (1995).
10. W.M.Theis, K.K.Bajaj, C.W.Litton and W.G.Spitzer, Appl. Phys. Lett. **41**, 70 (1982).
11. R.S.Leigh and R.C.Newman, J.Phys. C:Solid State Phys. **15**, L1045 (1982).
12. D.A.Robbie, M.J.L.Sangster, E.G.Grosche, R.C.Newman, T.Pletl, P.Pavone and D.Strauch, Phys. Rev. B **53**, 9863 (1996).
13. E.G.Grosche, Ph.D. Thesis, University of London (1997).
14. R.C.Newman, Semicond. Sci. Technol. **9**, 1749 (1994).
15. M.J.Ashwin, R.C.Newman and Muraki, J. Appl. Phys. **82**, 137 (1997).
16. R.Jones and S.Öberg, Semicond. Sci. Technol. **9**, 2291 (1994).
17. C.Domke, Ph.Ebert, M.Heinrich and K.Urban, Phys. Rev. B**54**, 10288 (1996).
18. J.Gebauer, R.Krause-Rechberg, C.Domke, Ph.Ebert and K.Urban, Phys. Rev. Lett., **78**, 3334 (1997).
19. M.J.L.Sangster, R.C.Newman, G.A.Gledhill and S.B.Upadhyay, Semicond. Sci. Technol., **7**, 1295 (1992).
20. D.W.Fischer and M.O.Manasreh, J. Appl. Phys. **68**, 2504 (1990).
21. E.G.Grosche, R.C.Newman, D.A.Robbie, R.S.Leigh and M.J.L.Sangster unpublished work (1997).
22. S.R.Morrison and R.C.Newman, J. Phys. C : Solid St. Phys. **7**, 619 (1974).
23. B.R.Davidson, R.C.Newman, T.J.Bullough and T.B.Joyce, Phys. Rev. B**45**, 17,106 (1994)
24. J.Wagner, R.C.Newman and C.Roberts, J. Appl. Phys, **78**, 2431 (1995).
25. D.T.Hon, W.L.Faust, W.G.Spitzer and P.F.Williams, Phys. Rev. Lett. **25**, 1184 (1970)
26. J.Wagner, R.C.Newman, B.R.Davidson, S.P.Westwater, T.J.Bullough, T.B.Joyce, C.D.Latham, R.Jones and S.Öberg, Phys. Rev. Lett., **78**, 74 (1997).
27. R.Jones and S.Öberg, Mater. Sci. Forum **143-147**, 253 (1994).
28. B.R.Davidson, R.C.Newman, J.Wagner, C.C.Button, C.Latham and R.Jones, unpublished work (1997)
29. M.D.Sciacca, A.J.Mayur, H.Kim, I.Miotkowski, A.K.Ramdas and S. Rodriguez, Phys. Rev. B **53**, 12878 (1996).
30. M.Ramsteiner, P.Kleinert, K.H.Ploog, J.Oh, M.Konagai and Y.Takahashi, Appl. Phys. Lett. **67**, 647 (1995).

Materials Science Forum Vols. 258-263 (1997) pp. 11-18
© 1997 Trans Tech Publications, Switzerland

OPTICALLY-INDUCED DEFECTS IN Si-H NANOPARTICLES

M J Caldas, R J Baierle, E Molinari[1], and S Ossicini[1]

Instituto de Física, Universidade de São Paulo, São Paulo, SP, Brasil

[1] INFM and Dipartimento di Fisica, Università di Modena, I-41100 Modena, Italy

Key Words: surface reconstruction, porous Si, Hydrogen in Si

Abstract.
We study the behavior of perfectly hydrogenated Si nanoparticles, under optical excitation. We use semiempirical selfconsistent techniques within the Hartree-Fock formalism, specially parametrized to reproduce key properties of the crystalline environment for the Si atom. We find that the optical absorption spectra of particles ranging in size from 29 to 71 Si atoms evidence both quantum confinement and relaxation effects, with optical gaps in the green-blue region. These particles show however strength for luminescence at much lower energy, related to localised surface defects created by gap-light excitation. These defects involve two surface Si atoms and a H-atom, in a Si-H-Si bridge configuration, and we propose they should be the active luminescent centers in porous Si.

Introduction.

The optical properties of nanometer-size structures are currently the object of much debate, both from the experimental and theoretical points of view, since quantum confinement may force a behavior not seen for the same material in the bulk. In this scenario, Si nanoparticles are interesting in that they show efficient luminescence, in the visible range. Furthermore, even if their optical behavior shows a clear dependence on the particle size, several aspects of photoluminescence experiments appear to be size independent and are not understood in terms of pure confinement of bulk-like electronic states. Si particles with diameter in the nanometer size range can be realised [1] through microwave plasma decomposition or by laser breakdown of silane, and are thought to be the structures responsible for the photoluminescence of porous Si. The optical properties of samples composed of such particles show intriguing features: *a*) the absorption edge shows an exponential tail, and blue-shifts with decreasing particle size from around 1.2 eV for diameters $\geq$ 10 nm, to around 2.5-3 eV for diameters of 2 nm; *b*) there are at least two channels for luminescent decay, a blue-green fast channel, and a red-orange slow channel (R-PL); *c*) in contrast to the absorption energy, the R-PL energy is virtually size-independent, but the intensity increases with decreasing average size of particles in a sample; *d*) the PL behavior is very sensitive to sample preparation, oxidation, and temperature.

Several hypothesis have been advanced to explain the above behavior, apart from quantum confinement, including alien species such as siloxanes or polisilanes, interfacial states (Si/SiO_2), or surface saturation defects (dangling bonds), and theoretical modelling is clearly desirable. However, in spite of the impressive progress in theory in the past decades, a reliable theoretical description of these systems is still very difficult. *Ab-initio* density-functional techniques can give quantitative answers to questions on the ground-state properties of unit cells with around 10^2 atoms, while atomistic molecular dynamics may be sucessfully applied to geometries of unit cells of the order of 10^4 atoms. Unfortunately, none of these approaches are at this time suitable for the study of optical properties of complex, finite nanostructures, because of the need to account for atomic relaxation at a microscopic level, and to treat the optical properties consistently from the smallest cluster limit, where correlation effects are expected to be important, up to large crystallites. Quantum semi-

empirical techniques, on the other hand, are usually parametrized for small organic molecules, where the sp^3 hybridization is not relevant.

This difficulty is apparent from the data shown in Table I, where we collect results for the energy of the first optical transition of Si particles, with perfectly hydrogenated surfaces, obtained from different models; we see that for any of the sizes studied, the transition energy can differ by more than 1.5 eV from one model to another. Even accounting for the difference between models, this discrepancy is unexpected, and arises from the fact that we are dealing with structures at the limit between molecules and solids, where both localization and delocalization effects can play an important role.

Table I : *Gap energy of H-saturated Si nanoparticles calculated through different models. The number of atoms in the particle is indicated in the first column. Ref. 2:supercell, pseudopotentials within Local Density Approximation (LDA),plane-waves basis set; Ref. 3: LCAO basis set, LDA, constant shift of +0.6 eV in gap energy; Ref. 4: MNDO, standard parametrization PM3; Ref. 5: empirical tight-binding, nearest neighbors only. An estimate can be made for a particle with around 70 Si atoms from Ref. 6, empirical pseudopotentials, LDA with excitonic corrections, gap ~2.9eV.*

Number of Atoms	Transition Energy (eV)			
	Ref. 2	Ref. 3	Ref. 4	Ref. 5
10	4.62	5.10	3.43	—
17	—	5.05	3.10	—
29	3.32	4.95	2.76	—
35	—	4.90	2.74	2.95
66	2.95	3.98	2.62	—
87	—	4.05	3.10	—
123	2.45	3.60	2.45	—
239	—	3.50	—	1.68

To address this problem, we decided to work within the Hartree-Fock plus Configuration Interaction framework, since there might be Stokes shifts involved and therefore structural relaxations *and* correlation effects might have to be investigated in the excited states. The complexity of the problem however constrains us to work with semiempirical techniques, which we briefly describe below.

Model and Methods

We adopt two techniques from the Neglect of Diatomic/Differential Overlap (NDO) family, which start from the usual Hartree-Fock variational procedure, with the mean-field wavefunctions (Molecular Orbitals, MO) expanded in Linear Combinations of Atomic Orbitals $\Phi_\mu(\mathbf{r})$ (LCAO). The NDO techniques all derive from the same basic approximations, namely: the frozen-core approximation, so that only valence-shell electrons are treated selfconsistently; a minimum-basis set for the LCAO, so that for Si or O only valence s and p orbitals are included; all electronic and nuclear energies are written in parametric form, but parameters are associated with particular elements, not situations, and are transferrable from one situation to another; and finally, to keep the number of two-electron two-center integrals manageable, the overlap element is neglected ($\Phi_\mu\Phi_\sigma d\mathbf{r}=0$). It is important to note that the real overlap between orbitals, ultimately responsible for bonding, is brought back into the calculation through the one-electron 'resonance' integrals, and that the electronic structure is obtained through a full selfconsistent iterative procedure.

Each NDO Hamiltonian is designed for obtaining optimal results for a given set of properties. We adopt the MNDO/AM1[7] (Modified NDO/ Austin Model 1) approximation for the study of structural properties, due to the multipole expansion used for the two-center two-electron integrals, which is very apropriate to the study of geometries; and the ZINDO/CI[8] (Zerner's Intermediate NDO/ Configuration Interaction) approximation for the optical properties, due to the special s-p interaction factors that optimize transition energies, and to the CI method for describing excited states. The difficulty lies, in both cases, in that the standard parametrizations are incapable of

reproducing the properties of crystalline material, and are thus inadequate for the study on hand. To solve this problem, we introduce new parametrizations, which we call NDO/Crystal: to do that we developed Bloch-periodic versions of the NDO codes, which we use mainly for the task of reparametrizing the methods for the Si (and O) atom. The mathematical framework includes expansion in Bloch-sums, built from the same minimum atomic basis sets used in the regular molecular versions. We use enlarged cells, and Chadi-Cohen special **k**-points for the density-matrix summation in the Brillouin Zone. The total energy is calculated adopting a neighborhood-approximation cut-off radius for the interactions (we attain convergence including third neighbors). The method is described in detail elsewhere.

Our parametrization ensemble includes the bulk Si and α-quartz crystals, and small relevant molecules such as silane, disilane and disiloxane. For MNDO we obtain best fits to the geometries and vibrational properties of the molecules, and for the lattice parameters of the crystals, within 4% of the experimental value. For the Si bulk crystal we adjusted parameters to obtain not only the bulk modulus (within 12% error, compared to 87% with the usual parametrization), but also phonon energies for the high-symmetry Γ, X and L points, which we fit within 8 % error. For ZINDO we obtained best fits to the optical spectra and first ionization potentials of the small molecules, and for the valence band properties and optical gap character of the crystals, always using the geometries obtained with MNDO/Crystal. We obtain the correct symmetries, and fair valence bandwidth for both crystals (we are focusing on the first optical transitions, so the lower valence states were not optimised), and correct indirect gap character for Si, with however the expected overestimation of gap energy, and underestimation of conduction bandwidth, that are recognised to be due to lack of correlation effects.

The inclusion of correlation effects through CI is not applicable to the infinite periodic solid. It is however crucial to our parametrization that we have an estimate of these effects: to do that we study nanocrystals, simulated by clusters in the perfect (theoretical) lattice geometry, saturated by pseudo-atoms. These pseudo-Si atoms are chosen so as to level-out the atomic charge density inside the nanocrystal, maintaining the charge hybridization obtained for the periodic crystal. CI is then performed for these nanocrystals, and the gap extrapolated to infinite radius gives the estimate we need. We show in Fig. 1(a) the results for Si, and we see that our value is extremely close to the experimental value. It is also relevant that the gap transition is essentially HOMO-LUMO (Highest Occupied-Lowest Unoccupied MO), and that these orbitals preserve the character of the (indirect) gap-edge orbitals obtained for the bulk.

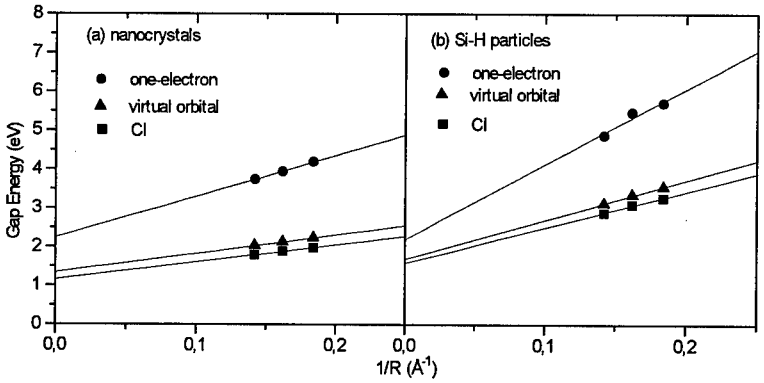


Figure 1: *Energy of the first optical transition for Si nanocrystals (a) and nanoparticles (b), plotted against the inverse radius 1/R (R is a characteristic length, given by the distance to the center of the structure of the outer Si shell). We show the Hartree-Fock one-electron value (always HOMO-LUMO for these transitions), the value including virtual orbital correction, and the CI value.*

Results and Discussion

Once the techniques are reparametrized, we use the standard molecular versions to calculate the structural (MNDO/Crystal) and optical (ZINDO/Crystal) properties of Si nanoparticles, with the surfaces perfectly hydrogenated. We studied [9,10] nanoparticles in T_d and D_{3d} symmetries, containing from 17 to 71 Si atoms (diameters from 0.4 to 1.5 nm), allowing all the atoms in the particle to relax. The first finding is that even for particles with as few as 29 Si atoms, in tetrahedral arrangement, the vibrational spectrum already reproduces quite well the phonon dispersion of the bulk. We show in Fig. 2 the vibrational spectrum for two particles, with 35 and 44 Si atoms, where we see clearly also the Si-H surface modes (there is a slight shift in Si-H modes carried over from the parametrization, since we did not change any parameter for the H atom).

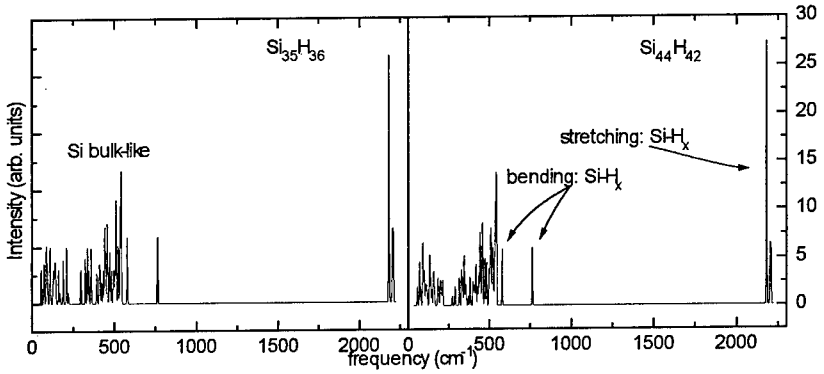


Figure 2: *Vibrational spectra obtained through MNDO/Crystal for the particles $Si_{35}H_{36}$ (a) and $Si_{44}H_{42}$ (b). We indicate the Si bulk-like modes and the surface Si-H modes.*

There occurs for all particles a non-linear relaxation that is responsible for a split-off Si-Si mode, with energy slightly higher than the ΓO energy, since there is always a compression of the first shell towards the central atom. These results are relevant to the debate on the dimensionality of the luminescent structures in po-Si, since it is shown that particles of this size may cause the phonon lines seen [11] experimentally.

For the optimum geometry, we calculate through ZINDO/Crystal/CI the optical spectra for all nanoparticles studied. For any one particle the spectrum is rich, but with no transitions in the red-orange region, as we show in Fig. 3 for two different-symmetry particles.

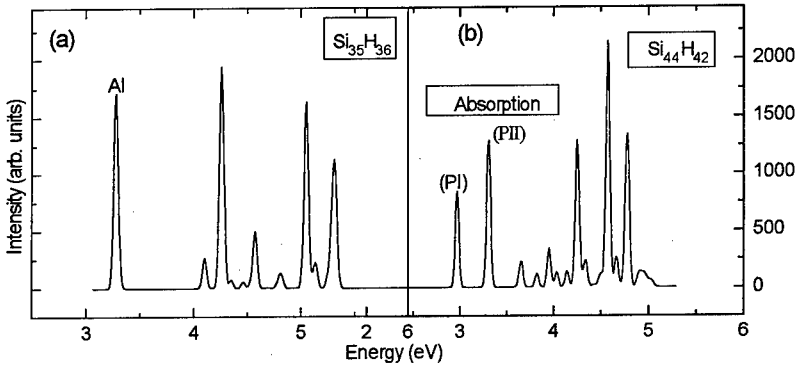


Figure 3: *Optical spectra for (a) $Si_{35}H_{36}$ and (b) $Si_{44}H_{42}$ calculated through ZINDO/Crystal/CI, in the relaxed ground state geometry; the lines are gaussian-broadened by 0.01 eV. The first peaks can be traced in more than 85% to the HOMO-LUMO one-electron trasition; the LUMO symmetry is a_1 in both cases, but the HOMO symmetry is lowered from t_2 of T_d in (a) to a_1+e of C_{3v} in (b).*

We show in Fig. 1(b) results for the first optical transition of the three largest particles, which may be compared to Fig. 1(a) for the corresponding (in size and strucuture) nanocrystals. We find thus that the energy gap for particles in this diameter range is size dependent, showing the expected confinement effects. However, comparing Fig. 1(a) and (b), we also see that there is a large opening of the gap in these hydrogenated relaxed particles, that comes directly from the compression already discussed for the central shells. In fact, if we analyse the first optical transition into one-electron excitations (Fig. 4), we find that again it is essentially a HOMO-LUMO transition.
If we now look at the charge distribution of these orbitals, we find that they concentrate mostly on the central shells of the particle (Fig 4(b,c)), so we may classify the first optical transition as crystalline. Indeed, the Hydrogen atoms do not contribute significantly to any of the transitions seen below 5 eV. It is unreasonable to try and extrapolate from the data in Fig. 1(b) to find a diameter range where we might find transitions in the red, since the relaxation effect should certainly decay with increasing size of the particle: accordingly, this extrapolation would lead to a gap of 1.5 eV even for an 'infinite Si-H particle'.

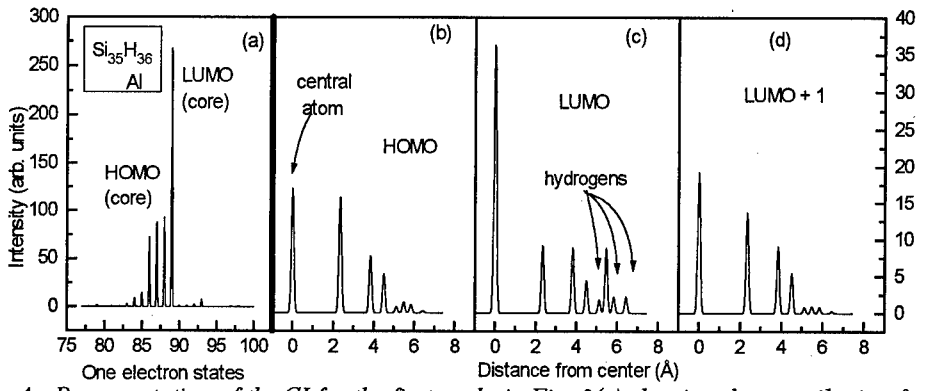


Figure 4: *Representation of the CI for the first peaks in Fig. 3(a) showing the contribution from the molecular orbitals to the first excited state of the $Si_{35}H_{36}$ nanoparticle, and we see it is essentially created by the HOMO-LUMO transition; similar results are obtained for the other particles. The spatial localisation for these orbitals is shown in parts (b) HOMO t_2; (c) LUMO a_1; and (d) LUMO+1. The probability density associated with a typical atom in a given shell is plotted vs the distance from the center of the particle. All peaks correspond to Si shells except those marked hydrogen, which correspond to the H surface shells.*

Summarizing our results so far, we find that the optical gap of Si-H particles, in the stable relaxed geometry, shows a blue shift with respect to bulk Si that is due to both confinement and relaxation effects. In agreement with most previous theoretical results [2-5], for particles in the diameter range 1.5-2 nm, the first optical transition lies around 3 eV, too high to account for the R-PL in po-Si; also, this first transitions are crystalline in character, which is compatible with the size dependence but appears conflicting with the data on po-Si, where we see a large dependence of the R-PL on the surface [1] conditions. There is however another important datum: for all studied particles, the first optical transition is essentially a HOMO-LUMO one-electron excitation. This on the one hand explains why different treatments of correlation give very similar results: there is none or extremely little configuration mixing for these transitions (This is not the case for higher-lying lines in the spectra). On the other hand, it allows us to study the excited state reached under illumination: we simply study through MNDO/Crystal the properties of the particle with one electron taken from the HOMO to the LUMO. With the geometry optimised for this electronic excited state, we again study the optical properties, through ZINDO/Crystal/CI.

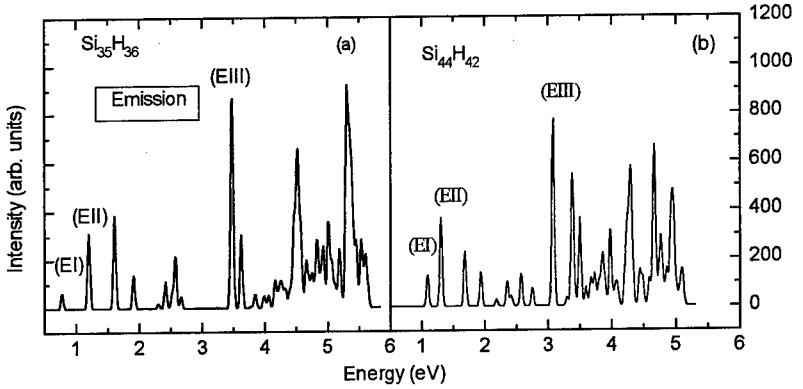


Figure 5: *Optical spectra for the (a) $Si_{35}H_{36}$ and (b) $Si_{44}H_{42}$ calculated through ZINDO/Crystal/CI, in the relaxed excited state geometry; the lines are gaussian-broadened by 0.01 eV.*

We show in Fig. 5 the spectra so obtained for the particles $Si_{35}H_{36}$ and $Si_{44}H_{42}$, which must be compared to Fig 3. The difference is striking: the first transition is drastically red shifted, and the region from 1 to 3 eV is now completely filled with lines. It must be noted first that, since the difference is so marked, these are the spectra more properly associated with the luminescence; the spectra in Fig. 3(a) should correspond to absorption only. Secondly, that these optical spectra are obtained for the first excited electronic state of each particle, reached though the HOMO-LUMO excitation; thus, only the lower lines in the spectra are likely to be seen in luminescence. Finally, the similarity of the effect for the two particles is also remarkable.

We next investigate the origin of the lower peaks. Results are very similar for the two particles: we find that there is now a clear configuration mixing effect, and the transitions mainly start from the HOMO, and involve both the LUMO and a second virtual state. Figure 6 depicts the analysis of the first peak in emission for the particle $Si_{35}H_{36}$ and we note that if the LUMO is still crystalline in character, the HOMO is however very different from the HOMO of the ground state. It is no longer degenerate, and shows a very large density concentration over just two Si atoms at the surface of the cluster. The other virtual state involved, LUMO+1, also shows this localised character.

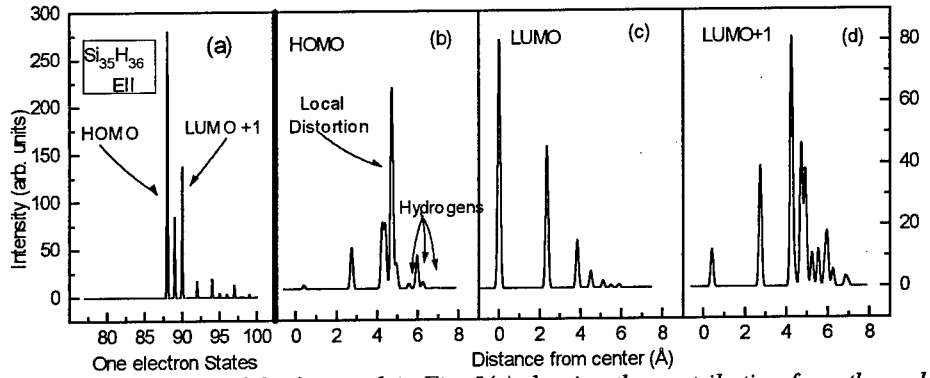


Figure 6: *Representation of the first peak in Fig. 5(a) showing the contribution from the molecular orbitals to the optical transiton; we see it is now a mixed transition. The spatial localisation for the relevant orbitals is shown in parts (b) HOMO; (c) LUMO; and (d) LUMO+1; all orbitals are now singly degenerate: note the localisation of the HOMO and LUMO+1.*

What we find in fact is that the particle in the excited state undergoes a strong spontaneous distortion extremely localised on two neighboring surface Si atoms, each bonded to just one H atom.

In the distortion the Si atoms bend and stretch their bond by 0.26 Å, keeping the distance to their internal neighbors almost unchanged. At the same time, one of the H atoms moves to bridge the bond, so that a surface configurational defect is created, with no complete rupture of any bonds in the particle. We show in Fig. 6 a scheme of the defect, depicting one 6-fold ring that includes the Si-H-Si bridge and reaches to the center of the particle. If we analyse the bond order in this bridge-defect configuration we find that the H-atom is bonded almost equally to both Si atoms, and that the Si atoms maintain 40% of the regular bond strength to each other.

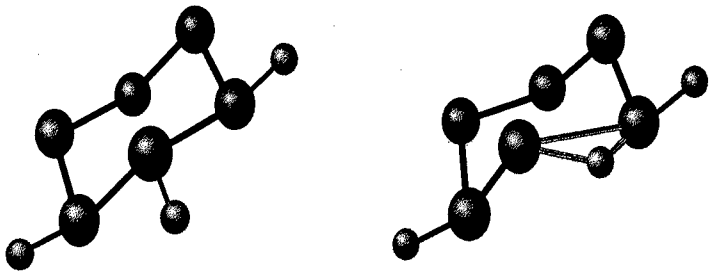


Figure 7. *Scheme of the bridge-defect, showing a 6-fold Si ring that reaches to the center of the particle, in the normal ground state (a) and in the excited state bridge configuration (b); results for the* $Si_{44}H_{42}$ *particle.*

It is relevant to note that this bridge-defect has a considerable oscillator strength for optical decay, so we might expect efficient luminescence from such a center. On the other hand, it is highly unstable relative to the normal surface configuration, and there is no evidence for a metastable (local minimum) distorted configuration in the ground state. So once the center optically decays, it should decay non-radiatively back to the normal surface configuration. In other words, we do not expect dangling-bond creation [12] or optical bleaching [13] in this case.

An earlier suggestion by Allan and coworkers [14] to explain the luminescence in po-Si invoked a surface defect: by removal of the H atoms saturating neighboring Si surface atoms, a surface dimer could be created, and the authors show that by stretching such a dimer one could create an efficient optical decay center, similar to the bridge defect. Our results show that there is no need for actual built-in defects, since this bridge is photocreated by the absorption process on perfectly H-saturated nanoparticles. It requires, however, a 'soft' environment, ideally provided by the surface of such particles, since there is considerable distortion of the atoms involved.

The luminescent process in po-Si has been called 'exciton trapping'. What our study indicates is that indeed the absorption process might be said to create an exciton, since the transition so clearly involves just the two one-electron levels and could be described as creating an electron-hole pair. The situation after the 'exciton trapping' is however more complex, since there is considerable configuration mixing between an extended (LUMO) and a localised (LUMO+1) electron state.

We find another distortion (breathing) mode for the excited state, from which there is also efficient optical activity; this symmetric relaxed configuration is however much higher in energy than the bridge defect state.

Our results allow then for a consistent explanation of the photoluminescence processes in Si-H nanoparticles, and in po-Si. For a given size distribution in a sample, we have a distribution of absorption thresholds that result in an exponential tail; for each particle, the first optical absorpion originates in the crystalline core and the gap is size dependent, showing quantum confinement effects. Once in the excited state it can decay through a symmetric state, Stokes-shifted by $\approx$ 0.2-0.3 eV, that is, in the blue-green region for particle diameters around 2 nm; due to the (symmetric) mode of relaxation, it should be a fast channel. The H surface atoms are not involved in either absorption, or blue-green luminescence. The R-PL is associated with the photocreated bridge-defect, and, due to the extremely localised character of the defect wavefunction, is 'pinned' in energy. We do not

have an estimate for the decay rate: since the distortion is very large the Jahn-Teller coupling term could slow the process down, or it could be that the decay is not directly to this luminescent excited state, but passes through some intermediate state. The presence of H atoms is essential to the red-orange luminescence, as is also the softness of the environment: the intensity of luminescence should increase with decreasing particle size.

Acknowledgements

The authors wish to thank Brazilian agencies FAPESP and CNPQ, and Italian agency CNR; the work was partially performed with use of computer facilities at LCCA-USP.

References

[1] Y. Kanemitsu, Phys. Rep. **263**,1-91 (1996), and references therein.
[2] M. Hirao, and T. Uda, Surf. Sci **306**, 87 (1994).
[3] B. Delley, and E. F. Steigmeier, Phys. Rev B **47**, 1397 (1993).
[4] R. Kumar, Y. Kitoh, K. Shegematsu, and K. Hara, Jpn. J. Appl. Phys. **33**, 909 (1994).
[5] Tu Huaxiang, Ye Ling, and Xie Xide, Phys. Rev. B **48**, 10978 (1993).
[6] L-W. Wang and A. Zunger, J. Phys. Chem. **98**, 2158 (1994).
[7] M. J. S. Dewar, E. G. Zoebish, E. F. Healy, and J. J. P. Stewart, J. Am. Chem. Soc. **107**, 3902 (1985).
[8] J. Ridley, and M. Zerner, Theoret. Chem. Acta **32**, 111 (1973).
[9] R. J. Baierle, M. J. Caldas, E. Molinari, and S. Ossicini, Braz. J. Phys. **26**, 631 (1996).
[10] R. J. Baierle, M. J. Caldas, E. Molinari, and S. Ossicini, Solid St. Commun. **102**, 545 (1997).
[11] P. D. J. Calcott, K. J. Nash, L. T. Canham, M. J. Kane, and D. Brumhead, J. Phys. Condens. Matter **5**, L91 (1993)
[12] X. Zhou, G.D. Watkins, K.M. McNamara Rutledge, R.P. Messmer and S. Chawla, Phys. Rev. B **54**, 7881 (1996).
[13] M. J. Caldas, J. Dabrowski, A. Fazzio and M. Scheffler, Phys. Rev. Lett. **65**, 2046 (1990); M. J. Caldas, and E. Molinari, Solid State Commun. **89**, 493 (1994).
[14]G. Allan, C. Delerue, and M. Lannoo, Phys. Rev. Lett. **76**, 2961 (1996).

Materials Science Forum Vols. 258-263 (1997) pp. 19-26
© 1997 Trans Tech Publications, Switzerland

DEFECTS AND DOPING IN III-V NITRIDES

Chris G. Van de Walle[1] and Jörg Neugebauer[2]

[1]Xerox Palo Alto Research Center, Palo Alto, California 94304, USA
[2]Fritz-Haber-Institut, Abt. Theorie, Faradayweg 4–6, D-14195 Berlin, Germany

Keywords: GaN, nitrides, first-principles calculations, vacancies, H, Mg, O

Abstract

We present a theoretical study of point defects and impurities in GaN. Sources of n-type doping are investigated: nitrogen vacancies are too high in energy, but silicon and oxygen readily incorporate. The properties of oxygen, including DX-center formation, support it as the main cause of unintentional n-type conductivity. Gallium vacancies are the likely source of the yellow luminescence. An investigation of various acceptor impurities indicates that Mg is still the acceptor of choice for p-type doping. The role of hydrogen during acceptor doping is discussed. We also find that compensation of acceptors by nitrogen vacancies may occur, likely leading to the observed persistent photoconductivity.

1. Introduction

GaN is successfully being used for green, blue, and UV light emitters and for high-temperature or high-power applications [1]. Light-emitting diodes [2] are already being produced in large quantities for use in applications ranging from traffic lights to full-color displays. Nakamura and coworkers have also achieved various milestones in the fabrication of laser diodes, including room-temperature CW (continuous wave) operation [3]. In addition, GaN is a very promising material for high-frequency and high-power devices [4] and for solar-blind detectors [5]. The ability to control doping is crucial for all of these applications; wide-band-gap semiconductors such as GaN have long suffered from lack of control of the doping levels. In this paper we discuss how a theoretical approach for native defects and dopant impurities, combined with state-of-the-art first-principles calculations, can be used to understand the various factors that govern doping.

Native defects have often been invoked to explain doping problems. Specifically, in GaN the nitrogen vacancy has traditionally been thought to be the source of n-type conductivity. Our first-principles investigations, however, indicate that nitrogen vacancies are high-energy defects in n-type GaN, and thus are unlikely to form in large concentrations [6]. We have proposed that unintentional impurities such as oxygen and silicon are the actual cause of the observed unintentional n-type doping [7]. These impurities are calculated to be shallow donors with high solubilities. Additional support for this assignment comes from the finding that oxygen (but not Si) behaves as a DX center in GaN under pressure, in agreement with recent experimental observations [8].

After a description of the theoretical approach in Section 2, we will summarize our main results for native defects in Section 3. In Section 4 we will discuss n-type doping and the behavior of oxygen and silicon. A major concern for optoelectronic devices is the presence of alternate

recombination channels, such as the "yellow luminescence" (YL), which occurs mainly in n-type GaN. Gallium vacancies are the most likely source of this YL [9].

p-type doping of GaN has become possible through a post-growth activation step in MOCVD-grown material. Hydrogen plays a crucial role in this process. The behavior of hydrogen in GaN is broadly similar to that in other semiconductors, including the stability of H^+ in p-type material and the negative-U character (in this case with a very large magnitude of U) [10, 11]. Intriguing differences occur, however, for instance in the structure of hydrogen-acceptor complexes. In Section 5 we will summarize results for hydrogen in GaN. Results for interactions between hydrogen and native defects will also be presented.

The specific role of hydrogen in p-type doping will be addressed in Section 6. This section also discusses other aspects of acceptor doping in GaN. p-type doping levels are still lower than desirable for low-resistance cladding layers and ohmic contacts. Achieving higher hole concentrations with Mg as the dopant has proved difficult; various explanations have been proposed for this limitation. Our investigations of compensation mechanisms [12] have revealed that the determining factor is the solubility of Mg in GaN, which is limited by competition between incorporation of Mg acceptors and formation of Mg_3N_2; incorporation of Mg on interstitial or substitutional nitrogen sites was found to be unfavorable. We will also discuss the prospects of other acceptor impurities for achieving higher doping levels [13]. We have also studied the interaction between O and Mg acceptors. The presence of oxygen during growth is detrimental to achieving p-type doping in the nitrides.

2. Theoretical approach

Key parameters in our approach are obtained from first-principles calculations that do not require any adjustable parameters or any input from experiment. The computations are founded on density-functional theory [14], using a supercell geometry and soft Troullier-Martins pseudopotentials [15]. The effect of d electrons in GaN is taken into account either through the so-called non-linear core correction [16] or by explicit inclusion of the d electrons as valence electrons; the latter proved to be necessary for obtaining accurate results in certain cases [17]. Further details of the computational approach can be found in Refs. [6], [18], and [19]

A key quantity describing the behavior of defects and impurities is their *formation energy*, E^f. The formation energy determines the equilibrium concentration of impurities or native defects according to the expression

$$c = N_{\text{sites}} \exp^{-E^f/k_B T} \tag{1}$$

where N_{sites} is the number of sites the defect or impurity can be incorporated on, k_B the Boltzmann constant, and T the temperature. Equation (1) shows that defects with a *high* formation energy will occur in *low* concentrations.

The formation energy is not a constant but depends on the growth conditions. For example, the formation energy of an oxygen donor is determined by the relative abundance of O, Ga, and N atoms, as expressed by the chemical potentials μ_O, μ_{Ga} and μ_N, respectively. If the O donor is charged (as is expected when it has donated its electron), the formation energy depends further on the Fermi level (E_F), which acts as a reservoir for electrons. Forming a substitutional O donor requires the removal of one N atom and the addition of one O atom; the formation energy is therefore:

$$E^f(\text{GaN:O}_\text{N}^q) = E_{\text{tot}}(\text{GaN:O}_\text{N}^q) - \mu_O + \mu_N + qE_F \tag{2}$$

where $E_{tot}(GaN:O_N^q)$ is the total energy derived from a calculation for substitutional O, and q is the charge state of the O donor. E_F is the Fermi level. Similar expressions apply to other impurities and to the various native defects. We refer to Refs. [6] and [20] for a more complete discussion of formation energies and their dependence on chemical potentials.

Note that the Fermi level E_F is not an independent parameter, but is determined by the condition of charge neutrality. However, it is informative to plot formation energies as a function of E_F in order to examine the behavior of defects and impurities when the doping level changes. As for the chemical potentials, these are variables which depend on the details of the growth conditions. For ease of presentation, we set these chemical potentials to fixed values in the figures shown below; however, a general case can always be addressed by referring back to Eq. (2). The fixed values we have chosen correspond to Ga-rich conditions [$\mu_{Ga} = \mu_{Ga(bulk)}$], and to maximum incorporation of the various impurities, with solubilities determined by equilibrium with Ga_2O_3, Si_3N_4, and Mg_2N_3.

3. Native defects

Our first-principles results for native defects were described in detail in Ref. [21]. One general conclusion is that self-interstitial and antisite defects are high-energy defects in GaN, and are thus unlikely to occur. Nitrogen vacancies (V_N) behave as donors, which means that their formation energy is higher in n-type material than in p-type [see Eq. (2)]. Nitrogen vacancies are therefore unlikely to form in n-type GaN, and hence they cannot be responsible for n-type conductivity. The low formation energy of V_N in p-type GaN, however, makes it a likely compensating center for acceptor doping, as will be discussed in Section 6. In n-type GaN the lowest-energy native defect is the gallium vacancy (V_{Ga}), a triple acceptor. This defect plays a role in donor compensation, as well as in the frequently observed yellow luminescence. Both aspects will be discussed in the next section.

4. n-type doping

Figure 1 summarizes our results for native defects and impurities relevant for n-type doping. As discussed in Section 3, nitrogen vacancies have too high a formation energy to be responsible for n-type conductivity in GaN. In contrast, Fig. 1 shows that O and Si have relatively low formation energies in n-type GaN, and can thus be readily incorporated. Both O and Si form shallow donors in GaN. The slope of the lines in Fig. 1 indicates the charge state of the defect or impurity [see Eq. (2)]: Si_{Ga}, O_N, and V_N all appear with slope +1, indicating single donors.

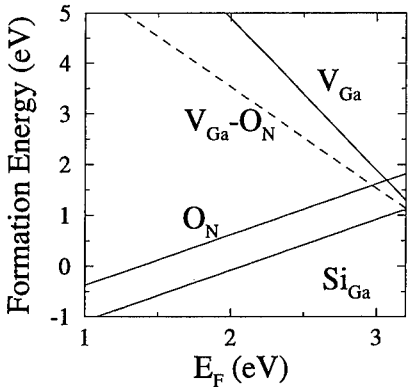


Figure 1: Formation energy vs. Fermi energy for native defects (nitrogen and gallium vacancies), donors (oxygen and silicon) and the V_{Ga}-O_N complex. The zero of Fermi energy is located at the top of the valence band.

Oxygen had been considered a potential source of n-type conductivity in GaN by Seifert *et al.* [22] and by Chung and Gershenzon [23]. Still, the prevailing conventional wisdom, attributing the n-type behavior to nitrogen vacancies, proved hard to overcome. Recent experiments have now confirmed that unintentionally doped n-type GaN samples contain silicon or oxygen concentrations high enough to explain the electron concentrations. Götz *et al.* [24] reported electrical characterization of intentionally Si-doped as well as unintentionally doped samples, and concluded that the n-type conductivity in the latter was due to silicon. Götz *et al.* have also recently carried out SIMS (secondary-ion mass spectroscopy) and electrical measurements on hydride vapor phase epitaxy (HVPE) material, finding levels of oxygen or silicon in agreement with the electron concentration [25].

High levels of n-type conductivity have always been found in GaN bulk crystals grown at high temperature and high pressure [26]. It has recently been established that the characteristics of these samples (obtained from high-pressure studies) are very similar to epitaxial films which are intentionally doped with oxygen [27, 28]. The n-type conductivity of bulk GaN can therefore be attributed to unintentional oxygen incorporation. The high-pressure experiments have also shown that freezeout of carriers occurs at pressures exceeding 20 GPa [8, 26, 28, 29]. Originally this observation was interpreted as consistent with the presence of nitrogen vacancies, since the V_N donor gives rise to a resonance in the conduction band, which emerges into the band gap under pressure. However, the observations are also entirely consistent with a "DX-like" behavior of the oxygen donor.

We have carried out extensive calculations for oxygen in GaN under pressure, as well as in AlGaN alloys [30]. Under compression the oxygen impurity assumes an off-center configuration: a large outward relaxation introduces a deep level in the band gap [31]. This behavior explains the carrier freezeout in GaN under pressure. Silicon donors do not exhibit this transition, consistent with experiment [8]. Alloying with AlN increases the band gap similar to the application of hydrostatic pressure; one therefore expects that the behavior of the impurities in AlGaN would be similar to that in GaN under pressure. Explicit calculations for oxygen in AlN indeed produce DX behavior [30]. These results are consistent with the observed decrease in n-type conductivity of unintentionally doped $Al_xGa_{1-x}N$ as $x > 0.4$ [32].

As a final comment on Fig. 1 we note that gallium vacancies (V_{Ga}^{3-}) have relatively low formation energies in highly doped n-type material (E_F high in the gap); they could therefore act as compensating centers. Yi and Wessels [33] have found evidence of compensation by a triply charged defect in Se-doped GaN. We have also proposed that gallium vacancies are responsible for the "yellow luminescence" (YL) in GaN, a broad luminescence band centered around 2.2 eV [9]. The origins of the YL have been extensively debated; as discussed in Refs. [9] and [34], the calculated properties of the gallium vacancy are in good agreement with experimental results.

5. Hydrogen

Hydrogen also has strong effects on the properties of GaN. Many growth techniques, such as metal-organic chemical vapor deposition (MOCVD) or hydride vapor phase epitaxy (HVPE) introduce large concentrations of hydrogen in the growing material. The behavior of hydrogen in GaN was analyzed in detail in Refs. [10] and [11]. We found that hydrogen incorporates more readily in p-type than in n-type GaN. In p-type GaN H behaves as a donor (H^+), compensating acceptors. Hydrogen can bind to the Mg acceptors with a binding energy of 0.7 eV. The structure of the resulting complex is unusual in that H does not sit next to the Mg, but

actually binds to a N atom which is a neighbor of the acceptor. As a direct consequence the vibrational frequency of the complex is *not* representative of a Ga-H bond, but rather of a N-H bond. The calculated vibrational frequency is 3360 cm^{-1}. This value does not include anharmonic effects; these may lower the frequency considerably in the case of N-H vibrations, by as much as 170 cm^{-1} [35]. Götz *et al.* [36] have reported a value of 3125 cm^{-1} for this local vibrational mode.

We have recently also studied the interactions of hydrogen with native point defects in GaN [37]. Since antisites and self-interstitials are very unlikely to form in GaN (see Section 3) we have focused on H interacting with vacancies. This interaction is often described in terms of tying off of dangling bonds. This picture does not apply in the case of the nitrogen vacancy, which is surrounded by Ga atoms at a distance of 1.95 Å from the center of the vacancy; a typical Ga-H bond distance is too large for more than one H to fit inside the vacancy. The calculated binding energy of the $(V_N H)^{2+}$ complex, expressed with respect to interstitial H in the positive charge state, is 1.56 eV; the formation energy of this complex is included in Fig. 2. We have proposed that this complex is involved in the appearance and disappearance of photoluminescence (PL) lines during post-growth annealing of Mg-doped layers grown by MOCVD [38].

For the Ga vacancy (V_{Ga}), we find that one, two, three or four H atoms can be accommodated in the vacancy, and levels are removed from the band gap as more hydrogens are attached. Distinct N-H bonds are formed, with a bond length of about 1.02 Å and vibrational modes between 3100 cm^{-1} and 3500 cm^{-1}. Hydrogenated gallium vacancies with one or two H atoms behave in much the same way as the unhydrogenated kind; they may therefore contribute to compensation of donors as well as to the yellow luminescence.

6. *p*-type doping

Magnesium has emerged as the acceptor dopant of choice in GaN. It has been found, however, that hole concentrations obtained with Mg doping are limited. In addition, it is well known that Mg-doped GaN grown by MOCVD needs to be subjected to post-growth treatments such as low-energy electron-beam irradiation [39] or thermal annealing [40] in order to activate the acceptors. All of these features can be addressed by our first-principles results, which are summarized in Fig. 2.

The Mg acceptor (Mg_{Ga}) has a low enough formation energy to be incorporated readily in GaN. We have also investigated other positions of Mg in the lattice, such as on substitutional N sites (Mg_N) and on interstitial sites (Mg_i), always finding much larger formation energies [12]. We therefore conclude that Mg overwhelmingly prefers the Ga site in GaN, the main competition being with formation of Mg_2N_3, which is the solubility-limiting phase. It would be interesting to investigate experimentally whether traces of Mg_2N_3 can be found in highly Mg-doped GaN.

Other potential sources of compensation are also illustrated in Fig. 2. The nitrogen vacancy, which had a high formation energy in *n*-type GaN (see Fig. 1), has a significantly lower formation energy in *p*-type material, and could act as a compensating center. Figure 2 shows that V_N can occur in a 3+ as well as a + charge state; the +/3+ transition is characterized by a large lattice relaxation [21]. Compensation by nitrogen vacancies may therefore be responsible for the observed persistent photoconductivity effects [41]. The metastability is associated with the different position of the A_1 state near the valence band in the +1 and +3 charge states; this state is occupied with two electrons the +1 charge state, and empty for the 3+ charge state.

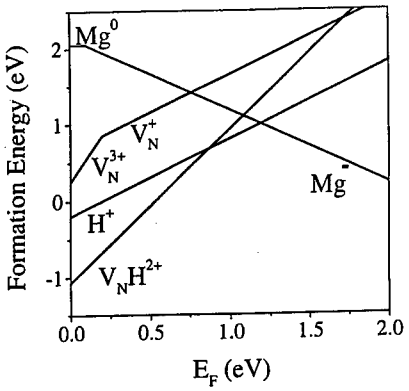


Figure 2: Formation energy as a function of Fermi level for Mg in different configurations (Ga-substitutional, N-substitutional, and interstitial configuration). Also included are the native defects and interstitial H.

Figure 2 also shows that hydrogen, when present, has a formation energy much lower than that of the nitrogen vacancy. In growth situations where hydrogen is present (such as MOCVD or HVPE) Mg-doped material will preferentially be compensated by hydrogen, and compensation by nitrogen vacancies will be suppressed. The presence of hydrogen is therefore beneficial – at the expense, of course, of obtaining material that is heavily compensated by hydrogen! Fortunately, the hydrogen can be removed from the active region by treatments such as low-energy electron-beam irradiation [39] or thermal annealing [40]. A more complete discussion of the role of hydrogen in GaN is given in Refs. [10] and [11].

For Mg, we thus conclude that achievable doping levels are mainly limited by the solubility of Mg in GaN. We have investigated other candidate acceptor impurities, and evaluated them in terms of solubility, shallow *vs.* deep character, and potential compensation due to incorporation on other sites [13]. None of the candidate impurities exhibited characteristics exceeding those of Mg. In particular, we perceive no noticeable advantage in the use of Be, which has been suggested as a superior dopant.

Last but not least we note the importance of avoiding any type of contamination during growth of *p*-type GaN. For instance, the oxygen formation energy shown in Fig. 1 clearly extrapolates to very low values in *p*-type GaN. Any oxygen present in the growth system will therefore be readily incorporated during *p*-type growth. In addition, complex formation between oxygen and magnesium can make oxygen incorporation even more favorable: we find that oxygen binds to Mg with a binding energy of 0.6 eV.

7. Conclusions

To maintain the rapid progress in development of GaN-based devices, a fundamental understanding is required of the behavior of point defects and dopants. First-principles calculations can greatly assist in providing a framework for understanding doping problems. Specific results for donor and acceptor doping have been presented in this paper. The main conclusions for *n*-type GaN are that (i) nitrogen vacancies are *not* responsible for unintentional *n*-type conductivity; (ii) Si and O donors can be incorporated in large concentrations, likely causing unintentional *n*-type doping; (iii) oxygen (but not silicon) behaves as a *DX* center in GaN under pressure and in AlGaN alloys; and (iv) gallium vacancies are the likely source of the yellow luminescence. For *p*-type GaN we found that (i) Mg is still the acceptor of choice; (ii) the resulting hole concentration is limited due to Mg solubility; (iii) incorporation of Mg on interstitial sites or antisites is not a problem; (iv) hydrogen has a beneficial effect on *p*-type doping

because it suppresses compensation and enhances acceptor incorporation; and (v) compensation by nitrogen vacancies may occur, likely causing the observed persistent photoconductivity.

Acknowledgements

This work was supported in part by DARPA under agreement no. MDA972-95-3-0008.

References

[1] For a recent review, see F. A. Ponce and D. P. Bour, Nature **386**, 351 (1997).

[2] S. Nakamura, M. Senoh, and T. Mukai, Jap. J. Appl. Phys. **32**, L8 (1993).

[3] S. Nakamura, M. Senoh, S. Nagahama, N. Iwasa, T. Yamada, T. Matsushita, Y. Sugimoto, and H. Kiyoku, Appl. Phys. Lett. **69**, 4056 (1996).

[4] M. A. Khan, Q. Chen, C. J. Sun, J. W. Wang, M. Blasingame, M. S. Shur, and H. Park, Appl. Phys. Lett. **68**, 514 (1996).

[5] D. Walker, X. Zhang, P. Kung, A. Saxler, S. Javadpour, J. Xu, and M. Razeghi, Appl. Phys. Lett. **68**, 2100 (1996).

[6] J. Neugebauer and C. G. Van de Walle, Phys. Rev. B **50**, 8067 (1994).

[7] J. Neugebauer and C. G. Van de Walle, Proc. ICPS-22 (World Scientific, Singapore), p. 2327 (1995).

[8] C. Wetzel, T. Suski, J. W. Ager III, E. R. Weber, E. E. Haller, S. Fischer B. K. Meyer, R. J. Molnar, and P. Perlin, Phys. Rev. Lett. **78**, 3923 (1997).

[9] J. Neugebauer and C. G. Van de Walle, Appl. Phys. Lett. **69**, 503 (1996).

[10] J. Neugebauer and C. G. Van de Walle, Phys. Rev. Lett. **75**, 4452 (1995).

[11] J. Neugebauer and C. G. Van de Walle, Appl. Phys. Lett. **68**, 1829 (1996).

[12] J. Neugebauer and C. G. Van de Walle, Proc. Mater. Res. Soc. Symp. **395**, 645 (1996).

[13] J. Neugebauer and C. G. Van de Walle, Proc. ICPS-23 (World Scientific, Singapore), p. 2849 (1996).

[14] P. Hohenberg and W. Kohn, Phys. Rev. **136**, B864 (1964); W. Kohn and L. J. Sham, *ibid.* **140**, A1133 (1965).

[15] N. Troullier and J. L. Martins, Phys. Rev. B **43**, 1993 (1991).

[16] S. G. Louie, S. Froyen, and M. L. Cohen, Phys. Rev. B **26**, 1738 (1982).

[17] J. Neugebauer and C. G. Van de Walle, Proc. Mater. Res. Soc. Symp. **339**, 687 (1994).

[18] R. Stumpf and M. Scheffler, Comp. Phys. Commun. **79**, 447 (1994).

[19] J. Neugebauer and C. G. Van de Walle, Proc. Mater. Res. Soc. Symp. **408** (1996).

[20] C. G. Van de Walle, D. B. Laks, G. F. Neumark, and S. T. Pantelides, Phys. Rev. B **47**, 9425 (1993).

[21] J. Neugebauer and C. G. Van de Walle, in Festkörperprobleme/Advances in Solid State Physics, Vol. **35**, ed. R. Helbig (Vieweg, Braunschweig/Wiesbaden), p. 25 (1996).

[22] W. Seifert, R. Franzheld, E. Butter, H. Sobotta, and V. Riede, Cryst. Res. & Technol. **18**, 383 (1983).

[23] B.-C. Chung and M. Gershenzon, J. Appl. Phys. **72**, 651 (1992).

[24] W. Götz, N. M. Johnson, C. Chen, H. Liu, C. Kuo, and W. Imler, Appl. Phys. Lett. **68**, 3114 (1996).

[25] W. Götz , J. Walker, L. T. Romano, and N. M. Johnson, Proc. Mater. Res. Soc. Symp. **449**, 525 (1997).

[26] P. Perlin, T. Suski, H. Teisseyre, M. Leszczyński, I. Grzegory, J. Jun, S. Porowski, P. Boguslawski, J. Bernholc, J. C. Chervin, A. Polian, and T. D. Moustakas, Phys. Rev. Lett. **75**, 296 (1995).

[27] C. Wetzel, T. Suski, J. W. Ager III, W. Walukiewicz, S. Fisher, B. K. Meyer, I. Grzegory, and S. Porowski, Proc. ICPS-23 (World Scientific, Singapore), p. 2929 (1996).

[28] P. Perlin, T. Suski, A. Polian, J. C. Chervin, W. Knap, J. Camassel, I. Grzegory, S. Porowski and J. W. Erickson, Proc. Mater. Res. Soc. Symp. **449**, 519 (1997).

[29] C. Wetzel, W. Walukiewicz, E. E. Haller, J. W. Ager III, I. Grzegory, S. Porowski, and T. Suski, Phys. Rev. B **53**, 1322 (1996).

[30] C. G. Van de Walle (to be published).

[31] D. J. Chadi and K. J. Chang, Phys. Rev. Lett. **61**, 873 (1988).

[32] H. G. Lee, M. Gershenzon, and B. L. Goldenberg, J. Electron. Mat. **20**, 621 (1991).

[33] G.-C. Yi and B. W. Wessels, Appl. Phys. Lett. **69**, 3028 (1996).

[34] C. G. Van de Walle and J. Neugebauer, Proc. Mater. Res. Soc. Symp. **449**, 861 (1997).

[35] B. G. Johnson, P. M. W. Gill, and J. A Pople, J. Chem. Phys. **98**, 5612 (1993).

[36] W. Götz, N. M. Johnson, J. Walker, D. P. Bour, M. D. McCluskey, and E. E. Haller, Appl. Phys. Lett. **68**, 3725 (1996)

[37] C. G. Van de Walle (to be published).

[38] W. Götz, N. M. Johnson, J. Walker, D. P. Bour, and R. A. Street, Appl. Phys. Lett. **68**, 667 (1996).

[39] H. Amano, M. Kito, K. Hiramatsu, and I. Akasaki, Jpn. J. Appl. Phys. **28**, L2112 (1989).

[40] S. Nakamura, N. Iwasa, M. Senoh, and T. Mukai, Jpn. J. Appl. Phys. **31**, 1258 (1992).

[41] C. Johnson, J. Y. Lin, H. X. Jiang, M. A. Khan, and C. J. Sun, Appl. Phys. Lett. **68**, 1808 (1996); J. Z. Li, J. Y. Lin, H. X. Jiang, A. Salvador, A. Botchkarev, and H. Morkoc, *ibid.* **69**, 1474 (1996).

Materials Science Forum Vols. 258-263 (1997) pp. 27-34
© 1997 Trans Tech Publications, Switzerland

A PROGRAMME FOR THE FUTURE?

A M Stoneham

Centre for Materials Research, Department of Physics and Astronomy, University College London, Gower Street, London WC1E 6BT, UK

Keywords: defects, processing, excited states, semiconductors.

Abstract This paper sums up some of the ideas and implications of recent work on defects in semiconductors. The developments are reviewed under the various driving forces in micro-electronics: Ultimate miniaturisation; Ultimate speed; Minimum power for operation; Reliability of the processes producing microelectronic components; Reliability of these components in performance; and the photonics link, *photonics* meaning that which can be done with lasers, optical fibres, etc., whether exploiting intensity, coherence, control of duration, or control of polarisation.

Introduction

We all know that the main driving forces in semiconductor applications have come from microelectronics, and especially from the information technologies and communications. We should be just as clear how fast these changes happen. 25 years ago, the largest computers had a capability similar to a PC. 10 years ago, many people did not even have a PC, none had portables, and few had serious graphics; 5 years ago, there was no World Wide Web. These are not casual examples, nor even unique to the last few years.

The 1860 Pony Express over the Rockies was superseded by the telegraph in the following year. Many 1970 predictions of electronics c.1995. Moore's famous "Law" for the doubling time for the number of devices on a chip is not what it was (12 months in the 1960s, 18 months in the mid 1980s, 24 months in the 1990s, and perhaps 36 months over the next 10 years) but is still very impressive [1]. Nor should one doubt the changes in communications: the Cu of the 1970s (1200 repeaters to span the Atlantic, one every 4km , with 144 Mb/s) was vastly inferior to glass fibres with Er amplifiers (80 repeaters, one every 100km; 10^8 Mb/s). Just as one should not doubt the speed of change, one should not ignore the implications for materials, or for the defects or dopants which control their behaviour.

We can hardly doubt that these developments in microelectronics affect the questions which we should ask about defects in semiconductors, since these defects (in the most general sense) often decide what is possible. Defect control underlies both processing and performance of semiconductor devices. When microelectronics and its applications change, this should impact on what we do, especially if we are training students responsibly for the challenges of the next century. How well is the science and application of defects and defect processes responding to changes in microelectronics?

Technology as a push to new ideas

The semiconductor industry has a Roadmap [2], the industry's best (or, at least, informed) judgements of achievable trends. For example [3], "The rate of new materials adoption is a looming problem ... perhaps four new materials at each of the 0.18m and 0.13m levels ..." The science of

defects in semiconductors should provide the understanding and the capabilities for the industry in the early years of the 21st century. This year's science is the engineering of the next decade. Are we being successful? If not, is that because technology has solved the problems and is getting on with the job? Or is it because we haven't defined the right questions? Even worse, could it be that we aren't smart enough?

If the context is microelectronics, then what are the major issues? This is an open-ended question, but certainly for microelectronics the issues include the following:
- Ultimate miniaturisation;
- Ultimate speed;
- Minimum power for operation;
- Reliability of the processes producing microelectronic components;
- Reliability of these components in performance;
- The photonics link. By *photonics* I mean anything that can be done with lasers, optical fibres, and so on, whether exploiting intensity, coherence, control of duration, or control of polarisation.

The scientific emphasis is different, and rightly so. There are new (or newish) ideas, some of which may lead to major new developments. These might include self-organisation, metastability, recombination-enhanced processes and other non-equilibrium phenomena, a wide range of non-radiative transitions, quantum effects (variously defined), and those features like alloy disorder and the local electric fields which become important for very small region sizes or for nanodots (which need not have high symmetry, contrary to the wishes of many theorists).

Again, it is useful to look back. The science base has brought methods, insights and understanding - how has it been used? One contribution which basic semiconductor science makes is clearly through the scientists and technologists which it trains. Education and skill development are still major contributions from national laboratories as well as universities; moreover, there is a predicted shortage of trained staff in areas of chip manufacture. But what of understanding? Often, the industry uses knowledge to avoid an issue [4]. Who now worries about the impurities which plagued silicon in the 1960s? Who worries about dislocations in standard Si (which are still a challenge for the nitrides or for Si/Ge)? What happened to swirl defects? All these seem to have gone, because technology found a way round the problems. Understanding speeded that solution, and gave confidence that nothing worse was likely, but most of the solution was complete before the science was fully established. So, what of more recent challenges? What has happened to DX and EL2? Mainly, these have been eliminated by restricting the range of compositions used, i.e. by the systematics, rather than the interpretation, of the defects. What about diffusion in silicon, a problem which becoming even more important as device features become smaller (and we must remember that 98% of the microelectronics applications use silicon, not compound semiconductors)? *Despite some excellent work, this particular major issue of semiconductor defect science is neither fully understood nor evident as a major theme in semiconductor studies.* [5] Are these problems too hard for us? Or are they being reported at other meetings?

In the following sections, I shall mention some of the ideas and themes at the present meeting. My aim is to identify issues, rather than to review what could hardly hope to be more than and incomplete and personal survey.

Ultimate Miniaturisation

The theme of miniaturisation takes different forms according to the number of dimensions which are seriously small: dots, lines, and layers show different problems.

Miniaturisation implies replication. Conventional processing looks inadequate for ultimate miniaturisation, and this has stimulated ideas. Eaglesham [5] observes that, by 1999, the critical dimensions in silicon devices will be 90nm, and that this is about the same distance as defects move in the transient enhanced diffusion (TED) which occurs in typical manufacturing processes. He remarks as well that silicon interstitial diffusion rates derived (whether from theory or experiment) differ by many orders of magnitude. The current approaches of extrapolation are not likely to be reliable for the smaller future devices, where lower-energy implantation will be needed. Diffusion-controlled phenomena could well limit future processing developments and device operation. Yet, as noted above, even for one of the most basic defects in the dominant material, we have serious gaps in our knowledge.

Special effects in nanodots Some of the effects are loosely associated with confinement: charge is quantised, so there are single-electron effects; Planck's constant is not zero, so we must remember that electrons are waves. The charge quantisation condition for single-electron devices. For these, electrostatic energies are central, and the radii imply dots of perhaps 10,000-20,000 atoms. The exciton confinement condition for optical switching favours smaller dots, of perhaps 200-500 atoms. Fabrication is daunting by conventional methods. There prove to be many ways of making dots, from biological and chemical to self-assembly. Could self-organisation of nanoscale structures at semiconductor surfaces (plus continued controlled deposition of material) be the answer? Scheffler's discussion [6] suggested one can indeed exploit the elastic energies and their competition with interfacial energies in these highly inhomogeneous systems. The preparative methods emerging will always be opportunistic to some degree, since there are many processes which can compete with self-organisation, and these can be sensitive to details of temperature and deposition rates. Theory is showing the potential to be a quantitative guide.

Once the dots have been created, what do they do which is more than one of the confinement effects mentioned above? They may have excited state instabilities, partly because confinement leads to larger energy localisation, and the surface will often have sites for easy defect generation. This qualitative argument seems to be true in some cases, at least. Caldas [7], in showing this for optically-induced defects in Si:H, also demonstrated how good computer experiments can point to phenomena (like new sorts of relaxed excited states) which were not anticipated. Dots also show novel features because of their surface elastic conditions (no shear stresses for a free dot, for example); this has consequences for exciton dynamics, rather than defect dynamics [8].

Ultrafine lines The scanning probe microscopies are beginning to have impact, and the exploitation of an STM to write on a hydrogen-saturated surface is fascinating. It is less clear whether it will ever provide writing at sufficient speed to offer a new and practical lithography [9]. Self-organisation takes new forms for lines [10] and it will be good to see how these ideas develop.

Thin layers Molecular Beam Epitaxy (MBE) is a mature technology, although with much to be done in the control needed for delta-doping or for alloy strain layers like SiGe. Intrinsic modulation doping was reported for InP [11]; defects in SiGe were surveyed in [12] and [13].

The general issues emerging in all these forms seem to be these. First, elastic energies are important. Stress/strain and fields can drive migration, as well as determining which structure is favoured. Secondly, since strain energies are important, dislocations are a concern. This was

evident in the work on strain-relaxed SiGe strain layers [13]. Dislocation-related states ican result. Thirdly, when one attempts band gap engineering, it is natural to exploit alloys (like SiGe, or AlGaAs). As scales become smaller, so do alloy fluctuations become a problem. Fourthly, low-dimensional systems have instabilities which are not always evident from larger systems. This means that effects often neglected, like quantum effects (including zero point motion) may matter.

Nanodefects If a quantum dot is created, comprising perhaps 200 atoms, will a simple point defect (adatom, vacancy, interstitial) affect the performance? It is clear that a charged defect will affect matters; the electric field will separate the electron and hole of an exciton, and certainly influence recombination. Certain other defects might reasonably be called nanodefects, these being defects on the scale of some of the nano-features (and clearly larger than point defects). Examples illustrate parallels with other nano-phenomena, and include *nanotubes* in GaN [14] and an array of *nanoholes* [15] on an Si surface, showing some degree of self-organisation under an electron beam. Self-organisation in three dimensions under irradiation is well known through the void lattice [16].

Ultimate Speed

Less was said explicitly about enhancing the speed of operation of microelectronic devices. Many possible limits can be recognised: carrier mobility limits, excited state dynamics limits, electron-electron scatter limits, phonon vibration limits, and even excited state coherence limits. High electron velocities imply large mobilities and the largest acceptable electric fields; it was perhaps surprising that little was said about the insulation and dielectric problems implied.

The benefits of modulation doping were noted, including intrinsic modulation doping [11]. One remaining limit on speed comes from remote charged defects, such as those in layers other than that in which carrier transport is occurring [17]. New materials, such as isotopically-engineered Ge, permitted [18] a reassesment of quantitative models for ionised impurity scatter.

Reliable Processing

We cannot ignore economics, either the capital costs of fabrication plants, or the actual process steps (perhaps tens or hundreds of steps). Wafer sizes tend to increase to give similar numbers of devices per process step. Robust processing is crucial. Falster [19] discussed many general aspects of the behaviour of grown-in point defects in CZ-Si and their importance in the 64Mbit era and beyond. Some of the more specific processing topics include the following:

Exploiting hydrogen Hydrogen has many virtues. In GaN [20] it may enhance the Mg solubility, it may compensate, or it may suppress N vacancies in p-GaN. It can act as a passivator in lithography for ultrafine selective oxidation [9] or for putting down ultrafine metal lines. But what can be said with certainty about H in c-Si? 20 years ago, the answer was that it wasn't present, and if it were present, it couldn't be seen. In 1983, we [21] showed that H_2 was significantly more stable than separate H atoms. It gradually became clear that there were alternative competing forms. Recent work suggested that the H_2 molecule had indeed been seen, but with a Raman frequency appropriate for the vaccum, rather than an interstice [22]:. The view emerging seems to be that the moelcules are in voids, rather than interstices, and are assoicated with H platelets, planar aggregates of hydrogen [23].

Worrying about oxygen Oxygen does not share hydrogen's virtues. It is still a major unsolved source of worry in the major semiconductor, Si.. Processing defects, like the thermal

donors, is better documented rather than better understood [24]. In the clustering process, is O_2 a rapid diffuser, or is there a catalytic process related to O_2 speeding interstitial O_i hopping [25]? Oxygen is also a potential problem in GaN, e.g. as a donor if one wants p-GaN.

Status of Fe and other metals The Roadmap [1] demands very tight controls on Fe in the not too distant future. Achieving this needs both a systematic analysis of the tendencey to contamination, gettering, and minority carrier lifetimes for given thermal histories [26]. This analysis identifies the need for progress in the fundamental science of metal adsorption from cleaning solutions. Electrochemistry and associated surface phenomena are again critical.

General points from and beyond the Roadmap Obvious fundamental areas include the importance of surface issues, like metal adsorption, thermal budget issues, possible alternative processes like low-temperature Si epitaxy, and transients: the competition between equilibrium and non-equilibrium process steps. The Roadmap is, of course, not comprehensive, since there will always be new science and unforseen technology. Such topics might include whether or not scanning probe microscopies will develop into tools valued for more than diagnostics. When will it make sense to use scanning probe methods? How could we exploit the "laboratory on a tip"? Applications may be either the scanning probe itself, or in combination with other methods, cf the use of positrons and the STM to characterise defects in highly-doped GaAs:Si, [27] or use of infrared and STM characterisation [28]. Another question might be whether Bose-Einstein condensates ever be useful in lithography? Claims are often made by those with condensates, but do not yet appear credible.

Reliability in Performance

The role in performance ranges from effective passivation to prolonging high-performance lifetime. The improvements on replacing protonic H by D in gate oxides were impressive, allowing reductions in channel lengths by 25% with no performance loss [9] The oxide is not itself a semiconductor, but clearly any charge trapping in the gate oxide affects charge transport in the adjacent semiconductor. Unintended defects, such as defect clusters in Si, also impact on the performance of large area devices [29].

In operating devices, non-radiative transitions are often undesirable. They are usually less rapid in wide-gap materials (radiative transition rates rise as the transition energy rises; non-radiative rates tend to fall, since a greater number of phonons is needed) but more important when they happen, since the enrgy released is greater and can have a bigger effect. Metastable states and alternative charge states are undesirable; enhanced diffusion, by whatever means, is a problem. The itopics in these areas included the degradation of II-VI laser diodes [30], anion-site vacancies as donor and acceptor-like defects [31], and the way that an H plasma affects dislocation motion [32].

Low power operation is an important aim. Moves to lower power operation; heat disposal and temperature control involve the nature of the substrate in heat dissipation, as well as the active components of the device. Reduction in feature sizes affect the heat fluxes and may give opportunities for novel approaches. There is a need for lower dielectric constant insulators for lower power consumption (corresponding to low CV^2f, with C = capacity, V = voltage, and f = frequency; information storage can need the opposit, namely higher dielectric constants). Perhaps the most striking illustration of lower power demands comes from outside the microelectronics area. Nitride light-emitting diodes are already being used in pilot schemes for traffic lights. This

application was achieved without our understanding and preliminary science, which should give us cause for concern.

Radiation damage continues to be both a means of processing (e.g., N implantation into ZnSe [33] and a mechanism for defect generation. Predictions of the evolution of vacancy aggregates [34] suggest that a 6-vacancy in silicon should be especially stable. This defect will surely develop into a vacancy loop at a later stage, and the way in which it evolves should be interesting.

Identifications, analytical approaches and diagnostics

These are the tools which aid the solution of the main challenges. Positron annihilation continues to give valuable results, such as the correlation of positive Ga vacancies in GaN with the yellow luminescence. If these positive vacancies do correspond to removing a Ga+ ion (so they correspond to the so-called V° centres in II-VIs), and if the yellow luminescence is indeed associated with the defect, this cannot be the small polaron type of transition known from absorption experiments in the II-VIs. Scanning probe microscopies have been most successful in conjunction with other methods, largely because STM/AFM methods do not have a good spectroscopy. Optically-detected magnetic resonance and allied methods continue to be a powerful methods in suitable cases, such as the ODMR of as-grown and electron-irradiated GaN and AlN [35] and electrically and optically detected magnetic resonance in GaN-based LEDs [36]

Photonics

Photonics is pushing us to new properties, laser techniques, near-field optics, and so on. Photonics implies electronic excited states. This means that different tools may be needed, especially for theorists. The moves to larger energy gaps (as for nitrides) mean that more energy is localised, and there are more opportunities for the generation or propagation of defects. There are opportunities for some neat defect engineering, and especially for exploitation of Er [37]. Photonics has its own needs for fine-scale structures, here meaning those such as the control of refractive index on the scale of optical wavelengths.

Theory and understanding

Theory works at several levels: to give a framework; to scope an area; to provide an accurate quantitative tool which complements experiment. The large band gaps of nitrides imply important excited state phenomena, as already noted. Methods which cannot tackle these phenomena (even if called a priori or first principles) need to do better. Other developments are making things easier. The smallest units (such as nanodots) are showing more interesting phenomena ($\hbar$ finite, electrons as waves, alloy fluctuations). Fewer atoms should mean more sophisticated theory, and new chances for closer interaction with experiment.

Conclusions

This could be the point to write a programme for the next few years. This I will not do. Surprises are to be enjoyed and exploited, not suppressed. "The man who draws up a programme for the future", wrote Karl Marx [38], "is a reactionary."

1. Dan Rose 1997 Solid State Technology, March 1997 issue p 45.

2. *The National Technology Roadmap for Semiconductors* 1994 SIA Semiconductor Industry Association, 4300 Stevens Creek Boulevard, San Jose, CA 95129, USA.
3. Dave Anderson 1997 Solid State Technology, March 1997 issue p 57
4. L C Kimerling 1991 MRS Bulletin, December 1991 issue, p.42
5. See the special issue of *Physics World* for November 1995, and especially the articles by John Poate (p.15), David Eaglesham (p.41) and Yoshio Nishi (p.25).
6 M Scheffler, 1997 this meeting.
7 M J Caldas, 1997 this meeting.
8 A M Stoneham, 1997, submitted.
9 J Lyding 1997, this meeting
10 N T Bagraev et al, 1997, this meeting.
11 W M Chen et al, 1997, this meeting.
12 P Kringhoj et al, 1997, this meeting.
13 P M Mooney and Kai Shum, 1997, this meeting.
14 Z Lillienthal-Weber et al, 1997, this meeting.
15 S Takeda, 1997, this meeting.
16 A M Stoneham 1975 pps 1121-1235 of "Fundamental Aspects of Radiation Damage" U S ERDA-CONF 751006 (edited M T Robinson and F W Young).
17 D Wasik et al, 1997, this meeting.
18 K M Itoh et al, 1997, this meeting.
19 R Falster, 1997, this meeting.
20 C van der Walle, 1997, this meeting.
21. A M Mainwood and A M Stoneham 1983 Physica **116B** 101-105; A M Mainwood and A M Stoneham 1984 J Phys **C17** 2513
22 M Kitajima, 1997, this meeting.
23 A W R Leitch et al, 1997, this meeting.
24 R Jones (editor) 1996 "Early stages of Oxygen precipitation in Silicon", Dordrecht: Kliewer.
25 S A McQuaid and R Falster, 1997, this meeting.
26 L C Kimerling, 1997, this meeting.
27 J Gebauer et al, 1997, this meeting.
28 R C Newman et al, 1997, this meeting.
29 B L Sopori 1997, this meeting.
30 K Nakano and A Ishibashi 1997, this meeting.
31 J Chadi 1997, this meeting.
32 Y Yamashita et al, 1997, this meeting.
33 K Marbach et al, 1997, this meeting.
34 S Estreicher, 1997, this meeting.
35 G D Watkins et al, 1997, this meeting.
36 W E Carlos and S Nakamura 1997, this meeting.
37 A R Peaker et al 1997, this meeting.
38. Karl Marx, letter to Beesley, in "Marx-Engels Selected Correspondence 1846-1895", translated Dona Torr 1943 London: Lawrence and Wishart; quoted by Alan Mackay 1977 "The Harvest of a Quiet Eye" Bristol: Institute of Physics Publishing.

Materials Science Forum Vols. 258-263 (1997) pp. 35-40
© 1997 Trans Tech Publications, Switzerland

Preceding Page Blank

THE HYDROGEN-SATURATED SELF-INTERSTITIAL IN SILICON AND GERMANIUM

M. Budde[1], B. Bech Nielsen[1], P. Leary[2], J. Goss[2], R. Jones[2], P.R. Briddon[3], S. Öberg[4] and S.J. Breuer[5]

[1]Institute of Physics and Astronomy, University of Aarhus, Denmark
[2]Department of Physics, University of Exeter, UK
[3]Department of Physics, University of Newcastle upon Tyne, UK
[4]Department of Mathematics, University of Luleå, Sweden
[5]Edinburgh Parallel Computing Centre, University of Edinburgh, UK

Keywords: Si, Ge, H, self-interstitial, IR spectroscopy, uniaxial stress, *ab initio* theory

Abstract.
Infrared absorption spectroscopy is used to study H-related point defects in H^+-implanted Si (Si:H) and Ge (Ge:H). The absorption lines at 743.1, 748.0, 1986.5 and 1989.4 cm^{-1} in Si:H and at 700.3, 705.5, 1881.8 and 1883.5 cm^{-1} in Ge:H are shown to originate from the same defect containing two equivalent H atoms. Uniaxial stress experiments show that the defects have monoclinic-II symmetry, and the orientations of the two Si-H or Ge-H bonds are determined. The structure and the local vibrational modes of the self-interstitial binding two H atoms (IH_2) are calculated with LDF cluster theory. The symmetry, bond-orientations and isotopic frequency-shifts calculated for IH_2 are in excellent agreement with those observed for the 743.1-, 748.0-, 1986.5- and 1989.4-cm^{-1} modes in Si:H and for the 700.3-, 705.5-, 1881.8- and 1883.5-cm^{-1} modes in Ge:H.

Introduction.

The vacancy and the self-interstitial are the fundamental intrinsic point defects in crystalline Si and can be produced by irradiation. The vacancy in Si has been studied in great detail [1], and it is one of the best-characterised defects in any crystalline material. In contrast, the self-interstitial in Si has never been observed directly. Instead, the irradiation induces a comparable number of substitutional impurities like B, C, Al or Ga to move into interstitial positions [1]. It is believed that the self-interstitials are mobile during the irradiation process and react with the substitutional impurities to form interstitial impurities [1]. Our present knowledge about the self-interstitial is based on studies of the products of such reactions [1] and on theoretical calculations [2,3,4,5,6]. The theoretical calculations suggest that the neutral self-interstitial has a <110>-split structure as shown in Fig. 1 (a) and that it can trap one or two H atoms [6,7]. The addition of H only moderately (0.66 Å, see ref. [6]) changes the positions of the two central Si atoms. Therefore, an experimental determination of the microstructure of IH_2 will provide a direct check of the credibility of the theoretical structures of the IH_2, IH and I defect sequence.

In Si:H, a series of Si-H stretch-modes are observed in the range 1800-2250 cm^{-1} together with Si-H bend-modes in the range 700-850 cm^{-1}. Of particular interest for this work is the 1980-cm^{-1} mode first observed by Stein at room temperature [8]. Later, this mode has been observed in H-doped Si irradiated with electrons [9], neutrons [10] or γ-rays [11], and it has been found to split into a doublet of lines at 1987 and 1989 cm^{-1} at 10 K [9]. The two lines are always observed with equal relative intensities, independent of production and annealing, and are assigned to the same defect [9,10]. These observations led Xie *et al* [10] to assign the 1987- and 1989-cm^{-1} lines to the vacancy

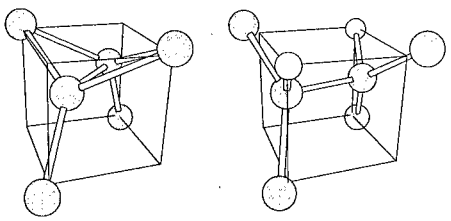


Figure 1. The calculated structure of (a) the self-interstitial and (b) IH_2 in Si [6].

containing two H atoms VH_2. This assignment, however, disagrees with recent work [12], in which absorption lines at 2121 and 2144 cm^{-1} were identified as the Si-H stretch-modes of VH_2. Thus, the origin of the 1987- and 1989-cm^{-1} lines remains unclear.
In this work, four Si-H modes at 743.1, 748.0, 1986.5 and 1989.4 cm^{-1} and four Ge-H modes at 700.3, 705.5, 1881.8 and 1883.5 cm^{-1} are studied. Only the results on the 1986.5- and 1989.4-cm^{-1} stretch-modes in Si:H and on the 1881.8 and 1883.5 cm^{-1} stretch-modes in Ge will be presented in this paper. A full presentation of the work will be published elsewhere [13].
The four modes in each material are shown to originate from the same defect, containing two equivalent H atoms. Uniaxial stress measurements show that the defect has monoclinic-II symmetry, and the orientations of the two Si-H and Ge-H bonds are determined. Based on the experimental evidence, the four Si-H and Ge-H modes are assigned to IH_2 in Si and Ge. The experimental results are compared with the results of *ab initio* calculations on IH_2 in Si and Ge. All calculated properties are in close agreement with those observed.

Experimental.
Samples cut from high-resistivity, Fz, single crystals of Si and Ge were implanted with H^+ and/or D^+ at 30K. The implantations were performed at 50-100 different energies in the range from 680 – 2500 keV for H^+ and 840 – 3000 keV for D^+. The dose at each energy was adjusted in order to result in a uniform concentration of implants of 0.02 or 0.05 at.%. Samples were produced with equal concentrations of H and D in overlapping profiles. After the implantation, the samples were stored at room temperature. The samples for the uniaxial stress measurements were bar-shaped and had dimensions 2×2×10 mm^3. The long sides of the samples were aligned with [100], [111] or [110] directions, and the implantations were performed into one of the 2×10 mm^2 faces.
The infrared absorption measurements were performed at either 10 K or 77 K with a Nicolet, System 800, Fourier-transform spectrometer. The spectral resolution was better than 1 cm^{-1}.

Results and discussion.
The absorption spectra of Si:H and Ge:H are shown in Fig. 2. In Si:H, about 10 sharp absorption lines are observed in the range 700-850 cm^{-1} together with about 20 sharp absorption lines in the range 1800-2250 cm^{-1}. These lines are known to reflect the excitations of H-related local vibrational bend- and stretch-modes, respectively [14]. The lines of particular interest to this work are shown in the in-sets of Fig. 2.
In Ge:H, similar series of lines are observed in the ranges 650-800 cm^{-1} and 1750-2100 cm^{-1} (see Fig. 2), which have been assigned to Ge-H bend-modes and Ge-H stretch-modes [15], respectively. Located approximately in the middle of the stretch-mode range of Ge:H is a doublet of lines at 1881.8 and 1883.5 cm^{-1}. Another doublet of lines at 700.3 and 705.5 cm^{-1} is observed in the bend-mode range. Within 0.3%, the frequencies of the four Ge-H modes scale with the four Si-H modes specified above. The average frequency ratio between the similar Ge-H and Si-H modes is 0.945, which is within the range of ratios 0.896 to 0.965 obtained for similar modes in germane (GeH_4) and silane (SiH_4) [16]. This strongly indicates that the four Si-H and Ge-H modes originate from defects with essentially the same structures in the two materials.
An isochronal annealing sequence was performed in which the samples were annealed for 30 min. at each temperature, starting at room temperature and going up to ~500°C in steps of ~20°C. The absorbance spectrum was measured after each step. The four lines within each set always appear with the same relative intensities, independent of the annealing temperature and of the implanted dose. This strongly suggests that the four lines originate from the same defect. All other lines in Fig. 2 have different annealing behaviours and do, therefore, not originate from this defect. The set of four lines disappear together at ~225°C in Si and at ~200°C in Ge. This difference in annealing temperature of the defect in Si and Ge is comparable to that of the H_2^* defect in the two materials [14,15].

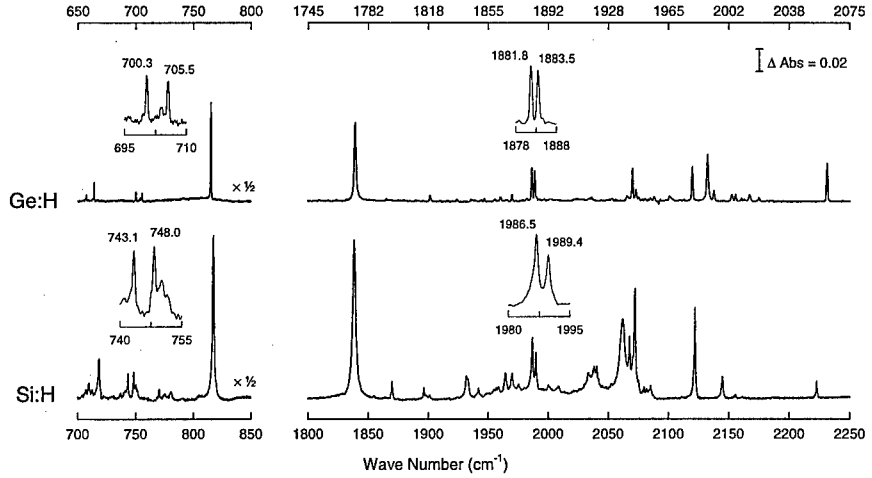


Figure 2. Absorbance spectra of Si:H and Ge:H measured at 10 K. The in-sets show the lines of particular interest to this work.

Spectra measured on Si:H+D are shown in the upper part of Fig. 3. Apart from the lines observed in Si:H or Si:D, three additional lines are observed at 745.7, 1447.3 and 1987.8 cm^{-1}. In Ge also three additional lines are observed at ~703, 1358.4 and 1882.8 cm^{-1}. These three lines in each material have the same annealing behaviours as the six lines in the single-isotope samples and are, therefore, ascribed to the isotopically mixed configurations of the same defect. The observation of only two additional stretch-mode, of which one involves H and the other involves D, indicates that the defect contains two equivalent H atoms.

Both the 1881.8- and 1883.5-cm^{-1} lines in Ge:H split into three components when uniaxial stress is applied along the [100] axis, as shown in Fig. 4. This implies that these absorption lines either correspond to one-dimensional modes of a defect with triclinic, monoclinic-II or orthorhombic-II symmetry [17], or to a two-dimensional mode of a centre with tetragonal symmetry [18]. The presence of two equivalent Ge-H bonds is only compatible with tetragonal and orthorhombic-II symmetries, if the two bonds are aligned with the same <100> axis. This, however, would imply that only one of the two stretch modes is infrared active, in conflict with the observation of two lines of almost equal intensity. Apart from the trivial triclinic symmetry, only monoclinic-II symmetry is in accordance with the splitting for [100] stress and the observation of two stretch-modes. Defects with monoclinic-II symmetry are invariant under the symmetry operations of the C_2 point group with the C_2 axis parallel to a <100> direction. Hence, uniaxial stress applied along any direction different from <100>, will lower the symmetry of the defect to triclinic. Moreover, stress-induced frequency shifts are obtained that are comparable to the splitting of the 1881.8- and 1883.5-cm^{-1} lines without stress. Consequently, uniaxial stress applied along e.g. the [111] direction may induce a mixing of the two Ge-H stretch-modes.

In order to include such second-order effects in the analysis of the response of the modes to uniaxial stress, the vibrational Hamiltonian of the system under stress is

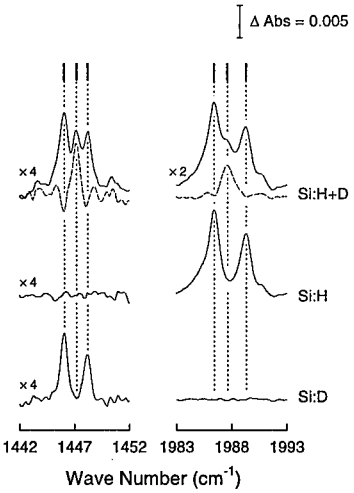


Figure 3. The isotopic shifts for the Si-H stretch-modes. The dotted curve is the Si:H+D spectrum subtracted with the single-isotope spectra.

diagonalised. The vibrational Hamiltonian of the system under stress is defined as the vibrational Hamiltonian at zero stress *plus* the stress-induced change to the potential expanded to first order in the components of the stress tensor. The diagonalisation is performed separately for the ground state and the two (fundamental) singly-excited states, which is justified by the fact that the stress-induced shifts in frequency are three orders of magnitude smaller than the level separation between the ground state and the singly-excited states. The differences between each of the two eigenvalues of the singly-excited states and the eigenvalue of the ground state give the transition frequencies for the excitations that are observed experimentally. The relative intensities of the two transitions depend on the orientations of the induced dipole moments of the two Ge-H bonds. Since the two bonds are equivalent and interrelated through the C_2 rotation, only the orientation of the induced dipole moment for one of the bonds needs to be specified with respect to the C_2 axis. This is done with a polar angle θ and an azimuthal angle φ, where θ is the smallest positive angle between the bond dipole moment and the C_2 axis, and φ is the smallest angle between a {100} plane and the plane spanned by the induced bond dipole moment and the C_2 axis. Then, the angle θ can be obtained from the relative intensities of the two absorption lines observed without stress.

The angle φ can be determined from the absorption profile observed with uniaxial stress. The profiles of the two absorption lines observed without stress are nearly Gaussian and have equal width. We assume that the two lines remain Gaussian and that the widths are unaltered when stress is applied. For a given orientation of the defect, the shifts in position and amplitude of the two Gaussians due to the uniaxial stress are calculated from the theory described above. The overall theoretical absorption profile at a given strength and direction of the uniaxial is a superposition of the profiles for each of the 24 different orientations of the defect. Using the positions, widths and relative intensities of the two lines observed at zero stress, we are left with seven parameters $\mathcal{A}_1$, $\mathcal{A}_2$, $\mathcal{A}_3$, $\mathcal{A}_4$, $\mathcal{B}_1$, $\mathcal{B}_2$ and φ which describe the theoretical absorption profile under uniaxial stress for any polarisation (ε) of the infrared light. The parameters $\mathcal{A}_i$ and $\mathcal{B}_j$ represent the influence of the stress tensor on the vibrational levels and are treated as fitting parameters. The theoretical profiles are fitted to the profiles observed at the maximum stresses along [100], [111] and [110], with the light polarised parallel and perpendicular to the stress direction. The theoretical frequency shifts and absorption profiles corresponding to the best fit are shown together with the experimental data in Fig. 4. The theoretical results are in excellent agreement with the observations. The angles

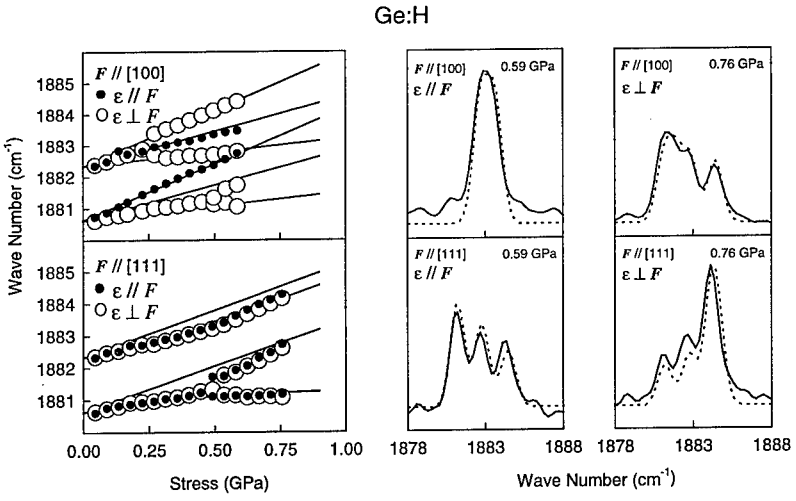


Figure 4. Frequency shifts and absorption profiles for the Ge-H lines at 1881.8 and 1883.5 cm^{-1} under [100] and [111] stress. The solid lines in the left figure and the dotted lines in the middle and right figure are the best-fit theoretical results for a monoclinic-II centre.

that specify the orientations of the induced bond dipole moments are $\theta = 45° \pm 1°$ and $\varphi = 3° \pm 5°$ for the two Ge-H stretch-modes. For a stretch-mode, we expect the induced bond dipole moment to be along the bond and, hence, the angles θ and φ obtained also specify the directions of the two Ge-H bonds. The θ and φ values show that the two Ge-H bonds are nearly aligned with [011] and [0$\bar{1}$1] for a defect with the C_2 axis along [001].

We have not been able to study the stress-response of the Ge:H lines at 700.3 and 705.5 cm^{-1}, as these lines are below the detection limit in the uniaxial stress experiments.

The Si-H lines at 743.1, 748.0, 1986.5 and 1989.4 cm^{-1} are less sensitive to uniaxial stress than the Ge-H lines discussed above. At 77 K none of the four lines are observed to split into three components for stress along [100]. Even at liquid He temperature, where the width of the absorption lines is reduced, a splitting into three components is observed only for the 748.0-cm^{-1} line. The observed responses of the four Si-H lines to uniaxial stress are, however, fully consistent with that of a centre with monoclinic-II symmetry and an angle φ close to zero. The polar angle in Si is $\theta = 48° \pm 1°$.

The experiments strongly suggest that the 743.1-, 748.0-, 1986.5- and 1989.4-cm^{-1} lines in Si:H and the 700.3-, 705.5-, 1881.8- and 1883.5-cm^{-1} lines in Ge:H reflect the same type of defect in the two materials. The defect contains two equivalent H atoms and has monoclinic-II symmetry. The bond directions are given by the angles $\varphi = 3° \pm 5°$ and $\theta = 45° \pm 1°$ in Ge and $\theta = 48° \pm 1°$ in Si. The φ angle could not be determined accurately in Si, but since all the other data suggest that the defects essentially are identical, we expect this angle to be close to zero, which is fully consistent with the data. Theoretical calculations have shown that the IH_2 defect in Si has monoclinic-II symmetry, and the Si-H bond directions are given by $\varphi = 9°$ and $\theta = 46°$ [6]. We conclude that the set of four absorption lines observed in both in Si and Ge originate from the IH_2 defect.

Calculations.

To provide further support to the assignments made in the previous section, the structure and local vibrational modes of IH_2 in Si and Ge are calculated with *ab initio* theory.

The *ab initio* calculations are performed with the LDF cluster method AIMPRO [19]. One host atom and two H atoms are added to a tetrahedral 71-atom Si or Ge cluster terminated with 60 H atoms. The self-consistent energy and the forces on the atoms are calculated, and all 72 host atoms and 2 H atoms at the defect core are allowed to relax until the minimum energy configuration is obtained. The H atoms at the surface are fixed during this procedure. The second derivatives of the energy between the 8 central atoms are calculated directly, while the derivatives between the remaining atoms are found from a Musgrave Pople potential given previously [19]. Then, the dynamical matrix of the cluster is constructed, and the local vibrational modes along with their isotope shifts are calculated.

The structure of the ground state configuration of IH_2 in both Si and Ge is very similar to those given previously in Si [6,7] (see Fig. 1(b)). The calculated local vibrational mode frequencies of IH_2, IHD and ID_2 are presented in Table I. Compared to the observed frequencies, the calculated stretch-mode frequencies are 8% too high in Si and 9% too high in Ge. Such deviations are typical for the theoretical method, and may be ascribed to the overbinding caused by density-functional theory and to anharmonic effects. In both Si and Ge, the theory predicts that for the stretch-modes,

	Mode	Frequency (cm^{-1})		
		IH2	*ID₂*	*IHD*
Si	*symmetric*	2144.7 (1989.4)	1540.2 (1448.2)	2143.8 (1987.6)
	asymmetric	2142.9 (1986.5)	1539.9 (1446.1)	1540.1 (1447.3)
Ge	*symmetric*	2056.7 (1883.5)	1462.5 (1359.0)	2055.1 (1882.8)
	asymmetric	2053.3 (1881.8)	1460.1 (1357.6)	1461.3 (1358.4)

Table I. The calculated stretch-mode frequencies of IH_2, ID_2 and IHD in Si and Ge. The observed frequencies are given in parentheses.

the *symmetric* mode has higher frequency than the *asymmetric* mode, in agreement with our observations. Moreover, the small splittings of the two stretch-modes of IH_2 and ID_2 are roughly reproduced by the calculations (see Table I). The calculated stretch-frequencies of *IHD* deviate by less than 0.1 cm^{-1} from the average frequency of the two stretch-modes of IH_2 and ID_2. Hence, the calculated isotopic shifts for the stretch-modes are in excellent agreement with experiment. The Si-H bond directions of IH_2 are given by $\theta = 46°$ and $\varphi = 10°$, and the Ge-H bond directions by $\theta = 46°$ and $\varphi = 8°$. These values are in excellent agreement with the experimental results of $\theta = 48° \pm 1°$ in Si and $\theta = 45° \pm 1°$ and $\varphi = 3° \pm 5°$ in Ge, and strongly support our assignments.

Acknowledgements.
This work was supported by the Danish National Research Foundation through Aarhus Center for Advanced Physics (ACAP). We thank the HPCI for an allocation of computer time on the Cray T3D at Edinburgh and the SP2 at Daresbury. S.Ö. thanks NFR and TFR in Sweden for financial support and also PDC at KTH for computer time on the SP2.

References.

[1] G.D. Watkins, in *Materials Science and Technology* Vol 4, edited by W. Schröter (VCH, Weinheim, 1991).
[2] Y. Bar-Yam and J.D. Joannopoulos, Phys. Rev. Lett. **52**, 1129 (1984).
[3] R. Car, P.J. Kelly, A. Oshiyama and S.T. Pantelides, Phys. Rev. Lett. **54**, 360 (1985).
[4] P.E. Blöchl, E. Smargiassi, R. Car, D.B. Laks, W. Andreoni and S.T. Pantelides, Phys. Rev. Lett. **70**, 2435 (1993).
[5] D.J. Chadi, Phys. Rev. B **46**, 9400 (1992).
[6] C.G. Van de Walle and J. Neugebauer, Phys. Rev B **52**, R14320 (1995).
[7] P. Deák, L.C. Snyder, M. Heinrich, C.R. Ortiz and J.W. Corbett, Physica B **170**, 253 (1991).
[8] H.J. Stein, J. Electronic Mat. **4**, 150 (1975).
[9] T.S. Shi, G.R. Bai, M.W. Qi and J.K. Zhou, Mater. Sci Forum **10-12**, 597 (1986).
[10] L.M. Xie, M.W. Qi and J.M. Chen, J.Phys.: Condens. Matter **3**, 8519 (1991).
[11] Y.C. Du, Y.F. Chang, X.T. Meng and H.Y. Sheng, Sci. Sin. A, **30**, 176 (1987) (in Chinese).
[12] B. Bech Nielsen, L. Hoffmann, M. Budde, R. Jones, J. Goss and S. Öberg, in *Defect in Semiconductors 18*, Vols. 196-201 of Materials Science Forum, edited by M. Suezawa and H. Katayama-Yoshida (Trans-Tech, Aedermannsdorf, Switzerland, 1995) p. 933.
[13] M. Budde, B. Bech Nielsen, P. Leary, J. Goss, R. Jones, P.R. Briddon, S. Öberg and S.J. Breuer, submitted to Phys. Rev. B
[14] See e.g. J.D. Holbech, B. Bech Nielsen, R. Jones, P. Sitch and S. Öberg, Phys. Rev. Lett **71**, 975 (1993).
[15] M. Budde, B. Bech Nielsen, R. Jones, J. Goss and S. Öberg, Phys. Rev. B, (1996).
[16] *American Institute of Physics Handbook*, 3rd ed. edited by D.W.E. Gray (McGraw-Hill, New York, 1972), p. 7-189.
[17] A.A. Kaplyanskii, Opt. Spectrosk. **16**, 557 (1964) [Opt. Spectrosk. (USSR) **16**, 1031(1964)].
[18] A.E. Hughes and W.A. Runciman; Proc. Phys. Soc. London, **90**, 827 (1967).
[19] R. Jones, Phil. Trans. Roy. Soc. London Ser. A **341**, 351 (1992).

Materials Science Forum Vols. 258-263 (1997) pp. 41-46
© 1997 Trans Tech Publications, Switzerland

MATRIX-INDUCED ISOTOPE SHIFT OF A VIBRATIONAL MODE OF INTERSTITIAL OXYGEN IN GERMANIUM

B. Pajot[1], E. Artacho[2], L. I. Khirunenko[3], K. Itoh[4] and E. E. Haller[5]
[1]GPS, tour 23, Université D. Diderot, 2 place Jussieu, 75251 Paris cedex 05, FRANCE
[2]Instituto Nicolás Cabrera and Departamento de Física de la Materia Condensada, C-III Universidad Autónoma de Madrid, 28049 Madrid, SPAIN
[3]Institute of Physics, NASU, Prospect Nauki 46, 252650 Kiev 22, UKRAINE
[4]Department of Applied Physics and Physico-Informatics, Keio University, 3-14-1 Hiyoshi Kohoku-ku, Yokohama 223, JAPAN
[5]Lawrence Berkeley Laboratory and University of California, Berkeley, CA 94720, USA

Keywords : monoisotopic Ge, oxygen, IR spectroscopy, local modes, phonon coupling

Abstract. Under high-resolution, the asymmetric mode of Ge_2O in germanium shows Ge isotope shifts related to Ge mass or to anharmonicity changes. We present here evidence of very small shifts between the position of lines in natural Ge and in quasi-monoisotopic Ge which are related to the change of the average mass of the matrix and we propose an explanation for this.

Introduction.

Natural Ge (average mass 72.60 amu) contains isotopes ^{70}Ge, ^{72}Ge, ^{73}Ge, ^{74}Ge and ^{76}Ge, with relative abundances of 0.205, 0.274, 0.078, 0.365 and 0.078, respectively. Doping with oxygen introduces isolated interstitial O (O_i) bonded to two nearest Ge neighbours. The Ge-O-Ge bridge has an apex angle near 140° and from a Ge-O bond-length of 0.17 nm, the Ge···Ge distance is estimated to be 0.29 nm compared to a normal value of 0.245 nm. The O_i vibrations in germanium produce a broad IR mode at 856 cm^{-1} and a weaker (and still broader) feature at 1260 cm^{-1} (room temperature) [1]. The former is attributed to the antisymmetric motion (ν_3 or A_{2u} mode) of the Ge-O-Ge unit combined with internal rotation of the O atom and the latter to a combination of the ν_3 mode with a symmetric motion of the same unit. These vibrational modes are comparable, *mutatis mutandis*, to some of the modes observed in silicon containing dispersed oxygen [2]. Near liquid helium temperature (LHeT) and under high spectral resolution, the ν_3 mode splits into an apparently complicated structure, made of about 25 sharp lines. This is due to the isotopic shifts (ISs) from natural Ge combined with resolved internal rotation of O about the Ge···Ge axis [3].
In the early 1990's, isotopically-enriched Ge crystals became available for physical investigations and the O_i spectrum in these materials at LHeT showed a simplification of the vibrational structure because some isotopic combinations were absent or at least greatly reduced in intensity [4,5].
We present and discuss the results of absorption measurements of the ν_3 mode performed at LHeT and at room temperature with appropriate resolutions in natural and quasi-monoisotopic (qmi) Ge samples. The measurements allow an accurate measurement of different Ge ISs. They also show the role of the interaction of the lattice phonons with the ν_3 mode, responsible for small frequency changes of the same modes in qmi and in natural Ge.

Results and discussion.

Absorption measurements have been performed at 1.6, 6 and 295 K using a BOMEM DA3$^+$ Fourier-transform spectrometer (FTS) using either a Si bolometer operated at 4.2 K or a MCT detector at 77 K. The LHeT spectra were obtained using the maximum apodised resolution (0.013 cm^{-1}) of the FTS and the room temperature spectra with a resolution of 1 or 2 cm^{-1}. Natural Ge:O samples were grown at Métallurgie Hoboken Overpelt, Belgium (now Union Minière) and another natural Ge sample was diffused with oxygen at the University of Paderborn (Germany). Ge:O samples enriched with isotopes ^{70}Ge, ^{73}Ge, ^{74}Ge or ^{76}Ge at concentrations between 88 and 95% were grown at the University of Kiev and at the Lawrence Berkeley Laboratory

The vibration-rotation structure of the ν_3 mode

Near 10 K, four vibration-rotation lines, labelled I, II, III and IV in order of decreasing energy, are associated with each isotopic Ge_2O combination [4]. They are sharp, with full width at half maximum (FWHM) near 0.04 cm^{-1} (line IV is a little bit broader (~0.06 cm^{-1})). These lines are due to some kind of vibration-rotation of O_i and in a spectroscopic description, they can be taken as $\Delta N = 1$, $\Delta J = 0$ transitions with $J = 0$ for line I. The low-energy rotational transitions have been directly observed near 1 K by phonon spectroscopy [6]. With ^{16}O, the initial states of lines II, III and IV are separated from the ground state by 1.5, 5.4 and 11 cm^{-1}, respectively [5,6]. This explains why at temperatures normally achieved with standard optical cryostats ($\geq$ 1.3 K or 0.9 cm^{-1}), lines I and II are always observed together. Lines III and IV require higher temperatures to be detected and line III is barely seen below 2 K.

From this, it could be inferred that the ν_3 mode could be resolved into 60 lines in natural Ge at 6 K. This is not the case, however, because:

1) line IV is weak and hard to detect in natural Ge (it was first observed in qmi Ge [4])

2) combinations with the same average mass (AM) of the Ge atoms, but different isotopes, like $^{72}Ge_2O$ and $^{70}GeO^{74}Ge$, vibrate at very close frequencies so that they are difficult to resolve or sometimes even to detect because of their small intensity. This limits the number of lines partially or totally resolved observed in natural Ge at 6 K to about 25. At 1.6 K, because of the depopulation of the levels, the situation still simplifies as only lines I and II are observed for each combination.

The Ge isotopic shift

The relation between the AMs and the G-O-Ge isotope combination is given in Table 1. This Table shows that there are eleven distinct AMs and that eight of them correspond to a single combination.

Table 1. 1) Correspondence between the AMs, the isotopic combinations and their contributions to the total normalised intensity in natural Ge and 2) comparison between Ge ISs for line I in natural Ge at LHeT with the calculated ones (^{16}O). The reference is $^{76}Ge_2O$ (AM 76) and the experimental uncertainty is ± 0.004 cm^{-1}. The position of line I($^{76}Ge_2O$) is 860.962 cm^{-1}.

AM	Ge combination	Contribution	IS_I (cm^{-1}) (observed)	IS (cm^{-1}) (calculated)
70	70-70	0.0420	2.961	3.918
71	70-72	0.1120	2.439	3.230
71.5	70-73	0.0320	2.190	2.902
72	72-72 + 70-74	0.2251		
	(72-72)	(0.0751)		
	(70-74)	(0.1500)		
72.5	72-73	0.0427	1.668	2.210
73	73-73 + 72-74 + 70-76	0.2379		
	(73-73)	(0.0060)		
	(72-74)	(0.2000)		
	(70-76)	(0.0319)		
73.5	73-74	0.0569	1.179	1.558
74	74-74 + 72-76	0.1757		
	(74-74)	(0.1330)		
	(72-76)	(0.0427)		
74.5	73-76	0.0122	0.712	0.943
75	74-76	0.0569	0.468	0.619
76	76-76	0.0060	-	-

The ISs of these eight combinations for lines I and II can thus be measured without interference. The shifts of line I with respect to ^{76}Ge are given in Table 1 for natural Ge, but these shifts are practically independent of the line considered. The measured ISs of Table 1 are systematically higher than those deduced from the data of [5] by 0.01 to 0.02 cm^{-1}. This comes from the fact that in ref. 5, the value of $I(^{76}Ge_2O)$, measured in a qmi ^{76}Ge sample, is higher by 0.015 cm^{-1} than the value measured in natural Ge. This difference will be discussed later. By comparison, when taking $I(^{76}GeO^{74}Ge)$ at 861.430 cm^{-1} as a reference, the ISs in natural Ge and those from ref. 5 agree within 0.003 cm^{-1}.

The frequencies of the antisymmetric mode for the different AMs have been calculated by first principles calculations as in [2]. The values obtained by this calculation are reasonably close to the ones observed: for $^{70}Ge_2O$, a value of 877.7 cm^{-1} is obtained, to be compared to 863.90 and 857.1 cm^{-1} measured at LHeT (line I) and 295 K, respectively. The ISs deduced from these calculations (last column of Table 1) are about 30% larger than the observed ones. Semi-empirical determinations of the ISs have also been obtained considering a puckered Ge-O-Ge pseudo-molecule [3,5]. A fit of the ISs is obtained by adjusting the value of the apex angle 2α of Ge-O-Ge and an interaction mass m' representing the interaction between the pseudo molecule and the crystal [3]. A good fit is obtained for $2\alpha = 140°$ and m' = 11.6 amu. This value of the apex angle is the same as obtained from the calculation of first-principles potential wells [2]. The fitting values of ref. 5 ($2\alpha = 111°$ and m' = 23.1 amu) give a difference of 0.02 cm^{-1} between the observed and fitted shift for the $^{70}Ge_2O$ and $^{76}Ge_2O$ combinations in natural Ge and this could be related to the choice of the frequency of $^{76}Ge_2O$ in the ^{76}Ge qmi sample.

At room temperature, the Ge ISs can only be measured by comparing the peak absorption in different qmi Ge samples. The comparison is possible with the LHeT values only for the "pure" combinations (two Ge atoms alike). The shift between qmi ^{70}Ge and qmi ^{76}Ge at 295 K is 3 cm^{-1}, very close to the LHeT value of 2.96 cm^{-1}.

Table 1 shows that AMs 72, 73 and 74 correspond each to two, three and two configurations, respectively, but the table shows also that the contribution of $^{73}Ge_2O$ (73-73) is negligible with respect to (72-74) and (70-76) in natural Ge. However, two configurations with the same AM do not vibrate exactly at the same frequency because of symmetry and anharmonicity differences, and under high-resolution, lines corresponding to different combinations with the same AM can be partially resolved, as shown in Fig. 1. A fit of the spectrum with the components expected shows that for a

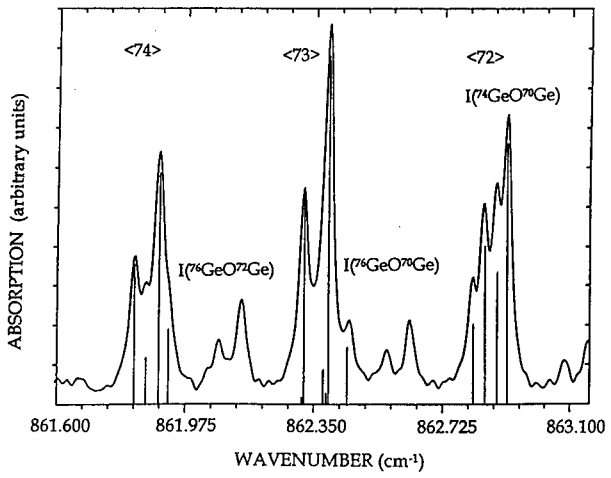


Figure 1: Detail of the ν_3 absorption in natural Ge at 1.6 K The bars scale the measured intensity of the $^{70}Ge_2O$ doublet by the respective contributions (Table 1) of the different doublets with AMs 72, 73 and 74. The components I and II of the doublets are ~ 0.07 cm^{-1} apart and the intensity ratio I/II is 1.64.

given AM, the most symmetric combination has the lowest frequency. Realistic calculation [2] of the frequencies of combinations with the same AMs has been performed whose results agree well with the observation, as shown in Table 2, taken from [2]. Lines due to combinations not observed in

Table 2. Comparison of the observed isotopes shifts IS(I) and IS(II) for lines I and II due to different GeOGe isotopes combinations with the same Ge average mass with the calculated ones [2]

	<Ge>	IS(I) Obs. (cm^{-1})	IS(II) Obs. (cm^{-1})	Calcul. (cm^{-1})
$^{72}GeO^{74}Ge$ - $^{73}Ge_2O$	73	0.006	-	0.010
$^{72}GeO^{76}Ge$ - $^{74}Ge_2O$	74	0.031	0.032	0.040
$^{70}GeO^{74}Ge$ - $^{72}Ge_2O$	72	0.033	0.032	0.044
$^{70}GeO^{76}Ge$ - $^{72}GeO^{74}Ge$	73	0.063	-	0.084

natural Ge can be measured accurately in qmi samples (^{73}Ge samples, for instance). However comparison of frequencies obtained with qmi and natural Ge samples must be used with care in the determination of these symmetry-induced shifts because of possible interferences with Ge matrix-induced shifts to be discussed later.

The frequencies of lines I and II for the most intense combinations of $Ge_2{}^{18}O$ have been measured in ref. 5. The corresponding shifts are slightly larger than the ones with ^{16}O: the experimental differences between the (I($^{70}Ge_2O$)-I($^{76}GeO^{74}Ge$)) ISs for ^{18}O and ^{16}O is 0.17 cm^{-1} while the calculation yields a difference of 0.19 cm^{-1}, in good agreement with the experiment. As for ^{16}O, here again the calculated frequencies are reasonably close to the observed ones.

Matrix-induced line shifts

In qmi ^{76}Ge, the frequencies of the Ge_2O lines at LHeT are found to be systematically larger than in natural Ge by ~ 0.010-0.015 cm^{-1} (the $^{76}Ge_2O$ frequencies measured in the ^{76}Ge qmi samples are in good agreement with those reported in ref. 5). This shift is small indeed, but reproducible for the different qmi ^{76}Ge samples investigated. It is shown in Figure 2 for the $^{76}GeO^{74}Ge$ doublet. It is difficult to measure a reliable shift for qmi ^{74}Ge because the accuracy on the $^{74}Ge_2O$ frequencies in

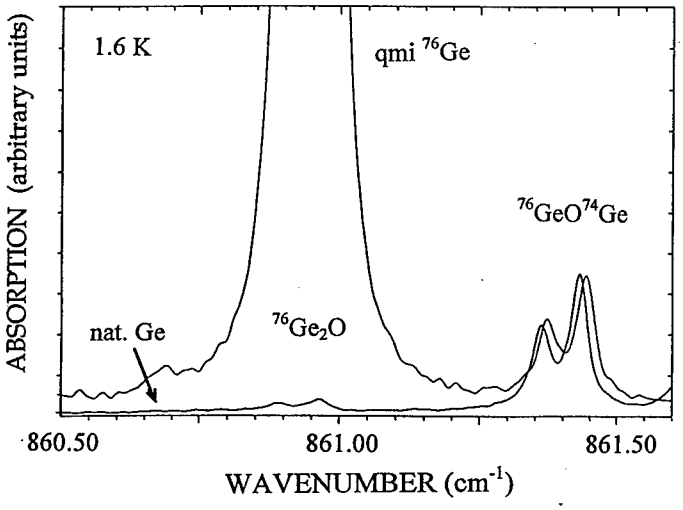


Figure 2: Low-energy part of the ν_3 absorption in natural Ge, superimposed on the absorption of qmi ^{76}Ge containing 9.2% ^{74}Ge showing the shift of the doublet of the $^{76}GeO^{74}Ge$ combination, observed in both samples. Note the weak $^{76}Ge_2O$ doublet in natural Ge. One abscissa division is 0.05 cm^{-1}.

natural Ge is not as good because of the interference with $^{76}GeO^{72}Ge$ with AM 74, but a small positive shift (~0.05 cm^{-1}) was found for $^{74}GeO^{76}Ge$ in qmi ^{74}Ge. The comparison with qmi ^{70}Ge and natural Ge could be made only on line III of $^{70}Ge_2O$ at 1.6 K because lines I and II were too intense in this qmi ^{70}Ge sample, and with $^{70}GeO^{72}Ge$. For both combinations, a negative shift ~ 0.01 cm^{-1} was measured. If we keep the concept of an interaction mass between the pseudo-molecule and the

surrounding lattice to fit the ISs, the observation can be translated into saying that the interaction is weaker (respectively larger) with ^{76}Ge (respectively ^{70}Ge).

The ν_3 mode is superimposed on the 3-phonon continuum of the germanium lattice [7]. Part of this spectrum is shown for natural Ge at 295 K in Figure 3, with a bar at the position of the ν_3 mode, on the high-energy side of the maximum due to a 3TO combined DOS. A possible qualitative explanation of the above result can be found by assuming that, at LHeT, the O_i lines are broadened by interaction with the 3-phonon continuum of germanium. This interaction must be small in order to

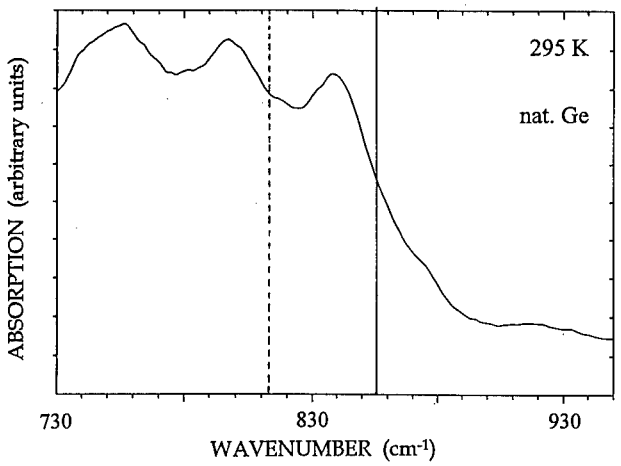


Figure 3: Absorption of the Ge lattice in the 3-phonon region at 295 K. The solid bar shows the position of $\nu_3(^{16}O)$ and the dashed one the position of $\nu_3(^{18}O)$.

account for the widths observed and it is related to the combined density of states (DOS) of the lattice phonons. We argue that this coupling produces also a shift of the lines depending on the value of the DOS on which the lines are superimposed. Near LHeT, this DOS is about 2.3 times less intense than at room temperature and it is shifted toward higher energies by about 10 cm^{-1} but this shift is nearly compensated by the corresponding high-frequency shift of the ν_3 mode. The point is that the value of the DOS at a given frequency is not the same in ^{76}Ge, in natural Ge and in ^{70}Ge. At a given frequency, when natural Ge is replaced by ^{76}Ge, the DOS becomes the same as at a frequency about 25 cm^{-1} higher in natural germanium [8,9]. This means that in this case, the interaction of the ν_3 modes with the lattice will be somewhat smaller in ^{76}Ge than in natural Ge and it should produce a positive shift of the line as well as a reduction of the linewidth. The experimental results do show a relative increase of the frequencies of the lines by $\sim 1.2 \times 10^{-5}$ in ^{76}Ge compared to natural Ge, but a reduction of the line width is impossible to detect. The same argument, but inverted, should hold for ^{70}Ge to explain the negative shift of the ν_3 modes: the positive shift of the DOS with respect to natural Ge would increase the interaction of the ν_3 modes with the lattice, hence decreasing the frequencies. The absolute order of magnitude of the observed shifts is the same for ^{70}Ge and ^{76}Ge, but this point cannot be discussed significantly now. In qmi ^{73}Ge, only a comparison of the ^{73}GeO^{72}Ge lines with those in natural Ge is possible and no shift is observed.

The lattice constant of crystals depends on the isotopic composition [10,11]. This can be related to the effect of the anharmonicity on the vibration amplitude of the atoms, which shows that the heavier the atom, the smaller the amplitude of vibration. The lattice constant of ^{76}Ge is smaller than that of natural Ge and an extrapolation of the results of the lattice constant measurements of ^{74}Ge crystals [10] to ^{76}Ge gives a relative decrease of the lattice parameter of about 4×10^{-5} with respect to natural Ge at LHeT. This decrease should produce the equivalent of a hydrostatic stress on the Ge-O-Ge quasi-molecule. An estimation of this stress considering the reduction of the lattice constant as the resulting strain is about 10 MPa. The hydrostatic piezospectroscopic coefficient of ν_3 is positive in both silicon and GaAs [12] and presumably in germanium. The hydrostatic piezospectroscopic coefficient of ν_3 in germanium has not yet been determined, but if we take the

same value as in GaAs (0.2 cm^{-1}/GPa [13]), we deduce a positive shift of the lines in ^{76}Ge crystals five times smaller than the observed value. Hence, it seems that the change of the lattice constant in qmi materials contributes only to a fraction of the line shift reported here.

Conclusion

The matrix-induced shifts reported here can be due to the difference between the amplitude of the 3-phonon DOS in qmi Ge and in natural Ge, combined with the effect of compression or dilatation stress on the O_i centre due to changes of the lattice constants between qmi and natural Ge. The $\nu_3(^{18}O)$ mode occurs in a spectral region where the 3-phonon DOS is flatter so that a smaller difference between qmi ^{76}Ge or ^{70}Ge and natural Ge due to the first effect is expected. A difference comparable to that for $\nu_3(^{16}O)$ would indicate that the effect of stress is predominant. Other matrix-induced line shifts have also been observed in the rotational spectra by phonon spectroscopy [14]. These shifts, which show an influence of the surrounding matrix are larger (typically 0.1 cm^{-1}) and inverse of the ones reported here. Stress effects are usually much larger on electronic transitions than on vibrational modes and they are probably involved in the shift of the N3 centre in diamond between $^{13}C_{dia}$ and natural diamond [15].

Acknowledgements

We acknowledge fruitful discussions with K. Laßmann. This work has been supported by the European Community (INTAS), the DGICYT of Spain and U.S. National Science Foundation.

REFERENCES

1. W. Kaiser, J. Phys. Chem. Solids **23**, 255 (1962).
2. E. Artacho, F. Ynduráin, B. Pajot, R. Ramírez, C. P. Herrero, L. I. Khirunenko, K. M. Itoh and E. E. Haller, Phys. Rev. **B56**, 15 August 1997.
3. B. Pajot and P. Clauws in Proc. 18th International Conference on the Physics of Semiconductors, ed. O. Engström (World Scientific, Singapore, 1987) pp. 911-914.
4. L. I. Khirunenko, V. I. Shakostov, V. K. Shinkarenko and F. M. Vorobkalo, Fiz. Tekh. Poluprovodn. **24**, 401 (1990) (Sov. Phys. Semicond. **24**, 663 (1990).
5. A. J. Mayur, M. D. Sciacca, M. K. Udo, A. K. Ramdas, K. Itoh, J. Wolk and E. E. Haller, Phys. Rev. **B49**, 16293 (1994).
6. M. Gienger, M. Glaser and K. Laßmann, Solid State Commun. **89**, 285 (1993).
7. S. J. Fray, F. A. Johnson, J. E. Quarrington and N. Williams, Proc. Phys. Soc. **85**, 153 (1965).
8. H. D. Fuchs, C. H. Grein, C. Thomsen, M. Cardona, W. L. Hansen, E. E. Haller and K. Itoh, Phys. Rev. **B43**, 4835 (1991).
9. M. Cardona, P. Etchegoin, H. D. Fuchs and P. Molinàs-Mata, J. Phys.: Condens. Matter **5**, A61 (1993).
10. R. C. Buschert, A. E. Merlini, S. Pace, S. Rodriguez and M. H. Grimsditch, Phys. Rev. **B38**, 5219 (1988).
11. P. Pavone and S. Baroni, Solid State Commun. **90**, 295 (1994).
12. D. R. Bosomworth, W. Hayes, A. R. L. Spray and G. D. Watkins, Proc. Roy. Soc. **A317**, 133 (1970).
13. C. Song, B. Pajot and C. Porte, Phys. Rev. **B41**, 12330 (1990).
14. N. Aichele, U. Gommel, K. Laßmann, F. Maier, F. Zeller, E. E. Haller, K. M. Itoh, L. I. Khirunenko, V. Shakovtsov, B. Pajot, E. Fogarassy and H. Mussig, this conference.
15. G. Davies, I. Kiflawi, G. Sittas and H. Kanda, this conference.

Materials Science Forum Vols. 258-263 (1997) pp. 47-52
© 1997 Trans Tech Publications, Switzerland

ISOTOPIC SHIFTS OF THE ROTATIONAL STATES OF INTERSTITIAL OXYGEN IN GERMANIUM

N. Aichele[1], U. Gommel[1], K. Laßmann[1], F. Maier[1], F. Zeller[1], E.E. Haller[2], K.M. Itoh[3], L.I. Khirunenko[4], V. Shakhovtsov[4*], B. Pajot[5], E. Fogarassy[6], and H. Müssig[7]

[1]Universität Stuttgart, 1. Physikalisches Institut, Pfaffenwaldring 57, D–70550 Stuttgart, GERMANY

[2]Lawrence Berkeley National Laboratory and University of California, Berkeley, CA 94720 USA

[3]Department of Applied Physics and Physico–Informatics, Keio University, 3-14-1, Hiyoshi, Kohoku–ku, Yokohama 223, JAPAN

[4]Institute of Physics of Ukrainian National Academy of Sciences, Prospect Nauki 46, 252650 Kiev–22, UKRAINE

[5]Groupe de Physique des Solides, Tour 23, Université Denis Diderot, 2 place Jussieu, F–75251 Paris Cedex 05, FRANCE

[6]CNRS, Laboratoire PHASE, 23 rue du Loess, F–67037 Strasbourg Cedex 2

[7]United Monolithic Semiconductors GmbH, Wilhelm–Runge–Str. 11, D–89081 Ulm, GERMANY

*deceased

Keywords: Ge:O, isotope shift, phonon spectroscopy

Abstract. By phonon spectroscopy we find in isotopically enriched Ge:O_i crystals Ge–isotope associated shifts of the rotational resonances that are larger than compatible with the linewidth in natural Ge if only the rotation of the quasi–free Ge_2O molecule is considered. Because of the reduced isotope scattering of the phonons in the enriched Ge the position of higher excited states could be determined. This may improve the estimate of the height of the axial potential barrier.

Introduction

A series of phonon scattering resonances between .18 meV and 4.08 meV has been found in Ge:O that can be associated with rotational states $E_l = [\hbar^2 / 2 \cdot I] \cdot l^2$; $(l = 0, \pm1, \pm2, ...)$ of interstitial oxygen up to $l = \pm5$ [1]. I is the momentum of inertia of the rotating entity. The state $l = \pm3$ is split by .28 meV into states $3^{\downarrow}$ and $3^{\uparrow}$ by perturbation of the angular potential ditch from the neighbouring Ge–tripods. It follows that the axial barrier against radial oscillation in the $_{Ge}/^{O}\backslash_{Ge}$ complex must be distinctly higher and the radial distance of the potential minimum determining the rotation larger than for Si:O_i. There the much higher transition energies, starting with 3.63 meV to the first excited state, are compatible with a nearly stretched configuration with small I [2, 3]. For rigid rotation of a free $_{Ge}/^{O}\backslash_{Ge}$ quasi–molecule around its inertial axis parallel to <111> one would have $I = \mu \cdot R^2$, where $\mu = m \cdot q/(1+q)$ with $q = 2M/m$ is the reduced mass made up by the germanium masses $2M$ and the oxygen mass m and R the distance of the oxygen from the Ge–Ge axis. From the fit to the resonance energies this would lead to $R = 93$ pm (as compared to 22 pm in Si) and to small Ge–isotope shifts within the observed linewidth.

Such an estimate disregards the fact that the quasi–molecule is tied to the surrounding lattice and its motion. To unravel the relative contributions of O, its nearest Ge neighbours, and the lattice to the motional states of the complex, it should be helpful to determine the O– and Ge–related isotope shifts of the resonances. The determination of the latter shifts requires isotopically enriched, quasi–monoisotopic (qmi) Ge crystals. An additional advantage of such crystals is the reduced isotope scattering of high–frequency phonons, which could allow the observation of resonant states at energies higher than in natural Ge (^{n}Ge). The knowledge of

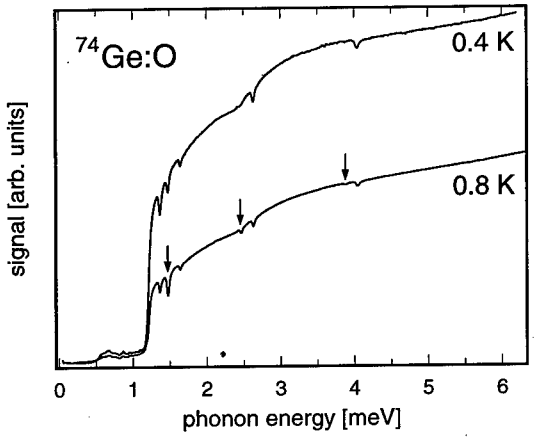


Figure 1: Phonon transmission spectra above 1.18 meV (Sn–detector threshold) of the ^{74}Ge–enriched sample. At the lower bath temperature of .4 K the signal is higher due to the increased detector sensitivity. The transitions (↓) from the thermally populated first excited state at .18 meV increase with temperature. All lines are shifted downward in energy as compared to ^{n}Ge. Doublets around 4.6 meV and 5.6 meV are not visible with this sensitivity.

the position of higher excited states should improve an estimate of the height of the central barrier.

We report on such measurements which show that the Ge–associated shifts are distinctly larger and the ^{18}O–associated shift is smaller than calculated with the above free–molecule assumption. The Ge–associated shifts are even larger than compatible with an isotope–induced inhomogeneous linewidth of the resonances in natural germanium if one assumes that only the nearest Ge–neighbours contribute to the shifts. This indicates some average coupling of the lattice to these low–energy excitations.

In addition, a higher resonance around 5.8 meV (position depending on Ge–isotope) is observed which probably belongs to the rotational state $l = \pm 6$. A weak further resonance near 4.75 meV is possibly associated with a transition to the first excited radial state. If so, this could mean a central barrier of about 12 meV.

Experimental

One ^{74}Ge:O sample (87.7% enrichment, $[O_i] = 6.7 \cdot 10^{21}\,m^{-3}$) was Czochralski–grown at the University of Kiev [4], three other samples:
^{76}Ge:O [$\approx$ 89.1%, $\approx 5 \cdot 10^{22}\,m^{-3}$], ^{73}Ge:O [96.7%, $5.5 \cdot 10^{22}\,m^{-3}$], ^{70}Ge:O [95.7%, $15 \cdot 10^{22}\,m^{-3}$], were grown by the vertical Bridgman method at the Lawrence Berkeley National Laboratory

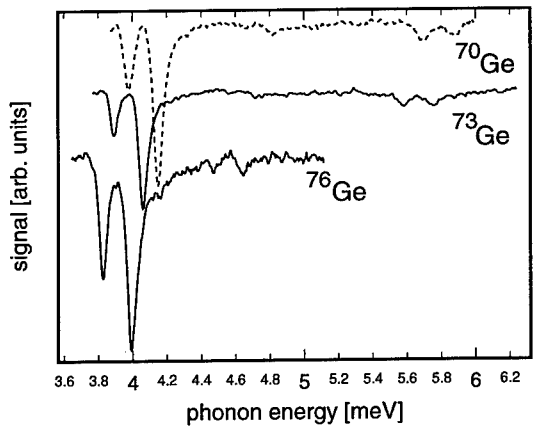


Figure 2: Transmission spectrum (baseline subtracted) at higher energies through Ge:O_i enriched by the isotopes 70, 73, and 76. The doublets around 4 meV belong to $l = \pm 5$ [1] and those around 5.8 meV possibly to $l = \pm 6$ of the ground state series. (The ^{76}Ge spectrum ends where the critical current of this specific emitter junction is reached.) The weak doublets around 4.7 meV could be due to transitions to the first excited radial state.

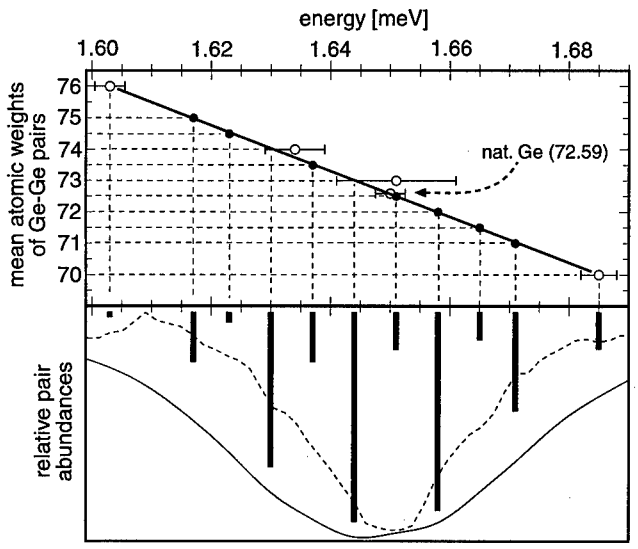


Figure 3: Position of the transition $l = 0$ to $l = 3^{\uparrow}$ for various Ge–isotopes. The position in ^{n}Ge fits well with its average mass into the linear interpolation. Lower part: Superposition of the various resonances (approximated by Lorentzians with linewidth 25 μeV) according to the relative abundances of the possible Ge–pair combinations in ^{n}Ge. The resultant effective linewidth is distinctly larger than the experimental linewidth in ^{n}Ge at low oxygen concentration (broken line).

[5]. The oxygen contents and the isotopic enrichments were determined by high resolution IR–spectroscopy from the integrated and relative intensity of the isotopic components of the oxygen absorption in the 860 cm^{-1}–band [6].

Whereas in Si at higher oxygen concentrations the natural ^{18}O content is detectable by phonon spectroscopy [7, 8] this will be difficult in Ge since the resonances are broader and they overlap where they are strong. To the best of our knowledge, the only Ge material reported in literature as being doped in the bulk with ^{18}O [9] is no longer available. With germanium oxide being volatile, doping in the bulk with ^{18}O by diffusion is problematic. Doping in a surface layer turned out to be feasible by either implantation or by laser–melting of the surface in an oxygen ambient. The implantation/annealing parameters were quite similar to those used for the investigation of oxygen implantation to produce isolating GaAs layers [10]. The parameters for laser–doping may as yet not be optimized; O_i was detected only by IR.

Tunnelling junctions were prepared by evaporation and oxidization of Al– and Sn–films for phonon emitters and detectors, respectively. Temperature was varied between about .4 K and 1.2 K in a ^{3}He–bath cryostat to determine the temperature dependence of the linewidth and to distinguish transitions starting from thermally occupied levels. Due to repeated phonon scattering at higher oxygen concentrations the apparent linewidths of the resonances will be larger than the true linewidths. At lower oxygen concentrations the reduced signal–to–noise ratio resulted in larger error bars of at most $\pm 8\,\mu$eV which can be improved by increased measuring times.

Results

Figure 1 shows a phonon transmission spectrum of the ^{74}Ge enriched sample (low $[O_i]$) above the threshold of the Sn–detector (1.18 meV). Transitions from the ground state to the rotational states $l = 3^{\downarrow}$ and $3^{\uparrow}$, ± 4, ± 5 can be discerned in this diagram. The lines marked by an arrow belong to transitions starting from $l = \pm 1$ and therefore decrease with decreasing temperature. All line positions are shifted to lower energies than in ^{n}Ge. The linewidth of the transitions from the ground state (about 30 μeV) do not noticeably change with temperature, i.e., lifetime broadening does not significantly contribute to the measured linewidth. In a sample of ^{n}Ge with similar oxygen content the linewidth is somewhat broader, namely about 35 μeV. So, possibly

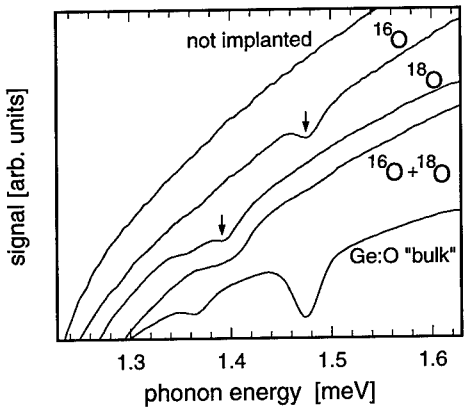


Figure 4: Transmission spectra of non-implanted, ^{16}O–, ^{18}O–, and (^{16}O + ^{18}O)–co–implanted Ge in the range around the $l = \pm 1$ to $l = 3^{\uparrow}$ transition ($\downarrow$). The origin of the satellite in the ^{18}O–implanted sample is not clear. The resonances in the co–implanted sample are broadened possibly by the higher dose applied. The measured oxygen isotopic ratio (1.06) of the resonance frequency is smaller than expected (1.125) if oxygen alone would rotate.

there is an additional broadening mechanism, be it by larger internal strains in this specific sample or by Ge–isotopic shifts in ^{n}Ge in general.

Ge–isotopic shifts are found in all the qmi samples. This is shown in Fig. 2 specifically for the high–energy part of the spectrum where the shifts are larger than at lower energies. This figure also shows weak doublets at about 4.8 meV, previously found in a thin sample of ^{n}Ge [7, 8], and another transition at about 5.8 meV detected only in the qmi samples because of the reduced isotope scattering. The average mass dependence is quite accurately represented by a linear fit as shown in Fig. 3 for the $l = 0$ to $l = 3^{\uparrow}$ transition. This linear interpolation allows to predict hypothetical line positions and intensities for the 15 combinations which should occur if the line in natural Ge is inhomogeneously broadened by a superposition of the lines due to the different isotopic combinations. The resultant inhomogeneous line shape for natural Ge is distinctly broader than the experimental one (Fig. 3).

Though ^{18}O–doping by implantation or laser–melting was only in a surface layer of less than 1μm it could be detected by IR absorption in both cases whereas by phonon spectroscopy only in the implanted layer and only the strongest transition $l = \pm 1$ to $l = 3^{\uparrow}$ was detected (Fig. 4). If only the oxygen would rotate a value of $E/E' = m'/m = 18/16 = 1.125$ would be expected in the rigid rotator approximation whereas the observed ratio is only 1.06. This again suggests an accompanying motion of the Ge–neighbours in the rotation.

Discussion

The existence of a Ge isotope shift connected with the hindered rotation of O_i could be expected for appropriate displacement r of the Ge–Ge axis from the rotation axis (see also [12]): $I = 2 \cdot Mr^2 + m(R+r)^2 = m \cdot R^2[g^2q + (1+g)^2]$, where $g = r/R$ is positive or negative for co– or counter–rotation of the Ge, respectively.

The corresponding ratio for the variation with M for given m is $E/E' = [(G+q')/(G+q)]$, where $G = [(1+g)/g]^2$, assuming $g \neq 0$ and not to depend on the isotopic mass. The observed ratios of 1.02 and 0.98 for ^{73}Ge v. ^{70}Ge and ^{73}Ge v. ^{76}Ge, respectively, can be approximated by $g = 0.46$ and $g = 0.49$ or $g = -0.24$ and $g = -0.25$, respectively. For these values of g one obtains for the oxygen isotopic ratio nearly identical values around 1.063 very close to the experimental value of 1.06. (1.097 would be expected for rotation around the axis of inertia of the Ge_2O–molecule.) For ^{70}Ge one would then obtain $R = 43$ pm and $r = 19$ pm for co–rotation and $R = 83$ pm $r = -20$ pm for counter–rotation.

Large values of $|r|$ should imply a large lattice interaction. It is suggestive to include an effective interaction mass by replacing M by $M(1+x)$ in the case of monoisotopic Ge. Its inclusion will also help to reduce r. The effect is, however, only small: Taking e.g. x as large as 0.8 a good fit to the O– and Ge–isotopic shifts is obtained for g = 0.30 as well for g = -0.19, i.e. for co– and

counter–rotation.
The consistency of numbers could be fortuitous: Assuming that g and x are independent of the isotopic masses does not lead to a compatible set of equations for the determination of these parameters. The value of x = .8 taken here is also rather large as compared to x ≈ .16 obtained in ^{n}Ge [6] or to x ≈ .31 obtained in qmi Ge [11] for the isotope dependence of the antisymmetric ν_3 mode where Ge inherently participates in the high frequency motion of the Ge_2O complex. Besides, both values of g appear to be rather large in view of the fact that the angular hindering potential amplitude of the rotating entity reflecting the symmetry of the neighbouring tripods is only .28 meV [1]. On the other hand, a large lattice interaction could reconcile the observed linewidth of the resonances in ^{n}Ge by some averaging: If only the immediate Ge neighbours would determine the shifts then the superposition of the various isotopic shifts according to the abundances of the possible Ge-pair combinations would lead to too large a linewidth in ^{n}Ge as evident from Fig. 3. It might be helpful, therefore, to separate the contributions by determining the line shapes of the resonances in an oxygen–doped 50%/50% ^{76}Ge/^{70}Ge–crystal.
A contribution of the lattice might be mediated via anharmonic coupling to higher modes of the complex. Coupling between the low–energy rotational states and the ν_3 mode is evident and well known from the fine structure of the 860 cm^{-1} band which has been investigated in recent years by high–resolution IR techniques revealing isotopic shifts of the band for the various Ge–isotopic pair combinations in ^{n}Ge as well as in isotopically enriched crystals [6, 4, 11, 12]. Also for this band differences have been observed for corresponding isotopic shifts in natural and qmi germanium [12, 13] that have been ascribed to coupling with lattice phonons.
A Ge–isotopic shift depending on the average lattice mass does not necessarily include a Ge–rotation: E.g. the isotope dependence of the lattice constant via anharmonicity in the zero–point motion could in principle change the rotator potential. The effect seems, however, to be too small by about two orders of magnitude if one argues as follows: The measured relative change of the ^{74}Ge/^{n}Ge lattice constants is about $-15 \cdot 10^{-6}$ at low temperatures [15]. The measured shift of the 2.66 meV resonance under <111>–uniaxial stress is -.8 meV/GPa [1]. If we translate the stress via the elastic constant into a macroscopic strain and assume this to be equivalent to the change in lattice constant then we obtain a shift of only .3 μeV as compared to the 40 μeV measured.
Regarding the interpretation of the observed higher resonances one possible explanation is obtained from a fit to the level scheme calculated with a model potential by Yamada–Kaneta et al. [3]. In this case the level at 4.74 meV in ^{n}Ge is due to the transition to the first excited 2D radial state and the line near 5.8 meV the transition to the rotational state $l = \pm 6$ of the ground state series. In this scheme one would expect the $l = \pm 1$ state of the excited radial series near 5.1 meV. Its observation may be difficult if the phonon transition probability is small. (See [14] for a discussion of phonon interaction in the case of Si:O_i.) From the fit within this model one would obtain ≈12 meV for the height of the axial barrier.
A good fit to the experimental data is also possible in terms of a non–rigid rotator model with a harmonic potential taking into account the centrifugal distortion [12] as was similarly done in the case of Si:O_i [2]. From this fit the next rotational level $l = \pm 6$ is also expected near 5.7 meV but the first excited radial level at about 9.2 meV. A correspondingly large central barrier of about 236 meV is reported [12] to result from first–principles total–energy calculations. A help for the interpretation of the observed levels at 4.75 meV and 5.8 meV may come from additional measurements: Whereas under <111>–uniaxial stress the ground rotational states decrease in energy by the increased momentum of inertia there should be an increase for the first excited radial state series by an increase of the axial barrier. Also, FIR transitions to these states might be measureable in absorption, or, more indirectly, by photon/phonon sequential transitions.
In conclusion we find that by the investigation of the low–lying resonant states in oxygen–doped qmi germanium with phonon spectroscopy (PS) substantial new information has been obtained that may help to obtain an improved understanding of the dynamics of interstitial oxygen in

germanium. Relevant additional data regarding the coupling of these states to the lattice and the assignment of the observed higher resonances are expected from FIR or combined FIR/PS absorption, from the growth of oxygen–doped Ge–isotopic mixtures, and from the stress dependence of the level positions.

Acknowledgement
Helpful discussions with E. Artacho, Madrid, W. Eisenmenger, Stuttgart, H. Yamada–Kaneta, Kawasaki, and financial support from the European Community (INTAS) and the Deutsche Forschungsgemeinschaft are gratefully acknowledged.

References

[1] M. Gienger, M. Glaser, and K. Laßmann, Sol. St. Comm. **86**, 285 (1993)

[2] D. R. Bosomworth, W. Hayes, A. R. L. Spray and G. D. Watkins, Proc. Roy. Soc. Lond. A **317** 133 (1970)

[3] H. Yamada–Kaneta, C. Kaneta, and T. Ogawa, Phys. Rev. **B 42** 42(15), 9650 (1990)

[4] L. I. Khirunenko, V. I. Shakhovtsov, V. K. Shinkarenko, and F. M. Vorobkalo, Sov. Phys. Semicond. **24** 663 (1990)

[5] K. Itoh, W.L. Hansen, E.E. Haller, J.W. Farmer, V.I. Ozhogin, A. Rudnev, A. Tikhorimov, J. Mat. Res. **8** 1341 (1993)

[6] B. Pajot and P. Clauws, Proc. of the 18th Int. Conf. on Phys. of Semic., Stockholm 1986, ed. by O. Lindström, World Scientific, Singapore, Vol. 2, 911 (1987)

[7] K. Laßmann, Mat. Sci. Forum **196–201** 1563 (1995), Proc. of the 18th Int. Conf. on Defects in Semiconductors, Sendai 1995, M. Suezawa, H. Katayama–Yoshida, eds.

[8] K. Laßmann, Proc. of PHONONS 95, Sapporo, 1995, Physica B **219&220**, 730 (1996)

[9] R.E. Whan, Phys. Rev. **140A** 690 (1965)

[10] H. Müssig, C. Wölk, H. Brugger, Inst. Phys. Conf. Ser. **136** 529 (1993)

[11] A.J. Mayur, M. Dean Sciacca, M.K. Rudo, A.K. Ramdas, K. Itoh, J. Wolk, and E.E. Haller, Phys. Rev. **B49** 16293 (1994)

[12] E. Artacho, F. Ynduráin, B. Pajot, R. Ramírez, C.P. Herrero, L.I. Khirunenko, K.M. Itoh, E.E. Haller, Phys. Rev. **B56**, No 7, 15 Aug. 1997

[13] B. Pajot, E. Artacho, L.I. Khirunenko, K.M. Itoh, E.E. Haller, these Proceedings

[14] H. Yamada–Kaneta, these Proceedings

[15] R.C. Buschert, A.E. Merlini, S. Pace, S. Rodriguez, M.H. Grimsditch, Phys. Rev. **B38** 5219 (1988)

Materials Science Forum Vols. 258-263 (1997) pp. 53-58
© 1997 Trans Tech Publications, Switzerland

DLTS COMBINED WITH PERTURBED ANGULAR CORRELATION (PAC) ON RADIOACTIVE ^{111}In ATOMS IN Ge

Ch. Zistl[1], R. Sielemann[1], H. Hässlein[1], S. Gall[1], D. Bräunig[1], J. Bollmann[2]
[1]Hahn-Meitner-Institut Berlin, Glienicker Str. 100, D-14109 Berlin, Germany
[2]Humboldt Universität Berlin, Invalidenstr. 110, D-10115 Berlin, Germany

Keywords: germanium, In-, Cd-impurities, In-vacancy pairs, DLTS, PAC-technique.

Abstract. We have combined two different techniques to study deep level defects in Germanium on a microscopic scale: Deep Level Transient Spectroscopy (DLTS) and Perturbed Angular Correlation (PAC). The combining element is the use of radioactive probe atoms on which both techniques are focused. For this purpose radioactive ^{111}In atoms are implanted in Ge subsequently prepared as Schottky contact. During the decay to ^{111}Cd DLTS is measured repeatedly. A level at E_V+0.15 eV ***increasing*** in concentration according to the lifetime of ^{111}In can be assigned to the daughter atom ^{111}Cd. In a further series of experiments additional electron irradiation is performed on the ^{111}In-doped samples and the DLTS again is measured repeatedly. A new level at E_V+0.33 eV is detected which ***decreases*** with the ^{111}In lifetime. In the course of the DLTS measurements PAC was measured on the same samples. From those spectra the trapping of a defect at the ^{111}In probes can be deduced characterized by a quadrupole interaction frequency ν_Q=52 MHz. Since this is the only defect component seen in the PAC spectra (except for the substitutional component), we identify this component with the defect seen by DLTS. In former PAC measurements we have identified the trapped defect as a neutral monovacancy. From this correspondence we assign a ^{111}In-V pair to the decreasing DLTS level.

Introduction.

Deep Level Transient Spectroscopy (DLTS) is an important, well established method to study deep centers in semiconductors [1]. A weakness of this method, however, is that DLTS does not contain information on the chemical nature and microscopic structure of the observed defects. This deficiency makes it difficult to correlate DLTS with structural sensitive methods like, e.g., Electron Paramagnetic Resonance (EPR). In recent developments it was shown that chemical information may be added by applying DLTS to radioactive impurity atoms [2,3]. The decay of unstable elements then may lead to a decrease or increase of a measured DLTS signal depending on whether a decay or a formation of a certain deep level is observed, see Fig.1. Even more complex situations may be observable like the formation of a pair consisting of two radioactive atoms [4]. A common situation in defect physics is the interaction of impurity atoms with intrinsic defects. As an example, dopant atoms might interact with intrinsic defects like vacancies and self-interstitials thereby changing the free carrier concentration from the value of the dopant concentration. In such a case one would like to have a structure sensitive technique to correlate with DLTS in order to arrive at an atomistic understanding of the observed effects.

In the following we report on experiments to exemplify such a correlation. For this purpose we perform DLTS on radioactive impurities which at the same time serve as probe atoms for the Perturbed Angular Correlation technique (PAC). Two types of experiments are performed: in the first the decay of radioactive ^{111}In to ^{111}Cd is monitored by repeated DLTS scans in the course of the decay. In this experiment one expects to observe the increase of a signal due to the emerging ^{111}Cd deep level originating from the DLTS-invisible shallow ^{111}In level. In the second type the

^{111}In doped samples are additionally electron irradiated to produce single Frenkel pairs, i.e., vacancies and self-interstitials. Formation of pairs with the ^{111}In atoms may then lead to additional deep levels, either directly in form of ^{111}In-defect pairs or following the transmutation in form of ^{111}Cd-related defects.

In addition we perform PAC experiments on the same samples. PAC is a radioactive probe technique which is sensitive to the immediate neighborhood of the probes on an atomic scale. If pair formation between the ^{111}In probe and a defect occurs an electric field gradient is induced at the probe leading to a nuclear quadrupole interaction measured on the $5/2^+$ state of the ^{111}Cd daughter nucleus by means of a γ-γ perturbed angular correlation experiment (PAC). A recent review of this technique is given in [5].

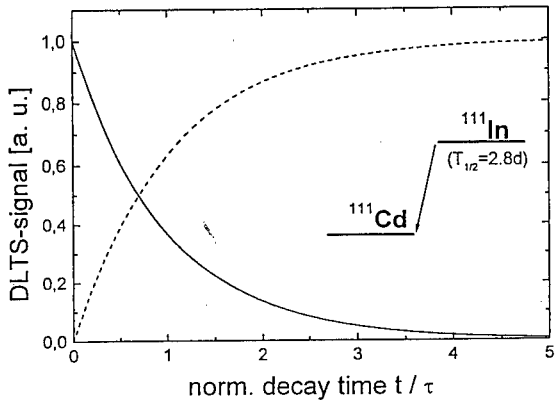


Fig. 1: Principle of decreasing (related to ^{111}In) and increasing (related to ^{111}Cd) DLTS signal versus decay mean-life of the ^{111}In activity.

Experimental.

Ge crystals (p(Ga)-type) with doping concentrations of $2\cdot10^{15}$ cm^{-3} were implanted with the well known PAC probe nucleus ^{111}In ($T_{1/2}$ = 2.8 d). The implantation was performed with a recoil implantation technique [6] which results in a rather uniformly implanted zone of 4 μm thickness. The concentration of radioactive probe atoms amounts from about $1\cdot10^{13}$ cm^{-3} to $2\cdot10^{14}$ cm^{-3} depending on the implantation condition chosen and is small compared to the initial doping concentration. Following the probe implantation an annealing in a sealed capsule under low Ar pressure at 600°C is performed to remove the implantation damage and to electrically activate the probe atoms. Subsequently Schottky contacts including the radioactive probes were prepared by evaporating Al after proper sample treatment. DLTS measurements were performed for a variety of samples either with or without additional electron irradiation (electron energy = 1.2 MeV; typical fluences $1\cdot10^{15}$ cm^{-2} to $2\cdot10^{16}$ cm^{-2}) .The samples without electron irradiation are also used to monitor the implantation process showing that unwanted impurities amount to at most the concentration of the ^{111}In probe atoms. In additional experiments also inactive impurities were implanted for a broader view on the impurity and/or irradiation aspects [7]. In this paper we will mainly concentrate on the ^{111}In implanted samples and the comparison with the related PAC. The PAC experiments were performed alternating with the DLTS scans on the same probes over a span dictated by the lifetime of ^{111}In.

Results and Discussion.

Figure 2 shows DLTS spectra of a sample implanted with ^{111}In and subsequent annealing without additional electron irradiation. The spectra were taken at various times during the decay of the ^{111}In activity. The time zero was taken at the end of the implantation. There is a strong level at approximately 90 K the intensity of which grows with increasing time. A second level at

approximately 115 K is always present in our spectra but has no time dependence in its intensity. It is related to our implantation conditions. Figure 3 shows the peak height of the 9o K level as function of the decay time . This time-dependent height was fitted with a function

$$N(t) = N_0 + N_1 (1 - \exp(-t/\tau)). \quad (1)$$

In this formula τ is the radioactive decay meanlife, N_1 is the saturation value of the peak height for long times and N_0 is a possible intensity already present at the beginning of the measurement. The solid line is a fit with the meanlife of ^{111}In = 98 h. The good fit with this parameter shows, that the level emerging at 9o K must be ascribed to a deep level associated with ^{111}Cd. The intensity N_0 is zero within the accuracy of our measurement showing on the one hand that no stable Cd is produced during the implantation (along with the ^{111}In intensity) and that the small fraction which has already decayed from ^{111}In during implantation is not detectable. The saturation value N_1 deduced from the fit and converted with the background doping concentration to a ^{111}Cd concentration is $2.5 \cdot 10^{13}$ cm^{-3}. This number agrees quite well with our estimation of the implanted ^{111}In activity. We note, however, that no correction has been made to this number for a possible inhomogeneous implantation profile which might result in an estimated error of at most 30%.

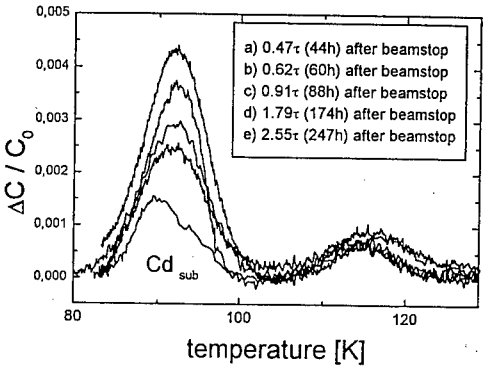


Fig. 2: DLTS signals for radioactive ^{111}In in Ge measured at various times during the decay to ^{111}Cd (time increasing from bottom to top (a - e)).

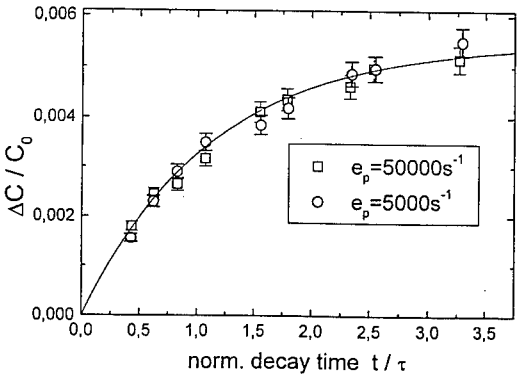


Fig. 3: DLTS peak height of the 90 K level of Fig. 2 as function of the ^{111}In decay time. Different symbols correspond to different rate windows.

Since ^{111}In is a shallow acceptor in Ge one expects it to occupy a substitutional lattice site. Any recoil energies involved in the ß-decay to ^{111}Cd (< 1eV mostly due to the emission of a neutrino) are small compared to the displacement energy in Ge (about 20 eV), hence for the daughter ^{111}Cd also a substitutional site (which is corroborated by our PAC results) is expected acting as a double acceptor. Concerning the electronic properties an Arrhenius plot of the 90 K level extracted from DLTS measurements with varying rate windows was produced which yields a level energy $E_{Cd} = E_V + 0.15(1)$ eV. From the measured lower limit of the hole trapping cross section

Coulomb attraction can be deduced showing that the level must be an acceptor. Since the first acceptor level is expected very close to the valence band [8] and we observe only one level we assign our level to the second acceptor level, $Cd^{2-/-}$.

In further experiments the ^{111}In implanted samples were additionally electron irradiated with a fluence of $1 \cdot 10^{16}$ cm^{-2}. Subsequently a DLTS spectrum was measured, displayed in Fig. 4. A rough survey shows that the spectrum contains 4 peaks. We give here a short assignment of these peaks obtained from a large variety of supporting experiments [7]. The peak at 90 K is due to the Cd level obtained in the decay of ^{111}In as presented above which in addition has a component at almost the same temperature which is produced by the additional electron irradiation. The peak at about 120 K is also due to the additional electron irradiation. The small peak at about 165 K is a small byproduct of the ^{111}In implantation procedure. The large peak at 210 K is the most interesting in this context: it is strong at the beginning of the successive DLTS measurements and then decays with the meanlife of the ^{111}In activity according to:

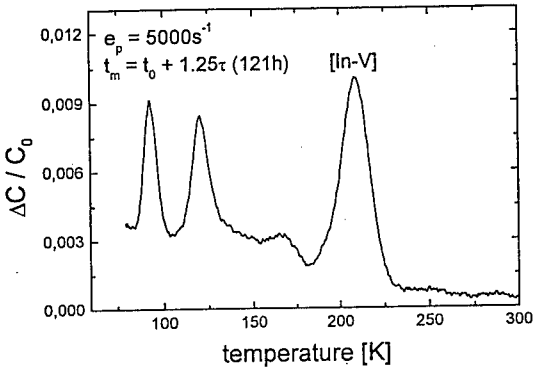


Fig. 4: DLTS signals of ^{111}In doped and electron irradiated Ge. Spectrum taken at 121 h after ^{111}In implantation.

$$N(t) = N_0 \exp(-t/\tau). \qquad (2)$$

The levels at 120K and 165K, respectively, do not show peak height variations in the successive measurements. In Fig. 5 we have plotted the peak height of the 210K level as function of the delay time after the implantation procedure. A fit according to (2) yields a lifetime of 98 h showing that the decaying deep level is associated with a radioactive ^{111}In atom. The initial concentration of the active ^{111}In-complex (N_0) evaluated from the capacity change and the background doping concentration is $10(3) \cdot 10^{13}$ cm^{-3}. An evaluation of the level energy from an Arrhenius plot yields E_V +0.33(1) eV.

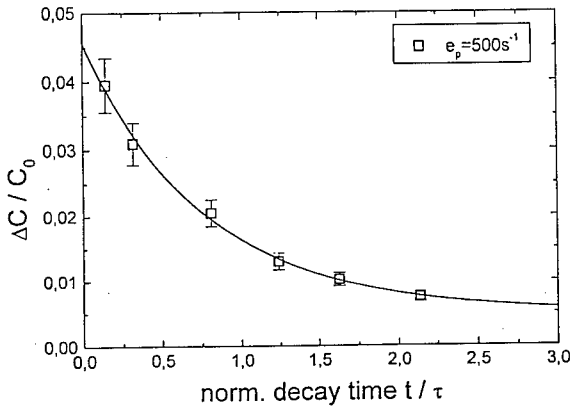


Fig. 5: Peak heights of the ^{111}In-V signal (from Fig. 4 versus decay time. The curve represents a fit of Eq. 2.

In general the interpretation of DLTS spectra of samples containing impurity atoms and subjected to additional electron irradiation is to a certain degree speculative due to the above

mentioned insensitivity with respect to the chemical identity and the structure of the defects involved. In the experiments discussed so far chemical sensitivity could be obtained for the levels associated with the radioactive In. To study the intrinsic defects in Ge and their interaction with the shallow acceptor In in more detail we have been applying the microscopically sensitive PAC technique in a variety of experimental situations [9,10]. The recent progress of this work is presented at this conference [10]. The important PAC experiment directly relating to the DLTS experiment of the irradiated sample was performed as follows: alternating with the DLTS scans the sample was measured with the PAC spectrometer at room temperature.

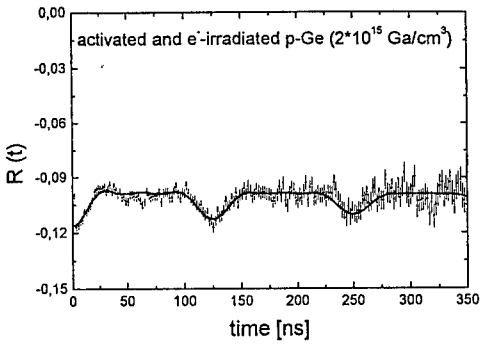


Fig. 6: PAC spectrum of ^{111}In implanted and electron irradiated Ge. The fitted frequency is the vacancy signal and corresponds to the ^{111}In-V peak of the DLTS spectrum in Fig. 4.

Figure 6 shows a PAC spectrum measured at room temperature (with electron irradiation at 77 K). This spectrum shows one defect component characterized by a quadrupole frequency ν_Q = 52 MHz. In detailed experiments [10] we have shown that this defect is due to a neutral monovacancy trapped at the ^{111}In probe, ^{111}In-V. A further parameters of this defect pair obtained by PAC is the geometrical structure: the pair is oriented in <111> crystal directions [11] and is axially symmetric. The formation temperature was also determined as 2oo(5) K corresponding to a migration energy of the vacancy of 0.5(1) eV. Since this is the only observable defect associated with the probe (the rest of the spectrum shows ^{111}In on unperturbed substitutional sites) we identify this defect with the level seen by DLTS at E_V + 0.33 eV. Another interesting feature is the fact that from PAC the interaction strength of the monovacancy with the In probe and the Ga dopants, respectively, can be compared. It turns out, that In is about 100 times more effective than Ga in attracting neutral vacancies which can also be demonstrated by DLTS [7].

We finally remark that we have undertaken these combined experiments also in n-type Ge where a different type of defect formation with the ^{111}In probe can be monitored by PAC upon electron irradiation [9,10]. Our DLTS spectra, however, so far do not show a level undergoing a change related to the nuclear transmutation [7].

Conclusion.

We have presented an example of a study in which two different experimental techniques are combined to give atomic-level information on a specified point defect and its interaction with dopant atoms in a semiconductor. These two techniques are the structure- and element-sensitive PAC and the DLTS. The combining bond is the use of radioactive impurity atoms, in our case ^{111}In, which is the probe nucleus for PAC and by its characteristic decay time serves as an additional label to identify the corresponding DLTS level. In this way structural, kinetic and electrical parameters for the monovacancy-In defect complex in Ge could be obtained. We have chosen Ge for this study since detailed defect information from PAC was already available [9,10], in particular a conclusive identification of the monovacancy and, to a high degree of certainty, also of the self-interstitial. Other semiconductors, however, are also suited for such studies. Further investigations in Ge with the aim of finding a DLTS signal related to the trapping of the

self-interstitial at the ^{111}In probes are presently under way. With the unique identification of the In-related defects in the DLTS spectra one also has in some cases an additional handle to unveil the nature of other defect levels appearing [7]. A detailed publication of the work presented here will follow.

Acknowledgement.

We thank N. Achtziger and W. Witthuhn (Universität Jena) for their supporting interest and helpful discussions.

References.

1. D.V. Lang, J. Appl. Phys. **45**, 3023 (1974).
2. J.W. Petersen and J. Nielsen, Appl. Phys. Lett. **56,** 1122 (1990).
3. M. Lang, G. Pensl, M. Gebhard, N. Achtziger, M. Uhrmacher, Appl. Phys. **A53,** 95 (1991).
4. N. Achtziger and W. Witthuhn, Phys. Rev. Lett. **75**, 4484 (1995).
5. Th. Wichert, Hyperf. Int. **97/98**, 135 (1996).
6. R. Sielemann, H. Hässlein, M. Brüssler, H.Metzner, Mater. Sci. Forum **83-87**, 1109 (1992).
7. Ch. Zistl, Thesis, Hahn-Meitner-Institut Berlin and Universität Jena, 1997, unpublished.
8. Landolt-Börnstein, New Series **III/22b**, 98 (1989).
9. H. Hässlein and R. Sielemann, Hyperf. Int. **(C), 1**, 203 (1996).
10 H. Hässlein, R. Sielemann, Ch. Zistl, this conference.
11. U. Feuser, R. Vianden and A.F. Pasquevich, Hyperf. Int. **6o**, 829 (1990).

Materials Science Forum Vols. 258-263 (1997) pp. 59-64
© 1997 Trans Tech Publications, Switzerland

MICROSCOPIC STUDY OF THE VACANCY AND SELF-INTERSTITIAL IN Germanium BY PAC

H. Hässlein, R. Sielemann and Ch. Zistl
Hahn-Meitner-Institut Berlin, Glienicker Str. 100, D-14109 Berlin, Germany

Keywords: germanium, vacancy, self-interstitial, In-impurities, irradiation, PAC-technique.

Abstract. We have employed two different techniques of Frenkel pair production in combination with the Perturbed Angular Correlation method (PAC) to study and identify the basic intrinsic defects in Germanium. In one of the techniques the PAC probe atom ^{111}In serves as primary knock-on atom due to a 29 eV recoil energy from a neutrino produced in the nuclear decay of the probe's precursor, ^{111}Sn. This leads to the production of single Frenkel pairs with the ^{111}In probe adjacent to a vacancy identifying this defect. In the other technique the Ge crystals are electron irradiated leading to the trapping of two different defects at the ^{111}In probes. Detailed studies of this trapping behavior as function of temperature and Fermi level are performed. One of the trapped defects is identified as the monovacancy from comparison with the neutrino recoil experiment, the second defect is assigned to a trapped self-interstitial. This assignment is based on exclusion of alternatives on the one hand and by indirect kinetic information from the neutrino recoil. An acceptor state for the vacancy at $E_V + 0.20$ eV is deduced. Long range migration of the neutral vacancy and the interstitial takes place at 200(5) K and 220(5) K, respectively.

Introduction.

The elementary defects in Germanium have attracted intensive research for a long time and numerous results have been obtained by application of mostly electrical techniques [1,2]. However, contrary to the case of silicon [3], no microscopic identification of either the vacancy or the self-interstitial has yet been accomplished. This is mainly due to the fact that methods suited to give microscopic information like Electron Paramagnetic Resonance (EPR) have for various reasons only limited success when applied to Ge. Thus, a definite assignment of the collected data to the basic defects and their properties is still missing and interpretation of the results has remained speculative.

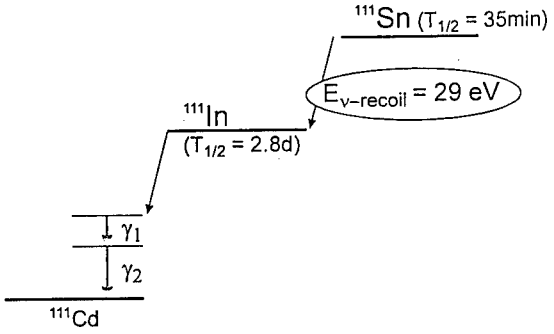


Fig. 1: Simplified decay scheme of the PAC probe ^{111}In with precursor ^{111}Sn.

In our experiments we use the PAC technique on the probe nucleus ^{111}In which is able to monitor a defect which is in the immediate neighborhood of the PAC probe. In such a case an electric field gradient is induced at the probe nucleus leading to a nuclear quadrupole interaction measured on the $5/2^+$ state of the

^{111}Cd daughter nucleus by means of a γ-γ angular correlation experiment. A recent review can be found in Ref. [4].

We apply the PAC technique in two different ways: in the first way the Ge samples are doped with the ^{111}In probes followed by defect introduction via electron irradiation at 77 K. In a subsequent annealing process the defects are mobilized and may be trapped at the probes if an attractive interaction exists. In the second way defects are produced by using the ^{111}In probe simultaneously as the primary knock-on atom. This is accomplished by starting the PAC technique not on the usual ^{111}In activity but on the radioactive precursor ^{111}Sn. In its decay to ^{111}In a high energy neutrino is emitted leading to a recoil energy of 29 eV. This is just above threshold for the production of single Frenkel pairs centered on the ^{111}In atom on which subsequently PAC is measured. In this way Frenkel pair production can be studied microscopically [5]. Figure 1 shows the decay scheme of ^{111}In with its precursor ^{111}Sn feeding the $5/2^+$ state in ^{111}Cd.

Electron Irradiation Experiments.

P-type (Ga) and n-type (Sb) Ge single crystals in a wide range of acceptor/donor concentrations were used in the experiments. The ^{111}In probes were introduced by a recoil implantation technique leading to low probe concentrations of about $5 \cdot 10^{13}$ cm^{-3} with a constant depth profile up to 4μm [5]. Following implantation the samples were annealed in an Ar atmosphere at 600°C for 10 min to remove the implantation damage. Subsequently measured PAC spectra at room temperature always show a completely flat spectrum proving that all of the probe atoms are in a defect free environment which for the shallow acceptor In in Ge is the substitutional site. After annealing the samples were irradiated with 1.2 MeV electrons at 77 K to a fluence of $5 \cdot 10^{16}$ cm^{-2} producing almost exclusively single Frenkel pairs. Subsequently, two types of experiments were performed: isochronal annealing experiments to study the trapping behavior of the irradiation induced defects as function of temperature on the one hand and experiments in variously doped material to study the Fermi level dependence of the trapping process. Some preliminary results were reported in [6].

(a) Isochronal Annealings

Figure 2 shows results of the isochronal annealing experiments (10 min) in p-type Ge. Two defect components f_1 and f_2 characterized by quadrupole interaction frequencies ν_{Q1} = 54 MHz and ν_{Q2} = 420 MHz appear in the PAC spectra at T_{ann} = 200 K (ν_{Q1}) and 220 K (ν_{Q2}), respectively (measured at 77 K). These frequencies were first reported in [7,8] and in [9]. It was also shown that both components are oriented along the <111> directions [9]. Only speculative interpretations could be given at that time. Our annealing spectra now show that the trapping for these defects occurs well separated but closely together within 20 K. The stability for both defect components extends to about 400 K and is again rather close together but also well separated.

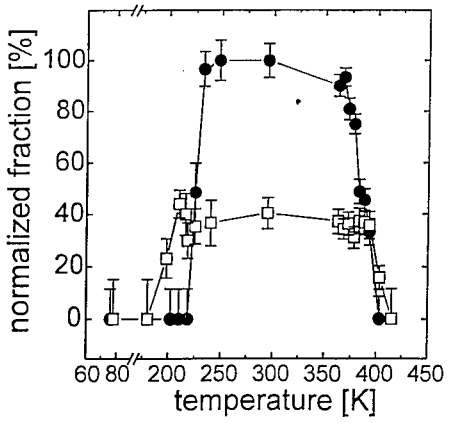


Fig. 2: Normalized fractions f_1 (squares) and f_2 (circles) measured at 77 K versus annealing temperature in p-type Ge.

Above this temperature thermal dissociation of the probe-defect complexes occurs.

(b) Doping Dependence Of Trapping Behavior

Figure 3 shows PAC spectra of variously doped Ge samples and Fig .4 shows the trapping behavior of the defects f_1 and f_2 extracted from the PAC spectra as function of the carrier concentration of the electron irradiated Ge crystals. For all these results annealing experiments were performed to check the temperature dependence of the probe-defect pair formation process. It turned out that trapping always occurred around 200 K already known from Fig. 2 or not at all up to temperatures of 600 K. Therefore the carrier concentration was measured by Hall effect around 200 K which allowed to determine the Fermi level (from the carrier concentration) at the temperature where the defect trapping occurs. Since between electron irradiation at 77 K and the later Hall effect measurements at 200 K the crystals were stored at room temperature, there is some unwanted additional annealing which, however, is small compared to the annealing between 77 K and 200 K and should only little influence the Fermi level determination. It is clearly seen that the occurrence of f_1 and f_2 depends on carrier concentration. f_1 is present only in p-type Ge for carrier concentrations $p>10^{15}$ cm^{-3} with a fraction of about 5 to 8% but is absent in n-type Ge. f_2, on

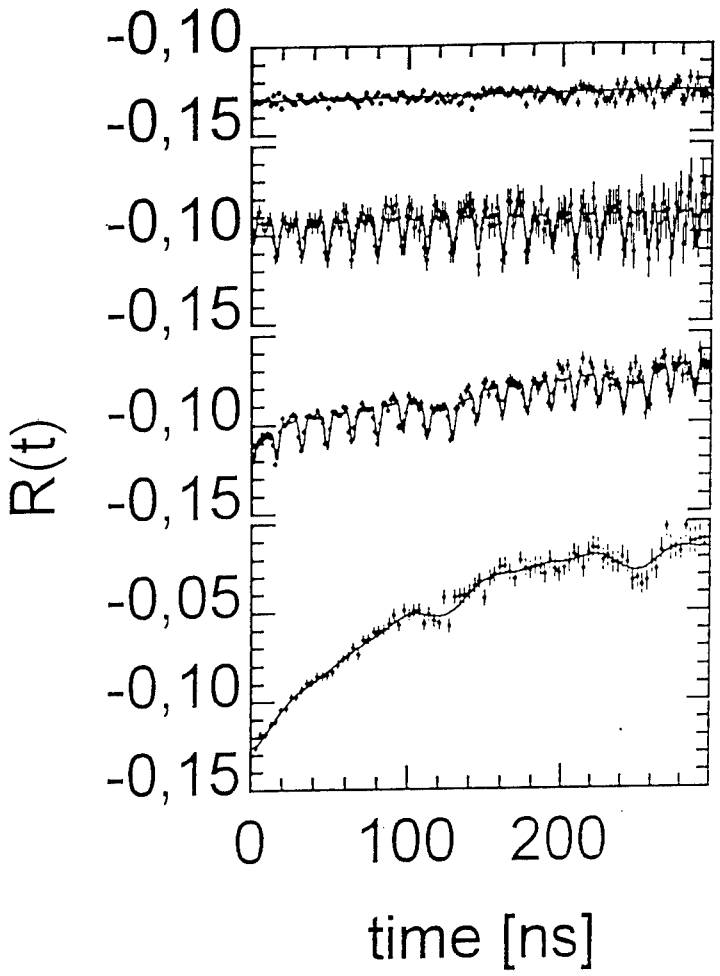


Fig. 3: PAC spectra of variously doped Ge samples. From top:(1) completely annealed (n-type); electron irradiated: (2) lightly n-doped, (3) medium p-doped, (4) heavily p-doped.

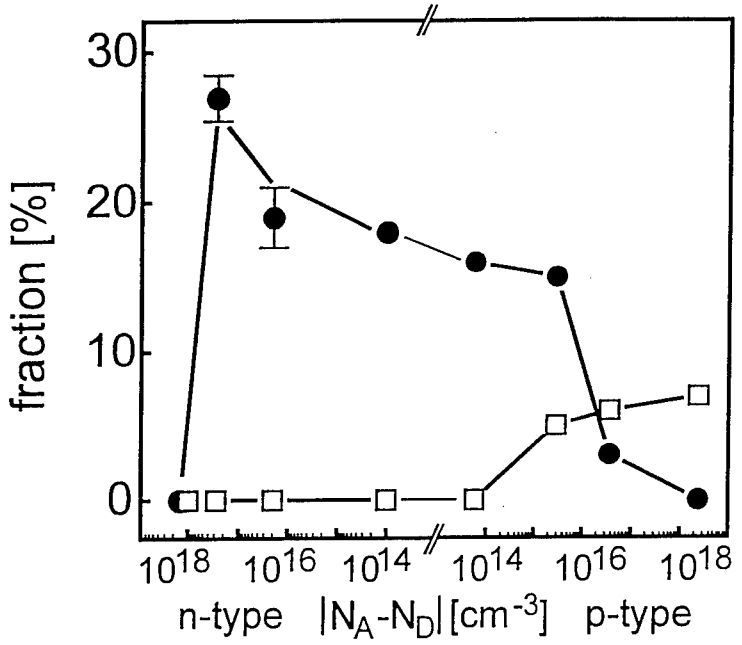


Fig. 4: Trapping behavior of f_1 (squares) and f_2 (circles) as function of the carrier concentration in n- and p-type Ge deduced from the PAC spectra.

the other hand, is present with a large fraction around 20% in a wide range from n- to p-doped material but ceases to be present for both high n- and high p-doping.

Neutrino Recoil Experiments.

Most of these experiments have been reported previously [5,10]. In these experiments the ^{111}Sn probe atoms (Fig.1) are recoil implanted into the Ge crystals analogously to the ^{111}In atoms. After implantation the recoil damage is annealed and the sample cooled down to 4.2K. Subsequently ^{111}Sn decays to ^{111}In imparting a recoil of 29 eV to the ^{111}In atoms. Thus Frenkel pair production takes place in an otherwise defect-free environment. It turned out that the neutrino recoil only leads to a measurable defect component in p-type material. This defect component has the quadrupole interaction frequency ν_Q = 54 MHz which leads us to conclude that this defect is identical to ν_{Q1} measured in the electron irradiation experiments reported above. No further defect is created, in n-type material there is no defect production at all. Isochronal annealing experiments show that the neutrino-induced defect disappears from the PAC spectra between 200 K and 273 K in contrast to the annealing of the identical defect (ν_{Q1}) around 400 K (see Fig.2) produced by trapping after electron irradiation. Present experiments aim to measure the annealing temperature of the neutrino-induced defect more precisely but are not yet conclusive.

Discussion.

Though it is rather clear that the appearance of f_1 and f_2 at the PAC probes after electron irradiation is due to the trapping of irradiation induced intrinsic defects a positive identification of these defects remains a difficult task since the fingerprint of a defect, the quadrupole interaction frequency, cannot be reliably calculated. Thus identification has to be done by properly conducted experiments. The key for identification is the neutrino-recoil experiment. Since the recoil energy

of 29 eV is just sufficient to produce one and only one Frenkel pair in Ge ν_{Q1} must be the association of the ^{111}In probe with one of the two Frenkel pair partners. Since the same defect also appears after electron irradiation (pair formation after long range defect migration) the defect configuration must be one which can be formed by both the recoil and the trapping process. This only leaves a monovacancy adjacent to the ^{111}In probe atom as a possible configuration as is discussed in more detail in Ref. [10]. The different thermal stability in the recoil- and trapping experiment is due to the different microscopic environment: in the recoil experiment the invisible Frenkel partner, the self-interstitial, is in close vicinity and annihilates with the vacancy which is bound in the 54 MHz configuration (correlated recombination). After trapping, however, the vacancy is bound to the probe without a nearby self-interstitial, the defect disappears when the vacancy breaks the attractive bond to the probe and migrates away (dissociation).

Identification of the defect leading to f_2 cannot be made in a direct way. We use two lines of arguments to make an assignment: on the one hand we have performed a variety of additional experiments to exclude the possibility that unintentional trapping of impurity atoms may lead to this defect. These experiments rest mainly on irradiation experiments with widely varying fluences and by using Ge crystals with different degrees of purity. Additionally impurity atoms were introduced on purpose (H;Cu). In a second type of experiments we varied the Fermi level of the crystals during the PAC experiments in situ [11] to check whether a different charge state of the already identified defect f_1 might be responsible for f_2. Both types of experiments lead us to conclude that f_2 is, like f_1, due to trapping of an intrinsic defect which by exclusion of alternatives then must be the self-interstitial. On the other hand, there is some information in the neutrino-recoil experiment directly linked to the self-interstitial: the correlated recombination between 200 and 273 K is due to the interstitial migration. The fact that pair formation leading to f_2 occurs at 22o K then is directly in accord with our interstitial assignment. Present experiments just under way are performed to narrow the temperature range where correlated recombination occurs sufficiently down for a precise comparison with the trapping experiment.

Having identified f_1 and f_2 we can interpret the trapping behavior as a function of the samples' carrier concentration in terms of a Fermi level dependent process which changes the charge states of the defects (Fig. 4). Since the ^{111}In probes are negatively charged shallow acceptors, trapping at these probes can only take place if an attractive interaction exists. This leaves for the vacancy only the charge state + or 0. Since the Ga dopants are also negative but extend to concentrations $>10^{18}$ cm^{-3} (3 orders of magnitude higher than the vacancy/self-interstitial concentration [12]) a hypothetical V^+ would be attracted by the In probes as well as by the Ga dopants and reduce and ultimately cancel the ^{111}In-V pair formation in conflict with the observation (Fig. 4). Thus one can infer that the observed ^{111}In-V pairing must be driven by elastic interaction between the oversized ^{111}In and a neutral V to form In-V pairs whereas the Ga dopants fit into the Ge lattice producing a much smaller interaction to V.

The fact that for $p<10^{15}$ cm^{-3} no formation of f_1 takes place can then be explained by a change of the charge state $V^\circ \rightarrow V^-$ which quenches the attractive interaction. Based on this model that ^{111}In-V pair formation is possible only when V is neutral we can determine the V acceptor level $E_{Vac}(-/o)$ from Fermi-Dirac statistics. The concentration of ionized vacancies $[N_{Vac}]^-$ is related to the total vacancy concentration by

$$\frac{[N_{Vac}]^-}{[N_{Vac}]} = \frac{1}{1 + g_{Vac} \exp\left(\frac{E_{Vac}(-/0) - E_F}{kT}\right)}$$

where g_{Vac} is a degeneracy factor which we take as 1. Figure 4 shows the transition from V° to V^- (trapping to non-trapping). Taking the respective Fermi levels from the Hall measurements around

200 K we obtain an upper and lower limit for $E_{Vac}(-/0)$ which we write: $E_{Vac}(-/0) = E_V+0.20(4)$ eV.

The trapping behavior of the self-interstitial leaves more possibilities for the interpretation and will be discussed in detail in a forthcoming publication. In this case, however, again a negative charge state can be excluded when trapping is observed.

Conclusion.

We have produced and microscopically studied the ^{111}In-vacancy pair and by exclusion of alternatives to a high degree of certainty also the ^{111}In-interstitial pair by applying the PAC technique. From analysis of the pair formation process a deep acceptor level at E_C + 0.20 eV for the vacancy is deduced. We were able to disentangle an annealing stage around 200 K which is repeatedly reported in the literature: we show that both vacancies and self-interstitials undergo long range migration in this temperature range separated by only 20 K.

Acknowledgement.

Experimental work of M Brüßler and H. Metzner at the beginning of this work is acknowledged. We thank V.V. Emtsev (St. Petersburg) for performing the Hall measurements and many stimulating discussions.

References.

1. V.V. Emtsev, T.V. Mashovets, V.V. Mikhnovich and N.A. Vitovskii, Rad. Effects and Defects in Solids **111-112,** 99 (1989).
2. J.C. Bourgoin, P.M.Mooney and F. Poulin, Inst. Phys. Conf. Ser. No. **59**, 33 (1980); N. Fourches, G. Walter and J.C. Bourgoin, J. Appl. Phys. **69**, 2033 (1991).
3. G.D. Watkins, Mat. Sci. For. **143-147**, 9 (1994).
4. Th. Wichert, Hyperf. Int. **97/98**, 135 (1996).
5. R. Sielemann, H. Hässlein, M. Brüssler, H. Metzner, Mater. Sci. Forum **83-87**, 1109 (1992).
6. H. Hässlein and R. Sielemann, Hyperf. Int. **(C), 1**, 203 (1996).
7. M. Brüssler, H. Metzner, R. Sielemann, Mat. Sci. For. **38-41**, 1205 (1989).
8. M. Brüssler, H. Metzner, R. Sielemann, Hyperf. Int. **60**, 809 (1990).
9. U. Feuser, R. Vianden, A.F. Pasquevich, Hyperf. Int. **60**, 829 (1990).
10. Th. Wichert, N. Achtziger, H. Metzner, R. Sielemann in „Hyperfine Interactions of Defects in Semiconductors" ed. G. Langouche (Amsterdam: Elsevier) pp.79 (1992).
11. H. Hässlein, Ph. D. Thesis, Freie Universität Berlin, 1993, unpublished.
12. St. Bausch, H. Zillgen, P. Ehrhart, Mat. Sci. Forum **196-201**, 1141 (1995).

Materials Science Forum Vols. 258-263 (1997) pp. 65-70
© 1997 Trans Tech Publications, Switzerland

LOCALIZATION OF NONDEGENERATE ELECTRONS AT RANDOM POTENTIAL OF CHARGED IMPURITIES

M.S.Kagan, E.G.Landsberg, and N.G.Zhdanova

Institute of Radioengineering and Electronics of RAS
11, Mokhovaya, 103907 Moscow, RUSSIA

Keywords: quantum interference effects, localization, percolation, transport phenomena

Abstract.
The low temperatures mobility saturation and the negative magnetoconductivity in a nondegenerate 3D electron gas in compensated Ge were observed and shown to be due to strong and weak localization effects.

Introduction.

Scattering electrons by charged impurities leads to the mobility edge (ε_c) existence and localisation of electrons with the energy below ε_c. The conductivity of a degenerate electron gas depends on Fermi level (ε_F) position. At the temperature T=0 a system behaves as a metal when $\varepsilon_F > \varepsilon_c$, and as an insulator when $\varepsilon_F < \varepsilon_c$. However, at very low but finite temperatures, the conductivity of a semiconductor can be made sufficiently high even at $\varepsilon_F << \varepsilon_c$, on the dielectric side of a metal-insulator transition, by means of photoexitation of carriers from impurities. In this case the electron gas is nondegenerate. Due to Boltzman distribution function, only exponentially small number of electrons having energy within the narrow band of the order of kT above the mobility edge should give the main contribution to the conductivity at low T as $kT < \varepsilon_c$. The electron-electron interaction is negligible because of small electron concentration. For nondegenerate electron gas, the magnitude of a random potential of charged impurities and the mobility edge value does not depend on free electron concentration which can be varied in a wide range with exciting light intensity.
Transport phenomena become considerably influenced by mobility edge existence as the wavelength λ of an electron of mean thermal energy is of the order of its mean free path, l (the Ioffe-Regel condition). This strong localisation condition can be easily fulfilled in compensated semiconductors doped with deep charged impurities.

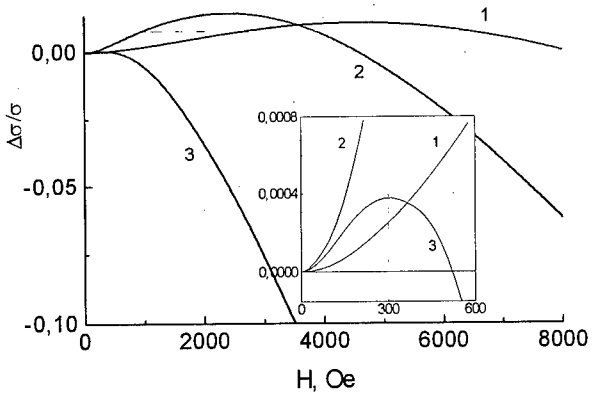


Fig. 1. Magnetoconductivity vs magnetic field for samples with various random potential, γ. The insert shows the initial part of the curves. γ, meV: 1 - 5.7, 2 - 2.5, 3 - 1.2

Experiment.

We studied *n*-type *Ge* crystals doped with deep *Cu* acceptors and partially compensated with shallow *Sb* donors so that triply and doubly negatively charged copper ions were in action. The *Sb* concentration was of $1.5*10^{15}$ to $1.2*10^{16}$ cm^{-3}. At thermal equilibrium the Fermi level is near the upper *Cu* level (0.26 eV below the conduction band edge). At low T free electron concentration was

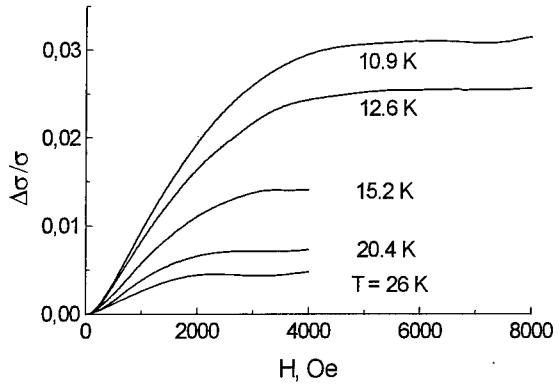


Fig. 2. Negative magnetoresistance of the sample with γ =2.5 at different T

ensured by impurity-band light excitation from deep centers. The shallow donor population at the temperatures as they are frozen out was shown to be controlled by direct donor-acceptor (D-A) recombination and depended on exciting light intensity, I [1]. The donor population is small due to the D-A recombination. So, practically all impurity centers are charged (Cu^{3-}, Cu^{2-}, and Sb^{+} ions).

The random Coulomb potential caused by a disorder in space positions of charged impurities spreads out the impurity levels. The random potential magnitude, γ, was determined (i) from the dependence of concentration of free electrons produced by electric-field ionization of shallow donors on the donor quasi-Fermi level position controlled by photoexcitation of deep acceptors, and (ii) from the dependence of D-A recombination coefficient on I and T [1]. The γ values are given in the Table.

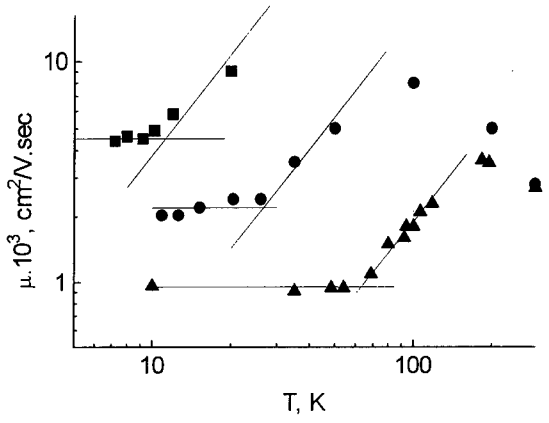


Fig. 3. Temperature dependence of electron mobility

Due to strong charged impurity scattering, the necessary condition for weak localisation effects, $\tau_\varphi >> \tau$ (τ is the mean free time due to elastic scattering, τ_φ is the electron-wave dephasing time governed by inelastic scattering), is satisfied. As a result, the negative magnetoresistance (MR) was observed. The MR data were reconstructed from measurements of the alternating current $\tilde{i} = \tilde{H} di/dH$ caused by modulated magnetic field $H = H_0 + \tilde{H}$, $\tilde{H} << H_0$, i.e. $\tilde{i} \propto d\sigma/dH$ (σ is the conductivity) [2].

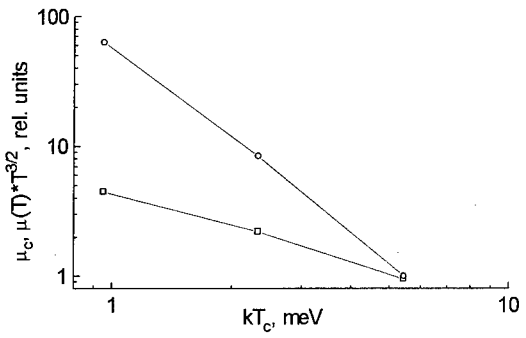


Fig. 4. The mobility in saturation and $T^{3/2}$ regions vs kT_c

Shown in Fig.1 is the magnetic field dependence of the relative transverse MR for the sample with Sb concentration of $1.5*10^{15}$ cm^{-3} at different T. MR data shown in Fig.2 are obtained for samples with various impurity concentrations (different γ). Note the negative MR (NMR) at low fields and positive classical H^2 dependence at higher fields. The NMR occured in a range of weak H, $\mu H/c << 1$ (μ is the electron mobility, c is light velocity), as classical MR is small is a result of magnetic-field suppression of quantum

interference corrections to the conductivity.

The NMR values and the magnetic field range of NMR decrease both with increasing T and decreasing γ. The change of NMR sign at higher fields is caused by transition to the classical dependence $\Delta\sigma/\sigma \propto (\mu H/c)^2$. The mobilities of the samples with different γ determined from the slopes of these H^2 dependences are shown in Fig.3. At the temperatures below some critical value T_c, the mobility is saturated, $\mu=\mu_c$. At $T>T_c$, the usual $T^{3/2}$ dependence (shown by straight lines) is observed. The kT_c value turns out to be close to γ value. The saturated mobility, μ_c, is inversely proportional to γ. On the other hand, the coefficient at the $T^{3/2}$ dependence is proportional to γ^3 (Fig.4). This shows that charged-impurity scattering is not single-center one even in this range of T.

The saturated values of NMR are also proportional to the random potential magnitude. It can be seen in Fig.5 where H dependence of NMR for samples with different γ is represented for nearly the same kT/γ ratio (here the classical H^2 dependence is subtracted from experimental MR curves).

Discussion.

The Ioffe-Regel condition for strong localisation, $\lambda \approx l$, is equivalent to: $\varepsilon_c \approx \hbar/2\tau$, and can be used to found the mobility edge energy, ε_c. Using the low-temperature value of $\tau = \tau_c = m\mu_c/e$ (m is the electron effective mass, e is the elementary charge), we obtain ε_c values being surprisingly close to γ.

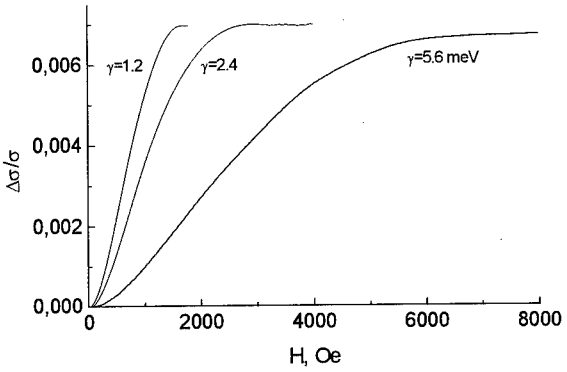


Fig. 5. The negative magnetoresistance at $kT/\gamma \approx$ const

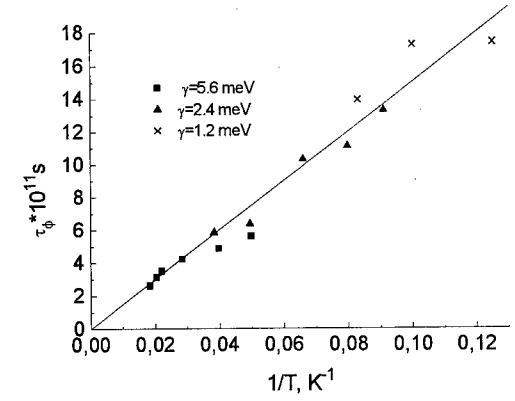


Fig. 6. Electron-wave dephasing time vs $1/T$ for different γ

Thus, the saturated mobility value is single-electron conductivity at the mobility edge and is connected with the random Coulomb potential magnitude.

The main difficulty for the quantitative description of the magnetic field suppression of quantum corrections to the conductivity by means of the present theory of weak localisation [3,4] is the assumption $\lambda << l$. Nevertheless, as the first attempt, we used the expression derived for a degenerate three-dimensional electron gas [3,4],

$$\frac{\Delta\sigma}{\sigma} = \frac{1}{48}\left(\frac{\tau_\varphi}{\tau}\right)^{3/2}(\omega_c\tau)^2, \qquad (1)$$

for description of the experimental NMR at low magnetic fields (in $-H^2$ region). Here $\omega_c=eH/mc$ is the cyclotron frequency, τ being determined from $\mu=e\tau/m$. The values of τ_φ found from the initial parts of MR curves are plotted in Fig.6. The main feature of the curves is the linear dependence of τ_φ on $1/T$. In our case $\tau_\varphi = \tau_{ac}$, the acoustic-phonon scattering time [4]. As $\tau_{ac} \propto \varepsilon^{-1/2}T^{-1}$ and $\varepsilon \approx \varepsilon_c$, this accounts for the $1/T$ dependence of τ_φ. The energy dependence of τ and τ_φ should not influence on $\Delta\sigma/\sigma$ at low H; even assuming their classical energy dependence, we have $\Delta\sigma/\sigma \propto \tau^{1/2}\tau_\varphi^{3/2} \propto (\varepsilon^{-3/4})(\varepsilon^{3/4})=\text{const}(\varepsilon)$. One can see from Fig.6 that the dephasing time values are of

two orders of magnitude more than the mean free time due to impurity scattering. We tried also to compare the theory and the experimental data by means of averaging single-electron quantum corrections over Boltzman distribution function. The magnetic field dependence of NMR was calculated with expression:

$$\frac{\Delta\sigma}{\sigma} = \frac{\int_{\varepsilon_c}^{\infty} d\varepsilon \nu^2 \tau(\lambda^2 / l l_H) \exp(-\varepsilon / kT)\rho(\varepsilon) f_3(l_\varphi / l_H)}{\int_{\varepsilon_c}^{\infty} d\varepsilon \nu^2 \tau(1-\frac{\lambda^2}{l^2}) \exp(-\varepsilon / kT)\rho(\varepsilon)}, \qquad (2)$$

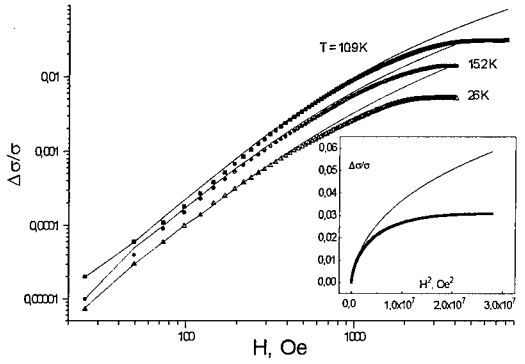


Fig. 7. Comparison of the experimental NMR with theory

Here $\lambda=\hbar/2m\varepsilon$ is the wavelength of an electron of energy ε, $l=v\tau$ is the mean free path of an electron, v is its velocity, $l_H = (c\hbar/eH)^{1/2}$ is the magnetic length, $\rho(\varepsilon)\propto\sqrt{\varepsilon}$ is the density of states, $l_\varphi = D\tau_\varphi$, D is diffusion cofficient, f_3 is the function introduced in [3]. The factor $(1-\lambda^2/l^2)$ is due to the requirement for the conductivity to be zero at the mobility edge. The energy dependences of the quantities involved were assumed to be classical. The condition $\varepsilon_c = \hbar/2\tau_c$ was taken into account, so the the mobility edge energy was as only fitting parameter. Its value coincides well with that obtained as shown above. The theoretical NMR is compared with the experimental results in Fig.7. Shown in the insert is the upper plot in $(\Delta\sigma/\sigma, H^2)$ plane. It is seen that Eq. 2 can describe the NMR only at sufficiently low H. One can see also that the energy dependence of kinetic coefficients is essential and becomes more pronounced at higher temperatures.

Let's now regard the most striking experimental facts. They are (i) low-temperature mobility saturation and (ii) sharp transition to it from $T^{3/2}$ dependence. The saturated values of relative NMC depend on charged impurity concentration and don't exceed several per cents although NMC should be of the order of unity for conducting electrons having energies near the mobility edge (iii). The magnetic length at which the negative MC is saturated is much less than the mean free path in contrast to the theoretical prediction (iv).

Consider first the NMR features. Small saturated values of NMR and low characteristic magnetic fields show at a suppression of electron interference on closed trajectories of small radii. The reason for vanishing short closed trajectories is the long-scale random potential of charged impurities. At the percolation threshold, most of possible closed electron trajectories should be of the order of optimal fluctuation radius [5]. In other words, an electron should pass around random potential "hills" for being coherently scattered. So, the probability of small closed trajectories and, as a consequence, the values of quantum corrections to the conductivity should be heavily diminished. At low magnetic fields, as the magnetic length, $l_H = (c\hbar/eH)^{1/2}$, is larger than the scale of random potential, quantum corrections to the conductivity are as for three-dimensional system and fit the theory of weak localisation though the condition $\lambda \approx l$ is fulfilled in the experiment.

The same reasons can be used to explain the mobility behaviour. Electrons can not move in the random potential when their energy becomes less than that of classical percolation threshold. Near the percolation threshold the system should behave as one-dimensional wire net [5]. Therefore, the

mobility edge should be at some energy above the percolation threshold as the electron wavelength is of the order of size of a "bottleneck" in the percolation net. This size can be estimated as $\lambda=\hbar/2m\gamma$. To find the mobility we consider the percolation net as the system of 1D channels where electrons can move without scattering. The conductivity value is then of the order of $e^2/\hbar$. The specific conductivity of a random net is determined by the conductivity of a typical net element and is in this case $e^2/\hbar R$, R is the random potential scale. To obtain the mobility we should multiply it by the volume of one electron, (it is $\lambda^2 R$), and divide by the elementary charge. We get finally $\mu = e\lambda^2/\hbar = e\hbar/2\ m\gamma$. This value coincides surprisingly with the experimental value. Note that the above expression is equivalent to the condition $\gamma = \hbar/2\tau$. So, this mobility is the quantum limit of one-electron conductivity, i.e. Mott's minimum metallic conductivity.
The sharp turn in the temperature dependence of mobility is likely due to the change of conductivity geometry from 3D continual one to 3D "wire net".

Conclusion.
Localization of free electrons at the presence of charged impurities is due to mobility edge existence. The latter, in turn, is believed as a result of interference of electron waves at multiple coherent backscattering. On the other hand, a disorder in charged-center positions gives rise a random Coulomb potential and classical percolation threshold. The question is what is the physical cause for the mobility edge in this case. The data presented here shows that for a system of charged scatterers, the mobility edge arises due to quantum percolation and not due to multiple coherent backscattering. For this reason, the quantum corrections to the conductivity caused the electron wave interference on closed trajectories turn out to be small, as well as the negative magnetoconductivity resulting from the magnetic field suppression of the interference.

This work was supported in part by Grant No 97-02-16819 from Russian Basic Research Foundation.

References.
1. N.G.Zhdanova, M.S.Kagan, E.G.Landsberg, and V.V.Petrishchev, Sov. Phys. ZhETP Lett., **58**, 529 (1993)
2. A.M.Bolibok, M.S.Kagan, E.G.Landsberg, Sov. Phys. ZhETP, **67**, 367 (1988)
3. A.Kawabata, J. Phys. Soc. Japan, **49**, 628 (1980)
4. B.L.Al'tshuler, A.G.Aronov, A.I.Larkin, and D.E.Khmel'nitskii, Sov. Phys. JETP, **54**, 411 (1981)
5. B.I.Shklovskii and A.L.Efros, Electronic Properties of Doped Semiconductors, Springer, Heidelberg (1984)

Materials Science Forum Vols. 258-263 (1997) pp. 71-76
© 1997 Trans Tech Publications, Switzerland

RESONANCE ACCEPTOR STATES AND THz GENERATION IN UNIAXIALLY STRAINED p-Ge

I.V.Altukhov, E.G.Chirkova, M.S.Kagan, K.A.Korolev, V.P.Sinis, K.Schmalz[1], M.A.Odnoblyudov[2], I.N.Yassievich[2]

Institute of Radioengineering & Electronics of Russian Academy of Sciences
11, Mokhovaya, Moscow, 103907, Russian Federation
[1] Institute for Semiconductor Physics, Walter-Korsing-Str. 2, 15230 Frankfurt (Oder), Germany
[2] Ioffe Physico-Technical Institute, 26, Politechnicheskaya, St.Petersburg, Russian Federation

Abstract.
The spectrum of stimulated THz emission from uniaxially compressed p-Ge is presented. The peaks corresponding to different optical transitions from resonance to ground and excited states of an acceptor were observed in the spectrum of stimulated emission. The peaks were identified by means of a comparison of experimental data with calculated acceptor level positions in dependence on pressure. The mechanism of a population inversion due to free carrier accumulation near energies of resonance acceptor states based on the resonance scattering is proposed.

Introduction.

Stimulated emission of far-infrared radiation has been observed in p-Ge at strong electric and magnetic fields [1] and shown to be due to population inversion of the valence subbands. We observed a stimulated emission in p-Ge without any magnetic field but under uniaxial stress [2]. In this report we present experimental evidence and some theoretical model for population inversion of strain-split acceptor levels in uniaxially compressed p-Ge in strong electric fields. The main peak of stimulated far-IR emission is shown to be due to the intracenter radiative transition between resonance s-state and localized p-excited state.

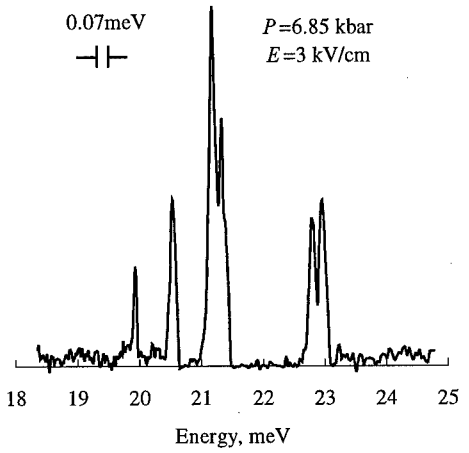


Fig.1. The spectrum of stimulated emission. $\boldsymbol{E}\|\boldsymbol{P}\|[111]$ The peak at 21.2 meV corresponds to the optical transitions between the resonance 1s and $2p_{\pm1}$ acceptor states.

Experimental.

The gallium-doped Ge crystals with Ga concentration of $3*10^{13}$ to 10^{14} cm^{-3} were used in the experiment at liquid helium temperature. The samples of a square cross section of 0.5 to 1 mm^2 and 6 to 10 mm long were cut in the [111] or [100] crystallographic directions. Uniaxial pressure P and electric field E were applied along the samples (z -direction). Voltage pulses of 0.2

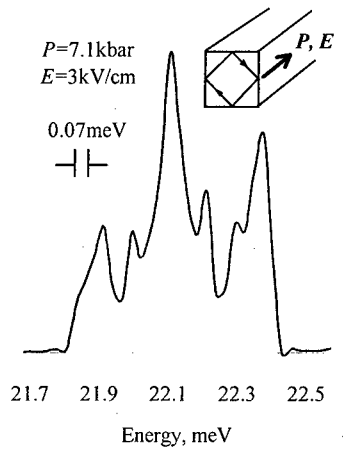


Fig.2. The mode structure of the main peak in the spectrum of stimulated emission. The sample cross section is of 1*1mm^2.

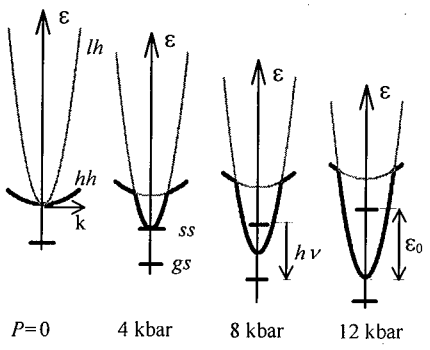


Fig.3. The valence band structure and the acceptor level positions for various values of *P*. Heavy-hole and light-hole bands are denoted by *hh* and *lh*, and ground and split-off acceptor states are denoted by *gs* and *ss*, respectively. ε_0 is the optical phonon energy. For convenience the hole subbands are shown here as for electrons.

to 1 μs duration were applied to two contacts positioned on the long (lateral) plane of the sample. The distance between the contacts was from 4 to 9 mm.

Far-infrared luminescence was registered by the cooled gallium-doped Ge photodetector. For the samples with planes parallel within 4`, the steep rise in radiation intensity up to 10^3 times was observed at some threshold stress P_c. The minimum P_c value was 4 kbar. The jump in radiation was accompanied by the jump-like rise in current (up to 10 times).

The resonator formed in our case by well-parallel sample planes was necessary to obtain the stimulated emission. Indeed, the jump in emission (and in the current) disappeared after rough grinding of one of the long sample planes. Polishing and etching restored the resonator and the stimulated emission appeared again.

The spectrum of stimulated radiation from compressed p-Ge measured by the grating monochromator is shown in Fig.1. It consists of several peaks. The peak energies increased with pressure. The energy of the most intensive peak (21.2 meV in Fig.1) is varied from 21.2 to 42 meV by increasing pressure from 6.85 to 11 kbar at $\boldsymbol{P} \| [111]$.

The main peak measured in more details shows the structure caused by resonator modes (Fig.2). The line spacing (≈0.11 meV) for the specimen with the cross section of 1*1 mm^2 coincides with that found from the condition $N\lambda=nL$, where λ is the radiation wavelength, n is the refractive index (n=4 for Ge), L is the optical path length, and N is an integer. This shows that in our case, as in [3], the optical resonator is formed due to total internal reflection from

lateral crystal planes (see the insert in Fig.2).

Discussion

Uniaxial deformation removes the degeneracy of the valence band of Ge at k=0 and splits it into two subbands separated by the energy gap proportional to the applied pressure P (the proportionality factor is about 4 and 6 meV/kbar for $\boldsymbol{P}$ parallel to [100] and [111] crystallographic directions, respectively [4]). The degenerate ground state of an acceptor is also split into two states. The energy separation $\delta\varepsilon$ between the split-off state and the ground state increases with strain. Fig.3 represents schematically the p-Ge valence band structure and the positions of the split-off and ground states for different pressures.

At certain pressures ($P\approx$4 kbar for $\boldsymbol{P}\,||\,$[111] and $P\approx$3 kbar for $\boldsymbol{P}\,||\,$[100]) the split-off state enters into the valence band continuum (band scheme for 4 kbar in Fig.4) and creates the resonance state while the ground state remains in the forbidden band. The series of exited states related both to ground and split-off states should exist also in the gap and the continuum, respectively.

In strong electric field the acceptor ground state located in the forbidden band becomes empty due to impact ionization while the split-off state being in the valence band is filled to some degree. Holes arriving into the valence band is driven by electric field in z-direction and their momentum p_z increases. One can assume, that the scattering is practically absent as holes have energy ε less than the resonance state energy ε_0. However, the holes near this energy undergo the strong resonance scattering and are accumulated in the resonance state. The inverted population of hot holes at the energy close to that of the resonance s-state can be the result of the strong resonance scattering. We have got the expression for the scattering probability:

$$w_{\varepsilon,\theta_0,\theta} = n\frac{\hbar^2\gamma_1^{3/2}}{m_0^{3/2}}\frac{\varepsilon_0}{\varepsilon^{3/2}}\frac{\left(\frac{\varepsilon}{\varepsilon_0}\right)^2}{\left(1-\frac{\varepsilon}{\varepsilon_0}\right)^2+\left(\frac{\Gamma}{\varepsilon_0}\right)^2}G\left(\frac{E_{def}}{\varepsilon},\theta_0,\theta\right)$$

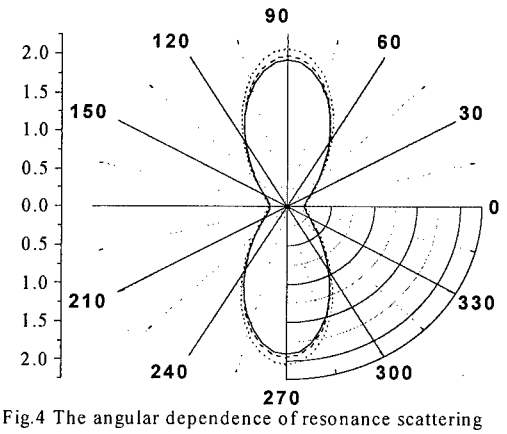


Fig.4 The angular dependence of resonance scattering probability for three value of incident angle θ_0:
(·····) 0, (- - - - -)π/4, (———)π/2

where n is impurity concentration, E_{def} is the splitting of valence band top, Γ is the broadening of resonance state ($\Gamma \ll \varepsilon_0$), G is the function which defines the angular dependence of scattering, θ_0 and θ are the incident and scattering angles, respectively. The angles are counting from z-direction. Our calculations show that the dependence from θ_0 is practically absent. On the contrary, there is a strong dependence from angle θ, which is demonstrated for

$\varepsilon = \varepsilon_0$ in Fig.4. Because this type of angular dependence of the scattering probability accumulates carriers with momentum directions perpendicular to electric field, it contributes to inversion. Due to the intensive exchange between continuous spectrum and the resonance state, their population is controlled by energy distribution function and thus by heating electric field.

The calculations of the spectrum of localized and resonance acceptor levels were performed by the variational method for high pressure limit (impurity states are considered in approximation of independent valence subbands). The calculated energies of optical transitions from the resonance 1s state to the localized 1s- and $2p_{\pm1}$ states and the experimental stress dependence of the energy of the main peak are shown in Fig.5. The comparison allows us to identify the main peak as the resonance 1s to $2p_{\pm1}$ transition and the peak at 19.9, 20.5 (see Fig.1) as the transitions from resonance 1s to $2p_0$, 2s respectively. The peak of energy 23 meV is supposed to be radiative transition of hot free holes of energy equal to s-resonance level to 1s localized state. The linewidth for different peaks is of 0.2 to 0.5 meV. The reason for the wide spectral maxima may be the broadening of the resonance acceptor state being in the continuum [5].

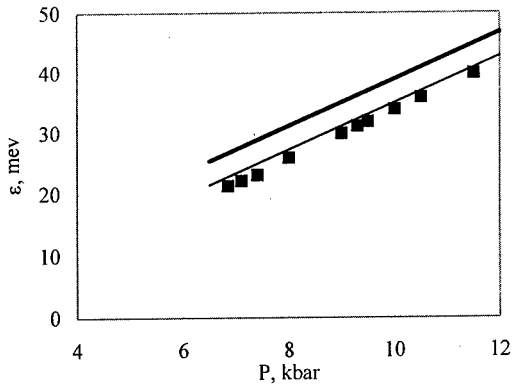


Fig.5. The energy of the main peak of stimulated radiation vs stress. Solid lines show the calculated energy of optical transitions from resonance -1s state to $2p_{\pm1}$ (lower line) and 1s localized states.

The minimum pressure for the stimulated emission to be observed is just that at which the resonance state appears (see band scheme in Fig.3). The energy splitting of the acceptor states is about 10 meV in this case (Fig.5). On the other hand, the stimulated radiation intensity decreases sharply [6] as the split-off acceptor state begins to depopulate via hole transitions to the valence band edge assisted by optical-phonon emission (see the band scheme for 12 kbar in Fig.3). The value of $\delta\varepsilon$ for depopulating the split-off acceptor state is about 42 meV. Thus, these data confirm that the intracenter inversion can arise as the split-off state enters into the valence band and exist until optical phonon-assisted hole transitions to the valence band edge depopulate the resonance state. The energy range of the stimulated emission is expected to be from 10 to 41 meV.

Conclusion.

In summary, the data obtained show that the stimulated far-infrared emission in uniaxially compressed p-Ge is due to the electric field induced population inversion of strain-split acceptor states. The necessary condition for the inversion is the resonance state appearance. The possibility of a strong frequency tuning by stress is shown. The spectral lines connected with the exiting states referred to the ground acceptor state were observed in the spectrum of the stimulated emission. It should be noted that the mechanism of far-infrared stimulated emission in p-Ge based on the population inversion of strain-split acceptor states seems to be promising also for acceptor doped two-dimensional structures. In such structures the acceptor states are split by strain and/or space quantization without any external pressure. It will be shown that the stimulated emission of far-infrared radiation in heating electric field.

This work was supported by RFBR grants No. 97-02-16820 and No. 96-02-17352 and Volkswagen-Stiftung grant.

REFERENCES.
1. A.A.Andronov. The highly non-equilibrium hot-hole distributions in germanium. "Spectroscopy of Nonequilibrium Electrons and Phonons", edited by C.V.Shank and B.P.Zakharchenya (1992)
2. I.V.Altukhov, M.S.Kagan, K.A.Korolev, V.P.Sinis, and F.A.Smirnov. JETP, **74,** 404 (1992).
3. A.A.Andronov, I.V.Zverev, V.A.Kozlov, Yu.N.Nozdrin, S.A.Pavlov, and V.N.Shastin. JETP Lett., **40**, 804, (1984).
4. G.L.Bir and G.E.Pikus, Symmetry and Strain-Induced Effects in Semiconductors (Wiley, New York, 1974).
5. A.K.Ramdas, S.Rodriguez, Rep.Prog.Phys., **44**, 1297, (1981).
6. I.V.Altukhov, E.G.Chirkova, M.S.Kagan, K.A.Korolev, V.P.Sinis, and I.N.Yassievich. Phys. Stat. Sol. (b) **198**, 35 (1996)

Materials Science Forum Vols. 258-263 (1997) pp. 77-82
© 1997 Trans Tech Publications, Switzerland

IONIZED IMPURITY SCATTERING IN ISOTOPICALLY ENGINEERED, COMPENSATED Ge:Ga,As

K. M. Itoh [1], T. Kinoshita [1], W. Walukiewicz [2], J. W. Beeman [2], E. E. Haller [2, 3], J. Muto [1], J. W. Farmer [4], and V. I. Ozhogin [5].

[1] Keio University, 3-14-1, Hiyoshi, Kohoku-ku, Yokohama, 223 Japan

[2] Lawrence Berkeley National Laboratory and [3] UC Berkeley, Berkeley, California 94720, USA

[4] University of Missouri, Columbia, MO 65211, USA

[5] Kurchatov Institute of Atomic Energy, 123182 Moscow, Russia

Key words: Ionized impurity scattering, Mobility, Compensated semiconductors

Abstract. Ionized-impurity scattering of holes has been studied in isotopically engineered p-type Ge:Ga,As samples with compensation ratios between 0.08 and 0.61. Experimentally measured Hall mobilities at temperatures between 10 and 300 K are quantitatively compared with existing theories of ionized impurity scattering in highly compensated semiconductors. We find fair agreement with the theory based on the correlated distribution of ionized impurity centers.

Introduction

The development of a method to accurately determine the compensation ratio K ($K \equiv$ [minority impurity concentration] / [majority impurity concentration]) in a given semiconductor has become important especially for recent studies of defects that hinder heavy doping in compound semiconductors. An appropriate method for finding K depends on the majority impurity concentration N of the given material. For the case of heavily doped semiconductors with $N>N_C$ (where N_C is the critical concentration for the degenerate to non-degenerate semiconductor transition) ionized impurity scattering limits the free carrier mobility significantly up to room temperature. Since the degree of ionized impurity scattering depends strongly on K, it is possible to find K in crystals with high N solely from room temperature mobility measurements. [1] A method to determine K based on mobility does not work in high purity materials ($N < 0.001N_C$) since the contribution of ionized impurity scattering becomes too small. An alternative method for pure materials is far-infrared absorption spectroscopy in which electric-field-broadening of impurity absorption peaks is used to determine K. [2] Finding K in moderately doped materials ($0.001N_C < N < N_C$) has been somewhat challenging. The impurity absorption method cannot be employed because the concentration broadening due to overlaps of impurity wavefunctions overwhelms the broadening due to the electric fields arising from ionized impurities. The mobility method, on the other hand, may be applicable but measurements down to low temperatures ($T<50$ K) are necessary. At high temperatures the contribution of phonon deformation scattering becomes more significant than that of ionized impurity scattering.

Because the determination of the compensation based on mobility requires an accurate scattering theory, the quantitative understanding of the scattering cross-sections of ionized impurities in compensated semiconductors is crucial. Up to now the Brooks-Herring theory [3] has been used widely to calculate ionized impurity scattering. The theory was developed originally for lightly compensated semiconductors and has been used successfully at high temperatures for materials with K values ranging from 0 to 1 and for materials with $K<0.2$ over a wide temperature range. [4] A number of attempts have been made to modify Brooks-Herring theory for heavily compensated materials at low temperatures. [5, 6] However their applicability has never been tested.

In this work we present a direct comparison between experimental and theoretical mobilities for temperatures between 10 and 300K using highly compensated, p-type Ge:Ga,As samples with N ranging from $0.003N_C$ to $0.006N_C$ ($N_C \approx 2\times10^{17}$ cm^{-3} for Ga in Ge). We were able to test the applicability of various theoretical approaches to calculate low temperature mobilities in compensated semiconductors.

Theory

The three models for ionized impurity scattering which were used to compute the mobility for our Ge:Ga,As compensated samples are; (i) Brooks-Herring model [3], (ii) Falicov-Cuevas model [5], and (iii) Stern model. [6]

Brooks and Herring derived a simple Yukawa potential V(r) for electron scattering by an ionized impurity center in semiconductors ;

$$V(r) = \frac{Z e^2}{\varepsilon r} \exp(-r/L_D) \tag{1}$$

where Ze is the charge of the scattering center and L_D is the screening length. There are two different screening mechanisms in doped semiconductors affecting L_D: screening of the scattering potential by (i) free carriers and (ii) other surrounding ionized centers (self-screening).

The expression for the former mechanism L_D(free carrier) is given by:

$$L_D(\text{free carrier}) = \frac{1}{e}\left(\frac{\varepsilon k_B T}{4\pi}\right)^{1/2} n^{-1/2} \tag{2}$$

where n is the free carrier concentration. As $T\rightarrow 0$, $n\rightarrow 0$ exponentially, i.e., $L_D(\text{free carrier})\rightarrow\infty$. Therefore, screening due to free carriers is significant only at high temperatures.

The screening length L_D(ion) due to ionized impurity self-screening is given by:

$$L_D(\text{ion}) = \frac{1}{e}\left(\frac{\varepsilon k_B T}{4\pi}\right)^{1/2}\left[\frac{(N_{MJ}-N_{MN}-n)(N_{MN}+n)}{N_{MJ}}\right]^{-1/2} \tag{3}$$

where N_{MJ} and N_{MN} are the concentration of majority and minority impurities, respectively. L_D(ion) vanishes at high temperatures where $n\approx N_{MJ}-N_{MN}$. Therefore, the effect of the self-screening becomes significant only at low temperatures where $n<N_{MJ}-N_{MN}$. The Brooks-Herring expression for L_D used in Eq. (1) is obtained by adding the inverse squares of Eq. (2) and Eq. (3):

$$L_D = \frac{1}{e}\left(\frac{\varepsilon k_B T}{4\pi}\right)^{1/2}\left[n + \frac{(N_{MJ}-N_{MN}-n)(N_{MN}+n)}{N_{MJ}}\right]^{-1/2}. \tag{4}$$

Finally the scattering rate τ_{ion}^{-1} in Brooks-Herring model is given by:

$$\tau_{ion}^{-1} = \frac{\pi N_I Z^2 e^4}{(2m^*)^{1/2}\varepsilon^2}\left[\ln(1+\gamma^2) - \frac{\gamma^2}{1+\gamma^2}\right] E^{-3/2} \tag{5}$$

$$\text{with} \qquad \gamma^2 = 8 m^* E L_D^2/\hbar^2, \tag{6}$$

where N_I is the ionized impurity concentration and E is the energy of an incident electron.

In the course of deriving Eq. (1), Brooks and Herring linearized the source term in Poisson's equation assuming that $eV(\mathbf{r})/k_BT$ is much smaller than unity. Falicov and Cuevas [5] explicitly pointed out that this condition is not satisfied in highly compensated semiconductors at low temperatures. They solved Poisson's equation without resorting to the expansion. Falicov and Cuevas further proposed that the ionized impurity distribution at low temperature is not random but is correlated, i. e., it is "frozen" in the state of minimum potential energy. They formalized their idea by using a simple temperature independent exponential correlation function between acceptors and donors and derived the scattering rate as:

$$\tau_{ion}^{-1} = \frac{\pi N_I Z^2 e^4}{(2m^*)^{1/2}\varepsilon^2}\left[\ln(1+\gamma_{FC}^2) + \frac{\gamma_{FC}^2}{1+\gamma_{FC}^2}\right] E^{-3/2} \tag{7}$$

$$\text{with} \quad \gamma_{FC}^2 = 8 m^* E a_c^2/\hbar^2, \quad a_c = [8\pi(N_{MJ}-N_{MN})]^{-1/3}. \tag{8}$$

Eq. (7) differs from the Brooks-Herring expression Eq. (5) only in that the sign of the last term within large parentheses is positive and that the temperature dependent L_D is replaced by the static temperature independent correlation length a_c.

Stern, on the other hand, did not take into account the correlation effect proposed by Falicov and Cuevas, but included the effect of the impurity level broadening due to the Coulomb fields arising from randomly distributed ionized impurities. [6] Kane proposed that the linearization of Poisson's equation, i.e., the Brooks-Herring expression, is valid when the number of screening sites within a sphere of radius L_D is greater than unity. [7] Stern argued that this criterion is barely satisfied for highly compensated semiconductors even at low temperature. [6] He

Table 1 Values of [Ga], [As], and K for each sample

Sample	[Ga] ($x10^{14}$ cm^{-3})	[As] ($x10^{14}$ cm^{-3})	compensation ratio K
A	6.5	0.5	0.08
B	8.0	2.7	0.34
C	8.3	3.3	0.40
D	9.0	4.4	0.49
E	11.3	6.9	0.61

calculated the modified screening length L_{DS} at T=0 due to the level broadening:

$$L_{DS} = s\,(8\,\pi^2\,N_{MN})^{-1/3} \qquad (9)$$

where s is a function of K graphically given in Ref. 6. The scattering rate proposed by Stern is given by replacement of L_D(ion) [Eq. (3)] by L_{DS} [Eq. (9)] in the Brooks-Herring model.

The original theories of Falicov and Cuevas and of Stern both assumed that the screening by free carriers at low temperatures is negligibly small. However, we include here the screening due to free carriers [Eq. (2)] when we use these models to calculate the temperature dependence of the Hall mobility for our Ge:Ga,As samples. It is also important that we include scattering by other mechanisms such as acoustic and optical phonon deformation potential scattering and neutral impurity scattering. Our calculation does not contain any adjustable parameters, i. e., a direct quantitative comparison with experimental results is possible. The details of our calculation have been described in Ref. 8 with the differences that we include optical phonon deformation scattering and that we calculate the Hall mobility rather than the drift mobility.

Experimental

We have produced a series of p-type Ge:Ga,As samples of constant net-impurity concentration N_{Net}=[Ga]-[As]=$5x10^{14}cm^{-3}$ with the compensation ratio (K=[As]/[Ga]) ranging between 0.082 and 0.6. Neutron-transmutation-doping of isotopically engineered Ge allows for such a precise control of very uniform doping. A detailed description of sample preparation is given in Ref. 9. Table 1 shows [Ga], [As], and K for five samples prepared for this work.

Hall and resistivity measurements were performed in order to determine the Hall mobility as a function of temperature. Disk-shaped (~6mm diameter, ~0.5 mm thick) samples with four boron implanted contacts in van der Pauw configuration were employed. The magnetic induction used for Hall effect measurements was 0.3 T.

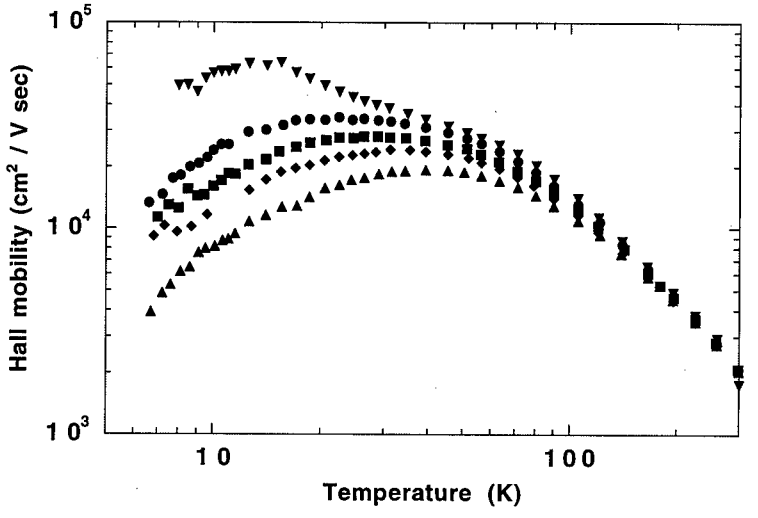


Fig. 1 Experimentally measured Hall mobilities in samples A (▼), B (●), C (■), D (◆), and E (▲).

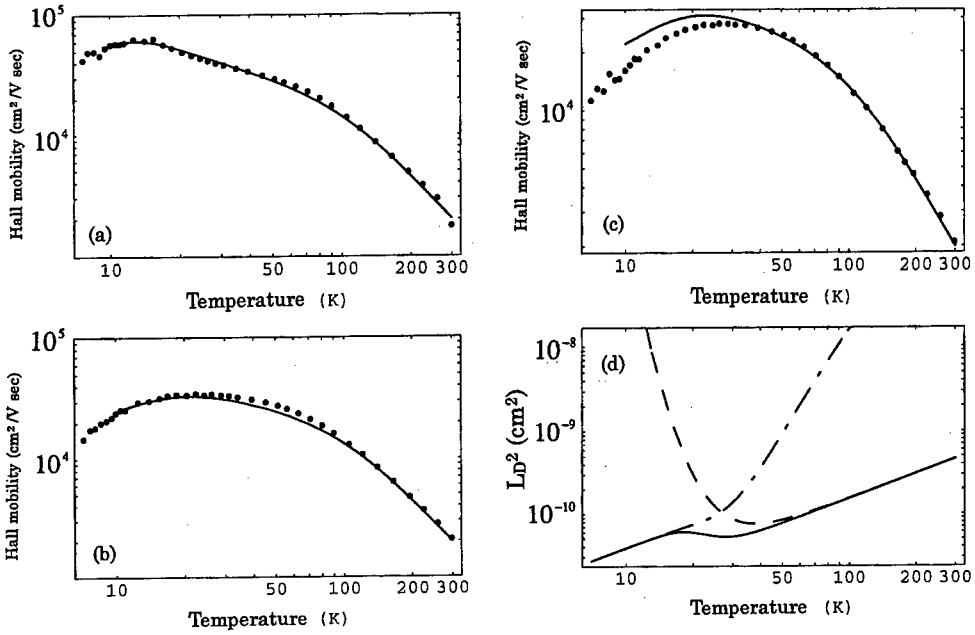


Fig. 2 Comparison between Brooks-Herring calculations (solid curve) and experimentally measured mobilities (●) in samples (a) A, (b) B, and (c) C. Contributions of L_D^2(ion) (broken curve) and L_D^2(free carrier) (dashed curve) to total L_D^2 for sample C are shown in (d).

Results and discussions

Figure 1 shows experimentally measured Hall mobilities in samples A-E (K=0.08-0.61). The low temperature mobilities decrease with K as expected. These experimentally measured curves will be compared with theoretical calculations using the above mentioned three different ionized impurity scattering models. Figure 2 (a), (b), and (c) show comparisons of the measured mobilities with the calculations based on Brooks-Herring model in samples A (K=0.08), B (K=0.34), and C (K=0.40), respectively. While these calculations agree very well with the mobilities in the less compensated samples A and B, the deviation between calculation and the experiment is observed for sample C at T<40 K. In order to demonstrate the origin for this low temperature disagreement, we show the contribution of L_D(free carrier) and of L_D(ion) to L_D for sample C in Fig. 2. (d). It is clear that L_D is dominated by L_D(free carrier) above 40 K and by L_D(ion) below 40 K, i. e., L_D(ion) estimated by Brooks and Herring is too small for such highly compensated semiconductors. This result is expected for the reasons given by Falicov and Cuevas and/or by Stern, but we demonstrate it experimentally for the first time. The deviation at low temperatures between Brooks-Herring calculations and experimental mobilities becomes more severe for samples D (K=0.49) and E (K=0.61) as seen in Fig. 3. (b) and (c), respectively. L_D(ion) given by Brooks and Herring is also too small for these cases.

Figure 3 (a), (b), and (c) show the comparisons between experimentally determined Hall mobilities and theoretical calculations based on the three different ionized impurity scattering models for samples C (K=0.40), D (K=0.49), and E (K=0.61), respectively. The theoretical curves are based on (i) Brooks-Herring model (broken curve), (ii) Falicov-Cuevas model (solid curve), and (iii) Stern model (dashed curve). For K<0.3 all the three models predict essentially the same mobilities for T between 10 and 300 K and they agree very well with the experiments. For samples C and D [Fig. 3. (a) and (b)], Brooks-Herring model and Stern model overestimate the experimental low temperature Hall mobility at T=20 K by 25% while overestimation due to Falicov-Cuevas model is less than 10%. For sample E the degree of overestimation at T=20 K by Brooks-Herring model becomes ~35% while that of Falicov-Cuevas and Stern models becomes

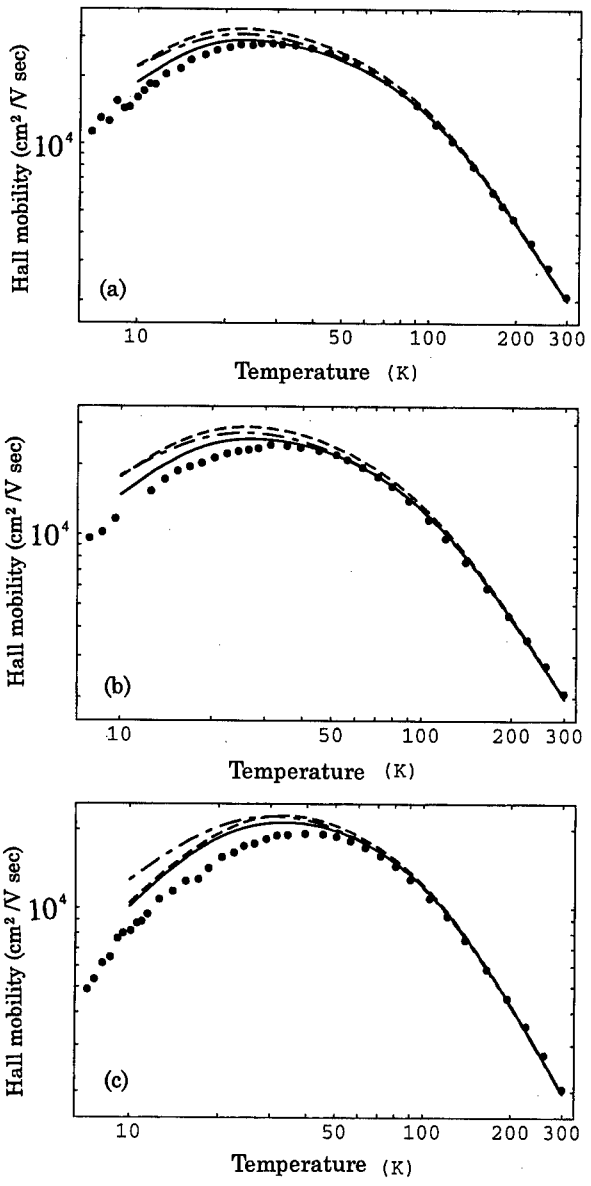


Fig. 3 Comparison between calculations and experimentally measured mobilities (●) in samples (a) C, (b) D, and (c) E. Calculations are by Brooks-Herring model (broken curve), Falicov-Cuevas model (solid curve), and Stern model (dashed curve).

comparable. The experimental mobility at T=20 K and Falicov-Cuevas and Stern models agree within 25% for sample E. We therefore conclude that the Falicov-Cuevas model leads to the best agreement with the experimental mobilities in all samples and for all temperatures. Stern model may be appropriate only for samples with high K.

It is not surprising to find significant experimental deviations from the Brooks-Herring calculations for the high K samples at low temperatures. Stern model does not work as well as expected possibly because he derived Eq. (9) assuming absolute zero temperature only. The Falicov and Cuevas model works quite well for all samples throughout the temperature range we investigated. Unfortunately the agreement with the experiment is not perfect most likely because of the zero order estimation they used in deriving the correlation function a_c [Eq. (8)]. (Falicov and Cuevas did not use a rigorous form of Coulomb interactions between ionized impurities for deriving a_c.) However, it should be emphasized that Falicov and Cuevas's approach of solving Poisson's equation without resorting to the expansion and their idea of a spatially correlated distribution of ionized impurities at low temperatures bring the results of theory and experiment much closer than the other two models. The existence of the correlated ion distribution was indeed confirmed in our recent optical absorption measurements on highly compensated semiconductors. [2]

Summary and conclusions

We have measured the Hall mobility in a series of compensated isotopically engineered, p-type Ge:Ga,As crystals. The quantitative comparison between the experimentally measured mobility and theoretical calculations has shown that the widely used Brooks-Herring approach is not applicable to heavily compensated semiconductors (K>0.3) in the temperature range below 50 K. Among the theories we considered, the ionized impurity scattering cross-section proposed by Falicov and Cuevas based on a spatially correlated ionized impurity distribution is the most appropriate model for describing the low temperature mobility in highly compensated materials.

Acknowledgments

The work at Keio was supported in part by Kanagawa Academy of Science and Technology Research Grants and in part by grant in aid from the Ministry of Education, Japan. The work at Berkeley was supported by US NASA W17605 and US DOE DE-AC03-76SF00098.

References

[1] W. Walukiewicz, et. al., J. Appl. Phys. **50**, 889 (1979).
[2] K. M. Itoh, et. al., Phys. Rev. B **53**, 7797 (1996).
[3] H. Brooks, Adv. Electr. Electr. Phys., **7**, 85 (1955).
[4] D. Chattopadhyay and H. J. Queisser, Rev. Mod. Phys. **53**, 745 (1981).
[5] L. M. Falicov and M. Cuevas, Phys. Rev. **164**, 1025 (1967).
[6] F. Stern, Phys. Rev. B **9**, 4597 (1974).
[7] E. O. Kane, Phys. Rev. **131**, 79 (1963).
[8] K. M. Itoh, et. al., Phys. Rev. B **50**, 16995 (1994).
[9] K. M. Itoh, et. al., Appl. Phys. Lett., **64**, 2121 (1994).

Materials Science Forum Vols. 258-263 (1997) pp. 83-90
© 1997 Trans Tech Publications, Switzerland

DEFECTS IN SiGe

Arne Nylandsted Larsen
Institute of Physics and Astronomy, University of Aarhus, DK-8000 Aarhus C, Denmark

Keywords: SiGe, molecular-beam epitaxy, defects, diffusion, E-centre

Abstract

The quality of molecular-beam epitaxy (MBE) grown SiGe alloys layers is discussed from a defect-study point of view. It is shown that strain-free $Si_{1-x}Ge_x$ alloy layers of $x \leq 0.50$ can be grown of a quality sufficient for many types of defect studies. Two examples of the use of MBE grown SiGe layers for defect studies are discussed, namely the diffusion of Sb and the pinning behaviour of the Sb-vacancy pair.

1. Introduction

Epitaxial layers of SiGe are mainly known from their use in fast, silicon-based microelectronics, e.g. as strained SiGe-base layers in hetero-junction bipolar transistors [1] or as relaxed graded layers in III-V/Si optoelectronic integration [2], and a large amount of research has been put into the optimization of the growth procedures for these purposes. However, the steady improvement of the crystalline and electrical quality of the layers has not only made them interesting from an applied point of view but also from a more fundamental [3]; there are now epitaxial SiGe layers available of an electrical and crystalline quality sufficient for many types of defect studies.

Using epitaxial-growth techniques, such as molecular-beam epitaxy (MBE) or chemical-vapour deposition (CVD), layers of high-crystalline quality of strain-relaxed material of any composition as well as layers of tensile- and compressive-strained material can be grown on silicon substrates; in these layers tailored impurity distributions can be included during the growth. Hence, the band gap, and the size and type of strain can be varied over fairly wide ranges, offering a flexible system for studies of the influence of these parameters on defects in Si and Ge, in very well-defined samples.

Bulk-grown $Si_{1-x}Ge_x$ crystals are also becoming available, and very recently Cz-grown crystals with $x=0.15$ were reported [4]. Compared to epitaxial layers they have the advantage of larger thicknesses; however, local impurity distributions cannot be included during growth and strain cannot easily be incorporated.

In this paper we will mainly be concerned with strain-relaxed SiGe layers grown on graded SiGe buffer layers as these layers can be grown to thicknesses which easily allow for defect studies. The growth of strain-relaxed layers of crystalline $Si_{1-x}Ge_x$ of any x, on a <100>-Si substrate, with a sufficiently low concentration of as-grown defects such that intentionally induced defects can be studied, has been and still is a challenging task. The progress in growing these layers will be reviewed with the main emphasis on our own MBE-based efforts which, for the time being, has resulted in layers of $x \leq 0.50$ of sufficient quality for defect studies. As examples of the use of strain-relaxed SiGe in defect studies, results from investigations of the diffusion of Sb in SiGe [5,6] and of proton-irradiation induced Sb-vacancy pairs [7] will be presented.

2. Strain-Relaxed SiGe Layers

The lattice constant of relaxed $Si_{1-x}Ge_x$ can be approximated with the parabolic expression [8]:

$$a(x) = 0.02733x^2 + 0.1992x + 5.431 \text{ (Å)}$$

An alloy layer of, e.g. x=0.30 has a lattice mismatch of 1.1% to Si and a critical thickness for dislocation-free growth of about 100Å [9]. For layer thicknesses above this critical thickness dislocations will develop with misfit segments parallel to and near the interface, and with threading segments running through the layer to the surface [9]. When a fully relaxed $Si_{0.7}Ge_{0.3}$ layer is grown directly on Si, the resulting density of threading dislocations is typically in the range of 1×10^{10} and 1×10^{11} cm^{-2} [10]. It was already realized in the seventies by Abrahams et al. [11] for the growth of III-V compounds that the concentration of threading dislocations could be reduced significantly by grading the composition. This growth procedure has been successfully taken over by the SiGe community [3,12]; thus between the Si substrate and the SiGe top layer a compositionally graded buffer layer is included (Fig. 1). For a properly chosen growth procedure the effect is a reduction of the threading dislocations in the top layer of more than a factor of 10^7 [12]. The mechanism behind this reduction, is a combination of increased dislocation-glide distance and annihilation of threads with antiparallel Burgers vectors [3,13]. Figure 2 shows a cross-section transmission-electron microscopy picture of a $Si_{0.65}Ge_{0.35}$ structure having a 3.5μm thick linearly graded buffer layer and a ~1μm thick uniform top layer. The growth parameters for this structure (and for the structures mentioned below) were a grading rate of 10%Ge/μm, a grading start at ~0% Ge, and a substrate temperature of 800°C. It can be appreciated that there is a very high density of misfit dislocations in the graded buffer layer and no threads in the top layer. From a large number of strain-relaxed SiGe layers on graded buffer layers grown in our MBE system, we can quantify the dislocation density in the uniform top layer as given in Table 1. The MBE-growth rate is typically 3-5Å/sec; thus, a $Si_{0.50}Ge_{0.50}$ structure with a 4μm top layer takes about 10 hours to grow. There is some activity going on to reduce the long growth time which in particular becomes a problem as x is approaching 1. Osten and Bugiel [10] have demonstrated that by adding a controlled amount of C to the graded buffer layer a strain-relaxed top layer of $Si_{0.70}Ge_{0.30}$ with a dislocation density of less than 1×10^5 cm^{-2} could be grown on a graded buffer layer of only 1μm. Very recently, Linder et al. [14] have obtained promising results with only a thin (0.1-0.2μm) Si buffer grown at low temperature between the substrate and

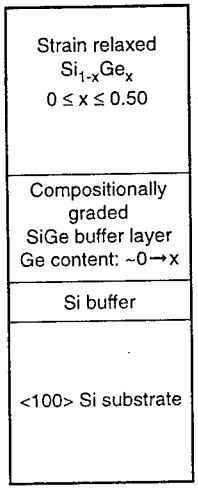


Fig. 1 Schematic structure of an epitaxially grown, strain-relaxed $Si_{1-x}Ge_x$ sample.

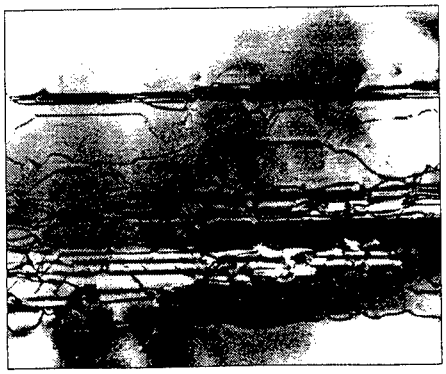


Fig. 2 Cross-section TEM picture of an epitaxial, strain-relaxed $Si_{0.65}Ge_{0.35}$ structure grown on <100>Si. The graded buffer layer is 3.5μm thick and the uniform top layer is 1μm.

the uniform top layer and no compositionally graded layer; for $Si_{0.85}Ge_{0.15}$ a dislocation density of about $1\times10^4 cm^{-2}$ was obtained. For many defect studies SiGe layers with dislocation densities equal to those given in Table 1 are sufficient.

Table 1: Dislocation density in strain-relaxed $Si_{1-x}Ge_x$ layers grown at 800°C on compositionally graded buffers with a composition grading of 10%Ge/μm.

x	Dislocation Density [cm^{-2}]
≤0.25	~1×10^5
0.25 - 0.35	~5×10^5
0.35 - 0.50	~1×10^6

We have further investigated the structural quality of the uniform-top layers by measurement of detailed

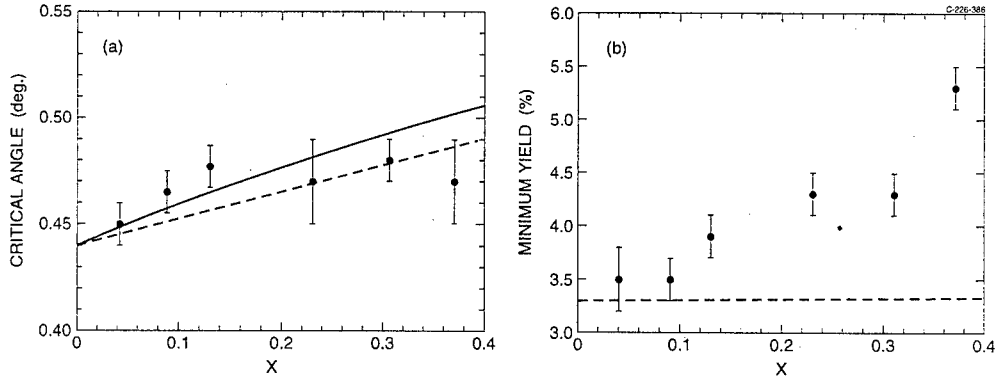


Fig. 3 Critical angles (a) and normalized minimum yields (b) for <100>-axial channeling in $Si_{1-x}Ge_x$ as a function of x. The dashed curves are linear interpolations between values for Si and Ge; the solid curve is corrected for the $Z^{½}$ dependence, where Z is the average atomic number. From ref. [15].

channeling-angular scans using 2-MeV α-particles, and compared the results to Monte Carlo simulations [15,16,17]. Figure 3 shows measured critical angles for channeling and minimum channeling yields as a function of the composition x. There is a good agreement between the measured critical angles and the theoretical expectations for perfect crystals; however the minimum yield is too high and increases with increasing Ge content. We have shown [16] that this behaviour is consistent with a compositionally dependent mosaic spread, which is ~0.1° for x=0.37. A similar conclusion was reached by Mooney et al. [18] based on x-ray diffraction measurements. We speculate that this mosaic spread originates from the misfit-dislocation structure in the graded buffer layer which can create non-uniform stress films influencing the film growth.

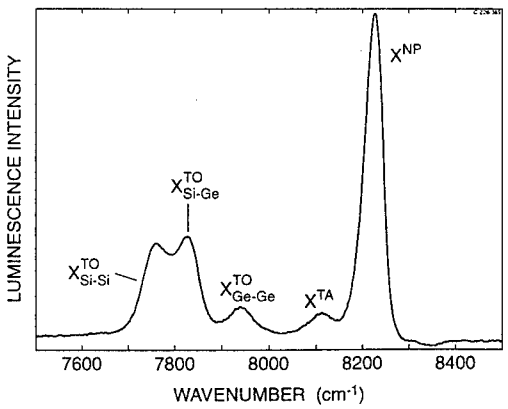


Fig. 4 Photoluminescence spectrum of a $Si_{0.6}Ge_{0.4}$ strain-relaxed layer for an excitation wavelength of 457.9nm. From ref. [19].

Photoluminescence (PL) measurements have been mainly performed in order to optimize the growth procedures. The PL spectra are dominated by near band gap excitonic luminescence with an intense sharp no-phonon transition; this, as well as the observation of well-distinguished phonon modes, (Fig. 4)

indicates a high quality of the SiGe layers. The PL measurements were of decisive importance for our decision of using a substrate-growth temperature ≥750°C [20].

The layers are doped n- or p-type during growth with Sb or B, respectively, from effusion cells. Layers grown without an intentional doping become n-type in our system with a dopant concentration of 1-5×10^{13}cm^{-3}. We have observed that in the strain-relaxed SiGe layers the concentration of deep levels as determined by deep level transient spectroscopy (DLTS) is reduced significantly as compared to the case of Si growth; we ascribe this to a gettering effect of the misfit dislocations in the graded buffer layer. The concentration of deep levels is found from DLTS measurements to be smaller than 5×10^{11}cm^{-3} in unintentionally doped layers and smaller than 2×10^{12}cm^{-3} in both p- and n-type layers doped to less than 1×10^{16}cm^{-3}. It has been crucial for our defect studies to achieve such a low concentration of deep levels.

3. Defect Studies with SiGe

3.1. Diffusion of Sb

The diffusion of Sb in Si is known to precede predominantly by the vacancy-assisted mechanism via the formation of Sb-vacancy pairs (E-centre mechanism) [21], and is believed to do so also in Ge [22], although to our knowledge there is no experimental evidence in Ge for this quality. Thus, we consider Sb in SiGe alloys for an excellent test specie to study vacancy-mediated diffusion as a function of the Ge content.

A determining advantage of the epitaxial methods compared to traditional bulk-crystal methods to grow structures for defect studies is that very well defined impurity profiles can be incorporated during growth into the layer in which the diffusion will be studied. This has been utilized in the present case where a Sb spike is buried in the SiGe top layer centred about 2000Å from the surface. The Sb peak concentration is kept below 1×10^{19}cm^{-3} to prevent Sb from precipitating during diffusion and to ensure that the diffusion precedes in the intrinsic regime, by keeping the Sb concentration below the intrinsic carrier concentration at the diffusion temperature.

Figure 5 shows representative chemical profiles measured by secondary ion-mass spectrometry (SIMS) from as-grown and heated samples together with calculated profiles [6]. The diffusivity was found to be time independent and well characterized with a concentration independent diffusion coefficient, in agreement with the chosen doping level. It can be appreciated from the figure that the diffusivity in $Si_{0.70}Ge_{0.30}$ is higher than that in $Si_{0.80}Ge_{0.20}$. The extracted activation energies of Sb diffusion are plotted in

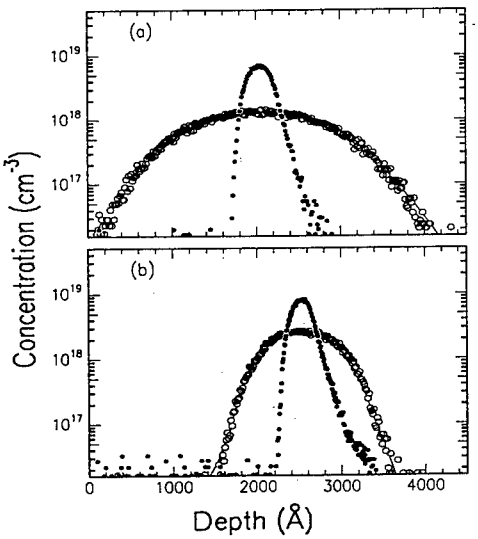


Fig. 5 Chemical profiles of Sb in $Si_{1-x}Ge_x$, as-grown (•), heated (○), and calculated (solid line); (a): x=0.3, (b): x=0.2. The heating temperature and time was 851°C and 24 hours, respectively. From ref. [6].

Fig. 6 together with a literature value for that of Ge. Also shown in Fig. 6 as a solid line is a linear interpolation between the Si and Ge activation energies. The measured activation energies are significantly higher that the linearly extrapolated values. According to Hu [23], the activation energy for E-centre diffusion is given as

$$Q = H_f + H_m - \Delta E_b$$

where H_f and H_m are the vacancy formation and migration enthalpies, respectively, and ΔE_b is the binding energy between the Sb and the vacancy in the third nearest neighbour position to the Sb atom. None of these terms are expected to scale linearly between Si and Ge and, moreover, could scale independently. Thus, one should not *a priori* expect a linear dependence. We have tried a very simple concept which is only meant to indicate a possible route for the modelling [6]. This concept is based on the observation that the vacancy has to pass two energy barriers in order to reach the saddle point for E-centre diffusion. In this simple model it is assumed that the higher of the two barriers is the determining factor, thus only in the case of two Ge barriers is the activation energy equal to that for Ge. Assuming a binomial distribution of atoms in the alloy, a quadratic expression for the activation energy is obtained:

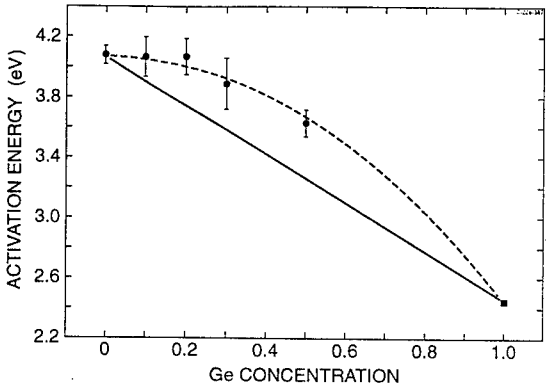


Fig. 6 Extracted activation energies as a function of Ge content (•); also shown is a linear interpolation between the pure Si and Ge values (solid line) and an interpolation based on the qualitative explanation, see text (dashed line). The value for pure Ge is a mean value of the values given by Sharma [26]. From ref. [6].

$$Q(x) = (1-x^2)\cdot Q(Si) + x^2\cdot Q(Ge).$$

The result of this simple approach is also shown in Fig.6 as the dashed curve, and the agreement with the experimental values is surprisingly good.

3.2. The Sb-Vacancy Pair

The group V - vacancy complex, the E-centre, plays a central role in the vacancy-assisted diffusion of P, As, or Sb in Si and SiGe, as has been demonstrated above in the case of Sb. The E-centre has an acceptor level in the upper part of the energy gap, at around E_C - 0.42eV, the exact position being dependant on the group-V element involved. At the diffusion temperature, e.g. at 1000 °C, the band gap in Si will be reduced to 0.72eV from 1.12eV at room temperature. The question is now what happens to the acceptor level of the E-centre when the temperature is increased to the diffusion temperature. Two different scenarios are depicted in Fig. 7: If the level is pinned to

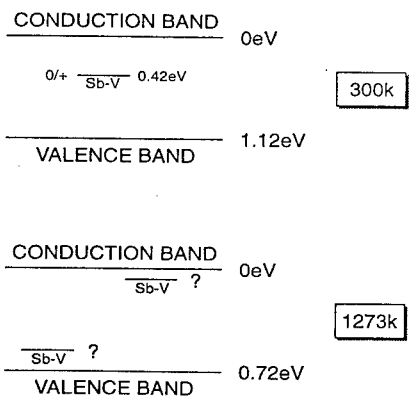


Fig. 7 The position of the acceptor level of the Sb-vacancy pair in the conduction band at the two mentioned temperatures (see text).

the valence band, at 1000°C it will be placed at E_C - 0.02eV, and the complex will be neutral during diffusion; if, on the other hand, the level is pinned to the conduction band, it will be placed in the lower part of the band gap, and the complex will be negatively charged during diffusion. The charge state of the complex is of course of decisive importance for its diffusivity and, moreover, influences its equilibrium concentration.

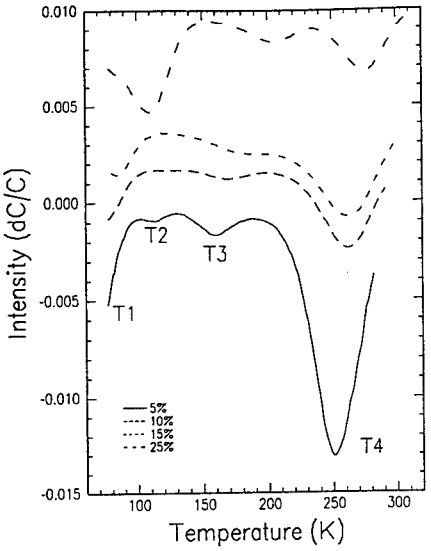


Fig. 8 DLTS spectra of $Si_{1-x}Ge_x$ strain-relaxed layers after irradiation with identical doses of 2-MeV protons. The spectra are from top to bottom for x=0.25, 0.15, 0.10, and 0.05, respectively. Only the spectrum for the x=0.05 sample follow the y axes; the other spectra are shifted arbitrarily but drawn to scale. The spectra were all recorded using a repitition rate of 1.0kHz. From ref. [7].

We have studied the pinning behaviour of the acceptor level of the E-centre in Si by varying the composition of strain-relaxed $Si_{1-x}Ge_x$ from x=0 to x=0.25 [7]; in this composition range the band gap changes at room temperature from 1.12eV to 1.02-eV, respectively, and the band gap is determined by the Si-like X conduction-band minimum in the whole composition range.

Either Schottky or p^+n diodes, doped to about 5×10^{15}Sb/cm^3, were irradiated with 2-MeV protons at room temperature to doses of about 1.5×10^{12}cm^{-2}. Typical DLTS spectra from the different SiGe alloy layers are shown in Fig. 8. Four lines can be distinguished in the spectra. From activation energies, apparent capture-cross sections, and annealing temperatures they have been identified as originating from interstitial carbon C_i (T_1), the interstitial carbon-substitutional carbon pair C_i-C_s (T_2), the divacancy (T_3), and the E centre (T_4) [7,24]. We have up to now only studied the E-centre as a function of composition, and in the following only this centre will be discussed.

It appears from Fig.8 that 1) the E-centre signal moves to higher temperature with increasing Ge content, 2) the size of the signal is reduced with increasing Ge content and 3) the half width of the peak is within 5% independent of the Ge content. Figure 9 shows the activation energy (enthalpy) relative to the conduction band edge and the apparent capture cross section as a function of composition extracted from Arrhenius plots of the thermal emission rate, corrected for the T^2 dependence. The apparent capture cross section σ_{na} is equal to $\sigma_{na} = \chi_n \sigma_n$, where χ_n is the entropy factor and σ_n the capture cross section. We have measured σ_n as a function of composition and found that it is inde-

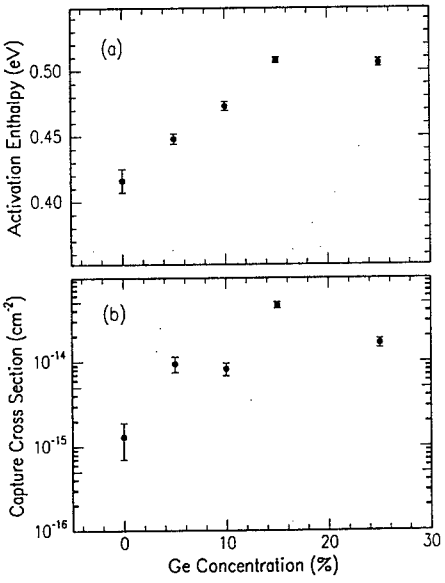


Fig. 9 Activation enthalpies (a) and apparent capture cross sections (b) for the Sb-V defect extracted from Arrhenius plots. The indicated uncertainties are only statistical ones from least-squares fits to the Arrhenius plots; the systematic uncertainties are estimated to be of the order of 5% on the activation enthalpies, and 10% on the capture cross sections. From ref. [7].

pendent of composition. Thus χ_n could be determined as a function of composition and then used to correct the activation enthalpy given in Fig. 9a to obtain the Gibbs free energy. The Gibbs free energy gives the true position of the level in the band gap, and as shown in Fig.10 the position of the E-centre level in the band gap is independent of composition; thus, the acceptor level of the E-centre is pinned to the conduction band. The average energy-position of the level relative to the conduction band is found from Fig. 10 to be $E_{Sb-V} = (0.41 \pm 0.02)$ eV.

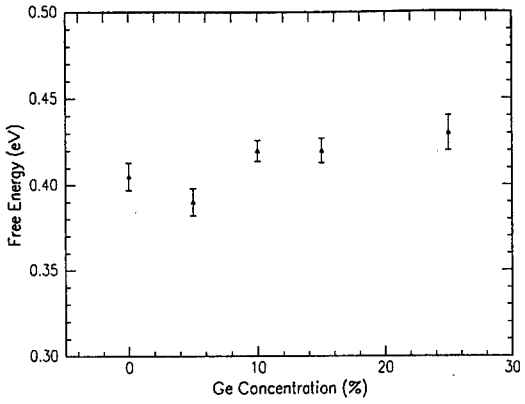


Fig. 10 Gibbs-free energy of the Sb-V defect as a function of composition. The uncertainties are statististical uncertainties only; the systematic uncertainties are estimated to be of the order of 5%. From ref. [7].

We can now understand the two other properties of the E-centre DLTS signal mentioned above. The reduced intensity with increasing Ge composition is due to the fact that the level moves deeper into the band gap and then starts to communicate also with the valence band. As the DLTS signals shown in Fig. 8 is due to electrons emitted from the E-centre level to the conduction band, and as the energy difference is independent of composition, there will be no broadening of the signal due to the statistical fluctuation of Ge atoms around the E-centre [25].

4. Conclusions

Strain-relaxed, epitaxial-grown $Si_{1-x}Ge_x$ alloy layers on Si substrates are very attractive for defect studies for several reasons: The band gap can be changed independent of temperature or external pressure making it possible to study band-gap sensitive phenomena such as the pinning behaviour of deep levels in the band gap. The composition can be changed gradually from Si to Ge which might shed light on physically processes such as impurity diffusion which is known to be different in Si and Ge for a number of impurities. Finally, very well defined impurity profiles can be incorporated in the layers during the growth which is very attractive for diffusion studies. However, a prerequisite for such studies is that material of a sufficient quality is available. We have demonstrated that this is actually the case for $Si_{1-x}Ge_x$ layers of $x \leq 0.50$, and we are convinced that this upper limit will move further up in the near future. The use of strain-relaxed SiGe alloy layers for defect investigations have been exemplified by the studies of Sb diffusion and the pinning behaviour of the Sb-vacancy pair.

Acknowledgement

This work has been supported by the Danish National Research Foundation through the Aarhus Centre of Advanced Physics (ACAP), the Danish Natural Scientific Research Council, and the Centre for Nano-Structures (CNAST) under the Danish Materials Development Program, MUPII. Thanks are due to Per Kringhøj, Sergey Shiryaev, and John Lundsgaard Hansen for many fruitful discussions.

References

1. A. Gruhle and A. Schüppen, Thin Solid Films **294**, 246 (1997)
2. E.A. Fitzgerald, Y.H. Xie, D. Monroe, P.J. Silverman, J.M. Kuo, A.R. Kortan, F.A. Thiel, and B.E. Weir, J.Vac.Sci.Technol. B **10**, 1807 (1992)
3. E.A. Fitzgerald and S.B. Samavedam, Thin Solid Films **294**, 3 (1997)
4. N.V. Abrosimov, S.N. Rossolenko, W. Thieme, A. Gerhardt, and W. Schröder, J.Cryst. Growth 174, **182** (1997)
5. P. Kringhøj, S.Yu. Shiryaev, and A. Nylandsted Larsen, Phys.Rev.Lett. **76**, 3372 (1996)
6. A. Nylandsted Larsen and P.Kringhøj, Appl.Phys.Lett. **68**, 2684 (1996)
7. P. Kringhøj and A. Nylandsted Larsen, Phys.Rev. B **52**, 16333 (1995)
8. H.-J. Herzog, in "Properties of Strained and Relaxed Silicon Germanium" ed. E. Kasper (EMIS Datareviews Series No.12 1995) p.49
9. R. Hull, ibid 8, p. 17
10. H.J. Osten and E. Bugiel, Appl.Phys.Lett. **70**, 2813 (1997)
11. M.S. Abrahams, C.J. Buiocchi, and G.H. Olsen, J.Appl.Phys. **46**, 4259 (1975)
12. F.K. LeGoues, B.S. Meyerson, and J.F. Morar, Phys.Rev.Lett. **66**, 2903 (1991)
13. S.Yu. Shiryaev, Phil.Mag.Lett. **68**, 195 (1993)
14. K.K. Linder, F.C. Zhang, J.-S. Rieh, P. Bhattacharya, and D. Houghton, Appl.Phys.Lett. **70**, 3224 (1997)
15. E.V. Monakhov and A. Nylandsted Larsen, Nucl. Instrum. and Meth. in Phys. Res B **108**, 399 (1996)
16. E.V. Monakhov and A. Nylandsted Larsen, Nucl. Instrum. and Meth. in Phys. Res B **117**, 71 (1996)
17. E.V. Monakhov, S.Yu.Shiryeav, A.Nylandsted Larsen, J. Hartung, and G. Davies, Thin Solid Films **294**, 43 (1997)
18. P.M. Mooney, F.K. LeGoues, J.O. Chu, and S.F. Nelson, Appl.Phys.Lett. **62**, 3464 (1993)
19. J. Hartung, G. Davies and A. Nylandsted Larsen, unpublished results
20. A. Nylandsted Larsen, J. Lundsgaard Hansen, R. Schou-Jensen, S. Yu. Shiryaev, P. Riis Østergaard, J. Hartung, G. Davies, F. Jensen, and J. Wulff Petersen, Physica Scripta T **54**, 208 (1994)
21. P.M. Fahey, P.B. Griffin, and J.D. Plummer, Rev.Mod.Phys. **61**, 289 (1989)
22. W. Frank, U. Gösele, H. Mehrer, and A. Seeger, in "Diffusion in Crystalline solids" eds. G.E. Murch and A.S. Nowick (Academic, New York 1984)p.63
23. S.M. Hu, Phys.Stat.Sol. B **60**, 595 (1973)
24. C. Budtz-Jørgensen and A.Nylandsted Larsen, unpublished results
25. A. Mesli, P. Kringhøj, and A. Nylandsted Larsen, to be published
26. B.L. Sharma, Defects and Diffusion Forum **70-71**, 1 (1990)

Materials Science Forum Vols. 258-263 (1997) pp. 91-96
© 1997 Trans Tech Publications, Switzerland

ACCEPTOR STATES IN BORON DOPED SiGe QUANTUM WELLS

K.Schmalz[*], M.S.Kagan, I.V.Altukhov, K.A.Korolev, D.V.Orlov, V.P.Sinis, S.G.Tomas[**], K.L.Wang[**], and I.N.Yassievich[***]

Institute of Radioengineering and Electronics of RAS, 11, Mokhovaya, 103907 Moscow, RUSSIA.
[*] Institute for Semiconductor Physics, Walter-Korsing str., 2, 15230 Frankfurt (Oder), Germany
[**] University of California, 66-147KK Engineering IV, Los Angeles, CA 90095, USA
[***] A.F.Ioffe Physico-Technical Institute of RAS, 26, Politekhnicheskaya, 194021 St.Petersburg, RUSSIA

Keywords: *SiGe* quantum wells, transport properties, acceptor states

Abstract.
The temperature dependences of lateral conductivity and hole mobility in *SiGe* quantum well structures selectively doped with boron are presented. The boron A^+ centers are found to exist and determine the low-temperature conductivity. The activation energy of conductivity at higher temperatures is shown to be determined by the energy distance between strain-split boron A^0 centers. The model of two-stage excitation of free holes including the thermal activation of holes from the ground to split-off state and next tunneling into the valence band is proposed. The binding energy of A^+ centers and the energy splitting of boron ground states by strain are found.

Introduction.

Selectively doped *SiGe* quantum well structures (QWs) are of great interest for study of acceptor states which are degenerate in bulk material and should be split in two-dimensional (2*D*) systems due to space quantization and/or strain. The energy positions of ground and exited states of an acceptor can be controlled in a wide range by alloy composition, QW width, doping level and space position of an acceptor center. In this report, the binding energies of 2*D* positively charged (A^+) acceptor states and strain-splitting energy of neutral (A^0) states in boron doped *SiGe* QWs for structures with the same QW width and doping level and different alloy composition are determined. So-called A^+ states (acceptors binding an additional hole) [1,2] are of specific interest as they should exist in *SiGe* QWs in thermal equilibrium in contrast to bulk material where they can appear only due to excitation, e.g., by light. Similar D^--states of donors have been investigated in GaAS/GaAlAs structures [3,4].

Experiment.

The *p*-type *Si/SiGe/Si* QWs MBE-grown pseudomorphically on the *n*-type *Si* substrate and selectively doped with boron were used for conductivity and magnetoconductivity measurements at the temperatures of 4 up to 300 K. The *SiGe* layer of 20 nm thickness was sandwiched between undoped *Si* buffer (130 nm wide) and cap (60 nm) layers. The *SiGe* QW was uniformly doped with boron; the *B* concentration was of $3*10^{17}$ cm^{-3}. The content of *Ge*, *x*, in *SiGe* alloy was 0.1 and 0.15, respectively. Two boron delta layers with *B* concentration of $2*10^{11}$ cm^{-2} positioned within the buffer and cap layers on the distance of 30 nm from each QW interface were used to obtain A^+ centers inside the QW. The buffer delta layer should also supply holes to form the *p-n* junction between the *p*-layers and the *n*-substrate. This hole concentration N_{pn} was calculated by the expression: $N_{pn} = (\kappa N_d \Phi/2\pi e^2)^{1/2}$, κ is the dielectric constant, N_d is the donor concentration in the substrate, Φ is the initial difference of Fermi energies in *n*- and *p*-regions ($\Phi \approx 1$ eV), taking into account the total depopulation of donors in space charge region. From the measurements of donor-bound exciton luminescence, we have $N_d \approx 2*10^{14}$ cm^{-3} for the QWs with x=0.1 and $N_d \approx 5*10^{14}$ cm^{-}

[3] for x=0.15. (We are indebted to A.S.Kaminskiy for obtaining this data.) So, we get that the concentration in the buffer delta layer is diminished by $N_{pn} \approx 5*10^{10}$ cm^{-2} and $8.5*10^{10}$ cm^{-2} for above structures.

The contacts were deposited on the p-type side of structures so that the p-n junction prevented from a current along the substrate.

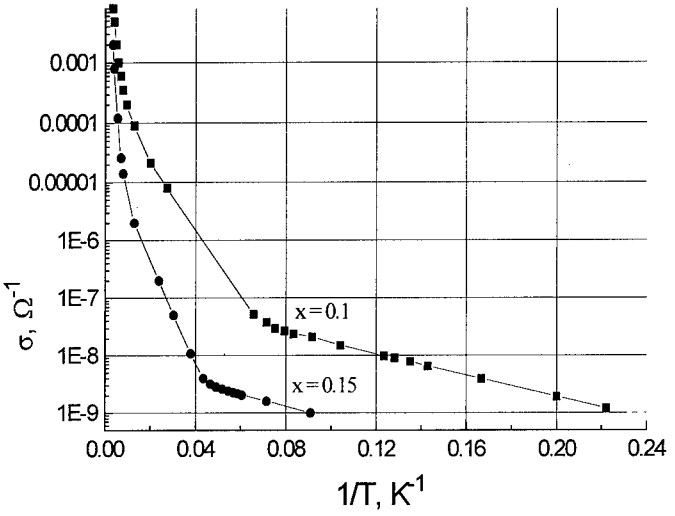


Fig.1. Temperature dependence of conductivity.

Figure 1 shows, in log-1/T scale, the temperature dependence of conductivity along the *SiGe* layer for the samples with 0.1 and 0.15 *Ge* content, x. One can see two activation-law regions in the curves. The low-temperature activation energy is approximately 2 meV and practically coincides for the samples with different *Ge* content. The activation energy at higher temperatures ($T \geq 20$ K) is of 12 ± 1 meV for x=0.1 and 19 ± 1 meV for x=0.15. The hole mobility, μ, was determined from the measurements of transverse magnetoconductivity by means of the expression $\Delta\sigma/\sigma = (\mu H/c)^2$ (σ is the conductivity, H is the magnetic field, c is the light velocity). The temperature dependence of μ is shown in Fig.2. The maximum in the $\mu(T)$ dependence points at the change of scattering mechanism. Note the comparatively high mobility values.

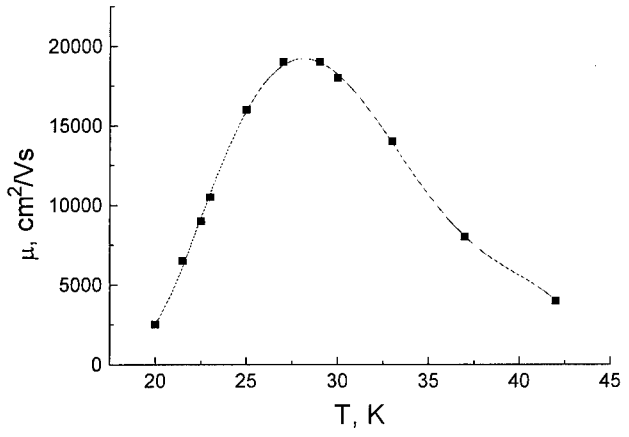


Fig.2. Temperature dependence of hole mobility for x=0.1.

Discussion.

There are two possible explanations of the observed exponential temperature dependence of conductivity. First, the low-temperature activation energy (≈ 2 meV) can be due to the thermally activated hopping conductivity. In dependence on the Fermi level (ε_F) position, the hopping can be over neutral (A^0) boron states if $\varepsilon_F \approx \varepsilon^0$, ε^0 is the A^0 binding energy, or positively charged A^+ states if $\varepsilon_F \approx \varepsilon^+$, it is A^+- centers binding energy. The main argument against the hopping is the low conductivity observed. Really, at the given doping level in QW, $3*10^{17}$ cm^{-3}, the mean distance

between impurities (≈ 8 nm) is of the order of the effective Bohr radius of impurity, which can be estimated by the expression $a_B \approx \hbar/\sqrt{2m\varepsilon_B}$. Using linear interpolation of *GeSi* parameters between *Si* and *Ge*, we get $a_B \approx 2.5$ nm for A^0 and ≈10 nm for A^+ states [5]. Because of strong overlapping impurity states, the specific (on square) conductivity value can not be less than 1 - 10 kOhm (see, f.i., [6] for references). It is several orders of magnitude more than the experimental values.

The second possible origin of 2 meV activation energy can be the thermal hole emission from A^+ states. The calculation of the A^+ binding energy [6] gives just $\varepsilon^+ \approx 2$ meV, being weakly dependent on *Ge* content in *SiGe* alloy. The necessary condition for conductivity due to thermal activation of A^+ centers is the Fermi level to be near ε^+ at low temperatures. Let's now discuss this possibility for our samples. Shown in Fig.3 is the schematic view of the valence band potential profile of the QW structures investigated. Due to charged *B*-delta layers, two barrier regions with linear potential distribution should appear outside of QW. To find the Fermi level position and then the temperature dependence of free hole concentration we used the following set of equations:

$$N_{1,2} = N_\delta \cdot \{1 + \exp[-(\varepsilon_\delta - \varepsilon_{1,2})/kT]\}^{-1},$$

$$N - N^- - N^+ = N \cdot \{1 + \exp[-(\varepsilon_0 - \varepsilon_F)/kT]\}^{-1},$$

$$N^+ = N\{1 + \exp[-(\varepsilon^+ - \varepsilon_F)/kT]\}^{-1},$$

$$\varepsilon_1 = \varepsilon_F - \Delta + (4\pi e^2 d/\kappa)[N_1 - (N_2 - N_{pn}) + N^+ - N^- + p],$$

$$\varepsilon_2 = \varepsilon_F - \Delta + (4\pi e^2 d/\kappa)[-N_1 + (N_2 - N_{pn}) - N^+ + N^- - p],$$

$$N_1 + N_2 + N^- = N^+ + p.$$

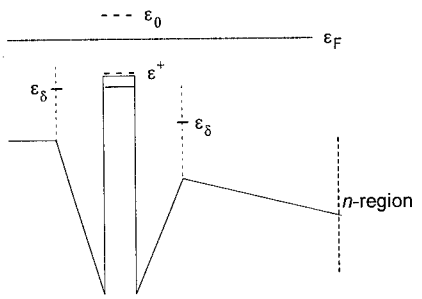


Fig.3. Schematic view of *SiGe* QW valence band structure.

Here $N_{1,2}$ are the concentrations of empty (negatively charged) *B* centers in the cap and buffer δ-layers, respectively, N_δ and N is the *B* concentration in δ-layers and in *SiGe* QW, N^+ and N^- are the concentrations of positively and negatively charged *B* centers in the QW, $p = N_v exp(\varepsilon_F/kT)$ is the free hole concentration and N_v is the density of states in the QW, ε_δ, ε_0, and ε^+ are the binding energies of *B* centers in *Si*, and boron-A^0 and A^+ centers in the *SiGe* QW, Δ is the valence band offset, d=30 nm is the distance between the δ-layers and QW interfaces, κ is the dielectric constant. The QW top energy was taken for zero. The calculated temperature dependence of hole concentration p for x=0.1 and for different δ-layer doping level is presented in Fig.4. The main feature of curves is the absence of a free hole density saturation at the temperatures of depopulation of the A^+ level which should exist at similar conditions in the bulk material. The reason for such a behavior is the absence of local charge neutrality and "horizontal" redistribution of carriers between the QW and δ-layers with changing temperature.

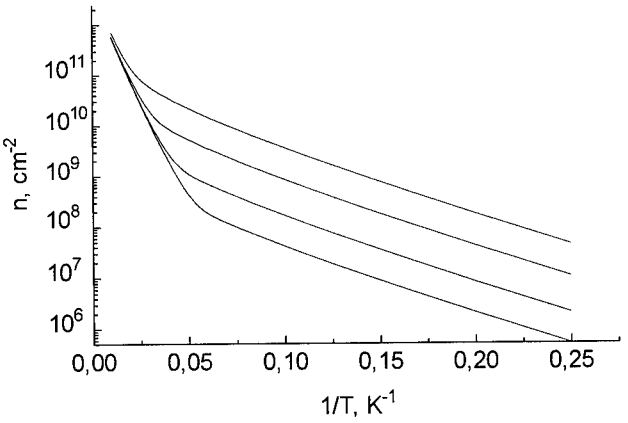


Fig.4. Calculated temperature dependence of hole concentration in QW at various δ-layer doping level.

The values of the binding energies of A^0 and A^+ centers, ε_0 and ε^+, was varied to fit the experimental curve. The

parameters for the best fit are the following: ε_0 = 24 meV and 36 meV for x=0.1 and x=0.15, respectively, ε^+= 2 meV and N_δ =10^9 cm^{-2} for both structures. Thus the low-temperature activation energy is the binding energy of the boron A^+ centers in QW. However, the extra hole concentration supplied into QW turns out to be two orders less than the doping level of δ-layers. The only reason for this seems to be *Si* surface states which can accumulate almost all holes from the δ-layers.

The origin of activation energy at higher temperatures is not so obvious. It should be one half of boron-A^0 binding energy because the Fermi level lies between the valence band edge and the B^0 ground state as it is filled. So, the observed high-temperature activation energies, 12 and 18 meV, correspond to 24 and 36 meV B^0 binding energies. These values are, however, quite surprising. Indeed, the binding energy of shallow impurity should decrease with increasing both *Ge* content and strain, it is quite the contrary to the experiment. Moreover, the value of ε_0 = 24 meV seems not to be real for x=0.1.

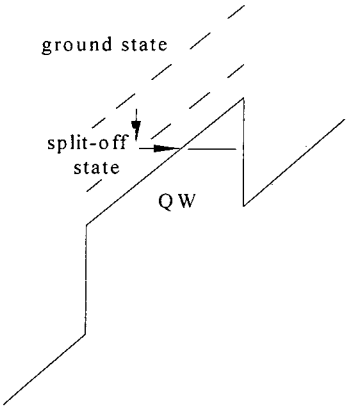


Fig.5. Scheme of conductivity activation by tunneling.

The only energy which could agree with the above values of ε_0 is the energy difference between acceptor levels split by strain. Indeed, the splitting energy of the ground acceptor state found by means of linear interpolation between *Si* and *Ge* is ≈ 15 and 25 meV for x=0.1 and x=0.15, respectively. This is close to the experimental activation energies. (Note that the estimation of the energies by interpolation is very approximate.) The splitting energy can be as the activation one only if holes can pass from the split-off state into the valence band without activation, that is by tunneling. It is impossible in the scheme of flat bands. On the other hand, we have seen from the experiment that almost all holes from the δ-layers accumulate in the surface states making the surface charged. So, the potential across the structure should appear inclining the valence bands. The scheme of potential distribution for this case is shown in Fig.5. One can see from this scheme that the conductivity in this case can be controlled by two-stage process: first, the thermal activation of holes from the ground to split-off state takes place and then hole tunneling into free hole band creates the conductivity. To estimate the possible potential drop across the structure, let's remember an empirical law that for most homeopolar semiconductors the Fermi energy is fixed on the surface near 1/3 of the energy gap from the valence band. It is ≈ 0.4 eV for *Si*. The QW width is 5 times less than the structure width. So, the potential drop on the QW is of ≈ 80 meV. Of course, this estimation is too rough but it shows that the proposed model can be real. Thus, the arguments for the model are (i) the increasing activation energy of conductivity with *Ge* content, (ii) small additional hole concentration supplied from δ-layers into the QW, and (iii) charging the surface and arising the potential drop across the QW, as a consequence.

Summary.

The experimental data presented give evidence for existence of A^+ centers in *B* doped *SiGe* QW structures in thermal equilibrium. The thermal emission of holes from these centers determines the conductivity along the QW at low temperatures. At higher temperatures, the conductivity is shown to be due to thermal activation of holes from the ground to strain-split *B* states following by hole tunneling into the QW valence band. The tunneling is made possible due to a potential drop across the QW which arise due to hole capture at surface states of the *Si* cap layer making the surface charged. Note that in structures with doping profile and level investigated, it is possible to find the energy splitting of acceptor levels by strain from temperature dependence of conductivity.

This work was supported in part by Grants No 96-02-17352 and 97-02-16820 from RFBR, No 97-10-55 from Russian Ministry of Science and Technology and Volkswagen Stiftung Grant.

References.

1. E.M.Gershenzon, Yu.P.Ladyzhenskii, and A.P.Mel'nikov, JETP Lett., **14**, 380 (1971)
2. E.E.Godik, Yu.A.Kuritsyn, and V.P.Sinis, JETP Lett., **14**, 377 (1971).
3. S.Huant, S.P.Najda, and B.Etienne, Phys.Rev.Lett., **65**, 1486 (1990).
4. D.M.Larsen, S.Y.McCann, Phys.Rev.B, **46**, 3966 (1992).
5. K.Schmalz, I.N.Yassievich, K.L.Wang, and S.G.Tomas, Phys.Rev.B (1997), in print
5. B.I.Shklovskii and A.L.Efros, Electronic Properties of Doped Semiconductors, Springer, Heidelberg (1984)
6. I.N.Yassievich, K.Schmalz, M.A.Odnobludov, and M.S.Kagan, Proc. 7th Int.Conf. on Modulated Semicond. Structures, 152, Spain (1995)

Materials Science Forum Vols. 258-263 (1997) pp. 97-102
© 1997 Trans Tech Publications, Switzerland

SUBSTITUTIONAL CARBON IN Ge AND $Si_{1-x}Ge_x$.

L. Hoffmann[1], J. C. Bach[1], J. Lundsgaard Hansen[1], A. Nylandsted Larsen[1], and B. Bech Nielsen[1], P. Leary[2], R. Jones[2], and S. Öberg[3],
[1]Institute of Physics and Astronomy, Aarhus University, DK-8000, Aarhus C, Denmark
[2]Department of Physics, University of Exeter, EX44QL, Exeter, United Kingdom
[3]Department of Mathematics, University of Luleå, S-95 187, Luleå, Sweden

Key Words: Carbon, Ge, $Si_{1-x}Ge_x$, IR-spectroscopy, ion-channeling, *ab-initio* calculations

Abstract. In the present work, carbon is implanted into monocrystalline Ge and into relaxed epitaxial MBE-grown $Si_{1-x}Ge_x$. The samples are studied with infrared absorption spectroscopy along with ion-channeling studies on the Ge samples. Finally, *ab-initio* local density functional cluster theory is applied to calculate the structure and the local vibrational modes of substitutional carbon, C_s, in Ge.
After implantation of $^{12}C^+$ in Ge at room temperature and subsequent annealing at 350 °C, a sharp absorption line is observed at 531 cm^{-1}. By isotope substitution, it is concluded that the 531 cm^{-1} line represents a local vibrational mode of a single carbon atom. From ion-channeling measurements on samples annealed at 450 °C, it is found that 31±3 % of the carbon atoms are located at substitutional sites. The population of the substitutional site and the intensity of the 531 cm^{-1} mode have identical annealing behavior and it is concluded that the 531 cm^{-1} mode is the three-dimensional T_2 stretch mode of C_s in Ge. The calculated frequency and isotope shift for this mode are in good agreement with the observations.
In $Si_{0.65}Ge_{0.35}$, two broad absorption lines are observed at ~551 and ~592 cm^{-1} after implantation of $^{12}C^+$ and subsequent annealing at 550 °C. From measurements on samples implanted with $^{13}C^+$ and co-implanted with $^{12}C^+$ and $^{13}C^+$ we conclude that these lines represent local vibrational modes of defects containing a single carbon atom. In $^{13}C^+$ implanted $Si_{1-x}Ge_x$ samples that contain 15 to 50 % Ge a number of modes are observed in a frequency range from ~510 to ~610 cm^{-1}, i.e., in the range of C_s in Ge and in Si. From the experimental findings it is concluded that substitutional carbon in $Si_{1-x}Ge_x$ binds to both Si and Ge.

Introduction

Carbon is an important impurity in Si and it forms a range of complexes [1] among which C_s is the most prominent [2,3]. This defect has tetrahedral symmetry and gives rise to a single three-dimensional local vibrational mode (T_2 mode) at 607 cm^{-1} [2]. C_s is also expected to exist in crystalline Ge due to the similar chemical properties of Si and Ge. However, the lengths of C-C and Ge-Ge bonds differ by 2.09 Å. This implies that a considerable strain field will be introduced around C_s in Ge and, therefore, the defect may be unstable. $Si_{1-x-y}Ge_xC_y$ layers of arbitrary thickness and low dislocation density can be grown on pure Si [4,5] in contrast to $Si_{1-x}Ge_x$ layers [6]. The reason is that the carbon atoms compensate the 4 % mismatch between the Si and Ge lattice constants. This makes C_s an interesting and important defect in $Si_{1-x}Ge_x$ compounds. So far, only the Si-C mode at 607 cm^{-1} has been observed in such materials and it remains unknown whether Ge-C bonds are formed [4,5,7].
In the present work, C_s in Ge and in $Si_{1-x}Ge_x$ are identified experimentally.

Experimental

Samples cut from single-crystalline float-zone Ge or relaxed epitaxial MBE-grown $Si_{1-x}Ge_x$ [8,9] were implanted with $^{12}C^+$ or $^{13}C^+$. The implantations were carried out at room temperature with 17 energies in the range from 50 to 450 keV. The dose implanted at each energy was adjusted to yield a nearly

uniform depth profile (3×10^{20} cm^{-3} in Ge and 1×10^{20} cm^{-3} in $Si_{1-x}Ge_x$) extending from 0.1 to 0.8 μm below the surface in Ge and from 0.1 to 1.0 μm in $Si_{1-x}Ge_x$. The beam was swept vertically and horizontally to ensure a homogeneously lateral distribution. The surfaces of the samples used for channeling measurements were perpendicular to a <100>, a <110>, or a <111> crystal axis. The infrared absorption measurements were carried out at 8 K and a resolution of ~4 cm^{-1} with a Nicolet, System 800, Fourier-transform spectrometer. The channeling measurements on Ge samples were carried out with a 1300 keV deuteron beam. The implanted ^{12}C atoms were probed by means of the nuclear reaction $^{12}C(d,p)^{13}C$ detecting the 3.25 MeV protons. Further details of the channeling technique and the experimental setup are given in Ref. [10,11,12].

Theoretical calculations

The structure and the local vibrational mode frequencies of C_s in Ge were calculated using *ab-initio* local density functional cluster theory on 71- and 131-atom tetrahedral clusters, $Ge_{35}H_{36}$ and $Ge_{71}H_{60}$, where the central Ge atom was replaced by carbon and the dangling bonds on the surface of the cluster were terminated by hydrogen. Further details of the method are given in Ref. [12,13]. The 71- and 131-atom clusters yielded almost identical structures, with the Ge-C bond lengths within 1.3 % of each other. The results for the 131-atom cluster are given below.

The energy minimization results in a configuration where C_s exerts a large tensile strain on the surrounding atoms. The Ge-C bond lengths are 2.046 Å, 18 % shorter than the bulk Ge-Ge bond length of 2.407 Å. As a result of this, the Ge-Ge back bonds are increased in length by 1.6 % to 2.447 Å. The highest vibrational mode frequency is 516 cm^{-1}, well above the Raman frequency at 304 cm^{-1}. This mode is triply degenerate (T_2) and involves the vibration of the carbon atom, and to a much lesser extent, its four neighbors. The frequency of the mode drops by 19 cm^{-1} when ^{12}C is substituted with ^{13}C.

Results and discussion

C_s in Ge. After implantation of $^{12}C^+$ in Ge and subsequent annealing at 450 °C, a single sharp absorption line is observed at 531 cm^{-1} (see Fig. 1). The line shifts down to 512 cm^{-1} when ^{12}C is substituted by ^{13}C. The frequency ratio is 1.037, i.e. very close to $\sqrt{13/12}$. This establishes that the line represents a local vibrational mode of carbon. No additional modes appear after co-implantation of $^{12}C^+$ and $^{13}C^+$ into overlapping profiles. Thus, the 531 cm^{-1} mode originates from a defect containing a single carbon atom.

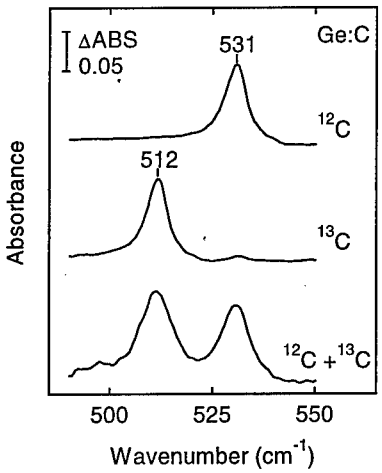


Figure 1. Absorbance spectra measured at 9 K on Ge samples annealed at 450 °C after implantation with $^{12}C^+$, $^{13}C^+$, or equal doses of both isotopes.

The angular distributions of proton and deuteron yields around the three major axes are shown in Fig. 2. For all three axes, there is a dip in the proton yield when the beam is aligned with the axis. The widths of the dips are close to those for backscattered deuterons, but the normalized minimum yields for the protons are much higher than those for the deuterons. Only a substitutional site or near-substitutional sites are consistent with broad dips in yield for all three major axes [14]. A significant fraction of the carbon atoms is consequently located at substitutional or near-substitutional sites. The solid lines through the datapoints in the figure represent the best fit to the data. In this analysis, the yield curves for C_s have been assumed equal to the host

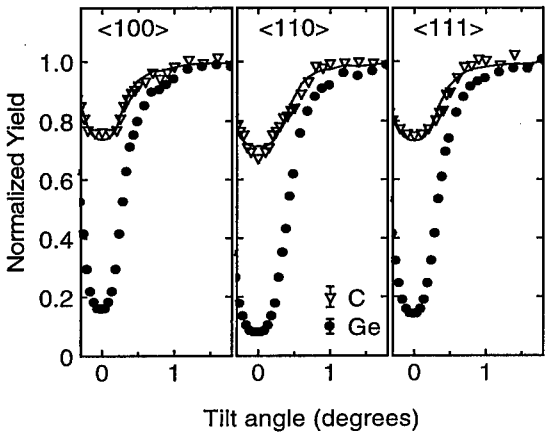


Figure 2. Angular distributions of normalized yield measured around the <100>, <110>, and <111> axes after annealing at 450 °C. The best fit (solid line) is obtained with 31±3 % carbon at substitutional sites, while the remaining carbon atoms are randomly located. The fit is obtained using the host curve data (•) to approximate the curve for C_s. Typical statistical uncertainties are indicated.

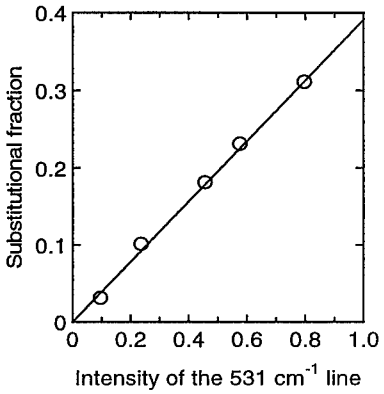


Figure 3. The population of carbon atoms at substitutional sites is shown as a function the intensity of the 531 cm^{-1} line. The channeling and infrared absorption measurements were carried out on the same sample after isochronal annealing at several temperatures. The data shown were measured after annealing at temperatures in the range from 450 to 700 °C.

dips in yield of backscattered deuterons. The fit corresponds to 31±3 % of the carbon atoms located at substitutional sites while the remaining 69∓3 % are located randomly.

Channeling and infrared absorption measurements were carried out on the same sample after isochronal annealing at several temperatures, starting at 350 °C and moving up to 700 °C in steps of ~50 °C. The 531 cm^{-1} mode begins to appear at 350 °C and reaches maximum intensity at 450 °C. Annealing at a higher temperature leads to a decrease in the intensity, and eventually at 700 °C, the mode has disappeared. It was not possible to carry out channeling measurements when the annealing temperature was below 450 °C due to insufficient recrystallization, so the channeling measurements were carried out at and above 450 °C. The population of the substitutional site has been determined quantitatively as a function of annealing temperature. It is maximal at 450 °C and decreases at higher temperatures and subsequently at 700 °C it is gone. The result of the analysis of the two sets of data is shown in Fig. 3 where the population of the substitutional sites is shown as a function of the intensity of the 531 cm^{-1} mode. It is evident from Fig. 3 that the annealing of the 531 cm^{-1} mode occurs parallel to the depopulation of the substitutional site, thus, the 531 cm^{-1} mode originates from a defect involving a single substitutional carbon atom.

The concentrations of C_s in our samples are ~10^{20} cm^{-3}, and are thus orders of magnitude higher than that of any other impurity. Therefore, the involvement of other impurities can be disregarded. The same argument cannot be used to rule out the involvement of intrinsic defects in the structure. However, it is hard to imagine that a carbon atom interacting with a vacancy-type or interstitial-type defect would be located exactly at a substitutional site. Moreover, the symmetry of such a defect would be lower than tetrahedral in which case at least two carbon modes should be expected, but only one is observed. On this basis, we identify the 531 cm^{-1} mode as the triply degenerate T_2 mode of isolated C_s in Ge.

The *ab-initio* calculations provide further support for our identification. The calculated frequency of the local vibrational mode of C_s is 516 cm^{-1}, well within the 100 cm^{-1} limit, which is typical of the method. Furthermore, when ^{12}C is substituted with ^{13}C the calculated mode drops by 19 cm^{-1}, which compares extremely well with the experimental reduction.

C_s in $Si_{1-x}Ge_x$. Infrared absorption measurements were carried out on a $Si_{0.65}Ge_{0.35}$ sample implanted with $^{12}C^+$ after isochronal annealing at several temperatures, starting at 300 °C and moving up to 900

°C in steps of ~50 °C. Two broad absorption lines at ~551 and ~592 cm^{-1} appear at 550 °C. The total intensity of the lines is constant until 800 °C, where the intensity starts to decrease, and at 900 °C the lines have disappeared. A selection of the absorbance spectrum of a $Si_{0.65}Ge_{0.35}$ sample implanted with $^{12}C^+$ is shown in Fig. 4 after annealing at 700 °C. In a $Si_{0.65}Ge_{0.35}$ sample implanted with $^{13}C^+$ a similar couple of lines are observed a factor of 1.03 lower in frequency. Therefore, the lines represent local vibrational modes of carbon. In a $Si_{0.65}Ge_{0.35}$ sample containing equal amounts of $^{12}C^+$ and $^{13}C^+$ a very broad line is observed. However, after subtraction of the absorption originating from the isotopic pure configurations, no additional modes appear (see Fig. 4). Thus, the modes originate from defects, which contain a single carbon atom.

The carbon related modes in $Si_{1-x}Ge_x$ ($0 \leq x \leq 1$) depend on the Ge concentration. Fig. 5 shows ^{13}C-related modes in pure Si, in pure Ge, and in $Si_{1-x}Ge_x$ after annealing at 750 °C [15]. The single T_2 mode of C_s observed in pure Si broadens and shifts downwards when the Ge concentration of the samples are increased from 0 to 50 %. Moreover, additional carbon-related modes are observed in samples containing Si and Ge. One mode is at a higher frequency than the T_2 mode of C_s in Si. This mode is observed at ~600 cm^{-1} in the $Si_{0.85}Ge_{0.15}$ sample and shifts down to ~585 cm^{-1} in the $Si_{0.5}Ge_{0.5}$ sample. A second mode is on the low-frequency side of the T_2 mode of C_s in Si. This mode shifts down from ~542 to ~525 cm^{-1} when the Ge concentration is increased from 15 to 50 %. Finally, a low-

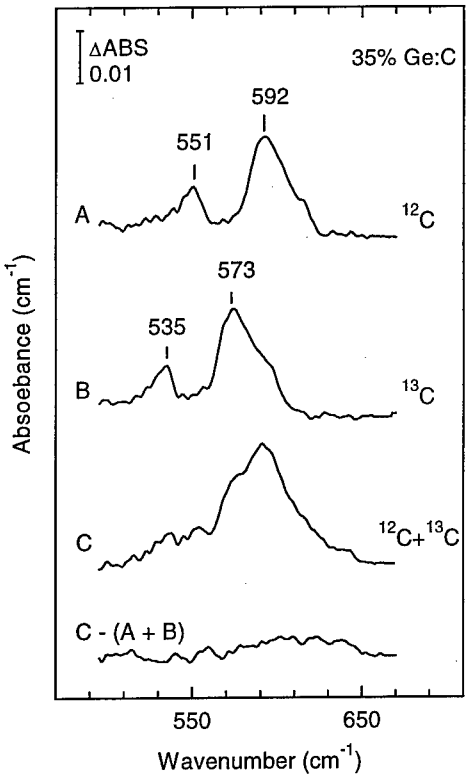


Figure 4. Absorbance spectra measured on $Si_{0.65}Ge_{0.35}$ samples annealed at 700 °C after implantation with $^{12}C^+$, $^{13}C^+$, and co-implantation with equal doses of each isotope. The spectrum at the bottom is a result of subtraction of the absorption originating from the isotopic pure samples from the absorption originating from the co-implanted sample.

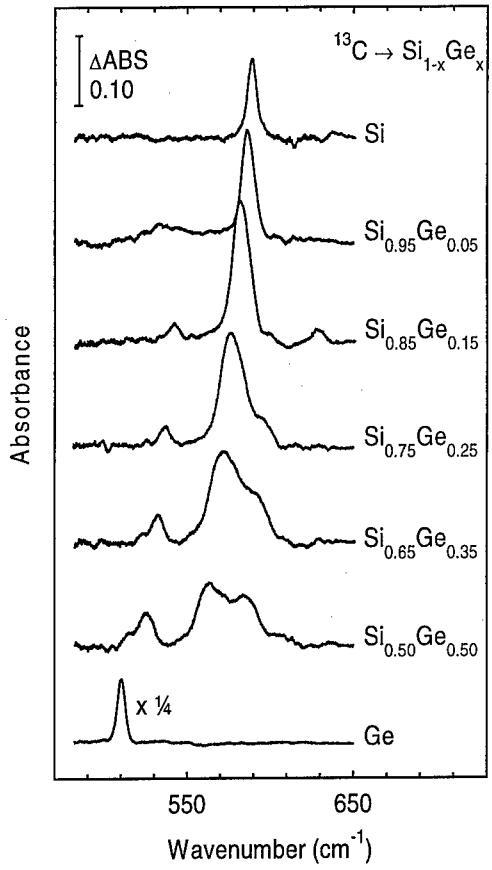


Figure 5. Absorbance spectra measured on $^{13}C^+$-implanted $Si_{1-x}Ge_x$ samples ($0 \leq x < 1$) after annealing at 750 °C. The absorbance spectrum for the Ge sample is measured after annealing at 550 °C.

intensity peak is observed at ~522 and at ~514 cm^{-1} in $Si_{0.65}Ge_{0.35}$ and in $Si_{0.5}Ge_{0.5}$, respectively. The intensity of the carbon-related modes varies as a function of the Ge concentration. The intensity of the Si-C related T_2 mode decreases, while the other modes gain intensity when the Ge concentration increases from 0 to 50 %.

In order to qualitatively understand how the carbon-related modes depend on the Ge concentration, we will focus on the $Si_{0.85}Ge_{0.15}$ sample, where three carbon-related modes are resolved (see Fig. 5). In this sample, two C_s defects are expected to prevail, C_s surrounded by four Si atoms, denoted Si_4:C, and C_s surrounded by three Si and one Ge atom, denoted Si_3Ge:C. The former defect gives rise to a single T_2 mode, while the latter has C_{3v} symmetry and gives rise to two carbon-related modes, a Si-C mode (E) and a Ge-C mode (A_1). Thus the 542 cm^{-1} mode is a A_1 mode. From the spectra, it seems like the 582 cm^{-1} mode is a T_2 mode and, therefore, the 600 cm^{-1} mode is a E mode. This assignment seems reasonable as the Si-C bonds are longer (i.e. the frequency is lower) in the Si_4:C defect than in the Si_3Ge:C defect where the long Ge-C bond will cause a shortening of the Si-C bonds [16]. The same modes are expected for the $Si_{0.75}Ge_{0.25}$ sample. However, the intensity of the E and A_1 modes will increase as the Si_3Ge:C defect will be more probable in a sample with 25 % Ge compared with a sample with 15 % Ge, in agreement with the experimental observations (see Fig. 5). In the $Si_{0.65}Ge_{0.35}$ sample three defects will prevail; Si_4:C, Si_3Ge:C, and Si_2Ge_2:C. The latter defect has C_{2v} symmetry and gives rise to three carbon-related modes, one Si-C mode (B_1), one Ge-C mode (B_2), and one Si/Ge-C mode (A_1). Therefore, six modes are expected in all, three Si-C, two Ge-C, and a mixed Si/Ge-C mode. In Fig. 5 only four modes are resolved, two high- and two low-frequency modes, but the high frequency modes are very broad, indicating that they originate from a superposition of a number of sharper modes. An assignment of the modes is therefore not possible, but is seems reasonable that the two low-frequency modes are Ge-C modes, while the two broad high-frequency modes are Si-C and Si/Ge-C modes.

The general trend seen on the spectra in Fig. 5 is that all modes shift downwards when the Ge concentration is increased from 15 to 50 %. This may be explained by the fact that the lattice constant increases as a function of the Ge concentration, as the lattice constant of Ge is 4 % larger than that of Si. When the lattice constant increases the Si-C and Ge-C bonds are extended, i.e., the frequency is lowered, in agreement with the observations.

Summarizing, the absorption lines observed in the frequency range from ~510 to ~610 cm^{-1} in $^{13}C^+$ implanted $Si_{1-x}Ge_x$ samples are identified as local vibrational modes of defects involving a single carbon atom. The modes are found in the range of C_s in pure Ge and in pure Si, and a simple model where it is assumed that the modes originate from C_s bound to four atoms (Si and Ge) can qualitatively account for the experimental data

Conclusion

The C_s defect in Ge has been identified by a combination of infrared absorption spectroscopy, ion channeling and *ab-initio* theory. The defect is observed after carbon implantation and subsequent annealing above 350 °C and it possesses a local vibrational T_2 stretch mode at 531 cm^{-1}. The calculated frequency is in good agreement with the observed frequency and the calculated isotope shift is in excellent agreement with our observations.

On basis of the identification of C_s in Si [2] and in Ge, the same defect is identified in $Si_{1-x}Ge_x$, where it is found that carbon binds to both Si and Ge.

Acknowledgements

This work has been supported by the Danish National Research Foundation through Aarhus Center for Advanced Physics (ACAP). P. Leary and R. Jones thank the HPCI for computer time on the T3D where some of this work was carried out. S. Öberg thanks NFR and TFR in Sweden for financial support and also PDC at KTH for computer time on the SP2.

References

[1] For a recent review, see G. Davies and R. C. Newman, in *Handbook on semiconductors*, edited by T. S. Moss (Elsevier Science, Amsterdam, 1994), Vol. 3b, p. 1557
[2] R. C. Newman and J. B. Willis, J. Phys. Chem. Solids **26**, 373 (1965).
[3] J. W. Strane, S. R. Lee, H. J. Stein, S. T. Picraux, J. K. Watanabe, and J. W. Mayer, Appl. Phys. **79**, 637 (1996).
[4] K. Eberl, S. S. Iyer, S. Zollner, J. C. Tsang, F. K. LeGoues, Appl. Phys. Lett. **60**, 3033 (1992).
[5] B. Dietrich, H. J. Osten, H. Rücker, M. Methfessel, and P. Zaumseil, Phys. Rev. B **49**, 17185 (1994).
[6] *GeSi strained layers and their applications*, edited by A. M. Stoneham, and S. C. Jain (Bristol: Institute of Physics Publishing, 1995).
[7] N. Herbots, P. Ye, H. Jacobsson, J. Xiang, S. Hearne, and N. Cave, Appl. Phys Lett. **68**, 782 (1996).
[8] A. Nylandsted Larsen, J. Lundsgaard Hansen, R. Schou Jensen, S. Y. Shiryaev, and P. Riis Østergaard, Phys. Scri. **T54** 208 (1994).
[9] E. V. Monakhov, S. Y. Shiryaev, A. Nylandsted Larsen, J. Hartung, and G. Davies, to be published in J. Cryst. Growth
[10] L. C. Feldman, J. W. Mayer, and S. T. Picraux, *Materials Analysis by Ion Channeling* (Academic Press, New York, 1982).
[11] B. Bech Nielsen, Phys Rev B **37**, 6353 (1988).
[12] L. Hoffmann, J. C. Bach, B. Bech Nielsen, P. Leary, R. Jones, and S. Öberg, Phys. Rev. B **55**, 11167 (1997).
[13] R. Jones, Phil. Trans. Roy. Soc. London Ser. A **341**, 351 (1992).
[14] B. Bech Nielsen, Phys Rev B **37**, 6353 (1988).
[15] The local vibrational mode of C_s in Ge is measured after annealing at 550 °C, as the mode has disappeared after annealing at 750 °C.
[16] In a real crystal the four Si and Ge atoms in the Si_3Ge:C defect are pushed outwards along <111> directions and hereby the Si-C bonds are extended. However, the Si-C bonds in the Si_3Ge:C defect will presumably still be shorter than in the Si_4:C defect.

Materials Science Forum Vols. 258-263 (1997) pp. 103-108
© 1997 Trans Tech Publications, Switzerland

Ge CONTENT DEPENDENCE OF THE INFRARED SPECTRUM OF INTERSTITIAL OXYGEN IN CRYSTALLINE Si-Ge

D.Wauters and P.Clauws
University of Gent, Department of Solid State Sciences,
Krijgslaan 281-S1, B-9000 Gent, Belgium

Keywords : silicon-germanium, silicon, oxygen, vibrational mode, infrared spectroscopy

Abstract

The germanium content dependence of the low temperature infrared absorption due to interstitial oxygen in bulk crystalline $Si_{1-x}Ge_x$ has been investigated for $0.024 < x < 0.066$. The appearance of new components in the 1130 cm^{-1} band as well as the shift to lower wavenumbers is explained as an effect of the perturbation of Si-O-Si centres by Ge neighbours at different distances, in agreement with an earlier study applying to lower x-values (H. Yamada-Kaneta et al., Phys. Rev. B47, 9338 (1993)). Calculations show that in the x-range presently considered the relative occurrence of different centres becomes strongly dependent on the distribution of the Ge atoms and a good agreement with the experimental data at 5 to 53K is obtained for the case of a random distribution. Observations concerning the 1206 cm^{-1} and 1748 cm^{-1} absorption are also briefly described.

1. Introduction

In silicon and germanium dispersed oxygen impurities occupy interstitial sites (O_i). The defect gives rise to a characteristic vibrational absorption band in the mid-infrared range, situated at 1107 cm^{-1} in silicon and at 855 cm^{-1} in germanium (room temperature values), which has been attributed to the anti-symmetric stretching mode ν_3 of a Si-O-Si or Ge-O-Ge quasimolecule (the A_{2u}-mode in D_{3d} symmetry). At liquid helium temperatures (LHeT) the bands resolve into a number of narrow lines in agreement with the isotopic abundance of nearest Si or Ge neighbours [1,2]; additional structure which depends on the temperature originates from the two-dimensional motion of the oxygen perpendicularly to the ⟨111⟩ defect axis (hot transition) and is for both semiconductors well explained by the anharmonic coupling model worked out by Yamada-Kaneta et al. [3-5].
A number of cases intermediate between the two defects above may be expected to exist in oxygen rich Si-Ge alloys, depending on the position of the oxygen with respect to neighbouring Si and Ge atoms; among these, oxygens bonded to one Si and one Ge would probably be the most promising for a study using infrared spectroscopy.
In [4] Yamada-Kaneta et al. investigated the infrared spectrum of O_i in $Si_{1-x}Ge_x$ for small x values up to 0.0134. New components were observed in the 1130 cm^{-1} band (and also in the 1206 cm^{-1} and 30 cm^{-1} bands) which were attributed to Si-O-Si perturbed by Ge atoms at neighbouring sites. The present paper deals with a similar study for x-values between 0.024 and 0.066. At this higher Ge contents the kind of distribution of the Ge atoms in the silicon matrix is expected to become important with respect to the occurrence of different O_i centres as would be reflected in the relative weight of spectral components; we also hoped for an increasing chance to detect absorption from Si-O-Ge species.

2. Experimental

The four $Si_{1-x}Ge_x$ samples used in this study were cut from Czochralski-grown Si-Ge crystals with different nominal Ge concentration. The x-values of the samples as calculated from mass-density measurements taking account of the variation of average bond length with x, were 0.024, 0.039, 0.059, 0.066 respectively, with an estimated uncertainty of 0.001 and in fair agreement with XPS

reference measurements. The samples with the two lowest x-values were singly crystalline, the other two polycrystalline.
The infrared transmission measurements were made with a FT-IR instrument equipped with a LHe cryostat. The O_i concentration was determined from the magnitude of the 1130 cm^{-1} absorption band at room temperature using the IOC-88 calibration factor of 3.14×10^{17} cm^{-2} [6] (since the width of this band was found to decrease slightly with increasing x, the integrated absorption was used rather than the amplitude). The O_i concentration of all four samples was found to lie within the range of $(4 \text{ to } 5)\times10^{17}$ at/cm^3. In all samples most absorption which can be assigned to oxygen is found in a band around 1130 cm^{-1} (LHeT) as shown in the spectra of Fig.1. In this figure the absorption of a Cz-Si sample (x = 0) has been included for comparison. With x increasing the peak located at 1136.4 cm^{-1} for x = 0 gradually decreases in amplitude while shifting to lower wavenumbers; for x = 0.059 and 0.066 it is present as a shoulder to the left side of the band. Simultaneously new absorption develops at the lower wavenumber side; as will be discussed in section 4, this absorption originates from two distinct components at about 1127 and 1118 cm^{-1}. The observations being very similar to those in [4] for lower x, we have adopted the same labels for the components, i.e. O_i-I for the shifted peak and O_i-II and O_i-III for the components at lower wavenumbers. Despite the higher x-values used in the present study no ν_3 bands of O_i could be traced which may originate from centres involving a Ge-O bond. Calculation of the ν_3 frequency of a Si-O-Ge quasimolecule using the change in reduced mass with respect to O_i in silicon and germanium, yields an estimated intermediate value somewhere around 1000 cm^{-1}, much lower than the components of the 1130 cm^{-1} band. This seems to confirm the assumption in [4] that formation of direct Ge-O bonds in $Si_{1-x}Ge_x$ would be energetically unfavourable. Besides the 1130 cm^{-1} band, O_i related lines at 1206 and 1748 cm^{-1} (values in silicon) were also observable in the Si-Ge samples. Their evolution with x will be discussed in section 5.

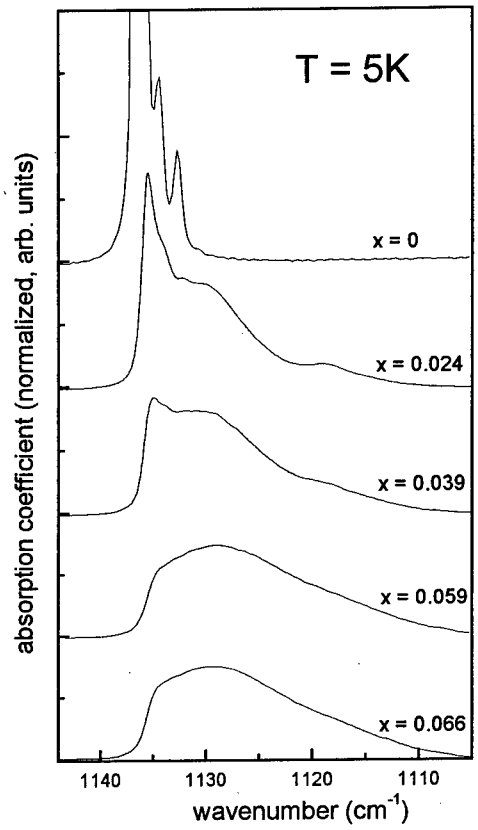


Figure 1. Germanium content dependence of the 1130 cm^{-1} absorption due to interstitial oxygen in $Si_{1-x}Ge_x$, measured at 5K and corrected for lattice absorption. Resolution = 0.5 cm^{-1}. The absorption of the different samples has been scaled to the same oxygen concentration.

3. Distribution of the Ge atoms and relative weight of O_i-centres

In the paper by Yamada-Kaneta et al. [4] the O_i-III and O_i-II components of the 1130 cm^{-1} band are regarded as ν_3 lines from Si-O-Si centres shifted to lower wavenumber as a result of the perturbative action of a Ge impurity at respectively a second nearest and a third nearest neighbouring site with respect to the oxygen. The O_i-I line which remains closer to the ν_3 position in silicon was assigned

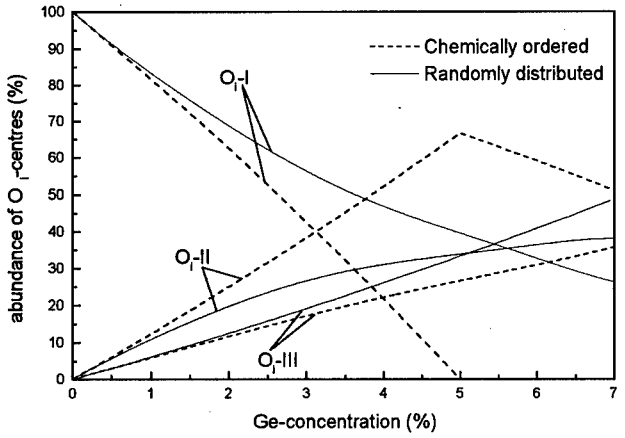


Figure 2. Calculated relative occurrence of O_i-I, O_i-II and O_i-III centres in $Si_{1-x}Ge_x$ with increasing Ge content for the case of homogeneously distributed (dashed lines) and randomly distributed Ge atoms (full lines).

to all other (less perturbed) Oi centres with Ge at longer distances. With these assignments the relative importance of the spectral components were found to agree with the calculated relative occurrence of the three kinds of centres considered, assuming the Ge impurities are distributed homogeneously in the silicon matrix. However, when a similar calculation is made for the higher x values of our samples, no agreement can be found with the relative weight of the components in the spectra of Fig.1, the O_i-I peak e.g. being predicted to disappear much faster than observed. This is most probably an effect of a more complex distribution of Ge which becomes more apparent at higher x-values.

Disregarding possible segregation (clustering) of Ge, the alternative for an equal spacing of Ge atoms (known as chemical or binary ordering) is a distribution at random. To calculate the fraction of different O_i centres in case of a random distribution of Ge we use the following procedure. A silicon cell of 512 atoms is defined with a fraction x of the Si atoms (chosen at random in the cell) substituted with Ge. This supercell is surrounded with identical copies in order to correctly define the surrounding of atoms at the edges of the central cell. The different O_i centres are counted by an algorithm checking each of the Si-Si bonds in the cell and finding the position of the Ge atom nearest to the bond centre. The whole procedure is repeated with the Ge atoms randomised again, until a statistical average is obtained. The result of the calculation is plotted in Fig.2 (full lines) where it may be compared with the corresponding result for a uniform distribution (dashed lines). It is e.g. clearly seen that for a uniform distribution the O_i-I centres disappear near $x = 0.05$ while for a random distribution a much slower decrease is predicted in agreement with the experiments. At the lowest x-values however the calculated fractions are less model dependent, explaining why in [4] a good agreement with the experiment is obtained assuming a uniform distribution.

4. Deconvolution of the 1130 cm^{-1} absorption band

The calculated results for the case of randomly distributed Ge makes it possible to decompose the LHeT 1130 cm^{-1} band consistently for all samples. Since in the model the O_i-II and O_i-III species are singly defined centres, the fitting procedure starts from the assumption that the wavenumber position of the respective components should remain nearly unchanged for different values of x, while the ratio of their integrated absorption to the total absorption in the band equals the calculated fraction at the corresponding x-value. The line form was similar to the $x = 0$ spectrum (including the isotopic fine structure), broadened to a width yielding the best fit. Subtraction of

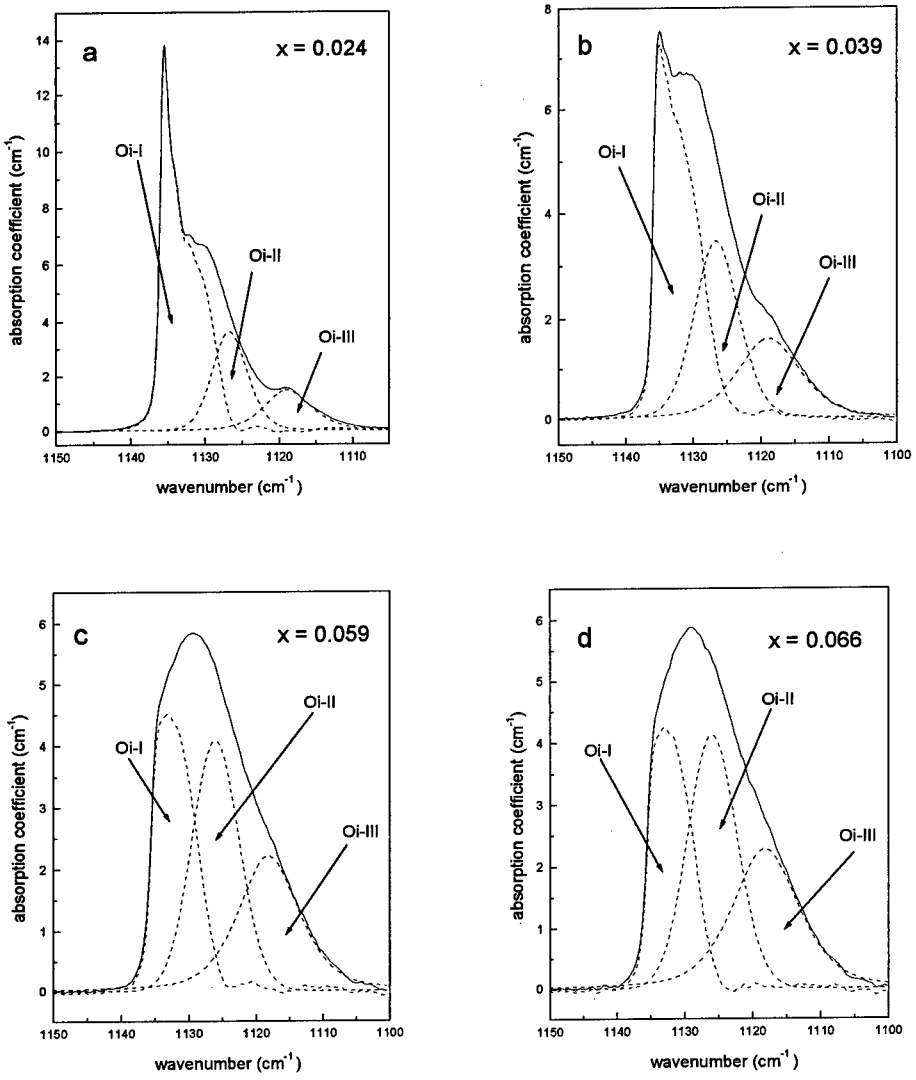


Figure 3. Decomposition of the 1130 cm^{-1} absorption band (T = 5K) due to interstitial oxygen in $Si_{1-x}Ge_x$. Resolution = 0.5 cm^{-1}. O_i concentration in units 10^{17} at/cm^3 : (a) : 4.97 , (b) : 4.90 , (c) : 4.15 , (d) : 4.54

the fitted O_i-III and O_i-II components from the total absorption yields the O_i-I component. The results of the fitting procedure are shown in Fig.3. O_i-II and O_i-III components are found at about 1127 and at 1118.5 cm^{-1} with slight variations in line width. The O_i-I component however is found to gradually shift to lower wavenumbers while its detailed structure is lost; the shift of the O_i-I maximum is also displayed in Fig.4. It is interesting to note that using the same procedure we succeeded to fit the x = 0.0134 spectrum of [4] consistently to the above results and it may be seen that the corresponding O_i-I maximum fits nicely into the sequence of Fig.4.

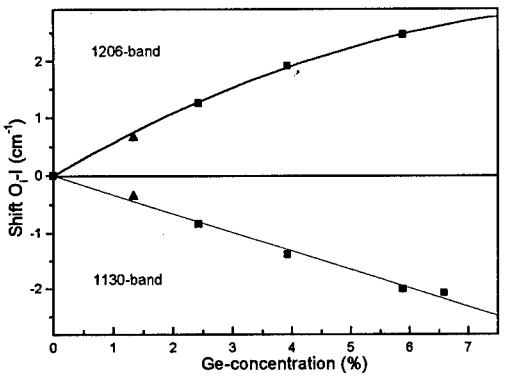


Figure 4. Shift of the peak maximum of the O_i-I component in the 1130 cm^{-1} and 1206 cm^{-1} absorption bands in $Si_{1-x}Ge_x$ as a function of germanium content, with respect to the peak maximum in silicon (LHeT).
■ : this study
▲ : Yamada-Kaneta et al. [4]

The changes in the O_i-I spectrum may be readily explained by considering that this spectrum is in fact the resultant of overlapping components due to all the remaining O_i centres for which the nearest Ge atom is further away than a third nearest neighbour. Within this set the average distance from a Ge will however also decrease with x increasing and the somewhat more perturbed centres will rapidly prevail over the less perturbed ones. This is confirmed by a more refined version of the calculation program where up to nine distinct O_i centres were defined; these results will be published elsewhere.

In addition to the LHeT experiments all samples have also been measured at a series of more elevated temperatures up to 53K. As in silicon this leads to additional absorption in the 1110 - 1130 cm^{-1} range originating from "hot transitions" involving higher levels in the ladder of two-dimensional oscillator states (in particular the 1st and 2nd hot transitions starting at the $|0,\pm1,0\rangle$ and $|0,\pm2,0\rangle$ coupled states in the notation used in [3]). The spectra were successfully decomposed by the same fitting procedure as for the LHeT components. In the 1st hot transition spectrum, components were found at 1116.5 and 1122 cm^{-1} for O_i-III and O_i-II and a O_i-I component shifting with increasing x from 1128 to 1127 cm^{-1}. More details about the spectra at elevated temperature will be published elsewhere.

5. Other absorption bands of O_i in $Si_{1-x}Ge_x$

The most obvious effect on the 1206 cm^{-1} band (LHeT) is the drastic decrease of the integrated absorption with increasing x, in contrast to the 1130 cm^{-1} band where no significant variation was observed. This reduction, which was also reported in [4] and may be attributed to a smaller oscillator strenght for the perturbed centres, is in the present case seen to continue for higher x until only about 30% of the absorption in silicon remains at x = 0.066. We also confirm the presence of a component developing at about 1213 cm^{-1} assigned to O_i-II. Using the relative weights from the random model we estimate the oscillator strenght of O_i-II at (16 ± 7)% of that of O_i-I, which is within the range mentioned in [4] and close to the theoretically calculated value in the same paper. The O_i-I component is again observed to shift with increasing x, however towards higher wavenumbers. The positions of O_i-I maxima are plotted in Fig.4 where they may be compared with those of the 1130 cm^{-1} band. Again the result from [4] fits into the sequence.

A weak band corresponding with the 1748 cm^{-1} band in silicon [7] could also be detected in the $Si_{1-x}Ge_x$ samples which regarding the poor signal-to-noise ratio can only be described in a qualitative manner. The overall absorption in the band is clearly displaced to lower wavenumbers with x increasing; this displacement seems however faster than in the case of the 1130 cm^{-1} band. No change in integrated absorption could be observed.

6. Conclusions

In the present study experimental results have been obtained which are in good general agreement with similar results presented by Yamada-Kaneta et al. [4] and they seem to confirm the basic ideas concerning the origin of the O_i-related absorption in silicon-rich Si-Ge developed by the latter authors.

In order to explain the detailed behaviour of the absorption at the higher Ge concentrations used in our investigation, we found it however necessary to accept a random distribution of Ge atoms in the silicon matrix. With this assumption it was possible to fit consistently the changes of the 1130 cm^{-1} absorption at different Ge contents and temperatures, to the calculated relative concentrations of Si-O-Si centres perturbed by more or less distant Ge neighbours. The different analysis as compared to [4] leads to somewhat different peak positions of assigned spectral components, with possible implications for the corresponding energy level diagrams. This is e.g. the case for the "hot transition" lines which we separated from the "cold transition" spectrum by subtracting an appropriate fraction of the latter from the spectra at elevated temperatures, a procedure considered to better avoid introduction of "false" components.

So far only the nearest Ge position was taken into account for the definition of the different O_i species, neglecting possible additional perturbation by other Ge atoms nearby. Although a further differentiation of this kind seems difficult to include in the analysis, similar complexities may explain at least part of the broadening of the O_i-II and O_i-III lines. Most needed seems however to elucidate the physical origin of the perturbation of oxygen centres by Ge atoms which gives rise to the line shifts.

Acknowledgements

The Si-Ge material used in this work has been grown at Union Minière Electro-Optic Materials, Olen (Belgium). The authors also wish to thank Prof. S. Hoste and Prof. L. Fiermans and their co-workers (University of Gent), respectively for the mass-density and the XPS experiments.

References

1. B. Pajot, E. Artacho, C.A.J. Ammerlaan and J-M. Spaeth, J.Phys. Condens. Matter **7**, 7077 (1995)
2. B. Pajot and P. Clauws, Proc. ICPS-18, World Scientific, Singapore, 911 (1987)
3. H. Yamada-Kaneta, C. Kaneta and T. Ogawa, Phys. Rev. **B42**, 9650 (1990)
4. H. Yamada-Kaneta, C. Kaneta and T. Ogawa, Phys. Rev. **B47**, 9338 (1993)
5. A.J. Mayur, M.D. Sciacca, M.K. Udo, A.K. Ramdas, K. Itoh, J. Wolk and E.E. Haller, Phys. Rev. **B49**, 16293 (1994)
6. A. Baghadi, W.M. Bullis, M.C. Croarkin, Y. Li, R.I. Scace, R.W. Series, P. Stallhofer and M. Watanabe, J. Electrochem. Soc. **136**, 2015 (1989)
7. E.Artacho, A. Lizón-Nordström and F.Ynduráin, Phys. Rev. **B51**, 7862 (1995)

Materials Science Forum Vols. 258-263 (1997) pp. 109-114
© 1997 Trans Tech Publications, Switzerland

OPTICAL INVESTIGATION OF Ge-RICH $Ge_{1-x}Si_x$ ($0 \leq x \leq 0.1$) ALLOYS

M.Franz[1], K.Pressel[1], K.F.Dombrowski[1], H.Rücker[1], A.Barz[2], P.Dold[2], and K.W.Benz[2]
[1] Institute for Semiconductor Physics, Walter-Korsing-Str. 2,
15230 Frankfurt (Oder), Germany
[2]Kristallograph. Institut, Universität Freiburg, Hebelstr. 25, 79104 Freiburg, Germany

Keywords: SiGe, defects, photoluminescence, absorption, Raman, phonons, local modes

ABSTRACT We have investigated Ge-rich $Ge_{1-x}Si_x$ bulk crystals with Si concentrations up to 12% by photoluminescence, infrared absorption, and Raman spectroscopy. The full widths at half maximum values between 2 meV and 5 meV for the near band edge luminescence are the smallest reported in literature up to now. These small linewidths, which increase with rising Si content, demonstrate the excellent sample quality. Sb and Te doped samples show luminescence lines, which shift with the excitonic band edge for increasing Si concentrations. They are caused by deeply bound excitons. The luminescence linewidth of 1.5 meV at 2 K is only about one half of the near band edge luminescence linewidth. We compare Raman and far infrared absoption measurements of the Ge-rich $Ge_{1-x}Si_x$ samples in the range of 390 cm^{-1}. We are able to distinguish between the local vibrational mode of substitutional silicon and SiGe related phonon modes. These experimental observations are confirmed by the anharmonic Keating model. Observation of the silicon isotopes proves that the absorption is caused by silicon, and gives a fingerprint of the excellent sample quality.

INTRODUCTION

SiGe offers many possibilities for electronic and optical devices like HBTs, MODFETs and detectors. Especially SiGe heterostructures used for HBTs are of growing importance for mainstream applications [1]. But also for bulk crystals several interesting applications exist, e.g. solar cells [2], X-ray optics [3], SiGe substrates for niche markets. Si and Ge are miscible over the whole composition range. This provides a good opportunity to study fundamental alloy properties. In this paper, we investigate alloy properties reflected in the bound exciton luminescence of doped and nominally undoped samples and study the influence of silicon incorporation on the phonon spectra of the Ge host. We used different optical methods, i.e. PL, infrared absorption, and Raman spectroscopy to investigate Ge-rich $Ge_{1-x}Si_x$ bulk crystals.

EXPERIMENTAL

The $Ge_{1-x}Si_x$ crystals were grown by the vertical Bridgman method in a monoellipsoid mirror furnace. The crystals have a diameter of 9 mm and a length of 30-40 mm, the maximum Si concentration is 12%. From these crystals samples with a thickness of 0.9 to 1.5 mm were cut. We investigated nominally undoped crystals and intentionally doped crystals. The shallow acceptors of group III and shallow donors of group V, as well as the chalcogenes Se and Te served as dopants. The photoluminescence (PL) and absorption measurements were performed with a BOMEM DA8.02 Fourier-transform infrared spectrometer. For PL measurements we excited the samples with the 514.5 nm line of an Ar^+ ion laser. The luminescence signal was detected by a liquid nitrogen cooled Ge detector. The Raman measurements were performed with a Dilor triple Raman spectrometer with a microscope entrance in backscattering configuration. The scattering was excited by the 514.5 nm line of an Ar^+ ion laser. The orientation of the samples is (111), the incident and scattered light was polarized perpendicular to each other.

DETERMINATION OF THE ALLOY COMPOSITION

The accurate knowledge of the alloy composition is important for the interpretation of the optical spectra. We measured the lattice constant of the samples with the Bond method [4], which is a very accurate X-ray diffraction method. We calculated the Si concentration by linear interpolation

between the lattice constants of Ge and Si, which is valid for Ge-rich samples. Additionally, we determined the alloy composition from PL spectra. Weber and Alonso [5] derived experimentally an equation which connects the excitonic band edge and the alloy composition. On the Ge-rich side of the alloy the excitonic band edge E_{gx} varies linear with the Si concentration x according to

$$E_{gx} = 0.74\text{-}1.27x \text{ eV} \qquad (1)$$

The Si concentration can be determined from the PL lines of the near band edge bound exciton emission as described in Ref. [5]. The Si concentration can also be determined from band edge absorption measurements at low temperatures. Absorption measurements give a hint of the homogeneity of the samples with respect to the alloy composition. With a light spot of a few millimeters in diameter a large volume of the sample is examined, including concentration fluctuations over the whole thickness. Only for homogeneous samples a clear fingerprint of the absorption thresholds can be observed. The results for the alloy composition determined by the Bond method, PL, and absorption measurements are in good agreement. We found only discrepancies of less than 0.1% Si.

PHOTOLUMINESCENCE RESULTS

Typical PL spectra of the nominally undoped samples obtained at 2 K are shown in Fig. 1. At this temperature the emission of bound excitons (X) and the corresponding phonon replica are observed. The full widths at half maximum (FWHMs) for the excitonic no-phonon (NP) lines of our samples are between 2.2 and 5 meV (Fig. 2). These values, which are the best values reported up to now, show the excellent crystal quality of our samples. The FWHM increases with rising Si content as plotted in Fig. 2 for different doped and nominally undoped samples. From statistical arguments Schubert et al. [6] derived an equation for the FWHM of bound excitons ΔE_{exc} of binary semiconductor alloys as a function of the alloy composition x. A purely random distribution of the different alloy elements is assumed.

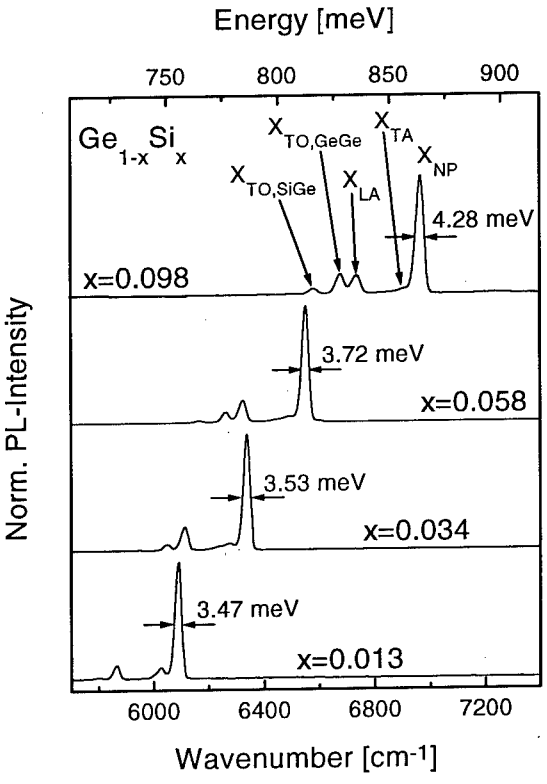


Fig. 1. Near band edge PL spectra recorded at 2 K for nominally undoped samples with different Si concentrations. X indicates bound exciton, the indices specify the nature of the participating phonons (NP: no phonon).

$$\Delta E_{exc} = 2.36 \cdot \frac{dE_g}{dx} \cdot \left(\frac{x(1-x)}{N \cdot V_{exc}} \right)^{\frac{1}{2}} \qquad (2)$$

The factor dE_g/dx describes the change of the band gap with alloy composition. For $Ge_{1-x}Si_x$ dE_g/dx is a constant value on the Ge-rich side of the alloy referring to equation (1). N is the density of lattice sites and V_{exc} is the volume of an exciton. The factor x(1-x) describes the alloy fluctuation. We plotted Eq. (2) in Fig 2 as a function of the Si concentration, assuming an excitonic radius of 70 Å. The comparison of the theoretical function with the measured values tentatively explains the increase of the FWHM with increasing Si content to be caused by alloy fluctuations. Nevertheless, more effects exist which cause an increase of the

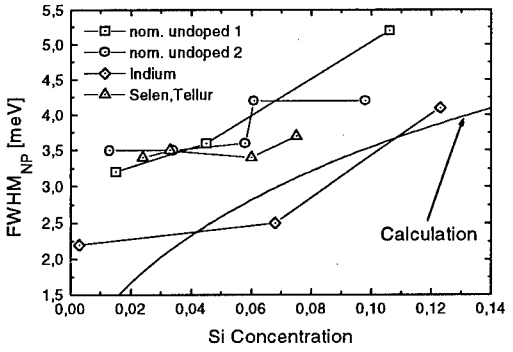


Fig. 2. FWHM of bound exciton NP line recorded at 2 K as a function of the Si concentration for different doped and undoped samples. The calculation was made with use of Eq. (2).

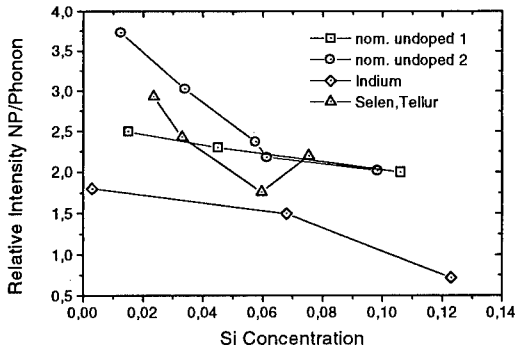


Fig. 3. Relative intensity of NP to phonon luminescence recorded at 2 K for different doped and undoped samples.

linewidth, i.e. internal stress and crystal defects. An increase of the linewidth on the Si-rich side of the alloy was reported by Lyutovich et al. [6], whereas Weber and Alonso reported a decrease of the FWHM on the Ge-rich and Si-rich side of the alloy [4]. The PL intensity of the NP line relative to the phonon replica is shown in Fig. 3. The NP emission decreases with increasing Si content. In Ge the LA phonon emission is the strongest, in Si the TO emission has the highest intensity. As shown in Fig. 1, the TO phonon emissions (TO_{GeGe} and TO_{SiGe}) increase with rising Si content. The

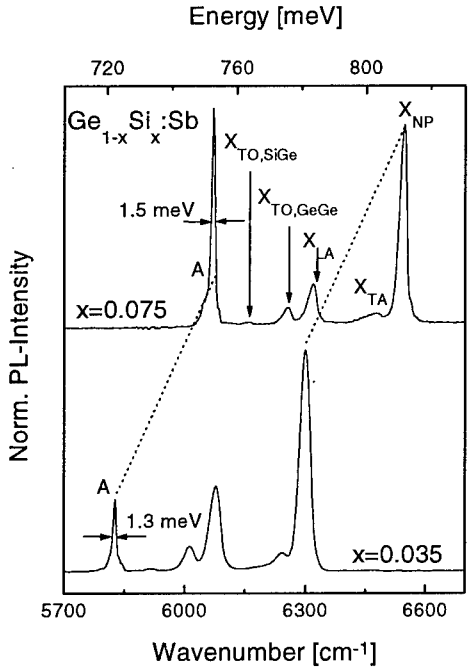


Fig. 4. Deep center luminescence, indicated by A for two Sb doped samples with different Si concentrations recorded at 2 K.

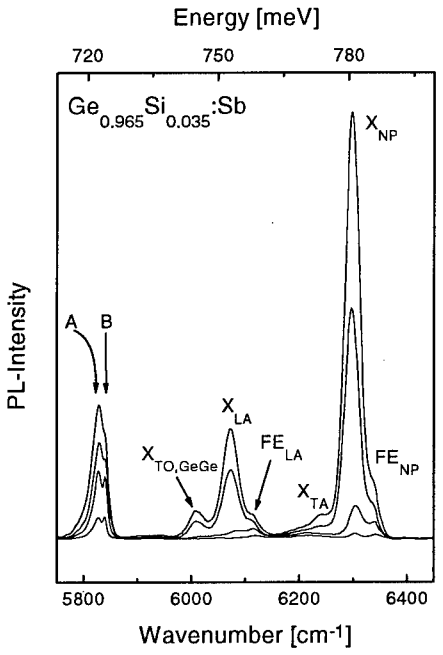


Fig. 5. PL spectra obtained at 5 K for different excitation powers. The spectra with increasing intensity were recorded for 25 mW, 50 mW, 75 mW, and 100 mW.

stronger phonon coupling with increasing Si concentration results in a decrease of the NP emission relative to the phonon emission. In the literature it has been argued that with increasing Si concentration scattering at potential fluctuations within the range of the impurity potential enhances the probability of the NP recombination. This effect is overcompensated by stronger phonon coupling.

In Sb and Te doped samples we observe a deep center luminescence, about 60 meV below the bound exciton NP emission. The shift with the band edge (Fig. 4) is typical for a bound exciton. The emission consists of at least two peaks in dependence of the sample. We observe no phonon coupling. The FWHM is only between 1.3 and 1.5 meV (depending on the sample) compared to the X_{NP} linewidth of 3.5 meV. Figure 5 shows spectra of the sample with x=0.035 obtained at 5 K for different excitation powers. Two lines, which are 1.5 meV apart, are clearly distinguishable. The energetically lower line is indicated by A. It is the same luminescence as observed at 2 K (Fig. 4), the second line is indicated by B. With increasing excitation the intensity of line A increases stronger than line B. The two lines correspond to two different deeply bound excitons. For the lowest excitation of 25 mW only weak free (FE) and bound exciton luminescence is detectable in addition to the defect luminescence. The deeply bound exciton luminescence saturates with increasing excitation while the free and bound exciton emission increases strongly. The deep center luminescence is detectable up to 60 K. Although these deeply bound exciton emissions have been found in Te and Sb doped samples no correlation could be found with these dopants.

PHONON SPECTROSCOPY BY FAR INFRARED ABSORPTION AND RAMAN

Both infrared absorption and Raman spectra reveal phonon contributions in the range of 300 cm^{-1} (Ge-Ge), 390 cm^{-1} (Si-Ge), and 450 cm^{-1} (Si-Si). In this paper we focus on the modes in the range of 390 cm^{-1}. Figure 6(a) and 6(b) show absorption spectra and Raman spectra in the range of the SiGe phonon modes, respectively. In absorption measurements a weak absorption at 372 cm^{-1} and a single line at about 390 cm^{-1} appears. The latter line shifts from 387.7 cm^{-1} for a concentration of 1.3% Si to 391.0 cm^{-1} for a concentration of 9.8% Si. The linewidth increases simultaneously. In Raman measurements we observe a peak at the same energetic position. This line shows the same shift to higher energies with rising Si content as observed for absorption measurements. Additionally, a

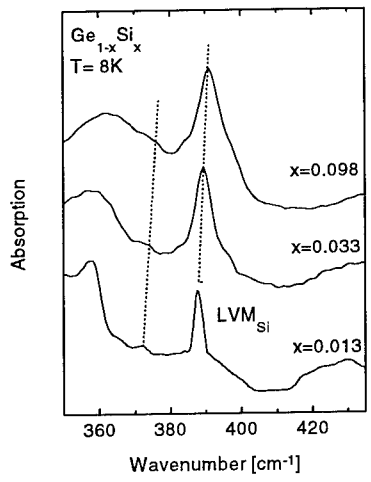


Fig. 6 (a). Absorption spectra for samples with different Si concentrations recorded at 8 K (LVM: local vibrational mode).

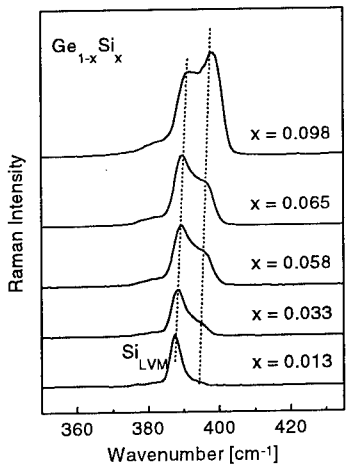


Fig. 6 (b). Raman spectra for samples with different Si concentrations recorded in the spectral range of the SiGe mode (LVM: local vibrational mode).

further line appears at the high energy side of the first peak. The intensity of this line increases strongly with increasing Si content. For low Si concentrations the vibration at about 390 cm^{-1} in Raman and absorption spectra is attributed to the local vibrational mode (LVM) [9,10] of Si in Ge. We identify the nature of this peak by the isotope effect of Si. Natural Si has three stable isotopes ^{28}Si, ^{29}Si and ^{30}Si with abundances of 92.2%, 4.7%, and 3.1%, respectively. Due to the different masses the vibration frequencies of the isotopes are slightly different. With the assumption that the force constant is the same for all isotopes the frequency difference of the LVM of the heavier isotopes ^{29}Si and ^{30}Si with respect to ^{28}Si are given by

$$\frac{\omega_{29}}{\omega_{28}}=\sqrt{\frac{m_{28}}{m_{29}}} \Rightarrow \Delta\omega = 7cm^{-1}, \quad \frac{\omega_{30}}{\omega_{28}}=\sqrt{\frac{m_{28}}{m_{30}}} \Rightarrow \Delta\omega = 13cm^{-1}$$

Due to the high quality of our samples we were able to resolve the LVM of all the three Si isotopes. Figure 7 shows the Raman spectrum of a sample with a concentration of 1% Si. The vibrational energies of the different isotopes are ω_{28} = 389 cm^{-1}, ω_{29} = 383 cm^{-1}, and ω_{30} = 378 cm^{-1}. The intensity ratios of the peaks correspond to the natural abundances of the Si isotopes. Due to the two phonon background and the weak absorption of the local mode, the isotope effect is not observable in absorption. By adding more Si atoms to the crystal the LVM develops into a SiGe like optical phonon. In Raman spectra a further SiGe like optical phonon appears on the high energy side of the local vibrational mode and increases in intensity with rising Si content. The Si_{LVM} is Raman and infrared active and gives rise to the line at about 390 cm^{-1}. Gaisler et al. also observed the two contributions in their Raman spectra for low Si concentrations of relaxed $Ge_{1-x}Si_x$ layers [13]. They interpreted this effect with the increasing influence of Si atoms in the vicinity of an isolated Si atom on the Ge-Si bond length and thus on the frequency of the LVM. But following this interpretation the high energy lines should also be observable in absorption measurements. The behavior of the Raman and absorption modes of the SiGe vibration can theoretically be described by application of the anharmonic Keating model [11] to SiGe alloys. In a simple picture the $Ge_{1-x}Si_x$ crystal consists of two fcc sublattices. Each sublattice is occupied by the same number of Si atoms, which is reasonable for a purely random distribution of the atoms in the alloy. The oscillation of these two sublattices against each other results in a SiGe phonon, which is Raman but not infrared active. Therefore the SiGe phonon causes the additional high energy lines observed

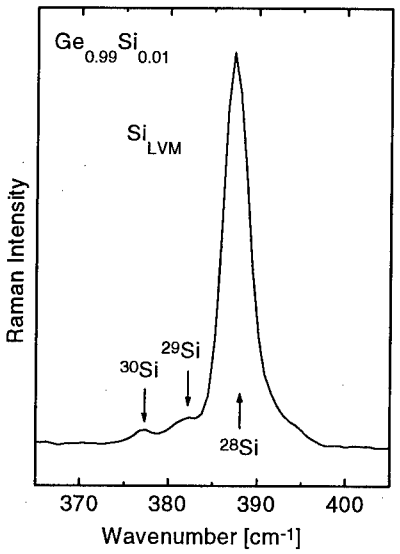


Fig. 7. Raman spectrum of the LVM of Si in Ge. The Si concentration of the sample is 1%. One can see the vibration of the different Si isotopes.

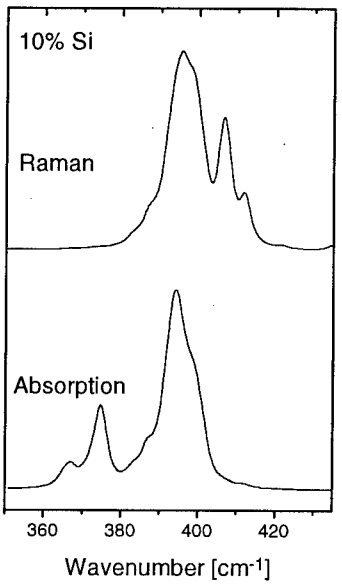


Fig. 8. Raman and Absorption spectra calculated with the anharmonic Keating model.

in Raman spectra but not in absorption. Figure 8 shows a calculated Raman and absorption spectrum for a Si concentration of 10%. The calculation shows a line at about 390 cm^{-1} for both absorption and Raman and the additional Raman active mode on the high energy side. The difference in experiment (Fig. 6 (b)) and theory (Fig. 8) of the intensity ratio of the two Raman lines can be either explained by inaccuracy of the Keating model or sample quality. Gaisler et al. [13] observed different intensity ratios compared with ours caused by different sample quality. The phonon mode observed in absoption at about 370 cm^{-1} appears also in the measurement as indicated in Fig. 6(a). Details of the calculations will be published elsewhere [12].

SUMMARY

We have investigated $Ge_{1-x}Si_x$ bulk crystals grown by the vertical Bridgman method. The small FWHM of the near band edge luminescence lines and the observation of a Si isotope effect in Raman measurements demonstrate the excellent sample quality. The increasing linewidth of the bound exciton luminescence with rising Si concentration occurs due to alloy fluctuations, while enhanced phonon coupling reduces the NP relative to phonon intensity, overcompensating the fluctuation effect. In PL we observe luminescence from deeply bound excitons which have a linewidth of only half of the near band edge bound exciton emission. The luminescence line shifts with the excitonic band edge for increasing Si concentration and is detectable up to 60 K. The vibrational modes observed in absorption spectra at about 390 cm^{-1} are caused by the LVM of silicon. In Raman spectra we observe in addition to the mode at 390 cm^{-1} contributions of SiGe related phonons at 400 cm^{-1}. Their intensity increases significantly with rising Si content. The Raman and infrared spectra can be explained with the anharmonic Keating model.

ACKNOWLEDGMENTS

The authors are indebted to Dr. J. Kräußlich of the University of Jena for the X-ray diffraction measurements. The support of Prof. B. Dietrich is gratefully acknowledged as well as the financial support of the DFG (BE 896/7-2, PR 493/3-2).

REFERENCES

1. D.L. Harame, J.H. Comfort, J.D. Cressler, E.F. Crabbe, J.Y.-C. Sun, B.S. Meyerson, and T. Tice, IEEE Transactions on Electron Dev. 42, 455 (1995), part I and part II
2. J.H. Werner, S. Kolodinski, H.J. Queisser, Phys. rev. Lett. 72, 3851 (1994)
3. A. Erko, F. Schaefers, W. Gudat, N.V. Abrosimov, S.N. Rossolenko, V. Alex, S. Groth, W. Schroeder, Nuc. Instr. and Methods in Phys. Research A 374, 408 (1996)
4. W.L. Bond, Acta Cryst. 13, 814 (1960)
5. J.Weber and M.I.Alonso, Phys. Rev. B 40, 5683 (1989)
6. E.F. Schubert, E.O. Göbel, Y. Horikoshi, K.Ploog, and H.J. Queisser, Phys. Rev. B 30, 813 (1984)
7. A.S. Lyutovich, K.L. Lyutovich, V.P. Popov, and L.N. Safronov, Phys. Stat. Sol. (b) 129, 313 (1985)
8. H.D. Fuchs, C.H. Grein, M.I. Alonso, and M. Cardona, Phys. Rev. B 44, 13120 (1991)
9. D.W. Feldman, M. Ashkin, and J.H. Parker, Jr, Phys. Rev. Lett. 17, 1209 (1966)
10. A.E. Cosand and W.G. Spitzer, J. Appl. Phys. 42, 5241 (1971)
11. H. Rücker and M. Methfessel, Phys. Rev. B 52, 11059 (1995)
12. M. Franz, K. Pressel, K. Dombrowski, H. Rücker, B. Dietrich, A. Barz, P. Dold, K.W. Benz, submitted for publication to Phys. Rev. B
13. V.A. Gaisler, O.A. Kuznetsov, I.G. Neizvestnyl, L.K. Orlov, M.P. Sinyukov, and A.B. Talochin, Sov. Phys. Solid State 31, 2006 (1989)

Materials Science Forum Vols. 258-263 (1997) pp. 115-120
© 1997 Trans Tech Publications, Switzerland

Electrical characterization of electron beam induced defects in epitaxially grown $Si_{1-x}Ge_x$

M. Mamor, F. D. Auret, S. A. Goodman, G. Myburg, P.N.K. Deenapanray and W. E. Meyer
Physics Department, University of Pretoria, Pretoria 0002, South Africa

Keywords: SiGe, Schottky diodes, barrier height, DLTS, electron beam metallization, defects.

Abstract

Schottky barrier diodes (SBDs) were formed on n-and p-type epitaxially grown $Si_{1-x}Ge_x$ (x = 0.0 to 0.2) strained films by electron beam (EB) deposition of Ti and Sc. The barrier height of Sc on $Si_{1-x}Ge_x$/Si and the defects introduced during EB deposition of Sc have been investigated as a function of Ge composition in $Si_{1-x}Ge_x$. The barrier height (ϕ_{bp}) to strained p-type films followed the same change as the band-gap with increasing Ge-content. These results suggest that (ϕ_{bn}) on n-type films does not exhibit composition dependence and seems to be evidence of Fermi level pinning relative to the conduction band. We have used deep level transient spectroscopy (DLTS) to study the electronic properties of defects introduced during EB deposition. The most prominent defect observed in n-$Si_{1-x}Ge_x$ after EB deposition has a level at E_c - 0.44 eV. The energy level of this defect was not influenced by a change in Ge-content, indicating that it is pinned to the conduction band. In p-$Si_{1-x}Ge_x$, the activation energy of the main defect was found to decrease with increasing Ge-content and followed the same trend as the band-gap variation $E_g(x)$ in $Si_{1-x}Ge_x$/Si, suggesting that this defect is also pinned to the conduction band.

Introduction

$Si_{1-x}Ge_x$/Si heterostructures are of great interest because of their potential application in heterojunction devices and their compatibility with Si integrated circuit technology [1,2]. The rapid decrease of the band-gap of strained $Si_{1-x}Ge_x$ epitaxially layers with Ge fraction makes this material suitable for a wide variety of electronic device applications [3]. Device fabrication requires metallization, which is one of the most critical processing steps in device processing. Metallization is also extremely important for the electrical characterization of metal/semiconductor interfaces. A technique which is frequently used for semiconductor metallization is electron beam (EB) deposition, especially due to its ability to evaporate high melting point metals and the enhancement of the adhesion of the deposited layer onto the substrate [4]. However, apart from these advantages, EB deposition also has some disadvantages. During EB deposition, the semiconductor surface is exposed to x-rays which introduce crystal damage at and close to its surface [5]. This damage affects the electrical and optical properties of the semiconductor and the defects thus introduced will influence the characteristics of devices fabricated on it. Studies on Si and GaAs have shown that the barrier heights (ϕ_b) of Schottky barrier diodes (SBDs) formed on n-and p-type material, *after* exposing it to low energy particles, are decreased and increased [5-7], respectively. Deep level transient spectroscopy (DLTS) [8] revealed that this is due to electrically active defects formed when particles impinge on the material, and that the degree of particle-induced barrier height modification increases with increasing defect concentration [5].

Several investigations have been conducted to characterize defects introduced during EB deposition on Si and GaAs [5,7,9] but very little "or no" information is available regarding the influence of EB deposition on defect introduction in $Si_{1-x}Ge_x$. In this work, we study the properties of defects in $Si_{1-x}Ge_x$ induced by EB deposition of Sc or Ti as a function of Ge-content. In addition, the

dependence of the Schottky barrier height on Ge-content and on the influence of stray electrons produced during EB deposition is also investigated.

Experimental details

The SiGe layers were grown by chemical vapor deposition (CVD). The growth temperature was between 625 and 700 °C. The boron and phosphorous doping of the epitaxial SiGe layers as determined by capacitance voltage (C-V) measurements was of the order of $8 \times 10^{16} - 1 \times 10^{17}$ cm^{-3}. The carrier density of the epitaxial layers was uniform. For all x, the germanium content is uniform within the $Si_{1-x}Ge_x$. The Ge-content ($0 < x < 0.2$) was determined by Rutherford backscattering spectrometry (RBS). The degree of strain relaxation was measured by x-ray diffraction using the (400) and (211) reflection planes for the determination of the perpendicular and parallel lattice constants, respectively. After wet chemical cleaning using trichloroethylene, isopropanol and oxide etching using diluted HF:H_2O (1:50) solution, the samples were inserted in a high vacuum system in which the pressure recovered to 10^{-8} mbar. Circular Sc or Ti contacts, 0.77 mm in diameter and 200 nm thick, were deposited onto the $Si_{1-x}Ge_x$, through a metal contact mask by EB evaporation.

The Schottky barrier height (SBH) was determined using current voltage (I-V) measurements at room temperature. As a result of the lower barrier height with higher Ge-content, these SBDs exhibit a high effective series resistance (R_s) yielding non-linear forward characteristics. Therefore, the SBH was determined from the reverse saturation current measurements. Thermionic emission was assumed to govern current transport under reverse bias. For lower Ge-content, the barrier height was determined using either forward I-V characteristics or directly from a measurement of the current at a reverse voltage $V_r = 1$. The saturation current, I_s is described by [10]

$$I_s = A^* S T^2 \exp[-\phi_{bp} / kT] \qquad (1)$$

where S is the SBDs surface area and A^* is the effective Richardson constant for $Si_{1-x}Ge_x$. A^* was calculated by using a linear dependence on the composition.

The EB evaporation-induced defects in the $Si_{1-x}Ge_x$ epilayer were characterised using a lock-in amplifier based deep level transient spectroscopy (DLTS) [8] system. The DLTS "signatures" (energy level, E_t, in the band-gap and apparent capture cross-section, σ_a) of the defects were determined from Arrhenius plots of T^2/e vs $1/T$, where e is the emission rate at a temperature T. In order to minimize electric field assisted emission [11], small biases and pulses were used ($V_r = V_p = 0.3$V).

Two sets of samples were prepared. The first set consisted of $Si_{1-x}Ge_x$ "*to be used as a reference*" with different x and was shielded from stray electrons originating at the EB filament during metal depositions. In order to examine the influence of EB evaporation of Sc and Ti on the characteristics of metal/$Si_{1-x}Ge_x$ and to study the defects introduced in $Si_{1-x}Ge_x$ during EB deposition, the second set was not shielded during deposition and was used to study the EB induced defects in $Si_{1-x}Ge_x$.

Results and Discussion

A. p-type $Si_{1-x}Ge_x$

1) I-V measurements

Figure 1 shows the variation of SBH as a function of Ge fraction. Also shown in Fig. 1 is the band-gap for strained alloys versus composition [12]. For control samples, the SBH decreases when the Ge fraction increases ($\phi_{bp} = 0.57 \pm 0.01$eV and 0.43 ± 0.01 for $x = 0$ and 0.2, respectively). After EB deposition (*without shield*), the SBH decreases from 0.62 eV to 0.46eV when x increases from 0 to 0.2. The composition dependence of (ϕ_{bp}) for diodes fabricated with and without shielding agrees well with that of the band-gap E_g (x) [12]. Therefore, the variation observed cannot be related

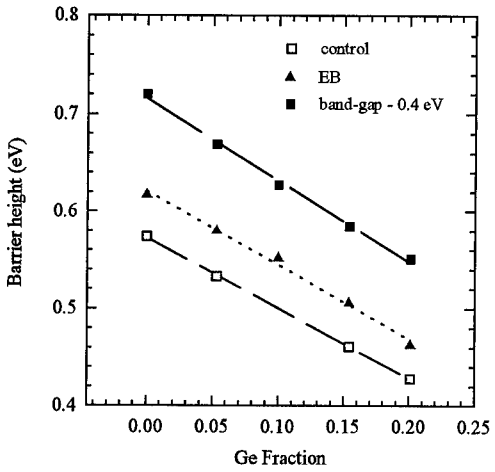


Figure 1: Correlation of strained SiGe band-gap change (filled squares) and the barrier height variation with Ge-content for Sc deposited on p-$Si_{1-x}Ge_x$ by EB evaporation, (control samples, open squares) and without shielding samples from stray electrons (solid triangles).

to the formation of defects but to the Ge-content. However, a theoretical model [13] indicates that the major part of the band gap variation ΔE_g in $Si_{1-x}Ge_x$/Si heterojunctions is contained in the valence band ($\Delta E_v = \Delta E_g$). Recent experimental results [14] indicate that the barrier height of W/p-$Si_{1-x}Ge_x$ for fully relaxed films follows the same trend as the valence band offsets between $Si_{1-x}Ge_x$ and Si.

Figure 1 also illustrates that the diodes deposited without shielding exhibit higher barrier heights than those deposited with shield. The higher barrier height formed in the presence of stray electron irradiation can be understood if it is assumed that these stray electrons introduce donor-like [7] defects at and below the surface of the semiconductor during metallization. The presence of electrically active defects after stray electron irradiation will be verified below by the DLTS results.

2) DLTS measurements

The DLTS results of control diodes, fabricated at a rate of 10 Å/s, and positioned to prevent stray electrons from reaching the p-SiGe, indicated that no defects with peaks between 40K and 300K from x = 0.0 to 0.1, are present in detectable concentrations ($< 10^{-5} \times N_a = 10^{12}$ cm^{-3}). In samples with higher Ge-content (x = 0.15 and 0.2) we detected two defects which we believe may be ascribed to slight relaxation present in the films with high Ge fraction.

Figure 2 depicts the DLTS spectra from samples fabricated by depositing Sc without shielding the p-$Si_{1-x}Ge_x$ from stray electrons originating at the filament. For all the investigated compositions, EB metallization of p-$Si_{1-x}Ge_x$ introduced one prominent (He2) and some minor (He1, He3, He4) hole traps of which the properties are given in Table I. Furthermore, note that the peak temperature of He1 and He2 in Table I are higher than in Fig. 2. This is because the "signatures" were determined under low electric field, while the curves in Fig. 2 were recorded at $V_r = 1$ and $V_p = 1.6$V. This causes a higher field in the depletion region which, in turn, results in enhanced emission and a peak shift to lower temperature.

Table 1: Electronic properties of the prominent hole trap He2 and minor defect He1 introduced during EB evaporation of Sc on epitaxially grown p-$Si_{1-x}Ge_x$/Si.

Defect label	*Ge-content*	*Activation energy* E_t *(eV)*	*Capture cross section* σ_a *(cm^2)*	*Peak temperature* T_{peak}[(b)] *(K)*
He2	0.00	0.525	9.4×10^{-14}	241.7
He2	0.053	0.467	5.1×10^{-14}	221.8
He2	0.10	0.403	2.4×10^{-14}	199.6
He2	0.15	0.350	2.4×10^{-14}	175.8
He1	0.10	0.509	8.1×10^{-14}	236.2
He1	0.15	0.502	9.6×10^{-14}	231.6

(b) Peak temperature at a lock-in amplifier frequency of 46 Hz, i.e. a decay time constant of 9.23 ms.

Figure 2 also illustrates that all the defect peaks with the exception of He1, shift towards lower temperature with increasing Ge-content. We suggest that this effect is due to a change in the band-gap with Ge-content. The DLTS spectra in Figure 2 further reveal that for $x > 0.1$, a new defect He1 with a peak at 226 K was detected. Furthermore, note that the peak temperature of this defect does not exhibit a strong composition dependence and it appears that this defect could only be detected in SiGe with $x > 0.1$. This defect has a level at $E_v + 0.50$ eV. The energy level of this defect was not influenced by a change in Ge-content, indicating that it is pinned to the valence band. We suggest that the most probable reason for this is the high Ge-content and this defect could be a Ge-related defect introduced by electrons during metallization.

From Arrhenius plots for He2 and He1, constructed from temperature scans performed at different pulse frequencies, we have extracted the activation energy E_t and the apparent capture cross section σ_a ; these parameters are given in Table I. Figure 3 shows the activation energy E_t of He2 as function of Ge fraction (x) for fully strained films. Also shown in Fig. 3 is the band-gap for strained alloys versus composition [12]. The composition dependence of E_t follows the same trend as the energy of the band-gap E_g (x).

A linear dependence of E_t (x) on E_g (x) in the form of

$$E_t(x) = 1.3E_g(x) - 0.94 \qquad 0 < x < 0.15 \qquad (2)$$

can be deduced. The slight increase in the slope from unity is not yet understood, but may be ascribed to some compressive strain which is induced during metallization. The good agreement between the change in E_t and E_g suggests that the He2 observed in p-$Si_{1-x}Ge_x$ is the same as that observed in p-Si and that this level is pinned relative to the conduction band for all the Ge-contents investigated. Thus, the reduction in activation energy is relative to the valence band as shown in the inset of Figure 3. Following this argumentation, our results are consistent with the fact that the main part of the band gap variation in $Si_{1-x}Ge_x$/Si heterojunction is contained in the valence band [13].

B. n-type $Si_{1-x}Ge_x$

For each n-SiGe epitaxial layer of different Ge-content, a control sample was fabricated using a resistively deposited contact which is known to introduce no defect in Si. No electrically active

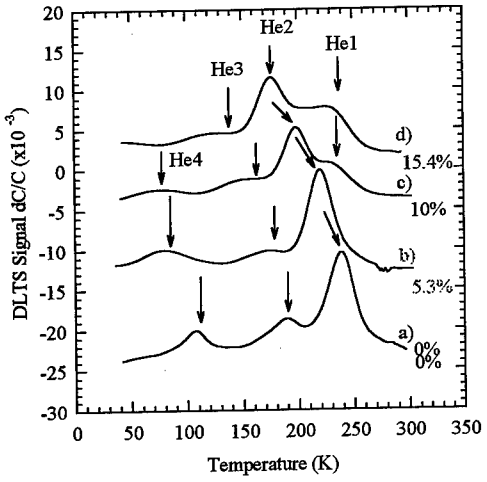


Figure 2: DLTS spectra of EB deposited Sc SBDs on p-$Si_{1-x}Ge_x$ with different Ge-content, a quiescent reverse bias (V_r) of 1 V and forward bias (V_p) of 1.6 V were used. The lock-in amplifier frequency was 46 Hz.

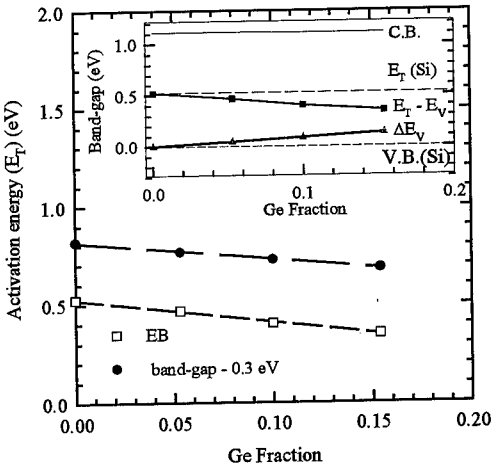


Figure 3: variation of $Si_{1-x}Ge_x$ band-gap (solid circles) and the activation energy of the most prominent defect (open squares) as a function of Ge-content. correlation of the activation energy change and the valence band change relative to silicon with Ge-content is shown in the insert.

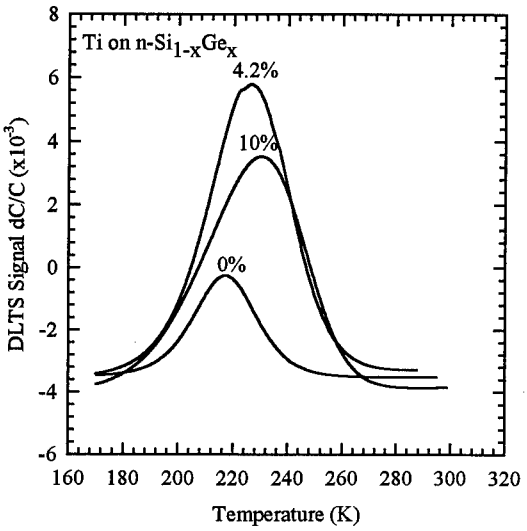


Figure 4: .DLTS spectra of Ti SBDs deposited by EB deposition on n-$Si_{1-x}Ge_x$ strained films with different Ge-content. All curves were recorded at a lock-in amplifier frequency of 46 Hz, $V_r = 1$ V and $V_p = 1.2$ V.

defects were detected in these control samples between 16 K and 300 K [15], thus we attribute all the DLTS peaks observed in the EB metallization samples to EB depositions induced defects.

Figure 4 depicts DLTS spectra of Ti SBDs on n-$Si_{1-x}Ge_x$ which were recorded at a quiescent reverse bias ($V_r = 1$ V) and a forward bias ($V_p = 1.2$ V). For x = 0 to 0.1, the most prominent defect observed in n-$Si_{1-x}Ge_x$ after EB deposition has a level at E_c - 0.44 eV. It is important to note that the energy level of this main defect was not influenced by a change in Ge-content, suggesting that it is pinned to the conduction band. This defect has a similar DLTS "signature" as one introduced during sputter depositiion of Au on n-type $Si_{1-x}Ge_x$ [15].

The DLTS spectra in Fig. 4 show that the main defect observed in n-Si is located at about 217 K. A slight shift of the peak towards higher temperatures (from 217 to 230 K) is clearly observed with increasing Ge-content. This shift is not yet understood, but may be ascribed to an increase in strain with an increase in Ge-content. After annealing the n-Si samples for 30 min at 180 °C, there was no drastic change in the DLTS peak height of this defect. This defect is, therefore, believed to be either the second charge state of the divacancy $V_2^{-/0}$, or the vacancy-phosphorous complex (V-P). It is also possible that it is the combination of V-P and $V_2^{-/0}$. In order to better understand these phenomena, isochronal annealing as a function of Ge-content are presently being performed to study the thermal behaviour of the V-P and the divacancy $V_2^{-/0}$ in SiGe.

Conclusions

In conclusion, the composition dependence of the Schottky barrier height of Sc deposited with and without electron shielding on strained p-$Si_{1-x}Ge_x$ films follows the same trend as the band-gap variation with Ge-content. It is also found that the barrier height is lower for SiGe not exposed to stray electrons and increased for a given Ge-content, when the SiGe films were not shielded during deposition. Thus, the surface damage layer effectively provides net donor-like and other gap states.

DLTS measurements confirmed the presence of defects introduced when the substrate was not shielded during metallization. We have shown, firstly, that EB metallization on p-$Si_{1-x}Ge_x$ introduced a set of defects, He2 being the most prominent for all compositions investigated. Secondly, the activation energy of this major defect decreases with increasing Ge-content. These results suggest that this defect introduced in p-$Si_{1-x}Ge_x$ is the same as that observed in p-Si and that this defect is pinned relative to the conduction band. For the first time, a direct relation is reported between the activation energy of EB induced defects and the band-gap variation in strained p-$Si_{1-x}Ge_x$.

The most prominent defect observed in n-$Si_{1-x}Ge_x$ after EB deposition of Ti SBDs has a level at E_c - 0.44 eV. The energy level of this defect is not influenced by a change in Ge-content, indicating that is pinned to the conduction band.

We gratefully acknowledge the financial assistance of the Foundation for Research Development and the Carl and Emily Fuchs Institute for Microelectronics.

References

1. G. L. Zhou and H. Morkoc, Thin Solid Films **231**, 125 (1993).
2. M. Arienzo, S. S. Iyer, B. S. Meyerson, G. L. Patton and J. M. C. Stork, Appl. Surf. Sci. **48**, 377 (1989).
3. S. S. Iyer, G. L. Patton, J. M. C. Stork, B. S. Meyerson and D. L. Harame, IEE. Trans. on Elect. Devices. **36**, 2043 (1989).
4. Y. G. A. Sai-Halasz and J. Gazecki, Appl. Phys. Lett. **45**, 1067 (1984).
5. G. Myburg and F. D. Auret, J. Appl. Phys. **71**, 6172 (1992).
6. F. D. Auret, S. A. Goodman, G. Myburg and W. E. Meyer, J. Vac. Sci. Technol. B **10**, 2366 (1992).
7. M. O. Paz and F. D. Auret, Mat. Res. Soc. Proc. **25**, 619 (1984).
8. D. V. Lang, J. Appl. Phys. **45**, 3014 (1974).
9. F. D. Auret and P. M. Mooney, J. Appl. Phys. **55**, 984 (1984).
10. S. S. Cohen and S. SH. Gildenblat, in *Metal Semiconductore Contacts*, Academic Press, Vol. 13 (1986).
11. J. Frenkel, Phys. Rev. **54**, 647 (1938).
12. D. Dutartre, G. Bremond, A, Souifi and T. Benyattou, Phys. Rev. B **44**, 115252 (1991).
13. C. G. Van de Walle and R. Martin, Phys. Rev. B **34**, 5621 (1986).
14. V. Aubry, F. Meyer, P. Warren and D. Dutartre, Appl. Phys. Lett. **63**, 2520 (1993).
15. S. A. Goodman and F.D.Auret, Jpn. J. Appl. Phys. **36**, 633 (1997).

Materials Science Forum Vols. 258-263 (1997) pp. 121-126
© 1997 Trans Tech Publications, Switzerland

LATTICE DEFECTS IN $Si_{1-x}Ge_x$ EPITAXIAL DIODES INDUCED BY 20-MeV ALPHA RAYS

H. Ohyama[1], J. Vanhellemont[2, 3], E. Simoen[2], C. Claeys[2], Y. Takami[4], K. Hayama[1], H. Sunaga[5], J. Poortmans[2] and M. Caymax[2]

[1]Kumamoto National College of Technology, 2659-2 Suya Nishigoshi Kumamoto, 861-11 Japan
[2]IMEC, Kapeldreef 75, B-3001 Leuven, Belgium
[3]Present address: Wacker Siltronic AG, D-84479 Burghausen, Germany
[4]Rikkyo University, 2-5-1, Nagasaka Yokosuka Kanagawa, 240-01 Japan
[5]Takasaki JAERI, 1233 Watanuki Gunma, 370-12 Japan

Key words : $Si_{1-x}Ge_x$ epitaxial layer, 20-MeV alpha ray irradiation, radiation damage, deep levels

Abstract. Results are presented of an extended study on the induced lattice defects and their effects on the degradation of $Si_{1-x}Ge_x$ diodes, subjected to a 20-MeV alpha ray irradiation. The degradation of the electrical device performance increases with increasing fluence, while it decreases with increasing germanium content and energy. In the $Si_{1-x}Ge_x$ epitaxial layers, electron capture levels associated with an interstitial - substitutional boron complex are induced by the irradiation. The influence of the radiation source on device degradation is discussed taking into account the number of knock-on atoms and the nonionizing energy loss (NIEL). The radiation source dependence of performance degradation is attributed to the difference of mass and the probability of nuclear collision for the formation of lattice defects.

Introduction

The utilization of sattelites for broadcast and weather forecast is now an essential factor in our information intensive society. From these requirements, extensive studies concerning the development of semiconductor devices which can operate reliably in the space radiation environment have been undertaken on a wide scale. It is well known that $Si_{1-x}Ge_x$ devices have an excellent performance with respect to high speed, large current and direct transition. Some results on the degradation and its recovery of $Si_{1-x}Ge_x$ devices by electron, neutron and proton irradiation have been reported so far [1-2].

In the present paper, the degradation of the electrical performance and the induced lattice defects of $Si_{1-x}Ge_x$ diodes, which are irradiated at room temperature with 20-MeV alpha rays, are investigated as a function of germanium content and fluence. The radiation source dependence of degradation is discussed by comparing the results with those after irradiation with neutrons and electrons. In order to examine the recovery behavior of the induced deep levels and the device performance, isochronal thermal annealing is carried out for temperatures ranging from 75 to 300 ^{o}C. Moreover, the effects of the induced lattice defects on the performance degradation is also presented.

Experimental

n^+-Si/p^+-$Si_{1-x}Ge_x$ diodes fabricated on strained $Si_{1-x}Ge_x$ epitaxial layers grown on Cz silicon substrates, were used in this study. The active boron concentration of the strained $Si_{1-x}Ge_x$ epitaxial layers for diodes, which were grown on silicon substrates using an ultra high vacuum chemical vapour deposition system (UHV CVD) at a growth temperature of 630 ^{o}C and a deposition pressure of 0.26 Pa, was about 6 x 10^{17} cm^{-3}. The germanium content of the $Si_{1-x}Ge_x$ epilayer of nominal

thickness 100 nm was x = 0.08, 0.12, and 0.16. A boron implantation at an energy of 55 keV was performed to make the base contact. The active diode windows were defined by standard photolithography, whereafter 200 nm undoped polysilicon was grown by atmospheric CVD at a temperature of 610 °C. The polysilicon was then implanted twice with phosphorous, i.e first a 3 x 10^{15} cm^{-2} implantation at 55 keV followed by an implantation of 10^{15} cm^{-2} at 20 keV. The n^+ polysilicon was used to form the n^+ region for diodes. The diode area was between 10^2 and 10^4 μm^2. More details on the diode process are described in a previous paper [2].

Diodes without applied bias voltage were irradiated at room temperature by a 20-MeV alpha ray in the AVF cyclotron in TIARA at the Takasaki Radiation Chemistry Research Establishment. The fluence of the alpha ray was varied between 10^{10} and 10^{13} $1/cm^2$. The diodes were also irradiated by fast 1-MeV neutrons at room temperature in the irradiation tube of the Rikkyo University reactor (Triga Mark II). The neutron fluence was varied between 10^{12} and 10^{14} n/cm^2. Morever, 1-MeV electron irradiations using the linear electron accelerator at the Takasaki JAERI (Dynamitron) were performed at room temperature. The electron fluence was varied from 10^{13} to 10^{15} e/cm^2.

The current/voltage (I/V) and capacitance/voltage (C/V) characteristics of the diodes were measured. The hole and electron capture levels in the $Si_{1-x}Ge_x$ epitaxial layer of the diodes were studied using deep level transient spectroscopy (DLTS). The applied filling pulse was ranging from -1 to 0.5 V to observe electron capture levels in the base region and from -1 to 0 V in the collector region. The capacitance/temperature (C/T) characteristics were recorded simultaneously with the DLTS spectra. To investigate the recovery behavior of the irradiated diodes, isochronal thermal anneals were carried out at temperatures between 75 and 300 °C under nitrogen flow. An annealing time of 15 min. was chosen and the temperature was varied with steps of 25 °C with an accuracy of 1 °C. After each annealing step and subsequent cooling of the devices, the electrical performance and induced deep levels of the devices were measured.

Results and discussion

Figure 1 (a) shows typical DLTS spectra revealing the presence of electron capture levels in x = 0.12 diodes for different fluence of 20-MeV alpha rays. As shown in this figure, only hole capture levels are observed below 1 x 10^{13} $1/cm^2$, while both electron and hole capture levels are detected for 5 x 10^{13} $1/cm^2$. The electron capture levels shown in figure are most likely associated with an interstitial boron complex [3-6] and are related to the increase of reverse current and the decrease of capacitance in $Si_{1-x}Ge_x$ epitaxial layer. Fig. 1 (b) shows the corresponding C/T profile. For 5 x 10^{13} $1/cm^2$, a severe decrease of capacitance due to the deactivation of substitutional boron atoms is observed. The same electron capture levels are also induced in x = 0.08 and 0.16 diodes.

Figure 2 (a) and (b) show the typical I/V and C/V characteristics for the x = 0.12 diodes, which are irradiated by 20-MeV alpha ray for different fluences, respectively. From figure 2a it is noted that both the reverse and forward current increase. The forward current is lower after irradiation for a forward voltage (V_F) larger than 0.5 V. The reason for this might be an increased resistivity of the Si substrate. It is found from figure 2b that the capacitance in the $Si_{1-x}Ge_x$ epitaxial layer decreases by irradiation due to the deactivation of active boron atoms. The performance degradation increases with increasing alpha particle fluence. The deactivation of boron is related with the formation of interstitial boron as mentioned below and is the main responsible for the increase of the reverse current.

Assuming a linear relationship between damage increase and fluence, one can calculate a damage coefficient for the reverse current (K_I), which can be defined by the following equation.

$$I_R(\Phi) = I_R(0) + K_I \Phi \qquad (1)$$

where Φ is the alpha ray fluence. I_R (Φ) and I_R (0) are the reverse current at V_R = - 1 V after and before irradiation.

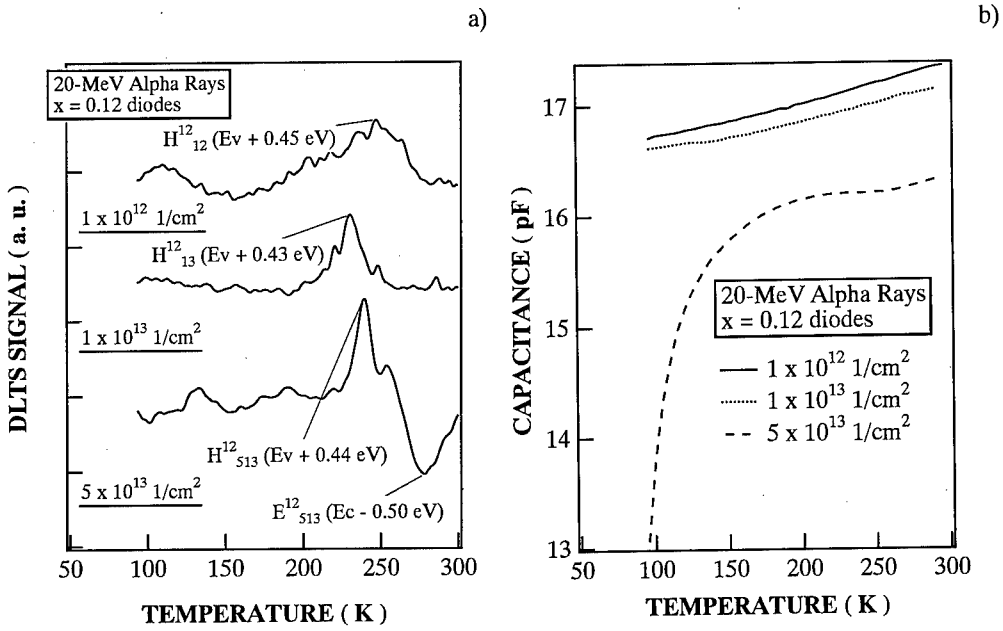


Figure 1 : DLTS (a) and C/T (b) spectra for x = 0.12 diodes irradiated by 20-MeV alpha rays.

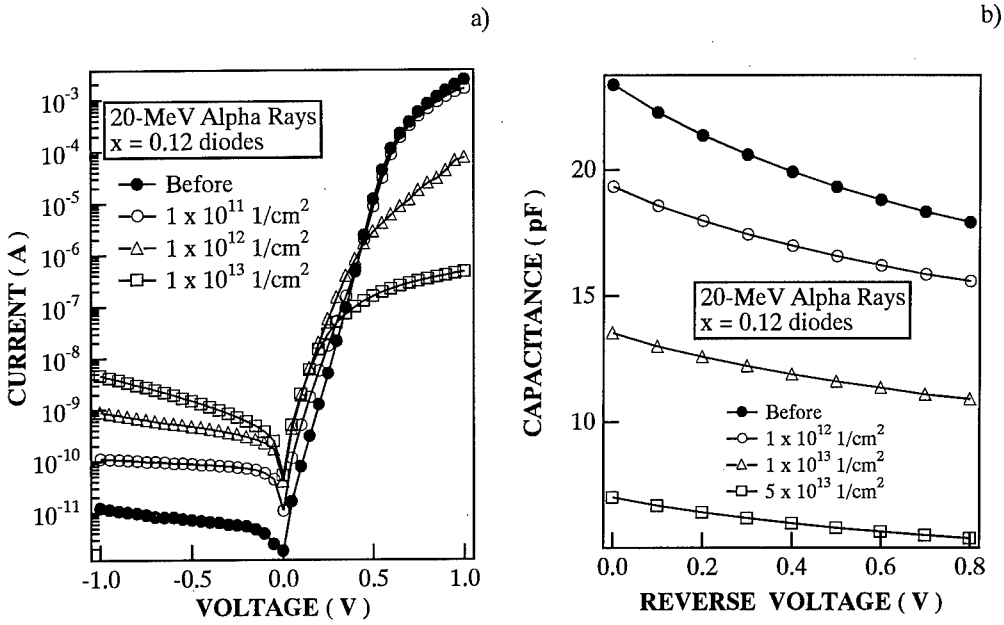


Figure 2 : Influence of 20-MeV alpha ray irradiation on I/V (a) and C/V (b) characteristics for x = 0.12 diodes.

K_I values of diodes, which are irradiated by 20-MeV alpha rays, for different germanium content calculated by this equation are listed in table 1 (a) and decreases with increasing germanium content. A similar dependence of the damage coefficient on the germanium content is observed for proton, neutorn and electron irradiations. Table 1 (b) summarises the respective K_I, the number of knock-on atoms (N_d) and the nonionizing energy loss (NIEL) of x = 0.12 diodes for 20-MeV protons, 1-MeV fast neutrons and 1-MeV electrons. For diodes with the same x, K_I for alpha ray irradiation is nearly the same as that for proton and neutron irradiation. One can also calculate N_d and NIEL in x = 0.12 diodes for 20-MeV alpha ray irradiation as 1240 cm^{-3} and 1.4 x 10^{-2} $MeVcm^2g^{-1}$, respectively [7]. The values are about a few times larger than those for proton and neutron irradiation. Based on these consideration, the radiation source and germanium content dependence of performance degradation is thought to be attributed to the difference of mass and the possibility of nuclear collision for the formation of lattice defects.

Tabel 1 : K_I for different germanium content, subjected to 20-MeV alpha rays (a) and K_I, N_d and NIEL of x = 0.12 diodes for different radiation sources (b).

a)

	x = 0.08	x = 0.12	x = 0.16
K_I (Acm^2)	7.5 x 10^{-21}	5.2 x 10^{-21}	1.8 x 10^{-21}

b)

	20-MeV Protons	1-MeV Neutrons	1-MeV Electrons
K_I	8.0 x 10^{-21} ($p^{-1}Acm^2$)	6.2 x 10^{-21} ($n^{-1}Acm^2$)	6.0 x 10^{-24} ($e^{-1}Acm^2$)
N_d (cm^{-3})	992	295	1.18
NIEL ($MeVcm^2g^{-1}$)	8.5 x 10^{-3}	4.5 x 10^{-3}	27 x 10^{-6}

Figure 3 (a) and (b) shows the results of 15 min isochronal anneals of I/V and C/V characteristics of x = 0.12 diodes, which are irradiated by a 20-MeV alpha ray with a fluence of 1 x 10^{12} $1/cm^2$. As shown in those figures, the performance degraded by irradiation recovers by thermal annealing and the recovery increases with increasing annealing temperature.

In order to quantify the recovery behavior, the unrecovered fraction of the reverse current (f_I), the annealing rate ($1/\tau_I$) and the activation energy (Ea) are defined as:

$$f_I = -\frac{I_{AA} - I_A}{I_A - I_B}, \quad f_I = \exp\left(-\frac{\tau}{\tau_I}\right) \text{ and } \frac{1}{\tau_I} = \nu_0 \exp\left(-\frac{E_a}{kT}\right) \qquad (2)$$

where I_{AA} and I_A denote the current after and before annealing, respectively, I_B is the current before irradiation, t is the annealing time, k the Boltzmann constant and ν_0 and T the frequency factor and annealing temperature, respectively. Similar equations are used to calculate E_a of the capacitance.
Based on these equations, E_a of reverse current and capacitance is calculated to be about 0.35 and 0.33 eV, respectively and are slightly larger than those for 20-MeV proton irradiation. This result means that the increase of reverse current by alpha ray irradiation is closely related to the decrease of capacitance in the $Si_{1-x}Ge_x$ epitaxial layer which is mainly caused by the radiation induced deep level.

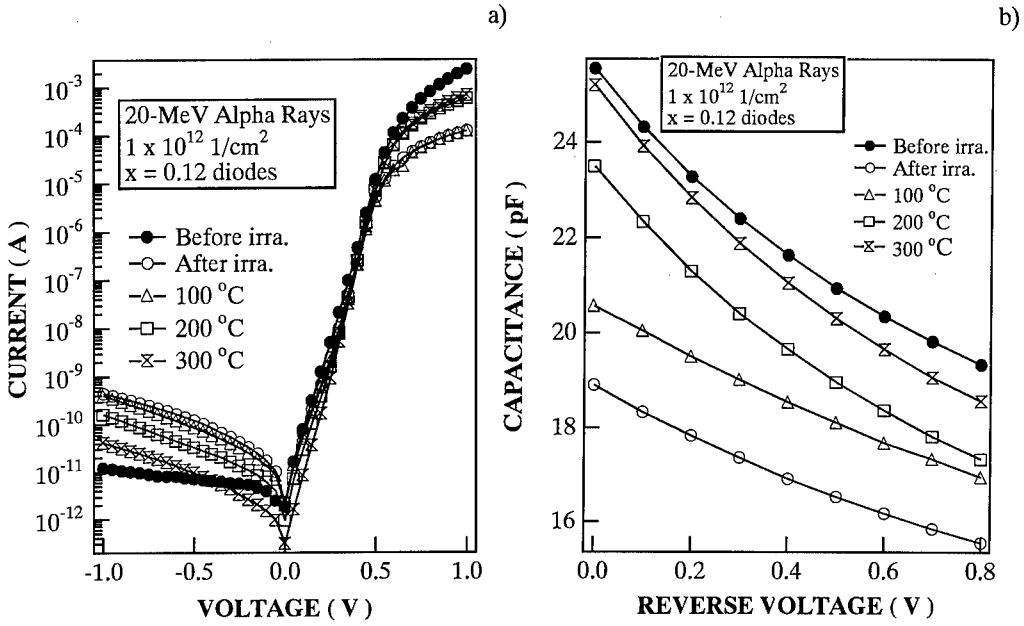


Figure 3 : Recovery behavior of I/V (a) and C/V (b) characteristics of 20-MeV alpha irradiated x = 0.12 diodes following isochronal annealing.

Conclusions

The main conclusions which can be made from the present study are:
1. After 20-MeV alpha ray irradiation, electron capture levels, associated with the interstital boron complex, and hole capture levels are induced in the $Si_{1-x}Ge_x$ epitaxial layers for high fluence, while only hole capture levels for low fluence have been observed by DLTS.
2. The degradation of the electrical performance of $Si_{1-x}Ge_x$ devices increases with increasing fluence, while it decreases with increasing germanium content.
3. The damage coefficient for alpha ray irradiation is nearly the same as for neutron and proton irradiation and is about three orders of magnitude larger than that for electron irradiation. This difference is due to the different number of knock-on atoms, which is correlated with the difference of mass and the possibility of nuclear collisions for the formation of lattice defects.
4. The degraded performance recovers by thermal annealing. The activation energy of reverse current and capacitance for x = 0.12 diodes irradiated by 20-MeV protons with a fluence of 1 x 10^{12} 1/cm^2 is 0.35 and 0.33 eV, respectively and is slightly larger than those for a 20-MeV proton irradiation.

Acknowledgement

Part of this work was supported by Giant-in-Aid for Scientific Research (No. 07555105 and No. 09045063) from the Japanese Ministry of Education for Science.

References

1. H. Ohyama, J. Vanhellemont, Y. Takami, K. Hayama, H. Sunaga, J. Poortmans and M. Caymax, IEEE Trans. Nucl. Sci., **41**, 2437 (1994).

2. H. Ohyama, J. Vanhellemont, Y. Takami, K. Hayama, H. Sunaga, J. Poortmans and M. Caymax, IEEE Trans. Nucl. Sci., **42**, 1550 (1995).
3. L. C. Kimerling, M. T. Asom, J. L. Benton, P. J. Drevinsky and C. E. Caefer, Materials Science Forum, **38-41**,141 (1989).
4. K. L. Wang, Y. H. Lee and J. W. Corbett, Appl. Phys. Lett., **33**, 547 (1978).
5. P. M. Moony, L. J. Süli, J. D. Gerson and J. W. Corbett, Phys. Rev. B, **15**, 3836 (1977).
6. L. C. Kimerling, M. T. Asom, J. L. Benton, P. J. Drevinsky and C.E. Caefer, Materials Science Forum, **38-41**, 141 (1989).
7. H. Ohyama, J. Vanhellemont, Y. Takami, K. Hayama, H. Sunaga, J. Poortmans and M. Caymax, Appl. Phys. Lett., **69**, 2429 (1996).

Materials Science Forum Vols. 258-263 (1997) pp. 127-132
© 1997 Trans Tech Publications, Switzerland

POSITRON ANNIHILATION STUDY OF ELECTRON-IRRADIATED SILICON-GERMANIUM BULK ALLOYS

Atsuo Kawasuso, Sohei Okada, Ichiro Yonenaga[1], Tatsuya Honda[1] and Masashi Suezawa[1]
Japan Atomic Energy Research Institute, Takasaki Establishment,
1233 Watanuki, Takasaki, 370-12, JAPAN
[1]Institute for Materials Research, Tohoku University, Sendai, 980, JAPAN

Keywords : SiGe, positron lifetime, Doppler broadening, electron irradiation, vacancy, annealing

Abstract. As-grown and electron-irradiated Si_xGe_{1-x} bulk crystals (x=0-0.82) have been studied using positron annihilation spectroscopy. Bulk positron lifetime and Doppler parameters were found to change from the value for Ge to that for Si with increasing Si fraction x. However, the dependence was non-monotonic at around x=0.20. Theses results seem to be correlated with the abrupt change of the band gap energy of Si_xGe_{1-x}. After 3 MeV electron irradiation, vacancy-type defects giving rise to the lifetime of 280 ps and 330 ps were detected for $0.63 \leq x \leq 0.82$ and $0.20 \leq x \leq 0.40$. However, no vacancy components were observed for $x < 0.20$. The composition-dependent vacancy production was interpreted in terms of the thermal stability of vacancies with the composition. Through the annealing experiment for the $Si_{0.82}Ge_{12}$ specimen after irradiation, it was found that vacancy-clustering upon heating was suppressed and considerably shifted to high temperatures as compared with the case of Si.

Introduction

Silicon-germanium (Si_xGe_{1-x}) alloy forms a complete series of solid solution [1]. By changing the alloy composition, physical parameters such as lattice constant and band gap energy can be controlled at arbitrary values between those of Si and Ge [2-6]. It is greatly interesting to study defect properties in Si_xGe_{1-x} alloy from a fundamental view point. Positron annihilation technique is a powerful tool not only to study electronic state but also to detect vacancy-type defects in crystalline solids. It is extensively applied to the study of defects in semiconductors [7]. Despite, the properties of vacancy-type defects in Si_xGe_{1-x} alloy have not been adequately studied so far. In this work, we investigated the annihilation characteristics of positrons in Si_xGe_{1-x} bulk state and also the properties of vacancy-type defects induced by electron irradiation.

Experimental

Specimens used in this work were undoped Czochralski-grown p-type Si_xGe_{1-x} crystals (x=0~0.82). The detail of the growth condition of the crystals was reported in Ref. 8. The residual carrier density was of the order of 10^{15} cm^{-3}. The dislocation density was determined to be of the order of 10^4 cm^{-2} by counting the number of etch-pit. The specimens were irradiated with 3 MeV electrons at the fluence of $1x10^{18}$ e^-/cm^2 at about 70℃ using a dynamitron accelerator in the Japan Atomic Energy Research Institute. Isochronal annealing up to 700 ℃ with a temperature step 25 ℃ for 20 min was carried out using an electric furnace in a dry argon ambience.

The positron source (^{22}NaCl ~0.4 MBq) was sandwiched by two specimens and positron lifetime was measured using a conventional spectrometer at room temperature. After subtracting the source and background components, lifetime spectrum was decomposed into two lifetime components (bulk and defect) using a computer program of PATFIT-88 [9]:

$L(t)=(I_1/\tau_1)\exp(-t/\tau_1)+(I_2/\tau_2)\exp(-t/\tau_2)$, where I_i (i=1,2) are the intensities ($I_1+I_2=1$) and τ_i are the lifetimes. If the two-state trapping model [10] is a good approximation, the above lifetimes are give by $\tau_1=1/(\tau_B^{-1}+\kappa)$, $\tau_2=\tau_D$, where τ_B is the positron lifetime in the bulk state, τ_D the positron lifetime at vacancy-type defects, and κ the positron trapping rate due to the vacancy-type defects $\kappa=(I_2/I_1)(1/\tau_B-1/\tau_2)$. The trapping rate is proportional to the concentration of defects. The validity of the analysis based on the trapping model can be checked by the difference of the lifetime τ_1 determined by the fitting procedure and that expected from the trapping model. Doppler broadening measurement of the annihilation γ-rays was also performed using conventional two-γ coincidence method with two pure Ge detectors. About 10^5 counts at peak position (511 keV) were accumulated in each spectrum. The typical signal to noise ratio was about $5x10^3$. The line shape parameters (S and W) were determined.

Results and Discussion

A. Positron annihilation in the bulk state

Figure 1 shows Doppler broadening spectra obtained for Ge, $Si_{0.63}Ge_{0.37}$ and Si specimens. The energy shift ΔE=1 keV corresponds to the electron momentum p=0.54 a.u. The spectrum for Ge is broader than that for Si in the high momentum region (i.e., ΔE > 3 keV). The spectrum for $Si_{0.63}Ge_{0.37}$ shows an intermediate shape between Ge and Si. The above result suggests that core electrons of Ge have a higher contribution to the annihilation of positrons than that of Si. It is in good agreement with recent theoretical calculations [11,12]. Figure 2(a) shows the dependence of the line shape parameters (S and W) on the Si fraction x. Here, S and W parameters were

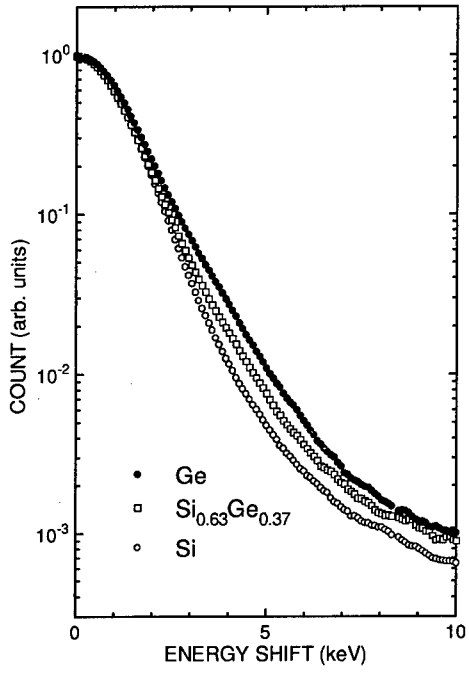


Fig.1 Doppler broadening spectra. Energy shift ΔE=1keV corresponds to electron momentum p=0.54 a.u.

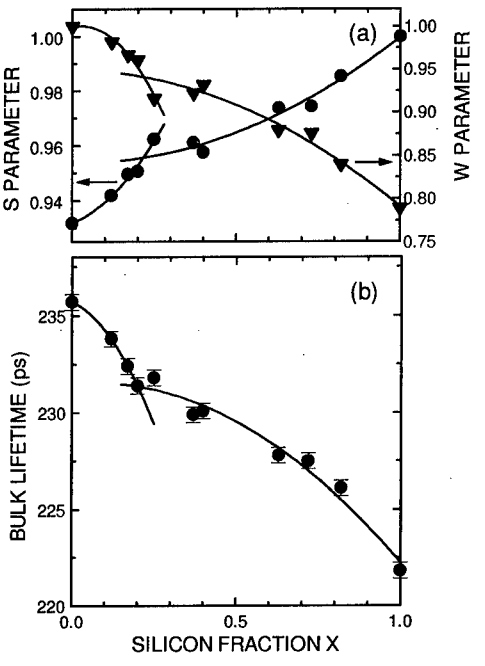


Fig. 2 (a) Doppler parameters (S&W) and
(b) bulk lifetime as a function of x.

normalized by the values of Si and Ge, respectively. These parameters vary between the values for Ge and Si depending on x. The mirror-like behaviors of S and W parameters simply show that the increase (or decrease) in the annihilation rate with core electrons correlates with the decrease (or increase) in the annihilation rate with valence electrons, or vice versa. It should be noted that the variation of the parameters with x is discontinuous at around x=0.20. This is discussed later.

For the as-grown specimens, the two-component analysis of lifetime spectra was not available and hence only one lifetime component was obtained. This shows that positrons annihilate through the delocalized state and not through the trapped state at defects. As shown in Fig. 2(b), although the bulk lifetime changes from 235.6±0.6 ps (bulk lifetime for Ge) to 221.8± 0.6 ps (bulk lifetime for Si) by changing x, the dependence is non-monotonic at around x=0.17-0.20 as well as the cases of S and W parameters.

Now we discussed about the non-monotonic change of the bulk lifetime and Doppler parameters. Since the lattice constant of Si_xGe_{1-x} bulk crystal obeys approximately to Vegard's law [2,3], it is simply expected that the bulk lifetime and Doppler parameters have monotonic dependences on the alloy composition. Therefore, the non-monotonic change of the bulk lifetime and Doppler parameters at around x=0.17~0.20 could not be explained by Vegard's law. It is also hardly expected that the non-monotonic change reflects some ordered structures as observed for Si/Si_xGe_{1-x} strained superlattice, since Si_xGe_{1-x} bulk forms a completly random system [13,14]. Here, it is interesting to note that the above non-monotonic change is similar to that of the band gap of Si_xGe_{1-x} alloy at x=0.15~0.25 due to the switch of conduction band minima from the Ge-like L points to the Si-like X points [2,4-6]. Possibly, the non-monotonic change is explained as the change in positron annihilation characteristics which is related to the change in the electronic structure of Si_xGe_{1-x} alloy. The positron annihilation rate with valence electrons is basically determined by the valence electron density felt by positrons. The annihilation rate is enhanced by the correlation effect that positrons tend to gather electrons around themselves. According to Bandt and Reinheimer [15], the enhancement factor is a function of dielectric constant. Puska shows that the enhancement factor for semiconductors may be given by $(1-1/\varepsilon)$, where ε is the dielectric constant [16]. This means that electrons respond to positrons through the dielectric polarization. The dielectric constant of semiconductors correlates with the band gap. The dielectric constant for Si_xGe_{1-x} varies depending on the alloy composition [17]. It is therefore expected that the bulk lifetime of Si_xGe_{1-x} alloy is expected to show a non-monotonic change at which the band gap changes discontinuously.

B. Vacancy production by electron irradiation

Figure 3 shows the positron lifetime spectra for the $Si_{0.82}Ge_{0.18}$ specimen before and after 3 MeV electron irradiation. An apparent increase in the lifetime is observed suggesting the introduction of vacancy-type defects due to irradiation. Figure 4 shows the positron lifetimes (τ_1 and τ_2) and the intensity (I_2) after the irradiation as a function of x. It is found that the lifetime τ_1 agrees well with that expected from the two-state trapping model. This assures that the first and second components are related to the positron annihilations in the bulk and vacancy-type defects, respectively. As seen from Fig. 4, (i) no second lifetime component due to vacancy-type defects is observed for $x \leq 0.17$, (ii) the lifetime τ_2~330 ps related to vacancy-type defects is observed for $0.20 \leq x \leq 0.40$ and the intensity has a plateau up to x=0.40 and (iii) the lifetime τ_2 decreases to 280 ps and the intensity increases for $x \geq 0.63$.

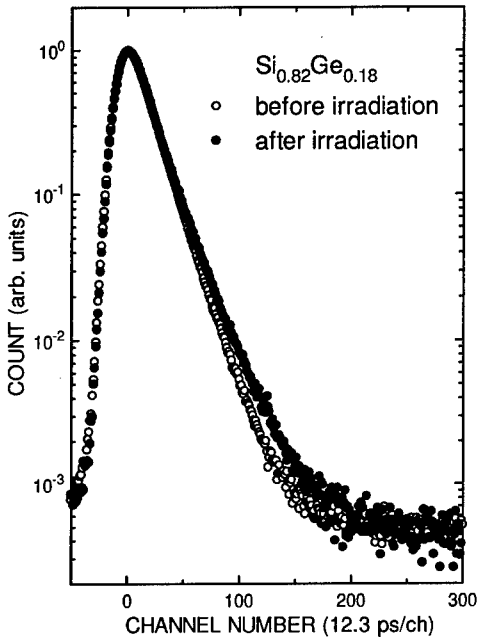


Fig.3 Positron lifetime spectra for the $Si_{0.82}Ge_{0.18}$ specimen before and after 3 MeV electron irradiation with a fluencen of $1x10^{18}$ e$^-$/cm^2.

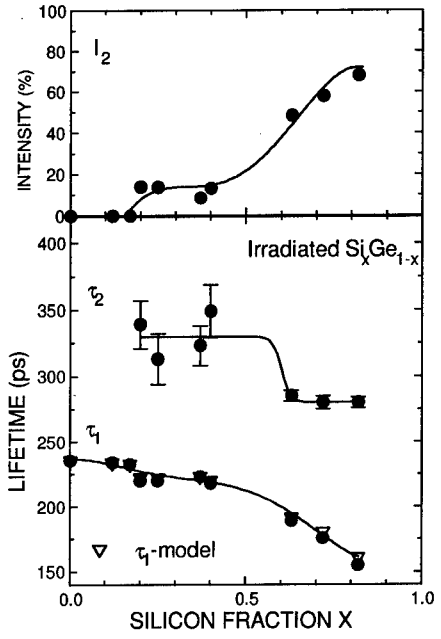


Fig.4 Positron lifetimes τ_1 and τ_2 and intensity I_2 obtained for 3 MeV electron irradiated Si_xGe_{1-x} as a function of Si fraction x.

Monovacancies in Ge are reported to disappear far below room temperature [18]. Divacancies in Ge were proposed to be unstable even at room temperature [19]. Thus, it is probable that both monovacancies and divacancies may disappear in the Ge-rich region ($x \leq 0.17$) since the crystals have a character similar to Ge. The absence of vacancy clusters in the region is explained in terms of the rapid disappearance of divacancies before agglomeration. Monovacancies in Si are also mobile and disappear at sinks or form divacancies or vacancy-impurity complexes below room temperature [20]. Divacancies in Si are stable at room temperature and to form vacancy clusters such as quadrivacancies at 300-350℃ [21, 22]. It is therefore expected that divacancy-like defects and vacancy-impurity complexes are the major defect species in the Si-rich region ($x \geq 0.63$) since the crystals have a character similar to Si. The observed lifetime τ_2~280 ps in the region seems to be an weighted average among these vacancies. The lifetime τ_2~330 ps in the intermediate region ($0.2 \leq x \leq 0.40$) suggests the presence of vacancy clusters larger than divacancies. Probably vacancies have intermediate mobilities between those in Si and Ge. It is therefore expected that divacancies move or dissociate slowly so that vacancy clusters such as trivacancies and quadrivacancies can be formed.

It is interesting to note that vacancies start to survive at x=0.17~0.20 where the conduction band minima switch from the Ge-like X points to the Si-like L points. This indicates that the stability of vacancies in Si_xGe_{1-x} alloy is related to the electronic structure of the alloy. It is probably because the electronic structure of crystal correlates with the strength of crystal bonding. For instance, the increase in the band gap energy is closely related to the increase in the strength of crystal bonding in the case of group IV semiconductors. Since the motion of a vacancy requires the

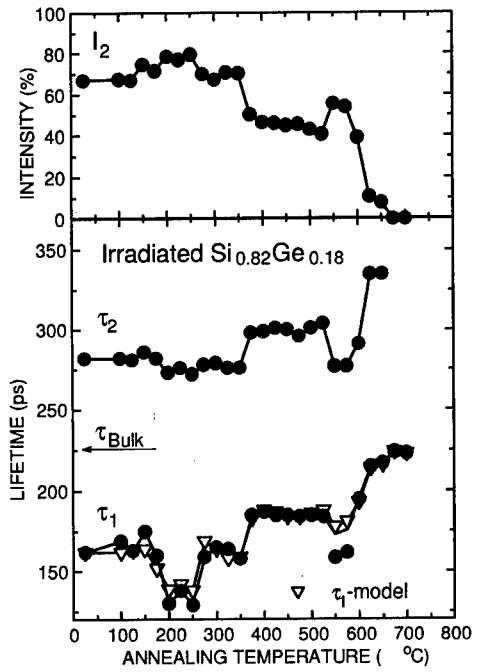


Fig. 5 Positron lifetimes (τ_1 and τ_2) and intensity I_2 for the irradiated $Si_{0.82}Ge_{0.18}$ specimen as a function of annealing temperature.

bond cuttings of the neighboring atoms, the stability of vacancies may depend on the detailed electronic structure of crystal.

C. Annealing of irradiation-induced vacancies

Figure 5 shows annealing behaviors of lifetimes and intensity for the $Si_{0.82}Ge_{0.18}$ specimen irradiated with 3 MeV electrons at a fluence of $1x10^{18}$ e^-/cm^2. The lifetime τ_1 agrees with that expected from the trapping model suggesting the second lifetime component represents vacancy-type defects. The lifetime τ_2 is about 280 ps and changes as 280 ps → 275 ps → 300 ps → 275 ps → 330 ps at 150℃, 350 ℃, 550 ℃ and 600 ℃, respectively. At these annealing temperatures, the intensity I_2 increases and then decreases, increases again and finally diminishes. At 700 ℃, intensity I_2 reaches the detection limit and the lifetime τ_1 fully recovers to the bulk lifetime.

It is known that in the case of lightly doped Si small vacancies generated by electron irradiation develops to large vacancy clusters upon heating and hence the positron lifetime has a tendency to increase at elevated temperatures [22]. Whereas in the heavily doped case vacancy-impurity interaction is a dominant process and hence positron lifetime does not increase drastically and sometimes decreases [23]. The above results seems to be similar to the case of heavily doped Si. Probably, vacancy-impurity interaction is a dominant defect reaction below 600 ℃. If we think that this specimen ($Si_{0.82}Ge_{0.18}$) is a heavily Ge-doped Si, vacancies at Si site easily interact with Ge atoms. Since the atomic radius of a Ge atom (1.23 Å) is slightly larger than that of a Si atom (1.17 Å), the dilatational strain field may be formed around Ge atom site. Thus, vacancies will be bound at Ge atom site. The lifetime of positron trapped at a vacancy-Ge complex may be shorter as compared to as isolated vacancy since the effective open volume of the complex is smaller due to the larger atomic radius of a Ge atom. In addition, excess core electrons of a Ge atom also results the shortening of the positron lifetime. Possibly, the decreases in the lifetime τ_2 at 150 ℃ and 550 ℃ may be caused by the combination of vacancy-type defects with Ge atoms. The increases in the lifetime τ_2 at 350 ℃ and 600 ℃ may be caused by the dissociation of vacancy-Ge complexes and/or vacancy-clustering. The lifetime τ_2 ~330 ps observed after the annealing at 600 ℃ is comparable to the lifetime of a positron trapped at trivacancy or quadrivacancy in Si. For instance, quadrivacancies in Si are formed due to the migration and combination of divacancies at 300~350 ℃. The above clustering temperature 600℃ is somewhat higher as compared to the case of Si. This indicates that the existence Ge atoms retards the growth of vacancy-clusters.

Summary

The results of this work are summarized as follows: The bulk positron lifetime and Doppler parameters of Si_xGe_{1-x} bulk crystal show a non-monotonic change at around x=0.17~0.20. This phenomenon is very similar to the abrupt change of the band gap width of Si_xGe_{1-x} bulk crystal. In irradiated Si_xGe_{1-x} crystals vacancy-type defects are observed for $x \geq 0.20$ but not for $x \leq 0.17$. This implies that the mobility of vacancies depends on the electronic structures of crystal itself. From the annealing behavior of the positron lifetime, it is found that vacancy-clustering is suppressed unlike to the case of lightly-doped Si. This may be due to the strong interaction between vacancies and Ge atoms.

Acknowledgment

We thank Mr. H. Sunaga of the Japan Atomic Energy Research Institute for his help in electron irradiation.

References

1. J. P. Dismukes and L. Ekstrom, Trans. Metall. Soc. AIME, **223**, 672(1965).
2. E. R. Johnson and S. M. Christian, Phys. Rev. **95**, 560 (1954).
3. J. P. Dimuske, L. Ekstrom and R. J. Paff, J. Phys. Chem. **68**, 3021 (1964).
4. J. Weber and M. I. Alonso, Phys. Rev. B**40**, 5683 (1989).
5. R. Braunstein, A. R. Moore and F. Herman, Phys. Rev. **109**, 659 (1958).
6. E. F. Kustov, E. A. Mel'nikov, A. A. Sutchenkov, A. I. Levadnii and V. A. Filikov, Sov. Phys. Semicond. **17**,481(1983).
7. P. A. Kumar, K. G. Lynn and D. O. Welch, J. Appl. Phys. **76**, 841 (1994).
8. I. Yonenaga, A. Matsui, S. Tozawa, K. Sumino and T. Fukuda, J. Cryst. Growth **154**, 275(1995).
9. P. Kirkegaard, N. J. Pederson and M. Eldrup, PATFIT-88, Riso-M-2704(1989).
10. R. N. West, Adv. Phys. **22**, 263(1973).
11. M. Alatalo, H. Kauppinen, K. Saarinen, M. J. Puska, J.Mäkinen, P. Hautojärvi and R. M. Nieminen, Phys. Rev. **B51**, 4176 (1995).
12. M. Alatalo, B. Barbiellini, M. Hakara, H. Kauppinen, T. Korhonen, M. J. Puska, K. Saarinen, P. Hautojärvi and R. M. Nieminen, Phys. Rev. **B54**, 2397(1995).
13. A. Qteish and R. Resta, Phys. Rev. B**37**, 1308(1989).
14. A. Qumazd and J. C. Bean, Phys. Rev. Lett. **55**,765(1985).
15. W. Brandt and J. Reinheimer, Phys. Rev. **8**, 3104(1970).
16. M. J. Puska, S. Mäkinen, M. Manninen and R. M. Nieminen, Phys. Rev. **B39**, 7666 (1989).
17. E. Schmidt, Phys. Stat. Sol. **27**, 57 (1968).
18. R. E. Whan, Phys. Rev. **140**, A690 (1965).
19. M. Hirata, Inst. Phys. Conf. Ser. **23**, 164 (1975).
20. G. D. Watkins, J. R. Troxell and A. P. Chatterjee, Inst. Phys. Conf. Ser. **46**, 16(1979).
21. G. D. Watkins and J. W. Corbett, Phys. Rev. **138**, A543 (1964).
22. A. Kawasuso, M. Hasegawa, M. Suezawa, S. Yamaguchi and K. Sumino, Materials Science Forum **175-178**, 423(1995).
23. A. Kawasuso, M. Hasegawa, M. Suezawa, S. Yamaguchi and K. Sumino, Appl. Surface Sci. **85**, 280 (1995).

Materials Science Forum Vols. 258-263 (1997) pp. 133-138
© 1997 Trans Tech Publications, Switzerland

ELECTRONIC PROPERTIES OF DEFECTS INTRODUCED IN n- AND p-TYPE $Si_{1-x}Ge_x$ DURING ION ETCHING

S.A. Goodman, F.D. Auret, M. Mamor, P. N. K. Deenapanray and W.E. Meyer
Physics Department, University of Pretoria, Pretoria, 0002, SOUTH AFRICA

Key Words : SiGe, ion etching, particle irradiation, defects,

Abstract. Surface processing, and in particular dry or plasma etching of semiconductors is a key technology for device processing. As ion assisted etching becomes more widely and routinely applied for device fabrication, especially for smaller dimensions, it is important to understand the damage introduced by the processing itself. Low energy particle bombardment also plays an important role in controlling the growth and properties of MBE grown Si and SiGe layers. We have used deep-level transient spectroscopy (DLTS) in an investigation of the electronic properties of defects introduced in phosphorus doped n-type $Si_{1-x}Ge_x$ (x = 0 to 0.25) during 1 keV He-ion-etching and those introduced by 0.75 keV Ar-ion etching of boron doped p-type $Si_{1-x}Ge_x$ (x = 0 to 0.15). The defects introduced during this ion etching are compared to those detected after α-particle irradiation, sputter deposition and electron beam deposition (no shielding of secondary electrons).

Introduction

Recent advances in the growth of strained SiGe on graded SiGe buffer layers has led to the development of heterostructures with superior carrier transport properties [1]. The gap in performance between n- and p-type SiGe devices is expected to shrink, which could possibly lead to the development of more complementary structures using SiGe [2]. The fabrication of these electronic and optoelectronic devices involve a series of processing steps. During processing steps, such as particle bombardment during thin film growth to enhance dopant incorporation [3] and ion-etching, the material is exposed to energetic particles. It is well known that exposure of semiconductors to energetic particles can lead to defect introduction. As ion assisted etching becomes more widely and routinely applied for device fabrication, especially for smaller dimensions, it is important to understand the damage introduced by the processing itself. Low energy particle bombardment also plays an important role in controlling the growth and properties of MBE grown Si and SiGe layers [4].

Experimental

For this study epitaxial SiGe layers were grown by chemical vapor deposition (CVD). A lightly doped ($4 - 6 \times 10^{16}\,cm^{-3}$) Si buffer layer was first grown between 625 and 700°C on (100) p^+ and n^+ silicon substrates for p- and n-type SiGe, respectively. The boron and phosphorous doping of the epitaxial SiGe layers as determined by capacitance voltage (C-V) measurements was between 1×10^{17} and $3 \times 10^{17}\,cm^{-3}$. The carrier density profiles of the layers were uniform. The SiGe layer thickness and dopant concentrations have been selected to avoid the potential interference from the Si / SiGe interface when conducting the DLTS [5] measurements. The n- and p-type sample specifications are listed in Table 1. From Table 1 it can be seen that the n-type epilayers are relaxed to a certain degree. This relaxation is probably due to some

Table 1.
n- and p-SiGe sample specifications

Carrier density (cm^{-3})	% Ge	% relaxation	SiGe thickness (nm)
n-type			
2.5×10^{17}	25	25	280
2.5×10^{17}	15	63	435
3.0×10^{17}	10	18	480
2.0×10^{17}	4	0	500
5.0×10^{16}	0	N/A	3000
p-type			
5.0×10^{16}	0	N/A	3000
1.0×10^{17}	5	0	380
1.0×10^{17}	10	0	386
1.0×10^{17}	15	0	280

tetragonal distortion of the cubic lattice cell of the SiGe or to a lesser due to the introduction of misfit dislocations [6]. From X-ray diffraction measurements, it was confirmed that there was no lattice relaxation in the p-SiGe epilayers. The thickness of the strained p-type epitaxial layers varies between 280 nm for material containing 15 % Ge and 386 nm for the 5 % Ge material. The thickness of the 5, 10 and 15 % Ge epilayers are well below the experimentally [7] and theoretically [8,9] calculated critical layer thickness (h_c). After wet chemical cleaning using trichloroethylene and isopropanol and etching using a buffered HF : H_2O (1 : 50) solution, the p-type samples were exposed to 0.75 keV Ar-ions in a modified high vacuum evaporator system, and the n-type material to 1 keV He-ions in the ultra-high vacuum system of an Auger electron spectroscopy (AES) system. After Ar-ion etching, circular Ti contacts, (0.77 mm in diameter and 200 ± 5 nm thick), were deposited onto the p-$Si_{1-x}Ge_x$ through a metal contact mask by electron-beam (e-beam) evaporation. A shield was positioned such that no stray electrons from the filament were able to reach the ion etched surfaces. After He-ion etching the n-type samples they were again chemically cleaned and etched prior to the resistive evaporation of Au Schottky contacts through a metal contact mask. The circular Au Schottky contacts, were 200 ± 5 nm thick and 0.77 mm in diameter. After Schottky diode fabrication, ohmic contacts were formed on the backside of both conductivity type samples using a Ga/In eutectic. For control purposes, a sample that had not undergone ion etching, was metallised in parallel under identical conditions as the ion etched material.

Results and discussion

n-$Si_{1-x}Ge_x$

DLTS of control samples, recorded using resistively deposited contacts, indicated that no defects with peaks between 15 K and 300 K are present in appreciable concentrations in the unprocessed n-$Si_{1-x}Ge_x$ ($0 \leq x \leq 0.25$). From inspection of Fig. 1, where the DLTS spectra of Si, where $x = 0$ (curve (a)) and $x = 0.04$ (curve (b)) are presented, it is evident that several electron defects are introduced during the He-ion etching process. After etching Si, where $x = 0$, four electron defects, EHe1, EHe2, EHe4 and EHe6 were introduced in the band gap. When $Si_{0.96}Ge_{0.04}$, is sputter etched with He-ions, two additional defects EHe3 and EHe5 are introduced. When comparing the defects detected after He-ion etching (curves a and b of Fig. 1) to those detected after 5.4 MeV α-particle irradiation (curves a and b, Fig. 2) and to those after sputter deposition (curves c and d, Fig. 2), it was noted that certain defects introduced during the He-ion etch process have the same DLTS "signatures" as defects after the sputter deposition processes (ES1 – ES7), but none were the same as those introduced during the α-particle irradiation. In Si seven discrete level defects (DLDs) were detected (ES1 - ES7), with ES4 and ES5 being the dominant defects in the spectra. In the $Si_{1-x}Ge_x$ ($x > 0$) the same 7 defects are detected, however, they are masked by the presence of a band of continuous level defects [10] (CLDs) in the band gap of the SiGe. Thus both DLDs and CLDs are detected in the material containing Ge. Defects EA1

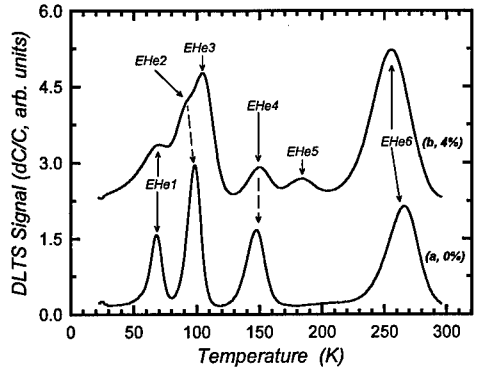


Figure 1. DLTS spectra of n-$Si_{1-x}Ge_x$ ($0 < x < 0.04$), after 1.0 keV He-ion etching. Spectra were recorded at a LIA frequency of 46 Hz.

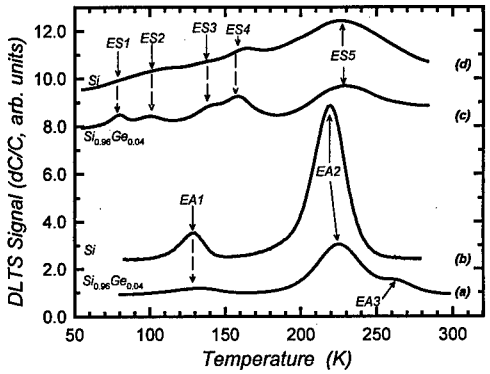


Figure 2. DLTS spectra of n-$Si_{1-x}Ge_x$ ($x = 0$ and 0.04), after 5.4 MeV alpha particle irradiation (a & b) and after sputter deposition of Au, (c & d).

and EA2 are detected in both Si and SiGe. These defects are believed to be the two charge states of the divacancy (EA1: $V^{-/-}$ and EA2: $V^{-/o}$) [11], it is also possible that EA2 is the vacancy-phosphorous complex (V-P) or a complex of a V-P center with a divacancy. Defect EA3, however, is only detected in material containing Ge. It has been found that the defects introduced by low (1 keV) and high energy (5.4 MeV) He-ion bombardment of Si are totally different [12]. This finding is in sharp contrast to the He-ion bombardment of epitaxially grown n-GaAs, where four defects in low energy bombarded GaAs were the same as the main defects introduced during high energy He-ion bombardment [13]. A comparison of the DLTS "signatures" of these defects with those detected after 5.4 MeV α-particle irradiation using a radionuclide and RF sputter deposition of Au SBDs is presented in Table 2. From this comparative study it is evident that EHe3 detected after He-ion etching of material containing Ge is similar to ES2 detected after sputter deposition of Au on material containing Ge. Defect EHe4, detected in material where there is no Ge, is similar to defect ES4 detected in the same material. From this table it is also evident that EA2 and EA3 have the same position in the band gap, however, they are observed at different temperature positions in the DLTS spectra, because of the large difference (factor of at least 100) in their capture cross-section. The DLTS signature of EA3 was approximated by graphical manipulation and subtracting the spectra obtained for the material containing no Ge from the spectra of the material with 4 % germanium. From this section of the study we believe defect EHe5 is definitely related to the presence of germanium as the EHe5 concentration increases with increasing Ge content. Defect

Table 2. DLTS "signatures" of defects introduced during He-ion etching, and α-particle irradiation of n-type $Si_{0.96}Ge_{0.04}$ and sputter deposition of n-type Si.

Defect label	E_T (eV)	$\sigma_n \times 10^{-16}$ (cm^2)	T_{peak} (K) at 46 Hz
EHe1	0.11	0.09	75
EHe2	—	—	—
EHe3	0.19	3.6	108
EHe4	0.28	1.7	157
EHe5	0.36	3.7	193
EHe6	0.52	4.7	267
ES1	0.135	2.6	80
ES2	0.175	3.3	100
ES3	0.175	0.002	137
ES4	0.299	6.7	158
ES5	0.431	2.7	229
ES6	—	—	—
ES7	0.583	1.7	310
EA1	0.24	2.3	136
EA2	0.44	7.6	226
EA3	0.44	0.07	274

The value of E_T is the depth of the energy level below the conduction band. All DLTS spectra were acquired under the following DLTS pulse conditions: a quiescent reverse bias (V_r) of 0.5 V and a forward bias (V_p) of 0.8 V. The scan rate was 0.08 $K.s^{-1}$.

EHe4 on the other hand, is related to the presence of Si, as the EHe4 concentration decreases with increasing Ge content.

p-$Si_{1-x}Ge_x$

As illustrated in Fig. 3, 0.75 keV Ar-ion etching introduced numerous defects in p-SiGe. It is also evident that certain defects are only present in material that contains Ge. Figure 4 depicts the DLTS spectra of one of the major defects (HAr2a), detected in Ar-ion etched p-$Si_{0.95}Ge_{0.05}$ a defect (He2) detected after electron beam deposition of Ti (no shielding of secondary electrons) and Hal5 detected after 5.4 MeV alpha particle

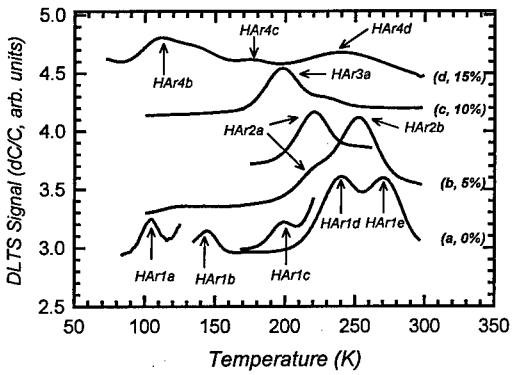


Figure 3. DLTS spectra of p-$Si_{1-x}Ge_x$ ($0 < x < 0.15$), after 0.75 keV Ar-ion etching. Spectra were recorded at a LIA frequency of 46 Hz.

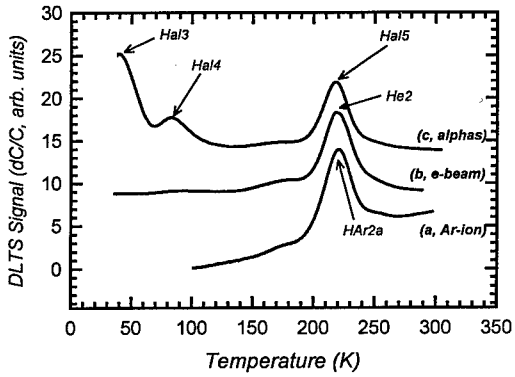


Figure 4. DLTS spectra of p-$Si_{0.95}Ge_{0.05}$ after 0.75 keV Ar-ion etching (a), after e-beam deposition with no shielding (b) and after α-particle irradiation (c).

irradiation. A comparison of the DLTS "signatures" of an Ar-ion induced defect as a function of increasing Ge content and comparing this to the change in band gap (assuming that the majority of the band gap change is taken up in the valence band) [14] revealed that the activation energy followed a certain trend. Taking the band gap change into account it was speculated that defect HAr1d detected in p-Si is the same as HAr2a, HAr3a and HAr4c detected in material with 5, 10 and 15 % Ge, respectively. This defect activation energy dependence with change in Ge content is illustrated in Fig. 5. In order to confirm this initial speculation, DLTS depth profiling was performed by recording spectra at fixed V_r but incrementing V_p in small steps from one scan to the next. The approach of Zohta *et al* [15] was then used to obtain the defect concentration as a function of depth below the interface. Figure 6 illustrates the defect distribution profile of the four defects introduced in material with different Ge contents that are believed to be the same defect. Although defect HAr4c detected in the material with 15 % Ge has the same profile shape it has a slightly lower concentration, this is possibly due to inaccuracies in the DLTS profiling caused by the defect's broad DLTS peak due to alloy broadening. From previous studies we believe that the defect concentration should increase exponentially towards the surface, the region of uniform defect distribution may be accounted for by incomplete defect filling near the surface due to pinning of the Fermi level caused by the region of high disorder near the surface resulting from the impinging Ar-ions. From this evidence we conclude that it is indeed the same defect. This defect which is pinned to the conduction band has an introduction rate which is independent of Ge content. A comparison of defect signatures after the three different defect introduction processes mentioned above is listed in Table

3. Defect HAr1d is also detected in α-irradiated material (Hal2) and electron beam prepared material (He2), defects HAr2a, Hal5 and He2 (5 %) are also similar. In material with 10 % Ge, defect HAr3a has similar electronic properties as Hal7 and He2.

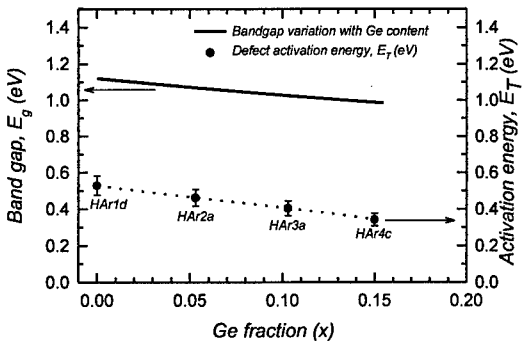


Figure 5. Calculated band gap change with variation in Ge content. Change in activation energy of the major defect detected in Ar-ion irradiated p-SiGe.

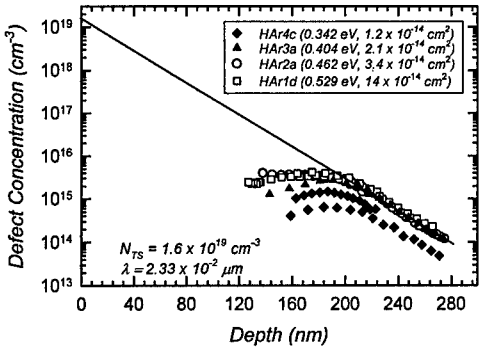


Figure 6. Depth profiles of the major defect in 0.75 keV Ar-ion etched p-SiGe. The characteristic length and surface defect concentration are derived [16].

Table 3. DLTS "signatures" of defects introduced by 0.75 keV Ar-ion etching, 5.4 MeV α-irradiation and electron beam deposition (no shielding) in p-$Si_{1-x}Ge_x$ (0 < x < 0.15).

5.4 MeV alpha particles					***0.75 keV Ar-ion etching***				
Defect label	*% Ge*	*E_T (eV)*	*σ_n x 10^{-16} (cm^2)*	*T_{peak} (K) (46 Hz)*	*Defect label*	*% Ge*	*E_T (eV)*	*σ_n x 10^{-16} (cm^2)*	*T_{peak} (K) (46 Hz)*
Hal1	*0*	*0.165*	*10*	*117.9*	*HAr1a*	*0*	*0.166*	*6.2*	*104.8*
Hal2	*0*	*0.525*	*960*	*241.5*	*HAr1b*	*0*	*0.258*	*33*	*143.4*
Hal3	*5*	*0.078*	*3.5*	*54.3*	*HAr1c*	*0*	*0.373*	*42*	*199.0*
Hal4	*5*	*0.134*	*2.1*	*90.9*	*HAr1d*	*0*	*0.529*	*1400*	*239.9*
Hal5	*5*	*0.464*	*530*	*220.0*	*HAr1e*	*0*	*0.559*	*160*	*274.0*
Hal6	*10*	*0.090*	*1.4*	*65.0*	*HAr2a*	*5*	*0.462*	*340*	*222.7*
Hal7	*10*	*0.400*	*280*	*196.6*	*HAr2b*	*5*	*0.540*	*320*	*258.2*
Electron beam					*HAr3a*	*10*	*0.404*	*210*	*201.6*
He1	*10*	*0.509*	*810*	*236.2*	***HAr4a***	*15*	*0.126*	*140*	*69.9*
He1	*15*	*0.502*	*960*	*231.6*	*HAr4b*	*15*	*0.155*	*1.2*	*105.2*
He2	*0*	*0.525*	*940*	*241.7*	*HAr4c*	*15*	*0.342*	*120*	*176.3*
He2	*5*	*0.467*	*510*	*221.8*	*HAr4d*	*15*	*0.467*	*130*	*233.6*
He2	*10*	*0.403*	*240*	*199.6*					
He2	*15*	*0.350*	*240*	*165.8*					

Conclusions

From this study, it is evident that He-ion etching of n-$Si_{1-x}Ge_x$ ($0 \le x \le 0.25$) introduced six discrete level electron traps (EHe1 - EHe6) in the band gap two of which could only be detected for $x \neq 0$. From a comparison of the DLTS "signatures" of our work and reported works, we have shown that three of these defects (EHe2, EHe4 and EHe6) are the same as those detected in silicon. For material containing as little as 4 % germanium two additional defects are detected (EHe3 and EHe5). It was seen that these He-ion induced defects are positioned close to the metal-semiconductor interface.

The possibility of field enhanced emission influencing the DLTS peak positions and hence the "signatures" must be taken into count when these parameters are compared to other results. When comparing only those defects detected in material containing Ge the following conclusion can be made: Defect EHe3 is similar to ES2 and EHe4 is possibly the same defect as ES4. Contrary to what is observed in n-type epitaxial GaAs, the defects introduced in Si by low and high energy He-ion bombardment are not the same. The incident energy and angle of incidence may possibly influence the defect formation mechanism in SiGe.

A defect (HAr1d) introduced in p-SiGe during Ar-ion etching was also detected after alpha-particle irradiation and e-beam deposition. This defect was introduced at the same rate regardless of the Ge content and has an activation energy which changes to the same degree as the band gap of the strained p-SiGe with increase in Ge content. The defect is pinned to the conduction band and has a similar concentration profile in the range of Ge contents investigated in this study. A defect with a similar DLTS "signature" was detected by Troxell [17], however, the structure is as yet unresolved. The concentration of this dominant defect detected very close to the interface, was extrapolated from 2×10^{19} cm^{-3} at the surface to the 10^{14} cm^{-3} range at 280 nm from the surface. From TRIM [18] calculations these low energy Ar-ions are only expected to penetrate the SiGe approximately 0.3 nm. The question arises why do the Ar-ion induced defects penetrate the SiGe much deeper than the penetration depth of the incident particle? It is believed that interstitials created in the Ar damaged near surface region diffuse into the material [19] forming pairs and complexes. This diffusion is an important phenomenon for the device physicist, in particular where shallow junction devices are concerned.

References

1. K.Ismail, J.O. Chu, and B.S. Meyerson, Appl. Phys. Lett., **64**, 3124 (1994).
2. M.Arafa, P. Fay, K. Ismail, J.O. Chu, B.S. Meyerson, and I. Adesida, IEEE Electron Device. Lett. **17**, 449 (1996).
3. R.A.A. Kubiak, W.Y. Leong and E.H.C. Park, J. Electrochem. Soc. **132**, 2738 (1985).
4. W.-X. Ni, G.V. Hansson, I.A. Buyanova, A. Henry, W.M. Chen, and B. Monemar, Appl. Phys. Lett. **68**, 238 (1996).
5. D.V. Lang, J. Appl. Phys. **45**, 3014 (1974).
6. K.W. Nauka, Proc. 22nd Int. Conf. on the Physics of Semiconductors, Canada, (1994).
7. J.C. Bean, L.C. Feldman, A.T. Fiory, S. Nakahara, and I.K. Robinson, J. Vac. Sci.. Technol. **A2**, 436 (1984).
8. J.W. Matthews and A.E. Blakeslee, J. Cryst. Growth **27**, 118 (1974).
9. R. People and J.C. Bean, Appl. Phys. Lett. **47**, 322 (1985).
10. F.D. Auret, S.A. Goodman, G. Myburg and W.E. Meyer, J. Vac. Sci. Technol., **B10**, 2366 (1992).
11. B.G. Svennsson, C. Jagadish, A. Hallen and J. Lalita, Proc. IBMM95, Canberra, Australia (1995).
12. F.D. Auret, P.N. K. Deenapanray and S.A. Goodman, unpublished.
13. F.D. Auret, S.A. Goodman, Accepted, Appl. Phys. Lett. **71** (1997).
14. C.G. van de Walle and R. Martin, Phys. Rev. B **34**, 5621 (1986).
15. Y. Zohta and M. O. Watanabe, J. Appl. Phys., **53**, 1809 (1982).
16. E. Grussel, S. Berg and L.P. Andersson, J. Electrochem. Soc. **127**, 1573 (1980).
17. J.R. Troxell, Solid State Electronics, **26**, 539 (1983).
18. J.F. Ziegler, J.P. Biersack and U. Littmark, "The Stopping and Range of Ions in Solids", vol. 1, Ed. J.F. Ziegler, Pergamon Press, New York, 1985
19. J.L. Benton, Mat. Res. Soc. Symp. **262** 1027 (1992).

Materials Science Forum Vols. 258-263 (1997) pp. 139-144
© 1997 Trans Tech Publications, Switzerland

THE ROLE OF NON-RADIATIVE DEFECTS IN THERMAL QUENCHING OF LUMINESCENCE IN SiGe/Si STRUCTURES GROWN BY MOLECULAR BEAM EPITAXY

I.A. Buyanova, W.M. Chen, G. Pozina, B. Monemar, W.X. Ni and G.V. Hansson
Department of Physics and Measurement Technology, Linköping University, S-581 83 Linköping, SWEDEN

Keywords: non-radiative defects, SiGe, Si, MBE, luminescence, ODMR, thermal quenching

Abstract.
The dominant mechanism responsible for thermal quenching of photoluminescence from SiGe quantum wells (QWs) grown by Molecular Beam Epitaxy (MBE) is shown to be the thermal activation of an efficient non-radiative recombination channel, with a rather low activation energy of about 2 - 5 meV. A post-growth hydrogen treatment is demonstrated to be only moderately effective in passivating the non-radiative defects and in reducing thermal quenching. Post-growth thermal annealing at high temperature (e.g. > 500 °C) is, on the other hand, shown to be highly effective and leads to a nearly complete removal of the non-radiative defects. Experimental evidence is provided for the dominant mechanism responsible for this improvement. It is due to a reduction of grown-in non-radiative defects such as vacancy-related complexes, monitored in the Optically Detected Magnetic Resonance (ODMR) experiments. Selective optical excitation above and below the bandgap of the Si barriers has been used to determine the relative contributions of non-radiative recombination channels present in the SiGe QWs and the Si barriers.

Introduction.
Recent rapid advances in modern epitaxial growth techniques have enabled the fabrication of high quality Si epilayers and Si-based low-dimensional artificial structures, and have awaken the long-sought desire for efficient Si-based light detectors and emitters, aiming at a monolithic integration of both optical and electronic devices based on the mature Si technology. However, a severe thermal quenching of the luminescence below room temperature has so far prevented this material system from practical applications for light-emitting devices operating at room temperature. Even though several mechanisms for the severe thermal quenching have been discussed in the literature in terms of surface recombination [1] and the presence of non-radiative channels which are thermally activated [2, 3], a definite experimental evidence as to the chemical identity of the defects has been lacking. This has thus deterred any deliberate elimination of these non-radiative channels and has undermined efforts in improving the radiative efficiency of the material.

Most recently we have revealed [4], by the optical detection of magnetic resonance (ODMR) technique, several efficient grown-in non-radiative centers in undoped and B-doped Si epilayers and SiGe/Si heterostructures grown by molecular beam epitaxy (MBE). A dominant defect is proven to be the vacancy-oxygen (V-O) complex in Si. Experimental evidence on the formation mechanisms of these non-radiative defects has been provided as being due to a low surface adatom mobility and a lower desorption rate of O contamination from the growing surface during low temperature growth, and also due to ion bombardment as occurs e.g. during potential enhanced doping. In this work, we provide direct evidence that these non-radiative defects are largely responsible for a rapid thermal quenching of luminescence from SiGe quantum wells (QWs). Based on the gained knowledge, educated attempts are made to remove these non-radiative defects by using different post-growth treatments, such as hydrogenation and thermal annealing. A post-growth hydrogen treatment is demonstrated to be only moderately effective in passivating the non-radiative defects and in reducing thermal quenching. Post-growth thermal annealing at high temperature (e.g. > 500 °C) is, on the other hand, shown to be highly effective and leads to a nearly complete removal of the non-radiative defects monitored in the ODMR experiments. These results correlate very well with effects of hydrogenation and thermal annealing on the non-radiative defects monitored in the ODMR experiments. Selective optical excitation above and below the bandgap of the Si barriers has been used to determine the relative contributions of nonradiative recombination channels present in the SiGe QWs and the Si barriers.

Samples and methods.
The samples studied in this work include undoped SiGe/Si single or multiple QWs (MQWs), grown on (100) Si substrate by MBE with a Balzers UMS 630 Si-MBE system. The growth rate was 1-2 Å/sec. For comparison, structures grown both at low temperature ~ 420 °C and at high temperature ~

620 °C were studied. Undoped thin Si epilayers grown at the same temperature were also studied to separate the contribution from Si barriers. The undoped Si samples consist of a 1000 Å undoped Si buffer layer, followed by a 2000 Å undoped Si layer. The undoped SiGe/Si QWs are typically 32 Å wide with the Ge composition of about 20 %. All the structures were finally capped by a 1000 Å undoped Si layer. Post-growth hydrogen treatment was done at around 200 °C for 60 min. inside a quartz reactor with a remote dc H plasma at a pressure of 2.0 mTorr. The post-growth thermal annealing was carried out at 500 °C for 15 min. in an argon gas environment.

The photoluminescence (PL) experiments were carried out with an Oxford variable temperature cryostat, where the sample temperature could be varied between 2 K and 300 K. The 514.5 nm and 1090 nm lines of an Argon-ion laser were used for optical excitation. PL emissions were first dispersed by a Jobin-Yvon 0.5 m double grating monochromator and then collected by a cooled North-coast Ge-detector. The ODMR experiments were performed at the X-band (9.23 GHz) using a modified Bruker ER-200D ESR spectrometer, equipped with a TE_{011} microwave cavity with optical access in all directions. PL emissions from the samples, under illumination of the UV multilines (333.6 - 363.8 nm) of an Ar^+ laser, were monitored by a cooled Ge detector. The ODMR signal was obtained by detecting a synchronous change in the PL with field modulation of the magnetic field. A derivative lineshape of the ODMR is observed in this case when the magnetic field is modulated on and off the spin resonance conditions.

Experimental results and discussion.

In Figure 1 we show temperature dependent PL spectra from the SiGe/Si QWs. The detected PL emission is cause by the recombination of excitons confined within the QWs, and corresponds to the no-phonon (X^{NP}), transverse optical (X^{TO}) and transverse acoustic (X^{TA}) phonon assisted transitions. At liquid helium temperature sharp and intense excitonic lines are observed from the SiGe/Si QWs grown at both 420 °C and 620 °C, which is usually considered as an evidence of a superior quality of the material. An increase in measuring temperature, however, causes a rapid decrease of the intensity of the QW-related emissions. The PL quenching is more drastic for the samples grown at low temperatures - Fig.1a, where the SiGe emission can no longer be detected for temperatures as low as 40 K. The PL thermal behavior is better for the structure grown at 620 °C, where the QW-related emission can be detected up to 140 K - Fig. 1b. A qualitatively similar temperature dependence of the PL was observed when using 514 nm and 1090 nm excitation sources, i.e. for both above and below barrier excitation conditions. A quantitative analysis of the Arrhenius plot of the integrated PL intensity (Fig. 2 a and b) suggests that quenching occurs with the activation energy of about 3 meV. The obtained value is much smaller than the energy depth of the SiGe QW,

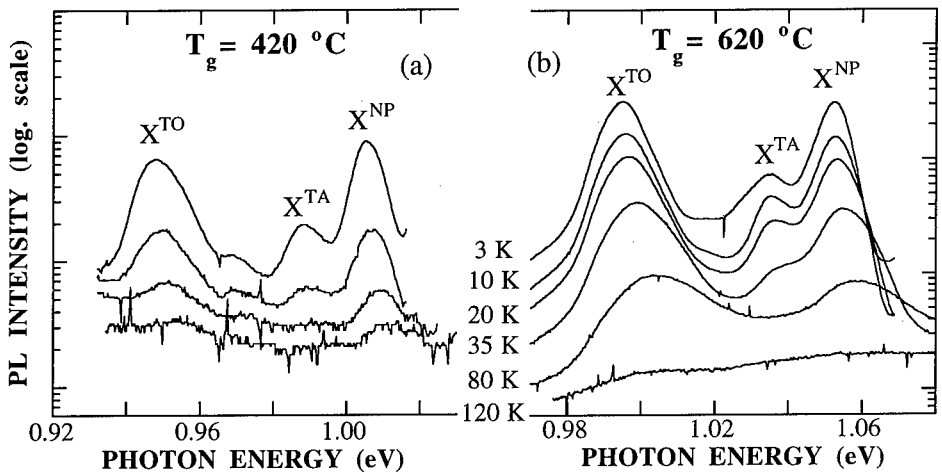


Fig.1. (a) and (b) - Temperature dependent PL spectra of Si/SiGe/Si QW structures grown at 420 °C and 650 °C, respectively.

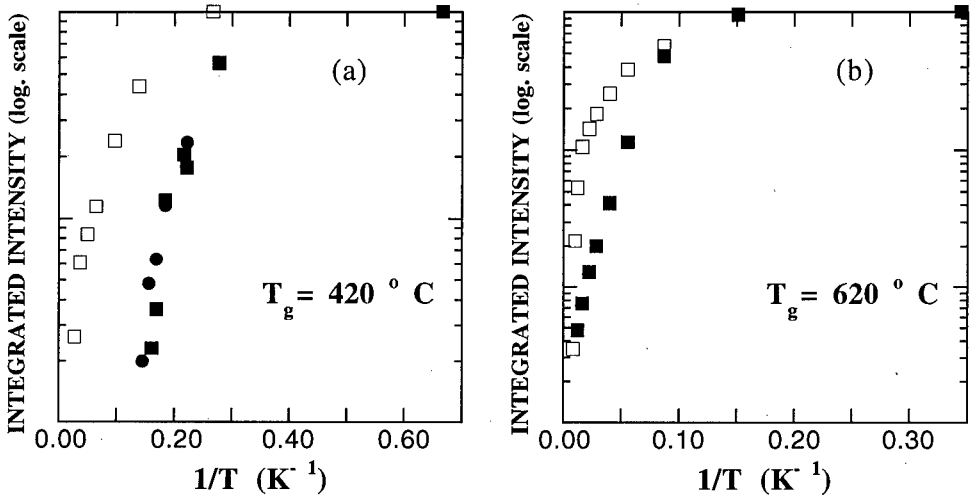


Fig. 2. Arrhenius plots of the integrated PL intensity measured from the Si/SiGe/Si QWs grown at 420 °C (a) and 620 °C (b) under 514 nm (squares) and 1060 nm (circles) excitations. Open and filled symbols correspond to the excitation power of 7 W/cm^{-2} and 0.35 W/cm^{-2}, respectively.

which is approximately 80 meV in our structures. The onset of thermal quenching can be somewhat postponed by increasing the excitation power, without changing, however, the activation energy of the PL quenching- Fig. 2 a and b.

The situation can be improved by post-growth treatments, such as hydrogenation and annealing as demonstrated in Fig. 3a for the single QW (SQW) structure, grown at 420 °C. The PL thermal quenching in the hydrogenated samples occurs at much higher temperatures than in the as-grown sample. However, a premature quenching of a low activation energy ~ 4 meV (seen by an additional shoulder in the Arrhenius plot, Fig. 3a) is still obvious. A more significant improvement of the PL thermal behavior can be achieved by thermal annealing. For the SQW structure after annealing the

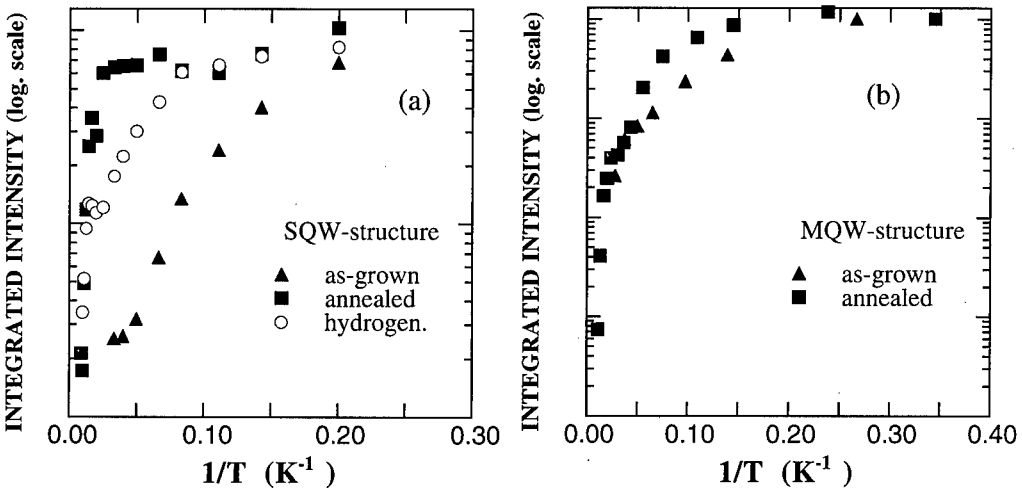


Fig. 3. Effect of post-growth treatments on the PL thermal behavior detected from the Si/SiGe/Si SQW (a) and MQW (b) structures grown at 420 ° C. The excitation wavelength is 514 nm.

integrated PL intensity from the QWs remains unaffected by increasing measuring temperature until the intrinsic activation from the QWs of a finite depth is reached - Fig. 3a. The effect of the post-growth treatments is much weaker for the MQW structure, where intrinsic activation from the QW can not be reached even after annealing - Fig. 3b.

A rapid thermal quenching of the PL from the SiGe/Si QW structures has in the past been discussed in terms of fast surface recombination [1] or the presence of strong non-radiative recombination centers [2, 3]. In the SiGe/Si heterostructures grown by the chemical vapor deposition (CVD) technique PL thermal quenching was shown [1] to occur via thermal activation of nonequilibrium carriers from SiGe QWs. The luminescence efficiency at high temperatures in such structures is controlled by a surface recombination rather than by bulk SiGe or Si properties and can be substantially improved by proper surface passivation. For MBE-grown SiGe/Si heterostructures PL quenching was suggested [2, 3] to occur due to the thermal activation of some competing nonradiative channels, located presumably in the Si barriers [2]. The chemical identity of these competing defects, as well as the formation mechanism was not previously understood.

The very low (≈ 2-4 meV) activation energy of the thermal quenching of the QW-related PL indicates [5] the prevalence of thermally activated nonradiative pathways in carrier recombination in MBE-grown Si/SiGe quantum structures. Due to this nonradiative recombination the loss of the photocreated carriers occurs well before they can be thermally activated from the SiGe QW. This competing channel can be partially saturated with increasing photoexcitation, as evident from the shift towards higher temperatures of the "knee" in the Arrhenius plot with increasing excitation power - see Fig. 2a and b. The qualitatively similar PL thermal behavior detected under above- and below barrier excitation indicates that non-radiative centers are located both in the Si barriers and the SiGe QW. These non-radiative defects are more readily introduced during the low-temperature growth conditions, since PL quenching occurs at significantly lower temperatures for the structures grown at 420 °C - Fig.1. The defects can be partially removed by post-growth treatments, among them thermal annealing is shown to be the most efficient - Fig.3a.

In order to identify the nonradiative defects responsible for the fast thermal quenching of the QW-related PL we employ the optically detected magnetic resonance (ODMR) technique. Using ODMR method we were able recently to identify some of the dominant non-radiative defects in MBE-grown Si and SiGe/Si structures [4]. One of the dominant defects, for example, was shown to be the vacancy-oxygen (V-O) complex. This complex has previously been demonstrated [6] to be the predominant defect introduced after bombardment of CZ Si by high energy particles (e.g. electrons).

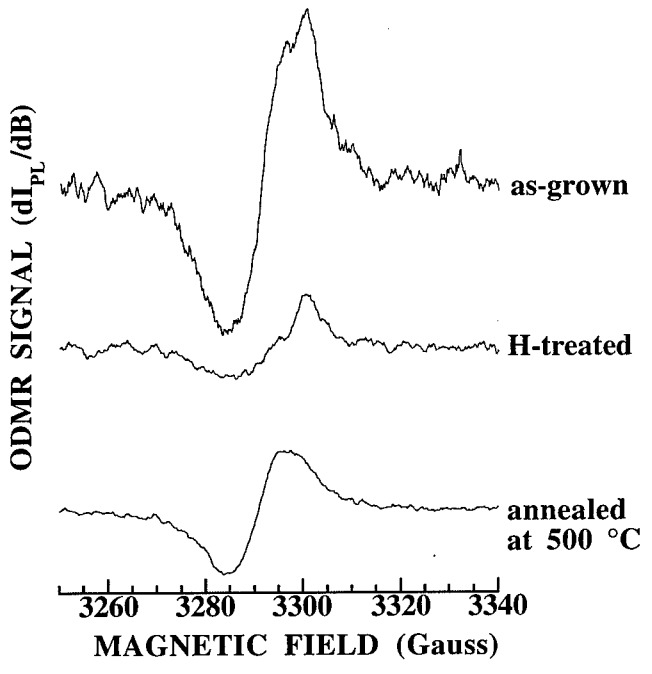


Fig. 4. ODMR specra obtained from a SiGe/Si SQW structure grown by MBE at 420 C before and after post-growth treatments.

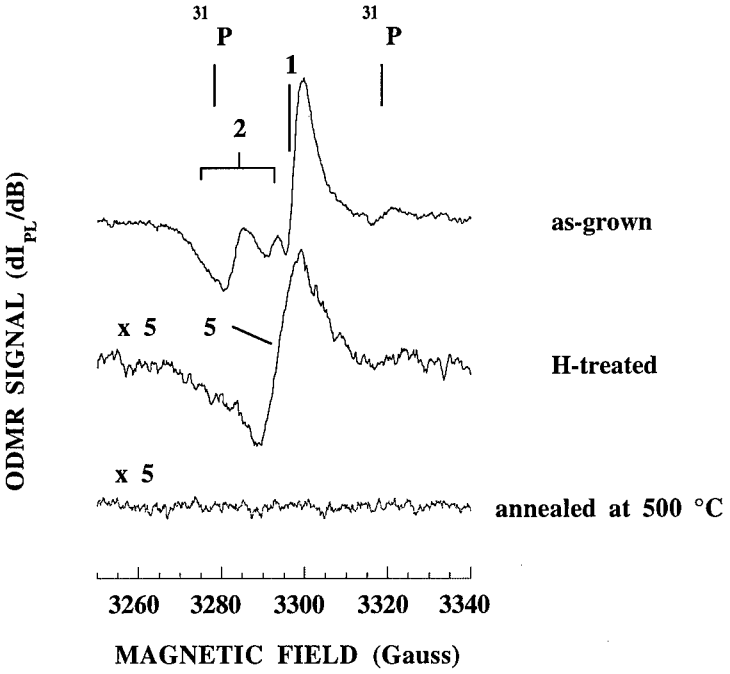


Fig.5. ODMR spectra obtained from the Si layers grown by MBE at 420 °C before and after post-growth treatments. The ODMR spectrum from the as-grown layer is composed from three contributions denoted as ^{31}P, 2 and 1, originating from three different defects.

We showed that these defects can also be introduced in the as-grown MBE Si and related structures grown at low temperatures, as a result of a low surface adatom mobility and a low oxygen desorption rate during the low temperature growth. The formation of the V-O complex can particularly be promoted by the occurrence of ion bombardment during e.g. potential-enhanced doping. This defect is known to be annealed out at a temperature higher than 500 °C, from previous studies [6] on bulk CZ Si.

To examine the role of the V-O complex and other non-radiative defects in the thermal quenching of the PL from the SiGe QWs, a corresponding study of these defects by the same post-growth treatments has been carried out. Fig.4 displays the ODMR spectra from the as-growth and post-growth treated samples. As it can be seen, the ODMR lines are not well resolved in the SiGe/Si structures, possibly due to strong overlapping of contributions from both the SiGe QWs and the Si barriers. A reduction of the ODMR signal strength can, however, be observed after the post-growth treatments. Such a reduction indicates a decrease in the concentration of the corresponding non-radiative defects, responsible for the improvement in the thermal quenching of the QW PL. To separate the contribution by the Si barriers, a parallel study of the Si epilayers grown under identical conditions but without the SiGe layer(s) is done. The resulting ODMR spectra from both as-grown and post-growth treated Si epilayers are illustrated in Fig.5. Here a narrower ODMR linewidth due to the absence of the strained SiGe enables a positive identification of each ODMR line to its corresponding defect. It is clearly shown that the V-O defect can be nearly completely removed by either hydrogenation or by thermal annealing at 500 °C, in agreement with the previously reported annealing behavior for this defect in bulk CZ Si [6]. It can also be noticed that there is still a defect remaining in the hydrogen treated sample (signal 5). The origin of this remaining defect is still unknown, argued to be (a) either already present in the as-grown material but obscured by the much stronger ODMR signals "2" and "1" from the V-O complex or (b) introduced by the hydrogen treatment. The effect of the thermal annealing on removing the non-radiative defects is proven to be strongest.

The effect of the post-growth treatments on the non-radiative defects and on the thermal quenching of the QW-related PL correlates remarkably well, establishing a direct link between these defects and the

PL thermal quenching. It is therefore believed that the non-radiative defects in the Si barriers are to a great extent responsible for the rapid thermal quenching of the PL from the SiGe QWs, via strong competing carrier capture and recombination processes in the barriers so that less non-equilibrium carriers can be trapped and recombine in the SiGe QWs. We need to point out, however, that post-growth treatments are less efficient in removing non-radiative defects from the MBE-grown SiGe material. This is evident from the preliminary PL thermal quenching observed in the annealed MQW structures - Fig. 3b, as well as from the existence of nonradiative recombination in the SiGe quantum structures, grown at 620 °C - Fig. 1b and 2b. The broader width of the ODMR lines detected from the SiGe quantum structures, unfortunately, has prevented us from a definite identification of non-radiative defects in the SiGe material.

Conclusions

In summary, we have provided experimental evidence that grown-in non-radiative defects are largely responsible for the rapid thermal quenching of luminescence from MBE-grown SiGe QWs. A post-growth hydrogen treatment is demonstrated to be only moderately effective in passivating the non-radiative defects and in the reducing thermal quenching. Post-growth thermal annealing at high temperature (e.g. > 500 °C) is, on the other hand, shown to be highly effective and leads to a nearly complete removal of the non-radiative defects in the Si barriers monitored in the ODMR experiments. By removing these non-radiative defects and thus the shunt pass for carrier recombination, a significant improvement in the thermal quenching behavior of luminescence from the SiGe/Si single QW structures has been achieved. The thermal quenching, in this case, is dominated by the intrinsic thermal activation of the holes from the QWs. For the multi QW structure, the effects of the post-growth treatments are less pronounced due to the existence of thermally stable non-radiative defects of unknown origin, located in the SiGe material. This work points out that further efforts are needed to improve the quality of the MBE-grown Si barriers and SiGe material, in order to achieve efficient light emission of the SiGe/Si quantum structures at room temperature in practical device applications.

References

1. A. St. Amour, J. C. Sturm, Y. Lacroix, and M.L.W. Thewalt. Appl. Phys. Lett. **65**, 3344 (1994).
2. S. Fukatsu and Y. Shiraki. J. Crystal Growth **150**, 1025 (1995).
3. H. M. Latuske, U. Mantz, K. Thonke, R. Sauer, F. Schäffler and H. J. Herzog in "Proc. 22nd Int. Conf. Phys. of Semiconductors" ed. D. J. Lockwood (Singapore: World Scientific), pp.1233-1236 (1995).
4. W.M. Chen, I. A. Buyanova, W.-X. Ni, G. V. Hansson, and B. Monemar. Phys. Rev. Lett. **77**, 4214 (1996).
5. J. Bourgoin and M. Lannoo. "Point defects in semiconductors II. Experimental aspects" ed.M. Cardona, P. Fulds and H.-J. Queisser (Berilin: Springer-Verlag), p. 295 (1983).
6. G. D. Watkins and J. W. Corbett. Phys. Rev. **121**, 1001 (1961).

Materials Science Forum Vols. 258-263 (1997) pp. 145-150
© 1997 Trans Tech Publications, Switzerland

GOLD-RELATED LEVELS IN RELAXED $Si_{1-x}Ge_x$ ALLOY LAYERS: A STUDY OF THE PINNING EFFECT

A. Mesli[1], P. Kringhøj[2] and A. Nylandsted Larsen[2]
[1]Laboratoire de Physique et Applications des Semiconducteurs, UPR 292, CNRS, Boîte postale 20, F-67037 Cédex, France
[2]Institute of Physics and Astronomy, University of Aarhus, DK-8000 C, Denmark

Keywords: silicon, SiGe alloys, transition metals, deep levels, DLTS.

Abstract. The question of the pinning behavior of the gold-donor and acceptor-levels is addressed in the present investigation. Gold doped n^+p and p^+n diodes of relaxed, epitaxial $Si_{1-x}Ge_x$ of $0 \leq x \leq 0.25$ are characterized with deep level transient spectroscopy (DLTS). Based on thermodynamic concepts, it is unambiguously concluded that both levels are pinned to the conduction band. A new effect related to the impact of the statistical distribution of Ge atoms into the lattice on the full width at half maximum of the DLTS peaks is clearly observed.

1.Introduction

In spite of the enormous attention addressed to point defects in silicon, some of their fundamental aspects are still far from being understood. Among them the pinning behavior of the levels introduced into the gap by specific chemical species or structural defects constitute a major issue in a variety of diffusion controlled phenomena or life time engineering. The motivation in the present work concerns the gold related levels in silicon. The question as to whether or not the donor and acceptor levels are pinned either to the conduction or to the valence band or to neither of them remains open. Concerning the acceptor level, three approaches have been followed to answer this question: i) from fits to the emission rates, it has been demonstrated that the level is pinned to the valence band [1]; ii) from photo capacitance measurements, the opposite conclusion of a pinning to the conduction band has been shown [2]; finally, iii) from hydrostatic pressure measurements it has been found that the acceptor level moves independently from the band edges [3].
Here, we propose to use $Si_{1-x}Ge_x$ alloys to handle the pinning question. Such compound allows for a much more sensitive handling of the gap than is possible for Si either by pressure variation [3] or by the sole temperature dependence of the gap [2]. Figure 1 (a) illustrating the impact of the temperature shows that an increase from 200 K to 300 K reduces the enthalpy of the gap by a few meV only. On the other hand, Fig. 1(b) shows that the Ge fraction x of the alloy will induce a gap shrinkage of 100 meV at any given temperature for x varying from 0 to 25 %, thus stressing the advantage of using this alloy to solve the question of the pinning effect.

2.Thermodynamic concepts

A point defect may be considered as a thermodynamic sub-system immersed into the surrounding semiconductor thermostat, exchanging both free carriers and phonons. This approach has the merit of assigning a clear physical meaning to the quantities describing the carrier - exchange rates between a given level and the allowed bands [4, 5]. Applying such a concept, the thermostat is defined by its gap, also defined as the increase in Gibbs free energy $\Delta G_{cv}(T)$ corresponding to an increase by one in the number of electron - hole pairs at constant temperature and pressure,

$$\Delta G_{cv}(T) = \Delta H_{cv}(T) - T\Delta S_{cv}(T) \qquad (1)$$

where $\Delta H_{cv}(T)$ and $\Delta S_{cv}(T)$ are, respectively, the enthalpy and entropy change resulting from an electron - hole pair generation. Experimentally, Varshni [6] found for $\Delta G_{cv}(T)$ the expression,

$$\Delta G_{cv}(T) = \Delta G_{cv0} - \frac{\alpha T^2}{\beta + T} \qquad (2)$$

where $\Delta G_{cv0} = \Delta H_{cv0}$ are the values of ΔG_{cv} and ΔH_{cv} at 0 K and α and β are adjustable parameters. Alex et al. [7] found $\alpha = (4.9\pm0.2)\times10^{-4}$ eV/K, $\beta = (655\pm40)$ K and $\Delta G_{cv0} = 1.169$ eV. Using the relations above and the thermodynamic definitions, $\Delta H_{cv}(T)$ may now be calculated,

$$\Delta H_{cv}(T) = \Delta H_{cv0} + \frac{\alpha\beta T^2}{(\beta + T)^2}. \qquad (3)$$

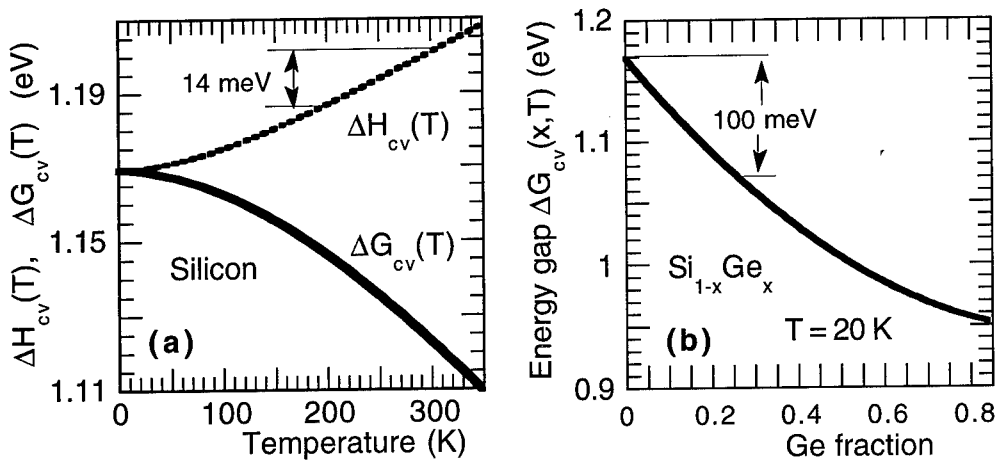


Fig.1: (a) Gibbs free energy (lower curve) and enthalpy (upper curve) of silicon as a function of temperature: (b) Composition dependence of the energy gap in $Si_{1-x}Ge_x$ alloy for $x < 0.85$ % [10].

The same reasoning applies to extract $\Delta S_{cv}(T)$ [8]. As shown in Fig. 1(a), the Gibbs free energy $\Delta G_{cv}(T)$ decreases with temperature. This decrease results from an increase of the entropy term accompanying the generation of an electron - hole pair. Applying the same concepts to the defect, the carrier-exchange rates, established at thermal equilibrium, are given by,

$$e_{n(p)} = c_{n(p)}(T) N_{c(p)}(T) exp\left[-\frac{\Delta G_{n(p)}(T)}{kT}\right], \tag{4}$$

where the different quantities have their usual meaning [8] and $\Delta G_{n(p)}(T)$ is expressed by a relation similar to Eq. (1). From the thermodynamic point of view, the pinning behavior has some consequences on the functions defined above. For instance, if the defect-related level is pinned to the conduction band, ΔG_n is constant. Therefore, according to the definition of entropy and owing to the energy conservation law [8],

$$\Delta S_n(T) = -\frac{\partial \Delta G_n}{\partial T} = -\frac{\partial\left[\Delta G_{cv}(T) - \Delta G_p(T)\right]}{\partial T} = 0, \tag{5}$$

from which it follows that the total entropy change when exciting a hole from the level to the valence band, $\Delta S_p(T)$, is equal to $\Delta S_{cv}(T)$. The treatment is thus simplified if we are probing the transition from the defect level to the conduction band, characterized by a constant ΔH_n. However, in the case of hole transition from the level to the valence band, the enthalpy $\Delta H_p(T)$ is given by,

$$\Delta H_p(T) = \Delta H_{cv}(T) - \Delta H_n. \tag{6}$$

Using Eq. (3), Eq. (6) becomes,

$$\Delta H_p(T) = \left[\Delta H_{cv0} - \Delta H_n\right] + \frac{\alpha\beta T^2}{(\beta + T)^2}, \tag{7}$$

where the term in brackets is the hole-emission enthalpy at 0 K. The Arrhenius treatment of Eq. (4) is straightforward if the function $c_{n(p)}(T)$ is known. Experimentally, the temperature range accessible is however narrow, allowing only a slight variation of the different functions. To overcome this difficulty, an alternative means of affecting the gap is to use the $Si_{1-x}Ge_x$ alloy [9,10]. Figure 1(b) shows that an increase of x from 0 to 25 % shrinks the gap by 100 meV. The solid curve represents the expression as obtained by Weber al. [34] from excitonic transitions at 20 K and corresponds to,

$$E_g(x, T = 20K) = 1.155 - 0.43x + 0.206x^2 \quad eV. \tag{8}$$

This equation is restricted to the range $0 < x < .85$ where the Si-like [100] X-conduction-band holds. Our experimentally investigated domain is entirely included in this range. The temperature at which Weber et al. [10] recorded their measurements is low enough for the approximation, $E_g(x, T = 20K) = \Delta G_{cv}(x, T = 0) = \Delta H_{cv}(x, T = 0)$ to be valid. Figure 1(a) shows, indeed, that below 20 K both ΔH_{cv} and ΔG_{cv} correspond to the values at 0 K. On the other hand, by investigating the temperature range $50 K < T < 300$ K, Braunstein et al. [9] have shown that the two variables which affect the band gap, namely T and Ge fraction x are independant. Under such conditions, the enthalpy of the electron - hole pair generation process in the alloy, expressed as a function of both x and T, is given by,

$$\Delta H_{cv}(x,T) = \Delta H_{cv}(x,0) + \frac{\alpha\beta T^2}{(\beta + T)^2}, \tag{9}$$

where the first term in the right hand side corresponds to relation (8). It follows that in the case of the level being pinned to the conduction band, ΔH_n is independent on both x and T. We get therefore,

$$\Delta H_p(x,0) = \Delta H_{cv}(x,0) - \Delta H_n. \tag{10}$$

In this relation $\Delta H_{cv}(x,0)$ represents the semi-empirical formula (8) derived by Weber et al. [10].

3.The amphoteric activity of gold

Based on deep level transient spectroscopy, we investigate below the carrier exchanges between the gold levels and the allowed bands. To distinguish between the donor (d) and acceptor (a) levels we assign a second subscript to the emission rates e_n and e_p and their corresponding thermodynamic functions. The donor level (0/+), located in the lower half of the band gap, acts as a pure hole trap whether it is analyzed in pure Si or in $Si_{1-x}Ge_x$ alloy: its interaction with the conduction band remains thus negligible even in the case where the full shrinkage of the gap of the alloy is taken up by ΔH_{nd}. As a consequence, the inequality $e_{pd} >> e_{nd}$ holds, at least up to x=30 %. The acceptor state (0/-), however, is a midgap level and thus susceptible to interact simultaneously with both the conduction and the valence band which is essential in $Si_{1-x}Ge_x$. In a reverse biased p^+n junction, under steady state conditions the fraction of the neutral charged state is given by,

$$\frac{[Au]^o}{[Au]^{tot}} = \frac{e_{na}}{e_{na} + e_{pa}}, \tag{11}$$

where e_{na} and e_{pa} are defined according to Eq. (4), and $[Au]^{tot}$ represents the total electrically active gold concentration. When carrying out DLTS in such an asymmetric diode, formed in pure silicon, $e_{na} > e_{pa}$. Thus, the fraction of gold that switches from the negatively charged state (filled state) to the neutral charge state (empty state) is close to unity. However, when analyzing the $Si_{1-x}Ge_x$ alloy, two cases must be distinguished. If the acceptor level is pinned to the valence band, the shrinkage of the gap is taken up by ΔH_{na}, which enforces the condition $e_{na} >> e_{pa}$. Thus, a significant shift to lower temperatures of the DLTS peak would be observed without any change in its amplitude. However, in the opposite case of a pinning to the conduction band, e_{pa} should no longer be neglected. A slight shift of the DLTS peak may still be observed but a drastic reduction of its amplitude is expected from Eq. (11).

4.Experimental conditions

Relaxed $Si_{1-x}Ge_x$ layers with x varying from 0 to 25 % were grown by molecular beam epitaxy (MBE) on (100) Si substrates using the compositional grading techniques as described elsewhere [11]. Both p^+n and n^+p diodes were fabricated by first growing a 4 µm thick layer doped with 2 - $5x10^{15}$ cm^{-3} of, respectively, antimony or boron; on top of this layer, a 0.5 µm thick layer doped to a very high concentration of, respectively, boron or antimony (~ 10^{19} cm^{-3}) was grown. Gold was diffused at 800°C into the mesa diodes, formed by chemical etching of photolithography-defined areas. DLTS spectra were recorded with a Semitrap spectrometer using the lock-in principle to process the capacitance transient signal [12].

5.Experimental results

5.1. The gold donor level.

Plots of conventional DLTS spectra, restricted to temperatures lower than 200 K, as obtained from gold doped n^+p are shown in Fig 2. We observe both an increase in the full width at half maximum (FWHM) of the peaks and their shift toward lower temperatures for increasing Ge composition. The first point will be discussed later. The observed shift corresponds to a decrease in the activation energy for the hole exchange rate. Qualitatively, this indicates that the level is at least partially pinned to the conduction band. Quantitatively, this shift can be described very simply considering the gold donor level as a pure trap as stated above. Therefore, the electron emission rate e_{nd} is negligible compared to the hole emission rate e_{pd}, thus allowing the factor $e_{pd} / (e_{pd} + e_{nd})$ to be approximated to unity. In consequence, for a given rate window, the DLTS peak heights do not depend upon the Ge fraction x which is confirmed in Fig. 2. Assuming the hole capture cross section to be temperature independent, and the hole effective mass as essentially determined by its value in silicon

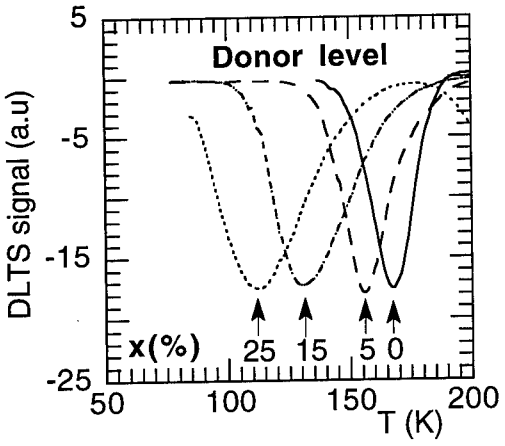


Fig. 2: DLTS spectra from Au-diffused n^+p $Si_{1-x}Ge_x$ diodes. The pulse voltage sequence was from -3V to 0V.

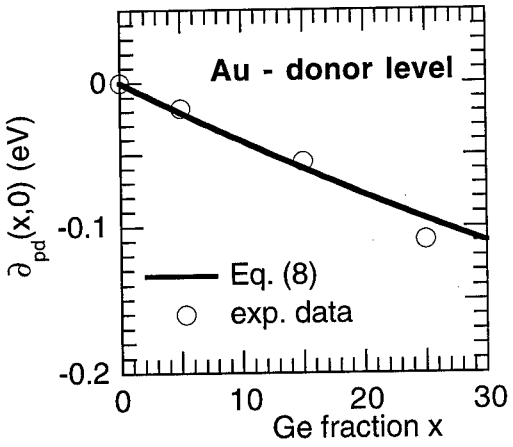


Fig. 3: The hole ionisation enthalpy at 0 K, as a function of Ge fraction x (open circles), compared to the semi-empirical Eq. (8).

[13], and provided $\Delta S_{pd}(x,T)$ is known, the Arrhenius treatment of Eq. (4) is straightforward. Using Eqs (9) and (10) we get,

$$\frac{e_o \exp\left(f(T_m)/kT_m\right)}{T_m^2 \exp\left(\Delta S_{pd}(x,T_m)/k\right)} = C\exp\left(-\Delta H_{pd}(x,0)/kT_m\right) \qquad (12)$$

where the T_m's are the temperatures at the maxima of the DLTS peaks, recorded at different experimental rate windows e_o; $f(T_m)$ is the temperature dependent function detailed in Eq. (9); the pre-exponential factor C at the right hand side of Eq. (12) is a constant including $\sigma_{pd}(x)$. Equation (12) assumes that the gold donor level is pinned to the conduction band as expected from Fig. 3. On the other hand, to satisfy the thermodynamic condition expressed through Eq. (5), $\Delta S_{pd}(x,T_m)$ is taken to be equal to $\Delta S_{cv}(0,T_m)$, the contribution of pure silicon. The extracted hole emission enthalpies at 0 K, $\Delta H_{pd}(x, 0)$, allow us to get the Ge composition dependent differential quantity,

$$\partial_{pd}(x,T=0) = \Delta H_{pd}(x,T=0) - \Delta H_{pd}(x=0,T=0), \qquad (13)$$

where $\Delta H_{pd}(x = 0, T = 0)$ is the hole emission enthalpy in pure silicon at 0 K. Equation (13) predicts that in the case of a pinning to the conduction band, the plot of $\partial_{pd}(x,T = 0)$ versus x will coincide with the gap shrinkage. Figure 3 shows indeed that the hole emission enthalpy follows entirely the gap decrease at 0 K, independently determined by Weber et al. [10] (see Eq. (8)). This result allows us to unambiguously state that the gold donor level is totally pinned to the conduction band, thus supporting the conclusions drawn by Wong et al. [14] from transport analysis carried out in pure silicon.

5.2.The gold acceptor level: Interaction with the conduction band

DLTS spectra from $Si_{1-x}Ge_x$ alloy layers on p^+n diodes are shown in Fig. 4. Here, in principle, we probe the electron transition from the acceptor level to the conduction band. Therefore, the observed shift toward lower temperatures of the peak, for increasing Ge fraction x, could correspond to an increase in the electron-emission rate. As this is a thermally activated process, the shift would be a consequence of a decrease in the electron-emission enthalpy, thus excluding any pinning of the acceptor level to the conduction band. This assertion cannot however be valid as it ignores the particularity of the acceptor level of being a midgap level, thus interacting with both allowed bands. Such a possibility, being excluded in pure silicon, because $e_{na} >> e_{pa}$, has to be reconsidered in $Si_{1-x}Ge_x$, as for increasing Ge fraction, a non negligible gap shrinkage occurs. But, if this condition is

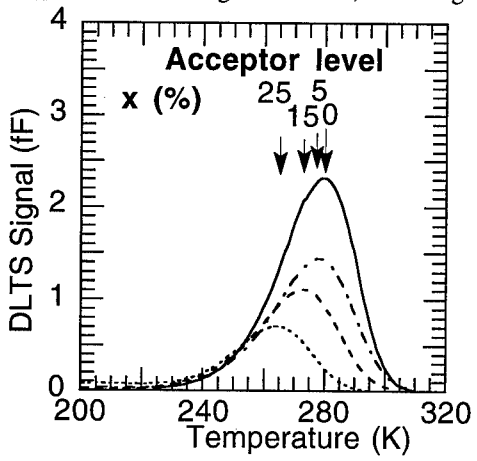


Fig.4: DLTS spectra as obtained from gold doped p^+n - $Si_{1-x}Ge_x$ diodes for different x.

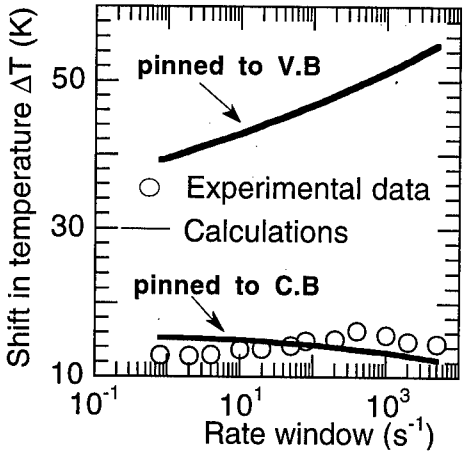


Fig. 5: The temperature shift of DLTS peak maxima $\Delta T = T_m(Si) - T_m(Si_{0.75}Ge_{0.25})$ as a function of the rate windows. The solid curves represent the two possibles cases.

necessary it is not sufficient. Indeed, the double interaction of the gold acceptor with both the valence and the conduction band needs a pinning to the conduction band. Then, the increase of e_{pa} with x implies both a shift toward lower temperatures of the peaks and a decrease of the their heights according to Eq. (11). This is clearly shown in Fig. 4. Therefore, both the shift and the reduction of the peak height result from a simultaneous interaction of the gold acceptor with both bands and a pinning to the conduction band. This statement is confirmed in Fig. 5 where we plot the temperature shift ΔT as a function of the experimental rate window. In the same figure we report theoretical simulations detailed elsewhere for both kinds of pinning [8]. The displayed results clearly favour a pinning to the conduction band. The consequence is a tremendous increase in the corresponding DLTS signal in p-type alloys, so far considered as a small relaxation in pure silicon [8].

6.The impact of a Ge fluctuation

The interesting feature that appears in Fig. 2 is related to the degradation of the full width at half maximum (FWHM) of the peaks with increasing Ge content. However, the width of the DLTS signal of the acceptor related peak extracted from n-type material remains unchanged (Fig. 4). Fig. 6 reports the behavior of the FWHM in all possible configurations, including the hole transition from the acceptor level, reported elswhere [8]. The first observation to be made is that the degradation of the FWHM concerns only the hole transitions. The electron transition from the acceptor level (solid squares in Fig. 6), does not exhibit any change in the FWHM. We believe that this effect stems from a local Ge fluctuation or disorder in the $Si_{1-x}Ge_x$ alloys. The occupation of the substitutional lattice sites by Si or Ge is assumed to be purely statistical [10]. The main effect of the resulting distribution is a variation in band gap energy arround an averaged value, produced by local fluctuations in the alloy composition x. Taking into account the experimentally [15] and theoretically [16] established fact that the variation of the gap in $Si_{1-x}Ge_x$ alloys is entirely taken up by the valence band, the mechanism underlying the hole-to-valence band transition from a level pinned to the conduction band is schematically shown in Fig. 7. It is clear that the fluctuation of the valence band and the pinning effect has a direct impact on the FWHM of the transition that is probed. The consequence of this

fluctuation is that for a level pinned to the conduction band, e_n is given by Eq. (4) while e_p is distributed among a range of values. It is easy to see from Fig. 7 that transitions to the conduction band should not exhibit any degradation of the FWHM.

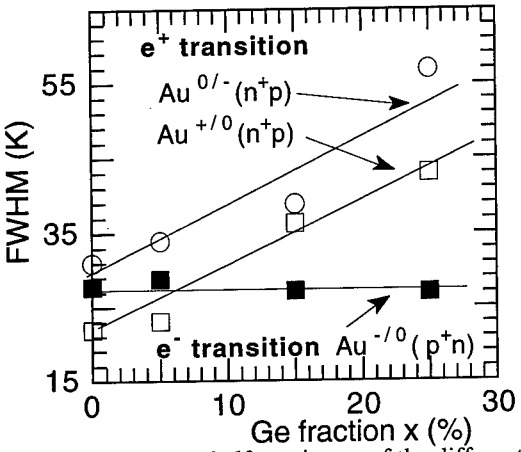


Fig.6: Full width at half maximum of the different transitions corresponding to gold levels.

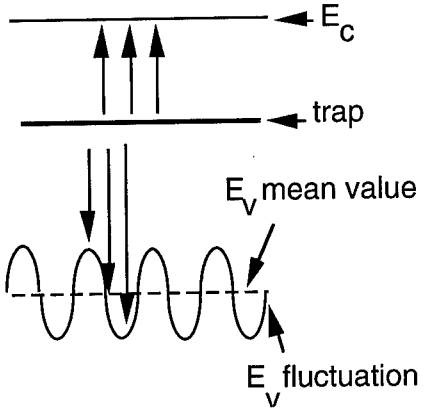


Fig.7: A schematic representation of the consequence of the pinning effect and Ge fluctuation on the transitions.

6.Conclusion

The improvement of the epitaxial growth of relaxed $Si_{1-x}Ge_x$, opens up a new approach in the study of the pinning behavior of the energy levels in the band gap. The large shrinkage of the bandgap of the alloy for increasing Ge fraction, has allowed us to demonstrate that both gold donor and acceptor levels are pinned to the conduction band. It has been stressed that the acceptor level has to be treated with great care as it possesses the important property of being a recombination-generation center.
A new and interesting phenomenon has been observed related to the FWHM of the DLTS peaks. The FWHM was found to increase with increasing Ge content when probing hole transition to the valence band but not when probing electron transition to the conduction band. This is suggested to be an effect of the statistical nature of the occupation of the substitutional lattice site by Si and Ge together with the previously established facts that the variation of the energy gap in the $Si_{1-x}Ge_x$ with varying x is entirely taken up by the valence band.

Acknowledgements

This work was supported by the Danish National Research Foundation through the Aarhus Center of Advanced Physics (ACAP) and the Danish Natural Scientific Research Council. Thanks are due to J. Lundsgaard Hansen for the MBE growths and to F. Nikolajsen for help with the experiments. We are thankful to Dr. J. Weber for useful suggestions and P. Montgomery for his valuable comments.

References

1. S.D. Brotherton and J. Bicknell , J. Appl. Phys., **49**, 667 (1978)
2. O. Engstrom and H.G. Grimmeiss, Appl. Phys. Lett., **25**, 413 (1974)
3. G.A. Samara and C.E. Barnes, Phys. Rev., **B35**, 7575 (1987)
4. C.D. Thurmond, J. Electrochem. Soc., **122**, 1133 (1975)
5. O. Engstrom and A. Alm, Solid-State Electr., **21**, 1571 (1978)
6. Y.P. Varshni, Physica, **34**, 149 (1967)
7. V. Alex, S. Finkbeiner, and J. Weber, J. Appl. Phys., **79**, 6943 (1996)
8. A. Mesli, P. Kringhøj, and A. Nylandsted Larsen, to be published
9. R. Braunstein, A.R. Moore, and F. Herman, Phys. Rev., **109**, 695 (1958)
10. J. Weber and M.I. Alonso, Phys. Rev., **B40**, 5683 (1989)
11. A. Nylandsted Larsen, R.S. Jensen, S. Shiryaev, P.R. Østergaard, J.Hartung, G. Davies, F. Jensen, and J. Wulff Petersen, Phys. Scr., **54**, 208 (1994)
12. F. Nikolajsen, P. Kringhøj, and A. Nylandsted Larsen, Appl. Phys. Lett., **69**, 1743 (1996)
13. M. Rieger and P. Vogel, Phys. Rev., **B48**, 14276 (1993)
14. D.C. Wong and C.M. Penchina, Phys. Rev., **B12**, 5840 (1975)
15. J. Weber and M.I. Alonso, in Defect Control in Semiconductors, ed. K. Sumino, Elsevier Science Publishers B.V. (North- Holland), 1990, p. 1453
16. C.G. Van de Walle, and R.M. Martin, Phys. Rev., **B34**, 5621 (1986)

Materials Science Forum Vols. 258-263 (1997) pp. 151-158
© 1997 Trans Tech Publications, Switzerland

DISLOCATION-RELATED ELECTRONIC STATES IN STRAIN-RELAXED $Si_{1-x}Ge_x$/Si EPITAXIAL LAYERS GROWN AT LOW TEMPERATURE

P.M. Mooney and Kai Shum[1]
IBM T.J. Watson Research Center
PO Box 218 Yorktown Heights, NY 10598 USA
[1]Electrical Engineering Department, City College of CUNY,
New York, NY 10031 USA

Keywords: SiGe, dislocations, D-lines, interdiffusion, strain, hole traps, photoluminescence, DLTS

Abstract. Strain-relaxed step-graded $Si_{1-x}Ge_x$/Si structures having low densities of threading dislocations are used as buffer layers for modulation-doped field-effect transistors (FETs). Low temperature photoluminescence (PL) and deep level transient spectroscopy (DLTS) have been used to study the electronic states associated with threading dislocations in $Si_{1-x}Ge_x$ layers grown at 550°C. We show that the energy shift of the D1 photoluminescence line upon annealing is due to strain-driven interdiffusion of Ge and Si at the dislocation core and results in an anti-crossing of the D1 and D2 lines. Two dislocation-related hole traps were observed by DLTS in concentrations which correlate with the oxygen concentration in the film, suggesting that they may be defect complexes involving oxygen at dislocations. Models for the origin of the D lines and the nature of electronic states of dislocations are reviewed in light of these and other recent experimental and theoretical results.

Introduction.

Strain-relaxed epitaxial $Si_{1-x}Ge_x$ layers grown on Si(001) substrates are needed as substrates for field-effect transistors having a strained Si or strained $Si_{1-x}Ge_x$ layer as the electron or hole channel [1,2] or for other applications such as the integration of III-V optical devices on Si [3]. Relaxed $Si_{1-x}Ge_x$ layers having low threading dislocation densities ($\leq 10^6$ cm^{-2}) have been reported by a number of groups [3-5]. The low defect densities were achieved by increasing the Ge mole fraction of the alloy gradually, either continuously or in steps, in order that dislocation nucleation occurs at low mismatch strain [6]. These defect densities are sufficiently low that carrier transport at room temperature, or even at low temperature, is not affected [7]; however, for device and circuit reliability and for other potential applications it is important to understand the defect-related electronic states and their effects on the properties of relaxed $Si_{1-x}Ge_x$ layers. Because of the low threading dislocation densities, step-graded buffer layer structures are ideal samples for studies of dislocation-related electronic states by a variety of experimental methods.

60°misfit dislocations in plastically deformed Si have been studied for many years and their structure is well-known [8,9]. However, although there is also a large body of literature on their electronic properties, neither the microscopic origins of the four photoluminescence lines associated with dislocations nor many of the various deep levels observed by DLTS measurements have been determined conclusively. Both the photoluminescence and DLTS spectra depend strongly on the method of sample preparation and thermal history of the sample [6]. Similarly, the photoluminescence and DLTS spectra of $Si_{1-x}Ge_x$ layers grown by different methods at different temperatures vary significantly [6].

Identification of the electronic states associated with dislocations has been hampered by the difficulty in distinguishing between the intrinsic states of dislocations (e.g. reconstruction defects, kinks, or jogs) and states of impurity atoms or defect complexes at the dislocation core or in the strain field of the dislocation. Electron spin resonance experiments in plastically deformed float zone Si prepared at very low temperature yielded a variety of spectra, which were categorized by their thermal stability [10].

Spectra annealing out at T≤500 °C were identified as isolated vacancy complexes, the same defects as had been observed in electron irradiated silicon. Spectra annealing out at temperatures between 500 °C and 800 °C were modeled as vacancy complexes at the dislocation core. States remaining after annealing at T≤800°C are believed to be states intrinsic to the dislocations, since dislocations are also present after high temperature annealing. However, it is difficult to rule out the presence of impurities such as oxygen and carbon, which are always present in Si in detectable concentrations, or transition metals, which are known to be gettered at dislocations.

Here we describe the results of low temperature PL and DLTS measurements on relaxed $Si_{1-x}Ge_x$ layers grown at 550 °C. Detailed annealing studies show that there is a large energy shift of the D1 photoluminescence line which results in an anti-crossing of the D1 and D2 lines. The energy shift of D1 has the same thermal activation energy as strain-enhanced out-diffusion of Ge from strained $Si_{1-x}Ge_x$ quantum wells. This behavior demonstrates that D1 is not a phonon replica of D2 and underscores the vital role of the local strain in determining the energies of the electronic states of dislocations. The intensities of the two dominant hole traps observed by DLTS in as-grown $Si_{0.7}Ge_{0.3}$ layers correlate with the oxygen concentration in the film and therefore may originate from point defect complexes involving oxygen at the dislocation. Their annealing behavior indicates that the origin of the DLTS peaks is different from that of the D-lines.

Sample Preparation.

The relaxed $Si_{1-x}Ge_x$/Si(001) structures prepared for these experiments were grown by ultra-high vacuum chemical deposition (UHV/CVD) [11]. They consist of a layer about 0.5-1 μm thick in which the Ge mole fraction x was increased in steps followed by a 0.5-3.5 μm-thick uniform composition $Si_{1-x}Ge_x$ layer. Fig. 1 is a cross-sectional transmission electron micrograph of a typical step-graded structure showing the misfit dislocations in the step-graded layer and also at the top of the Si substrate and the bottom of the uniform composition $Si_{1-x}Ge_x$ layer. A threading arm can be seen going up toward the top surface of the $Si_{1-x}Ge_x$ layer. Some structures were un-doped. Others were doped during epitaxial growth to form a one-sided abrupt p-n^+ junction about 500 Å from the top surface of the uniform composition layer. Pieces of the undoped structures were each annealed for 10 minutes in dry N_2 ambient at various

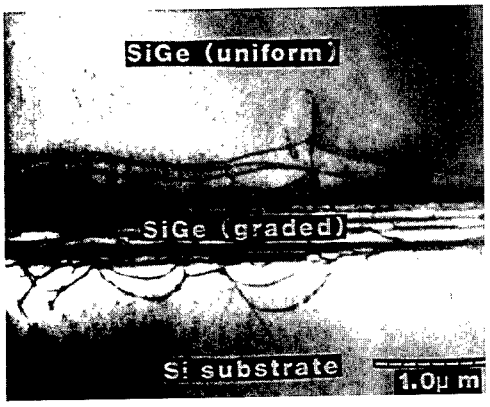


Fig.1. Cross-sectional transmission electron micrograph of a step-graded $Si_{1-x}Ge_x$ buffer layer. The dark lines are 60° misfit dislocations.

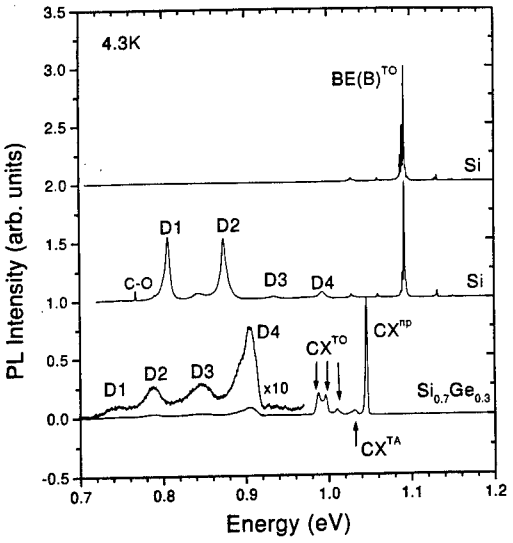


Fig. 2. Normalized PL spectra of Si and strain-relaxed $Si_{0.7}Ge_{0.3}$.

temperatures up to 800 °C. As described in detail elsewhere [12], mesa diodes were fabricated from the doped structures, either as-grown or after annealing at 700 °C, for DLTS measurements. Threading dislocations in the upper part of the relaxed $Si_{1-x}Ge_x$ layer were probed in both experiments. In order to compare our results with previous studies in plastically deformed Si, dislocations were introduced into the upper part of a Czochralski (CZ) Si wafer by growing an epitaxial $Si_{0.85}Ge_{0.15}$ layer, which was subsequently removed by etching. The dislocation density was varied by increasing the thickness (and thus the degree of strain relaxation) of the $Si_{0.85}Ge_{0.15}$ layer. In this way both the mechanism of dislocation formation and the thermal history of the Si samples are the same as our $Si_{1-x}Ge_x$ samples.

Photoluminescence Results.

Figure 2 shows low temperature PL spectra for three different samples. The top spectrum is from a zone refined Si wafer. The only luminescence observed is near-band-edge recombination, in this case the phonon-assisted recombination of excitons bound to boron acceptors. The middle spectrum is from a CZ silicon wafer in which dislocations were introduced as described above. This spectrum is also dominated by the near-band-edge emission. However, the four D-lines known to be associated with dislocations are also present [13]. The four D-lines are broader in samples having higher dislocation densities. All four are still present after a 10 min. anneal at 800 °C, and the energy shift of all of them upon annealing is negligible [14].

The bottom spectrum in Fig. 2 was taken from an un-doped relaxed $Si_{0.7}Ge_{0.3}$ layer. Note that the near-band-edge emission and the D-lines are shifted to lower energy, since the bandgap of the $Si_{1-x}Ge_x$ alloys is smaller than that of Si. In this spectrum the dominant feature of the near-band-edge luminescence is the no-phonon line due to recombination of excitons confined at potential wells caused by fluctuations in alloy composition [15]. The transverse acoustic and transverse optical phonon replicas of this line are also clearly observed. As the excitation power density is increased, a somewhat broader line at slightly lower energy emerges and becomes dominant. This broader line was originally attributed to the recombination of excitons bound to phosphorous [15]. However, recent detailed measurements and analysis, including a comparison of the measurement temperature dependence of this line with that due to excitons bound to boron in an intentionally B-doped layer, have clearly shown that the origin of this line is the recombination of biexcitons [16]. Free exciton recombination has also been observed at very high excitation power density [15].

The four dislocation-related D-lines are also clearly observed in the low temperature PL spectrum of the relaxed $Si_{0.70}Ge_{0.30}$ layer in Fig. 2; however, they are broader than in the Si wafer and their relative intensities are also different. We found that the relative intensities of the D-lines vary from sample to sample as does their intensity compared to the near-band-edge luminescence. The latter is detected only in samples having uniform composition layers greater than about 1.5 μm, probably because of carrier diffusion into the step-graded region in structures with thinner uniform composition layers. Fig. 3 shows normalized PL spectra for two other $Si_{1-x}Ge_x$ layers as-grown (550 °C) and after 10 minute anneals at the temperature indicated. The thinner (1.0 μm) $Si_{0.75}Ge_{0.25}$ layer shows only the four D-lines, whereas the thicker (3.5 μm) $Si_{0.70}Ge_{0.30}$ layer shows the near-band-edge luminescence as well. Both the near-band-edge luminescence and the four D-lines were also observed in a 3.5 μm-thick $Si_{0.83}Ge_{0.17}$ sample.

The large energy shift of the D1 and D2 lines is very interesting. In contrast, both the D3 and D4 lines as well as the confined exciton line have a negligible energy shift upon annealing. In the $Si_{0.75}Ge_{0.25}$ layer, both D1 and D2 shift continuously with annealing. Their energy separation varies with the annealing temperature and has a minimum value of 41 meV in the sample annealed at 675 °C [14]. The D1 line is initially less intense than D2; however, the intensities of the two lines are nearly equal in the sample annealed at 675 °C, i.e. when they are closest together in energy, and after annealing at higher temperatures the D2 line is less intense than D1. In fact the D2 line is difficult to detect in samples annealed at $T \geq 725$ °C. The initially decreasing and subsequently increasing energy difference between the two states and the transfer of intensity from D2 to D1 are typical features of an anti-crossing of two energy levels. In contrast, the D1 line in the $Si_{0.70}Ge_{0.30}$ layer is no longer detectable after annealing at

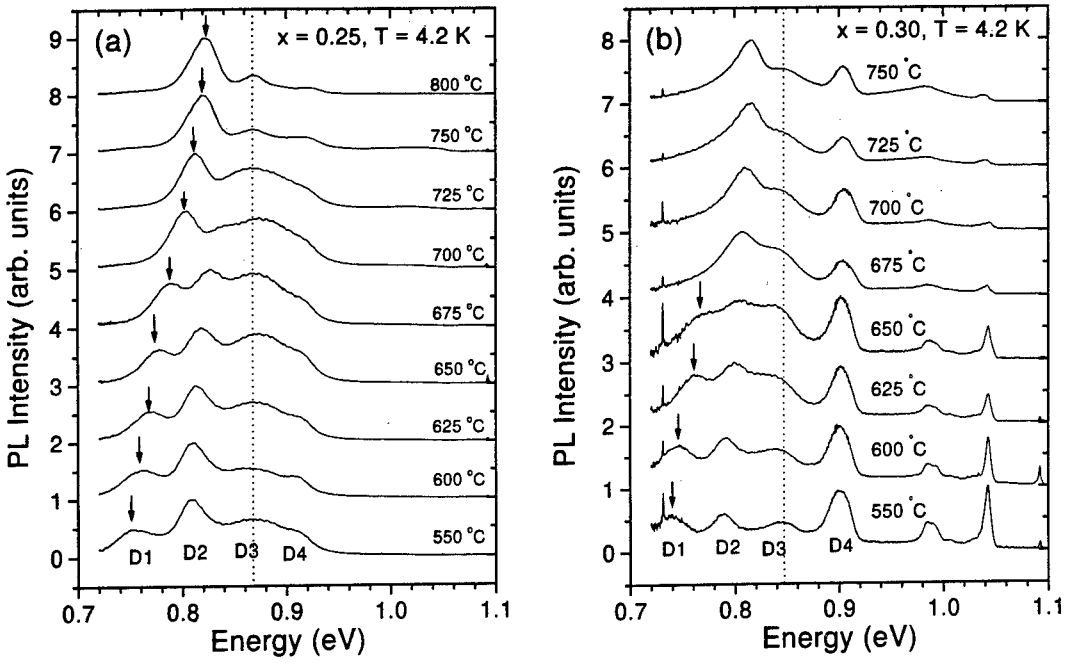


Fig. 3. Low temperature PL spectra for two as-grown and annealed $Si_{1-x}Ge_x$ buffer layers.

650 °C. Here the D1 line disappears before the two levels interact and thus the anti-crossing of D1 and D2 is not observed. Nevertheless, the energy shift of D1 is clearly observable after annealing at low temperature.

Figure 4 shows the energy shift of the D1 line in three layers of different alloy composition. The inset shows the confined exciton energy in the $Si_{0.70}Ge_{0.30}$ layer for comparison. These data indicate the expected variation of the energy position of the D1 line in the as-grown samples [17]. However, after annealing at T≥750 °C, the energy of the D1 line in both $Si_{0.83}Ge_{0.17}$ and $Si_{0.75}Ge_{0.25}$ layers is independent of the alloy composition. Note that the energy of the confined exciton line is essentially constant compared to the relatively large energy shift of the D1 line, indicating that the average strain in the layer, and hence the bandgap, is essentially unchanged after annealing.

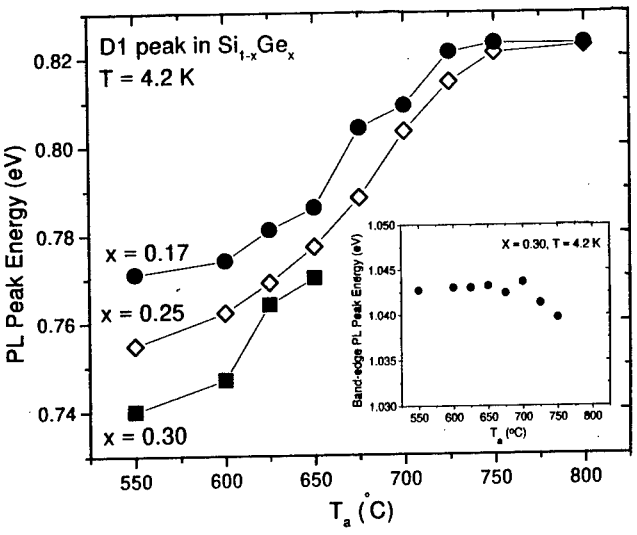


Fig. 4. Energy shift of the D1 line in three $Si_{1-x}Ge_x$ layers. The inset shows the energy shift of the confined exciton in the $Si_{0.7}Ge_{0.3}$ layer.

The continuous energy shifts of D1 and D2 suggest that changes in the local band structure occur upon annealing. Shifts in the energies of D1 and D2, previously observed in isothermal annealing experiments, have been modeled in terms of strain-driven interdiffusion of Si and Ge at the dislocation core [18]. We have shown that this model is consistent with the energy shift of D1 [14,19]. Assuming that the energy shift of the D1 line is the result of strain relaxation at the dislocation by interdiffusion of Si and Ge, the energy shift is then proportional to the change in alloy composition. The energy shift of the D1 line, E=E(T_a)-E(550 °C), can be expressed in terms of the thermal activation energy for the interdiffusion of SiGe using the expression $E(kT_a)^{3/2}=B(x)\exp(-2E_a/3kT_a)$, where B(x) is defined as $E_g(x)3(\pi/2)^{1/3}(AD_0t_0)^{2/3}$ [14,19]. The constant A was calculated using the values of D_0 and E_a determined from measurements of the out-diffusion of Ge from SiGe quantum wells [20]. At these annealing temperatures, interdiffusion is a local effect; the atoms move distances of only a few nanometers.

Figure 5 shows Arrhenius plots for the D1 and D2 lines in the $Si_{0.75}Ge_{0.25}$ and $Si_{0.70}Ge_{0.30}$ samples. The thermal activation energy for D1 in the $Si_{0.70}Ge_{0.30}$ layer is 2.39 eV, in excellent agreement with that found for strain-driven out-diffusion of Ge from $Si_{1-x}Ge_x$ quantum wells [18,20]. However, this plot shows clearly that the energy shift of D2 is much smaller than that of D1 and that no interaction between the two levels occurs in this sample. The activation energy for the energy shift of D1 at low annealing temperature is 2.44 eV in the $Si_{0.75}Ge_{0.25}$ layer. The energy shift of D2 is much larger in this layer and results from the interaction with D1 at annealing temperatures ≥675 °C. A similar value of the thermal activation energy, 2.52 eV, was found from the energy shift of D1 in the $Si_{0.83}Ge_{0.17}$ layer, and the anti-crossing of the D1 and D2 lines was observed as well. Both the D1 and D2 levels were clearly detected in this sample, even after the anneal at 800 °C. Note that temperature at which D1 (or D2 which becomes D1-like as a result of the anti-crossing) anneals out decreases with increasing Ge mole fraction in these relaxed $S_{1-x}Ge_x$ layers.

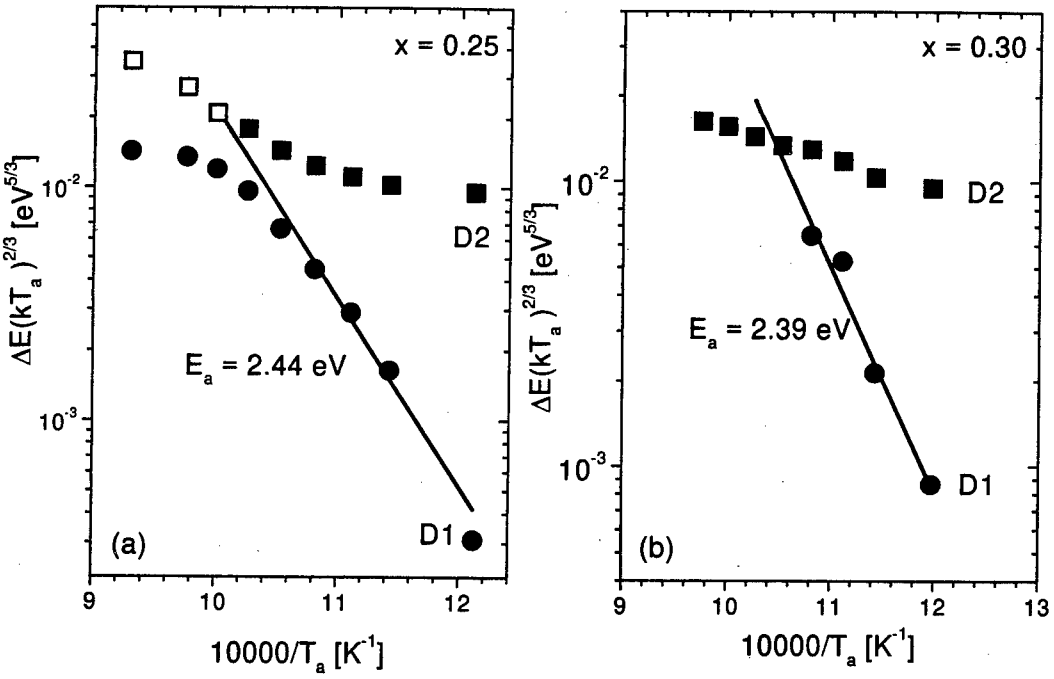


Fig. 5. Activation energy plots for the $Si_{0.75}Ge_{0.25}$ and $Si_{0.70}Ge_{0.30}$ layers. Open symbols have larger unertainty than solid symbols.

DLTS Results.

DLTS measurements were performed on step-graded buffer layer structures having n^+-p junctions near the upper surface of the uniform layer [12]. Fig. 6 shows DLTS spectra for several different B-doped $Si_{1-x}Ge_x$ layers. No dislocations were seen in the $Si_{0.98}Ge_{0.02}$ layer by transmission electron microscopy and no DLTS peaks were observed either. The most intense DLTS peaks observed in the $Si_{1-x}Ge_x$ layers having higher Ge mole fraction are from two hole traps. The amplitude of both DLTS peaks was found to increase logarithmically with the filling pulse duration, indicating that these traps are associated with extended defects, not isolated point defects. The capture rates were found to be independent of the measurement temperature indicating that there is no significant lattice relaxation when the charge state of the trap changes. Thus the thermal emission activation energy is essentially equal to the change in enthalpy required to thermally ionize the filled trap. Thermal emission activation energies of 0.06 and 0.14 eV were found for the two traps when x≈0.3; the activation energies were larger at lower x.

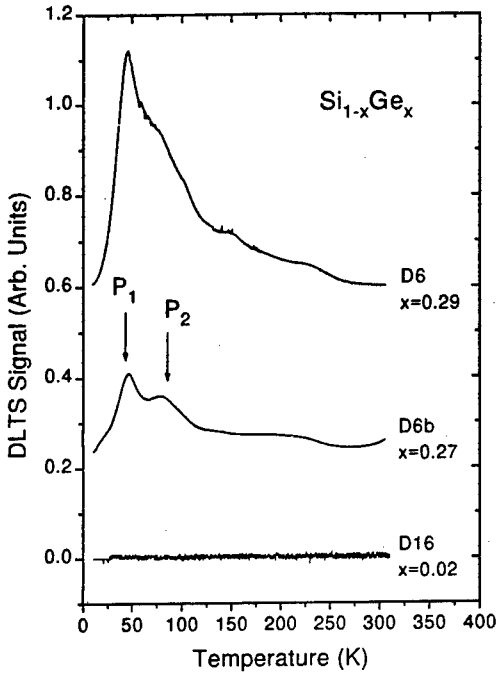


Fig. 6. DLTS spectra for B-doped relaxed $Si_{1-x}Ge_x$ buffer layers. The rate window was 49.1 s^{-1}. The reverse bias voltage was -2.0V and the filling pulse was 0V for 1.0 ms.

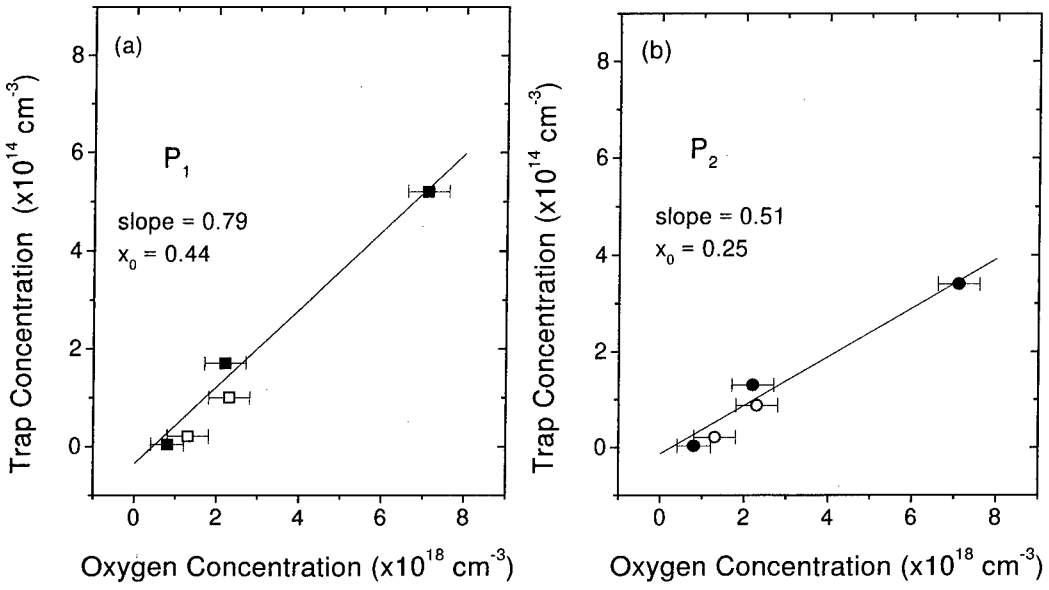


Fig. 7. Trap concentration vs.oxygen concentration for the teo hole traps. Solid and open symbols indicate layers grown at 560 and 500°C respectively. The lines are fits to the solid data points.

The amplitudes of both traps were reduced by more than a factor of two in devices fabricated on pieces of the same wafer which had been annealed at 700 °C for 10 minutes. Thermal stability arguments based on the EPR results in Si showing that point defect complexes at dislocations anneal out in the temperature range from about 550-850 °C, suggest that these hole traps originate at point defect complexes trapped at the dislocations. The same hole traps were observed as minority carrier traps in a P-doped layer, indicating that neither boron or phosphorous is a constituent of these defect complexes. Fig. 7 shows plots of the DLTS peak intensity as a function of the oxygen concentration in buffer layer structures having comparable threading dislocation densities, 2-4x10^7 cm^{-2}. These data suggest that oxygen may be a constituent of the point defect complexes [12].

An obvious question to ask is whether these two hole traps have the same origin as any of the D-lines. The available data suggest that they do not. The energies of the D1 and D2 transitions are close to what they would need to be if they involved the recombination of electrons with holes bound to the two trap states. However, the two DLTS peaks show no energy shift upon annealing and their annealing temperature is not the same as that of either D1 or D2 in $Si_{0.7}Ge_{0.3}$. In addition the variation of the D1 and D2 energies with alloy composition does not appear to be consistent with that of the hole traps.

Discussion.

The D-lines have been studied for many years and their microscopic origin is controversial. They fall into two groups, with D1 and D2 having similar characteristics which differ from those of D3 and D4 [21,22]. Two different models have been proposed for the D-lines. In one proposal, the origin of the luminescence is not the dislocations itself, but occurs only when the dislocation is decorated with transition metal impurities [23,24]. A curious aspect of this model is that the energies of the D-lines apparently do not depend on the impurity species [23]. Cathodoluminescence measurements (~10μm resolution) indicate that D3 and D4 correlate more closely with the dislocation core than do D1 and D2 [23]. Thus it has been suggested that D1 and D2 arise from impurities or defects trapped in the strain field of the dislocation rather then the dislocation itself. Other doping experiments rule out transition metal precipitates at dislocations as the origin of the D-lines, but to not rule out the presence of individual transition metal atoms at the dislocation core [25]. It was also found that the intensities and polarization of the D-lines depend strongly on the direction of detection and from symmetry arguments it was proposed that the D2 transition (and it's phonon replica D1) originate at the stacking fault ribbon separating the 30° and 90° partial dislocations of the dissociated 60° misfit dislocations [25].

Our PL data clearly show that the D1 and D2 lines have very different annealing characteristics. The interaction (anti-crossing) upon annealing indicates that D1 has a much larger strain shift than D2. Thus D1 cannot be a phonon replica of D2. Consistent with calculations showing changes in the electronic structure at stacking faults in Si [26], spatially resolved (2 Å resolution) electron energy loss spectroscopy (EELS) measurements at the stacking fault ribbon of dislocations in $Si_{1-x}Ge_x$ show changes in the density of states lying above the bottom of the conduction band and no changes in the conduction band edge compared to the bulk material [27]. These results cast doubt on the proposal that D1 and D2 originate at the stacking fault.

Recent theoretical work demonstrates the importance of intrinsic dislocation states. Recent calculations of the electronic structure of a perfectly reconstructed straight 90°edge dislocation in Si show that the local strain pushes states from the valence band about 200 meV into the gap, creating a quantum well for holes at the dislocation [28]. Calculations of kinks at the 30° [29] and 90° [30] partial dislocations also show energy levels pushed into the bandgap. EELS measurements in the regions of the partial dislocation cores show electronic levels in the bandgap [27]. Further work is necessary to understand the origin of the states observed in these experiments and the role of impurities at the dislocation core.

Conclusions.

Relaxed $Si_{1-x}Ge_x$ buffer layers having relatively low densities of threading dislocations have been studied using PL and DLTS. Two hole traps, suggested to originate at point defect complexes involving oxygen,

were observed and an anti-crossing of the D1 and D2 luminescence lines was found to occur due to strain relaxation by local interdiffusion of Si and Ge upon annealing. The latter results appear to conflict with the proposal that these lines originate at the stacking fault ribbon of the dissociated 60° dislocations. Clearly further work is needed to understand the microscopic origins of dislocation-related electronic states observed in Si and $Si_{1-x}Ge_x$.

Acknowledgments.
The buffer layer structures were grown by J.O. Chu and the p-n junction diodes were fabricated by C.P. D'Emic, who did the annealing. The transmission electron micrograph (Fig. 1) was provided by F.K. LeGoues. This work was partially supported by AFOSR grant No. F49620-93-1-0619.

References.

1. K. Ismail, S.Rishton, J.O. Chu, K. Chan, S.F. Nelson and B.S. Meyerson, IEEE Electron Device Lett. **EDL-14,** 473 (1994).
2. M. Arafa, K. Ismail, J.O. Chu, B.S. Meyerson and I. Adesida, IEEE Electron Devcie Lett. **EDL-17**, 1, (1996).
3. E.A. Fitzgerald, Y.H. Xie, D. Monroe, P.J. Silverman, J.M. Kuo, A. R. Kortan, F.A. Theil, and B.E. Weir, J. Vac. Sci. Technol., **B10**, 1807 (1992).
4. B.S. Meyerson, K.J. Uram, and F.K. LeGoues, Appl. Phys. Lett. **53**, 2555 (1988); F.K. Legoues, B.S. Meyerson, and J.F.Morar, Phys. Rev. Lett. **66**, 2903 (1991).
5. D. Dutartre, P. Warren, F. Provenier, F. Chollet and A. Pério, J. Vac. Sci. Technol. **A12**, 1009 (1994).
6. P.M. Mooney, Materials Science and Engineering **R17**, 105 (1996) and references therein.
7. K. Ismail, Solid State Phen. **47-48**, 409 (1996).
8. Helmut Alexander and Helmar Teichler, in *Electronic Structure and Properties of Semiconductors*, Ed. W. Schröter(VCH, Weinheim, 1991) pp. 249-319.
9. Koji Sumino, Handbook on Semiconductors, Vol. 3, Ed. T.S. Moss, (Elsevier Science, 1994) p.73.
10. C. Kisielowski-Kemmerich, Phys. Stat. Sol. (b) **161**, 11 (1990).
11. B.S. Meyerson, Appl. Phys. Lett. **48**, 797 (1986).
12. P.M. Mooney, et al. to appear in J. Appl. Phys., July 15, 1997.
13. E. Lightowlers and V. Higgs, Phys. Stat. Sol. (a) **138**, 665 (1993).
14. Kai Shum, P.M. Mooney, and J.O. Chu, Mat. Res. Soc. Symp. Proc. **442**, 325 (1997).
15. L.P. Tilly, P.M. Mooney, J.O. Chu and F.K. LeGoues, Appl. Phys. Lett. **67**, 2488 (1995).
16. Kai Shum, P.M. Mooney, L.P. Tilly and J.O. Chu, Phys. Rev. B **55**, 13058 (1997).
17. J. Weber and M.I. Alonso, in Defect Control of Semiconductors, Ed. K. Sumino (Elsevier Science Publishers, New York, 1990) p. 1453.
18. K. Tanaka, M. Suezawa and I. Yonenaga, J. Appl. Phys. **80**, 6991 (1996).
19. Kai Shum, P.M. Mooney and J.O. Chu, to appear in Appl. Phys. Lett., August 25, 1997.
20. P. Baucaud, et al., J. Appl. Phys. **80**, 1414 (1996).
21. R. Sauer, et al., Appl. Phys. **A36**, 1 (1985).
22. S. Fukatsu, et al., Appl. Phys. Lett. **68**, 1889 (1996).
23. V. Higgs, E.C. Lightowlers, C.E. Norman and P. Knightley, Mat. Sci. Forum **83-87**, 1309 (1992).
24. A.R. Peaker, et al., Proc. 2nd Symp. on Defects in Silicon, Electrochemical Soc., **91-9**, 125 (1991).
25. K. Weronek, J. Weber, A. Höpner, F. Ernst, R. Buchner, M. Stefaniak and H. Alexander, Materials Sci. Forum **83-87**, 1315 (1992).
26. L.F. Mattheis and J.R. Patel, Phys. Rev. B **23**, 5384 (1981).
27. P.E. Batson, Proc. Microscopy. Soc. of America, Ed. G.W. Bailey and M.N. Elliman, 1995, p. 276.
28. Feng Liu, Mark Mostoller, V. Millman, M.F. Chisholm and Theodore Kaplan, Phys. Rev. B **55**, 17192 (1995).
29. Y. Huang, J. Spence and O. Sankey, Phys. Rev. Lett. **74**, 3392 (1995).
30. S. Őberg, P.K. Stich, R. Jones and M.I. Heggie, Phys. Rev. B **51**, 13138 (1995).

Materials Science Forum Vols. 258-263 (1997) pp. 159-164
© 1997 Trans Tech Publications, Switzerland

DISLOCATION ACTIVITIES IN BULK GeSi CRYSTALS

I. Yonenaga and K. Sumino[1]
Institute for Materials Research, Tohoku University, Sendai 980-77, Japan
[1]Nippon Steel Corporation, Futtsu 293, Japan

Key Words: GeSi, dislocations, dislocation velocity, alloy hardening, crystals growth

Abstract. The mechanical strength and dislocation velocity in bulk single crystals of GeSi alloy grown by the Czochralski technique were investigated by compressive deformation tests and the etch pit technique, respectively. In the temperature range 450 - 700°C and the stress range 3 - 24 MPa the dislocation velocity in $Ge_{1-x}Si_x$ in the composition range x = 0.004 - 0.080 decreases monotonically with an increase in the Si content, reaching about one seventh of that in pure Ge at x = 0.080. The velocity was determined as functions of the stress and the temperature. The stress-strain curve in the yield region of GeSi alloy in the temperature range lower than about 600°C was temperature-sensitive and was similar to those of Ge and Si However, the yield stress of the alloy became temperature-insensitive at high temperatures. It increases with increasing Si content in the composition range x = 0 - 0.4. The yield stress was dependent on the composition as being proportional to $x(1 - x)$. Built-in stress fields in GeSi alloy caused by local fluctuation of the alloy composition together with dynamic development of solute atmosphere around dislocations, are thought to suppress the dynamic activities of dislocations and result in the strengthening of GeSi alloy.

Introduction.

GeSi alloy is of important in view of its variable band gap and lattice parameter according to the alloy composition. GeSi alloy for opto electronic applications is usually grown as thin films on substrates by various epitaxial techniques. Introduction of misfit dislocations is unavoidable in hetero epitaxial structure when the film thickness exceeds the critical value. Though dislocations affect the electrical and optical properties of GeSi alloy and limit its application to various devices, only little is known about their dynamic properties such as the generation and motion of misfit dislocations at the film/substrate interface[1-6]. Biaxial stress inherent to heterostructure hinders the quantitative study of the native properties of dislocations. Dynamic properties of dislocations in the GeSi system have often been assumed to be similar to those in Si or Ge and little attention has been paid to the unique properties of dislocations which appear due to alloying. The present authors found that the flow stresses of GaAsP and InAsP alloys have athermal components that are absent in GaAs, GaP, InAs and InP compounds[7,8]. It is of interest to investigate the dynamic activities of dislocations in GeSi alloy using bulk crystals and to deduce their unique properties brought about by alloying.

This paper reports the dislocation velocities and mechanical properties of GeSi alloy which were investigated with bulk crystals grown by the Czochralski technique and compares them with those of elemental Ge and Si crystals.

Experiment.

$Ge_{1-x}Si_x$ bulk alloy crystals were grown by the Czochralski technique. Seeds prepared from a Si crystal oriented to parallel to the [111] or [001] were used for the growth of crystals of most alloy compositions. For alloy of low Si content seeds were prepared from a Ge crystal of the [111] orientation. The pulling rate for growth was in the range of 0.5 - 2.0 mm/h. The details of the growth procedure and apparatus are described in the previous paper[9]. The composition of the alloy was determined by means of energy dispersive X-ray (EDX) spectroscopy.

Velocities of dislocations were measured in specimens prepared from single crystals with Si contents up to x = 0.080 and with low grown-in dislocation densities of about 10^3 cm^{-2}. Rectangular shaped specimens 2 x 3 x 15 mm^3 in size with the long axis along the $[\bar{1}10]$ and side surfaces parallel to the (111) and $(11\bar{2})$ were finished by chemical polishing with the reagent 5HNO_3:1HF at 30 - 40°C. The specimen was stressed at elevated temperature by three-point bending in a vacuum. The bending axis was parallel to the $[11\bar{2}]$. Dislocations were generated

from a scratch drawn on the (111) surface along the long axis at room temperature with a diamond stylus. Displacements of dislocations caused by stressing were measured by the etch pit technique with the Billig etchant [10] at 80°C.

Mechanical properties were investigated in specimens prepared from single crystals or specimens prepared from single crystalline part of the ploycrystals developed near the seed, with Si contents up to x = 0.4 and with grown-in dislocation densities of 10^3 - 10^5 cm^{-2}. Rectangular shaped specimens 2.7 x 2.7 x 10.7 mm^3 in size were finished by chemical polishing. The compression axis was parallel to the [123] with the side surfaces parallel to the (111) and (541). Compression tests were conducted under a constant strain rate using an Instron-type machine at elevated temperatures.

The dislocation velocities and the mechanical properties of crystals of high purity Ge and Si with grown-in dislocation densities of about 10^4 cm^{-2} were compared with those of the alloy.

Results.

Crystal Growth

Figure 1 shows a GeSi alloy crystal grown from the melt of an initial composition of x_{m0} = 0.02. The pulling direction was parallel to the [001] and the pulling rate was 1.0 mm/h. The development of four {111} facets confirms the growth of a single crystal through the length of the grown crystal. The composition at the growth start position is x_0 = 0.11 and changes gradually to low Si content along the growth direction due to the preferential consuming of Si from the melt during the growth. A single crystal 20 mm in diameter and 60 mm in length with variable composition 0.004 < x < 0.03 along the [111] growth direction was successfully obtained with the pulling rate 2.0 mm/h.

Single crystals were successfully grown for alloys of low Si contents, while single crystal parts were obtained only in the regions near the seeds for alloys of intermediate and high Si contents, which may be related to the occurrence of constitutional supercooling.

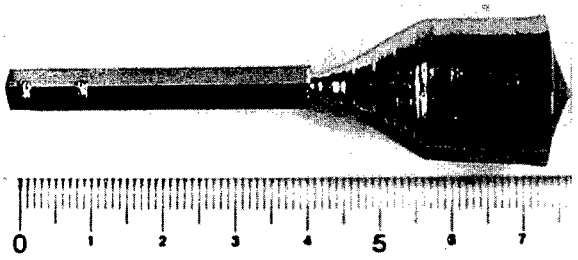


Fig. 1. GeSi alloy crystal grown by the Czochralski technique. The composition at the start position of the growth is x = 0.11.

Variation in the alloy composition within a grown crystal was quantitatively determined by EDX. For any grown crystal the composition changes spatially in such a way that the Si content gradually decreases along the pulling direction, implying that Si in the melt is preferentially consumed and taken into the crystal during the growth. Such composition variation within the grown crystal along the growth direction can well be described in terms of the complete mixing model of the melt [11], if the gravity effect caused by a large difference in the densities of Ge and Si is taken into account.

Dislocation velocity

Dislocations were generated preferentially from a scratch drawn on the surface. The velocity was measured as a function of the temperature in the range 450 - 700°C and that of the resolved shear stress in the range 3 - 24 MPa. Figure 2 shows how the velocity of 60° dislocations at 450°C under a shear stress of 20 MPa depends on the composition of the GeSi alloy. It is seen that the velocity of dislocations in the GeSi alloy decreases monotonically with an increase in the Si content and reaches about one seventh of that of dislocations in pure Ge at x = 0.080.

Figure 3 shows the velocities of 60° dislocations at various temperatures plotted against the shear stress in the $Ge_{1-x}Si_x$ alloys with x = 0.016, 0.047 and 0.080 together with that in pure Ge. The logarithm of the velocity of dislocations is linear with respect to the logarithm of the stress at all temperatures and for all Si contents with the approximately same slope.

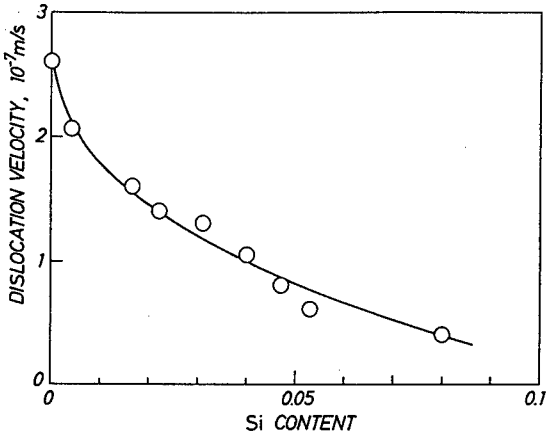


Fig. 2. Velocities of 60° dislocations in the GeSi alloy at 450°C under a shear stress 20 MPa as dependent on the Si content.

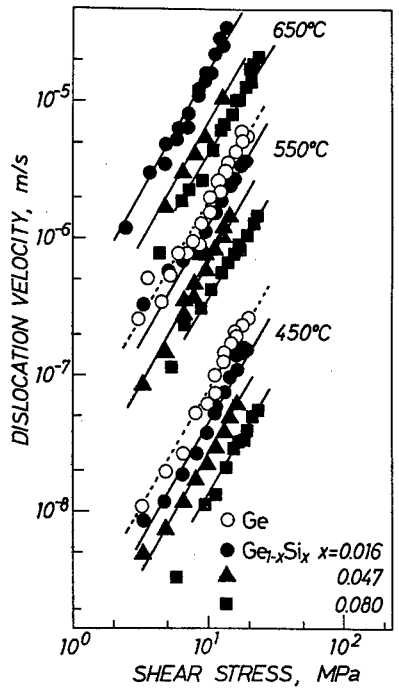


Fig. 3. Velocities of 60° dislocations in the GeSi alloys of various Si contents at 450, 550 and 650°C as dependent on the shear stress together with those in Ge.

The velocity v of 60° dislocations in the $Ge_{1-x}Si_x$ alloys in the composition range $x = 0.004$ - 0.080 can well be expressed as a function of the shear stress τ and the temperature T by the following empirical equation:

$$v = v_0 (\tau / \tau_0)^m \exp(-Q / k_B T), \quad (1)$$

where τ_0=1 MPa and k_B is the Boltzmann constant. The experimentally determined magnitudes of v_0, m and Q in GeSi and Ge are given in Table 1. The magnitudes of the parameter m in the alloys are same as that in Ge and those of Q are only slightly different from that in Ge. This may be related to rather small Si contents in the alloys investigated. The activation energy Q obtained in the present investigation is larger than that reported for Ge-rich GeSi thin films [5].

Table 1. Magnitudes of v_0, m and Q for 60° dislocations in $Ge_{1-x}Si_x$ and pure Ge.

Crystal	v_0(m/s)	m	Q (eV)
Ge	2.9×10^2	1.7	1.62 ± 0.05
$Ge_{1-x}Si_x$ ($x = 0.016$)	4.6×10^2	1.7	1.68
($x = 0.047$)	2.8×10^2	1.7	1.68
($x = 0.080$)	2.3×10^2	1.6	1.70

Mechanical property

Stress-strain behaviour of GeSi crystals with Si contents up to $x = 0.4$ was investigated at various temperatures under a shear strain rate of 1.8×10^{-4} s^{-1}. Figure 4 shows the stress-strain curves of the GeSi alloy of $x = 0.10$. At temperatures lower than 600°C the stress-strain curves of the specimens were characterised by a stress drop followed by an increase in the stress with the strain.

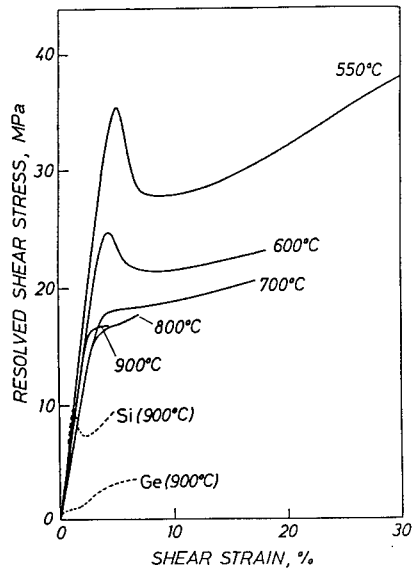


Fig. 4. Stress-strain curves of GeSi alloy of $x = 0.10$ at various temperatures under a strain rate of 1.8×10^{-4} s^{-1}. Dashes lines are those of Si and Ge at 900°C.

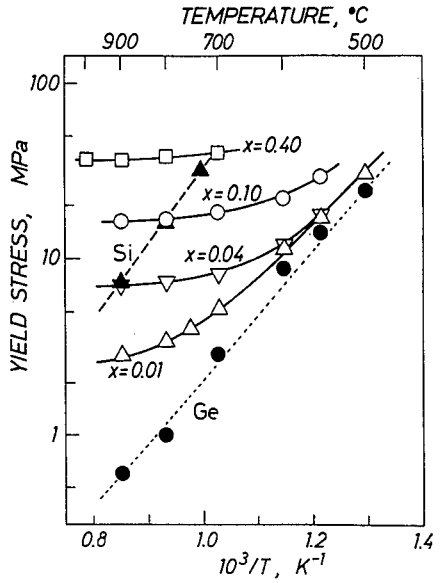


Fig. 5. Yield stresses of the GeSi alloys plotted against the reciprocal temperature for deformation under a strain rate of 1.8×10^{-4} s^{-1}.

Such a stress drop after the upper yield point is commonly observed in various semiconductors, such as Si, Ge, GaAs etc. at relatively low temperatures. Contrarily, at temperatures higher than 700°C, no stress drop is seen in the stress-strain curve and the level of the flow stress of the alloy is much higher than those of pure Si and Ge crystals.

The lower yield stresses of the $Ge_{1-x}Si_x$ alloy with $x = 0.01$, 0.04, 0.10 and 0.40 and also those of Si and Ge, for comparison sake, are plotted against the reciprocal temperature in Fig. 5 for the deformation under a shear strain rate of 1.8×10^{-4} s^{-1}. The logarithms of the yield stresses in Si and Ge are linear with respect to the reciprocal temperature in the whole temperature range investigated. The same holds in a limited temperature range of 500 - 700°C for the alloy of $x = 0.01$ and in a range of 550 - 600°C for the alloy of $x = 0.04$ and 0.10. In such temperature ranges the yield stresses of the alloys are close to that of Ge. The temperature dependencies of the yield stresses of the alloys become much weaker in a higher temperature range. Such a temperature range expands toward the low temperature side with an increase in the magnitude of x. Thus, the yield stresses of the GeSi alloys are nearly constant with respect to the temperature and are much higher than that of Ge in the high temperature range. Siethoff observed the temperature-dependent lower yield stresses of Si crystals doped with Ge up to $x = 0.016$ similar to that of pure Si[12]. This may be attributed to rather low Ge contents and also to the fact that deformation temperature was too low to render the temperature-independent yield stress appreciable in his SiGe alloys.

Figure 6 shows the dependence of the yield stress of the $Ge_{1-x}Si_x$ alloys under a shear strain rate of 1.8×10^{-4} s^{-1} at 900°C on the Si content x. The yield stress increases with increasing Si content in the composition range $x = 0$ - 0.4 investigated. Since the yield stresses of the alloys with $x > 0.10$ are much higher than that of pure Si, the maximum of yield stress is presumed to exist in the range $x = 0.5$ - 1.0. Such a composition dependence differs significantly from the composition dependence of the room temperature hardness of the GeSi alloys obtained with a Knoop indentor with a 25 g load for 10 s shown by open triangles in Fig. 6. The hardness at room temperature

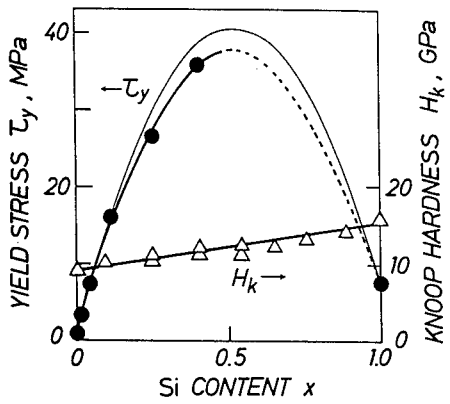


Fig. 6. Yield stresses τ_y of the GeSi alloy plotted against the Si content x for deformation at 900°C under a strain rate of 1.8×10^{-4} s^{-1} together with Knoop hardness H_k. The thin line shows the $x(1-x)$ fitting.

increases linearly with the Si content up to $x = 1$. This might be related to the fact that the yield stresses of the GeSi alloys are not much different from that of Ge at low temperatures.

Discussion.

The velocities of dislocations in the $Ge_{1-x}Si_x$ alloys with $x = 0.004$ - 0.080 are a little lower than that in Ge crystals in the temperature range 450 - 700°C . This may account for rather small difference between the yield stresses of the alloys of these compositions and that of Ge observed in such a temperature range.

The flow stress of a crystal in any deformation stage consists of two components. One is the effective stress that is necessary to move dislocations at a certain velocity against the intrinsic resistance (Peierls potential) of the crystal via a thermally activated process. The other is the athermal stress that is the component necessary to overcome any resistance not thermally surmountable and depends weakly on the temperature. If we assume that alloying results in a drastic increase of the Peierls potential and reduces the dislocation velocity, we may expect that the stress drop at the yield point should be more remarkable in GeSi alloy than in Ge on the basis of dislocation dynamical treatment of yielding in semiconductors [13]. Furthermore, the strengthening effect caused by alloying should become less remarkable as the temperature is increased. Neither is in agreement with the present experimental results. The variation in the yield stress with temperature in the GeSi alloys can be interpreted to show that the flow stress of the alloy has an athermal stress component that is absent in Ge and Si. Such athermal stress component related to alloying becomes large with an increase in the Si content up to $x = 0.5$.

There are some possible origins for athermal stress related to alloying, as discussed in the previous papers on GaAsP and InAsP alloys[7,8]. Short-range order of $L1_1$ structure is reported to exist in strained layer superlattice thin layers grown on substrates by molecular beam epitaxy or metal organic chemical vapour deposition by some research groups [14-16]. It can result in an extra stress of athermal nature to move dislocations, since the motion of a dislocation destroys the short-range order along its slip plane and produces an interface of excess energy along its slip plane[17]. However, it is difficult to detect the ordered structure in bulk GeSi alloy [18].

Long-range stress may be induced with a relation to the local fluctuation of the alloy composition in a crystal. Since the bond lengths of Si and Ge differ by about 4 %, local fluctuation of the alloy composition in the crystal, causing the development of small regions enriched with Si or Ge, may induce a long-range stress field that cannot be surmounted thermally by dislocations. The composition dependence of the athermal stress estimated for $Ge_{1-x}Si_x$ is given by the $x(1 - x)$ relation, as shown by a thin line in Fig. 6. This means that dislocations in GeSi alloy move by repeating bowing out processes around the long range stress fields.

The dynamic development of a solute atmosphere around a dislocation during deformation at high temperatures leads to an extra stress necessary to release the dislocation from the solute atmosphere.

In fact, the Portevin-LeChatelier phenomenon was observed as many fine serrations on the stress-strain curve in the deformation under a low strain rate. Such characteristic is interpreted as being caused by repeated locking and releasing processes of dislocations due to the interaction with impurities as observed in highly doped GaAs with impurities[19]. Though the releasing process of a dislocation from its solute atmosphere is a thermally activated one, the development of solute atmosphere around the dislocation is more enhanced at higher temperature. Thus, the contributions of these effects to the flow stress compensate each other and may give rise to temperature-insensitive resistance to the dislocation motion, apparently looking like an athermal stress.

Either or both of the local fluctuation of alloy composition or/and the dynamic development of solute atmosphere around dislocations are thought to suppress the dynamic activity of dislocations and result in the strengthening of bulk GeSi alloy at elevated temperatures. Direct observations of such effect on the dynamic activity of an individual dislocation is a task in the future.

Conclusion.

The mechanical strength and the dislocation velocity in bulk single crystals of $Ge_{1-x}Si_x$ alloy grown by the Czochralski method were investigated. The dislocation velocity in the composition range $x = 0.004$ - 0.080 can be expressed by an empirical equation as a function of the stress and the temperature. The dislocation velocity decreases with an increase in the Si content, reaching about one seventh of that in pure Ge at $x = 0.080$. The stress-strain behaviour in the yield region of the GeSi alloys is similar to that of Ge and Si in the temperature range lower than about 600°C. The yield stress of the alloys is temperature-insensitive at high temperatures and increases with increasing Si content from $x = 0$ to 0.4. The composition dependence of the yield stress follows the $x(1 - x)$ relation. Built-in stress fields related to local fluctuation of the alloy composition, together with dynamic development of solute atmosphere around dislocations, seem to suppress the activity of dislocations and bring about the hardening of the GeSi alloy.

Acknowledgement.

The authors express their gratitude to Mr. A. Matsui and Dr. T. R. Mchedlidze of the Institute for Materials Research, Tohoku University for their assistance.

References.

1. G. G. Tuppen and C. J. Gibbings, J. Appl. Phys. **68**, 1526 (1990).
2. D. C. Houghton, Appl. Phys. Lett. **57**, 2124 (1990).
3. R. Hull, J. C. Bean, D. Bahnck, L. J. Peitcolas, K. Short and F. C. Unterwald, J. Appl. Phys. **70**, 2052 (1991).
4. Y. Yamashita, K. Maeda, K. Fujita, N. Usami, K. Suzuki, S. Fukatsu, Y. Mera and Y. Shiraki, Phil. Mag. Lett. **67**, 165 (1993).
5. R. Hull, J. C. Bean, L. J. Peitcolas, B. E. Weir, K. Prabhakaran and T. Ogino, Appl. Phys. Lett. **65**, 327 (1994).
6. D. D. Perovic and D. C. Houghton, "Microscopy of Semiconducting Materials 1995", ed. A. G. Cullis and A. E. Staton-Bevan (Bristol, IOP Publishing) pp. 117-134(1995).
7. I. Yonenaga, K. Sumino, G, Izawa, H. Watanabe and J. Matsui, J. Mater. Res. **4**, 361(1989).
8. I. Yonenaga and K. Sumino, "8th Symposium Record of Alloy Semiconductor Physics and Electronics" ed. A. Sasaki (Kyoto, Organization of Special Project Research on Alloy Semiconductor Physics and Electronics) pp. 187-194(1989).
9. I. Yonenaga, A. Matsui, S. Tozawa, K. Sumino and T. Fukuda, J. Crystal Growth **154**, 275 (1995).
10. P. R. Camp, J. Electrochem. Soc. **102**, 586 (1955).
11. E. Scheil, Z. Metallk. **34**, 370(1942).
12. H. Siethoff, Mater. Sci. Eng. **4**, 155 (1969).
13. K. Sumino, "Handbook of Semiconductors Vol. 3" ed. S. Mahajan,(Amsterdam: Elsevier Science B. V.) pp. 73 - 181(1994).
14. A. Ourmazd and J. C. Bean, Phys. Rev. Lett. **55**, 765 (1985).
15. F. K. LeGoues, V. P. Kesan and S. S. Iyer, Phys. Rev. Lett. **64**, 40(1990).
16. E. Müller, H. -U. Nissen, K. A. Mäder, M. Ospelt and H. von Känel, Phil. Mag. Lett. **64**, 183 (1991).
17. J. C. Fisher, Acta Metall. **2**, 9 (1954).
18. D. Stenkamp and W. Jäger, Phil. Mag. **A65**, 1369 (1992).
19. I. Yonenaga and K. Sumino, J. Appl. Phys. **71**, 4249 (1992).

Materials Science Forum Vols. 258-263 (1997) pp. 165-170
© 1997 Trans Tech Publications, Switzerland

SCHOTTKY DIODES ON $Si_{1-x-y}Ge_xC_y$ ALLOYS: MEASUREMENT OF BAND OFF-SET BY DLTS

M.Serpentini, G.Brémond
Laboratoire de physique de la martière (UMR 511), insa de Lyon, bât.502,
20 av.A.Einstein, 69621 Villeurbanne cedex, France
F.Meyer
Institut d'electronique fondamentale, CNRS URA 22, bât.220,
Université Paris Sud, 91405 Orsay cedex, France

Keywords : $Si_{1-x-y}Ge_xC_y$, DLTS, Schottky contact,Tungstene, band-offset , strain

Abstract
In this paper, an original method to evaluate the band offsets values in the SiGeC/Si(100) system is proposed using DLTS spectroscopy performed on W/p-SiGeC/p-Si(100) samples. We have worked on pseudomorphic SiGeC layers with C content varying from 0% to 1.25% to observe the change over from compressive to tensile strain. We have detected three levels. One is located near the Schottky contact W/SiGeC, an other is located in the bulk and the third is situated at the SiGeC/Si interface. We suppose that this latter is an intrinsic defect and can be referred to the vacuum state or the minimum energy of the conduction band. Consequently its activation energy variations versus [C] follows the band structure and in particularly the band offset. Its activation energy increases up to 0.8% C and decreases after. This suggests that ΔEv and ΔEc decrease with C content respectively for compressive and tensile strained layers in good agreement with recent reported results.

Introduction

It is well known at the present time that C incorporation in pseudomorphic $Si_{1-x}Ge_x$ compensates strains. Consequently, the critical thickness is pushed back and a ratio 1:12 between C and Ge leads to the lattice match on Si **[1,2]** Furthermore, recent photoluminescence results showed that the band-gap energy increases by 20-26 meV/%C for compressive strained SiGeC layers while it decreases by 57-65 meV/%C for tensile strained $Si_{1-y}C_y$ layers **[3-6].**
Although few electrical properties of this new ternary alloy have been reported, the band offset is one of the main property features in electronic devices such as MODFET or heterojunction Bipolar Transistor (TBH).**[4]**. So its knowledge is fundamental, but remains questionable up to now in the SiGeC/Si system.
In this study, we propose an estimation of the band offset in the SiGeC/Si(100) system by using DLTS measurements on W/p-type Schottky diodes versus C content. Recent studies have showed that tungsten Schottky contacts have a good quality. More details on W metallization on SiGeC materials are available elsewhere **[7]**.

Experimental details

Samples were grown on p-type substrate using RTCVD (Rapid Thermal Chemical Vapor Deposition). After a RCA cleaning, a HF dip and a thermal flash cleaning at 1000 °C under a hydrogen flow, a 100 nm silicon buffer was grown at 900 °C under a working pressure of 1 Torr.
The 100 nm SiGeC layer was grown at 550 °C with silane (SiH_3), germane (GeH_3) and methylsilane (SiH_3CH_3) as precursor gas. Carbon has been substitutionnaly incorporated up to 1.25% and Ge content was 10%. XRD (X-ray diffraction), infrared spectroscopy and Rutherford backscattering spectroscopy were performed to confirm the high structural quality of the SiGeC layers. P-type doping was obtained by using diborane (B_2H_6), Secondary Ion Mass Spectroscopy measurements have given 6-8 10^{17} at / cm^3 for the SiGeC films and 1-2 10^{15} at / cm^3 for the Si substrate. The buffer

was non intentionally doped. More details of the structure growth are given in **[8]**. W deposition has been achieved in a magnetron-DC sputtering system. Schottky contacts were defined by photolithography and selective etch **[7]**. SiGeC films were compressively strained for weak C contents (from 0% to 0.74%) and lightly tensile strained for the higher content (from 1% to 1.25%).
We have performed electrical measurements such as Current-Voltage, Capacitance-Voltage, and DLTS (Deep Level Transient Spectroscopy) on these samples. I-V and C-V were accomplished to be sure of the integrity of the Schottky diode to perform DLTS measurements. C-V was used to obtain the doping profiles and to determine the Schottky barrier height with a working frequency of 100 kHz **(Tab.1)**.

	$Si_{0.9}Ge_{0.1}$	$Si_{0.896}Ge_{0.1}C_{0.004}$	$Si_{0.892}Ge_{0.1}C_{0.008}$	$Si_{0.89}Ge_{0.1}C_{0.01}$	$Si_{0.887}Ge_{0.1}C_{0.013}$
Vbi (eV)	0.40	0.68	0.54	0.55	0.48

Table 1 : Schottky barrier heights

In order to have coherent results, admittance spectroscopy have also been performed.
Here is a brief DLTS description: The diode is placed under reverse bias Vr which creates a depleted region with a capacitance. An electrical pulse excitation of height Hp is applied and the level is momentarily full. The level is emptying during the pulse duration time tp. After the pulse excitation off, the capacitance change in an exponential transient. This transient is measured at two times t1 and t2 versus temperature using a double boxcar and the DLTS signal corresponds to C(t2)-C(t1)
According to C-V **(fig.1)** and I-V results we have chosen to apply 0.5 V as Vr and 1.5 V as Hp in order to examine the whole SiGeC film with 100 kHz as work frequency and 1 ms as filling-time tp.

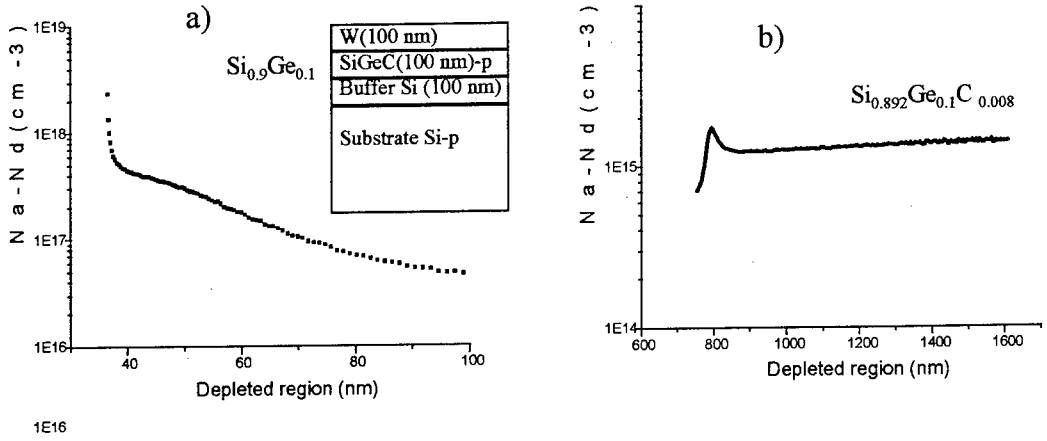


Figure 1 : doping profiles of $Si_{0.9}Ge_{0.1}$ (a) and $Si_{0.892}Ge_{0.1}C_{0.008}$ (b)
a) : The depleted region is located in the SiGe layer
b) : The located region is located in the bulk region
We presume that C intoduces a compensation effect

Experimental results
For the C-free sample, the depleted region at 0.5V reverse bias was located at about 100 nm from the Schottky contact. This allowed us to confirm a p-doping around of $6\text{-}8.10^{17}$ at/cm^3 in the SiGe layer. For the samples containing C, the more the carbon content increases, the more the depleted region is located far in the bulk region. We conclude that the carbon incorporation introduces a compensation effect in the SiGeC layer.
By performing DLTS versus electrical field Vp, three levels have appeared **(fig.2)**. We called them D1, D2 D3.

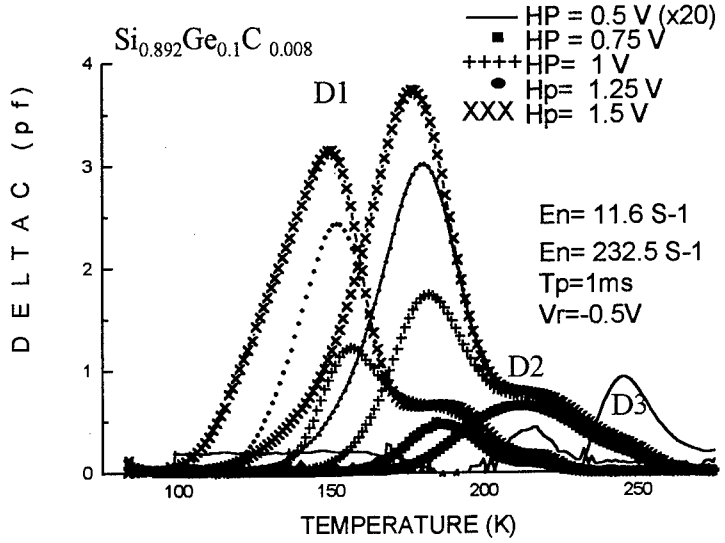


Figure 2 : DLTS spectra of $Si_{0.892}Ge_{0.1}C_{0.008}$ versus Hp for two emission rates.
We observe that D3 immediately appears while D2 and D1 appears when Hp>Vbi.

The **figure 3** gives the Arrhenius plots corresponding to the DLTS signatures of all the measured traps.

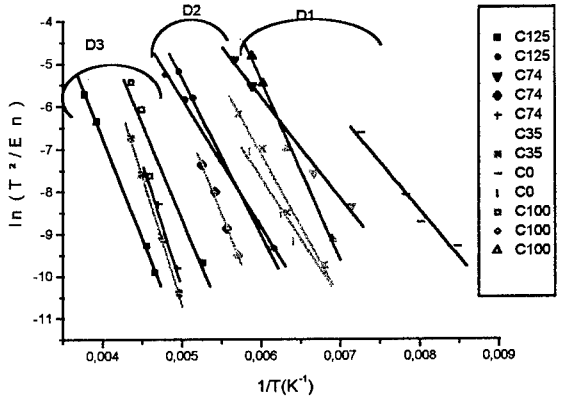


Figure 3: Arrhenius plots for all levels.
We have classed the defects in three groups D1,D2 D3, versus their activation temperatures.

We have reported in **table 2** the results for the $Si_{0.9}Ge_{0.1}$ and $Si_{0.892}Ge_{0.1}C_{0.008}$ samples for comparison. **Table 3** gives the activation energy results on all the samples. D1 only appears when the electrical excitation is superior to the Schottky barrier but we did not detect it in all the samples. D3 appears in all samples containing C because we were able to probe the buffer and substrate regions in these structures. Furthermore, for D1 and D2 we observed a Poole-Frenkel effect. DLTS versus reverse bias has been achieved and the ratio $\Delta C/C_r^3$ has been calculated for each sample. This ratio is constant for D1 and D2 which strongly suggests that these defects are located close to the surface of the SiGeC/Si interface, in good agreement with DLTS results.

Finally; C-V and DLTS results lead us to conclude that D1 and D2 are situated in the SiGe or SiGeC layer, D1 is a surface defect at the W/SiGeC interface and D2 is an interfacial defect at the SiGeC/Si interface while D3 is located in the bulk or buffer region.

Vp (V)	$Si_{0.9}Ge_{0.1}$		$Si_{0.892}Ge_{0.1}C_{0.008}$		
	D1 (eV)	D2(eV)	D1(eV)	D2(eV)	D3(eV)
1	0.20±0.02	0.30±0.03	0.18±0.02	0.34±0.03	0.43±0.04
0.5	0.28±0.03	0.31±0.03	0.29±0.03	0.37±0.04	0.43±0.04
0		0.32±0.03			0.43±0.04

Table 2 : DLTS results versus Vp for the C-free sample and the $Si_{0.892}Ge_{0.1}C_{0.008}$ sample

Energy	$Si_{0.9}Ge_{0.1}$	$Si_{0.896}Ge_{0.1}C_{0.004}$	$Si_{0.892}Ge_{0.1}C_{0.008}$	$Si_{0.89}Ge_{0.1}C_{0.01}$	$Si_{0.887}Ge_{0.1}C_{0.013}$
D1 (eV)	0.20±0.02		0.18±0.02	0.30±0.03	
D2 (eV)	0.29±0.03	0.30±0.03	0.34±0.03	0.32±0.04	0.26±0.03
D3 (eV)		0.52±0.06	0.40±0.04	0.41±0.04	0.41±0.04

Table 3 : DLTS results with 0.5V as reverse bias and 1.5V as electrical excitation

We have examined the hole trapping behavior versus the filling-pulse duration**(fig.4)** The saturation of the DLTS signal rapidly occurs. A logarithmic dependence of DLTS peak height on filling-pulse duration and a broadened DLTS peak-width are both characteristic properties of carrier trapping at dislocations **[9,10].** So, in regard with the **figure 4** we identify the three levels as being related to rather punctual defects than extended ones as dislocations. Photoluminescence results agreed with the good structural quality of the layer by the non-observation of the dislocations lines.

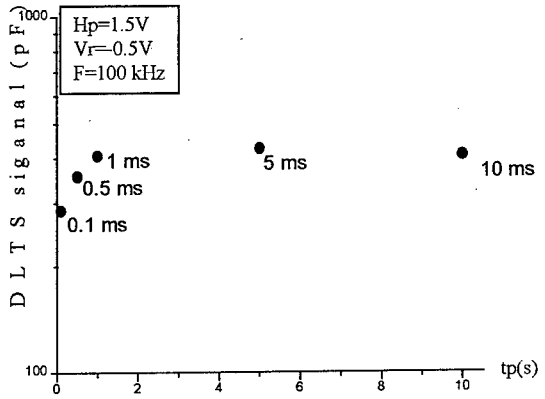


Figure 4: Hole trapping D2 behavior versus filling-pulse. This establishes that D2 is a punctual defect (This is the same behavior for the other levels).

Discussion about the determination of the band offsets in the SiGeC/Si system

Several investigations have been achieved to study the effect of carbon on the valence band offset of compressively strained $Si_{1-X-Y}Ge_XC_Y/Si(100)$ heterojunctions**[11,12]**. They found a decrease of 25-30 meV as 1% carbon was added and for a Ge content of 20.6% with admittance spectroscopy

The measurement of low value of band offset using single heterostructure requires a very good interface quality with adapted doping profile conditions in the layers on each side. This is fundamental in order to form a bi-dimensionnal gaz of carriers at the interface allowing to examine their emission through the band offset barrier. This is not really the case in our study. In fact, the doping is not well

adapted due to the compensation effect of the carbon incorporation and the low doping of the Si buffer and substrate. Then, another point is to consider the change versus the C content of the energy for a deep level taken as an energy reference. In the preceding part we have remarked a particular behavior of the activation energy of the D2 level versus C content **(see fig.5)**. Up to 0.8%C, its binding energy measured from the valence band increases, but it decreases after for y=1% and y=1.25%. Note that the perfect strain compensation happens for about [C]=0.9%. So, this drastic energy change corresponds to the transition from compressive to tensile strain. Consequently, the energy band structure is affected and also the band offset.

First, we can argue that D2 is an intrinsic defect of the SiGeC/Si interface and it could be referred to an internal energy reference of the structure. So, its binding energy variation would be directly connected to the valence band offset variation versus C content. Taken into account a broaden analysis of our results due to the lack of good accuracy of our DLTS measurements, we found **(fig.5)** a valence band offset energy decrease of 50±15 meV/%C for compressive strained SiGeC layers. This result is in good accordance with the expected evolution of the ΔEv versus C content as described in recent papers**[11,12]**.

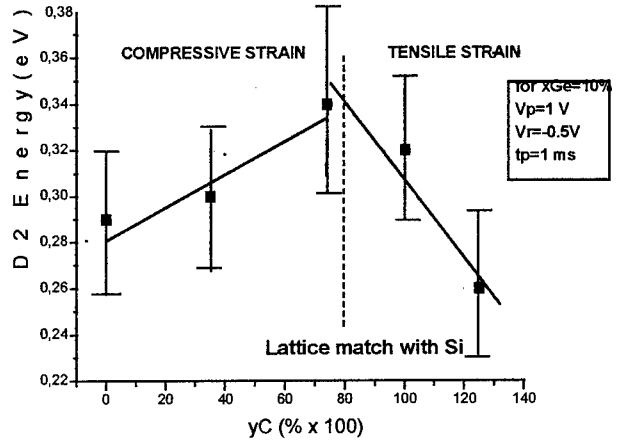


Figure 5 : Activation energy of D2
We observe :
- The transtion from type I to type II band structure correponding with the perfect compensation of the strains at [C]=0.8%
-An increase of (50 ∓15) meV/%C for compressive strain
-A decrease of (115∓ 45) meV/%C for tensile strain

However, if we follow this track, the increase of ΔEv for tensile strained SiGeC layer doesn't agree the expected ΔEv evolution which would be keep at least constant. So, we have to hypothesize that the D2 level is referred to the conduction band minimum energy . So, we can consider that the energy between the conduction band and the D2 level is constant. In that case, the evolution of its energy measures the decrease of ΔEv for compressively strained SiGeC layers and the increase of ΔEc in tensile strained SiGeC layers. This is possible because i) change in band gap of SiGe as carbon was added is mainly accommoded in the valence band for compressively strained SiGeC layers [12]; ii) we measure by DLTS the energy of the D2 level related to the Si valence band energy when the one of SiGeC becomes lower.We have found δΔEc=115±45 meV/%C in good agreement with recent published papers**[11,6].**

Conclusion

To sum up this work, we have performed C-V, I-V , admittance spectroscopy and DLTS on W/SiGeC Schottky diodes. We have found a defect situated at the SiGeC/Si interface. Its activation energy increases with [C] for compressively strained SiGeC films and decreases with [C] for tensile strained films. Considering that this level was referred to the conduction band minimum energy as being an intrinsic heterojunction defect , we have proposed a shift of the band offsets corresponding to the shift of its activation energy versus C content. Furthermore, our results showed the transition from compressive to tensile strain which may correspond to the transition from type I to type II band alignment.

Acknowledgments

The authors thank J.L..Regolini from the CNET Meylan for providing the samples and are grateful to H.Gamez, A.Daami and A.Souifi for their help in materials characterization.

References

[1] K.Eberl, S.S.Iyer, S.Zollner, J.C. Tsang, and F.K. LeGous, Appl.Phys.Lett. **60**, .3033 (1992)
[2] J.L.Regolini, F.Gisbert, G.Dolino, and P.Boucaud, Mat.Lett **18**, .57 (1993)
[3] St-Amour, C.W.Liu, J.C.Sturm, Y. Lacroix and M.L.W. Thewalt, Appl. Phys. Lett. **67**,3915 (1995)
[4] L.D.Lanzerotti, A.St Amour, C.W.Liu and J.C.Sturm, IEEE Electron Device Letters **17**, 334 (1996)
[5] P.Boucaud, C.Francis, F.H.Julien, J.-M.Lourtioz, D.Bouchier, S.Bodnar, B.Lambert and J.L.Regolini, Appl.Phys.Lett. 64, pp.875 (1994)
[6]] K.Brunner, W.Winter and K.Eberl, Appl.Phys.Lett. **69**,1279 (1996)
[7] M.Mamor,F.Meyer, D.Bouchier, G.Vialaret, Mat.Res.Soc.Symp.Proc.**379**, 137 (1995)
[8] V.Aubry-Fortuna in "Papers at SIMC'9, ed.IEEE, pp.231_234 (1996)
[9] P. Omling, E.R. Weber, L. Montelius,H. Alexander, J. Michel, Phys. Rev. B, **32**, 6571 (1985); T.Wosinsky, J.Appl.Phys,.**65**, 1566 (1989)
[10] P.N.Grillot; S.A.Ringel, E.A.Fitzgerald, G.P.Watson and Y.H.Xie, J.Appl.Phys, **77**, 3248 (1995)
[11] B.L.Stein, E.T.Yu, E.T.Croke, A.T.Hunter, T.Laursen, A.E.Bair, J.W.Myaer, and C.C.Ahn, Appl.Phys.Lett. **70**, 3413 (1997)
[12] C.L.Chang, A.St-Amour, J.C. Sturm, in "Papers at IEDM", ed. IEEE, pp.257 (1996)

Materials Science Forum Vols. 258-263 (1997) pp. 171-178
© 1997 Trans Tech Publications, Switzerland

MOLECULAR-DYNAMICS SIMULATIONS OF MICROSCOPIC DEFECTS IN SILICON

Stefan K. Estreicher[1] and Peter A. Fedders[2]
[1]Physics Department, Texas Tech University, Lubbock, TX 79409, USA
[2]Physics Department, Washington University, St.Louis, MO 63130, USA

Keywords: molecular-dynamics, theory, hydrogen diffusion

Abstract. A variety of molecular-dynamics (MD) techniques are being used to predict properties of defects in semiconductors. Simulated quenching provides local and global minima of complicated potential surfaces, while constant temperature simulations lead to the prediction of vibrational frequencies, diffusivities, and defect interactions. Thermodynamic quantities such as the entropy are also being calculated. This paper contains a non-technical overview of the key ingredients and implementations of MD simulations. As an example, the diffusivity of H in Si is discussed.

I. Introduction.

Molecular-dynamics (MD) simulations are a theoretical tool of growing importance (for recent reviews, see Refs. [1,2]). A number of methodologies are applied to macroscopic problems (such as wafer bonding[3]) as well as to microscopic (localized) defects. Many authors produce 'movies' showing atoms vibrating, impurities hopping around or bouncing off surfaces, all of it calculated in real time. Such visualizations help enormously when it comes to convincing an audience (and oneself). MD simulations give a new set of coordinates at every time step. Since one calculates 10^n time steps where n ranges from 3 to 6, the amount of data generated is huge. It is now the computer itself that reads the output of the calculation and turns it into pictures. The process is so appealing that it is easy to believe the results.

This paper discusses at a non-technical level the various methodologies, their strengths and drawbacks, and contains a few examples. Space is much too short for a comprehensive review of the topic. My goal is to give the reader a flavor of the computations involved, the approximations made, and the tricks used.

II. Overview of the methodologies.

Classical MD simulations use the Born-Oppenheimer approximation to separate the nuclear and electronic problems. The temperature T is included via the kinetic energy of the nuclei, which becomes an explicit part of the total energy. This kinetic energy is only a small fraction of the total energy. However, it can dominate the gradient of the energy. Note that for quantum solids such as He, treating the ions classically leads to drastic errors. For semiconductors, this is usually not important, especially at high T as phonons destroy the coherence. However, tunneling cannot be described. If one is studying the vibrational modes of a system, the classical limit means $k_B T > \hbar\omega$ where ω is the relevant frequency. MD is an intrinsically high-temperature technique.

The nuclei are treated classically, that is one solves Newton's laws of motion with forces obtained from the total energy via the Hellman-Feynman theorem.[4] There are a number of efficient algorithms[5] to obtain the equations of motion for each nucleus. The various MD methods differ in the way the electronic part of the energy is computed, that is how

Schrödinger equation is solved. This is the most difficult and computer-intensive part of the problem. The various MD methods can be subdivided into four broad groups:[1,2] semiempirical potentials, empirical tight-binding, *ab-initio* plane waves, and *ab-initio* tight-binding. Of course, hybrid methods exist as well. These groups differ in the way the quantum mechanical part of the calculation is done.

Semiempirical potentials give rise to the simplest and fastest MD codes. One decides on a functional form for the total energy of a system of particles and the forces between them. The parameters are adjusted to reproduce some set of experimental data or accurate total-energy calculations. The simplest methods use pair and three-center potentials, more sophisticated ones involve calculating for a given atom the equivalent of an effective field which includes all the surrounding atoms.[6] The key problem is *transferability.* The parameters are fit to some bonding configuration, and there is no guarantee that different types of bonding will also be well described. The best-known empirical method for Si is that of Stillinger and Weber.[7]

Empirical Tight-Binding (ETB) methods explicitely solve the one-body Hamiltonian matrix whose eigenvalues approximate the electronic energies. The electronic eigenstates are written as a linear combination of localized (atomic-like) orbitals,[8] and the sum of the occupied eigenvalues is the attractive electronic contribution to the energy. One must add a repulsive interaction, which is obtained by some fitting procedure. Orthogonal TB methods assume that the basis functions are mutually orthogonal, which is a rather drastic approximation but simplifies the computations enormously. The radial part of the basis functions is cut off smoothly at some distance from the nucleus, typically 3Å in the case of Si. Semiempirical parameters are used to fit the repulsive potentials and some hopping integrals. The parameters are often fit to reproduce selected properties of crystalline silicon.

The methods involve an $N \times N$ matrix diagonalization, which is an N^3 process, where N is the size of the basis set. However, the programs are rather simple to write. Further, the band gap is fit and presumably comes out right. This type of approach also has transferability problems. The most widely used ETB Hamiltonians for force calculations are those of the Goodwin-Skinner-Pettifor type.[9] Non-orthogonal ETB Hamiltonians have been proposed,[10,11] and they appear to be more transferable than orthogonal ones. Tang *et al.* compared the formation energies of the vacancy and self-interstitial in Si calculated with various potentials,[12] and report quite a spread not only in the defect formation energies but the lowest energy configurations as well.

Ab-initio methods are so named because they contain no experimental input. All of the methods used for MD simulations are based on density-functional (DF) theory,[13] often within the local density approximation (LDA). In principle, one could do MD simulations based on *ab-initio* Hartree-Fock (HF). However, this method scales as N^4 (N is the basis set size), which makes it much too slow for that purpose. Pseudopotentials[14] are introduced so that only the valence electrons are treated explicitely. The choice of pseudopotentials is dictated by the basis set. Plane-wave calculations require 'soft' pseudopotentials, in particular for elements with strong potentials, such as O, F, or $3d$ transition metals.

Two types of basis sets are used: *plane waves*, with functions included up to some cutoff energy (typically 8 to 16 *Ry*), and *local basis*, with sets of atomic-like orbitals centered on each ion (typically s, p, or even d). Plane waves are often associated with the *Car-Parrinello* (CP) approach, while local basis are referred to as *ab-initio tight-binding.*

In 1985, CP[15] revolutionized *ab-initio* MD simulations with what is now known as the CP method. Usually, it is taken to mean an MD simulation using a plane wave basis set and an iterative minimization scheme to solve the electronic problem with the self-consistent DF equations. Plane waves work well because of the great speed of fast Fourier transforms. The

key contribution of CP was to show that an actual diagonalization of the huge matrix is not necessary. Instead, they use a fictious Lagrangian to calculate the LDA energy. The method still involves $\sim N^3$ computations per iteration, where N is the number of atoms times the number of plane waves per atom (usually 100 to 1,000). A similar (but faster) method was developed by Scheffler and his group.[16]

The local basis method was developed by Sankey and co-workers.[17] The set consists of pseudo-atomic orbitals (PAOs) calculated within the LDA. The use of minimal basis sets reduces the variational freedom but speeds up the calculations. The PAOs are (smoothly) cut at some distance from the nucleus. This distance must be short otherwise each atom overlap with all the others and the computation time becomes excessive. In the case of Si, a typical cutoff radius is of the order of $5\,a_B$, that is two Si atoms more than $10\,a_B$ apart do not overlap. The eigenvalues and eigenvectors are easily expressed in terms of the PAO's, which is very helpful in interpreting the results. The faster version of the code uses the linearized, non self-consistent, version of DF theory (Harris functional[18]), which is quite good in situations which do not involve too much charge transfer. The fully self-consistent version is slower.

A few comments about energy gaps and eigenvalues are in order. First, within the LDA, the DF method produces gaps that are considerably too small. In most cases, this won't matter much. However, it can introduce errors in the total energy if there are occupied states in (or near) the conduction band. Such errors can often be removed by considering the appropriate *differences* in total energy. Second, the eigenvalues are computed as a contribution to the total energy, but they are not the only contribution. Thus, the meaning of the energy eigenvalues is not exactly the same as in a simple single-particle picture. Third, the eigenvalues themselves change as the occupation of single particle states changes. In any case, it is difficult to predict the position of energy levels in the gap - especially unoccupied ones - and very little is known about conduction band states. Ultimately, the difference in energy between two (global) states of a system must be computed by comparing their total energies, not eigenvalues. Special care must be taken not to over-interpret the energy eigenvalues.

Order N methods, $O(N)$, are so named because the CPU time increases linearly with the size of the system (for large systems). *Ab-initio* methods or ETB are of order N^3 because the diagonalization of an $N \times N$ matrix involve $\sim N^3$ operations. For such methods, current practical limits are supercell sizes of about a hundred atoms and simulation times of the order of 10 ps or so. There is presently a vigorous quest for quantum mechnical methods which scale linearly with the size of the problem. This is a competitive and fast-moving field. The methods are normally orthogonal tight-binding, and each atom only overlaps with a few nearest-neighbors. As a result, the matrices are sparse. The codes can be parallelized, which tremendously increases their computational efficiency. The mathematical details are tricky, and complete discussions are given in Refs. [19-21]. $O(N)$ methods heavily approximate the electronic problem. They are best at high T, when the ions have a large kinetic energy which makes their behavior much less dependent on the details of the potential energy surface.

III. Practical aspects and tricks.

MD simulations of defects in semiconductors are done in periodic supercells. In the case of Si, a typical cell contains 64 atoms and equivalent points in adjacent cells are 11 Å apart. In such cells, 4 k-points in the Brillouin zone are used for the calculation. Larger cells most often restrict the reciprocal-space sampling to just the Γ point (k=0).

Typical time steps range from 0.1 fs up to 5.0 fs. The shorter times must be used when dealing with a light atom such as H, while longer times are appropriate for something heavy and slow like Ga. Thus, even simulations involving 10^6 time steps represent only something like a ns real time. For *ab-initio* methods, the practical limit is of the order of 10 ps.

At each step, the quantum mechanical problem must be solved as fast as possible (may be one minute of CPU time or less). By comparison, a (single-point) large basis set *ab-initio* HF calculation in a 44 Si-atoms cluster with no symmetry takes days (weeks) of CPU time. The MD game is one of 'give-and-take', where one sacrifices accuracy in exchange for speed or size, and vice-versa. If the recent progress in computer power continues to increase, the balance will shift in favor of longer *ab-initio* simulations in larger clusters. However, it is not likely that the million-atom cell and the ns simulation will become routine anytime soon.

Typical uses of MD simulations include crystal growth and melting, ion implantation, wafer bonding, as well as the calculation of vibrational frequencies, the search for global or local minima of a potential energy surface, the simulations of defect reactions and diffusivities, the calculations of thermodynamic properties, etc. Some types of calculations require large temperature gradients, others keep T=const. for as long as computationally tractable. Since the initial ionic velocities are assigned randomly (usually, a gaussian distribution corresponding to the desired initial temperature), the cell must always be allowed to equilibrate for several hundred time steps before any calculation is done.

Simulated quenching consists in removing a fraction of the ionic kinetic energy every few time steps (the reverse process - simulated annealing - is also possible). It mimics the cooling down of the material. However, computer quenching occurs much faster (real time) than can be done in the lab: the temperature drops from a very high value to near zero within less than a ns! This method allows a search for local (fast quench) and global (slow quench) minima of the potential energy surface. Note that one really wants the minima of the free energy, and this has already been calculated in some cases.[22]

If one deals with a large defect with many degrees of freedom, the number of local minima increases dramatically. In order to find the global minimum of the energy, one must quench many times, starting with a large variety of initial configurations to make sure that the global minimum has been reached. When dealing with systems containing atoms with very different masses, such as H in Si, it is often useful to set the mass of H to a value close to that of Si. This results in the same final configuration, allows one to use a longer time step and, most of all, prevents undesirable oscillations of the energy.

Constant-temperature simulations are limited to reactions occurring very fast. A thermostat must be used to control the temperature.[23] Simulations lasting several thousand Δt's are common at the *ab-initio* level, those lasting a few hundred thousand Δt's require approximate methods. 'Long' simulations last $\sim 10\,ps$ (*ab-initio*) up to a ns (ETB or $O(N)$ methods). Note that the forces are calculated and Newton's equations solved at each time step. Therefore, the accumulation of systematic errors is not a serious problem, even in very long simulations. In any case, it is desirable to speed up slow reactions. One can of course raise the temperature, and then all the reactions occur faster. But the importance of electronic excited states increases, and these are normally not included (although, the finite-temperature version of DF theory can be used[24]). Again, there is a price to pay for speeding things up. A number of other tricks are commonly employed.

Kicks of one (or more) atom(s) can be used to simulate e.g., the capture of a phonon. A kick may consist in assigning some high initial velocity to an ion. One could also underestimate the initial lattice relaxation around a defect. The size of a kick must be sufficient to force the reaction. The process must be carefully controlled in order to make sure that all one does is speed up a slow reaction. This implies a good understanding of the processes that are likely to take place. The extra energy associated with a kick is rapidly absorbed by the phonon bath. An extreme case involves assigning a kinetic energy of several keV's to one atom in order to study the effects of ion implantation.[25]

In order to find a diffusion path one can **freeze some degrees of freedom** by assigning a large mass to some nuclei, thus restricting their motion. One can also **force the diffusion** by pushing one or more ions in the desired direction, for example by cancelling any component of the net force pointing in the opposite direction. In the 'adiabatic trajectory' approach,[26] the diffusing atom is forced to move at a small constant speed along a predetermined path while the other atoms in the supercell continuously relax in response to its motion.

IV. Example: H in c-Si.

Many point defects and defect reactions have been studied using MD simulations. The list includes interstitial H,[27-30] the vacancy (V),[12,31-35] the self-interstitial,[11,32-34] H—O,[30] H—V,[32] and V—V[36] interactions, etc.

The case of H is a good example because it has been studied at several levels of MD theory. Experimentally, the situation is clear only at high temperatures, where the data of Van Wieringen and Warmoltz (WW)[37] are universally accepted. They measured the diffusivity $D = 9.41 \times 10^{-3}\ \exp\{-0.48\, eV/kT\}\ cm^2/s$ in the range $1240 < T < 1480\, K$. At lower temperatures, measurements of H diffusivity give values that are in most cases (but not always) much below the extrapolation of the WW values. The diffusion of H is trap-limited,[38] and the data depend on the Fermi level, the type of sample (e.g, FZ vs. CZ), the impurity and defect content, the hydrogenation conditions, and on the type of experiment.

Most *ab-initio* (static) calculations[39] predict that H is found in three charge states, H^- (at the tetrahedral interstitial (T) site), H^0 (stable at the bond-centered (BC) site and metastable near the T site), and H^+ (at the BC site). These states are labeled H_T^-, H_{BC}^0, H_T^0, and H_{BC}^+, respectively. One experiment[40] has been interpreted as showing that H has negative-U properties, which would simplify the issue since H^0 would always be unstable. In particular, only H_{BC}^+ would exist in p-type Si and only H_T^- in n-type Si. However, this experiment and its interpretation have been challenged and the issue is not resolved.[40] Muon-spin rotation data above room temperature can only be understood if several states of muonium coexist. There are other data that are difficult to explain if only one charge state of H is present in a given sample. The MD studies of H diffusion have clarified some the issues.

Buda *et al.*[27] studied H^+ in a 128 Si atoms cell at the *ab-inito* CP level in the range $1000 - 1950\, K$ with a time step of $0.12\, fs$. The longest simulation lasted $4\, ps$.
Boucher and DeLeo[28] studied H^0 in a 64 Si atoms cell at the orthogonal ETB level with the Goodwin *et al.*[9] potential for Si–Si interactions and a Harrison-type potential for Si–H interactions. The latter had to be scaled to get the abolute minimum of the potential energy for H at the BC site. The time step was rather long, $\Delta t = 0.35\, fs$, and simulations were performed up 120,000 Δt's for $1050 < T < 2000\, K$.
Panzarini and Colombo[29] went from 1800 to $800\, K$ for H^0 in a 64 Si atoms cell with an ETB approach similar to the one above, but using their own Si–H potential, fitted to silane. Their simulations lasted $25\, ps$, with one run extended to $300\, ps$! The time steps were $0.5\, fs$ above and $1.0\, fs$ below $1000\, K$.
Park *et al.* discussed some aspects of H diffusion within their studies of O–H[30] and V–H[32] interactions. They use the *ab-initio* tight-binding method of Sankey *et al.*[17] in 64-atoms cells, a time step of $0.2\, fs$, and temperatures above $1000\, K$.

These MD simulations of H diffusion, done at three levels of theory, give insights into how the methods compare. Some results are independent of the methodology, the time step, the cell size, and other factors. But there are many differences in the finer details, and important differences occur at low T.

All the authors agree that both H_{BC}^+ and H_{BC}^0 hop from BC to BC site without spending much time in interstitials sites such as T where the electron density is low. There are differences

in exactly how H gets from one BC site to the other, how long it stays around a given BC site, which sites it visits while oscillating, etc. These differences can be due to the charge, (+1 vs. 0), different potentials for Si–H interactions, and other reasons. Figure 1 shows the trajectories calculated by the first three authors at comparable temperatures.

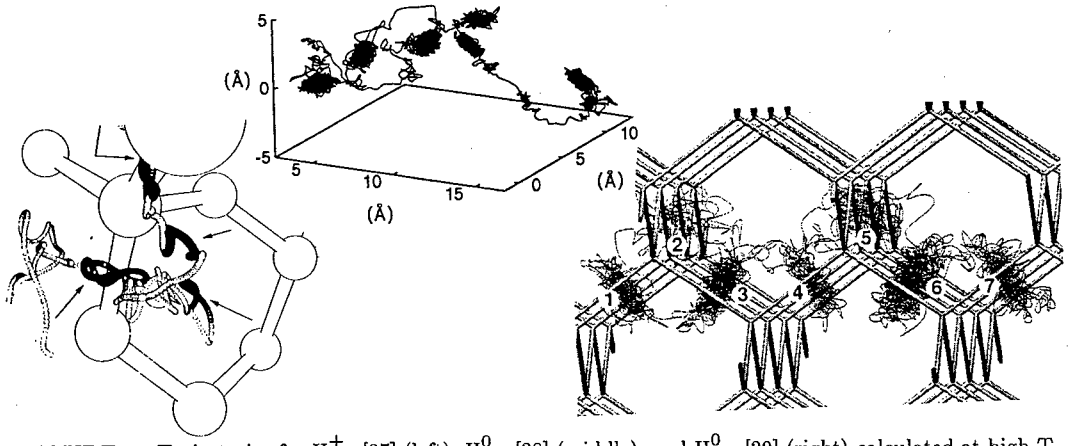


FIGURE 1: Trajectories for H^{+}_{BC}[27] (left), H^{0}_{BC}[28] (middle), and H^{0}_{BC}[29] (right) calculated at high T. The diffusion is characterized by rapid hops between BC sites after long times at one particular site.

Above $1,200\,K$ or so, the calculated diffusivities are in good agreement with the WW data. The most computer intensive calculation[27] produced just three values of the diffusivity, and all are above the WW value. It is possible that H_{BC} diffuses faster in the + than the 0 charge state, and that the measured value is the average diffusivity of several charge states in the sample, with H spending a fraction of the time as H^{+} and another as H^{0}. The fit of the three theoretical points to an Arrhenius law gives the activation energy for diffusion $E_a = 0.33 \pm 0.25\,eV$. The high-T diffusivities in Refs. [28,29] are remarkably close to the WW one ($D = 6.91 \times 10^{-3}\,\exp\{-0.45\,eV/kT\}\,cm^2/s$ in Ref. [28]). However, in Ref. [29] and below $1200\,K$, they drop substantially below the extrapolated WW value. It is not clear if the shift toward smaller values (which is experimentally observed) is to be expected in defect- and impurity-free Si. It is usually believed that the diffusion becomes trap-limited instead. Figure 2 shows the calculated diffusivities.

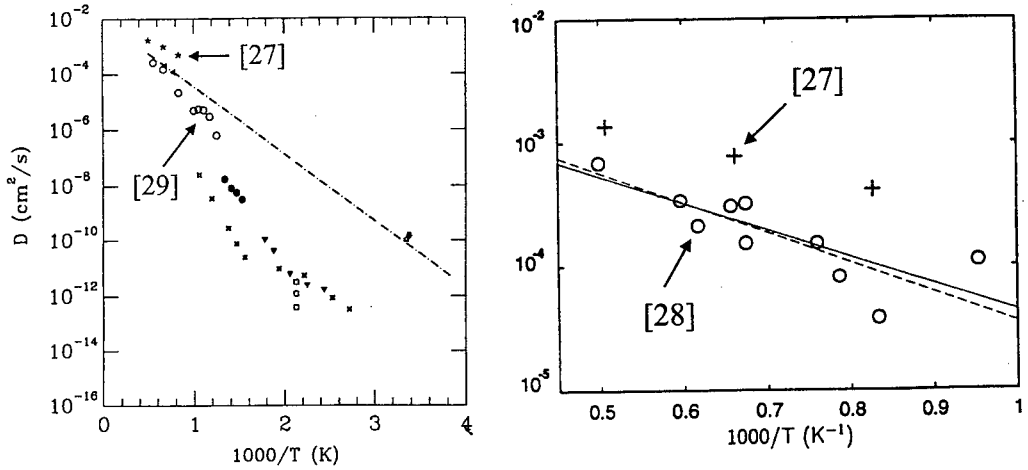


FIGURE 2: Diffusivity of H in Si. The line shows the extrapolation of the WW data. **Left:** the three stars are from Ref. [27], the open circles from Ref. [29]. The other points are various exprimental data. **Right:** the three crosses are from Ref. [27], the open circles from Ref. [28].

A final note from Ref. [30]: Park and co-workers report that while H^0_{BC} hops along BC–BC paths, H^0_T hops even faster along T–T paths. H^0_T is metastable, may be 0.5 eV or so above H^0_{BC}. However, a substantial relaxation of a Si–Si bond (typically, 2.35 to 2.85 Å) is required for H to reach a BC site. Given H^0_T, the BC site may be hard to reach, because H^0_T hops to an adjacent T site before two Si atoms have enough time to relax and render the BC site a minimum of the potential energy. This situation changes at very high T and/or near a strained region of the crystal (in Ref. [30], this was caused by interstitial O, and H^0_T readily self-traps at a BC site in the vicinity of O). Thus, the mobility of H may be unexpectedly high in some regions of the crystal. Thus, the issue of H diffusion in Si is still not fully understood.

The potential energy surfaces for H (obtained by quenching down to 0 K) show very substantial differences when calculated at different levels of MD theory. As expected, the CP method[27] predicts results that are very close to those obtained with various *ab-initio* (static) methods (for a review, see Ref. [39]). However, in Ref. [28], the minimum of the potential surface occurs for H^0_T (instead of H^0_{BC}), and the Si–H potential had to be scaled appropriately. On the other hand, in Ref. [29], the hexagonal interstitial site became a local minimum of the potential energy, almost degenerate with the BC site (at the *ab-initio* level,[39] the hexagonal site is always a saddle point of the energy for H). However, the methods seem to work much better at high temperatures.

Acknowledgements: The work of SKE is supported in part by the grant D-1126 from the R.A. Welch foundation and the contract RAD-7-17652-01 from the National Renewable Energy Laboratory. The work of PAF is supported in part by the NSF grant DMR 93-05344.

References.

1. S.K. Estreicher and P.A. Fedders, in *Computational Studies of New Materials*, ed. D.A. Jelski and T.F. George (World Scientific, Singapore, to be published).
2. D.A. Drabold, in *Amorphous Insulators and Semiconductors*, ed. M.F. Thorpe and M.I. Mitkova (Kluwer, Dordrecht, 1997).
3. See e.g., K. Scheerschmidt, D. Conrad, and U. Gösele, Comp. Mat. Sci. **7**, 40 (1996).
4. R.P. Feynman, Phys. Rev. **56**, 340 (1939).
5. L. Verlet, Phys. Rev. **159**, 98 (1967).
6. For a review of semiempirical methods, see A.E. Carlsson, Sol. St. Phys. **43**, 1 (1990).
7. F.A. Stillinger and T.A. Weber, Phys. Rev. B **31**, 5262 (1985).
8. See P. Vogel, H.P. Hjalmarson, and J.D. Dow, J. Phys. Chem. Sol. **44**, 365 (1983).
9. L. Goodwin, A.J. Skinner, and D.G. Pettifor, Europhys. Lett. **9**, 701 (1989); J. Mercer and M.Y. Chou, Phys. Rev. B **47**, 9366 (1993); Q. Li and R. Biswas, Phys. Rev. B **50**, 18090 (1994).
10. M. Menon and K.R. Subbaswamy, Phys. Rev. B **47**, 12754 (1993) and **48**, 8398 (1993).
11. L.M. Canel, A.E. Carlsson, and P.A. Fedders, Phys. Rev. B **48**, 10739 (1993).
12. M. Tang, L. Colombo, and T. Diaz de la Rubia, MRS Proc. **396**, 33 (1996).
13. P. Hohenberg and W. Kohn, Phys. Rev. **136**, 864 (1964); W. Kohn and L.J. Sham, Phys. Rev. A **140**, 1133 (1965).
14. G.B. Bachelet, D.R. Hamann, and M. Schlüter, Phys. Rev. B **26**, 4199 (1982).
15. R. Car and M. Parrinello, Phys. Rev. Lett. **55**, 2471 (1985).
16. R. Stumpf and M. Scheffler, Comp. Phys. Comm. **79**, 447 (1994); M. Brockstedte, A. Kley, J. Neugebauer, and M. Scheffler, Comp. Phys. Comm. (to be published).

17. O.F. Sankey and D.J. Niklewski, Phys. Rev. B **40**, 3979 (1989).
18. J. Harris, Phys. Rev. B **40**, 1770 (1985); W.M.C. Foulkes and R. Haydock, Phys. Rev. B **39**, 12520 (1989).
19. S. Goedecker and M. Teter, Phys. Rev. B **51**, 9455 (1995).
20. L. Colombo, Ann. Rev. Comp. Phys. **IV**, 147 (1996).
21. P. Ordejón, D.A. Drabold, R.M. Martin, and M.P. Grumbach, Phys. Rev. B **51**, 1456 (1995) and refs. therein.
22. See e.g., R. Car, P. Blöchl, and E. Smargiassi, Mat. Sci. For. **83-87**, 433 (1992).
23. S. Nose, Mol. Phys. **52**, 255 (1984) and J. Chem. Phys. **81**, 511 (1984).
24. P.L. Silvestrelli, A. Alavi, M. Parrinello, and D. Frenkel, Phys. Rev. Lett. **77**, 3149 (1996).
25. See e.g., T. Diaz de la Rubia and G.H. Gilmer, Phys. Rev. Lett. **74**, 2507 (1995).
26. C. Wang, Q.-M. Zhang, and J. Bernholc, Phys. Rev. Lett. **69**, 3789 (1992).
27. F. Buda, G.L. Chiarotti, R. Car, and M. Parrinello, Phys. Rev. Lett. **63**, 294 (1989).
28. D.E. Boucher and G.G. DeLeo, Phys. Rev. B **50**, 5247 (1994).
29. G. Panzarini and L. Colombo, Phase Trans. **52**, 137 (1994) and Phys. Rev. Lett. **73**, 1636 (1994).
30. Y.K. Park, S.K. Estreicher, and P.A. Fedders, in *Early Stages of Oxygen Precipitation in Silicon*, ed. R. Jones (Kluwer, Dordrecht, 1996), p. 179.
31. C.Z. Wang, C.T. Chan, and K.M. Ho, Phys. Rev. Lett. **66**, 189 (1991).
32. Y.K. Park, S.K. Estreicher, C.W. Myles, and P.A. Fedders, Phys. Rev. B **52**, 1718 (1995).
33. T. Sinno, Z.K. Jiang, and R.A. Brown, Appl. Phys. Lett. **68**, 3028 (1996).
34. P.E. Blöchl, E. Smargiassi, R. Car, D.B. Laks, W. Andreoni, and S.T. Pantelides, Phys. Rev. Lett. **70**, 2435 (1993).
35. M. Tang, L. Colombo, J. Zhu, and T. Diaz de la Rubia, Phys. Rev. B (in print).
36. S.K. Estreicher, J.L. Hastings, and P.A. Fedders, Appl. Phys. Lett. **70**, 432 (1997); J.L. Hastings, S.K. Estreicher, and P.A. Fedders, Phys. Rev. B (in print).
37. A. Van Wieringen and N. Warmoltz, Physica (Utrecht) **22**, 849 (1956).
38. S.J. Pearton, J.W. Corbett, and M.J. Stavola, *Hydrogen in Semiconductors* (Springer-Verlag, Berlin, 1992).
39. S.K. Estreicher, Mat. Sci. Engr. R **14**, 319 (1995).
40. N.M. Johnson, C. Herring, and C.G. Van de Walle, Phys. Rev. Lett. **73**, 130 (1994); C.H. Seager, R.A. Anderson, and S.K. Estreicher, Phys. Rev. Lett. **74**, 4565 (1995).

Materials Science Forum Vols. 258-263 (1997) pp. 179-184
© 1997 Trans Tech Publications, Switzerland

COMPARISON OF MUONIUM (HYDROGEN) DYNAMICS IN GERMANIUM AND SILICON

R.L. Lichti[1], K.H. Chow[2], S.F.J. Cox[3], T.L. Estle[4], B. Hitti[5], and C. Schwab[6]

[1]Department of Physics, Texas Tech University, Lubbock, TX 79409, USA
[2]Sherman Fairchild Labs, Lehigh University, Bethlehem, PA 18015, USA
[3]ISIS, Rutherford Appleton Laboratory, Chilton OX11 0QX, UK
[4]Department of Physics, Rice University, Houston, TX 77251, USA
[5]TRIUMF, Vancouver, BC V6T 2A3, Canada
[6]Centre National de la Recherche Scientifique, PHASE, 67037 Strasbourg, France

Keywords : Hydrogen, Muonium, Dynamics, Diffusion, Germanium, Silicon

Abstract. The dynamics of transitions among the various sites and charge states of muonium (Mu) in Si and Ge are compared. At high temperatures longitudinal depolarization data reveal rapid muonium charge cycles from repeated electron capture and ionization. In Ge separate 0/+ cycles involving Mu^0_{BC} and Mu^0_T begin near 200K, while a three–step cycle involving both neutral centers is observed above 400K in Si. An additional state joins the Ge charge cycles only above 350K. A site change from T to BC occurs near room temperature for Mu^0 in Si and much slower bi-directional Mu^0 site changes begin near 100K in Ge. BC to T site transitions accompanied by electron capture are seen in both materials. Details of the transition processes and the associated dynamic parameters are extracted and compared, and implications for the analogous hydrogen impurities are briefly discussed.

Introduction

Hydrogen is now well known to modify electrical and optical properties of semiconductors.[1] This occurs by formation of complexes with other impurities which moves defect related energy levels into or out of the gap. The dominant charge states of isolated hydrogen and their diffusion characteristics partially control these interactions. Even though much can be inferred regarding isolated hydrogen from the properties of H-related complexes, the most direct results are from studies of muonium (Mu), an unstable pseudo-isotope of hydrogen in which a positive muon replaces the proton.[2] We have investigated the dynamics of muonium in various semiconductors, focusing recently on Ge. The site-changes and charge-state transitions which govern diffusion of hydrogen have been identified. In this paper we compare Mu dynamics in Ge with our earlier results for Si.

In both Si and Ge, as well as many other semiconductors, muonium forms four distinct states, which we label as Mu^0_{BC}, Mu^+_{BC}, Mu^0_T, and Mu^-_T to identify the site and charge-state. The Mu^0 centers associated with the tetrahedral (T) interstices are far more mobile than any of the other states. The bond-centered (BC) configuration has the lowest energy for Mu^0 in silicon; however, theoretical calculations for Ge predict that the two neutral centers have very similar energies and suggest that relative site stabilities are reflected in hydrogen passivation effectiveness.[3] Level-crossing spectra [4] for Mu^0_{BC} and EPR results for H^0 in Si [5] have established the equivalence of H^0_{BC} and Mu^0_{BC}. Our recent work on Mu dynamics in Si [6-8] and GaAs [9,10] have shown that a series of charge-state transitions into and out of the highly mobile Mu^0_T state are crucial to the diffusive properties of Mu and H. We have investigated longitudinal depolarization rates related to rapid charge–state transitions in an ultra-pure germanium sample and have re-evaluated previous μSR spin precession data on Mu^0 centers. The present results show that the relationship between site changes and charge–state transitions is somewhat different for Ge compared to either Si or GaAs. More complete details of the data and analysis for Ge, and our arguments for state and transition assignments, will be published elsewhere; we concentrate here on results obtained thus far.

Charge–State Transitions

In silicon RF driven magnetic resonance measurements [7,8] in a series of n– and p–type samples yielded a full description of the dynamics for eight separate transitions among the four observed Mu states. All but one of these involve a change in the muonium charge state, the lone exception being a site change for Mu^0 from the metastable T-site to the BC ground state configuration. The single–site charge–state transitions $Mu^0_{BC} \rightarrow Mu^+_{BC}$ and $Mu^-_T \rightarrow Mu^0_T$ occur either by hole capture or by thermal ionization depending on doping concentrations and temperature, while the reverse transitions occur by electron capture. Additional e^- capture transitions were identified, accompanied by a BC to T site change resulting in $Mu^+_{BC} \rightarrow Mu^0_T$ and $Mu^0_{BC} \rightarrow Mu^-_T$ state changes. At very low temperatures optical excitation initiates a combined h^+ capture and site–change transition of $Mu^0_T \rightarrow Mu^+_{BC}$.[11] Above about 400K in intrinsic Si and shifted somewhat in doped samples, the electron capture and loss transitions become very rapid on the μs time scale leading to rapid cycles of the muonium charge state, muon–spin depolarization, and signal loss in traditional μSR spin precession or RF resonance measurements. Above the onset temperature for Mu charge cycles essentially all information is derived from depolarization rates in magnetic fields applied parallel to the initial muon spin direction.

A peak in the depolarization rate *vs* temperature, as shown for Si [6] and Ge in Fig. 1, provide the primary signature for these rapid cyclic Mu charge–state transitions. The magnetic field dependences (not shown) provide information pertinent to identifying the Mu^0 center involved in the cycle and properly scaling transition rates with the hyperfine frequency.[6] During each cycle a random e^- spin orientation is introduced into the combined (μ^+, e^-) spin system of Mu^0 upon e^- capture. This randomness is transferred to the muon during the Mu^0 lifetime by the hyperfine interaction, thereby decreasing the muon polarization. Each cycle is most effective as a depolarization source when the neutral–state lifetime matches the hyperfine period. Fits of the full temperature and field dependences of the measured longitudinal depolarization rates yield the hyperfine constant, thus the Mu^0 identity, and the rates for both transitions in a two–state cycle, or equivalently parameters for the temperature dependence of those rates.

Silicon: A two–state description of the charge–cycle depolarization identified Mu^0_T as the active center in Si even though the BC configuration is the neutral ground state.[6] Subsequent comparison of transition rates from RF resonance data at lower temperatures [7] confirmed a three–state cycle initiated by ionization of Mu^0_{BC} to Mu^+_{BC} with an energy of 0.22eV, followed by e^- capture along with a site change to the metastable Mu^0_T with a net activation energy of 0.40eV, and completed by the Mu^0 site change back to the BC ground state with a barrier of 0.38eV. The depolarization takes place in the Mu^0_T stage ($A_T \simeq 2000$MHz) since at these temperatures the Mu^0_{BC} lifetime is extremely short compared to its hyperfine period ($A_{BC} \simeq 100$MHz) such that minimal loss occurs in the BC state. In n-type Si we do see depolarization from a 0/+ charge cycle at the BC site just above Mu^0_{BC} thermal ionization at 150K. At temperatures where the three–state cycle is observed, this BC charge cycle also causes no depolarization.

Additionally in n–type samples Mu^-_T is formed via e^- capture by Mu^0_T and is very stable at low temperatures. For donor concentrations above the mid–$10^{14} cm^{-3}$ range this fraction is large enough that Mu^-_T ionization to Mu^0_T is observed, giving an ionization energy of 0.66eV in the latest fits. Combining all of this information we conclude that the true muonium charge dynamics in silicon are quite complicated. At high temperatures extremely rapid, but essentially invisible, e^- capture/ionization cycles occur in the BC configuration, with an occasional three–state cycle initiated by e^- capture into the mobile T-site neutral which produces the observed muon depolarization. In heavily–doped n–type samples Mu^-_T dominates the diamagnetic Mu fraction at temperatures below its ionization, but once ionization occurs that fraction appears to join existing 0/+ charge cycles in all samples examined to date. An additional depolarization mechanism is present in n-type materials, known as spin–exchange or spin–flip scattering between conduction electrons and Mu^0 centers. This process yields features very similar to charge cycles, and needs to be correctly included in depolarization analysis. We have not thus far re-analyzed all of the existing depolarization data on Si with complete charge–state and spin flip scattering dynamics included.

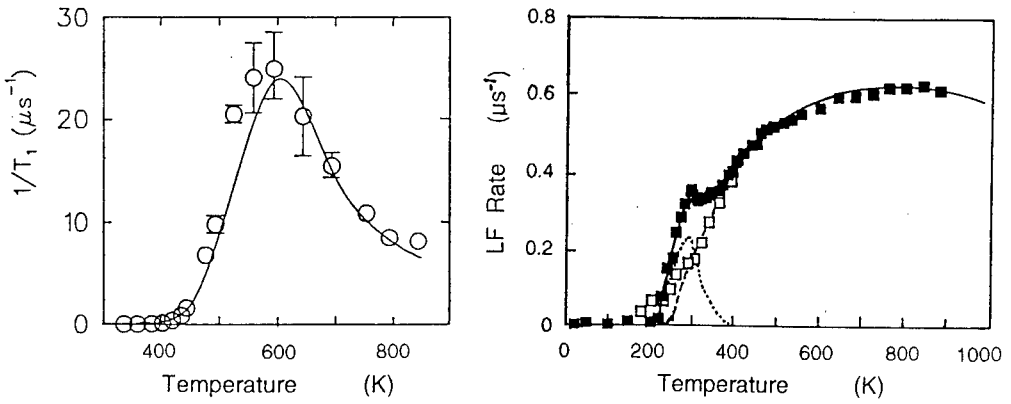


Figure 1. Low–field temperature–dependent longitudinal muon–spin depolarization rates related to rapid muonium charge–state cycles for intrinsic samples of (a) Silicon, and (b) Germanium. Transverse field μSR spin–precession relaxation rates are included in (b) up to 400K. The curves are from fits to a two–state model, with two separate cycles required in Ge.

Germanium: The situation is somewhat different for Ge, with two peaks clearly seen in the depolarization data of Fig. 1b for the intrinsic sample. The field dependence of these rates shows a definite change in details in the region between 300 and 400K verifying a change in the dynamics. In attempting to fit these data to the two–state model we found that the data from 350K to the highest temperatures gave consistent results while below 350K we obtained considerably different parameters. Extending the high temperature fits below 350K gave a curve which fell very close to the rapid rise in the transverse–field μSR relaxation rates shown in Fig. 1b. We therefore included transverse field points from roughly 300K onward in a final fit for the high temperature charge cycle. Parameters from the temperature dependence and field dependences at 350K, 410K, 501K, and 603K were then compared for consistency. These parameter sets fell within overlapping error estimates, confirming that each curve was probing the same physical processes. We then substracted the resulting curve from the lower temperature data and fitted the remainder to a second two–state charge cycle.

The hyperfine parameters from initial fits indicated that the higher temperature cycle was due to depolarization at Mu_T^0 and fit attempts using specific process assignments implied an electron ionization and capture cycle involving a positive charge state, theoretically expected to be Mu_{BC}^+. Based on the Si results, the capture step should be activated: however, fits to an activated rate yielded a slightly negative barrier when standard expressions for the ϵ^- concentration and a constant capture cross section were included. An alternative is to allow the total process cross section to vary more generally with temperature, which gave a better fit and cross sections which decreased as T^{-2}. Carrier capture processes initiated by optical illumination of Ge at low temperatures also appear to show combined charge and site changes with little or no thermal energy involvement.[11] We have chosen to use this latter fit in reported results although the interpretation remains open. The $Mu_T^0 \rightarrow Mu_{BC}^+ + \epsilon^-$ transition process implied by the higher temperature charge cycle in Ge yields a "thermal ionization" energy of about 0.170eV more or less independent of the expression for capture rates, the precise hyperfine parameter, or the subset of the relevant data which was used. This value was also obtained from the rise of diamagnetic spin–precession amplitude near 200K assuming a Mu_T^0 ionization process.[2] It is however, two orders of magnitude greater than the energy from relaxation rates related to the disappearance of the Mu_T^0 spin–precession signal near 100K.[2] This disagreement in the transverse field μSR data has remained a problem for over a decade. The charge–cycle data and the robustness of the fit results for the ionization step confirm the larger value as the Mu_T^0 "ionization" energy with the stipulation that the overall process most likely includes a site change for the muon, not just loss of an electron.

Fits of the remaining smaller peak near 300K show that a much smaller hyperfine constant is required, on the order of 50 to 100MHz, consistent with an assignment of Mu^0_{BC} as the relevant neutral center. Using our best fit to the temperature dependence data for the main cycle as the subtraction function, this second peak yields a Mu^0_{BC} ionization energy of 0.215eV and a constant capture cross section of about 2500Å^2 over the relatively narrow region where this cycle is visible. These parameters are thus assigned to a 0/+ charge cycle with the muon remaining in the BC configuration. Parameters listed in Table 1 are from a best fit to the data in Fig. 1b; slightly different but consistent values are obtained using the constant–temperature field dependences as well.

An additional diamagnetic Mu state is apparent in the Ge longitudinal depolarization data. This state constitutes 14 to 17% of the muons as a "prompt" fraction and is non-relaxing in both longitudinal and transverse field measurements. Its intensity is transferred into the charge cycles between 350 and 400K with an activation energy of 0.75eV which is greater than the Ge band gap at those temperatures. A Mu^-_T state might be a possibility for this center; however, we argue that if the measured energy is related to thermal loss of a electron from Mu^- it implies an energy level outside the gap for which such a process would not be expected. We have therefore concluded that this signal is most likely related to a bound state of Mu with an impurity. Since ultra-pure Ge may contain electrically inactive impurities such as silicon, carbon, or oxygen to levels approaching $10^{14} cm^{-3}$, muonium paired with one of these impurities becomes a good candidate for this additional state. Furthermore, in time–integral RF-μSR data on the same sample, a state with a very similar temperature dependence dominates the diamagnetic intensity, amounting to roughly 50% of the implanted muons. The increased amplitude for later times implies slow formation of that state and appears to be fully consistent with a model in which the highly mobile Mu^0_T encounters an impurity and is trapped. This probably occurs via charge–exchange scattering and coulomb capture, although we have no direct evidence to support this amount of detail. In Ge samples intentionally doped with Si the low–temperature μSR relaxation rates for Mu^0_T increase proportional to the Si concentration, consistent with this type of interaction with an iso-electronic impurity.[2]

Mu^0 Site Transitions in Ge

In silicon the observed Mu^0 site transition was found to be intimately involved in the visible high–temperature charge cycle; however, for germanium the charge cycles occur separately with each neutral communicating with a common Mu^+ state. Assuming the assignment of ionization energies obtained from the charge–cycle data is correct, we are still left with the question of low energies associated with the disappearance of the Mu^0 spin–precession signals at much lower temperatures. Both μSR signals rapidly broaden and become invisible above about 100K. Our re-analysis combining all the published data (References in [2]) yield 0.019eV for Mu^0_T and 0.030eV for Mu^0_{BC} with frequency prefactors below 100MHz in both cases. Bi-directional site changes are the best candidates for these features if one rules out ionization. This assignment is consistent with a common disappearance if the site energies are essentially identical as predicted. Additional support comes from a fit of the longitudinal relaxing amplitudes in the range of 10 to 150K well below the onset of charge cycles. We used a simplified model for the depolarization due to Mu^0 site changes and obtained slightly higher energy barriers and lower prefactors, but overall consistent results. The above barrier heights imply that the BC configuration remains slightly preferred for Mu^0 in germanium, but that the barrier between the two sites is extremely small compared to the analogous barriers in silicon or diamond. Additionally, the low prefactors suggest that these transitions may be initiated in Ge by accoustic phonons rather than by optical phonons as in the other two elemental materials. The muonium motion in going from BC to T is most likely normal to the bond direction, which is relatively unimpeded structurally. Upon comparing the various muonium transition rates in gemanium we find that although Mu^0 site changes begin at fairly low temperatures they remain quite slow due to the small prefactors and are much slower than either Mu^0 ionization rate well below the 220K onset of cyclic charge–state transitions.

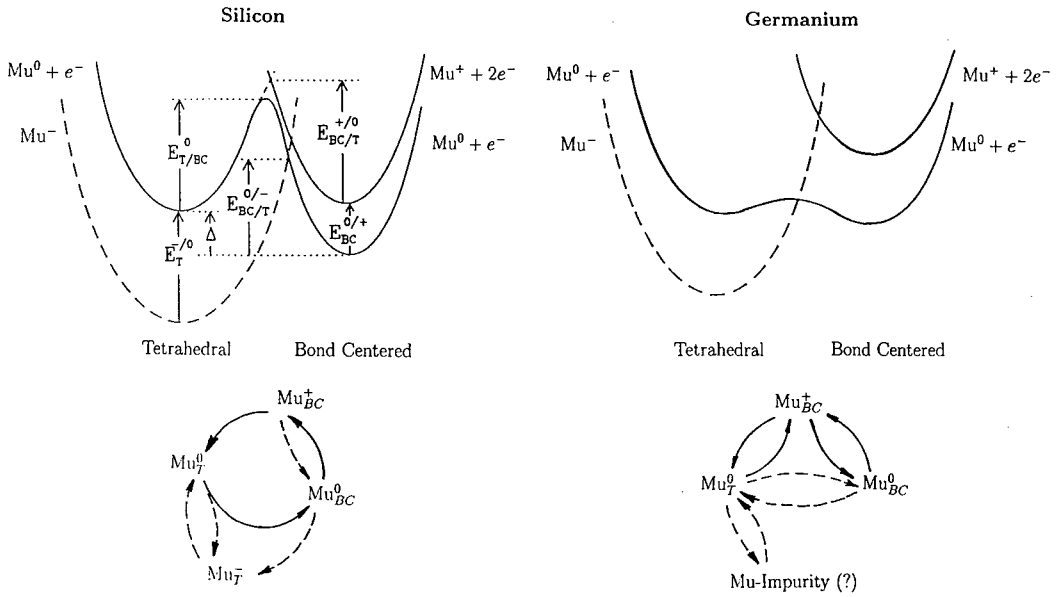


Figure 2. Configuration coordinate diagrams for muonium or hydrogen in (a) Silicon and (b) Germanium resulting from the dynamics of the observed Mu transitions along with a schematic representation of those transitions. Full lines show the dominant cycles related to diffusion. Measured energy parameters are given in Table 1.

Conclusions

We have analyzed longitudinal muon-spin depolarization rates for an intrinsic germanium sample, finding evidence for two separate 0/+ muonium charge-state cycles which are active above 200K. A small rate peak near 300K is assigned to a $Mu^0_{BC} \rightleftharpoons Mu^+_{BC} + e^-$ electron ionization and capture cycle, and a much broader and higher-temperature peak is associated with a similar $Mu^0_T \rightleftharpoons Mu^+_{BC} + e^-$ cycle. The ionization energies resulting from this analysis are two orders of magnitude larger than the energies associated with the common low-temperature disappearance of the Mu^0_{BC} and Mu^0_T transverse-field μSR signals which we have re-assigned to bi-directional T $\rightleftharpoons$ BC site transitions for Mu^0. Additional checks support this assignment. We have indirect evidence for a pairing interaction of muonium with an electrically inactive impurity, which we suggest may be Si, C, or O, known to be present at significant levels in

Table 1. Comparison of Mu energy parameters in Si and Ge and the transition processes from which they were derived. The Si values are from RF-μSR results [7,8] and Ge values are from this work.

Mu Transition	Parameter	Silicon	Germanium
$Mu^0_{BC} \rightarrow Mu^+_{BC} + e^-$	$E^{0/+}_{BC}$	$0.22 \pm 0.01 eV$	$0.215 \pm 0.009 eV$
$Mu^0_T \rightarrow Mu^+_{BC} + e^-$	$E^{0/+}_{T/BC}$	two steps	$0.174 \pm 0.003 eV$
$Mu^-_T \rightarrow Mu^0_T + e^-$	$E^{-/0}_T$	$0.66 \pm 0.07 eV$	
$Mu^0_T \rightarrow Mu^0_{BC}$	$E^0_{T/BC}$	$0.38 \pm 0.04 eV$	$0.019 \pm 0.002 eV$
$Mu^0_{BC} \rightarrow Mu^0_T$	$E^0_{BC/T}$		$0.030 \pm 0.005 eV$
$Mu^0_{BC} + e^- \rightarrow Mu^-_T$	$E^{0/-}_{BC/T}$	$0.30 \pm 0.01 eV$	
$Mu^+_{BC} + e^- \rightarrow Mu^0_T$	$E^{+/0}_{BC/T}$	$0.40 \pm 0.02 eV$	zero

electronically ultra-pure germanium. This bound state dissociates near 350K yielding a binding energy of 0.748 ± 0.002eV according to our fit to the disappearance of a non-relaxing fraction in the depolarization measurements. Fairly convincing evidence of bound Mu states and the mobility features discussed below suggest that neutral Mu (and probably H) should have no trouble reaching impurities. Similar information regarding the charged centers must await ongoing experiments on doped germanium.

A summary of the results to date for muonium transition dynamics in Si and Ge are presented in Fig. 2 with energy values compared in the accompanying table. In addition, carrier–capture cross sections are consistent with direct geometric interactions (10-20Å^2) for capture by neutral centers, while those for capture by the charged centers are very much larger (2000-3000Å^2) fully consistent with Coulomb capture. This agreement with expectations gives added confidence that we have properly identified transition processes and have used appropriate expressions for transition rates.

In comparison to muonium behaviour in Si, the current results for Ge indicate very much smaller barriers to Mu^0 site changes and indicate that the Mu^0 configuration energies are essentially equal in the T and BC locations as predicted theoretically. These results further imply that muonium diffusion, and by analogy hydrogen diffusion, as a neutral atom procedes through both sites, although the T-site species is highly mobile in its own right. The dominant Mu charge cycle for Ge implies that high–temperature diffusion of Mu and H is dominated by motion of the T-site neutral center even when it is not the equilibrium state. This result is very similar to the diffusive behaviour which we previously concluded occurs in Si and GaAs, although the details are somewhat different for each material. We strongly suspect that this will prove to be a general conclusion for high–temperature hydrogen diffusion in most semiconductors for which the mobility of a T-site neutral hydrogen or muonium far exceeds that of any of the other centers.

Acknowledgements

Portions of this work have been supported by the United States National Science Foundation, The Robert A. Welch Foundation, the Engineering and Physical Sciences Research Council of the United Kingdom, the Natural Sciences and Engineering Research Council of Canada, and a NATO Collaborative Research Grant.

References

[1] *Hydrogen in Compound Semiconductors*, ed. by S.J.Pearton, Mat. Sci. Forum **148-149** (1994).
S.J.Pearton, J.W.Corbett, M.Stavola, *Hydrogen in Crystalline Semiconductors* (Springer, 1992).
Hydrogen in Semiconductors, ed. by J. Pankove and N.M. Johnson (Academic Press, 1990).
[2] A review of older data on Mu in semiconductors: B.D. Patterson, Rev. Mod. Phys. **60**, 69 (1988).
[3] S.K. Estreicher and Dj.M. Maric, Phys. Rev. Lett. **70**, 3963 (1993).
[4] R.F. Kiefl, *et al.*, Phys. Rev. Lett. **58**, 1780 (1987); Phys. Rev. Lett. **60**, 224 (1988).
[5] Yu.V. Gorelkinski and N.N. Nevinnyi, Zh. Tekh. Fiz. **13**, 105 (1987).
B. Bech-Nielsen *et al.*, Mat. Sci. Forum **143-147**, 909 (1994).
[6] K.H. Chow, *et al.*, Phys. Rev. B **47**, 16004 (1993).
[7] S.R. Kreitzman, *et al.*, Phys. Rev. B **51**, 13117 (1995).
[8] B. Hitti, *et al.*, Hyperfine Int. **105**, 321 (1997).
[9] R.L. Lichti, Phil. Trans. A **350**, 323 (1995).
[10] K.H. Chow, *et al.*, Phys. Rev. Lett. **76**, 3790 (1996).
[11] R. Kadono, *et al.*, Phys. Rev. Lett. **73**, 2724 (1994); Hyperfine Int. **105**, 303 (1997).

Materials Science Forum Vols. 258-263 (1997) pp. 185-190
© 1997 Trans Tech Publications, Switzerland

HYDROGENATION AND PASSIVATION OF B IN Si BY BOILING IN WATER PRESSURIZED UP TO 10 ATM

Y. Ohmura, K. Abe, M. Ohtaka, A. Kimoto and M. Yamaura[1]
Department of Electronic Engineering, Iwaki Meisei University,
[1] Department of Fundamental Science, Iwaki Meisei University,
Iwaki, Fukushima 970, JAPAN

Keywords : hydrogen, acceptor, passivation, Si, B, water boiling

Abstract. It has been found, by C-V profiling, sheet-resistivity or IR-absorption measurements, that passivation of B in Si by high-pressure water boiling for 6 hrs is enhanced up to 8 atm, but, beyond 8 atm, it decreases. This hydrogenation behavior is understood in terms of competing, high-temperature annealing effect. The annealing rate shows an activation energy of 0.7 eV, which may be associated with dissociation of H from the passivated B center.

Introduction.

Hydrogen in semiconductors has been an attractive subject for more than three decades. It is well known that hydrogen incorporated in p-type semiconductors passivates or neutralizes the electrical activity of acceptors[1]. Hydrogenation or passivation has been confirmed through measurements of sheet- or spreading resistance, C-V carrier profile, infrared free hole absorption or hydrogen-acceptor local vibration mode. Hydrogen injection has mostly been performed by the exposure of samples heated at several hundred ℃ to hydrogen plasma. Tavendale et al. have boiled p-type silicon wafers with different resistivities at atmospheric pressure and have shown, by the C-V carrier profile, that the hole concentration decreased near the surface region due to neutralization of acceptors[2]. Recently, we showed that more elevated-temperature(～120 ℃) boiling enhances the hydrogenation and results in significant modification of B-doped Si comparable with hydrogen-plasma processing[3]. In this work, hydrogenation experiment has been extended to 10 atm and 180 ℃. Annealing effect on hydrogenated samples has also been studied.

Experimental.

Samples used are 0.5 Ω cm boron-doped p-type silicon wafers for C-V measurement and boron-implanted ones for sheet resistivity and IR absorption measurements. A dose of 1×10^{16} ^{11}B ions/cm^2 were implanted at 100 keV into 10 Ω cm n-type Si wafers. Implanted wafers were annealed at 1000 ℃ in an N_2 atmosphere. The junction depth was measured at 1.5 μ m using spherical drilling and staining techniques. High-pressure boiling was performed in deionized water in a stainless-steel autoclave which can operate up to 200 ℃ and 100 atm and is equipped with a stirring propeller. The autoclave was heated from the outside. The water temperature, not the pressure, was controlled at fixed values. The pressure measured by the Bourdon-tube pressure gauge at a temperature was almost the same as that reported as the temperature-pressure relationship. Before boiling, the wafers were etched in an HF solution for the native oxide removal. After boiling, Al was

evaporated both on the front surface (through the stencil mask) and the rear surface for the Schottky and Ohmic contacts, respectively, for the C-V measurement, without further etching. Some of the p^+-n wafers boiled were employed for annealing experiment. Annealing was performed in an Ar gas in a gold-plated furnace.

Results.

Figure 1 shows C-V carrier profiles for samples boiled at different pressures for 6 hrs. As the boiling pressure(temperature) increases from 4 to 5 and 8 atm, the hole concentration decreases more and more. However, when the pressure increases further to 9 atm, the hole concentration again begins to increase. At 10 atm, the concentration rather approaches that for unboiled samples.

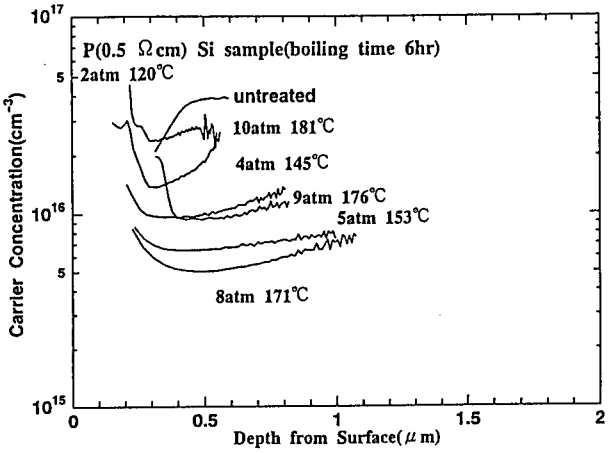


Fig. 1 C-V carrier profile for p-Si wafers boiled at different pressures for 6 hrs.

Figure 2 shows sheet resistivities for p^+ layers of B-implanted p^+-n wafers as a function of boiling pressure. The wafers have also been boiled for 6 hrs. The sheet resistivity starts from about 16 Ω/□ for the unboiled sample and increases to a value as high as 27 Ω/□ at 8 atm, which indicates that about 38 % of $1\times10^{16}/cm^2$ implanted B acceptors in Si have been neutralized, provided the hole mobility does not change during boiling. However,

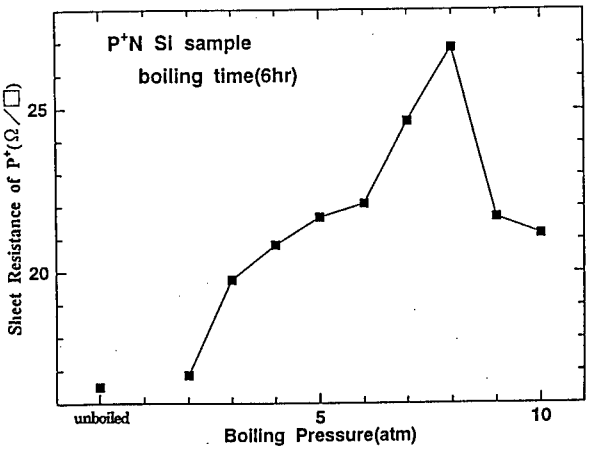


Fig. 2 Sheet resistivity of p^+-n wafers as a function of boiling pressure (6 hrs boiling).

as the boiling pressure exceeds 8 atm, the sheet resistivity suddenly decreases. This behavior is similar to that in Fig. 1 for C-V carrier profiles for p-type wafers. Evidence that the sheet resistivity increase is due not to hole mobility degradation but to hole concentration decrease is given by the IR free carrier absorption. Figure 3 shows room-temperature

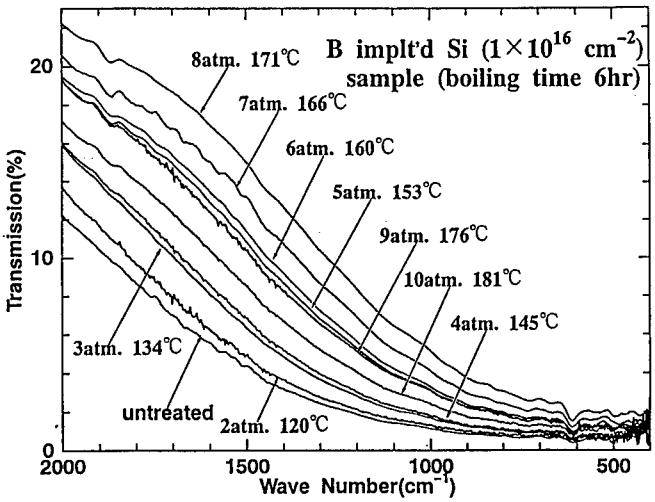


Fig. 3 IR absorption for p^+-n wafers boiled for 6 hrs at different pressures.

IR absorption spectra for the same wafers as used in Fig. 2. In the unboiled sample, the transmission is the least due to the ample, 1×10^{16} holes/cm^2. As the boiling pressure increases from 2 atm, the hole concentration decreases due to neutralization of B, and hence the transmission increases. It is observed that, for some of the spectra where the transmission has highly increased, there is a small dip due to ^{11}B-H local vibration mode at about 1870 cm^{-1}. The transmission increase, however, ends at 8 atm and drops towards 9 and 10 atm. The behavior in Fig. 1 through 3 that neutralization due to 6 hrs boiling reaches the maximum at 8 atm and decreases beyond 8 atm, differs from the behavior forecast at 2 atm boiling[3] that the higher is the boiling pressure and hence the temperature, neutralization develops further. The ion product of H-related species in water, $[H^+][OH^-]$ continues to increase in this temperature range[4]. An annealing experiment has been

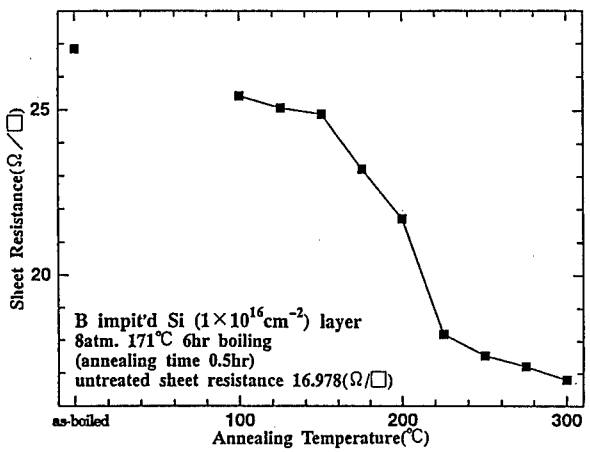


Fig. 4 Annealing behavior of sheet resistivity for 8 atm 6 hrs boiled wafer.

performed. Figure 4 shows a plot of the sheet resistivity against the annealing

temperature for one of the most passivated p^+-n wafers which was boiled at 8 atm for 6 hrs. Annealing was performed isochronally for 30 min in a gold-plated furnace with a flow of Ar gas. It is observed that annealing of H-passivated B takes place, though very slightly, at a temperature as low as 100 ℃. However, the main annealing stage seems to exist near 200 ℃, for 30 min annealing. Stavola et al have reported a result of an isochronal annealing similar to Fig. 4 for B-implanted surface layers[5]. The IR free hole absorption curves corresponding to this sheet resistance annealing one is shown in Fig.5.

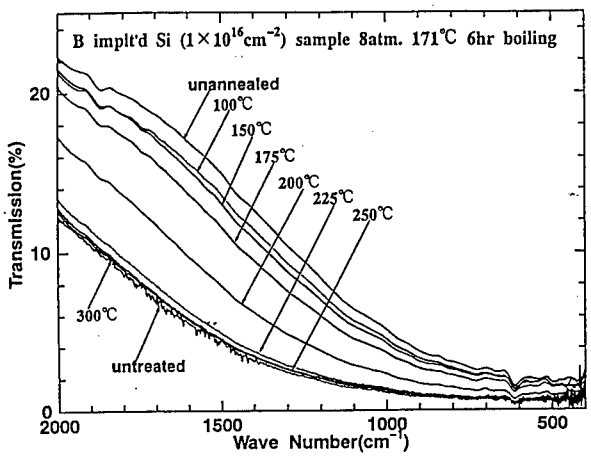


Fig. 5 IR absorption curves for hydrogenated p^+-n wafers showing the change during annealing.

In Fig. 5, the least absorption(best transmission) curve is of course that for unannealed sample which is subject to 8 atm, 6 hrs boiling. As the annealing temperature increases, the transmission degrades. It is observed that the transmission shows a drastic decrease from 175 ℃ to 225 ℃, which corresponds very well to the sheet resistivity annealing behavior in Fig. 4.. In order to investigate the annealing behavior fundamentally, an isothermal annealing experiment has been performed.

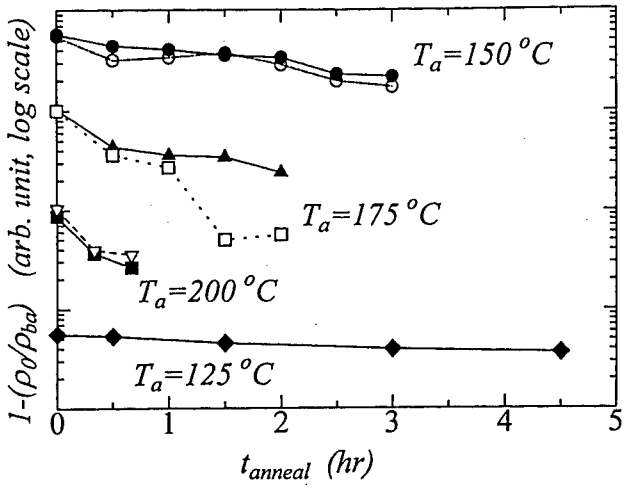


Fig. 6 Fractional sheet resistivity change with annealing time.

Figure 6 shows the fractional sheet resistivity change with the isothermal annealing time from 125 ℃ to 200 ℃ for 2 atm boiled, hydrogenated wafers. It is found that the annealing proceeds exponentially with the annealing time. The vertical axis ($1-\rho_0/\rho_{ba}$) corresponds to the fractional concentration of hydrogenated B atoms, where ρ_0 and ρ_{ba} denote sheet resistivities for unboiled and boil-annealed wafers, respectively. Figure 7 shows these annealing rates as a function of annealing temperature. It has been found that

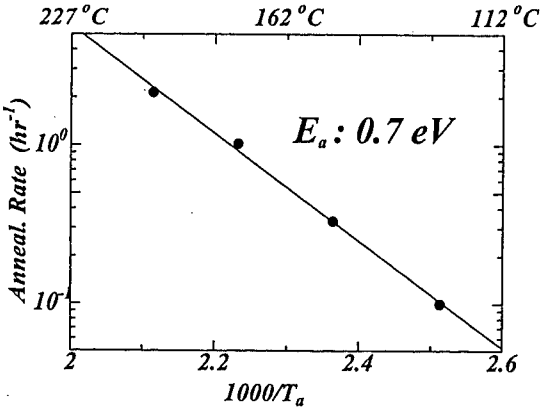


Fig.7 Annealing rate as a function of temperature.

the annealing rate exhibits an activation energy of 0.7 eV. This activation energy is almost the same as a dissociation energy for the B-H complex by Herrero et al[6], but is somewhat small compared with that determined through C-V measurement reported by Zundel and Weber[7], which might be due to a large B concentration difference between B implanted layer and normally B doped wafer.

Summary.

The C-V carrier profile for p-type Si wafers and sheet resistivity and IR free hole absorption as a function of boiling pressure(temperature) show that, for 6 hrs boiling, hydrogenation increases with pressure up to 8 atm, but decreases towards 9 and 10 atm. On the other hand, the dissociation of H from the passivated B accelerates with increasing temperature(pressure). Thus, it may be understood that the above mentioned passivation behavior is the result of two competing processes, neutralization due to the increase of H-related species in water with temperature and the enhanced annealing of passivated B at the elevated temperature. It is found that the annealing rate has an activation energy of 0.7 eV, which may be associated with dissociation of H from passivated B.

References.

1. "Hydrogen in Crystalline Semiconductors" ed. S. J. Pearton, J. W. Corbett and M. Ṣtavola (Springer-Verlag, Berlin, 1992).
2. A. J. Tavendale, A. A. Williams, and S. J. Pearton, Appl. Phys. Lett. **48**, 590(1986).
3. Y. Ohmura, Y. Otomo, Y. Tago, N. Terakado, and T. Satoh, Appl. Phys. Lett. **67**, 64(1995).
4. "Electrochemical data" ed. D. Dobos (Elsevier Scientific Publishing Co. Amsterdam (1975).

5. M. Stavola, S. J. Pearton, J. Lopata, and W. C. Dautremont-Smith, Phys. Rev. **B 37,** 8313(1988).
6. C. P. Herrero, M. Stutzmann, and A. Breitschwerdt, Phys. Rev. **B 43**, 1555(1991).
7. T. Zundel and J. Weber, Phys. Rev. **B 39**, 13549(1989).

Materials Science Forum Vols. 258-263 (1997) pp. 191-196
© 1997 Trans Tech Publications, Switzerland

LOW TEMPERATURE HYDROGEN DIFFUSION IN SILICON: INFLUENCE OF SUBSTRATE QUALITY AND THE SURFACE DAMAGE

M. I . Symko, Bhushan L. Sopori, Robert Reedy, and Kim M. Jones

National Renewable Energy Laboratory, 1617 Cole Boulevard, Golden, CO 80401, U.S.A.

Key words: hydrogen, silicon, passivation, diffusion

Abstract

Hydrogen passivation of defects and impurities is becoming a necessary step for achieving high efficiency solar cells on materials from some photovoltaic (PV) vendors[1,2]. Even though hydrogen passivation is a common technology, relatively little is known on the diffusion and passivation mechanisms of hydrogen in silicon. For example, it is not known why solar cells fabricated on the material from some vendors improve considerably more than others. Vendors who utilize this passivation may see a 20% increase in the cell performance, making it a remarkable process for those who benefit. There are other intriguing observations, the degree of passivation for solar cells fabricated on the material from the same vendor vary with the hydrogenation technique. Likewise, if the growth parameters of the material are changed, the degree of passivation can also change.

Introduction

Recently, it has been observed that passivation of impurities and defects can occur as a byproduct of nitridation by a PECVD process, and during annealing Al contacts in a forming gas ambient. While the traditional techniques of hydrogenation such as ion implantation, and plasma processes have yet not been well understood, possibility of low temperature diffusion from a molecular ambient or deep diffusion from a short exposure to hydrogen ions in a PECVD are clearly challenging and important from a technological view point.

A partial answer to these questions came from the proposed hypothesis that a vacancy mechanism is involved in the diffusion of hydrogen at low temperatures[3]. It suggests that a process, which injects vacancies during hydrogenation, can be very efficient passivating technique. This mechanism concurs with the finding that the vacancy is one of the strongest traps for hydrogen and can readily form complexes with specific defects and impurities[3]. Furthermore, some theoretical support to this mechanism comes from Hartree Fock type of ab initio calculations that show a (V-H) complex has a lower migration barrier compared to the interstitial H[4].

This paper describes our studies aimed at developing better understanding of the mechanisms that lead to the dependence of hydrogen passivation on the (i)

material quality and (ii) occurrence of passivation when a solar cell is annealed in a FG ambient. Because deep diffusion of hydrogen is a prerequisite for passivation, the initial work has emphasized studies on the diffusion behavior of hydrogen. We show that the value of hydrogen diffusivity depends on the substrate quality, in particular on the concentration of frozen-in, vacancy-related defects. We also show that the damage created during the passivation technique or by processes that precede device formation (such as formation of an N/P junction), is instrumental in hydrogen diffusion.

Experimental

In order to determine the influence on substrate quality we have measured diffusivity of deuterium in silicon samples obtained from different vendors. These samples had different C and O concentrations, and crystal growth speed. They consist of Czochralski (CZ), float zone (FZ), cast polycrystalline (CP), edge defined growth (EFG) ribbon and laser recrystallized (LRC) ribbon. These samples were all in the resistivity range typically used for solar cells, about 1 Ω-cm. Deuterium was diffused by low energy implantation at 1.5 KeV, 250 °C, for 30 minutes, and the depth profiles were measured by SIMS.

To understand the role of the surface damage on the diffusivity, a detailed study was executed in which the samples were given different degrees of surface damage and annealed in hydrogen or deuterium bearing gas. The surface damage was introduced by mechanical polishing on a silicon carbide pad or by polishing with Al_2O_3 grit on a Suba IV pad. Grit sizes (ranging from 10 um to 0.01 um), pressure, and polishing times were used to control the degree of damage. The samples were then annealed in a forming gas containing deuterium or hydrogen. Similar samples, but without the surface damage, were annealed in the same runs as reference samples.

Sample's were prepared under the following conditions, we will call this the standard anneal:

- Damage free polish[5] followed by a low pressure mechanical 0.3 um (desired grit) grit surface damage
- Removal of oxide layer by HF
- FG anneal @ 400 ° C for 1 hour, followed by a rapid cool down.

Silicon substrates with a N/P junction from American Solar Energy (EFG ribbon) were also included. However, these samples were not mechanically damaged.

RESULTS

Our objective was to examine if the results agree with the proposed diffusion model that invokes vacancy assisted diffusion. This model of vacancy assisted diffusion is depicted in Figure 1. In this model, the molecular hydrogen dissociates as a result of interaction with the vacancies available due to surface

damage, and diffuses into the bulk as H^+ or {H-V}. We propose that vacancies are also available in the bulk of the material that can form additional {H-V} complexes and assit in the diffusion of hydrogen. This suggests that material containing high concentrations of vacancy related defects will have deeper penetration of hydrogen in a given process, thus leading to a better passivation. This mechanism explains all observations on hydrogen passivation. For example, a rapid diffusion of hydrogen during nitridation is expected because nitridation injects vacancies and that some surface damage is inevitable during a PECVD process. Theoretical calculations have shown that the formation of the {H-V}. complex is favored to that of the Si-H bond by more than 2 eV[6].

In the following section we will discuss how this model can explain experimental observations.

(i) ***Substrate Quality***

Figure 2 shows the measured diffusivity of Si samples from various vendors. These materials are CZ, FZ, cast polycrystalline, EFG (RP1), and LRC(RP2). It can be concluded that the diffusivity varies from PV silicon material to single crystal silicon material. The highest diffusivity is for that of the LRC, with a growth rate of 2.54 cm per minute, with low C & O concentrations of < 1 ppma each. The EFG material was next highest with a rate of 1.27 cm per minute and a high C concentration. The cast poly was grown at a rate of 1 mm per minute. The CZ and FZ material were both grown at low rates. This leads to a strong conclusion that the diffusivity increases with an increase in crystal growth speed, increase in C concentration and a decrease in O concentration - conditions that favor vacancy formation in the crystal growth.

(ii) ***SurfaceDdamage***

The initial in-diffusion of molecular hydrogen with a surface damage was found to be quite intriguing. Starting with a hydrogen rich surface, molecular hydrogen is thought to be split into its atomic form by a surface damage, as illustrated in the diffusion model of figure 1. Figure 3 shows the SIMS deuterium profiles of samples with and without surface damage. The damage was produced with a 10 um grit. Clearly, a deep diffusion of D occurs with the presence of surface damage. Although polishing with a 10 μm grit may appear quite a severe condition, TEM and SEM analyses have shown the surface roughness was less than 2 μm and that the damage was confined to less than 0.2 μm. With a surface roughness on the order of a few tenths of a micrometer, one can expect a preponderance of vacancies at the surface. With this type of surface, fast H^+ or {H-V} diffusion will occur.

Characterization by TEM was done to determine the degree of surface damage produced from the various grits and by a P/N junction. These results showed that a polishing procedure creates a surface roughness and a lattice damage (or a stress) similar to that of the P/N junction. The surface roughness (and damage) is a function of many variables. These include the size, hardness of grit, pressure and pad quality. Figure 4 is an SEM picture showing the surface morphology of a

sample polished with 0.3 um grit size. The roughness of the surface, as measured by SEM and Dektak, was considerably smaller than the grit size.

Figure 5 shows D profiles in CZ and FZ samples, both polished with 0.3 μm grit. As expected, a deeper diffusion into FZ sample is observed. This is again explainable on the basis of the propensity of oxygen for quenching the vacancy generation during crystal growth. Figure 6 shows the measured profiles in ribbon samples in which polishing was done with different grit sizes - ranging from 0.01 for different polishing conditions. It can be seen from this figure that the diffusivity increases with surface roughness. This apparent variation in the diffusivity can be explained if we consider that the damaged surface absorbs hydrogen and acts as a "limited" diffusion source. Thus, at lower levels of surface damage, diffusion occurs from a source where the hydrogen concentration may be varying.

Conclusions

From the experiments described herein, we have shown that vacancies play a major role in the hydrogen diffusion process. We propose that a {H-V] complex is formed; such a complex can have diffusivities approaching that of a mono-vacancy[7]. Other results, not discussed in this paper indicate that interstitial diffusion and vacancy mechanism exist simultaneously, the latter being dominant at low temperatures.

We have also shown that hydrogen diffusion from a molecular ambient can be mediated by the surface damage. A further thought is that the surface damage will follow the reaction:

$$H_2 + V \rightarrow (H\text{-}V) + H^+$$

We believe that the damage at a phosphorus diffused N/P junction is sufficient to cause in-diffusion of hydrogen. This result is consistent with theoretical work, which suggests that a hydrogen molecule can simultaneously dissociate in the vicinity of a vacancy. A similar effect can occur during PECVD nitridation.

References

1. A. Chari, P. de Mierry, A. Meinikh, and M. Aucouturier, " Impurity and Defect interaction in polycrystalline silicon for photovoltaic applications: The Role of Hydrogen, Rev. Phys. appl. , vol. 22, pg 655, 1987
2. Jacques I. Pankove, N. Johnson, "Hydrogen in Semiconductors", Semiconductors and Semimetals, volume 34
3. B.L. Sopori et al.; Solar Energy Materials and Solar Cells, (41,42), 1996, 159-169
4. M.A. Roberson, and S.K. Estreicher, Phys. Rev. B 49, 17040 (1994)
5. B. L. Sopori, T. Nilsson, and M. McClure, J. Electrochemical Society; Solid State science and technology, January, 1981
6. S. K. Estreicher, Mater. Sci. Eng. Rep. 14,1 (1995)

7. D. M. Maric, P.F. Meier, and S.K. Estreicher, Phys. Rev. B 47, 3620 (1993-1)

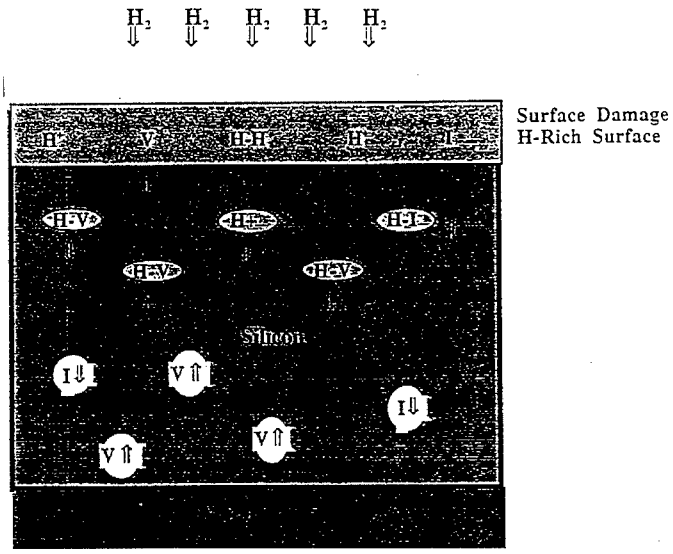


Figure 1. Hydrogen diffusion model

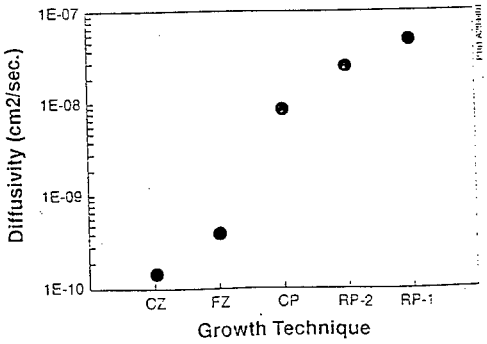


Figure 2. Diffusivity values obtained from different vendors

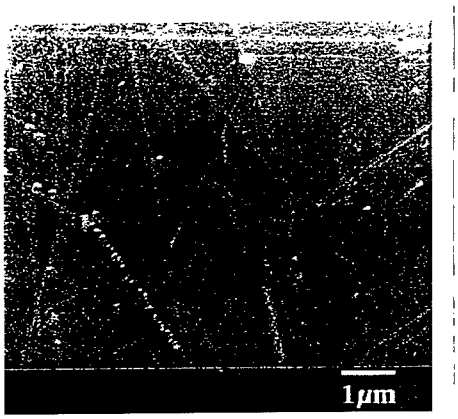


Figure 3. The surface roughness of a FZ sample after polishing with a 0.3 μm Al_2O_3 grit measured by SEM and dektak.

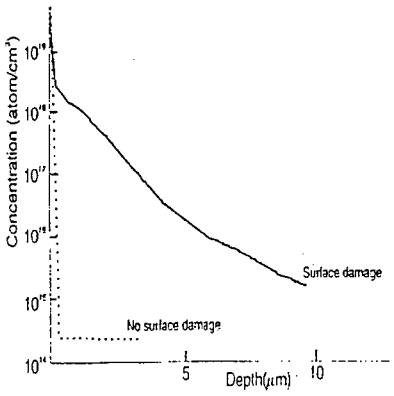


Figure 4. Hydrogen diffusion profiles in an EFG ribbon, produced by anneal annealing in a FG ambient with and without surface damage.

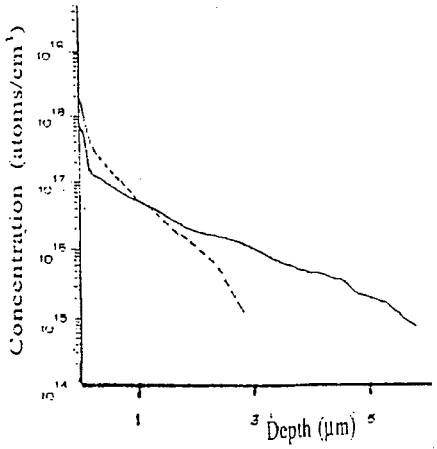


Figure 5. SIMS deuterium profile of and FZ samples polished with a 0.3 μ m grit and annealed in D_2 containing forming gas (400 °C/1hr)

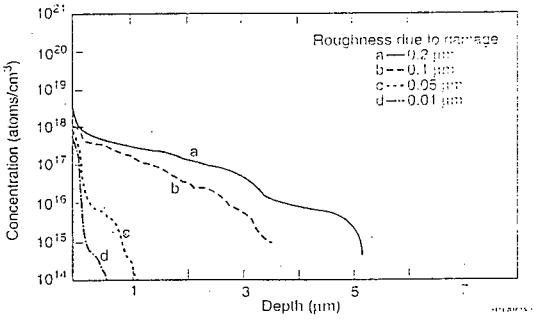


Figure 6. SIMS deuterium profile CZ of an LRC ribbon with various grit sizes applied to substrates. (a) 0.2 μ m, (b) 0.1 μ m, (c) .05 μ m, (d) .01 μ m. The deuterium depth does increase with surface damage.

Materials Science Forum Vols. 258-263 (1997) pp. 197-202
© 1997 Trans Tech Publications, Switzerland

MECHANISM OF ULTRASONIC ENHANCED HYDROGENATION IN POLY-Si THIN FILMS

Sergei Ostapenko
Center for Microelectronics Research, University of South Florida,
4202 Fowler Avenue, Tampa, Florida 33620, U.S.A

Keywords : ultrasound treatment, hydrogenation, dangling bonds, luminescence.

Abstract. Ultrasound treatment (UST) was applied to improve electronic properties of polycrystalline silicon (poly-Si) films on glass. A strong decrease of sheet resistance by a factor of two orders of magnitude was observed in hydrogenated films at UST temperatures lower than 100°C. The UST effect is accompanied by improvement of a film electrical and optical homogeneity as confirmed by spatially resolved photoluminescence (PL) study. By applying UST at higher temperatures up to 280°C, a dramatic increase of infra-red photoluminescence (PL) intensity is observed in films obtained by solid-phase crystallization of amorphous silicon. UST enhances the PL band at 0.7eV, and also stimulates a new luminescence maximum at about 0.9eV related to the amorphous fraction of poly-Si films. Activation energy of the UST effect is 0.33eV. A new mechanism of ultrasonic stimulated hydrogen detrapping followed by a fast hydrogen diffusion and passivation of non-radiative centers in polycrystalline and amorphous Si films is suggested.

Introduction.

Poly-Si thin films on glass are promising materials for thin film transistor in active matrix liquid crystal displays and a new generation of thin-film solar cells. Compared with transistors using hydrogenated amorphous silicon (α-Si) films, poly-Si transistors have improved operational parameters due to a substantially higher electron mobility. However, grain boundary and interface defects in poly-Si lead to high off-state current and affect threshold voltage. A conventional approach to passivate these defect states and to reduce inter-grain barriers for electron transport is hydrogenation. Plasma hydrogenation using radio frequency or electron cyclotron resonance technique was proven to be effective to improve transport properties of poly-Si. The hydrogen defect passivation occurs in two steps: plasma penetration and a subsequent atomic hydrogen diffusion. The diffusion of hydrogen in poly-Si is slow compared with single crystal silicon due to a trapping at grain boundaries [1], typically resulting in a long hydrogenation time and electrical inhomogeneity within passivated regions of poly-Si. The trap-limited hydrogen diffusivity in poly-Si films is described by an activation energy of 1.3 to 1.5eV with a diffusion coefficient given by

$$D_H = D_{ho} \times (N_i/N_t) = D_o \exp(-E_o/kT) \times \exp(-\Delta E/kT) \quad (1)$$

where D_{Ho} is the hydrogen diffusivity in crystalline Si with an activation energy E_o=0.48eV; Ni/Nt is a fraction of interstitial to trapped hydrogen; and ΔE is a binding energy of trapped atomic hydrogen of the order of 1eV [2]. A suppression of hydrogen trapping can enhance the passivation of defect states to benefit transport properties of hydrogenated poly-Si films.

A new approach to enhance hydrogenation efficiency using the Ultrasound Treatment (UST) was reported recently [3]. Defect engineering using the method of UST was proven to be extremely beneficial in polycrystalline materials where ultrasound vibrations enhance an interaction between extended lattice defects, like grain boundaries and dislocations, with mobile point defects [4]. It was reported that the atomic hydrogen is a specifically suitable object for ultrasound stimulated defect reactions in poly-Si thin films [3,5]. In this paper, key experiments of the UST enhanced

hydrogenation are reviewed, and a new mechanism of UST stimulated hydrogen detrapping discussed.

Samples and experimental.

Semi-insulating silicon films with thickness of 0.3 to 0.5μm were deposited at 625°C and 550°C on Corning 7059 glass by low pressure chemical vapor deposition. The 625°C films had a crystallite structure with the average grain-size of 100nm, while the films deposited at 550°C were amorphous. The α-Si films were annealed at 550°C in a nitrogen flow to develop <111> oriented crystalline structure. Using annealing time from 8 to 75 hours, a set of samples with a different fraction of crystalline to amorphous phases was designed. Raman spectra of thermally recrystallized films enabled to determine this fraction from the intensity ratio of the crystalline peak at 520cm^{-1} to amorphous peak at about 480cm^{-1}. Poly-Si films were also obtained by eximer laser recrystallization of α-Si and compared to films deposited at 625°C. Only one Raman peak at 520cm^{-1} due to poly-Si was observed, which proves a high level of crystallinity in both previous cases. The poly-Si films were selectively plasma hydrogenated using a pattern defined by an opening in an Al mask. This enabled us to study UST effects by comparing hydrogenated with non-hydrogenated areas on the same film. The hydrogenation was performed at 300°C in a parallel plate RF plasma system operating at a 100ccm H_2 flow with 0.3Torr pressure and 200W radio frequency power or using a low pressure electron cyclotron resonance (ECR) plasma system.

For UST experiments, ultrasonic vibrations were generated in poly-Si films through a glass substrate using a circular piezoelectric transducer (PZT-5A). For good acoustic contact, a sample was pressed against a transducer front surface using a spring or vacuum contact. UST transducers operated at resonance frequency of radial vibrations of 25KHz or 70KHz. The amplitude of sample vibrations in acoustic contact with the transducer was monitored "in-situ" by a calibrated contact acoustic probe. The maximum acoustic strain amplitude on a film surface was of the order of 10^{-3}. Temperature of a sample under UST was stabilized from 50°C to 280°C and measured by a thermocouple attached to the film surface. The upper UST temperature was limited by a Curie point of the piezoelectric transducer. UST processing at elevated temperatures was performed in nitrogen ambient with a rate of N_2 flow of 5 l/min. A control sample from the same poly-Si wafer was kept without ultrasound at exactly the same temperature to separate a possible effect of thermal processing on material properties. Detail parameters and operational principles of automatic UST station can be found in [6].

The UST effect was monitored by measurements of sheet resistance at room temperature using the four-point-probe method. Concurrently, spatially resolved photoluminescence (PL) and nano-scale contact potential difference (CPD) mapping were performed. Details of CPD method using atomic force microscope are published elsewhere [4]. Photoluminescence at 4.2 to 300K was analyzed using a SPEX 500M spectrometer coupled with cooled Ge or PbS detector. An Ar^+-laser 514nm line with power from 30 to 80 mW was used as a PL excitation source.

Results.

Plasma hydrogenation applied to poly-Si films reduces resistance by a factor of one order of magnitude due to increased electron mobility after passivation of grain-boundary defects.

A decreased resistance is saturated to a minimum value of the order of 10^9 Ω/sq after 3 to 5hr RF plasma processing of 0.35μm films. In the films where the plasma hydrogenation process was not completed, we observed the additional dramatic reduction of sheet resistance by a factor of *two orders* of magnitude after UST as shown in Fig. 1. Resistance in non-hydrogenated region was practically not changed after the UST. Notice, that UST-induced reduction of sheet resistance occurs at temperatures lower than 100°C, which is specifically beneficial for large scale poly-Si transistor applications requiring low-cost substrates with low thermal stability.

Another feature of the UST effect is reveled by the resistance distribution within the same poly-Si film. In Figure 1, the UST induced change of resistance in two regions of the same hydrogenated film is presented. Initially, a more than one order of magnitude variation in resistance was reduced to approximately 10% after a few consecutive steps of UST.

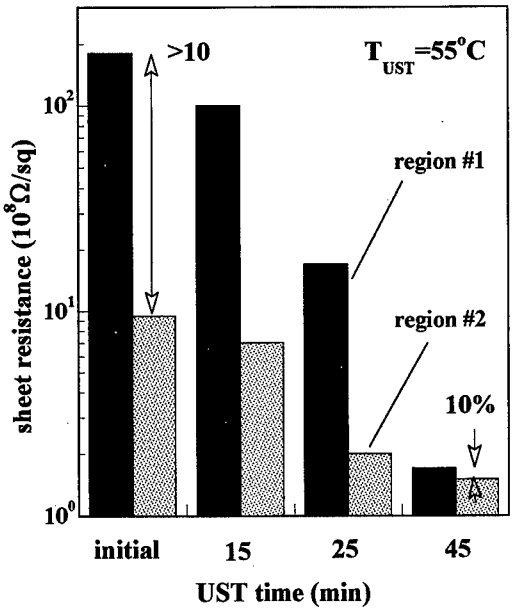


Fig.1 UST reduces resistance in hydrogenated poly-Si films due to improved passivation of dangling bonds.

Based on these findings, it was suggested that ultrasound vibrations applied to hydrogenated films can promote the process of defect passivation with atomic hydrogen. This statement is justified by the following spatially resolved PL study, and directly observed using nano-scale contact-potential difference mapping [3].

It was reported that PL spectroscopy allows defect monitoring in poly-Si films, and is specifically sensitive to the state of film hydrogenation [7]. At 4.2K the band-tail recombination dominates in PL spectrum of films deposited at 625°C. With increasing temperature, the band-tail luminescence is strongly quenched and deep 0.7eV PL band is retained and persists at room temperature.

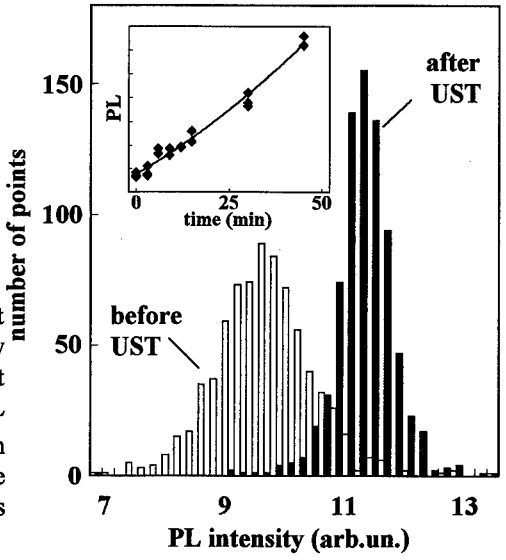


Fig.2 UST increases PL intensity and improves homogeneity of PL mapping due to redistribution of the hydrogen.

A similar PL band ($h\nu_{max}$=0.68eV) was observed previously in Cz-Si thermally annealed for 64hr at 450°C, and attributed to oxygen precipitates [7]. Notice, that our poly-Si samples were annealed under very similar conditions (75hr at 550°C). The intensity of 0.7eV PL band was used to monitor the UST effect on improvement of recombination properties of poly-Si. The increase of 0.7eV PL band intensity versus ECR plasma hydrogenation time is shown in Fig. 2 (insert). The PL increase occurs due to hydrogen passivation of non-radiative recombination centers at grain boundaries [7]. PL mapping technique with resolution of 100μm was applied to monitor a distribution of recombination centers and changes after UST. The results are presented in Figure 2 as two PL histograms of exactly the same hydrogenated film area prior to and immediately after the UST performed at 80°C for 1hr. The average PL intensity after UST exhibits an additional 25-30% increase and also narrowing by a factor of two of the half-width of the PL histogram. This result is consistent with UST improvement of resistance homogeneity shown in Figure 1.

It was assumed the UST is a thermally activated process which can be substantially facilitated at temperatures above 100°C. To verify this, thermally recrystallized at 550°C poly-Si films were subjected to UST at temperature up to 280°C [5].

The PL spectrum of poly-Si thin films at 77 K is dominated by "oxygen" related band at 0.7eV (Fig. 3). Luminescence intensity of as-deposited films was lower than sensitivity limit of PL set-up. By increasing annealing time of 550°C films up to 75 hours, it was found that the intensity of 0.7eV band monotonously increases by a factor of ten in 75hr annealed samples compared to 8-12hr annealed films. Therefore, the intensity of 0.7eV band can be used to monitor changes of recombination properties in the poly-Si phase of films.

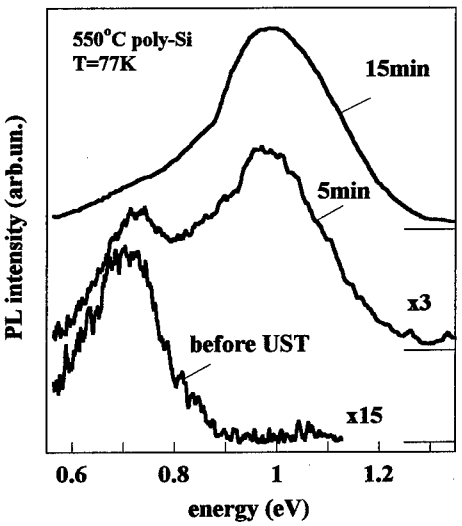


Fig.3 UST activation of 0.9eV PL band in α-Si phase of thin films: T_{UST} =250°C.

After UST was applied at T_{UST}=150-280°C, two noticeable changes in PL spectrum were observed (Fig. 3). The first is the increase of the 0.7eV band intensity by a factor of 2 to 4 in different samples, which is consistent with data of low-temperature UST processing of hydrogenated poly-Si films (Fig.2). The second effect is a strong UST activation of a "new" broad PL band with a maximum at 0.92 - 0.98eV and half-width of 260meV at 77K (referred hereupon as 0.9eV band). We notice that a dramatic enhancement of 0.9eV band exceeding *two orders* of magnitude compared to untreated sample requires only a few minutes of UST processing performed at 250-280°C. After UST activation of luminescence is completed (5min @280°C), the PL spectrum is entirely dominated by the 0.9eV band (Fig. 3).

UST processing was performed at different temperatures between 150 and 280°C. Corresponding points of isothermal kinetics of the 0.9eV band at two temperatures and their single-exponential fits are shown in Figure 4. For a comparison, the picture also comprises PL kinetics of a control sample annealed without UST at 280°C, which proves that the effect of 0.9eV band activation is entirely UST related. The UST kinetic is characterized by a time constant of 3min at 280°C which increases to 25min at 150°C. From the Arrhenius plot of UST time constant we find the UST activation energy: E_{UST}=0.33 +/- 0.05eV.

We have strong arguments that UST activated 0.9eV band is related to a residual amorphous phase of recrystallized poly-Si films.

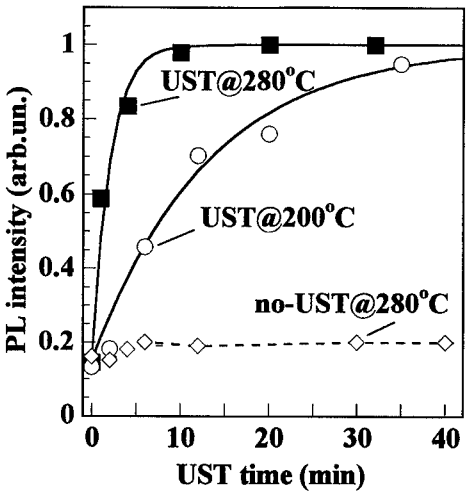


Fig.4. Isothermal UST kinetics of 0.9eV band activation (points), and exponential fit (solid).

The saturated intensity of the 0.9eV band after completion of UST processing is a function of 550°C annealing time, and therefore, depends on a fraction of α-Si phase in the films as proved by Raman spectroscopy: the 0.9eV band has a maximum intensity in films with significant fraction of α-Si phase, and is gradually decreased in films where the poly-Si phase is dominating. The UST activation of 0.9eV band is also negligible in poly-Si films either deposited at 625°C or recrystallized using an eximer laser. Furthermore, parameters of 0.9eV band are very close to a "defect" PL band previously observed in hydrogenated α-Si films [9]. We conclude, that UST promotes a passivation of non-radiative centers in the α-Si phase of recrystallized films.

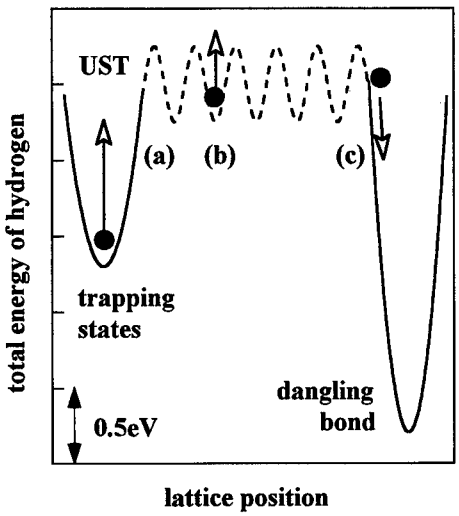


Fig.5. The model of UST enhanced hydrogenation in poly-Si and α-Si thin films.

Discussion: UST mechanism.

It is known that after plasma hydrogenation the total hydrogen concentration in poly-Si films can exceed the number of non-passivated dangling bonds by as much as two orders of magnitude [10]. In 550°C LPCVD films obtained by decomposition of silane (SiH_4) and annealing at 550°C, the concentration of trapped residual hydrogen can approach 10%. Therefore, a significant reservoir of trapped electrically non-active hydrogen is available in UST processed films to accomplish a defect passivation.

It is suggested that UST enhances the hydrogenation in a three-step mechanism schematically shown in Fig. 5: (a) UST hydrogen releasing from trapping states, (b) fast H-diffusion, and (c) hydrogen capture at dangling bonds. It is obvious that UST promotes a release of hydrogen from traps by a reduction of the hydrogen binding energy ΔE defined in Eq. (1). A physical reason of such UST induced hydrogen detrapping is a selective absorption of the ultrasound by grain boundaries and other extended crystal defects where hydrogen can reside. Being liberated from traps, hydrogen will diffuse with the diffusion coefficient of crystalline Si: $D_H=9.4\cdot10^{-3}$ x exp (-0.48eV/kT) [cm^2/sec]. The UST activation energy 0.33eV is close to activation of H diffusion in silicon (0.48eV). A possible reduction of this energy can be attributed to UST stimulated diffusion of hydrogen [4]. The diffusion length of H migration under UST ($T_{ust}=280^oC$, $\Delta t=3$min) can be estimated as $L=(D_H\cdot\Delta t)^{1/2}=76\mu m$. This value substantially exceeds a 100nm grain-size of poly-Si films, which explains why liberated hydrogen atoms can quickly approach non-radiative centers in poly-Si and α-Si phases.

It is known that the binding energy of hydrogen can be substantially perturbed in strained grain-boundary regions. As an example, the binding energy in strained Si-H-Si configuration linearly varies with stretching of Si-Si bond-length in a rate of 0.46eV per 0.1A [11]. This value is taken to estimate UST effect on hydrogen binding. Under the ultrasound, a dynamic stress field generates regions of local expansions and tensions. Amplitude of the average acoustic strain in our UST study is small, of the order of 10^{-3}, and corresponds to bond stretching of 2.5 x 10^{-3}. However, it is anticipated that elastic constants of grain boundaries are smaller than that at inter-grain regions. In this case, UST stress will generate a strong local strains at grain boundaries. To quantify the effect, we consider the ratio of grain-boundary volume to inter-grain volume as 1% for 100nm grain size. The amplitude of acoustic strain in grain boundary will approach 10^{-1} corresponding to 10% stretching of bond-length by 0.25. As a result, the reduction of hydrogen binding energy by about 1eV is expected. This rough estimation requires a comprehensive theoretical analysis.

Acknowledgments.
Expert assistance of A. U. Savtchouk, G. Nowak, Y. Koshka, T. Ruf, and J. M. Zhang in experiments is acknowledged. The author thanks J. Lagowski, L. Jastrzebski, J. Werner, and N. H. Nickel for helpful discussion. The work was partially supported by NREL contract No. XD-2-11004-5.

References.

1. W.B.Jackson, N.M.Johnson, C.C.Tsai, I.-W. Wu, A.Chiang, and D.Smith, APL, **61**, 1670 (1992).
2. N.H.Nickel, N.M.Johnson, and C.Van der Walle, Phys.Rev.Lett, **72**, 3393 (1994).
3. S.Ostapenko, L.Jastrzebski, J.Lagowski, and R.K.Smeltzer, APL, **68**, 2873 (1996).
4. S. Ostapenko, N.E. Korsunskaya, M.K.Sheinkman, and S.Koveshnikov, "Defect engineering in semiconductors using ultrasound treatment" in *Encyclopedia of Electrical and Electronics Engineering*, (editor J.G.Webster), in press.
5. Y.Koshka, S.Ostapenko, T.Ruf, and J.M.Zhang, APL, **69**, 2537 (1996).
6. http://www.eng.usf.edu/CMR/smd
7. A.U.Savchouk, S.Ostapenko, G.Nowak, J.Lagowski and L.Jastrzebski. APL, **67**, 82 (1995).
8. M.Tajima, J.Cryst.Growth, **103**, 1 (1990).
9. R.A.Street, Advances in Physics, **30**, 593 (1981).
10. N.H.Nickel, N.M.Johnson, and W.B.Jackson, APL, **62**, 3285 (1993).
11. C.G.Van de Walle and N.H.Nickel, Phys.Rev.B, **51**, 2636 (1995).

Materials Science Forum Vols. 258-263 (1997) pp. 203-210
© 1997 Trans Tech Publications, Switzerland

HYDROGEN MOLECULES IN CRYSTALLINE SILICON

M. Kitajima, K. Ishioka, K.G. Nakamura, N. Fukata[1], K. Murakami[1], J. Kikuchi[2] and S. Fujimura[2]

National Research Institute of Metals, 1-2-1 Sengen, Tsukuba, 305 Japan
[1]Institute of Materials Science, University of Tsukuba, Tsukuba, 305 Japan
[2]Process Development Division, Fujitsu Ltd., Kawasaki, 211 Japan

Keywords : H_2, crystalline Si, hydrogen atom treatment, Raman scattering

Abstract
Hydrogen molecules in crystalline silicon treated with hydrogen atoms are investigated using Raman scattering spectroscopy. The rotational and vibrational Raman lines of hydrogen molecule are observed at 590 cm^{-1} and 4158 cm^{-1}, respectively. The Raman measurements show that H2 concentration has a maximum for hydrogenation at 400 °C. The vibrational Raman line of hydrogen molecules is broad and asymmetric due to inhomogeneous broadening originated from various configurations in crystalline silicon. Successive treatment with hydrogen and deuterium atoms showed that Si-H bonds formed by hydrogenation play little role in the formation of hydrogen molecules.

Introduction.

Hydrogen in semiconductors has been examined extensively with various experimental and theoretical methods. Hydrogen in crystalline silicon has several possible configurations. It terminates dangling bonds on the surface, and passivates acceptors, donors and deep level impurities in the bulk by forming complexes with the dopants [1,2]. Several experimental studies have observed {111} platelets [3,4] and metastable diatomic hydrogen complex [5] formed in heavily doped n-type silicon.

Theoretical calculations have predicted that hydrogen molecule is stable at tetrahedral interstitial sites in silicon with its axis along a <100> (or <111>) direction [6,7,8,9]. There are also several experimental results that suggest indirectly the existence of hydrogen molecules in crystalline silicon [10,11,12,13,14]. Murakami and his group have inferred a formation of hydrogen molecules in n-type silicon after hydrogenation at temperatures between 250 to 400 °C from the hydrogenation-temperature dependence of the line width of the electron spin resonance (ESR) spectrum of conduction electrons [10, 11]. Recently, we have confirmed for the first time the existence of hydrogen molecules in crystalline silicon by detecting their vibrational and rotational Raman lines in heavily doped n-type crystalline silicon treated with hydrogen atoms [15,16,17,18]. Interactions of the hydrogen molecules with conduction electrons in the crystalline silicon have been studied [29]. For other semiconductors, hydrogen molecules in GaAs have also been observed by means of Raman scattering spectroscopy and exhibited a Raman shift lower than that in Si [19]. This suggests the importance of further study on the matrix effect , i.e., ionicity, lattice constant, etc. of crystals, to Raman shift of hydrogen molecules.

In the present paper, we report a detailed study on hydrogen molecules in crystalline silicon by means of Raman measurements. The hydrogenation-temperature dependence of the formation of hydrogen molecules has been examined. Successive treatments with atomic hydrogen and with atomic deuterium have been performed to investigate the formation mechanism of hydrogen molecules. The configuration and the thermal stability of hydrogen molecules in crystalline silicon are also briefly described.

Experimental.

p-type [100] FZ Si (80-100 Ωcm) wafers were used as crystalline Si samples. The samples were treated with atomic hydrogen from a hydrogen plasma at substrate temperatures between 60 to 600 °C for 3 hours. The experimental setup is shown in Fig. 1. The hydrogen plasmas were generated by microwave irradiation in a cavity. The samples were placed 60 cm apart from the plasma to suppress damage from the activated species. H_2O gas (0.05 Torr) was added to H_2 gas (0.95 Torr) to suppress recombination of hydrogen atoms at quartz wall surfaces. We also performed deuterium atom treatment by using D_2 and D_2O instead of H_2 and H_2O, respectively. The substrate temperature during hydrogenation was monitored using interference of an infrared light from InGaAsP laser (λ= 1310 nm) reflected on both surfaces of the wafers mirror-polished, since conventional thermocouples react with hydrogen atoms and lead to an overestimation of the temperature. The substrate temperature during the hydrogen atom treatment was controlled to an accuracy of ±2.5 °C. Details of the method of hydrogenation were reported elsewhere [26]. The depth profiles of hydrogen and deuterium in crystalline silicon were obtained from secondary ion mass spectroscopy (SIMS) measurements. The silicon sample treated at 400 °C exhibited a peak with a concentration of ~ 5 x 10^{20} /cm^3 at around 40 nm and had a total amount of hydrogen (areal concentration) ~ 5 x 10^{15} atoms/cm^2. We also performed chemical etching of the samples in a 1 : 25 mixture of 5 % HF and 50 % HNO_3 aqueous solutions to estimate the depth profile of H_2 in Si from Raman measurements.

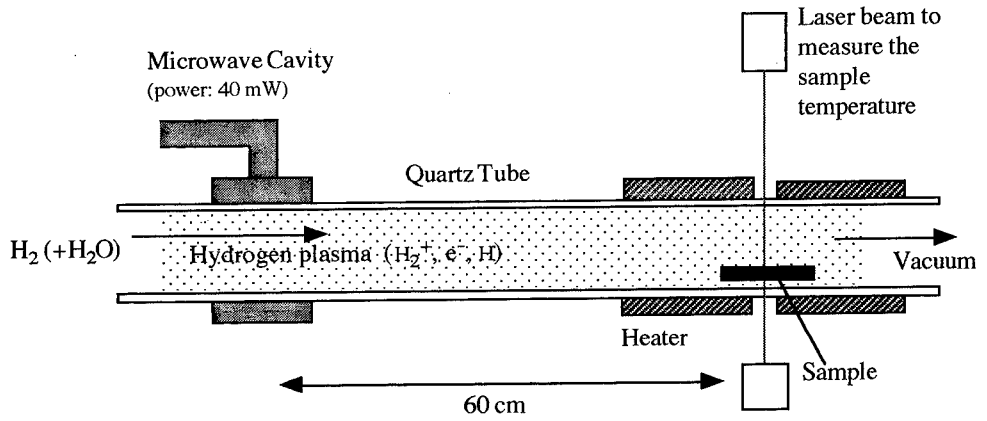


Fig.1 Schematic drawing of the hydrogenation system.

Raman scattering measurements were performed at room temperature and at 90K. A cw argon-ion laser with a wavelength of 514.5 nm was used as an excitation source. Scattered light was collected in a 90° configuration, analyzed using a triple grating monochromator with a wavenumber resolution of 0.7 cm^{-1}, and detected with a spectrometric multichannel analyzer. Raman spectra were measured in Raman shift ranging from 300 to 4300 cm^{-1}.

Results and Discussion.

Figure 2(a) shows a Raman spectrum of crystalline Si after treatment with atomic hydrogen at 400 °C. Raman lines observed at around 590 cm^{-1} and 4158±3 cm^{-1} were assigned to the $S_0(1)$ rotational line and the Q_1 vibrational line of H_2, respectively. A broad and asymmetric Raman band at around 2100 cm^{-1} was attributed to the stretching of Si-H bonds in crystalline silicon. The Raman spectrum is very similar in the line shape with that of heavily doped n-type crystalline Si after hydrogen atom

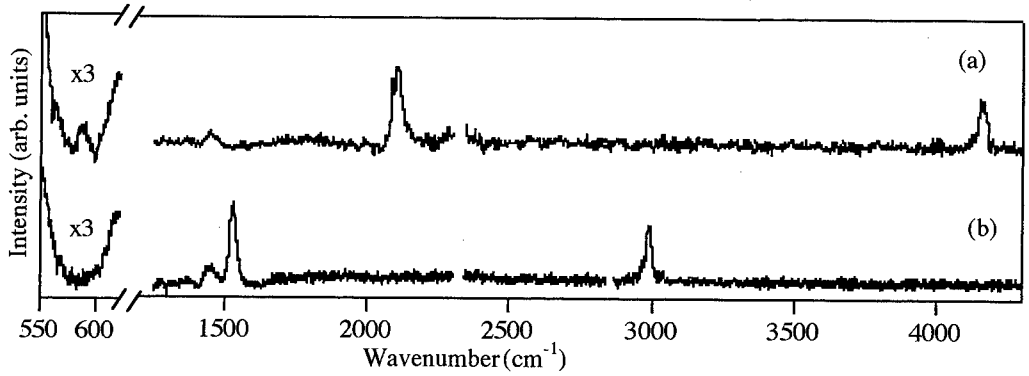


Fig. 2 Typical Raman spectra of crystalline Si (a) after treatment with H atoms at 400 °C and (b) after treatment with D atoms at 400 °C.

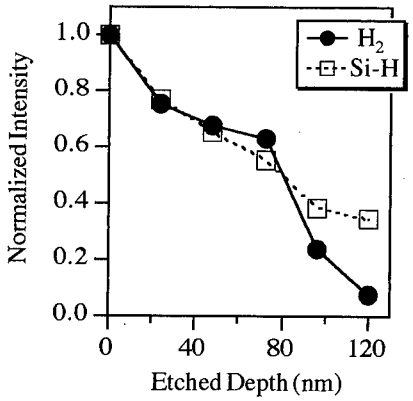


Fig. 3 Raman intensities of the vibrational line of H_2 and the Si-H stretching line after sequential chemical etching. The intensities are normalized by those before etching (etched depth = 0).

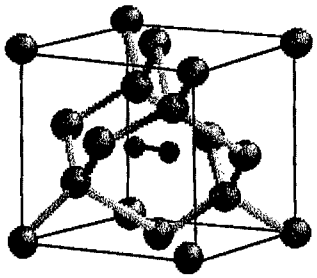


Fig. 4 Model for H_2 in Si crystal; H_2 is trapped in the tetrahedral site of Si, with its axis oriented in the <100> direction.

treatment at 400 °C [15,16,17,18]. Figure 2(b) shows a Raman spectrum of crystalline Si treated with deuterium atoms at 400 °C. The Raman lines associated with H_2 or Si-H were not detected, but the Q_1 vibrational line of D_2 at 2990 cm^{-1} and the Si-D stretching line at 1530 cm^{-1} were observed. The isotope shift confirms the existence of hydrogen molecules in crystalline Si.

The depth profile of H_2 in Si was obtained by performing sequential chemical etching of the surface layers. In Fig. 3 is plotted the intensity of the Q_1 vibrational line of H_2, together with that of Si-H stretching, as a function of etching depth. Fig. 3 indicates that H_2 has a depth distribution of about 100 nm from the surface, which is comparable to that of the H concentration measured with SIMS [18]; in other words, H_2 exists not only near the surface but in bulk Si crystal. A most

plausible trapping site of H_2 is the tetrahedral interstitial site in crystalline Si illustrated in Fig. 4, which was predicted by theoretical calculations [6,7,8,9].

Figures 5 and 6 show the rotational and vibrational lines of H_2, respectively, for Si crystal treated with atomic hydrogen at various temperatures. The intensities of the rotational and vibrational lines are largest at hydrogenation temperature of 400 °C, while that of the Si-H stretching line has a maximum at 250 °C, as shown in Fig. 7. The Raman shift of the vibrational line of H_2 was almost constant at 4158±3 cm^{-1}, while the width decreases with increasing hydrogenation temperature. The vibrational line of H_2 is significantly asymmetric with a shoulder at around 4130 cm^{-1} for crystalline Si hydrogenated at 250 °C, which corresponds to the maximum formation of Si-H. The main peak at 4160 cm^{-1} is attributed to H_2 trapped in the tetrahedral sites in well-ordered silicon lattice, whereas the shoulder around 4130 cm^{-1} is inferred to arise from H_2 in the tetrahedral sites distorted by the existence of Si-H bonds in the vicinity. We have investigated the difference between p-type and heavily-doped n-type crystalline silicon samples. However, there was no significant difference in hydrogenation-temperature dependence of the Raman spectra [18].

It is noted that the widths of the rotational and vibrational lines in Figs. 5 and 6 are always much larger than those of gaseous or solid hydrogen molecules [20,21], while the Raman shifts are comparable. The line width of the vibrational line decreased with increasing hydrogenation temperature, from ca. 50 cm^{-1} for 180°C hydrogenation to 30 cm^{-1} for 500°C hydrogenation. The broadening of the Raman lines of H_2 is too large to be explained by high-pressure gaseous H_2. In fact, the vibrational Raman line of gaseous H_2 at a pressure of 200 MPa, the pressure of gaseous H_2 in voids in amorphous silicon [22,23], has a width no more than 3 cm^{-1} [24]. On the other hand, for H_2 dissolved in vitreous silica the spectral width is about 20 cm^{-1} at room temperature and exhibits significant narrowing with decreasing measurement temperature [25]. The temperature - dependent

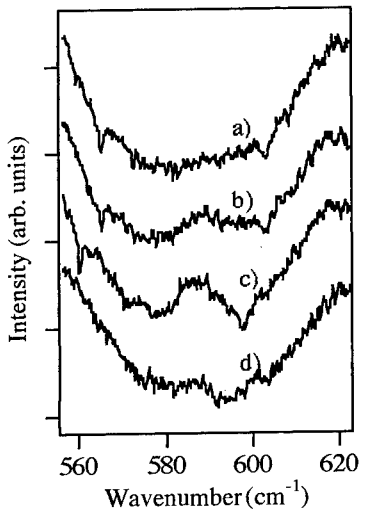


Fig. 5 The rotational Raman line of H_2 in crystalline Si treated with H atoms at (a) 250 °C, (b) 350 °C, (c) 400 °C and (d) 500 °C.

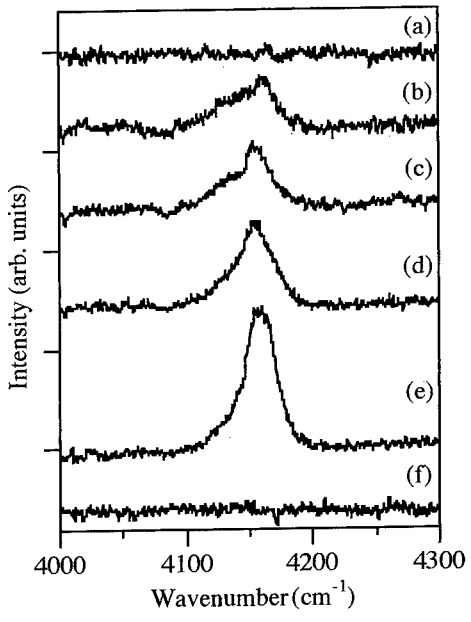


Fig. 6 The vibrational Raman line of H_2 in crystalline Si (a) before hydrogenation, and after hydrogenation at (b) 180 °C, (c) 250 °C, (d) 300 °C, (e) 400 °C, and (f) 600 °C.

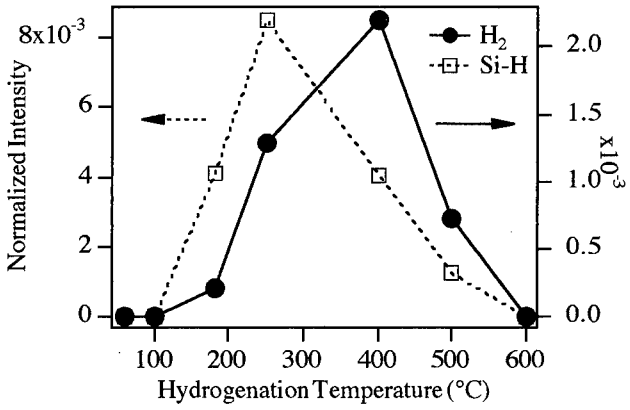


Fig. 7 The Raman intensities of the vibrational line of H_2 (closed circle) and the Si-H stretching line (open square) as functions of substrate temperature during hydrogenation. The Raman intensities are normalized by that of the optical phonon line of silicon at 521 cm^{-1}.

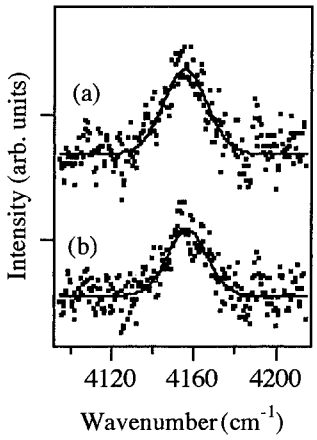


Fig. 8 The vibrational Raman line of H_2 in silicon treated with atomic hydrogen at 400°C measured at (a) 90 K and (b) room temperature.

part of the width is explained in terms of collisional or motional broadening while the temperature-independent width ascribed to inhomogeneous broadening. To examine the origin of the large width in the present study, Raman measurements were also performed at 90 K. Figure 8 shows the vibrational line of H_2 measured at 90 K and room temperature in the same experimental configuration. No significant difference was observed upon lowering the temperature to 90 K, indicating that the broadening is not attributed to collisional broadening in high pressure gas or other motional broadening, but predominantly to inhomogeneous broadening due to various configurations in Si crystal. We consider that most H_2 molecules are trapped, isolated in the tetrahedral interstitial sites, in well-ordered bulk crystalline Si, as shown in Fig. 4. The width obtained experimentally in the present study, about 30 cm^{-1}, is also comparable to the distribution in the vibrational frequency of H_2 in different orientations in the tetrahedral site in Si obtained from *ab initio* calculations [9].

The hydrogenation-temperature dependence in Fig. 7 shows that H_2 is formed at higher temperature (400 °C) than Si-H formation (250°C). To investigate the formation mechanism of H_2, especially the role of Si-H bonds in the formation of H_2, successive deuterium and hydrogen atom treatments were carried out on crystalline Si. Figure 9 shows the Raman spectra of crystalline Si treated with D atoms at 250 °C for 3 hours and successively with H atoms at 250 °C for 4 hours. H atom treatment in addition to D atom treatment induced the vibrational line of H_2 at 4158 cm^{-1} and Si-H stretching around 2100 cm^{-1} and reduced the Si-D stretching at 1530 cm^{-1}; it affected little the vibrational line of D_2 at 2990 cm^{-1}. In the wavenumber region around that of gaseous HD (~3630 cm^{-1}, indicated by an arrow), however, no Raman signal was detected after H atom treatment. The result suggests that Si-H (Si-D) bonds play no important role in the formation of hydrogen molecule; that is to say, most

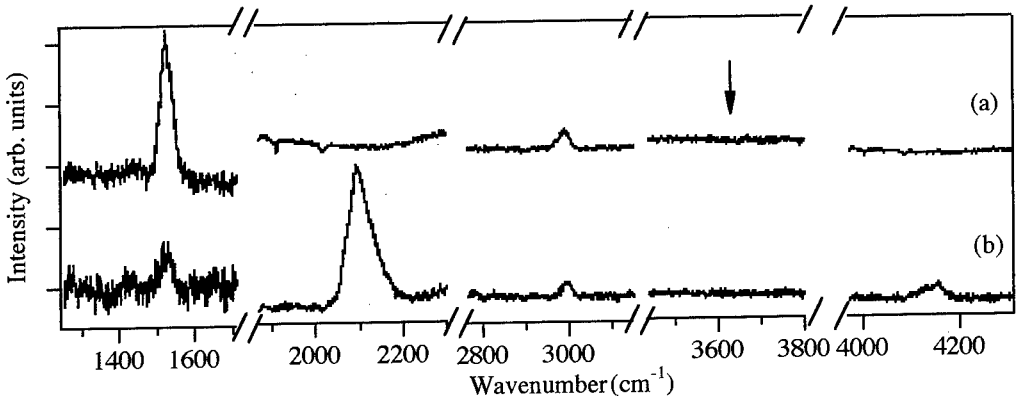


Fig. 9 Raman spectra of crystalline Si (a) after treatment with D atoms at 250 °C for 3 hours and (b) successively after treatment with H atoms at 250 °C for 4 hours. The frequency of gaseous HD (~3630 cm^{-1}) is shown with an arrow.

of H_2 molecules are not formed via H abstraction from Si-H bond. Further H/D atom treatment is in progress to investigate the formation mechanism of H_2 systematically.

In order to investigate the thermal stability of H_2 in Si, we performed thermal annealing at temperatures from 300 to 500 °C for 20 minutes after a treatment with hydrogen atoms at 250°C for 3 hours, and measured changes in the intensity and the shape of the vibrational line of H_2. The intensity was almost constant up to 400 °C with a similar line shape, indicating that H_2 is stably trapped in the crystalline silicon up to ≈ 400°C. The intensity decreased drastically after annealing at 450 °C, and disappeared after annealing at 500 °C. The decrease in the Raman intensity above 400 °C is not ascribed to the dissociation but to the diffusion of H_2 in crystalline silicon. [27].

The effect of crystal disorder on the formation of H_2 was examined to understand trapping sites for H_2 in crystalline Si. We made Raman measurements on crystalline, microcrystalline and amorphous Si treated with atomic hydrogen. A vibrational line of H_2 was observed in crystalline and microcrystalline Si after hydrogenation, and the intensity in microcrystalline is one fifth of that observed in crystalline Si. No Raman signal due to hydrogen molecule was observed in amorphous Si. The results imply that H_2 is trapped in non-damaged, well-ordered bulk crystal [28].

Conclusion.

Hydrogen molecules are observed in crystalline silicon treated with hydrogen atoms at substrate temperatures between 180 and 500 °C. The vibrational and rotational Raman lines of hydrogen molecule in crystalline silicon are observed at 4158 cm^{-1} and 590 cm^{-1}, respectively, and their intensities are largest for hydrogenation at 400 °C. The broad and asymmetric Raman spectrum of H_2 suggests that the configurations for the hydrogen molecules are not unique in crystalline silicon. We infer that most hydrogen molecules are isolated at the tetrahedral sites in well-ordered silicon crystal lattice with various molecular orientations. The hydrogen molecules are stably trapped there up to about 400 °C. Among the formation mechanisms of hydrogen molecules, abstraction of H atoms from Si-H bonds is not dominant.

The physics and chemistry of hydrogen molecules in crystalline silicon are not well understood. We need more studies using probing techniques such as ion channeling to determine the trapping sites, ESR and NMR to know the nuclear magnetic properties of hydrogen molecules in crystalline semiconductors. It is also of importance to make a systematic study of the matrix effect on the formation of hydrogen molecules. Finally, the effects and dynamic behaviors of the molecular hydrogens in semiconductors must be clarified for further development of the present semiconductor devices such as Si-LSI, GaN photodiode, etc. which include hydrogen impurities.

ACKNOWLEDGMENTS

We thank H. Haneda and I. Sakaguchi for the SIMS measurements and S.Sasaki and S. Tateishi for their assistance in experiments.

References.

1. J. I. Pankove and N. M. Johnson, "Hydrogen in Semiconductors" Semiconductors and Semimetals 34 (Academic Press, New York, 1991); S. J. Pearton, J. W. Corbett, and M. Stavola, "Hydrogen in crystalline semiconductors" (Springer-Verlag, Berlin, 1991).
2. K. Bergman, M. Stavola, S. J. Pearton and J. Lopata, Phys. Rev. B **37**, 2770 (1988).
3. N. M. Johnson, F.A. Ponce, R. A. Street and R. J. Nemanich, Phys. Rev. B **35**,4166 (1987).
4. J. N. Heyman, J. W. Ager , E. E. Haller, N. M. Johnson, J. Walker and C. M. Doland, Phys. Rev. B **45**, 13363 (1992).
5. J.D. Holbech, B. Bech Nielsen, R. Jones. P. Sitch and S. Öberg, Phys. Rev. Lett. **71**, 875 (1993).
6. D. J. Chadi and C. H. Park, Phys. Rev. **B52**, 8877 (1995).
7. C. G. Van. de Walle, Phys. Rev. B **49**, 4579 (1994).
8. K. G. Nakamura, K. Ishioka, M. Kitajima and K. Murakami, Solid State Commun. **101**, 735 (1997).
9. K.G. Nakamura and M. Kitajima, Jpn. J. Appl. Phys. **36**, pp. 2004 (1997).
10. N. Fukata, S. Fujimura and K. Murakami, Materials Sci. Forum **196-201**, 873 (1995).
11. N. Fukata, S. Sasaki, S. Fujimura, H. Haneda and K. Murakami, Jpn. J. Appl. Phys. **35**, 3937 (1996).
12. M. Stutzmann, W. Beyer, L. Tapfer and C. P. Herrero, Physica B **170**, 240 (1991).
13. N. M. Johnson and C. Herring, Phys. Rev. B **38**, 1581 (1988).
14. P. Stallinga, T. Gregorkiewicz, C. A. J. Ammerlaan and Yu. V. Gorelkinskii, Phys. Rev. Lett. **71**, 117 (1993).
15. K. Murakami, N. Fukata, S. Sasaki, K. Ishioka, M. Kitajima, S. Fujimura, J. Kikuchi and H. Haneda, Phys. Rev. Lett. **77**, 3161 (1996).
16. N. Fukata, S. Sasaki, K. Murakami, K. Ishioka, M. Kitajima, S. Fujimura, J. Kikuchi and H. Haneda, Jpn. J. Appl. Phys. Lett. **35**, L1069 (1996).
17. K. Ishioka, K. G. Nakamura, M. Kitajima, N. Fukata, S. Sasaki, K. Murakami, J. Kikuchi, S. Fujimura and H. Haneda, Appl. Surface Science **117/118**, 37 (1997).
18. N. Fukata, S. Sasaki, K. Murakami, K. Ishioka, K.G. Nakamura, M. Kitajima, S. Fujimura, J. Kikuchi, and H. Haneda, Phys. Rev. B, in press (1997).
19. J. Vetterhoffer, J. Wagner, and J. Weber, Phys. Rev. Lett. **77**, 5409 (1996).
20. B. P. Stoicheff, Can. J. Phys. **35**, 730 (1957).
21. S. S. Bhatnagar, E. J. Allin and H. L. Welsh, Can. J. Phys. **40**, 9 (1962).
22. Y. J. Chabal and C. K. N. Patel, Phys. Rev. Lett. **53**, 210 (1984).
23. J. B. Boyce and M. Stutzmann, Phys. Rev. Lett. **54**, 562 (1985).
24. A. D. May, V. Degen, J. C. Stryland and H. L. Welsh, Can. J. Phys. **39**, 1769 (1961).
25. C. M. Hartwig and J. Vitko, Phys. Rev. B **18**, 3006 (1978).
26. J. Kikuchi, S. Fujimura, M. Suzuki, and H. Yano, Jpn. J. Appl. Phys. **32**, 3120 (1993).
27. N. Fukata, K. Murakami, K. Ishioka, K. G. Nakamura, M. Kitajima, H. Haneda, S. Fujimura, and J. Kikuchi, in this proceedings.

28. K. Ishioka, K. G. Nakamura, M. Kitajima, N. Fukata, K. Murakami, S. Fujimura, and J. Kikuchi, in this proceedings.
29. K. Murakami, N. Fukata, S. Sasaki, K. Ishioka, M. Kitajima, S. Fujimura, J. Kikuchi, and H. Haneda, Proc. Material Res.Soc. **442**, 269 (1997).

Materials Science Forum Vols. 258-263 (1997) pp. 211-216
© 1997 Trans Tech Publications, Switzerland

THERMAL STABILITY OF HYDROGEN MOLECULE IN CRYSTALLINE SILICON

N. Fukata, K. Murakami, K. Ishioka[1], K.G. Nakamura[1], M. Kitajima[1], S. Fujimura[2], J. Kikuchi[2] and H. Haneda[3]

Institute of Materials Science, University of Tsukuba, 1-1-1 Tennoudai, Tsukuba, 305 Japan
[1]National Research Institute of Metals, Tsukuba, 305 Japan
[2]Process Development Division, Fujitsu Ltd., Kawasaki, 211 Japan
[3]National Institute for Research in Inorganic Materials, Tsukuba, 305 Japan

Keywords : diffusion , hydrogen molecule, silicon, thermal annealing, Raman scattering

Abstract. Thermal stability of H_2 formed in crystalline silicon by hydrogenation at 250 °C was investigated by performing thermal annealing. Isochronal annealing was done between 300 and 500 °C, and isothermal annealing at 300, 400, and 420 °C was performed up to 200 minutes. The Raman intensity of hydrogen molecule was observed to decrease after thermal annealing at and above 400 °C, while its line shape was almost constant. The result indicates that hydrogen molecule is stably trapped in silicon below 400 °C. The intensity decay is ascribed to the diffusion of H_2 out of the region probed by Raman measurements, since the activation energy of the intensity decay estimated from thermal annealing was comparable to a calculated potential barrier between hydrogen molecules at a tetrahedral site and at a hexagonal site of silicon.

Introduction.

Hydrogen is incorporated into semiconductors during various steps of processing, and affects their electronic properties by passivating shallow-level dopants and deep-level impurities. The diffusion of hydrogen in silicon has been investigated extensively with various experimental techniques [1]. Johnson and Herring investigated the spatial distribution of hydrogen resulting the diffusion through *p-n* junction using secondary ion mass spectrometry [2]. They observed highly immobile neutral form of hydrogen accumulated in excess of local boron concentration, and ascribed it to H_2. However, there have been no direct experiments for the diffusion and dissociation of hydrogen molecule in crystalline silicon.

Recently we presented the first direct observation of hydrogen molecules H_2 in crystalline silicon using Raman scattering spectroscopy [3-7]. The Raman lines of H_2 were observed for silicon hydrogenated at temperatures between 180 °C and 500 °C, and their intensities had a maximum for hydrogenation at 400 °C. The vibrational Raman line of H_2 was very broad and asymmetric, consisting of at least two components, especially for samples hydrogenated at relatively low temperatures such as 250 °C. We inferred H_2 to be trapped isolated at the tetrahedral (T_d) interstitial sites in silicon based on experimental results [8] and theoretical calculations [9,10]. However, the origins of the large width and asymmetry of the vibrational line, as well as the formation mechanism of H_2 in silicon, are remain ambiguous.

In the present study we performed thermal annealing on crystalline silicon hydrogenated at 250 °C to investigate the thermal stability of hydrogen molecules, which are inferred to be trapped predominantly isolated in the T_d sites of silicon but a few of them also in other configurations for silicon hydrogenated at this temperature. Thermal annealing was carried out isochronally on a hydrogenated silicon at temperatures ranging 300 - 500 °C to investigate the trapping sites and formation mechanisms of H_2. More detailed information such as the activation energy of the intensity decay was obtained from isothermal annealing at relatively low temperatures.

Experimental.

p-type [100] floating-zone Si wafers were used as crystalline Si samples. Hydrogenation was performed on the silicon samples at 250 °C for 3 hours by remote downstream treatment of hydrogen atoms [4,5]. This method suppresses hydrogen ions and electrons flowing down to the sample, and introduces only hydrogen atoms into the sample without a significant damage on the surface. The temperature of the samples during hydrogenation was monitored using interference of a 1310 nm light from an InGaAsP laser reflected on both sides of the wafers mirror polished, and controlled with an

accuracy of ± 2.5 °C. Details of the hydrogenation method were described elsewhere [4,5].

Thermal annealing on the hydrogenated silicon samples was performed in an atmosphere of flowing highly-pure N_2 gas to prevent oxidation and contamination by carbon and other elements. The temperature during annealing was controlled with an accuracy of ± 5 °C. Isochronal annealing was carried out on a hydrogenated sample accumulatively at temperatures ranging 300 - 500 °C, for 20 minutes. Isothermal annealing was done at 300, 400 and 420 °C, respectively.

All the Raman scattering measurements were performed at room temperature after each annealing. A cw argon-ion laser with a wavelength of 514.5 nm was used as an excitation source. Scattered light was collected in a 90° configuration, analyzed using a triple grating monochromator with a wavenumber resolution of 0.7 cm^{-1}, and detected with a spectrometric multichannel analyzer.

Results and Discussion.

Figure 1 (a) and (b) show Raman spectra of silicon hydrogenated at 250 °C before and after isochronal annealing. The broad Raman band at 4160 cm^{-1} in Fig. 1(a) is the Q_1 vibrational line of H_2, and the one at around 2100 cm^{-1} in Fig. 1(b) the Si-H stretching band. The intensities of the vibrational line of H_2 and the Si-H stretching band after the annealing are plotted in Fig. 2. Annealing up to 400 °C scarcely affected the intensity and the line shape of the vibrational line of H_2. The intensity decreased abruptly after annealing above 400 °C and disappeared after annealing at 500 °C. However, for the silicon hydrogenated at 500 °C, the Q_1 line of H_2 was clearly observed and the intensity was about one half compared with that for the silicon hydrogenated at 400 °C [5]. On the other hand, the Si-H stretching band changed gradually in its intensity and line shape with increasing annealing temperature. It is noted that the intensity of H_2 does not increase while that of Si-H decreases with increasing annealing temperature up to 400 °C. This indicates the formation of H_2 following the thermal dissociation of Si-H is negligible.

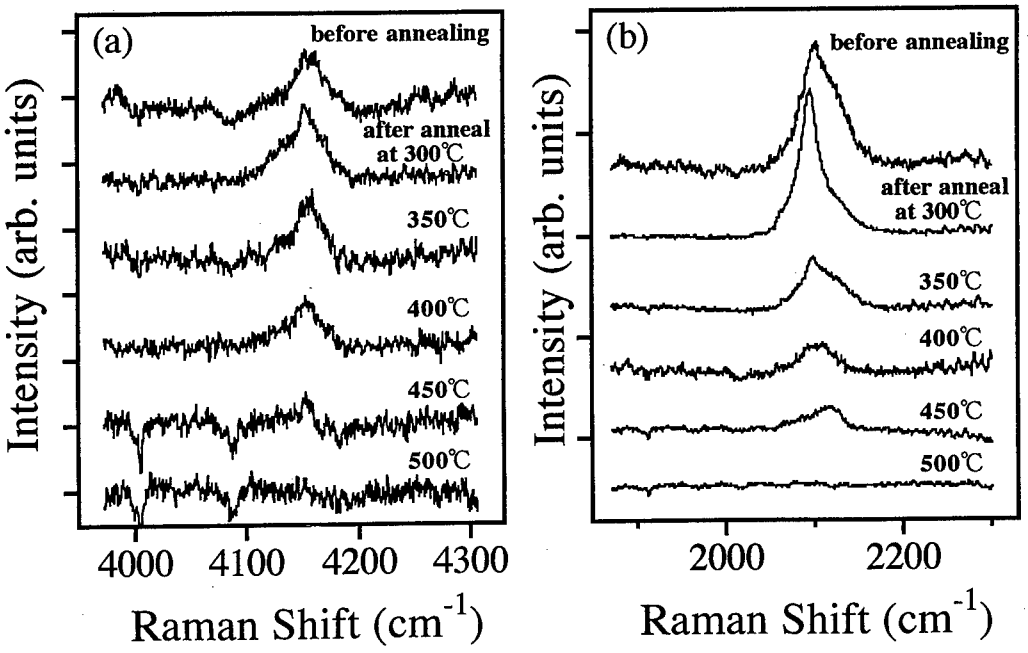


Fig. 1 Raman spectra of crystalline Si hydrogenated at 250 °C after accumulative thermal annealing at different temperatures for 20 minutes, respectively; (a) the Q_1 vibrational line of H_2, and (b) the Si-H stretching band.

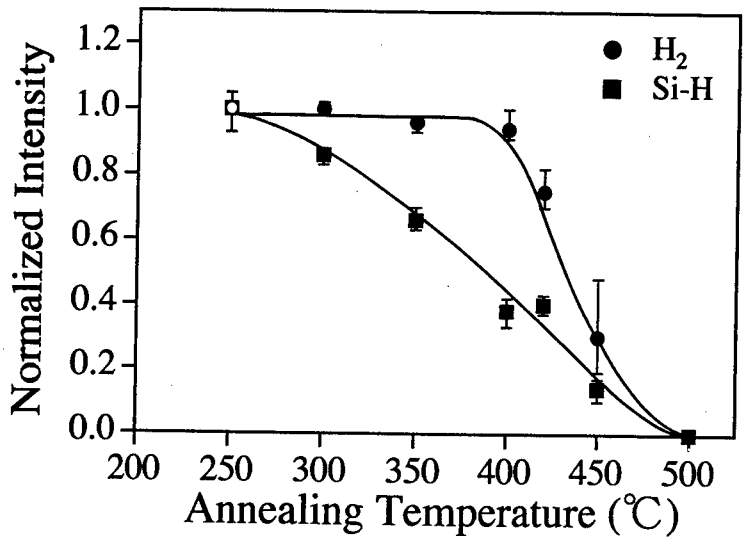


Fig. 2 The intensities of the Q_1 vibrational line of H_2 and the Si-H stretching band after successive annealing at different temperatures for 20 min at each temperature. The intensities are normalized with those before annealing, which are plotted at 250 °C (the temperature of hydrogenation of the sample).

The vibrational line of H_2 for crystalline silicon hydrogenated at 250 °C can be decomposed into at least two components, a main peak at 4160 cm^{-1} and a shoulder around 4130 cm^{-1}. The main peak at 4160 cm^{-1} is attributed to H_2 trapped in the T_d sites in well-ordered silicon lattice, whereas the shoulder around 4130 cm^{-1} is inferred, from the hydrogenation-temperature dependence of its intensity, to arise from H_2 in the T_d sites distorted by the existence of Si-H bonds in the vicinity [5]. It is noted that in Fig 1 the vibrational line of H_2 after annealing up to 400 °C is very similar to the initial one before annealing, being very broad and asymmetric. This result is in contrast to narrower and more symmetric line shape for crystalline silicon hydrogenated at 400 °C [5], and indicates that the thermal stability of H_2 in different configurations, corresponding to 4160 cm^{-1} and 4130 cm^{-1} components, is comparable. No change in the line shape obtained in the present study suggest that the thermal stability of the H_2 molecules in different configurations in silicon is very similar.

The decrease in the intensity of Si-H is attributed to its thermal dissociation. After annealing at 300 °C the shoulder at 2130 cm^{-1} in the Si-H band, which is plausibly attributed to Si-H bonds in platelets [5], disappeared. This result is in accordance with the thermal stability of {111} platelets observed with transmission electron microscopy [11]. The sharp peak at 2100 cm^{-1} vanished after further annealing at 450 °C, but a small peak around 2120 cm^{-1} remain after annealing at 450 °C. This is consistent with the inference that 4130 cm^{-1} shoulder in the H_2 Raman line, which remains at least up to 400 °C annealing, is trapped in sites that is related to Si-H bonds.

To investigate the mechanism of the disappearance of H_2 by thermal annealing in more detail, isothermal annealing at relatively low temperatures such as 300, 400 and 420 °C was performed on crystalline silicon hydrogenated at 250 °C. The intensity of the vibrational line of H_2 after annealing is plotted as a function of accumulated annealing time in Fig. 3. Annealing at 300 °C for 3 hours hardly affected the intensity of H_2. The intensity decays with time for annealing at 400 and 420 °C, faster for annealing at higher temperature.

The decrease in the intensity by isothermal annealing was fitted to an exponential decay written by

$$I = I_0 \exp(-t/\tau), \qquad (1)$$

where I_0 and I are the Raman intensity of H_2 before and after annealing, respectively, t the

accumulated annealing time, and τ a time constant. A decay rate of the intensity of H_2 can be defined by the inverse of the time constant. Figure 4 shows an Arrhenius plot of the decay rate ($1/\tau$) obtained from the isothermal and the isochronal annealings. The decay rate was roughly fitted by a single exponent with an activation energy of 1.6±0.4 eV.

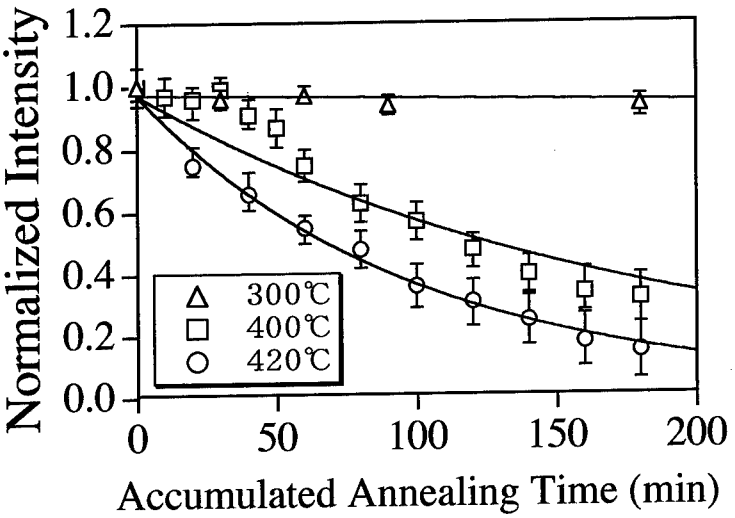


Fig. 3 The intensities of the Q_1 vibrational line of H_2 after annealing at 300, 400 and 420 °C as functions of accumulated annealing time. The intensities are normalized with those before annealing, which are plotted at zero annealing time. The solid curves represent exponential fitting curves represented by eq. (1).

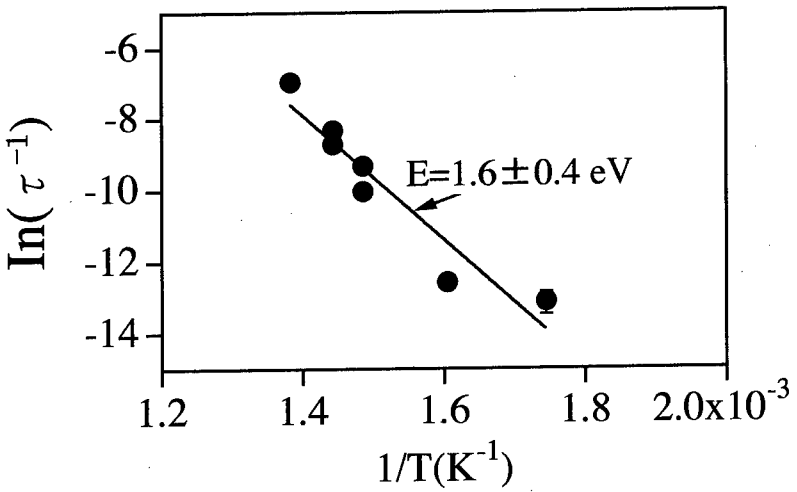


Fig. 4 Arrhenius plot of the decay rate ($1/\tau$). The solid line represents a fitting using a single exponent, which gives an activation energy of 1.6±0.4 eV.

There are two possible explanations for the decay of the Raman intensity of H_2 under thermal annealing. One is that H_2 escapes from the probed region (about 1000 nm from the surface in crystalline silicon) through a diffusion process, and the other is dissociation of H_2 to two H atoms. We calculated the energies of the diffusion and the dissociation of H_2 in silicon using an *ab initio* Hartree-Fock method and a silicon cluster model ($Si_{10}H_{16}$) [9,10]. The calculation showed the most

stable site of H_2 in silicon is the T_d site. The energy barrier for diffusion of H_2 at a T_d site to the next T_d site through a hexagonal (H_{ex}) site was calculated to be 1.47 eV. The calculated energy barrier is compared with the results reported by other authors ; 1.74 eV in Ref. [12], 1.1 eV in Ref. [13]. The dissociation energy of H_2 at a T_d site into two H atoms is calculated to be 2.93 eV. The calculated dissociation energy is compared with the results reported by other authors [12,14-16]. The calculated diffusion barriers are comparable to the experimentally estimated activation energy of the decay rate, but the calculated dissociation energies are much higher. From these result, therefore, the decrease in the intensity of the Raman intensity of H_2 is therefore attributed to the diffusion of H_2 out of the region probed with Raman measurements.

The diffusion coefficient of H_2 in silicon was estimated to be an order of 10^{-14} cm^2/sec at 400 °C using the calculated value of 1.47 eV as the diffusion activation energy, Debye frequency as the jump frequency, and the distance between Td-Hex-Td sites as the jump distance. This diffusion coefficient is lower than 4 - 5 orders of magnitude lower than that for atomic hydrogen in silicon [1].

In conclusion we performed thermal annealing on hydrogenated crystalline silicon to investigate the thermal stability of H_2. The intensity of the vibrational line of H_2 decreased after annealing above 400 °C. The activation energy of the decay of the Raman intensity of H_2 is estimated and consistent with a calculated potential barrier between a T_d site and a H_{ex} site of silicon, suggesting that the intensity decay is due to the diffusion of H_2 from a T_d site through a H_{ex} site. Little change in the Raman line shape of H_2 in different configurations is very similar.

Acknowledgment.
The authors thank S. Sasaki, S. Tateishi and K. Nakanoya for their assistance in the experiments.

References.

1. C. Herring and N.M. Johnson, in "Hydrogen in Semiconductors", ed. J. I. Pankove and N. M. Johnson, (Academic Press, New York) pp.225-347 (1991).
2. N. M. Johnson and C. Herring, Phys. Rev. **B38**, 1581(1988).
3. K. Murakami, N. Fukata, S. Sasaki, K. Ishioka, M. Kitajima, S. Fujimura, J. Kikuchi, and H. Haneda, Phys. Rev. Lett. **77**, 3161 (1996).
4. N. Fukata, S. Sasaki, K. Murakami, K. Ishioka, M. Kitajima, S. Fujimura, and J. Kikuchi, Jpn. J. Appl. Phys. **35**, L1069 (1996).
5. N. Fukata, S. Sasaki, K. Murakami, K. Ishioka, K.G. Nakamura, M. Kitajima, S. Fujimura, J. Kikuchi and H. Haneda, to be published in Phys. Rev. **B**.
6. K. Ishioka, K.G. Nakamura, M. Kitajima, N. Fukata, S. Sasaki, K. Murakami, J. Kikuchi, S. Fujimura, and H. Haneda, Appl. Surface Science **117/118**, 37 (1997).
7. M. Kitajima, K. Ishioka, K.G. Nakamura, N. Fukata, K. Murakami and S. Fujimura, in this Proceedings.
8. N. Fukata, S. Sasaki, K. Murakami, K. Ishioka, K.G. Nakamura, M. Kitajima, S. Fujimura, J. Kikuchi and H. Haneda, submitted to Jpn. J. Appl. Phys.
9. K.G. Nakamura, K. Ishioka, M. Kitajima, and K. Murakami, Solid State Commun. **101**, 735 (1997).
10. K.G. Nakamura and M. Kitajima, Jpn. J. Appl. Phys., **36**, 2004 (1997).
11. N. M. Johnson, F. A. Ponce, R. A. Street, and R. J. Nemanich, Phys. Rev. **B35**, 4166 (1987).
12. S. K. Estreicher, M. A. Robberson, and Dj. M. Maric, Phys. Rev. **B50**, 17018 (1994).
13. C. G. Van de Walle, Y. Bar-Yam, and S. T. Pantelides, Phys. Rev. Lett. **60**, 2761 (1988).
14. C. G. Van de Walle, Phys. Rev. **B49**, 4579 (1994).
15. R. Jones, Phyica **B170**, 181 (1991).
16. P. Deak, L. C. Snyder and J. W. Corbett, Phys. Rev. **B37**, 6887 (1988).

Materials Science Forum Vols. 258-263 (1997) pp. 217-222
© 1997 Trans Tech Publications, Switzerland

EMISSION AND CAPTURE KINETICS FOR A HYDROGEN-RELATED NEGATIVE-U CENTER IN SILICON: EVIDENCE FOR METASTABLE NEUTRAL CHARGE STATE

V.P.Markevich, L.I.Murin*, T.Sekiguchi, and M.Suezawa
Institute for Materials Research, Tohoku University, Sendai 980-77, JAPAN
***Institute of Solid State and Semiconductor Physics, P.Brovki str. 17, Minsk 220090, BELARUS**

Keywords: silicon, hydrogen-related center, emission, capture, electronic structure, metastable state

Abstract. The results of study of electron emission and capture processes for an amphoteric (having a donor and an acceptor levels) hydrogen-related center with negative-U properties in crystalline silicon are presented. It is found that only singly negatively and singly positively charged states of the defect are stable, but for the description of the transient process between these states thermodynamically unstable neutral charge state should be taken into account. Two local energy minima in configurational space are suggested to be present for this state. A non-equilibrium occupancy statistics for the negative-U centers with such an electronic structure has been developed and analytical expression for the time constant of the occupancy transient process (τ_f) is obtained. Experimentally observed $\tau_f^{-1}(1/T)$ dependencies were described perfectly by applying the developed statistics and the values of energy barriers for the electron capture and emission were determined.

Introduction.

At present a great number of defect systems displaying metastable properties is known in semiconductors including the well known and technologically important EL2 in GaAs, DX-centers in AlGaAs, bistable thermal donors in Si etc.(e.g. see reviews [1,2] and Refs. therein). An important information on the electronic structure and properties of metastable defects has been obtained from the studies of the carrier emission and capture kinetics. However very often there are appreciable discrepancies in some parameters of the same center determined by different investigators. The main reason of this is the complexity of the processes of emission and capture of charge carriers for metastable defects. These centers can exist in different configurations available for the same charge state. So, carrier emission or capture can be followed by the transformation of defect configuration towards the stable one. There is no non-equilibrium occupancy statistics developed for such centers in a general case and often it is rather difficult to interpret experimental data adequately.

Recently a new metastable hydrogen-related (MHR) defect with negative-U properties was discovered in hydrogenated Czochralski-grown silicon crystals [3,4]. This center is one of the dominant electrically active defects in Si:O,H crystals, irradiated with fast electrons and heat-treated at 300-400 °C. It was found that electronic properties of the MHR center are similar to those of the DX centers in III-V compound semiconductors. The center possesses a shallow donor and a deep acceptor levels with inverted order of their location in the gap. Positions of the levels were determined from the results of Hall effect and infrared absorption measurements as $E(-/0) = E_C - 0.11$ eV and $E(0/+) = E_C - 0.043$ eV [4-6]. It is known that the defects with such electronic properties are only stable in singly negatively and singly positively charged states. However, transitions between these stable states goes through a metastable neutral charge state and manifestation of this state can be observed upon investigation of the transient processes. A preliminary study of emission and capture processes for the MHR center indicated the existence of two local energy minima in configurational space for the neutral charge state of the defect [7]. Further evidence for the existence of such a metastable neutral charge state of the MHR center is presented in this paper. Non-equilibrium occupancy statistics for the negative-U centers with intermediate metastable states is developed and applied for the description of emission and capture kinetics and determination of characteristics of the MHR center.

Experimental.

Czochralski-grown silicon crystals doped with phosphorus ($N_P = 5 \cdot 10^{14} \div 5 \cdot 10^{15}$ cm^{-3}) have been studied. Hydrogen was introduced into the samples by heat-treatments in a H_2 gas ambient at 1000-1200 °C with following rapid cooling. Irradiation with fast electrons (3.5 MeV in energy, $2 \cdot 10^{12}$ $cm^{-2}s^{-1}$ in electron beam intensity) was performed at room temperature. Post-irradiation heat-treatments were carried out in argon atmosphere. Shottky barriers for capacitance measurements were prepared by evaporation of gold on the samples.

Deep level transient spectroscopy (DLTS) measurements were carried out in the temperature range 30-300 K. To obtain more exact information on the electron emission and capture processes isothermal capacitance transient spectroscopy (ICTS) measurements were done at different fixed temperatures. Capacitance transients were measured in the range 10^{-4}-10^{2} s by means of a Sanwa MI-416 capacitance meter. The length of the filling pulse was varied in the range 10^{-6}-10^{0} s. The changes in the square of diode capacitance (C^2) were analyzed to find the concentrations and characteristics of the traps. C-V and Hall effect measurements were used for the determination of free carrier concentration in the samples.

Experimental results.

Figure 1 shows DLTS spectra, recorded with different emission rate windows, for an hydrogenated irradiated sample ($\rho_0 = 1$ Ω·cm) after annealing at 350 °C. The most intense peak seen in the spectra in the temperature range of 70-100 K is related to the ionization of the MHR center [5]. Growth of the magnitude of this peak with the measurement temperature indicates the temperature-dependent capture rate of free electrons by the trap. It should be pointed out that an analysis of DLTS spectra based on a commonly used "temperature of the peak maximum" method can lead to significant errors in determination of trap parameters in the case of changeable magnitude of DLTS peak. For example, the analysis of DLTS spectra shown in Fig. 1 by means of this method gives the wrong values of activation energy of emission and capture cross section of electrons for the MHR center, 0.17 eV and $1.2 \cdot 10^{-13}$ cm^2, respectively. Correct values of the trap parameters can be derived from ICTS measurements.

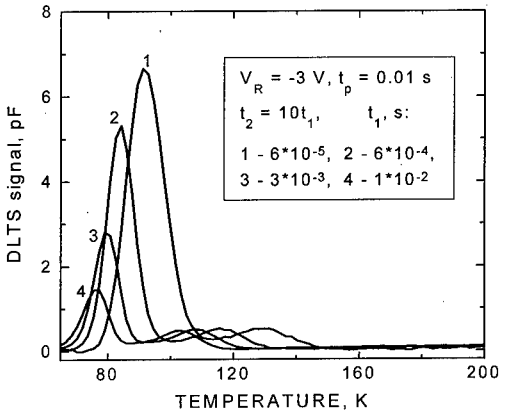


Fig. 1. DLTS spectra of a hydrogenated (at T = 1200 °C) and irradiated with fast electrons (F = $1.6*10^{16}$ cm^{-2}) Cz-Si sample after annealing at 350 °C.

Time transients of the square of diode capacitance are presented in Fig. 2. The transients were taken for the sample whose DLTS spectra are shown in Fig. 1. The observed $C^2(t)$ dependencies are consistent with a mono-exponential process of emission and are described well by the equation

$$C^2(t) = (C_\infty)^2 - \Delta C_{p0}^2 \exp(-e_n t) = (C_\infty)^2 - 2A_0 N_f \exp(-e_n t) \quad , \qquad (1)$$

where $(C_\infty)^2$ is the steady-state value of C^2 (at $t \to \infty$) for an appropriate temperature and reverse bias, ΔC_{p0}^2 is the deviation of C^2 from the steady-state value after filling pulse, N_f is the concentration of filled traps, and e_n is the emission rate; $A_0 = q\varepsilon A^2 / 2(V_{bi} + V_R)$, where q is an elementary charge, ε is the permittivity of material, A is the area of Shottky contact, V_{bi} is the diffusion voltage of the diode, and V_R is the reverse bias voltage. Because charge state of the MHR center changes from single negative to single positive in the process of ionization (negative U manifestation), factor 2 occurs in the second term of the right-hand part of Eq. (1). Calculated in

accordance with Eq. (1) $C^2(t)$ dependencies were fitted to the experimentally observed ones and the values of e_n and ΔC_{p0}^2 (N_f) were determined by means of such a fitting.

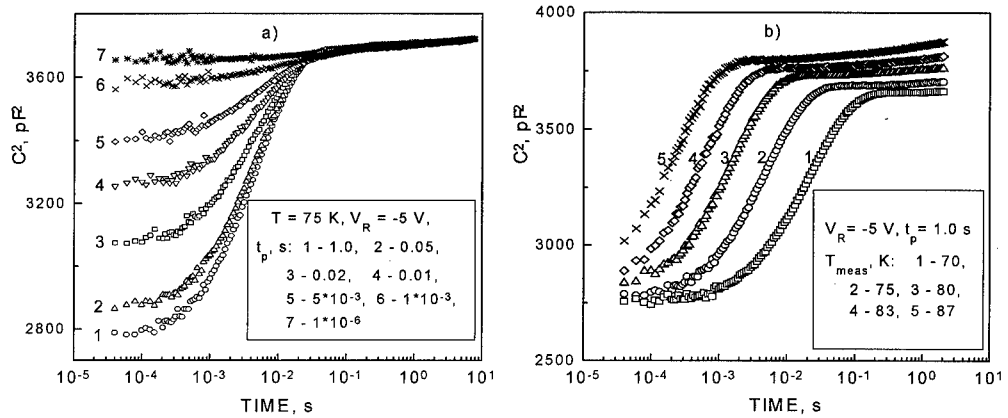


Fig. 2. Time transients of the square of diode capacitance taken a) at 75 K after filling pulse of different length and b) at different temperatures after pulse of 1.0 s length.

Figure 3 shows the capture kinetics for the MHR center at different temperatures. Analysis of these kinetics showed that the trap-filling process at a fixed temperature can be considered as a mono-exponential growth to the maximum value of N_f $(N_f)_{max}$ with increase in the filling pulse length, i.e.

$$\Delta C_{p0}^2 = 2 A_0 N_f = 2 A_0 \left(N_f\right)_{\max} \left[1 - \exp\left(-t_p / \tau_f\right)\right] , \qquad (2)$$

where t_p is the length of filling pulse, and τ_f is the time constant of the process. Solid lines in Fig. 3 present the dependencies calculated according to Eq. (2) with appropriate choice of $\left(N_f\right)_{max}$ and τ_f.

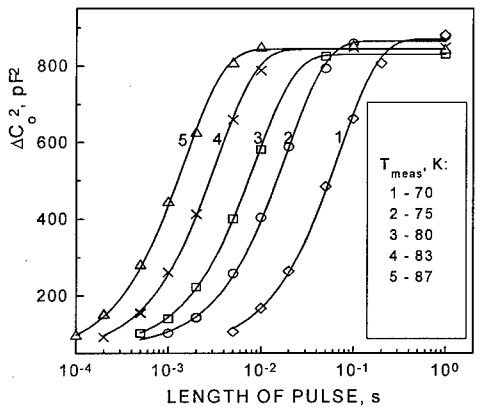


Fig. 3. Changes in the square of a diode capacitance at different temperatures as a result of occupancy of the MHR center with electrons after filling pulse of various length.

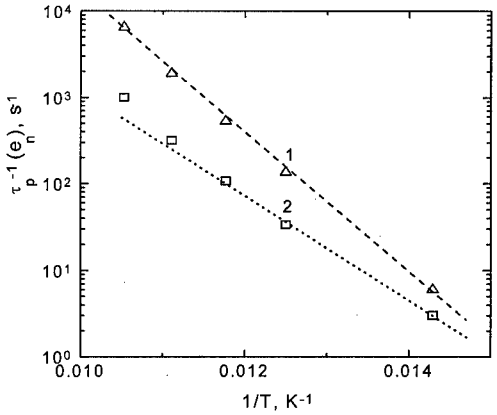


Fig. 4. Temperature dependence of (1) emission rate and (2) the inverse time constant of the trap-filling process for the MHR center in an irradiated and heat-treated (T = 350 °C) Si:O,H sample with initial resistivity ρ_0 = 5 Ω·cm.

Temperature dependencies of the emission rate (e_n) and the inverse time constant of the filling process (τ_f^{-1}) for the MHR center in a hydrogenated Cz-Si sample are shown in Fig. 4. The activation energy of the emission process is determined from the dependence of $e_n T^{-2}(1/T)$ as ΔE_e = 0.15 eV. Two different slopes are apparent in the $\tau_f^{-1}(1/T)$ dependence. It is thought that the time

constant of the trap-filling process for a negative-U center can be expressed via the emission and capture rates as [8]

$$\tau_f^{-1} = e_n + c_n fn = e_n + \sigma_n v_{th} fn \quad , \tag{3}$$

where σ_n is the capture cross section of electrons by the trap, v_{th} is the average thermal velocity of electrons, n is the density of free electrons and f is a function related to the occupancy probability of an upper level of the center. Two slopes in the $\tau_f^{-1}(1/T)$ dependence can be observed when one or another terms in the right-hand side of Eq. (3) is dominant. It follows from Eq. (3) that τ_f^{-1} value should always exceed the value of e_n but the experimental data presented in Fig. 4 are not consistent with this statement $((e_n)_{exp} > (\tau_f^{-1})_{exp})$. Electric field in reverse-biased Schottky diodes can be an origin of the enhanced electron emission from traps but it is found that the field-enhanced emission cannot account for the unusual ratio of the emission and capture rates related to the MHR center. It is known also that for the defects with phonon-assisted emission and capture processes the activation energy of emission is a sum of thermal ionization energy and an energy barrier for the electron capture [9]. Thermal ionization energy of the singly negatively charged state of the MHR center was determined earlier as $\Delta E(-/0) = 0.11$ eV [5]. In accordance with a simple calculation the activation energy for the electron capture (ΔE_c) should be 0.04 eV ($\Delta E_c = \Delta E_n - \Delta E(0/+) = 0.15 - 0.11 = 0.04$ eV). However, this value differ significantly from the minimum possible ΔE_c value of about 0.12 eV, determined from the analysis of trap-filling process (low-temperature part of curve 2 in Fig. 4).

Discussion.

It was proposed in Ref. 7 that peculiar features of emission and capture processes related to the MHR center could be associated with the existence of an intermediate metastable configuration for the neutral charge state of the defect. Appropriate configurational coordinate diagram of the center is shown in Fig. 5. In accordance with this diagram four different states (D^-, X^0, H^0, and H^+) are available for the center and transitions between the stable D^- and H^+ states must occur via the thermodynamically unstable X^0 and H^0 states, i.e.,

$$D^- \longleftrightarrow X^0 + e^- \longleftrightarrow H^0 + e^- \longleftrightarrow H^+ + 2e^- \, . \tag{4}$$

The changes in density of states can be described by the following system of differential equations:

$$\begin{aligned}
\frac{dN_{D^-}}{dt} &= c_{nX} n N_{X^o} - e_{nD} N_{D^-}, \\
\frac{dN_{X^o}}{dt} &= e_{nD} N_{D^-} - c_{nX} n N_{X^o} + \omega_2 N_{H^o} - \omega_1 N_{X^o}, \\
\frac{dN_{H^o}}{dt} &= \omega_1 N_{X^o} - \omega_2 N_{H^o} - e_{nH} N_{H^o} + c_{nH} n N_{H^+}, \\
\frac{dN_{H^+}}{dt} &= e_{nH} N_{H^o} - c_{nH} n N_{H^+}, \\
\frac{dn}{dt} &= e_{nD} N_{D^-} - c_{nX} n N_{X^o} + e_{nH} N_{H^o} - c_{nH} n N_{H^+}.
\end{aligned} \tag{5}$$

where $e_{nD(H)}$ and $c_{nX(H)}$ are the emission and capture coefficients defined in a common manner ($e_n = c_n N_c \exp(-\Delta E_c/kT)$, $c_n = \sigma_o v_{th} \exp(-\Delta E_c/kT)$), $\omega_{1(2)} = \omega_{01(02)} \exp(-\Delta E_{1(2)}/kT)$ are the rates of structural rearrangement, n is the electron concentration, N_D^-, N_X^o, N_H^o and N_H^+ are densities of the appropriate states of the MHR center ($N_D^- + N_X^o + N_H^o + N_H^+ = N_{MHR}$).

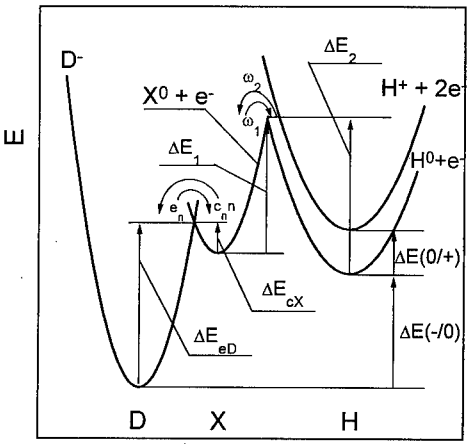


Fig. 5. Configurational coordinate diagram of the MHR center.

The full solution of the system (5) is rather complicated. However, taking into consideration that the reaction rates differ significantly and some of the states are in quasiequilibrium and assuming that $N_{MHR} << n$ (n = const) we could pass from such a system to an ordinary differential equations of the first order. Analytical expressions for the changes in the density of states could be obtained easily by solution of such equations. In particular, the changes in the density of the singly negatively charged state of the defect at a constant temperature after the deviation from equilibrium are expressed by a simple equation

$$\Delta N_{D^-}(t)=\left(\Delta N_{D^-}\right)_0 exp(-t/\tau), \qquad (6)$$

where $\left(\Delta N_{D^-}\right)_0$ is the initial deviation from the equilibrium density of the D^- state and τ is the time constant of the process. This time constant depends on the reaction rates as

$$\tau^{-1}=\frac{\omega_1 e_{nD}+c_{nx} n\,\omega_2 f_H}{\omega_1+c_{nx} n}, \qquad (7)$$

where $f_H=N_{H^0}/\left(N_{H^0}+N_{H^+}\right)=\left\{1+\exp\left[-\left(E_F-E(0/+)/kT\right)\right]\right\}^{-1}=\left\{1+\left(N_C/n\right)\exp\left[-\left(E_C-E(0/+)/kT\right)\right]\right\}^{-1}$ is the relative occupancy function of the H^0 state. Eq. (7) can be expressed in a usual form

$$\tau^{-1}=e_n^{eff}+c_n^{eff} n \qquad (8)$$

with

$$e_n^{eff}=e_{nD}\left(1+c_{nX} n/\omega_1\right)^{-1},$$
$$c_n^{eff}=c_{nX}\,\omega_2\,\omega_1^{-1} f_H\left(1+c_{nx} n/\omega_1\right)^{-1}. \qquad (9)$$

The analysis of Eqs. (7-9) has shown that several different terms with their characteristic activation energies and power dependence on the free carrier concentration can be dominant in $\tau^{-1}(1/T)$ dependence with respect of the Fermi level position (E_F) and the $c_{nx}n/\omega_1$ ratio.

Emission or capture becomes a dominant process when Fermi level crosses an occupancy level E(-/+){E(-/+) = 1/2[E(-/0)+E(0/+)]} of a negative U defect.

For E_F>E(-/+) capture is more effective and $\tau^{-1}\approx c_n^{eff} n$. In principle, in this case up to four different terms can occur in the equation for $\tau^{-1}(1/T)$ depending on the position of Fermi level relative to E(0/+) level of a center and the $c_{nx}n/\omega_1$ ratio. Power dependence of τ^{-1} on the free carrier concentration can vary from 0 to 2 in these terms.

For E_F<E(-/+) emission is a dominant process ($\tau^{-1}\approx e_n^{eff}$). If $c_{nx}n<<\omega_1$ the emission process is similar to that one of the usual centers. If $c_{nx}n>>\omega_1$ then $e_n^{eff}\approx e_{nD}\,\omega_1/c_{nx}n$ and the effective emission rate should vary in inverse proportion to the electron concentration.

The dependencies of $\tau^{-1}(1/T)$, experimentally observed in our study and calculated in accordance with Eq. (7-9) with appropriate choice of parameters are presented in Fig. 6. It is found that ΔE_{cx} barrier is relatively small for the MHR center and a $c_{nx}n>>\omega_1$ case occur when studying

trap-filling process. Consequently $c_n^{eff} n = \omega_2 f_H$ and $e_n^{eff} \approx e_{nD}\omega_1/c_{nx}n$ for the MHR center in the considered temperature region and the range of free carrier concentration. Besides, in this range $E_F<E(0/+)$ and f_H can be expressed as $f_H \approx (n/N_C)\exp[\Delta E(0/+)/kT]$. Finally, it results in

$$c_n^{eff} n = \frac{\omega_{20} n}{N_c}\exp\left(-\frac{\Delta E_2 - \Delta E(0/+)}{kT}\right),$$
$$e_n^{eff} = \frac{N_c \omega_{10}}{n}\exp\left(-\frac{\Delta E_{eD} + \Delta E_1 - \Delta E_{cX}}{kT}\right) \quad (10)$$

for the MHR center. In the depletion region of the diode (under reverse bias conditions) the ratio $c_{nx}n/\omega_1 << 1$ should occur and $e_n^{eff} \approx e_{nD}$.

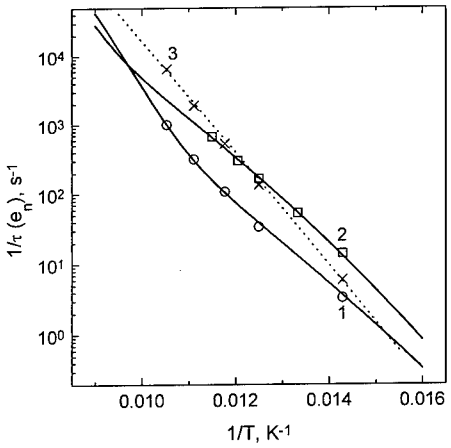


Fig. 6. Temperature dependencies of (1,2) inverse time constant of the trap-filling process and (3) emission rate for the MHR center in the samples with different initial resistivity: 1,3 - 5 Ω·cm; 2 - 1 Ω·cm. Solid lines are calculated ones according to Eqs. (7-10) with the fitting parameters given in text.

From the fitting procedure of experimental results in accordance with Eqs. (7-10) the values of ΔE_2 - $\Delta E(0/+)$ and ΔE_{eD} + ΔE_1 - ΔE_{cx} were derived as 0.12 eV and 0.27 eV, respectively. Activation energy of electron emission from the D^- state (ΔE_{eD}) was found to be 0.15 eV. Taking into account the value of $\Delta E(0/+)$ determined earlier as 0.043 eV [4], we found that $\Delta E_2 \approx 0.16$ eV and ΔE_1 - $\Delta E_{cx} \approx 0.12$ eV. Separate determination of the ΔE_1 and ΔE_{cx} values was not possible from the experimental data obtained. Unfortunately, limited characteristics of our capacitance meter do not allow us to carry out the measurements at higher temperatures and observe an unusual power dependence of τ^{-1} on the free carrier concentration ($\tau^{-1} \sim 1/n$).

Concluding remarks.

Finally, it should be noted that practically all the parameters of metastable defects can be deduced from the analysis of experimentally obtained $\tau_f^{-1}(1/T)$ dependencies. Usual DLTS measurements with a constant filling pulse length make it possible to determine only the emission rate e_n since in the depletion region of the diode the electron recapture processes do not occur. So, to detect the existence of intermediate states and to determine parameters of metastable defects correctly the careful studies of capture processes in a wide range of temperatures and in crystals with different doping levels are required in addition. Such an approach was successful for the explanation of some peculiar features of emission and capture processes related to the MHR center in silicon and determination of parameters of this defect.

References.

1. G.D. Watkins, Reviews of Solid State Science **4**, 279 (1990).
2. L. Dobaczewski and J.M. Langer, Mater. Sci. Forum **65-66**, 433 (1990).
3. F.P. Korshunov *et al*, Dokl. Akad. Nauk Belarus **38**, 35 (1994).
4. V.P. Markevich *et al*, J. Appl. Phys. **76**, 7347 (1994).
5. V.P. Markevich *et al*, Mater. Sci. Forum **196-201**, 945 (1995).
6. V.P. Markevich and L.I. Murin, Fiz. Tekh. Poluprovodn. [Semiconductors] **30**, 1186 (1996).
7. B.A. Komarov *et al* in "Proc. of the 23rd Intern. Conf. on the Physics of Semicond." ed M. Scheffler and R. Zimmermann (Singapore: World Scientific) pp. 2593-2596 (1996).
8. L.F. Makarenko and L.I. Murin, Phys. Stat. Sol. (b) **145**, 241 (1988).
9. C.H. Henry and D.V. Lang, Phys. Rev. B **15**, 989 (1977).

Materials Science Forum Vols. 258-263 (1997) pp. 223-228
© 1997 Trans Tech Publications, Switzerland

IR STUDIES OF SI-H BOND-BENDING VIBRATIONAL MODES IN SI

S.Zh.Tokmoldin and B.N.Mukashev
Institute of Physics and Technology, Kazakstan Ministry-Academy of Sciences, Almaty, 480082, KAZAKSTAN. E-mail: serik@satsun.sci.kz

Keywords: crystalline silicon, atomic hydrogen, IR local vibrational modes

Abstract. The IR isotope analysis of Si-H bond-stretching and bond-bending local vibrational modes in proton-implanted crystalline silicon are performed. New data on the identification of Si-H bond-bending IR absorption bands are obtained. It is shown that bond-bending bands are split into two separated groups related to vacancy-type and interstitial-type complexes as in the case of the bond-stretching bands.

Introduction.

Hydrogen (H) implantation into crystalline silicon (Si) leads to appearing of very complicated IR absorption spectra caused by local vibrational modes of bonded H atoms [1-3]. At present time there are a lot of experimental and theoretical data on the nature of bond-stretching bands [4,5]. However the analysis of bond-bending spectra is very difficult because of

- bond-bending Si-H bands in the range 500-800 cm^{-1} are broad;
- weak or unresolved splitting are characteristic of the bands;
- there is not direct correlation with behavior of the bond-stretching bands;
- there is a very intensive phonon absorption in the bond-bending range.

In comparison with bond-stretching range there are only a few IR bands in the bond-bending range. This fact indicate that the bond-bending vibrational frequencies of complexes with similar structure may be closed to each other. We have found correlation between total intensities for some groups of bond-stretching and bond-bending IR bands.

Experimental results.

In this work we have studied IR spectra of Si crystals with impurity concentration of $N_{P,B} < 10^{14}$ cm^{-3} and N_0, $N_C < 10^{15}$ cm^{-3}. The samples were implanted by energetic E=30 MeV protons and E=25MeV deuterons at doses of 3×10^{16}-10^{18} ion/cm^2 and beam current of 0.1-0.7 $\mu A/cm^2$. Various thickness aluminum screens were used for ion energy reducing up to ~3 MeV to prevent samples heating. The samples were glued onto a water-cooled aluminum holder and the temperature was kept at $<50^0$C.

IR spectra of implanted Si:H and Si:D samples were measured in differential mode with unimplanted refereeing Si sample in the wavenumber range of 500-2300 cm^{-1} and temperatures of 80K and 300K. Typical Si:H and Si:D IR spectra at 300K are shown in Fig. 1. Top one is a redrawn Si:H spectrum with wavenumber scale reduced by a isotope shift factor of ~1.37. There is a good similarity of the spectrum with the Si:D spectrum in the whole range excepting for a neighborhood of the 480 cm^{-1} TO-phonon line which considerably affects the absorption related to Si-D bond-bending modes.

We have studied both dose dependence and annealing behavior of Si-H bond-bending bands in the 500-800 cm^{-1} range in comparison with Si-H bond-stretching bands in the 1900-2250 cm^{-1} range. Dose dependence showed monotonous increasing of bond-bending bands intensities similar to dose dependence of the main Si-H bond-stretching bands. However no direct correlation in the dose dependence data only was found to separate groups of bond-stretching and bond-bending bands arisen from the various type vibrational modes of any H-related complexes.

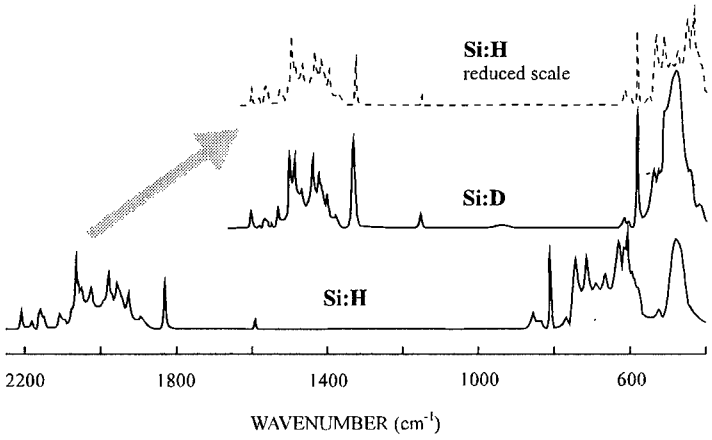


Figure 1. Typical IR spectra at 300K for Si:H and Si:D samples implanted by H^+ and D^+ ions.

Figure 2 shows the main Si-H bond-stretching and bond-bending bands annealing behavior derived from the spectra measured at 300K. It is seen good correlation for bands at 634 cm^{-1} with 2211 cm^{-1}, at 668 cm^{-1} with a doublet at 2161 cm^{-1} and 2184 cm^{-1} (weak band), at 694 cm^{-1} and 588 cm^{-1} with a doublet at 2104cm^{-1} and 2120 cm^{-1}. The 610, 718 and 750 cm^{-1} bond-bending bands show no direct correlation with any separate Si-H bond-stretching band. However there are plain correlation between the 610 cm^{-1} band and the summarized intensities of the 2161, 2120, 2104 and 2067 cm^{-1} bands as well as between the doublet at 718 and 750 cm^{-1} and the summarized intensities of the 1950 and 1960 cm^{-1} bands.

Thus, the annealing behavior data allow to separate the following groups of both bond-bending and bond-stretching Si-H local vibrational modes:

a) 2211 cm^{-1} and 634 cm^{-1},
b) 2161, 2184 cm^{-1} and ~610, 668 cm^{-1},
c) 2104, 2120 cm^{-1} and ~610, 694, 588 cm^{-1},
d) 1950 cm^{-1} and 718, 750 cm^{-1},
e) 1960 cm^{-1} and 718, 750 cm^{-1}.

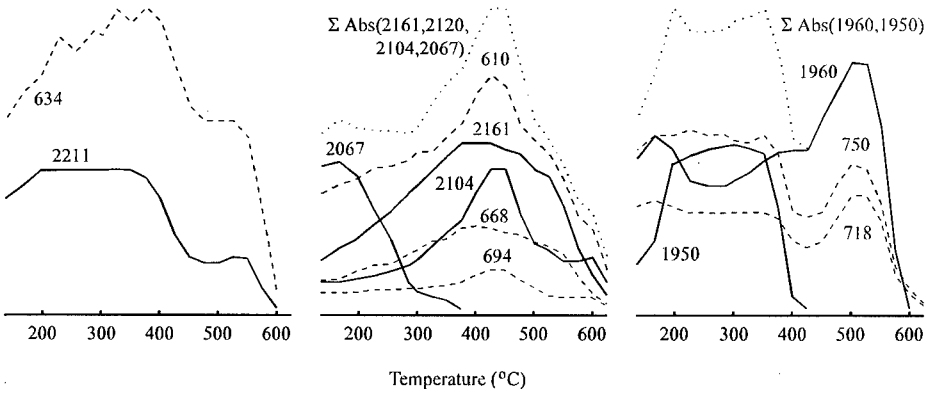


Figure 2. Annealing behavior of the main Si-H bond-bending and bond-stretching bands

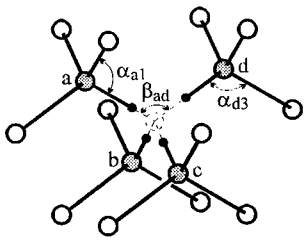
Discussion.

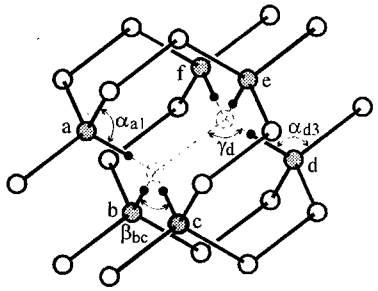
In [6] we performed isotope study of the Si:H spectrum in the 1900-2250 cm^{-1} bond-stretching range and found a difference in the temperature dependence of an anharmonicity between the bands lying above and below 2000 cm^{-1}. This allowed us to identify the bands above 2000 cm^{-1} with vacancy-type centers and the bands below 2000 cm^{-1} predominantly with interstitial-type centers. The same trend was also shown in other works both theoretically [7-9] and experimentally [10-12].

In [10] we showed that the most intensive Si-H bond-stretching bands in the 2000-2250 cm^{-1} range are related to the H-decorated intrinsic vacancy (V) and divacancy (V_2). The assignment was as follow: VH_4 - 2211 cm^{-1}, V_2H_6 - the doublet at 2184 and 2161 cm^{-1}, V_2H_4 - the doublet at 2104 and 2120 cm^{-1}, V_2H_2 - the 2067 cm^{-1}.

Thus the data on annealing behavior correlation between bond-bending and bond-stretching Si-H bands illustrated in Fig. 2 lead us to assumption that bond-bending Si-H bands are split into two separated groups related to vacancy-type and interstitial-type centers as in the case of the bond-stretching Si-H bands: the bands in the range 580-690 cm^{-1} may be assigned to the vacancy-type centers and the bands in the range 710-780 cm^{-1} may be assigned to the interstitial-type centers.

Figures 3(a) and 3(b) show Si-H bond structure in the vicinity of V and V_2. Because of Si-H bonds may be considered as dipoles with a small negative charge of ~-(0.2-0.3)e^- at the H atoms [13] the doublet structure of some Si-H bond-stretching bands indicates that there is a large resonance Si-H dipole interaction, sufficient to consider VH_n and V_2H_m (n=1,..,4; m=1,..,6) as "quasi-molecules". This allows to analyze the vibrational properties of various H-vacancy complexes using a group theory. The results of this analysis for VH_n are given in Table 1.





VH_1 $\alpha_{a1}+\alpha_{a2}+\alpha_{a3}=0$

VH_2 $\alpha_{a1}+\alpha_{a2}+\alpha_{d1}+\alpha_{d2}+\beta_{ad}=0$

VH_3 $\alpha_{a1}+\alpha_{c1}+\alpha_{d1}+\beta_{ac}+\beta_{ad}+\beta_{cd}=0$

VH_4 $\beta_{ab}+\beta_{ac}+\beta_{ad}+\beta_{bc}+\beta_{bd}+\beta_{cd}=0$

(a)

V_2H_6 $\beta_{ab}+\beta_{ac}+\beta_{bc}+\gamma_a+\gamma_b+\gamma_c=0$

$\beta_{de}+\beta_{df}+\beta_{ef}+\gamma_d+\gamma_e+\gamma_f=0$

(b)

Figure 3. H-decorated Si-bonds in the vicinity of intrinsic vacancy-related defects in c-Si.

It is seen in Fig. 3(a) and 3(b) that the distances between Si-H bonds located around two neighboring vacant sites are about twice in comparison with those for Si-H bonds located around one and the same vacant site. Hence the Si-H dipole interaction around a vacant site must be about one order greater than in the case of two neighboring vacant sites. Therefore the assumption is that V_2H_m may be considered as a weak $VH_s \oplus VH_t$ (s,t=0,1,2,3) pair, the vibrational properties of which are similar to those of VH_n. Indeed a trigonal character of the doublet at 2161 and 2184 cm^{-1} related to V_2H_6 [10] was observed in uniaxial stress experiments [14].

Table 1. IR active Si-H local vibrational modes in the vicinity of a vacancy in c-Si.

Symmetry	T_d	C_{3v}		C_{2v}	C_s
Center	VH_4	VH_3	VH	VH_2	VH
Bond-stretching modes	F_2	A_1 E	A_1	A_1 B_1	A'
Bond-bending modes	F_2	A_1 2 E	E	A_1 B_1 B_2	A' A"

In [12] the doublet at 2161 and 2184 cm^{-1} was assigned to VH_3. VH_3 has a dangling bond and, therefore, it is a deep acceptor-like center. In [11] we argued that in Si:H the complexes with even number of H atoms predominate owing to the effective interactions of H^+ with acceptor-type complexes containing odd number of H atoms. Hence the correlation in behavior of the 2161 and 2184 cm^{-1} doublet and the 2210 cm^{-1} band related to VH_4 must be observed. However no dose and annealing behavior data were found to support this assumption.

The group theory analysis (Table 1) predicts the following vibrational modes for various vacancy-H complexes:

a) 1 bond-stretching and 1 bond-bending modes - for VH_4;
b) 2 bond-stretching and 3 bond-bending modes - for VH_3 and V_2H_6 (as $VH_3 \oplus VH_3$);
c) 2 bond-stretching and 3 bond-bending modes - for VH_2 and V_2H_4 (as $VH_2 \oplus VH_2$).

In the last case the $VH_3 \oplus VH_1$ pair is also available. One can see a good conformity of the experimental data (Fig.2) with the predictions. The closed frequencies of some bond-bending Si-H modes may be explained by similar structure of the VH_n-like weak-bonded units in the $VH_s \oplus VH_t$ complexes.

Let's now consider the possible configurations for H-decorated self-interstitial complexes.

According to [15] self-interstitial Si_i atom is very mobile even at very low temperatures and up to now it was not directly observed. One of possible configuration of this defect is a <001> Si interstitialsy proposed in [16]. The self-interstitials were observed experimentally as complexes including several Si_i atoms. Those are Si-B3 <001> split interstitial [16], Si-A5 two <001> split interstitial [17] and S-P6 di-interstitial [18] centers. Tentative configurations of the Si-B3 and Si-A5 centers [16,17] may be considered as consisting of two structural units similar to the Si interstitialsy.

The <001> Si interstitialsy (here we refer it as the I-center) may be stabilized by two H atoms with the formation of the IH_2 center (Fig. 4(a)). It was suggested for the first time in [19] where the IR spectra of Si crystals grown in hydrogen atmosphere were studied. Figures 4(b)-4(d) show similar tentative configurations for H-decorated Si-P6, Si-B3 and Si-A5 centers, respectively.

The IH_2 center has a <100> C_2-symmetry. As in the case of above discussed vacancy-type centers the IH_2 vibrational properties are determined by two Si-H dipoles which may be considered as a Si_2H_2 "quasi-molecule" with the <100> C_2-symmetry. So according to the group theory it is expected that a self-interstitial complex consisting of one or more Si_2H_2 structures has at least two Si-H bond-stretching A + B modes and three Si-H bond-bending A + 2 B modes. Indeed we have

observed a doublet bond-bending Si-H bands at 718 and 750 cm^{-1} and the additional splitting of the 1950 and 1960 cm^{-1} Si-H bond-stretching bands appeared due to the decreasing of measurement temperature up to 80 K. Then as in the case of vacancy-type centers the good conformity of the experimental data (Fig.2) with the theoretical predictions is seen.

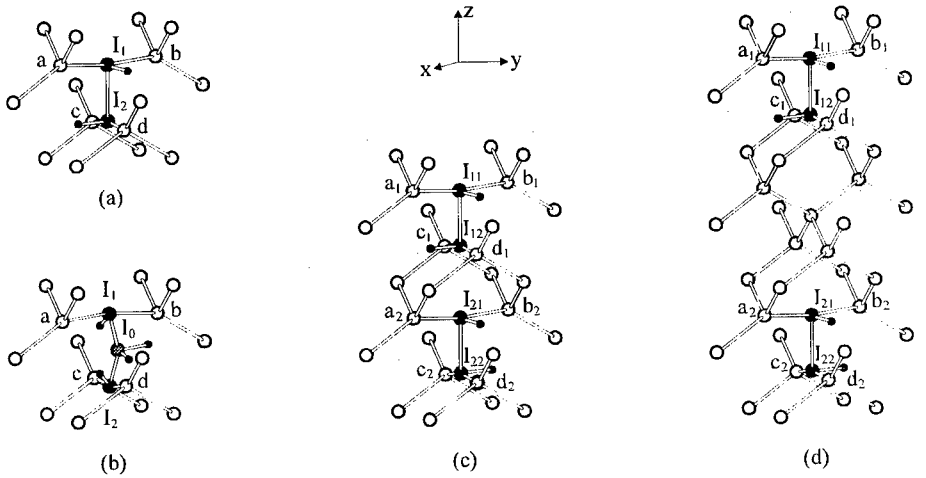


Figure 4. Tentative configurations for H-decorated self-interstitials in c-Si.

It is seen in Fig. 4(c) and 4(d) that the tentative configurations of the H-decorated Si-B3 and Si-A5 centers consist of the Si_2H_2 "quasi-molecules" like the IH_2 center. So the vibrational properties of all these three centers are expected to be nearly closed to each other. Indeed it is necessary to note that the frequencies of two groups of the Si-H bond-stretching and bond-bending bands at 1950, 718 and 750 cm^{-1} as well as 1960, 718 and 750 cm^{-1} bands are well closed to the frequencies of the bands at 1946, 791 and 812 cm^{-1} which were tentatively assigned in [19] to the IH_2 center. Taking into account the temperature stability of the self-interstitial complexes [16,17] the bands at 1950 and 1960 cm^{-1} may be tentatively assigned to the H-decorated Si-A5 and Si-B3 centers, respectively. Figure 2 shows that the centers connected with the 1950 and 1960 cm^{-1} bands are more stable than the Si-A5 and Si-B3 centers disappeared near 170^{0}C [17] and 500^{0}C [16], respectively. This is apparently a general feature because the same trend is characteristic of the vacancy-type VH_4 and V_2H_6 centers.

Conclusions.

The data presented show direct correlation between the Si-H bond-stretching and bond-bending IR absorption bands and lead to conclusion that the Si-H bond-bending bands related to vacancy-type and interstitial-type centers are located separately in different spectral ranges as in the case of Si-H bond-stretching bands.

The data allow also to propose some tentative assignments of the Si-H bond-stretching and bond-bending modes to H-decorated vacancy-type and interstitial-type centers. Additional studies are needed to support the assignments.

Acknowledgments.

This work was partially funded by the Science Foundation of the Ministry of Science - Academy of Sciences of the Republic of Kazakstan.

References.

1. H.J.Stein, J.Electr.Mat. **4**, 157 (1975).
2. N.N.Gerasimenko, M.Rolle, L.-J.Cheng, Y.H.Lee, J.C.Corelli and J.W.Corbett, Phys.Stat.Sol(b) **90**, 689 (1978).
3. B.N.Mukashev, K.H.Nussupov, and M.F.Tamendarov, Phys.Lett. **72A**, 381 (1979).
4. S.J.Pearton, J.W.Corbett, M.Stavola, Hydrogen in Crystalline Semiconductors (Springer-Verlag, 1992).
5. S.M.Mayers, M.Baskes, H.K.Birnbaum, J.W.Corbett, G.G.DeLeo, S.K.Estreicher, E.E.Haller, P.Jena, N.M.Johnson, R.Kirchheim, S.J.Pearton, M.J.Stavola, Rev.Mod.Phys. **64**, 559 (1992).
6. B.N.Mukashev, M.F.Tamendarov, and S.Zh.Tokmoldin in ICDS-15, ed. G.Ferenczi, Mat.Sci. Forum (Switzerland: Trans Tech Publications) **38-41**, pp. 1039-1044 (1989).
7. V.V.Frolov and B.N.Mukashev, Phys.Stat.Sol. (b) **148**, K105 (1988).
8. P.Deak, M.Heinrich, L.C.Snyder, and J.W.Corbett, Mater.Sci.Eng. **B4**, 57 (1989).
9. P.Deak, L.C.Snyder, M.Heinrich, C.R.Ortiz, and J.W.Corbett, Physica **B170**, 253 (1991).
10. B.N.Mukashev, S.Zh.Tokmoldin, and M.F.Tamendarov in Defect Control in Semiconductors, ed. by K.Sumino (North-Holland: Elsevier Science Publishers) pp. 429-434 (1990).
11. B.N.Mukashev, S.Zh.Tokmoldin, M.F.Tamendarov, and V.V.Frolov, Physica **B170,** 545 (1991).
12. B.B.Nielsen, L.Hoffmann, and M.Budde, Mat.Sci.Eng. **B36**, 259 (1996).
13. M.Cardona, Phys.Stat.Sol.(b) **118**, 463 (1983).
14. B.B.Nielsen and H.G.Grimmeiss, Phys.Rev. **B40**, 12403 (1989).
15. G.D.Watkins, Chenese J.Phys. **15**, 92 (1977).
16. K.L.Brower, Phys.Rev. **B14**, 872 (1976).
17. Y.H.Lee, Y.M.Kim, and J.W.Corbett, Rad.Eff **15**, 77 (1972).
18. Y.H.Lee, N.N.Gerasimenko, and J.W.Corbett, Phys.Rev. **B14**, 4506 (1976).
19. T.S.Shi, L.M.Xie, G.R.Bai, and M.W.Qi, Phys.Stat.Sol.(b) **131,** 511 (1985).

Materials Science Forum Vols. 258-263 (1997) pp. 229-234
© 1997 Trans Tech Publications, Switzerland

OPTICAL ABSORPTION DUE TO HYDROGEN BOUND TO INTERSTITIAL Si IN Si CRYSTAL GROWN IN HYDROGEN ATMOSPHERE

Masashi Suezawa
Institute for Materials Research, Tohoku University, Sendai 980-77, JAPAN

Keywords : Si, hydrogen, interstitial, optical absorption

Abstract. We studied optical absorption spectrum of Si crystal grown in a hydrogen ambient. Specimens were grown by the floating-zone grown method in hydrogen atmosphere of 1 atm. Optical absorption spectra of those specimens were measured at 6 K. Many optical absorption lines were observed in the range of 1900 to 2200 cm^{-1}. They were observed only when the concentrations of carbon or boron were high. To understand these results, we refered a report according to which so-called A-type swirl, an interstitial type dislocation loop, was observed when impurities of smaller covalent radius than that of Si were doped. Hence we concluded that the above optical absorption lines were due to localized vibration of hydrogen atoms bound to interstitial Si atoms.

Introduction.

We studied optical absorption spectra of Si crystals grown in hydrogen atmosphere and concluded that many optical absorption lines observed at around 2000 cm^{-1} were due to localized vibration modes of hydrogen atoms bound to interstitial Si atoms.

In this section, we briely reviewed studies on point defects existed at high temperature in Si and then studies on defects in Si grown in hydrogen atmosphere. Point defects existed at high temperature in Si crystals are responsible for the self-diffusion and diffusion of substitutional impurities. Moreover, they are recently known to generate so-called secondary defects, for example, A-swirl, D-swirl and negative crystals, which existed in as-grown Si crystals[1]. They disturbe the uniformity of electrical properties of wafers. Consequently they are harmful for integrated circuits. Hence many reports have been published to explain the generation processes of the secondary defects from vacancies (V_{Si}) and interstitials(I_{Si})[2-6].

However, little is known on the properties of such defects at high temperatures since it is difficult to study them. We therefore think that it is still important to investigate their high temperature properties, such as the equilibrium concentration, the formation energy and the migration energy. There are only a small number of papers on the point defects in Si at thermal equilibrium at high temperatures. Dannefaer et al.[7] studied point defect in Si at high temperature with the measurement of positron life time which was sensitive to vacancy-type defects. They determined the formation energy of vacancy to be 3.6 ± 0.2 eV. However Seeger's group[8] and Lynn's group[9] did not detect vacancies with positron annihilation method. Okada measured lattice constants at high temperatures. Combining his data with Okaji's data on the temperature dependence of specimen length, Okada[10] concluded that the concentration of V_{Si} was higher than that of I_{Si}. He did not determine the formation energy of vacancy since the temperature dependence of the concentration of (V_{Si}-I_{Si}) was not simple. Comparing Dannefaer et al.'s result with Okada's one, we noticed a peculiar feature that the concentration of V_{Si} determined by Dannefaer et al. was smaller than that of V_{Si}-I_{Si} determined by Okada.

There seems another way to study point defects existed at high temperature, namely, the study of optical absorption lines in Si crystals grown in hydrogen atmosphere since they coincided with those observed in proton-implanted crystals. This strongly suggests that those lines are related to hydrogen bound to isolated point defects, such as V_{Si} and I_{Si}. It is still open question whether the point defect is V_{Si} or I_{Si}. Some researchers claimed that the defect was I_{Si}. Shi et al.[11], for example, proposed that point defect was I_{Si}, and claimed that the concentration of I_{Si} was larger than that of V_{Si} at thermal equilibrium. On the other hand, Xie et al.[12] proposed that the point defect responsible for the above optical absorption lines was vacancy. Recently, Bech Nielsen et al. [13] studied optical absorption spectra of Si after H^+ implantation from both of experimental and theoretical view points and concluded that the point defect was V_{Si}.

As shown in the above, there is still controversy about the defect responsible for the above optical absorption lines. Even so (or therefore), it is interesting for us to study optical absorption spectra of Si crystals grown in hydrogen atmosphere since it seems possible to know the point defects existed at high temperatures from such a study as discussed already. One peculiar point is as follows: From the study on the defects generated due to irradiation of high energy electrons at low temperature, V_{Si} and I_{Si} are known to have very high diffusion rates and therefore they seem to be impossible to be detected in the as-grown crystal.

We measured the optical absorption spectra of Si crystal grown in hydrogen atmosphere, concentrating on the effect of dopants on the spectra. From the effect of dopants, we concluded that the observed optical absortion spectra were due to hydrogen bound to I_{Si}.

Experimental.

Specimens were grown in hydrogen atmosphere of 1 atm. with the floating-zone grown method using a high-frequency induction coil for zone-melting. Starting materials were phosphorus-doped ($5x10^{12}$, $2.4x10^{15}$ cm^{-3}) and boron-doped ($1.5x10^{16}$ cm^{-3}) Si crystals grown by the floating-zone grown method. In the case of heating of a Si crystal by the induction coil, we need to pre-heat the crystal. We adopted three methods as shown in Fig. 1. In the case of (b) and (c) in Fig. 1, we heated the split-type carbon sheath which was removed after the crystal temperature became high enough to be heated by the induction coil. In the case of (a), the crystal was heated by the carbon chuck which was heated by the induction coil. The growth velocity was mainly 0.2 mm/min. The diameter of specimens was about 12 mm in most cases.

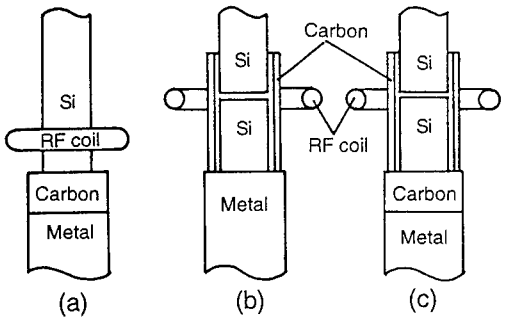


Fig. 1 Methods of pre-heating of specimens.

Optical absorption spectra of specimens were measured at 6 K with an FT-IR equipment. The thickness of specimen was about 6 mm and the resolution was 0.25 cm^{-1}.

Results.

Figure 2 displays an optical absorption spectrum of n-type specimen. Those peaks were found also in proton-implanted specimens as will be shown in Fig. 3. Hence, these peak are thought to be

related to vibration of hydrogen atom bound to an isolated point defect. Among several peaks, a sharp peak at about 2223 cm^{-1} has been studied extensively. Bech Nielsen et al.[14], for example, determined the symmetry of defect responsible for this peak with the measurement of response of this peak for uniaxial stresses.

Figure 3 shows a summary of absorption peaks observed in specimens grown in hydrogen atmosphere and proton-implanted specimens. Cui et al.[15] observed those peaks at room temperature. If we consider the temperature dependence of peak positions, many of their peak positions coincided with ours. Some of the peak positions in the crystal grown in hydrogen atmosphere coincide with those of proton-implanted ones. Hence we concluded that many defects in the as-grown crystal were the same as those of proton-implanted ones, namely, hydrogen atoms bound to isolated point defects.

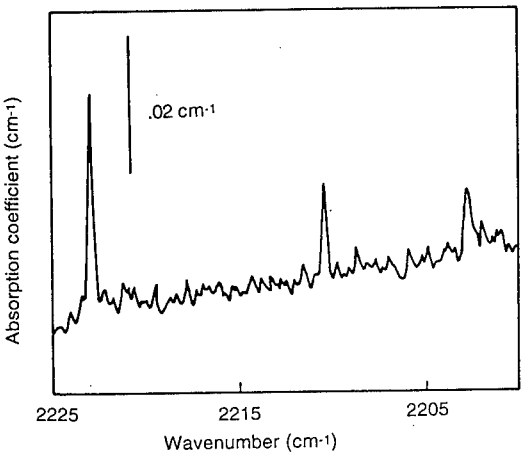


Fig. 2 Optical absorption spectrum of a specimen grown in hydrogen atmosphere with a growth velocity of 0.2 mm/min.

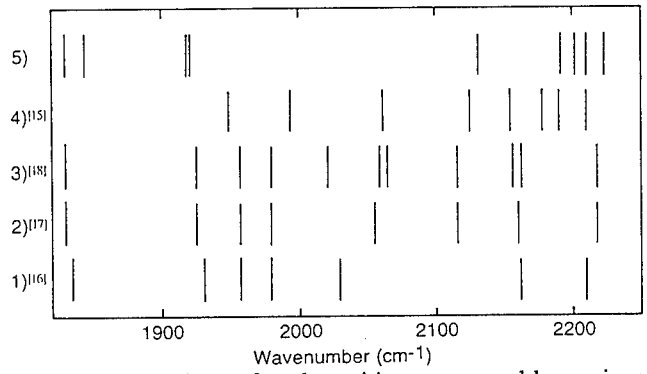


Fig. 3 Comparison of peak positions measured by various authors. 1)~3): proton-implanted, 4)&5): grown in hydrogen atmosphere, 5): present work.

Interesting point of our results was the effects of impurities. At first, the above absorption peaks were observed when we used (a) or (c) in Fig. 1 for pre-heating the crystals. Those crystals included high concentration of carbon, about $5x10^{16}$ cm^{-3}. The surfaces of carbon chucks of (a) and (c) were slightly whitish, suggesting reaction of them with residual oxygen. Hence carbon was probably doped to crystals because of CO gas coming from those chucks. We did not observe the spectrum of Fig. 2 when we used (b) in Fig. 1 for pre-heating the crystal. The grown crystal with the use of (b) in Fig. 1 included only a small amount of carbon. We therefore thought that there might be an impurity effect for the appearance of absorption peaks in Fig. 2. In this context, we reminded Abe's study on the effect of impurity for the generation of swirls[16]. He observed A-swirl, agglomerates of I_{Si}, and D-swirl, agglomerates of V_{Si}, when he doped impurities of smaller covalent radii and larger ones than that of Si, respectively.

We therefore examined the effect of impurity for the appearance of the spectrum of Fig. 2. We grew crystal from p-type Si doped with about $1.5x10^{16}cm^{-3}$ boron atoms which have smaller covalent radius than that of Si. We observed the same spectrum as that of Fig. 2 with slightly

weaker intensity. When we doped Sn about $5x10^{18}cm^{-3}$ during crystal growth with (a) in Fig. 1, we did not observe the spectrum in Fig. 2. As Sn has larger covalent radius than that of Si, vacancies generated by doping Sn probably over-compensated I_{Si} generated by C doping. In summing up the above results, we concluded that the optical absorption peaks observed around 2000 cm^{-1} were due to localized vibration of hydrogen atoms bound to I_{Si}.

Discussion.

In the following, we discuss about the effect of impurity for the formation energy of I_{Si}. Abe's results strongly suggested that the dominant point defects at high temperatures depended on the doped impurity. He qualitatively explained his results by assuming elastic interaction between impurity and point defect such as V_{Si} and I_{Si}. We slightly extend his explanation as follows.

First, we discuss about the heat of solution of interstitial impurity in Si. If the impurity is Si, it is interstitial Si, I_{Si}. The reason for this discussion is that the covalent radius of substitutional impurity affects the volume of interstitial site and hence may affect the formation energy (E_f) of I_{Si}. From the dependence of the heat of solution of interstitial impurity, we can probably evaluate the effect of volume of interstitial site on E_f.

We assume that the heat of solution (E. This is E_f when the impurity is Si.) is composed of two terms, namely, contributions from the chemical energy ($E_{chem.}$) and the elasic energy ($E_{elas.}$). We also assume that the elastic energy is proportional to the square of a misfit ε defined by Eq. 1,

$$\varepsilon = (R - R_0) / R_0 \qquad (1)$$

, where R and R_0 are the atomic radius of impurity and the covalent radius of Si, respectively.

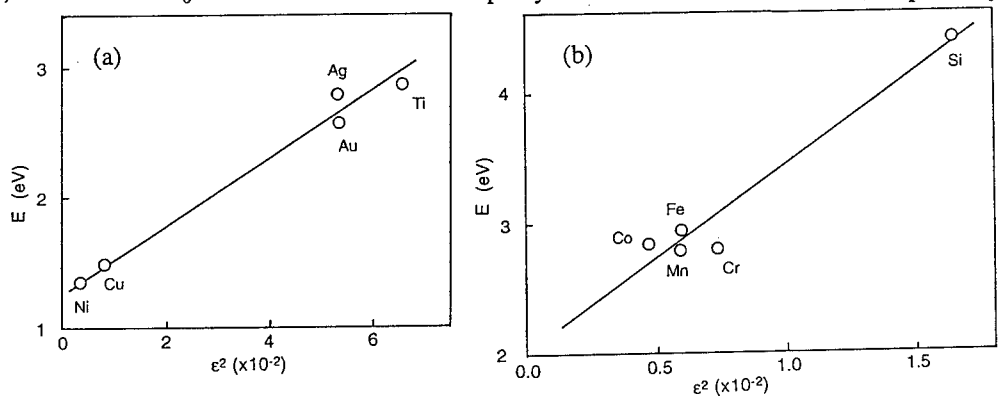


Fig. 4 Relation between the heat of solutions of interstitial impurities and their misfits.

Consequently the heat of solution is given by Eq. 2 ;

$$E = E_{chem.} + 8\pi\mu\varepsilon^2 R_0^3 \qquad (2)$$

, where μ is the shear modulus. To check the validity of the above assumptions, we plotted the heat of solution of interstitial impurity in Si as the function of ε^2 as shown in Figs. 4(a) and (b). Metallic interstitial impurities in Si were known to be classified in two groups as shown in Fig. 4. From the proportional coefficient of Figs. 4(a) and (b), we estimated μ. In the case of Fig. 4(a), it was about 1.6 times larger than that of Si. In the case of Fig. 4(b), on the other hand, it was about 9 times larger than that of Si. The former result seems to support the above assumptions. In the latter case, the discrepancy between the estimated value and the expected value, i.e., the shear modulus of Si, is very large. We think that there is some mechanism to enlarge the apparent shear

modulus in the case of impurities plotted in Fig. 4(b) since the above assumptions (Eq.(2)) seems to be realized in Fig. 4(a). We need more consideration to explain the above discrepancy.

A smaller covalent radius of substitutional impurity is probably equivalent to a larger volume of interstitial site, and consequently smaller misfits for interstitial impurities. According to Fig. 4(b), if the volume of interstitial site is 2 % larger than the ordinary one near a smaller substitutional impurity, the effective volume at neighboring interstitial site becomes large and the formation energy of interstitial atom decreases by about 1 eV. Such a large reduction of formation energy of interstitial (I_{Si}) probably explain the observed result. Such I_{Si} probably has a high diffusion rate, but becomes immobile by making pair or complex with hydrogen atoms after crystal growth in hydrogen atmosphere.

From the above experimental results, we can conclude that the concentration of thermal I_{Si} in high purity Si is smaller than that in Si doped with $1.5x10^{16}cm^{-3}$ boron atoms.

The reason for the existence of many peaks is probably due to various number of hydrogen atoms bound to interstitial Si atoms. To clarify this experimentally, we need to study on Si grown in deuterium atmsophere and a mixed gas of hydrogen and deuterium.

Conclusions.

We studied optical absorption spectra of Si crystals grown in hydrogen atmosphere and obtained following conclusions.

Several optical absorption peaks were observed at around 2000 cm-1 in the above crystals. They coincided well with the previous studies on similar crystals and also those observed in proton-implanted crystals. In our case, they were observed only when carbon contamination occurred or boron concentration was high. When tin was doped, the above optical absorption peaks were not observed even when the carbon concentration was high. According to the above experimental results, we interpreted that the above absorption peaks were related to hydrogen bound to interstitial Si atoms, not to vacancies.

Acknowledgement

The author thanks T. Sugawara of the Core Laboratory of Crystal Science of the IMR for growing Si crystals in hydrogen armosphere. This work was partly supported by a Grant-in-Aid for Scientific Research (1997 and 1998) on Kiban-B from the Ministry of Education, Science and Culture, Japan.

References.

1. T.S. Plaskett, Trans. Metall. Soc. AIME **233**,809(1965)
2. V.V. Voronkov, J. Cryst. Growth **59**, 625(1982)
3. T.Y. Tan and Y. Goesele, Appl. Phys. **A37**, 1(1985)
4. W. Wijaranakula, J. Electrochem. Soc. **139**, 604(1992)
5. R. Habu, I. Yunoki, T. Saito and A. Tomiura, Jpn. J. Appl. Phys. **32**, 1740(1993)
6. R.A. Brown, D. Maroudas and T. Sinno, J. Cryst. Growth **137**, 12(1994)
7. S. Dannefaer, P. Mascher and D. Kerr, Phys. Rev. Lett. **56**, 2195(1986)
8. R. Wurschum, W. Bauer, K. Maier, A. Seeger and H.E. Schaefer, J. Phys. Condens. Matter **1**, SA33(1989)
9. J. Throwe, T.C. Leung, B. Nielsen, H. Huomo and K.G. Lynn, Phys. Rev. **B40**,

12037(1989)
10. Y. Okada, Phys. Rev. **B41**, 10741(1990); *ibid.* **B45**, 6352(1992)
11. T.S. Shi, L.M. Xie, G.R. Bai and M.W. Qi, Phys. Stat. Sol.(**b**)**131**,511(1985)
12. L.M. Xie, M.W. Qi and J.M. Chen, J. Phys. **C3**, 8519(1991)
13. B. Bech Nielsen, L. Hoffmann, M. Budde, R. Jones, J. Goss and S. Oberg, Materials Sci. Forum **196-201**, 933(1995)
14. B. Bech Nielsen, J. Olajos and H.G. Grimmeiss, Phys. Rev. **B39**, 3330(1989)
15. S.F. Cui, Z.H. Mai and L.Z. Qian, Scientia Scinica **A27**,213(1984)
16. H.J. Stein, J. Electronic Mater. **4**, 159(1975)
17. N.N. Gerasimenko, M. Rolle, L.J. Cheng, Y.H. Lee, J.C. Corelli and J.W. Corbett, Phys. Stat. Sol.(b)**90**,689(1978)
18. B.N. Mukashev, K.H. Nussupov and M.F. Tamendarov, Phy. Lett.**72A**, 381 (1979)
19. T. Abe, Oyo Buturi (in Japanese) **59**, 272(1990)

Materials Science Forum Vols. 258-263 (1997) pp. 235-240
© 1997 Trans Tech Publications, Switzerland

TRAPPING SITE OF HYDROGEN MOLECULE IN CRYSTALLINE SILICON

K. Ishioka , K.G. Nakamura, M. Kitajima, N. Fukata[1], K. Murakami[1], S. Fujimura[2], J. Kikuchi[2]

National Research Institute of Metals, 1-2-1 Sengen, Tsukuba, 305 Japan
[1]Institute of Materials Science, University of Tsukuba, Tsukuba, 305 Japan
[2]Process Development Division, Fujitsu Ltd., Kawasaki, 211 Japan

Keywords : H_2; microcrystalline and amorphous Si, Raman scattering; *ab initio* calculation

Abstract. We have investigated trapping sites for H_2 in crystalline Si by examining the effect of crystal disorder on the formation of H_2 and by performing *ab initio* calculation. Raman measurements have been carried out on crystalline, microcrystalline and amorphous Si treated with atomic hydrogen. A vibrational line of H_2 has been observed in crystalline and microcrystalline Si after hydrogen atom treatment, and the intensity in microcrystalline is one fifth of that observed in crystalline Si. No Raman signal due to hydrogen molecule has been observed in amorphous Si. The results imply that H_2 is trapped in non-damaged, well-ordered bulk crystal. *Ab initio* calculations using $Si_{10}H_{16}$ cluster to simulate Si crystal indicate that H_2 is most stable at the tetrahedral site with a vibrational frequency quite close to that observed for H_2 in crystalline Si.

Introduction.

Hydrogen introduced in semiconductors form complexes with other impurities and crystal defects. It terminates the surface and dislocations [1,2], passivates donor/acceptor dopants [1,3], and forms platelets [4,5] and non-molecular diatomic hydrogen complex H_2* [6], depending on the substrate temperature during hydrogenation. Theoretical calculation predicted that molecular hydrogen (H_2) is stable in the tetrahedral sites in crystalline Si [7-10], while from experimental studies the formation of the interstitial molecular hydrogen was inferred only indirectly [11-13]. Recently we presented the first direct observation of H_2 in crystalline Si after hydrogen atom treatment by using Raman scattering spectroscopy [14-17]. A most plausible trapping site for hydrogen molecule is the tetrahedral site of Si crystal, which was predicted by the theoretical calculations.

Infrared (IR) absorption study showed that hydrogen injected into defective silicon gathers and terminates void surfaces by forming Si-H bonds more favorably than H_2 formation in voids [2]. On the other hand, molecular hydrogen in microbubbles was observed in heavily hydrogenated amorphous Si using nuclear magnetic resonance (NMR) [18] and IR absorption [19]. The molecular hydrogen in microbubbles is under such high pressure as 2000 atm that enables the detection by means of IR absorption. It is also known that implantation of hydrogen or deuterium ions leads to a formation of bubbles in crystalline materials such as metals and alloys [20,21].

Thus, to elucidate the trapping site of H_2 in crystalline Si, we have to examine if hydrogen molecules are trapped in defects, dislocations or voids that might be formed during hydrogenation. In the present study we have investigated the trapping site of H_2 in crystalline Si both in experimental and theoretical aspects. We have examined the effect of crystal defects by treating crystalline, microcrystalline and amorphous Si with atomic hydrogen under the same condition and comparing the formation of H_2 using Raman measurements. Hydrogen has also been introduced in crystalline silicon by means of hydrogen ion implantation to check the formation of hydrogen bubbles. Potentials of H_2 in the silicon clusters ($Si_{10}H_{16}$) have been calculated using the *ab initio* Hartree-Fock method, and the vibrational frequency of H_2 has been compared with the experiment.

Experimental.

p-type [100] floating-zone Si wafers were used as crystalline Si (*c*-Si) samples. Microcrystalline Si (μ*c*-Si:H) film of thickness of 760 nm and amorphous Si (*a*-Si:H) film of 930 nm were deposited on glass substrates using plasma CVD method. A flow rate of 1 sccm SH_4 was applied for deposition of *a*-Si:H, and 1 sccm SH_4 was diluted with 39 sccm H_2O for μ*c*-Si:H. Gas pressure of 50 mTorr and substrate temperature of 300 °C were maintained during the deposition. The average grain size of

the μc-Si:H sample was estimated to be 7 nm from the Raman line shape of optical phonon of Si [22]. The concentration of hydrogen in μc-Si:H and *a*-Si:H films was 2.9 and 6.4 atm.% hydrogen, respectively. To eliminate the effect of the hydrogen a hydrogen-free amorphous Si (*a*-Si) sample was also made by implanting *c*-Si with 40 keV P^+ at a dose of $1x10^{15}$ cm^{-2} and then with 80 keV P^+ at $2x10^{15}$ cm^{-2} and used.

All the Si samples, *i.e.*, *c*-Si, μc-Si:H, *a*-Si:H and hydrogen free *a*-Si, have been treated with atomic hydrogen in a downstream of hydrogen plasma for 3 hours. The samples were placed 60 cm apart from the plasma to suppress damage from activated species. The substrate temperature of the samples was maintained at 400 °C during the hydrogen atom treatment (HAT), for the formation of H_2 in *c*-Si is maximum around 400 °C [15,16]. The depth distribution of hydrogen atoms in *c*-Si after the HAT was obtained from secondary ion mass spectrometry (SIMS) measurements to range to 400 nm from the surface, and the areal density was estimated to be about $1x10^{16}$ cm^{-2} [16]. Details of the hydrogen atom treatment have been reported elsewhere [3].

c-Si was also implanted with hydrogen ion with an energy of 10 keV and doses up to 10^{17} cm^{-2} at room temperature for introduction of both defects and hydrogen. Thermal annealing on the implanted sample was performed in an electronic furnace in an N_2 atmosphere, accumulatively at temperatures ranging 300 - 600 °C, for 20 minutes at each temperature, to check the formation of hydrogen bubbles.

Raman scattering measurements were performed at room temperature unless otherwise noted. A cw argon-ion laser with a wavelength of 514.5 nm was used as an excitation source, whose probe depth is about 1000 nm in *c*-Si and about 100 nm in *a*-Si.. Scattered light was collected in a 90° configuration, analyzed using a triple grating monochromator with a wavenumber resolution of 0.7 cm^{-1}, and detected with a spectrometric multichannel analyzer. Raman spectra were measured for Raman shifts ranging from 300 to 4300 cm^{-1}.

Computational.

All calculations were performed with the GAUSSIAN 94 program [23]. The geometrical structure was computed at the Hartree-Fock self-consistent field level of theory with basis sets 3-21G, 6-31G and 6-31G**. Applying different basis sets caused very little difference [24], so we present here only the result performed with 6-31G. The Berny geometry optimization algorithm was used. Silicon cluster ($Si_{10}H_{16}$) was used to simulate Si crystal lattice, where H atoms were put to hold sp^3 configurations of Si bonds. At first, the full geometry optimization was performed for the $Si_{10}H_{16}$ cluster with initial parameters of the Si-Si bond length of Si crystal (2.35 Å), the Si-H bond length of silane molecule (1.48 Å) and the sp^3 configuration [25]. H_2 was put inside the optimized $Si_{10}H_{16}$ cluster, and a geometry optimization was performed again taking into account the relaxation of the cluster.

Results and Discussion.

Figure 1 shows typical Raman spectra of *c*-Si before and after HAT. HAT at 400°C for 3h did not affect the Raman line shape of the optical phonon of Si at 520 cm^{-1}, which is used as a criterion of the lattice disorder [21]. This makes sure that crystal lattice has no significant macroscopic disorder due to HAT. HAT introduces two distinct Raman-active hydrogen-related defects in *c*-Si; one is H_2 that gives rise to the Q_1 vibrational line at 4158 cm^{-1} and the $S_0(1)$ rotational line at 590 cm^{-1}, and the other Si-H bonds giving rise to the stretching mode around 2100 cm^{-1}. The assignment of the Raman lines was confirmed by isotope substitution of hydrogen with deuterium [14,16].

The Raman spectrum of the *c*-Si sample after HAT was not affected by chemical etching of the surface layer up to 10 nm, which might be damaged even under the remote-treatment with atomic hydrogen. The concentrations of H_2 and Si-H were obtained from the Raman intensities after successive chemical etching. They have peaks about 80 nm from the surface and depth distribution of about 200 nm, being consistent with the depth profile of hydrogen obtained from SIMS measurement. These suggest that H_2 is trapped in bulk crystal silicon.

The vibrational line of H_2 has a Raman shift quite close to that of gaseous hydrogen, whereas the full width at half maximum is about 30 cm^{-1}, much larger than that of gaseous [26] or solid hydrogen [27]. The width is too large to be explained by high-pressure gaseous H_2; the Raman width of H_2 at 2000 atm, which corresponds to the pressure in microbubble in *a*-Si:H [19], is no more than 3 cm^{-1} [28]. In addition, the broadening arising from high pressure H_2 should be accompanied by a significant frequency shift. To examine the origin of the remarkably large width of H_2 we varied the temperature during the Raman measurement. The Raman spectrum of H_2 in *c*-Si was not affected by lowering the measurement temperature down to 90 K, indicating the width is not dominated by collisional or motional broadening but by some inhomogeneous broadening such as different trapping sites and orientations of H_2 in *c*-Si [17]. These results support that the hydrogen molecules in *c*-Si are not gas in bubbles.

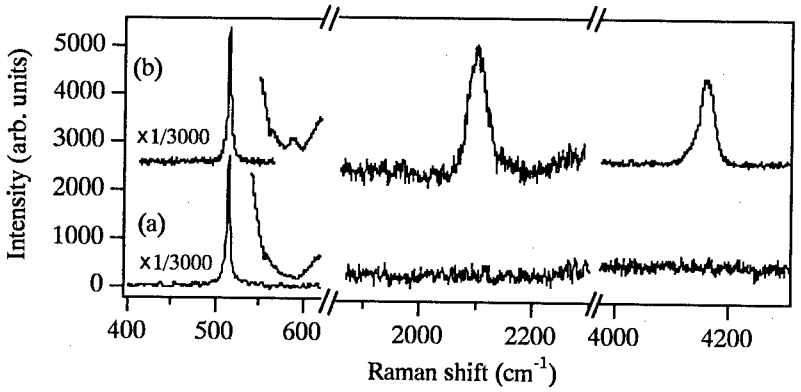


Fig. 1 Typical Raman spectra of crystalline Si (*c*-Si) (a) before and (b) after hydrogen atom treatment (HAT) at 400 °C for 3h.

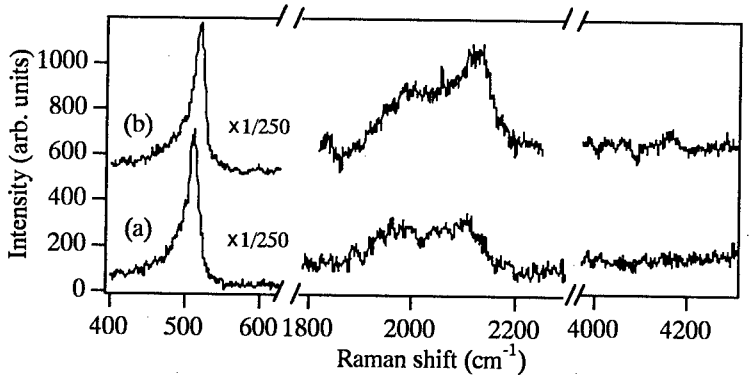


Fig. 2 Raman spectra of microcrystalline Si (μ*c*-Si:H) (a) before and (b) after HAT at 400 °C for 3h.

Figure 2 shows typical Raman spectra of μ*c*-Si:H before and after HAT. μ*c*-Si:H before HAT contains 2.9 atm.% hydrogen bonded to Si, which gives rise to a broad Raman band of Si-H stretching around 2000 cm^{-1}, but no Raman signal due to H_2 was observed before HAT. After HAT at 400 °C for 3h, the vibrational Q_1 Raman line of H_2 was observed. The Raman shift, 4158 cm^{-1} and the full width at half maximum, 31 cm^{-1}, were quite similar to those observed for *c*-Si after HAT, while the intensity relative to that of the optical phonon line of Si was about 1/5. Figure 3 shows typical Raman spectra of *a*-Si:H and hydrogen free *a*-Si before and after HAT. *a*-Si:H before HAT contains 6.4 atm.% hydrogen with a broad Raman band of Si-H stretching around 2000 cm^{-1} but no Raman signal due to H_2. Neither for *a*-Si:H nor for hydrogen-free *a*-Si after HAT was observed Raman line of H_2 in the wavenumber range of 4000 - 4300 cm^{-1}. Figures 2 and 3 imply

that crystal disorders in Si such as defects, voids and dislocations do not play an important role for the formation or trapping of H_2; on the contrary, they impede the formation and/or trapping of H_2 during HAT. In other words, H_2 is trapped stably only in non-defective bulk crystal of silicon.

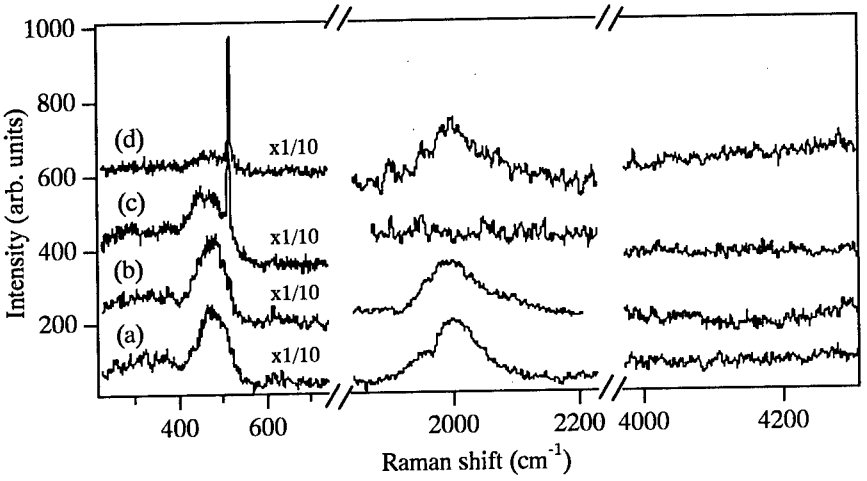


Fig. 3 Raman spectra of hydrogenated amorphous Si (*a*-Si:H) (a) before and (b) after HAT at 400 °C for 3h, and Raman spectra of hydrogen-free amorphous Si (*a*-Si) (c) before and (d) after HAT at 400 °C for 3h.

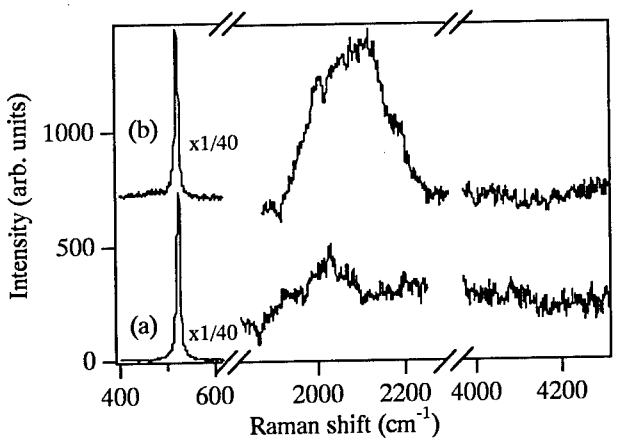


Fig. 4 Raman spectra of *c*-Si implanted with hydrogen ions at room temperature with an energy of 10 keV and a dose of (a) 10^{16} cm^{-2} and (b) 10^{17} cm^{-2}.

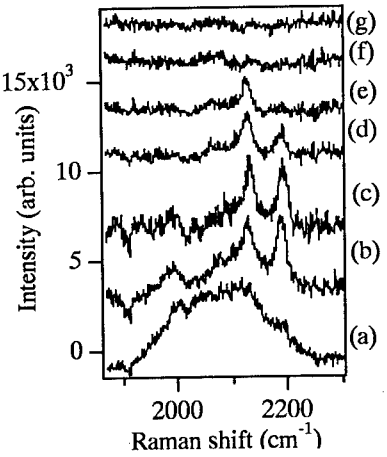


Fig. 5 Si-H stretching Raman band in *c*-Si implanted with 10^{17} cm^{-2}, 10 keV hydrogen ions (a) before anneal and after accumulative anneal at (b) 300 °C, (c) 350 °C, (d) 400 °C, (e) 450 °C, (f) 500 °C and (g) 550°C for 20 min, respectively.

Figure 4 shows Raman spectra of *c*-Si implanted with hydrogen ions with an energy of 10 keV and doses up to $1x10^{17}$ cm^{-2}. After the implantation Raman band of Si-H stretching was observed around 2000 cm^{-1}, but no Raman signal of H_2 in the wavenumber range of 4000 - 4300 cm^{-1}. We performed thermal annealing on the implanted *c*-Si to check the formation of bubbles of H_2. After furnace annealing at 300 °C the Raman band of Si-H stretching changed drastically in the line shape, as shown in Fig. 5, indicating rearrangement of metastable Si-H bonds. Further anneal up to 600°C decreased the intensity of the Si-H stretching band due to thermal dissociation of Si-H bonds. Raman

components at around 1980 cm^{-1}, 2180 cm^{-1} and 2120 cm^{-1} diminished at different annealing temperature, corresponding to different structure of Si-H bonds (*e.g.*, isolated Si-H, H_2*, platelets). However, no Raman signal of H_2 was observed throughout the annealing. The results imply that the formation of bubbles of H_2 is negligible in silicon even after ion implantation.

Potentials of hydrogen molecules in the silicon clusters ($Si_{10}H_{16}$) were calculated using the *ab initio* Hartree-Fock method. After the geometry optimization of the cluster ($H_2/Si_{10}H_{16}$) the Si-Si bond length was 2.43 Å, 3.4% longer than that of the initial cluster; the $Si_{10}H_{16}$ cluster was expanded by insertion of H_2. Figure 6 shows the optimized structure of the $H_2/Si_{10}H_{16}$ cluster. H_2 has minimum energy at a tetrahedral (Td) interstitial site of the cluster, with the molecular axis oriented almost along (100) direction. At a hexagonal (Hex) site H_2 has an energy 1.5 eV higher than at the Td site. The difference in the potential energy between the Td and the Hex sites corresponds to the diffusion barrier, and is much larger than the thermal energy of room temperature (~25 meV), suggesting that H_2 does not diffuse but is trapped stably in the Td site. Mulliken charge analysis showed that H_2 was almost neutral (-0.094). Frequency analysis was performed for the optimized geometry of the $H_2/Si_{10}H_{16}$ cluster. The vibrational frequency of H_2 was calculated with a harmonic approximation and scaling factor [29] of 0.89, and estimated to be 4393 cm^{-1}. The calculated vibrational frequency of H_2 in the $Si_{10}H_{16}$ cluster represents reasonably the experimentally obtained frequency, 4158 cm^{-1} for H_2 in *c*-Si and μ*c*-Si:H. The calculations support that H_2 is trapped in the Td site of *c*-Si, being isolated from surrounding Si atoms, *i.e.*, without any significant electronic interaction. It is noted, however, that surrounding Si atoms affect slightly the bond length H_2 in the way that the vibrational frequency varies by about 30 cm^{-1} depending on the molecular orientation at the Td site. The variation of the vibrational frequency for different orientations might be an origin of the anomalously large width of the vibrational line of H_2 obtained experimentally for *c*-Si and μ*c*-Si:H.

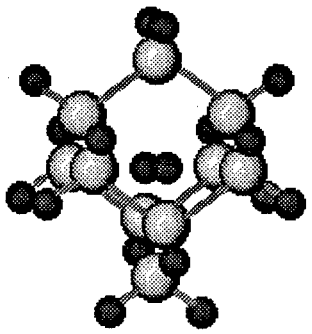


Fig. 6 The optimized structure of the $H_2/Si_{10}H_{16}$ cluster. Large bright balls and small dark ones represent Si and H atoms, respectively. H_2 has minimum energy at a tetrahedral (Td) interstitial site of the cluster.

In conclusion we have treated crystalline, microcrystalline and amorphous Si with atomic hydrogen and compared the formation of H_2 using Raman spectroscopy. The smaller Raman signal of H2 in microcrystalline compared with crystalline Si and the absence of the Raman signal of H_2 in amorphous Si suggest that H_2 is formed and trapped not in vacancies, dislocations or voids but in an interstitial site of non-defective crystalline Si. The results of hydrogen-ion implantation on *c*-Si also support this model. We have also calculated the potential energy of H_2 in $Si_{10}H_{16}$ cluster. The calculations show that H_2 is most stable at the tetrahedral site of the cluster with a vibrational frequency quite close to that observed for H_2 in crystalline Si after hydrogen atom treatment. The calculated results also support that H_2 observed in crystalline Si is trapped isolated in the tetrahedral interstitial site.

Acknowledgment.

The authors thank Dr. S. Yamazaki for supplying the *a*-Si:H and μ*c*-Si:H samples, and for S. Sasaki and S. Tateishi for their assistance in the experiments.

References.

1. J. I. Pankove and N. M. Johnson, "Hydrogen in Semiconductors" (Academic Press, New York, 1991) and references therein.
2. H.J.Stein, S.M.Myers and D.M. Follstaed, J. Appl. Phys. **73**, 2755 (1993).
3. N. Fukata, S. Sasaki, S. Fujimura, and K. Murakami, Jpn. J. Appl. Phys. **35**, 3937 (1996) .
4. N. M. Johnson, F. A. Ponce, R. A. Street, and R. J. Nemanich, Phys. Rev. **B35**, 4166 (1987).
5. J. N. Heyman, J. W. Ager , E. E. Haller, N. M. Johnson, J. Walker and C. M. Doland, Phys. Rev. B **45**, 13363 (1992).
6. J.D. Holbech, B. Bech Nielsen, R. Jones, P.Sitch and S. Öberg, Phys. Rev. Lett. **71**, 875 (1993).
7. C. G. Van de Walle, Phys. Rev. **B49**, 4579 (1994).
8. D.J. Chadi and C.H. Park, Phys. Rev. **B52**, 8877 (1995).
9. K.G. Nakamura, K. Ishioka, M. Kitajima, and K. Murakami, Solid State Commun. **101**, 735 (1997).
10. K.G. Nakamura and M. Kitajima, Jpn. J. Appl. Phys., **36**, 2004 (1997).
11. N. M. Johnson and C. Herring, Phys. Rev. **B38**, 1581(1988).
12. M. Stutzmann, W. Beyer, L. Tapfer, C. P. Herrero, Physica **B170**, 240 (1991) .
13. P. Stallinga, T. Gregorkiewicz, C. A. J. Ammerlaan, and Y. V. Gorelkinskii, Phys. Rev. Lett. **71**, 117 (1993).
14. K. Murakami, N. Fukata, S. Sasaki, K. Ishioka, M. Kitajima, S. Fujimura, J. Kikuchi, and H. Haneda, Phys. Rev. Lett. **77**, 3161 (1996).
15. N. Fukata, S. Sasaki, K. Murakami, K. Ishioka, M. Kitajima, S. Fujimura, and J. Kikuchi, Jpn. J. Appl. Phys. **35**, L1069 (1996).
16. N. Fukata, S. Sasaki, K. Murakami, K. Ishioka, K.G. Nakamura, M. Kitajima, S. Fujimura, J. Kikuchi and H. Haneda, Phys. Rev. **B** in press (1997).
17. K. Ishioka, K. G. Nakamura, M. Kitajima, N. Fukata, S. Sasaki, K. Murakami, J. Kikuchi, S. Fujimura and H. Haneda, Appl. Surf. Sci. **117/118**, 37 (1997).
18. J. B. Boyce and M. Stutzmann, Phys. Rev. Lett. **54**, 562 (1985).
19. Y. J. Chabal and C. K. N. Patel, Phys. Rev. Lett. **53**, 210 (1984).
20. K. Niwase, T. Ezawa, T. Tanabe, M. Kiritani and F.E. Fujita, J. Nucl. Mater. **203**, 56 (1993).
21. Y. Murase, A. Hasegawa, N. Yamamoto, J. Nagakawa, and H. Shiraishi, J. Nucl. Sci. and Technol. **33**, 239 (1996).
22. H. Richter, Z. P. Wang and L. Ley, Solid State Commun. **39**, 625 (1981).
23. Gaussian 94, Revision C.3, M.J. Frisch, G.W. Trucks, H.B. Schlegel, P.M.W. Gill, B.G. Johnson, M.A. Robb, J.R. Cheeseman, T. Keith, G.A. Petersson, J.A. Montgomery, K. Raghavachari, M.A. Al-Laham, V.G. Zakrzewski, J.V. Oritz, J.B. Foresman, J. Cioslowski, B.B. Stefanov, A. Nanayakkara, M. Challacombe, C.Y. Peng, P.Y. Ayala, W. Chen, M.W. Wang, J.L. Andres, E.S. Replogle, R. Gomperts, R.L. Martin, D.J. Fox, J.S. Binkley, D.J. Defrees, J. Baker, J.P. Stewart, M. Head-Gordon, C. Gonzalez, & J.A. Pople, Gaussian, Inc., Pittsburgh PA (1995).
24. K.G. Nakamura, K. Ishioka, M. Kitajima. A. Endou, M. Kubo and A. Miyamoto, submitted to Phys. Rev. **B**.
25. D.R. Lide and H.P.R. Frederikse, "CRC Handbook of Chemistry and Physics" (CRC Press, Baca Raton, 1995).
26. B.P. Stoicheff, Can. J. Phys. **35**, 730 (1957).
27. S. S. Bhatnagar, E. J. Allin and H. L. Welsh, Can. J. Phys. **40**, 9 (1962).
28. A.D. May, V. Degen, J.C. Stryland and H.L. Welsh, Can. J. Phys. **39**, 1769 (1961).
29. J.B. Foresman and A. Frisch, "Exploring Chemistry with Electronic Structure Methods", (Gaussian, Inc., Pittsburgh), p.78 (1993).

Materials Science Forum Vols. 258-263 (1997) pp. 241-246
© 1997 Trans Tech Publications, Switzerland

FORMATION AND STRUCTURE OF HYDROGEN MOLECULES IN CRYSTALLINE Si

AWR Leitch*, V Alex and J Weber
Max-Planck-Institut für Festkörperforschung, Heisenbergstrasse 1, D-70569 Stuttgart, Germany

Keywords : hydrogen, silicon, Raman spectroscopy

Abstract
We report on a Raman spectroscopy study of H_2 molecules in crystalline Si after treatment in a hydrogen plasma. Both P-doped (*n*-type) and B-doped (*p*-type) Si having resistivities ranging from 0.07 to 2000 Ωcm were investigated. A new Raman line at 3629 cm^{-1} is attributed to the vibrational excitation of the HD molecule in Si. It is found that the formation and annealing characteristics of the H_2 molecule in Si shows similar behaviour to that of the SiH platelets formed during plasma treatment. The results strongly suggest that the H_2 molecules giving rise to the measured Raman line are located within the voids created by the platelets.

Introduction

Hydrogen is an important impurity in Si and has therefore been studied by many groups in recent years.[1] The ability of hydrogen to passivate many electrically active impurities and defects in Si is now well documented. Theoretical calculations[2-4] have predicted the formation of a stable hydrogen dimer in Si, either in the form of H_2^*, in which one hydrogen is in the body-centered (BC) position while the other is in the antibonding (AB) position, or as the H_2 molecule[5], positioned at or near the interstitial tetrahedral (T) site within the Si lattice. Although many experimental results (such as the annealing of hydrogenated B-doped Si[6]) have been explained in terms of the formation of such dimer species, direct experimental evidence for their existence in crystalline Si has proved to be difficult to obtain.

Infrared (IR) modes measured in p^+-implanted Si by Holbech *et al.*[7] gave the first evidence for the presence of the H_2^* defect in Si. The same defect could be generated in hydrogen-enriched Si by electron irradiation.[8] Very recently, Murakami *et al.*[9] measured a Raman line at 4158 cm^{-1} in hydrogenated Si, which they identified as the vibrational excitation of the isolated H_2 molecule in Si, thereby confirming the existence of H_2 molecules within the Si lattice. At the same time similar Raman spectroscopy results were reported for the isolated H_2 molecule in hydrogenated GaAs.[10]

An important question that needs to be addressed has to do with the position within the Si lattice of the H_2 molecules giving rise to the reported 4158 cm^{-1} Raman signal. Murakami *et al.*[11] have argued that the Raman signal they have measured comes from the H_2 molecule situated at or close to the T site. An alternative explanation would be that the H_2 signal comes from H_2 molecules trapped within the voids formed by the SiH platelets. Transmission electron microscopy (TEM) studies have indicated that the SiH platelets, which are formed near the surface during the H-plasma treatment of the Si, contain a high density of hydrogen at pressures of the order of 1 GPa.[12]

In this paper we have used Raman spectroscopy to study the formation of H_2 in Si. We show that the H_2 is at all times associated with the presence of SiH platelets in the Si. We have also examined the annealing behaviours of both the H_2 and the SiH Raman lines, in order to give clarity to the structure of the H_2 molecule in crystalline Si.

Experimental details

Float-zone < 111> Si wafers doped with either phosphorus (*n*-type) or boron (*p*-type) and having a range of doping concentrations (0.07 Ωcm to 2000 Ωcm) were studied. Hydrogen was introduced into the wafers by exposing them to a remote DC hydrogen plasma at typically 200 °C for 3 to 8 hours. The hydrogen pressure was held constant at 1.5 mbar. For some samples the hydrogen atmosphere was replaced by either deuterium, or a mixture consisting of 50:50 H_2:D_2. Raman measurements were performed at room temperature, using the focused 488 nm line of an Ar-ion laser for excitation. The incident laser intensity was typically 300 mW. The backscattered Raman signal was analysed without polarisation using a 0.3 m single grating spectrometer and detected with a cooled Si-CCD detector array. Appropriate holographic notch filters were used to reduce the scattered laser light. The full spectral range up to 4500 cm^{-1} was investigated.

Results

Figure 1 shows the Raman spectra obtained after exposure of 0.07 Ωcm P-doped Si to the various plasmas. Curve (a) shows the Raman peak measured at 4157 cm^{-1} after exposure to a pure H_2 plasma. Using a pure D_2 plasma resulted in a peak at 2991 cm^{-1} (curve (b)); while the H_2:D_2 mixture gave rise to the lines at 4157 cm^{-1}, 2991 cm^{-1} as well as at 3629 cm^{-1} (curve(c)). These three lines are interpreted as vibrational excitations of isolated H_2, D_2, and HD molecules in crystalline Si, respectively. This is the first report of a Raman frequency for the HD molecule in crystalline Si. The ratio of the frequencies of the H_2 signal to the D_2 signal is 1.39, close to the $\sqrt{2}$ value expected from the isotope shift. None of these Raman lines were present in the material before hydrogen-plasma treatment. These spectra therefore give convincing evidence for the presence of H_2 molecules in crystalline Si.

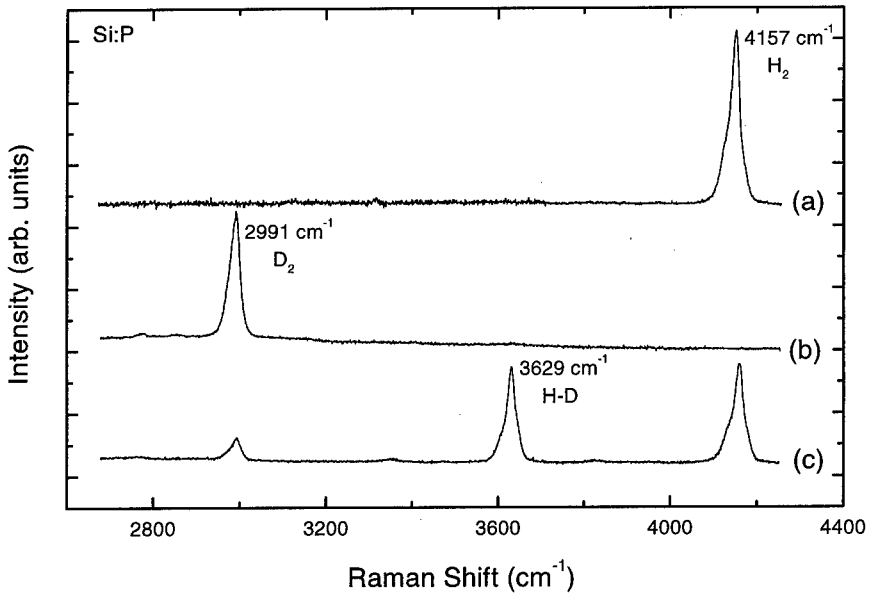


Figure 1: Room temperature Raman spectra of Si:P, after exposure at 200 °C for 8 hours to: a) H_2 plasma; b) D_2 plasma; and c) H_2:D_2 (50:50) plasma.

Matrix	H_2 (cm^{-1})	D_2 (cm^{-1})	HD (cm^{-1})	FWHM (cm^{-1})	Reference
Si	4157 ± 2	2991 ± 2	3629 ± 2	25	*this work*
Si	4158 ± 3	2990 ± 2	-	34	9
GaAs	3934.1	2842.6	3446.5	3.0	10
H_2 (gas)	4161.13	2993.55	3632.06		13
H_2 (liquid)	4153.78	2987.99	3623.65	0.3	14
H_2 (solid)	4151.8	2985.46	3621.85	0.4	14

Table 1: Summary of the reported Raman frequencies for H_2. The FWHM values refer to the linewidths of the H_2 Raman line.

The results of Fig. 1 are summarised in Table 1, together with the values recently reported for Si[9] and GaAs[10] and the measured Raman frequencies for H_2, D_2 and HD molecules in the solid, liquid and gas phases.[13,14] We briefly draw attention to two points that will be discussed further: Firstly, the Raman frequencies for H_2 in Si are seen to best match the values reported for gaseous H_2, while those for H_2 in GaAs are 100 - 200 cm^{-1} lower. Secondly, while the line-width of the H_2 signal in Fig. 1 is sharper than what was recently reported by Murakami *et al.*[9], it is still much broader than the value for H_2 in GaAs as well as for H_2 in the solid, liquid or gas phases.

Figure 2 shows the Raman spectra measured for p-type Si after H-plasma treatment at 200 °C. The intensities of the H_2 Raman lines are essentially the same for each of the doping densities, and compare well with the Raman lines for n-type Si seen in Fig. 1. It would appear from these spectra that the formation of the H_2 molecule is as efficient in *p*-type Si as in *n*-type Si. This result is interesting, as it is accepted that interstitial hydrogen exists as H^{+1} in *p*-type Si, while in *n*-type it is H^0 or H^{-1}. Thus the formation reactions for the H_2 molecule should be different in both cases.

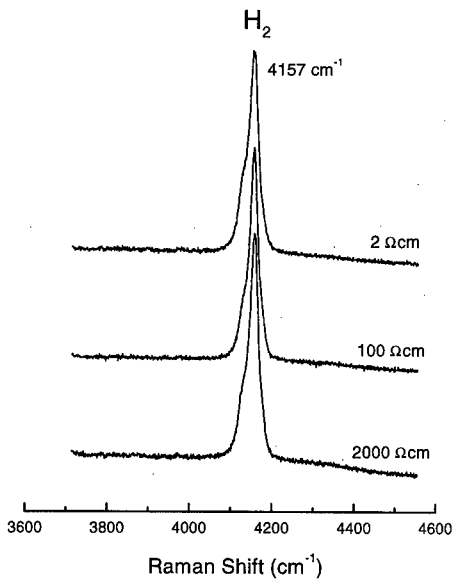


Figure 2: Raman spectra of the H_2 molecule in B-doped Si, for different resistivities.

The influence of sample temperature during plasma treatment was also investigated. It is found that temperatures as low as 75 °C are sufficient for forming the H_2 molecule. At 75 °C the Raman signal for the H_2 molecule is small and broad. As the temperature during plasma treatment is increased, the Raman signal becomes sharp and intense, reaching a maximum at temperatures of 200 - 300 °C.

The SiH platelets that are also formed during plasma treatment have a broad Raman band around 2100 - 2200 cm^{-1}. Polarised Raman measurements[15] have indicated that the band consists of two or more lines, and that the relative strengths of the lines depend on the thermal history of the sample. It is important to note that for all the samples we have investigated, the SiH Raman signal always accompanies the H_2 Raman line. While the capture cross sections for the H_2 and SiH Raman

signals in Si have not been determined and it therefore makes no sense to compare absolute intensities, we have observed that an intense SiH signal always accompanies an intense H_2 signal. These are all indications that the H_2 and the SiH platelets are in some way related.

An important question has to do with the depth of the H_2 molecules giving rise to the Raman line at 4157 cm^{-1}. Based on absorption data for 488 nm (the laser line) in Si[16], we estimate that the excitation radiation is absorbed within the first 250 nm from the surface. Murakami *et al.*[11] reported that after etching 10 nm off the sample, the H_2 Raman line remained. They therefore concluded that the H_2 molecules must be situated at T sites within the Si lattice, deeper than the plasma-damaged region near the surface. They made no mention however of the Raman signal from the SiH platelets. It is known[15] that the platelets can extend 100 - 200 nm or more into the Si. To investigate this further, we have etched approximately 50 nm off a H-plasma treated sample, by sequentially boiling the Si in water followed by rinsing in HF. We find that both the SiH and the H_2 Raman signals are reduced, but are still measurable. At a depth of about 25 nm, both SiH and H_2 signals are approximately 85 % of the intensity measured from the unetched sample. This indicates that the SiH platelets appear to extend into the Si at least as deep as the H_2 molecules, giving further indication that they are related.

It was noted that the line-width of the H_2 Raman signal in Si is always broad, about two orders of magnitude larger than that of gaseous H_2. Murakami *et al.*[11] have suggested that the broad Raman line may come from the metastabilities of hydrogen molecules located at several sites near the tetrahedral interstitial site and with several stable directions for the molecular axis, in addition to the interaction between hydrogen molecules and Si lattice phonons. Subsequently, Nakamura and Kitajima[17] attributed the broad line-width to an orientation effect of H_2 at the T site in the Si crystal. In all our spectra we have observed a shoulder on the high energy side (around 4129 cm^{-1}) of the H_2 Raman line (see Fig. 2), which contributes to the broadening. No dependence of the line-width on the sample temperature (from 4 to 300 K) was detected. We have been able to resolve the shoulder by a series of isochronal anneals up to 500 °C. Figure 3 shows some of the Raman spectra after 20 min anneals at increasing temperatures. Firstly, the SiH platelets signal (fig. 3(a)) is seen to reduce intensity within this range. The SiH peak at 2132 cm^{-1} moves to lower energies (2112 cm^{-1}),

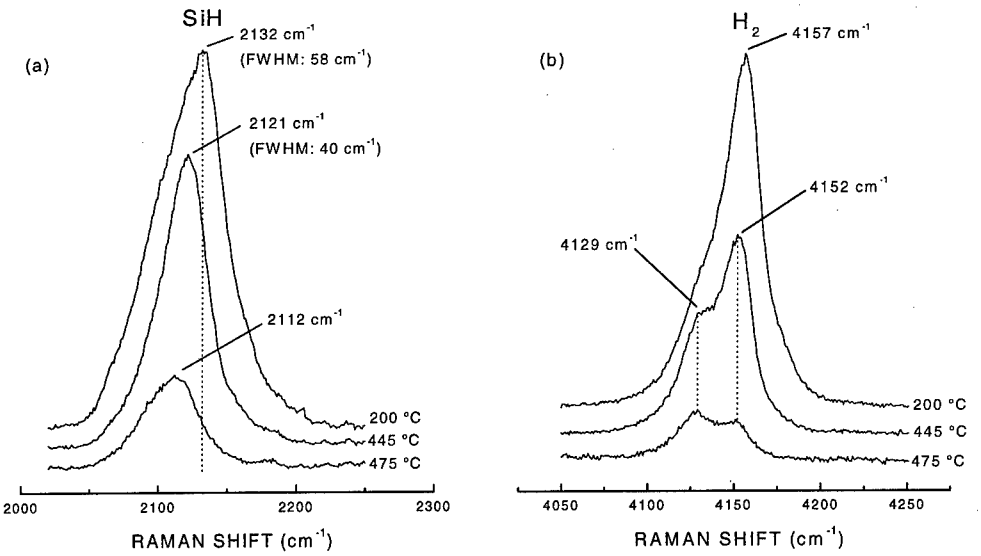


Figure 3: Raman spectra of a) SiH platelets; and b) H_2 molecules, in H-plasma treated Si:P, after 20 min anneals at 445 and 475 °C.

decreasing in line-width at the same time. Secondly, the H_2 Raman signal (fig. 3(b)) also decreases in intensity, with the peak position at 4157 cm^{-1} moving slightly to 4152 cm^{-1}, while the peak at 4129 cm^{-1} (previously only visible as a shoulder) becomes dominant. If the broad line-width was simply caused by an orientation effect of the H_2 molecules located at the T site in the Si lattice, as suggested by Nakamura and Kitajima[17], we would have expected the two peaks (at 4152 cm^{-1} and 4129 cm^{-1}) to have reduced intensity at the same rate. This is clearly not the case.

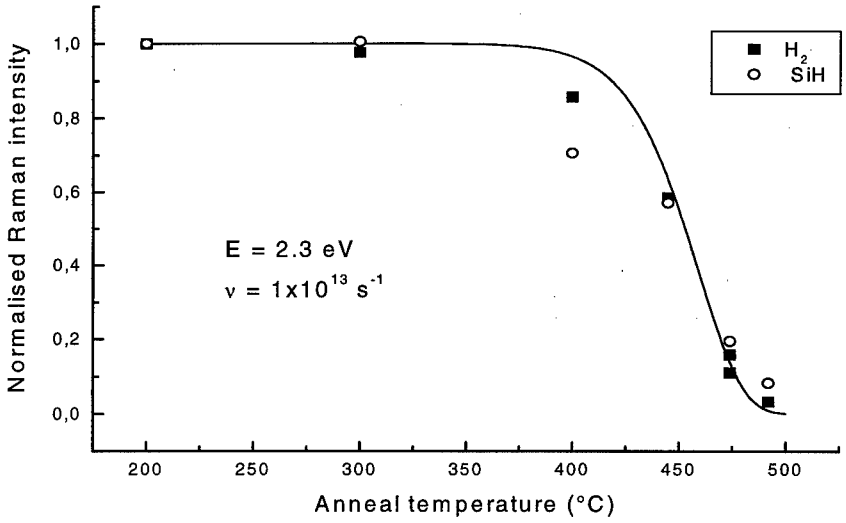


Figure 4: Normalised intensities of the SiH and the H_2 Raman signals in Si:P, after 20 min isochronal anneals. The solid line is a fit to the data, assuming first-order kinetics.

Figure 4 shows the integrated intensities of the SiH and the H_2 Raman signals as function of annealing temperature. The data has been normalised to the intensities measured immediately after plasma treatment at 200 °C. Both signals are seen anneal out at approximately the same rate within the range 400 - 500 °C. The fact that they show the same annealing behaviour strongly suggests that the SiH platelets and the H_2 molecules are correlated. Assuming that the annealing of the SiH and H_2 signals obeys first-order kinetics and assuming a jump frequency of 10^{13} s^{-1}, we obtain an energy of 2.3 eV for the process. It may be noted that Beyer,[18] when measuring the effusion of hydrogen from a < 111> Si surface, calculated a free energy of desorption of 2.2 eV. As the platelets break up (resulting in a decrease in the SiH Raman signal), the high concentration of H_2 molecules will reduce, either by effusion from the surface, or by diffusing deeper into the material.

Finally, we discuss the actual Raman frequency (4157 cm^{-1}) measured for the H_2 molecule in Si. It was noted (table 1) that the Raman frequency compares well with the frequency reported for isolated H_2 molecules in the gaseous phase. Assuming that the H_2 molecule was at the T site within the Si lattice, one would expect some perturbation of the molecule by the Si lattice, resulting in a weakening of the molecular bond and a decrease in the measured Raman frequency. This is indeed what is found for GaAs, where the frequency measured for H_2 in the GaAs matrix is about 100 - 200 cm^{-1} lower than that of gaseous H_2. The fact that this frequency shift is not measured for H_2 molecules in Si, argues in favour of the molecule being located in voids formed by the platelets, where the H_2 is expected to be present in high densities.

To conclude, we have measured the Raman signal of the H_2 molecule in crystalline Si. We have found that it is stable up to temperatures of 400 °C. The SiH platelets and the H_2 molecules exhibit similar annealing characteristics. All indications are that the H_2 molecules are located within the voids formed by the SiH platelets, which are generated during the H-plasma treatment.

Acknowledgements
We gratefully acknowledge the continued interest and support of Prof. H.-J. Queisser. We thank S.K. Estreicher for useful discussions. The technical assistance of W. Heinz and W. Krause is appreciated.

References

* Permanent address: Department of Physics, University of Port Elizabeth, PO Box 1600, Port Elizabeth 6000, South Africa.
1. *Hydrogen in Semiconductors*, edited by J.I. Pankove and N.M. Johnson, Semiconductors and Semimetals Vol 34 (Academic Press, New York, 1991).
2. C.G. Van de Walle, Phys Rev **B 49**, 4579 (1994).
3. D.J. Chadi and C.H. Park, Phys Rev **B 52**, 8877 (1995).
4. S.K. Estreicher, Mater. Sci. Eng. **R14**, 319 (1995).
5. J.W.Corbett, S.N. Sahu, T.S. Shi and L.C. Snyder, Phys. Lett. **A 93**, 303 (1983).
6. T. Zundel and J. Weber, Phys Rev **B 43**, 4361 (1991).
7. J.D. Holbech, B. Bech Nielsen, R. Jones, P. Stitch and S. Öberg, Phys. Rev. Lett. **71**, 875 (1993).
8. R.C. Newman, Phil. Trans. R. Soc. Lond. **A 350**, 215 (1995).
9. K. Murakami, N. Fukata, S. Sasaki, K. Ishioka, M. Kitajima, S. Fujimura, J. Kikuchi and H. Haneda, Phys. Rev. Lett. **77**, 3141 (1996).
10. J. Vetterhöffer, J. Wagner and J. Weber, Phys. Rev. Lett. **77**, 5409 (1996).
11. K. Murakami, N. Fukata, S. Sasaki, K. Ishioka, K.G. Nakamura, M. Kitajima, S. Fujimura, J. Kikuchi and H. Haneda, in Proceedings of the Materials Research Society Symposium Vol. 442 ed. J. Michel, T. Kennedy, K. Wada and K. Thonke (Pittsburgh: Materials Research Society) pp. 269-274 (1997).
12. S. Muto, S. Takeda and M. Hirata, Phil. Mag. **A 72**, 1057 (1995).
13. B.P. Stoicheff, Can. J. Phys. **35**, 730 (1957).
14. S.S. Bhatnagar, E.J. Allin, and H.L. Welsh, Can. J. Phys. **40**, 9 (1962).
15. J.N. Heyman, J.W. Ager III, E.E. Haler, N.M. Johnson, J. Walker and C.M. Doland, Phys Rev **B 45**, 13363 (1992).
16. G.E. Jellison and F.A. Modine, Appl. Phys. Lett. **41**, 180 (1982).
17. K.G. Nakamura and M. Kitajima, Jpn. J. Appl. Phys. **36**, 2004 (1997).
18. W. Beyer, Physica **B 170**, 105 (1991).

Materials Science Forum Vols. 258-263 (1997) pp. 247-252
© 1997 Trans Tech Publications, Switzerland

STRUCTURE AND CHARGE-STATE-DEPENDENT INSTABILITY OF A HYDROGEN-CARBON COMPLEX IN SILICON

Y. Kamiura, N. Ishiga, S. Ohyama, and Y. Yamashita
Faculty of Engineering, Okayama University,
3-1-1, Tsushima-naka, Okayama 700, Japan
(E-mail: kamiura@elec.okayama-u.ac.jp)

Keywords : silicon, hydrogen, carbon, stress, DLTS

Abstract. We have studied the symmetry and structure of a hydrogen-carbon (H-C) complex in Si and the bonding nature of its electronic state by means of DLTS technique under uniaxial stress. Application of <111> and <110> compression stresses splitted the DLTS peak into two as ratios of 1:3 and 2:2, respectively, which were the ratios of the low-temperature peak to the high-temperature one. No splitting was observed under <100> stress. These results clearly indicate the trigonal symmetry of the H-C complex and the anti-bonding nature of its electronic state, and are consistent with the previously proposed model, where hydrogen occupies the bond-centered site between carbon and silicon atoms. We have studied the stability of the complex by annealing with and without reverse bias applied to the Schottky junction. The complex was unstable outside the depletion region, where it was annihilated with an activation energy of 0.7 eV, while inside it was relatively stable and the activation energy was 1.3 eV. From these results, we have concluded that the complex becomes unstable in the neutral charge state by capturing an electron from the conduction band.

Introduction.

It has been established that atomic hydrogen not only passivates electrically active donors and acceptors but also electrically activates neutral impurities like substitutional carbon by forming a hydrogen-carbon (H-C) complex [1-5]. It acts as an electron trap, E3, with a donor level at E_c-0.15eV. We have discovered that this complex is stable at and above room temperature in the dark but is easily dissociated under the illumination of band gap light below room temperature [3, 4], and have suggested that the dissociation occurs via so-called recombination-enhanced dissociation, in which the electronic energy released by the electron-hole recombination at the E3 trap level is converted into local vibrational energy to induce the atomic motion of hydrogen. However, there is still an alternative possibility that electronic excitation alters the charge state of the H-C complex to induce substantial changes in charge distribution inside and around the complex and reduces the potential barrier height for the dissociation [5]. Thus, the dissociation mechanism has not been clear yet. In addition, there has been no experimental information available on the atomic and electronic structures of the H-C complex, though some theoretical calculations indicated that the bond-centered (BC) configuration where hydrogen resides between carbon and silicon atoms is the most stable structure [6-8].

In the present work, we have applied DLTS technique under uniaxial stress [9] to study the symmetry and structure of the H-C complex and the bonding nature of its electronic state. We have also performed systematic experiments on the stability of the complex, and present here data on the activation energies and frequency factors determined for the dissociation process under various conditions such as under illumination, in the dark and with or without the application of reverse bias to the Schottky junction. On the basis of the present results, we construct a configurational coordinate diagram showing the potential for hydrogen motion around carbon and discuss the dissociation mechanism of the complex together with its structural model.

Experimental procedure.

We used two FZ grown n-type silicon crystals with phosphorus densities of $1.5x10^{14}$ and $5.9x10^{14}$ cm^{-3}. Their oxygen and carbon densities were less than $1x10^{16}$ and about $1x10^{16}$ cm^{-3}, respectively. Samples for the normal DLTS measurement were cut from the former crystal into a size with dimensions of 2x3x1 mm^3. For the stress DLTS measurement, many samples were cut from the latter crystal into a square pillar with dimensions of 1x1x6 mm^3, the longest of which was parallel to <100>, <110> or <111> directions. Hydrogen injection was performed by chemical etching at 20°C for 5 min. The hydrogenated samples were prepared for DLTS measurements by forming Au Schottky diodes. Capacitance DLTS measurements were performed typically at a rate window of 114 s^{-1}. In the stress DLTS measurement, compression stresses up to 1.2 GPa were applied to the samples along their longest dimension. Other details were the same as published previously [2].

The symmetry of the atomic structure.

Figure 1 shows the results of the stress DLTS measurements. Solid curves are measured spectra, and broken ones are the fitting using the usual DLTS function. In the fitting, we considered the presence of maximum three peaks: the splitted peaks of the E3 trap at 75-95K and an unidentified peak around 115K. The peak of the E3 trap, which is seen at 93K under no stress (a), is splitted

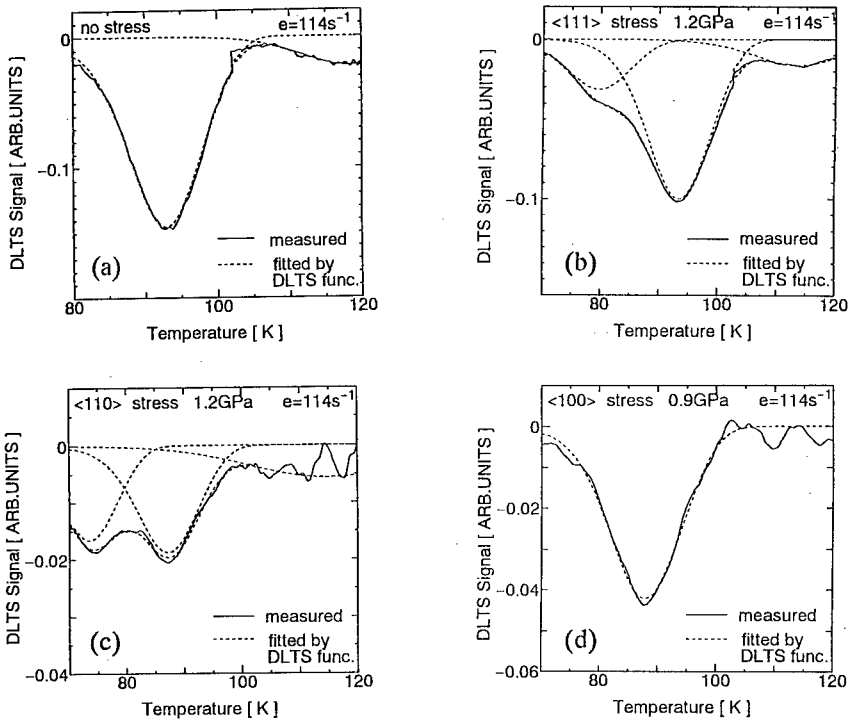


Figure 1. DLTS spectra of the E3 trap under no stress (a) and under compression stresses along <111> (b), <110> (c) or <100> (d) directions. Solid curves are measured spectra, and broken ones are the fitting using the usual DLTS function considering the presence of maximum three peaks: the splitted peaks of the E3 trap at 75-95K and an unidentified peak around 115K. Application of <111> and <110> stresses splits the E3 trap peak into two as intensity ratios of 1:3 and 2:2, respectively, which are the ratios of the low-temperature peak to the high-temperature one. There is no splitting under <100> stress. These results clearly indicate the trigonal symmetry of the H-C complex.

Table 1. The trap density in 10^{12} cm^{-3} determined by the fitting. N_0 represents the density of an unsplitted peak under no stress, while N_1 and N_2 represent the densities of the low-temperature and high-temperature peaks, respectively.

	under no stress	under a stress of 1.2 GPa	
orientation	N_0	N_1	N_2
<111>	30.0	7.2	22.0
<110>	13.0	5.9	6.9

under compression stresses along <111> (b) and <110> (c) directions into two as intensity ratios of 1:3 and 2:2, respectively (Table 1), which are the ratios of the low-temperature peak to the high-temperature one. There is no splitting under <100> stress (d) . Since the electronic state of the H-C complex is not orbitally degenerate according to the theoretical calculation of Kaneta and Katayama-Yoshida [8], the peak splitting reflects the lift of orientational degeneracy by the stress. Therefore, the above results clearly indicate the trigonal symmetry of the H-C complex, and are consistent with the previously proposed model [4], where hydrogen occupies the BC site between carbon and silicon atoms, and also agree well with the results of recent theoretical calculations [6-8].

Bonding nature of the electronic state.

Figure 1(b) and Table 1 shows that the intensity ratio of the low-temperature peak to the high-temperature one is 1:3 under a compression stress along the <111> direction. This means that the applied stress induces the energy of one configuration of the H-C complex, whose <111> symmetrical axis along the C-H-Si bond is parallel to the applied stress, to become higher than those of the other three configurations among four <111> equivalent orientations of the symmetrical axis. We have analyzed data on the <111> stress dependence of energy levels of the splitted peaks considering the stress dependence of the lower-lying band of splitted conduction band manifolds, and have found that the stress raises both of the energy levels of splitted peaks and increases their energies linearly with stress but in different magnitudes. The energy level of the low-temperature peak has a strong stress dependence (45±5 meV/GPa), while the high-temperature one has only a weak dependence (8±4 meV/GPa). These results clearly indicate that the compression stress component parallel to the symmetrical axis raises the energy of the C-H-Si bond, suggesting its anti-bonding nature. This is in excellent agreement with the prediction of the theory [8].

Stress-induced preferential alignment of the complex.

We have observed stress-induced preferential alignment of the complex, which was completely aligned by the annealing at 250K for 50 min under a <110> stress of 1 GPa. This alignment was monitored by DLTS as the increase of relative intensities of the high-temperature peak to the low-temperature one. This can be reasonably understood by the increase in bonding energy under a compression stress parallel to the bonding direction. On the other hand, no alignment was observed at 120K even for long annealing time as long as 5 hours. The observation of the stress-induced alignment of any hydrogen-related complex is of particular significant, because there has been only few information available on the dynamical properties of hydrogen in semiconductors at low temperatures. Our forthcoming goal is to study the motion of hydrogen around carbon in various charge states by observing the relaxation of stress-induced alignment of the H-C complex under various conditions such as under illumination, in the dark and with or without the application of reverse bias to the Schottky junction. Since carbon is an isoelectronic impurity in Si, such motion can compare with that of free hydrogen in crystalline silicon. Our experiments are now in progress.

Dissociation of the complex under various conditions.

We have observed that the illumination with white light enhances the dissociation of the H-C complex while the application of reverse bias to the Schottky junction suppresses it [3, 4]. The E3 trap existing only outside the depletion region of the junction becomes unstable to be dissociated. Annealing kinetics under zero bias and reverse bias is entirely different. For zero-bias annealing, the dissociation is gradually slowed down as the annealing proceeds and kinetics deviates from first order. On the contrary, kinetics completely obeys first order for reverse-bias annealing. This difference suggests that the back reaction to form the H-C complex begins to dominate as the dissociation goes forward. On reverse-bias annealing, the hydrogen released by the dissociation may be negatively charged in n-type Si [10, 11] and be swept away by strong junction fields from the region probed by DLTS. This leads to no back reaction occurring to form the complex, resulting in a simple first-order kinetics representing the dissociation alone. On zero-bias annealing, the region probed by DLTS is outside the depletion region and has no junction fields, so that hydrogen stays around carbon to form the complex again after its dissociation. This results in the slowing down of dissociation and the deviation from first order kinetics. In any case, the initial annealing process reflects the dissociation of the complex alone, and can be approximated to first-order reaction. Figure 2 shows the temperature dependence of reciprocal time constant, $1/\tau$, for the initial annealing process of the H-C complex under various conditions such as under illumination, in the dark and with or without the application of reverse bias, V_R, to the Schottky junction. For the reverse-bias annealing in the dark, the activation energy, E, for the annihilation is 1.3 eV and the frequency factor, ν, is $2\text{x}10^{14}$ s^{-1}. These values are consistent with the thermal dissociation of the H-C complex by the usual atomic jump of hydrogen being released from carbon. For the zero-bias annealing, E is much lower; 0.5 eV under illumination and 0.7 eV in the dark. The values of ν are also even smaller, 10^6-10^7 s^{-1}. This means that there is another dissociation path with a low activation energy and a

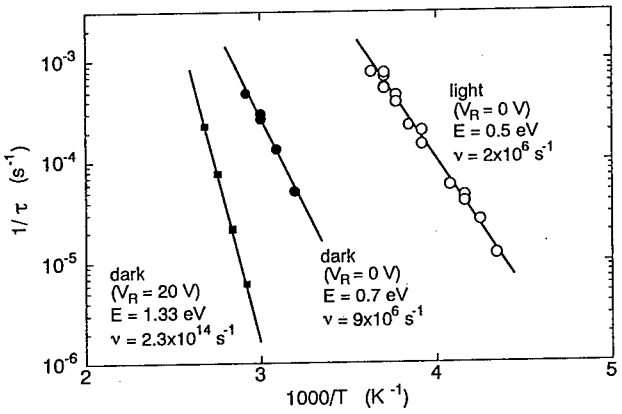


Figure 2. Temperature dependence of reciprocal time constant, $1/\tau$, for the initial annealing process of the H-C complex under various conditions such as under illumination, in the dark and with or without the application of reverse bias, V_R, to the Schottky junction. For the reverse-bias annealing in the dark, the activation energy, E, for the annihilation is 1.3 eV and the frequency factor, ν, is $2\text{x}10^{14}$ s^{-1}. For the zero-bias annealing, E is much lower; 0.5 eV under illumination and 0.7 eV in the dark. The values of ν are also smaller, 10^6-10^7 s^{-1}.

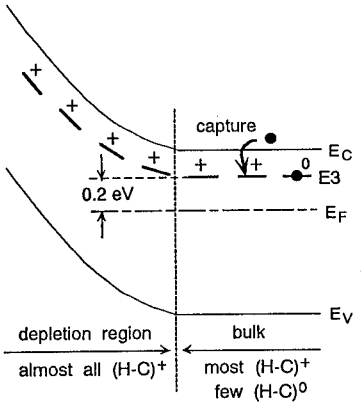


Figure 3. The charge states of the H-C complex near the Schottky junction. Substantially all the complexes existing inside the depletion region are in the positive-charge state, while outside a few of the complexes are in the neutral state and are unstable. The complex in the positive-charge state successively becomes neutral and unstable by capturing an electron from the conduction band.

small frequency factor. The magnitude of ν strongly suggests that the capture of an electron by the E3 trap from the conduction band is a rate-limiting step of this dissociation path. This is consistent with the observation that the E3 trap existing only outside the depletion region is dissociated.

Dissociation mechanism.

We have found that the H-C complex becomes unstable outside the depletion region in the dark as well as under illumination. Since no hole is available in the valence band in the dark, the recombination does not occur, clearly indicating that the cause of the instability should be due to the charge-state effect. The charge states of the complex are schematically illustrated in Fig. 3, where substantially all the H-C complexes existing inside the depletion region are in the positive-charge state while so are most of the complexes outside as well but a few of them are in the neutral state. There is no other difference concerning the situation of the complex between the inside and outside of the depletion region. Therefore, we must ascribe the instability of the complex outside the depletion region to this difference in level occupation. This leads us to conclude that the H-C complex becomes unstable by capturing an electron from the conduction band to change its charge state to neutral. If some complexes are dissociated in the neutral state, the average occupation of their electronic levels deviates from that in thermal equilibrium. This drives an unoccupied trap to capture an electron from the conduction band to maintain thermal equilibrium. Thus, the capture of an electron and the subsequent dissociation continuously occurs to reduce the density of the complex on zero-bias annealing. This mechanism reasonably explains that the rate-limiting step in the dissociation is the capture of an electron and why the dissociation is suppressed on reverse-bias annealing.

Considering the results of recent theoretical investigations [6-8], we propose that the BC configuration of the H-C complex in the neutral state is unstable with no binding among hydrogen, carbon and silicon. This may be understood in the following way. The positive charge state of the complex has yield the binding because the positive charge of a proton is present inside the negatively charged bonding between carbon and silicon. However, the neutral complex no longer has such binding and becomes unstable. This means that the activation energy of hydrogen motion should be comparable

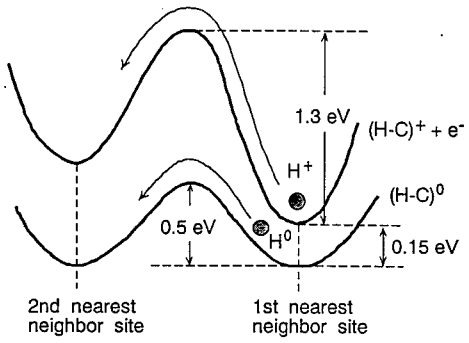


Figure 4. Configurational coordinate diagram illustrating the total energy of the H-C complex in the positive and neutral charge states. The upper curve represents the potential for hydrogen in the positive charge state around carbon. Hydrogen must overcome the binding with carbon and silicon when it moves apart from carbon. The lower curve shows that hydrogen moves freely in the neutral state without any attractive force exerted by carbon and silicon.

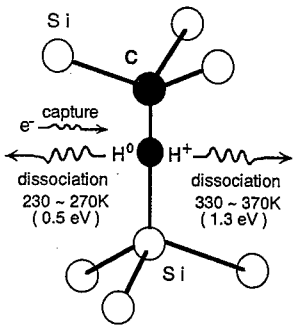


Figure 5. Summary of the dissociation of the complex using its atomic model. When its charge state remains positive by reverse-bias application, the complex is dissociated by atomic jump of hydrogen with an activation energy of 1.3 eV. If the charge state of the complex is changed to neutral by capturing an electron, the barrier height is lowered to 0.5 eV to enhance the dissociation of the complex.

with that of isolated hydrogen, which was measured as 0.5 eV by hydrogen diffusion experiments [12]. This value is actually the same as the activation energy of the dissociation of the complex on zero-bias annealing under the illumination of white light (Fig. 2). Therefore, we interpret that the complex captures an excess electron created in the conduction band by above-gap excitation or accepts an electron from the valence band by below-gap excitation, and loses the binding to be dissociated with an activation energy of 0.5 eV. On the other hand, the activation energy on zero-bias annealing in the dark is 0.7 eV, which is 0.2 eV higher. This can be explained as follows. As we discuss in the preceding paragraph, the continuous dissociation of the complex needs the capture of an electron from the conduction band to maintain thermal equilibrium. This process involves the thermal activation of an electron from the Fermi level to the trap level. Accordingly, the dissociation needs an additional activation energy, which is the energy difference between the both levels and can be estimated to be 0.2 eV under our experimental conditions (Fig. 3).

On the basis of the above discussion, we can draw a configurational coordinate diagram illustrating the total energy of the H-C complex in the positive and neutral charge states (Fig.4). The upper curve represents the potential for hydrogen in the positive charge state around carbon. Hydrogen must overcome the binding with carbon and silicon when it moves apart from carbon. In the neutral state, hydrogen moves freely without any attractive force exerted by carbon and silicon (lower curve of Fig. 4). Figure 5 demonstrates the summarizing illustration of the dissociation of the complex using its atomic model. When its charge state remains positive by reverse-bias application, the complex is dissociated by atomic jump of hydrogen with an activation energy of 1.3 eV. If the charge state of the complex is changed to neutral by capturing an electron, the barrier height is lowered to 0.5 eV to enhance the dissociation of the complex.

Acknowledgements.
We thank M. Hayashi, Y. Nishiyama, Y. Matsuda of Okayama University for their assistance in our experiments. We express thanks to Dr. K. Endo of Mitsubishi Materials Silicon Co., Ltd. for his supplying carbon-rich FZ silicon crystals.

References.

1. A. Endrös, Phys. Rev. Lett. **63**, 70 (1989).
2. M. Yoneta, Y. Kamiura and F. Hashimoto, J. Appl. Phys. **70**, 1295 (1991).
3. Y. Kamiura, M. Yoneta and F. Hashimoto, Appl. Phys. Lett. **59**, 3165 (1991).
4. Y. Kamiura, M. Yoneta, Y. Nishiyama and F. Hashimoto, J. Appl. Phys. **72**, 3394 (1992).
5. Y. Kamiura, M. Tsutsue, M. Hayashi, Y. Yamashita and F. Hashimoto: in *Defects in Semiconductors 18*, edited by M. Suezawa and H. Katayama-Yoshida, Materials Science Forum **196-201** (Zurich: Trans Tech Publications) pp. 903-907 (1995).
6. D. M. Maric, P. F. Meier and S. K. Estreicher, Phys. Rev. **B47**, 3620 (1993).
7. Y. Zhou, R. Luchsinger, P. F. Meier, H. U. Suter, D. Maric and S. K. Estreicher: in *Defects in Semiconductors 18*, edited by M. Suezawa and H. Katayama-Yoshida, Materials Science Forum **196-201** (Zurich: Trans Tech Publications) pp. 891-895 (1995).
8. C. Kaneta and H. Katayama-Yoshida: in *Defects in Semiconductors 18*, edited by M. Suezawa and H. Katayama-Yoshida, Materials Science Forum **196-201** (Zurich: Trans Tech Publications) pp. 897-901 (1995).
9. L. C. Kimerling, J. L. Benton, K. M. Lee and M. Stavola, in *Microscopic Identification of Electronic Defects in Semiconductors*, edited by N. M. Johnson, S. G. Bishop and G. D. Watkins, Mater. Res. Soc. Symp. Proc. **46**, (Pittsburgh: Materials Research Society) pp. 3-12 (1985).
10. A. J. Tavendale, S. J. Pearton and A. A. Williams, Appl. Phys. Lett. **56**, 949 (1990).
11. J. Zhu, N. M. Johnson and C. Herring, Phys. Rev. **B41**, 12354 (1990).
12. A. V. Wieringen and N. Warmoltz, Physica **22**, 849 (1956).

Materials Science Forum Vols. 258-263 (1997) pp. 253-258
© 1997 Trans Tech Publications, Switzerland

THE TRAPPING OF HYDROGEN AT CARBON DEFECTS IN SILICON

Alison Mainwood

Physics Department, King's College London, Strand, London WC2R 2LS

Keywords: Silicon, hydrogen, carbon, migration, local vibrational modes.

Abstract

An approximate molecular orbital method, including Car-Parrinello-like dynamics, has been used to model the migration and vibration of hydrogen and hydrogen-carbon complexes in silicon. The local vibrational mode spectra and the reorientation of the hydrogen within the complexes are simulated. Different di-carbon-hydrogen defect structures appear to form if a hydrogen is trapped by the di-carbon defect than if a carbon-hydrogen interstitial complex is trapped by a substitutional carbon atom.

Introduction

Hydrogen is very mobile in silicon, either as a single interstitial occupying a bond-centred position[1], or in one of the diatomic forms. One of the surprising results to emerge over the last few years is the number of defects in silicon which contain hydrogen[2]. It is undetectable in its normal forms until it is trapped by another defect. It affects the optical (and electrical) activity of that defect, so its diffusion through the silicon can be traced, by the photoluminescence from defects activated (or de-activated) by the trapping of hydrogen[2]. One of the defects which traps hydrogen is a carbon substitutional atom, converting the isoelectronic defect into a deep donor[3]. It is also trapped by the di-carbon defect[4], with a substantial re-ordering of the carbon atoms. Hydrogen, in whatever site it occupies, has local vibrational modes (LVM) associated with it[5], and it is from these much experimental information can be derived.

This paper looks at how hydrogen and hydrogen-carbon defects can be modelled. Because hydrogen is so much lighter than the silicon atoms, but in many defects is in self-trapped sites, treating it in a classical way is not valid. However, a simple prescription for the quantum mechanical modelling of such defects was explained by Flynn and Stoneham[6].

The paper applies this prescription to the migration of isolated interstitial hydrogen through silicon, and the same method is used when the carbon-hydrogen and di-carbon hydrogen defects are modelled. The paper also looks at the modelling of LVM spectroscopy.

Modelling

The computational model uses Car-Parrinello-like dynamics and an approximate molecular orbital technique (AEA Technology's CHEMOS code) to simulate the migration and dynamics of the hydrogen's migration, vibration and trapping near the carbon.

Migration of hydrogen

Hydrogen has a very low mass, so when we look at its path as it migrates through a solid, we need to use a quantum mechanical treatment. The stable site is a bond-centred interstitial position[1] which is a self-trapped site: that is, until the silicon lattice relaxes outwards to accomodate the hydrogen, the site is not a stable one. However, the silicon atoms move much slower than the hydrogen, so in a classical sense, it is difficult for the hydrogen to be trapped at all.

A quantum mechanical particle samples all the possible configurations. When it is trapped in one site, it can sample any neighbouring sites, and as the lattice deforms due to the phonons present, the energies of these neighbouring sites will change. If the particle's energy at its present site (including the lattice distortion) is the same as that at the new site, it can hop across. Then the energy of activation of the hop it just the energy to distort the lattice such that the energies in the two sites are matched. This is derived mathematically by Flynn and Stoneham[6].
The activation energy for migration of the single hydrogen interstitial atom, derived by this method is 0.20 eV.

Local vibrational modes
The dipole moment of the full defect and surrounding crystal can be calculated at each time step (usually 1 fs), as well as the positions of all the atoms and their potential and kinetic energy.

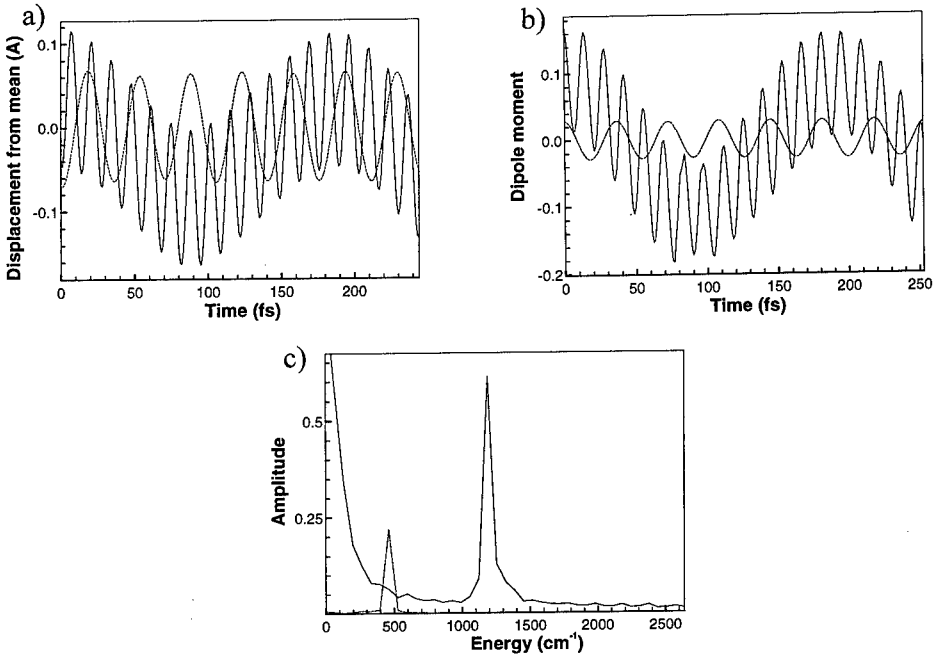


Figure 1: The deviation of a) the position and b) the dipole moment from equilibrium, of the anti-bond hydrogen atom in the H_2* defect in silicon, as it vibrates in along the (111) direction. c)The local mode spectrum corresponding to the dipole moment in b).

The Fourier transform of the dipole moment, gives the spectrum in the infrared which corresponds to the LVM spectrum, including the polarisation. Fig. 1c shows that the vibration in Fig. 1b gives a plausible LVM spectrum. The experimental local mode energies are 1838 cm^{-1} and 817 cm^{-1}[7], showing that the model gives rather low estimates of vibrational energies. The resolution of the spectrum is inversely proportional to the time over which the vibration is recorded, and hence to the computer time used. Since many defects or local modes vibrations are not infrared-active, it can be misleading to equate the vibrational

frequencies to the LVM spectrum. The spectra derived here can be compared directly to their experimental equivalents.

Hydrogen trapped at carbon

Carbon is present in all types of silicon as substitutional atoms. It is substantially smaller than the silicon atom it replaces, leading to a contraction of the lattice around it[8]. Hence, when the bond-centred hydrogen attaches itself to the carbon, some of the strain in the lattice is relieved. The gain in energy when the carbon traps an interstitial hydrogen atom is 1.7 eV.
The orientation of the defect will rotate if the hydrogen hops from one of the carbon bonds to another, as is shown in Fig. 2. As before, it is not adequate to calculate the energy barrier over which the hydrogen moves either with the silicon atoms frozen or with them free to relax - a quantum mechanical treatment is necessary. However, using this method, the activation energy for the hydrogen's hop is very high - about 4.7 eV. It is very difficult to investigate all the structures such that the final and initial states have the same energy, so this estimate is an upper limit. However, its large value, compared to the migration energy of the hydrogen itself derived above by the same method, indicates that the defect is more likely to dissociate than to reorient itself.

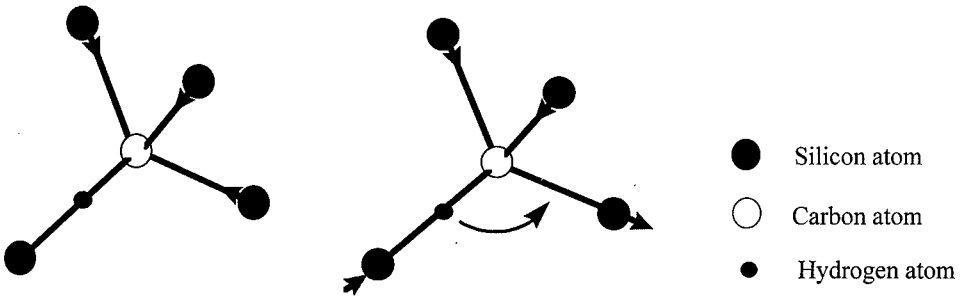


Figure 2: The carbon-hydrogen defect, showing the hop that the hydrogen needs to make to reorient the defect.

In this structure, the hydrogen can vibrate parallel or perpendicular to the C-H-Si bond. Figure 3 shows the dipole moment and the LVM spectra that arise from these vibrations.

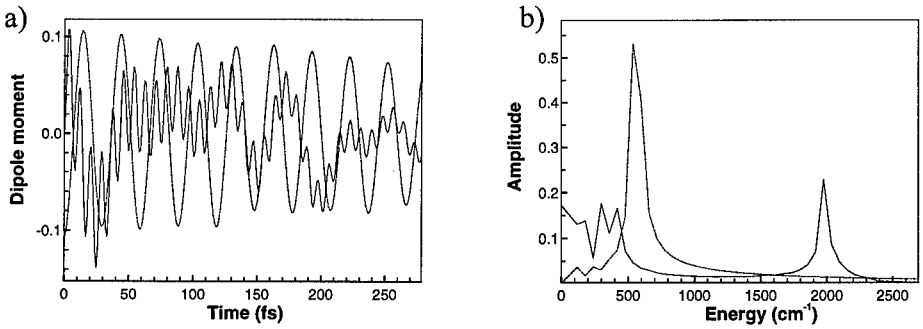


Figure 3: a) Variations of dipole moments and b) LVM spectra derived from them of the carbon-hydrogen defect, with the hydrogen vibrating parallel (solid lines) and perpendicular (broken lines) to the C-H-Si bond.

A DLTS signal has been associated with the positive charge state of this defect with a deep donor level at 0.16 eV below the conduction band edge[3], and it appears to capture an electron and dissociate with an activation energy of 0.7 eV[9]. There is no experimental evidence for it reorienting.

Hydrogen trapped at the di-carbon centre

Previous work, incorporating several experimental and theoretical techniques[4,10], has shown that when silicon containing carbon is irradiated, a metastable defect containing two carbon atoms forms. The two forms of this defect are: the A-form in which a (001) carbon split interstitial is trapped next to a carbon substitutional atom (C_i-C_s), and the B-form in which both the carbons are at neighbouring substitutional sites, with a silicon interstitial on a buckled bond between them (C_s-Si_i-C_s). They are illustrated in Fig. 4, with the higher energy structure which consists of the two carbons sharing a site $(C\text{-}C)_s$.

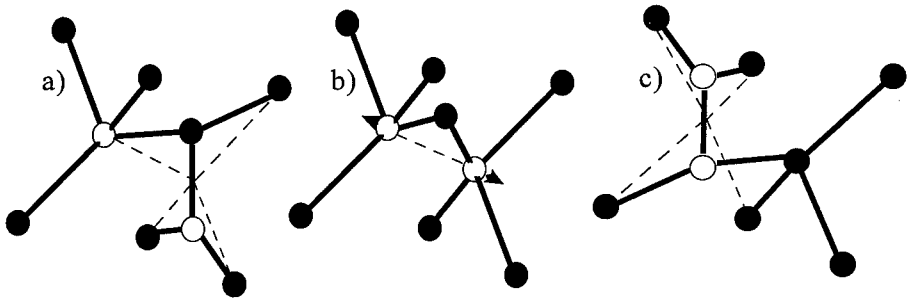


Figure 4: Configurations of the di-carbon defect, a) the A-form (C_i-C_s), b) the B-form (C_s-Si_i-C_s) and c) a higher energy structure $(C\text{-}C)_s$.

The defect is formed when irradiation produces vacancies and silicon interstitials which displace carbon substitutional atoms, which are trapped at other carbon substitutional atoms. If, in addition, there are mobile hydrogen atoms (or complexes) in the crystal, they may also trap hydrogen:

$$\begin{aligned} C_i + C_s &\rightarrow (C_i\text{-}C_s) \quad \text{or} \quad (C_s\text{-}Si_i\text{-}C_s) \\ (C_i\text{-}C_s) + H_i &\rightarrow (C\text{-}C\text{-}H) \\ \text{or} \quad (C_s\text{-}Si_i\text{-}C_s) + H_i &\rightarrow (C\text{-}C\text{-}H) \end{aligned} \qquad (1)$$

Leary et al[11] investigate the possibilities of this process from another perspective - the interstital carbon-hydrogen complex is both very stable and highly mobile, and if it is trapped by another substitutional carbon, the same or another structure of the di-carbon-hydrogen defect may form:

$$\begin{aligned} C_i + H_i &\rightarrow (C\text{-}H)_i \\ (C\text{-}H)_i + C_s &\rightarrow (C\text{-}C\text{-}H) \end{aligned} \qquad (2)$$

Using either process, the di-carbon-hydrogen complex should form readily if the energy is lower than that of the constituent defects. In these calculations, an energy of 2.7 eV is released when the di-carbon defect captures a hydrogen atom.

However, in contrast to the results of Leary et al [11,12], who find that the most stable structure of the complex is like that shown in Fig. 4c, with the hydrogen attached to one of the carbon atoms, I find a lower energy structure with the carbons as in Fig. 4b with the hydrogen attached to a back bond of one of the carbon atoms, although the other structure is also stable. These two structures are shown in Fig. 5.

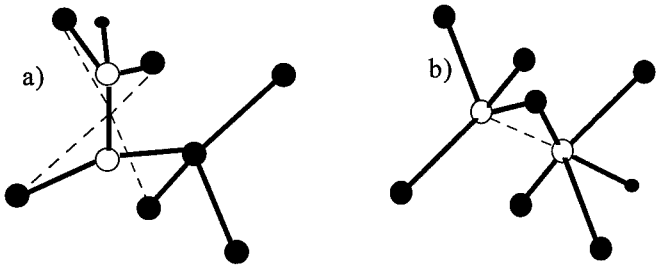


Figure 5: Alternative configurations of the di-carbon-hydrogen defect:
a) as calculated by Leary et al[11], b) these calculations.

Hydrogen was placed at several sites near the di-carbon complex, so that the trapping could be simulated. It was repelled by the B-form of the di-carbon complex if it approached from sites away from the (111) axis of the defect, but formed the structure shown in Fig 5b, when the hydrogen approached one of the carbon substitutional atoms near that axis. Neither of the two stable configurations of the di-carbon defect could be persuaded to re-order, on trapping the hydrogen, into the structure suggested by Leary et al[11,12]. That structure arises quite naturally from the trapping of the $(C\text{-}H)_i$ by a carbon substitutional atom, as shown in Eqn. 2, as his paper indicates. Its local modes agree well with those of the photoluminescence system, the T-line[12].

Therefore, we suggest that when the di-carbon-hydrogen complex forms by the di-carbon defect capturing a hydrogen atom (Eqn. 1) it may form a different structure to that which forms when a carbon interstitial atom captures an interstitial carbon-hydrogen complex (Eqn. 2). The latter is the defect responsible for the T-line, the former may be present in the same material or in samples produced under different conditions, for example when hydrogen is introduced after irradiation and annealing have caused the formation of the di-carbon defects. Local vibrational modes of both structures caused by the vibration of the hydrogen, are shown in Figure 6.

Conclusions

It is necessary to use a quantum mechanical treatment of the migration of hydrogen; a classical picture is misleading.

Hydrogen is trapped readily at isoelectronic defects (as well as dopants) in silicon. Substitutional carbon traps interstitial hydrogen with a gain in energy of 1.7 eV. The metastable di-carbon defect can also trap interstitial hydrogen with a gain in energy of 2.7 eV, but may form a different structure than that which forms when the substitutional carbon traps a mobile interstitial carbon-hydrogen complex.

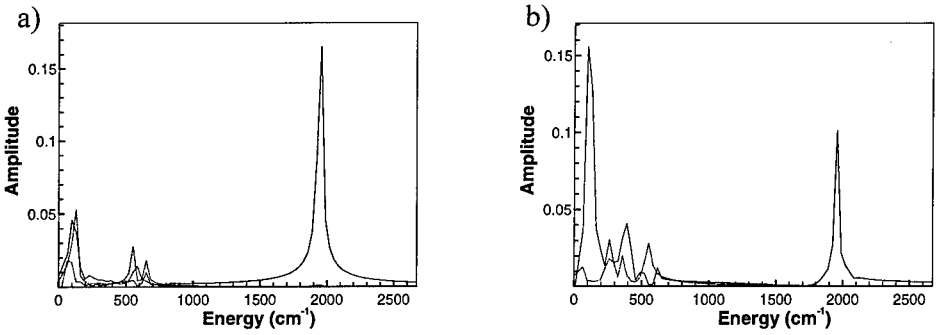


Figure 6: Local vibrational modes of the two structures of the di-carbon defect illustrated in Fig. 5a and 5b respectively. The vibrations are parallel (solid lines) and perpendicular (broken lines) to the C-H bond.

Acknowledgments:
This work was supported by the Engineering and Physical Science Research Council, U.K.

References:

[1]M. C. R. Symons, Hyp. Int. **17-19,** 771 (1984); T. L. Estle, S. K. Estreicher and D. S. Marynick, Hyp. Int. **32**, 637 (1886)
[2] E. C. Lightowlers, Mat. Sci. Forum **196-201**, 817 (1995)
[3] A. Endros, Phys. Rev. Lett. **63**, 70 (1989)
[4] G. Davies and R. C. Newman, in "Handbook on Semiconductors, Vol. 3", ed. S. Mahajan, (Elsevier Science B. V.) 1994, p 1557, and references therein.
[5] e.g. R. C. Newman, "Infrared studies of crystal defects" (Taylor and Francis: London) 1973, p1-187.
[6] C. P. Flynn and A. M. Stoneham, Phys. Rev. **B1**, 3996 (1970)
[7] B. Bech Nielsen, J. D. Holbech, R. Jones, P. Sitch and S. Oberg, Mat. Sci. Forum **143-147**, 845 (1994)
[8] J. A. Baker, T. N. Tucker, N. E. Moyer and R. C. Buchert, J. Appl. Phys. **39**, 4368 (1968)
[9] Y. Kamiura, M. Tsutsue, M. Hayashi, Y. Yamashita and F. Hashimoto, Mat. Sci. Forum **196-201**, 903 (1995).
[10] R. Jones, S. Oberg, P. Leary and V. Torres, Mat. Sci. Forum, **196-201**, 785 (1995), A. Mainwood, Mat. Sci. Forum **196-201**, 1589 (1995)
[11] P. Leary, S. Oberg, P. R. Briddon and R. Jones, paper P1 75 at this conference;
[12] A.N. Safonov, E. C. Lightowlers, G. Davies, P. Leary, R. Jones and S. Oberg, Phys. Rev. Lett. **77**, 4812 (1996).

Materials Science Forum Vols. 258-263 (1997) pp. 259-264
© 1997 Trans Tech Publications, Switzerland

THE M-LINE (760.8 meV) LUMINESCENCE SYSTEM ASSOCIATED WITH THE CARBON-HYDROGEN ACCEPTOR CENTRE IN SILICON.

A.N.Safonov and E.C.Lightowlers.

Physics Department, King's College London, Strand, London WC2R 2LS, United Kingdom.

Keywords:carbon, hydrogen, silicon, photoluminescence.

Abstract.
Further investigations of the M-line (760.8 meV) photoluminescence system are reported. Analysis of the magnetic field perturbation data shows that the transition occurs between a shallow effective mass-like state and a deep state of a paramagnetically active acceptor centre. The position of the deep (-/0) level is located at E_c-0.37 eV. Isotope shifts and splitting of the zero-phonon line and the local vibrational mode features show that the centre contains one hydrogen atom and two or more carbon atoms. The mechanism of the defect formation is discussed.

Introduction.

The M-line luminescence system, with zero-phonon line at 760.8 meV, appears in radiation damaged silicon after subsequent thermal treatment in the temperature range 300-600°C. This band has been known for a long time to be associated with a carbon containing centre [1], but more recently it was shown also to contain hydrogen [2,3]. There are several carbon and hydrogen containing luminescence centres of high thermal stability created by thermal treatment after radiation damage in either Czochralski (CZ) or float zone (FZ) Si. Apart from M-line, these include the T-line (935.1 meV) and the I-line (965.0 meV) systems which in some cases can be created by thermal treatment of CZ silicon alone [2,4]. Since carbon and hydrogen are two common contaminants in Si and all of these defects are stable up to 600°C and create electronic levels in the band gap, it is of both technological importance and scientific interest to establish their electronic and atomic structures and the mechanism of their formation.

The atomic structure of the T-line centre has been identified recently as a ⟨100⟩ oriented carbon pair occupying a substitutional site with a hydrogen atom attached to a one of the carbon atoms [5]. The I-line appears to have a very similar configuration, modified probably by the presence of an oxygen atom [6]. Surprisingly, these two centres involve a pair of carbon atoms arranged in a form totally different from the di- carbon G-line centre [7]. Both of them, in contrast to the latter contain a C-C bond. In this paper we report a preliminary analysis of the local vibrational modes associated with the M-line centre which suggests that its atomic structure, particularly the configuration of the carbon atoms, has a similarity with the structure of the G-line centre. Also we present a more detailed analysis of the magnetic field perturbation measurements on the M-line which shows that, similar to the T- and I-line centres the M-line centre creates a deep acceptor level in the band gap and is paramagnetic in its neutral state.

Experimental details.

The material employed in these measurements was FZ Si with either $[^{12}C]= 2\times10^{17}cm^{-3}$ or $[^{12}C]=5\times10^{16}$ cm^{-3} and $[^{13}C]=7\times10^{16}$ cm^{-3}. This was saturated with $1.5\times10^{16}cm^{-3}$ H_2 or D_2 by heating in flowing gas for 30 minutes at 1300°C and rapidly cooling in silicone oil [8].

The samples were either neutron irradiated with a Cd ratio of 25 to total flux of 1.2×10^{17} cm^{-2} neutrons, or 2 MeV electron irradiated with a flux of 4×10^{17} cm^{-2}. They were then then annealed for 30 minutes at 390°C. They were etched in 10:90 HF:HNO_3 mixture before and after all heat treatments. Photoluminescence measurements, with 514.5-nm Ar^+ laser excitation, were carried out using either a Nicolet 60SX or a Bomem DA8 Fourier-transform spectrometer fitted with a North Coast Ge diode detector, or a Cincinnati Electronics InSb diode detector cold-windowed at 2.74 μm for energies below 0.7 eV. The Zeeman experiments were carried out with a magnetic field up to 5.0 T, in an Oxford Instruments drip feed cryostat fitted with a Helmholtz pair of superconducting coils.

Results and discussion.

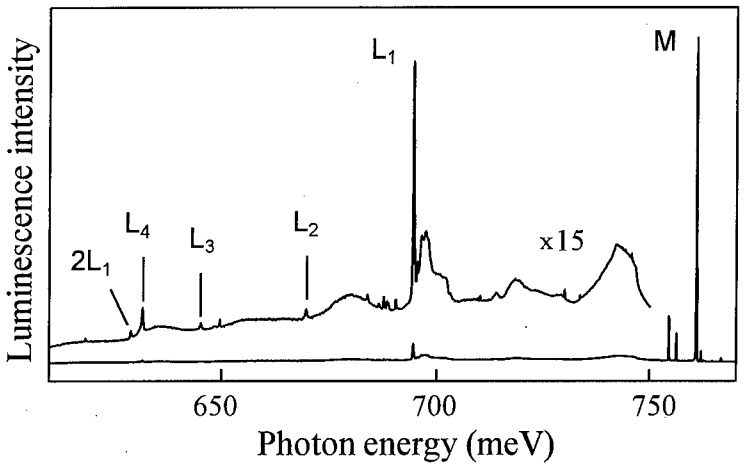


Fig.1 Photoluminescence spectrum of the M-line obtained at 4.2 K from hydrogenated FZ silicon with [C] ~ 2 x $10^{17}cm^{-3}$.

Figure 1 shows the M-line photoluminescence spectrum obtained at 4.2 K, with a resolution of 0.12 meV, from FZ material containing ^{12}C and H. The spectrum is dominated by the zero-phonon transition at 760.8 meV, labelled M, which is accompanied at lower energies by a broad side band of phonon-assisted transitions associated with the perturbed lattice modes and by sharp local mode satellites L_i. There are also some zero-phonon lines and phonon-assisted features in the spectrum associated with other defects. The features between 680 and 690 meV are considered to be local mode satellites related to the two strong zero-phonon lines just below the M-line. However, this has not been clarified yet because these zero-phonon lines are always created along with the M-line under conditions for optimising the strength of the M-line. The spectra recorded at temperature above 10 K contain an additional sharp feature M(E) at 2.8 meV higher energy than the M-line. The ratio of the M(E) and M intensities with increasing temperature follows an exponential law close to the Boltzmann thermal population factor for the two excited states of the same centre separated by $\sim$ 2.8 meV. It has been demonstrated previously that the M-line has a relatively large hydrogen-deuterium isotope splitting (0.33 meV) [3] and a very small carbon isotope shift, but not resolvable splitting [1], which implies that the centre contains at least one hydrogen and one carbon atom. The shifts and splitting of the L_2, L_3 and L_4 local mode features, to be described later, confirm the presence of one hydrogen atom and either two or more carbon

atoms.

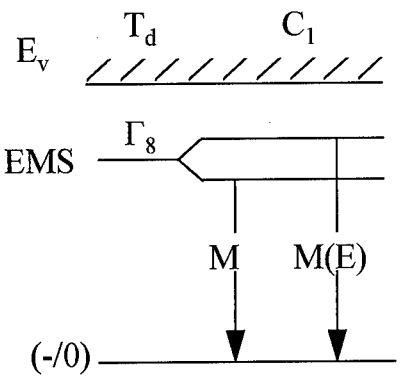


Fig.2 Schematic energy level diagram of the transitions responsible for the M and M(E) zero-phonon lines.

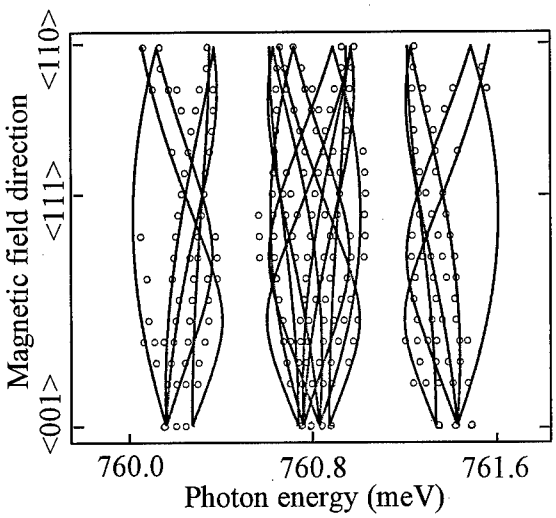


Fig.3 Circles show the positions of the M-line Zeeman components measured at 5 T for different directions of the magnetic field. The lines are calculated as described in the text.

We have reported previously that under magnetic field and uniaxial stress perturbations the M-line undergoes a rather complicated splitting into a large number of components reflecting the low symmetry of the defect [3]. It was shown that the uniaxial stress response in its linear limit and the structure of the Zeeman spectra can be accounted for by a standard perturbation approach based on pure symmetry arguments, and that both the stress and the magnetic field effects are consistent with triclinic symmetry of the centre. Basically, the M-line corresponds to a transition between two orbitally nondegenerate states which split into doublets in a magnetic field. However, the origin of the states involved in the transition was not identified. A more detailed analysis shows that the presence of two zero-phonon lines and the behaviour under external field perturbations are consistent with transitions between the levels of an acceptor type centre which is paramagnetically active in its neutral state. The ground state of the system corresponds to a neutral centre with a hole occupying a deep (-/0) level created by the defect core potential. Under optical excitation from an argon laser, such a centre can be ionised by transfering the hole into the valence band or, equivalently, by transfering an electron from the valence band into the (-/0) state. Once ionised, the negatively charged defect creates a Coulomb-like hole attractive potential and can bind a hole in shallow effective-mass like states (EMS) which are detected in luminescence as the excited states of the system. Fig.2 shows schematically the energy level diagram explaining the origin of the luminescence lines. This type of optical transitions has been observed for many other luminescence systems, including the T- and I-line [9,6], and has several characteristic features common for all of them, for example, the existence of closely lying excited states which interact under external field perturbations. The latter gives rise to strong nonlinear behaviour at relatively small applied stresses. The magnitude of the stress induced interaction in this case is primarily determined by the characteristics of the valence band maxima. Also, luminescence lines of this type exhibit strong anisotropy of the Zeeman splitting. To explain the origin of such anisotropy and also to demonstrate the validity of above description in the

case of the M-line, we will consider the effect of the magnetic field in more detail.
Figure 3 shows the angular variation of Zeeman splitting at 5 T where the circles correspond to the experimental data and lines are the calculated fit obtained with the two basic assumption described below. First, we assume that the hole in the ground state is a spin-like particle with $s = \frac{1}{2}$, which is commonly the case for deep level states in Si and, therefore, it splits isotropically in a magnetic field. Second, we consider that the lowest energy EMS excited states observed in photoluminescence can be described in the basis of $\Psi_{3/2}$ states of the Γ_8 group, similar to the ground states of the shallow acceptor centres. In the symmetry lowering field of the defect core potential, fourfold degenerate Γ_8 states split into two Kramers doublets resulting in the M and M(E) zero-phonon lines. The effect of a magnetic field with components B_x, B_y, B_z on these states can be account for by Hamiltonian [10]

$$H^h(B) = \mu_B \left(g_1 \sum_i B_i J_i + g_2 \sum_i B_i J_i^3 \right) + H_o \qquad (1)$$

where J_i are the angular momentum operators, μ_B is the Bohr magneton and g_1, g_2 are the hole g-factors. The second part of the Hamiltonian

$$H_o = -b_1 \sum_i (J_i^2 - I)\epsilon_{ii}^o - \frac{d_1}{\sqrt{3}} \sum_{ij} \{J_i J_j\} \epsilon_{ij}^o \qquad (2)$$

with $\{J_i J_j\} = 1/2(J_i J_j + J_j J_i)$, describes the symmetry lowering perturbation of the short-range defect field in terms of internal strain components ϵ_{ij}^o. The ϵ_{ij}^o are not necessarily the real strain but one of the ways to account for the effect of the core potential on the Γ_8 hole states. The fit shown in Fig.3 has been obtained with the hole parameters g_1=1.1, g_2=0.03 , b_1=-1.8 eV, d_1=-5.4 eV and electron g-factor g_e=1.97. The zero strain components used are $\epsilon_{YY}^o = 0.33 \times 10^{-3}$ and $\epsilon_{ZZ}^o = -0.33 \times 10^{-3}$, referred to the defect axes, where Y and Z lie in the $[1\bar{1}0]$ plane and deviate by 20° from the $\langle 110 \rangle$ and $\langle 001 \rangle$ directions, respectively. Although the excited state of the transition splits into a doublet in a magnetic field it can not be regarded as spin $s = \frac{1}{2}$ state. The wavefunction of this effective-mass like state contains a mixed combination of orbital (ℓ=1) and spin ($s = \frac{1}{2}$) components which does not correspond to any particular moment. As a consequence, all the transitions between the split sublevels of the excited state and ground spin-like state are allowed in a magnetic field. This fact, together with a strong anisotropy of the effective mass-like state splitting, explains the relatively large number of the Zeeman components.
The binding energy of the hole in this shallow state can be estimated from the temperature-dependence measurements which provide a value close to 35 meV. In turn, using this value and the energy of the optical transition we can estimate the position of the deep (-/0) level as E_c-0.37 eV.
The strong nonlinearity in the stress response of the M-line reported in reference 3 is consistent with the presence of two closely lying excited states and is most likely associated with the interaction between them. However, a full quantitative analysis of the stress data requires the knowledge of the M(E)- line splitting which is difficult to obtain due to the weak intensity of the line.
It is well established that the centre responsible for the M-line contains both carbon and hydrogen. Measurements which have been carried out on a wide range of materials provide no evidence that oxygen, any group III and V elements, or any other impurities which could be present or inadvertently incorporated, are involved. The studies of the zero-phonon line and local modes in material containing a hydrogen-deuterium mixture give no indication that

the centre contains more than one hydrogen atom. This is also consistent with a paramagnetic activity of the defect which requires an odd number of hydrogen atoms being involved in the complex provided its atomic components include only carbon and hydrogen. Taking into account the results of recent theoretical calculations predicting a high mobility of C-H pair in Si [11], it is difficult to imagine that the M-line centre, with such high thermal stability and low symmetry, contains only one carbon atom. Although a small shift and broadening of the zero-phonon line can be detected in mixed carbon isotope material [1] this provides no information about the number of carbon atoms involved. It should perhaps be noted that isotope structure of zero- phonon lines does not unambiguously reflect the atomic composition of the defect. For example, the structure of the T-line in material with a ^{12}C and ^{13}C mixture has only two components although the centre contains C-C bond. The presence of this bond can be clearly seen in the splitting of the local modes satellites [5]. We will discuss now some results of preliminary measurements on the isotope structure of the local modes associated with the M-line centre, which are shown in Fig.4.

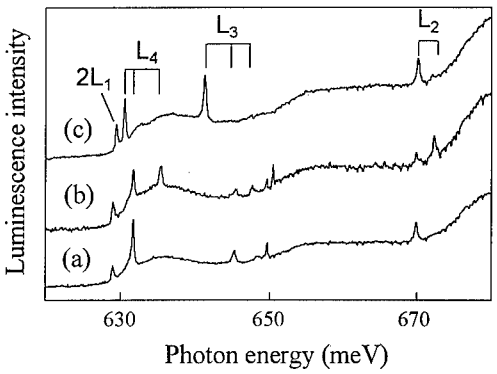


Fig.4 Photoluminescence spectra of the local vibrational modes associated with the M-line obtained from material containing (a) H+^{12}C , (b) H+ ^{12}C+ ^{13}C, (c) D+ ^{12}C

The strongest local mode feature L_1 shown in Fig.1 has no carbon isotope shift or splitting and there is only a small shift to higher energy in deuterated material due to the shift of the zero-phonon line. Consequently it is not included in Fig.4. The features at $\sim$ 650 meV have been found in some hydrogenated samples but not in deuterated material and probably are not related to the M-centre. Spectra (a) and (b) in Fig.4 obtained from hydrogen material containing just ^{12}C or a ^{12}C:^{13}C $\sim$ 1.4:1 mixture, respectively, show that the local modes L_2, L_3 and L_5 are all carbon-related and undergo large carbon-related isotope shifts. Comparing spectra (a) and (c), it can be seen that L_3 and L_4 have large hydrogen-deuterium isotope shifts while L_2, like L_1, has only a small shift associated with that of the zero- phonon line. These data suggest the presence of at least two carbon atoms at different locations. One of them is probably attached to a hydrogen atom and is involved in the L_3 and L_4 vibrations which have both carbon and hydrogen isotopes shifts. Another one gives rises to L_2 which is not affected by hydrogen-deuterium substitution. The doublet structure of all the modes in mixed carbon isotope material suggests that there is little coupling between the carbon atoms.

We noted above that there is a similarity between the structures of the M-line and the G-line centres. Recent investigations of the G-line spectra in mixed carbon isotope materials, which will be reported elsewhere, revealed that the centre responsible for this system has a local mode with an energy and carbon isotope shift similar to that of the L_2 mode of the M-line centre. This has an energy of 733.5 cm^{-1} (90.94 meV) and a ^{13}C-^{12}C shift of -19.5 cm^{-1} (-2.42 meV) which implies that the vibration primarily involves only one carbon atom. Note

that the ratio of $hv_{12}/hv_{13} \sim 1.028$ in this case is very close to the ratio expected for an isolated Si-C pair. The presence of almost identical local modes in the M-line and G-line spectra strongly suggests that both defects contain a carbon atom at the same location. As stated earlier, the M-line centre in contrast with the other carbon-hydrogen related centres is only created in radiation damaged silicon after annealing at temperatures above 300°C. The major carbon related defect in irradiated silicon disappearing at temperatures $\sim$ 250-300°C is the di-carbon centre responsible for the G-line. This would suggest that the formation of the M-centre involves an interaction between a carbon pair and hydrogen. Together with other evidence [12], it would also suggest that the uncoupled di-carbon pair which forms the G-centre does not break up when the centre is destroyed, rather that it changes configuration and possibly becomes mobile. Further investigations are in progress to provide more information about the structures and mechanisms of formation of the M-line, G-line and other carbon containing centres.

Acknowledgement This work was supported by the Engineering and Physics Sciences Research Council (UK).

References.

[1] E.Irion, N.Burger, K.Thonke and R.Sauer, J. Phys. C: Solid State Phys. **18**, 5069 (1985).
[2] A.N.Safonov and E.C.Lightowlers, Mat. Sci. Forum **143-147**, 903 (1994).
[3] A.N.Safonov, E.C.Lightowlers and G.Davies, *Proc. 22nd Int. Conf. on The Physiscs of Semiconductors* (World Scientific, Singapore, 1995) p.2239.
[4] E.C.Lightowlers, R.C.Newman, and J.H.Tucker, Semicond. Sci. and Tech. **9**, 1370 (1994).
[5] A.N.Safonov, E.C.Lightowlers, G.Davies, P.Leary, R.Jones, S.Öberg, Phys. Rev. Lett. **77**, 4812 (1996).
[6] J.Gower, G.Davies, E.C.Lightowlers and A.N.Safonov, this conference.
[7] L.W.Song, X.D.Zhan, B.W.Benson, and G.D.Watkins, Phys. Rev. B **42**, 5765 (1990).
[8] M.J.Binns, S.A.McQuaid, R.C.Newman and E.C.Lightowlers, Semicond. Sci. Technol. **8**, 1908 (1993).
[9] A.N.Safonov, E.C.Lightowlers and G.Davies, Mat. Sci. Forum **1196-201**, 909 (1995)
[10] G.L.Bir and G.E.Pikus, *Symmetry and Strain-Induced Effects in Semiconductors*, (Halsted, New York, 1974).
[11] P.Leary,S.Öberg, P.R.Briddon and R.Jones, this conference.
[12] E.C.Lightowlers and A.N.Safonov, this conference.

Materials Science Forum Vols. 258-263 (1997) pp. 265-270
© 1997 Trans Tech Publications, Switzerland

INTERSTITIAL CARBON-HYDROGEN DEFECTS IN SILICON

P. Leary[1], S. Öberg[2], P. R. Briddon[3], and R. Jones[1]

[1] Department of Physics, University of Exeter, Exeter, EX4 4QL, United Kingdom
[2] Department of Mathematics, University of Luleå, Luleå, S95 187, Sweden
[3] Department of Physics, University of Newcastle upon Tyne, Newcastle, NE1 7RU, United Kingdom

Keywords: carbon interstitial, hydrogen, silicon, *ab initio* theory

Abstract. Interstitial carbon, in contrast with substitutional carbon, forms defects with hydrogen which are both electrically active and stable to high temperatures. *Ab initio* cluster calculations show that the most primitive defect, C_iH, diffuses very rapidly and is expected to complex with many other impurities notably C, H and O. We describe here the structure and properties of $C_{i,n}H_m$ defects where n and m are less than 3. The most stable defects of the type $C_iC_sH_m$ have very different structures when $m = 0$ and when $m > 0$. In the former case, the C-C bond is metastable and only C-Si-C bonds are formed. However in the second case, the presence of a H atom stabilises the C-C bond. These results are supported by experiment. We show that the vibrational modes of the C_s-C_iH defect are close to those observed for the T-photoluminescent centre and this defect is passivated when complexed with a further H atom. This defect then provides the first example of a fully characterised carbon centre containing a C-C bond.

Introduction

The introduction of either carbon or hydrogen into silicon can have advantageous effects with regards to device reliability and performance. Carbon can be introduced from graphitic contaminants or carbonaceous gases present during growth and predominantly occupies a substitutional site, C_s, having no gap levels. The electrically active interstitial carbon defect C_i is formed upon the capture of a mobile self-interstitial, I, by the C_s defect. The $C_i^{+,0,-}$ defect is one of the most important centres in radiation damages silicon, and it is well established that it adopts a $\langle 100 \rangle$ C-Si split-interstitial with C_{2v} symmetry – see for example [1, 2] and references therein. Thus, C_i can act as a sink for mobile I defects, and suppress transient enhanced diffusion. The barrier for migration of C_i is $\approx$0.8 eV, and therefore the defect is mobile above room temperature and migrates and complexes with a variety of other defects and impurities such as O_i and C_s [2]. However, these defects are only stable to around 300°C, and hence cannot be used to probe self-interstitial generation in the interesting temperature range 450-600°C, where both thermal donor formation and oxygen precipitation takes place. It would be of interest to locate interstitial C defects which are stable in this region.

Hydrogen in silicon has also been intensively investigated in recent years [3], however the absolute concentration of the molecular interstitial is uncertain. Evidence also exists for the formation of H_2 molecules in Si [4] in plasma treated material, which, unless situated near a second defect are infra-red inactive. Furthermore photoluminescence experiments [5], have shown that hydrogen is present in heat treated silicon, even when it was not intentionally introduced – an important finding. Most of the results on interstitial hydrogen have come from muon-spin resonance experiments (μSR) with $\mu^{-,0}$ occupying the T_d site and $\mu^{0,+}$ occupying the bond-centred (BC) site [6]. The defect is therefore bistable, a result supported by theory

[7]: $H^{+,0}$ preferentially occupies the BC site, whereas the T_d site is the ground state for H^-. The barrier for the migration of the interstitial H defect is believed to be low, suggesting that it can migrate to and complex with other defects, often passivating their electrical and/or optical activity [3].

The interaction between H and C_s has recently been investigated [8, 9]. These defects although electrically active, are of minor technological importance as they have low dissociation energies, breaking up when T>100°C. Minaev and Mudyri [10] observed several sharp PL lines from CZ-Si annealed between 450°C and 600°C. The presence of oxygen and carbon in many of these was deduced from sample statistics. The intensities of some of these PL lines can be dramatically increased by the deliberate incorporation of both H and C. Isotopic analysis of these lines shows that many of these defects contain carbon (eg the P and H centres) and both carbon and one hydrogen (I, M, and T centres), but only provide a lower bound to the number of atoms in the defect. [5, 11, 12, 13, 14]. Of primary interest here is the the T-line (935.1 meV), the most extensively studied of these defects. The zero-phonon line displays isotope shifts with both ^{13}C [11] and hydrogen [13] implying that the defect contained at least one C and one H atom. The symmetry of the defect giving rise to the line was also found to be C_{1h}. However, C-isotopic shifts of an LVM, observed as a phonon replica to the T-line, demonstrated that the defect contained two C atoms. In [15] all LVMs along with their isotope shifts were detailed, and these results, along with *ab initio* calculations have determined the microscopic structure of the defect. This consists of a ⟨100⟩ oriented C-CH pair occupying a single lattice site, the structural model is discussed in more detail later. If the H concentration is large, with respect to C, the T-line disappears.

This paper is concerned with a theoretical investigation of the interaction C_i with H, and subsequent reactions with other H and C_s atoms. The calculations described here are based on local density cluster theory with large hydrogen terminated clusters. Two clusters, a ⟨111⟩ oriented 86 atom cluster $Si_{44}H_{42}$, and a tetrahedral 131 atom cluster $Si_{71}H_{60}$, were modified for all of the calculations presented here. Details of the method have been described previously [16]. All atoms were relaxed in these calculations, with full symmetry constraints.

The C_i-H_n defects

The isolated C_i defect possesses two undercoordinated atoms (C and Si) and therefore H can bond to either of these atoms forming a ⟨100⟩ oriented defect with H bonded to C (Figure 1a), or with H bonded to Si. These configurations are labelled $(C_iH)_{\langle 100\rangle}Si$ and $C_i(SiH)_{\langle 100\rangle}$ respectively. There is then the possibility of a structural change to a bond centred (BC) defect with either the C-H unit at the centre of a Si-Si bond $(C_iH)_{BC}Si$ (Figure 1b), or with a Si-H unit at the centre of a C_s-Si bond $C_s(Si_iH)_{BC}$. The presence of H lowers the symmetry of all of these defects to C_{1h}.

Two of the structures possessed almost degenerate energies in the neutral charge state: with $(C_iH)_{BC}Si$ possessing an energy 0.03 eV above $(C_iH)_{\langle 100\rangle}Si$, which was the ground state structure. The other structures were less stable by at least 0.47 eV. The binding energy of H with C_i in the ⟨100⟩ form was evaluated by placing H in a BC site distant from C_i, yielding an energy of 2.8 eV. The near degeneracy in the energies of the ⟨100⟩ and BC forms is surprising in view of the very different bonding patterns. In the isolated C_i defect these two configurations possessed very different energies [1] and it is the presence of H which stabilises the BC form. Since the BC site lies on a possible diffusion trajectory of C_i, the results suggest that the defect should be highly mobile.

The saddle point for this migration path was found by the following procedure: the initial cluster coordinates in each run were linearly interpolated between the relaxed ⟨100⟩ and ⟨111⟩

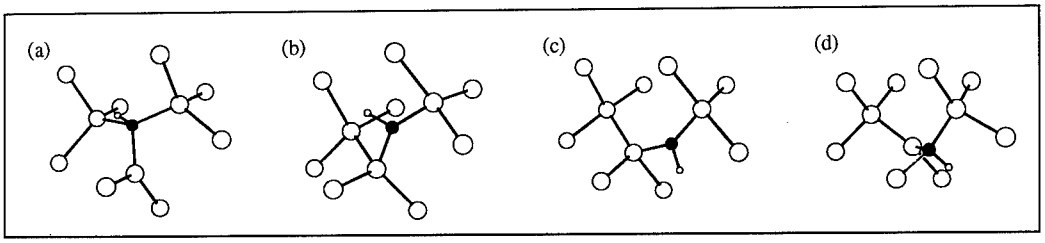


Fig. 1. The possible configurations of the C_i-H defect in Si, and the defect migration path: (a) the $(C_iH_{\langle 100\rangle})$Si configuration, (b) the (C_iH_{BC})Si configuration, (c) the (C_iH_{BC})Si configuration with the rotated CH unit, and (d) reformation of the $(C_iH_{\langle 100\rangle})$Si structure. The black circles represent carbon, and the small and large white circles hydrogen and silicon respectively.

bond centred forms illustrated in Fig. 1a-b. Thus these coordinates are simply $(1-\alpha)R_1 + \alpha R_2$ where R_i describes the $\langle 100\rangle$ and $\langle 111\rangle$ forms respectively, followed by a constrained relaxation. The energies of each run versus α are shown in Fig. 2 (α_1). The calculated barrier for conversion of the $\langle 100\rangle$ to BC form is ~0.27 eV. A second constrained run to calculate the energy required for the 120° rotation of the C_i-H unit in the BC defect (Fig. 1b-c) was performed (α_2) and gave a barrier of 0.16 eV for this process. The migration step is complete when the $\langle 100\rangle$ defect is reformed, Fig. 1d. From these results, it is clear that the migration energy for C_iH is extremely low, around 0.3 eV, and therefore we expect the C_i-H defect to be an extremely reactive unit, rapidly migrating to and complexing with other defects present in the material.

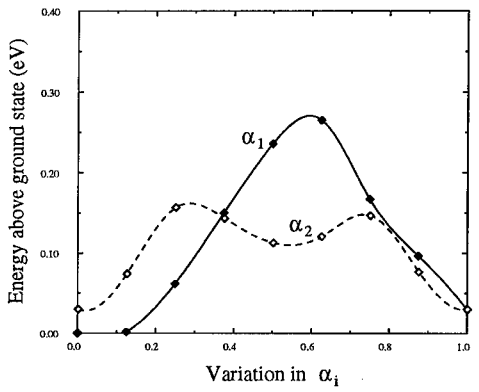


Fig. 2. The energy as a function of α for the restructuring and rotation of C_i-H.

Both configurations give rise to a singly occupied mid-gap level, consistent with a single electron occupying a dangling p-orbital. Hence the defects are paramagnetic in the neutral charge state with $S = \frac{1}{2}$. The charged C_i-H defects were also investigated, and it is clear that the difference in energy between the two forms was much greater here: in the negative charge state, the BC structure proved to be lowest in energy — being 0.55 eV below the $\langle 100\rangle$ structure. Conversely, in the positive charge state the $\langle 100\rangle$ oriented defect lay 0.72 eV below the BC configuration. This greater difference in energy will affect the diffusion barrier, it is likely that the $\langle 100\rangle$ and the BC configurations are the saddle points for the negative and positively charged defects respectively, and the diffusion energy is now comparable to, but still lower than that of neutral C_i (experimental 0.8 eV, theory 1.1 eV [1]).

Capture of a second hydrogen atom leads to an electrically inactive and immobile defect.

Two configurations of C_i-H_2 were investigated, with H passivating the dangling bond of the C_i-H defect. Here, the BC C_i-H_2 defect proved to be the lowest energy configuration, and should be stable enough to enable detection of its local vibrational modes. The LVMs of both the C_i-H and C_i-H_2 defects have been calculated and will be discussed elsewhere.

The $(C_i\text{-}H_n)C_s$ defects

Another possible reaction which C_i-H might undergo is trapping by C_s. As well as the capture of C_iH by C_s, a C_s-(C_i-H) defect could potentially be formed by the capture of H by the di-carbon defect. There are many possible structures for this defect and several were investigated. Of these, two structures both with C-C bonds possessed significantly lower energies than any of the others. These are denoted $C_s(C_iH)_{\langle 100\rangle}$ and $C_s(C_iH)_{BC}$ and are illustrated in figure 3 (a) and (b) respectively. The first of these was the ground state configuration lying 0.28 eV below the latter structure.

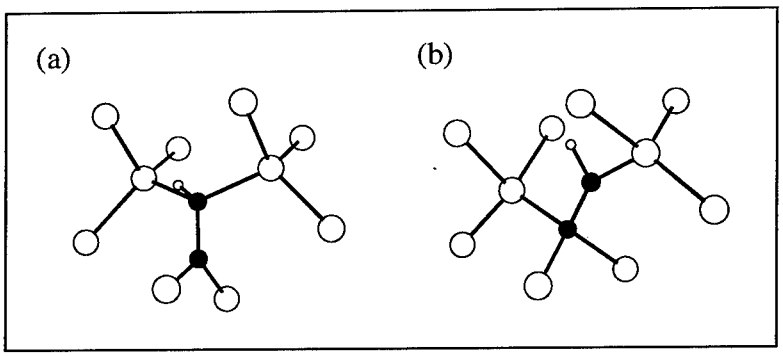


Fig. 3. The two low energy configurations of the $(C_i\text{-}H)C_s$ defect in Si.

It is interesting to note that contrary to the di-carbon centre, the formation of a C-C bond is favoured in these defects. The neutral ground state is paramagnetic with $S=\frac{1}{2}$, and is isoelectronic with the IA configuration of the C_i-P_s defect which has been investigated experimentally. The Kohn-Sham eigenvalues indicate that the defect gives rise to one gap level which contains one electron. This occurs around mid-gap, and is related to a non-bonding p-orbital on the undercoordinated carbon atom.

The defect has been assigned to the 0.9351 eV PL centre, or T-centre, which creates a deep electron trap at E_c-0.2 eV. The structure and vibrational modes of the ground state structure and their relationship with the modes observed for the T-centre has been described previously [15], and given in Table 1. Analysis of the Zeeman splitting of the PL line confirms that the neutral state of the T-line defect is paramagnetic with $S=\frac{1}{2}$ consistent with the singly occupied Kohn Sham level from the calculation. The binding energy of C_iH to C_s was estimated by the introduction of the separated defects into the cluster, a value of 0.8 eV was obtained.

In samples with large concentrations of H, the intensity of the T-line is greatly reduced. One possible explanation is that the C_i-H precursor defect traps a second H atom, becoming immobile thus blocking the formation of the T-centre. A second possibility is that the T-centre rapidly traps a second H atom. Here, we investigated three possible configurations of the C_2-H_2 defect: a) $\langle 100\rangle$ oriented defect labelled $(C_2H_2)_{\langle 100\rangle}$, b) a BC defect, with a C_i-H_2 unit between C_s and a Si neighbour, labelled $(C_2H_2)_{BC}$, and finally c) $(C_2H_2)_{\langle 110\rangle}$ where two (C-H) units share a lattice site a $\langle 110\rangle$ orientation. The symmetry of these three configurations was constrained

Table 1. Comparison between calculated and (experimental) local vibrational modes L5 and L4, cm^{-1}, for $C_s(C_iH)_{100}$ and the T-centre, along with their downward isotope shifts.

Sym	Mode	^{12}C-(^{12}C-H)		Δ^{12}C-(^{13}C-H)		Δ^{13}C-(^{12}C-H)		Δ^{13}C-(^{13}C-H)	
A	L5	1097.8	(1056.0)	19.2	(18.0)	20.7	(27.0)	40.8	(45.0)
A	L4	743.6	(796.0)	1.0		22.0	(25.0)	23.1	(25.0)
Sym	Mode	^{12}C-(^{12}C-D)		Δ^{12}C-(^{13}C-D)		Δ^{13}C-(^{12}C-D)		Δ^{13}C-(^{13}C-D)	
A	L5	1102.2	(1052.0)	17.1	(16.5)	24.3	(20.5)	42.3	(38.0)
A	L4	713.7	(759.0)	0.9		16.6	(16.5)	17.3	(16.5)

to C_2, C_{1h} and C_{2v} respectively. The most stable defect is $(C_2H_2)_{\langle 100\rangle}$, where H saturates the C radical in the T-centre, being at least 1.0 eV below the next lowest energy structure. The defect is analogous with the hydrogenated self-interstitial defect (Si_iH_2) which also has a $\langle 100\rangle$ orientation [18, 19] with C_2 symmetry. Again the calculations of the LVMs of all these defects will be published elsewhere.

Discussion

It is clear that many defects can arise when H complexes with interstitial carbon. We found that the binding energy of H with C_i is very large, $\sim$ 2.8 eV, and consequently such defects should be readily formed in irradiated material or annealed CZ-Si. The neutral defect exists in two almost degenerate structures consisting of a $\langle 100\rangle$ oriented and bond centred pair. The bond centred form has a similar structure to O_i. Its migration barrier is 0.4 eV and this low value implies that the defect would easily migrate through the lattice readily forming complexes. The centre gives rise to a singly occupied $S=\frac{1}{2}$ gap state. The negative charge centre is stable in the BC form while the $\langle 100\rangle$ form is favoured in the positive charge state.

The binding energy of C_iH with C_s is 0.8 eV and the resulting $\langle 100\rangle$ oriented C-C pair, with H bonded with one C radical, is identified with the T photoluminescent (0.9351 eV) centre. The calculated local vibrational modes and their isotope shifts are in good agreement with observations on this centre [15]. The formation of the T-centre by this reaction is more likely than the pairing of H with a di-carbon defect as the latter is not stable beyond $\sim$ 300°C. The T-centre can be observed when CZ-Si is annealed to 450°C, or when H soaked FZ-Si containing C is irradiated and subsequently annealed around 450°C. The annealing is probably necessary to break up H molecules and silicon interstitial aggregates.

The C_i-H centre can be passivated by further H trapping. Such a centre would be be immobile and its formation would block the production of T-centres. Alternatively, T-centres themselves could trap a second H atom forming the inert C_s-C_i-H_2 defect.

There are of course many other possible defects formed, which are beyond the scope of this current work, among these are the reaction of the migrating C_i-H with O, N and other CH defects. It seems likely that CH forms very similar defects to those of isoelectronic impurities such as N or P. For example, we have already pointed out that the C-CH pair is isoelectronic with C_i-P_s. More recent work [17] has showed that a N_iO_{2i} defect is a candidate for the shallow thermal donor, and if N is replaced by CH, there is little change in the structural or electronic properties. It is likely then that such complexes are responsible for some of the other yet unidentified PL lines in Si. The presence of these centres provides further evidence that the thermal treatment of CZ Si leads to the generation of self-interstitials. The stability of such centres over this temperature range (450-600°C) where thermal donors are produced may provide a means for monitoring Si_i production.

S. Öberg thanks NFR and TFR in Sweden for financial support. He also thanks PDC at KTH in Sweden, for computer time on the SP2. We also thank the HPCI committee of the EPSRC for computer time on the T3D where some of these results were derived.

References

[1] P. Leary, R. Jones, S. Öberg, and V. J. B. Torres, Phys. Rev. B, **55**, 2188, (1997).

[2] G. Davies, and R. C. Newman, in *Handbook on Semiconductors*, **3**, ed. by S. Mahajan, Elsevier (1994), p 1557.

[3] S. J. Pearton, J.W.Corbett and M.Stavola, *Hydrogen in Crystalline Semiconductors* (Springer-Verlag, Berlin Heidelberg, 1992).

[4] K. Murakami, N. Fukata, S. Sasaki, K. Ishioka, M. Kitajima, S. Fujimura, J. Kikuchi, and H. Haneda, Phys. Rev. Lett. **77**, 3161 (1996).

[5] E. C. Lightowlers, Mat. Sci Forum **196-201**, 817 (1995).

[6] Phil. Trans. R. Soc. Lond. A, **350** 169-333, *Ed.* S. F. J. Cox, A. M. Stoneham, and M. C. R. Symons, (1995).

[7] C. G. Van de Walle, P. J. H. Denteneer, Y. B. Yam, and S. T. Pantelides, Phys. Rev. B **39**, 10791 (1989).

[8] A. Endrös, Phys. Rev. Lett. **63**, 70 (1989).

[9] Y. Kamiura, M. Tsutsue, M. Hayashi, Y. Yamashita and F. Hashimoto, Materials Science Forum **196-201**, 903, (1995).

[10] N. S. Minaev, and A. V. Mudryi, Phys. Stat. Solidi (a) **68**, 561 (1981).

[11] E. Irion, N. Burger, K. Thonke, and R. Sauer, J. Phys. C: Solid State Phys. **18**, 5083 (1985).

[12] A.N. Safonov and E.C. Lightowlers, Mat. Sci. Forum **143-147**, 903 (1994).

[13] A. N. Safonov, E. C. Lightowlers, and G. Davies, Materials Science Forum **196-201**, 909, (1995).

[14] E. C. Lightowlers, R. C. Newman, and J. H. Tucker, Semicond. Sci. and Tech. **9**, 1370 (1994).

[15] A. N. Safonov, E. C. Lightowlers, G. Davies, P. Leary, R. Jones, and S. Öberg, Phys. Rev. Lett. **77**, 4812, (1996).

[16] R. Jones, Phil. Trans. Roy. Soc. Lond. A, **350**, 189, (1994).

[17] C. P. Ewels, R. Jones, S. Oberg, J. Miro, and P. Deak Phys. Rev. Lett. **77** , 865 (1996).

[18] C. G. Van de Walle, and J. Neugebauer, Phys. Rev. B **52**, 14320 (1995).

[19] B. Bech Nielsen, M. Budde, J. Goss, P. Leary, R. Jones, and S. Öberg, Unpublished.

This article was processed using the LaTeX macro package with TTP style

Materials Science Forum Vols. 258-263 (1997) pp. 271-276
© 1997 Trans Tech Publications, Switzerland

LOW-TEMPERATURE MIGRATION OF HYDROGEN AND INTERACTION WITH OXYGEN

K. Bonde Nielsen, B. Bech Nielsen, and J. Hansen
Institute of Physics and Astronomy, University of Aarhus, DK-8000 Aarhus C, Denmark

Keywords: hydrogen, oxygen, silicon, ion-implantation, diffusion

Abstract. Low-dose proton implantation into n-type silicon below 80 K initiates the formation of two deep donor centres containing hydrogen. The centres, E3' and E3", have been observed by deep-level transient spectroscopy carried out *in situ* with as-implanted samples. The centres have very similar emission rates, and are discerned only because they form and anneal differently. In the neutral charge state E3' anneals in10 min. at 100 K while E3" anneals in ≈ 50 ms at 75 K. These anneals lead to the same negatively charged acceptor-type centre from which both E3' and E3" can be recovered: E3' by forward-bias injection, and E3" by exposing the sample to band-gap light. The E3' recovery is associated with fast migration of hydrogen, while E3" recovers instantly without migration. In the positive charge state E3' anneals in the range 200 - 240 K as a result of hydrogen migration and trapping at oxygen, while E3" anneals in a two-step process through E3". The centre for recovery of E3' and E3" anneals in the range 230 - 270 K restrained by hydrogen-oxygen interaction. We discuss the annealing scenario with reference to present understanding of isolated hydrogen in silicon. The previous identification of E3' with bond-centre hydrogen is maintained. We suggest that E3" is a perturbed form of E3' but a definite assignment is not obtained.

Introduction

A general approach to studies of hydrogen-defects in silicon has been to incorporate hydrogen by diffusion. It has been inferred from the dynamics [1] of donor and acceptor passivation that hydrogen atoms migrate interstitially through one or more of the three natural charge states of isolated hydrogen (H^-, H^0, and H^+) , and it is anticipated that both a donor level and an acceptor level exist. The actual diffusion path depends on the position of the Fermi level relative to the levels of the hydrogen solute and involves trapping and detrapping on intrinsic defects or impurities, including hydrogen itself. Eventually, new secondary electrically active defects will form, or existing electrically active defects will neutralise through the interaction of hydrogen with lattice imperfections or adjacent impurities. In order to study the primary interstitial defects in stable form one must avoid the formation of the secondary defect structures. To achieve this, protons may be implanted at low temperature where hydrogen and most intrinsic defects are immobile. Then, the subsequent evolution in the defect scenario with increasing temperature can be followed by means of *in situ* applications of standard techniques for characterisation of semiconductor defects.

The theoretical consensus [2] is that the global minimum in the H^- total-energy surface is the interstitial tetrahedral site. The associated defect, $H^-(T)$, is an acceptor. Similarly, the H^0 and H^+ surfaces have global minima at centres of Si-Si bonds giving rise to the defects $H^0(BC)$ and $H^+(BC)$, which are filled and ionised donors, respectively. As a consequence, hydrogen is an amphoteric impurity always counteracting the prevailing doping. At sufficiently low temperature $H^+(BC)$ becomes stable in p-type silicon and $H^-(T)$ becomes stable in n-type silicon, whereas $H^0(BC)$ may exist only in the metastable form in the sense that for all positions of the Fermi level either $H^+(BC)$ or $H^-(T)$ has lowest total energy. However, neutral and negatively charged interstitial hydrogen may coexist as stable defects at low temperature in n-type material because the energy of $H^-(BC)$ exceeds that of $H^0(BC)$, and a barrier prevents the conversion from $H^0(BC)$ to $H^-(T)$.

Many problems related to hydrogen defects remain unsolved. The bond-centre donor level has been assigned from a combination of results [3-6] obtained by Electron Paramagnetic Resonance (EPR) and Deep-Level Transient Spectroscopy (DLTS). However, no direct spectroscopic identification of the acceptor level has been obtained. It has been recognised [7] that the presence of

interstitial hydrogen leads to significant enhancements of the rate of diffusion of oxygen and related processes, such as the enhancement of the rate of thermal donor formation [8] and the incorporation of hydrogen in shallow thermal donors [9]. These observations require elucidation of oxygen-hydrogen structures and the interactions that occur during the defect evolution in low temperature anneal.

This contribution presents the results of DLTS measurements carried out *in-situ* after proton implantation at low temperature. The study extends work [6] in which a metastable hydrogen centre was identified in n-type silicon and assigned to bond-centred hydrogen. The associated DLTS signal is known as E3'. In this work we identify a new centre which is closely related to E3'. The new centre is labelled E3". The formation and annealing of both centres will be investigated with particular emphasis on the role of oxygen impurities in the annealing scenario.

Measurements and Results

A series of p^+n or Schottky diodes were prepared on n-type silicon substrates, and protons (or deuterons) were implanted through the diode junction into the substrate. Subsequently, the created defect structures and their thermal evolution were studied by means of *in-situ* DLTS carried out at low temperature in between successive annealing steps. The corresponding distributions of the charge associated with ionised defects were simultaneously examined by means of capacitance voltage profiling (CV). The implantation energy was chosen to give an implantation depth in the middle of the depletion layer corresponding to 20 V reverse bias over the diode. For a 10 Ωcm sample this energy is about 450 KeV. A typical dose was in the range from 10^9 - 10^{10} cm^{-2}, chosen to give less than 20% distortion of the initial dopant concentration as measured by CV profiling. As indicated by the frequency scans depicted in Fig. 1 two almost identical signals can be generated in the implanted samples. The two signals can be distinguished only because the E3'' peak decays very fast when electrons are supplied by removal of the bias, while E3' anneals thermally by first order kinetics and exhibits normal Arrhenius behaviour [6]. Either of the two peaks can be regenerated after the decays, but in basically different ways. The E3" signal can be recovered by illumination of a reverse-biased diode with a Nd:YAG laser. The recovery saturates in the order of one second by laser exposure of the sample backside (10^{-3} W through a 1 mm^2 hole). When the implantation signal (i.e. E3' after zero-bias implantation) is removed by annealing, then E3" acquires by illumination more than 75% of the strength of the initial signal, whereas less than 5 % of E3' itself is recovered. In contrast, 75 % of E3' can be effectively recovered in p^+n samples by forward-bias injection of holes [6]. The order of recovery of E3' by hole injection and E3" by illumination is reversible. Both signals lead to defects in the singly positive charge state as verified by CV profiling.

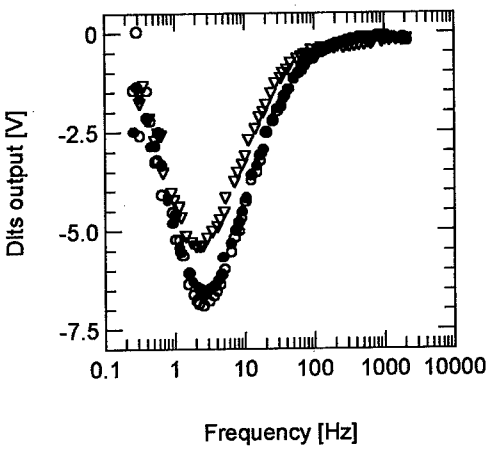


Fig. 1 DLTS frequency scans comparing as-implanted E3' (filled circles) with the E3'+ E3" signal after illumination (open circles) and the E3" signal after zero-bias annealing and illumination (triangles).

The annealing characteristics suggest that two metastable configurations of implanted hydrogen exist which convert to, and can be recovered from, a third configuration which is not observable by DLTS in the temperature range where it is thermally stable. This concealed configuration is in the singly negative charge state [6] as verified by comparison of CV profiles measured before and after annealing. Further evidence for the connection between E3' and E3" is presented in Fig. 2 The saturation of the E3' signal as a function of the duration of the forward-bias injection is shown,

together with the sum E3' + E3''. The graphs indicate the decrease of the amount of E3'' that can be generated concurrent with the E3' saturation.

It is a crucial point that the annealing / recovery cycle of E3' is associated with enhanced diffusion of hydrogen. This is illustrated in Fig. 3 where CV donor profiles obtained before and after annealing of E3' is compared. After the fourth annealing / injection cycles an E3' DLTS profile was also measured. This profile is included in the figure and reveals that hydrogen is now dispersed over the entire depletion region of the diode in accordance with the CV profiles. In contrast, recycling of E3" by successive bias removals and light exposures occurs without redistribution of hydrogen. However, already dispersed hydrogen shows in the spatial distribution of E3".

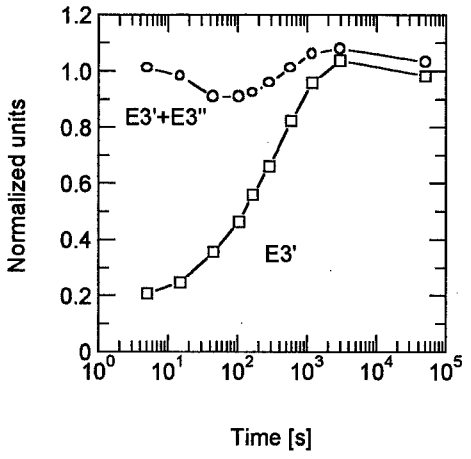


Fig. 2 Generation of E3" on top of E3' by illumination. Signal strengths are shown as a function of injection time for E3' at 1.5 Acm^{-2} current density and normalised to the initial E3" signal as generated after zero-bias annealing prior to injection.

The principal results regarding the annealing kinetics of the E3' centre have been presented previously [6] the zero-bias annealing is governed by a thermally activated jump of hydrogen away from a metastable location in the lattice, the annealing stage is associated with a neutral E3' centre capturing one electron. Also, the reverse-bias annealing of the E3' centre is governed by a first order process with an activation enthalpy $\Delta H = 0.44 \pm 0.01$ eV and pre-exponential factor $\nu \approx 1.3 \times 10^8$ s^{-1} [6]. The value of the pre-exponential factor indicates that diffusion may be involved. Just as in the case of zero-bias annealing, both E3' and E3" signals can be recovered after the annealing. This indicates that zero-bias and reverse-bias annealing of E3' eventually leads to identical, or very similar, negatively charged centres.

The reverse-bias annealing stage can be associated with the trapping of migrating H^+ on natural occurring oxygen impurities. This pertains to both CZ and FZ silicon as can be inferred from Fig.4 where CZ and FZ isochronal annealing data are compared In the analysis the activation enthalpy for H^+ jumping in the lattice is fixed to the value $\Delta H = 0.44$ eV deduced from the isothermal data. In this way the fits to the experimental data depend only on the pre-exponential factors which should come out proportional to the oxygen concentration, if we can assume that natural interstitial oxygen make up the principal sinks for trapping of migrating hydrogen. The shift between the CZ and FZ annealing temperatures shown is in agreement with this assumption. Moreover, their absolute values may be assessed linking the rate constant of annealing to the long-range diffusion constant. The analysis results in a trapping radius of $R_{trap} \approx 3$ Å, which is a reasonable magnitude.

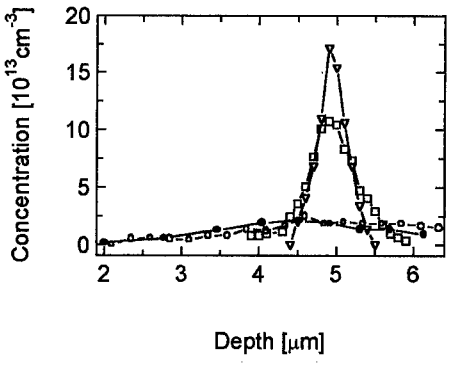


Fig. 3 Recovery after zero-bias annealing. CV profiles revealing the injection-induced migration of hydrogen. As-implanted (triangles), after first annealing and injection, (squares), after fourth annealing and injection. (circles), and E3' DLTS profile after fourth annealing and injection (filled circles).

As mentioned earlier, the E3" centre in the neutral charge state is essentially unstable in

comparison with E3'. The graphs depicted in Fig. 5 demonstrate that E3" converts thermally to E3' in FZ material of low dopant density. The E3' intensity was recorded after completion of each step in an isochronal annealing sequence under reverse-bias. Prior to each step (n) the E3' from the previous step was removed by zero-bias annealing at 105 K, whereafter the E3" signal was retrieved by light exposure. The plot of ingrown E3' is normalised to the strength of E3" regenerated prior to each step. In addition, the isochronal intensity ratios E3"(n)+E3'(n) normalised in the same way are shown, together with the ratios E3'(n)/E3'(n-1) obtained for another diode in the same annealing sequence. The ingrowth of E3' from E3" and its subsequent annealing have been analysed assuming a two-step process in which the E3" anneal is governed by a single jump. We use the constants of the E3' annealing as fixed parameters in the analysis and fix the pre-exponetial factor of the E3" annealing to 10^{13} s^{-1}. The model explains the bell-shaped ingrowth of E3' with $\Delta H_{E3"} = 0.75\pm0.15$ eV as a conservative estimate for the activation enthalpy.

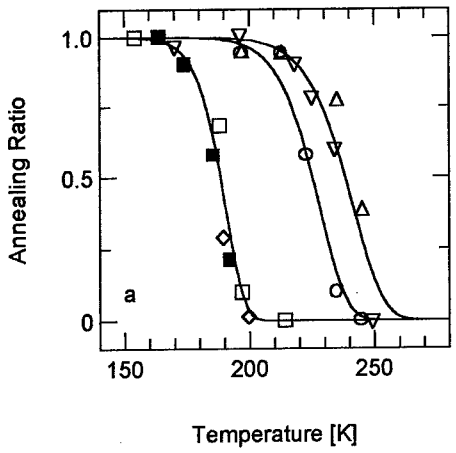


Fig. 4 (a) The E3' isochroal annealing in FZ and CZ silicon. Data for different 10 Ωcm CZ diodes (squares), different 60 Ωcm FZ diodes (triangles) and the a 10 Ωcm FZ diode (circles) are shown. The fits have been obtained with $\Delta H = 0.44$ eV from isothermal data.

According to our analysis and discussion above the annealing of E3' and E3" leads to a common state. We have investigated the annealing of that state and find that it anneals at about 260 K in CZ silicon and 230 K in FZ silicon.

Discussion

As already mentioned, the E3' signal has been assigned previously to the deep-donor level of bond-centred hydrogen [3-6]; i. e. to the transition $H^0(BC) \rightarrow H^+(BC) + e_{cb}$. The observation of two closely spaced deep-donor levels, one associated with E3' and one associated with E3", raises the question whether the previous interpretation of E3' is affected. We introduce the qualitative configuration scheme depicted in Fig. 6. This scheme contains the main features agreed upon theoretically. The consensus is that H^+ and H^0 have minimum energy at the BC site and H^- at the T site. In addition several authors predict a metastable configuration of H^0 at either an antibonding site or the interstitial tetrahedral site, see Ref. [2] and references therein for details.

The scheme relates the E3' signal to the ionisation of H^0 at the BC position and exhibit, as a main feature, the prediction that $H^0(BC)$ is metastable in n-type silicon with a fairly low barrier for transforming to $H^-(T)$. The charge-state-converting zero-bias annealing observed may therefore be anticipated if E3' is associated with the BC site. Also, in accordance with experiment, the scheme indicates an annealing process that is governed by a single atomic jump followed by the capture of a conduction electron.

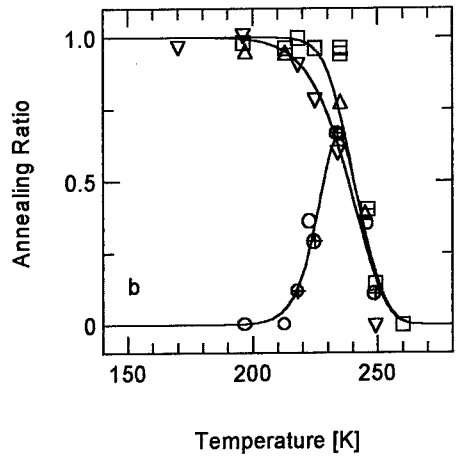


Fig. 5 The thermal conversion from E3'' to E3' measured for two different diodes and modelled as explained in the text. Circles represent grown-in E3', squares E3'' annealing, and triangles E3' annealing. An activation barrier $\Delta H = 0.75\pm0.05$ eV results.

Since our annealing data do not exhibit any significant dependence on sample resistivity we conclude that the rate-limiting step is to overcome the barrier in the H^0 total-energy surface rather than a capture process. The scheme also indicates, how the observed redistribution of hydrogen during the regeneration of E3' by hole-injection may be understood. The redistribution can be accounted for by a sequence of processes where holes are captured to form neutral interstitial hydrogen, expected to be highly mobile in the open regions of the lattice, with subsequent recapture of electrons at T-sites competing with jump to a BC-sites. We may envisage this as charge-state controlled diffusion with a flat pathway in the H^0 potential leading, eventually, to the formation of H^0(BC) and thereby recovery of E3'. In the scheme is further indicated a barrier for H^+ jumping out of the BC site. We identify this barrier with that of the diffusion-to-sink model for the E3' reverse-bias annealing.

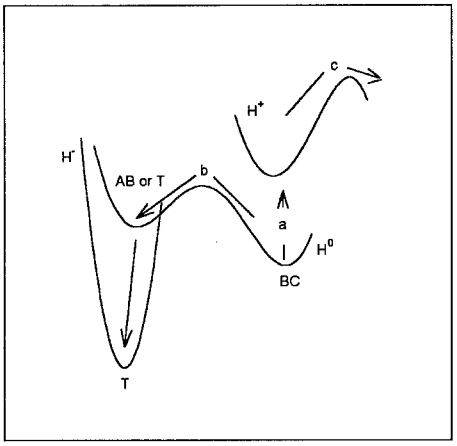


Fig. 6 Sketch total-energy diagram for H^+, H^0 and H^- in n-type silicon to illustrate the annealing-recovery scenario discussed in the text. The arrows indicate (a) E3' emission, (b) E3' zero-bias-annealing, and (c) E3' reverse-bias annealing.

The observation of two closely spaced deep-donor levels of hydrogen, one associated with E3' and one associated with E3", raises the question of how to incorporate the E3" centre consistently in the scheme. A straight-forward interpretation compatible with the observed annealing characteristics of E3" would be to introduce a second donor state in the low-density area of the crystal with a barrier (0.75 eV) opposing the conversion to H^+(BC), and essentially no barrier opposing the conversion to H^-(T) when conduction electrons are made available. If a donor state with these characteristics exists it could be formed by light-enhanced emission from the acceptor state H^-(T) during reverse-bias with the implication that the time spent in the H^0(AB or T) state must be short compared to the time needed for conversion to H^0(BC). Such a process would comply with our observation of an almost instantaneous generation the E3" signal by illumination, with only very little E3' generated simultaneously. The trouble with this interpretation is to understand physically how metastable interstitial hydrogen in the low-density area of the crystal can be positively charged, even in a diode space-charge layer. Intuitively, one would expect such a state to capture an electron from the valence band. Furthermore, the similarity of the E3' and E3" levels would be fortuitous. An alternative interpretation would be that E3' and E3" both represent bond-centre hydrogen with E3" destabilised as a consequence of an altered relaxation around the centre. Different relaxation's for E3' and E3" could arise because the centres are produced differently. However, without a perturbing adjacent defect it is difficult to understand how the conversion E3" $\rightarrow$ E3' restoring such relaxation can be opposed by a barrier as high as 0.75 eV.

Nevertheless, it is attractive to envisage E3" as destabilised form of E3'. If, like the observed migration of hydrogen during forward-bias recovery of E3', we can assume that fast diffusion also occurs during implantation and zero-bias annealing we may associate E3' with the unperturbed bond-centre site for hydrogen, and E3" with a perturbed form of that site, or vice versa. In accordance with the minute likelihood of implanted hydrogen coming at rest close to a vacancy or a self-interstitial generated in its own collision cascade we rule out at once that E3" could be a simple vacancy/interstitial associated defect.

The most obvious candidate for a trap is oxygen. Even in FZ material the diffusion range needed to form a perturbed centre directly during implantation is only $\approx$ 0.1 μm, to be compared with an implantation straggling of $\approx$ 0.4 μm. A diffusion range of that order would not be revealed in the

measured profiles. Therefore, direct trapping at oxygen can neither be ruled out nor verified. We emphasise that E3" forms in full strength after the first zero-bias annealing subsequent to the implantation, therefore, if the formation involves diffusion to a trap (oxygen) this must imply that migration through the lattice is much faster than the capture H^0(AB or T) $\rightarrow$ H^-(T). Another implication would be that the recovery centre for E3' and E3" is most likely a perturbed form of the acceptor state H^-(T).

We must conclude that the incorporation of E3" in the defect scenario remains an unresolved puzzle. We maintain (from the correlation with EPR data [5]) that E3' rather than E3" represents normal bond-centre hydrogen. Clearly oxygen plays a role in the annealing/recovery scenario. Our data strongly suggest that oxygen and hydrogen interact during the reverse-bias annealing of E3'. It is very difficult to explain the shift in annealing stage between CZ and FZ samples in any other way than diffusion of interstitial hydrogen to an oxygen trap. Regarding the reservoir annealing we suggest a scenario in which encounters between hydrogen and oxygen delay the migration of interstitial H^0 released from H^-(T) (or a perturbed version of that centre). This scenario is attractive, although undeniably very tentative, because the slowing down of hydrogen migration could be associated with speeding up of oxygen migration. Indeed, as briefly mentioned in the introduction, enhanced oxygen diffusion has been observed in hydrogen-rich silicon. If the structures associated with the weak transient bonding of hydrogen and oxygen indicated by the annealing data can be revealed (by infrared absorption) it may give a clue to answering the important question of how the experimentally established enhanced diffusion of oxygen in hydrogenated silicon is catalysed.

Acknowledgement

This work has been supported by the Danish National Research Foundation through the Aarhus Center for Advanced Physics (ACAP).

References

[1] J.I. Pankove and N. M. Johnson (editors), *Hydrogen in Semiconductors*, Semiconductors and Semimetals, Volume 34 (Academic Press, INC., New York, 1991)
[2] S.K. Estreicher, Materials Science & Engineering, **R14** (1995)
[3] Yu.V. Gorelkinskii and N.N. Nevinnyi, Physica **B170** 155 (1991)
[4] Yu.V. Gorelkinskii and N.N. Nevinnyi, Mater. Sci. Engineering **B36** 133 (1996)
[5] B. Bech Nielsen, K. Bonde Nielsen, and J.R. Byberg, Mater. Sci. Forum, **143-147** 909 (1994)
[6] B. Holm, K. Bonde Nielsen, and B. Bech Nielsen, Phys. Rev. Lett. **66** 2360 (1991)
[7] A.R. Brown, M. Claybourn, R. Murray, P.S. Nandra, R.C. Newmann, and J.H.Tucker, Semicond. Sci..Technol. **3** 591 (1988)
[8] H.J. Stein and S.K Hahn, Appl. Phys. Lett. **56** 63 (1990)
[9] S. A. McQuaid, R. C. Newman, and E. C. Lightowlers, Semicon. Sci. Technol. **9** 1736 (1994)

Materials Science Forum Vols. 258-263 (1997) pp. 277-282
© 1997 Trans Tech Publications, Switzerland

ANOMALOUS SHIFT OF THE 1075 cm^{-1} OXYGEN-HYDROGEN DEFECT IN SILICON

B. Hourahine[1], R. Jones[1], S. Öberg[2], and P. R. Briddon[3],

[1] Department of Physics, The University of Exeter, Exeter, EX4 4QL, United Kingdom
[2] Department of Mathematics, University of Luleå, Luleå, S-97187, Sweden
[3] Department of Physics, The University of Newcastle upon Tyne, Newcastle upon Tyne, NE1 7RU, United Kingdom

Keywords: *ab initio* theory, oxygen, hydrogen molecule, water molecule, Si

Abstract. First principles calculations are carried out on i) hydrogen and ii) water molecules trapped near an interstitial oxygen atom in Si. We find that it is possible for these molecules to cause an upward shift in the antisymmetric stretch mode of O_i when H is replaced by D, which could explain the anomalous shift in the 1075 cm^{-1} O-H related local vibrational mode. Both these molecules lead to modes in the 3500-4000 cm^{-1} region but those of the H_2 lie close to those recently detected using Fourier transform infra-red spectroscopy.

Introduction

Evidence that the diffusivity of oxygen in Si around 350-450° C is enhanced by H comes from an increased generation rate for thermal double donors [1], and in the decrease in the activation energy for O reorientation between the ⟨111⟩ bond centre (BC) sites occupied by the O atom [2]. There are several models of the effect but they all suppose that H sits close to O, in a weakly bonded configuration, and forms a stronger bond when O hops from one BC site to another. This stronger binding leads to a decrease in the barrier energy from 2.6 to about 1.8 eV.

Previous calculations of ours [3] found neutral H to be stable at an anti-bonding site to the O atom. However Estreicher [4] and Ramamoorthy and Pantelides [5] both found an adjacent BC site to be favoured, with the latter giving an energy difference of 0.2 eV with the anti-bonding site. In spite of these differences, the theoretical prediction of a stable O-H defect is clear and the first experimental observation of a possible O-H defect has created much interest.

Markevich *et al.* [6] diffused H into Cz-Si at high temperature (900-1200° C) and detected a vibrational band at 1075.1 cm^{-1}. This band shifted *upwards* by 1.3 cm^{-1} in the case of deuterium implying the presence of H in the defect. In mixed H, D samples, only two modes were detected suggesting the defect contains one H atom. The band was not detected in FZ-Si and thus the presence of oxygen in the defect was inferred from its presence in the material. Assuming the transition dipole moment is the same as that of the 1136 cm^{-1} interstitial oxygen defect, the concentration of O-H pairs was estimated to be about 1.1×10^{15} cm^{-3} – which is close to the equilibrium concentration of atomic hydrogen at 1200° C in Si [7]. Thus during the quench a significant fraction of H is trapped by oxygen.

The effect of a heat treatment is unusual. The IR intensity decreased between 100 and 125° C but the defect reformed upon a subsequent anneal at 50° C. Only for temperatures above 350° C were the defects irreversibly removed. No electrical activity was associated with the O-H defect which is surprising in view of the fact that isolated H introduces a donor level (E3′) at $E_c - .16$ eV and possibly a mid-gap acceptor level [8].

Further work has been carried out by the Imperial College group [9]. Here H was introduced into Cz-Si crystals 17 mm thick by in-diffusion at high temperatures. The 1075 cm^{-1} band appears with a broad background and is composed of a peak at 1075.1 cm^{-1} and a shoulder at 1075.8 cm^{-1}. In the deuterated case, the peak shifts upwards to 1076.6 cm^{-1} and the shoulder to around 1076 cm^{-1}. These findings, together with data in the mixed H-D case, were interpreted as showing that, contrary to the previous study, the defect contained two H atoms.

The 1075 cm^{-1} displayed satellite lines lying 1.7 and 3.8 cm^{-1}, below the main peak. Similar satellites are found in the spectra of O_i and are due to ^{29}Si-^{16}O-^{28}Si and ^{30}Si-^{16}O-^{28}Si defects. Moreover, the intensities of the 1075 cm^{-1} satellites were in line with the expected ^{29}Si and ^{30}Si isotopic abundances (including a factor of two for the location of the heavier Si atom) and confirms that O is part of the defect and is in its normal BC location, *ie.* bonded with two Si atoms.

The infra-red measurements also revealed sharp H related modes at 3789, 3731 and 3618 cm^{-1} which shifted downwards by approximately a factor of $\sqrt{2}$ in the D case. The 3731 and 3789 modes are close to those of a water molecule (3756 and 3652 cm^{-1}) and are far away from the frequencies ascribed to H_2 molecules in Si by Raman scattering studies [10]. These occur around 4158 cm^{-1} in hydrogenated, and 2990 cm^{-1} in deuterated, material.

Thus our first conjecture was that a molecule of H_2O was bound to O_i. However, it became clear that this molecule could not explain the observed H-D modes which, in our opinion, can only be explained by a hydrogen molecule. This then leads to the question of their infra-red activity. However, there are several reports of infra-red activity of H_2 absorbed onto zeolites such as NaA [11]; the H_2 mode is shifted downwards from its gas value by 83 cm^{-1} as well as being infra-red active. The explanation given is that the local electrical field polarises the molecule, so that the H atoms become inequivalent and their separation slightly longer than in the gas. Other workers find downward shifts of 200 cm^{-1} [12] but even these are much less than the 543 cm^{-1} required here. There are, however, other cases, notably involving a transition metal, where large downward shifts in the H_2 mode occur and the molecule becomes IR active [13]. However, these molecules are not especially stable.

A further finding [9] is that the higher two modes at 3789 and 3731 cm^{-1} are associated with O but the third is not. Upon annealing, there is a drop in the intensity of the two higher modes and a correlated increase in the intensity of the lowest. The suggestion was made that the molecule is trapped in two distinct but energetically similar sites near O_i and these give rise to the two higher modes. Upon annealing the molecule drifts away to a third site, responsible for the lowest mode. This third site is possibly associated with a another impurity such as C, N or a transition metal. Of great importance is the fact that only one H-D mode is detected for each defect showing the H atoms are equivalent.

We shall in this paper discuss possible mechanisms for the anomalous increase in frequency for the 1075 cm^{-1} O related mode. We use an *ab initio* local density functional cluster method (AIMPRO) to evaluate both the structure of the defects and their vibrational modes. Typically 134 or 151 atom clusters centred on a Si atom or on a T_d interstitial site were used. Details of the technique have been given elsewhere [14] and a previous application has dealt with H_2 molecules in GaAs where the molecule is found to lie at a T_d cage site [15].

We first discuss our findings relating to a H_2 molecule close to O_i and then discuss the case of a water molecule.

Hydrogen Molecule

There are several obvious locations for the molecule close to O_i but since the binding between the molecule and the O atom is so weak, these are close in energy and difficult to distinguish.

Furthermore, it seems that there are a large number of configurations differing in the orientation of the molecule and all of these have to be considered as candidate structures.

We suppose that the molecule resides near the T_d site and oxygen decorates one of the nearby Si-Si bonds. There are two almost degenerate low energy configurations which have similar modes. We first consider the case when the O atom bridges a $[11\bar{1}]$ Si-Si bond forming part of the surrounding cage as shown in Fig. 1. The centre of the molecule in the relaxed configuration then lies near a mirror plane containing the Si-O-Si bonds and is oriented along $[1\bar{1}0]$, *ie.* perpendicular to the Si-O-Si bond and the mirror plane. The O-Si bonds are 1.62 Å and the Si-O-Si angle is 172.5°. The H_2 bond length is 0.77 Å with both H atoms about 2.37 Å away from O_i. Each H atom lies 2.55 and 2.99 Å away from the Si neighbours of O_i. The vibrational modes of the cluster are given in table 1.

The H_2 stretch mode at 3855 cm^{-1} is lower than that calculated for an isolated molecule. With the present method, this occurs at 4424.8 cm^{-1}: about 10% higher than the observed value, although anharmonicity must play a significant role in this overestimate. The molecular frequency depends on the size of the surrounding cage. The 3855 cm^{-1} mode lies close to the experimental modes around 3750 cm^{-1} associated with oxygen. The two H atoms are almost equivalent and this explains why only one H-D mode is present although the calculations show a 10 cm^{-1} splitting caused by deviations from ideal σ_h symmetry.

The mode at 1129.8 cm^{-1} is clearly due to O_i as it shifts downwards by only 0.3 cm^{-1} when D replaces H but by 52 cm^{-1} with ^{18}O. This is comparable with the 51 cm^{-1} shift observed in the 1136 cm^{-1} mode of O_i when ^{18}O replaces ^{16}O. The small downward shifts with D demonstrate that there is very little direct coupling between O_i and the molecule and this is essential to our arguments, based on anharmonicity, if an upward shift is to be seen in the deuterated case. It is not clear why the experimental O mode is shifted downwards by as much as 65 cm^{-1} from that of isolated O_i.

The modes at 733 to 577 all involve the movement of H and none has been detected so far. They represent H_2 bend and librational modes. Their shifts with ^{18}O given in table 1 demonstrate that many of them involve the movement of O.

Of particular interest here is the mode at 577 cm^{-1}. This represents a librational mode as the two H atoms are displaced almost parallel to their bond. We now argue that the anomalous frequency shift of the 1075 cm^{-1} band is to be understood through an anharmonic coupling between an overtone, or combination band, of these low frequency modes and the O mode resulting in a Fermi resonance. Let $|n_{\rm Ox}>$ be the n'th oscillator state for the vibrations of the oxygen atom whose fundamental occurs at $\nu_{\rm O}$ = 1129.8 cm^{-1}, and $|m_{\rm H}>$ be the m' th state for a mode whose frequency, $\nu_{\rm H}$, is about half that of the O_i mode, *ie.* the modes in the region of 550 cm^{-1}. The states of the coupled system are then described by linear combinations of $|n_{\rm Ox}, m_{\rm H}>$. The effect of anharmonicity, V, is to couple together these states and second order perturbation theory gives the shift in the energy of the $|1_{\rm Ox}, 0_{\rm H}>$ state to be dominated by

$$\frac{<1_{\rm Ox}, 0_{\rm H}|V|0_{\rm Ox}, 2_{\rm H}>^2}{(\nu_{\rm O} - 2\nu_{\rm H})}.$$

This follows as the energy denominator is particularly small for these modes. The perturbation is negative for the 577 cm^{-1} mode and lowers the energy of the $|1_{\rm Ox}, 0_{\rm H}>$ state, and hence that of the fundamental transition. On the other hand, when H is replaced by D, as the frequency of this mode drops below 575 cm^{-1}, then the perturbation acts to raises the energy of the state. Thus the two cases reinforce the tendency to depress the O mode in the H case below that of D. Another ways of describing the effect is an anti-crossing between the O mode and an overtone of the librational mode. If this mechanism is correct, there has to be unreported modes in the 550 cm^{-1} region.

Although the Fermi resonance explains the anomalous isotope shift of the O_i mode there remains the problem of its infra-red activity. However, during the stretching of the H-H bond, there is a slight displacement of the O atom and this causes an induced dipole moment. We have calculated this by determining the change in the dipole moment of the cluster when the atoms are displaced in line with the normal coordinates of each mode. The magnitude of the transition dipole moment, δp, is given in the last column of table 1. The integrated infra-red intensity is then proportional to the square of this quantity. We find the most intense mode to be the O mode at 1130 cm^{-1}. Its effective charge would be $\sqrt{M_O}\delta p$ or about 1.4 e. This is about one-third of the known value and this underestimate may either be a basis effect or due to differences between the local electrical field at the defect and the macroscopic field. Assuming the latter, then the integrated intensity of the 3856 cm^{-1} H_2 mode can be related to that of the O mode. We find that it is about 4% of the O related 1130 cm^{-1} mode. The observations [9] give the effective charges of each of the H modes to be about $0.1e$ (M = 0.5 a.m.u.) and as that of O_i is 3.5 e, it implies that the integrated intensity of the H mode is 2.6 % of the O_i mode, and is in reasonable agreement with the calculation. However, the theory finds that the intensity of the 655 cm^{-1} mode should be comparable with the O stretch mode.

We have also investigated other positions for the molecule. A second and almost degenerate configuration occurs when the molecule lies close to a C_2 axis passing through O_i. This has similar modes to the first and could account for the second defect which is observed. A third possibility is that the molecule lies along the Si-O-Si axis near a T_d site. This site is stable but the molecule is then close to the Si neighbour of O_i and this results in an O related mode that is strongly coupled with H in conflict with the experiment. However, the energy of this structure appears to be lower than that shown in Fig. 1 by 0.5 eV. This may be a due to the proximity of O_i to the surface of the cluster and further investigations are needed to clarify the most stable configuration.

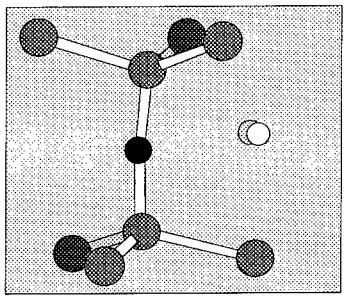


Fig. 1. Schematic illustration of O_iH_2 defect.

Water Molecule

The O-H bonds of the isolated molecule are calculated to be 0.96 Å and H-O-H angle equal to 107.9°. These are close to the experimental values of 0.957 Å and 104.5°. The vibrational modes are given in table 2 and compared with the experimental values [16].

We notice that although the two O-H stretch modes at 3521.6, 3352.1 (H_2) and 2571.8, 2432.7 (D_2) cm^{-1} lie close to those observed in Si, there is no mode in the HDO case lying in the region mid-way between these values. This is because there is little direct coupling between the H atoms. Thus the observed H-D modes around 3300 cm^{-1} cannot be explained. This argument is now shown to be unaffected by inserting the molecule into a cluster containing an O_i defect.

The O-H lengths and angle of the water molecule placed near an interstitial T_d site are 0.99 Å and 109°. The effect of the cluster is then to weaken the O-H bonds. This molecular species is probably metastable and would in practice dissociate forming H_2 and O_i defects. The local modes are given in table 2 and demonstrate the absence of any H-D mode around 3000 cm^{-1}.

$(H_2)_i$	$(HD)_i$	$(DH)_i$	$(D_2)_i$	$^{18}O_i+(H_2)_i$	δp
This work					
3855.6	3339.5	3350.1	2726.7	3855.6	0.07
1129.8	1129.7	1129.6	1129.5	1078.1	0.34
733.3	685.6	690.6	678.6	731.4	0.08
696.2	663.2	654.6	653.7	685.3	0.32
655.3	650.1	645.0	630.9	649.0	0.33
643.6	627.6	627.4	536.3	638.9	0.14
630.6	539.5	542.6	533.6	622.6	0.30
576.7	536.0	536.1	532.8	576.1	0.17
Experiment					
3788.9	3304.3	2775.4			
3730.8	3285.3	2716.0			
3618.3	3264.8	2714.9			
1075.1		1076.6			

Table 1: Local vibrational modes (cm^{-1}), and transition dipole moment, δp, a.u., for the $(H_2)_i$, $^{16}O_i$ complex (unless otherwise labelled).

$(H_2O)_i$	$(HDO)_i$	$(DHO)_i$	$(D_2O)_i$	$(H_2O)_i{}^{18}O_{bc}$
Water in Si				
3521.6	3354.9	3519.2	2571.8	3521.6
3352.1	2560.3	2444.2	2432.7	3352.1
1512.3	1373.0	1309.6	1114.7	1512.3
1100.3	1100.1	1099.2	1095.3	1046.4
723.5	689.4	697.6	682.5	723.0
708.6	681.6	653.2	651.6	708.5
659.6	616.0	617.0	594.8	659.6
591.2	576.4	580.9	576.4	591.1
Free Water				
Experiment				
3756		3707	2788	
3657		2727	2671	
1595		1402	1178	
This work				
3755	3710	3708	2752	
3659	2691	2692	2635	
1574	1380	1379	1153	

Table 2: Local vibrational modes (cm^{-1}), for the $(H_2{}^{16}O)_i$ molecule (with $^{16}O_{bc}$ nearby, unless otherwise labelled).

The mode at 1100 cm^{-1} is the antisymmetric stretch mode of O_i. This drops by 54 cm^{-1} for $^{18}O_i$ — the oxygen mass on the water remaining ^{16}O. We notice that in the D_2 case, the 1512 cm^{-1} bend mode drops and couples strongly with the 1100 cm^{-1} O_i mode. In fact the two modes at 1095 and 1115 cm^{-1} involve substantial amplitude on O_i. This can be seen as these modes shift to 1111 and 1044 cm^{-1} for $^{18}O_i$. For a fictional mass on the hydrogen atoms of 2.5 a.m.u, the bend mode of water lies at 1011.7 cm^{-1} and below that of the O_i mode which has been pushed *upwards* to 1100.6 cm^{-1}. This demonstrates that a molecule of water can cause an upward displacement of the local mode due to O_i in favourable cases. However, as emphasised above, the observed H-D vibrational modes rule out this molecule as responsible for the effect.

Discussion

The calculations have shown that a H_2 molecule is stable in two almost degenerate configurations near O_i and possesses a H-H stretch mode whose frequency is much lower than the gas value. This mode is very weakly coupled with the antisymmetric stretch mode of O_i which causes it to become infra-red active. The anomalous upward shift of the O-mode with D can be explained through a Fermi resonance interaction with librational modes of the molecule around 530 cm^{-1}. Such modes have not been reported and experimental investigations in this region are called for. The fact that only one H-D mode is reported shows that the H atoms are equivalent. These two degenerate configurations would explain the experimental observation of two close vibrational modes [9]. This assignment raises a question over the interpretation of the modes attributed to H_2 seen in plasma-irradiated material at 4158 cm^{-1} [10]. Our calculations

show that the frequency of the molecule increases rapidly with the size of the surrounding cage and we suggest that the latter defects are molecules inside voids created by plasma etching.

The question arises as to whether the molecule influences the migration of O_i. It seems difficult to give a mechanism based on the proximity of the molecule. If the molecule temporarily dissociated for a time long enough for an enhanced migration of O_i to occur by coupling with atomic H, then the activation barrier for the molecular dissociation would have to be lower than 1.8 eV. Since it is believed that the dissociation energy for the reaction $H_2 \rightarrow 2H_{BC}$, is 1.74 eV [17] then this seems unlikely as the barrier to the dissociation would have to be greater than this. O_i however acts as a trap for the molecule and this might be important in processes involving oxygen precipitation which at some unknown stage involve the production of Si_i.

S. Öberg thanks NFR and TFR in Sweden for financial support. He also thanks PDC at KTH in Sweden, for computer time on the SP2. We also thank the HPCI committee of the EPSRC for computer time on the T3D where some of these results were derived. We thank Ron Newman for communicating results prior to publication and both him and Emil Roduner for very useful discussions.

References

[1] R. C. Newman, R. Jones in *Oxygen in Silicon*, edited by F. Shimura, *Semiconductors and Semimetals*, edited by R. K. Willardson and A. C. Beer, **42**, page 289- 352, Academic Press, 1994.
[2] M. Stavola, J. R. Patel, L. C. Kimerling, and P. E. Freeman, Appl. Phys. Lett., **42**, 73 (1983).
[3] R. Jones, S. Öberg, A. Umerski, Material Science Forum, **83-7**, 551-62, (1991)
[4] S. Estreicher, Phys. Rev. **B 141**, 9886 (1990).
[5] M. Ramamoorthy, and S. T. Pantelides, in *Early Stages of Oxygen Precipitation in Silicon,* ed. R. Jones, NATO ASI Series (3. High Technology) Vol. 17, Kluwer Academic Publishers, Dordrecht, 319-27 (1996), p 197.
[6] V. P. Markevich, M. Suezawa, and K. Sumino, Mater. Sci. Forum, **196-201**, 915 (1995).
[7] M. J. Binns, S. A. McQuaid, R. C. Newman, and E. C. Lightowlers, Semincon. Sci. and Technol., **8**, 1908 (1993).
[8] N. M. Johnson, C. Herrig, and C. G. Van de Walle, Phys. Rev. Lett., **73**, 130 (1994).
[9] R. E. Pritchard, M. J. Ashwin, R. C. Newman, J. H. Tucker, E. C. Lightowlers, M. J. Binns, R. Falster, and S. A. McQuaid, this conference.
[10] K. Murakami, N. Fukata, S. Sasaki, K. Ishioka, M. Kitajima, S. Fujimura, J. Kikuchi, and H. Haneda, Phys. Rev. Lett, **77**, 3161 (1996).
[11] E. R. Cohen de Lara, Mol. Phys., **66**, 479 (1989).
[12] V. B. Kazansky, V. Yu. Borovkov, and L. M. Kustov, in *Proceedings of the 8th International Confererence on Catalysis* , Berlin Dechema Verlag Chemie, Weinheim, 1984 vol. 3 p 3.
[13] G. J. Kubas, Acc. Chem. Res., **21**, 120 (1988).
[14] R. Jones, and P. R. Briddon, *Identification of Defects in Semiconductors*, ed. M. Stavola, *Semiconductors and Semimetals*, treatise editors, R. K. Willardson, A. C. Beer, and E. R. Weber, Academic Press.), in press (1997).
[15] S. J. Breuer, R. Jones, P. R. Briddon, S. Öberg, Phys. Rev. B., **53**, 16289-96 (1996).
[16] K. Nakamoto, *Infrared and Raman spectra of inorganic and coordination compounds*, 3rd Edn., John Wiley, New York (1978).
[17] C. G. Van de Walle, Phys. Rev. B **49**, 4579 (1994).

This article was processed using the LaTeX macro package with TTP style

Materials Science Forum Vols. 258-263 (1997) pp. 283-288
© 1997 Trans Tech Publications, Switzerland

VIBRATIONAL ABSORPTION FROM OXYGEN-HYDROGEN (O_i-H_2) COMPLEXES IN HYDROGENATED CZ SILICON

R. E. Pritchard[1], M. J. Ashwin[1], R. C. Newman[1], J. H. Tucker[1], E. C. Lightowlers[2], M. J. Binns[3], R. Falster[3], and S. A. McQuaid[3]

[1] IRC for Semiconductor Materials, The Blackett Laboratory, Imperial College, London SW7 2BZ, U. K.

[2] Department of Physics, King's College London, Strand, London WC2R 2LS, U. K.

[3] MEMC Electronic Materials Inc., 501, Pearl Drive (City of O'Fallon) P.O. Box 8, St. Peters, Missouri 62276 U. S. A.

Keywords : Si, oxygen, hydrogen, infrared absorption

Abstract. IR absorption spectra of CZ silicon heat treated in H_2 gas show absorption at 1075 cm^{-1} due to perturbed interstitial oxygen atoms. Three weak hydrogen stretch modes at 3789, 3731 and 3618 cm^{-1} are also detected and the two highest frequency modes are found to correlate in strength with the 1075 cm^{-1} absorption. For deuterated samples and samples heated in a H_2/D_2 mixture, ν_{DD} and ν_{HD} analogues are detected for all three modes. The frequencies of these lines and their isotopic shifts indicate that the defect centres responsible must be hydrogen molecules with weakened bonds that acquire small dipole moments as a result of interactions with either adjacent O_i atoms (ν_1 and ν_2 centres) or a second impurity/defect (ν_3 centres). Annealing treatments imply that the O_i -H_2 complexes dissociate for $T \geq 70°C$ and the resulting H_2 molecules either diffuse to interstitial sites (IR-inactive centers) or to sites where additional ν_3 defects are formed.

Introduction.

Defect centres present in Czochralski (CZ) silicon pre-heated in hydrogen gas at ~1200°C give rise to infrared (IR) vibrational absorption at 1075.1 cm^{-1}. It has been demonstrated that hydrogen atoms are incorporated in these defects since the absorption shifts to 1076.6 cm^{-1} when samples are pre-heated in deuterium gas [1]. These absorption features are not detected in low oxygen content float-zone (FZ) silicon samples suggesting that oxygen is also a constituent of the centre [1].

We now show that the 1075 cm^{-1} absorption is due to bond-centred interstitial oxygen atoms (O_i) perturbed by an adjacent hydrogen molecule, an O_i -H_2 complex, rather than a hydrogen atom. Using high resolution, very low noise IR absorption spectroscopy, we demonstrate that these molecules acquire dipole moments and give rise to two weak high frequency vibrational modes as a result of interactions with the adjacent O_i atoms. Detection of a third high frequency absorption mode from perturbed hydrogen molecules in both CZ and FZ Si indicates that these molecules are trapped at sites adjacent to an unknown defect centre (X).

Experimental Details.

High quality as-grown CZ Si ($[O_i]$ ~10^{18} cm^{-3}) lightly doped to 5 x 10^{14} cm^{-3} with either boron or phosphorus and with carbon concentrations below the detection limit of 2 x 10^{15} cm^{-3} were prepared as samples with thicknesses from 3 to 17 mm. The samples were heated in the range 1000-1300°C in either H_2, D_2 or mixtures of the two gases at atmospheric pressure and then cooled rapidly by dropping them into silicone oil at room

temperature or they were heated in a quartz tube that was withdrawn rapidly from the furnace and plunged into water. One of the 17 mm thick hydrogenated samples was given low temperature isochronal annealing treatments (10 min) in the range 70 -370 °C. Samples of high resistivity FZ Si, boron-doped CZ Si ([B] = $7x10^{16}$ cm^{-3}) and phosphorus-doped CZ Si ([P] = $2x10^{16}$ cm^{-3}) were also given high temperature annealing treatments. Fourier transform infrared (FT-IR) absorption spectra were measured (10 K) with a Bruker IFS 113v operated at a resolution of 0.1 cm^{-1}.

Results.

Vibrational absorption from perturbed O_i atoms.

Figures 1a and 1b show vibrational absorption from hydrogenated and deuterated lightly-doped CZ Si samples respectively. The localised vibrational mode (LVM) at 1084.9 cm^{-1}, with two associated low energy satellite features, is due to isolated $^{18}O_i$ atoms and the LVM at 1077.5 cm^{-1} is due to $^{18}O_i$ atoms in their first excited pseudo-rotational state [2]. The hydrogen-related feature (Fig.1a) has a peak at 1075.1 cm^{-1} and a high energy shoulder at 1075.8 cm^{-1}. By deconvoluting these features into two Voigt profiles [3], the relative strengths (P_H : S_H) is found to be 3:1 for a number of samples. For deuterated samples, the main peak shifted to 1076.6 cm^{-1} with an unresolved low energy shoulder close to 1076 cm^{-1}. Deconvolution of these two features into Voigt profiles gave P_D:S_D=2:1.

On closer inspection, weak satellite features (S_1 and S_2) are evident on the low energy sides of the main deuterium- and hydrogen- related peaks. The separations of these satellites from the main peaks are close to 2 cm^{-1} and 4 cm^{-1}, similar to values observed for the weak satellites of the principal $^{18}O_i$ mode at 1085 cm^{-1} and the satellite structure of the principal $^{16}O_i$ mode at 1136 cm^{-1}. In the latter two cases, the O_i atoms are incorporated into the Si lattice as interstitial, bond-centred impurities with two direct bonds to silicon atoms: the relative strengths of the satellites are related to the natural isotopic abundances of silicon, namely ^{28}Si (92.3 %), ^{29}Si (4.7 %) and ^{30}Si (3.0 %) [2]. The observation of satellite structure for the features P_H and P_D with the same relative strengths and energy separations as the satellite structure of bond-centred O_i atoms demonstrates that the new lines are indeed due to the vibrations of a bond-centred $^{16}O_i$ atom perturbed by adjacent H(D) atoms.

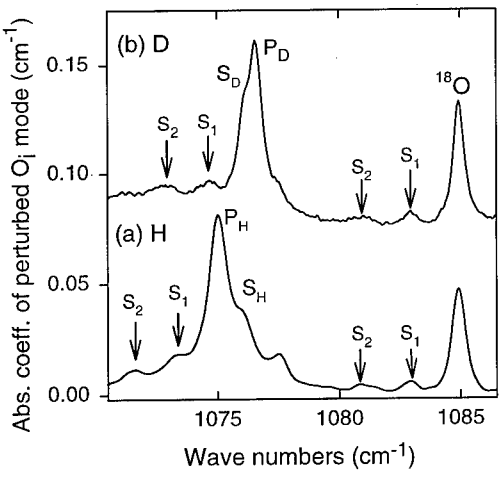


Fig. 1. *IR absorption spectra from CZ Si samples pre-heated in (a) hydrogen gas and (b) deuterium gas.*

IR absorption spectra from lightly doped CZ Si samples annealed in a mixture of H_2 and D_2 gas are now analysed. It was expected that the resulting IR absorption near 1075 cm^{-1} would simply be a linear addition of the two spectra shown in Fig. 1 in the appropriate proportions. For samples heated in 50:50, 75:25 and 25:75 mixtures of H_2:D_2, it was impossible to synthesise the observed spectra using this procedure. For example, for the spectrum obtained from the sample heated in

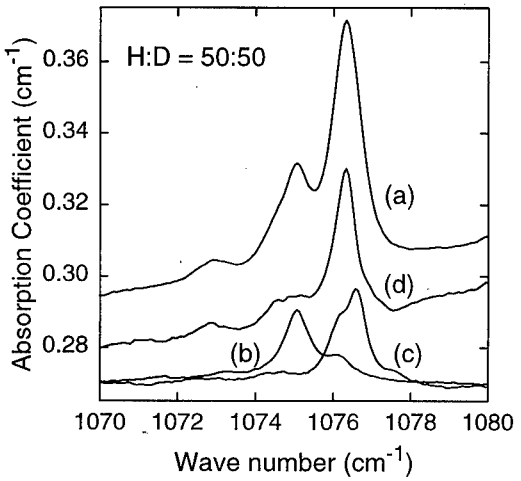


Fig. 2 *IR spectra of samples heated in (a) 50:50 H:D mixture, (b) H_2 gas,(c) D_2 gas, plotted in the strength ratios 4:1:1.(d) Spectrum of the extracted "HD" component.*

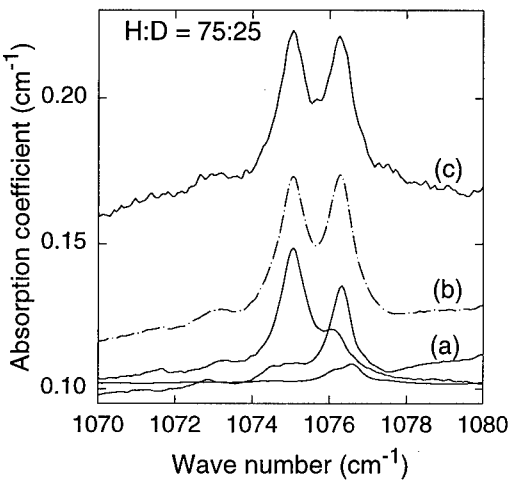


Fig. 3 *IR spectra for (a) the 3 contributions from H_2 , D_2 and HD pairs, (b) synthesised spectrum and (c) measured spectrum.*

the 50:50 H_2:D_2 mixture (Fig. 2a), a strong peak is observed at 1076.1 cm^{-1} (lower in energy by 0.5 cm^{-1} than the main D-related peak) and a weaker feature at P_H=1075.1 cm^{-1}. It is concluded that the perturbation of the O_i vibrational modes cannot be due to the presence of a *single* H(D) atom.

The possibility that the O_i atom is perturbed by two equivalent H atoms was considered next. There would be contributions to the IR absorption profile from H-H, H-D and D-D components: for a 50:50 mixed sample their relative strengths should be 25:50:25. To deduce a possible H-D component, 25 % each of the H and D spectra (Figs. 2b and c) was subtracted from the experimentally measured 50:50 mixed spectrum (Fig. 2a). The extracted profile (Fig. 2d) is essentially a single line at 1076.3 cm^{-1}. This H-D profile was then used to synthesize spectra from samples annealed in 75:25 and 25:75 H:D mixtures. Very close agreement between the synthesised and measured spectra (see Fig. 3 for 75:25 mixture) implies that the complex giving rise to the absorption close to 1075 cm^{-1} is due to an O_i atom perturbed by *two* H atoms. The observation of two components to the IR absorption from hydrogenated and deuterated samples (Fig. 1), suggests that two types of O_i-(H-H) centres are formed with slightly different structures. We now present IR absorption measurements of the hydrogen vibrational modes of these complexes.

Direct observation of LVMs due to H-H, H-D, and D-D pairs.

IR spectra from the hydrogenated lightly doped CZ samples (thickness > 5mm) reveal the presence of three very weak but sharp (Δ = 0.1-0.2 cm^{-1}) lines ν_{1HH}, ν_{2HH}, and ν_{3HH} (Fig. 4 and Table 1) in the spectral region 3600 - 3800 cm^{-1} where there is a high spectral density of absorption lines from atmospheric water. In deuterated samples, a corresponding set of 3 lines ν_{1DD}, ν_{2DD}, and ν_{3DD} is observed (Table 1) with ν_{2DD} occurring as a close doublet. For samples heated in a 50:50 mixture of H_2:D_2, all of the ν_{HH} and ν_{DD} modes are detected but no additional structure close in frequency to these modes is found. However, a further three lines ν_{1HD}, ν_{2HD}, and ν_{3HD} are observed with frequencies essentially mid-way between the ν_{HH} and ν_{DD} modes (Table 1). We shall show that these observations

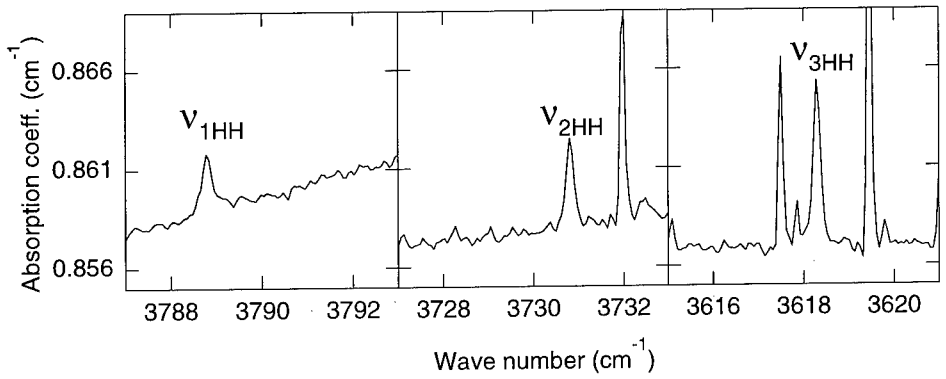


Fig. 4 *High resolution IR spectra showing the high frequency hydrogen stretch modes from H-H pair defects (ν_1, ν_2 and ν_3). The additional lines close to ν_{2HH} and ν_{3HH} are due to absorption from atmospheric water molecules.*

demonstrate the presence of three types of defect (ν_1, ν_2, and ν_3) each incorporating two hydrogen atoms that are bonded directly to each other.

For a number of hydrogenated samples, together with data from the isochronally annealed sample, it was found that the integrated absorptions of both ν_{1HH} and ν_{2HH} modes correlated with that of the 1075 cm^{-1} absorption. It follows that the ν_{1HH} and ν_{2HH} modes correspond to hydrogen modes of the O_i-(H-H) complexes. One of these modes must correspond to the peak, P_H, of the 1075 cm^{-1} absorption and the other mode to the shoulder, S_H. The ν_{3HH} mode showed a weak anti-correlation with the 1075 cm^{-1} absorption and therefore should be associated with H-H centres located at sites remote from O_i atoms. This latter proposal was verified by the detection of ν_{3HH}, ν_{3HD} and ν_{3DD} in a FZ Si sample ([O_i] =2 x 10^{15} cm^{-3}) that had been heated in a 50:50 H_2:D_2 mixture. As expected, the ν_1 and ν_2 modes were not detected in this sample.

Preliminary isochronal annealing experiments (70-370°C) on a hydrogenated CZ sample showed increases in the strength of the ν_{3HH} mode and reductions in the strengths of ν_{1HH}, ν_{2HH} and 1075 cm^{-1} absorption from 70-110°C. At higher temperatures up to 370°C, there was no further increase in the strength of ν_{3HH} even though the absorption

Defect	ν_{HH} (cm^{-1})	ν_{HH}/ν_{HD}	ν_{HD} (cm^{-1})	ν_{HD}/ν_{DD}	ν_{DD} (cm^{-1})	ν_{HH}/ν_{DD}
ν_1(Si)	3788.9	1.147	3304.3	1.191	2775.4	1.365
ν_2(Si)	3730.8	1.136	3285.3	1.210	2716.0 2714.9	1.374
ν_3(Si)	3618.3	1.108	3264.8	1.235	2642.5	1.369
H_2(Si) [4]	4157	1.145	3629	1.213	2991	1.390
H_2(GaAs) [5]	3934.1	1.141	3446.5	1.212	2842.6	1.384
H_2 (gas) [5]	4161.1	1.146	3632.1	1.213	2993.6	1.390

Table 1. *Energies (cm^{-1}) of the IR vibrational modes (ν_1, ν_2 and ν_3) of H_2, D_2 and HD pair defects observed in Si and the observed Raman transitions of H_2, D_2 and HD molecules in different environments. The frequency ratios are also given.*

strengths of the three correlated modes continued to decrease until their strengths were less than 10 % of their initial values for $T > 150$ °C. This indicates that there is a net loss of detectable hydrogen at the higher anneal temperatures.

In earlier work on hydrogenated CZ Si [6], it was found that high boron-doping levels ($>10^{16}$ cm^{-3}) inhibit the formation of the centres giving rise to the 1075 cm^{-1} absorption. We have now examined highly boron- and phosphorus-doped samples and the ν_{3HH} mode was the only high frequency mode observed, implying that O_i-(H-H) centres were not present. In n-type material, H-P pairs are not detected and so the lattice locations of all in-diffused H atoms is not known. In p-type material (boron-doped), 30 % of the H atoms were paired with boron acceptors and it was speculated that the remaining 70 % are incorporated as molecules. Annealing such samples at ~ 175°C led to the formation of additional H-B pairs [6]. It could now be speculated that this so-called "hidden" hydrogen is in the form of H-H pair defects that we detect as ν_3 centres in the present CZ and FZ samples.

Discussion.

The important new result of this work is the observation of high frequency vibrational modes of defects incorporating pairs of H-H, D-D and H-D atoms (Table 1) and we now consider possible models for the structure of these ν_1, ν_2 and ν_3 defect centres.

Even though the ν_{1HH}, ν_{2HH} and ν_{3HH} modes occur in the spectral region of strong absorption by O-H modes, we find that the assignment of the pair defect to an H_2O molecule is untenable. The gaseous H_2O molecule has three IR-active modes at 3756, 3652 and 1595 cm^{-1} [7] and so, in principle, the two associated high frequency anti-symmetric and symmetric modes could correspond to ν_{1HH} and ν_{2HH}. For the D_2O molecule, the anti-symmetric and symmetric modes shift to 2789 cm^{-1} and 2666 cm^{-1} respectively, close to the ν_{1DD} and ν_{2DD} frequencies. The crucial point is that for the HDO molecule, the anti-symmetric mode occurs at 3707 cm^{-1} and the symmetric mode at 2727 cm^{-1}. These shifts are incompatible with the measurements for ν_{1HD} and ν_{2HD} (Table 1).

The presence of ν_{HD} modes with frequencies essentially mid-way between those of ν_{HH} and ν_{DD}, implies unambiguously that for each centre (ν_1, ν_2 and ν_3), the two atoms must be bonded directly to each other as a molecule (see Table I for a comparison with data for H_2 molecules). The frequency ratios, ν_{HH} /ν_{DD}, for the three centres all have values close to 1.37 (Table 1) compared with values close to 1.39 for the isolated H_2 molecule in Si [4]. The smaller ν_{HH}/ν_{DD} ratios obtained for the ν_1, ν_2 and ν_3 defects implies that the H_2 molecules present in these centres interact with an adjacent impurity atom of low mass.

The correlated ν_1 and ν_2 modes must be due to hydrogen molecules trapped at sites adjacent to O_i atoms and we now consider possible structures of these O_i-H_2 complexes. A possibility is that *two* H_2 molecules are trapped by one O_i atom. As a result of coupling, many high frequency hydrogen modes would be expected due to the large number of H/D combinations. However, we only observe two high frequency hydrogen modes associated with the oxygen complexes. Furthermore, the probability that two H_2 molecules are captured by a common O_i atom is negligible on a statistical basis. A more plausible model is that a single H_2 molecule can occupy two different lattice sites adjacent to an O_i atom. This would account for both the ν_1 and ν_2 modes and the two components to the perturbed oxygen mode. Another possibility is that, again, one H_2 molecule is trapped at an O_i atom but that the two components to the perturbed oxygen mode (P and S, Fig. 1) are due to H_2 molecules present as either ortho- or para-hydrogen [5]. The

observed strength ratios (P:S) are 3:1 for hydrogenated samples and 1:2 for deuterated samples which correspond to the expected concentrations of ortho- and para-hydrogen. However, there is no direct evidence for this interpretation since their frequency separation (57 cm^{-1}) is much larger than the separation observed for H_2 molecules in GaAs (8 cm^{-1}) [5].

The arguments presented above lead to the conclusion that only one H_2 molecule is trapped at a site close to an O_i atom. The configuration of the molecule must be such that there is a redistribution of electron density between the 2 H atoms due to the electro-negative O_i atom so that the molecule acquires a dipole moment. A reduction in electron density of the H-H bond can explain the reduced H_2 vibrational frequencies for the ν_1 and ν_2 modes. Since the molecule is trapped, however, its free rotation should be hindered and so it seems unlikely that we are observing modes of ortho- and para- hydrogen. The lowest energy mode labelled ν_3 must be due to a H_2 molecule trapped by an impurity/defect other than oxygen and possible candidates are carbon and nitrogen. Further work is under way to explore these possibilities. During annealing it is implied that there is both a transfer of H_2 molecules from O_i atoms to this second trap and a net loss of detectable H_2 molecules. The latter observation could be explained by the diffusion of molecules to low energy, interstitial sites [8] remote from either impurity where they would have no dipole moment.

Conclusion.

Detection of the ν_1, ν_2 and ν_3 modes implies that hydrogen is incorporated predominately as molecules in as-quenched undoped Si. These molecules become trapped at O_i atoms in CZ Si and at another impurity (X) in FZ and CZ Si. Trapping is inferred because (a) the H_2 vibrational frequencies are significantly lower than the Raman frequencies obtained for the free molecule (4161 cm^{-1}), isolated H_2 molecules in Si (4157 cm^{-1}) and H_2 molecules in GaAs (3926 cm^{-1}), and (b) the molecules must acquire a dipole moment to account for their IR activity. Nevertheless, the estimated dipole moments per unit displacement are small (~0.1*e* compared with 3.5*e* for the O_i atom in Si) [3] so that it is feasible that they arise as a result of local internal electric fields.

Acknowledgements.

The UK authors thank the Engineering and Physical Sciences Research Council for financial support of the contracts (GR/K 96977 and (GR/K 30995).

References.

1. V.P Markevich, M. Suezawa, and K. Sumino, Mater. Sci. Forum **196-201**, 915 (1995).
2. Pajot, in "Oxygen in Silicon", ed. F. Shimura, Willardson, A.C. Beer, and E.R. Weber, Semiconductors and Semimetals **42** (Academic: San Diego) pp.191-249 (1994).
3. R.E. Pritchard, M.J. Ashwin, J.H. Tucker, R.C. Newman, E.C. Lightowlers, M.J. Binns, S.A. McQuaid, and R. Falster, submitted to Phys. Rev. B (1997).
4. J. Weber, private communication (1997).
5. J. Vetterhöffer, J. Wagner, and J. Weber, Phys. Rev. Lett. **77**, 5409 (1996).
6. M.J. Binns, S.A. McQuaid, R.C. Newman, and E.C. Lightowlers, Semicond. Sci. Technol. **8**, 1908 (1993).
7. K. Nakamoto, in "Infrared and Raman Spectra of Inorganic and Co-ordination Compounds" (John Wiley: New York, 1978).
8. C.G. Van de Walle, Phys. Rev. **B**, 4579 (1994).

Materials Science Forum Vols. 258-263 (1997) pp. 289-294
© 1997 Trans Tech Publications, Switzerland

THE I CENTRE : A HYDROGEN RELATED DEFECT IN SILICON

Joanne Gower, Gordon Davies, E.C. Lightowlers and A.N. Safonov
Physics Department, King's College London, Strand, London WC2R 2LS, U.K.

Keywords: Hydrogen, luminescence, silicon, isoelectronic centre.

Abstract. The I-line luminescence system with zero-phonon transitions at 965.0 and 967.4 meV is created when Czochralski silicon is electron irradiated and subsequently annealed at temperatures greater than 400 °C. We report here that the centre contains two inequivalent carbon atoms and one hydrogen atom and that the uniaxial stress and Zeeman perturbations are consistent with a paramagnetic centre possessing monoclinic I symmetry. We propose that the core of the centre is a C-C-H complex, similar to that of the T-centre, perturbed by the presence of an oxygen atom.

Introduction

In recent years there has been significant interest in the effects of hydrogen at defect centres in silicon. Hydrogen passivates dangling bonds and is used widely in semiconductor manufacturing because of this property. More recently it has also been shown to be a constituent of several photoluminescence centres [1]. This paper reports a detailed study of an hydrogen related centre in silicon, known as the 'I-centre' with comparisons made to the well understood T-centre [2]. Isotope substitution suggests the centre contains a single hydrogen atom and two inequivalent carbon atoms. Analysis of uniaxial stress and magnetic field perturbations shows that the centre possesses monoclinic I symmetry. The excited state of the centre can effectively be described using the simple model of a tightly bound electron orbited by an effective mass hole.

Experimental

The samples used in this study were mainly Czochralski (CZ) silicon with high concentrations of both carbon and oxygen, typically [C] ~ 2 x 10^{17} cm^{-3} and [O] ~ 10^{18} cm^{-3}. Samples were saturated with 1.5 x 10^{16} cm^{-3} H or D by heating in flowing gas for 30 minutes at 1300°C and rapidly cooling in silicone oil [3]. The samples were electron irradiated with a total flux of 2 x 10^{17} cm^{-3} 2 MeV electrons and then annealed for 30 minutes at a temperature between 450 - 500 °C. Photoluminescence measurements were carried out on either a Nicolet 60SX or a Bomem DA3 Fourier transform spectrometer fitted with a North Coast cooled Ge diode detector with excitation by a 514 nm Ar^+ laser. Uniaxial stress measurements were made using stresses of up to 0.16 GPa and Zeeman experiments were made with magnetic fields up to 4.5 T, both using 12 x 2 x 2 mm^3 X-ray oriented samples.

Isotope Structure of the Local Mode Satellites

It has previously been shown that the I-centre contains hydrogen and carbon [4] from the effect on the zero-phonon line of doping with different isotopes. However the zero-phonon line is perturbed by the effects of one C atom. Here we show that there are at least two C atoms in the centre using the effects of isotopic substitution on the local mode satellites. The local modes are labelled following the T-centre [2]. Figure 1 shows the effects of isotope doping on the L3 mode, with a quantum of 543 cm^{-1} in the ^{12}C, H material. Figure 1a shows the effect of approximately equal doping with ^{12}C and ^{13}C. The presence of four lines with comparable intensities shows that two C atoms at inequivalent sites are involved in the motion. Figure 1b shows similar ^{12}C, ^{13}C material but doped with D instead of H. Changing the ^{12}C:^{13}C ratio to 1:5 results in the expected intensity changes (Fig. 1c), and using ^{12}C, ^{14}C approximately doubles the splitting relative to ^{12}C, ^{13}C (Fig. 1c and d), again as expected.

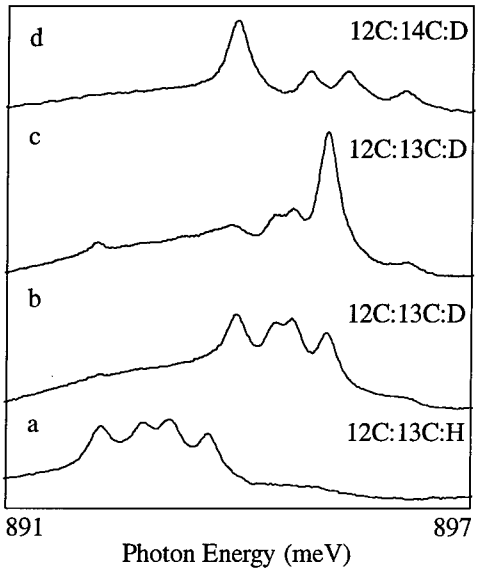


Figure 1. Luminescence from the I-line L3 local mode showing the effects of mixed carbon isotopes and deuterium on the energy of the lines.

Contrary to a previous report [6] there is no evidence that an oxygen atom is present at the centre other than the strong requirement that the photoluminescence has only been observed in Czochralski silicon. ^{18}O:^{16}O:H and ^{18}O:^{16}O:D samples have been studied, but no splittings of either the zero phonon line or local modes have been observed. The position of the local modes and the experimentally observed isotopic shifts are comparable with those of the T-line and are shown in Tables 1 and 2. The similarities suggest that the I-centre is also a split carbon-carbon interstitial with a single hydrogen atom bonded to a carbon atom (Reference [5] discusses the formation of this centre in detail). The L1 and L4 modes for the I-line are not observable as they lie under the zero-phonon line and L3 mode respectively.

Mode	12C-(12C-H)	Δ12C-(13C-H)	Δ13C-(12C-H)	Δ13C-(13C-H)
L2	543.08 (531.5)	(4.0)	5.7 (2.0)	(3.8)
L3	586.94 (567.5)	4.4 (7.5)	7.2 (3.0)	11.1 (10.0)
L5	(1056.0)	(18.0)	(27.0)	(45.0)

Table 1. Comparison between the I and (T)-centre vibrational modes (cm^{-1}) for C-(C-H) defects, along with their downward isotope shifts.

Mode	12C-(12C-D)	Δ12C-(13C-D)	Δ13C-(12C-D)	Δ13C-(13C-D)
L2	536.6 (528)	(1.3)	5.49(2.5)	(7.7)
L3	578.31(558.5)	4.17(5.3)	5.78 (2.5)	9.39 (7.7)
L5	1054.5 (1056)	12.2(16.5)	29.1(20.5)	44.6(38.0)

Table 2. Comparison between the I and (T)-centre vibrational modes (cm^{-1}) for C-(C-D) defects, along with their downward isotope shifts.

Uniaxial Stress and Zeeman Perturbations

The ionisation energy of the exciton bound to the I-centre has been found to be 39 meV. This is typical in silicon for an effective mass particle bound by the Coulomb potential to a defect with a single charge. Consequently after the decay of the bound exciton the I-centre is still uncharged. In the ground state the charge of the proton is assumed to be balanced by one electron. We show below that when an exciton is bound, the two electrons spin-pair, leaving the hole as the effective mass particle. The uniaxial stress and Zeeman experiments can be modelled by simply considering the effects on the electrons and on the hole separately.

Figure 2 shows spectra of the I-centre's two zero-phonon transitions (ZP1 and ZP2) at 25 K. Clearly visible for ZP2 is the presence of 2, 3 and 4 components in the <001>, <111> and <110>

stress directions respectively. This is consistent with the centre possessing monoclinic I symmetry[7]. Figure 3 shows the energy of the I-centre as a function of the applied stress.

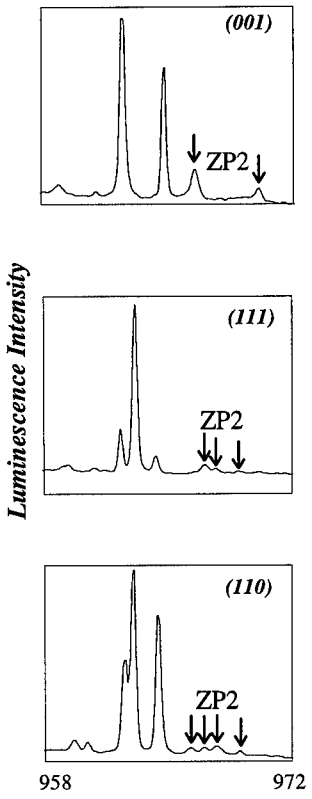


Figure 2. Luminescence of the I-centre's two zero-phonon transitions measured at 25 K and uniaxial stresses of 0.16 GPa.

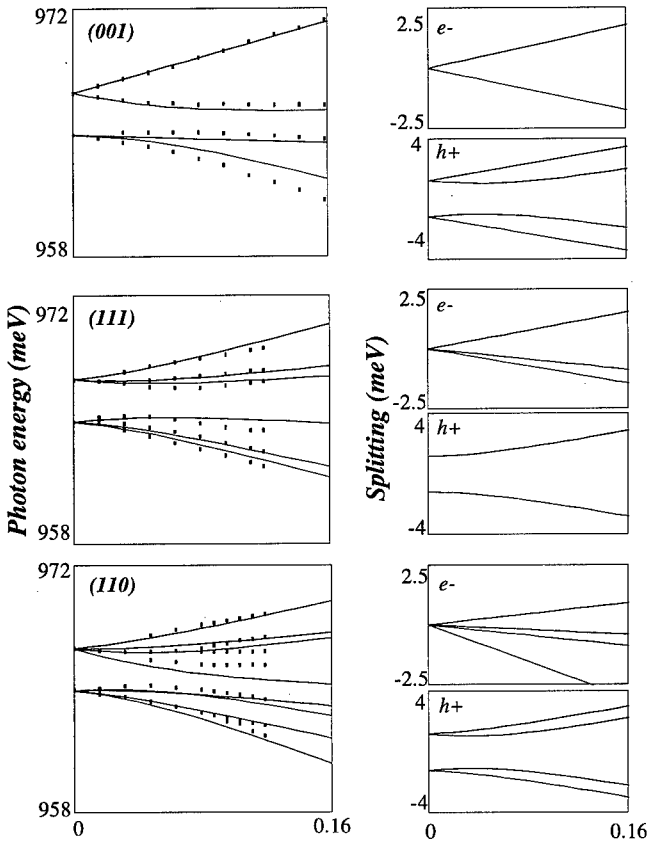


Figure 3. Energy of the I-centre as a function of applied stress. Points are experimental values, lines are calculated as described in the text. Right column shows the hole and electron splittings separately as a function of the applied stress.

We assume that the electrons are trapped in a non-degenerate orbital state at the centre. A representative monoclinic I centre has local axes X, Y, and Z along $00\bar{1}$, $\bar{1}10$ and 110 respectively with the reflection plane perpendicular to [110]. The electron is perturbed by [7]:-

$$\Delta E = A_1 s_{ZZ} + A_2 (s_{XX} + s_{YY}) + 2A_3 s_{XY} + 2A_4 (s_{YZ} - s_{XZ}) \qquad \text{Equation (1)}$$

The effect of the applied stress is assumed to be linear and in the complete fit of Fig. 3 can be described by the Kaplyanskii coefficients A_1 = 11.05, A_2 = -10.91, A_3 = -8.31 and A_4 = 5.65 meV/GPa. We treat the effective mass hole as orbiting in a strain field created by the I-centre. The hole is then derived from the valence band maximum perturbed by the effect of the axial centre. We parameterise the perturbation by an effective "internal stress", S_i, created by the defect. In addition

we need to consider the effects of the external stress, applied experimentally. Both stresses perturb the valence band maxima in the same way. This perturbation is :-

V/V	$+3/2$	$+1/2$	$-1/2$	$-3/2$
$+\frac{3}{2}$	$-\frac{B}{2}S_\theta$	$-\frac{C}{\sqrt{3}}(S_{xz}-iS_{yz})$	$-\frac{B}{2}S_\varepsilon+\frac{i}{\sqrt{3}}CS_{xy}$	0
$+\frac{1}{2}$	$-\frac{C}{\sqrt{3}}(S_{xz}+iS_{yz})$	$+\frac{B}{2}S_\theta$	0	$-\frac{B}{2}S_\varepsilon+\frac{i}{\sqrt{3}}CS_{xy}$
$-\frac{1}{2}$	$-\frac{B}{2}S_\varepsilon-\frac{i}{\sqrt{3}}CS_{xy}$	0	$+\frac{B}{2}S_\theta$	$\frac{C}{\sqrt{3}}(S_{xz}-iS_{yz})$
$-\frac{3}{2}$	0	$-\frac{B}{2}S_\varepsilon-\frac{i}{\sqrt{3}}CS_{xy}$	$\frac{C}{\sqrt{3}}(S_{xz}+iS_{yz})$	$-\frac{B}{2}S_\theta$

where $S_\theta = 2S_{zz} - S_{xx} - S_{yy}$, $S_\varepsilon = \sqrt{3}\,(S_{xx} - S_{yy})$ and the quantisation of the valence band states is the [001] crystal axis. The hydrostatic shifts are included in the A_1 and A_2 of the electron . The stress tensor components will obviously differ depending on the direction of the stresses and the effects of the internal and external stress can simply be summed.

The data can be fitted very simply by taking S_i along the [001] axis of the defect with a magnitude of 0.085 GPa splitting the Γ_8 valence band into two states V_1 and V_2. When no external stress is applied this splitting is the energy difference between the two states associated with the I-centre. ZP1 is a transition to a state which is derived from an admixture of the m_j = |3/2,1/2> and |1/2,1/2> states, and ZP2 corresponds to a transition to the m_j = |3/2,3/2> band. The fit given by this model is shown by the solid lines on fig. 3. It uses the parameters B = 14.0 meV/GPa and C = 48.0 meV/GPa. B and C for the pure valence band are 22.6 and 52.5 meV/GPa respectively. The modification of B and C reduces the magnitude of the valence band splitting when external stress is applied.

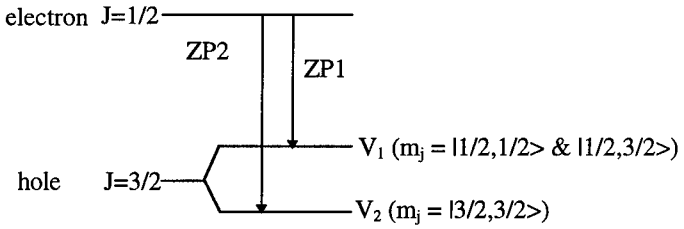


Figure 4. Energy level diagram of Γ_8 valence band and observed transitions for I centre.

The Zeeman experiments are modelled by assuming the ground state is a single spin 1/2 particle (the electron provided by the hydrogen atom) possessing no orbital angular momentum. When a magnetic field is applied its energy is split by $\pm\mu_B m_s g_s B$. The excited state is again a spin 1/2 particle but this time it is the hole since the two electrons fill the outer shell of the hydrogen atom and are spin paired. The hole is in an effective mass like orbital and so possesses orbital angular momentum as well as spin angular momentum. The magnetic perturbation matrix for the hole is given by:-

V/V	$+3/2$	$+1/2$	$-1/2$	$-3/2$
$+\frac{3}{2}$	$GB_1 - \varepsilon$	$\frac{GB_2}{\sqrt{3}}$	0	0
$+\frac{1}{2}$	$\frac{GB_2^*}{\sqrt{3}}$	$\frac{GB_1}{3} + \varepsilon$	$\frac{2}{3}GB_2$	0
$-\frac{1}{2}$	0	$\frac{2}{3}GB_2^*$	$-\frac{GB_1}{3} + \varepsilon$	$\frac{GB_2}{\sqrt{3}}$
$-\frac{3}{2}$	0	0	$\frac{GB_2^*}{\sqrt{3}}$	$-GB_1 - \varepsilon$

where $2\varepsilon = 2.4$ meV is the splitting of the hole states produced by the pure [001] internal stress. $G = (\mu_B g_l + 1/2\mu_B g_s) = 1.95\mu_B$ where μ_B is the Bohr magneton, $B_1 = B_z$ and $B_2 = B_x + iB_y$.

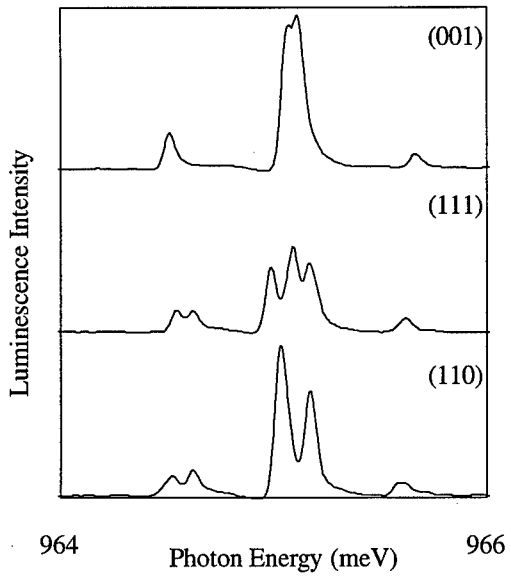


Figure 5. Luminescence of the I centre measured at 4.2 K (ZP2 not observable) with B along <001>, <111>, and <110> crystal axes and equal to 4.5 T.

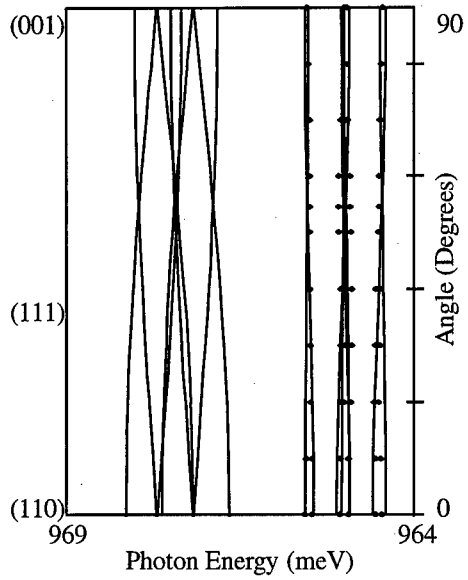


Figure 6. Energies (points) of the components of the I line split by a 4.5 T magnetic field as a function of the direction of the field (measured at 4.2K hence ZP2 not observable). The lines are calculated as described in the text.

Discussion

So far we have shown that the defect has a core consisting of two inequivalent carbon atoms with a hydrogen bonded to one carbon atom and is dependent on oxygen. The defect binds an electron tightly, presumably pairing with the single electron of the hydrogen atom to form a closed shell, and has an effective mass hole orbiting. These properties are very similar to those of the T centre [2,8] excepting the internal strain which is significantly larger for the I centre producing an energy difference between the two states of 2.4 meV compared with 1.8 meV for the T centre.

There is no direct evidence from isotope shifts of an oxygen atom being in the centre. However the centre is only observed in oxygen rich silicon implying that one (or more) oxygen atoms are involved in the centre. The T centre is stable at annealing temperatures up to 600 °C [8], i.e. it is stable at the formation temperature of the I centre (450 - 500 °C). At these temperatures the oxygen atoms in silicon are known to be mobile, as seen in the production of thermal donors. The obvious model is thus that an O atom has approached and been trapped at a T centre. The location of the O atom is not known. We note an apparent parallel with the production of the "P" centre (zero-phonon line 767 meV) in heavily oxygen doped silicon, as an oxygen-perturbed version of the "C" centre (zero-phonon line 789 meV).

Conclusion

We have demonstrated that the I-centre (zero-phonon energy 965 meV) is chemically similar to the T -centre (935 meV) with direct evidence for the involvement of one hydrogen atom and two carbon atoms. We have no direct evidence for oxygen at the centre except the need for oxygen rich silicon. We have shown that the uniaxial stress and magnetic field data can be modelled very simply by assuming a tightly bound electron and an effective mass hole.

Acknowledgements

This work was supported by the EPSRC, and Joanne Gower thanks EPSRC for the provision of a research studentship.

References

[1] E.C. Lightowlers & Gordon Davies, Early stages of oxygen precipitation in Silicon, P303, (1996)
[2] A.N. Safonov et al, Phys Rev Lett. P4812, Vol 77, No 23 (1996)
[3] M.J. Binns et al, Semicond. Sci. Technol. P1908, 8 (1993)
[4] E.C. Lightowlers, R.C. Newman & J.H. Tucker, Semicond. Sci. Technol. P1370, 9 (1994)
[5] P.Leary et al , these proceedings.
[6] J.E. Gower et al, Early stages of oxygen precipitation in Silicon, P463, (1996)
[7] A.A. Kaplyanskii, Opt. Spectrosc. P329, 16 (1964)
[8] A.N. Safonov, E.C. Lightowlers & Gordon Davies, Mater. Sci. For. P909, Vol 196 - 201 (1995)

Materials Science Forum Vols. 258-263 (1997) pp. 295-300
© 1997 Trans Tech Publications, Switzerland

THEORY OF GOLD-HYDROGEN COMPLEXES IN SILICON

A Resende[1], J Goss[1], P R Briddon[2], S Öberg[3] and R Jones[1]

[1] Department of Physics, The University of Exeter, Exeter, EX4 4QL, United Kingdom
[2] Department of Physics, The University of Newcastle upon Tyne, Newcastle upon Tyne, NE1 7RU, United Kingdom
[3] Department of Mathematics, University of Luleå, Luleå, S-97187, Sweden

Keywords: *ab initio* theory, Si, Au, H, G complex, passivation.

Abstract. Spin-polarised local density functional cluster calculations are carried out on substitutional Au and Au–H_n complexes in Si. Slater's transition argument and Janak's theorem are combined to discuss the donor-acceptor levels of the defects and the results are compared with experiment. The calculations give a good account of the donor/acceptor levels of Au and the Au–H pair. They confirm that the G1, G2 and G4 levels are due to Au–H. Au–H_3 is found to be an electrically inactive defect and may be identified with the passive defect found experimentally.

Introduction

Transition metals are important impurities in Si as they possess deep levels in the bandgap and interfere with the properties of devices. For example, they reduce storage time in MOS dynamical memory cells and lead to the formation of dark current spikes in CCDs.

Gold as an isolated impurity in silicon is one of the most studied defects in semiconductors. This is mainly due to its technological important and to its pivotal role in the understanding of the electronic properties of transition metal impurities in semiconductors. Elements like gold, platinum, silver or even titanium, are commonly used to produce metallic contacts. Our understanding of the impurities at the far right of the periodic table is based on the "vacancy model" [1]. This maintains that their electronic activity is controlled by the levels of the vacancy. Since, the vacancy can be passivated [2], there is a possibility that the transition metal impurity can also be passivated and this has been found in the case of Au [3].

Background experimental results

The amphoteric behaviour of gold in silicon has been a matter of controversy for many years. Only recently [4] has it been unequivocally established that substitutional gold introduces two levels in the band gap. These deep acceptor and donor levels lie at $E_c - 0.54$ and $E_v + 0.35$ eV respectively. The ground state of the substitutional Au^0 impurity has C_{2v} symmetry, tetragonally distorted, spin state $\mathcal{S} = 1/2$ and configuration $b_2^{\uparrow\downarrow} b_1^{\uparrow} a_1^0$ [5], with $g_{\|} \approx 2.8$ and $g_{\perp} \approx 0$. The distortion is in agreement with the predictions of the vacancy model. The defect can reorientate easily at cryogenic temperatures ($T < 4$ K) [6] suggesting a very small departure from T_d symmetry. Surprisingly, no EPR signal has been attributed to the defect and this is understood to arise by a rapid tunnelling between two equivalent C_{2v} configurations [7] driven by a *dynamical* Jahn-Teller effect. This makes the g_{xx} and g_{yy} components of the g tensor very small and hence the microwave $\Delta m_J = \pm 1$ transitional probability becomes very low and the

EPR spectrum difficult to observe. This model is supported by recent theoretical work using the same methods as those described here [8]. The theory finds that Au^0 distorts along the [100] direction by ~ 0.18 Å with small shifts of the neighbouring Si atoms. The barrier to the reorientation is then only ~ 0.01 eV and the defect might be expected to tunnel easily between symmetric configurations.

We concentrate in this paper on the energy levels of the defect and the effect of H upon them. The first study on the influence of H on the gold centre was reported by Pearton and Tavendale [3] using samples exposed to a plasma between 150 and 350°C. A substantial loss of the Au activity was reported which could, however, be partially reactivated by annealing at 400°C. No effect was found for samples annealed in hydrogen gas.

Wet-chemical etching is another process commonly used to introduce hydrogen into the samples. This process has some advantages over the the use of a plasma. H is introduced at room temperature, without any damage to the wafer surface, and leads to the formation of Au–H defects which posses distinct deep levels [9]. These defects disappear around ~150°C and are transformed to a passive defect if sufficient H is available. Such H could be released from the dissociation of P-H defects. The passive defect is destroyed by annealing beyond 200°C. This temperature is lower than that found by Pearton and Tavendale, probably because they heated the sample in the presence of the plasma, which provided a continuous source of H. Pt-H_2 defects appear to be more stable, forming around ~400°C .

The Au–H defects formed in wet-chemical etching have been studied by Sveinbjörnsson *et al* [10]. Four new deep levels named G1–G4 were observed in the DLTS spectra. G1 is an acceptor level observed in n-type material with an activation energy of 0.19 eV. G2 and G3 are hole traps detected in p-type Si and located at $E_v + 0.21$ and $E_v + 0.47$ eV respectively. G4 was detected in both n- and p-type samples and showed similar characteristics to those of the gold acceptor level. It was suggested that G1, G2 and G4 are levels of the *same* Au–H defect, probably Au complexed with a single H atom, but the PA complex contained additional H atoms. However, the DLTS study did not reveal the number of H atoms in the defects. Little is known about the G3 defect.

A very recent study on the electron- and hole-capture kinetics of Au–H complexes in Si has been carried out using Minority Carrier Transient Spectroscopy (MCTS) [11]. This technique, combined with DLTS, allowed the determination of acceptor and donor levels using only one type of material and is a useful technique for defects with multiple levels. The main conclusion refers to the nature of the G1, G2 and G4 levels. Davidson and Evans confirmed that these levels are all produced by the same Au–H complex but G1 was shown to be a double acceptor level.

Method

Ab initio spin-polarised local density functional cluster theory (AIMPRO) was used to explore the properties of Au–H defects. Full details of the technique have been given before and will not be repeated here [12]. Large tetrahedral H-terminated clusters, containing 131 and 297 atoms with the configurations $Si_{71}H_{60}$ and $Si_{181}H_{116}$ respectively, were used in this investigation. The basis consisted of N Cartesian s, p Gaussian orbitals sited on each atom. N independent d-orbitals were sited on the Au atom. The charge density is fitted to M Gaussian functions. In this study, (N, M) are: Au(6,12), Si(4,5) and H(2,3). The pseudo-wave functions were expanded in independent combinations of the N Gaussian orbitals on atoms at the centre of the cluster but a fixed linear combination of the N orbitals was used on those outside the defect core. The pseudopotentials were those of Bachelet *et al*. These were placed on all atoms except H. The

self-consistent energy was found together with the analytic forces on each atom. The structure was then relaxed using a conjugate gradient algorithm.

This method has been successfully applied to the study of Ni and Ni–H complexes in silicon [13] as well as the ferrocene molecule [14] and Ni defects in diamond [15].

Of particular interest here are the donor and acceptor energy levels associated with the defects. But there are several problems relating to the formalism in extracting these levels. The acceptor or $(-/0)$ level, relative to the conduction band, is simply the energy difference between a negatively charged and neutral defect with an additional electron in the lowest conduction band state. Suppose d is the Kohn-Sham energy level of the highest occupied level associated with the ionised defect and let c be the Kohn-Sham level associated with the conduction band minimum. Now, provided the relaxation of the defect when the electron is promoted between these levels can be ignored, the difference in the energies of these configurations is, according to Slater's transition state argument and Janak's theorem, simply the difference in the d and c levels found for an electronic configuration corresponding to half-occupancy, *i.e*, one-half a electron is removed from the level d and placed in level c. If this were the only approximation, the errors would be very slight. Unfortunately, density functional theory is not strictly applicable to the excited state configuration and as such band gaps are substantially underestimated. However, the use of a H-terminated cluster often leads to a band gap which exceeds the experimental one and is a consequence of the large confining potential exerted on the cluster by the terminating H atoms. In diamond, these two effects tend to cancel with the result that the gap is fortuitously in agreement with the experimental gap. The use of the Slater scheme to calculate excitation energies then leads to values in reasonable agreement with known optical transitions [16]. Unfortunately, in silicon the cluster band gaps are between a factor three and four too large. To deal with this problem, we have chosen to scale the Slater's transition state energies by the ratio of the correct Si band gap and the cluster gap. This has the effect of severely reducing all the donor-acceptor levels. In an analogous way, donor levels can be found by promoting half a electron from the valence band to the lowest unoccupied defect level corresponding to the positively charged defect. The technique is easily extended to second acceptor or donor levels. While the approach is not completely satisfactory, it does lead to levels in known cases which are within 0.2-0.3 eV of experiment, although it appears that the levels found are deeper than the experimental ones.

The substitutional Au centre

An 131 atom cluster with a neutral Au placed at its centre was fully relaxed, keeping the H terminators fixed. The gap contains a t_2 level containing three electrons and the configuration is taken to be $t_2^{\uparrow\uparrow}t_2^{\downarrow}$, consistent with $\mathcal{S} = 1/2$. The charge density was averaged over the three degenerate t_2 states and the self-consistent energy and forces acting on the atoms found. This procedure prevents a Jahn-Teller distortion [13]. Such distortions have been investigated by breaking the symmetry and relaxing in a specific electronic configuration [8, 13] but the t_2 splitting is very small and of no importance to the calculation of the donor and acceptor levels. The Au-Si lengths were 2.76 Å.

The positions of the five innermost atoms, including the impurity, were then inserted into a 297 atom cluster. An additional half electron was added to the $t_2^{\downarrow}$ level and another half added to the nearest a_1 empty level which is taken to be the conduction band bottom. The difference between these levels then gave an estimate of the $(-/0)$ acceptor level. In a similar way, the donor level was found by promoting half a electron to the t_2 level of the positively charged defect from the three levels lying beneath this defect level (and taken to represent thee valence band top). These energies were then rescaled as described above to compensate for the cluster

band gap. With the present basis, the band gap in the 297-atom cluster without any impurities is 3.51 eV. The scaling factor is then 0.33 and the resulting estimates for the levels are given in Table 1.

The deep acceptor level at $E_c - 0.63$ eV compares well with the experimental value of 0.54 eV. The donor level at $E_v + 0.45$ eV is deeper than than the experimental value of 0.35 eV. A second acceptor level lay at $E_c - 0.017$ eV. There is no evidence for this shallow level and it presumably lies above the conduction band minimum. The sum of the $(0/+)$ and $(-/0)$ levels is 1.08 eV which is almost equal to the energy gap 1.16 eV, whereas the experimental sum is 0.89 eV. The latter differs from the gap because of the Hubbard U term. It is clearly a failing of the present theory to account for this term properly.

Table 1. Comparison between experimental [10, 11] and calculated energy levels ΔE for the gold centre and Au–H complex (G complex).

Defect	Peak	Calc. (eV)	Expt. (eV)
Si:Au^0	Au$(-2/-)$	0.017	—
	Au$(-/0)$	0.63	0.54
	Au$(0/+)$	0.45	0.35
Au–H	G1$(-2/-)$	0.36	0.19
	Au$(-/0)$ + G4	0.63	midgap
	G2$(0/+)$	0.39	0.21

Au–H_n

We investigated the Au–H_n complexes when H lies both at anti-bonding sites outside the nearest neighbour shell of Si atoms to the impurity, and inside the shell. Similar sized clusters were used as in the Au defect discussed above.

For the $\mathcal{S} = 0$ Au–H defect, the H atom lies near a bond centred site as illustrated in Fig. 1. This configuration is more stable than the AB one by ~ 0.2 eV. The Au-H and H-Si lengths are 1.78 and 1.57 Å respectively with an Au-H-Si angle of 118°. The difference in energy between a configuration where the H atom is constrained to lie along [100] with C_{2v} symmetry is 0.15 eV and this represents an estimate of the energy barrier to reorientation.

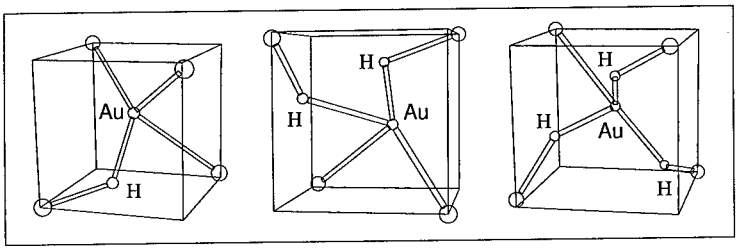


Fig. 1. Relaxed structure of the Au_{Si}–H_n in Si, $n = 1, 2$ and 3. Box edges mark the {100} directions. Note the increasing $\measuredangle$(Au-H-Si) with increasing number of H atoms.

The t_2 level (Fig. 2) now contains four electrons and is split and displaced downwards in the gap by the proton. Inevitably, this will decrease the donor and deepen the acceptor levels — as observed for G2 and G4 —, and encourages the possibility of a second acceptor level. The Slater method locates the acceptor $(-/0)$ level at 0.63 eV which is the same as that of Au. This agrees with the assignment of the mid-gap G4 level. A second acceptor $(-2/-)$ level is found at $E_c - 0.36$ eV and about 0.17 eV deeper that the $(-2/-)$ G1 level. The donor $(0/+)$ level at $E_v + 0.39$ eV is slightly lower than that of Au at $E_v + 0.45$ eV and is 0.17 eV above

G2. Given that the levels are generally deeper than about 0.1–0.2 eV, the results support the finding that the G1, G2, G4 levels all arise from the same defect which contains just one H atom. In addition, they support the claim that the G3 level at $E_v + 0.47$ eV cannot arise from this defect.

Table 2. Bond lengths for the different complexes. The bottom row of the table gives the distance (d) of the Au atom from the centre of the cluster. Bond lengths in Å.

Bond	Au^0	Au–H	$Au–H_2$	$Au–H_3$
Au–Si	2.76	2.60/2.61/2.48	2.45/2.66	2.45
Au–H	—	1.78	1.72/1.81	1.84/1.84/1.70
H–Si	—	1.57	1.53/1.65	1.67/1.50/1.50
d	0	0.26	0.63	0.60

Adding additional H atoms to the defect will fill the t_2 level and shift it downwards (Fig. 2). The level becomes filled for $Au–H_3$. The H atoms prefer to be inside the vacancy as the energy of this structure is 0.8 eV below that of the outside configuration. Two H atoms are strongly bonded to the Si radicals with lengths of 1.50 Å whereas the third is 1.67 Å from a third radical and 1.64 Å from Au. The gold atom is displaced off-site by ~ 0.6 Å along [100]. The defect has $\mathcal{S} = 0$ and the filled Kohn-Sham levels now are low lying and there are no empty gap levels. Thus the defect cannot act as an acceptor. The donor level as calculated by Slater's method is placed at $E_v + 0.18$ eV. Since our method leeds to deeper levels by ~ 0.2 eV than observed, the defect may identify $Au–H_3$ with the passive PA complex. This suggests that the Au–H defect is passivated by a direct combination with a mobile hydrogen molecule.

The $Au–H_2$ and $Au–H_4$ defects are electrically and magnetically active but will not be discussed here. It seems unlikely that the G3 level is one of these defects.

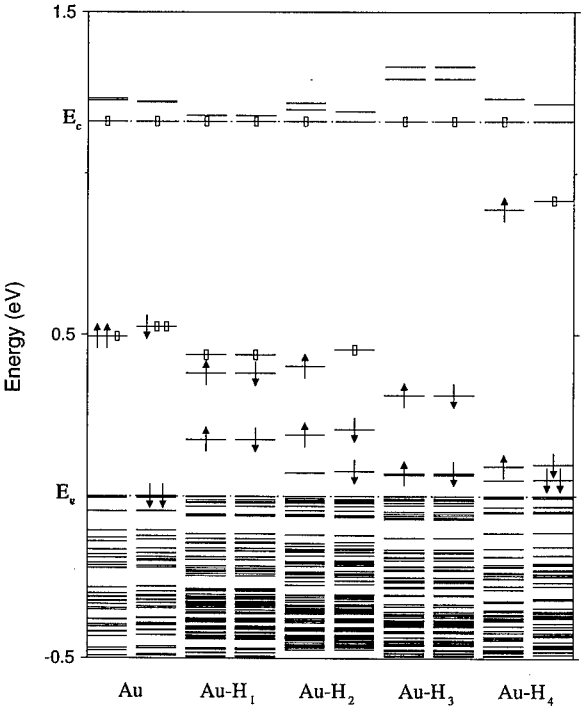


Fig. 2. One-electron Kohn-Sham eigenvalues in the vicinity of the gap for the Au_{Si}-H_n complexes in their relaxed configurations, with $n = 1, \cdots, 4$. Arrows indicate filled spin states, boxes indicate empty one-electron states (these are only shown in region of the gap).

In conclusion, our calculations have found:

1. The substitutional Au centre has (0/+) and (0/−) levels within 0.2 eV of the experimental values and a second acceptor level lies close to (and probably in) the conduction band;

2. The Au–H complex is diamagnetic and more stable with H close to Au near a bond centred configuration. The reorientation energy for Au is close to 0.15 eV;
3. The Au–H defect has deeper acceptor and more shallow donor levels than Au. We find the $(-2/-)$, $(0/-)$, $(0/+)$ levels within 0.2 eV of those of G1, G2 and G4 which are associated with one defect;
4. Two further H atoms add to Au–H by saturating two of the Si dangling bonds. The defect is diamagnetic;
5. Au–H_3 has no acceptor levels and a shallow donor level. We identify it with the passive defect first detected by Pearton and Tavendale;
6. Au–H_2 and Au–H_4 are electrically and magnetically active defects with deep levels.

Acknowledgements

S Öberg thanks NFR and TFR in Sweden for financial support. He also thanks PDC at KTH in Sweden, for computer time on the SP2. We also thank the HPCI committee of the EPSRC for computer time on the CRAY T3D where most of these results were derived.

References

[1] G D Watkins, *Physica* **B117–B118**, 9 (1983).

[2] B. Bech Nielsen, L. Hoffmann, M. Budde, R. Jones, J. Goss, and S. Öberg, *Materials Science Forum* **196-201**, 933, (1995).

[3] S J Pearton and A J Tavendale, *Phys. Rev* **B26**, 7105 (1982).

[4] J W Petersen and J Nielsen, *Appl. Phys. Lett.* **56**, 1122 (1990).

[5] M Kleverman, A Thilderkvist, G Grossman, H G Grimmeiss and G D Watkins, *Sol. State Commun.* **93**, 383 (1983).

[6] G D Watkins and M Kleverman, *Phys. Rev. Lett.* **67**, 1149 (1990).

[7] G D Watkins and P M Williams, *Phys. Rev.* **B52**, 16575 (1995).

[8] P R Briddon (To be published).

[9] W Jost and J Weber, *Phys. Rev* **B54**, 11038 (1996); W Jost, J Weber and H Lemke, *Semicond. Sci. Technol.* **11**, 22 (1996).

[10] E Ö Sveinbjörnsson and O Engström, *Phys. Rev.* **B52**, 4884 (1995).

[11] J A Davidson and J H Evans, *Semicond. Sci. Technol.* **11**, 1704 (1996).

[12] To appear in *Identification of Defects in Semiconductors*, edited by M Stavola and *Semiconductors and Semimetals*, treatise editors, R. K. Willardson, A C Beer and E R Weber (Academic Press).

[13] R Jones, S Öberg, J Goss, P R Briddon and A Resende, *Phys. Rev. Lett.* **75**, 2734 (1995).

[14] A Resende, R Jones, S Öberg, P R Briddon and B R Eggen (unpublished)

[15] J Goss, A Resende, R Jones, S Oberg and P R Briddon, *Materials Science Forum* **196-201**, 67–72, (1995).

[16] J P Goss, R Jones, S J Breuer, P R Briddon and S Öberg, *Phys Rev Lett* **77**, 3041 (1996).

This article was processed using the LaTeX macro package with TTP style

Materials Science Forum Vols. 258-263 (1997) pp. 301-306
© 1997 Trans Tech Publications, Switzerland

ELECTRICALLY ACTIVE SILVER-HYDROGEN COMPLEXES IN SILICON

N. Yarykin[1], J.-U. Sachse, J. Weber and H. Lemke[2]
Max-Planck-Institut für Festkörperforschung, Heisenbergstraße 1, D-70569 Stuttgart, Germany
[1]Institute of Microelectronics Technology RAS, 142432 Chernogolovka, Moscow Region, Russia
[2]TU Berlin, Institut für Werkstoffe der Elektrotechnik, Jebensstraße 1, D-10623 Berlin, Germany

Keywords : silicon, silver, hydrogen, DLTS

Abstract. The effect of hydrogenation during wet chemical etching in acid solutions on the energy levels in silver doped n- and p-type silicon is studied by deep-level transient spectroscopy. It is observed that along with known acceptor and donor levels of substitutional silver a number of novel deep-level centres appear near the etched surface. The depth profiles of the deep-level centres are investigated depending on time and temperature of the reverse- and zero-bias annealing processes. The novel centres are silver–hydrogen complexes containing only one silver atom and one or more hydrogen atoms. The striking similarities of silver–hydrogen and gold–hydrogen complexes are discussed.

Introduction

The study of the interaction of hydrogen with impurities is currently stimulated by the possibility to create electrically inactive impurity–hydrogen complexes. The hydrogenation of transition metals seems to be of great practical importance as a simple method to influence the lifetime of minority carriers. In this paper we study the behavior of silver under hydrogenation. The results are compared with the already published data on Au–H complexes [1, 2].

The literature on the electrical properties of silver doped silicon is rather limited [3, 4 and references therein]. This is certainly due to the high diffusion temperatures needed to obtain a noticeable concentration of electrically active silver [3]. However, the results available show definitely that Ag in Si results in at least two deep levels: an acceptor level near the middle of the gap and a donor level 0.34-0.40 eV above the top of the valence band.

Contrary to gold, the isoelectronic analogue of silver, no study on silver–hydrogen interactions is known. However, chemical etching followed by annealing at moderate temperatures leads to a decrease of the silver acceptor [5] and donor [6] concentrations. The possibility of electrically active silver–hydrogen complexes is discussed in Ref. [5].

Experimental

Floating-zone silicon crystals doped with phosphorus ([P] = $2 \cdot 10^{14}$ cm^{-3}) or boron ([B] = $1.5 \cdot 10^{14}$ cm^{-3}) are used in the present work. Silver is introduced during crystal growth [4], the concentration of the electrically active Ag-levels is ~15% of the shallow dopants. The hydrogenation of the samples is produced during wet chemical etching in acid solution $HF : HNO_3 : CH_3COOH$ (1 : 2 : 1). Etching rate is at about 20 μm/min. The Schottky contacts of 2 mm diameter are fabricated by vacuum metal evaporation, Au on n-type and Al on p-type crystals. Ohmic contacts are produced by scratching an eutectic InGa alloy on the back side of the samples. Some chemically etched samples are annealed at temperatures 200-500°C for one hour in Ar atmosphere. No additional surface treatment is performed in this case before Schottky diode fabrication.

The measurements are performed on a computerized DLTS system with a lock-in amplifier as a correlator. Energy levels are determined from the Arrhenius plots of the thermal emission rate using the standard T^2 correction. The spatial distribution of the deep-level centres is calculated by digital differentiation of the DLTS signal dependence on the filling pulse amplitude at a fixed reverse bias. The inhomogeneous profile of the shallow dopants which is determined by CV measurements is properly included in the evaluation of the deep-level depth profiles.

Results and discussion

P-type Si, reverse bias annealing

Previous investigations on p-type Si crystals doped with transition metals (for instance gold [1]) established that almost all hydrogen atoms injected in the crystal during chemical etching are trapped by boron and no (or very small concentrations of) hydrogen–transition metal complexes can be detected immediately after etching. The same situation is found in silver doped samples. The dotted line in Fig. 1 shows the DLTS spectrum from a chemically etched sample without any additional treatment. Only the DLTS H1-peak of the silver donor level is detected (see Table 1). A small peak at ~260 K can be associated with the weak hole emission from the mid-gap silver acceptor level.

Hydrogen introduced in the near surface region is drifted into the bulk by reverse bias annealing (RBA) at moderate temperatures [7]. This process is monitored by the formation of the dip in the active boron concentration profile obtained from CV measurements (Fig. 2, dotted curve). After such a treatment 3 new peaks appear in the DLTS spectrum: H2, H3 and a small peak at 66 K (Fig. 1, solid curve). The spatial distributions of these new centres (except the latter) and the silver donor level are shown in Fig. 2. It is seen that the concentration of the substitutional silver donor follows qualitatively the CV profile and shows a dip at 5÷9 μm, the new defects exhibit a maximum approximately at the same depth. Moreover, the reduction of the silver donor concentration is approximately equal to the sum of the concentrations of the H2- and H3-defects. These findings give strong evidence for the association of these new defects with two different silver–hydrogen complexes. The centre responsible for the DLTS peak at 66 K has a maximum concentration in the

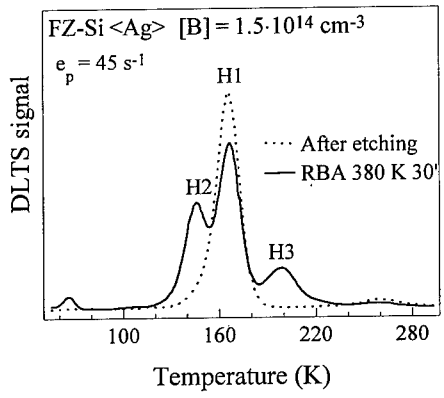


Figure 1. DLTS curves taken in p-type Si ⟨Ag⟩ immediately after chemical etching and following reverse bias annealing (RBA).

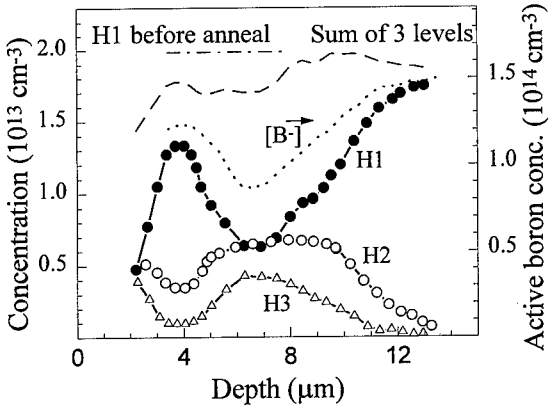


Figure 2. Concentration profiles of the deep-level centres measured in p-type Si ⟨Ag⟩ after 2h reverse bias annealing at 380 K. The distribution of electrically active boron [B^-] is also shown.

hydrogen-rich region and seems also to be hydrogen-related. However, its concentration reaches a saturation at a very early stage of the annealing, when hydrogen and silver atoms are still available. The saturation level is low compared to the silver concentration and we believe that this defect is most probably not silver-related.

In all experiments the H2- and H3-centres have maximum concentration approximately at the same depth. However, their formation kinetics at 380 K are quite different: the H2-centre increases much faster at early stages of annealing and the concentrations of these two centres become comparable only after long annealing times. The quantitative analysis of the kinetics observed shows that such behavior is in agreement with the assumption that the H3-centre is formed by addition of another hydrogen atom to the H2-centre. The H3-defect is therefore most probably an Ag–H_2 complex.

For longer (several hours) anneals at 380 K the sum concentration of all silver-related deep-level centres also reveals a dip in the region of the maximum hydrogen concentration. This implies that during further hydrogenation silver atoms are transfered into electrically inactive complexes (Ag-H_X, $X \geq 3$).

N-type Si, room temperature etching

In contrast to p-type crystals and in accordance with the results of previous investigations on n-type Si ⟨Au⟩ [1, 2], the effect of hydrogenation during chemical etching on the DLTS spectrum of n-type samples is observed without any additional treatment. The dotted line in Fig. 3 shows the DLTS spectrum taken at high reverse bias and relatively small filling pulse amplitude. Under these measurement conditions only the centres located at 9÷11 μm from the etched surface (where the effect of etching is negligible) contribute to the signal. This curve is dominated by the E1-peak at 258 K, which can be identified with the substitutional silver acceptor level (see Table 1). A small shoulder at ~ 200 K was detected in all the investigated samples. It is not clear at the moment if the corresponding defect is silver-related, the concentration is always small compared to the concentration of the silver acceptor and does not affect the transformations considered below. The nature of the defect level at ~ 200 K and the behavior under hydrogenation will not be discussed in this paper.

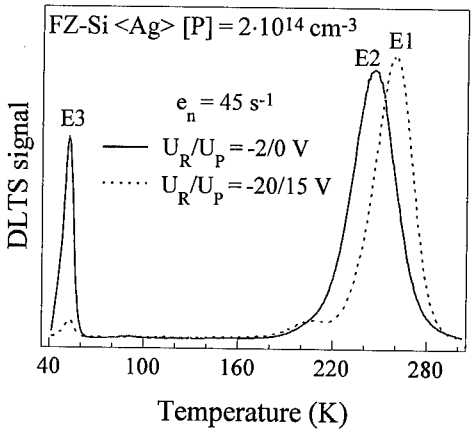


Figure 3. DLTS curves taken at different reverse bias / filling pulses in n-type Si ⟨Ag⟩, which was chemically etched before Schottky diode fabrication.

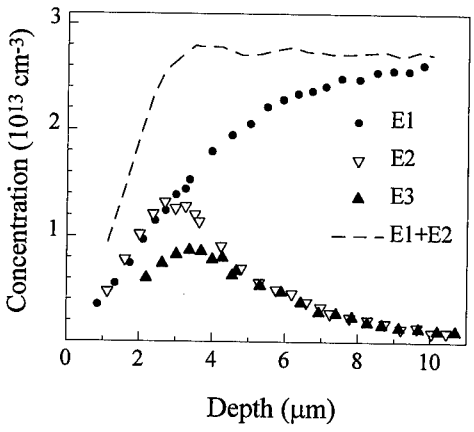


Figure 4. Concentration profiles of the deep-level centres after chemical etching of n-type Si ⟨Ag⟩.

The solid curve in Fig. 3 shows the DLTS signal from the near surface region of the same sample. It is seen that in this region the E1-peak becomes much smaller while two other peaks of approximately the same amplitude appear. The similar change in the DLTS spectrum was interpreted in [5] as a shift of the silver acceptor peak towards lower temperatures. Under the conditions presented in Fig. 3 the average electric fields in the regions from which the electron emission is studied are small ($< 8 \cdot 10^3$ V/cm) and equal within 20%. Therefore, the great peak shift (> 10 K) can not be attributed to the weak field dependence of the emission from the silver acceptor level [8]. We have indications that the shifted DLTS line is composed of two lines, the unshifted E1 peak and a new hydrogen induced line E2. The parameters of the E1- and E2-levels presented in Table 1 are obtained by the deconvolution of the capacitance transient into two exponential decays. There is no report on the E3 peak in the literature. The small peak at 88 K seems to be identical to the S-peak in Ref. [5]. As in the case of the peak at 66 K in p-type samples, this peak is always small compared to the silver-related peaks and possibly not silver-related.

The depth profiles of the centres with the highest concentration are presented in Fig. 4. At greater depths (4÷10 μm from the surface) the concentrations of the E2- and E3-centre coincide within the accuracy of the measurements. The sum of the concentrations of the E1 and E2 (or E3) centres is nearly constant for a depth deeper than 3 (4) μm and is equal to the initial electrically active silver concentration. This behavior indicates that E2 and E3 are two levels of the same defect, the defect originates from substitutional silver atoms due to hydrogenation.

Table 1. Energy levels, majority carrier capture cross sections $\sigma_{n,p}$ and assignment of the deep levels observed in silver-doped silicon. E_A and $\sigma_{n,p}$ are both determined from the Arrhenius plot of the thermal emission rates.

Level	Activation energy E_A (eV)	σ_n or σ_p (cm^2)	Assignment
E1	$E_C - 0.56$	$7.5 \cdot 10^{-15}$	$Ag^{-/0}$
E2	$E_C - 0.45$	$2.4 \cdot 10^{-16}$	$(Ag–H)^{-/0}$
E3	$E_C - 0.09$	$6.7 \cdot 10^{-16}$	$(Ag–H)^{--/-}$
H1	$E_V + 0.37$	$9.7 \cdot 10^{-14}$	$Ag^{0/+}$
H2	$E_V + 0.28$	$6.6 \cdot 10^{-15}$	$(Ag–H)^{0/+}$
H3	$E_V + 0.38$	$2.1 \cdot 10^{-15}$	$(Ag–H_2)$

The CV-measurements at different temperatures reveal the acceptor character of the E2-level. Therefore, the E3-level should exhibit the properties of a double-acceptor. The capture of a second electron should be influenced by an electrostatic barrier. Indeed, the capture cross section of this level measured by variation of the filling pulse width is found to be approximately 100 times smaller than determined by emission and shown in Table 1 and exhibits a strong temperature dependence.

The concentration of all deep-level centres vanishes near the surface (see Fig. 4), where the maximum hydrogen concentration exists. Apparently, high hydrogen concentrations leads to a full passivation of all silver-related deep levels in the upper half of the gap. In p-type Si ⟨Ag⟩ we have already detected a reduction of all deep-level centres in the hydrogen-rich region after long term

annealing at 380 K. Therefore, the electrically active silver–hydrogen complexes seem to be intermediate stages of the total passivation of the silver levels.

The great difference in concentrations of the E2- and E3-levels in the region of 2÷4 μm from the surface is not completely clear now. Most probably, another centre with the level similar to that of the E2-centre contributes to the DLTS signal. Taking into account that the H3-level in p-type crystals has already been assigned to the Ag–H_2 complex, the difference discussed can be tentatively ascribed to another level of this defect. Note that the formation of this defect in n-type Si is expected in this region, in which the concentration of hydrogen is higher than in deeper layers but not sufficient for a total passivation of the electrical activity of the silver-related centres.

Annealing at higher temperatures

Annealing of both n- and p-type crystals at temperatures $T_{ann.} \geq 200°C$ is performed after chemical etching without Schottky contacts. No new levels are observed in concentrations comparable to those of the silver-related centres discussed above. The main effect of annealing in the range $200°C \leq T_{ann.} \leq 350°C$ consists in a further decrease of the silver acceptor and donor concentration near the surface, an increase of the total number of silver–hydrogen complexes and a notable shift of their profiles deeper into the crystal. Such a shift is shown in Fig. 5 for the E3-level in n-type Si and the H2-level in p-type Si.

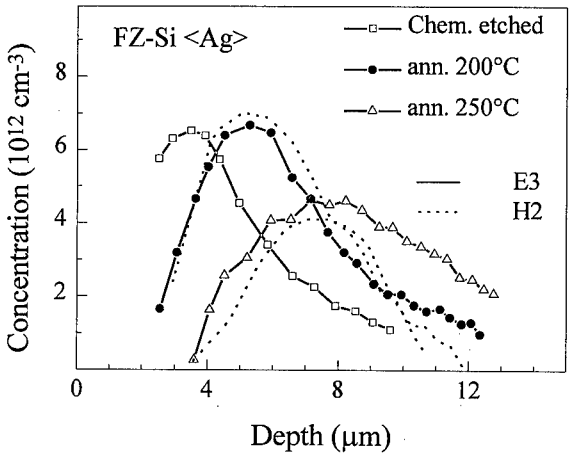


Figure 5. Spatial distribution of the E3-level after chemical etching and subsequent annealing. Dotted lines show the H2-centre distribution measured in p-type Si ⟨Ag⟩ after the corresponding annealing. E3- and H2-concentrations were normalized according to the initial silver concentration in n- and p-type samples.

The Fermi level position during annealing at $T_{ann.} \geq 200°C$ in our moderately doped (~ $2 \cdot 10^{14}$ cm^{-3}) samples is located approximately in the middle of the gap. Both H–B and H-P pairs are unstable at these annealing temperatures. Due to the coincidence of the E3- and H2-profiles after annealing at 200÷300°C (Fig. 5) we assign both levels to the same centre. In addition, the identical profiles give evidence for a similar distribution of hydrogen in n- and p-type silicon at higher temperatures. Annealing expands the near surface region in which no deep-level defects exist in n- and p-type crystals and only electrically inactive silver-hydrogen complexes are formed.

Increasing the annealing temperature up to 400÷500°C results in the disappearance of all deep-level centres attributed to silver–hydrogen complexes. Simultaneously, the profiles of the silver acceptor and donor levels become flat with the concentration of electrically active substitutional silver being equal to that in the initial crystals. This means that all the silver–hydrogen complexes (including those electrically inactive) are unstable under such annealing conditions. The exact value of the annealing temperature resulting in destruction of silver–hydrogen complexes seems to depend on the cooling rate after annealing. Apparently part of the free hydrogen remains in the crystal and interacts with silver during cooling.

Conclusion

We have studied the interaction of hydrogen with substitutional silver atoms. An electrically active Ag–H complex is formed at room temperature in n-type Si and at least at 370 K in p-type Si. This complex has an acceptor level at $E_C - 0.45$ eV, a second acceptor level at $E_C - 0.09$ eV, and a donor level at $E_V + 0.28$ eV. Adding another hydrogen atom results in the formation of an Ag–H_2 complex, which reveals an energy level at $E_V + 0.38$ eV. Further hydrogenation leads to the formation of electrically inactive silver-hydrogen complexes. Annealing at $T_{ann.} \geq 400$°C destroys all silver–hydrogen complexes and restores the electrical activity of the isolated silver atoms.

The comparison of the results in Ag doped samples with the published data on Au doped samples exhibits the similar structure of energy levels in these two systems. The substitutional silver and gold atoms reveal amphoteric behavior, the donor and acceptor levels of both impurities are difficult to distinguish by DLTS. The complex of these transition metals with one hydrogen atom gives three new levels in the gap: E3, E2, and H3 for Ag–H and G1 ($E_C - 0.19$ eV), G4 ($E_C - 0.53$ eV), and G2 ($E_V + 0.21$ eV) for the Au-H pairs [1]. Both E3 and G1 show a temperature dependent capture cross section [9]. The two levels E2 and G4 reveal only a small energy shift from the position of the original acceptor levels. The H3 and G3 ($E_V + 0.47$ eV) levels can be correlated by their similar formation kinetics. However, there is a remarkable difference in the thermal stability of silver–hydrogen and gold–hydrogen complexes (400-500°C for Ag–H vs. 250-300°C for Au–H).

Acknowledgements

We thank H. J. Queisser for his interest and support and E. Ö. Sveinbjörnsson for helpful discussions. The technical assistence of W. Heinz is acknowledged. N. Y. is grateful for the support by the Deutsche Forschungsgemeinschaft (436 RUS 113/166).

References

1. E. Ö. Sveinbjörnsson and O. Engström, Phys. Rev. B **52**, 4884 (1995).
2. A. Parakhonsky, O. Feklisova, N. Yarykin and S. Karelin, Semiconductors **30**, 362 (1996).
3. K. Graff "Metal Impurities in Silicon-Device Fabrication" (Springer-Verlag, 1995).
4. H. Lemke in "High Purity Silicon IV", edited by C. L. Claeys, P. Rai-Choudhury, P. Stallhofer, and J. E. Manrits (The Electrochem. Soc., Pennington, NJ) Proc.Vol. **96-13**, p. 272 (1996).
5. H. Feichtinger and E. Sturm, Material Science Forum **143-147**, 111 (1994).
6. H. Lemke, Physica Status Solidi (a) **94**, K55 (1986).
7. T. Zundel and J. Weber, Phys. Rev. B**39**, 13549 (1989).
8. L. D. Yau and C. T. Sah, Phys. Status Solidi A **6**, 561 (1971) .
9. N. Yarykin, J.-U. Sachse and J. Weber, to be published.

Materials Science Forum Vols. 258-263 (1997) pp. 307-312
© 1997 Trans Tech Publications, Switzerland

PALLADIUM-HYDROGEN RELATED COMPLEXES IN SILICON

J.-U. Sachse, J. Weber and H. Lemke[1]
Max-Planck-Institut für Festkörperforschung, Heisenbergstraße 1, D-70569 Stuttgart, Germany
[1]TU Berlin, Institut für Werkstoffe der Elektrotechnik, Jebensstraße 1, D-10623 Berlin, Germany

Keywords: hydrogen, transition metals, silicon

Abstract

The electrical properties of palladium-hydrogen related defects in n- and p-type silicon are studied by deep-level transient spectroscopy (DLTS). Wet-chemical etching leads to the formation of several electrically active and at least one passive Pd-H complexes. Depth profile measurements and heat treatments enable us to distinguish between different palladium-hydrogen related centers. The correlation between hydrogen induced levels in palladium and platinum doped silicon is discussed.

Introduction

Hydrogen is known to interact with transition metals in silicon by passivation of their deep levels and by formation of electrically active transition metal-hydrogen complexes [1,2]. An example for a 5d transition metal is platinum where several Pt-H complexes have been detected [3,4]. Palladium as the 4d relative of platinum exhibits almost identical electronic properties. This is explained by the so called "vacancy model" which is based on structural similarities between the substitutional Pd and Pt defect with the vacancy in silicon [5]. It is expected that the close relationship of the isolated substitutional defects leads to similar transition metal-hydrogen complexes. However, no information is yet available concerning the formation and the properties of palladium-hydrogen related defects. In this study we present evidence for hydrogen induced electrically active and passive Pd complexes in Si and compare the results with Pt doped silicon.

Experimental

We used phosphorus- or boron-doped float zone or Czochralski silicon with doping concentrations in the range of 1×10^{14} - 1×10^{16} cm^{-3}. Palladium was introduced during crystal growth [6] or by diffusion at temperatures between 800 °C and 1000 °C. The total concentration of electrically active palladium reached 1×10^{13} - 5×10^{14} cm^{-3}. Hydrogenation of the samples was performed by wet-chemical etching in a 1:2:1 mixture of HF, HNO_3 and CH_3COOH before evaporation of the Schottky contacts (Al for p-type Si, Au for n-type Si). In addition, hydrogen incorporation during wet-chemical etching was avoided by cleaving the samples and evaporation of the contacts directly onto the surface without any further surface treatment.
The experimental set-up is a computerized lock-in deep level transient spectroscopy (DLTS) system. The shallow dopant concentration profiles are determined by capacitance-voltage (CV) measurements at room temperature (1 MHz). DLTS concentration profiling was used to determine the distribution of the deep levels. The profiles are calculated taking into account the nonuniform shallow dopant profiles.

Results

A typical DLTS spectrum of a palladium doped p-type silicon sample after wet etching is shown in Fig. 1a. We observe two dominant DLTS peaks at 165 K and at 70 K. These signals can be assigned to the single [7,8] and double donor level of substitutional palladium [9,10].
In addition to the two Pd donor levels, a small peak labeled H(280) is detected at 280K in the etched sample. This signal increases after annealing at 370 K for 30 min while the substitutional palladium signals decrease by the same amount (Fig. 1b). A heat treatment at 400 K leads to a further enhancement of H(280) as shown in Fig. 1c. At the same time three new levels appear in the spectrum, H(45), H(55) and H(140), and the two palladium donor signals are drastically reduced.
Annealing at temperatures between 450 and 550 K results in a decrease of all observed peaks without the occurance of new signals. While H(45), H(55) and H(140) vanish after one hour at 550 K, level H(280) is slightly more stable, but anneals out after several hours at 650 K. Furthermore, we observe for temperatures above 600 K an enhancement of the Pd donor signals. A one hour heat treatment at 750 K leads to a complete recovery of the Pd donor signals and their intensities agree with the initial values after wet-chemical etching.
Figure 2 shows the depth profiles of the shallow and deep levels after etching and after a heat treatment at 370 K applying a reverse bias of -8 V to the Schottky diode. After wet etching we observe a reduction of the net active boron concentration in the region close to the surface (solid line in Fig. 2a). This passivation is caused by the introduction of hydrogen during the etching and the formation of electrically inactive B-H pairs [11]. The corresponding depth profiles of the deep levels after etching are shown in Fig. 2b. Level H(280) is only detected close to the sample surface where hydrogen has been incorporated while the Pd single and double donor profiles are uniform.

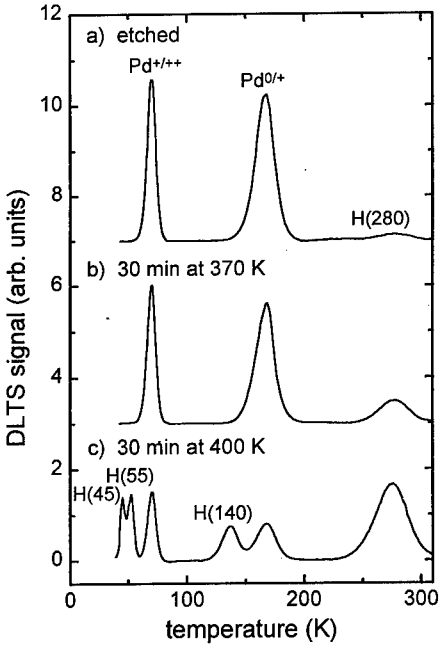


Figure 1 DLTS spectra of Pd doped p-type Si. a) after etching; b) after etching and subsequent zero bias annealing at 370 K for 30 min; c) after etching and subsequent zero bias annealing at 400 K for 30 min. The emission rate is 42 s^{-1}.

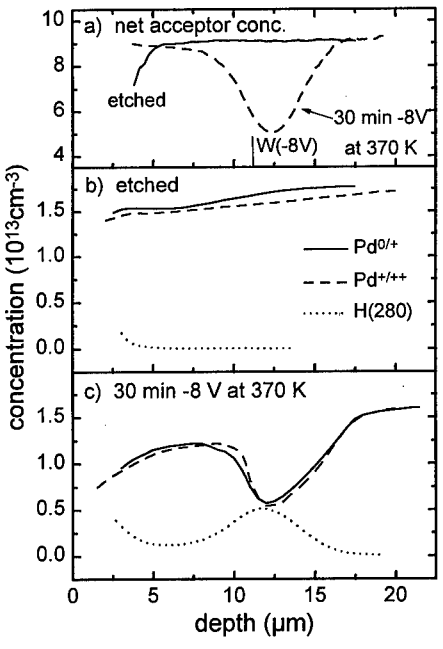


Figure 2 a) Depth profiles of the net boron acceptor concentration in an etched sample and after a subsequent reverse bias annealing at 370 K for 30 min using a reverse bias of -8 V; b) Depth profiles of the palladium related defects $Pd^{0/+}$, $Pd^{+/++}$ and H(280) after etching; c) Depth profiles after an additional reverse bias annealing.

Level	Activation energy E_A (eV)	σ_n or σ_p (cm^2)	Assignment
E(60)	E_C - 0.10	$1 \cdot 10^{-18}$ (57K)	Pd-H related
Pd(115)	E_C - 0.23	$3 \cdot 10^{-15}$	$Pd^{-/0}$
E(160)	E_C - 0.29	$2 \cdot 10^{-16}$	Pd-H related
E(200)	E_C - 0.43	$7 \cdot 10^{-16}$	Pd-H related
H(280)	E_V + 0.55	$2 \cdot 10^{-17}$	Pd-H related
Pd(165)	E_V + 0.31	$6 \cdot 10^{-16}$	$Pd^{0/+}$
H(140)	E_V + 0.23	$5 \cdot 10^{-16}$	Pd-H related
Pd(70)	E_V + 0.14	$1 \cdot 10^{-16}$ (70K)	$Pd^{+/++}$
H(55)	E_V + 0.08	$2 \cdot 10^{-17}$	Pd-H related
H(45)	E_V + 0.07	$1 \cdot 10^{-18}$	Pd-H related

Table 1 Activation energy levels determined from Arrhenius plots of the emission rates, capture cross sections $\sigma_{n,p}$ determined by variation of the filling pulse length and the assignment of the deep levels observed in Pd doped silicon. The activation energies of E(60) and Pd(70) are field dependent and the values are given from extrapolation to zero field. The temperature dependence of the capture cross sections has been measured for all levels. E(60) and Pd(70) have thermally activated capture cross sections, while the values of $\sigma_{n,p}$ do not show a temperature dependence for the other levels.

Annealing under reverse bias affects the depth profiles of both the shallow and the deep defects dramatically. The boron-hydrogen pairs dissociate in the surface region resulting in a reactivation of boron. The released positively charged hydrogen drifts to the end of the space charge region where new B-H pairs are formed causing the dip in the net boron profile at a depth of 12 μm (dashed line in Fig. 2a). At the same time we observe an increase of the concentration of H(280) at the same depth accompanied by an equal reduction of the Pd single and double donor concentrations as shown in Fig. 2c. This strongly suggests that H(280) is caused by a palladium-hydrogen complex.

The behavior of the levels which are formed at higher temperatures (H(45), H(55) and H(140)) resembles H(280). All these signals are maximized at the same depth as H(280) after the reverse bias annealing (not shown). This suggests that they also belong to palladium-hydrogen complexes. The different Pd-H related levels in p-type silicon can be distinguished by their depth profiles and thermal stabilities. We find that H(45) and H(55) belong to the same complex while H(140) and H(280) are caused by different centers.

After heat treatments below 450 K the sum of the concentrations of all the Pd related centers agrees with the initial palladium concentration in the etched sample. This is not the case for annealing at higher temperatures, where we observe a decrease in the total Pd concentration in the region where hydrogen is concentrated. Since this behavior is not detected in cleaved samples which are free of hydrogen we tentatively assign this effect to the formation of an electrically passive Pd-H complex. Such a passivation of palladium was previously reported [12].

In cleaved n-type silicon only the acceptor level of substitutional Pd is observed as shown in Fig. 3a [7,8]. In contrast to p-type Si, the DLTS spectrum has already changed dramatically after wet-chemical etching (Fig. 3b). The Pd acceptor signal decreases significantly while three new peaks appear in the spectrum labeled E(60), E(160) and E(200). The corresponding values for activation energies and capture cross sections are presented in Table 1. It should be noted that level E(60) shows an electric field dependence of the activation energy and a thermal activation of the electron capture cross section.

At higher temperatures we observe a decrease of all signals. E(60) and E(160) anneal out between 500 K and 550 K while E(200) disappears at 650 K. At temperatures above 600 K the Pd acceptor recovers and after a one hour heat treatment at 750 K the acceptor signal has regained its initial intensity as in the cleaved sample.

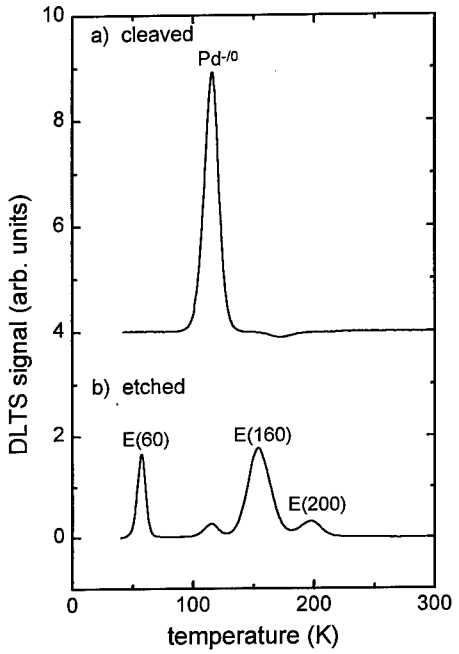


Figure 3 DLTS spectra of Pd doped n-type Si. a) cleaved sample; b) after etching. The emission rate is 42 s^{-1}.

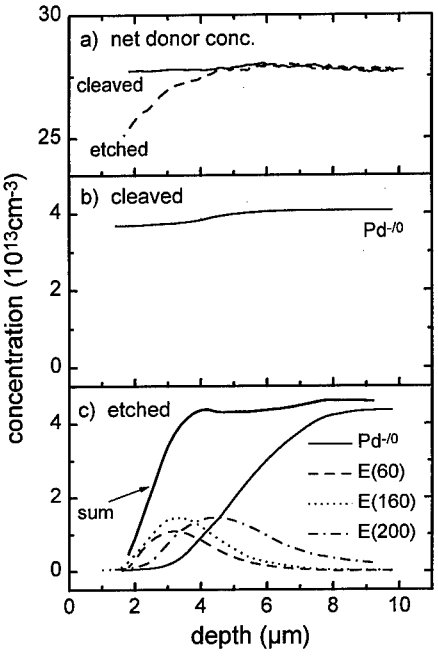


Figure 4 a) Depth profiles of the net phosphorus donor concentration in a cleaved sample and after etching; b) Depth profile of the Pd acceptor in a cleaved sample; c) Depth profiles of the palladium related defects $Pd^{-/0}$, E(60), E(160) and E(200) after etching.

Figure 4a shows the corresponding profiles of the net phosphorus donor concentration. For the cleaved sample we observe a flat profile, while a reduction of the net active phosphorus concentration is observed after etching in the region close to the surface (at depths ≤ 5 μm). The origin of this passivation is hydrogen diffusion into the surface region and the subsequent formation of passive P-H complexes [13].

The profile of the Pd acceptor is flat in the cleaved sample (Fig. 2b). After wet-chemical etching three additional palladium related levels appear: E(60), E(160) and E(200). All three levels have their maximum concentration within the depth where hydrogen has diffused in (3 - 5 μm) and decrease towards the bulk and the surface (Fig. 4b). The profiles of E(60) and E(160) are similar after etching in contrast to the E(200) profile which is always shifted to larger depths. E(60) decreases slightly faster during annealing at temperatures above 450 K than E(160). Therefore, we assign E(60), E(160) and E(200) to three different Pd-H complexes.

The sum of the concentration of all palladium related levels is also shown in Fig. 4b. At depths ≥ 4 μm the total concentration of electrically active palladium is uniform and equals the concentration in the cleaved sample while a reduction of the sum in the region close to the surface is observed. This region extends deeper into the bulk after annealing at temperatures above 450 K, but a heat treatment above 600 K results in a reactivation of electrically active palladium in the form of the substitutional palladium acceptor. The passivation and reactivation kinetics resemble the behavior in p-type silicon indicating that both in n- and p-type silicon a passive Pd-H complex is formed between 450 K and 600 K.

Discussion

DLTS depth profile studies reveal that wet-chemical etching of Pd doped silicon leads to the formation of several Pd-H complexes in p- and n-type samples. In n-type Si the Pd-H related defect levels are already observed directly after etching while an additional annealing step is needed to detect the complexes in p-type Si. These differences can be explained by the interaction between hydrogen and the shallow dopants. In p-type Si, most of the hydrogen is complexed with boron after etching. In contrast, pairing of phosphorus and hydrogen in n-type Si is less efficient, which enables a considerable formation of Pd-H complexes already at room temperature. Similar differences between the formation kinetics in p- and n-type Si have also been reported for other transition metal-hydrogen complexes [1,2,4]. In Fig. 5 the energy levels of both the isolated substitutional Pd defect and the Pd-H complexes are illustrated in an energy-level diagram. The three hydrogen related levels in n-type Si (E(60), E(160), E(200)) belong most probably to three different Pd-H complexes due to their different thermal stabilities and concentration depth profiles. In p-type Si the shallow levels H(45) and H(55) are most likely different charge states of the same center, while H(140) and H(280) are caused by different defects. Thus we assume that palladium also forms three different complexes with hydrogen in p-type material. In addition, we observe both in n- and p-type silicon an electrically inactive Pd-H complex.

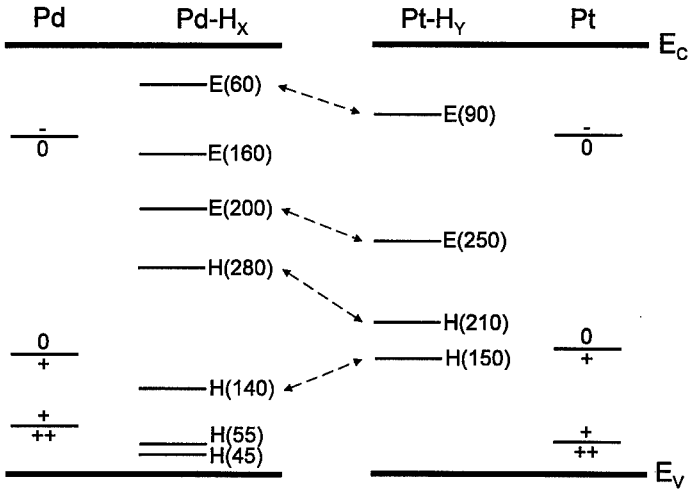


Figure 5 Energy-level diagram showing the levels of the isolated substitutional defects and the hydrogen-related levels for palladium and platinum.

Figure 5 also shows the energy levels of the substitutional defect and the hydrogen related complexes for platinum [4]. The close relationship between Pd and Pt is displayed by the fact that both transition metals do not only occur in the same charge states, but also the corresponding energy levels almost coincide.

We do not find such a complete agreement between both metals when we compare the hydrogen related defects. Especially, palladium seems to exhibit more hydrogen induced levels. Furthermore, it forms a passive complex with hydrogen which is not observed for platinum [4]. However, it is possible to correlate certain levels for both metals due to their electrical and thermal properties. These levels might be caused by hydrogen related complexes with the same structure containing the same number of hydrogen atoms. Possible candidates for such a correlation are connected by arrows in Fig. 5. The corresponding levels show similar thermal stabilities and concentration depth

profiles. Furthermore, common characteristic properties of E(60) (Pd) and E(90) (Pt) are the field dependence of the activation energy and a thermally activated capture cross section.
In Pt doped silicon the four hydrogen related levels have been assigned to at least three different Pt-H complexes [4]. Based on measurements with minority carrier injection and a comparison of the concentration depth profiles, an assignment of E(90) and H(210) to the same Pt-H complex cannot be excluded. This defect is a candidate for the PtH_2-complex observed by electron paramagnetic resonance (EPR) and vibrational spectroscopy [3]. The comparison in Fig. 5 shows that the corresponding levels in Pd doped silicon are E(60) and H(280) which are both shifted by about 100 to 150 meV towards the conduction band, compared to E(90) and H(210) in the Pt case. EPR and vibrational spectroscopy measurements are necessary to determine if a PdH_2-complex exists and if E(60) and H(280) are possibly energy levels of such a center.

Conclusion

In summary, we observe seven palladium-hydrogen related levels in Pd doped silicon after wet-chemical etching. At least two of them belong to the same center. In p-type Si a heat treatment is necessary to detect the defects. An additional electrically passive complex is formed in the hydrogen-rich region of the samples at temperatures between 450 and 600 K. Palladium tends to form more hydrogen related complexes than the electronically closely related platinum. However, a correlation of all Pt-H related levels to corresponding Pd-H related levels is possible. All Pd-H complexes anneal out between 500 and 700 K and the substitutional palladium concentration reaches ist initial value before hydrogenation.

Acknowledgements

We thank H. J. Queisser for his support throughout the work and E. Ö. Sveinbjörnsson for helpful discussions. We acknowledge the technical assistance of W. Heinz and W. Krause. We thank W. Zulehner (Wacker Siltronic AG) for the generous supply of the silicon wafers.

References

[1] E. Ö. Sveinbjörnsson and O. Engström, Phys. Rev. B **52**, 4884 (1995).
[2] W. Jost, J. Weber, and H. Lemke, Semicond. Sci. Technol. **11**, 525 (1996).
[3] S. J. Uftring, M. Stavola, P. M. Williams, and G. D. Watkins, Phys. Rev. B **51**, 9612 (1995).
[4] J.-U. Sachse, E. Ö. Sveinbjörnsson, W. Jost, J. Weber, and H. Lemke, Phys. Rev. B **55**, 16176 (1997).
[5] G. D. Watkins, Physica **117B & 118B**, 9 (1983).
[6] H. Lemke, in Semiconductor Silicon edited by H. R. Huff, W. Bergholz, and K. Sumino (Pennington, NJ: The Electrochemical Society 1994), p. 695.
[7] J. A. Pals, Solid-State Electron. **17**, 1139 (1974).
[8] E. Rubio, J. Vicente, M. Jaraiz, J. Arias, L. Bailón, and J. Barbolla, J. Appl. Phys. **69**, 298 (1991) and references therein.
[9] H. Lemke, phys. stat. sol. (a) **86**, K39 (1984).
[10] J.-U. Sachse, W. Jost, J. Weber, and H. Lemke, to be published.
[11] T. Zundel and J. Weber, Phys. Rev. B **39**, 13549 (1989).
[12] S. J. Pearton and E. E. Haller, J. Appl. Phys. **54**, 3613 (1983).
[13] A. L. Endrös, W. Krühler, and J. Grabmaier, Physica B **170**, 365 (1991).

Materials Science Forum Vols. 258-263 (1997) pp. 313-318
© 1997 Trans Tech Publications, Switzerland

EFFECTS OF HYDROGEN PLASMA ON DISLOCATION MOTION IN SILICON

Y. Yamashita, F. Jyobe, Y. Kamiura and K. Maeda[1]
Faculty of Engineering, Okayama University,
3-1-1, Tsushima-naka, Okayama 700, Japan
[1]Faculty of Engineering, University of Tokyo,
7-3-1, Hongo, Bunkyo-ku, Tokyo 113, Japan
(e-mail: yamasita@elec.okayama-u.ac.jp)

Keywords : silicon, dislocation, glide velocity, hydrogen plasma,

Abstract. We have measured the velocity of dislocation glide motion in phosphorus-doped FZ-silicon during hydrogen plasma irradiation, and, have found for the first time that the velocity was drastically promoted under hydrogen plasma by a factor of 10 to 100 in the temperature range of 390-480°C, and the activation energy of dislocation motion was reduced to 1.2eV from the value 2.3eV, in the dark. We exclude the possibility that the observed phenomenon is due to so called radiation-enhanced dislocation glide induced by plasma light, since no enhancement of dislocation motion occurred at all under nitrogen plasma with the same light intensity as hydrogen plasma, and hydrogen plasma irradiation with covers to prevent light exposure promoted dislocation motion as well. In addition, it is confirmed by spreading resistance measurements that hydrogen atoms were actually incorporated up to about 10 μm beneath the surface to passivate boron. This assures us that hydrogen atoms were incorporated to enough depths at the temperatures where dislocation velocity was measured. These results clearly indicate that hydrogen itself enhances dislocation motion. Some discussions are made on the enhancement mechanisms of dislocation motion.

Introduction.

Dislocations in semiconductors are electrically active and their motion is largely affected by their electronic states. For example, a well-known phenomenon is that the dislocation velocity is affected by the species and amount of dopant [1]. This means that the dislocation velocity depends on the Fermi level of semiconductors. Another effect is that dislocation velocity is extremely enhanced under the irradiation of laser light or electron beam [2]. This effect is known as radiation-enhanced dislocation glide (REDG), and is explained as the follow. Excess carriers generated by the irradiation of light or electron beam recombine at the dislocation level and the electronic energy released is converted to lattice vibrational energy through multi-phonon emission and effectively assists the dislocation motion. This mechanism is widely known as one of recombination-enhanced defect reactions. On the other hand, it has been intensively studied that the hydrogen incorporated in semiconductors interacts with electrically active defects and passivates their electrical activities [3]. On the basis of these facts mentioned above, we have conceived that if hydrogen atoms in semiconductors interact with dislocations, which are believed to have gap states originating in themselves, their mobility is possibly affected by hydrogen. In fact, it was reported that the flow stress of silicon single crystal is reduced under hydrogen plasma [4]. This strongly suggests that dislocation velocities may be promoted by means of hydrogen plasma irradiation. The purpose of the present work is to directly study the effects of hydrogen on dislocation motion in silicon. In our experiments, we measured dislocation glide velocities at various temperatures under hydrogen plasma and compared them to those measured in the dark. We have discovered for the first time that the dislocation velocities are actually promoted by hydrogen. We present the results here and discuss possible mechanisms of the enhancement.

Experimental procedure.

Samples used to measure dislocation velocities were phosphorus doped FZ Silicon ([P]=5.9x$10^{14}$$cm^{-3}$). The samples were cut from ingots into a rectangular form (about 2x15x0.5mm^3) with the (111) top face and the longest dimension along $[\bar{1}3\bar{2}]$ direction. After the samples were polished mechanically and etched chemically, they were scratched with a diamond point loaded 60gw. Then they were set in a four-point-bending apparatus to be given driving force for dislocation motion. Resolved sheer stress operating on dislocations of $[\bar{1}10]/(11\bar{1})$ slip system was always 68MPa in this study, and the dislocation concerned was 60° type. The double etching method was taken to measure the dislocation velocity. The Sirtl etchant consisting of CrO_3(50g), H_2O(100ml) and HF(100ml) was used to reveal the positions at which dislocations intersect the surface. Hydrogen plasma of 13.56MHz frequency with a power of 50W was operated to incorporate hydrogen into samples. The procedure of measuring dislocation velocities under hydrogen plasma is as follows. Dislocations were introduced by the first loading, and then the samples were exposed to hydrogen plasma at 540°C for 2 hours. During this pre-irradiation process, hydrogen atoms may be incorporated into the samples up to about 2mm that is calculated from the diffusion coefficient which are calculated by extrapolation to this temperature from what was measured at the higher temperature (D=1x$10^{-5}$$cm^2$/s [5]). This process makes sure that dislocations move in a hydrogen-rich environment during the whole second loading period, where the second load was given to the sample at a testing temperature under hydrogen plasma for the duration in which dislocations move by a distance of about 20~30μm. We also measured dislocation velocity under nitrogen plasma to study the effect of plasma light. The plasma conditions were the same as those of hydrogen except for no pre-irradiation process of nitrogen plasma. Spreading resistance (SR) measurements were also done to confirm the introduction of hydrogen atom into samples. Two kinds of crystals were used for SR measurements. One was the same as that used for dislocation velocity measurements and the other was p-type silicon with a boron density of 8.0x$10^{14}$$cm^{-3}$. The reason of using the latter crystal is that boron is known to be more easily passivated by hydrogen than phosphorus and more clearly shows the incorporation depth of hydrogen as the width of the high resistivity layer.

Dislocation velocities under hydrogen plasma irradiation.

Figure 1 shows the temperature dependence of dislocation velocities measured both under hydrogen plasma and in the dark. The velocities under hydrogen plasma are showed by filled circles and those in the dark by open circles. The latter depends on temperature in Arrhenius type, as have been well known. The activation energy was 2.3eV, which is slightly higher than the value, 2.1eV or 2.2eV, that were previously reported [6]. Under hydrogen plasma, the velocities are remarkably enhanced by a factor of 10 to 100 in the temperature range of 390~480°C, but no enhancement effect is seen at temperatures above 500°C. In the former temperature regime, the temperature dependence of dislocation velocities under hydrogen plasma also shows Arrhenius type, but the activation energy is lowered to 1.2eV. Moreover, the pre-exponential factor is several orders smaller than that in the dark. Around the transition temperature (about 500°C), the velocities under hydrogen plasma are discontinuously changed from the enhanced value to the normal one as measured in the dark. This change is far beyond the experimental errors. The reason for such a loss of enhancement is not clear. The above hydrogen-induced enhancement of dislocation motion observed for the first time in our experiments is phenomenologically similar to REDG. In fact, samples were irradiated by plasma light during plasma irradiation. However, the reduction in activation energy, 1.1eV, under hydrogen plasma is different from that of REDG, 0.8eV [2]. In the next section, we will describe the results of further experiments to investigate whether the plasma light enhances dislocation motion via REDG mechanism or hydrogen really plays an essential role in the enhancement.

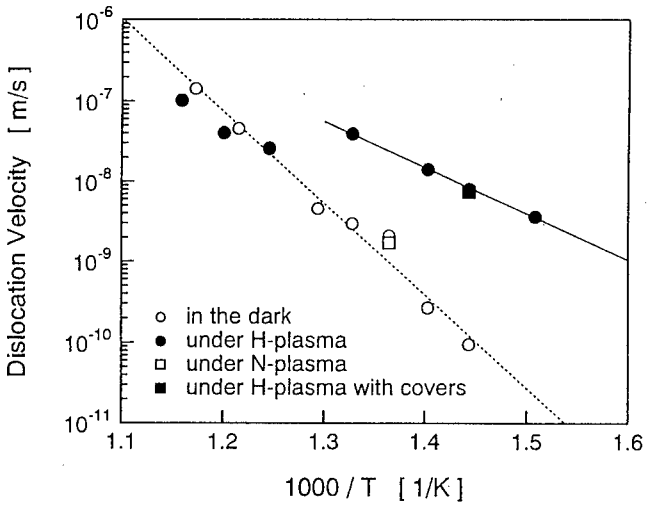


Figure 1. Temperature dependence of dislocation velocities. Filled circles show velocities measured under hydrogen plasma, and open circles show those in the dark. Below 480°C, dislocation velocities under hydrogen plasma are remarkably enhanced and the activation energy was reduced to 1.2eV from the value, 2.3eV, in the dark. The velocities measured under hydrogen plasma with a cover and nitrogen plasma without a cover are also shown by a filled and open square, respectively. See the next section.

Effects of plasma light on dislocation motion.

Hydrogen plasma irradiation may affect dislocation motion in two ways. One is attributed to the incorporation of hydrogen itself into the sample. The other is due to plasma light which may excite excess carriers and cause the enhancement by REDG mechanism. In order to check the latter possibility, we have measured dislocation velocities under nitrogen plasma. Although the emission spectra of both types of plasma are different, nitrogen plasma illuminated the sample with similar intensity to hydrogen plasma. This implies that similar amounts of excess carriers were created by both types of plasma. Nitrogen atoms incorporated in the sample plays no electrical role. Therefore, we could investigate only the effect of plasma light. The result was shown in Fig. 1 by an open square. The velocity measured under nitrogen plasma was obviously the same as that in the dark. We have done a more direct experiment where the samples were exposed to only hydrogen avoiding plasma light. We measured dislocation velocities under hydrogen plasma with covers. The sample was also covered during the pre-irradiation as well. Hydrogen atoms may have diffused to reach the sample surface through the side of covers, but plasma light should have gone straight and not reached the sample. The result was shown in Fig. 1 by a filled square. The measurement was done only at 420°C, but the obtained velocity was obviously the same as that without covers. When we used a larger cover, however, the velocities were intermediate values between the value under hydrogen plasma without covers and that in the dark. (This result is not shown in Fig. 1.) Since the scattered plasma light that reached the sample surface was too weak to give rise to REDG, we consider that the amount of hydrogen atoms incorporated into the sample was less in the case of using a larger cover. Anyway, these experimental results strongly suggest that the plasma light plays no or only little role in promoting the dislocation velocity in the case of hydrogen plasma irradiation. Therefore, the observed enhancement effect must be attributed to the hydrogen atoms themselves incorporated into samples.

Spreading resistance measurements.

We performed SR measurements to confirm the introduction of hydrogen atoms into samples. Figure 2(a) shows the result of SR measurements done on a similar sample in which dislocation velocities were measured under hydrogen plasma. The depth profile of resistivity of this sample (represented by filled circles) shows no difference from that with no treatment (represented by open circles). This does not necessarily suggest that hydrogen atoms were not incorporated into samples during hydrogen plasma irradiation. It has been established that phosphorus atoms are rather hardly passivated by hydrogen and that even if they are once combined with hydrogen, they are reactivated above 150°C. Since the loading temperatures (390~580°C) in our experiments were far above 150°C, phosphorus was not passivated at the loading temperatures. Hydrogen atoms incorporated during the loading period can have been combined with phosphorus atoms only after samples were cooled down below 150°C. However, hydrogen concentration must be lowered down to the solubility at 150°C which may be below $10^3 cm^{-3}$[7]. This may be the reason we could not detect obvious changes in resistivity. For the reason described above, it is the most important point that we should confirm whether the hydrogen atoms generated in plasma actually reach the surface of samples mounted in our bending apparatus. For this purpose, we used a silicon crystal doped with boron, which is known to be more easily passivated by hydrogen than phosphorus. A sample was exposed to hydrogen plasma in the bending apparatus for two hours at 120°C, and SR measurements were done. The results are shown in Fig. 2(b). It is clearly seen that resistivities in the near-surface region, which was about 10μm beneath the surface, were higher than those of an as-grown sample. This means that the hydrogen atoms generated in plasma certainly reach the sample surface. Since the penetration depth of hydrogen during two hours of the pre-irradiation at 540°C is estimated to be more than several hundreds of micrometer [5], we can suppose that dislocations moved in hydrogen-rich environment during the whole second loading period.

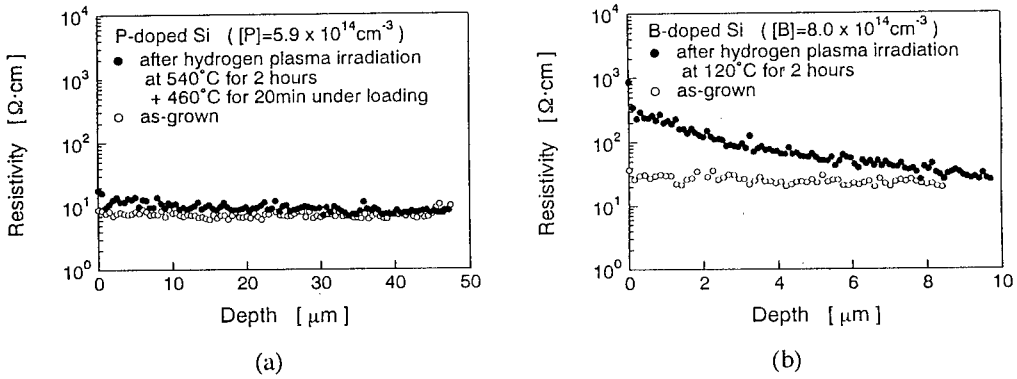


Figure 2. Depth profiles of resistivity measured by SR technique for the phosphorus-doped samples used in dislocation velocity measurements (a), and boron-doped samples (b). One of the former samples was given the same hydrogenation and temperature history as described in experimental procedure. One of the latter samples was exposed to hydrogen plasma at 120°C for two hours. In (a) and (b), filled circles show the results for hydrogenated samples in respective conditions and open circles show those for as-grown samples.

Enhancement mechanism of dislocation motion by hydrogen.

It is widely accepted that dislocation glide motion in semiconductors is controlled by the Peierls mechanism. On the basis of this mechanism, dislocation motion consists of two elementary processes. One is double kink formation process, that is, a part of straight dislocation segment lying in the trough of the Peierls potential overcomes the peak of the potential by thermal fluctuation and a

pair of kinks which have opposite signs to each other is generated. The other is kink migration process, that is, kinks with opposite signs migrate opposite directions along Peierls potential biased by stress and the separation of kink pair becomes large. As a result, the whole segment moves to the next trough. In covalent crystals like semiconductors, Peierls potential is high and the width of kinks is thought to be small. Accordingly, kinks experience the potential of lattice period, called Peierls potential of the 2nd kind, and their migration is thought to become diffusive. Within this picture of dislocation motion, the velocity of dislocation glide is formulated as follows[8]. If the dislocation length is short, a pair of kinks formed on the dislocation line moves in the opposite directions and sweeps the whole line. In this case, dislocation velocity, v, is in proportion to the number of double kink formation site, therefore, to dislocation length L, and is given by

$$v = \frac{2\nu_k \tau b h^2 d}{kT}\left(\frac{L}{2d}\right)\exp\left(-\frac{2F_k + E_m}{kT}\right), \quad (1)$$

where ν_K represents vibrational frequency of kinks, τ resolved shear stress, b the magnitude of the Burgers vector, h the distance between the adjacent Peierls troughs, d the lattice period along a dislocation line, k Boltzmann constant, T temperature, F_K the formation energy of single kink, and E_m the activation energy of kink migration. When dislocation length is long and plural kink pairs generate on it, kinks annihilate by colliding with each other. In this case, dislocation velocity is no longer dependent on the dislocation length and is given by

$$v = \frac{2\nu_k \tau b h^2 d}{kT}\exp\left(-\frac{F_k + E_m}{kT}\right). \quad (2)$$

Previously, dislocation velocity in bulk crystals was thought to be represent by Eq. (2). Recent study however suggests that long dislocations in bulk crystals are effectively partitioned by a characteristic length in which kink collision does not occur and that dislocation velocity in bulk crystals is represented by Eq. (1), in which L is substituted to partition length L_p [9]. Hereafter, we discuss the change of activation energy based on this new model, where the activation energy measured in the dark is $2F_K+E_m$. First we suppose that the reduction of activation energy is due to the passivation of kinks by hydrogen, which may have dangling bond and gap state. No enhancement observed in the high temperature regime may be explained by the dissociation of kink-hydrogen pairs. In this case, the observed reduction of activation energy, 1.1eV, in the low temperature regime corresponds to a change in $2F_K$ and the reduced amount of F_K is 0.55eV. This value should be the binding energy between a kink and hydrogen. This seems, however, so small that we can not explain that the enhancement does occur at temperatures up to 480°C, because the hydrogen-kink pair is thought to dissociate at such high temperatures. For example, in the case of boron passivation, the binding energy of B-H pair is known to be 1.28eV, and they dissociate around 150°C [3]. Therefore, we speculate that hydrogen-induced enhancement is due to rather dynamic effects. The mechanism may be as follows. A hydrogen atom which comes to a site on a dislocation attacks the covalent bond and weakens the atomic binding, so that the atomic jump accompanied by bond switching may become easier. In this model, the promoted elementary process of dislocation motion is different, depending on whether the dislocation site a hydrogen atom attacks is a straight dislocation site or a kink site. In the former case, the enhanced process is double kink nucleation process of the smallest size, and in the latter case, it is kink migration process. Such consideration is very similar to that of the REDG effects if we replace the site of hydrogen attack in the present case with the site of non-radiative recombination in the REDG case. Therefore, we can refer to the theoretical analysis of REDG effects reported by N. Maeda et al. [10]. The result of their analysis is shown in Table 1, where SD denotes straight dislocation sites, K kink sites, ΔE_S the reduction of smallest double kink nucleation energy, ΔE_K the reduction of kink migration energy. On the basis of their analysis, the promotion of smallest double kink nucleation process is necessary for the enhancement of dislocation motion in the case that kink collision does not occur. In this case,

the observed reduction of activation energy, 1.1eV, is ΔE_S. This means that the smallest double kink nucleation preferentially occurs at hydrogenated sites of dislocation lines. Because the number of those sites increases in proportion to the probability that hydrogen atoms encounter the dislocation, the pre-exponential factor of enhanced dislocation velocities is proportional to the hydrogen concentration. If the hydrogen concentration becomes so high that plural double kinks are formed in a partition length, the reduction of activation energy changes to the value of case I or II in Table 1 and the expression of dislocation velocity is also changes from Eq. (1) to Eq. (2). Accordingly, if we measure the activation energy of dislocation velocity for various hydrogen concentrations, it will change from the value, $2F_k+E_m-\Delta E_S$, to $F_k+E_m-(\Delta E_S+\Delta E_k)/2$ or $F_k+E_m-\Delta E_S/2$, by $F_k-(\Delta E_S-\Delta E_k)/2$ or $F_k-\Delta E_S/2$, respectively, as the hydrogen concentration increases. To examine the hydrogen concentration dependence of the activation energy is the future subject.

Table 1. The result of theoretical analysis of the REDG effects by N. Maeda et al. [10]. SD denotes straight dislocation sites, K kink sites, ΔE_S the reduction of smallest double kink nucleation energy, ΔE_k the reduction of kink migration energy. This analysis can apply to the present case provided that 'recombination site' is replaced by 'hydrogenated site'.

	Case	Recombination Site (Hydrogenated Site in the Present Case)	Reduction of Activation Energy
Kink Collision Case	I	SD+K	$(\Delta E_S+\Delta E_k)/2$
	II	SD	$\Delta E_S/2$
	III	K	$\Delta E_k/2$
No Kink Collision Case	IV	SD+K	ΔE_S
	V	SD	ΔE_S
	VI	K	0

Acknowledgments.
We thank K. Inoue and Y. Hakoda of Okayama University for their assistance in our experiments.

References.

1. J. R. Patel and L. R. Testardi, Appl. Phys. Lett. **30**, 3 (1977)
2. K. Maeda, "Dislocations in Solids" ed. F. R. N. Nabarro and M. S. Duesbery (Amsterdam: Elsevier Science) Chap. 54, pp. 445-504 (1996)
3. S. J. Pearton, J. W. Corbett and M. Stavola, "Hydrogen in Crystalline Semiconductors", (Berlin:Springer-Verlag) Chap. 4 (1992)
4. P. Haasen, M. Brede and T. Zhang, Inst. Phys. Conf. Ser. No **104**, 361 (1989)
5. A. Van Wieringen and N. Warmolts, Physica **22**, 849 (1956)
6. H. Alexander, "Dislocations in Solids" ed. F. R. N. Nabarro (Amsterdam: Elsevier Science) Chap. 35, pp115-234 (1986)
7. T. Ichimiya and A. Furuichi, Int. J. Appl. Radiat. Isot. **19**,573 (1968)
8. J. P. Hirth and J. Lothe, "Theory of Dislocations" 2nd ed. (Malabar, Florida:,Krieger) Chap. 15 (1992)
9. Y. Yamashita, K. Maeda, K. Fujita, N. Usami, K. Suzuki, S. Fukatsu, Y. Mera and Y. Shiraki, Philos. Mag. Lett. **67**, 165 (1993)
10. N. Maeda and S. Takeuchi, "Defect Control in Semiconductors" ed. K. Sumino (Amsterdam: North-Holland) pp1397-1402 (1990)

Materials Science Forum Vols. 258-263 (1997) pp. 319-324
© 1997 Trans Tech Publications, Switzerland

HYDROGENATION OF COPPER RELATED DEEP STATES IN n-TYPE Si CONTAINING EXTENDED DEFECTS

J. Kaniewski[1], M. Kaniewska[1], L. Ornoch[1], T. Sekiguchi[2], K. Sumino[2,3]

[1] Institute of Electron Technology, al. Lotników 32/46, 02-668 Warsaw, Poland
[2] Institute of Materials Research, Tohoku University, Sendai 980, Japan
[3] Nippon Steel Corporation 20-1 Shintomi, Futtu, Chiba 293, Japan

Keywords : Si, extended defects, copper related deep states, hydrogenation, DLTS.

Abstract.
Defect impurity levels have been examined in copper-diffused n-type Cz-Si. Specimens free of extended defects as well as containing dislocation loops or stacking faults were contaminated at 1100^0C and cooled slowly to room temperature. The level at about E_C - 0.14eV has been observed in all types of specimens. The thermal activation energy as well as concentration of the deep trap have been influenced by the presence of extended defects. This centre exhibiting acceptor-like character can be completely passivated at 400^0C with atomic hydrogen in Si free of extended defects. In the presence of dislocation loops as well as stacking faults passivation of the state is slightly limited. All other deep states have been passivated completely after hydrogen plasma treatment.

Introduction.
Copper is one of the common metallic impurities incorporated in Si during device fabrication. Cu diffuses into Si as positively charged interstitials [1]. Its solubility in Si is very high, of about $9x10^{17}cm^{-3}$ at 1100^0C [1]. This impurity is extremely rapid diffuser and is difficult to be retained in electrically active form even by quenching of diffused samples [1]. However, deep centres involving Cu are observed by Deep Level Transient Spectroscopy (DLTS) in heat treated silicon.
Most previous work concentrated on Si free from extended defects. Generally it is accepted that hole traps at E_V + (0.20-0.23)eV, E_V + (0.35-0.46)eV [2-5] are associated with Cu. Pearton and Tavendale [4] also observed an additional level at E_V + 0.53eV. These centres are passivated with atomic hydrogen and are restored at 400^0C [4]. With respect to the states in the upper part of the energy gap the situation is much less clear. Lemke [5] observed in n-type float zone silicon one copper related state at high concentration ($8x10^{13}$ cm^{-3}) at E_c - 0.16eV (after diffusion with metal at 1050^0C and slow cooling within 20 min) and identified it as another charge state of the two levels observed in the lower half of the gap. Brotherton *et al.* [3] found this deep level in copper diffused float zone Si after additional annealing at 200^0C for 30 min.
Recently few reports were published on the behaviour of Cu in the presence of well-characterized extended defects in Si. Kaniewska *et al.* [6] found copper related states in n-type vapour phase epitaxial silicon containing oxidation induced stacking faults (OSFs). As

revealed by DLTS the concentration of the deep trap was higher than $1x10^{14}$ cm^{-3} and the thermal activation energy of the trap changed from E_C - 0.25eV in samples diffused at 700^0C to E_C - 0.56eV in samples diffused at 950^0C. The behaviour observed in the presence of bulk stacking faults after contamination at 1100^0C was significantly different. In this case three deep states with thermal activation energy E_C - 0.17eV, E_C - 0.3eV and E_C - 0.44eV have been found [7]. The concentration of the lowest energy state was $\approx 3x10^{13}cm^{-3}$ as revealed by DLTS measurements.

Contamination of Si wafers with Cu is always associated with metal precipitates. The phase of Cu precipitates has been suggested to be a low temperature polymorph of Cu_3Si [8]. Therefore the precipitation of Cu is accompanied by a very large volume expansion of about 150%. The repeated precipitation of Cu results in: nucleation of Cu at pre-existing dislocation, growth of precipitate resulting in the emission of interstitials [9] and unpinning of the dislocation followed by the nucleation of a new precipitate. The characteristics of Cu precipitation in Si containing dominantly either bulk stacking faults or punched-out dislocations have been determined by transmission electron microscopy (TEM) and the electron-beam-induced current (EBIC) technique. Shen *et al.* [10,11] observed in Cz-Si that Cu precipitation depends on contamination level, cooling rate as well as on type of extended defect. Colonies of Cu precipitates developed irrespective of cooling rate, apparently originating from punched-out dislocations developed around oxygen precipitates. In heavily contaminated samples cooled fast from the contamination temperature, Cu also precipitated on Frank partial dislocations bounding stacking faults, During slow cooling, precipitation of Cu took place on Frank partials only in lightly contaminated but never in heavily contaminated specimens. It was concluded that punched-out dislocations are more favourable precipitation sites for Cu than Frank partials of stacking faults.

Here we present results of DLTS studies performed on the set of Si samples containing dislocation loops or stacking faults contaminated with Cu. Influence of hydrogenation on electrical activity of copper related states is discussed.

Experimental details.

Specimens were prepared from n-type, P-doped, 28 Ωcm Cz-Si grown in <111> direction, with an initial oxygen concentration of $1x10^{18}cm^{-3}$ and a carbon concentration less than $2x10^{16}cm^{-3}$. The specimens were contaminated with Cu from high purity foils during annealing for 1h at 1100^0C, performed in evacuated quartz capsules, followed by slow cooling to room temperature. Copper was diffused into three groups of samples:

- as grown, free of extended defects
- containing dislocation loops (DLs) at a density of $6x10^6cm^{-2}$
- containing stacking faults (SFs) at a density of $2x10^5cm^{-2}$.

High density of DLs and SFs was induced by oxygen precipitation by means of following multistep annealing: for DL - 600^0C/20h+725^0C/15h+1000^0C/15h, and for SF 725^0C/15h+1000^0C/15h, respectively. The reference specimens (AGRef), i.e. not intentionally contaminated, were also annealed at 1100^0C for 1h. The specimens were stored at room temperature for long time. The structure of extended defects generated during processing was studied by transmission electron microscopy and the results are presented elsewhere [7,10,11].

Hydrogen plasma treatment of all types of the samples was done at 400^0C for 30min in a clean metal-free plasma chamber made of high-purity quartz. The plasma was excited by microwave with a frequency of 2.45 GHz. The plasma pressure was about 10 torr.

Schottky contacts were formed by evaporation of Au. The DLTS studies were performed using computer controlled Semitrap DLS-82E system.

Experimental results.

As it was confirmed by DLTS spectra, presented in Fig. 1, as grown samples were free of deep states. However, the samples free of extended defects contaminated with copper exhibited three peaks; the main one at about 100K and two additional much smaller at about 175K and about 300K. The low temperature peak, of similar height was also found in

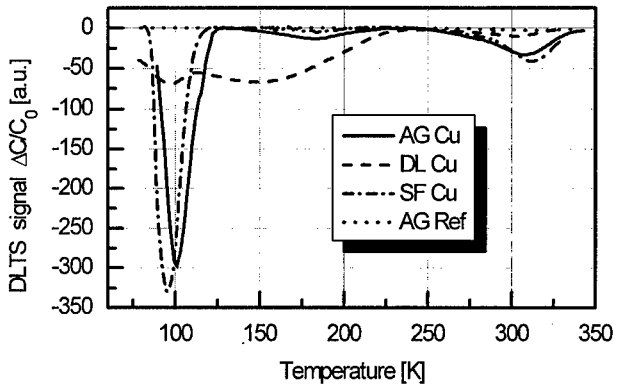


Fig. 1. DLTS spectra for the majority carrier traps in n-type Si: AGRef - as grown, AGCu - as grown contaminated with Cu, DLCu - containing dislocation loops and contaminated with Cu, SFCu - containing stacking faults and contaminated with Cu. Emission rate $e_n = 100s^{-1}$.

copper diffused samples containing SFs. In the case of copper diffused samples containing DLs, the low temperature peak is significantly reduced and additional peak at 150K appears. Due to the very high population changes of the low temperature level, DLTS technique did not allow for proper determination of deep trap concentration. Therefore capacitance-temperature characteristics were measured - Fig. 2. Huge capacitance changes are observed in the copper diffused samples. The effect was very pronounced since at liquid nitrogen temperature capacitance of the as grown material contaminated with Cu as well as that containing stacking faults and contaminated with Cu is very small. In the case of contaminated samples containing dislocation loops capacitance changes are significantly smaller.

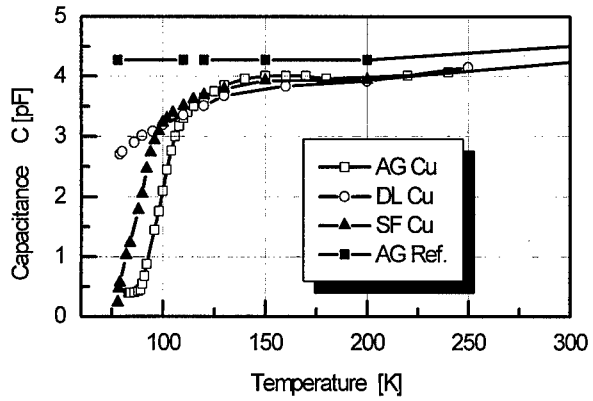


Fig. 2. Thermally stimulated capacitance of n-type Si samples: AGRef - as grown, AGCu - as grown contaminated with Cu, DLCu - containing dislocation loops and contaminated with Cu, SFCu - containing stacking faults and contaminated with Cu.

It is well known that deep levels introduced into silicon by metal contamination can be passivated by reaction with atomic hydrogen. The effect often is interpreted as a hydrogen passivation of dangling bonds. Therefore in order to provide a greater insight into a microstructure of the traps similar studies on samples additionally hydrogenated have been performed. DLTS spectra presented in Fig. 3 show that deep states completely disappear in contaminated samples free of extended defects. Simultaneously, in samples containing DLs or SFs the low temperature DLTS peak is significantly reduced. The changes in the deep trap concentration are better seen in Fig. 4. Only small thermally stimulated capacitance changes

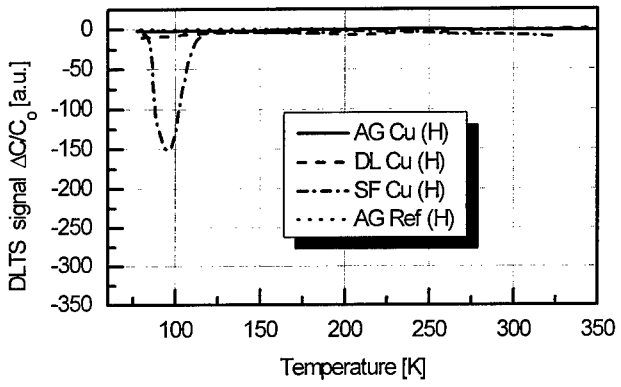


Fig. 3. DLTS spectra for the majority carrier traps in n-type Si: AGRef(H) - hydrogenated as grown, AGCu(H) - as grown contaminated with Cu and hydrogenated, DLCu(H) - containing dislocation loops contaminated with Cu and hydrogenated, SFCu(H) - containing stacking faults contaminated with Cu and hydrogenated. Emission rate $e_n = 100s^{-1}$.

were observed in samples containing dislocation loops or stacking faults contaminated with Cu - Fig. 4. The value of the capacitance changes is similar, independently on the type of extended defect.

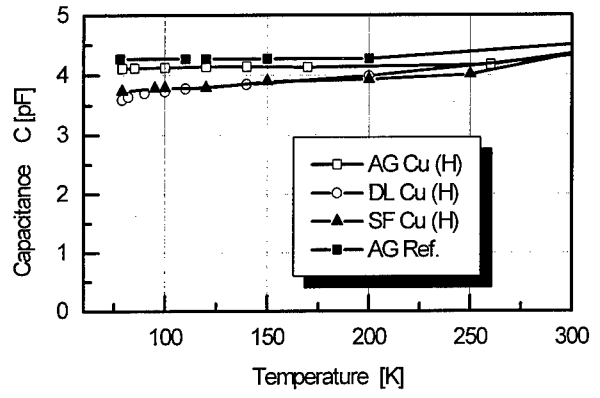


Fig. 4. Thermally stimulated capacitance of n-type Si samples: AGRef(H) - hydrogenated as grown, AGCu(H) - as grown contaminated with Cu and hydrogenated, DLCu(H) - containing dislocation loops contaminated with Cu and hydrogenated, SFCu(H) - containing stacking faults contaminated with Cu and hydrogenated.

Discussion.

The DLTS spectra in Fig. 1 and Fig. 3 show similar low temperature peak. It should, however, be noted that the DLTS peak appears at slightly different temperatures. The effect is also seen in the Arrhenius plot as determined from DLTS studies - Fig. 5. The thermal activation energy of the deep state in samples free of extended defects was found to be 0.14eV with respect to the conduction band. Arrhenius plots for the states in the presence of DLs and SFs are slightly

different and are shown in Fig. 5. For comparison results of Brotherton *et al.* [3] are also included. Capacitance changes (Fig. 2) suggest two possible origins of the low temperature peak; either Cu and P can easily form deep complex in Si and nearly all phosphorus atoms are complexed or this centre existing at high concentration exhibits acceptor like character trapping most of electrons. Pairing between copper (substitutional triple charged acceptor) and donor impurities have been considered by Hall and Racette [12]. However, it is supposed that the mechanism would be effective in highly P doped silicon [13].

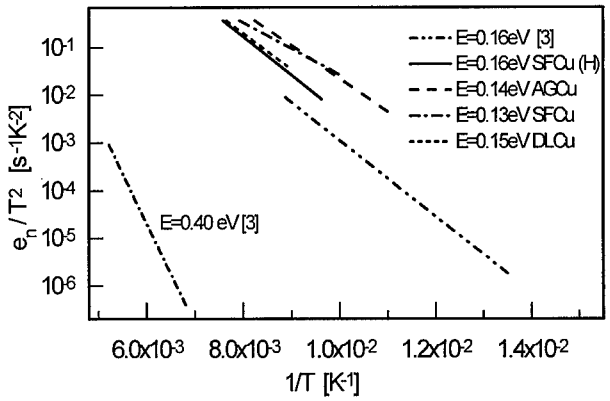


Fig. 5. Arrhenius plot of deep states involving copper in n-type Si.

Additional measurements of capture kinetics of electrons at this centre proved its repulsive character. Similar result was obtained by Brotherton *et al.* [3] for the level at E_C - 0.16eV (see Fig. 5). The electron capture cross section of $3x10^{-17}cm^2$ for the level would be remarkably low for such a shallow level if it were a neutral acceptor. Previous measurements of the electron capture cross section for neutral acceptor with different energy level would lead to expected value of $\sim 10^{-14}cm^2$. In view of this large difference it was concluded that the centre is negatively charged before electron capture. The experimental results show that low temperature peak is passivated after hydrogenation. It is predicted that hydrogen is most strongly attracted to defects or impurities with vacancy-like properties. Therefore it is expected that acceptors would be most susceptible to hydrogen passivation. All this support acceptor-like (probable multiple acceptor) character of the centre.

Repulsive behaviour of the centre for electron capture could suggest its correlation with extended defect like dislocation loop or stacking fault. However we did not found any correlation of this defect concentration with the extended defects (DLs or SFs), intentionally induced with high densities in the specimens studied. The SFs does not influence concentration of the E_C - 0.14eV level while in the presence of DLs its concentration was even lower than found in Cu contaminated as-grown specimens.

Similarities of DLTS characteristics of the low temperature trap and the trap labelled A or 1 at E_C - 0.19eV previously observed in Cu contaminated n-type Si containing oxidation induced stacking faults (OSFs) [6] suggest its common origin. Also in that case we were not able to find any correlation between distribution of the trap concentration and a penetration depth of OSFs induced at the surface.

Results from TEM and temperature dependent EBIC studies [10,11] showed that in heavily contaminated samples cooled slowly, similar to those studied here, dislocation loops were more favourable precipitation sites for Cu than Frank partials of stacking faults. Indeed in

DLTS spectra presented in Fig. 1 similar behaviour can also be found. In the case of sample contaminated with Cu and containing dislocation loops one can notice additional DLTS peak at about 150K, characteristic for cooper decorated extended defect [6]. Simultaneously the height of low temperature peak (at about 100K) is reduced, proving that significant part of diffused cooper atoms has been consumed by dislocation loops. The mentioned effect of copper decoration of Frank partials have not been found. Nevertheless, it should be stressed that the effect of decoration of dislocation loops cannot be always observed. Previously [7] in the similarly prepared specimens we did not notice any changes of electrical activity in the presence of dislocation loops. These discrepancies may be understood assuming changes in precipitation colonies being result of different cooling rate.

Conclusions.

We have demonstrated that in heavily contaminated and slowly cooled n-type Si specimens Cu forms deep centre with thermal activation energy about E_C - 0.14eV at high concentration. This centre exhibiting acceptor-like character captures electrons very effectively. In the presence of dislocation loops the concentration of the deep state is reduced due to simultaneous decoration of the dislocation loops. In n-type Si free of extended defects this deep level can be completely passivated at 400^0C with atomic hydrogen. In the presence of dislocation loops or stacking faults passivation of the deep state is limited. All other deep states have been passivated completely after hydrogen plasma treatment.

References.

1. E.R. Weber, Appl. Phys. **A30**, 1 (1983).
2. J. L. Benton and L.C. Kimerling, J. Electrochem. Soc. **129**, 2098 (1982).
3. S.D. Brotherton, J.R. Ayres, A. Gill, H.W. van Kesteren and F.J.A.M. Greidanus, J. Appl. Phys. **62**, 1826 (1987).
4. S.J. Pearton, A. and J. Tavendale, J. Appl. Phys. **54**, 1375 (1983).
5. H. Lemke, Phys. Stat. Sol. (a) **95**, 665 (1986).
6. M. Kaniewska, J. Kaniewski and A.R. Peaker, Mater. Sci. Forum **83**, 1457 (1992).
7. J. Jabłoński, J. Kaniewski, M. Kaniewska, T. Sekiguchi, L. Ornoch and K. Sumino, Mater. Sci. Forum **143-147**, 1517 (1994).
8. J.K. Solberg, Acta Crystall. A **34**, 684 (1978).
9. M. Seibt and W. Schroter, Solid State Phenom. **19&20**, 283 (1991).
10. B. Shen, T. Sekiguchi, J. Jabłoński and K. Sumino, J. Appl. Phys. **76**, 4540 (1994)
11. B. Shen, T. Sekiguchi, R. Zhang,Y.Shi, Y.D. Zheng and K. Sumino, Phys. Stat. Sol. (a) **155**, 321 (1996)
12. R.N. Hall and J.H. Racette, J. Appl. Phys. **35**, 379 (1964).
13. E.R. Weber and D. Gilles, Defects Control in Semiconductors, ed. K. Sumino (North-Holland, Amsterdam, 1990) p. 89.

Materials Science Forum Vols. 258-263 (1997) pp. 325-330
© 1997 Trans Tech Publications, Switzerland

HYDROGENATION OF DEEP DEFECT STATES IN n-TYPE Si CONTAINING EXTENDED DEFECTS AND TRANSITION METAL (Ni or Fe)

M. Kaniewska[1], J. Kaniewski[1], L. Ornoch[1], T. Sekiguchi[2], K. Sumino[2,3]

[1] Institute of Electron Technology, al. Lotników 32/46, 02-668 Warsaw, Poland
[2] Institute of Materials Research, Tohoku University, Sendai 980, Japan
[3] Nippon Steel Corporation 20-1 Shintomi, Futtu, Chiba 293, Japan

Keywords : Si, extended defects, nickel and iron related deep states, hydrogenation, DLTS.

Abstract.
Deep Level Transient Spectroscopy (DLTS) was used to characterise deep defect states in n-type Cz-Si contaminated with Ni or Fe in the presence of dislocation loops or stacking faults. Emission characteristics of the states have been found to be dependent on the kind of metal as well as the type of extended defect. They became similar to each other after hydrogenation, which partially passivated the states. Two deep levels showing the emission characteristics similar to those of A and C_1 deep traps (Omling's notation) present in plastically deformed Si have been observed.
Fe related deep level at about E_C - 0.5eV, often reported in literature, is found to be thermally unstable and its characteristics depend on annealing at temperatures higher than 100^0C.

Introduction.

Presently, Czochralski grown Si (Cz-Si) is a basic material, commonly used in semiconductor technology. Various kinds of microdefects are introduced into Si wafers during high temperature processing for device fabrication due to oxygen precipitation. The main defects are extended defects, such as bulk stacking faults bounded by Frank partial dislocations and punched-out dislocations. Meanwhile, Si wafers are easily contaminated by metallic impurities at high temperatures, especially those exhibiting high diffusivity and solubility. Therefore, the behaviour of Ni and Fe as common 3d-metallic contaminants in such environment is essential.
Present knowledge on Ni and Fe related deep states is mainly based on the results obtained on Si free from extended defects. Ni, similarly as Cu, diffuses into Si as positively charged interstitials [1]. Its solubility is very high, of about $4x10^{17}cm^{-3}$ at 1100^0C. Its diffusivity does not vanish at room temperature although the value of diffusivity decreases drastically. It is, however sufficiently high to enable both out-diffusion of atoms to the wafer surfaces and precipitation by homogeneous nucleation mechanism. Large discrepancies are noted regarding electrical properties of Ni in Si. There are few studies of nickel in silicon using space-charge transient techniques. Graff and Pieper [2] reported only one donor level at E_V + 0.15eV with a capture cross-section of $2.7x10^{-15}cm^2$. This is in disagreement with the work of Pearton and Tavendale [3], who observed three levels at E_V + 0.18eV, E_V + 0.21eV and E_V + 0.33eV with capture cross sections of $6x10^{-15}$ cm^2 , $\cong 10^{-20}$ cm^2 and 10^{-20} cm^2, respectively, in Ni-doped p-type silicon. Indusekhar and Kumar [4] found Ni related levels definitely at E_V + 0.32eV and probably at

E_V + 0.28eV and E_V + 0.50eV. Additionally, a complicated annealing behaviour of main Ni-related level was reported and was explained on the basis of the formation and dissociation of a Ni-vacancy complex. Lemke [5] observed by DLTS a donor level at E_V + 0.17eV and an acceptor level at E_C - 0.38eV and interpreted them as related to Ni^+ and Ni^-, respectively. After contact fabrication or annealing at temperatures lower than 400^0C decreases in the concentrations of both Ni^+ and Ni^- in the surface regions of crystals were observed. Reactions were associated with the production of about ten impurity centres including that at E_C - 0.22eV when Pd-contacts were used. Nakashima *et al* [6] concluded that E_V + 0.16eV and E_C - 0.45eV levels are associated with different charge state of Ni at substitutional sites. Mostly Ni has been introduced by diffusion. On the other hand, Rohatgi *et al.* [7] investigated the deep levels due to various impurities incorporated during the Czochralski growth of silicon and did not detect any level due to Ni. Fe, in contrast to Ni diffuses as neutral interstitials. Its solubility is about $2x10^{15}cm^{-3}$ at 1100^0C. The diffusivitiy of this lighter 3d transition metal is too small to enable out-diffusion or precipitation by homogeneous nucleation mechanism. This metal can be quenched in on interstitial sites. The corresponding donor level is located at E_V + 0.4eV as determined by DLTS [8 and Ref. therein]. In p-type Si pairing of interstitial Fe atoms with shallow acceptors is observed. The second level at E_C - (0.5-0.6)eV in Si:Fe, with large spread of value of activation energy, have been often reported [8 and Ref. therein].

Recently it has been found by Shen *et al.* [9] that segregation behaviour of Ni and Fe on extended defects depends not only on the species of impurities, but also significantly on the cooling rate of the specimen after contamination. In slowly cooled specimens Ni decorates Frank partials weakly. A high density of Ni precipitates was found on Frank partials when specimens were cooled fast. Fe decorated Frank partials both in slow and fast cooled specimens. However, the amount of Fe on Frank partials was larger in slow cooled specimen than in a fast cooled one.

DLTS studies performed on n-type Cz-Si specimens containing stacking faults, slowly cooled after contamination with Ni, revealed two deep levels at concentrations $\geq 1x10^{13}cm^{-3}$ at E_C - 0.21eV and E_C - 0.44eV [10]. In the case of Fe contaminated samples the spectra were dominated by a deep trap at E_C - 0.54eV and deep centres at E_C - 0.49eV and E_C - 0.19eV were present only in low concentration. It has been concluded that in the presence of stacking faults the levels revealed in DLTS spectra are displaced towards lower temperatures, and their thermal activation energies are lowered after higher level contamination with Ni.

Experimental details

Specimens were prepared from n-type, P-doped, 28 Ωcm Cz-Si grown in the <111> direction, with an initial oxygen concentration of $1x10^{18}$ cm^{-3} and a carbon concentration less than $2x10^{16}$ cm^{-3}. The specimens were contaminated from high purity wires during annealing, performed in evacuated quartz capsules. Contamination with Ni was performed during 1h at 1100^0C whereas, with Fe during 4h at the same temperature 1100^0C, followed by slow cooling to room temperature. Metals were diffused into three groups of samples:

- as grown, free of extended defects
- containing dislocation loops (DLs) at a density of $6x10^6cm^{-2}$
- containing stacking faults (SFs) at a density of $2x10^5cm^{-2}$.

High density of DLs and SFs was induced by oxygen precipitation by means of following multistep annealing: for DL - 600^0C/20h+725^0C/15h+1000^0C/15h, and for SF-725^0C/15h+1000^0C/15h, respectively. Hydrogen plasma treatment for all types of samples was done at 400^0C, for 30min in a clean metal-free plasma chamber made of high-purity quartz. The plasma was excited by microwaves with a frequency of 2.45 GHz. The plasma pressure was about 10 torr.

Finally, Schottky barriers were fabricated by evaporating Au. DLTS studies were performed using computer controlled Semitrap DLS-82E system.

Experimental results.

Majority carrier DLTS spectra in samples contaminated with Ni are presented in Fig. 1. No well resolved peak have been found in as grown specimens diffused with Ni. Instead, almost featureless band in the (150-350)K temperature range have been detected which suggests the existence of a few deep levels at low concentrations, below $2x10^{12}cm^{-3}$. In the case of Ni-contaminated specimens with dislocation loops three well defined peaks of similar height have been observed at about 100K, 200K and 310K. In samples containing stacking faults, Ni related levels have been detected at high concentrations.

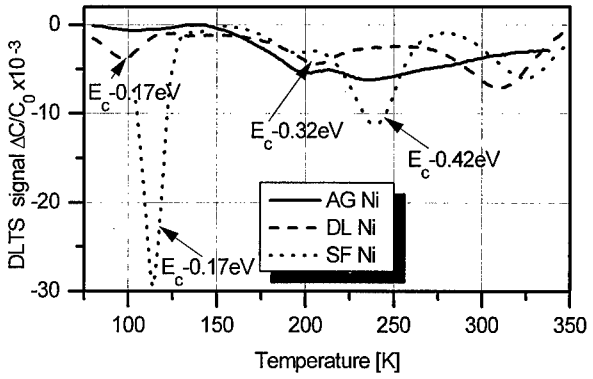


Fig. 1. DLTS spectra for the majority carrier traps in Ni diffused n-type Si; AGNi-as grown contaminated with Ni, DLNi-containing dislocation loops and contaminated with Ni, SFNi-containing stacking faults and contaminated with Ni. Emission rate $e_n = 100\ s^{-1}$.

Electrical properties of Si:Fe seems to be different from those of the Si:Ni. The DLTS spectra obtained for as grown Fe contaminated specimens show one dominant peak, above 300K-Fig. 2. The high temperature peak, together with two other peaks of similar heights at about 100K and 180K have been also observed in Fe contaminated specimens containing dislocation loops.

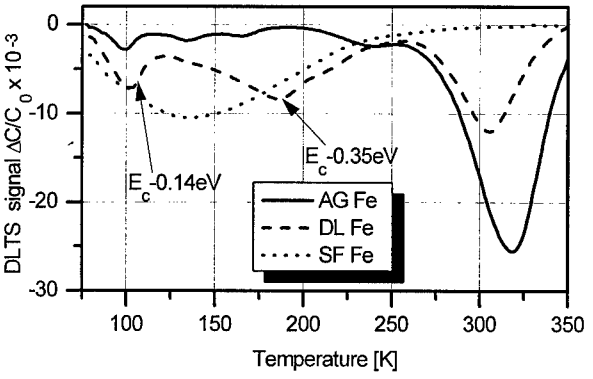


Fig. 2. DLTS spectra for the majority carrier traps in Fe diffused n-type Si: AGFe-as grown contaminated with Fe, DLFe-containing dislocation loops and contaminated with Fe, SFFe-containing stacking faults and contaminated with Fe. Emission rate $e_n = 100\ s^{-1}$.

These states were absent in Fe contaminated specimens containing dominantly stacking faults. In such specimens a broad band in DLTS signal has been detected. Hydrogenation has been found to be effective in passivation of the deep states detected in as grown specimens and in specimens containing stacking faults, both contaminated with Ni - Fig. 3.

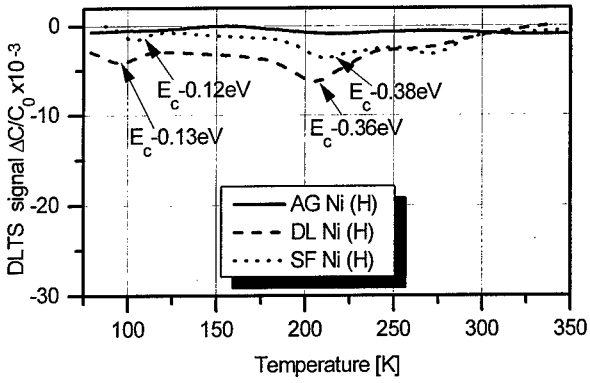


Fig. 3. DLTS spectra for the majority carrier traps in Ni diffused and hydrogenated n-type Si: AGNi(H)-as grown contaminated with Ni and hydrogenated, DLNi(H)-containing dislocation loops contaminated with Ni and hydrogenated, SFNi(H)-containing stacking faults contaminated with Ni and hydrogenated. Emission rate $e_n = 100\ s^{-1}$.

The concentrations of all deep centres in those groups of specimens were reduced by about one order of magnitude, to the values of about $5x10^{11}cm^{-3}$. In contrast to that no changes due to

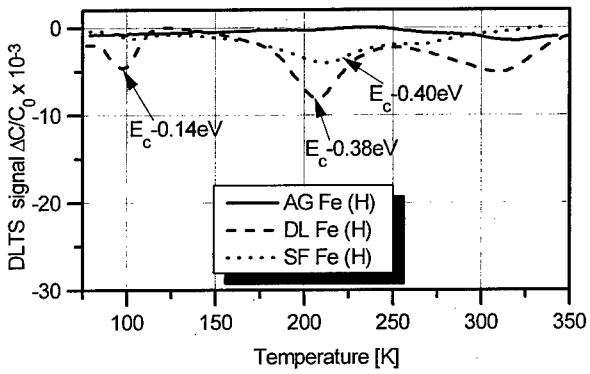


Fig. 4. DLTS spectra for the majority carrier traps in Fe diffused and hydrogenated n-type Si: AGFe(H)-as grown contaminated with Fe and hydrogenated, DLFe(H)-containing dislocation loops contaminated with Fe and hydrogenated, SFFe(H)-containing stacking faults contaminated with Fe and hydrogenated. Emission rate $e_n = 100\ s^{-1}$.

hydrogenation were observed for states at about 100K and about 200K in Si:Ni containing dislocation loops. Similar effect has been observed in specimens contaminated with Fe - Fig. 4. Only minor changes in DLTS spectra of the both deep centres have been found.

Discussion.

Comparison of the DLTS spectra in Figs. 1 and 3 gives some insight to the nature of the DLTS peaks associated with extended defects in specimens contaminated with Ni. In specimens containing stacking faults two peaks were found at about 120K and 230K before hydrogenation. The energy levels associated with these peaks were determined to be E_C - 0.17eV and E_C - 0.42eV, respectively. The levels are rather close to the levels, E_C - 0.21eV and E_C - 0.44eV, which were observed in a previous work on Si containing stacking faults and contaminated with Ni [10]. Hydrogenation reduces the concentrations of these deep levels and, at the same time, changes their thermal activation energies as seen in Fig. 3. The effect of hydrogenation is better seen in the Arrhenius plot in Fig. 5. The peak observed around 100K is labelled ***I*** while that around 200K is labelled ***II***. Hydrogenation of specimens containing stacking faults and contaminated with Ni results in the shift of both peaks to low temperatures, i. e. to the right hand side in Fig. 5. The plot of DLTS peaks at about 100K and 200K observed in specimens containing dislocation loops and contaminated with Ni are not shifted by hydrogenation as seen

in Fig. 5. It is interesting to note that the plot for the specimens containing stacking faults after hydrogenation almost coincides with those for the specimens containing dislocation loops.

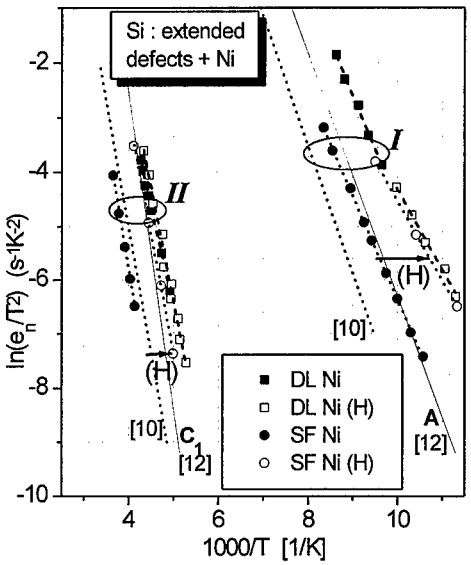


Fig. 5. Arrhenius plot of deep states involving Ni in the presence of extended defects in n-type Si.

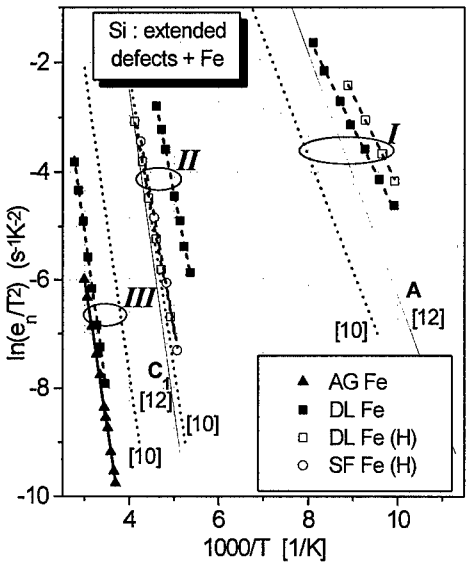


Fig. 6. Arrhenius plot of deep states involving Fe in the presence of extended defects in n-type Si.

The effects of hydrogenation on the deep levels in specimens doped with Fe are seen in Figs. 2, 4 and 6. A peak is observed at rather high temperature around 300K in as grown specimens and also in those containing dislocation loops. The level giving rise to this high temperature peak in as grown specimens is passivated almost completely by hydrogenation while some part of the level in dislocated specimens remains unpassivated. This level is thermally unstable and can be regenerated by annealing at temperature higher than about 100^0C. The energy of the level was determined to be E_C - 0.47eV. The Arrhenius plot for this level is labelled ***III*** in Fig. 6. The large discrepancy in the energies of deep levels reported by different authors [8 and Ref. therein, 10] might be attributed to the peculiar annealing behaviour of the level just mentioned. However, as seen in Fig. 1, the high temperature peak is observed also in specimens contaminated with Ni even though the height is small. Thus, the possibility that it results from unintentional contamination may not be excluded.

No well defined DLTS peaks have been obtained in specimens containing stacking faults and contaminated with Fe in contrast to the specimens contaminated with Ni. Only a broad band in the temperature range (80 - 250)K has been revealed in such specimens. Such a broad band was assigned to be related to stacking faults in a previous paper [11]. Contamination with Fe enhances the height of DLTS signal related to stacking faults by a factor of about 3 while conserving the broad character. Fe atoms in this type of specimens were observed to be precipitated on Frank partial dislocations bounding stacking faults by means of heterogeneous process [9].

Hydrogenation has been found to passivate the deep levels in Si containing stacking faults and contaminated with Fe. In specimens containing dislocation loops and contaminated with Fe the

states giving rise to the DLTS peaks at about 100K and 200K are not effectively passivated by hydrogenation. However, their emission characteristics are modified as seen their Arrhenius plots (groups labelled ***I*** and ***II***) in Fig. 6. It is worth noting that the emission characteristic of the level belonging to the group labelled ***II*** in specimens containing dislocation loops and that in specimens containing stacking faults coincide other after hydrogenation.

The Arrhenius plots in Figs. 5 and 6 obtained in the present work are compared with that for the deep levels, termed A and C_1 , in plastically deformed Si reported by Omling *et al.* [12]. The plot for the state A is rather close to that of the centre labelled ***I*** of the present work. That for the C_1 is very close to that of the centre labelled ***II***. These observations indicate that both the A and C_1 states are related to extended defects decorated with metallic impurities. Contamination of a specimen with metallic impurities is inevitable in plastic deformation of the specimen at an elevated temperature.

It is interesting to note that hydrogenation seems to modify the structure of an extended defect in the same way irrespective of the nature of the impurities segregated on the defect and also on the type of defect.

Conclusions.

DLTS studies of deep levels in n-type Si containing stacking faults or dislocation loops and contaminated with Ni or Fe have revealed two groups of deep levels which give rise to DLTS peaks at about 100K and 200K. Hydrogenation of the specimens modifies the emission characteristics of the two groups of levels in such a way that they become independent of the impurity species and the type of extended defects. The emission characteristics of the A and C_1 traps reported for plastically deformed Si are similar to those of the deep levels found in the present work.

Hydrogenation passivates the deep levels related to stacking faults more effectively than those related to dislocation loops.

References.

1. E.R. Weber, Appl. Phys. **A30**, 1 (1983).
2. K. Graff and H. Pieper , J. Electrochem. Soc. **128**, 669 (1981)
3. S.J. Pearton and A.J. Tavendale, J. Appl. Phys. **54**, 1375 (1983).
4. H. Indusekhar, V. Kumar, J. Appl. Phys. **61**, 1449 (1987).
5. H. Lemke, Phys. Stat. Sol. (a) **99**, 205 (1987).
6. A. Rohatgi, J. Davis, R. Hopkins and P. McMullin, Solid-State Electron. **26**, 1039 (1983)
7. H. Nakashima, T. Sadoh, H. Kitagawa and K. Hashimoto, Mater. Sci. Forum **143-147**, 761 (1994).
8. K. Graff, Mater. Sci. Eng. **B4**, 63, (1989)
9. B. Shen, T. Sekiguchi, R. Zhang, Y. Shi, Y.D. Zheng, and K. Sumino, Phys. Stat. Sol. (a) **155**, 321 (1996).
10. J. Jabłoński, J. Kaniewski, M. Kaniewska, T. Sekiguchi, L. Ornoch and K. Sumino, Mater. Sci. Forum **143-147**, 1517 (1994).
11. M. Kaniewska, J. Kaniewski and A.R. Peaker, Mater. Sci. Forum **83-87**, 1457 (1992).
12. P. Omling, E.R. Weber, L. Montelius, H. Alexander and J. Michel, Phys. Rev. B **32**, 6571 (1985).

Materials Science Forum Vols. 258-263 (1997) pp. 331-336
© 1997 Trans Tech Publications, Switzerland

METASTABLE DEFECTS AND RECOMBINATION IN HYDROGENATED AMORPHOUS SILICON

E. Morgado[1] and R.T. Henriques[2]

Instituto Superior Técnico, Technical University of Lisbon, Av. Rovisco Pais,1000 Lisboa, Portugal
[1]Department of Electrical Engineering and Centro de Física Molecular
[2]Department of Chemical Engineering

Keywords: amorphous silicon, metastable defects, recombination, ESR, PDS.

Abstract. Metastable defects have been created by light exposure in thin films of a-Si:H. Effects on the electronic properties have been investigated and the interpretation is based on a proposed recombination model. Changes in the defect density have been measured by Photothermal Deflection Spectroscopy (PDS) and Electron Spin Resonance (ESR) for different exposure times. The samples have been also characterized by dark conductivity and photoconductivity as a function of light flux. A number of parameters have been monitored along the photodegradation process: Fermi level position, dangling bond density, Urbach slope, density of paramagnetic centers, photoconductivity and the exponent of its light intensity power dependence. The experimental results are consistent with numerical calculations with a recombination model involving localized band tail states and one class of correlated dangling-bond states. The calculations allow to explain light-soaking effects on the transport and recombination properties of the a-Si:H films as a consequence of changes in the electronic occupation of the gap states produced by light-induced defects.

Introduction

The photodegradation of the electronic properties of a-Si:H is a subject of extensive research since the performance of a-Si based devices is significantly affected by exposure to light, with emphasis for p-i-n structured photovoltaic cells. Since the discovery of the Staebler-Wronsky effect [1] many attempts to explain the mechanisms of generation of metastable defects in a-Si:H by exposure to light have been proposed [2]. In the present paper we concentrate on the relations between the light-induced defects and the degradation of the photoconductivity in a-Si:H. The observed experimental trends are explained with the help of numerical calculations with a recombination model which takes into account the characteristic features of the density of states in the gap of amorphous silicon.

Experimental

The experiments have been performed on a nitrogen doped a-Si:H sample produced by r.f glow-discharge in a N_2-SiH_4 gas mixture and details are described elsewhere [3]. Degradation of the film has been performed with light from a tungsten-halogen lamp at an incident power density of 100 mW/cm^2. Glass substrates were used for the conductivity and Photothermal Deflection Spectroscopy (PDS) measurements, and crystalline silicon substrates were used for the Electron Spin Resonance (ESR) measurements. ESR spectra were collected in a BRUKER ESP300 X-band spectrometer at room temperature (294 K). The microwave power was 0.32 mW at 9.45 GHz and the modulation amplitude was 5.0 G_{pp} for all spectra. The density of paramagnetic centers was obtained from the intensity of the g = 2.0055 line in the spectra which is related to the neutral state of the Si dangling bond defect and is presented in relative units. The defect density was estimated from the excess integrated absorption in the PDS spectra, $N(cm^{-3}) = 7.9 \times 10^{15} \int \exp(\alpha - \alpha_0 \exp(E/E_0))$, where E_0 is the Urbach parameter [4]. E_0 was estimated after differentiating the PDS absorption spectrum, since the density of states in the gap N(E) is proportional to $d\alpha/d(h\nu)$, where α is the absorption coefficient and $h\nu$ is the radiation energy [5] Photoconductivity measurements were performed under white light in the range of photogeneration rates $G \approx 10^{18} - 10^{21}$ cm^{-3} s^{-1}, using

neutral density attenuation filters. All the measurements have been performed on the same film after subsequent steps of degradation.

The recombination model

In the present paper we report results of numerical calculations with a recombination model involving exponential band tails of localized states and one class of correlated dangling-bond states. The recombination kinetics are assumed to obey Shockley-Read statistics. Only transitions between localized and extended states are considered. Simmons-Taylor statistics [6] describes the occupation of the conduction and valence band tails of localized states, with exponential energy distributions $N_{ct}(E) = N(E_c) \exp [(E - E_c)/E_{oc}]$ and $N_{vt}(E) = N(E_v) \exp [(E_v - E)/E_{ov}]$; E_c and E_v are the mobility edges of the conduction and valence bands, respectively. The dangling-bond defect is represented by correlated discrete levels for the states of charge D^+, D^0, D^- with occupancies f^+, f^o, f^- ruled by correlated electron statistics [7].

It was already shown that the model can reproduce the Fermi level, light intensity and temperature dependences of photoconductivity and carrier lifetimes including the phenomena of thermal quenching and supralinearity [8, 9].

The basic equations are:

i) The equilibrium of charge flows in the conduction band,

$$G = R_{db} + R_{ct} + R_{vt} , \qquad (1)$$

where G is the photogeneration rate and $R_{db,ct,vt}$ are net recombination rates (i.e., including capture and emission terms) for, respectively, the dangling-bond states, the conduction band-tail states and the valence band-tail states.

ii) The charge neutrality equation, where it is assumed that the conduction band-tail states are acceptor-like and the valence band-tail states are donor-like ,

$$n - p + N_D f^- - N_D f^+ + n_t - p_t = Q , \qquad (2)$$

where n an p are the free electrons and holes, respectively, N_D is thr defect density, n_t is the density of trapped electrons in the conduction band tail and p_t is the density of trapped holes in the valence band tail .

The term Q in Eq. (2) accounts for the charge in the dopant centers and is zero for undoped material, positive for n-type and negative for p-type. It is assumed that the occupation of dopant states is not significantly altered neither by light nor by temperature.

Results

In Figs. 1, 2 and 3, the experimental results are shown as a function of light exposure time; lines are drawn as guides for the eye. In Fig. 2, the magnitude of steady-state photoconductivity is shown for two values of the photogeneration rate used *in the measurement.* The values of the γ exponent of the light intensity dependence of the photoconductivity, $\sigma_{ph} \alpha G^{\gamma}$, represented in Fig. 3 were obtained in the range $G = 10^{20} - 10^{21}$ cm^{-3} s^{-1}. The position of the Fermi level relative to the conduction band (E_c-E_F) was estimated from the measurement of the dark conductivity at room temperature and by using the conductivity prefactor $\sigma_o = 150\ \Omega^{-1}$ cm^{-1}[10]. The annealed sample has a value E_c-$E_F \approx 0.43$ eV which is consistent with the n-type doping effect of nitrogen in a-Si:H.

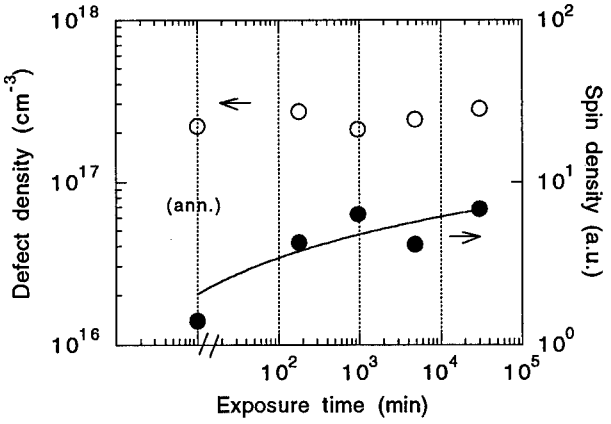


Fig. 1 - Density of defects estimated by PDS and relative density of paramagnetic centers measured by ESR, as functions of light exposure time.

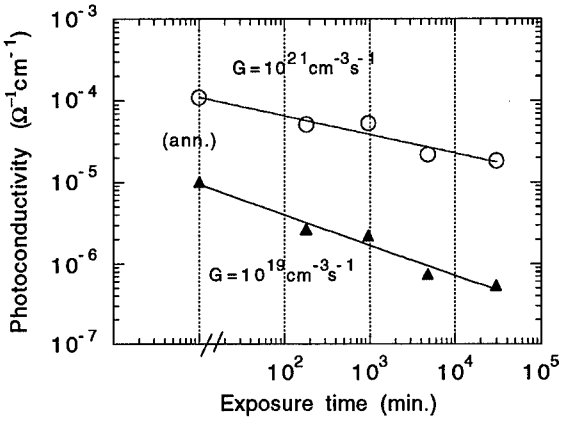


Fig. 2 - Photoconductivity magnitude after different light exposure times.

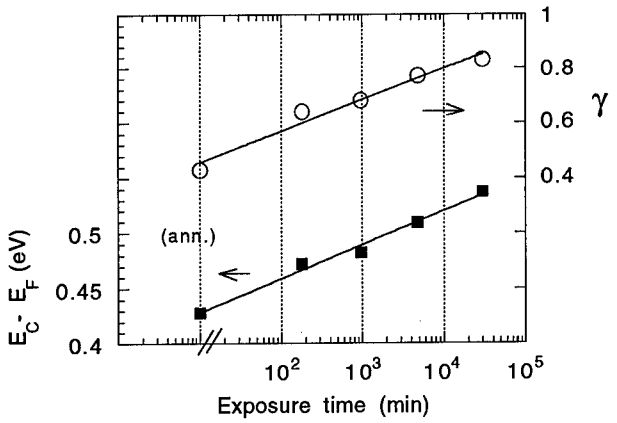


Fig. 3 - Fermi level position and the exponent γ of the light intensity dependence of photoconductivity as functions of the degradation time.

In the calculations, the D^0 state is located 1 eV below the conduction band edge and the correlation energy is 0.4 eV [11]. From the PDS measurements the reciprocal slope of the valence band tail has been estimated as $E_{ov} = 0.056$ eV. As the conduction band tail has a reciprocal slope of about 60% of the valence band tail [12], we have adopted $E_{oc} = 0.034$ eV. The capture cross section of the band tail states is $\sigma_t = 10^{-17}$ cm^{-2} [13], the capture cross sections of the D^0 state for electrons and holes are $\sigma_n^0 = \sigma_p^0 = 2 \times 10^{-16}$ cm^2 and the capture cross sections of the charged D^+ and D^- states for electrons and holes are $\sigma_n^+ = \sigma_p^- = 10^{-15}$ cm^2 [14], the temperature is T = 300 K. In Fig. 4, the photoconductivity data is for $G = 10^{20}$ cm^{-3} s^{-1} and the γ exponent was calculated in the range $G = 10^{20} - 10^{21}$ cm^{-3} s^{-1}. The position of the Fermi level for different values of the metastable density of defects N_D was calculated from the charge neutrality condition.

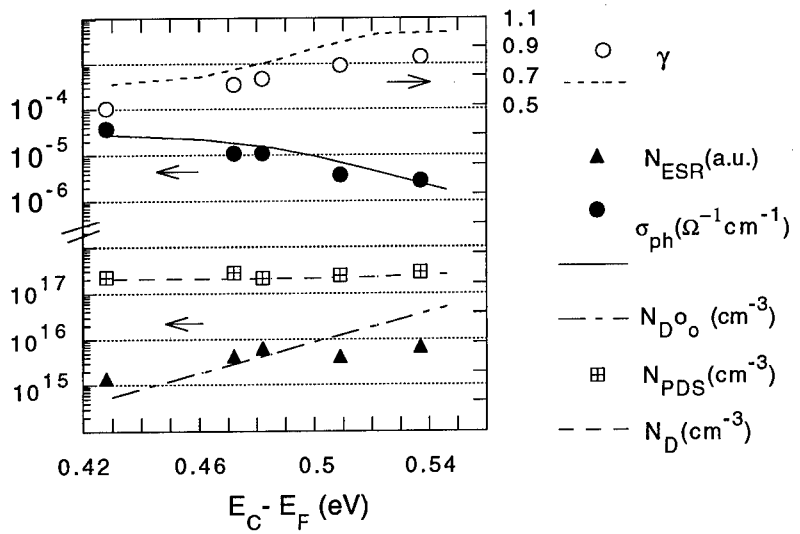


Fig.4 - Comparison between the experimental data and the model results. The symbols are the data and the lines are the results of the calculations.

Discussion

A particular feature of the present ligh-soaking study is that, in the range of light exposure times up to 500 hours, the defect density deduced from PDS does not change significantly and the apparent variations are within the usual error range for these kind of measurements. This can be related to the fairly high density of defects of the annealed state of that sample [2], which is consistent with the corresponding Fermi level position E_c-$E_F \approx 0.43$ eV [15]. However, as is shown in Fig. 2, the photoconductivity decreases by an order of magnitude over the degradation process The fair agreement between the experimental trends and the model results ilustrated in Fig. 4 is a good support for the interpretation. The decrease in the photoconductivity magnitude can be explained by the shift of the Fermi level towards the middle of the gap (Fig. 4) and the consequent increase of the density of D^0 states, N_{D^0} in the dark, which are the dominant recombination centers for electrons. The intensity of the ESR signal is a measure of the density of D^0 centers and also increases with the exposure time (Figs. 1 and 4). The increase of the exponent γ is induced by the shift of the Fermi level, as previous modelling has shown [8]. As can be seen in Fig.4, the model predicts a very small increase of the dangling bond density over the studied range of energies in agreement with the PDS data.

Conclusions

Light-induced effects on the room temperature photoconductivity and its light intensity dependence, on the Fermi level position, on the total defect density and on the paramagnetic spin density, have been studied in a nitrogen doped a-Si:H thin film. The experimental trends can be explained and reproduced by numerical simulations with a recombination model involving one class of correlated silicon dangling bond states and exponential band tails of localized states The increase in the metastable defect density induces the shift of the Fermi level towards the middle of the gap, leading to an increase of the density of the D^0 neutral centers, which are the principal recombination centers for electrons in the studied temperature and light intensity experimental conditions, therefore producing a decay in the photoconductivity magnitude, while the γ exponent approaches unity. The consistency of the simulation results with the experimental data contributes to the validation of the proposed recombination model,which has already been successful in previous simulation studies, and gives new insight into the photodegradation of the electronic properties in a-Si:H..

Acknowledgements

The present work was supported in part by Junta Nacional de Investigação Científica under the project PBIC/C/CTM/1385/92.

References

1. D.L. Staebler and C.R. Wronsky, Appl. Phys. Lett. 31, 292 (1977)
2. M. Stutzmann, Phil. Mag. B **60**, 531 (1989).
3. E. Morgado, J. Non-Cryst. Solids **139**, 248 (1992)
4. W. B. Jackson and N.M. Amer, Phys. Rev. B **25**, 5559 (1982)
5. K. Pierz, H. Mell and J. Terukov, J. Non-Cryst. Solids **77/78**, 547 (1985)
6. J. G. Simmons and G.W. Taylor, Phys. Rev. B **4**, 502 (1971).
7. F. Vaillant, D. Jousse and J.-C. Bruyère, Phil. Mag. B **57**, 649 (1988)
8. E. Morgado, J. Non-Cryst. Solids **164-166**, 627 (1993)
9. E. Morgado, Defect Diffus. Forum **134-135**, 39 (1996)
10. J. Stuke, J. Non-Cryst. Solids **97-98**, 1 (1987)
11. P. G. Le Comber and W. E. Spear, Phil. Mag. B **53**, L1 (1986).
12. T. Tiedje, J. M. Cebulka, D. L. Morel and B. Abeles, Phys. Rev. Lett. **46**, 1425 (1981)
13. J. M. Marshall, R. A. Street and M. J. Thompson, Phil. Mag. B **54**, 51 (1986)
14. A. Doghmane and W. E. Spear, Phil. Mag. B **53**, 463 (1986).
15. K. Pierz, W. Fuhs and H. Mell, Phil. Mag. B **63**, 123 (1991).

Materials Science Forum Vols. 258-263 (1997) pp. 337-340
© 1997 Trans Tech Publications, Switzerland

TRACING DIFFUSION BY LAPLACE DEEP-LEVEL SPECTROSCOPY

K. Bonde Nielsen[1] and L. Dobaczewski[2]
[1]Institute of Physics and Astronomy, University of Aarhus, DK-8000 Aarhus C, Denmark
[2]Institute of Physics, Polish Academy of Sciences, Al Lotnicow 42/46 Warsaw, Poland

Keywords: Laplace DLTS, diffusion, ion-implantation, hydrogen, silicon

Abstract. Proton implantation in n-type silicon at temperatures below ≈ 80 K generates a metastable deep donor defect ascribed to hydrogen at the bond centre site in the silicon lattice. The defect anneals at ≈ 100 K forming a negatively charged acceptor structure. In implanted p^+n diodes the donor state can be recovered by forward-bias injection of holes. The recovery broadens the primary straggling profile of the hydrogen implant. We have applied Laplace deep-level spectroscopy to study this profile broadening. It is demonstrated that quantitative measures of the diffusion broadening of narrow deep donor layers can be obtained by peak-shape analysis. This novel method rests upon the electric-field dependence of donor emission rates, and utilises the high emission-rate resolution offered by the Laplace technique. We show that diffusion lengths in the micron range may be derived.

Introduction

One of the standard applications of deep-level transient spectroscopy (DLTS) is to investigate spatial distributions of defect species in depletion layers of diode structures. This may include studies of impurity diffusion, decoration of radiation damage, and interactions between defects in general. The high resolution offered by Laplace DLTS [1] can be utilised to investigate the diffusion broadening of an implanted impurity layer without having to carry out defect profiling in the usual way. In the case of a deep donor the electric-field dependence of the emission rate (the Poole-Frenkel effect) provides a convenient transformation between the scales of emission-rate and depth. As a result, with sufficiently good resolution, a quantitative evaluation of diffusion lengths in the micron range may be obtained from shape analysis of the Laplace signal. This work tests the method in a study of injection enhanced migration of interstitial hydrogen in silicon using the E3'' deep-donor signal of hydrogen [2] as a vehicle to trace the migration.

Measurements and Results

The introduction of the Laplace transform method of capacitance transient analysis in conventional DLTS makes a substantial improvement in terms of the resolution obtainable [1]. A particular feature of the technique is its ability to recognise the difference between a case when the transient consists of a close series of discrete mono-exponential components and a case when the transient non-exponentialilty is a result of a continuous distribution of the defect parameters. This distribution is visualised as a DLTS-signal spectrum function on the logarithmic scale of the emission rates. The spectral distribution is the mathematical representation of the Laplace-transform inverse function of the capacitance transient. See Ref. [1] and references therein for details.

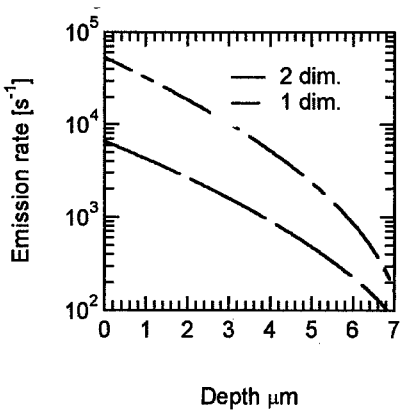


Fig. 1 An example indicating the relation between emission rate and depth. A Coulomb-field rate-dependence has been assumed and graphs representing the one-dimensional as well as the two-dimensional model [3] are shown. The graphs have been calculated for a 20 V reverse-biased 10 Ωcm n-type silicon diode.

In the Laplace method it is not necessary to make any a priory assumptions about the functional shape of the spectrum, except that all decays are exponential in the same direction. The transient-deconvolution algorithm is based on the so-called Tikchonow regularisation method and the current

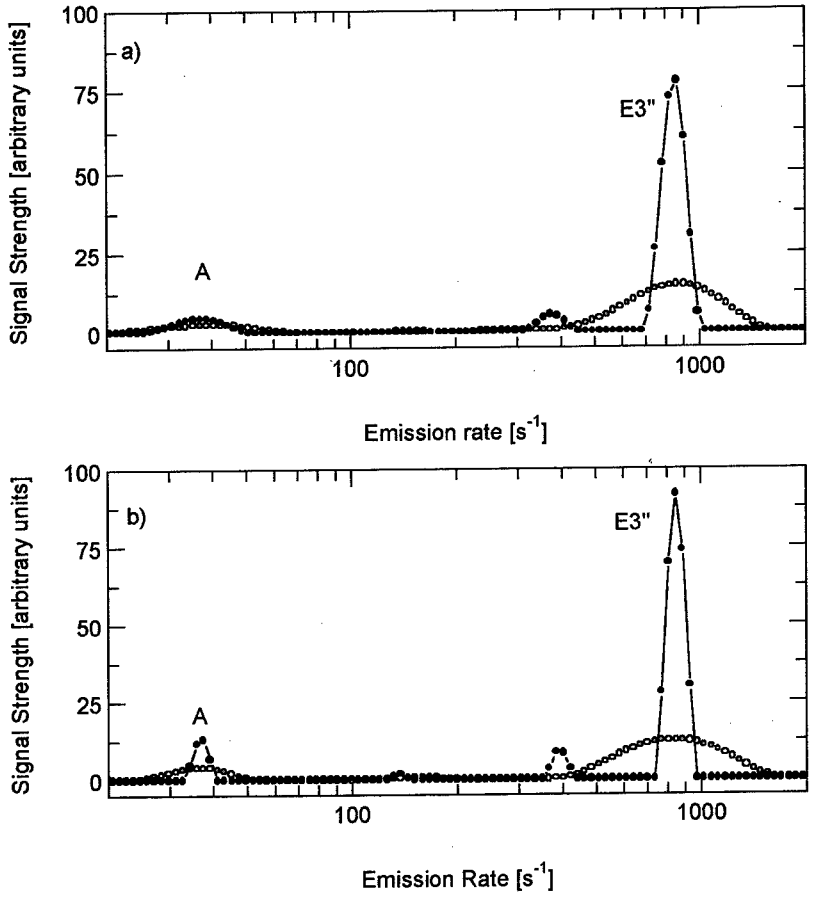


Fig. 2 Laplace DLTS spectra indicating the injection-induced broadening of the E3'' signal. Two different numerical realisations of the deconvolution algorithm have been used to analyse the same capacitance transient. The resulting spectra are shown in a) and b). The markers (•) and (o) indicate data obtained before and after injection, respectively. The peak labelled (A) is the oxygen-vacancy A-centre signal.

version allows for parallel use of alternative different numerical realisations of the algorithm. These different realisations must lead to consistent deconvoluted spectra in order to achieve the necessary level of confidence in the analysis.

As briefly mentioned in the introduction, the Poole-Frenkel effect connects the distribution of the exponential transients contained in the Laplace signal to the depth distribution of the corresponding deep donor. To indicate the sensitivity in the conversion between the two distributions Fig. 1 depicts of the emission rate versus depth for a typical case (10 Ωcm n-type silicon and 20 V reverse bias). The individual graphs represent the one-dimensional Coulomb-field model and its two-dimensional extension [3]. As indicated in the figure, an implantation depth of $\approx$ 4 μm should be attempted to obtain suitable sensitivity and diffusion space. After proton implantation at low temperature we can assume that the distribution of hydrogen-related defects is represented by a Gaussian defect profile. We further assume that this profile stays Gaussian during diffusion

broadening. When the effective shallow dopant concentration is homogeneous the relation between emission rate (e_n) and depth (x) can be represented mathematically as

$$\log(e_n) = \alpha\sqrt{\beta - x} + \gamma \qquad (1)$$

where, in the actual case, the constants α, β and γ can be obtained from a measurement of the Pole-Frenkel shift as function of reverse bias. If the dopant concentration can not be considered homogeneous the relation between depth and field (reverse bias voltage) must be obtained separately by capacitance-voltage profiling and used to modify the above relation. An underlying Gaussian depth distribution causes the Laplace DLTS signal, plotted on a logarithmic emission-rate scale, to appear with a skewed Gaussian-like shape. It is implied in the analysis that the natural linewidth of the Laplace signal is negligible compared to the diffusion-broadened signal.

Having shown in principle how the Laplace technique may be utilised to obtain diffusion lengths we test its applicability in practical work using the hydrogen E3'' donor signal [2] as a suitable test case. Figure 2 shows the Laplace spectra resulting from deconvolution of the same experimental capacitance transient using two alternative numerical methods with different convergence criteria in the analysis. As can be seen the main features of the spectra are very similar. In both cases a narrow hydrogen signal (E3'') is revealed prior to forward-bias injection, and after injection these E3'' signals broadens equally. The small signal, denoted (A) in the figure, originates from the oxygen-vacancy defect (the A-centre) and should not broaden being an acceptor signal. However, some broadening is in fact observed. This indicates the limitation of the technique namely that the shape of small features in the spectra may be influenced by nearby strong peaks. It should be noticed that the intensity of the A-centre peak is unaffected by the shape and size of the dominating E3'' signal.

Two strong donor signals (E3' and E3'') can be observed in n-type silicon diodes after low-dose proton implantation at temperatures below 80 K. These signals relate to primary interstitial defect structures of hydrogen from which secondary hydrogen-associated defects form during annealing of the sample. The study of the primary hydrogen defects, such as the migration indicated by the broadening of the E3'' signal, is therefore of fundamental interest for our understanding of the behaviour of the hydrogen impurity in silicon. We shall restrict our discussion to properties of E3'' which are relevant in the context of testing the diffusion application of Laplace DLTS. We refer to a

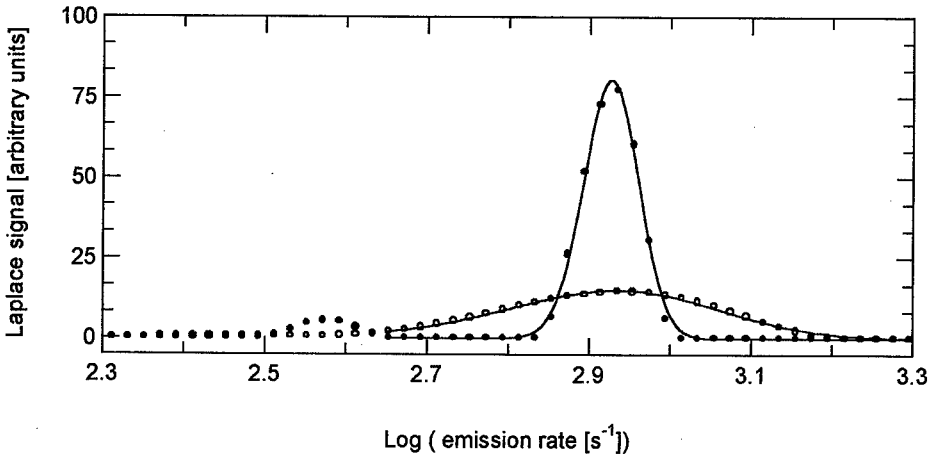


Fig. 3 Least squares analysis of the E3'' peak shape assuming an underlying Gaussian depth distribution. Equation 1 is used to relate emission-rate and depth. The resulting standard deviations are $\sigma = 0.43$ μm and $\sigma = 0.11$ μm for the diffused (o) and non-diffused (•) cases, respectively.

contribution presented elsewhere in these proceedings [2] for further details concerning the hydrogen donor signals. The circumstances regarding the E3'' formation is as follows: In as-

implanted samples (typically 10^{10} cm^{-2} for 10 Ωcm material) a different donor signal is present [4]. This signal is denoted E3' and is almost identical to E3''. The two signals are distinguished only because they form and anneal differently. The E3' signal disappear when the sample is annealed without bias at ≈ 100 K and a negatively charged acceptor-type hydrogen centre is formed [4]. From this centre, the E3'' signal can be generated by exposure of the sample to band-gap light [2], while the sample is kept under reverse bias. The E3'' signal is highly unstable when the bias is removed. In fact, it decays partly during the DLTS scans performed at 85 K. Also the E3' signal can be recovered, however, unlike E3'' by forward-bias injection of holes [2,4]. When the E3' centre is annealed once more after the recovery more than 75% the E3'' signal can again be generated by illumination now broadened as a result of hydrogen migration. The described scenario corresponds to the data of Fig. 2.

A least squares analysis of the diffusion broadening is presented in Fig. 3. The analysis is based on the Gaussian diffusion model discussed above with the constants of Eq. 1 specified using a measured Poole-Frenkel shift. The resulting standard deviations of the underlying depth distributions are $\sigma = 0.43$ μm and $\sigma = 0.11$ μm in the diffused and non-diffused cases, respectively. The corresponding diffusion length is about 0.3 μm, which is much larger than expected for thermal diffusion of hydrogen [2,5]. It may be noticed that the standard deviation in the non-diffused case comes out slightly smaller than that of the range straggling (≈ 0.15 μm). This may be traced back to the compensation effect of the implantation. In the analyses we have used the virgin-sample linear relation between depth and electric field. However, the actual (average) field varies more slowly than derived from this relation in the range of implantation straggling. Thus the analyses slightly underestimate the widths of the distributions particularly in the non-diffused case.

Conclusion

A novel application of Laplace DLTS has been introduced. We have shown by an example that peak-shape analysis of the Laplace transformed signal can be utilised to study diffusion broadening of narrow deep-donor distributions inside depletion layers of diodes. The method is free of complications coming from the Debye-tail, which may effect conventional DLTS profiling of narrow layers. The method is, however, limited to cases where the analysed peak is dominating in the Laplace spectrum. The hydrogen test case has revealed a remarkably fast injection-enhanced diffusion of hydrogen with a diffusion length that is many orders of magnitude larger than expected for thermal diffusion.

Acknowledgements

This work has been supported by the European Community grant No CIPA-CT94-0172, and the Danish National Research Foundation through the Aarhus Center for Advanced Physics (ACAP).

References

1. L. Dobaczewski, P. Kaczor, I. D. Hawkins, and A.R. Peaker, J. Appl. Phys. 76, 194 (1994)
2. K. Bonde Nielsen, B. Bech Nielsen, and J. Hansen, contribution to this conference
3. J. L. Hartke, J. Appl. Phys. 39, 4871 (1968)
4. B. Holm, K. Bonde Nielsen, and B. Bech Nielsen, Phys. Rev. Lett. 66, 2360 (1991)
5. A. Van Wieringen and N. Warmoltz, Physica, 22, 849 (1956)

Materials Science Forum Vols. 258-263 (1997) pp. 341-346
© 1997 Trans Tech Publications, Switzerland

DEFECTS IN AS-GROWN SILICON AND THEIR EVOLUTION DURING HEAT TREATMENTS

J. Vanhellemont, E. Dornberger, J. Esfandyari, G. Kissinger*, M.-A. Trauwaert, H. Bender**, D. Gräf, U. Lambert and W. von Ammon**
Wacker Siltronic AG, P.O. Box 1140, D-84479 Burghausen, Germany
***Institute for Semiconductor Physics, Walter-Korsing-Str. 2, D-15230 Frankfurt (Oder), Germany**
****IMEC, Kapeldreef 75, B-3001 Leuven, Belgium**

Keywords: grown-in defects, crystal pulling, Cz silicon, voids, silicon oxide precipitates

Abstract

The nature and stability of grown-in defects in Czochralski silicon is discussed as well as their dependence on crystal pulling conditions. It is shown that large voids are formed during crystal cooling by agglomeration of vacancies together with much smaller silicon oxide precipitates. During further thermal treatments the oxide precipitates become the dominant defects with a number density 2 to 4 orders of magnitude larger than that of grown-in voids. Defect nucleation and growth simulations illustrate the crucial role played by intrinsic point defects at the melt/solid interface.

Introduction

Most commercial silicon materials are grown using pulling conditions resulting in vacancy-rich crystals. The supersaturation of vacancies during crystal cooling leads to the formation of so-called D-defects which have a detrimental impact on the electrical properties of thin gate oxides [1-4] and have therefore been studied intensively during the last years [5-8]. Only recently, it was established that as-grown Czochralski silicon contains 10^5-10^7 cm^{-3} octahedral voids with diameters in the 100 nm range. The observed void density correlates well with the gate oxide and D-defect densities.
As interstitial oxygen is present in high concentration, oxide precipitate nuclei are also formed during crystal growth. Due to the slower diffusion of oxygen, the size of these nuclei is smaller than that of the D-defects while their number density is a few orders of magnitude higher.
In the present paper results are reported of an experimental and numerical investigation of grown-in point defect clusters as a function of crystal pulling conditions. Infrared light scattering and interference contrast techniques are used to measure the defect size and density distributions in as-grown and heat treated Czochralski silicon wafers. A large fraction of the grown-in defects is smaller than the size detection limit of the available analytical tools and is therefore not observed in the as-grown material. Increasing the defect sizes by thermal anneals allows to shift the initial defect sizes above the size detection limit and yields indirect information on the grown-in distribution.
The experimental observations can be reproduced with high accuracy by numerically simulating the whole pulling process. This includes not only intrinsic point defect incorporation but also homogenous nucleation and growth of voids and oxide nuclei during cooling of the crystal. Consistent estimates of the intrinsic point defect solubility and diffusivity can also be determined allowing to simulate a wide variety of crystal pulling processes with the same set of parameters.

Materials and techniques

Wafers are studied which were prepared from 150 and 200 mm crystals pulled with hot zone designs leading to different crystal cooling rates labelled A to E (cooling rate decreasing from A to E). All crystals were however pulled fast enough to obtain vacancy-rich material.

Low defect densities in the bulk of silicon wafers can be studied conveniently by non-invasive tools using near infrared (IR) light. IR interference contrast microscopy [9] and light scattering tomography (LST) [10] have been used to study the defect distributions in as-grown and annealed Cz wafers. After determination of accurate defect coordinates TEM analyses were performed using focused ion beam techniques to prepare thin foils containing the defect.

The nucleation and growth of defects is simulated using an integrated software package allowing not only to model the full crystal pulling process including the temperature distributions and the concentration of intrinsic point defects in the growing crystal [11] but also the precipitation processes during crystal growth and further thermal anneals [12]. Oxide or vacancy cluster formation is hereby simulated using rate equations for small clusters composed of less than 20 atoms. For larger clusters the required calculation power increases tremendously with the number of equations and therefor their growth is described by a single Fokker-Planck equation.

Results and discussion

Defects in as-grown Cz wafers: oxide precipitates versus voids

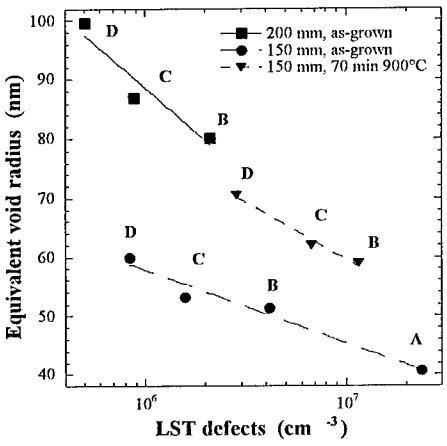


Fig. 1: Defect density vs size in as-grown silicon and after gate oxidation (70 min, 900°C) [4].

LST and IR interference contrast microscopy reveal defects in as-grown wafers with densities typically between 10^5 and 10^7 cm^{-3}. A clear correlation exists between density and size of the defects (Fig. 1) as expected for a homogeneous nucleation process. For many years there has been a discussion on the real nature of these defects i.e. oxide precipitates or vacancy clusters. Recently, TEM investigations have shown that the grown-in defects which are detected by light scattering tools are large octahedral voids with the internal surface covered by a thin amorphous layer which is probably SiO_x [7,8]. Figure 2 shows a typical defect in a B-type, 150 mm wafer [13]. The diameter of the voids ranges typically between 50 and 300 nm depending on the cooling rate of the crystal [11].

In the as-grown material SiO_x precipitate nuclei are too small to be detected. A special technique was developed to shift this size distribution above the detection limit of LST showing that also the grown-in oxide precipitate distribution depends strongly on the crystal pulling conditions [14].

The dominant defects which are expected in fast pulled material are thus vacancy and oxide clusters as a high supersaturation of both types of point defects is created during cooling of the crystal. Recent TEM results suggest that the large defects which are observed by LST and which give rise to the formation of COP are octahedral voids possibly partially filled with oxide. Also recent simulations of void formation yield results which are in excellent agreement with grown-in defect size and density distributions observed after different crystal pulling processes.

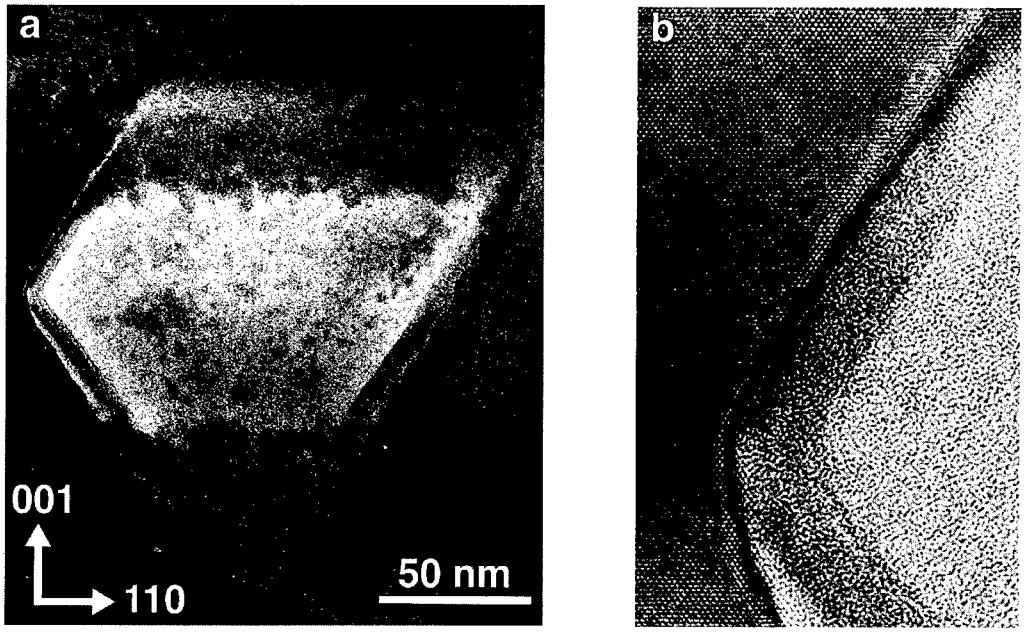


Fig. 2: a) Cross-section TEM image of a D-defect close to the wafer surface. b) High resolution image revealing a 5 nm thick amorphous layer on the inner surface of the void.

Nucleation and growth of precipitates in silicon

Cooling the silicon crystal from the melt temperature leads to a supersaturation of interstitial oxygen and self-interstitials and/or vacancies depending on the pull rate and axial thermal gradient [11]. The critical radius $r_c^{SiO_x}$ of a SiO_x precipitate is strongly influenced by the supersaturation of oxygen and intrinsic point defects while for voids only the vacancy supersaturation is involved,

$$r_c^{SiO_x} = \frac{2\sigma_{SiO_x}}{\frac{xkT}{\Omega_{SiO_x}} \ln \frac{C_{OI}}{C_{OI}^*} \left(\frac{C_V}{C_V^*}\right)^{\beta}} \quad \text{and} \quad r_c^{Void} = \frac{2\sigma_{Si}}{\frac{kT}{\Omega_{Void}} \ln \frac{C_V}{C_V^*}} . \qquad (1)$$

σ_{SiO_x} is the interface energy between oxide and silicon while σ_{Si} is the surface energy per unit area of silicon. The interstitial oxygen and the vacancy in the matrix are C_{OI} and C_V, respectively while their thermal equilibrium values are C_{OI}^* and C_V^*. The molecular volume Ω_{SiO_x} of all known silicon oxide phases is larger than the one of silicon (Ω_{Si}). It is assumed that this volume deficiency is relieved by the absorption of β vacancies from the matrix per precipitated oxygen atom.
Assuming that the nucleation of precipitates during the cooling process is homogeneous, the nucleation rate J of spherical particles is according to the classical nucleation theory given by

$$J \propto D_P \left(r_c C_P^0\right)^2 e^{-\frac{G(r_c)}{kT}} \quad \text{with} \quad G(r_c) = 4\sigma\pi r_c^2 + (G_V + E_s)\frac{4}{3}\pi r_c^3 \qquad (2)$$

D_P is the diffusion coefficient, C_P^0 the concentration, G the free energy for forming a nucleus with radius r_c . G_V is the free energy and E_s the strain energy per unit of precipitate volume.

In a first order approximation one expects an exponential relation between the size of the precipitates and the number density observed after crystal growth (Fig. 1). Equations (1) also illustrate the tight connection which exists between vacancy and oxygen behaviour. For a reliable prediction of oxygen precipitation kinetics one has therefore to consider at least the effect of a vacancy supersaturation and in a more refined simulation also the simultaneous formation of voids and oxide precipitates as well as consumption of vacancies by the growing precipitates and of oxygen by the growing voids.
For the calculation of the grown-in point defect cluster size and density a precipitation scheme is used in which the kinetics of clustering is described by rate equations for small cluster sizes (< 20 clustered molecules). Larger clusters are treated by an additional Fokker-Planck equation to calculate the overall size distribution. The coefficients of the resulting equations are modelled using phenomenological models of cluster free energy and assuming diffusion limited precipitation. Voids and oxide precipitates are considered to be spherical for simplicity. The defect radius r_x is calculated from the number of precipitated molecules n present in the precipitate

$$r_x = \left(\frac{3n\Omega_x}{4\pi}\right)^{\frac{1}{3}}, \qquad (3)$$

with $x = Si$ for a void and $x = SiO$ or SiO_2 for an oxide precipitate.
Nucleation is to a large extent determined by the interface energy σ between the precipitated phase and the surrounding matrix. In the present simulations interface energies of 1 (void) and 1.7 (SiO_2) Jm^{-2} were used [15]. In view of its high interface energy one needs a supersaturation of vacancies decreasing the critical radius of a SiO_2 particle to have significant nucleation.
The observed LST defect densities in the as-grown material are reproduced quite well by the calculated void densities. Figure 3 shows a comparison of the expected void and oxide precipitate density for different pulling processes with superimposed the defect density determined with LST and gate oxide tests. It turns out that the same supersaturation of vacancies which is assumed for the void nucleation leads to the expected SiO_2 particle nucleation. The figure also illustrates that there is no correlation between oxide precipitate density and GOI. An excellent agreement is obtained between the simulated and measured sizes only in case of voids (Fig. 4). The size of the oxide precipitates is in the range of 7 nm which is well below detection limit of available analytical tools. The simulated size corresponds with the oxide layer thickness on the internal surface of the void of which the growth is probably also oxygen diffusion limited. The density is however in the range between 10^8 and 10^{10} cm^{-3}, in excellent agreement with observations after further thermal anneals.

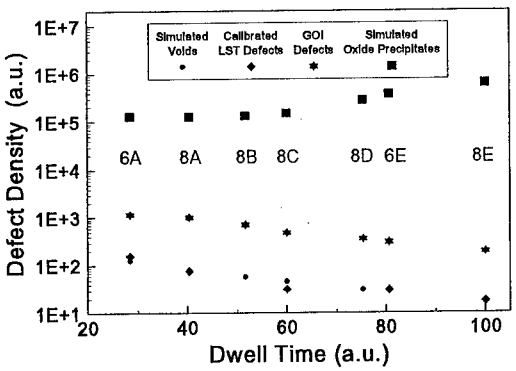


Fig. 3: GO, LST defect and calculated void and oxide precipitate densities in 150 (6) and 200 (8) mm as a function of the dwell time between 1050 and 900°C.

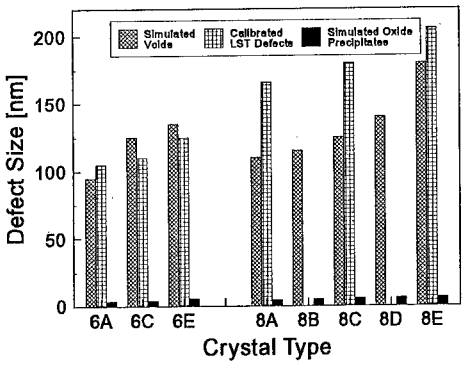


Fig. 4: Computed void and silicon oxide precipitate sizes compared with LST defect sizes observed in 150 and 200 mm crystals (6 and 8, resp.).

The size and density distribution of both voids and silicon oxide precipitates depends strongly on the crystal pulling conditions (Figures 2 and 5). Faster cooling leads to an increasing density of voids with smaller sizes. The results also show that voids are formed in the temperature window between 1050 and 900°C. Above 1050°C the vacancy supersaturation is quite low leading to a negligible nucleation rate. Below 900°C their is no more significant growth of voids. Shifting the oxide precipitate sizes above the detection limit of LST reveals indirectly grown-in size distributions expressed by the stability temperatures of the precipitates (Fig. 5) [14].

Defect evolution due to thermal anneals

IR interference contrast microscopy and LST analyses were performed on wafers before and after thermal anneals. The grown-in voids apparently grow also during thermal treatments as shown in Fig. 1 for a gate oxidation at 900°C for 70 min. Due to the low temperature anneal the grown-in oxide precipitates remain smaller than the detection limit of the techniques and still only the voids are observed. After prolonged heat treatments or using higher temperatures oxide precipitates become visible and due to their much larger density become the dominant defect in the observations. This is illustrated for a high/low/high treatment (1100°C, 6h + 750°C, 8h + 975°C, 9h) where a distribution of large oxide precipitates is formed with a density which is 3 orders of magnitude higher than that of the grown-in voids (Fig. 6) but still in agreement with the grown-in oxide precipitate density predicted by the simulation.

Also here the use of simulation to determine the evolution of the grown-in defect distribution during the thermal anneal is needed especially for the near surface region where devices will be fabricated [16]. For an accurate description, both outdiffusion of oxygen and vacancies should to be taken into account as well as Ostwald ripening processes.

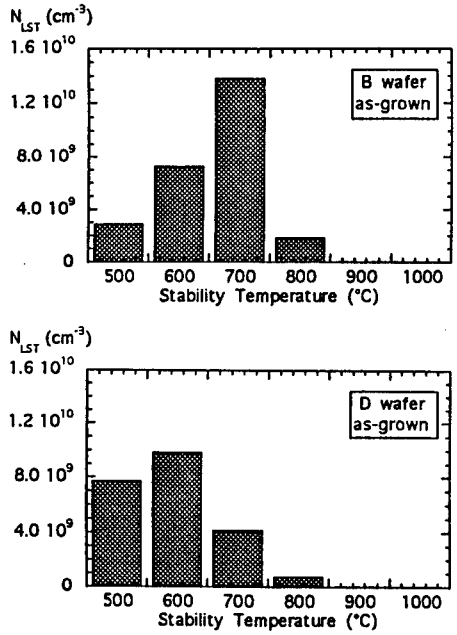


Fig. 5: LST determined grown-in defect spectrum obtained with sequential anneals [14].

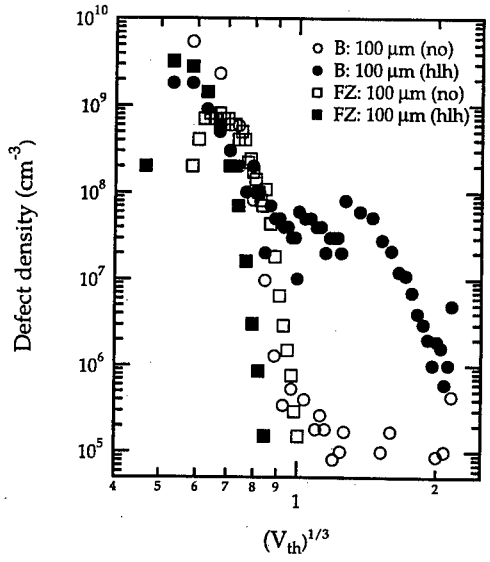


Fig. 6: Interference contrast microscopy defect distribution in as-grown (no) and annealed (hlh) B-type and FZ wafers [9]. The defect size is proportional to the third root of the threshold voltage V_{th} (> 1V).

Conclusion

Defect nucleation and growth during crystal growth can be simulated accurately using advanced simulators. Comparison with experimental data allows to determine fundamental material properties like solubility and diffusivity of intrinsic point defects. A consistent set of data could be determined allowing to simulate quantitatively defect nucleation and growth for a large range of Czochralski crystal pulling conditions.
The simulations show clearly that the large grown-in defects which are observed in as-grown Cz silicon are voids formed by vacancy agglomeration. In parallel a much higher density of small oxide precipitates are formed of which the size is below the detection limit of present analytical tools. Nevertheless as these precipitates determine the later oxygen precipitation behaviour their nucleation and its strong dependence on intrinsic point defects has to be understood quantitatively.

Acknowledgements

Part of the work has been supported by the Federal Department of Education and Research of Germany under contract M 2793 F/G. The authors alone are responsible for the contents. M.-A. Trauwaert is indebted to the Flemish institute for the promotion of scientific and technological research in industry (IWT) for her fellowship.

References

1. M. Itsumi, O. Nakajima and N. Shiono, J. Appl. Phys. **72**, 2185 (1992).
2. J.-G. Park, S. Ushio, H. Takeno, K.-C. Cho, J.-K. Kim and G.A. Rozgonyi, The Electrochem. Soc. Proc. Vol. **94-33**, 53 (1994).
3. I. Fusegawa, K. Takano, M. Kimura and N. Fujimaki, Mat. Science Forum **196-201**, 1683 (1995).
4. J. Vanhellemont, G. Kissinger, K. Kenis, M. Depas, D. Gräf, U. Lambert and P. Wagner, in: Early Stages of Oxygen Precipitation in Silicon, ed. R. Jones, Kluwer Academic Publishers, 493 (1996).
5. S. Sadamitsu, S. Umeno, Y. Koike, M. Hourai, S. Sumita and T. Shigematsu, Jpn. J. Appl. Phys. **32**, 3675 (1993).
6. W. Wijaranakula, J. Appl. Phys. **75**, 3678 (1994).
7. M. Itsumi, H. Akiya, T. Ueki, M. Tomita and M. Yamawaki, Jpn. J. Appl. Phys. **35**, 812 (1996).
8. M. Kato, H. Takeno and Y. Kitagawara, in 'Defects in Electronic Materials', 1996 MRS Fall Meeting, Mat. Res. Soc. Proc. in press.
9. M.-A. Trauwaert, K. Kenis, P.W. Mertens, M. Heyns, J. Vanhellemont, U. Lambert and D. Gräf, proceedings GADEST '97, in press (1997).
10. G. Kissinger, J. Vanhellemont, C. Claeys and H. Richter, Inst. Phys. Conf. Ser. **149**, 19 (1996).
11. E. Dornberger, J. Esfandyari, D. Gräf, J. Vanhellemont, U. Lambert, F. Dupret and W. von Ammon, Electrochem. Soc. Proc. Vol., in press (1997).
12. J. Esfandyari, C. Schmeiser, S. Senkader, G. Hobler, B. Murphy,J. Electrochem. Soc. **143**, 995 (1996).
13. H. Bender, J. Vanhellemont, R. Schmolke, submitted for publication in Jap.J.Appl.Phys.
14. G. Kissinger, D. Gräf, U. Lambert and H. Richter, J. Electrochem. Soc. **144**, 1447 (1997).
15. S. Senkader, G. Hobler and C. Schmeiser , Appl. Phys. Lett. **69**, 2202 (1996).
16. J. Vanhellemont, S. Senkader, G. Kissinger, V. Higgs, M.-A. Trauwaert, D. Gräf, U. Lambert and P. Wagner, J. Crystal Growth, in press.

Materials Science Forum Vols. 258-263 (1997) pp. 347-354
© 1997 Trans Tech Publications, Switzerland

AN INVESTIGATION OF THE POSSIBILITY THAT OXYGEN DIFFUSION IN CZOCHRALSKI SILICON IS CATALYZED DURING CLUSTERING

S.A.McQuaid, B.K.Johnson, R.Falster and K.F.Kelton[1]

MEMC Electronic Materials, 501 Pearl Dr., P.O. Box 8, St. Peters, MO63376, USA.
[1]Department of Physics, Washington University, St.Louis, MO 63130.

Keywords : silicon, oxygen, thermal donor, diffusion, clustering, precipitation.

Abstract. The rates of loss of isolated oxygen from solution at the lowest temperatures ($T < 400°C$) are close to those expected for O_i-O_i interaction in a dilute solution, yet the dependence of rates on $[O_i]$ at slightly higher temperatures ($400 < T < 500°C$) indicates that the predominant clusters formed contain many more then two atoms. The implication that the kinetics of O-clustering at low temperatures are anomalous coincides with the assumption that thermal donors consist of different numbers of clustered O-atoms. Attribution of the implied fast evolution of a series of clusters to rapid dimer diffusion does not appear to be consistent with observations relating to the defects subsequently detected. Even if aspects of this evolution suggest the involvement of self-interstitials ejected during clustering, no reasonable way has been found that these defects might account for the serial evolution of large O-clusters. A natural explanation of growth of a series of relatively large clusters is that a barrier to dimerization exists and that the rate of O_i-O_i interaction is much greater than that of $[O_i]$-loss. The assumption of a dilute solution seems to be questionable.

Introduction.

Oxygen atoms are incorporated in silicon crystals grown by the Czochralski method, due to the partial dissolution of the quartz crucible in which the melt is contained. The solid solution is highly supersaturated at temperatures below $\sim 1250°C$ and the equilibrium solubility decreases rapidly with temperature ($C_s = 9x10^{22}exp(-1.52eV/kT)cm^{-3}$) [1]. Yet despite the slow rate of cooling in the crystal puller ($\sim 100°C/h$), the oxygen atoms remain predominantly in isolated interstitial sites (O_i), giving rise to an infrared (IR) absorption band at $9\mu m$. Following anneals at high temperatures ($T > 700°C$) estimates of the diffusion coefficient of O_i ($D_{oxy} = 0.13exp(-2.53eV/kT)cm^2s^{-1}$) were derived from near-surface concentration profiles [2] and the results were independent of doping, crystallographic orientation or external conditions during the heat treatments. In the absence of evidence for the involvement of native defects, and the correlation with O_i reorientation rates derived from internal friction measurements [3] in the same temperature range and measurements at much lower temperatures ($T \leq 400°C$) of the rate of loss of stress-induced dichroism in the $9\mu m$-band [4], the mechanism was concluded to be hopping of O_i between adjacent interstitial sites.

During anneals of as-grown material at such high temperatures, the concentration of isolated oxygen atoms ($[O_i]$) decreases and precipitate sizes on average increase at rates corresponding to those expected for the arrival rate of O_i to the precipitate interface. The implied values of D_{oxy} are in agreement with measurements [1]. It has been argued that this precipitate growth could not occur unless the large local increase in strain were efficiently relieved in some way [5]. The observation of dislocation loops and/or stacking faults in annealed samples have been attributed to the clustering of self-interstitial (I) atoms ejected by the precipitates [6]. As-grown material can contain significant concentrations ($\sim 10^{10}cm^{-3}$) of nucleii for precipitation which form during cooling of the growing crystal. A high temperature ($> 900°C$) dissolution treatment of samples is usually a prerequisite for clear monitoring of the nucleation stage [7]. The rate at which nucleii form is significant at temperatures below 700°C. In contrast to predictions of classical nucleation theory, two optimum temperatures for nucleation were observed at $\sim 650°C$ and $\sim 500°C$ [8].

Extrapolation of the high temperature measurements of D_{oxy} implies that corresponding out-diffusion measurements should not be feasible for reasonable anneal times at $T < 700°C$. Surprisingly, such measurements have been reported which indicate enormous enhancements of D_{oxy} (by factors of up to 10^7 at 450°C). The earliest work [9] revealed widely varying effective values which, although always unexpectedly large, did not change systematically with anneal temperature ($550 < T < 700°C$), $[O_i]$ in the bulk or crystallographic orientation of the surface. Systematic variations of the effective value of D_{oxy} with changes of $[O_i]$ and anneal time were recently reported for anneals at 450°C [10], however the temporal variation is so strong that it is unclear whether the profile changed significantly during the heat treatments. Other work [11] provided evidence that the enhanced out-diffusion rates are associated with high concentrations of carbon ($[C_s] > 10^{17}cm^{-3}$) in the crystal. These data provide the most reliable evidence that D_{oxy} may be greatly enhanced (at least in the near surface regions) but given the inconsistencies it is difficult to conclude that long range diffusion in the bulk is enhanced to the extent implied during precipitate nucleation.

Donor defects form during anneals over the entire range of temperatures for which precipitate nucleation is significant [12]: shallow single donors and normal double thermal donors (TDs) [13] tend to predominate at higher and lower temperatures respectively. In fact, previously formed TDs (470°C) have been found to first anneal and then reform [14] during isothermal anneals at 620°C. From a technological point of view, TDs are of little direct importance but identification of the process(es) involved in their formation would provide valuable information about precipitate nucleation, particularly at low temperatures ($T \sim 500°C$).

Information derived from the study of defect formation.

During the early stages of low temperature ($T < 500°C$) anneals, a family of TDs form serially [13] and vibrational infrared (IR) absorption has been observed which appears to arise from O present in other unidentified defects [15]. In particular, two IR absorption bands at 1012 and 1006cm^{-1} seem to arise from nucleii necessary for TD formation (Fig. 1). The existence of such nucleii had previously been deduced from a systematic study of donor formation kinetics [16]. The incorporation of O in the core of the TDs has been established [17], and the discrete reductions of ionization energy with increasing index along the series is consistent with the successive incorporation of additional atoms. The implied attachment rates of this entity have long been known to be much greater than those expected for the arrival of randomly diffusing O_i in a dilute solution. Depending on initial assumptions, resolution of this discrepancy has been suggested to indicate either that the added atoms are native defects rather than O-atoms or that the reaction rates associated with O-clustering are anomalous. Conclusive structural identification of even the electrically active core of TDs has proved difficult, and the debate has become centered on whether [18] or not [19] an additional I-atom is involved.

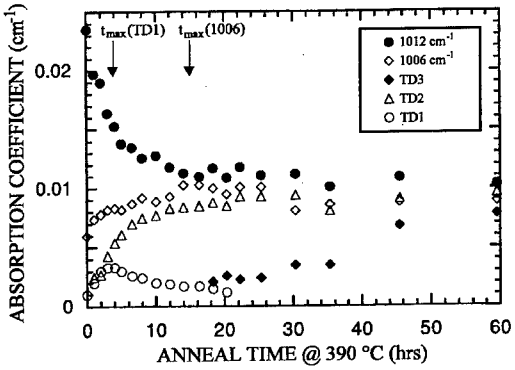


Figure 1. Evolution of defect concentrations during an isothermal anneal of as-grown material (Ref. 15).

Information derived from $[O_i]$-loss measurements.

The rates at which absorption in the 9μm band decreased during the anneals implied the loss of on average ~ 10 O_i atoms per TD formed. At the lowest temperatures ($T \leq 400°C$), the rates increased in proportion to $[O_i]^2$ in different samples and varied only slightly (by a factor of ~3) with increasing anneal time [20]. The process was accelerated in samples which had been heated

previously in H_2(g) and the larger diffusion rates were consistent with measured enhancements of the rates of reorientation of O_i in similarly treated material. On the basis of a uniform distribution of atoms and relatively insignificant concentration of additional sinks, the obvious interpretation would be that the rate of the process is controlled by that of interaction of two randomly diffusing O_i ($d[O_i]/dt=-2k_f[O_i]^2$). For a reasonable choice of capture radius ($r_c=5$Å), the implied values of D_{oxy} ($=k_f/4\pi r_c$) are close to an interpolation of measurements and values derived from the O_i reorientation rates at higher and lower temperatures respectively. The different time scales of reorientation and $[O_i]$-loss would be explained simply by their being first and second order reactions, respectively. Consideration of the whole serial reaction with similar rate coefficients for each step would lead to the conclusion that $[O_i]$-loss should cause increases of mainly $[O_2]$.

The kinetics of $[O_i]$-loss during anneals at moderately higher temperatures, while remaining fairly uniform with increasing anneal time, are less than are implied by an exptrapolation ($E_a=2.53$eV) of the lower temperature data. Their dependence on $[O_i]^x$ varied such that x increased from 2 to values of up to 8 at 500°C. The changes indicate the increasing effect of back reactions, but no way has been found to account for the observations by assuming that dimers dissociated if these defects would otherwise accumulate in the crystal during the anneals. Uniform reductions with anneal time require that the concentration of the dissociating cluster is already close to steady state with respect to $[O_i]$ as a result of some other reaction. The fact that no loss of $[O_i]$ is detectable before such reductions become evident would imply that this other process(es) is much faster (by a factor of >100) than the rate at which O_i in a dilute solution would be expected to diffuse to the dimer. Most importantly, explanation of the measured increases in order (x) of the reaction requires that the fast process(es) involves further O atoms. Specifically, if the formation of some large cluster (O_N) occurred rapidly following dimer formation then the increasing competition between dissociation and this transformation would cause the order to vary from $x=2$ to $N/2$ when the two processes were balanced and finally to $n=N$ when the rate of dissociation greatly exceeded that of the transfer of O from O_2 to O_N. Thus, the observed kinetics of $[O_i]$-loss could be explained if O_8 were forming rapidly following dimerization over the whole range of temperatures ($T\leq 500$°C) while the relative contribution of dissociation tended to be insignificant at temperatures at or below 400°C. In other words, the kinetics of $[O_i]$-loss imply that pairing of atoms is the rate limiting step in the formation of much larger O-clusters, a conclusion that would be consistent with the view that the various TDN are distinguished by their incorporation of different numbers of O-atoms.

Modeling investigations.

The implication that the kinetics of O-clustering are anomalous leads to obvious problems in deciding what can be assumed initially in a realistic model. This choice inevitably will influence conclusions about what gives rise to the unexpected behavior. Since the rate of loss of $[O_i]$ is close to the expected arrival rate of O_i at another such atom in a dilute solution, subsequent clustering reactions would have to be much faster than expected. While it seems difficult to justify values of $r_c>500$Å for the capture of neutral O_i by O_2, it has been argued that measurements of out-diffusion at low temperatures provide evidence that O_2 can diffuse rapidly [21].

O_2 clustering.

The observed kinetics of $d[O_i]/dt$ for $400\leq T\leq 500$°C could be explained entirely by dissociation of O_2, if the dimer otherwise diffused rapidly and reversibly combined with O_n ($n<5$) as an entity [22]. The simple assumption that O_2 did not form a stable complex on interaction with O_i would ensure that the dimers formed faster than they were trapped and a large flux of O_2 generally would give rise to the rapid and independent evolution of two series of clusters consisting of odd and even numbers of O-atoms. The assumption that dissociation rates decreased uniformly with increasing cluster size (where dissociation would have to involve the release of O_2 rather than O_i to avoid large reductions in the rate of $[O_i]$-loss at low temperatures) would favor the dominance of the odd-numbered series,

possibly related to TDs. Two additional assumptions were required to emulate the evolution of defect concentrations, exposing weaknesses in this type of explanation. The first was that r_c for capture of O_2 by the large stable clusters (taken to correspond to TD1-3) decreased with increasing size, so having envoked rapid diffusion of O_2 to greatly increase forward rates, these rates are then supposed to slow during clustering. The variation is contrary to reasonable expectation for the capture of O_i-atoms by clusters of increasing size. The second weakness arose in an attempt to correlate the TD-nucleii with smaller unstable clusters (O_3 and O_5) by deliberate choice of initial concentrations. It was not possible to reproduce the observation that the time required for absorption in the 1006cm^{-1} band to reach a steady state value was longer than that for [TD1] (Fig. 2a). The simulated steady state values for $[O_3]$ and $[O_5]$ at low temperatures (no dissociation) varied in proportion to $[O_i]^{1.3}$ and $[O_i]^{1.7}$ respectively, whereas the absorption in 1012 and 1006cm^{-1} bands in spectra of as-grown material [15] were almost direct proportional to $[O_i]$. A proportional dependence of cluster concentrations with $[O_i]$ and rapid arrival of O_2 to them could consistently be explained if a barrier existed which reduced the rate of the reaction between O_2 and O_i, but was smaller or absent for the corresponding reactions between O_2 and O_3 and between two O_is. However, the step-like variation of splitting of electronic absorption lines ($2p\pm$) with increasing index in the TDN series [13] suggests the addition of single atoms at each stage rather than pairs, and there is no evidence that concentrations of intermediate clusters (even numbered ones) are detected during the annealing of TDN at higher temperatures.

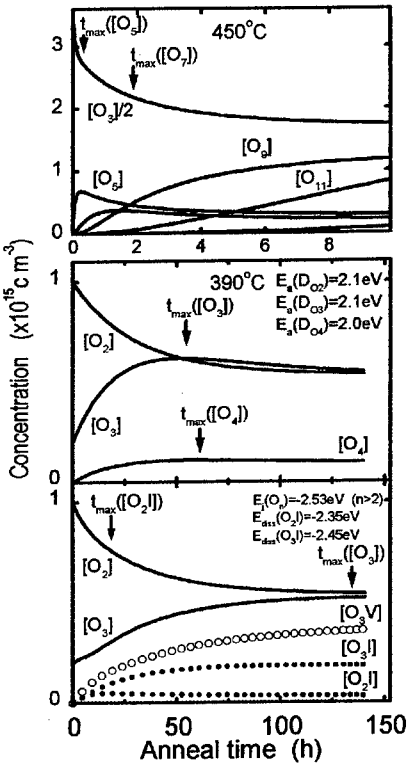


Figure 2 Variations in concentration of O-clusters with increasing anneal time for various serial reactions. The reversible clustering of rapidly diffusing dimers (a), rapid diffusion of O_2, O_3 and O_4 (b) and the latter with the further assumption of I-atom ejection by O_3 and reversible decoration of all clusters. The arrows indicate times at which maxima are established.

Rapid reaction between O_n and O_i.

An alternative explanation would be to suppose that all forward reactions in the serial reaction proceeded faster than that expected for the arrival of O_i. In order to account for the reverse reactions which become apparent at $T > 400$°C, dissociation of clusters containing up to 8 O-atoms would then have to be coupled, i.e., the respective forward and reverse rates would have to vary proportionally. Evolution of the first three members of the TD-series appears to be modified by back reactions in the same temperature range ($T \geq 427$°C) [16] as that implied by measurements of $[O_i]$-loss. Their effect was most pronounced in material with relatively low values of $[O_i]$, consistent with attributing these TDs to the smaller unstable clusters. If O-clusters reacted rapidly and irreversibly with O_i at low temperatures, their steady state concentrations would be expected to vary in proportion to $[O_i]$. On the other hand, the efficient trapping of O_n by O_i would imply that, even if the clusters diffused rapidly, the arrival rate of both O_n and O_i to any other defect would be similar. Thus, rapid evolution of an extended series of O-clusters would require that each and every corresponding forward rate were somehow faster than expected. Simply varying the forward reaction rates in this way cannot explain the longer time taken for the absorption strength in the 1006cm^{-1} band to reach steady state relative to that for TD1 (Fig. 2b), a limitation inherent to any serial reaction. In other words, if TD1 is converted to TD2 by the addition of an O_i atom, then the same process cannot be

expected to account for the distinction between 1006cm^{-1} and TD1. One way to resolve this problem is to suppose that the internal strain in the cluster giving rise to 1006cm^{-1} IR absorption band is sufficient to eject an I-atom and that TDs 1 and 2 are the result of I-decoration of the clusters giving rise to 1012 and 1006cm^{-1} bands (Fig. 2c). This model agrees with one proposed identification of the TD core [18] and with the loss of one C_s atom at the rate of between 2 and 3 O_i atoms during corresponding anneals of highly carbon doped material [23]. While the absence of evidence to support the formation of O_3V is at odds with this explanation, the underlying problem is that envoking I-ejection in this way does not account for the rapid arrival of O to the defects (undecorated dimer and trimers were supposed to diffuse rapidly in the simulation shown in Fig.2c). On the other hand, it has often been speculated that I-atoms might play some role in explaining the rapid arrival of O to TDs.

I catalysed diffusion of O_i.

If a catalyst were released during O-clustering which greatly enhanced the forward reaction rates, uniform rates of $[O_i]$-loss would not be expected in general. However, this contradiction with observation can be avoided under restricted conditions. If O_2 both ejected and trapped a rapidly diffusing I-atom, then the dominant defects formed during the anneal would be $[O_2I]$ and $[O_2V]$, while [I] would tend to a steady-state value independent of $[O_i]$ and given by the rate of its ejection by O_2. By setting the latter rate to be the same as that of O_i hopping, the assumption that the transient interaction of an I-atom with O_i caused a single diffusion jump would ensure that both normal and catalyzed hops would occur at the same rates (Fig. 3b). The alternative assumption that O_2I defects were unstable and that they dissociated by releasing $2O_i$ and an I-atom would ensure that the rate of catalyzed O_i hopping increased dramatically while the balanced catalysis of O_2 dissociation would maintain the overall rate of loss of $[O_i]$ (second order included). The rate of O_i-O_i interaction would then be much greater than that of $[O_i]$-loss. The catalyzed diffusion of O_i to O_nV and O_nI ($n>1$) would cause the number of O_i atoms per unit time to increase during the anneals, but this can be stabilized by allowing the I-atom to recombine with some O_nV larger than O_2V (e.g. O_4V in the simulation shown in Fig. 3c). Unfortunately, a low rate of recombination of I with O_2V turns out to be critical to the emulation of the $[O_i]$-measurements at low temperatures. The rate of $[O_i]$-loss is reduced by increasing the probability ($P > 10^{-4}$) of this recombination and the reduced rate would tend to a dependency on $[O_i]^3$. This gives rise to two obvious problems. First, treatments at temperatures at which such clustering would occur usually precede lower temperature anneals during which the loss of stress-induced dichroism is measured and, if a catalyst were accumulating in the crystal or condensing into some weakly bound complex during cooling, greatly enhanced rates of O_i reorientation would be expected but are not observed. Second, O_2V which is believed to give rise to an IR absorption band at 889cm^{-1} [24] is not detected following anneals of unirradiated material. Many variations of this model were investigated including assumptions that only clusters larger than O_2 ejected an I-atom, and that O_2V dissociated

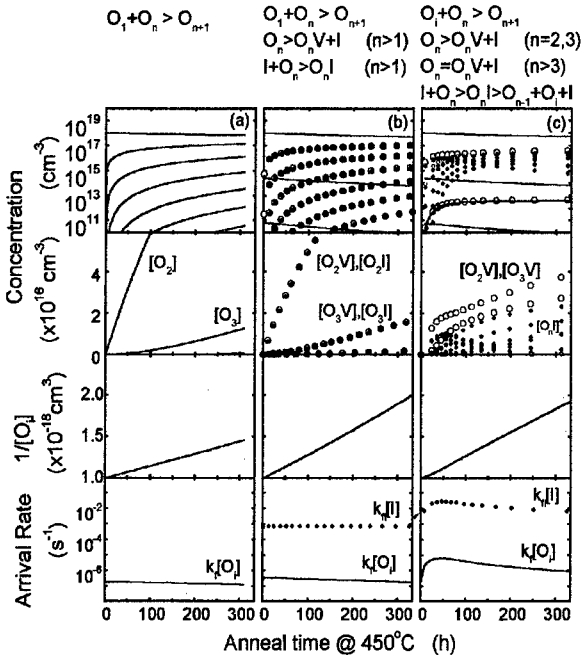


Figure 3. Simulation of the simplest serial reaction of O-clustering (a), I-atom release and capture by clusters with catalyzed D_{oxy} (b) and similarly catalyzed dissociation of O_n (c).

so catalysis of D_{oxy} by V occurred. In spite of these efforts, no other way was found that catalysis could account for the uniformity of the rates of $[O_i]$-loss revealed by the measurements.

I-O_i pair diffusion.

The simplest way to emulate the observed kinetics of $[O_i]$-loss remains to assume that they are controlled by the rate of O_i-O_i interaction and that D_{oxy} is normal. It is possible that a subsequent reaction between I and O_2 causes the redistribution of O via a rapidly diffusing I-O_i pair. This would be significant if O_2 caused the ejection and mainly $[O_3I]$ and $[O_2V]$ would be the predominant defects formed. The absence of evidence for the latter defect would therefore remain a problem. Similar dissociative release of OI along the O_nI series would result in dramatically decreasing concentrations of O_nI with increasing I and would merely change the number of O-atoms in the O_nI defect which predominated. In fact, the difference between the underlying rates of formation of O_2 and O_n ($n>2$) are accentuated by the assumed mechanism so that a serial reaction generally would not be expected. If the first cluster assumed to eject the I-atom were larger than O_2, the catalytic process would be insignificant, since I-generation would be much slower than that of O_2. It might be argued that I-O_i reacted only with O_nV, to explain the absence of absorption due to the latter defect.

V-O_n diffusion.

The problems associated with the absence of absorption bands attributed to O_2V, or O_3V in the spectra of annealed material can be avoided conveniently if these defects are supposed to diffuse rapidly. Conversion of O_2V to O_3V has been proposed to account for the exchange of absorption among different IR bands in the spectra of irradiated material during anneals at $\sim$475°C [24]. Supposing the transformation occurred by diffusion of O_2V, the implied barrier to diffusion would be only 2eV for the same prefactor as that for O_i diffusion. Rapid conversion of O_2 to O_3 could be explained in this way without implying that $[O_2V]$ should be greater than the IR detection limit, if both defects ejected I-atoms at relatively slow rates. However, it would be difficult to account for the observed evolution of defect concentrations with increasing anneal time if TDN corresponded to relatively unstable O_nI complexes (Fig. 2c) without implying that $[O_2V] > [O_2I]$ at some stage.

A barrier to O_2 formation.

Assuming that dimers are formed at the expected rate implies that subsequent reactions are anomalously fast. Yet the only defect whose steady state concentration clearly increases with increasing temperature in the temperature range below 450°C is that which gives rise to the 1012cm^{-1} absorption band [15], apparently the first cluster formed. Even if the transformations of subsequent defects occurred faster than the underlying rate limitation, there is no evidence that differences between the relative rates correspond to changes of activation energies: the measured relative concentrations of individual [TDN] for $N\geq 2$ did not change in material with high $[O_i]$ annealed over a wide range of temperatures ($395\leq T\leq 490$°C) [25]. Evidence that the concentrations of defects which give rise to the 1012 and 1006cm^{-1} bands in as-grown material are proportional to $[O_i]$ raises doubts about the conclusion that the rate of $[O_i]$-loss is that of O_i-O_i interaction [20]. Second order kinetics would be equally consistent with the loss of a large fraction of $[O_i]$ directly to these defects rather than to other O_i atoms. Inversely, steady state concentrations of clusters would be expected to vary proportionally with $[O_i]$ provided they trapped an O_i faster than they dissociated in the range of temperatures over which their concentrations were established. In the same temperature range at which back reactions are apparently significant ($T>400$°C), TDN ($N>3$) have been found to realign at rates smaller than that for O_i but with similar activation energies [26] and it was argued that the reorientation rate was limited by the diffusion of nearby O-atoms. If such motion occurred entirely within the donor complex then the process would be irrelevant to the O-agglomeration puzzle, unless reorientation corresponded to enormous diffusion jumps of the whole defect. However, the motion may involve atoms which would otherwise give rise to absorption at 9μm so that these diffusion steps would be equivalent to forward and reverse reactions, consistent with cluster instability at these

temperatures. If the rates of O_i-O_i interaction were much greater than those of $[O_i]$-loss, then rather than implying that reactions leading to formation of $O_n(n>2)$ were faster than expected, the conclusion would be that dimer formation was relatively slow. It has been argued that both strain and Coulombic interactions between two O_i-atoms would cause them to repel each other [27]. Of course the problem then would be to account for the large rates of O_i-O_i interaction relative to those expected on the basis of random diffusion in a dilute solution. As described above, an explanation in terms of catalytic reactions was found to be inconsistent with observations. If O-atoms were confined to small volumes within which their concentration was uniform and they diffused randomly, a local concentration greater than the average by a factor of 50 and a correspondingly reduced probability of dimer formation leads to rapid evolution of a series of O-clusters while the implied average rates of $[O_i]$-loss were similar to those measured (Fig. 4).

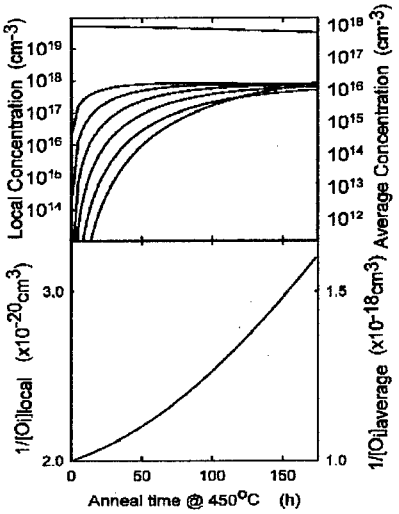


Figure 4. Effect of spatial correlation of O-atoms causing a local increase in concentration by a factor of 50 with a similar reduction in probability that O_2 forms relative to the rate of O_i-O_i interaction

Discussion and Conclusions.

Variations in dependence of the average rate of $[O_i]$-loss on average concentration indicate that pairing is the slowest step in the formation of clusters with larger numbers of O-atoms. Since the absolute rates are close to those expected for O_i-O_i interaction in a dilute solution, it would seem reasonable to suppose that subsequent reactions were anomalously fast. If O_2 diffused rapidly, the behavior could be accounted for in principle, but while proportionality between defect concentrations and $[O_i]$ would be expected if the dimers reacted with O_i, this same reaction would not, in general, lead to the rapid evolution of a series of clusters with larger numbers ($n>3$) of O-atoms. If clusters ejected I-atoms which then decorated others, some explanation for the observed evolution of defect concentrations [15] would be provided, but no way was found that I-atom interactions with either O_i or O_2 could account for the relatively fast arrival of O_i necessary for rapid formation of large clusters ($n>3$) without contradicting other experimental observations. The observed temperature dependence of the steady state absorption in the $1012cm^{-1}$ band *and* rapid evolution of a series of O-clusters would most naturally be explained, if a barrier existed to the first stage of clustering. The observation of back reactions in TDN evolution and realignment of TDN($N>3$) [26] in the same temperature range as that in which clusters smaller than O_8 seem to be unstable, suggest that a reversible exchange occurs between atoms in the matrix (O_i) and those in the defect. If these reactions accounted for a large fraction of the $[O_i]$-loss, the measured rates of $[O_i]$-loss at low temperatures would then have to be significantly slower than the average rate of O_i-O_i interaction and the observed correlation between $d[O_i]/dt$ and O_i-reorientation kinetics, would restrict the potential explanation to a) a much larger diffusion jump distance than the nearest neighbor separation, b) a large radius for capture of O_i by O_n and/or c) a spatially correlated distribution of O_i. The possibility that O_i and O_n kick-out I-atoms and rapid diffusion of O_nV occurs is difficult to rule out, particularly given the Coulombic attraction which can be expected between OV^- and donors. Unlike the assumption that O_2 diffused rapidly, such an explanation would be supported by the observed fast evolution of O_nV clusters during anneals of irradiated material [24]. But a much simpler explanation can be provided if the assumption of a dilute solution is discarded. Correlated concentration fluctuations, the potential importance of which has already been emphasized [28,29], could account for the rapid evolution without implying that D_{oxy} was greatly affected, provided that they were sufficiently large ($\Delta[O_i]$ greater than one order of magnitude and $>40\%$ of the atoms in the enriched areas). The short durations of effects of high temperature pretreatments ($\sim$30h at 427°C [16]), would then imply that the 'clouds' were not removed by the pretreatment,

or that they reformed rapidly (T > 800°C) during cooling. If such fluctuations were present then the kinetics of [O_i]-loss would depend not only on D_{oxy} but on their average concentration and spatial dimensions. The observed tendency for the number of O_i-atoms lost per unit time to increase in the simulation (Fig. 4) could be compensated by the depletion of [O_i] in the clouds, an effect not considered in this simulation and likely to be particularly important if the number of atoms in the fluctuations is small ($\sim$50 atoms), similarly the decreasing reaction rates along the TD series might be accounted for. In summary, the kinetics of [O_i]-loss indicate that dimerization is the slowest step in the formation of much larger clusters but the implication that reaction rates lead to steady state concentrations which vary in proportion to [O_i] leads to difficulties in distinguishing whether subsequent reactions are much faster than expected or that the pairing step is slow. No reasonable way has been found to explain rapid cluster evolution in a dilute solution by envoking reactions with interstitials, even if they are ejected by small clusters. Rapid diffusion of clusters (in one form or other) may occur although there is no evidence that such rates are associated with low activation energies. If the solid solution is composed of large correlated concentration fluctuations, long-range D_{oxy} need not be significantly enhanced.

1. F.M.Livingstone, S.Messoloras, R.C.Newman, B.C.Pike, R.J.Stewart, M.J.Binns, W.P.Brown and J.G.Wilkes, J.Phys.C **17**, 6253 (1984).
2. J.C.Mikkelson, Jr., Mat.Res.Soc.Symp.Proc. **59**,19 (1986);
3. P.D.Southgate, Proc. Phys. Soc. (London) **36**, 385 (1960).
4. J.W.Corbett, R.S.McDonald and G.D.Watkins, J. Phys. Chem. Solids **25**, 873 (1964).
5. S.M.Hu, Mat.Res.Soc.Symp.Proc. **59**, 249 (1986).
6. A.Bourret, Mat.Res.Soc.Symp.Proc., **59**, 223 (1986);
7. N.Inoue, K. Wada and J. Osaka, in "Semiconductor Silicon", ed. H.R.Huff, R.J.Kriegler, and Y.Takeishi (NJ, The Electrochemical Society), pp282-293 (1981).
8. H.Yamanaka, Jpn.J.Appl.Phys. **31**, 2519 (1992).
9. S.-Tong Lee, P.Fellinger, and S.Chen, J.Appl.Phys. **63**, 1924 (1988).
10. Y.Tokuda, M.Katayama and T.Hattori, Semicond.Sci.Technol. **8**, 163 (1993).
11. W.Wijaranakula, J.Appl.Phys. **68**, 6538 (1990).
12. V.Cazcarra and P.Zunino, J.Appl.Phys. **51**, 4206 (1980).
13. P.Wagner and J.Hage, Appl.Phys. **A49**, 123 (1989).
14. W.Götz, G.Pensl and W.Zulehner, Phys.Rev. **B46**, 4312 (1992).
15. J.L.Lindström and T.Hallberg, J.Appl.Phys. **77**, 2684 (1995), J.Appl.Phys.**79**, 7570 (1996).
16. L.I.Murin and V.P. Markevich in "Defect Control in Semiconductors", ed. K.Sumino (North-Holland), pp199-210, (1990).
17. J.Michel, J.R.Niklas, and J.M.Spaeth, Phys.Rev.B **40**, 1732 (1989).
18. P.Deák, L.C.Snyder and J.W.Corbett, Phys.Rev.B **45**, 11612 (1992).
19. D.J.Chadi, Phys.Rev.Let. **77**, 861 (1996).
20. S.A.McQuaid, M.J.Binns, C.A.Londos, J.H.Tucker, A.R.Brown and R.C.Newman, J.Appl.Phys. **77**, 1427 (1995).
21. U.Gösele, K.-Y.Ahn, B.P.R.Marioton, T.Y.Tan and S.-T.Lee, Appl.Phys.A **48**, 219 (1989).
22. S.A.McQuaid, R.C.Newman and E.Muñoz, Mat. Sci. Forum **196-201**, 1309 (1995).
23. R.C.Newman, A.S.Oates and F.M.Livingston, J.Phys.C **16**, L667 (1983).
24. J.W.Corbett, G.D.Watkins and R.S.McDonald, Phys.Rev. **135**, A1381 (1964).
25. M.Claybourn and R.C.Newman, Appl.Phys.Lett. **51**, 2197 (1987).
26. J.M.Trombetta, G.D.Watkins, J.Hage and P.Wagner, J.Appl.Phys. **81**, 1109 (1997).
27. J.Michel and L.C.Kimmerling in "Oxygen in silicon" ed. F.Shimura (Academic, San Diego), Chap.7 (1994).
28. A.Ourmazd, W.Schröter and A.Bourret, J.Appl.Phys.**56**, 1670 (1984).
29. K.F.Kelton and R.Falster, MRS Spring Meeting (San Francisco,.1997), to be published.

Materials Science Forum Vols. 258-263 (1997) pp. 355-360
© 1997 Trans Tech Publications, Switzerland

TEMPERATURE-DEPENDENT WIDTHS OF INFRARED AND FAR-INFRARED ABSORPTION LINES OF OXYGEN IN SILICON

H. Yamada-Kaneta
Process Development Div., Fujitsu Ltd.,
4-1-1 Kamikodanaka, Nakahara-ku, Kawasaki 211-88, Japan

Key words: Silicon, Oxygen, Impurity, Infrared absorption, Line width

Abstract. For temperatures below 70 K, we measured the widths of the absorption lines in the 1100- and 30-cm^{-1} bands of oxygen in silicon. Strong temperature dependences of the line widths observed for both bands were ascribed to the one-phonon transitions in the energy-level ladders of the 30-cm^{-1} excitation belonging to the ground and first excited states of the 1100-cm^{-1} mode. A formulation was given to the interaction between the two-dimensional low-energy anharmonic excitation of oxygen and the phonons. This clarified the selection rule for the phonon transitions, and suggested the essential phonon transitions for the observed behavior of the line widths. Origin for the extreme narrowness of the low-temperature 29.3-cm^{-1} line was also clarified.

I. Introduction

The bond-interstitial oxygen in silicon, the Si-O-Si center, causes the absorption bands at about 30 and 1100 cm^{-1}. The 30-cm^{-1} band, comprising the lines at 29.3, 37.7, 43.3 and 48.6 cm^{-1}, is ascribed to the two-dimensional (2D) low-energy anharmonic excitation (LEAE) due to bond-perpendicular motion of the oxygen [1, 2]. The 1100-cm^{-1} band, having three lines at 1136.4, 1128.2, and 1121.9 cm^{-1}, is attributed to A_{2u} local vibration containing the bond-parallel motion of the oxygen [2]. Due to the coupling between the 2D LEAE and the A_{2u} local mode, the energy level ladder of the 2D LEAE occurs for each of the ground and the first excited states of the A_{2u} local vibration (Fig. 4(a) of [2]). This energy-level scheme well explained the measured energies and intensities of these lines [2]. However, the strong temperature dependence of the line widths characteristic of these absorptions has not yet been described theoretically. Bosomworth et al. [1] reported that the width of the 29.3-cm^{-1} line rapidly increases with increasing temperature from 1.8 K to 35 K. Also for the 1100-cm^{-1} band, similar strong temperature dependence of the line width in the low-temperature region has been reported [3]. It attracts much interests that the lines in the 1100-cm^{-1} band, completely off-resonant to the host lattice phonons, have the temperature-dependent widths similar to that of the 29.3-cm^{-1} resonance line.

The purpose of this paper is to clarify the physical mechanism that causes these temperature dependences of the line widths. Constructing a model Hamiltonian, we quantitatively describe the temperature dependences of the line widths. Since available experimental data are insufficient, we first measure temperature dependence of the line widths for the 30- and 1100-cm^{-1} bands.

II. Experiment

Temperature dependence of the full width at half maximum (FWHM) of the lines in the 1100- and 30-cm^{-1} bands were measured with the maximum resolutions of 0.1 cm^{-1} and 0.01 cm^{-1}, respectively. Figure 1 is the spectrum of the 30-cm^{-1} band. All lines in the 30- and 1100-cm^{-1} bands were well fitted by Lorentzian curves. The results of measurement are plotted in Fig. 2. The FWHM of each line in both bands exhibits strong temperature dependence. The FWHM of the 29.3-cm^{-1} line was 0.09 cm^{-1} at 7 K, which is much smaller than the value 0.2 cm^{-1} obtained by Bosomworth et al. [1] with a resolution of 0.2 cm^{-1}. At low enough temperatures, the FWHM of the 29.3-cm^{-1} line is narrower by far than the other lines in the both bands.

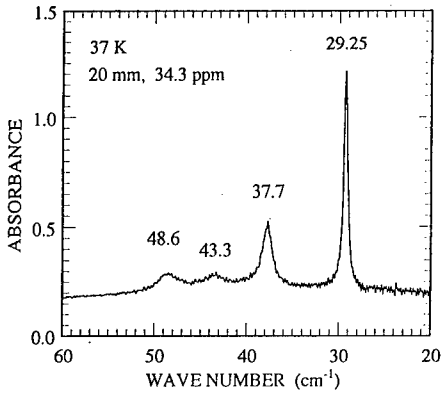


FIG. 1. The 30-cm^{-1} absorption band measured at 37 K for the oxygen concentration of 34.3 ppm and the sample thickness of 20 mm.

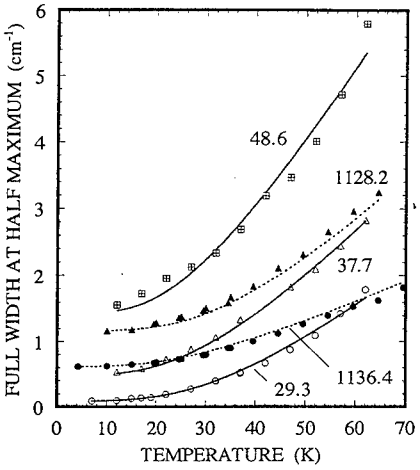


FIG. 2. Temperature dependence of the widths of the absorption lines in the 30- and the 1100-cm^{-1} bands. The experimental plots and the calculated theoretical curves are shown.

III. Model

We consider a silicon crystal containing a single Si-O-Si center. As the origin of the atomic displacements, we take the atomic configuration with the potential energy minimized under the D_{3d} symmetry, where the oxygen is at the center of symmetry forming linear Si-O-Si unit. Let (x, y) and z denote the bond-perpendicular and bond-parallel displacements of the oxygen, respectively, and q_j the displacement of the jth silicon atom. The Taylor expansion of the potential energy $U(x, y, z, q_1, q_2, q_3, \ldots)$ can be generally written as

$$U(x, y, z, q_1, q_2, q_3, \ldots) = V_{2D}(x,y) + V(z, q_1, q_2, q_3, \ldots) + W(x, y : z, q_1, q_2, q_3, \ldots) \quad . \tag{1}$$

The $V_{2D}(x,y)$ is the potential for the 2D LEAE in the static lattice. The last term is regarded as the interaction term between (x,y) and $(z, q_1, q_2, q_3, \ldots)$. We approximate the excitation due to $V(z, q_1, q_2, q_3, \ldots)$ as a system of harmonic vibrations dominated by the potential $V_H(z, q_1, q_2, q_3, \ldots)$. From the experimental fact that there exists the 1100-cm^{-1} mode localized at z displacement of the oxygen, we assume that V_H produces the local mode responsible for the 1100-cm^{-1} band, i.e., the A_{2u} local mode. So far this manner of treating the potential energy is the same as in our previous work [2]. Here we further assume that this A_{2u} local mode is completely localized at the oxygen. Thus, the V in (1) is expressed as

$$V(z, q_1, q_2, q_3, \ldots) \cong V_H(z, q_1, q_2, q_3, \ldots) \cong V_{A2u}(z) + V_P(q_1, q_2, q_3, \ldots) \quad . \tag{2}$$

The V_P is regarded as the potential for the host-lattice phonons perturbed by the presence of the oxygen. The interaction term in (1) can be generally written as

$$W(x, y : z, q_1, q_2, q_3, \ldots) = W_{2D\text{-}A2u}(x, y : z) + W_{2D\text{-}P}(x, y : q_1, q_2, q_3, \ldots) \quad . \tag{3}$$

Consequently, the potential energy U is approximated as

$$U \cong V_{2D}(x,y) + V_{A2u}(z) + V_P(q_1, q_2, q_3, \ldots) + W_{2D\text{-}A2u}(x, y : z) + W_{2D\text{-}P}(x, y : q_1, q_2, q_3, \ldots) \quad . \tag{4}$$

The interaction term between the A_{2u} mode and the other phonons is absent because of the harmonic approximation, $V \cong V_H$. Adding the kinetic energy $K_{2D}+K_{A2u}+K_P$ to (4), we obtain the total Hamiltonian, which is the sum of the following second quantized Hamiltonians:

$$H_{2D} = \sum_j \varepsilon_j a_j^\dagger a_j \ , \qquad H_{A2u} = \Delta \, | u >< u | \ , \qquad H_P = \sum_{\lambda,k} \omega_{\lambda k} b_{\lambda k}^\dagger b_{\lambda k} \ , \quad (5)$$

$$W_{2D\text{-}A2u} = | u >< u | \sum_j \Gamma_j a_j^\dagger a_j \ , \quad W_{2D\text{-}P} = \sum_{\substack{j,j' \\ (j \neq j')}} a_j^\dagger a_{j'} \sum_{\lambda,k} \left(\gamma^*_{\lambda k jj'} b_{\lambda k} + \gamma_{\lambda k j'j} b_k^\dagger \right) \ . \quad (6)$$

The H_{2D}, H_{A2u} and H_P describe the 2D LEAE, the A_{2u} local vibration and the host lattice phonons, respectively. The label j is the abbreviation of the labels (k, ℓ) that we used previously to specify the 2D LEAE eigenstates [1]: k $(= 0, 1, 2, \ldots)$ distinguishes the eigenstates having the same angular momentum ℓ $(= 0, \pm1, \pm2, \ldots)$. The diagonal interaction terms $(j = j')$ were neglected in $W_{2D\text{-}P}$. The A_{2u} local mode was simplified as the two-level system $\{ | d >, | u > \}$ with the energy Δ much higher than the maximum phonon energy.

IV. Method of calculation

For now, we omit the index λ. The problem for the A_{2u}-mode-coupled 2D LEAE is already solved since its Hamiltonian is diagonal with respect to $\{ | d > | j >, | u > | j > \mid j = 1, 2, 3, \ldots \}$:

$$H_{2D\text{-}A2u} \equiv H_{2D} + H_{A2u} + W_{2D\text{-}A2u} = | d >< d | \, H_{2D}^{(d)} + | u >< u | \, H_{2D}^{(u)} \ , \quad (7)$$

$$H_{2D}^{(d)} \equiv H_{2D} \ , \qquad H_{2D}^{(u)} \equiv \Delta + \sum_j \varepsilon_j' a_j^\dagger a_j \ , \qquad \varepsilon_j' \equiv \varepsilon_j + \Gamma_j \ . \quad (8)$$

The $H_{2D}^{(d)}$ and $H_{2D}^{(u)}$ give the energy-level ladders $\{\varepsilon_j \mid j = 1, 2, \ldots\}$ and $\{\Delta + \varepsilon_j' \mid j = 1, 2, \ldots\}$ of the A_{2u}-mode-coupled 2D LEAE. We refer to the states belonging to the former and the latter energy-level ladders as d-states and u-states, respectively. By means of the one-particle retarded Green's function, we calculate how the phonon coupling $w_{2D\text{-}P}$ causes finite width to the d-state energy levels. The expression for widths of the u-state energy levels can be simply obtained by substituting ε_j' into ε_j in the resultant expression for the d-state energy levels. The density distribution function of energy level for the state $| d >| j >$ is given by

$$\rho_j(E) = (-1/\pi) \ \mathrm{Im} << a_j \ ; a_j^\dagger >>_{E + i0_+} \ , \quad (9)$$

where the Heisenberg operator $a_j(t)$ of the retarded Green's function

$$<< a_j ; a_{j'}^\dagger >>_z \equiv -i \int_{-\infty}^{\infty} dt \ e^{izt} \, \theta(t) < \{ a_j(t) \, , a_{j'}^\dagger \} > , \qquad \mathrm{Im}\, z > 0 \ , \quad (10)$$

is driven by the Hamiltonian $H_{2D}^{(d)}+H_P+W_{2D\text{-}P}$. (If we deal with the u-state, then $a_j(t)$ is to be driven by $H_{2D}^{(u)}+H_P+W_{2D\text{-}P}$.) Once we obtain the Green's function in the form

$$<< a_j \ ; a_j^\dagger >>_z = \frac{1}{z - \varepsilon_j - \xi_j(z)} \ , \quad (11)$$

then, the FWHM of the density distribution function of energy level is given by $2 \mid \mathrm{Im} \ \xi_j(\varepsilon_j + i 0_+) \mid$. We adopted the equation of motion method (Eq. (3.7) of [4]) to calculate the Green's function. Using the original label (k, ℓ), the obtained expression for the FWHM is written as:

$$2 \mid \mathrm{Im} \ \xi_{k\ell}(\varepsilon_{k\ell} + i0_+) \mid = \sum_{\substack{k,\ell \\ (\neq k', \ell')}} [\, (1 + P_{k\ell,k'\ell'}) \, s_{k\ell,k'\ell'} + P_{k\ell,k'\ell'} \, s_{k\ell,k'\ell'} \,] , \quad (12)$$

$$P_{k\,\ell,k'\ell'} = 1/[\exp\{\beta(\varepsilon_{k\,\ell}-\varepsilon_{k'\ell'})\}-1]\ , \tag{13}$$

$$s_{k\,\ell,k'\ell'} \equiv 2\pi \sum_{\lambda,k} |\gamma_{\lambda k,k\,\ell,k'\ell'}|^2\ \delta(\varepsilon_{k\,\ell}-\varepsilon_{k'\ell'}-\omega_{\lambda k})\ . \tag{14}$$

The first and the second terms on the right side of (12) are interpreted as the contributions from the one-phonon emission and absorption processes, respectively. In fact, by the first order perturbation theory, we can show that $(1 + P_{jj'})\, s_{jj'}/\hbar$ and $P_{j'j}\, s_{j'j}/\hbar$ are the rates of the transition $|j> \rightarrow |j'>$ due to emission and absorption of a phonon in thermal equilibrium, respectively. Therefore, following Weisskopf and Wigner [5, 6], we calculate here the width $Y_{jj'}$ of the optical absorption line due to the transition $|j> \rightarrow |j'>$ as the sum of the FWHMs for the initial state $|j>$ and the final state $|j'>$ which are both calculated with (12).

V. 2D LEAE–Phonon Interaction

We assume that the 2D LEAE of the oxygen interacts only with the two adjacent Si atoms. Then, the interaction $W_{2D\text{-}P}$ is written in the following symmetrized form:

$$W_{2D\text{-}P}(x,y:\{q_j\}) = \sum_{\Gamma,\gamma} w_{\Gamma\gamma}(x,y)\ q_{\Gamma\gamma}\ , \qquad \Gamma = A_{1g}, E_u, E_g\ . \tag{15}$$

The $q_{\Gamma\gamma}$ are symmetrized displacements composed of the displacements of two adjacent Si atoms, which are shown in Fig. 3. The lowest order terms of the interaction potential $w_{\Gamma\gamma}$ are written as

$$w_{A1g} = c_{A1g}\, r^2\ , \tag{16}$$

$$w_{Eu\,x} = c_{Eu}\, x = c_{Eu}\, r\cos\phi\ , \qquad w_{Eu\,y} = c_{Eu}\, y = c_{Eu}\, r\sin\phi\ , \tag{17}$$

$$w_{Eg\,a} = c_{Eg}\,(x^2-y^2) = c_{Eg}\, r^2\cos 2\phi\ , \qquad w_{Eg\,b} = c_{Eg}\,(2xy) = c_{Eg}\, r^2\sin 2\phi\ . \tag{18}$$

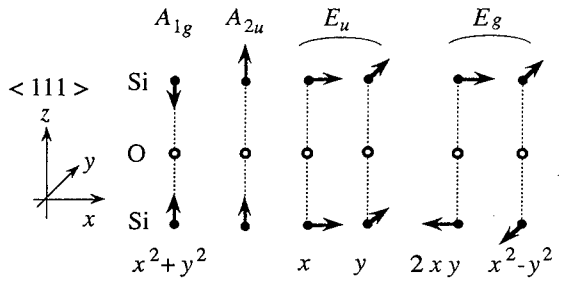


FIG. 3. Symmetrized displacements composed of the displacements of the nearest neighbor silicon atoms. The corresponding irreducible representations and the potential induced by each symmetrized displacement are also shown.

The potential induced by q_{A2u} was neglected, since such the potential is higher than the second with respect to (x, y). After brief manipulation using the phonon field operator, we see that the coupling constant is written as follows

$$\gamma^{*}_{\lambda k,k\,\ell,k'\ell'} = (\hbar/2\omega_{\lambda k})^{1/2} \sum_{\kappa,\alpha} u^{(\lambda k)}_{\kappa\alpha} \sum_{\gamma} A_{\kappa\alpha,\Gamma\gamma} <k\ \ell\,|\,w_{\Gamma\gamma}\,|\,k'\ \ell'>\ , \quad \Gamma = A_{1g}, E_u, E_g\ , \tag{19}$$

where $u^{(\lambda k)}_{\kappa\alpha}$ is the eigenvector of the unperturbed phonon belonging to $(\lambda, \boldsymbol{k})$, $A_{\kappa\alpha,\Gamma\gamma}$ is a matrix of symmetrizing transformation, κ (= 1, 2) specifies the Si atoms in the unit cell in which the oxygen is incorporated, and α (= x, y, z) denote the component of the Cartesian coordinates.

There is at most one kind of Γ that gives nonzero $<k, \ell\,|\,w_{\Gamma\gamma}|\,k', \ell'>$ for given (ℓ, ℓ'). This is why the summation with respect to Γ is absent from (19). Accordingly, the Γ in (19) indicates such the unique Γ that gives nonzero $<k, \ell\,|\,w_{\Gamma\gamma}|\,k', \ell'>$, if it exists. In other words, there is at

most one kind of symmetrized displacement that contributes to an $s_{k\ell,k'\ell'}$ in (14). In this meaning, the phonon transition rate $s_{k\ell,k'\ell'}$ is classified into the representation Γ of the symmetrized displacement. For $\ell-\ell' = 0, \pm 1, \pm 2$, the transition $|k, \ell> \rightarrow |k', \ell'>$ is caused by the phonon modes $(\lambda, \boldsymbol{k})$ containing the A_{1g}-, E_u-, E_g-displacements, respectively. For $|\ell-\ell'| \geq 3$, $<k,\ell|w_{\Gamma\gamma}|k',\ell'>$ vanishes. Thus we have only to take account of the phonon transitions that change ℓ by 0, ± 1 or ± 2. The other types of the transitions are irrelevant (negligible) for the present system. From (19), we find the important relation, $s_{k\ell,k'\ell'} = s_{k-\ell,k'-\ell'}$.

VI. Result of Calculation

Hereafter, we express $|k, \ell>$ by the abbreviated symbol $\ell^{(k)}$, where (k) stands for the primes whose number indicates the value of k. For example, $|0 \pm 1>$ and $|1, \pm 1>$ are abbreviated as ± 1 and $\pm 1'$, respectively, and $s_{0-1,10}$ as $s_{-1,0'}$. We have already known the energy levels for the d-state ($N=0$ state) and the u-state ($N=1$ state) (Fig. 4(a) in [2]). Figure 4 shows the phonon transitions between the d-states that we take into account in the present calculation. Also for the u-states, we assume the same type of the phonon transitions. In order to reduce the number of the adjustable parameters, we simplify the energy levels as in Fig. 5, instead of those in Fig. 4.

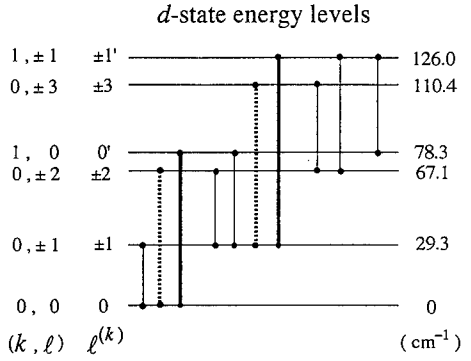


FIG. 4. The phonon transitions taken into account in the present calculation for the line widths. The transition through the A_{1g}-, E_u- and E_g-displacements are described by the bold lines, thin lines and dotted lines, respectively. Two types of the labeling, (k, ℓ) and $\ell^{(k)}$, are given to each eigenstate. The same types of transitions are assumed also for the u-states.

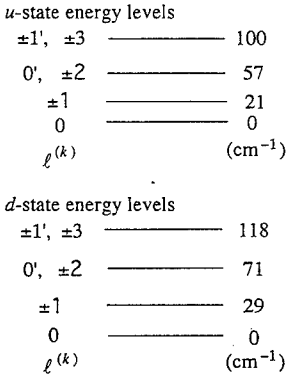


FIG. 5. Simplified energy level scheme used for the present calculation of the line width. The eigenstates belonging to each energy level are shown by means of the label $\ell^{(k)}$.

Consequently, from (12), the FWHM of the 29.3-cm^{-1} lines due to the optical transitions $|0, 0> \rightarrow |0, \pm 1>$, and that of the 1136.4-cm^{-1} line due to the transitions $|d>|0, 0> \rightarrow |u>|0, 0>$ are expressed, respectively, as follows:

$$s_{1,0} + 3\,P_{1,0}\,s_{1,0} + P_{2,0}\,(2\,s_{2,0} + s_{0',0}) + P_{2,1}\,(s_{2,1} + s_{0',0}) + P_{3,1}\,(s_{3,1} + s_{1',1} + s_{-1',1}), \quad (20)$$

$$2\,(P_{1,0} + \kappa^3_{1,0}\,P'_{1,0})\,s_{1,0} + (P_{2,0} + \kappa^3_{2,0}\,P'_{2,0})\,(2\,s_{2,0} + s_{0',0}) \,. \quad (21)$$

For small $|\boldsymbol{k}|$, we can assume $\gamma_{\lambda\boldsymbol{k},k\ell,k'\ell'} \cong g_{k\ell,k'\ell'}\,|\boldsymbol{k}|^{1/2}$. Thus from (14), $s_{k\ell,k'\ell'}$ for the u-states is easily obtained from that for the d-states by using $s^{(u)}_{k\ell,k'\ell'} \cong (\kappa_{k\ell,k'\ell'})^3\, s^{(d)}_{k\ell,k'\ell'}$, where $\kappa_{k\ell,k'\ell'} \equiv [(\varepsilon'_{k\ell} - \varepsilon'_{k'\ell'}) / (\varepsilon_{k\ell} - \varepsilon_{k'\ell'})]^{1/2}$. This is why the $(\kappa_{k\ell,k'\ell'})^3$ appears in (21). In (21), the prime added to the symbol $P_{jj'}$ indicates that this is concerned with the u-state energy levels.

Also for the other lines, the similar expressions are obtained. The curves in Fig. 2 are obtained by determining the values for $s_{k\ell,k'\ell'}$ in these formulas. $s_{1,0}$, $s_{1,0} + s_{2,0} + s_{2,1}$ and $s_{1,0} + s_{0',0} + 2s_{0',1}$, were determined from the widths of the 29.3-, 37.7- and 48.6-cm^{-1} lines measured at low enough temperature, i.e., the residual widths. The ratios $s_{2,1} / s_{1,0}$ and $s_{0',1} / s_{2,1}$ were determined from the corresponding ratios of the oscillator strength of absorption measured for the 29.3-, 37.7- and 48.6-cm^{-1} lines [7]. Since the phonon transition by the E_u displacement is the dipolar transition, the rate of such E_u phonon transition is closely related to the rate of electric dipole transition, i.e., the oscillator strength of absorption. The other values were determined by fitting the theoretical curves to the experimental plots. For the 1136.4- and 1128.2-cm^{-1} lines, the residual widths were adjusted to the experimental ones. The obtained values are given in Table I.

TABLE I. Classification of the phonon transitions and the values for the phonon transition rate.

Type of Symmetrized Displacement Responsible for Phonon transition $\mid k, \ell > \rightarrow \mid k', \ell' >$	Values for Phonon Transition Rate $s_{k'\ell',k\ell}$ (cm^{-1})
A_{1g}	$s_{0',0} = 1.26$
E_u	$s_{1,0} = 0.09$, $s_{2,1} = 0.15$, $s_{0',1} = 0.05$, $s_{3,2} + s_{1',2} = 2.37$, $s_{1',0'} = 2.54$
E_g	$s_{2,0} = 0.26$
Mixed	$s_{3,1} + s_{1',1} + s_{-1',1} = 5.2$

VII. Discussion

Since $s_{k\ell,k'\ell'}$ involves information on the phonon density of states (see (14)), direct comparison of the magnitude of $s_{k\ell,k'\ell'}$ should be made for the transitions with nearly equal transition energies. As shown in Table I, the $s_{0',0}$ for the transition energy 78.3 cm^{-1} is much larger than $s_{2,0}$ for the nearly equal transition energy. The former and the latter are caused by the phonons involving the A_{1g} and E_g displacement, respectively. This suggests that the corresponding A_{1g} matrix element $\langle 1,0 \mid w_{A1g} \mid 0,0 \rangle$ is much larger than the E_g matrix element $\langle 0,2 \mid w_{Eg\,\tau} \mid 0,0 \rangle$, τ = a, b. This would be a reasonable consideration because the interaction between the 2D LEAE and the bond-parallel displacements of the adjacent Si atoms (A_{1g} displacement) would be stronger than that between the 2D LEAE and the bond-perpendicular ones (E_g and E_u displacements). Therefore, the phonon transitions of the A_{1g} type is considered to be essential for the strong temperature dependence of the line widths for these bands.

The residual width 0.09 cm^{-1} of the 29.3-cm^{-1} line, being extremely small compared with the others of the 30-cm^{-1} band, is ascribed to the fact that there is only one phonon-transition that causes the residual width to this line. It is the phonon emission transition, $\mid 0, \pm 1 > \rightarrow \mid 0, 0 >$, which gives the width to the energy level of the state $\mid 0, \pm 1 >$. Moreover, the rate of this phonon transition $s_{1,0}$ is very small. This is why the 29.3-cm^{-1} line at low enough temperature is by far the narrower than the other lines in the 30-cm^{-1} band.

References

[1] D. R. Bosomworth, W. Hayes, A. R. L. Spray, and G. D. Watkins, Proc. R. Soc. London Ser. A **317**, 133 (1970).
[2] H. Yamada-Kaneta, C. Kaneta, and T. Ogawa, Phys. Rev. B **42**, 9650 (1990).
[3] B. Pajot, in Oxygen in Silicon (Semiconductors and Semimetals Vol. 42), edited by F. Shimura, (Academic Press, Boston, 1994), pp.191-249.
[4] Y. Kayanuma, H. Yamada, and S. Tanaka, J. Phys. Soc. Jpn. **54**, 2576 (1985).
[5] G. E. Stedman, J. Phys. C: Solid St. Phys. **3**, 1055 (1955).
[6] V. Weisskoph and E. Wigner, Z. Phys. **63**, 54 (1930); Z. Phys. **65**, 18 (1930).
[7] H. Yamada-Kaneta, unpublished.

Materials Science Forum Vols. 258-263 (1997) pp. 361-366
© 1997 Trans Tech Publications, Switzerland

THE OXYGEN DIMER IN SILICON: SOME EXPERIMENTAL OBSERVATIONS

T. Hallberg, J.L. Lindström, L.I. Murin[1] and V.P. Markevich[1]

Linköping University, Department of Physics and Measurement Technology, S-581 83 Linköping, Sweden
[1]Institute of Solid State and Semiconductor Physics, P. Brovki str. 17, Minsk 220072, Belarus

Keywords : Silicon, oxygen dimer, vibrational frequencies, annealing, binding energy

Abstract. The results of an experimental study of oxygen dimers in silicon are presented. Three infrared vibrational bands at about 1012, 1060 and 1105 cm^{-1} are shown to be related to oxygen dimers. This assignment is based on the correlation between the strengths of these bands and the interstitial oxygen concentration and on the analysis of changes in the intensity of these bands after heat-treatments in the temperature range 350-1000 °C. Isotopical shifts of the bands in the samples doped with ^{18}O gives additional support for the above identification. The binding energy of the oxygen dimer is found to be about 0.3 eV. It is estimated that the mobility of oxygen dimers should be about 4 orders of magnitude higher as compared with that of interstitial oxygen.

Introduction.

The oxygen dimer (O_2) should be the first step in the clustering process of oxygen in silicon. It was first suggested by Gösele and Tan in 1982 that fast-diffusing gas-like molecular oxygen could be responsible for the enhanced oxygen diffusion and thermal double donor (TDD) formation at T<500 °C [1]. It is now clear that such an oxygen molecule is not stable in the Si lattice, however, an oxygen dimer formed from two interstitial oxygen atoms (O_i) with a common Si neighbor can be stable in a certain configuration [2-7]. The binding energy for such a complex has been found to be in the range 0.1-1.0 eV. The activation energy for migration of the oxygen dimer could be significantly lower as compared with that of a single O_i atom [3,7], thus explaining enhanced oxygen diffusion and TDD generation. Important experimental results have shown that for T≥400°C there should be increasing significance of oxygen dimer dissociation, assuming that O_2 diffuse much more rapidly than isolated O_i atoms [8].
However, no experimental evidence for the existence of the oxygen dimer has been presented so far. Only in a recent paper of Stein and Medernach [9] an enhanced formation of vibrational infrared (IR) absorption bands at 1005, 1013 and 1063 cm^{-1} was observed in Cz-Si crystals heat-treated in H-plasma at 275 °C. One of these bands (1005 cm^{-1}) was suggested to be related to the oxygen dimer. Earlier some satellite lines near the 29.3 cm^{-1} O_i band were observed by means of high sensitive acoustic phonon spectroscopy [10]. These lines were assigned to the oxygen pairs because of the quadratic dependence of their intensity on the O_i concentration in the crystals. But these assignments [9,10] are rather tentative and in fact none of the oxygen dimer characteristics is known.
Recently the vibrational IR bands related to small oxygen clusters (TDDs and their precursors) were discovered [11-14]. It has been argued [15,16] that one of these bands (located at about 1012 cm^{-1}) is related to the oxygen dimer. This assignment was based mainly on some similarities between the expected annealing behavior of the oxygen dimer and that of the complex giving rise to the 1012 cm^{-1} band. In the present paper experimental evidence for this suggestion is given and some other IR absorption bands associated with the oxygen dimer are revealed.

Experimental.

In this study the IR absorption analysis was carried out using a Bruker IFS 113v Fourier Transform Infrared Spectrometer. The measurements were performed at room temperature and at 10 K, with a spectral resolution of 0.5-1.0 cm^{-1}. We used as-grown phosphorus and boron doped Cz-silicon samples of 2-60 Ωcm with an O_i concentration in the range $(4\text{-}15)\times10^{17}$ cm^{-3} and a substitutional carbon (C_s) concentration ≤ 10^{16} cm^{-3}. We also included a few samples with a high carbon concentration as well as samples doped with the isotope ^{18}O. The concentration of O_i and C_s was monitored by measuring the intensity of the well known absorption bands at 1107 [17] and 605 cm^{-1} [18], respectively. The heat-treatments (HTs) were performed in nitrogen ambient or in air and was followed by quenching in isopropyl alcohol.

Results and discussion.

An unique feature of the oxygen dimer is the ability to exist in Cz-Si crystals in a quasi-equilibrium concentration of 10^{14}-10^{16} cm^{-3} at high temperatures up to the Si melting point [16]. Thus, our study was focused on weak IR absorption bands related to oxygen complexes which survive after high temperature HTs.

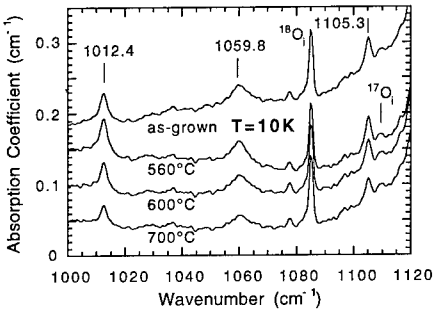


Fig. 1. IR absorption spectra measured at 10K for an as-grown sample and samples annealed for 30 minutes at 560, 600 and 700 °C.

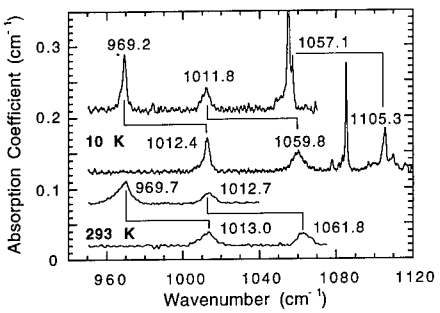


Fig. 2. Spectra (base line corrected) of as-grown ^{16}O and ^{18}O doped samples measured at 10 K and at RT. $[^{18}O_i]=1.2\times10^{18}$ cm^{-3}, $[^{16}O_i]=1.1\times10^{18}$ cm^{-3}, $[C_s]=1.5\times10^{17}$ cm^{-3} for ^{18}O sample and $[C_s]=5\times10^{15}$ cm^{-3} for ^{16}O sample.

Figure 1 shows typical IR absorption spectra at 10 K in the range 1000-1120 cm^{-1} for carbon-lean Cz-Si samples, as-grown and heat-treated for 30 minutes at 560, 600 and 700 °C. In all the spectra besides the well known bands related to the natural oxygen isotopes $^{18}O_i$ and $^{17}O_i$ there are three bands located at 1012.4, 1059.8 and 1105.3 cm^{-1}. At room temperature (RT) the first two bands were found to be positioned at about 1013.0 and 1061.8 cm^{-1}. The band at 1105.3 cm^{-1} is not possible to detect at RT because of disturbance from the strong 1107 cm^{-1} O_i band. In samples doped with the isotope ^{18}O the bands were shifted to 969.2, 1011.8 and 1057.1 cm^{-1} at 10 K and to 969.7 and 1012.7 at RT for the first two bands (see table I). These bands are shown in Fig. 2 for as-grown ^{16}O and ^{18}O samples (an additional band on the low energy side of the 1012/969 cm^{-1} band has also been reported previously [13,14]). A carbon-oxygen related band at about 1055 cm^{-1} is present in the ^{18}O material. This band can be found at about 1104 cm^{-1} in ^{16}O material [19]. It is interesting to note that when changing the temperature from RT to 10 K the positions of the 1012 and 1060 cm^{-1} bands slightly decreases while they would normally be expected to increase.

From the results in Fig. 2 it is evident that the bands are related to oxygen. However, an isolated O_i atom can not give rise to these bands. Their intensity was found to vary noticeably with the HT temperature (see Fig. 1) while the O_i concentration remained constant during these short-time anneals. Therefore these bands should arise from some oxygen-related complex. Since the 1012 cm^{-1} band was observed earlier even after dispersion treatments at 1100 [13] and 1350 °C [20] it appears likely that this complex could be the oxygen dimer.

According to estimations [16] very short times should be required to reach a dynamical equilibrium between O_i and O_2 (equilibrium state of dimer) at high temperatures. Our experimental results show that the equilibrium level of the bands at about 1012, 1060 and 1105 cm^{-1} for the lowest HT at 500 °C is attained within 30 minutes.

We will now analyze the quasi-equilibrium concentration $[O_2^{eq}]$ of the oxygen dimer in a simplified model of the formation kinetics of the O_2 complex, assuming that its mobility is much higher than that of O_i. We further assume that no traps such as carbon are present, that the reactions between O_2 and higher order complexes than O_i are insignificant as compared with reactions between O_i-O_i and O_2-O_i and ignoring back reactions of complexes of higher order than O_2. The formation kinetics can then be expressed as

$$\frac{d[O_2]}{dt} = k_1[O_i]^2 - k_{-2}[O_2] - k_3[O_2][O_i], \quad (1)$$

where $[O_i]$ and $[O_2]$ are the concentrations of O_i and O_2 and k_1, k_{-2} and k_3 are formation and dissociation rate constants. Taking into account the results from Ref. 8 assuming that oxygen dimer dissociation becomes the dominating process at higher temperatures (increasing in importance from 400 °C), $[O_2^{eq}]$ can be expressed as

$$[O_2^{eq}] = \frac{k_1}{k_{-2}}[O_i]^2. \quad (2)$$

In this case we expect a quadratic dependence for $[O_2^{eq}]$ on $[O_i]$. In Fig. 3 the integrated absorption coefficient (IA) of the band at 1012 cm^{-1} measured at RT is plotted vs. $[O_i]$ for as-grown samples and for samples annealed for 30 minutes at 700°C. Both curves show a quadratic dependence with $[O_i]$. The same results were also obtained when plotting the IA of the bands at 1012, 1060 and 1105 cm^{-1} measured at 10 K vs. $[O_i]$. For T<400 °C dissociation of O_2 should no longer be important and association processes will dominate [8]. In this case $[O_2^{eq}]$ will be according to

$$[O_2^{eq}] = \frac{k_1}{k_3}[O_i], \quad (3)$$

suggesting a linear dependence for $[O_2^{eq}]$ on $[O_i]$. Samples annealed at 370 °C long enough in order to obtain the quasi-equilibrium concentration of the complex giving rise to the 1012 cm^{-1} band (180 hours), show a linear dependence for the IA of the 1012 cm^{-1} band on $[O_i]$, according to Fig. 3. The same result was also obtained for the 1060 cm^{-1} band. Reliable measurements at 10 K of the bands at 1012, 1060 and 1105 cm^{-1} were not possible to obtain in this case, since electronic transitions of TDD complexes dominated the spectrum. These results demonstrate according to Eq. (2) and (3) that the complex giving rise to the bands at 1012, 1060 and 1105 cm^{-1} is most probably the oxygen dimer, since they show that two O_i atoms are involved in this complex. Figure 3 shows for the as-grown samples that the $[O_2]$ in these is frozen in during cooling when O_2 dissociation is dominating over association processes.

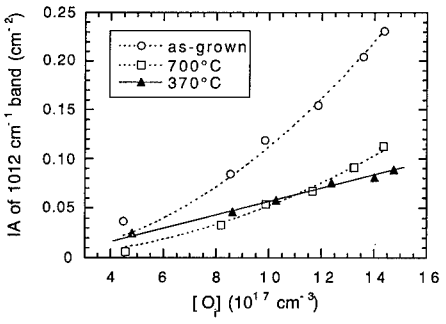


Fig. 3. The IA of the 1012 cm^{-1} band measured at RT plotted vs. $[O_i]$, showing a quadratic dependence for as-grown and 700 °C annealed samples, while there is a linear dependence for samples annealed at 370 °C.

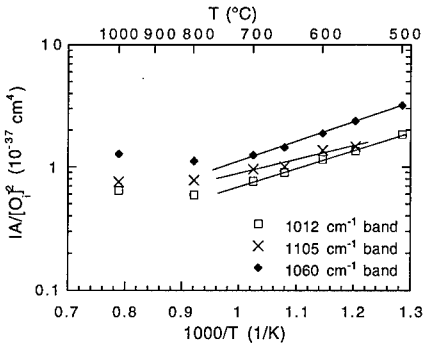


Fig. 4. Annealing temperature dependencies of the IA of the 1012, 1060 and 1105 cm^{-1} bands measured at 10 K, normalized to the square of the $[O_i]$.

One of the most important characteristics of the oxygen dimer is its binding energy. In the case of the existence of a dynamical equilibrium between O_i and O_2 the concentration of oxygen dimers can be expressed as [16,21]

$$[O_2^{eq}] = \frac{[O_i]^2 g_2}{[O_{SO}] g_1} \exp(\frac{E_{b2}}{kT}), \quad (4)$$

where g_1 and g_2 are the numbers of possible O_i and O_2 sites per unit cell ($g_1 = 4$ and $g_2 = 12$), E_{b2} is the oxygen dimer binding energy and $[O_{SO}]$ is the density of possible sites for O_i in the Si lattice ($[O_{SO}]=10^{23}$ cm^{-3}).

To determine the E_{b2} value we have studied the temperature dependence of the IA equilibrium level for the 1012, 1060 and 1105 cm^{-1} bands in the range 500-1000 °C. Figure 4 shows the corresponding experimental results. It is clearly seen that the plots obtained can not be described by a simple exponential function according to Eq. (4). There is a flat region in the range 800-1000 °C and only in the range 500-700 °C an exponential increase in IA with decrease in temperature is observed. Apparently the cooling rate after HTs used in the present study was insufficient to freeze an equilibrium state of dimers at T≥800 °C (in accordance with [16] the life-time of O_2 is <10 msec at T>800 °C). So in further analysis we have concentrated on the temperature region 500-700 °C.

It was deduced that the temperature dependencies of the IA of the bands at 1012 and 1060 cm^{-1} are characterized by the same slope of 0.3 eV. On the other hand it was revealed that the temperature dependence of the IA of the band at 1105 cm^{-1} is slightly different (see Fig. 4) and is characterized by a lower slope of about 0.2 eV. It should be pointed out that the data for this band are not so definitive as for the bands at 1012 and 1060 cm^{-1}. At low temperatures its position practically coincides with that of the band related to the C_S-O_i complex [22] and with bands related to electronic transitions of TDDs [23]. So it was rather difficult to determine properly the IA of the band at 1105 cm^{-1} in the samples containing TDDs (after HT at 500 °C) or carbon in concentration >10^{16} cm^{-3}.

From our results it can not be excluded that the 1105 cm^{-1} band could arise from some dioxygen configuration with a slightly lower binding energy, different from the main one (E_{b2} = 0.3 eV) giving rise to the bands at 1012 and 1060 cm^{-1}. This suggestion can also be confirmed from electron irradiations at about 280 °C [24] where the bands at 1012 and 1060 cm^{-1} are strongly enhanced while the band at 1105 cm^{-1} is not affected. In these experiments weak IR vibrational bands positioned at about 556 and 690 cm^{-1} where found to correlate with the 1012 and 1060 cm^{-1} bands (see Table I). For the further characterization of the oxygen dimer we will consider the value of E_{b2} = 0.3 eV as the most reliable one. It is worth noting that the most recent calculations [6] gave the close value of E_{b2} = 0.4 eV.

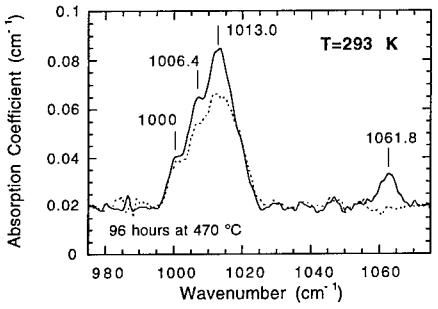


Fig. 5. Spectra for a sample annealed 96 hours at 470 °C, measured at RT. The solid spectrum was obtained by using a FZ-Si reference sample, the dotted by using the as-grown sample as a reference.

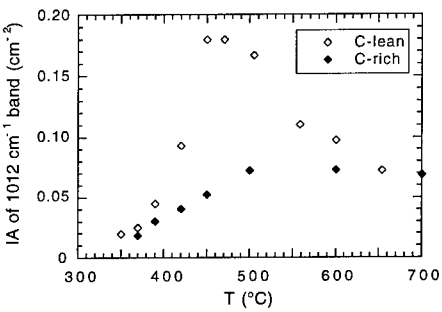


Fig. 6. The quasi-equilibrium level of the 1012 cm^{-1} band as a function of temperature, for carbon lean ([O_i]=1.0×10^{18}, [C_S]≤10^{16} cm^{-3}) and carbon rich ([O_i]=1.1×10^{18}, [Cs]≈3×10^{17} cm^{-3}) samples.

An identification of the band at 1012 cm^{-1} as arising from the oxygen dimer allowed us to reinterpret some previous data concerning the annealing behavior of this band at the TD formation temperatures [11-14]. It is evident now that there are two different kinds of oxygen complexes giving rise to the IR bands located at about the same position at 1012-1013 cm^{-1}: a) oxygen dimers which exist in as-grown crystals and can rapidly be transformed into the first types of TDDs during

the initial stages of HTs at 350-450 °C; b) higher order complexes formed after more prolonged anneals. This is clearly illustrated in Fig. 5 for a sample annealed at 470 °C for 96 hours, where a spectrum using a Float Zone Si reference (solid line) is compared with a spectrum using the as-grown sample before the anneal as a reference (dotted line). The dimer related bands at about 1013 and 1062 cm^{-1} (at RT) stays constant while a much broader structure is growing up at about 1012 cm^{-1} (an important conclusion made in Ref. 2 was that the oxygen dimers should be present in a quasi-equilibrium concentration throughout the anneals). This broader 1012 cm^{-1} band also has a related mode at about 744 cm^{-1} [13] which is not the case for the oxygen dimer. The case is similar for bands at 1005-1006 cm^{-1}. In as-grown samples a band is found at 1005.3 cm^{-1} (at RT) which has been suggested to be related to the trimer [15,16] while in annealed samples bands at 1006.4 cm^{-1} and at about 734 cm^{-1} have been found to correlate with the higher order TDDs (from TDD4 and up) [13].
In Ref. 13 we presented the temperature dependence (350-470 °C) of the equilibrium level of the 1012 cm^{-1} band, related to the here suggested oxygen dimer. Those data together with the new ones obtained after high temperature HTs (measurements at RT) are plotted in Fig. 6. It is seen that the maximum achievable equilibrium level of the 1012 cm^{-1} band ($[O_2^{eq}]$) corresponds to the temperatures of about 450-500 °C. At lower HT temperatures an essential decrease in $[O_2^{eq}]$ occurs. This fact together with the observed rapid transformation of "as-grown" dimers into the first TDD species [12] shows clearly that when decreasing the annealing temperature below 450 °C the capture processes of mobile dimers increasingly dominates.

Table I. The oxygen dimer related vibrational IR modes for $^{16}O_2$ and $^{18}O_2$ with their wavenumber positions and the full width at half maximum (Δ) values.

Dimer Mode	$^{16}O_2$, 293 K pos. / Δ (cm^{-1})	$^{16}O_2$, 10K pos. / Δ (cm^{-1})	$^{18}O_2$, 293 K pos. (cm^{-1})	$^{18}O_2$, 10K pos. (cm^{-1})
"1060"	1061.8 / 7	1059.8 / 6	1012.7	1011.8
"1012"	1013.0 / 6	1012.4 / 3	969.7	969.2
"690"	686.3 / 6	690.1 / 3	676.5	679.7
"556"	551.9 / 4	555.8 / 2	551.3	555.4
"1105" (?)	---	1105.3 / 3	---	1057.1

It is well known that the presence of carbon in a high concentration prohibits TDD generation in Cz-Si crystals. This phenomenon has been associated recently [8,15,25] with the capture of dimers by carbon. In the present study we have found that in fact the $[O_2^{eq}]$ in carbon rich samples is consistently lower as compared with carbon lean ones in the temperature interval 350-700 °C, according to Fig. 6. The latter result indicates the mobility of oxygen dimers as well as the efficiency of carbon related centers for their trapping.
Since it is expected that the diffusion of O_2 should be greatly enhanced as compared with single O_i diffusion we will make an estimate of this enhancement for T<400 °C by using Eq. (3) under quasi-equilibrium conditions for O_2. By expressing $k_1=8\pi r_{c1}D_{Oi}$ and $k_3=4\pi r_{c3}D_{O2}$, where r_c ($r_{c1}=r_{c3}$) and D are the appropriate capture radii and diffusion coefficients, and using half the value of the O_i calibration coefficient in order to calculate $[O_2^{eq}]$, we get that the ratio D_{O2}/D_{Oi} should be around 10^4. Applying the O_i calibration coefficient is rather doubtful, however, it can be used to obtain a rough estimation.
Finally we should also mention that preliminary theoretical calculations of vibrational IR bands related to the O_2 complex [26] show that strong bands are expected very close to 1012 and 1060 cm^{-1} while weaker modes should be found close to 556 and 690 cm^{-1}. From these calculations it is also expected that the mode at 556 cm^{-1} should not show a dependence on its position with isotopic mass changes of the oxygen atom, which is according to our results (Table I). However, in samples enriched with both ^{16}O and ^{18}O there are no mixed modes observed for the O_2 related bands, which is expected for a next-neighbor oxygen dimer structure. This peculiarity needs to be explained for a complete understanding of the oxygen dimer.

Summary.
We have revealed vibrational IR absorption bands related to the oxygen dimer in Si. The O_2 binding energy was determined to be equal to 0.3 eV and its quasi-equilibrium concentration was found to depend on the $[O_i]$ according to formation kinetics expected for the oxygen dimer. The latter result indicates that the oxygen dimer is stable below 400°C while O_2 dissociation processes dominate at

higher temperatures. From these results it is also expected that the migration of O_2 complexes is strongly enhanced as compared with a single O_i atom, where an enhancement factor of around 10^4 was estimated. We also conclude that the O_2 mode at about 1012 cm^{-1} should not be confused with a broader band at the same position appearing after prolonged heat-treatments.

Acknowledgments.
Financial support was received from Teknikvetenskapliga Forskningsrådet (TFR) and from the National Defense Research Establishment. We also acknowledge financial support from the Swedish Institute, making it possible for L.I. Murin and V.P. Markevich to visit Linköping University. We are also very thankful for communications with C. Ewels, R. Jones and S. Öberg regarding results from theoretical calculations on the oxygen dimer.

References.

1. U. Gösele and T.Y. Tan, Appl. Phys. A **28**, 79 (1982).
2. T.Y. Tan, R. Kleinhenz and C.P. Schneider, Mat. Res. Soc. Symp. Proc. **59**, 195 (1986).
3. L. C. Snyder, J. W. Corbett, P. Deák, and R. Wu, Mater. Res. Soc. Symp. Proc. **104**, 179 (1988).
4. P. J. Kelly, Mater. Sci. Forum **38-41**, 269 (1989).
5. M. Needels, J. D. Joannopoulos, Y. Bar-Yam, and S. T. Pantelides, Phys. Rev. B **43**, 4208 (1991).
6. D. J. Chadi, Phys. Rev. Lett. **77**, 861 (1996).
7. C. P. Ewels, R. Jones, and S. Öberg, in *Proceedings of the NATO Advanced Workshop on the Early Stages of Oxygen Precipitation in Silicon*, Exeter,U.K., 1996, edited by R. Jones, NATO ASI Series, 3. High Technology Vol. 17 (Kluwer Academic Publishers, Dordrecht, 1996), p. 141.
8. S. A. McQuaid, M.J. Binns, C.A. Londos, J.H. Tucker, A.R. Brown and R.C. Newman, J. Appl. Phys. **77**, 1427 (1995).
9. H. J. Stein and J. W. Medernach, J. Appl. Phys. **79**, 2337 (1996).
10. E. Dittrich, W. Scheitler, and W. Eisenmenger, Jap. J. Appl. Phys. **26**, Supplement **26-3**, 873 (1987).
11. J. L. Lindström and T. Hallberg, Phys. Rev. Lett. **72**, 2729 (1994).
12. J. L. Lindström and T. Hallberg, J. Appl. Phys. **77**, 2684 (1995).
13. T. Hallberg and J. L. Lindström, J. Appl. Phys. **79**, 7550 (1996).
14. J. L. Lindström and T. Hallberg, in *Proceedings of the NATO Advanced Workshop on the Early Stages of Oxygen Precipitation in Silicon,* Exeter,U.K., 1996, edited by R. Jones, NATO ASI Series, 3. High Technolodgy Vol. 17 (Kluwer Academic Publishers, Dordrecht, 1996), p. 41.
15. L. I. Murin and V. P. Markevich, in *Proceedings of the NATO Advanced Workshop on the Early Stages of Oxygen Precipitation in Silicon*, Exeter,U.K., 1996, edited by R. Jones, NATO ASI Series, 3. High Technolodgy Vol. 17 (Kluwer Academic Publishers, Dordrecht, 1996), p. 329.
16. L. I. Murin and V. P. Markevich, in *Proceedings of the 7th International Conference on Shallow-Level Centers in Semiconductors*, Amsterdam, 1996, edited by C. A. J. Ammerlaan and B. Pajot (World Scientific, Singapure, 1997), p. 339.
17. A. Baghdadi *et al.*, J. Electrochem. Soc. **136**, 2015 (1989).
18. R.C. Newman and J.B. Willis, J. Phys. Chem. Solids **26**, 373 (1965).
19. A.R. Bean and R.C. Newman, J. Phys. Chem. Solids **33**, 255 (1972).
20. B. Pajot and B. Gales, Mater. Res. Soc. Symp. Proc. **59**, 39 (1986).
21. C. Herring and N. M. Johnson, in *Hydrogen in Semiconductors,* edited by J. I. Pankove and N. M. Johnson, Semiconductors and Semimetals Vol. 34 (Academic, San Diego, 1991), p. 225.
22. Y. Shirakawa, H. Yamada-Kaneta, and H. Mori, J. Appl. Phys. **77**, 41 (1995).
23. P. Wagner and J. Hage, Appl. Phys. A **49**, 123 (1989).
24. J.L. Lindström, T. Hallberg, D. Åberg, B.G. Svensson, L. Murin and V.P. Markevich, in this conference preceedings.
25. U. Gösele, K.-Y. Ahn, B.P.R. Marioton, T.Y. Tan and S.-T. Lee, Appl. Phys. A **48**, 219 (1989).
26. Private communications with C. Ewels, R. Jones and S. Öberg.

Materials Science Forum Vols. 258-263 (1997) pp. 367-372
© 1997 Trans Tech Publications, Switzerland

FORMATION OF OXYGEN DIMERS IN SILICON DURING ELECTRON-IRRADIATION ABOVE 250 °C

J.L. Lindström, T. Hallberg, D. Åberg[1], B.G. Svensson[1], L.I. Murin[2] and V.P. Markevich[2]

Linköping University, Department of Physics and Measurement Technology, S-581 83 Linköping, Sweden
[1]Solid State Electronics, Royal Institute of Technology, S-164 40 Kista, Sweden
[2]Institute of Solid State and Semiconductor Physics, P. Brovki str. 17, Minsk 220072, Belarus

Keywords : Silicon, electron irradiation, defects, oxygen dimer, thermal donors

Abstract. The oxygen dimer should be a first step in clustering of oxygen atoms in silicon. It has been suggested to play an important role in the formation kinetics of the thermal double oxygen donors formed during heat-treatments below 500 °C. Recently strong experimental indications of the dimer have been presented and infrared vibrational bands at about 1012 and 1060 cm^{-1} have been assigned to an oxygen dimer. In this work a strong increase of these dimer related bands has been found in silicon crystals after electron (2 MeV) irradiation at elevated temperatures (250-300 °C). Additional related weaker vibrational bands also appear at about 556 and 690 cm^{-1} at 10 K. Simultaneously vacancy-oxygen related defects as well as thermal double donors are formed. In carbon-rich material the dimer formation is strongly suppressed. Different models for dimer formation are discussed and a model where a silicon self-interstitial is trapped by a dioxygen-vacancy center is suggested.

Introduction.

Defects formed in silicon during electron-irradiation and subsequent annealings have been the subject of extensive investigations [1,2]. In Czochralski-grown (Cz) materials several defects have been identified related to trapping by impurities of vacancies and interstitials formed during irradiation. The experimental results reported usually refer to irradiations at room-temperature (RT) or lower temperatures. During the following annealing procedures, new defect centers arise where typically oxygen and carbon related defects are the most frequently appearing.

Heat-treatments of as-grown Cz-Si in the range 350-500 °C give rise to different defects like the thermal donors and oxygen-carbon defects which also have been widely studied [1,2]. However, the combined effect of electron irradiation of samples kept at temperatures above 250 °C is not much explored. In one study the recovery kinetics of stress induced dichroism of the 1107 cm^{-1} oxygen IR band during electron irradiation at temperatures up to 320 °C was reported and revealed a strongly enhanced recovery rate at the higher temperatures [3].

The most common defects found after RT electron (MeV) irradiation like the A-center, the divacancy, E-centers and carbon-carbon and carbon-oxygen related centers anneal out to a large extent at temperatures below 300 °C. Electron-irradiation at temperatures above 250 °C is therefore anticipated to be a very different situation in terms of defect formation.

The A-center or the vacancy-oxygen center is the most frequently appearing defect in Cz silicon after irradiation. It can exist in at least two charge states VO^0 and VO^- and anneals out around 300 °C [4]. The annealing is suggested to be due to three different mechanisms: reaction with a fast diffusing species (carbon or silicon interstitial), dissociation and trapping of diffusing VO-centers by interstitial oxygen to form VO_2 centers. It has been suggested that the VO center diffuses faster in the negative charge state [5].

Due to the supersaturation of oxygen in Cz silicon below 1200 °C clustering of oxygen atoms occurs at temperatures where normal oxygen diffusion is important. The oxygen dimer (O_2) should be the first step in such a process. There have been several suggestions about the structure of such a dimer. It was first suggested that fast-diffusing gas-like molecular O_2 could be responsible for the enhanced oxygen diffusion and thermal double donor (TDD) formation at T<500 °C [6]. However, from theoretical studies [7-11] it has been found that such an oxygen molecule is not stable in the Si lattice. It has been suggested that an oxygen dimer formed from two interstitial oxygen atoms (O_i) with a common Si neighbor can be stable in a certain configuration.

From calculations the binding energy for such a complex has been found to be in the range 0.1-1.0 eV. It has been found that the activation energy for migration of the oxygen dimer could be significantly lower as compared with that of a single O_i atom [7,11]. This would explain the

enhanced oxygen diffusion observed for TDD generation. Experimental results have shown that for T>400 °C there should be increasing significance of oxygen dimer dissociation, assuming that O_2 diffuse much more rapidly than isolated O_i atoms [12].
So far no experimental evidence has been presented for the existence of the oxygen dimer. A recent paper of Stein and Medernach [13] presented results on an enhanced formation of vibrational infrared (IR) absorption bands at 1005, 1013 and 1063 cm^{-1} in Cz-Si crystals heat-treated in H-plasma at 275 °C. The band at 1005 cm^{-1} was suggested to be related to the oxygen dimer. Earlier some satellite lines near the 29.3 cm^{-1} O_i band were observed by means of high sensitive acoustic phonon spectroscopy [14]. These lines were assigned to the oxygen pairs because of the quadratic dependence of their intensity on the O_i concentration in the crystals. However, the assignments [13,14] are tentative and none of the oxygen dimer characteristics is known.
Vibrational IR bands related to small oxygen clusters (TDDs and their precursors) were recently discovered [15-18]. There has been suggestions [19,20] that one of these bands (located at about 1012 cm^{-1}) is related to the oxygen dimer. The assignment was mainly based on similarities between the expected annealing behavior of the oxygen dimer and that of the complex giving rise to the 1012 cm^{-1} band. Experimental evidence was very recently found for this assignment [21].
In an investigation on oxygen associated defects and thermal donors in silicon, a spectrum was presented from a sample partially irradiated at a temperature estimated to 200 °C [22]. In this spectrum strong absorption bands could be seen at 1012 and 1060 cm^{-1}. In the present paper an experiment is discussed where a non-equilibrium concentration of dimers is suggested to be formed during electron (2 MeV) irradiation at temperatures in the range 250-300 °C.
The bands discussed below are referred to as the 1012 (1012.4) band and the 1060 (1059.8) band corresponding to the spectral positions at 10 K. The positions at RT are 1013.0 and 1061.8 cm^{-1} respectively.

Experimental.
The samples used in this investigation were as-grown Cz-Si, doped with P to resistivities of about 60 Ωcm. The concentrations of interstitial oxygen (O_i) and substitutional carbon (C_s) were monitored by measuring the well known absorption bands at 1107 [23] and 605 cm^{-1} [24], respectively. We also included a few samples with a high carbon concentration as well as samples doped with the isotope ^{18}O. The samples were polished to an optical surface on two sides and the dimensions were 10×5×3 mm^3. The samples were irradiated in a temperature regulated holder in air at temperatures in the range 200-300 °C to different doses from 5×10^{16} to 1.5×10^{18} cm^{-2}, using 2.0 MeV electrons. The beam current was in the range 5-8 $\mu A/cm^2$.
IR absorption analysis was carried out using a Bruker IFS 113v Fourier Transform IR (FTIR) Spectrometer. A spectral resolution of 0.5-1.0 cm^{-1} was used and the samples were measured at 10 K and at RT. Heat-treatments (HTs) were performed in nitrogen ambient or in air.

Results and discussion.
From 2 MeV electron irradiations of Cz silicon at RT it is well established that the dominating IR absorption bands appearing in carbon-lean material at RT are the well-known vibrational bands related to the vacancy-oxygen center at 830 and 877 cm^{-1}. In carbon-rich samples bands at 862 and 1020 cm^{-1} related to the C3 and C4 centers also appear.
Figure 1 shows RT spectra for carbon-lean and carbon-rich samples irradiated at 280 °C as well as for an as-grown sample. In the spectrum from the carbon-lean sample we see four dominating bands at 889, 1005.3, 1013.0 and 1061.8 cm^{-1}. The 889 band is assigned to the dioxygen-vacancy center (VO_2) which is formed during annealing around 300 °C when the VO-center anneals out. The mechanism behind the formation is believed to be trapping of mobile VO pairs by interstitial oxygen atoms [4].
The 1012 and 1060 cm^{-1} bands have recently been suggested to originate from an oxygen dimer [21] and the band at 1005.3 cm^{-1} to an oxygen trimer [19,20]. This attribution contradicts previously published results where bands at the same positions are assigned to vibrational modes of oxygen clusters related to thermal donors developing during HTs in the temperature range 350-500 °C [15].
However, it is now evident that there are two kinds of oxygen complexes giving rise to the IR bands located at about the same position at 1012-1013 cm^{-1}, namely oxygen dimers which exist in as-grown crystals and rapidly are transformed into the first types of TDDs during HTs at 350-450 °C, and higher order complexes formed during prolonged anneals. The higher order complexes give rise

to a broader 1012 cm^{-1} band and besides have a related mode at about 744 cm^{-1} [17] which is not the case for the oxygen dimer. For bands at 1005-1006 cm^{-1} we have a similar situation. In Fig. 1 it can be seen that the strength of the 1012 cm^{-1} band in as-grown material is an order of magnitude smaller as compared to the irradiated carbon-lean sample. If we use a calibration coefficient comparable to half of that used for estimation of the $[O_i]$ (based on the integrated absorption coefficient), the concentration of dimers should after irradiation be about 6×10^{15} cm^{-3} which is much higher than the estimated equilibrium concentration at 280 °C which is around 10^{13} cm^{-3}.

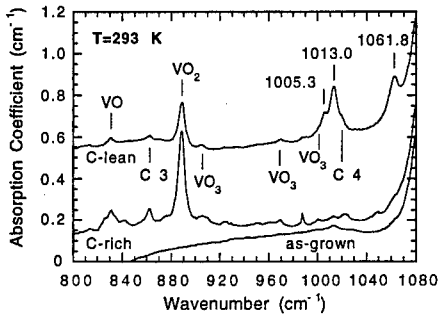


Fig. 1. Spectra measured at RT for as-grown and for samples electron irradiated at 280 °C to a dose of about 1×10^{18} e/cm². Bands at 1005.3, 1013.0 and 1061.8 cm^{-1} increase in the C-lean material ($[C_S]=5\times10^{15}$ cm^{-3}) but not in the C-rich material ($[C_S]=3\times10^{17}$ cm^{-3}). Bands related to vacancy-oxygen and carbon-oxygen complexes are also present in the spectra.

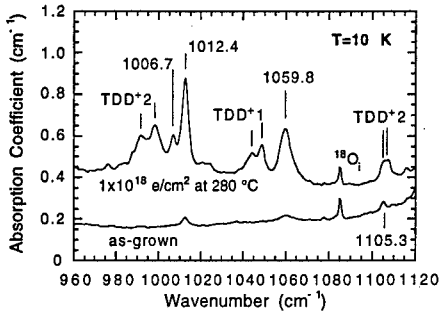


Fig. 2. Spectra measured at 10 K for an as-grown sample and for a sample electron irradiated at 280°C to a dose of about 1×10^{18} e/cm². Vibrational bands at 1006.7, 1012.4 and 1059.8 cm^{-1} increase together with the electronic transitions of TDD+1 and TDD+2.

In Fig. 2 the corresponding spectra for the carbon-lean samples measured at 10 K are presented. Besides the bands discussed above we can observe the well-known electronic transition bands related to TDD1 and TDD2. The TDDs normally develop after HTs in the range 350-500 °C. The fact that they are appearing already at 280 °C seems to be due to a fast oxygen diffusion during irradiation. Spectra from irradiations at lower temperatures (200-235 °C) did not show any differences from RT irradiations. The critical temperature seemed to be around 250 °C.

The position of the dimer related bands in Fig. 1 and 2 shows an unusual temperature dependence. A small shift to lower wavenumbers can be observed as the temperature is decreased from RT to 10 K. Typically there is a shift in the opposite direction for all other oxygen related vibrational bands in silicon.

The results in Fig. 1 and 2 show clearly that oxygen related defects are developing at 280 °C during electron irradiation. The concentration of VO (830 cm^{-1}) is low and the formation of VO_2 (889 cm^{-1}) occurs at a lower temperature than could be expected if the formation is caused by a mobile VO being trapped by an interstitial oxygen atom. One explanation for the latter observation could be that, due to a high degree of ionization during irradiation, we have VO in a negative charge state with increased mobility (ionization enhanced diffusion).

The situation for defect formation during irradiation is probably complex at 280 °C, due to a high degree of ionization combined with the instability of many of the radiation induced defects. The mechanisms behind the formation of dimers and TDDs is therefore not obvious. A movement of oxygen atoms could occur [3] from repeated trapping of fast diffusing vacancies (V) and self-interstitials (I) at an oxygen atom according to:

$$V+O_i \Rightarrow VO,\ VO+I \Rightarrow O_i \qquad (1)$$

This mechanism could cause the oxygen diffusion involved in the formation of TDDs. The formation of VO_2 is usually described by the reaction:

$$VO + O_i \Rightarrow VO_2 \qquad (2)$$

where VO is mobile (≥ 300 °C) and is trapped at an O_i atom. In the present case VO_2 might be formed both from a mobile VO being trapped by an O_i atom and a mobile O_i atom being trapped by a VO. The annihilation of VO_2 is usually observed at temperatures where normal oxygen diffusion is significant. The reaction is described by:

$$VO_2 + O_i \Rightarrow VO_3 \quad (3)$$

In Fig. 1 we observe absorption bands related to VO_3 (905, 969 and 1001 cm^{-1}) which again is an indication of mobile oxygen atoms.
Concerning the role for the I it is known to cause annihilation of vacancies and VO-centers. It should therefore be a possibility that I also interact with VO_2 centers in a reaction like:

$$VO_2 + I \Rightarrow O_2 \quad (4)$$

A possible backward reaction could be:

$$O_2 + V \Rightarrow VO_2 \quad (5)$$

The importance of the I is quite clear from the results in Fig. 1 where a spectrum from a carbon-rich sample irradiated at 280 °C is included. We can see an extremely strong effect on the dimer formation. The well-known Watkins replacement mechanism $I+C_s \Rightarrow C_i$ is a dominating reaction in the carbon-rich sample and will of course strongly suppress the reaction where dimers are formed due to reaction (4). It can also be noticed in Fig. 1 that the concentration of VO_2 becomes much stronger than in the carbon-lean sample which would be expected.

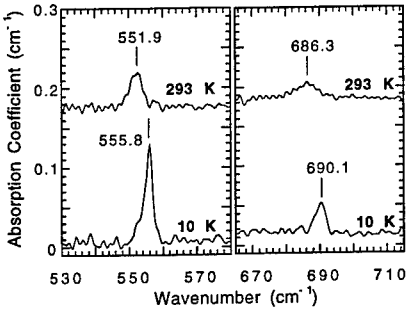


Fig. 3. Spectra of measurements at RT and at 10 K of vibrational IR bands correlated with the 1012 and 1060 cm^{-1} bands according to Fig. 4.

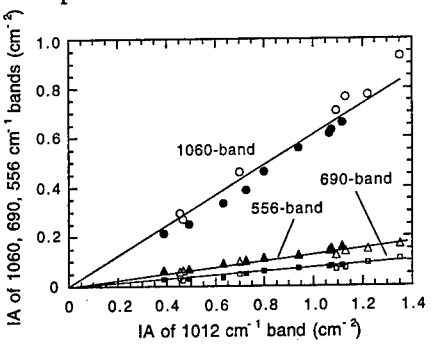


Fig. 4. The correlation between the 1012 cm^{-1} band and the 1060, 690 and 556 cm^{-1} bands for the creation (electron irradiation at 280°C, open symbols) and annihilation (filled symbols) of these bands. Electron irradiation doses of 1.0×10^{16}-1.6×10^{18} e/cm^2 were used.

If we assume that the calibration coefficient for the dimer (using the 1012 cm^{-1} band) and VO_2 is about the same we find that the sum of the concentrations of of these two defects is what we typically get for VO_2 from RT irradiation followed by annealing. This also supports the reaction (4). In the earlier studies, the 1012 cm^{-1} band was weak [15-18]. Now we have an order of magnitude stronger bands and we have the possibility to look for weaker modes related to the oxygen dimer. Our results show that there indeed are such bands as shown in Fig. 3. The strength of the bands are an order of magnitude weaker than the 1012 cm^{-1} band and at 10 K they are positioned at 555.8 (551.9 at RT) and 690.1 (686.3 at RT) cm^{-1}. Samples enriched with ^{18}O showed that there is an isotopic shift for the 690 cm^{-1} band but not for the 556 cm^{-1} band. In this respect the 556 cm^{-1} band behaves like the 515 cm^{-1} band related to O_i. The correlation between the bands assigned to the

oxygen dimer is illustrated in Fig. 4. The results are from both formation during irradiation and from annihilation of the dimer.
It has been suggested that the oxygen dimer is always present in Cz-Si in an equilibrium concentration due to a continuous formation and dissociation [20]. The equilibrium concentration has experimentally been found to have a maximum around 450-500 °C [21]. The lifetime of the dimer in the temperature range 450-500 °C is estimated to 10^5 s while the lifetime at 280 °C should be around 10^{14} s. The high non equilibrium dimer concentration obtained during irradiation at 280 °C should therefore decrease during a post heat-treatment at higher temperatures.

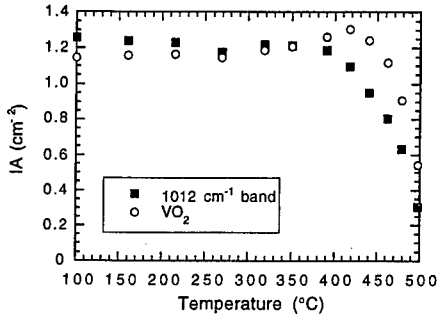


Fig. 5. Isochronal annealing of the dimer related 1012 cm^{-1} band and of the VO_2 complex. Measurements were carried out at RT.

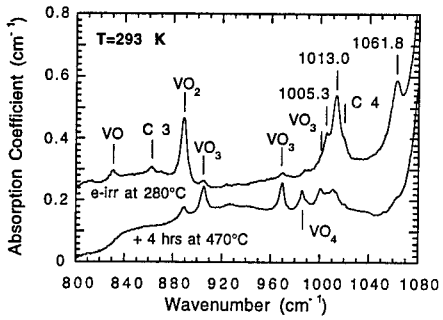


Fig. 6. Spectra measured at RT of a sample electron irradiated (1×10^{18} e/cm^2) at 280°C followed by HT for 4 hours at 470°C. Bands at about 1005, 1013 and 1062 cm^{-1} decrease together with the VO and VO_2 centers and the carbon-oxygen C3 and C4 complexes. Bands assigned to VO_3 and VO_4 and possibly also vibrational bands related to TDD2 and TDD3 increase.

Figure 5 shows the results of an isochronal annealing for both the dimer and VO_2. While the annealing of the dimer is dominated by a dissociation process to adjust to thermal equilibrium, the annealing of VO_2 is supposed to occur by a process where mobile oxygen atoms are trapped at VO_2 giving rise to VO_3. After 4 hours at 470 °C in Fig. 6 we can observe the growth of the VO_3 and VO_4 related bands [6]. A strong decrease of the dimer related bands to a strength somewhat higher than the equilibrium concentration at 470 °C (probably because the HT time was too short) is also observed. There are indications of the vibrational bands related to TDD2 and TDD3 at 988 and 999 cm^{-1}. A band at 986 cm^{-1} assigned to VO_4 is stronger than usually observed. This might be caused by a diffusing dimer trapped by VO_2.

Summary
We have found that electron irradiation at temperatures in the range 250-300 °C of Cz silicon gives rise to vibrational IR bands at 1059.8, 1012.4, 690.1 and 555.8 cm^{-1} at 10 K. These bands are assigned to the oxygen dimer. The formation of the dimer is suggested to be due to a reaction where the dioxygen-vacancy center traps a self-interstitial. A simultaneous development of TDDs and VO_3 indicates an enhanced oxygen diffusion during the irradiation.

Acknowlegements.
Financial support was received from Teknikvetenskapliga Forskningsrådet (TFR) and from the National Defense Research Establishment. We also acknowledge financial support from the Swedish Institute, making it possible for L.I. Murin and V.P. Markevich to visit Linköping University.

References.

1. *Oxygen in Silicon, Semiconductors and semimetals* , Vol. 42, ed. F. Shimura (Academic Press, Inc., 1994) ; *Proceedings of the NATO Advanced Workshop on the Early Stages of Oxygen Precipitation in Silicon, Exeter,U.K., 1996,* edited by R. Jones, NATO ASI Series, 3. High Technology Vol. 17 (Kluwer Academic Publishers, Dordrecht, 1996).

2. *Early Stages of Oxygen Precipitation in Silicon Proceedings of the NATO Advanced Workshop on the Early Stages of Oxygen Precipitation in Silicon,* Exeter,U.K., 1996, edited by R. Jones, NATO ASI Series, 3. High Technolodgy Vol. 17 (Kluwer Academic Publishers, Dordrecht, 1996).
3. A.S. Oates, R.C. Newman, J.M. Tucker, G. Davies and E.C. Lightowlers, Mat. Res. Soc. Proc. **59**, 59, (1986).
4. J.W. Corbett, G.D. Watkins and R.S. McDonald, Phys. Rev. **135**, A1381 (1964); J.L. Lindström and B.G. Svensson, Mat. Res. Soc. Symp. Proc., **59**, 45 (1986); J.L. Lindström and B.G. Svensson, Phys. Rev. B **34**, 8709 (1986).
5. T. Hallberg, J.L. Lindström, B.G. Svensson and K. Swiatek, Mat. Science Forum **143-147**, 1239 (1994)
6. U. Gösele and T.Y. Tan, Appl. Phys. A **28**, 79 (1982).
7. L. C. Snyder, J. W. Corbett, P. Deák, and R. Wu, Mater. Res. Soc. Symp. Proc. **104**, 179 (1988).
8. P. J. Kelly, Mater. Sci. Forum **38-41**, 269 (1989).
9. M. Needels, J. D. Joannopoulos, Y. Bar-Yam, and S. T. Pantelides, Phys. Rev. B **43**, 4208 (1991).
10. D. J. Chadi, Phys. Rev. Lett. **77**, 861 (1996).
11. C. P. Ewels, R. Jones, and S. Öberg, in *Proceedings of the NATO Advanced Workshop on the Early Stages of Oxygen Precipitation in Silicon*, Exeter,U.K., 1996, edited by R. Jones, NATO ASI Series, 3. High Technology Vol. 17 (Kluwer Academic Publishers, Dordrecht, 1996), p. 141.
12. S. A. McQuaid, M.J. Binns, C.A. Londos, J.H. Tucker, A.R. Brown and R.C. Newman, J. Appl. Phys. **77**, 1427 (1995).
13. H. J. Stein and J. W. Medernach, J. Appl. Phys. **79**, 2337 (1996).
14. E. Dittrich, W. Scheitler, and W. Eisenmenger, Jap. J. Appl. Phys. **26**, Supplement **26-3**, 873 (1987).
15. J. L. Lindström and T. Hallberg, Phys. Rev. Lett. **72**, 2729 (1994).
16. J. L. Lindström and T. Hallberg, J. Appl. Phys. **77**, 2684 (1995).
17. T. Hallberg and J. L. Lindström, J. Appl. Phys. **79**, 7550 (1996).
18. J. L. Lindström and T. Hallberg, in *Proceedings of the NATO Advanced Workshop on the Early Stages of Oxygen Precipitation in Silicon,* Exeter,U.K., 1996, edited by R. Jones, NATO ASI Series, 3. High Technolodgy Vol. 17 (Kluwer Academic Publishers, Dordrecht, 1996), p. 41.
19. L. I. Murin and V. P. Markevich, in *Proceedings of the NATO Advanced Workshop on the Early Stages of Oxygen Precipitation in Silicon*, Exeter,U.K., 1996, edited by R. Jones, NATO ASI Series, 3. High Technolodgy Vol. 17 (Kluwer Academic Publishers, Dordrecht, 1996), p. 329.
20. L. I. Murin and V. P. Markevich, in *Proceedings of the 7th International Conference on Shallow-Level Centers in Semiconductors*, Amsterdam, 1996, edited by C. A. J. Ammerlaan and B. Pajot (World Scientific, Singapure, 1997), p. 339.
21. T. Hallberg, J.L. Lindström, L. Murin and V.P. Markevich, in this conference proceedings
22. B. Pajot and B. Gales, Mater. Res. Soc. Symp. Proc. **59**, 39 (1986).
23. A. Baghdadi *et al.*, J. Electrochem. Soc. **136**, 2015 (1989).
24. R.C. Newman and J.B. Willis, J. Phys. Chem. Solids **26**, 373 (1965).

Materials Science Forum Vols. 258-263 (1997) pp. 373-378
© 1997 Trans Tech Publications, Switzerland

HIGH-FIELD EPR SPECTROSCOPY OF THERMAL DONORS IN SILICON

Ruud Dirksen, F. Berg Rasmussen[1], T. Gregorkiewicz, and C.A.J. Ammerlaan

Van der Waals–Zeeman Institute, University of Amsterdam,
Valckenierstraat 65-67, NL-1018 XE Amsterdam, The Netherlands

[1]Risoe National Laboratory, DK-4000 Roskilde, Denmark

Keywords: magnetic resonance, silicon, thermal donors

Abstract Thermal donors generated in p-type boron-doped Czochralski-grown silicon by a 450 °C heat treatment have been studied by high-field magnetic resonance spectroscopy. In the experiments conducted at a microwave frequency of 140 GHz and in a magnetic field of approximately 5 T four individual thermal donors species could be resolved. These were observed in their singly ionized TD^+ charge state. For the first time in the four decades of thermal donor research the g tensor values for specific members of the Si-NL8 family are given. Also the symmetry of the observed species is discussed.

Introduction

Thermal donors (TD's) constitute a long-standing puzzle in the materials science of silicon. Ever since their first observation [1] they presented a challenge to both experiment and theory. At this moment, some 40 years after their discovery, there exists no microscopic model of their structure, which would be capable of accounting for all the available experimental data. Also the theoretical picture is not complete and basic questions remain unanswered. This situation continues to exist as new findings often contradict each other and complicate rather than converge our understanding of the problem. Little progress is achieved in spite of the fact that TD's are easily generated in large concentrations and, as such, can be readily observed by a variety of experimental techniques commonly used for defect characterization. At the same time the shallow electrical character and wide-spread abundance make TD's relevant for device development, performance and stability.

While numerous methods have been applied in the studies of TD's the infrared absorption and magnetic resonance proved to be among the most informative. The infrared absorption spectroscopy was the first to reveal the major problem which hinders the progress in the structure determination of these centers - the multispecies character. In a recent absorption study [2] it was shown that upon prolonged treatment of oxygen-rich silicon in the 450 °C temperature range a series of 16 very similar, yet distinct, shallow double donors develop, with each species having its own generation and decay properties. This very characteristic feature of TD centers could be also confirmed by the high-resolution deep-level transient spectroscopy (DLTS) technique [3]. The electrical structure of TD's was shown to be well described by the effective mass theory, with a series of helium-like levels within approximately 180 meV below the bottom of the conduction band. In addition to those findings, the two deepest members of TD family were shown to have bistable properties, thus further complicating the picture.

In electron paramagnetic resonance (EPR) two spectra were assigned to thermal donors [4,5]: one of them, Si-NL8, has been identified as a singly ionized charge state TD^+; the other one, Si-NL10, has recently been shown to incorporate a single hydrogen atom and, consequently, identified as a TD-H complex, although another structural variation, involving an aluminum acceptor, is also possible [6]. For both Si-NL8 and Si-NL10 centers participation of oxygen has been established proving in this way the relation between TD's and this dominant impurity [7,8]. Another important conclusion from magnetic resonance studies was the overall orthorhombic-I (C_{2v}) symmetry found for both TD-related centers.

Generally, in magnetic resonance each center is characterized by its g tensor which describes the Zeeman interaction between spin S of the center and the magnetic field. Experience shows that the g tensor in practice identifies the defect and forms its unique fingerprint. The multispecies character should then be readily observable as a series of similar EPR spectra. In practice the resonance lines

of individual species overlap, resulting in line broadening. The annealing time development of TD species gives rise to a gradual, quasi-continuous change of line positions - the so called g-shifting effect. Such an effect leads to a lowering of anisotropy of the TD-related spectra for longer annealing times, in agreement with the simultaneous domination of the more shallow species. Actual EPR spectra of individual TD species could not be observed until now due to an insufficient resolving power of the available experimental setups, seriously hampering the value of the EPR technique in TD investigations. In view of the crucial role which magnetic resonance spectroscopy played in the past in the development of microscopic understanding of major defect centers, one may speculate that if this situation could be changed a flow of valuable information would follow. In this aspect the development of novel high-frequency magnetic resonance techniques offers new possibilities. These have been explored in the current study.

Experimental conditions

The experiments were performed with the newly constructed high-frequency D-band spectrometer operating at 140 Ghz. Its features and construction will be shortly described in the following.

The 140 GHz microwaves are generated by a high-stability 18 times frequency multiplier which is externally driven by a tunable CW synthesizer (HP 8671B) running at a frequency of approximately 7.7 GHz. The multiplied signal is fed through a band pass filter and an injection locked amplifier delivering 30 mW output power to the homodyne microwave bridge. The attenuators in the bridge are electronically tuned PIN diodes. A helium-cooled InSb crystal detects the power reflected from the cavity. The cylindrical cavity (radius 1.41 mm) has an unloaded quality factor Q of approximately 4500 and can be tuned by repositioning of its bottom. The sample is glued to the bottom of the cavity and rotated for changing its orientation with respect to the magnetic field. Measurements are done when tuned to dispersion. The magnetic field is supplied by a 6 T superconducting magnet (Cryogenic) with provisions for linear scanning. Modulation of the magnetic field is achieved by an additional coil wound around the cavity allowing for phase-sensitive detection at about 100 kHz. The temperature of the sample and cavity-insert is kept stable by a helium flow cryostat combined with a heater (Cryogenic). In order to calibrate the magnetic field, markers with well known resonance lines, such as Si:P and manganese, are mounted in the cavity together with the sample under study.

Experimental results and discussion

A. Preliminaries

As already mentioned, the resolving power of conventional EPR is insufficient to reveal the individual TD species. Figure 1 presents the angular dependence of the Si-NL8 spectrum commonly assigned to TD^+; the thin and the thick lines correspond to the experimental results as obtained in

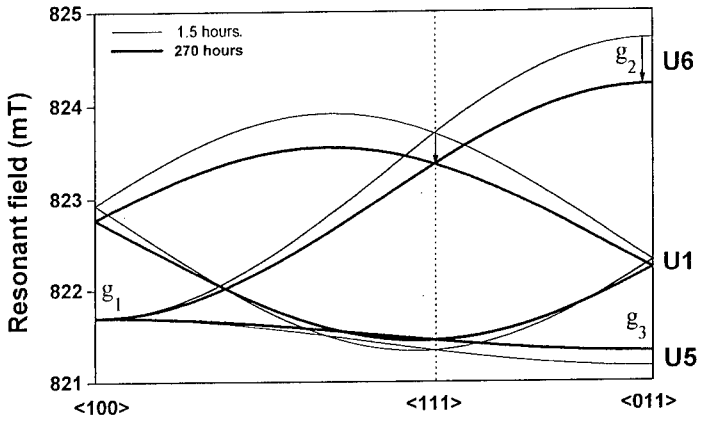


Figure 1: *The angular dependence of the Si-NL8 EPR spectrum as measured in the K microwave band for a Cz-Si:B sample annealed for 1.5 and 270 hrs - thin and thick lines, respectively.*

a sample annealed, respectively, for 1.5 and 270 hours. A clear g-shifting effect can be concluded: upon prolonged annealing the spectrum of orthorhombic-I symmetry type undergoes, what is observed as, a continuous transformation and becomes more isotropic. In the g tensor description this

corresponds to a gradual change of tensor components, with the most pronounced variation of the off-diagonal element g_{xy}. A similar effect has also been concluded for the other TD-related Si-NL10 center [5].

The g-shifting effect illustrated in Fig.1 is readily explained if we assume that the actual EPR spectrum represents a superposition of unresolved contributions of individual species. The relative (but also absolute) concentrations of these change with the annealing time resulting in a somewhat different overall signal. Since the shallower species with the more isotropic g tensors dominate at a later heat-treatment stage, the superimposed spectrum also becomes less anisotropic, in agreement with the experimental result depicted in Fig.1.

B. Individual Si-NL8$_i$ species

Although up to now the EPR spectra of individual TD's could not be resolved, the distinction was possible by Electron Nuclear DOuble Resonance (ENDOR). Such experiments have, again, been performed for both TD-related centers. In ENDOR one observes hyperfine interactions between the electron spin of the center and nuclear spins of atoms on which it is localized.

For the Si-NL8 center a ^{29}Si [9] and ^{17}O ENDOR [8] has been done revealing hyperfine interactions with ligand silicon atoms as well as with oxygen atoms forming (presumably) the essential part of the TD structure. In both cases different "shells" have been found and these have been postulated to arise from different TD species. A direct relation between a selected hyperfine interaction and the EPR center can be obtained in the so-called field-swept ENDOR (FSE); in case of Si-NL8 studies the available conditions did not allow for such a measurement. On the other hand, an attempt was made to correlate different ENDOR shells with TD species detected by IR absorption [10].

Also for the Si-NL10 center a vast body of experimental evidence has been collected. Similarly to Si-NL8, the individual species were resolved in ENDOR [11]. In this case, however, successful FSE measurements could identify several members of the Si-NL10 family. Although the separation of individual contributions was only possible for the single most anisotropic orientation and only close to the <011> crystal direction, i.e., in the vicinity of the U6 point indicated in Fig.1, the FSE technique was in that case capable of providing a very valuable structural information. Among the few separated species only one was found to have the "true" orthorhombic-I symmetry; for all the other ones a small monoclinic distortion was inferred. This finding is of crucial importance for the modeling of the TD structure, and will be further discussed in the next section.

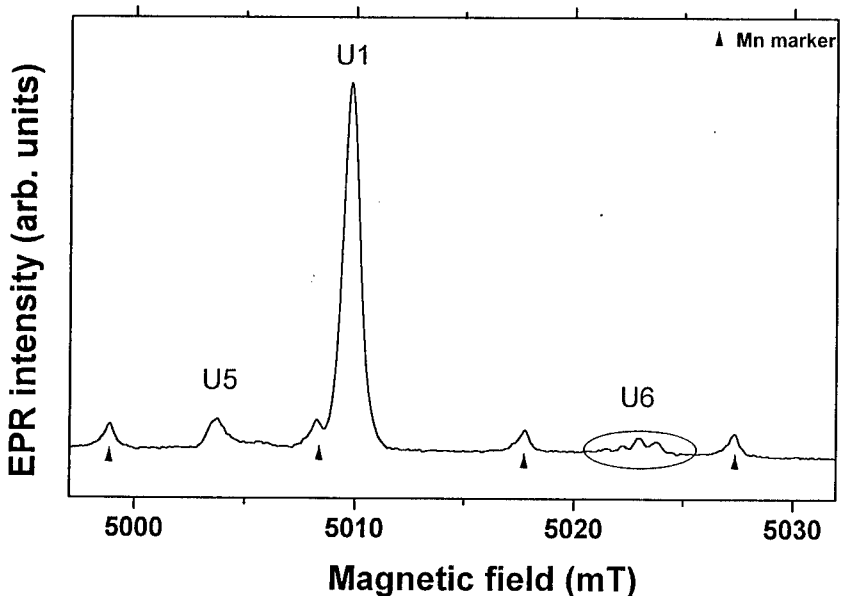


Figure 2: *The Si-NL8 EPR spectrum as obtained in the D-microwave band at 140 GHz with magnetic field parallel to <011>. The indicated splitting of the high-field component U6 shows the contributions of individual TD species. Mn markers are indicated.*

In addition to the ENDOR/FSE studies the Si-NL10 species were also investigated by high-field magneto-absorption [12]. In the experiment conducted for an Al-doped Czochralski-grown Si sample in a magnetic field of 12 T three different species were resolved. However, in view of a poor signal-to-noise ratio, the distinction was possible only for the U6 point, where the separation between the individual spectra is most pronounced; this allowed for an estimation of the specific g tensors.

Since the individual species are characterized by specific g tensors, the spectral separation between them is proportional to magnetic field. In the current study we take full advantage of that effect. Figure 2 shows the EPR spectrum as measured in the studied sample with the magnetic field of approximately 5 T parallel to the <011> crystallographic direction. The four evenly spaced resonances of equal intensity are due to manganese and serve as field markers. For a center of orthorhombic-I symmetry the spectrum in this direction contains three lines with 1:4:1 intensity ratio. Instead, in the figure the high-field line U6 is split into at least four components of different magnitude; their total integrated intensity is equal to that of the low-field resonance U5 at 5003.701 mT. We conclude that the observed splitting represents contributions of individual TD species whose spectra are well resolved in the high-field U6 point, and coincide for the low-field line (U5). Such a behavior is in good agreement with that expected from the g-shifting effect, as depicted in Fig.1. The measurement presented in Fig.2 is the first direct EPR identification of individual TD species observed here in their singly ionized charge state TD^+. We label these species Si-$NL8_1$–Si-$NL8_4$.

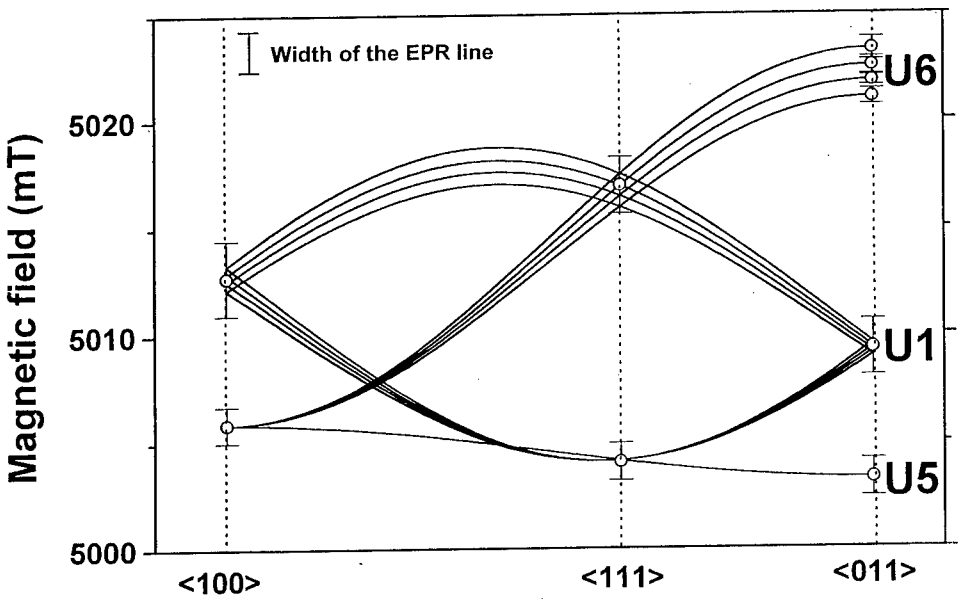


Figure 3: *The angular dependence of the Si-NL8 EPR spectrum as obtained in the D-microwave band at 140 GHz. Solid lines represent simulations for the individual TD species Si-$NL8_1$ to Si-$NL8_4$ with the parameters as summarized in Table I.*

Subsequently the whole angular dependence was measured. The result is illustrated in Fig.3 where experimental data are shown together with the computer fit under the assumption of orthorhombic-I symmetry. The resulting g tensors for the four species are summarized in Table I. Following the earlier discussion we identify the most anisotropic Si-$NL8_1$ as the basic TD present in our sample; it should be characterized by the most simple microscopic structure with (possibly) the smallest number of participating oxygen atoms and the lowest ionization energy level. The "later", less anisotropic species - Si-$NL8_2$–Si-$NL8_4$ - should represent larger structures, with gradually shallower electric levels. Careful inspection of the high-field line in Fig.2 reveals a possible presence of still further species; their presence can also be concluded from a broad high-field shoulder of the middle component - U1. Their field shift is, however, insufficient to determine the g tensors.

Table I: *g values of individual species of Si-NL8*

	$Si\text{-}NL8_1$	$Si\text{-}NL8_3$	$Si\text{-}NL8_3$	$Si\text{-}NL8_4$
g_1	1.99980	1.99980	1.99980	1.99980
g_2	1.99285	1.99317	1.99346	1.99376
g_3	2.00084	2.00084	2.00084	2.00084

C. Symmetry aspects

In the fitting of the angular dependence illustrated in Fig.3 the orthorhombic-I symmetry has been assumed, in line with the generally accepted symmetry properties of TD centers. However, when one considers now that in the current experiment individual species are separately probed, the natural assumption of the C_{2v} symmetry appears much less certain. In detail, if one accepts a general model that the TD development process comprises (interstitial) oxygen aggregation around a characteristic core of precisely orthorhombic-I symmetry and electrical character of a double donor, then it appears highly unlikely that this symmetry type would be preserved in the TD growth process. In order to maintain the orthorhombic-I symmetry for all the species the growth process would either have to take place along a <100> crystallographic direction (the two-fold defect axis), or would require the simultaneous addition of at least two oxygen atoms on symmetry-equivalent sites on both sides of the cluster. The first possibility is contradicted by the experimental data which indicate <011> as the growth direction; the latter one is highly improbable in view of the large number of components involved. Consequently, it is plausible that, when investigated separately, the majority of TD species would disclose symmetries lower than orthorhombic-I: monoclinic or general. We note here that such a growth-induced symmetry lowering has been concluded in case of the other TD-related EPR spectrum, Si-NL10, from the FSE studies [10]. In that case, among the four species investigated in some detail only one was determined to have a true C_{2v} symmetry type; for the other ones a small splitting of the orientations which coincide in U6 has been concluded. The magnitude of this splitting was shown to be (far) below the resolution of a K-band EPR experiment.

Although in the current study the experimental data could be satisfactorily fitted with orthorhombic g tensors, a possible lowering of the symmetry type has been given further attention. This is illustrated in Fig.4.

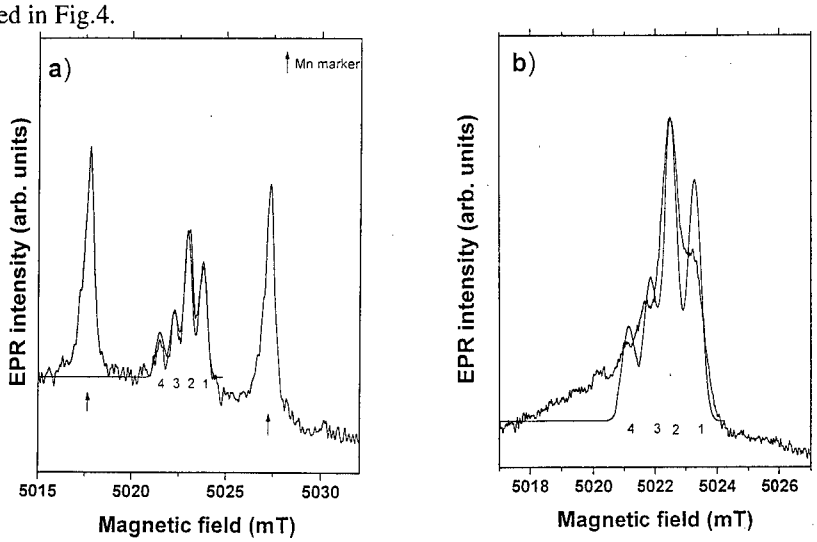


Figure 4: *Comparison of the measured and the simulated spectra with magnetic field oriented* **(a)** *along a <011> direction and* **(b)** *16° away from <011>. Only the resonance U6 from a single TD orientation is shown. A clear disagreement for the off-main-direction measurement can be observed.*

Figure 4(a) shows the EPR spectrum as experimentally observed in the high-symmetry U6 point. This measurement has been used to determine the intensity of individual components, and a simulation of the signal has been made. As can be seen the experimental form of the spectrum can be very

well reproduced. Subsequently, the intensity and the linewidth established in this way have been used to simulate the spectrum expected 16° away from the main direction. In Fig.4(b) this simulation is compared with the actual measurement: in this case the agreement is rather poor. The experimental result can be readily reproduced if we assume a small, unresolved splitting of components related to Si-$NL8_1$, Si-$NL8_3$, and Si-$NL8_4$. Therefore the current study offers strong indications that the growth process lowers the overall symmetry of the TD center from orthorhombic to, at least, monoclinic. However, even when performed at the frequency of 140 GHz, the experimental resolution of EPR appears insufficient to decide on the precise symmetry of the individual species.

In follow-up experiments currently on the way the growth/development of TD's will be further investigated. We hope that these studies will finally unravel the symmetry changes and, in this way, contribute to the understanding of the whole process.

Conclusions

The individual species of silicon TD's were for the first time resolved in EPR. They were observed in their singly-ionized charge state TD^+. From the measurements performed in a magnetic field of approximately 5 T and a microwave frequency of 140 GHz the g tensors for four centers, labeled Si-$NL8_1$–Si-$NL8_4$, have been determined. From an analysis of the form of the spectrum observed at approximately 16° away from the <011> main direction the true symmetry of the TD centers has been investigated; some indication has been found that some of the species present in the investigated crystal were of a symmetry lower than orthorhombic-I usually assigned to TD's.

Acknowledgements

The research has been partially sponsored by the *Stichting voor Fundamenteel Onderzoek der Materie* (FOM). The authors are grateful to Ir V. Krymov for his valuable contributions to instrumentation.

References

1. W. Kaiser, Phys. Rev. **105**, 1751 (1957).
2. W. Götz, G. Pensl, and W. Zulehner, Phys. Rev. B **46**, 4312 (1992).
3. L. Dobaczewski, P. Kamiński, R. Kozlowski, and M. Surma, Mater. Sci. Forum **196-201**, 669 (1995).
4. S.H. Muller, M. Sprenger, E.G. Sieverts, and C.A.J. Ammerlaan, Solid State Commun. **25**, 987 (1978).
5. T. Gregorkiewicz, D.A. van Wezep, H.H.P.Th. Bekman, and C.A.J. Ammerlaan, Phys. Rev. B **35**, 3810 (1987).
6. Yu.V. Martynov, T. Gregorkiewicz, and C.A.J. Ammerlaan, Phys. Rev. Lett. **74**, 2030 (1995).
7. T. Gregorkiewicz, D.A. van Wezep, H.H.P.Th. Bekman, and C.A.J. Ammerlaan, Phys. Rev. Lett. **59**, 1702 (1987).
8. J. Michel, J.R. Niklas, and J.-M. Spaeth, in *Defects in Electronic Materials*, ed. M. Stavola, S.J. Pearton, and G. Davies, Materials Research Society Symposia Proceedings, Vol.104, p.185 (MRS, Pittsburgh, 1988).
9. J. Michel, J.R. Niklas, J.-M. Spaeth, and C. Weinert, Phys. Rev. Lett. **57**, 611 (1986).
10. J. Michel, J.R. Niklas, and J.-M. Spaeth, Phys. Rev. B **40**, 1732 (1989).
11. T. Gregorkiewicz, H.H.P.Th. Bekman, and C.A.J. Ammerlaan, Phys. Rev. B **38**, 3998 (1988).
12. T. Gregorkiewicz, H.H.P.Th. Bekman, C.A.J. Ammerlaan, W. Knap, L.C. Brunel, and G. Martinez, Phys. Rev. B. **45**, 5873 (1992).

Materials Science Forum Vols. 258-263 (1997) pp. 379-384
© 1997 Trans Tech Publications, Switzerland

SHALLOW THERMAL DONORS IN ANNEALED CZ SILICON AND LINKS TO THE NL10 EPR SPECTRUM: THE RELEVANCE OF H, Al AND N IMPURITIES

R. C. Newman[1], M. J. Ashwin[1], R. E. Pritchard[1], J. H. Tucker[1], E. C. Lightowlers[2], T. Gregorkiewicz[3], I. S. Zevenbergen[3], C. A. J. Ammerlaan[3], R. Falster[4], and M. J. Binns[4]

[1] IRC for Semiconductor Materials, The Blackett Laboratory, Imperial College, London SW7 2BZ, UK

[2] Department of Physics, King's College London, Strand, London WC2R 2LS, UK

[3] Van der Waals-Zeeman Laboratorium, Universiteit van Amsterdam, Valckenierstraat 65-67, NL-1018 XE, Amsterdam, The Netherlands

[4] MEMC Electronic Materials Inc., 501, Pearl Drive (City of O'Fallon) P.O. Box 8, St. Peters, Missouri 62276, USA

Keywords : Si, oxygen, shallow thermal donors, infrared absorption, electron paramagnetic resonance

Abstract. Heat treatment of Czochralski Si at ~ 470 °C leads to the formation of shallow thermal donors (STDs) with ionisation energies of ~ 36 meV that are detected by infrared (IR) absorption. The STDs produced in hydrogenated samples (B, P or In-doped) are shown to incorporate H atoms and give rise to a distinct set of electronic transitions. A different family of lines is detected in Al-doped samples. Such samples also give rise to NL10 electron paramagnetic resonance (EPR) spectra and ENDOR measurements reveal the presence of H(D) or Al atoms in the defect cores. STD*N*(H) and STD*N*(Al) are produced simultaneously in hydrogenated Al-doped samples. Samples pre-heated in nitrogen gas at high temperatures show yet a third set of IR electronic transitions but ^{14}N is not detected by ENDOR. There is a suggestion that these centres incorporate a lattice vacancy. We demonstrate that there are at least three types of shallow thermal donors that have not always been distinguished by IR measurements in previous work.

Introduction.

Clustering of oxygen atoms in Czochralski (CZ) silicon annealed in the range $350 < T < 500°C$ leads to the formation of a family of double thermal donors, TD*N* [1,2] with $N = 1$ to 16. Individual members of this family are resolved by infrared (IR) measurements of the electronic transitions from either TD*N*^{0} or TD*N*$^+$. In their singly ionised charge state, the donors also give rise to the NL8 electron paramagnetic resonance (EPR) spectrum [3,4] and electron nuclear double resonance (ENDOR) measurements of ^{17}O-doped samples demonstrate the presence of O atoms in the TD cores [5]. ENDOR signals from other impurities (^{13}C, ^{14}N) are not detected (see, for example, Ref. 6). In spite of the wealth of information, there is still uncertainty about the detailed structure of these defects.

Another family of defects that gives rise to the less anisotropic EPR NL10 spectrum [7] is also generated in annealed CZ Si. NL10 is always stronger in samples doped with Al and ENDOR measurements confirm the presence of both oxygen and ^{27}Al in the defect cores [7,8]. However, the presence of ^{27}Al is not essential for the detection of NL10 and in other samples, an ENDOR signal from hydrogen has been observed [6,9]. In hydrogenated Al-doped material both ENDOR signals can be detected indicating that these defects can be of the type NL10(Al) or NL10(H). Again the detailed structure of these defects is not known but it resembles the TD structure with the addition of an Al atom, a H atom or possibly some other impurity or a defect.

Electronic IR absorption lines are detected at energies below ~ 300 cm^{-1} and recently their strengths have been linked with the strength of NL10(H) [6]. These IR absorption lines have been studied by many workers and correspond to a second family of donors that are known as shallow thermal donors, STD*N* [6, 10-15]. However, these absorption lines have not been differentiated into separate families of STD*N*s and so it is not clear whether or not the same donor defects have been examined in each study. For example, it has been shown that the STD defects responsible for the IR absorption lines reported in Ref. 6, must incorporate at least one H atom since the transitions shifted slightly to lower energies when H atoms were replaced by D atoms. Other workers have measured IR absorption in annealed Al-doped CZ Si below 300 cm^{-1} [15], but a well-resolved family of lines was not reported. There have also been many reports of STD transitions detected in nitrogen treated samples [11-14] and some workers have proposed that nitrogen is incorporated in these STD defect cores [11,14].

The aim of the present work is to clarify the situation by examining a range of annealed CZ samples: namely, hydrogenated material, Al-doped material and nitridated material. We will show that after suitable annealing treatments, these three types of samples can produce three different families of STD*N* absorption lines and three different types of ENDOR signal from their NL10 spectra. We link STD*N*(H) to NL10(H) and STD*N*(Al) to NL10(Al) but the third family of lines produced in nitridated material, STD*N*(X), does not link to an ENDOR signal from ^{14}N. The presence of nitrogen is not ruled out but, alternatively, a different defect/impurity may be incorporated in this donor core.

Experimental Details.

Most CZ Si samples (O_i ~ 10^{18} cm^{-3}) were given a thermal pre-treatment at 1200 - 1300 °C in Ar, H_2 (hydrogenation) or N_2 gas (nitridation) at atmospheric pressure for 30 - 60 min. The samples were then cooled rapidly by either dropping them directly into silicone oil, or the tube in which they were heated was plunged into water. The material was either aluminium doped ([Al] = 1 x 10^{15} cm^{-3}) or lightly boron-doped ([B] = 5 x 10^{14} cm^{-3}) , both with carbon concentrations less than 2 x 10^{15} cm^{-3}. The samples were then annealed in air or in a radio-frequency hydrogen plasma (13.56 MHz, 2 mbar, 40 W) in the range 470 - 650 °C for periods of up to 24 h. It was found that the various STD defects have different dissociation temperatures, allowing selective formation of a particular family of STDs by the choice of an appropriate anneal temperature. All samples were wedged and polished and IR spectra at ~ 10 K were obtained with a Bruker IFS 120 HR interferometer operated at a resolution of 0.25 cm^{-1}.

Results and Discussion.

Figure 1a shows the IR electronic absorption lines from the STDs in a hydrogenated boron-doped sample following an anneal at 470 °C for 22h. These lines (Table 1, column 1) relate to oxygen clusters that incorporate a hydrogen atom and were previously linked to the NL10 (H) EPR spectrum [6]. Annealing this material in air at 470 °C/16h without a pre-hydrogenation treatment produced the same STD centres at a lower concentration, indicating that hydrogen is present in the as-grown material. The absorption lines from the STDs generated in annealed Al-doped material (Fig. 1b) have different energies (Table 1, column 3) and so it is inferred that there are two types of STD centres, STD*N*(H) and STD*N*(Al). IR spectra from hydrogenated Al-doped material (Fig. 1c) show lines from both STD*N*(H) and STD*N*(Al) demonstrating that the two types of STD defect can co-exist in samples annealed at 470 °C. ENDOR measurements demonstrate that NL10(H) and NL10(Al) can also co-exist in such samples and so a new result from the present work is

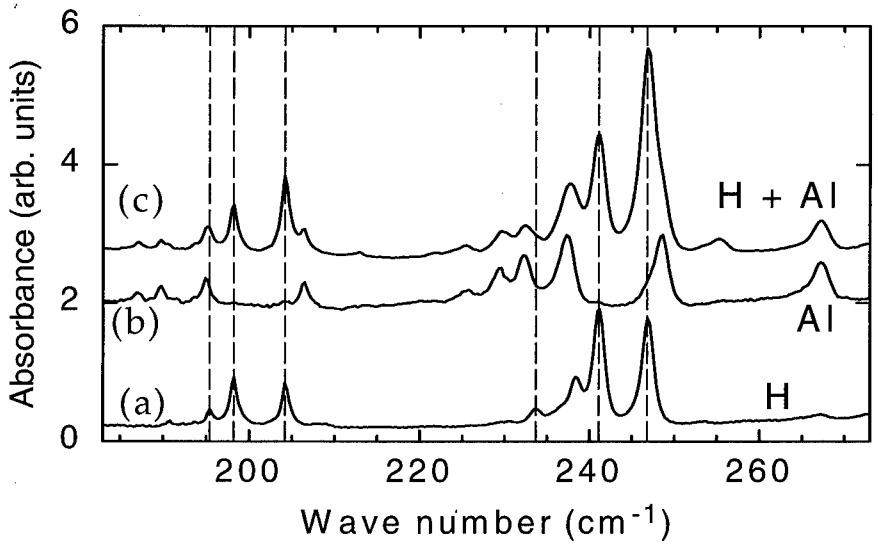


Fig. 1 *IR absorption lines (1s->2p_0 near 200 cm^{-1} and 1s->2p± near 240 cm^{-1}) detected in samples annealed at 470°C. (a) Hydrogenated boron-doped Si showing the* STDN(H) *spectrum, (b) Al-doped Si pre-heated in Ar showing the* STDN(Al) *spectrum, and (c) hydrogenated Al-doped Si showing the superposition of the* STDN(H) *and* STDN(Al) *spectra. The vertical lines are guides for the eye.*

that we can relate a family of absorption lines, STD*N*(Al), to the NL10(Al) spectrum. Both Al-doped and boron-doped material also showed strong absorption from TD centres following an anneal at 470 °C.

Hydrogenated samples of the boron- and Al-doped material, given a second anneal at 550 °C for 16h, showed no absorption from TD*N* centres and absorption from STD*N*(H) centres was barely visible. However, the same treatment given to the Al-doped sample, led to absorption from STD*N*(Al) that increased in strength by a factor of ~ 10 demonstrating that these centres are more stable than STD*N*(H). Following a further anneal of this sample at 650 °C/16h, the strengths of the STD*N*(Al) lines decreased by factors of 2-5, implying some degree of dissociation at this higher temperature.

In a nitridated boron-doped sample annealed at 470 °C/24h, IR absorption lines relating to STD*N*(H) dominated the spectrum, although other weaker lines were also present in the same spectral region. After a second anneal at 550°C/16h, the latter lines increased in strength by a factor of ~ 5 (Fig. 2a) while absorption from STD*N*(H) and TD*N* centres was greatly reduced. The STD transitions in this material (Table 1, column 4) are different from both the STD*N*(H) (Fig. 2b) and STD*N*(Al) (Fig. 2c) transitions and are labelled STD*N*(X) where X is an unknown component of the donor. For a nitridated boron-doped sample annealed at 650 °C/16h, all absorption from STD*N*(X) was lost showing that all these centres had dissociated after this long period of annealing.

The present IR absorption spectra demonstrate that at least 3 different types of shallow thermal donors can form in annealed CZ silicon. ENDOR measurements of the NL10 spectrum generated in a nitridated sample annealed at 550 °C did not reveal the presence of ^{14}N in the STD*N*(X) core. However, ^{29}Si ENDOR measurements revealed the presence of hyperfine interactions larger than those measured for the NL10(Al) spectrum. These differences are currently under investigation but there is a possibility that there is a third NL10 spectrum, labelled NL10(X), which we could relate to the STD*N*(X) transitions. X is an unknown constituent of the defect but the ENDOR measurements suggest that it is not

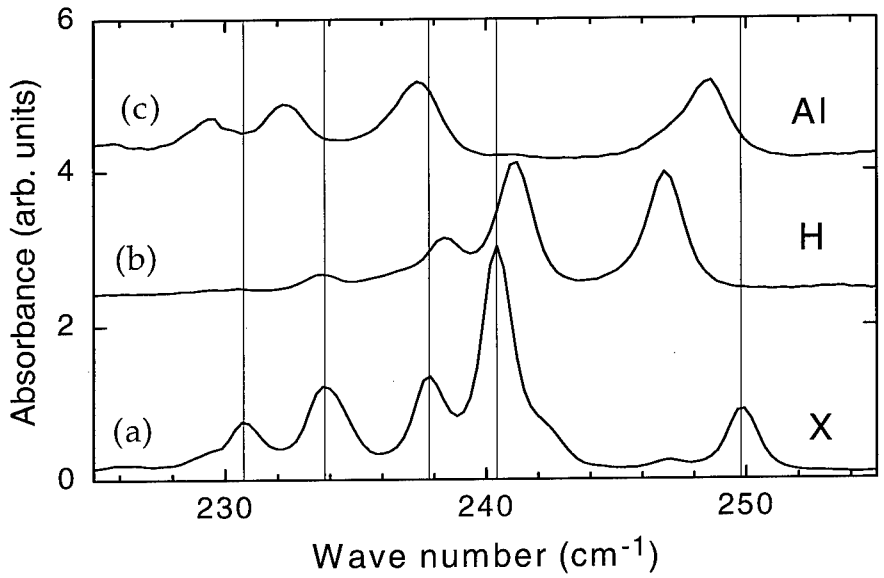


Fig. 2 *IR absorption lines (1s->2p±) of (a) the STDN(X) spectrum produced in Si pre-heated in nitrogen gas and annealed at 550°C, (b) the STDN(H) spectrum, and (c) the STDN(Al) spectrum.*

necessarily a nitrogen atom even though the material was annealed in N_2 gas. This conclusion is supported by IR absorption measurements of unannealed samples (float zone and CZ) nitridated at 1270 °C for 1 h. Localised vibrational modes from N-N pairs were not detected, indicating that the concentration of such pairs introduced by our procedure must be less than 10^{15} cm^{-3}. An alternative possibility is that vacancies are incorporated in the STD*N*(X) centres instead of nitrogen. It is well known from diffusion measurements of buried impurity marker layers that rapidly diffusing vacancies are produced at the surface of silicon samples heat treated at high temperatures in nitrogen gas [16]. This would include samples grown in a N_2 atmosphere, irrespective of whether or not the melts contained Si_3N_4. For crystals doped with Si_3N_4, the growth atmosphere has not always been specified but nitrogen atmospheres have been used.

We now compare the present IR measurements with published STD electronic energies (Table 1). The energies of the STD*N*(X) lines measured in our nitridated samples (N_2(Q)) coincide with those quoted in Ref. 11 for nitrogen-doped samples and those given in Ref. 12 for nitridated samples. The latter data were obtained by photo-thermal ionisation spectroscopy (PTIS) and agree with our IR absorption measurements for the same sample (column(a)). On the other hand, transitions measured for samples heated in N_2 gas and then annealed at 480°C [14] coincide with the STD*N*(H) transitions. At this lower anneal temperature, STD*N*(X) defects may also have been present but the transitions may have been obscured by stronger STD*N*(H) lines, as found in the present work. Finally, STDs have been reported in hydrogenated, electron-irradiated material [17] and may correspond to STD*N*(H) transitions. It was speculated that these centres incorporated both a lattice vacancy and hydrogen but the presence of hydrogen was not demonstrated.

We have suggested previously that STD*N*(H) and NL10(H) centres are TD*N* defects passivated by a single H atom [6,9]. However, our measurements show that STD*N*(H) is stable up to 500°C in contrast to deep-level transient spectroscopy (DLTS) measurements which show that passivated TDs (predominately TD1 and TD2) dissociate at ~ 200 °C [18]. Since the H atoms in these defects are most likely bonded to either O or Si, the DLTS

STDN(H)		STDN(Al)	STDN(X)			
H_2(Q)	(Ref. 14)		N_2(Q)	(a)	PTIS [12]	(Ref. 11)
		-	184.6			
187.4		187.0	187.8		188.0	
190.7		189.7	190.9	191.1	190.9	190.8
195.4		195.0	194.7	194.8	194.9	195.0
198.2	198.1[b]	198.3	197.6	197.7	197.6	197.7
					198.9	
204.2	204.2[b]	204.1		200.3		200.2
					203.8	
208.7		206.4	207.3	207.5	207.3	207.4
226.1		225.5				-
230.6		229.3	230.7		230.9	-
233.7		232.3	233.8	233.8	233.8	233.7
238.4	238.2	237.4	237.8	237.8	237.9	237.9
241.1	241.1[b]	-	240.4	240.4	240.4	240.5
-				242.5	242.4	242.4
246.8	246.7[b]		247.1		246.8	
-	249.7[b]	248.6	249.8	249.9	249.6	249.9
253.6						-
				256.9	257.0	-
	264.5					
			259.9	260.2	260.3	-
					264.2	
			266.6	266.7	266.5	266.7
267.1	267.2	267.3		268.9	268.7	268.8
273.0	273.3			274.1	273.9	
278.5	276.1	275.1	276.2	276.2	275.9	

TABLE 1. *The frequencies (cm^{-1}) of the IR transitions of STDN(H), STDN(Al) and STDN(X) shallow thermal donors and comparisons with published work. (a) Our IR data for a sample (MPI, Stuttgart) previously measured by PTIS (Ref. 12). (b) Lines also reported in Ref. 17 for irradiated, hydrogenated silicon. Q indicates quenched samples.*

measurements are consistent with the expectation that H-O and H-Si bonds would dissociate at $T \ll 500$ °C. We considered the possibility that STDN(H) defects are formed by H passivation of TDs as the samples cool to room temperature. To test this idea, a hydrogenated boron-doped sample was cut into two pieces that were annealed together at 470°C/16h. One piece was cooled rapidly by dropping it into liquid nitrogen while the other piece was cooled slowly over a period of 16 h. There was no difference in the strength of the resulting STDN(H) spectra suggesting that these defects are not formed during the cooling period. We conclude that STDN(H) centres have slightly different structures to hydrogen passivated TD centres.

Another possibility is that STDN(H) centres incorporate a carbon atom in the defect core. In this case, a stronger H-C bond would form which could be stable up to ~ 500 °C. This was investigated by annealing a hydrogenated, carbon contaminated sample ([C] = 2 x 10^{16} cm^{-3}) at a temperature of 470°C for 16h. However, this sample showed no IR absorption from STDN(H) centres and only very weak absorption from TDN centres and so we find no evidence to support this proposal. Evidently the hydrogen passivation of extended defects is more complex than the passivation of simple point defects.

Conclusions.

We have demonstrated that three types of STD defect relating to the clustering of oxygen atoms can exist in annealed CZ Si. Each defect gives rise to a characteristic family of IR electronic absorption lines and therefore can be distinguished by IR absorption spectroscopy. One type of STD defect is formed exclusively in Al-doped material and we relate STD*N*(Al) to NL10(Al). The second type of STD centre incorporates hydrogen and can be formed in *all* annealed CZ Si since H is always present at low concentrations in as-grown material. These defects also give rise to the NL10(H) spectrum. The third type of shallow thermal donor, STD*N*(X), is detected in nitridated material and incorporates a defect or impurity that we label X. The consensus view, based on circumstantial evidence, is still that X corresponds to a nitrogen atom since the absence of a ^{14}N ENDOR signal in the NL10(X) spectrum could be explained by a small overlap of the electron wavefunction with the nitrogen nucleus. Alternatively, we suggest that nitridation may act as a catalytic process for the formation of STD*N*(X), allowing X to be identified with a lattice vacancy. Finally, we note that the thermal stability of STD*N*(Al) centres is greater than that of STD*N*(X) centres that are, in turn, more stable than STD*N*(H) centres. The relative stability of the STD*N*(Al) defects is expected since the formation energy of Al_2O_3 (300 kcal/mol) is some 50 % greater than that of SiO_2. However, the high thermal stability of STD*N*(H) defects suggests that bonds other than H-Si and H-O are formed in these centres.

Acknowledgments

The UK authors thank the Engineering and Physical Sciences Research Council, UK, for financial support of the contracts GR/K96977 and GR/K30995 .

References

1. P. Wagner and J. Hage, Appl. Phys. A **49**, 123 (1989).
2. W. Götz, G. Pensl, and W. Zulehner, Phys. Rev. B **46**, 4312 (1992).
3. J. Michel, J.R. Niklas, and J.-M. Spaeth, Phys. Rev. B **40**, 1732 (1989).
4. K.M. Lee, J.M. Trombetta, and G.D. Watkins, in "Microscopic Identification of Electronic Defects in Semiconductors", ed. N.M. Johnson, S.G. Bishop, and G.D. Watkins, Mat. Res. Soc. Symp. Proc. **46**, 263 (1985).
5. N. Meilwes, J.-M. Spaeth, W. Götz, and G. Pensl, Semicond. Sci. Technol. **9**, 1632 (1994).
6. R.C. Newman, J.H. Tucker, N.G. Semaltianos, E.C. Lightowlers, T. Gregorkiewicz, I.S. Zevenbergen, and C.A.J. Ammerlaan, Phys. Rev. B **54**, R6803 (1996).
7. T. Gregorkiewicz, H.H.P.Th. Bekman, C.A.J. Ammerlaan, Phys. Rev. B **38**, 3998 (1988).
8. T. Gregorkiewicz, D.A. van Wezep, H.H.P.Th. Bekman, and C.A.J. Ammerlaan, Phys. Rev. Lett. **59**, 1702 (1987).
9. Yu. V. Martynov, T. Gregorkiewicz, C.A.J. Ammerlaan, Phys. Rev. Lett. **74**, 2030 (1995).
10. H. Navarro, J. Griffin, J. Weber, and L. Genzel, Solid State Commun. **58**, 151 (1986).
11. M. Suezawa, K. Sumino, H. Harada, and T. Abe, Jpn. J. Appl. Phys. **27**, 62 (1988).
12. J. Griffin, J. Hartung, J. Weber, H. Navarro, and L. Genzel, Appl. Phys. A **48**, 41 (1989).
13. A.G. Steele, L.C. Lenchyshyn, and M.L.W. Thewalt, Appl. Phys. Lett. **56**, 148 (1990).
14. A. Hara, J. Appl. Phys. **34**, 3418 (1995).
15. P. Kaczor, M. Godlewski, T. Gregorkiewicz, Mater. Sci. Forum **143-147**, 1185 (1994).
16. P.M. Fahy, P.B. Griffin, and J.D. Plummer, Rev. Mod. Phys. **61**, 289 (1989).
17. V.P. Markevich, I.F. Medvedeva, L. I. Murin, in "Early Stages of Oxygen Precipitation in Silicon", ed. R Jones NATO ASI series (Kluwer, Dordrecht) **17**, 103 (1996).
18. J. Weber and D. I. Bohne, in "Early Stages of Oxygen Precipitation in Silicon", ed. R Jones NATO ASI series (Kluwer, Dordrecht), **17**, 123 (1996).

Materials Science Forum Vols. 258-263 (1997) pp. 385-390
© 1997 Trans Tech Publications, Switzerland

FORMATION OF ULTRA SHALLOW DONORS IN SILICON BY LONG-TERM-ANNEALING AT 470 °C

D. Åberg, T. Hallberg*, B. G. Svensson,
J. L. Lindström*, and M. Kleverman**

Royal Institute of Technology, Solid State Electronics, P.O. Box E-229, S-164 40 Kista-Stockholm, Sweden

* Linköping University, Dep. Physics and Measurement Technology, S-581 83, Linköping, Sweden

**University of Lund, Solid State Physics, S-221 00, Lund, Sweden

Key Words: shallow thermal donors, oxygen clusters, electrical characterization

Abstract

Czochralski-grown and phosphorus-doped ($\sim 2 \cdot 10^{14}\text{cm}^{-3}$) silicon samples have been annealed at 470 °C in nitrogen ambient for durations between 1 h and 500 h. The samples were subsequently characterized by Fourier transform infrared absorption measurements , photo-thermal ionization spectroscopy, and in particular various electrical techniques such as four point probe resistivity measurements, admittance spectroscopy (ADSPEC), thermally stimulated capacitance measurements (TSCAP), capacitance-voltage measurements and deep level transient spectroscopy. An increasing concentration of free carrier electrons is observed at room temperature with increasing anneal time, reaching an almost constant value of $\sim 8 \cdot 10^{15}\text{cm}^{-3}$ after $\sim 25 - 50$ h. ADSPEC and TSCAP measurements performed at frequencies from 10^3 to 10^6 Hz for temperatures between 14 and 300 K revealed the presence of ultra shallow donors with level positions gradually shifting from ~ 35 meV to ~ 25 meV below the conduction band edge as a function of annealing time. The samples were examined both in the near surface region ($\leq 1\mu$m) and also at larger depths ($\sim 15\mu$m) after chemical etching, and within the experimental accuracy no variations in the concentration and energy position of the donors were observed. The donor complexes are most likely oxygen-related but not of the same origin as the so-called shallow thermal donors (STD's).

1 Introduction

Czochralski (Cz) grown silicon contains oxygen impurities in interstitial sites normally up to concentrations of 10^{18} cm^{-3}. This oxygen is super-saturated at temperatures below the melting point, and heat treatments therefore cause precipitates and clusters to form. Since 1954[1] it is known that heat treatments in the range 300-500 °C cause thermal donors (TD's) to be produced, and since then it is one of the most studied defect phenomenon in Si. TD's are known to contain oxygen, and over the years both thermal double donors (TDD's)[2, 3] and single donors, with more shallow energy position than TDD's and therefore called shallow thermal donors (STD's)[4, 5], have been found. The microscopical structures of the TD's are still not fully known, and the determination of these has proven to be one of the greatest challenges in defect physics of semiconductors.

The TDD's are known to exist in up to 16 different species [6, 7] with the neutral species having energy positions in the range of 69-53 meV below the conduction band edge (E_c), and the singly ionized species in the range 156-118 meV below E_c for the first nine evolving defects[8], with each new defect level approaching the conduction band. In parallel with the production of TDD's, the single donors STD's at 35-37 meV below E_c

emerge[8]. They give rise to IR electronic absorption bands below ~300 cm^{-1}[9] and an electronic paramagnetic resonance (EPR) signal called NL-10[10].

The STD has been argued to be formed either by an alternative clustering path to the TDD [11] or by singly passivating existing TDD[12, 13]. There is strong evidence from electronic nuclear double resonance (ENDOR) and EPR-measurements that hydrogen can be part of the STD core [12, 13], and that nitrogen affects the formation of both TDD's and STD's [5, 14, 15, 16]. Nitrogen has, however, never been identified as part of the core of STD, and it is disputed whether nitrogen exists as a catalyst or as a constitutient[11, 14, 15, 16]. Further, theoretical analysis has shown[17] that shallow defects could be constructed from either nitrogen-oxygen complexes or carbon-oxygen complexes with very similar electronic properties, which could explain how the STD defects have been created without the presence of nitrogen in several experiments [15, 18].

Hydrogen is another element of concern related to the STD's, as it has been shown to form five types of shallow donors [19]. McQuaid et al.[19] discussed the idea that STD's are different forms of singly passivated TDD's, and that one formation path is conversion of a deep donor to a shallow single donor by complexing with hydrogen. Another group proposed from electron-nuclear double resonance (ENDOR) measurements that NL-10 has hydrogen as part of its core[12]. Indeed, IR measurements made on annealed hydrogenated CZ Si samples show STD evolution where the positions of the vibrational bands shift when deuterium is used instead of hydrogen[13]. On these hydrogenated samples ENDOR measurements were made which inferred that the defects giving rise to STD's were partially passivated TDD's. No evidence of neither nitrogen nor carbon in the defects was found by these measurements.

Photo thermal ionization spectroscopy (PTIS) measurements on CZ Si annealed at 450 °C show an ionization continuum above 210 cm^{-1} (~26 meV)[9], and the aim of this contribution is to report on a set of thermal donors in this very shallow energy regime. These ultra-shallow thermal donors (USTD's) have been found to form in Cz-Si at 470 °C during long annealing times. They occur with a high concentration($\sim 10^{16}cm^{-3}$), and with energy levels closer to E_c than the STD's. They are single donors, and increase to a maximum concentration on the order of 10^{16} cm^{-3} after 100 hours. This is one order of magnitude higher than what have previously been reported for the STD's [8, 10], and in our experiments USTD's are the dominant electrical centers.

2 Experiments

The Si-material used throughout the experiments was as-received Cz-grown from Virginia Semiconductors, Inc. It was doped with phosphorus to $\sim 2 \cdot 10^{14}cm^{-3}$, with an intrinsic content of oxygen and carbon $\sim 7 \cdot 10^{17}cm^{-3}$ and $\leq 2 \cdot 10^{16}cm^{-3}$, respectively as determined by IR measurements. The samples were annealed in nitrogen atmosphere at 470 °C from 2h to 504h. Resistivity measurements using a 4-point probe were made on all samples. Schottky contacts of gold were grown on the samples after a standard surface cleaning procedure in order to enable electrical analysis by admittance spectroscopy (ADSPEC)[20], thermally stimulated spectroscopy (TSCAP)[20] and deep level transient spectroscopy (DLTS)[21]. The samples were mounted in TO5-headers and cooled using a closed cycle, double stage cryostat from APD Cryogenics, DE-202. The measurements were made from 14 K to room temperature at a reverse bias voltage of 5V. For measuring the temperature a Si-diode was mounted in a TO5-header with a symmetric position to that of the sample-header in the cryostat, to ensure maximum accuracy of the temperature reading. Measurements were conducted using a sweep frequency capacitance-voltage (C-V) meter, HP4284A, and as a result of the CV-curves, the concentration of free carriers was obtained as a function of temperature. Some selected samples were chemically etched to a depth of 15 μm in order to distinguish between surface and bulk effects. The

etchings was made in 80 °C KOH for 16 minutes during stirring. We also performed DLTS-measurements, using the same setup as described above plus a pulse generator HP8110A, and HP4280A 1MHz C(t)-meter for time resolved capacitance measurements. All the measurements were controlled by a PC via a GPIB bus.

3 Results and discussion

Figure 1 shows results from four point probe measurements performed at room temperature using samples annealed at 470 °C for different times between 2h and 504h. Compared to the initial electron concentration of 2×10^{14} cm^{-3}, given by the phosphorus donors, a large increase of more than one order of magnitude takes place within the first 50h before a maximum of almost 10^{16} cm^{-3} is reached at 100h. At longer times a gradual decrease occurs. The carrier concentration values are deduced from the measured resistivity data applying the so-called Irvin curve for phosphorus [22] and assuming a uniform distribution through the samples. This assumption is confirmed by carrier concentration versus depth profiles obtained from C-V measurements, which is illustrated in figure 2 displaying data from a sample annealed for 15h. A small decrease is only observed in the near surface region at depths less than $\sim 1.5\mu$m while a constant level occurs at large depths towards the bulk, as also substantiated by results from samples chemically etched to depths in excess of 15μm.

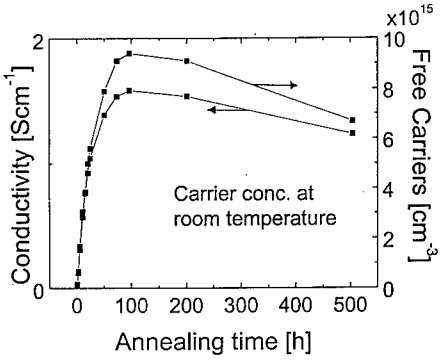


Figure 1: Carrier concentrations at room temperature as a function of annealing time at 470 °C.

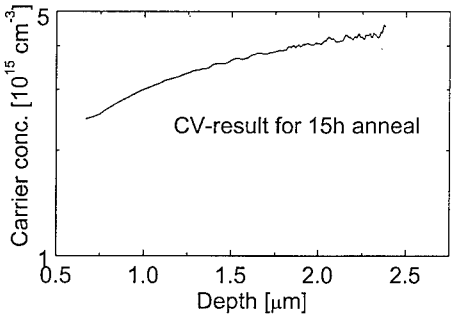


Figure 2: Carrier concentration at room temperature as a function of sample depth.

Conductance versus temperature curves obtained at a sampling frequency of 1MHz for samples annealed at 2h, 15h, 50h and 96h are compared with that for an as-grown sample in figure 3. In addition to the 'classical' TDD's and the phosphorus donor, one ultra shallow level is observed which shifts to lower temperatures and becomes increasingly dominant with increasing time, e.g., after 96h more than 80 % of the conduction electrons originate from this ultra shallow thermal donor (USTD). As expected, the level associated with the TDD's exhibit a minor shift with annealing time; their positions in the bandgap were also determined by low-temperature DLTS and found to be identical with that reported previously in the literature[2, 8, 7]. However the influence of the TDD's with respect to the total electron concentration is small and even in the sample annealed for 2h the relative contribution is less than 30 %. After 504h all the TDD's have essentially been annealed out while the USTD's still prevail with a concentration $6 - 7 \times 10^{15}$ cm^{-3}.

Arrhenius plots deduced from conductance versus temperature measurements at frequencies between 10^3 and 10^6 Hz (ADSPEC analysis) are shown in figure 4 for as-

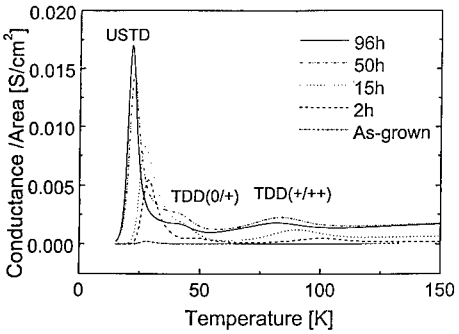


Figure 3: Conductance as a function of temperature changes with annealing temperature. Ultra shallow donors emerge.

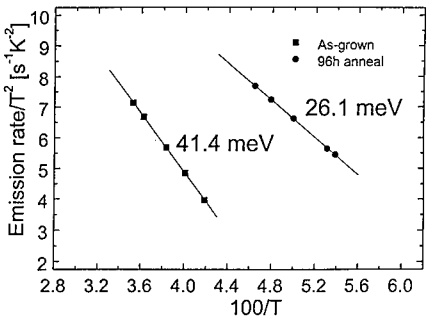
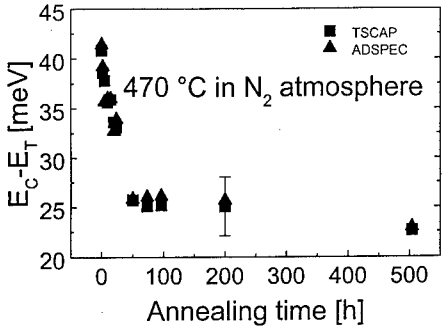


Figure 4: Arrhenius plot showing the difference in energy position for the most shallow significant defect in as-grown material and 96h annealed material.

grown sample and annealed (96h) samples. The value obtained for donor energy level in the as-grown sample ($\sim E_c$-41 meV) is associated with phosphorus while the position of the USTD level in the 96h annealed sample is significantly shallower ($\sim E_c$-26 meV). The capture cross sections extracted by extrapolation of the Arrhenius plots are in the range of $\sim 10^{-20}$ cm^2 for both levels. Further TSCAP and ADSPEC analysis of chemically etched samples yielded identical results for the energy positions as in figure 4, emphasizing that the existence of USTD's is a bulk phenomenon.

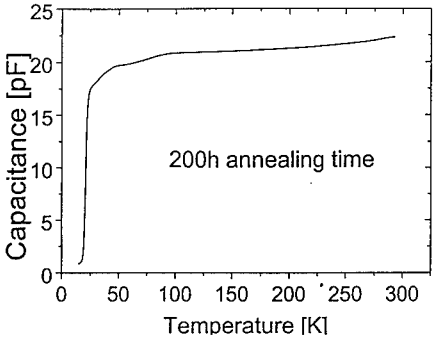
Figure 5 shows the position of the most shallow donor level as a function of the annealing time, and in particular, a rapid shift towards E_c occurs initially (up to $\sim$50h) while at longer times (more than $\sim$ 100h)the position remains almost constant. These data may indicate a gradual evolution of the USTD's up to a saturation in their concentration and that the atomic configuration is fully developed at longer times. In figure 6 the dominating contribution of the USTD's to the conduction electrons is illustrated by capacitance versus temperature data using a sample annealed for 200h. The TDD's give rise to a small but noticeable increase at $\sim 70 - 90$K (TDD(+/++)) and $\sim 35 - 45$K (TDD(0/+)) where the latter is more difficult to resolve since it follows closely after the contributions from the STD's and the phosphorus donors. PTIS measurements were performed on some selected samples and in addition to the distinct electronic transitions at $\sim E_c - 35$ meV, which exhibited concentrations of $\leq 10^{15}$ cm^{-3} and are associated with the STD's[9], a broad ionization spectrum was observed above ~ 200 cm^{-1}. The position of this spectrum corresponds to ≥ 23 meV below E_c and it is very tempting to make an association with the USTD's. In this context it should be mentioned that also Navarro et al. [9] found a broad ionization spectrum in their samples but no detailed discussion was given.

Finally, the formation kinetics of TD's has been investigated by numerous groups and a basic problem is to account for the fast formation rate of TDD's, STD's and now USTD's compared to the diffusivity of interstitial oxygen atoms. A common concept is to introduce a fast diffusing species like for example the oxygen dimer, which acts as a precursor to the TDD's but is not electrically active itself. Recently, an IR absorption band at 1012 cm^{-1} has been attributed to the oxygen dimer[23] and a broad sub-band at the same wavenumber is created subsequently and preliminary data indicate that the



Energy level position for the most shallow donors as a function of annealing temperature. As the positions shifts towards the conduction band, the concentrations of defects also increases.

Figure 5:



Capacitance as a function of temperature using a measurement frequency of 1MHz. The major increase occurs at such temperatures where the STD's or phosphorus are not ionized.

Figure 6:

strength of this broad band correlates with the concentration of USTD's. This correlation is to be investigated in further work.

4 Conclusions

The existence of ultra shallow thermal donors with concentrations as high as $\sim 10^{16}$ cm^{-3} and positions as shallow as E_c-25 meV is shown in Cz-Si samples annealed at 470 °C for times up to $\sim$ 500h. The STD's and the classical TDD's have previously been thought to cause the large increase of free carriers when annealing Cz-Si in the range 300-500 °C. There is now reason to question this, as we attribute the larger part of free carrier concentration in 470 °C annealed Cz-Si to originate from USTD levels between 25 meV and 35 meV below E_c. Further work is in progress to determine the thermal stability of the USTD's, and also to reveal their identity. Current data indicate that the USTD's are more stable than the TDD's (and the STD's).

Acknowledgement

Financial support by the Swedish Research Council for Engineering Sciences is acknowledged.

References

[1] C. S. Fuller, J. A. Ditzenberger, N. B. Hannay, and E. Buehler. *Phys. Rev.*, 96:833, 1954.

[2] P. Wagner and J. Hage. *Appl. Phys. A*, 49:123, 1989.

[3] P. Deak, L. C. Snyder, and J. W. Corbett. *Phys. Rev. B*, 45(20):11 612, 1992.

[4] J. A. Griffin, H. Navarro, J. Weber, L.Genzel, J. T. Borenstein, J. W. Corbett, and L. C. Snyder. *J. Phys. C*, 19:L579, 1986.

[5] M. Suezawa, K. Sumino, H. Harada, and T. Abe. *Jpn. J. Appl. Phys.*, 25(10):L859, October 1986.

[6] W. Götz, G. Pensl, and W. Zulehner. *Phys. Rev. Lett.*, 46:4312, 1992.

[7] T. Hallberg. PhD thesis, Linkping University, S-581 83 Linkping, Sweden, 1995.

[8] H. H. P. Th BEkman. PhD thesis, Natuurkundig Laboratorium der Universiteit van Amsterdam, Valckenierstraat 65, 1018 XE Amsterdam, The Netherlands, 1990.

[9] H. Navarro, J. Griffin, J. Weber, and L. Genzel. *Solid State Commun.*, 58(3):151, 1986.

[10] T. Gregorkiewicz, D. A. van Wezep, H. H. P. Th. Beckman, and C. A. J. Ammerlaan. *Phys. Rev. B*, 35(8):3810, 1987.

[11] J. A. Griffin, J. Hartung, and J. Weber. *Materials Science Forum*, 38-41:619, 1989.

[12] Yu V. Martynov, T. Gregorkiewicz, and C. A. J. Ammerlaan. *Phys. Rev. Lett.*, 74(11):2030, 13 March 1995.

[13] R. C. Newman, J. H. Tucker, N. G. Semaltianos, E. C. Lightowlers, T. Gregorkiewicz, I. S. Zevenbergen, and C. A. J. Ammerlaan. *Phys. Rev. B*, 54(10):6803, 1996.

[14] A. Hara, T. Fukada, T. Miyabo, and I. Hirai. *Appl. Phys. Lett.*, 54(7):626, 13 February 1989.

[15] A. Hara, I. Hirai, and A. Ohsawa. *J. Appl. Phys.*, 67(5):2462, 1 March 1989.

[16] D. Yang and D. Que. *J. Appl. Phys.*, 77(2):943, 15 January 1995.

[17] C P. Ewels and R. Jones. *Phys. Rev. Lett.*, 77(5):865, July 1996.

[18] B. J. Heijmink Liesert, T. Gregorkiewicz, and C. A. Ammerlaan. *Phys. Rev. B*, 47(12):7005, 1993.

[19] S. A. McQuaid, R. C. Newman, and E. C. Lightowlers. *Semicond. Sci. Technol.*, 9:1736, 1994.

[20] E. H. Rhoderick and R. H. Williams. Oxford University Press, 2 edition, 1988.

[21] D. V. Lang. *J. Appl. Phys.*, 45(7):3023, 1974.

[22] S. M. Sze. *Physics of Semiconductor Devices.* Wiley, 1981.

[23] L.I. Murin and V.P Markevich. To be published in the NATO ASI series, 1996.

Materials Science Forum Vols. 258-263 (1997) pp. 391-398
© 1997 Trans Tech Publications, Switzerland

LOCAL VIBRATIONAL MODES OF WEAKLY BOUND O-H COMPLEXES IN SI

B. Bech Nielsen[1], K. Tanderup[1], M. Budde[1], K. Bonde Nielsen[1], J.L. Lindström[2], R. Jones[3], S. Öberg[4], B. Hourahine[5], and P. Briddon[5].

[1] *Institute of Physics and Astronomy, University of Aarhus, DK-8000, Denmark.*
[2] *Department of Physics, Linköbing University, S-58183, Sweden*
[3] *Department of Physics, University of Exeter, EX44QL, United Kingdom.*
[4] *Department of Mathematics, University of Luleå, S-95187, Sweden.*
[5] *Department of Physics, University of Newcastle, United Kingdom.*

Keywords: Oxygen, Hydrogen, Complexes, Silicon, Local modes, Infrared absorption.

Abstract.
Local vibrational modes of two oxygen-hydrogen complexes have been identified with infrared absorption spectroscopy. Samples of intrinsic silicon and samples doped with ^{16}O or ^{18}O isotopes were implanted with protons and deuterons at ~20 K. After the implantation, infrared absorbance spectra were measured at 8 K on unannealed samples. An oxygen mode at 1077 cm^{-1} and a hydrogen mode at 1879 cm^{-1}, which originate from the same defect OH_I were observed in the as-implanted samples. Heat-treatment at 200 K produced a new center OH_{II} with modes at 1028 and 1830 cm^{-1}. OH_I anneals out at ~130 K while OH_{II} is stable up to ~240 K. OH_I and OH_{II} are tentatively identified with two complexes of interstitial oxygen and bond-centred hydrogen. *Ab initio* theory was applied to calculate the structure and local modes of three such complexes. The results qualitatively support our tentative assignments.

Introduction

Oxygen atoms are abundant impurities in crystalline silicon with concentrations ranging from about 10^{16} cm^{-3} in float-zone (Fz) material to 10^{18} cm^{-3} in Czochralski-grown (Cz) material. The importance of oxygen was realized in the early days of semiconductor technology and therefore, the properties of oxygen impurities in silicon have been addressed in numerous publications[1]. A large part of the activity has dealt with clustering of oxygen in Cz silicon[2]. The clustering is governed by the migration of oxygen and oxygen-related complexes. Of particular interest to this work, hydrogen in silicon is known to enhance the diffusion of oxygen about two orders of magnitude in the temperature range 250-400°C[3-6]. The enhancement is caused by a catalytic process, believed to involve an oxygen-hydrogen complex in which the activation energy associated with atomic jumps of the oxygen is reduced. Identification of the structure of this complex may provide us with a starting point for a detailed understanding of the catalytic process.

The interaction of hydrogen with interstitial oxygen (O_i) has been investigated theoretically by three groups[7-10], who all agree that in the minimum-energy configuration, no oxygen-hydrogen bond is formed. The calculated equilibrium structures differ, however. Estreicher[7] found that in the neutral charge state, the oxygen and hydrogen atoms occupy two neighbouring bond-centre (BC) sites. In contrast, Jones et al.[8,9] found that the stable site for the hydrogen atom is an antibonding (AB) site opposite to the interstitial oxygen. Recently, Ramamoorthy and Pantelides[10] found that in the neutral and positive charge states oxygen and hydrogen occupy two neighbouring BC sites while in the negative charge state the AB site opposite to the oxygen is the stable site for the hydrogen. The binding energies of the O_i-H_{BC} complex was found to be 0.5 eV, 0.3eV, and 0.4 eV for the positive, the neutral, and the negative charge states, respectively[10].

There is little experimental evidence for the existence of *O-H* complexes in silicon. Qi et al.[11] assigned Si-H stretch modes at 1894, 2123, and 2191 cm^{-1} to *O-H* complexes. These modes were observed in neutron-irradiated Fz silicon doped with hydrogen during growth. The assignments were based solely

on a positive correlation between the intensities of the Si-H modes and the intensity of the O_i mode at 1136 cm^{-1}. No oxygen modes related to centres responsible for the Si-H stretch modes were reported. Mukashev et al.[12,13] found two modes at 870 and 891 cm^{-1} in proton-implanted Cz silicon, which they ascribed to the A-centre (vacancy-oxygen complex) containing one and two hydrogen atoms. No correlated hydrogen modes were reported. A similar investigation was carried out by Tatarkiewicz and Witthuhn[14], who found no evidence for *O-H* complexes. Recently, Markevich et al.[15,16] succeeded in observing a local mode at 1075 cm^{-1} in Cz silicon, which had been heat-treated in a hydrogen atmosphere at 1200 °C and subsequently quenched at 0 °C. This mode shifted upwards in frequency by 1.3 cm^{-1} when the heat-treatment was done in a deuterium atmosphere[15], establishing that hydrogen is involved in the centre. From measurements on samples co-doped with hydrogen and deuterium it was concluded that the 1075-cm^{-1} centre contains a single hydrogen. Moreover, the mode was not observed in Fz material and it was concluded that the centre also contains a single oxygen. Very recent work by Pritchard and co-workers[17] suggests that the 1075-cm^{-1} band originates from defects which contain a hydrogen molecule and a single oxygen atom.

This paper reports on the observation of two weakly bound *O-H* complexes, denoted OH_I and OH_{II}. Oxygen and hydrogen local vibrational modes of both complexes have been observed with infrared absorption spectroscopy. It is directly shown that the two complexes each contain a single hydrogen and an oxygen. Based on the local mode frequencies and their relative intensities, it is suggested that both complexes consist of a bond-centred hydrogen in its positive charge state (H_{BC}^+) bound to a nearby interstitial oxygen. *Ab initio* local density functional cluster theory has been applied to calculate the structure and the local vibrational modes of O_i -H_{BC}^+ complexes with H_{BC}^+ located at the first-, second-, and third-nearest neighbour bond-centre sites to the interstitial oxygen. The results suggest that OH_I and OH_{II} correspond to structures with H_{BC}^+ occupying the second-, third-, or fourth-nearest neighbour bond-centre sites to an interstitial oxygen.

Experimental

Below a brief account of the experimental details is presented. A more thorough description is deferred to a subsequent publication. Samples with dimensions ~ 8 × 8 × 2 mm^3 were cut from ordinary Fz and Cz silicon with high resistivity. The oxygen concentrations were $\lesssim 5\times10^{15}$ cm^{-3} in the Fz samples and 5.5×10^{17} cm^{-3} in the Cz material. In addition a few samples were cut from material doped with the ^{18}O isotope. In this material, the concentration of ^{18}O was 9.0×10^{17} cm^{-3} and that of ^{16}O was 0.3×10^{17} cm^{-3}. The samples were mounted directly on the cold finger of a high-power closed-cycle helium cryostat (cryocooler), equipped for optical transmission measurements. With this setup, the sample temperature could be controlled in the range 8 - 320 K. The cylindrical vacuum shroud had four windows, two made from 5mm thick CsI crystals and two made from 0.2 mm thick aluminium foil. The vacuum shroud could be rotated without breaking the vacuum. Thus, it was possible to implant the samples at low temperatures through the aluminium windows and subsequently measure the infrared transmission through the CsI windows.

The samples were implanted with protons and/or deuterons at 30-60 different energies. The temperature of the sample was kept below 20 K during the implantation. The dose implanted at each energy was adjusted in order to obtain a rather uniform depth distribution of implants. The local concentration of hydrogen isotopes was 3.3×10^{17} cm^{-3}, and the profiles extended from the sample surface to a depth of 0.60 mm for protons and 0.30 mm for deuterons. In samples co-implanted with both isotopes, the hydrogen profile only extended to a depth of 0.30 mm to match the deuterium profile.

After the implantation, the cryostat was transported from the accelerator to the infrared spectrometer. The cryocooler was switched off during transport, but the temperature never exceeded 20 K. The cryostat was then mounted to a Nicolet, System 800, FTIR spectrometer, covering the spectral range from 600 to 5000 cm^{-1}. The resolution was 1.0 cm^{-1} , and the sample temperature was 8 K during measurements.

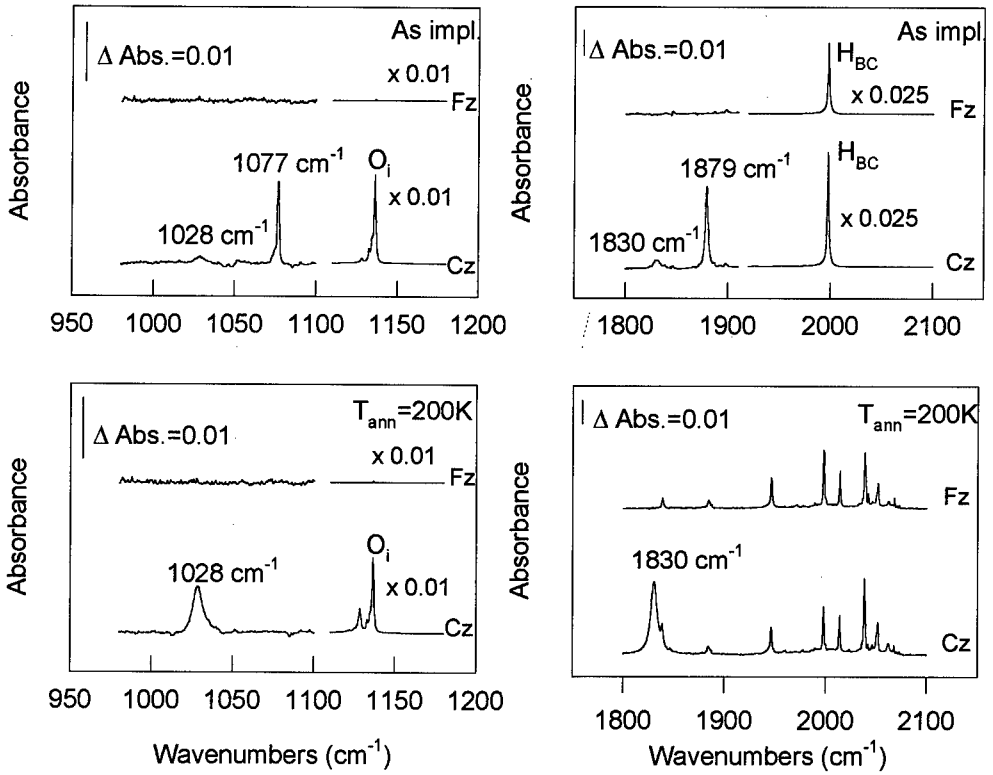


Fig. 1. Sections of absorbance spectra recorded after proton implantation and after annealing at 200 K.

Results and discussion

Sections of the absorbance spectra measured at 8 K directly after implantation of protons are shown in Fig. 1. In Fz material, only one major absorption line at 1998 cm^{-1} is observed. At 80 K, this line is broadened substantially and shifted down to 1990 cm^{-1}. Thus, it is the same line as that observed previously by Stein[18]. The line frequency shifts down with a factor of about $1/\sqrt{2}$ to 1449 cm^{-1} when protons are substituted by deuterons. Hence, the line represents a local vibrational mode of hydrogen, and in agreement with Stein[18], we assign it to a Si-H stretch mode. Recently, we have shown[19] that the annealing behaviour of the 1998-cm^{-1} mode is identical to that of the AA9-signal[20], which is known to originate from isolated hydrogen at the BC site. In addition, it was possible to show[19] that the 1998-cm^{-1} mode is related to the positive charge state of the defect (H_{BC}^{+}) . In Fz material, virtually all the implanted protons end up at BC sites. Since the implanted dose is known, we could deduce the effective charge η of the mode, which may be defined by the formula:

$$\int \alpha(\omega)\, d\omega = \frac{2\pi^2 N}{n_R c} \frac{\eta^2}{M} \qquad (1)$$

where α is the absorption coefficient, n_R the refractive index, c the velocity of light, and M the mass of the impurity. From this it was found that $\eta = 1.8e$, which is much larger than the values expected from theory for Si-H stretch modes of defects in their neutral charge state[21]

The spectra recorded on proton-implanted Cz material are also shown in Fig. 1. Four new lines absent in the Fz spectra are observed, two at 1028 and 1077 cm^{-1} close to the 1136-cm^{-1} mode of interstitial oxygen, and two at 1879 and 1830 cm^{-1} close to the 1998-cm^{-1} mode of bond-centred hydrogen. The lines at 1028 and 1830 cm^{-1} grow in intensity while the lines at 1077 and 1879 cm^{-1} disappear completely after a 15 min. heat-treatment at 200 K.

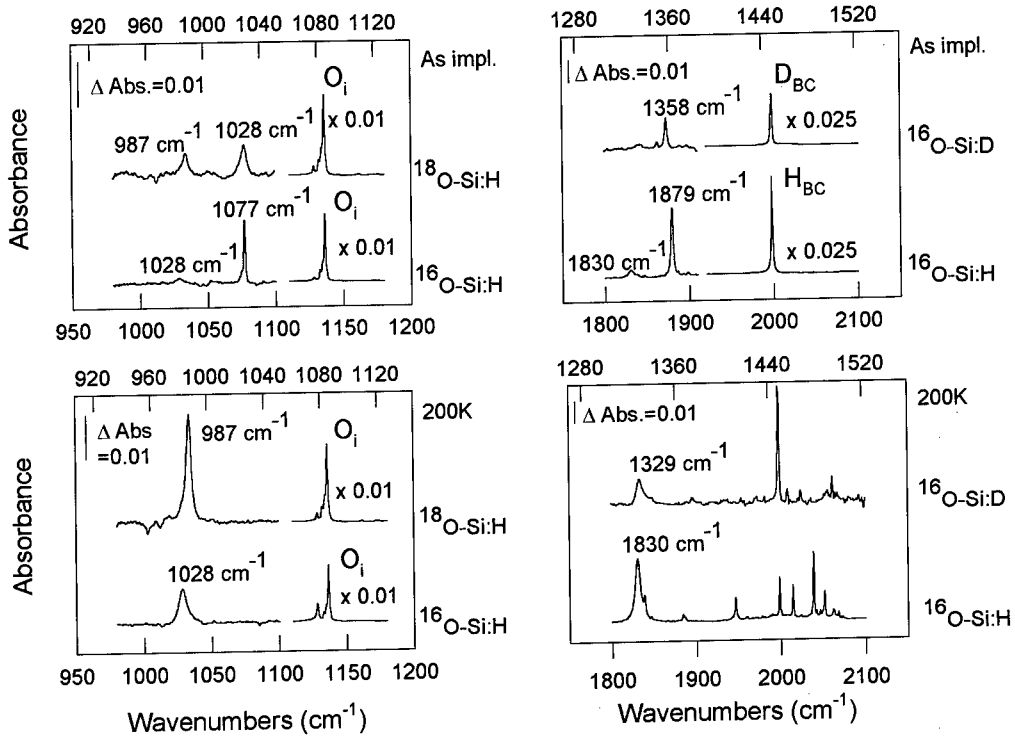


Fig. 2. Spectra measured on ^{16}O- or ^{18}O-doped samples implanted with protons or deuterons.

In Fig 2. spectra recorded on ^{16}O-doped (Cz) and ^{18} O-doped samples implanted with protons and deuterons are compared. The spectra measured just after the implantations show that the line at 1077 cm^{-1} shifts downwards in frequency to 1028 cm^{-1} when ^{16}O is substituted by ^{18}O, and that at 1879 cm^{-1} shifts downwards to 1358 cm^{-1} when protons are replaced by deuterons. This establishes that the lines at 1077 and 1879 cm^{-1} represent local vibrational modes of oxygen and hydrogen, respectively. The spectra recorded after heat-treatment at 200 K show similarly, that the line at 1028 cm^{-1} shifts to 987 cm^{-1} when ^{16}O is replaced by ^{18}O, and that the 1830-cm^{-1} line shifts to 1329 cm^{-1} when deuterons are implanted instead of protons. Hence, the 1028-cm^{-1} line represents an oxygen mode whereas the 1830-cm^{-1} line represents a local mode of hydrogen.

The intensities of the modes were measured at 8 K after each step in a sequence of 15-minutes annealings. The first annealing was carried out at 20 K, and the temperature was increased by 20 K between each step. After annealing at about 100 K, a new absorption line begins to overlap with the hydrogen mode at 1879 cm^{-1}, making it difficult to establish the annealing behaviour of the 1879-cm^{-1} mode accurately. Fortunately, the corresponding deuterium mode at 1358 do not overlap with other lines. The intensities of the 1077 and 1358 cm^{-1} modes as a function of annealing temperature are shown in Fig. 3 together with those for the modes at 1028 and 1830 cm^{-1}.

As can be seen from the figure, the modes at 1077 and 1358 cm^{-1} modes have identical annealing behaviour, and the same applies to the modes at 1028 and 1830 cm^{-1}. This suggests that the modes at

1077 and 1879 (and 1358) cm^{-1} originate from the same defect, as do the modes at 1028 and 1830 cm^{-1}. Since the effective charge is expected to be the same for different isotopes, the ratio $M_H I_H / M_O I_O$ should be a constant for hydrogen and oxygen modes associated with the same defect, independent of the mixture of hydrogen and oxygen isotopes. The ratio $M_H I_H / M_O I_O$ is within 20% constant for the ^1H / ^2H modes at 1879/1358 cm^{-1} and the ^{16}O / ^{18}O modes at 1077/1028 cm^{-1} in all the as-implanted samples. For the ^1H / ^2H modes at 1830/1329 cm^{-1} and the ^{16}O/ ^{18}O modes at 1028/987 cm^{-1}, the value of $M_H I_H / M_O I_O$ is constant within 10% in all samples annealed at 200 K. On this basis, we conclude that the ^{16}O and ^1H modes at 1077 and 1879 cm^{-1} originate from an oxygen-hydrogen defect denoted OH_I, and that the ^{16}O and ^1H modes at 1028 and 1830 belongs to another oxygen-hydrogen complex denoted OH_{II}.

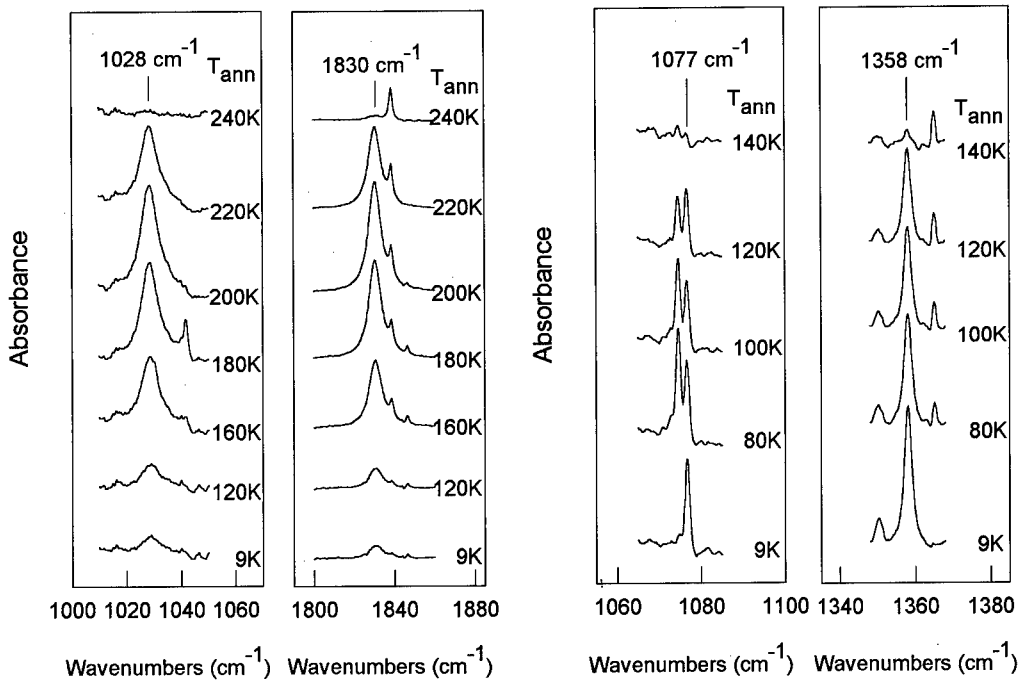


Fig. 3. Annealing behaviours of modes at 1077 and 1358 cm^{-1}, and modes at 1028 and 1830 cm^{-1}.

Information on the number of hydrogen atoms involved in OH_I and OH_{II} was obtained from spectra measured on Cz samples co-implanted with protons and deuterons. Besides the hydrogen and deuterium modes at 1879 and 1358 cm^{-1}, and at 1830 and 1329 cm^{-1}, no new modes were observed. Hence, OH_I and OH_{II} both contain a single hydrogen. Moreover, since oxygen is unable to migrate below room temperature, both centres most likely involve a single oxygen.

The frequencies of the modes observed for all isotopic configurations of the OH_I and OH_{II} centres are reproduced in Table I. As can be seen from the table, the hydrogen and deuterium modes of OH_I do not shift significantly when ^{16}O is substituted by ^{18}O. The ^{16}O mode at 1076.9 cm^{-1} has a minute shift of −0.2 cm^{-1} when deuterium is replaced by hydrogen. Such a small shift is at the limit of the spectral resolution and may be an artifact introduced by the background subtraction. Thus, the oxygen and hydrogen modes are almost decoupled in OH_I.

In contrast to this, a very small dynamical coupling between the oxygen and hydrogen modes in OH_{II} *is* observed. The hydrogen and deuterium modes of OH_{II} shift by -0.3 and 1.5 cm^{-1}, respectively, when ^{16}O is replaced by ^{18}O, and the ^{16}O frequency shifts upwards by 3.8 cm^{-1} when hydrogen is replaced by deuterium. Within the harmonic approximation, it is impossible to explain why the frequency increases

with the isotopic mass. We have no explanation at present, although a similar effect is seen for O-H_2 and interpreted as a Fermi resonance[22].

Table I: Local modes (cm^{-1}) of OH_I and OH_{II}.

	OH_I		OH_{II}	
Isotope mix	O-mode	H-mode	O-mode	H-mode
$^{16}O + {}^{1}H$	1076.9	1879.2	1028.5	1830.4
$^{16}O + {}^{2}H$	1076.7	1358.0	1032.3	1329.1
$^{18}O + {}^{1}H$	1028.3	1879.1	987.1	1830.1
$^{18}O + {}^{2}H$	1028.	1358.0	987.7	1330.6

The intensities of the hydrogen modes of OH_I and OH_{II} are larger than those of the corresponding oxygen modes. For OH_I, the intensity ratio is $I_H/I_O = 6.0\pm1.0$, whereas the value for OH_{II} is $I_H/I_O = 3.1\pm0.5$. The effective charges of different oxygen complexes appear to be similar to that of the 1136-cm^{-1} mode of interstitial oxygen ($\eta \sim 3.8e$)[23,24]. If the same effective charge is assumed for the oxygen modes of OH_I and OH_{II}, we may estimate the effective charges for the hydrogen modes from the intensity ratios given above and Eq. (1). We find that $\eta_H \sim 2.3e$ for OH_I and $\eta_H \sim 1.7e$ for OH_{II}. Now, the concentrations of OH_I and OH_{II} may be estimated from Eq. (1). The concentration of OH_I just after the implantation is $\sim 8\times10^{15}$ cm^{-3}, and the concentration of OH_{II} after annealing at 200 K is $\sim 2.8\times10^{16}$ cm^{-3}. This indicates that ~2% of the hydrogen atoms are trapped in OH_I complexes just after the implantation, whereas ~8% become trapped in OH_{II} complexes upon annealing at 200 K.

The hydrogen frequencies of the OH_I and OH_{II} complexes are typical for Si-H stretch modes but lie well below those for stretch modes of O-H bonds, at about 3700 cm^{-1}. Therefore, we assign the hydrogen modes to Si-H stretch modes, and we conclude that the oxygen and hydrogen atoms do not form a direct bond in the complexes OH_I and OH_{II}. Furthermore, the very small dynamical coupling between the vibrations of the oxygen and hydrogen atoms in OH_I and OH_{II} indicates that the two atoms are rather far apart. The frequencies of the oxygen modes associated with OH_I and OH_{II} are comparable to that of interstitial oxygen at 1136 cm^{-1}. Therefore, we assign the oxygen modes of OH_I and OH_{II} to interstitial oxygen which is perturbed by a single hydrogen.

The Si-H frequencies of OH_I and OH_{II} are more than 150 cm^{-1} lower than those associated with hydrogen in a vacancy[25]. Moreover, the Si-H bond in a vacancy is stable well above room temperature. Hence, we conclude that neither OH_I nor OH_{II} involve a hydrogen located inside a vacancy.

Hydrogen at an antibonding site (H_{AB}) is expected to have a rather low frequency, e.g. the hydrogen at the antibonding site in H_2^* oscillates at 1838 cm^{-1}[21]. However, normally an intense Si-H_{AB} wag mode is observed at about 800 cm^{-1}[21]. Such a mode has not been observed for OH_I and OH_{II}. Moreover, the calculated effective charge for the Si-H_{AB} mode in H_2^* was $0.41e$[21], well below the values of η_H found above. Thus, the hydrogen atom in OH_I and OH_{II} is not likely to occupy an antibonding site.

A bond-centre site for hydrogen in OH_I and OH_{II} is an attractive possibility. In all our spectra, the absorption band at 2770 cm^{-1} (3.61 μm), associated with the divacancy in its singly negative charge state, is observed[26,27].Therefore, the Fermi level E_F is within the range $E_c - 0.4\text{eV} \le E_F \le E_c - 0.23\text{eV}$. Since the donor level of isolated H_{BC} is at $E_c - 0.16$eV[28], we expect that an H_{BC} well separated from an O_i will be in its positive charge state. Support for this expectation is provided by two facts. Firstly, the effective charges corresponding to the hydrogen modes of OH_I ($2.3e$) and OH_{II} ($1.7e$) are both close to the value $1.8e$ associated with isolated H_{BC}^+. Secondly, OH_I and OH_{II} disappear after annealing at ~130 K and at~240 K, which is close to the temperature ~190 K where isolated H_{BC}^+ anneals out. Therefore, we tentatively identify OH_I and OH_{II} with O_i–H_{BC}^+ complexes. Since the dynamical coupling between oxygen and hydrogen is largest for OH_{II}, the oxygen-hydrogen distance is likely to be smallest in this complex.

To provide further evidence for these assignment, the structure and local vibrational modes of three O_i–H_{BC}^+ complexes, with the hydrogen located at the first-, second-, and third-nearest bond-centre site to the interstitial oxygen atom, have been calculated with *ab initio* theory. The calculations are based on local density functional cluster theory applied on a 150-atom cluster. The method has been described

Table II. Calculated local modes (cm^{-1}) of $O_iH_{BCj}^+$ (j=2,3)

	$O_iH_{BC2}^+$		$O_iH_{BC3}^+$		O_i	H_{BC}^+
Isotope mix	O	H	O	H	O	H
$^{16}O + {}^1H$	1050.7	1608.7	1043.1	1788.4	1104	2203
$^{16}O + {}^2H$	1050.3	1144.4	1042.9	1271.1	-	-
$^{18}O + {}^1H$	1000.7	1608.7	993.6	1788.4	-	-
$^{18}O + {}^2H$	1000.4	1144.3	993.4	1271.0	-	-

elsewhere[8,9,29], and further details will be presented in a subsequent publication. The calculated structures, denoted $O_iH_{BC1}^+$, $O_iH_{BC2}^+$, and $O_iH_{BC3}^+$ are presented in Fig. 4 and the local-mode frequencies are given in Table II. In addition, the frequencies calculated previously for isolated O_i[30] and H_{BC}^+[31] are shown for comparison. As can be seen from the Table, there is a significant drop in the H_{BC}^+ frequency when the hydrogen is moved towards the O_i from a distant BC site to the third-nearest BC-site to the O_i, because the Si-H-Si bond is elongated by the oxygen-hydrogen interaction. The frequency drops further when H_{BC}^+ is moved to the second-nearest BC-site to the O_i. This behaviour is qualitatively in good agreement with our observations. ***OH$_I$*** and ***OH$_{II}$*** both have smaller hydrogen frequencies than isolated H_{BC}^+. The fact that the Si-H frequency of ***OH$_I$*** is larger than that of ***OH$_{II}$*** indicates that the oxygen-hydrogen separation distance is smaller in the latter complex, as suggested above. Moreover, the calculated dynamical coupling is very small for $O_iH_{BC2}^+$ and $O_iH_{BC3}^+$, as can be inferred from the minute isotope shifts in Table II. In contrast, the isotope shifts found for the $O_iH_{BC1}^+$ complex are quite substantial, which renders this structure an unlikely candidate for ***OH$_I$*** and ***OH$_{II}$***.

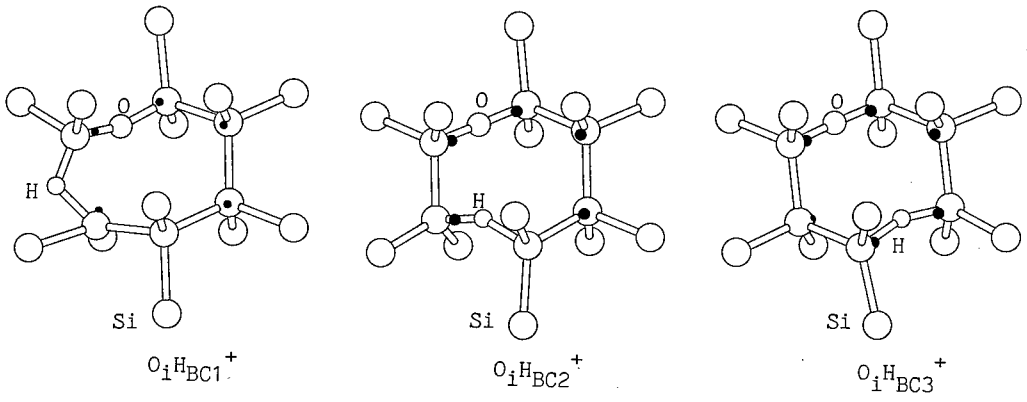


Fig. 4. Calculated structures of O_i-H_{BC}^+ defects. Unrelaxed lattice sites of silicon are indicated by (●)

Two oxygen-hydrogen complexes ***OH$_I$*** and ***OH$_{II}$*** have been identified. Both complexes contain a single hydrogen and a single oxygen atom. The complexes are stable only well below room temperature, indicating a weak binding between the hydrogen and oxygen atoms. ***OH$_I$*** and ***OH$_{II}$*** are tentatively identified as O_i-H_{BC} pairs in their positive charge state. This assignment is supported by *ab initio* calculations, which suggest that ***OH$_{II}$*** may represent an H_{BC}^+ located at the second- or third-nearest BC-site to O_i, and that H_{BC}^+ in ***OH$_I$*** occupies a third- or fourth-nearest BC-site to O_i.

Acknowledgement
This work has been supported by the Danish National Research Foundation through Aarhus Center for Advanced Physics (ACAP).

References

[1] See e.g. *Oxygen in silicon*, Vol. 42 of *Semiconductors and Semimetals*, Ed. F. Shimura (Academic Press, New York, 1994) Vol. 42 and references therein.
[2] See e.g. *Early Stages of Oxygen Precipitation in Silicon*,Ser.3-Vol. 17 of *NATO ASI Series*, Ed. R. Jones (Kluwer Academic Publishers, Dordrecht, 1996) and references therein.
[3] R.C. Newman, J.H. Tucker, and S.A. McQuaid in *"Defects in Semiconductors 16"*, Vol. 83-87 of *Materials Science Forum*, Eds G. Davies, G.G. DeLeo and M. Stavola (Trans Tech Publ., Zürich, 1992) p. 87.
[4] H.J. Stein and S. Hahn, J. Appl. Phys. **75**, 3477 (1994).
[5] S.A. McQuaid, M.J. Binns, C.A. Londos, J.H. Tucker, A.R. Brown, R.C. Newman, J. Appl. Phys. **77**, 1427 (1995).
[6] R.C. Newman in *"Early Stages of Oxygen Precipitation in Silicon"*,Ser.3-Vol. 17 of *NATO ASI Series*, Ed. R. Jones (Kluwer Academic Publishers, Dordrecht, 1996) p. 19.
[7] S.K. Estreicher, Phys. Rev. B **41**, 9886 (1990).
[8] R. Jones, S. Öberg, and A. Umerski in *"Defects in Semiconductors 16"*, Vol. 83-87 of *Materials Science Forum*, Eds G. Davies, G.G. DeLeo and M. Stavola (Trans Tech Publ., Zurich, 1992) p. 551.
[9] R. Jones, Phil. Trans. R. Soc. Lond. A **350**, 189 (1995).
[10] M. Ramamoorthy and S.T. Pantelides in *"Early Stages of Oxygen Precipitation in Silicon"*,Ser.3-Vol. 17 of *NATO ASI Series*, Ed. R. Jones (Kluwer Academic Publishers, Dordrecht, 1996) p. 197.
[11] M.W. Qi, G.R. Bai, T.S. Shi, and L.M. Xie, Materials Letters **3**, 467 (1985).
[12] B.N. Mukashev, M.F. Tamendarov, and S.Z. Tokmoldin in *"Defects in Semiconductors 15"*, Vol. 38-41 of *Materials Science Forum*, Ed. G. Ferenczi (Trans Tech Publ. , Aedermannsdorf, 1989) p. 1039
[13] B.N. Mukashev, S.Z. Tokmoldin, M.F. Tamendarov, and V.V. Frolov, Physica B **170**, 545 (1991).
[14] J. Tatarkiewicz and W. Witthuhn, Phys. Stat. Sol (b) **154**, K99 (1989).
[15] V.P. Markevich, M. Suezawa, and K. Sumino in *"Defects in Semiconductors 18"*, Vol. 196-201 of *Materials Science Forum*, Eds. M. Suezawa and H. Katayama-Yoshida (Trans Tech Publ., Zurich, 1995) p. 915
[16] V.P. Markevich, I.F. Medvedeva, and L.I. Murin in *"Early Stages of Oxygen Precipitation in Silicon"*,Ser.3-Vol. 17 of *NATO ASI Series*, Ed. R. Jones (Kluwer Academic Publishers, Dordrecht, 1996) p. 103
[17] R.C. Newman, *private communication*
[18] H.J. Stein, Phys. Rev. Lett. **43**, 1030 (1979).
[19] To be published
[20] Yu.V. Gorelkinskii and N.N. Nevinnyi, Sov. Tech. Phys. Lett. **13**, 45 (1987).
[21] J.D. Holbech, B. Bech Nielsen, R. Jones, P. Sitch, and S. Öberg, Phys. Rev. lett. **71**, 875 (1993).
[22] B. Hourahine, R. Jones, S. Öberg, and P. Briddon, this conference.
[23] A.S. Oates and R.C. Newman, Appl. Phys. Lett. **49**, 262, (1986).
[24] A.R. Bean and R.C. Newman, Solid State Commun. **9**, 271 (1971).
[25] B. Bech Nielsen, L. Hoffmann, and M. Budde, Materials Science and Engineering B **36**, 259 (1996), and B. Bech Nielsen, L. Hoffmann, and M. Budde, to be published
[26] F. Carton-Merlet, B. Pajot, D.T. Ton, C. Porte, B. Clearjaud, and P.M. Mooney, J. Phys. C **15**, 2239 (1982).
[27] J.H. Svensson, B.G. Svensson, and B. Monemar, Phys.Rev. B **38**, 4192 (1988).
[28] B. Holm, K. Bonde Nielsen, and B. Bech Nielsen, Phys. Rev. lett. **66**, 2360 (1991).
[29] R. Jones, Philos. Trans. R. Soc. London A **341**, 351 (1992).
[30] R. Jones, A. Umerski, and S. Öberg, Phys. Rev. B **45**, 11321 (1992).
[31] R. Jones, Physica B **170**, 181 (1991).

Materials Science Forum Vols. 258-263 (1997) pp. 399-404
© 1997 Trans Tech Publications, Switzerland

PHONON SCATTERING IN HEAT–TREATED CZ–SILICON

F. Zeller, C. Wurster, K. Laßmann, W. Eisenmenger

Universität Stuttgart, 1. Physikalisches Institut, Pfaffenwaldring 57, D-70550 Stuttgart, GERMANY

Keywords: phonon spectroscopy, oxide precipitates, Cz–silicon

Abstract

We investigated the phonon scattering in heat–treated Cz–silicon with different carbon concentrations by means of energy–resolved phonon spectroscopy with superconducting tunnelling junctions. The investigated samples were subjected to a typical "intrinsic gettering" thermal cycle (1100°C + 750°C + 1050°C). After the 1050°C step samples with measurable carbon content show a series of at least three relatively sharp absorptions above 3 meV, which we attribute to geometrical resonances caused by the excitation of geometric eigenvibrations of oxygen aggregates with sizes corresponding to the phonon wavelength. Comparison to infrared absorption is made.

Introduction

Acoustic phonon spectroscopy (PS in the following) with superconducting tunnelling junctions may provide information on nanoscopic crystal defects with sizes corresponding to phonon wavelengths. Like X–ray or small angle neutron scattering it is an integral method for the determination of size distributions down to some nanometers. This was first shown for Ca–colloids in electron–irradiated CaF_2 [1]. Another example is Cz–silicon, where oxygen-related precipitates are of great technological interest. A recent investigation [2] combining PS with IR measurements has revealed characteristic differences of the spectra and time–of–flight signals for carbon–lean and carbon–rich Cz–Si after various annealing steps. Here we report on analogous experiments, specifically investigating the effects of so–called high–low–high annealing sequences on the phonon transmission spectra, relating them to the variation of oxygen–defect–related components of the IR spectra.

Experimental

The investigated samples were cut from Cz–Si (provided by Wacker Siltronic) with low, medium and high substitutional carbon concentration, denoted L–C, M–C, and H–C in the following. The sample dimensions were $14 \times 14 \times 1.3\,mm^3$ with the <111>– or <100>–direction perpendicular to the largest cross section (Tab. 1 and Fig. 1). An annealing series consisted of a first short–term step (2 h) at 1100°C to dissolve grown–in complexes with concomitant out-diffusion of oxygen from the surface region, followed by isothermal annealing at 750°C up to 210 h for the generation of nuclei, and finally a sequence of shorter annealings at 1050°C for the growth of the oxygen precipitates. Annealings were carried out in an inert ambient. For the short high–temperature annealings the samples were moved into the centre of the furnace, which had already reached the operating temperature, and quenched in water afterwards. In case of the long low–annealings the samples were in the furnace during heating and cooling down. Immediately before annealings and IR measurements the crystal surface was etched in HF to remove the oxide layer. After each annealing step phonon and IR spectra were taken and a four point measurement of the resistivity performed.

For PS superconducting Al and Sn tunnelling junctions as phonon generators and detectors were evaporated onto opposite sides of the sample, which was cooled down to 1 K for the measurements. With this set–up the accessible energy ranges from $2\Delta_{det} = 1.2$ meV, the detector threshold at the Sn superconductor gap, up to about 8 meV, where isotope scattering in silicon

sample	orientation	annealing step	$[O_i]$ $[10^{17}cm^{-3}]$	$[C_s]$ $[10^{17}cm^{-3}]$	ϱ [Ωcm]
L–C	<100>	as received	14.2	$< 5 \cdot 10^{15}$	0.8
		2 h / 1100°C	14.5		2.4
		210 h / 750°C	2.8		2.3
		30 min / 1050°C	2.2		2.5
M–C	<111>	as received	15.0	0.3	18.2
		2 h / 1100°C	8.6	6.0	22.5
		210 h / 750°C	0.2	1.6	3.2
		30 min / 1050°C	3.3	3.0	145.7
H–C	<111>	as received	9.2	5.9	19.0
		2 h / 1100°C	7.8	4.5	20.8
		210 h / 750°C	1.1	1.5	1.3
		30 min / 1050°C	7.5	5.7	> 1700

Table 1: Oxygen and carbon concentrations, resistivity of the various samples after comparable annealing steps. Some of the isothermal annealings have been carried out in several time intervals, see Fig. 1.

may mask other scatterers. This range corresponds to transverse phonon wavelengths between some 18 nm and 2 nm which in the case of geometrical resonant scattering will be the range of characteristic resonant lengths. Phonons are also scattered by point defects as in the case of the lowest–energy transition of the interstitial oxygen O_i at 3.64 meV [3]. From the strength of this phonon absorption it is in principle possible to determine quantitatively the residual content after annealing down to concentrations of $\approx 5 \cdot 10^{13}$ cm^{-3} [4]. Phonon spectra of the annealed samples were taken in parallel to those of an as–grown reference sample cut from an adjacent region of the same crystal. Optimum energy resolution ($\approx 10\mu$eV) was not required by the width of the observed resonances, so it was set to about 20 μeV.
The IR–spectra have been obtained by FTIR spectroscopy with a resolution of 2 cm^{-1}. They were taken at room temperature and also at lower temperature using a continuous flow liquid helium cryostat, which allows cooling down to 3.5 K (measured with a Si–diode which was mounted close to the investigated sample). Oxygen and carbon concentrations ($[O_i]$ and $[C_s]$) were determined at room temperature with the conversion factors given in DIN 50438-1. If the oxygen content is strongly reduced by precipitation, low temperature IR measurements become necessary, allowing a separation of the 1136 cm^{-1}–O_i–absorption from the broad absorption around 1100 cm^{-1} caused by the oxygen–related complexes [5]. For the evaluation of the oxygen concentration the resolution of the instrument has then to be considered [6].

Results
Fig. 1 lists $[O_i]$, $[C_s]$ as well as the resistivity of the various samples after equivalent annealing steps. On the left side of Fig. 1 the variation of point defect concentrations and resistivity for sample M–C due to the annealing sequences is graphically depicted. $[O_i]$ decreases only little during the first high–annealing step at 1100°C, whereas $[C_s]$ strongly increases by a factor of $\approx$ 20 (Fig.1), apparently liberated from carbon-related complexes. The decay of oxygen and carbon content during the low–sequence follows the relationship $\Delta[C_s] = \frac{1}{2} \cdot \Delta[O_i]$, i. e. the agglomeration of O_i is accompanied by the removal of one carbon atom from its substitutional configuration, as was also found by Sun et al. [7]. The decrease of the resistivity can be related to the formation of so–called New Thermal Donors (NTD), which is favored in carbon–rich silicon. The phonon transmission spectrum after the first low–annealing step at 750°C is com-

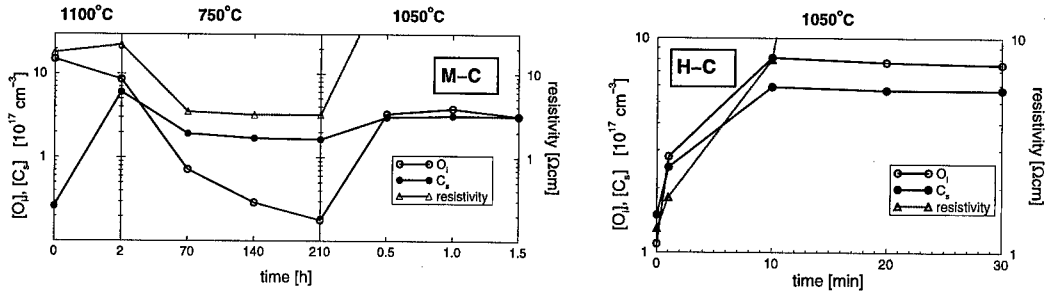


Figure 1: Variation of $[O_i]$, $[C_s]$ and resistivity of samples M–C and H–C with annealing time and tempeature.

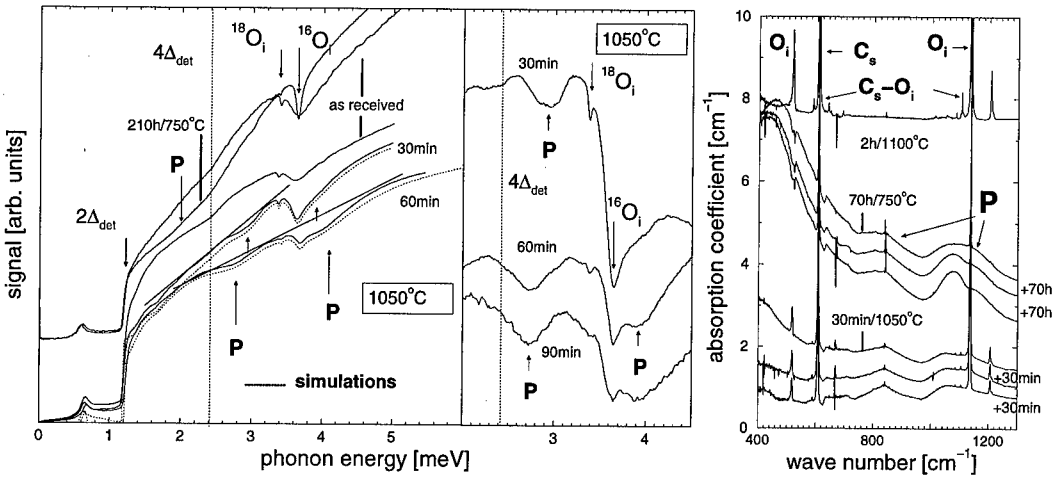


Figure 2: Phonon transmission spectra (left side) and IR absorption spectra (vertically shifted) of crystal M–C. Phonon scattering as well as IR–absorption, which is attributed to oxgyen precipitates or other agglomerates, are marked by the letter P. The right half of the left picture shows the phonon signal after subtracting a baseline as indicated on the left side. At $4\Delta_{det}$ there is a slight increase of signal slope which is caused by an increase of the detector sensitivity.

pared to the as–grown reference crystal in Fig. 2. Due to the high oxygen concentration before annealing there is instrumental broadening of the $^{16}O_i$–resonance at 3.64 meV whereas the $^{18}O_i$–resonance remains sharp because of the small concentration of the isotope (0.2%). Wiggles beyond the main resonance are resonances shifted by the mutual stress associated with O_i in close pair configurations [3]. The reduction of $[O_i]$ after annealing for 70 h at 750°C shows up as a narrowing of the line. In the region around 2 meV (marked by P) a depression of the phonon transmission signal is observed, which is typical for carbon–rich material [2] and could be caused by resonant phonon scattering at clusters with dimension $\lambda/2 \approx 5$ nm, with λ being the transverse phonon wavelength which belongs to 2 meV. This finding would be in agreement with the result of SANS measurements for 750°C annealings [5]. Prolonged annealing at 750°C does not seem to result in a significant change of position, depth or width of the absorption band, rather a further signal decrease over the whole energy range was observed.

The infrared spectra show two broad bands around 840 cm^{-1} and around 1100 cm^{-1}, the latter being related to the oxygen precipitates. The origin of the absorption at 840 cm^{-1} is not yet clear, it might be caused by SiC–clusters [8], but there have been other suggestions as well ([7], [9]). After the first 70 h intervall at 750°C the absorption increases only around 1100 cm^{-1}

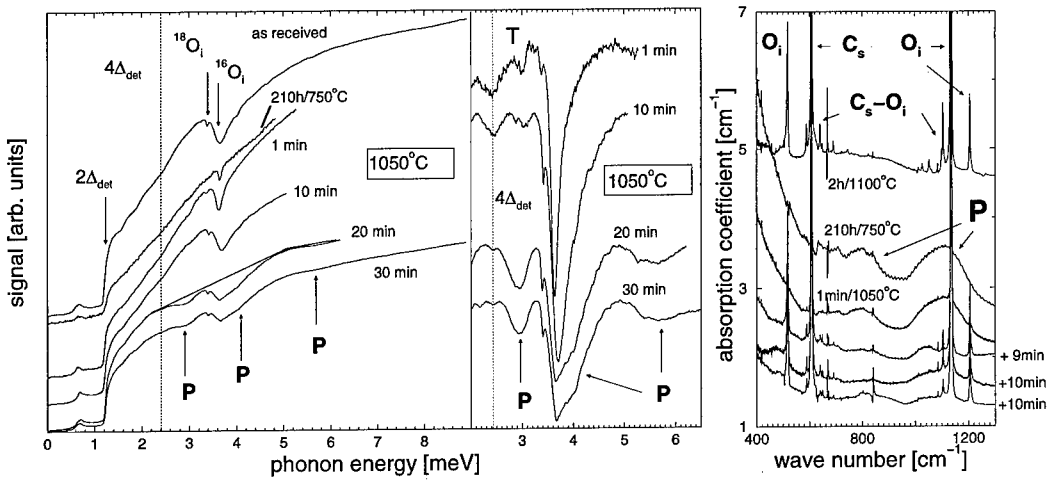


Figure 3: Phonon transmission spectra of crystal H–C (left side) and corresponding IR spectra. Notation as in Fig. 2. The structure at 2.4 meV of the "baseline–corrected" phonon signals is caused by an increase in detector sensitivity; the lines marked by T are precursors to the O_i–resonances due to phonons from a thermally excited side band with an energy higher by $2\Delta_{gen}$ than the main emission line.

(Fig. 2), indicating the presence of two types of oxygen precipitates with maximum absorption coefficients around 1070 cm^{-1} and 1150 cm^{-1}, respectively. After half an hour annealing at 1050°C the oxygen and carbon contents have apparently reached their equilibrium values, two oxygen atoms per one carbon atom having by now gone into solid solution, see Tab. 1 and Fig.1. The strong increase of the resistivity indicates that the NTDs are dissolved during the first 1050°C–intervall. The IR–absorption around 840 cm^{-1} remains nearly unaffected, whereas the 1100 cm^{-1} band decreases, probably since larger nuclei grow at the expense of smaller ones, which results in a smaller precipitate density. The asymmetric form of the 1100 cm^{-1} band remains, but the relative maximum shifts from ca. 1075 cm^{-1} to $\approx$ 1050 cm^{-1}.
The high–temperature step at 1050°C leads to narrow–band phonon absorption as is evident in Fig. 2. After 30 minutes at 1050°C at least two phonon resonances have developed, one at 2.9 meV, the other one overlapping with the $^{16}O_i$–absorption (also marked with P in the left diagram of Fig. 2). By a simulation as described in [4] a good fit to the phonon transmission spectrum [4] is possible if one assumes that these two resonances have identical line shapes and if one sets $[O_i] = 2.2 \cdot 10^{17}$ cm^{-3}, the corresponding IR value being $[O_i] = 3.3 \cdot 10^{17}$ cm^{-3} (Fig. 2, left diagram). The line positions and widths slightly change after further annealing steps with the lower–lying resonance energy decreasing to 2.75 meV, whereas the other resonance seems to shift to a slightly higher energy of 3.9 meV. The line width, as obtained by simulation, amounts to $\approx$ 0.6 meV after one hour at 1050°C. A steady state is reached after annealing for more than one hour, as is shown in Fig. 2, which also depicts the phonon spectra in the energy range around 3 meV after subtracting a "baseline".

The experiment was repeated with a H–C–sample in order to check whether these phonon resonances can be reproduced under the same annealing conditions, but with different defect concentrations. As there had been changes on a time scale of some ten minutes in the case of sample M–C, we have used shorter time intervals to focus on the initial stage of the 1050°C annealing. The time dependence of $[O_i]$, $[C_s]$ and resistivity are illustrated on the right side of Fig. 1. After half an hour annealing at 1050°C the oxygen concentration is $7.5 \cdot 10^{17}$ cm^{-3}, which is 82 % of the initial content (22 % in the case of sample M–C), whereas the amount of substitutional carbon atoms has nearly reached the level previous to heating. Moreover, Fig. 1

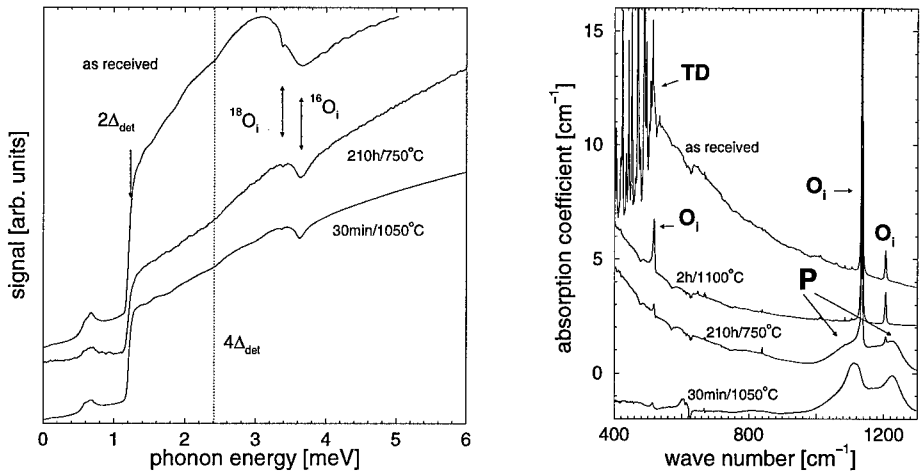


Figure 4: Phonon transmission spectra (left side) and IR absorption of crystal L–C. The series of sharp IR absorptions below 500 cm^{-1} of the as–received sample is caused by electronic excitations of thermal donors, which are annihilated after annealing at 1100°C for 2 hours. The IR spectrum at the bottom was measured at room temperature.

shows that both [O_i] and [C_s] seem to reach a relative maximum after about ten minutes at 1050°C (comparable to the results of Kung [10] in the case of a 750°C + 1050°C–treatment). The agglomeration of oxygen and carbon again causes broad–band IR absorptions around 830 cm^{-1} and 1100 cm^{-1}, the latter being more symmetrical after 210 h at 750°C (and after 30 min at 1050°C as well) than observed with sample M–C. After annealing for 30 minutes at 1050°C the phonon transmission spectrum shows additional resonant scattering, which is in remarkable agreement with the results obtained for sample M–C under the same conditions: the resonance at the lower energy has the same position and width in both cases. Differences in the line shape around the $^{16}O_i$–resonance can be explained by the higher oxygen concentration in sample H–C (Fig. 1). Since the critical current of the Al–emitter was high enough to extend the upper phonon energy range to more than 5 meV, an additional weak phonon resonance with minimum at $\approx$ 5.7 meV was found (see the two traces at the bottom of Fig. 3). Since the fraction of monochromatic phonons contributing to the detector signal decreases with increased generator voltage and because of increased isotope scattering line depths at higher energies cannot directly be compared to lower–energy resonances. Fig. 3 shows that during the first 10 minutes there is no significant change in the phonon transmission spectrum as compared to the 210 h / 750°C annealing, apart from a rapid increase in the depth and width of the oxygen resonance. The defects which cause the observed phonon resonances evolve between 10 and 20 minutes at 1050°C, the absorption widths and depths being comparable to the M–C–sample after 20 minutes already.

The IR spectra exhibit a similar time dependence upon annealing time: after one minute annealing at 1050°C the absorption coefficients of the agglomerate–related bands are nearly unchanged, although the O_i and C_s–absorptions strongly increase (Fig. 1 and 3). Further annealing leads to a decrease of both the 830 cm^{-1} and the 1100 cm^{-1}–absorptions. The latter is reduced to a weak band with maximum at 1040 cm^{-1} after 10 min at 1050°C (the corresponding phonon transmision spectrum is nearly identical that of the measurement of the reference sample, Fig. 3, left side). With subsequent annealings the peak at 1040 cm^{-1} becomes broader, its maximum shifting to higher wave numbers.

Fig. 4 shows the effect of the same high–low–high thermal cycle on a Si–crystal with low carbon content ($< 5 \cdot 10^{15}$ cm^{-3}). In contrast to samples M–C and H–C no distinct resonant phonon

scattering is observed both after 750°C– and 1050°C annealing. The O_i–resonance is stronger reduced than the IR oxygen absorption, which to our experience is typical of carbon–lean samples. This could be accounted for by an enhanced inelastic phonon scattering, masking the O_i–phonon–resonance [2]. In agreement with [7] the IR spectra show the well–known double–peaked band [9] with relative maxima at $\approx$ 1120 cm^{-1} and 1225 cm^{-1}, which has already developped after the 750°C long–term anneal. (No 1225 cm^{-1}–absorption was observed in another sample of the same crystal that had not been subjected to the 1100°C–pre–treatment.)

Discussion

The most striking result of our PS measurements is the appearance of rather narrow–band phonon scattering in carbon–doped Si–crystals after 1050°C annealing with pre–treatment at 1100°C + 750°C. The observed positions and line widths of the two lower resonances, which seem to be constant after annealing for more than one hour, correspond to transverse phonon wavelengths of $\lambda_{transv}/2 \approx (3.9 \pm 0.5)$ nm and (2.7 ± 0.5) nm. From the correlation with the corresponding IR spectra we conclude that they are caused by the excitation of geometric eigenvibrations of nm–sized aggregates. A change of size should result in a shift of the geometric phonon resonance, which is observed in the case of the absorption below 3 meV with increasing annealing time, the steady–state value of 2.75 meV or $\lambda_{transv}/2 \approx 3.9$ nm corresponding to the typical thickness of plate–like precipitates as observed in TEM (e. g. [11]). On the other hand, the IR absorption at 1225 cm^{-1}, which is *not* observed in these carbon–doped samples, is often attributed to plate–like oxygen precipitates [12]. The phonon resonance at 5.7 meV could then be interpreted as the λ–resonance of the higher harmonic mode of the 2.9 meV–resonance (for half an hour annealing at 1050°C). The origin of the absorption at 4 meV may be attributed to clusters with a different size distribution or to a different vibration mode of the defects causing the lower–lying resonance, the latter interpretation being perhaps more compatible with the similarity of the line shapes.

Acknowledgement

Financial support of the Deutsche Forschungsgemeinschaft is gratefully acknowledged.

References

[1] C. Wurster, K. Laßmann, W. Eisenmenger, Phys. Rev. Lett. **70**, 3451 (1993)

[2] G. Schrag, M. Rebmann, C. Wurster, F. Zeller, K. Laßmann, W. Eisenmenger, to be submitted for publication in phys. stat. sol. (a)

[3] E. Dittrich, W. Scheitler, W. Eisenmenger, Jap. Appl. Phys. **26-3**, 873 (1987)

[4] C. Wurster, E. Dittrich, W. Scheitler, K. Laßmann, W. Eisenmenger, W. Zulehner, Physica B **219 & 220**, 763 (1996)

[5] F.M. Livingston, S. Messoloras, R.C. Newman, J. Phys. **C17**, 6253 (1984)

[6] B. Pajot, Analysis **5**, 293 (1977)

[7] Q. Sun, K. H. Yao, J. Lagowski, H. C. Gatos, J. Appl. Phys. **67**(9), 4313 (1990)

[8] A. R. Bean, R. C. Newman, J. Phys. Chem. Solids **32**, 1211 (1971)

[9] F. Shimura, J. Appl. Phys. **59**, 3251 (1986)

[10] C. Y. Kung, J. Appl. Phys. **65**(12), 4654 (1989)

[11] K. Wada, H. Nakanishi, H. Takaoka, N. Inoue, J. Cryst. Growth **57**, 535 (1982)

[12] S. M. Hu, J. Appl. Phys. **51**(11), 5945 (1980)

Materials Science Forum Vols. 258-263 (1997) pp. 405-410
© 1997 Trans Tech Publications, Switzerland

DETERMINATION OF STOICHIOMETRY AND OXYGEN CONTENT IN PLATELIKE AND OCTAHEDRAL OXYGEN PRECIPITATES IN SILICON WITH FT-IR SPECTROSCOPY

O. De Gryse*, P. Clauws*, J. Vanhellemont **,§ and C. Claeys**
***Department of Solid State Sciences , University of Gent, Krijgslaan 281-S1, 9000 Gent, Belgium**
****IMEC, Kapeldreef 75, B-3001 Leuven, Belgium**
§ Presently at Wacker Siltronic AG, P.O. Box 1140, D-84479 Burghausen, Germany

Keywords: silicon, oxygen, precipitation, infrared spectroscopy

Abstract

p- and n-type Si wafers with interstitial oxygen concentrations in the range of (9-11)x10^{17} cm^{-3} were subjected to different thermal treatments. FT-IR measurements were performed at 300K and 6K. The absorption spectra of octahedral and platelet precipitates can be reconstructed well by the theory of absorption of light by small particles. An empirical relationship is deduced to determine the concentration of oxygen in both types of precipitates, with an estimated accuracy of 15%. Analysis of the spectra leads to the conclusion of an oxygen density of 3x10^{22} cm^{-3} and identification of the precipitates as consisting of SiO, which can be modeled as a mixture of SiO_2 and a-Si.

I. Introduction

Oxygen is one of the dominant impurities in Czochralski grown crystalline silicon. Being highly supersaturated it will precipitate into platelet and octahedral precipitates, depending on the annealing conditions [1,2], thus affecting the mechanical and electrical properties of the substrate [3]. In spite of many investigations during the last decades, a lot of questions remain unanswered. The purpose of the present article is twofold. First an empirical relationship is deduced to obtain the concentration of precipitated oxygen from the IR-absorption spectrum. Second the stoichiometry and microstructure of SiO_x precipitates are analyzed. In the literature different values of x have been proposed: Borghesi *et al.* found $x \approx 1.8$ on the basis of FT-IR spectra [4], EELS-experiments concluded $x \approx 1.2$ [5] or $x \approx 0.95$ [6]. Vanhellemont [7] analyzed TEM results of different authors using the theory of diffusion limited precipitate growth which led to $x \approx 1$.

II. Experimental

The investigated Si specimens contained an initial interstitial oxygen concentration between 9 and 11 x10^{17} cm^{-3} and are divided into four groups of annealing schemes.
The first set of specimens (i) received a series of pretreatments followed by a high-temperature step at 1000° C for a duration ranging from 1 to 32 h (Fig. 1.a). The second group (ii) received a nucleation step (800° C in N_2 for 24h) followed by a high-temperature step (3h, 1100° C in wet oxygen) (Fig. 1.b). The third group (iii) received a very long treatment at 750° C in N_2 ambient for 265 h in order to produce a high density of stable oxide precipitate nuclei. This was followed by a treatment at 1050° C in Ar for 2h (Fig.1.c). The last group (iv) received different pretreatments, followed by a high temperature step in order to investigate the dependence of the oxygen precipitation on the initial $[O_i]$ and the pretreatment [8].
The oxygen content before the annealing treatments was determined by measuring the height of the absorption peak at 1107 cm^{-1} at 300K, using the IOC88 standard calibration conversion factor of

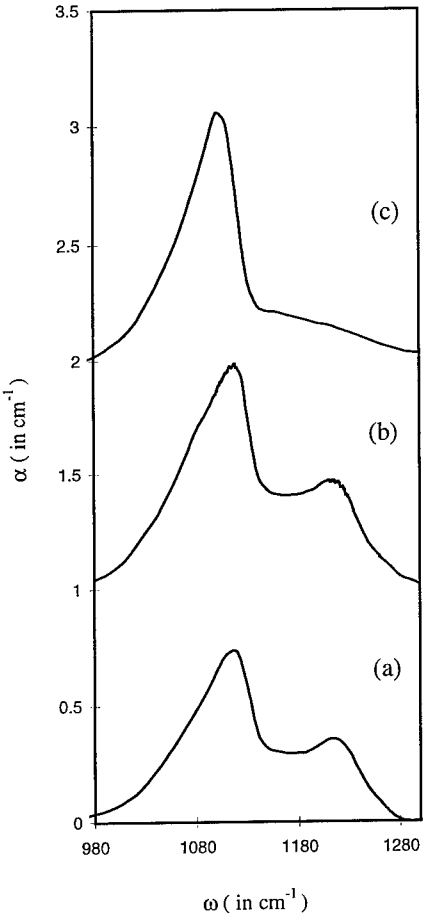


Figure 1 (top): Typical examples of absorption spectra: (a) group i (high temperature step for 32 h), (b) group ii (high temperature step for 3 h), (c) group iii (high temperature step for 2h). The spectra have been vertically shifted for clarity.

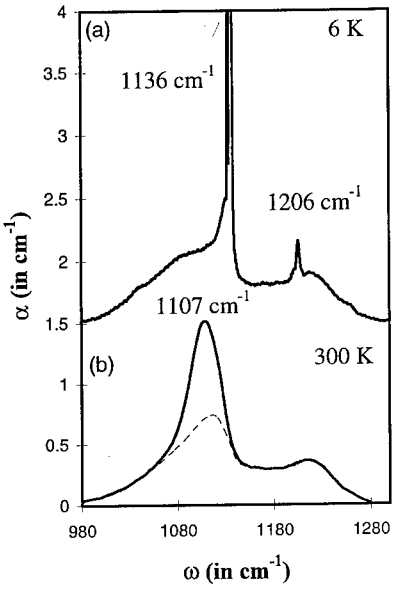


Figure 2: Typical example of group i: (a) spectrum at 6K ; (b) spectrum at 300K of precipitate bands + O_i absorption peak (solid line) and spectrum of isolated precipitates bands (dotted line). The spectra have been vertically shifted for clarity.

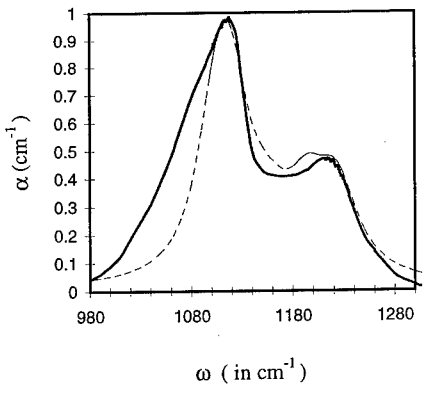


Figure 3 (right): Comparison between experimental spectrum (__) and simulation (--) of a specimen of group ii (see figure 1.b). $\omega_F \approx 1116$ cm^{-1} and $\omega_d \approx 1220$ cm^{-1}

3.14 x 10^{17} cm^{-2} [9]. The interstitial oxygen remaining after annealing was determined at 6K by measuring the height of the 1206 cm^{-1} peak, using the procedure outlined by Wagner [10] (fig. 2a). In this way the broad absorption peak at 300K belonging to the remaining interstitial oxygen could be removed by subtracting a scaled 1107 cm^{-1} absorption peak from the experimental spectrum, leaving the spectrum of precipitated oxygen only (Fig. 2b).

III. Simulation of the spectra

In this paragraph the theory of absorption of light by small particles will be briefly outlined and applied to the case of oxide precipitates in Si.

The absorption of spheroids in a nonabsorbing medium can be simulated well by the theory of absorption cross sections of small particles [11]. For low volume fractions it gives identical results as the effective medium approach [4,12,13].

Two conditions have to be fulfilled in order to use this theory: $2\pi.n.a/\lambda << 1$ (negligible retardation effects) and $2.\pi.\kappa.a/\lambda << 1$ (uniform electric field inside the spheroid), with n the refractive index and κ the extinction coefficient of the particle and a its characteristic size.

The absorption is determined by the polarizability (g) of the particle in the matrix. For oblate spheroids g becomes a diagonal tensor if the direction of the field vector coincides with the axes of the spheroid:

$$g_i = v.\frac{\epsilon_p - \epsilon_m}{\epsilon_m + L_i.(\epsilon_p - \epsilon_m)}, \qquad (1)$$

where ϵ_p and ϵ_m are the dielectric functions of the particle and the matrix, L_i the geometrical factor depending on the aspect ratio (the ratio of the small axis to the large axis) [11], with i = 1,2,3 indicating the axes of the spheroid (i = 3 for the small axis). The geometrical factors for oblate spheroids have the following properties : $L_1 = L_2 \leq L_3$, $L_1 + L_2 + L_3 = 1$; for a perfect disk $L_3 = 1$ and for a sphere $L_3 = 1/3$.

The platelet precipitates are known to lie in {100} planes [1,2]. Hence the direction of the axes of the spheroids will be rotated with respect to the direction of the incident field. In the case of non-polarized light incident on a host lattice with cubic symmetry the expression for the absorption cross section per unit of volume becomes:

$$C = \frac{k}{3}.\mathrm{Im}\{2.g_1 + g_3\}, \qquad (2)$$

with k the wavenumber in the surrounding medium.

The power absorption coefficient immediately follows : $\alpha = f.C$, with f the volume fraction.

The resonance frequency is given by the Fr $\bar{\text{h}}$lich frequency (ω_F) for a sphere and by the longitudinal optical frequency (ω_{LO}) for a perfect disk. For an oblate spheroid the resonance frequency will depend on the value of the eccentricity.

The aspect ratio was calculated [7,14,15] and checked against experimentally obtained values [15,16], resulting in a geometrical factor L_3 between 0.973 and 1.

We assumed that both kinds of precipitates have the same composition. This will be justified in section V. In order to simulate our experimental absorption spectra a dielectric function was needed yielding ω_F between 1110 and 1116 cm^{-1} and ω_{LO} around 1230 cm^{-1}. A set of dielectric functions for SiO_x from the literature were tested but only the dielectric function of Balz *et al.* [18] (given as a lorentzian oscillator model) meets all requirements. Unfortunately the stoichiometry was not given, but will be calculated in section V. A typical result of the simulation is shown in figure 3. The simulation gives a excellent overall fit, except in the low frequency region. Borghesi *et al.* [4] explained a similar effect as due to the coexistence of precipitates with different stoichiometry. However, it seems more reasonable to point the origin of this discrepancy to the use of an oscillator model, instead of the true dispersion of ϵ.

IV. Determination of the oxygen content in oxide precipitates

An empirical relationship to determine the concentration of precipitated oxygen will be deduced from the values of the interstitial oxygen disappeared during the treatments ($\Delta[O_i]$) and the absorption cross sections for spheres and spheroids.
The volume fraction of disks (d) and spheres (s) in the silicon matrix , is given by:

$$f_d = \left[C_S(\omega_F).\alpha(\omega_d) - C_S(\omega_d).\alpha(\omega_F)\right]/A$$

$$f_S = \left[C_d(\omega_d).\alpha(\omega_F) - C_d(\omega_F).\alpha(\omega_d)\right]/A,$$

$$A = C_d(\omega_d).C_S(\omega_F) - C_d(\omega_F).C_S(\omega_d), \qquad (3)$$

ω_F = 1110 cm^{-1} and ω_d = 1225 cm^{-1} the resonance frequencies for a sphere and an oblate spheroid with geometrical constant L_3 = 0.99, $\alpha(\omega)$ the total absorption coefficient and $C_i(\omega)$ the absorption cross sections per unit of volume with ϵ_m = 11.7 (SI-matrix) and ϵ_p from Balz *et al.* [18].
This leads in a quite straightforward way to a relationship allowing to determine the oxygen content in both types of precipitates.
The absorption peak due to octahedral precipitates can be converted into that of an equivalent disk by multiplying the absorption coefficient with $C_d(\omega_d)/C_S(\omega_F)$. This results in a set of couples for the platelet precipitates:

$$\left([O]_d^{\,eff}, \alpha^{eff}\right) = \left(\Delta[O_i].f_d/f_{tot},\ \alpha(\omega_d) - f_S.C_S(\omega_d)\right) \qquad (4)$$

and for octahedral precipitates :

$$\left([O]_S^{\,eff}, \alpha^{eff}\right) = \left(\Delta[O_i].f_S/f_{tot}\ ,\ \left[\alpha(\omega_F) - f_d.C_d(\omega_F)\right].C_d(\omega_d)/C_S(\omega_F)\right), \qquad (5)$$

with $f_{tot} = f_S + f_d$. The results are given in figure 4 along with the regression line which has a R^2 = 0.95. Substituting the formulas and the respective values in the equation of the regression line leads to:

$$[O]_d = 1.72.\alpha(\omega_d) - 0.18.\alpha(\omega_F), \qquad (6)$$

for the oxygen concentration in platelet precipitates and to:

$$[O]_S = 9.11.\alpha(\omega_F) - 1.40.\alpha(\omega_d), \qquad (7)$$

for the oxygen concentration in octahedral precipitates. In these equations α is given in cm^{-1} and [O] in units 10^{17} cm^{-3}.
The estimated accuracy is around 15%.

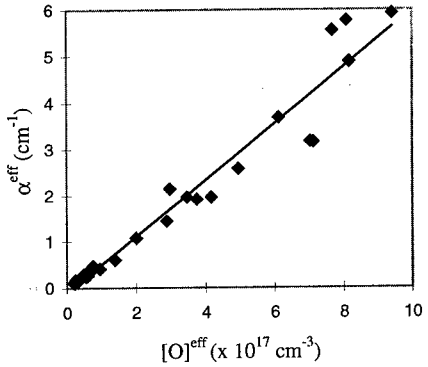


Figure 4 : Effective oxygen concentration versus effective absorption. The solid line represents: $\alpha^{eff} = 0.59 \times 10^{-17}.[O]^{eff}$

V. Determination of stoichiometry and microscopic structure of the precipitates

As already mentioned before $\omega_F \approx 1110$ cm^{-1} and $\omega_{LO} \approx 1230$ cm^{-1} in the present experimental spectra. A lot of literature has been devoted to SiO_x with $x \leq 2$. Basically two models exist to describe its microscopic structure. The first and a widely accepted model is the random bonding model (RBM) [19-23]. In the RBM SiO_x is composed of five different tetrahedra Si-(Si_{4-y} O_y) (y = 0,1,2,3,4) occurring with a probability determined by the stoichiometry. In this model SiO_x consists of one phase. In the microscopic mixture model (MMM) on the other hand SiO_x consists of two phases : amorphous silicon and amorphous SiO_2. Although in general this last model is not accepted, it is also recognized that SiO_x , which can be described by the RBM, is a metastable phase. During annealing and even at room temperature (after a period of years), SiO_x can decompose into a-Si and a-SiO_2 [23-25].

Two-phased SiO_x and one-phased SiO_x have distinct optical properties. The latter has an anti-symmetric vibration mode ω_{TO} which decreases linearly with decreasing x [20,21,22,26] while ω_{LO} - ω_{TO} increases with decreasing x [20]. On the other hand two-phased SiO_x has an ω_{TO} which increases with decreasing x, while ω_{LO} - ω_{TO} decreases with decreasing x [13,21]. In the present samples the following applies :

$$\omega_F(SiO_2) = 1100 < \omega_F(\text{exp}) \text{ and } \omega_{LO}(\text{exp.}) - \omega_F(\text{exp.}) < \omega_{LO}(SiO_2) - \omega_F(SiO_2),$$

where "exp." denotes experimentally determined values. This implies that the oxide precipitates from an optical point of view behave as an effective medium consisting of two phases which may be described by the MMM. Using the effective medium approach of Bruggeman [27] and the dielectric function of thermal SiO_2 [28] we obtain for SiO_x with $x \approx 0.95$: $\omega_{TO} = 1076$ cm^{-1}, $\omega_F = 1110$ cm^{-1} and $\omega_{LO} \approx 1233$ cm^{-1}. A similar value can be obtained by the following approach.

In SiO_2 there is an anti-symmetric mode (at 1075 cm^{-1}) in which the neighboring oxygen atoms move in phase (AS1) and an anti-symmetric mode (at 1190 cm^{-1}) in which the neighboring oxygen atoms move out of phase (AS2), while in both modes the neighboring Si-atoms are almost at rest [29]. The sum of the integrated mode strengths is proportional to the oxygen density [29]. Since SiO_x in this case behaves optically as consisting of two phases the integrated strength of the oscillator will be proportional to the density of oxygen oscillators as in the case of SiO_2. The strength is given by [29]:

$$\langle F_{AS1} \rangle + \langle F_{AS2} \rangle = \frac{1}{2.\pi^2} . \int_0^\infty \omega . [\epsilon''_{AS1}(\omega) + \epsilon''_{AS2}(\omega)] . d\omega \qquad (8)$$

For SiO_2 the following holds: $\langle F_{AS1} \rangle + \langle F_{AS2} \rangle \approx 52000$ and $[O]_{SiO2} \approx 4.6 \times 10^{22}$ cm^{-3}

Using the dielectric function of [18] we obtain : $\langle F_{AS1} \rangle + \langle F_{AS2} \rangle \approx 34000$, which results in $[O]_{SiOx} \approx 3.0 \times 10^{22}$ cm^{-3}. This value is close to the one found by Vanhellemont [7], based on the theory of diffusion limited precipitate growth and experimental values obtained by TEM.

Assuming the material consists of two phases x is given by :

$$x = \frac{2.[O]_{SiOx} . V_{Si}}{2 + [O]_{SiOx} . (V_{Si} - V_{SiO2})} \qquad (9)$$

with $[Si]_{Si} = 5 \times 10^{22}$ cm^{-3} ; $[Si]_{SiO2} = 2.25 \times 10^{22}$ cm^{-3} ; $V_{SiO2} = 4.5 \times 10^{-23}$ cm^3 ; $V_{Si} = 2.25 \times 10^{-23}$ cm^3 ; Substituting the values in (9) results in a value of $x \approx 1.0$.

This value is close to the ones already mentioned in the introduction [5-7], except for the value obtained by FT-IR [4]. The discrepancy with the value of $x \approx 1.8$ may be explained from the choice of dielectric function. The latter authors used an oscillator model for the dielectric function from $SiO_{1.8}$ consisting of one-phase (RBM). With a similar function [21] it is impossible to simulate the octahedral precipitates.

VI. Conclusion

Using a wide range of experimental IR-spectra an empirical relationship was deduced to obtain the concentration of oxygen precipitated into platelet and octahedral precipitates. From the positions of the resonance frequencies of the octahedral and platelet precipitates we can conclude that the precipitates consist of SiO_x with $x \approx 1$ which can be optically simulated by the MMM assuming a mixture of a-Si and a-SiO_2,.

Acknowledgements

This work was performed with financial support from the National Science Foundation (FWO).

References

1 W.A. Tiller, S. Hahn, F. A. Ponce, J. Appl. Phys. **59** (9), pp. 3255 (1986)
2 H. Bender, Phys. Stat.Sol. A **86**, pp. 245 (1984)
3 J. Vanhellemont, E. Simoen, G. Bosman, C. Claeys, A. Kaniava, E. Gaubas, A. Blondeel and P. Clauws, The Electrochem. Soc. Proc. Vol. **94-10**, pp. 670 (1994)
4 A. Borghesi, A. Piaggi, A. Sassella, A. Stella, B. Pivac, Phys. Rev. B **46**, pp. 4123 (1992)
5 R.W. Carpenter, I. Chan, H.L. Tsai, C. Varker and L.J. Demer, *Defects in semiconductors II*, ed. S. Mahajan and J.W. Corbett (North Holland, Amsterdam, 1983), p. 195
6 H.M. Skiff, H.L. Tsai and R.W. Carpenter, *Oxygen, Carbon, Hydrogen and Nitrogen in Crystalline Silicon*, ed. J.C. Mikkelsen, Jr., S.J. Pearton, J.W. Corbett and S.J. Pennycook (Materials Research Society, Princeton, NY, 1986) pp. 241
7 J. Vanhellemont, J. Appl. Phys. **78** (6), pp. 4297 (1995)
8 J. Vanhellemont, M. Libezny, E. Simoen, C. Claeys, P. Clauws and A. Blondeel, Proc. ICPS-22, Vancouver 1994, (World Scientific Singapore, 1995), pp. 2399
9 A. Baghdadi, W. Bullis, M. Croarkin, Y-Z Li, R. Scace, R. Series, P. Stallhofer, M. Watanabe, J. Electrochem. Soc. **136**, pp. 2015 (1989)
10 P. Wagner, Appl. Phys. A **53**, pp. 20 (1991)
11 C.F. Bohren, D.R. Huffman, *Absorption and Scattering of light by small particles*, John Wiley & Sons (1983)
12 S.M. Hu, J. Appl. Phys. **51** (11), pp. 5945 (1980)
13 L. Genzel, T.P. Martin, Surface Science **34**, pp. 33 (1973)
14 F.S. Ham, J. Phys. Chem. Solids **6**, pp. 335 (1958)
15 S.M. Hu, Appl. Phys. Lett. **48** (2), pp.115 (1986)
16 K. Sueoka, N. Ikeda, T. Yamamoto and S. Kobayashi, J. Appl. Phys. **74** (9) , pp. 5437 (1993)
17 K. Sueoka, N. Ikeda, T. Yamamoto and S. Kobayashi, J. Electrochem. Soc. **141** (12), pp. 3588 (1994)
18 T. Balz, R. Brendel, R. Hezel, J. Appl. Phys. **76** (8), pp. 4811 (1994)
19 H.R. Philipp, J. Phys. Chem. Solids **32**, pp 1935 (1971)
20 A. Lehmann, L. Schumann, H. Sobotta, V. Riede, U. Teschner and K. Hubner, Phys. Stat. Sol. B **111**, K103 (1982)
21 A. Lehmann, L. Schumann and K. Hubner, Phys. Stat. Sol B **121**, pp 505 (1984)
22 A.L. Shabalov and M. S. Feldman, Thin Solid Films **151**, pp. 317 (1987)
23 M. Nakamura, Y. Mochizuki , K. Usami, Y. Itoh and T. Nozaki, Solid. State Comm. **50** (12), pp. 1079 (1984)
24 K. Hubner, A.V. Shendrik and A.M. Praulinsh, Phys. Stat. Sol. B **118**, pp. 239 (1983)
25 J. Finster, D. Schulze and A. Meisel, Surface Science **162**, pp. 671 (1985)
26 P.G. Pai, S.S. Chao, Y. Takagi and G. Lucovski, J. Vac. Sci. Technol. A4 (3), pp. 689 (1986)
27 Ph. J. Roussel, J. Vanhellemont and H.E. Maes, Thin Solid Films **234**, pp. 423 (1993)
28 P. Grosse, B. Harbeke, B. Heinz, R. Meyer and M. Offenberg, Appl. Phys. A **39**, pp. 257 (1986)
29 C.T. Kirk, Phys. Rev. B **38** (2), pp. 1255 (1988)

Materials Science Forum Vols. 258-263 (1997) pp. 411-416
© 1997 Trans Tech Publications, Switzerland

INFLUENCE OF THE Li CONCENTRATION ON THE PHOTOLUMINESCENCE SPECTRA OF NEUTRON-IRRADIATED SILICON: PASSIVATION OF RADIATION INDUCED CENTERS.

F. Rodriguez[1], G. Davies and E.C. Lightowlers
Physics Department. King's College London, Strand, London WC2R 2LS, UK.
[1]On Sabbatical leave from the University of Cantabria (Spain)

Keywords: Radiation defects; Silicon; Passivation; Lithium

Abstract. The formation of radiation-induced centers in irradiated Li-doped Si and the passivation of different defects are investigated through photoluminescence. It is shown that centers C and D1+D2 are efficiently passivated by Li. Besides the well known four Li associated vacancy, a new Li complex involving at least four Li atoms has been identified in Si doped with high concentrations of Li.

Introduction

Lithium-related defects in silicon have received considerable attention due to the ability of Li to passivate defects and deep level impurities [1, 2]. Furthermore its high diffusivity, even at room temperature, makes it an efficient impurity for use in silicon devices [3]. This aspect has been exploited, for example, in solar cell applications where the incorporation of Li into Si increased the radiation tolerance [3]. In this work we investigate the formation of centers produced by neutron irradiation in Li-doped silicon as a function of the Li concentration and the annealing temperature by means of photoluminescence (PL). The use of this technique allows us to get evidence of the passivation processes of centers through variations in the intensities of the zero phonon lines (ZPLs) associated with the emission of bound excitons. In this paper we present new findings related to the passivation of very active centers for exciton trapping as well as evidence of the formation of new centers which dominate the low temperature PL spectrum. Isotope analysis reveals the existence of clusters involving several Li atoms in FZ n-type Si. Another center, observed in CZ p-type Si at 1096.9 meV, is identified as a major feature in the PL spectrum; it is not related to Li but shows an appreciable oxygen isotope shift.

Experimental

Three series of Li-doped silicon crystals have been employed throughout this work. The starting materials were Czochralski (CZ) 30 Ωcm p-type carbon-lean Si, Float zone (FZ) 60 Ωcm n-type oxygen-lean Si with [C] = 1.6×10^{17} cm^{-3} and FZ 1000 Ωcm oxygen- and carbon-lean Si. The three crystal series were doped with lithium by the diffusion technique. Lithium was diffused in for 30 minutes at drive-in temperatures between 300 and 550 °C. After removing the excess of Li from surface, samples were annealed for 2 hours at 600 °C in order to homogenise the Li distribution within the crystal. The Li concentration was estimated by the increase of the room temperature resistivity according to proper calibrated resistivity curves. Lithium concentrations ranging from 10^{14} to 10^{17} cm^{-3} were obtained by this procedure, the upper concentration corresponding to the limit for Li precipitation. The isotope structure was investigated using the same Li-doped Si crystals with different ^{6}Li:^{7}Li ratios as employed in a previous study [4]. The crystals were neutron irradiated with a dose of 1×10^{17} cm^{-2}. An isochronal annealing of 30 minutes was carried out in the three crystal series, between 100 and 600 °C. Photoluminescence spectra were obtained using a Nicolet 60XS and a Bomem DA3 Fourier Transform spectrometers fitted with North Coast Ge diode detectors. Most of the experiments were done with samples immersed in liquid helium at 4.2 K, and with excitation by a 514 nm Argon laser. Special care was paid for obtaining the photoluminescence spectra under the same experimental conditions for intensity analysis.

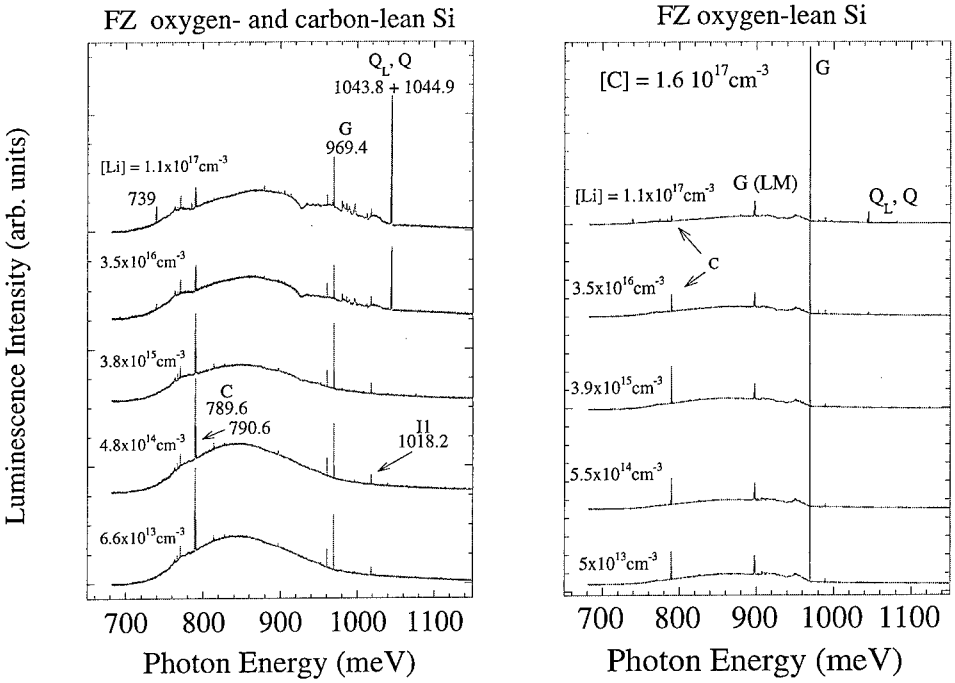


Figure 1. PL spectra at 4.2 K corresponding to the Li-doped series of FZ carbon- and oxygen-lean Si (left) and FZ oxygen-lean Si with [C] = $1.6x10^{17}$ cm^{-3} (right), neutron irradiated with a dose of $1x10^{17}$ cm^{-2} (non-annealed crystals).

Results and discussion

Radiation induced centers at room temperature

Figure 1 shows the photoluminescence spectra corresponding to the neutron irradiated FZ carbon-lean and carbon-rich Li doped Si, respectively. For [Li] < 10^{16} cm^{-3}, the spectra are dominated by ZPLs of centers C (789.6 meV) and G (969.4 meV) which correspond, respectively, to centers involving carbon and oxygen interstitials [5] and, two substitutional C and one Si interstitial [6]. For FZ carbon-enriched Si (right side spectrum of Fig. 1) the G line intensity is much higher than the C intensity, while the opposite occurs for the PL spectrum (not shown here) of CZ carbon-lean Si. In FZ carbon- and oxygen-lean Si (left side of Fig. 1) these lines exhibit similar intensities. Lines at 790.6, 960.7 and 1018.2 meV show appreciable intensity in this crystal. Although the structures of the centers responsible for these three lines are not known, the first line is observed upon neutron irradiation and is thought [7] to be associated with heavily damaged regions of the crystal. The 1018.2 meV line named I1 is the dominant feature in the PL spectra of irradiated FZ Si after annealing in the 150-350 °C range. Recent studies associate the defect responsible for this PL with the neutral divacancy [8].

As illustrated in Fig.1, the main influence of doping with Li is to reduce the C-line intensity for [Li] >10^{16} cm^{-3}, for this radiation dose, while for [Li] <10^{16} cm^{-3} the intensity is almost independent of the Li concentration. A similar behaviour is observed for the FZ carbon-enriched Si in Fig.1 but in this case the C-line intensity reduces by an order of magnitude. Such a reduction can be compared with the intensity of either the ZPL of the G center or the associated local mode (LM) component. The passivation process clearly observed in C is not so evident as for the G center whose corresponding ZPL slightly varies with Li (Fig.1) and is much less affected in the FZ carbon-rich Si of Fig. 1.

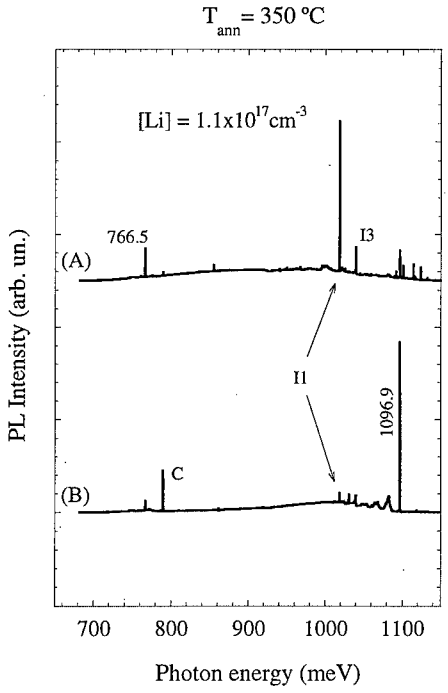


Figure 2. PL spectra at 4.2 K from carbon lean (A) FZ and (B) CZ Si, neutron irradiated and annealed at 350 °C for 30 minutes.

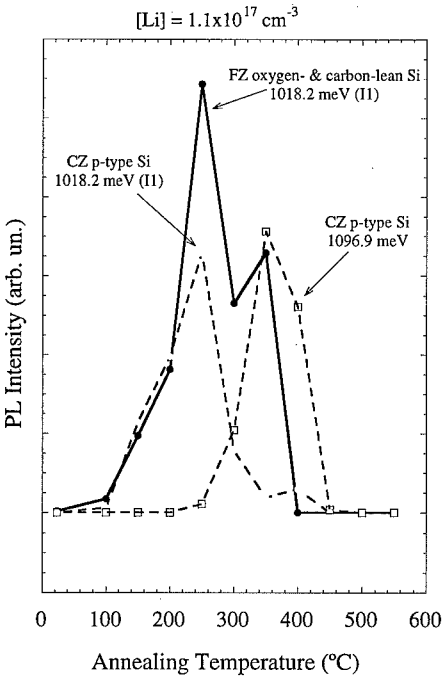


Figure 3. Variation of the ZPL intensity of I1 (1018.2 meV) and the new line at 1096.9 meV as a function of the annealing temperature.

In contrast to the passivation process directly revealed through the decrease of the C line intensity with Li, the presence of new lines at 739 meV and specially at 1043.8-1044.9 meV (Q and Q_L doublet) reflects the formation of Li-related centers for [Li] $>10^{16}$ cm^{-3}. In particular the presence of such a Q_L, Q doublet (L denotes low temperature component) is worthwhile since the defect corresponds to the four Li associated vacancy, Li_4-V (passivated vacancy). Interestingly, the intensity of the G and Q lines are time dependent upon annealing at room temperature. This effect has been evidenced by the decrease of the G line but mainly by the enhancement of the Q line observed over four weeks, reflecting the high diffusivity of Li at room temperature.

Isochronal annealing

Thermal treatments of annealing above 100 °C lead to important changes in the PL spectra of the three investigated series. Many new centers associated with different impurities are formed and later destroyed upon isochronal annealing at different temperatures. Although many of these PL lines have already been reported [2, 7, 10-13], several new lines associated with Li observed in this work for the first time. There is no space here to discuss all these lines.

Upon annealing at T_{ann} < 250 °C, the dominant G line progressively weakens [9] with T_{ann} while the I1 (1018.2 meV) grows to dominate the PL spectra from all samples of the three series. Annealing above 250 °C produces the I3 line (1039.7 meV) but the PL is still dominated by the I1 line up to 400 °C in the FZ crystals [9]. An exception to this behaviour is observed in CZ Si where the major contribution to the PL spectrum in the 300-400 °C annealing range is due to a new line at 1096.9 meV (Fig. 2). A line at 1096.2 meV was previously observed in Si irradiated with H^+ and H_2^+ ions [13], but its dominant presence in CZ crystals such as it appears in Fig. 2 had not been reported before [7, 14]. A detailed study of this line will be published in future, but it is worth pointing out hare that the associated center has monoclinic I symmetry and involves oxygen; these results have been deduced

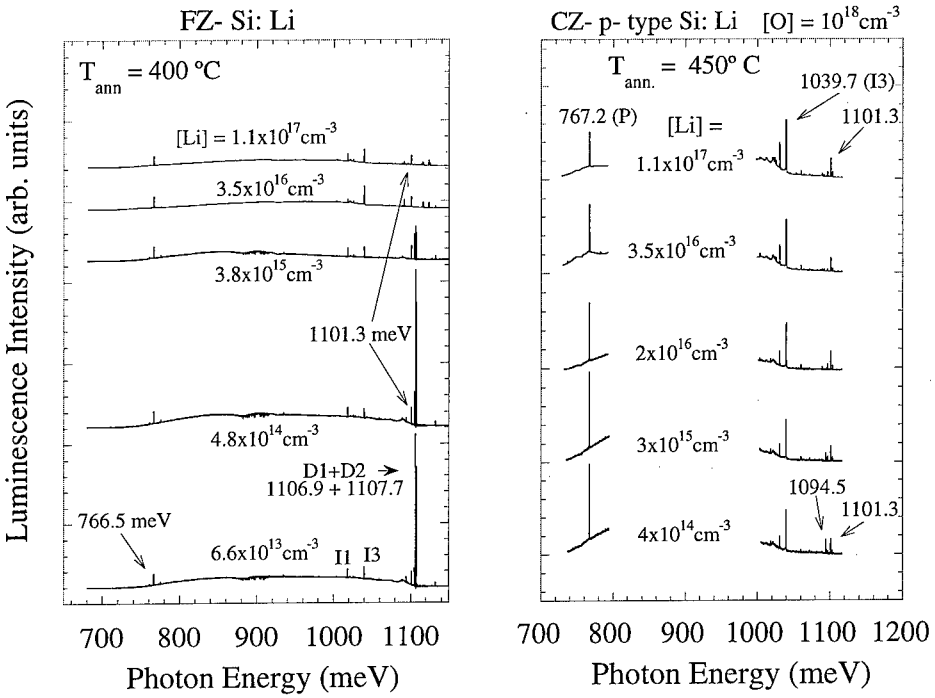


Figure 4. PL spectra at 4.2 K corresponding to the Li-doped series of FZ carbon- and oxygen-lean Si (left) and CZ p-type carbon-lean Si (right), neutron irradiated and annealed for 30 minutes at 400 and 450 °C, respectively.

from uniaxial stress experiments and from the observed isotope shift,
$E_{ZPL}(^{18}O) - E_{ZPL}(^{16}O) = + 0.037$ meV.
Figure 3 shows the variation in intensity of this line and of the I1 line in CZ- and FZ-crystals as a function of the annealing temperature. The observed variation suggests that the formation of this new line correlates with the decrease of I1, thus indicating that the new center may be formed by complexing the trigonal I1 center [15] with one (or more) interstitial oxygen. This idea supports the I1 center model as an intrinsic small cluster like the <111> split interstitial [16, 17], or the neutral divacancy [8] rather than the five vacancy model proposed in [18]. The PL spectra of Fig. 4 indicate that ZPL of centers I1, I3, 1096.9 meV does not show a strong Li-dependence. Since these centers are not directly passivated by Li (Fig. 4), they can be used as probes for quantitative estimates in PL techniques.
The most salient feature related to the passivation of centers is observed in FZ- Si between 300 and 500 °C. Fig. 4 shows the corresponding PL spectra for different Li concentrations. At these annealing temperatures the PL spectra are fully dominated by the D1+D2 (1106.9 and 1107.7 meV) lines. Although the defect responsible for these lines remains unknown and no isotope splitting has been reported [2], it is an isoelectronic center of trigonal symmetry [19]. As can be seen in Fig. 4 the center is very efficiently passivated by Li even for concentrations of about 10^{15} Li cm^{-3}, an order of magnitude lower than the concentration required to passivate the C center in the same crystal series. This result stresses the effectiveness of Li for neutralising highly efficient exciton trapping centers such as D1+D2. The right hand side of Fig. 4 shows another example of defect passivation, at the 1094.5 meV line, in CZ Si. Interestingly, there are several important centers formed in irradiated Si such as P (767.1 meV) or T (935.1 meV) which are not passivated by Li under the present experimental conditions even though the proposed structures of the centers includes unsaturated dangling bonds [14, 20-23].

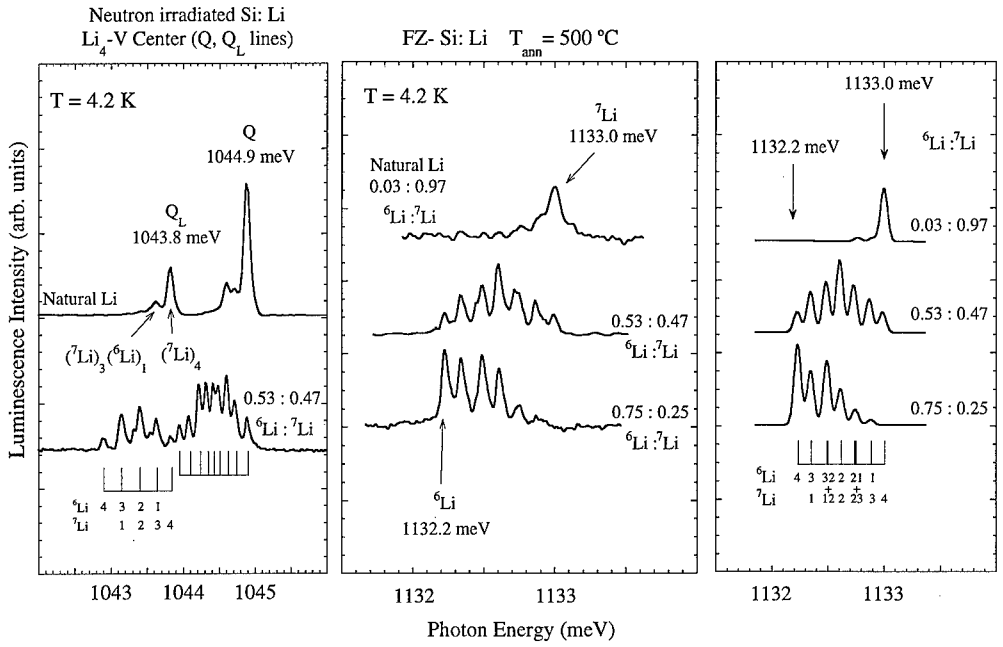


Figure 5. Isotope structure of the ZPL of the Q, Q_L center (left) and the new Li-related center at 1133.0 meV (middle) obtained from irradiated FZ Si with [Li] = $5x10^{17}$ cm^{-3}. The PL spectrum on the middle was obtained from annealing at 500 °C for 30 minutes. Resolution: 0.025 meV. The right hand side figure depicts the calculated isotope structure of the 1133 meV line on the basis of a four-atom Li defect consisting of two Li pairs with two inequivalent sites (D_{2h} symmetry). The spectra were simulated using Pearson profiles with the same width (0.075 meV) for all lines, and the intensity of each component calculated according to the model with the indicated isotope ratio.

Formation of Li centers: Isotope analysis.

There are many Li-associated lines in the PL spectra of either neutron- or electron- irradiated Si doped with [Li] > 10^{17} cm^{-3} after annealing. A survey of these lines can be found elsewhere [2, 7]. A well characterised center created in highly Li-doped Si after irradiation at room temperature is the four-atom Li associated vacancy, Li_4-V [4]. The corresponding ZPL dominates the low temperature PL spectrum (Fig. 1). The isotope splitting displayed by the ZPL in samples doped with different ^6Li to ^7Li ratios (Fig. 5) reveals the nearly tetrahedral symmetry of the four-atom Li center. The isotope splitting, $\Delta E_{iso} = E_{ZPL}(^7Li) - E_{ZPL}(^6Li) = 1043.8 - 1042.9 = +0.9$ meV is significantly higher than those measured for other Li-associated centers with ΔE_{iso} = 0.1 - 0.3 meV [7], suggesting that the defect involves several Li atoms. Upon annealing between 400 and 500 °C a new line at 1133.0 meV has been identified in the PL spectrum of the irradiated highly Li doped ($5x10^{17}$ cm^{-3}) FZ Si crystals. Its ZPL energy is close to that of the Li bound-exciton with emission of TA mode (1132.5 meV), but this Li+TA emission is observed in the PL spectrum at higher annealing temperatures or in non-radiated crystals. The isotope structure of the ZPL is shown in Fig. 5 for three ^6Li:^7Li ratios. The number of non-thermalised ZPLs observed in the PL spectrum (seven) together with the value of the isotope splitting between extreme lines, $\Delta E_{iso} = E_{ZPL}(^7Li) - E_{ZPL}(^6Li) = +0.8$ meV strongly suggest that the associated defect is a cluster of several Li atoms. Although the presence of seven equally spaced lines in the 0.53(^6Li):0.47(^7Li) spectrum suggests a six-atom Li defect as responsible for the 1133 meV line, the comparison between the observed intensity of each ZPL along the series and the calculated intensities for this center rules out this possibility. However other centers involving, for example, four

Li at non-equivalent sites may explain adequately both the ZPL splitting and the observed intensities along the series. For illustrative purposes, the right hand side of Fig. 5 shows the calculated spectra on the basis of a four-atom Li defect with two inequivalent sites. Although the simulation suggests that the proposed center is likely responsible for the ZPL structure, this must be only considered as a tentative model which is able to explain the experimental ZPL intensities. Further work using uniaxial stress data is required to confirm the center structure.

Acknowledgements
Thanks are due to Dr A. Safonov for fruitful discussions. One of us (FR) is indebted to the DGICYT (Grant Ref. PR95-282) for financial support. FR also thanks the Solid State Group at King's College for the hospitality and friendship extended to him during his Sabbatical. This work was financed by the Engineering and Physical Science Research Council (UK).

References

1. E. Ö. Sveinbjörnsson, S. Kristjansson and H.P. Gislason, J. Appl. Phys. **77**, 3146 (1995)
2. L.T. Canham, PhD Thesis, University of London (1983)
3. J.J. Wisocky, P. Rappaport, E. Davison, R. Hand, J.J. Lofersky, Appl. Phys. Lett. 9,44 (1966)
4. E.C. Lightowlers, L.T. Canham, G. Davies, M.L.W. Thewalt and S.P. Watkins, Phys. Rev. B. 29, 4517 (1984)
5. K. Winner and R.A. Street, J. Appl. Phys. 65, 2272 (1989)
6. P.McL. Colley and E.C. Lightowlers, Semicond. Sci. Technol. 2, 157 (1987)
7. G. Davies, Phys. Rep. **176**, 83 (1989) and references therein
8. S.K. Estreicher, J. Weber, A. Derecskei-Kovacs and D.S. Marynick, Phys. Rev. B. 55, 5037 (1997)
9. G. Davies, T.K. Kwok and T. Reade, Phys. Rev. B. 44, 12146 (1991)
10. T.K. Kwok, J. Lumin. 65, 327 (1995)
11. A.V. Mudryi, A.V. Yukhnevitch, Sov. Phys. Semic. 7, 117 (1973)
12. N.S. Minaev and A.V. Muddryi, Phys. Stat. Sol. (a) 68, 561 (1981)
13. V.I. Obodnikov, L.N. Safronov, L.S. Smirnov, Sov. Phys. Semicond. 10, 815 (1976)
14. E.C. Lightowlers and G. Davies, Proc. NATO Conference on Early stages of oxygen precipitation in Silicon, Exeter (1996) Pg. 303
15. G. Davies, E.C. Lightowlers and Z.E. Ciechanowska, J. Phys. C 20, 191 (1987)
16. J.W. Corbett, J.C. Bourgoin and C. Weigel, IOP Conf. Ser. 16, 1 (1973)
17. N.S. Minaev, A.V. Muddryi and V.D. Tkachev, Phys. Stat. Sol. (b) 108, k89 (1981)
18. V.D. Tkachev and A.V. Mudryi, IOP Conf. Ser. No 31, 231 (1977)
19. R. Sauer and J. Weber , Proc. ICDS 12, Amsterdam (1982)
20. W. Kurner, R. Sauer, A. Dornen and K. Thonke, Phys. Rev. B 39, 13327 (1989)
21. A.N. Safonov, E.C. Lightowlers, G. Davies, P. Leary, R. Jones and S. Öberg, Phys. Rev. Lett. **77**, 4812 (1996)
22. J. Wagner, A. Dornen and R. Sauer, Phys. Rev. B 31, 5561 (1985)
23. G. Davies, E.C. Lightowlers, R.A. Wooley, R.C. Newman and A.S. Oates, J. Phys. C 17, L499 (1984)

Materials Science Forum Vols. 258-263 (1997) pp. 417-422
© 1997 Trans Tech Publications, Switzerland

ELECTRIC-DIPOLE SPIN RESONANCE OF BE-DOPED SILICON

H. Schroth[1], K. Laßmann[1], Chr. Borgmann[2], and H. Bracht[2,3]
[1]Universität Stuttgart, 1. Physikalisches Institut,
Pfaffenwaldring 57, D-70550 Stuttgart, Germany
[2]Universität Münster, Institut für Metallforschung,
Wilhelm-Klemm-Straße 10, D-48149 Münster, Germany
[3]Lawrence Berkeley National Laboratory,
One Cyclotron Road, MS 2-200, Berkeley, CA 94720, USA

Keywords: Si:Be, double acceptor, hydrogen, deuterium, electric-dipole spin resonance

Abstract. Electric-dipole spin resonance (EDSR) spectra of silicon doped with beryllium by diffusion at temperatures between 945°C and 1180°C are presented. We find four spectra labelled Be-a to Be-d with trigonal symmetry. The IR spectra of these samples show the well known acceptor effective mass line series of substitutional beryllium (Be_s), beryllium-beryllium pairs (Be_2), beryllium-hydrogen pairs (BeH) and, in a sample heated in deuterium atmosphere, beryllium-deuterium pairs (BeD). It is proposed that Be-a and Be-b originate in BeH and BeD, respectively, while Be-c and Be-d may be spectra of Be paired with contaminants. By illumination of the samples a number of broad absorption lines appear in EDSR, reminiscent of the single acceptor spectrum of indium. However, a Hamiltonian similar to that used for effective mass acceptors does not well describe the angular dependence of all the lines. From the doping conditions it is not yet clear whether these absorptions are connected with the single hole state of Be_s^-.

Introduction

Silicon doped with beryllium has been extensively studied by optical methods. An acceptor centre with ionization energy of E_v + 191.9 meV was found by infrared absorption [1] and assigned to isolated substitutional beryllium by quenching and annealing studies [2]. This was confirmed by applying uniaxial stress, under which the lines split according to tetrahedral symmetry [3]. A slightly shifted line series indicates a ground state splitting of 0.51 meV and is explained by hole-hole interaction at the neutral double acceptor. Accordingly, by DLTS two levels are found at E_v + 190 meV and E_v + 440 meV [4]. Another acceptor centre with ionization energy of E_v + 145.8 meV is found in slowly cooled samples and identified as trigonal Be-Be pair [1, 2, 3]. Pairing of Be with hydrogen and deuterium has been studied with IR and FIR absorption [5, 6, 7]. The acceptor level of BeH at about E_v + 91 meV increases by nearly 1 meV by substituting H through D. In these pairs the H (or D) atom is believed to tunnel between equivalent positions in the vicinity of a substitutional Be atom. Peale et al. [7] inferred from the line shift under uniaxial stress that these positions are along the [111] directions, while theoretical work on this subject [8, 9, 10, 11] favours [100] energy minima.

Here we report on EDSR investigations of Be-doped Si intended to obtain alternative information on the structure and symmetry of the electronic states of Be-related defects. This variant of EPR has been previously used to investigate silicon doped with single acceptors [12] and the double acceptor Zn [13]. The single acceptors of group III could be understood by an effective mass Γ_8 ground state with quadratic contribution to the Zeeman splitting increasing with the depth of the acceptor. In contrast, no resonance could be attributed to Zn^- which may be regarded as an extreme case of a deep one-hole state (E_v + 600 meV). It might be instructive, therefore, to look for EDSR spectra related to Be^-, with E_v + 440 meV an intermediate case.

Experimental

For electric-dipole spin resonance (EDSR) a superconducting magnet cryogenic system with split pair magnets allowing static magnetic fields up to 7 T was used. The samples were placed at the centre of flat TM_{030} cavities, where the microwave electric field is at its maximum and the microwave magnetic field negligible. We used three cavities of different sizes for frequencies around 24, 34, and 60 GHz. Measurements were carried out between 1.8 K and 10 K. Additionally, IR absorption spectra were obtained at about 25 K using a Bio-Rad Fourier-transform infrared spectrometer equipped with a cold finger cryostat. Resolution was 2 cm^{-1}.

Sample Preparation and Characterization

The starting material for the samples was float-zone silicon, phosphorus-doped with resistivities of 5 Ωcm and 10 000 Ωcm, and boron-doped with resistivities of 1450 Ωcm and 2000 Ωcm. Flat cylinders, about 1.25 mm thick and with a diameter of 6.8 mm were cut, polished and etched before evaporating a thin layer of Be on one of the surfaces of each sample. Two or more of the cylinders were sandwiched together with the Be-plated surfaces in contact and put into cylindrical silicon crucibles. Contamination of the samples with stray impurities may be reduced this way and also reaction of Be with the quartz of the ampoule is suppressed. The samples were then sealed in quartz ampoules, either evacuated or with a gas filling of pure hydrogen or deuterium at about 250 mbar, heated to temperatures between 945°C and 1180°C for 30 minutes and quenched in ethylene glycole. Excess Be was finally removed with concentrated HCl. Altogether 13 samples doped with Be as described above were investigated and additionally a sample kindly supplied by R. E. Peale, that has been previously investigated by R. K. Crouch et al. (sample Nr. 269-4 in reference [2]). Data for some of the samples are collected in Tab. 1.

Samples diffused at temperatures above about 1000°C were of p-type after diffusion as expected. A typical IR spectrum of such a sample is shown in Fig. 1. We find substitutional Be and, for the highest temperatures, also Be-Be pairs. Surprisingly, we also detect BeH pairs in almost all samples. Most probably hydrogen is introduced by polishing and etching the samples before evaporating Be onto the surface. It should be noted that spectrum Be_{IV} found by Kleverman and Grimmeiss [14] in Be-doped, but not intentionally H-doped silicon can be also identified as BeH. In some of our samples the BeH pair concentration after diffusion in vacuum reached the values obtained by diffusion in H_2-atmosphere. In sample Nr. 3, diffused in D_2-atmosphere, we find both, BeD and BeH pairs. Diffusion temperatures below about 1000°C led to n-type conductivity of the samples, that turned to p-type by isothermal annealing at 600°C for 20 min. For one of the n-type samples the FIR absorption spectrum was additionally recorded, showing Li and LiO donor centres [15]. Experiments are carried out at present to find the source of this contamination. Possibly, the Be contained a small fraction of Li, a fast diffuser with high solubility. Except for weak BeH lines, no Be-related IR signal was found in such samples. On the other hand, no Li, LiO or one of the two BeLi centres [2] were found in the p-type samples diffused at higher temperatures.

sample	starting material		diffusion parameters			resistivity [Ωcm]	
Nr.	dopand	resistivity [Ωcm]	T [°C]	time [min]	ambient	plated side	back side
1	B	1450	1175	30	vacuum	1.8	2.0
2	P	5	1171	30	vacuum	0.35	180
3	P	5	1180	30	D_2	0.37	0.65
4	P	5	1180	30	H_2	50	50

Table 1: Data for some of the samples mentioned in the text. All these samples show p-type conductivity after Be diffusion.

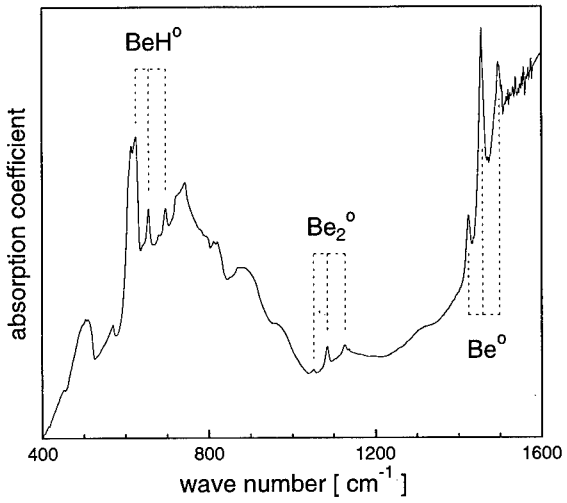


Figure 1: IR absorption of sample Nr. 2 at about 25 K, a representative example for the samples diffused at higher temperatures. Substitutional Be, Be-Be pairs and BeH pairs are visible, for which the strongest lines of the well known acceptor effective mass series are indicated. Although Be was diffused under vacuum in this sample, BeH pairs are present.

Results and Discussion

Below about 10 K we observe up to four trigonal EDSR spectra with varying absolute and relative strength depending on the doping conditions. These spectra, labelled Be-a, Be-b, Be-c, and Be-d, are not present in the starting material or in samples heat-treated without the addition of Be. As an example Fig. 2 (lower part) shows the EDSR signal of sample Nr. 3 diffused at 1180°C for 30 minutes in D_2-atmosphere. All four trigonal spectra are visible, each consisting of four lines according to the four equivalent trigonal axes in the crystal. The angular variation of the line maxima by rotation of the sample in the $(1\bar{1}0)$ plane is shown in the upper part of the figure and is typical for trigonal defect symmetry. The resonance field is at its minimum and the lines are narrow and weak if the magnetic field is aligned along the defect axis. With deviation from this direction the lines rapidly increase and broaden. No hyperfine structure could be resolved for any of the spectra, identification has to be based therefore on the comparison with infrared spectroscopy and circumstantial evidence. The situation is most clear for spectrum Be-b, which was very strong in the sample diffused in D_2-atmosphere (see Fig. 2) and not found in any of the other samples. We conclude that Be and D participate in the formation of this defect. This implies that the different isotopic masses of D and H lead to distinguishable EDSR spectra. Effects of the isotopic mass on spin resonance spectra have been observed for several centres in silicon, e. g. the tin-vacancy pair [16] or two Zn-related centres [13]. With IR absorption, not only BeD, but also BeH pairs are found in this sample. If more than one D atom would be needed to form the defect giving spectrum Be-b, further spectra should be visible according to all combinations of H and D atoms. Since this is not the case, we assume that only one D is involved. The number of Be atoms is not as clear. Crouch et. al. [5] report on Be_2H centres, Be_2D should as well exist. However, we do not observe them with IR absorption in our samples, so that spectrum Be-b rather should belong to BeD pairs. Since BeH pairs were found in almost all of our samples with IR spectroscopy, we tried to correlate their strength with one of the EDSR spectra. A gross proportionality is found for spectrum Be-a, the scatter in the data is within the experimental error expected from possible temperature differences in the IR measurements and a slightly varying EDSR sensitivity, that critically depend on the mounting of the sample. For spectrum Be-a, a peculiar temperature dependence is found. The line strength increases with increasing temperature and has a sharp maximum at about 2.8 K (see Fig. 3). Above this temperature, a strong broadening and decrease of the lines is observed. Thermalisation between several ground state levels would give a much broader temperature range. A simple model of a BeH centre accounting for the

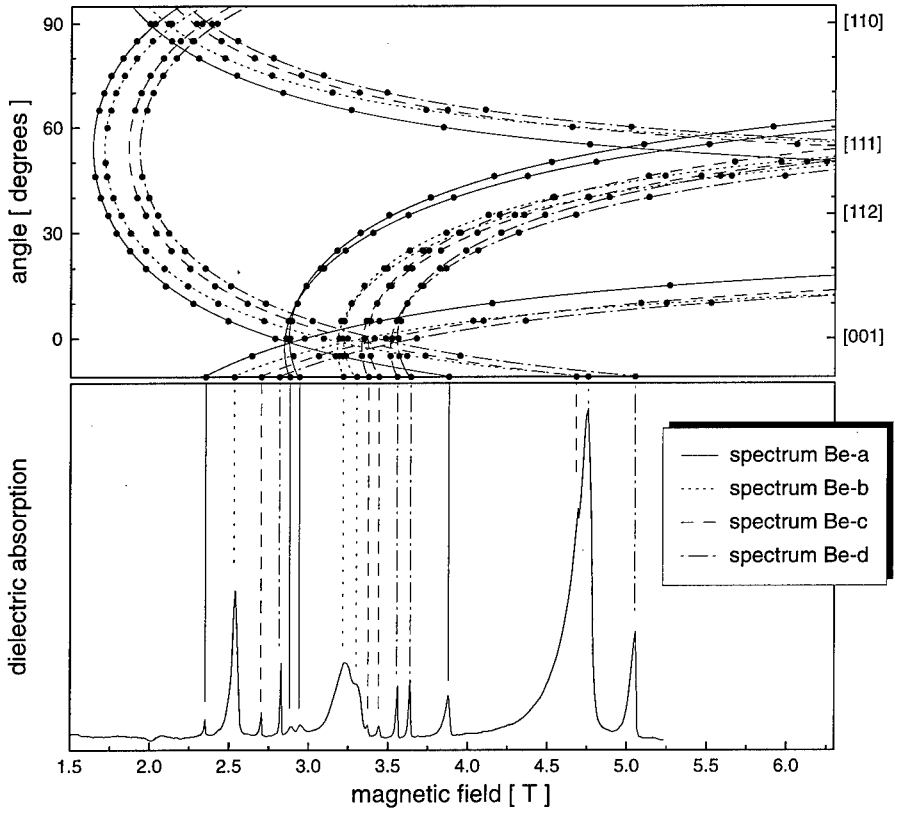


Figure 2: The EDSR signal of sample Nr. 3 is shown in the lower part of the figure, measured at a microwave frequency of 59.68 GHz and 1.97 K. The rotation pattern in the upper part shows the variation of the resonance fields for different directions of the magnetic field in the $(1\bar{1}0)$ plane of the sample.

trigonal symmetry might be analogous to the model for the BeLi centre discussed in ref. [7]: The hydrogen atom is situated in one of the tetrahedral interstitial sites next to the substitutional Be double acceptor and fills a silicon bond with its valence electron giving a single acceptor as a whole. The Γ_8 ground state of this acceptor is then split into two doublets by the trigonal crystal field. The effective g-values of $g_{||} = 2.59$ and $g_{\perp} = 0$ of spectrum Be-a may be accounted for by transitions between the $\pm$ 3/2 levels of this split Γ_8 ground state, so that the true value of $g_{||}$ would be one third of the effective value, namely 0.863, a value that is in close vicinity to the $g_{||}$-values observed for single acceptors in silicon [17]. The true $g_{\perp}$ and D values cannot be determined independently from the rotation pattern, good fits are obtained for D values large compared to the energy of the microwave quantum. The increase of spectrum Be-a with temperature may possibly be explained with a positive D, i. e. $\pm$ 3/2 levels lying above $\pm$ 1/2, however, one might then expext also transitions between the $\pm$ 1/2 levels, which are not observed. The strong decrease of spectrum Be-a above about 2.8 K may reflect the lost of the trigonal symmetry due to a dynamic process enhanced at higher temperatures, possibly the motion of the hydrogen atom. For spectrum Be-b a fairly good fit is possible with S = 3/2, $g_{||} = 0.829$, $g_{\perp} \approx 0.36$ and $|D| \approx 0.83$ cm^{-1} with slight deviations at the highest field values only. It is not clear, whether weak features visible in the FIR measurement of Muro and Sievers approximately 1.6 cm^{-1} from transition A and B of BeD (see Fig. 3 in ref [6]) are connected

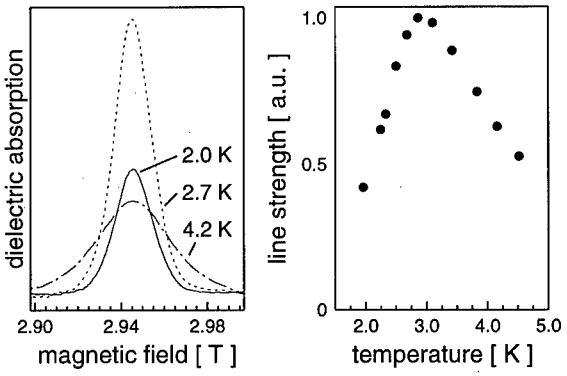


Figure 3: Temperature dependence of spectrum Be-a in sample Nr. 1 at 33.8 GHz. The magnetic field is at an angle of 16.5° from [001]. The resonance field of the centres oriented along the three other [111] directions is much lower, i. e. they have a larger magnetic field splitting.

with the zero field splitting 2D.

Spectrum Be-c is observed with approximately constant strength in all four samples that were P-predoped with 5 Ωcm and in none of the other samples. As visible in Fig. 2, it is rather weak compared to the other spectra. It is not yet clear, whether P is involved in this defect or if only a compensating donor is needed. Spectrum Be-d was very strong in almost all our samples. From the comparison with the IR measurements we can exclude that any of the trigonal spectra is correlated with Be-Be pairs. We assume that Be-c and Be-d are spectra of impurities paired with Be. Li was found in one of the samples with FIR absorption and neutral interstitial Fe in two of the samples with EDSR (electrically induced transitions are allowed and give a signal with g = 2.07 [18]). However, other contaminants cannot be excluded. Effective $g_{\|}$-values of spectrum Be-c and Be-d are 2.29 and 2.20, respectively, and the $g_{\perp}$ values are again in the vicinity of zero.

Somewhat similar to the situation in Zn-doped Si four broad lines appear after illumination of the samples in the 24 GHz measurement (Fig. 4). Line δ has no discernible angular dependence of the position with a g-value of 1.24. It is strongest with the magnetic field in a [110] direction and vanishes in the [001] direction. The strength of the other three lines is vice versa and they have a small angular variation of their g-values. In the [001] direction the g-value at 24.315 GHz is 0.877 for line α, 0.638 for line β, and 0.479 for line γ. With slight shifts in the g-values, the lines α, β, and δ are also observed at 34 GHz and line δ at 60 GHz, while the other lines would lie at magnetic field values exceeding the possible 7 T. These absorptions are reminiscent of the deeper of the single acceptors, for which the Γ_8 ground state exhibits a quadratic contribution to the Zeeman splitting giving three separate lines for the $\Delta m = 1$ transitions and one line for the $\Delta m = 2$ transitions [12]. We tried to fit the angular dependence of the lines α, β, and γ to the $\Delta m = 1$ transitions and the position of line δ to the $\Delta m = 2$ transitions of the Hamiltonian

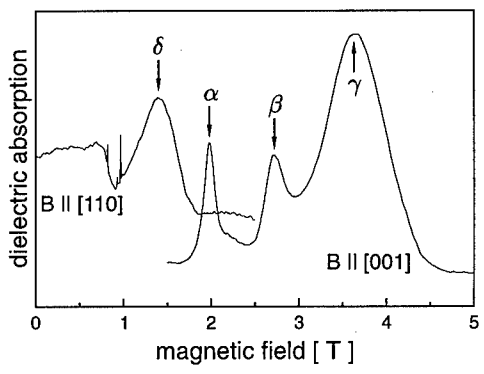


Figure 4: EDSR signal of the illuminated sample Nr. 2 at 24.315 GHz and 1.92 K.

commonly used for single acceptors [12]. However, no satisfactory agreement was obtained. Unfortunately, the lines decrease slowly after switching off the light. Therefore, no conclusive results could be obtained as to the temperature dependence so that the level ordering remains open. According to the IR results, the substitutional Be_s double acceptor is predominantly in the neutral charge state in our samples. Possibly, by illumination some Be_s atoms become singly ionized, giving the above signal. Samples with higher Be_s^- concentration are currently prepared to further investigate the origin of these lines.

Conclusion

Microscopic models for the BeH and BeD centres found with IR and FIR absorption have been controversely discussed during the last decade. Our results so far suggest that the EDSR spectra Be-a and Be-b are related to these centres. If so, the trigonal character has to be accounted for by any such model. No FIR experiments under uniaxial stress are reported so far, that could help to decide upon the defect symmetry. Phonon spectroscopy with superconducting tunneling junctions is a promising alternative with high sensitivity and resolution in this spectral region. Since natural Be consists to 100% of the isotope ^{9}Be, the investigation of isotope effects of Be, that could help to deduce the number of Be atoms involved, would need the use of ^{7}Be or possibly ^{10}B as diffusant, two isotopes that cannot easily be produced. Further experiments on samples with partially compensated Be centres are necessary to check for a possible correlation of the lines found after illumination with the deep one-hole state Be_s^-.

Acknowledgement

We are indebted to N. A. Stolwijk for helpful discussions. Financial support by the Deutsche Forschungsgemeinschaft is gratefully acknowledged.

References

[1] J. B. Robertson, R. K. Franks, Solid State Commun. **6**, 825 (1968)
[2] R. K. Crouch, J. B. Robertson, T. E. Gilmer, Phys. Rev. B **5**, 3111 (1972)
[3] J. N. Heyman, A. Giesekus, E. E. Haller, Mater. Sci. Forum **83-87**, 257 (1992)
[4] P. Stolz, thesis, University of Erlangen-Nürnberg, Germany (1990)
[5] R. K. Crouch, J. B. Robertson, H. T. Morgan, T. E. Gilmer, R. K. Franks, J. Phys. Chem. Solids **35**, 833 (1974)
[6] K. Muro, A. J. Sievers, Phys. Rev. Letters **57**, 897 (1986)
[7] R. E. Peale, K. Muro, A. J. Sievers, Phys. Rev. B **41**, 5881 (1990)
[8] E. Artacho, L. M. Falicov, Phys. Rev. B **43**, 12507 (1991)
[9] K. R. Martin, W. B. Fowler, Phys. Rev. B **44**, 1092 (1991)
[10] L. S. Chia, N. K. Goh, C. K. Ong, J. Phys. Chem. Solids **53**, 585 (1992)
[11] K. R. Martin, W. B. Fowler, Phys. Rev. B **52**, 16516 (1995)
[12] A. Köpf, K. Laßmann, Phys. Rev. Letters **69**, 1580 (1992)
[13] H. Schroth, K. Laßmann, H. Bracht, *The Physics of Semiconductors*, ed. by M. Scheffler and R. Zimmermann (World Scientific, Singapore), vol. 4, p. 2725 (1990)
[14] M. Kleverman, H. G. Grimmeiss, Semicond. Sci. Technol. **1**, 45 (1986)
[15] R. L. Aggarwal, P. Fisher, V. Mourzine, A. K. Ramdas, Phys. Rev. **138**, A882 (1965)
[16] G. D. Watkins, Solid State Commun. **17**, 1205 (1975)
[17] G. Feher, J. C. Hensel, E. A. Gere, Phys. Rev. Lett. **5**, 309 (1960)
[18] G. W. Ludwig, F. S. Ham, Phys. Rev. Lett. **8**, 210 (1962)

Materials Science Forum Vols. 258-263 (1997) pp. 423-428
© 1997 Trans Tech Publications, Switzerland

CADMIUM-RELATED DEFECTS IN SILICON: ELECTRON-PARAMAGNETIC-RESONANCE IDENTIFICATION

W. Gehlhoff, A. Näser, M. Lang[1] and G. Pensl[1]

Institut für Festkörperphysik, Technische Universität Berlin, Hardenbergstr. 36, D-10623 Berlin, Germany
[1]Institut für Angewandte Physik, Universität Erlangen-Nürnberg, Staudtstr.7, D-8520 Erlangen, Germany

Keywords : Si:Cd, EPR, DLTS, double acceptor, diffusion

Abstract. Electron paramagnetic resonance observations of the double acceptor centre cadmium in silicon are reported. The main centre labelled Cd(1) shows tetrahedral symmetry and can be described with an effective spin J=3/2. Based on the spectrum analysis and combining the results with earlier DLTS measurements, the Cd(1) centre has been identified as arising from the negative charge state of the isolated substitutional cadmium atom in silicon.

1. Introduction.

The group II impurities Zn and Cd in silicon have been extensively studied during the last many years [1-9]. The electronic properties have been determined from space charge and Hall measurements, and it has been concluded that both species occupy, in their isolated form, a regular substitutional lattice site and, lacking two electrons to be isovalent impurities, act as double acceptors [1,2,6,7]. Both elements show a pronounced tendency to form complexes with other impurities [4,5,8]. The atomic and electronic structure of isolated Zn and Cd has been discussed as that corresponding to isolated Pt^- and Au^0, respectively, and there is no generally accepted model for the electronic defect structure. The number of electrons in the 3d and 4d orbitals of the substitutional Zn/Cd (with configuration of the free neutral atom $3d^{10}4s^2/4d^{10}5s^2$) is in competition with the hybridised covalent bonds: $3d^8/4d^8$ (Ludwig-Woodbury model) or $3d^{10}/4d^{10}$ with two bound holes in the covalent bonds.
Very recently deep level transient spectroscopy was applied to radioactive impurities (DLTS-RI) in silicon [10]. It was demonstrated that the chemical nature as well as the number of probe atoms that participate in the considered defect centres can be identified by the time dependence of the concentration of the incorporated radioactive impurities and their daughter elements. The DLTS-RI method was also applied to radioactive $^{111}In^*$ atoms [6,7], a standard probe atom for the PAC-technique [9], which are transmuted into stable cadmium atoms. Besides two Cd-induced centres that contain one Cd atom each and a FeCd-pair, the singly and doubly charged state of the isolated double acceptor could be identified [6,7]. In spite of these studies, the microscopic structure of the Cd-induced centres, which is often revealed by means of electron paramagnetic resonance (EPR) spectroscopy, is not clear, because the DLTS-RI method gives no direct information on the microscopic structure of the centres involved. For the charge state Zn_s^-/Cd_s^- with one bound hole one might expect EPR or electric-dipole spin resonance (EDSR) spectra analogous to those observed for the single acceptors B, Al, Ga and In in Si [11]. On the other hand for the donor states Zn^+/Cd^+ the electronic configuration would be equivalent to the transition element impurities near the end of the $3d^n$ and $4d^n$ series which can be well described with the vacancy model [12] suggested some years ago by Watkins [13]. However, it seems that at least the donor-state Zn_s^+ does not exist. EPR or electric-dipole transitions of the isolated Zn_s^+ were not found up to now [5]. So far only various transition metal-pairs have been identified by EPR in samples with corresponding co-doping [4]. No EPR-results of Cd-related centres in Si have, as yet, been published.

In this paper the first EPR investigations of Cd-diffused silicon samples are reported. Samples identical to those used in Ref. [6] were used for our studies, allowing a direct comparison of EPR and DLTS results. From the observed Cd-related centres here only the centre labelled Cd(1) with the highest EPR-intensity is described and analysed. This Cd(1) centre shows the typical cubic angular dependence of the fine and hyperfine structures of a Γ_8-state. The chemical identification of the Cd(1)-defect is based on the agreement of the experimental hyperfine structure with the simulated one, considering the isotopic mixing of natural Cd isotopes with and without a nuclear spin.

2. Experimental details.

The samples used in this study were originally prepared for DLTS measurements some years ago [8,9]. From the set of samples those were selected which were prepared from p-type Czochralski grown silicon wafers with a boron concentration of 1.5×10^{16} cm^{-3}. The (100)-wafers were cut in rectangular samples of 5x6 mm^2, cleaned and then diffused with Cd in a sealed quartz ampoule which was evacuated. After the diffusion process which took place in a furnace at 1200^0 C for approximately 20 hours, the samples were subsequently quenched to room temperature. In some cases they were annealed at 600^0C for 1-2 minutes, to incorporate most of the cadmium atoms into the double-acceptor configuration. Finally, contacts were evaporated for the DLTS measurements on the front and backside of the samples. Details of the preparation are described in [6,7]. For the EPR measurements these contacts were removed and the samples were cut in smaller pieces of 2x5 mm^2 with the long edge oriented parallel to a <110> direction.

The EPR measurements were performed at the X-band using a Bruker ESP 300E spectrometer equipped with an Oxford ESR 900 helium gas-flow cryostat. The samples were mounted with their long dimension along the axis of a rectangular TE_{102} or a high sensitively TE_{011} cylindrical microwave cavity and in both cases perpendicular to the plane in which the magnetic field could be rotated.

3. Results and discussion.

Figure 1 displays the typical DLTS-spectra obtained for the set of samples investigated with the EPR method. The temperature scan reveals three Cd-related levels at the temperature of 78K, 178K and 220K, termed Cd(B1), Cd(B2) and $Cd^{-/o}$ respectively. The amplitudes of the three levels are strongly

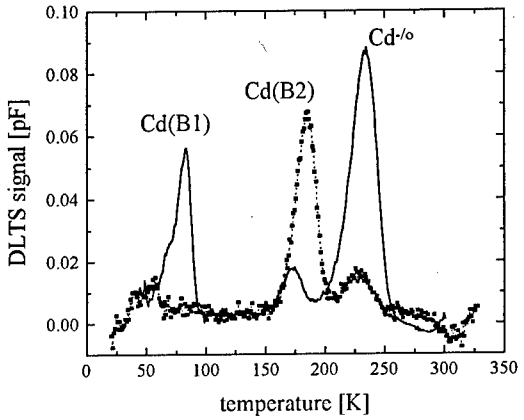


Fig.1: DLTS-spectra of Cd-diffused p-type silicon samples after quenching to room temperature without (dashed line) and with (solid line) an additional annealing for 2 min at 600°C.
([B]=1.5×10^{16} cm^{-3}; Cd-diffusion at 1200°C, 20 h).

dependent on the thermal treatment of the samples. After quenching from the diffusion temperature of 1200°C to room temperature, level Cd(B2) is dominant. The observed concentrations of the $Cd^{-/0}$ and Cd(B2) levels were about $1x10^{14}cm^{-3}$ and $5x10^{14}cm^{-3}$, respectively. Level Cd(B1) was formed at concentration approximately one order of magnitude lower. Additional rapid thermal annealing of the samples for 2 min at 600°C results in an increase of the concentration of the Cd(B1) and $Cd^{-/0}$ at the expense of the Cd(B2) level by about a factor five. $Cd^{-/0}$ was identified as the singly charge state of the Cd double acceptor with the energy level at E_v+(485±27) meV and Cd(B1) tentatively as a Cd-related complex of at least two atoms [6,7]. About the chemical nature of Cd(B2) no information was available.

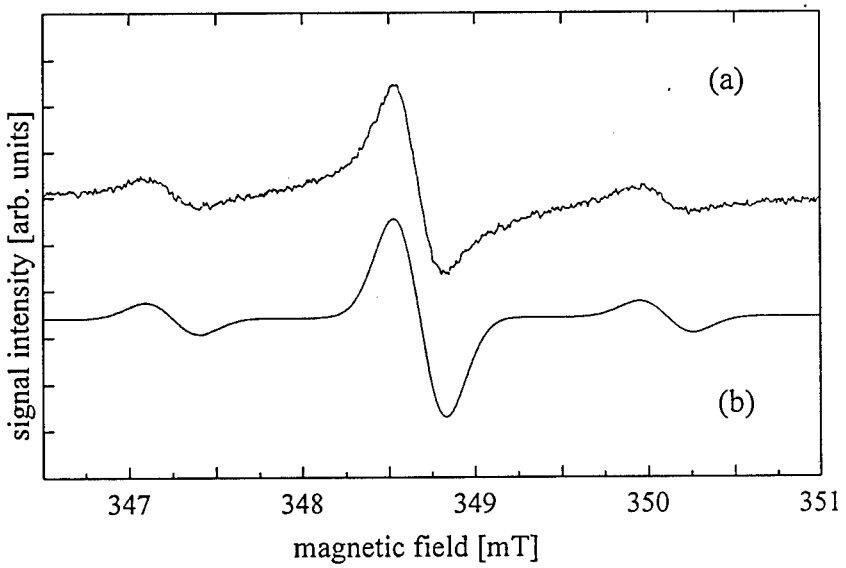


Fig. 2: EPR spectra of a Si:Cd sample for the magnetic field B || <100> showing the central component arising from Cd isotopes with I = 0 and the hyperfine structure due to the ^{111}Cd and ^{113}Cd nuclei with nuclear spin I=1/2.
(a) experimental spectrum at T=10K, microwave frequency ν = 9.477 GHz. (b) simulated spectrum assuming the natural abundance of the Cd isotopes. Details are given in the text.

The EPR measurements of the investigated p-type samples with a strong $Cd^{-/0}$ DLTS peak reveal, besides an isotropic signal with g = 2.0055 at low temperature, a weak angular dependent signal at g=1.9462±0.0005 which is shown in Fig. 2. Besides a strong central line a twofold splitting with the intensity ratio of 6:1 is observed. The spectrum shows a weak but characteristic angular dependence for centres in cubic environments. A stack plot of the spectrum for a rotation of the magnetic field in a {110} crystal plane is presented in Fig. 3. The chemical identity of this centre was verified by the well-resolved hyperfine structure and the observed intensity ratio of 6:1 between the central and the hyperfine lines. Cadmium has two isotopes with non-zero nuclear spin: ^{111}Cd and ^{113}Cd both with I=1/2 and a natural abundance of 12.75% and 12.26%, respectively. Because the line intensities depend only on the abundance of the isotopes for identical atoms and the line positions relate naturally to the magnetic moments of the isotopes, the excellent agreement between the experimental and simulated spectra (s. Fig. 2) provides evidence that the Cd(1) centre is arising from an isolated Cd centre. The ratio between the nuclear magnetic moments of the ^{111}Cd and ^{113}Cd isotopes is 0.956. Therefore, the expected difference of the hyperfine splitting for both isotopes is much smaller than the observed line width of 0.3mT, whereby the detection of the different hyperfine splitting for both isotopes is prevented. The superhyperfine interaction with the ^{29}Si isotope (I=1/2, natural abundance 4.70%) was neglected in the simulation procedure. Obviously, this is the reason for the visible difference in the line intensities on both sides of the central line.

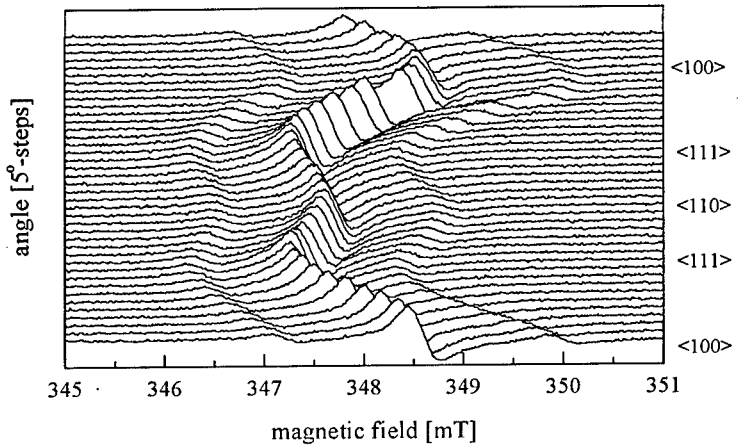


Fig. 3: Stack plot of the Si:Cd EPR signal at T = 10K in the X band. The magnetic field B is rotated by 5^0 steps in a {110} crystal plane.

The angular dependence in the line positions of the observed electron spin and hyperfine transitions can be described by the spin Hamiltonian (1) for a ground state with J=3/2 and a nuclear spin I=1/2 in cubic environment, which transforms like a Γ_8-state [14]

$$\mathbf{H} = g\beta\mathbf{B}\cdot\mathbf{J} + f\beta\{J_x^3 B_x + J_y^3 B_y + J_z^3 B_z - \frac{1}{5}(\mathbf{J}\cdot\mathbf{B})[3J(J+1)-1]\} + \sum_i A_i \mathbf{J}\cdot\mathbf{I}_i + F\{J_x^3 I_{i_x} + J_y^3 I_{i_y} + J_z^3 I_{i_z} - \frac{1}{5}(\mathbf{J}\cdot\mathbf{I}_i)[3J(J+1)-1]\} - g_N\beta_N\mathbf{B}\cdot\mathbf{I}_i , \quad (1)$$

where quadratic and higher Zeeman terms are omitted and the subscripts x, y, z denote the cubic crystal axis. The sum is taken on the two Cd isotopes ^{111}Cd and ^{113}Cd with nuclear spin I=1/2. Assuming that $g\beta\mathbf{BJ}$ is large in comparison with all the other terms in Eq.(1) and that $A\mathbf{JI}$ is always larger than the other terms involving **I**, the energy levels are given in first order by

$$E_{Mm_i} = g\beta BM + A_i Mm - g_N\beta_N Bm_i + (f\beta B + F_i m_i)\{M^3 - \frac{1}{5}M[3J(J+1)-1]\}p, \quad (2)$$

where M and m are the eigenvalues of the components along the magnetic field **B** of **J** and **I**, respectively. The frequencies ν_i of the EPR transitions (M-1$\leftrightarrow$ M, Δm=0) derived from Eq.(2) for i= (^{111}Cd, ^{113}Cd) are:

$$h\nu_i = (g - \frac{9}{5}fp)\beta B + (A_i - \frac{9}{5}F_i p)m_i \quad \text{for } M=-1/2\leftrightarrow+1/2$$

$$h\nu_i = (g + \frac{6}{5}fp)\beta B + (A_i + \frac{6}{5}F_i p)m_i \quad \text{for } M=\pm1/2\leftrightarrow\pm3/2 \quad (3)$$

According to equations (2) and (3), the angular dependence of the electron and hyperfine transitions in a cubic field is determined by the function p, which reads for rotation of the magnetic field **B** in a {110} plane

$$p = 1 - \frac{5}{4}\sin^2\theta(1+3\cos^2\theta), \quad (4)$$

where θ is the angle between the direction of **B** and the <100> axis in the plane. The experimental angular dependence of the -1/2$\leftrightarrow$+1/2 transition and of the hyperfine splitting are shown in Fig. 4.

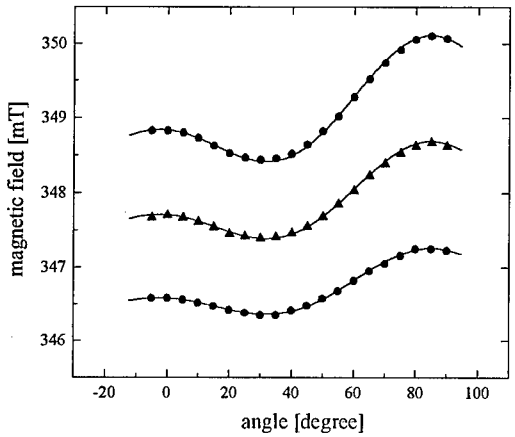


Fig. 4: Angular variation of the line positions of the Cd(1) signal for the Cd isotopes with nuclear spin zero (▲) and nuclear spin I=1/2 (•) for rotation of the magnetic field **B** in a {110} crystal plane. The solid curves are calculated with parameter set (5) obtained from the fit using the spin Hamiltonian given in Eq.(1).

The solid curves are calculated with the following parameters obtained from the fit of the line positions predicted by Eq.(1) to the experimental curves:

$$|g| = 1.9462\pm0.0005 \qquad |f| = 0.0024\pm0.0005 \qquad (5)$$
$$|A| = (21.6\pm0.2)10^{-4}\ cm^{-1} \qquad |F| = (2.42\pm0.02)10^{-4}\ cm^{-1},$$

where A and F are the average values of the Cd isotopes ^{111}Cd and ^{113}Cd since the difference in the twofold splitting of both isotopes with nuclear spin could not be resolved because of the reason described above. The relative signs were determined to be equal to: $gf > 0$ and $AF < 0$. The $\pm1/2 \leftrightarrow \pm3/2$ transitions are broadened beyond detection by random strains in the sample.

The agreement between the experimental angular dependencies with the predicted ones (Fig. 4) reveals that the Cd ion is located on the substitutional or the tetrahedral interstitial site. Based on symmetry arguments, it is not possible to favour a particular site. However, the proved cubic angular dependence described by the terms proportional to f and F in the spin Hamiltonian (1) indicates a strong coupling to the silicon lattice and consequently suggests the substitutional lattice site. This assumption is also supported by the observed temperature dependence (Fig. 5) and saturation behaviour of the EPR transitions with microwave power (Fig. 6) that reveal a strong lattice coupling. It is, therefore, reasonable to assume that the investigated cadmium centre occupies the substitutional position in silicon. The obtained EPR results with a degeneracy corresponding to J=3/2 are consistent with the negative charge state Cd^-. But it is also possible to assign this EPR spectrum to Cd^+ assuming the high-spin (S=3/2) ground state of the d^7 configuration or equivalently the ground state configuration $a_1^2t_2^3$ within the framework of the vacancy model. In both cases many electron effects must dominate. Assuming that the EPR spectra arise from the positive charge state Cd^+, the EPR investigations would reveal a different behaviour in comparison to the isoelectronic transition metal impurities Pd_s^- and Ag_s°. These impurities show a Jahn-Teller off-centre C_{2v} symmetry distortion and an electron spin S=1/2 in agreement with the vacancy model [12]. According to the DLTS results obtained for these samples, the charge state Cd^- is

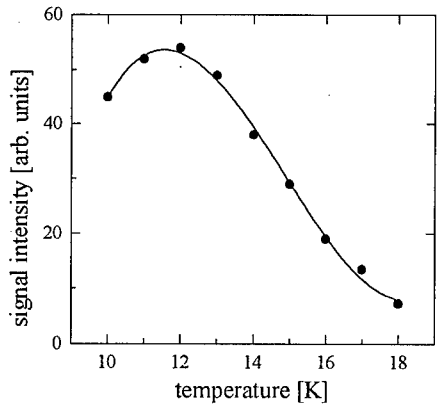


Fig. 5: Temperature dependence of the EPR signal intensity (peak-to-peak amplitude) of the Cd(1) signal.
Microwave power 13 mW, ν = 9.447 GHz
• experimental data — theoretical fit

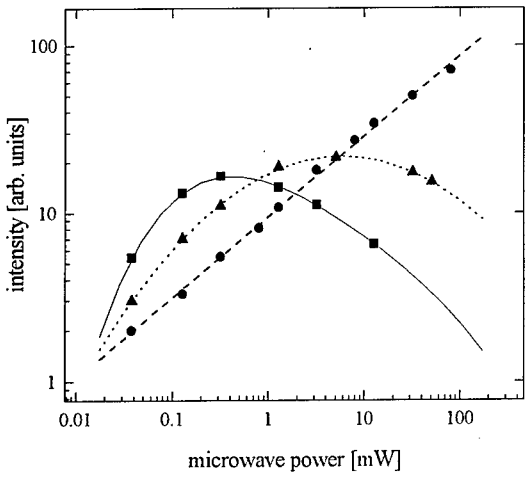


Fig. 6: Dependence of the EPR signal intensity (peak to peak amplitude) of the cubic Cd(1) signal on the microwave power at three different temperatures: 4K (■), 8K (▲), 12K (●) (rectangular resonator H_{102}, critical coupling, ν=9.477 GHz).

the most probable one. Therefore, we conclude that the observed spectra, labelled Cd (1), arise from the negative charge state of the cadmium atom which is located at the substitutional site.
In analogy to the isoelectronic, neutral, shallow single acceptors B°, Al°, Ga° and In°, the ground state of Cd^- can also be described with an effective spin S'=3/2. However, in contrast to these shallow acceptors, the parameters f and F of the multipole terms $\mathbf{J^3B}$ and $\mathbf{J^3I}$ in the spin Hamiltonian (1) are about one order of magnitude smaller for Cd^-.

4. Summary.

In Si-samples doped with cadmium, which reveal a strong $Cd^{-/0}$ level in DLTS spectra a new paramagnetic centre, called Cd(1), was observed using the EPR method. Based on the EPR spectrum analysis and the DLTS results obtained for the same samples this Cd(1) centre has been identified as the isolated substitutional cadmium atom in silicon with charge state Cd^-.

Acknowledgement

Parts of this work which were performed at the TU Berlin have received financial support from the BMBF under grant 03-GE4-TUB-5 which is gratefully acknowledged.

References.

1. S.S. Dyunaidov, N.A. Urmanov, M.V. Gafurova, phys.stat.sol. **A66**, K79 (1981)
2. S. Weiss, R. Beckmann, R. Kassing, Appl. Phys. **A50**, 151 (1990)
3. R.A. Casali, M.A. Caravaca, C. O Rodrigguez, Phys. Rev. **B54**, 16701 (1996
4. H. E. Altink, T. Gregorkiewicz. C.A.J. Ammerlaan, Solid State Comm. **75**, 115 (1990)
5. H. Schroth et al., Proc. ICPS-23, Berlin 1996, World Scientific 1996, Vol. 4, p.2725
6. M. Lang, G. Pensl, M. Gebhard , N. Achtziger , M. Uhrmacher, Appl. Phys. A 53, 95 (1991); Materials Science Forum **83-87**, 1097 (1992)
7. M. Lang, Thesis, Universität Erlangen-Nürnberg, 1993
8. S.E. Daly, E. Mcglynn, M.O. Henry, J.D.Campion, K.G. McGuigan, M.C. DoCarmo, M.H.Nazare, Materials . Science Forum **196-201** (1995) pp.1303-1308
9. Th. Wichert, N. Achtziger, H. Metzner, R. Sielemann, in "Hyperfine interaction of defects in solids", ed. G. Langouche (Amsterdam: Elsevier 1992), pp.77-156.
10. J.W. Petersen, J. Nielsen, Appl. Phys. Lett. **56**, 1122 (1990)
11. A. Köpf, K. Lassmann, Phys.Rev Lett. **69**, 1580 (1992)
12. G.D. Watkins, P.M. Williams, Phys. Rev. **B52**, 16575 (1995)
13. G.D. Watkins, Physica B+C, **117B-118B**, 9 (1983
14. A. Abragam and B. Bleaney,"Electron resonance transition ions", Dover Public., New York 1986

Materials Science Forum Vols. 258-263 (1997) pp. 429-436
© 1997 Trans Tech Publications, Switzerland

IRON IN *p*-TYPE SILICON: A COMPREHENSIVE MODEL

Song Zhao, Aimée L. Smith, Sang H. Ahn, Gerd J. Norga, Marlene T. Platero, Hiroshi Nakashima[1], Lucy V. C. Assali[2], Jürgen Michel, and Lionel C. Kimerling
Dept. of Materials Science & Engineering, M.I.T., Cambridge, MA 02139, USA
[1]Dept. of Electrical Engineering, Kyushu University, Fukuoka 812, Japan
[2]Instituto de Física da Universidade de São Paulo, CP 20516, São Paulo, SP, Brazil

Key words: gettering, Fe-acceptor pairs, solubility, precipitation, silicon processing

Abstract Contamination by transition metal impurities is a major concern in Si processing. The bulk contamination tendency is measured as the product of the metal ion diffusivity and its solubility in Si under processing conditions. In particular, iron (Fe) is incorporated as a highly mobile and soluble (Fe_i^+) species. Surface contamination during wafer cleaning is driven by liquid-solid equilibria dictated by the choice of cleaning solution. In Si solid solution Fe is a near-midgap recombination center. Due to its high mobility Fe in solution in *p*-Si normally exists in the form of an ion-pair with a negatively charged acceptor ion. Gettering, the removal of Fe from active device regions, is accomplished by designing remote regions of lower chemical potential (segregation gettering) or with a high density of heterogeneous nuclei for precipitation (relaxation gettering). This paper presents a comprehensive model for the deposition of Fe from liquid solution, the ion pair structure and stability, and the gettering of Fe from p/p^+ epilayers.

Introduction

Fe is a major contaminant in Si processing. During crystal growth Fe is not a major concern because of its low melt segregation coefficient, $k_{Fe(Si)}=8.0\times10^{-6}$ [1]. Reasonable care in melt preparation can assure bulk concentrations below $10^{11}cm^{-3}$. The prevalence of stainless steel vessels, transport lines and parts in a modern fabline presents ample opportunity for Fe to enter the Si matrix during processing. Understanding the control of Fe in Si is both of specific value for Fe and a guide for the control of all fast diffusing metals.

The areas of concern are the solid/liquid equilibria of Fe in cleaning and etching chemistry; the structure of isolated and paired Fe in the Si crystalline matrix; the factors determining the equilibrium Fe solubility in *p*-Si; and the kinetics of Fe gettering in both the segregation and relaxation regimes. For each subject area we construct models to describe the experimental observations and apply them to simulate and design gettering processes for p/p^+ epitaxial layers.

Fe Solubility in Wafer Cleaning Solutions

Metals exist as soluble ions in aqueous solutions. The solubility is governed by the redox reactions available to reduce the positively charged metal ions to neutral metal atoms on the Si surface or to insoluble oxide compounds. For high concentration acid solutions with radical species that form soluble complexes with the metal ion, the solubility is estimated by the electromotive series. Ions with ionization potentials positioned below the standard hydrogen potential (SHP) are reduced by electrons from the acid. Figure 1 shows the relative positioning of typical metals in HF (at a concentration of 1ppm) with the SHP and the Si Fermi level (E_F, referenced to the vacuum level) shown on the same scale. For adsorption on the Si surface, the electron transfer occurs from the Si E_F to the ion with the Si oxidation (etching) completing the circuit. Fe is above E_F, and deposition does not occur. Au is well below E_F and deposition to the Si surface is expected. For Cu, with an position near the Si E_F, both the deposition rate and morphology are dependent on E_F and quasi-E_F as affected by external illumination [2].

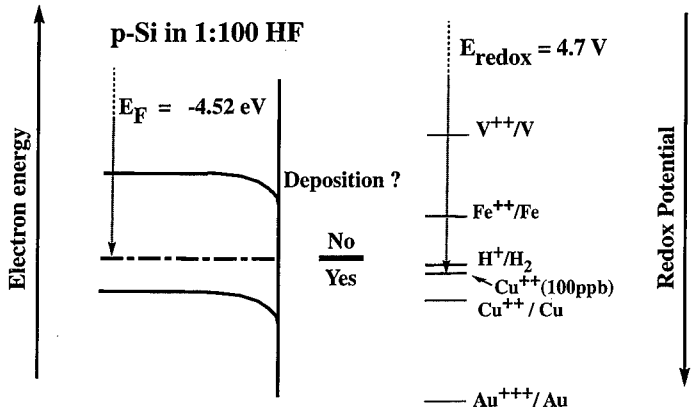


Figure 1: Band diagram for p-type Si in the dark compared against standard reduction potentials for various metals. Band-bending occurs at the Si surface due to the presence of surface states when immersed in dilute HF.

Table I: Standard reduction potential (E^o), surface lifetime (τ_{meas}), 1:100 HF exposure conditions, and calculated driving force (ΔG) for the cathodic reaction.

Redox System	E^o [V]	Exposure	τ_{meas} [ms]	ΔG [meV]
Au^{+++}/Au	1.692	100 ppb, 5 min	0.028	-1402
Cu^{++}/Cu	0.337	1 ppm, 10 min	0.220	-259
Fe^{++}/Fe	-0.440	1 ppm, 10 min	5.0	520
V^{++}/V	-1.175	1 ppm, 10 min	5.0	1258

The deposition of metals from HF can be measured directly by monitoring surface recombination velocity. We have constructed a contactless radio frequency photoconductance decay measurement apparatus for the measurement of minority carrier lifetime [3]. The Si surface in HF attains low surface recombination velocity, $S \approx 1.0$cm/s, by hydrogen termination of surface bonds. For long bulk minority carrier lifetime, $\tau > 100\mu$s, the measured lifetime is given by $d/2S$, where d is the wafer thickness. Table I shows a comparison of measured lifetimes for HF solutions intentionally contaminated with different metals. The predictions of the model of Figure 1 are validated. Fe will not deposit from HF to the Si surface.

For oxidizing solutions, the pH and oxidation potential of the solution are variables. Pourbaix diagrams provide a representation of the variation in metal solubility with these variables in terms of the possible reaction equilibria [4]. Figure 2 shows the Pourbaix diagram for Fe with the positions of the SC-1 and SC-2 "standard cleaning" solutions. SC-1 oxidizes the Si surface to remove organics and particles, but its position in the Fe_2O_3 phase field, indicates that Fe^{+++} is electron deficient and will leave solution and adsorb at the Si surface. Phase boundaries delineate the stability of a given ion concentration against the reducing potential of the solution. Higher oxidation potential and lower pH increase the Fe "gettering potential" of the solution.

Fe-Acceptor Pairs

Fe in Si can be regarded in much the same way as Fe in aqueous solution. The Fe exists as an ion (Fe_i^+, Fe_i^{++}), and the Si matrix behaves as a dielectric continuum (ϵ_r=11.7). Positively charged Fe ions are attracted to negatively charged acceptor dopants by long range Coulomb forces. The stable state for Fe in p-Si is the electrostatically bound pair with an acceptor dopant. Figure 3 shows the different

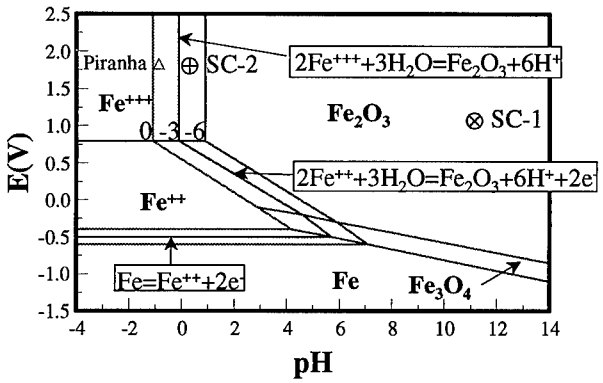


Figure 2: Pourbaix diagram for the Fe-H_2O system. Phase boundaries for 10^0, 10^{-3} and 10^{-6} molal concentration are shown.

pair structural configurations with the Fe_i occupying the TN position: the tetrahedral interstitial site in the Nth shell from the acceptor. The binding energy of these ion-pairs is E_B=0.60±0.05 eV for all Group III acceptors (B, Al, Ga, In). Thus, for temperatures below about 150°C a significant fraction of the Fe_i^+ is bound as $Fe_i^+B_s^-$ pairs. The statistics of this association reaction will be reviewed in the solubility section.

The constancy of E_B, independent of acceptor, is not completely understood. We have modified our previous model of the Fe-Acceptor pair to include strain and electrostatics, including charge polarization, explicitly [5, 6, 7]. The Fe-Si interatomic potential is expressed as [5, 6]

$$V_{\text{rep}}(r) = 4\epsilon[(\sigma/r)^6], \tag{1}$$

where r is the distance between atoms, and σ and ϵ are empirical parameters. σ and ϵ are fit to the Fe diffusivity with a charge state dependence observed in experiments [8, 9]. From the Fe_i migration energy data $E_M(Fe_i^+)$=0.68eV and $E_M(Fe_i^0)$=0.78eV, it is determined that, $4\epsilon[\sigma(Fe^+, Si)/a]^6$=$2.44\times10^{-3}$ eV and $4\epsilon[\sigma(Fe^0, Si)/a]^6$=$2.80\times10^{-3}$ eV (a=5.43Å, Si lattice constant) [7]. The elecrostatic term is written as

$$V_{\text{att}}(r) \approx \frac{1}{4\pi\epsilon_r\epsilon_0}[\frac{q_1q_2}{r} - \frac{1}{2}(\frac{a_2^3q_1^2}{r^4} + \frac{a_1^3q_2^2}{r^4})], \qquad \text{for } r \gg a_1 + a_2, \tag{2}$$

where a_1 and a_2 are the valence electron cloud spherical surface radii (74% of atom radius), q_1 and q_2 are the net charges on the ions. Local lattice relaxation is included by adjusting the acceptor-near neighbor Si atom bond lengths to the sum of the covalent radii, r_{cov}(A)+r_{cov}(Si), of Si and the acceptor (A). The acceptor identity enters in the polarization term ($V_{\text{att}}(r)$), the lattice relaxation term, and the interatomic repulsion term ($V_{\text{rep}}(r)$) [6, 7].

The competition between the hard core repulsion and electrostatic attractive forces determines the stable pair configuration. Table II lists for each pair the experimental and model values for the stable configuration, the pair binding energy and the migration barrier for near neighbor Fe_i jumps. The values agree well with experiments indicating that the polarizability and lattice relaxation corrections are appropriate. In particular, the charge state controlled metastable configurations have been verified by experiment.

Fe Solubility in *p*-Silicon

Ion pairing is not a factor in solubility or diffusivity at elevated temperatures (T>700°C). The fraction of paired Fe_i, f, as a function of acceptor concentration and temperature is given by the relation [15]

$$[Fe_i^+B_s^-]/([Fe_i^+][B_s^-]) = (1/ZN)\exp(E_B/kT), \tag{3}$$

Table II: Fe_iA_s Pair Structure, Binding Energy, and Near Neighbor Migration Barrier[(a)]

Pair	Stable Structure	Binding Energy E_B [eV]	Migration Barrier $\Delta V_{mig}(Fe_i^+)$ [eV]	
			T1→T2	T2→T1
$Fe_i^0B_s^-$	⟨111⟩[(b)] (⟨111⟩[10, 11])	0.01	1.02 (0.9-1.0[12])	0.92
$Fe_i^+B_s^-$	⟨111⟩ (⟨111⟩[10, 13, 14])	0.56 (0.65[15],0.58[16, 17])	0.90 (<1.1[18])	0.72 (0.75[18],0.65[15])
$Fe_i^+Al_s^-$	⟨111⟩ (⟨111⟩[19, 20, 21, 22])	0.58 (0.52[23])	0.65 (0.64[20, 23])	0.56 (0.75[22])
$Fe_i^+Ga_s^-$	⟨111⟩ (⟨111⟩[13, 22, 24])	0.53	0.60 (0.6[25])	0.58 (0.72[22])
$Fe_i^+In_s^-$	⟨100⟩[(c)] (⟨100⟩[13, 22, 26, 27])	0.55	0.57	0.69 (0.6[25],0.69[22])

(a) Experimental results are listed in brackets; (b) ⟨111⟩-trigonal symmetry; (c) ⟨100⟩-orthorhombic symmetry.

$$f \equiv [Fe_i^+B_s^-]/[Fe]_{total}, \quad \text{and} \quad [Fe]_{total} = [Fe_i^+B_s^-] + [Fe_i^+] + [Fe_i^0], \tag{4}$$

where Z is the configuration degeneracy (e.g., Z=4 for T1 site), and N=5.0×10^{22} cm^{-3} is the Si lattice site density. Figure 4 plots the Fe_iB_s pair concentration vs. temperature for a range of boron doping levels.

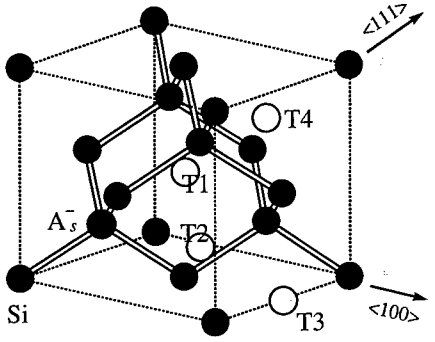


Figure 3: The Fe_iA_s pair configurational symmetry is determined by the Fe_i position relative to the A_s. The Fe_iA_s pair exhibits ⟨111⟩-trigonal symmetry if the Fe_i is at T1 or T4 site. The Fe_iA_s pair shows ⟨100⟩-orthorhombic symmetry if the Fe_i is at T2 site.

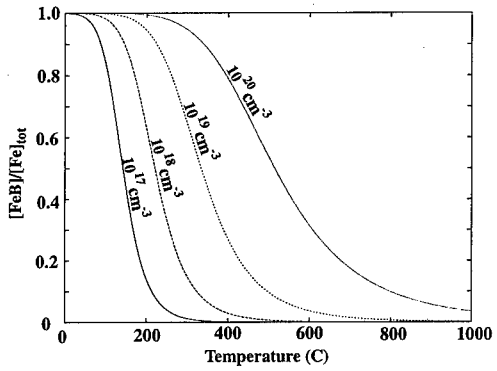


Figure 4: Fraction of $[Fe_iB_s]$ to total [Fe] in Si solid solution for various levels of boron doping as a function of temperature. Except for the highest doping level shown, the fraction of paired Fe_i is below 5% at typical processing temperatures.

The solubility (C_s) enhancement of Fe in p-Si is derived directly from the electron-hole equilibria as shown in the following equations describing impurity ionization, dopant activation, electron-hole recombination, and neutrality

$$Fe_i^0 \rightleftharpoons Fe_i^+ + e, \qquad B_s^0 \rightleftharpoons B_s^- + h, \qquad e + h \rightleftharpoons \emptyset, \tag{5}$$

$$[B_s^-] + n = [Fe_i^+] + p, \tag{6}$$

where $n \equiv$ [e] and $p \equiv$ [h]. This behavior is independent of pairing as the hole concentration in excess of the intrinsic level promotes the ionization and solution of Fe donors. Using the value of

Table III: Average initial precipitate size and density at 620°C and 700°C.

Temperature	$(Nr)_{ppt}$ [cm^{-2}]	r_{ppt} [nm]	N_{ppt} [cm^{-3}]
620°C	870	13	6.6×10^8
700°C	910	16	5.7×10^8

the $Fe_i^{0/+}$ donor level as E_V+0.38 eV and taking the level to be a constant proportion of the energy gap as the temperature varies, the solubility of Fe in Si may be calculated and plotted as shown in Figure 5. The ratio of C_s (p or p^+) to C_s (intrinsic) gives, k, the partition coefficient for Fe_i at a p/p^+ epilayer/substrate interface. Figure 6 displays the same data in the form of k vs. acceptor concentration.

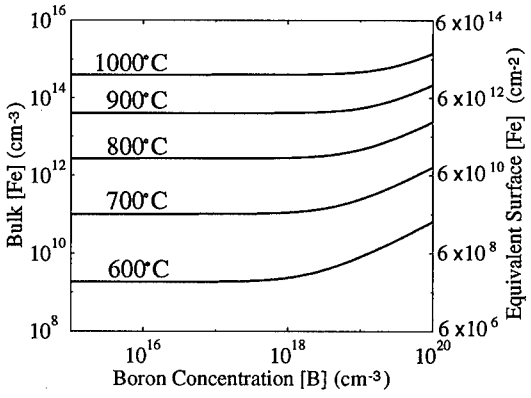


Figure 5: Fe solubility in Si, $C_s(Fe_i)$, increases with boron concentration [B] and temperature T.

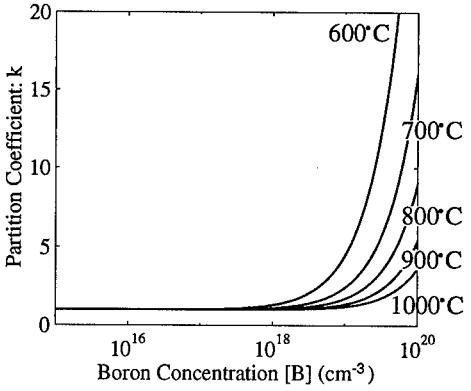


Figure 6: k is the ratio of Fe solubility, $C_s(Fe_i)$, in boron doped Si to that in intrinsic Si.

In supersaturated solutions Fe precipitates in a diffusion limited process that is dictated by the Fe diffusivity $D(Fe_i)$, and the heterogeneous nucleation site density N_{ppt}. The governing kinetic relation for the diffusion-segregation-nucleation process is given by [28]

$$\frac{\partial C}{\partial t} = \frac{\partial}{\partial x}\left[D\left(\frac{\partial C}{\partial x}\right)\right] + 4\pi r N_{ppt} D[C_s(Fe_i) - C], \tag{7}$$

where $C \equiv [Fe_i]$ and $D \equiv D(Fe_i)$. In Eq.(7), an uniform segregation profile has been assumed. r is the radius of a precipitate, $C_s(Fe_i)$ is the Fe solubility in silicon. Figure 7 plots the Fe concentration in solution, measured in the center of a wafer by DLTS, following saturation at 1000°C, quench in water, and annealing at 620°C and 700°C [29]. The data were analyzed according to the second term in Eq.(7) featuring the Fe precipitation process, and the values for the average precipitate size (r_{ppt}) and number density (N_{ppt}) are shown in Table III. As shown in Figure 7 the Fe concentration in solution decays asymptotically toward the Fe solubility at the heat treatment temperature. As predicted the time constant for precipitation is faster at higher temperatures [30], but the asymptotic limit is a higher concentration of Fe than $C_s(Fe_i)$ at the heat treatment temperatures. The heterogeneous nucleation of Fe pecipitation occurs at sites of oxygen precipitates. A Czochralski (Cz) grown wafer can be heat treated with a specific schedule to create a given nucleation site density.

Gettering of Fe

The fundamentals developed in the preceding sections can be applied to a comprehensive model for the behavior of Fe in Si. We give below application of this model to simulate the gettering of Fe

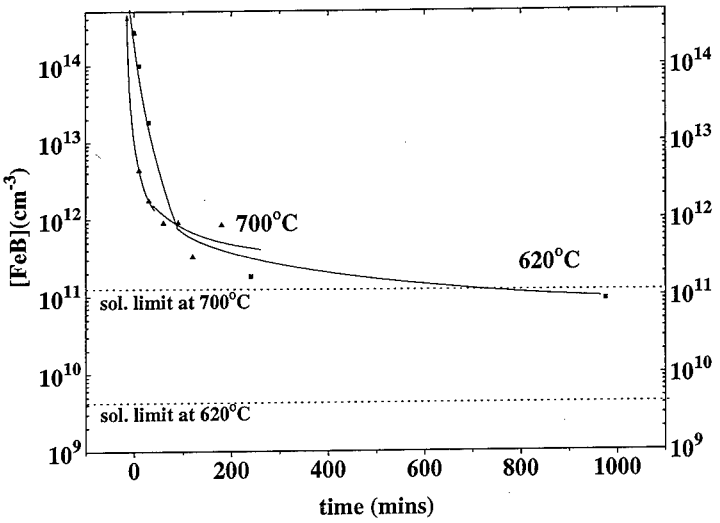


Figure 7: The $[Fe_iB_s]$ at the center of Fe-contaminated p-type Cz Si with Al backside contact is plotted against annealing time at 620°C and 700°C, respectively.

in p/p^+ epitaxial layers. The basic problem is reduction of [Fe] to levels of $10^{11}cm^{-3}$ in the fastest possible time for high yield processing. Fe is known to limit device performance by a variety of mechanisms that range from the role of Fe_iB_s as a recombination center to Fe precipitates acting as filamentary junction short circuits.

We model the roles of three mechanisms for localizing Fe outside the epilayer: segregation to the p^+ substrate, precipitation at internal gettering (IG) sites, and precipitation at damage sites on the backside of the wafer (BSD). Figure 8 shows a schematic drawing of the wafer and the results of the simulator for four different wafer designs. FZ (float-zoned) designates Si of low oxygen content with no heterogeneous sites. The wafer was saturated with Fe at 1000°C and gettered at 700°C. The Cz substrates contained 10^9cm^{-3} IG sites.

At short times segregation of Fe from the epilayer to the p^+ region occurs. However, due to the small values of k (<10), the Fe concentration remains well above the target value. At long times outdiffusion to the BSD sites are effective in reducing the epilayer Fe concentration for the FZ substrates. For the Cz substrates, the IG sites lower the substrate Fe concentration fairly rapidly and, in turn, reduce the epilayer concentration through the segregation coefficient (k) multiplier. Thus while segregation alone is insufficient, segregation with IG nucleated precipitation is very effective in reaching the target Fe concentration in reasonable times.

Figure 9 plots the Fe concentration vs. time for the epilayer, substrate and backside for all for wafer designs. The 700°C gettering temperature is effective in generating a supersaturated solution of Fe in Si. The low diffusivity of Fe at 700°C renders the BSD mechanism useless. However, the IG mechanism rapidly responds to the supersaturation and the epilayer is emptied of Fe to the target level of $10^{11}cm^{-3}$ by short range diffusion to the p/p^+ interface.

Summary

We present a comprehensive model for the chemical behavior of Fe in p-Si and apply this model to the design of gettering processes. In aqueous solution the deposition of Fe on the Si surface is

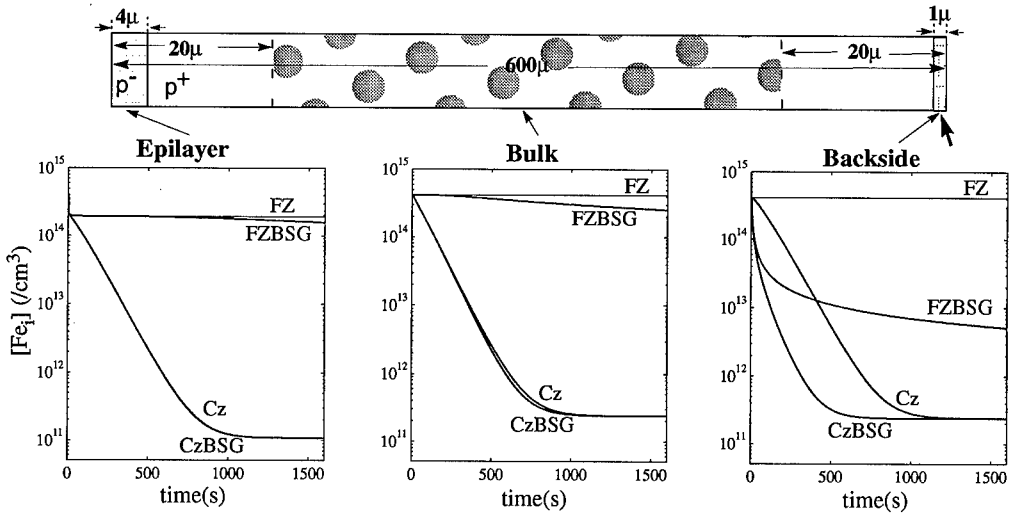


Figure 8: Competing gettering mechanisms for lightly doped epilayer on a p^+ substrate. FZ represents the float zone case with no internal gettering sites and no back surface damage. FZBSD is the case with no internal gettering sites but with back surface damage. Cz is the case with internal gettering sites such as those generated by the high-low-high gettering treatment and CzBSD is the case with both internal gettering and back surface damage. The plots show $[Fe_i]$ as a function of treatment time at 700°C.

governed by the oxidation potential of the solution and the reduction potential of Fe. The low Fermi level position in p-Si retards electron transfer to reduce Fe_i^{++} ion for deposition from HF. The binding energy for Fe-acceptor pairs was calculated using a semi-empirical model that includes local lattice relaxation and electrostatics, including charge polarization, explicitly. The model accurately predicts the observed pair configurations of Fe with B, Al, Ga and In. The dependence of Fe solubility in Si on p-doping was calculated and used to derive the partition coefficient for Fe at a p/p^+ interface as a function of doping and temperature. The precipitation of supersaturated solutions of Fe in Si was measured and fit to a model based on heterogeneous nucleation. These fundamental concepts were integrated into a single model to simulate the gettering kinetics of Fe in p/p^+ epilayers and evaluate the roles of segregation at the epilayer substrate interface and precipitation at IG and BSD sites.

Acknowledgements This work is supported by the National Renewable Energy Laboratory (NREL) and the Wafer Engineering and Defect Science (WEDS) Consortium.

References

[1] S. Wolf and R. N. Tauber, "*Silicon Processing for the VLSI Era*", Vol. **1**, p12 (Lattice Press, 1986).

[2] G. J. Norga, M. T. Platero, K. A. Black, A. J. Reddy, J. Michel, and L. C. Kimerling, J. Electrochem. Soc., **144**, 2801 (1997).

[3] H. M'saad, J. Michel, A. J. Reddy, and L. C. Kimerling, J. Electrochem. Soc., **142**, 2833 (1995).

[4] M. Pourbaix, "*Atlas of Electrochemical Equilibria in Aqueous Solutions*", p.389, (Pergamon, 1966).

[5] L. C. Kimerling, M. T. Asom, J. L. Benton, P. J. Drevinsky, and C. E. Caefer, Mater. Sci. Forum, **38-41**, 141-150 (1989).

[6] S. Zhao, L. V. C. Assali, and L. C. Kimerling, Mater. Sci. Forum, **196-201**, 1333 (1995).

[7] S. Zhao, L. V. C. Assali, G. H. Gilmer, and L. C. Kimerling, *to be published.*

[8] H. Takahashi, M. Suezawa, and K. Sumino, Phys. Rev. B **46**, 1882 (1992).

[9] T. Heiser and A. Mesli, Appl. Phys. Lett. **58**, 2240 (1991); Phys. Rev. Lett., **68**, 978 (1992).

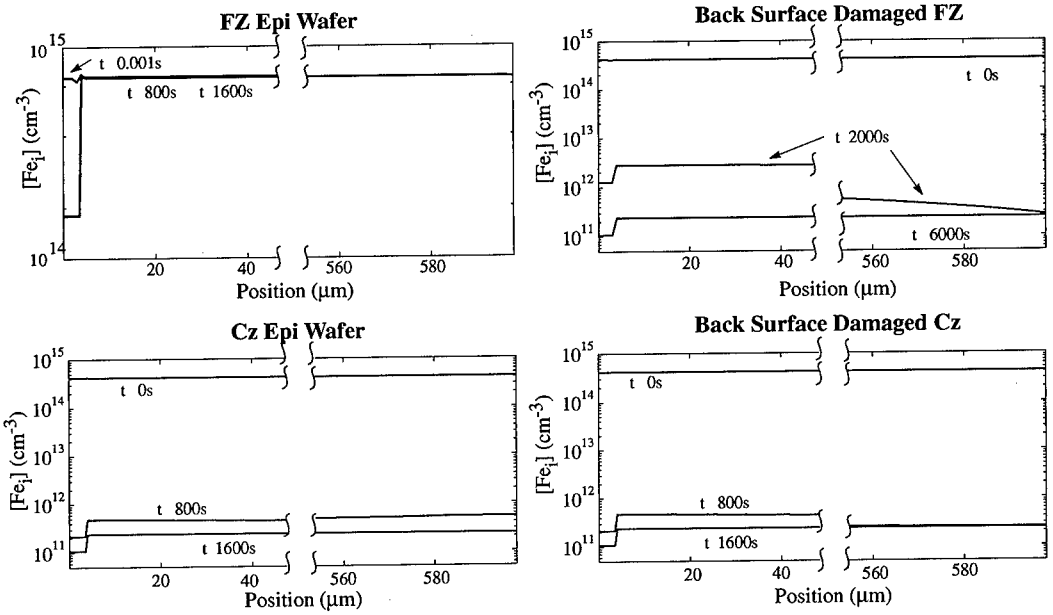


Figure 9: Epi-wafer [Fe_i] profiles after varying treatment times at 700°C after an indiffusion at 1000°C. FZ wafer assumes no bulk internal gettering sites where Cz assumes an internal gettering site density of 10^9 cm^{-3}.

[10] W. Gehlhoff and U. Rehse, Mater. Res. Soc. Symp. Proc., **262**, 507 (1992).
[11] S. Ghatnekar-Nilsson, M. Kleverman, P. Emanuelsson, and H. G. Grimmeiss, Mater. Sci. Forum, **143-147**, 171 (1994).
[12] H. Nakashima, *private communication*.
[13] G. W. Ludwig and H. H. Woodbury, Sol. State Phys., **13**, 223 (1962).
[14] W. Gehlhoff and K. H. Segsa, Phys. Stat. Sol. (b) **115**, 443 (1983).
[15] L. C. Kimerling and J. L. Benton, Physica **116B**, 297 (1983).
[16] H. Nakashima, T. Isobe, Y. Yamamoto, and K. Hashimoto, Jpn. J. Appl. Phys., **27**, 1542 (1988).
[17] W. Wijaranakula, J. Electrochem. Soc., **140**, 275 (1993).
[18] H. Nakashima, T. Sadoh, and T. Tsurushima, Phys. Rev. B **49**, 16983 (1994).
[19] J. J. van Kooten, G. A. Weller, and C. A. J. Ammerlaan, Phys. Rev. B **30**, 4564 (1984).
[20] W. Gehlhoff, K. Irmscher, and U. Rehse, Mater. Sci. Forum, **38-41**, 373 (1989).
[21] K. Irmscher, T. Kind, and W. Gehlhoff, Phys. Rev. B **49**, 7964 (1994).
[22] H. Takahashi, M. Suezawa, and K. Sumino, Mater. Sci. Forum, **83-87**, 155 (1992).
[23] A. Chantre and D. Bois, Phys. Rev. B **31**, 7979 (1985).
[24] W. Gehlhoff, K. Irmscher, and J. Kreissl, Lecture Notes in Phys., **301**, 262 (1988).
[25] A. Chantre and L. C. Kimerling, Mater. Sci. Forum, **10-12**, 387 (1986).
[26] W. Gehlhoff, P. Emanuelsson, P. Omling, and H. G. Grimmeiss, Phys. Rev. B **41**, 8560 (1990).
[27] W. Gehlhoff, P. Emanuelsson, P. Omling, and H. G. Grimmeiss, Phys. Rev. B **47**, 7025 (1993).
[28] T. Y. Tan, R. Gafiteanu, and U. Gösele, Proc. 6th NREL Workshop on the Role of Impurities and Defects in Si Dev. Proc., 110 (1996).
[29] S. H. Ahn, S. Zhao, A. L. Smith, L. L. Chalfoun, H. Nakashima, M. T. Platero, and L. C. Kimerling, Mater. Res. Soc. Symp. Proc., **442**, 169 (1997).
[30] D. Gilles, E. R. Weber, and S. Hahn, Phys. Rev. Lett., **64**, 196 (1990).

Materials Science Forum Vols. 258-263 (1997) pp. 437-442
© 1997 Trans Tech Publications, Switzerland

MÖSSBAUER SPECTROSCOPY OF Fe IN SILICON WITH THE NOVEL LASER -IONIZED $^{57}Mn^{+}$ ION BEAM AT ISOLDE

G. Weyer[a,c], S. Degroote[b], M. Fanciulli[c], V.N. Fedoseyev[d], G. Langouche[b], V.I. Mishin[d], A.-M. Van Bavel[b], A. Vantomme[b], and the ISOLDE Collaboration[a]

[a] PPE Division, CERN, CH-1211 Geneva 23, Switzerland

[b]Institute for Nuclear and Radiation Physics, Leuven University, B-3001 Leuven, Belgium

[c]Institute of Physics and Astronomy, University of Aarhus, DK-8000 Aarhus C, Denmark

[d]Institute of Spectroscopy, Russian Academy of Sciences, 142092 Troitsk, Russia

Keywords: Mössbauer spectroscopy, silicon, deep-level impurities, Fe impurities in silicon

Abstract. Radioactive $^{57}Mn^{+}$ ions have been implanted at the ISOLDE facility into variously doped silicon single crystals to study the lattice location and electronic configuration of ^{57}Fe daughter atoms by ^{57}Fe Mössbauer emission spectroscopy. Two single lines in the spectra are assigned to substitutional Fe_s and interstitial Fe_i, respectively. The isomer shift, i.e. electron density, for Fe_i has been found to depend on the doping of the crystals, this is attributed to the 0/+ band gap state of Fe_i. A model for the creation of both Fe_s and Fe_i in different charge states by the β^-- decay of ion implanted ^{57}Mn is proposed.

Introduction

Over 30 years of experimental efforts to identify the Mössbauer spectra of (differently charged) interstitial and substitutional Fe in silicon, comprising diffusion and implantation of radioactive ^{57}Co parent and stable ^{57}Fe Mössbauer isotopes as well as of Coulomb-excited ^{57m}Fe have led to a generally accepted identification of the spectrum for interstitial Fe, whereas conflicting interpretations still prevail for substitutional Fe [cf. refs.1, 2 and refs. cited there]. Here, we present first results obtained from ion implantations of radioactive $^{57}Mn^{+}$ parent isotopes, an approach, which is shown to have striking advantages over the previous experimental schemes; the results both corroborate and challenge previous interpretations as well as theoretical predictions and are shown to lead to a conceivable (re)interpretation.

Experimental procedures

Laser resonance ionisation has been applied to produce ions of radioactive Mn isotopes obtained from proton-induced fission in a UC_2 target at the ISOLDE on-line mass separator at CERN with a 1 GeV proton beam from the PS-Booster accelerator. The radioactive ion beams were found to have unprecedented intensity ($>10^8$/s for $^{57}Mn^{+}$) and purity owing to the efficiency and chemical selectivity of the laser ionisation scheme [3]. The $^{57}Mn^{+}$ ($T_{1/2}$ = 1.3 m) probe ions were implanted into n- and p-type silicon with an energy of 60 keV at 77 and 297 K to fluences $<10^{12}/cm^2$. A previously described implantation chamber was employed [4]; Mössbauer spectra were measured with an enriched potassiumferrocyanide absorber in transmission geometry. The isomer shifts are given at 297 K relative to α-iron.

Experimental results and discussion

^{57}Fe Mössbauer emission spectra measured at 297 K after the implantation of $^{57}Mn^{+}$ at that temperature into differently doped silicon crystals are shown in Fig. 1. These as well as corres-

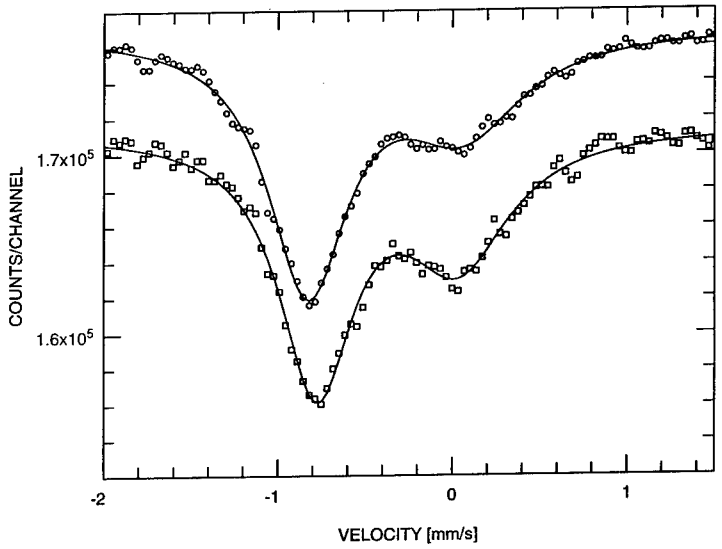


Fig. 1: Mössbauer emission spectra from ^{57}Mn implanted and measured at 297 K in silicon. Upper spectrum: intrinsic, n- and p-type material, lower spectrum (scaled by multiplication with 4): n^{+}-type material.

ponding spectra measured for implantation at 77 K could be analysed consistently in terms of three spectral components: two single lines and a quadrupole-split third line; the fits are indicated in the figure. Although the statistical accuracy of these first spectra is comparable to those previously published for different parent isotopes [cf. refs. 1,2, and 5], the analysis cannot be considered unequivocal. The presence of the two single lines, however, is unambiguous and the presence of a weak third quadrupole-split component (δ = .17(8) mm/s, ΔE_Q = 1.02(8) mm/s and 20% spectral intensity at 297 K) is justified because: 1. it leads to second order Doppler shifts for all lines between 77 and 297 K consistent with theory and 2. a strong annealing effect (within the lifetime of ^{57}Mn, τ = 1.9 min) is found for the quadrupole-split line, its spectral intensity decreases by about a factor of two between 77 and 297 K and leads to a corresponding increase mainly of one of the single lines. This analysis is furthermore in general agreement with that of in-beam spectra obtained from implanted Coulomb-excited ^{57m}Fe and annealing effects observed there for a similar quadrupole-split line at correspondingly higher temperatures due to annealing times of order 100 ns, i.e. the lifetime of the excited ^{57}Fe states [5]. A more detailed comparison of these effects in both experiments will be discussed in a forthcoming paper and the question of the hitherto unknown nature of this quadrupole-split "damage" site [5] will be addressed. Here we concentrate on the comparison and interpretation of the single lines, the (relative) parameters of which were found not to be critically affected by slightly different analysis procedures applied tentatively to the present data. The errors given take the uncertainty of the analysis procedure into account, the relative errors, relevant for the significance of a shift of lines in different spectra, are smaller.

It is noticable in Fig. 1 that the position of the dominating resonance line (at negative velocity, i.e. with a positive isomer shift) is shifted in the two spectra, whereas no such shift is indicated from the analysis for the other single line. The isomer shifts for the dominating line in n^+-Si, which was P doped to $(3\text{-}4)\cdot10^{20}/cm^3$ by ion implantation followed by rapid thermal annealing [6], is determined to δ = .75(2) mm/s, whereas in all other materials (intrinsic or up to $5\cdot10^{18}/cm^3$ B- or P-doped) the same, significantly higher value of δ = .80(2) mm/s is found (these spectra have been added in Fig. 1). The latter value is in reasonable agreement with that of ref. 5 (δ = .84(2) mm/s) for the only single line observed below 600 K, which has been unambiguously attributed to interstitial $Fe_i^{(0)}$ from the diffusional line broadening at higher temperatures [5]. Even when considering the slightly different analysis procedures, this value appears not consistent, however, with the value measured here for n^+-type material. The isomer shift for a second single line, observed only at much higher temperature in ref. 5, is roughly in agreement with the value for the second (weak) single line observed here, δ = -.01(3) mm/s, when the second order Doppler shift (SOD) is taken into account. This value is also in fair agreement with a value of δ = -.07(3) mm/s found for the only single line in the spectra after the implantation of radioactive $^{57}Co^+$ ($T_{1/2}$ = 270 d) precursor ions at 300 K and for 4 K implantations after annealing to 300 K. This line has been suggested to be due to substitutional Fe_s [1]. This assignment will be shown to be corroborated by the present results as discussed below. The concordant assignments of the two single lines found here simultaneously and in either of the above cited references to substitutional Fe_s ($\delta \approx$ -.04 mm/s) and interstitial Fe_i ($\delta \approx$ .8 mm/s) appears also well founded on the basis of theoretical calculations for their isomer shifts which yielded values (at 0 K, refs. 7/8, respectively) of: $\delta(Fe_s)$ = -.06/+.13 mm/s, $\delta(Fe_i^0)$ = .625/.89 mm/s, and $\delta(Fe_i^+)$ = .543/.81 mm/s. These are in sufficiently good agreement with the experimental values (corrected for SOD) to support the site assignments although the deviations amongst them and to the experimental values are considerable. However, given the site assignments of the lines to be correct, the questions arise whether the subtle but significant differences in the Fe_i isomer shifts in differently doped material can be related to Fe_i charge states and whether the presence or absence of interstitial or substitutional lines in the spectra can be understood on the basis of the possibly different implantation behaviour, i.e. resulting lattice location, of the three different radioactive probe atoms applied in the experiments. In this context the following considerations appear important to arrive at an (unified) interpretation of these results.

Firstly, we address questions related to the electronic effects of the nuclear decays, assuming for simplicity an (most likely) interstitial location of the implanted ions; analoguous arguments apply for a substitutional location. The band gap states for interstitial Mn_i and Fe_i, shown schematically in Fig. 2, and their electron/hole capture/emission rates have been determined mainly by deep-level transient spectroscopy [9-11]. Initially, for times < 10^{-12} s after the implantation, the charge states of (interstitially) implanted Mn, Fe, or Co ions can be assumed to be 1+ (if no 2+ states exist in the band gap). Owing to their long halflives both Mn_i and Co_i can generally assume their Fermi-level dependent thermal equilibrium charge states prior to their decay. This question is more critical in the in-beam experiments [5] within the lifetime of the excited nuclear ^{57m}Fe states (≈ 100 ns); in fact, for the n-type material employed ($3\cdot10^{12}$ P/cm^3), even without taking the effect of the radiation damage into account (see below), electron capture is unlikely to occur on the basis of the known rates for the 0/+ Fe_i band gap state [9]. Hence, contrary to the interpretation in ref. 5, we propose that the measured isomer

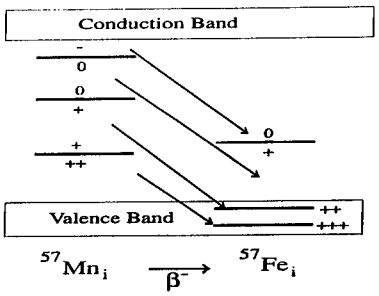


Fig. 2: Schematic band gap levels of interstitial Mn_i and Fe_i; the nuclear decay path from different Mn_i to Fe_i charge states is indicated by arrows.

shift for the single line is that of Fe_i^+ and not Fe_i^0. It is interesting to note that also the diffusion coefficient deduced from the line broadening for Fe_i [5] appears to be in slightly better agreement with that measured for Fe_i^+ than for Fe_i^0 in ref. 12, however, these diffusion coefficients are still a matter of debate [12,13]. Likewise, very high doping levels, i.e. electron capture rates, would be needed in the case of interstitial Co parent probe atoms as the ^{57}Co electron-capture decay is known to leave the ^{57}Fe daughter atoms in highly charged (non-equilibrium) states ($\leq 7+$). Although multiply charged valence band states can be assumed to be filled within times much shorter than the nuclear excited state lifetime [2], $Fe_i^{+/++}$ are likely to result, if a 2+ state should exist as suspected [14], unless the capture rates are comparable to the nuclear lifetime. This appears difficult to achieve if the radiation damage from the implantation is not completely annealed since this damage is known to introduce a locally high density of deep-level states in the band gap. The situation is different for implanted $^{57}Mn^+$ ions, which can assume their equilibrium charge state within the much longer ground state halflife and the subsequent β^-- decay is anticipated to affect the electronic structure much less severely as effectively only the nuclear charge changes by +1. For, e.g., Mn_i^- in equilibrium in n-type material, its decay leads to Fe_i^0, which is likewise the equilibrium charge state (cf. Fig. 2) and correspondingly this applies in intrinsic or moderately doped p-type material for the Fe_i^+ state. Thus, irrespective of whether or not the electron/hole capture rates allow for the Fe equilibrium state(s) to be reached, these are obtained "naturally" in the β^-- decay in favourable cases. These considerations then suggest that the Fe_i^0 state isomer shift has been measured in n^+-type, whereas Fe_i^+ results in all other types of material employed. That the Fe_i^0 state is not observed in n-type material can be attributed to the effect of the radiation damage and the same isomer shift value also for p-type material indicates that no multiply charged band gap states exist for Fe_i in contrast to Mn_i. The isomer shift value for interstitial Fe from the in-beam experiment, reinterpreted here as that for Fe_i^+, and the corresponding present result are, as pointed out above, in reasonable agreement, whereas the value assigned here to Fe_i^0 is significantly lower. This apparent consistency of the above interpretation is spoilt, however, on the one hand, by recent results from in-beam experiments [15] at 300 K for Fe_i in p-type material (B-doped to $10^{20}/cm^3$), yielding an isomer shift of δ = .75(3) mm/s, i.e. coincident with the value assigned here to Fe_i^0. On the other hand, from the calculations cited above an isomer shift difference of $\delta(Fe_i^+) - \delta(Fe_i^0) = -.08$ mm/s is predicted, in agreement with the results of ref. 15, but in disagreement with the results obtained here. It appears meaningless and difficult, however, to point at a most likely physical explanation for these deviations

because, as stated above, the statistical quality of all spectra measured so far does not yet allow for a unambiguous analysis/interpretation. In particular, the presence of a quadrupole-doublet in the analysis of all spectra does affect the position(s) of the single line(s) on the subtle scale considered in this context. In the present case at 297 K its spectral intensity of only 20% makes the position of the dominating single line probably less uncertain than for the in-beam experiments, where the quadrupole-split line dominates (66% intensity), and where furthermore its isomer shift changes apparently more than that of the single line for n- and p-type material [15]. This is not indicated in the analysis of the present data. Also, in the present experiments n^+-type and other type materials were measured alternatingly and the relative line shift was observed both at 77 and 297 K. In conclusion, the question whether or not the changes in the isomer shift of interstitial Fe are in accordance with the theoretical predictions for the 0/+ charge states remains open for the time being; this problem appears accessible, however, to experiments with ^{57}Mn. It should be noted in this context that although the electronic configuration of $Fe_i^{0/+}$ has been studied extensively by electron spin resonance and electron nuclear double resonance [e.g. 16,17] and a remarkable degree of agreement with calculated hyperfine interaction parameters has been concluded [7,18], the isomer shift measured by Mössbauer spectroscopy, which is directly proportional to the total electronic density, would still constitute a valuable, critical test of the theory.

Secondly, we address questions related to the lattice location of the implanted probe atom species. In the in-beam experiments the Fe concentrations are presumably below the solubility limit, whereas both for the Mn and Co implantation experiments this limit is exceeded at least for temperatures < 300 K. However, from the diffusivity of Mn_i [11] this is not expected to lead to clustering or segregation, whereas pair formation with dopant atoms could occur at 297 K in heavily-doped material within its lifetime. For Co implantations [1] the observed annealing effects at ≤ 300 K have been suggested to result from the reaction $Co_i + V \rightarrow Co_s$ with mobile vacancies, V, leading to substitutional Co_s. The analogous reaction with Fe might be indicated at correspondingly higher temperatures in the in-beam experiments. However, as for the present Mn experiments, the annealing reaction rather occurs by the simultaneous annealing of the "damage" site [5], dominant in all experiments at low temperature, where the local impurity surrounding is not known presently. In the Co and Fe cases, on the other hand, the recoil energy imparted on the decaying probe atom is too low to alter its lattice location. This situation is different for ^{57}Mn, where an average recoil energy of $\langle E_R \rangle$ = 20 eV is imparted on the ^{57}Fe nucleus. This may lead to its displacement from both an interstitial or a substitutional parent site (as well as from a "damage" site). Adopting from the in-beam experiments with Fe that - apart from the "damage" site - an interstitial lattice location is also most favourable for Mn in the implantation process, a substitutional relocation due to a replacement collision with the lattice atoms appears possible as the recoil energies exceed the Si displacement energy. From the mass difference between Si and Fe, this process should have a much lower probability, however, than an interstitial relocation. These relocation effects are proposed to be the origin of the 5-8% substitutional Fe location found at 77 K, where a much larger fraction ≈ 50% is located on interstitial sites. The strong annealing of the quadrupole doublet for 297 K implantations leads supposedly also for Mn to an increase mainly of the substitutional site fraction, which attains > 20% spectral intensity, however, also the interstitial fraction increases significantly. This may again be attributed to the recoil effects, which for energies slightly above the displacement threshold of substitutional Fe are expected to result in an interstitial relocation [19]. Thus irrespective of the lattice location of the Mn parent probes the Fe daughter atoms are anticipated to be relocated with considerable probability by the recoil energy involved in the nuclear decay, which leads to the (athermal) simultaneous

creation of both interstitial and substitutional Fe in particular. This lattice location is then maintained within the lifetime of the nuclear excited state of only 140 ns, up to 600 K for Fe_i as inferred from the in-beam experiments. The electronic configuration, on the other hand, is unlikely to be altered in the recoil process as it leads to velocities much smaller than electronic velocities. Subsequently, within the lifetime of the excited state, this appears possible only in highly doped material as argued before. The same isomer shift value determined in the present investigation for substitutional Fe_s in all types of material is therefore consistent with no band gap state of Fe_s as indicated also from theory [20]. The small difference in the isomer shift to that from the Co experiments can again be attributed to the insufficient spectral accuracy.
In summary, the experimental values for the isomer shifts of both interstitial and substitutional Fe in silicon can be considered as well established although the charge state dependence expected for $Fe_i^{0/+}$ has to be investigated further. The deviations of either of the two respective theoretical values appear significant, however, and may be indicative of, e.g., relaxational effects as proposed for Fe_s [14], which are not taken into account in the calculations.

This work was supported by the Belgian Fund for Scientific Research, the Russian Foundation for Basic Research (96-02-18331), INTAS (94-2053) and within the Center for CERN-Related Atomic and Nuclear Physics by the Danisch Natural Science Research Council.

References

1. G. Langouche, Hyp. Int. **72**, 217 (1992)
2. D.L. Williamson, L. Niesen, G. Weyer, R. Sielemann, and G. Langouche, in "Hyperfine Interactions of Defects in Semiconductors", ed. G. Langouche (Elsevier, Amsterdam), p. 1 (1992)
3. V.N. Fedoseyev, K. Bätzner, R. Catherall, A.H.M. Evensen, D. Forkel-Wirth, O.C. Jonsson, E. Kugler, J. Lettry, V.I. Mishin, H.L. Ravn, G. Weyer, and the ISOLDE Collaboration, Nucl. Instr. Meth. **B126**, 88 (1997)
4. G. Weyer, Nucl. Instr. Meth. **186**, 210 (1981)
5. P. Schwalbach, S. Laubach, M. Hartick, E. Kankeleit, B. Keck, M. Menningen, and R. Sielemann, Phys. Rev. Lett. **64**, 1274 (1990)
6. A. Nylandsted Larsen, P. Tidemand-Petersson, G. Weyer, Appl. Phys. Lett. **53**, 755 (1988)
7. M. Lannoo, A. Svane, H. Overhof and H. Katayama-Yoshida, in ref. 2, p. 379
8. J. Kübler, A.E. Kumm, H. Overhof, P. Schwalbach, M. Hartick, E. Kankeleit, B. Keck, L. Wende, and R. Sielemann, Z. Phys. **B92**, 155 (1993)
9. H. Lemke, phys. stat. sol. **(a)76**, 223 (1983)
10. K. Wünstel and P. Wagner, sol. stat. comm. **40**, 215 (1981)
11. H. Nakashima and K. Hashimoto, Mat. Sci. Forum **83-87**, 227 (1992)
12. T. Heiser and A. Mesli, Phys. Rev. Lett. **68**, 978 (1992) and Appl. Phys. Lett. **68**, 1868 (1996)
13. V. Koveshnikov and G. Rozgonyi, Appl. Phys. Lett. **66**, 860 (1995) and **68**, 1879 (1996)
14. S.H. Muller, G.M. Tuynman, E.G. Sieverts, C.A.J. Ammerlaan, Phys. Rev. **B25**, 25 (1982)
15. M. Hartick, P. Schwalbach, M. Ciani, M. Drodt, B. Keck, R. Sielemann, B. Stahl, L. Wende, and E. Kankeleit, Hyp. Int. **84**,317 (1994)
16. W. Gehlhoff and K.H. Segsa, phys. stat. sol. **(a)41**, K21 (1977)
17. J.J. van Kooten, E.G. Sieverts, and C.A.J. Ammerlaan, Phys. Rev. **B37**, 8949 (1988)
18. H. Weihrich and H. Overhof, Phys. Rev. **B54**, 4680 (1996)
19. R. Sielemann, L. Wende, and G. Weyer, Phys. Rev. Lett. **75**, 1542 (1995)
20. F. Beeler, O.K. Andersen, and M. Scheffler, Phys. Rev. **B41**, 1603 (1990)

Materials Science Forum Vols. 258-263 (1997) pp. 443-448
© 1997 Trans Tech Publications, Switzerland

RECOMBINATION-ENHANCED Fe ATOM JUMP OF Fe-ACCEPTOR PAIRS IN Si

Tohru Takahashi and Masashi Suezawa
Institute for Materials Research, Tohoku University, Sendai 980-77, JAPAN

Keywords : Si, Fe, Fe-acceptor pair, recombination-enhanced jump, ESR

Abstract.
We studied the recombination-enhanced jump of Fe atom between the first and second neighbor sites of group III acceptors in Si. Specimens were p-type Si doped with Al, Ga or In around 10^{15} atoms.cm^{-3}. Fe was doped with the vapor method, namely, annealing specimens at high temperature in Fe vapor followed by quenching. Specimens were annealed at 80℃ to generate the first and second neighbor Fe-acceptor pairs. The concentrations of those pairs were measured by ESR measurement at 10K. After annealing at around 150 K under optical excitation, the concentration of the first neighbor pair was decreased and that of the second neighbor pair was increased. Activation energies for the above changes were about 0.11, 0.08 and 0.02 eV for Fe-Al, Fe-Ga and Fe-In pairs, respectively. These are much smaller than that (about 0.8 eV) of thermal annealing alone. The optical threshold energies for the above phenomena corresponded to the energy difference between the bottom of conduction band and the energy levels of group III acceptors.

Introduction.

In this report, we showed our study on the recombination-enhanced jump of Fe atom between the first and second neighbor sites of group III acceptors in Si.

Chantre and Bois [1] found two kinds of donor levels associated with Fe-Al pairs and showed that they corresponded to the stable and metastable configurations of pairs. Kimerling and Benton [2] first showed that Fe in Fe-B pairs in Si showed recombination-enhanced dissociation below room temperature. According to them, Fe-B pairs were dissociated due to minority-carrier injection at temperatures low enough to prevent their thermal dissociation. Nakashima et al.[3] studied the above process in a more detailed manner after illumination or injection of minority carriers with the use of thermally stimulated capacitance (TSCAP) method and found some new energy levels. They interpreted those energy levels to be associated with the second and more distant neighbor pairs of Fe-B. It is, however, difficult to determine the kinds of neighbors by TSCAP method.

In contrast to the capacitance method, the ESR method is a powerful method to determine the kind of neighbors since it makes possible to determine the symmetry of neighbors. In really, Takahashi et al.[4] determined the energy difference between the first and second neighbor pairs of Fe-Al, Fe-Ga and Fe-In from the measurement of generation processes of those pairs by the ESR method. One of the interesting features of these pairs is that configurations of the stable and metastable

states are different; namlely, the first neighbor pair is the stable state for Fe-Al and Fe-Ga pairs while the second neighbor pair is the stable state for Fe-In pair. Hence one of the interesting point to investigate systematically the recombination-enhanced jump of Fe atom in these pairs is the direction of Fe atom jump; namely, whether it is from the stable to metastable state or from the first neighbor site to the second one.

For the study of recombination-enhanced Fe atom jump between the first and second neighbor sites, we applied the ESR method to discriminate clearly the concentrations of the first and second neighbor pairs. A part of this study was published elsewhere[5].

Experiment.

The Si crystals used in this study were grown by the floating-zone grown method. The concentrations of Al, Ga and In were $2x10^{15}$, $5x10^{15}$ and $3x10^{15}$ atoms.cm^{-3}, respectively. We cut out specimens from the above crystals in parallelpiped shape, 3.0x3.5x14.5 mm, the longest side of which was parallel to the [110] direction. After shaping and chemical polishing, we doped specimens with Fe with the vapor method; namely, we sealed specimens in evacuated quartz capsules together with pieces of high-purity Fe wire, annealed them at around 1100℃ and then quenched them in iced water. Fe-acceptor pairs were not detected just after quenching since the quenching rate was too high for such pairs to be generated during quenching. We annealed specimens at 80℃ for 2 hrs to generate Fe-acceptor pairs. After the above annealing, we detected ESR signals of both the first and second neighbor pairs.

We illuminated specimens at around 150 K in a continuous-flow-type liquid helium cryostat. Diffusion of Fe atom is almost impossible at this temperature without optical excitation. To determine the threshold energy for the optical excitation, we illuminated monochromatic light, which was generated with the uses of lenses, a halogen lamp and a grating monochromator. Spectral resolution was about 6 meV at 1.16 eV. In order to determine concentrations of Fe-acceptor pairs at various neighbors, we measured ESR of an X-band spectrometer at 10 K with the use of the above cryostat.

Results.

Figure 1 shows the ESR spectra of the first neighbor (Fig. 1(a)) and the second neighbor (Fig. 1(b)) Fe-Al pairs before (solid line) and after (dotted line) illumination with 1.2 eV photons at 150 K for 30 min. As is clearly shown, the intensity of the first neighbor pair decreases and that of the second one simultaneously increases due to the illumination of light. These results may come from the change of

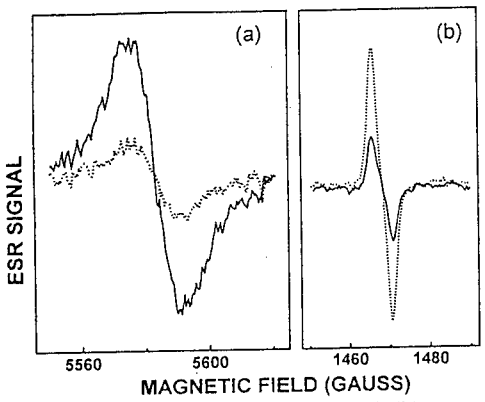


Fig. 1 ESR spectra of the (a) first and (b) second neighbor pairs of Fe-Al before (solid lines) and after (dotted lines) illumination of 1.2 eV photons at 150 K. Spectra were measured at 10 K.

charge states of the first and the second neighbor pairs to ESR inactive and to ESR active ones, respectively. It was clarified that this was not the case since the changes of Fig. 1 were not observed when we illuminated specimens at 10 K. Hence the changes in Fig. 1 are really caused by the change of Fe atom site from the first to the second neighbor site of Al since the electronic transition itself occurs even at low temperature.

Figure 2 shows the dependence of the illumination effect on the ESR intensities of the first and the second neighbor Fe-Ga pairs. Those intensities are proportional to the concentrations of pairs. From this figure, we noticed three features. The first is that the sum of the intensities of the first and the second neighbor pairs is almost constant suggesting that the change of Fe atom sites mainly occures between the first and the second neighbor site of Ga atom. The second is that the time constant for the change of intensity is shorter at higher temperatures, which suggests the contribution of thermal activation for Fe atom jump under the recombination-enhanced condition. Finally, the saturation intensity of the first neighbor pair seems not 0 but some finite value, which suggests the occurrence of Fe atom jump not only from the first to the second neighbor site of Ga but also from the second to the first one.

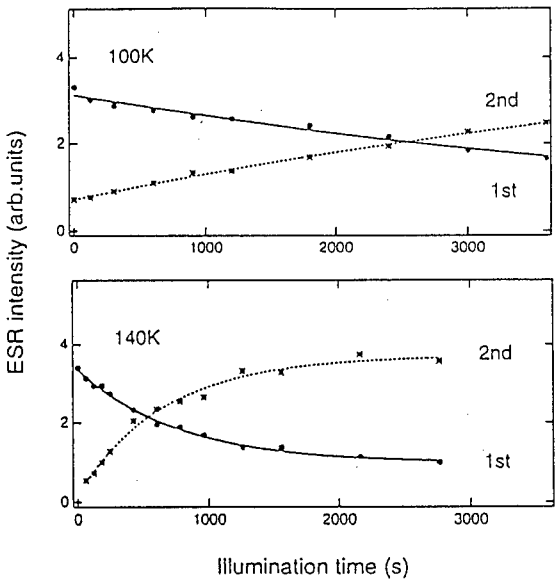


Fig. 2 The dependence of ESR intensities of the first and second neighbor Fe-Ga pairs on the illumination time at various temperatures.

Figure 3 shows the dependence of the illumination effect on the ESR intensities of the first and the second neighbor Fe-In pairs. In contrast to the case of Fe-Ga pair, the intensity of the first neighbor pair was weaker than that of the second neighbor pair. This

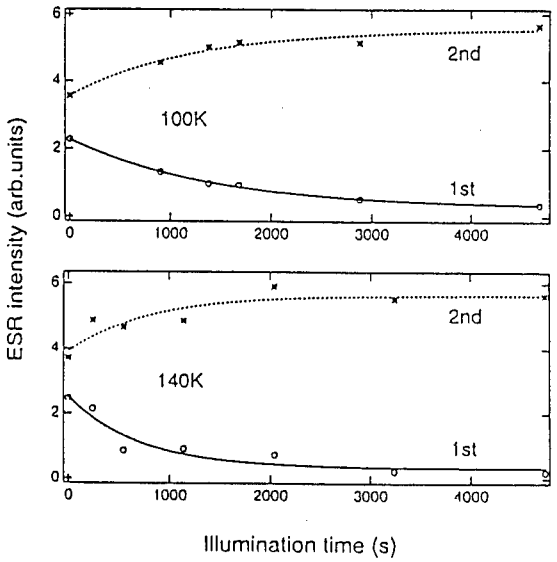


Fig. 3 The dependence of ESR intensities of the first and second neighbor Fe-In pairs on the illumination time at various temperatures.

comes from the fact that the second neighbor pair is the stable state in the case of Fe-In pair as mentioned in the introduction. The effect of illumination on the change of concentrations of neighbors, however, was similar to that of Fe-Ga pair. Hence we conclude that the net direction of Fe atom jump under the recombination- enhanced condition is not from the stable to metastable configurations but from the first to the second neighbor site of acceptor.

From the temperature dependence of time constant for the change of intensities of the first and the second neighbor pairs under illumination, we determined the activation energy for the recombination-enhanced motion. Table 1 shows the results together with the activation energy without optical excitation. As clearly shown in Table 1, the activation energies under optical excitation are much smaller than those under no-illumination.

Table 1 Activation energy under illumination ($E_{illumi.}$) and without illumination (E_0).

Pair	$E_{illumi.}$ (eV)	E_0 (eV)
Fe-Al	0.11	0.82
Fe-Ga	0.08	0.75
Fe-In	0.02	0.69

To determine the threshold energy of optical excitation for the recombination-enhanced Fe atom jump, we measured the dependence of the second neighbor concentration on the energy of illuminated photon. We analysed the data with the Lucovsky model which is known to be applicable for the optical transition of electrons between an energy level in the band gap and a band, for example, the conduction band. Table 2 shows the results together with the differences between the band gap energy and the threshold energies. From Table 2, we know that the threshold energies coincide well with the difference between the bottom of conduction band and acceptor levels of group III acceptors and therefore electrons are excited from ionized acceptors to the conduction band.

Table 2 Threshold energy (E_{th}) for the illumination effect. $E_{ion.}$ is the ground state energy of acceptor impurity.

Pair	E_{th}(eV)	E_g-E_{th} (meV)	$E_{ion.}$ (meV)
Fe-Al	1.095	65	69
Fe-Ga	1.087	73	73
Fe-In	0.99	170	156

Discussion.

Here we discuss about the recombination process of electrons and holes at energy levels of Fe-acceptor pairs, and the efficiency of the recombination energy for the jump of Fe atom .

In the case of Fe-B pair, Nakashima et al. [3] showed that the recombination of electrons and holes took place between the electron captured at the acceptor level of Fe-B pair and the hole captured at the donor level of Fe-B pair. We measured the DLTS spectrum to determine the acceptor level of Fe-Ga pair by injecting minority carriers refering to Brotherton's method [6]. We did not detect the acceptor level probably because the level was too shallow. According to our estimation taking the experimental condition of our DLTS measurement into consideration, the energy level should be nearer than 50 meV to the conduction band. This is probably the case also for Fe-Al and Fe-In pairs. The donor levels of Fe-group III acceptor have been reported already. Table 3 shows the

recombination energies determined from the difference between the acceptor levels, which were assumed to be between 0 and 50 meV, and the donor levels of Fe-group III acceptors.

As shown in Table 3, these energies are slightly larger than the magnitudes of the reduction of thermal activation energy due to the recombination enhancement. In the following, we will discuss about the mechanism of the recombination- enhanced reaction (Fe atom jump in our case) based on Table 3.

Roughly, two theories have so far been proposed to explain the recombination-enhanced reaction. Weeks et al.[7] proposed a model in which they described defect and its surroundings as a strongly coupled oscillators. The defect energized by the recombination dissipates energy to the oscillator and the recombination-enhanced reaction takes place. According to this model, whole of the recombination energy is transfered to the reaction. As shown in Table 3, this is not the case in our experiment. Sumi [8,9] proposed another model, the phonon-kick mechanism, in which he described the recombination-enhanced reaction in terms of chemical reaction coordinate diagram. He introduced a factor g which was the direction cosine between the recombination coordinate and the reaction coordinate. From the application of this theory to our experimental results, the factor g was estimated to be around 0.75. Therefore the recombination energy seems to be effectively used for the reaction.

Table 3 The recombination energy ($E_{recom.}$) defined as the difference between the acceptor level and the donor level of Fe-Acceptor pair. "Fraction" is defined as $(E_0-E_{illumi})/E_{recom.}$.

Pair	E_{recom}(eV)	E_0-E_{illumi}(eV)	Fraction
Fe-Al	0.91~0.96	0.71	0.78~0.74
Fe-Ga	0.88~0.93	0.67	0.76~0.72
Fe-In	0.84~0.89	0.67	0.80~0.75

The recombination-enhanced Fe atom jump occurs both directions between the first to the second neighbor site of acceptor as mentioned already. In really, the activation energies were the same for both directions. In such case, the saturation value after long duration of the recombination-enhanced motion is determined by the net jump rate, namely, number of atomic jump path from the first to the second neighbor site and vice versa of the acceptor atom, and populations at both sites, not by the stability, namely, the stable and metastable state. From the geometrical consideration, the ratio of the path number from the first to the second and vice versa are 3/4 and 2/4, respectively. Our experimental results were different from this value. We have not succeeded to explain the reason for this discrepancy.

Conclusions.

We studied the recombination-enhanced Fe atom jump between the first and second neighbor sites of group III acceptors, such as Al, Ga and In in Si and obtained following conclusions.

The activation energies for the Fe atom jump were much reduced, by about 0.66 eV, by the illumination. The optical threshold energy corresponded to the excitation of electrons from the acceptor levels of group III acceptors to the conduction band. About 75 % of the recombination

energy was supplied for the Fe atom jump.

References.

1. A. Chantre and D. Bois, Phys. Rev. **B31**,7979(1985)
2. L.C. Kimerling and J.L. Benton, Physica **B116**, 297(1983)
3. H. Nakashima, T. Sadoh and T. Tsurushima, Phys. Rev. **B49**, 16983(1994)
4. H. Takahashi, M. Suezawa and K. Sumino, Mater. Sci. Forum **83-87**, 155(1992)
5. S. Sakauchi, M. Suezawa and K. Sumino, J. Appl. Phys. **80**, 6198(1996)
6. S.D. Brotherton, J. Appl. Phys. **55**, 3636(1984)
6. J.D. Weeks, J.C. Tully and L.C. Kimerling, Phys. Rev. **B12**, 3286(1975)
7. H. Sumi, Physica **117B-118B**, 197(1983)
8. H. Sumi, Phys. Rev. **B29**, 4616(1984)

Materials Science Forum Vols. 258-263 (1997) pp. 449-454
© 1997 Trans Tech Publications, Switzerland

PRECIPITATION OF IRON IN FZ AND CZ SILICON

H. Hieslmair, A. A. Istratov, S. A. McHugo[‡], C. Flink, E. R. Weber

Materials Science Dept. University of California at Berkeley, Berkeley, CA, 94720 USA

[‡]Lawrence Berkeley National Laboratories, Berkeley, CA, 94720 USA

Keywords : iron, precipitation, Ham's Law

Abstract. Iron was precipitated in FZ silicon and Cz silicon with varying densities of oxygen precipitates, including Cz material with no oxygen precipitates. Computer simulations based on Ham's law were fitted to experimental data to obtain iron precipitation site densities. Iron precipitate densities were found to decrease with increasing precipitation anneal temperatures until ≈500°C, yielding a trap energy of 0.49±0.14 eV. Above 500°C, the precipitation site density remained approximately constant. Iron precipitate site densities increased with oxygen precipitate densities, and correlated with oxygen precipitate surface areas. Iron precipitate site densities in FZ material were found to be higher than in Cz with no oxygen precipitates. We suggest that vacancy agglomerations may be the dominant trapping defect in FZ.

Introduction.

Transition metal impurities in silicon such as Cu, Ni, and Fe are known to reduce device yields, and in photovoltaic (PV) devices, conversion efficiencies. In the integrated circuit (IC) industry, the direct introduction of metals from the melt during crystal growth is not probable if the necessary precautions are taken [1]. The contamination frequently occurs during cutting and polishing of wafers and processing steps during device fabrication. In the PV industry, cheaper starting materials and lower cost processes introduce significant amounts of metal impurities into the bulk material. Precipitation of these metals during cooling from high temperatures is an important process in both IC and PV industries. In the IC industry, oxygen precipitates are intentionally created in the bulk of the wafer in order to create precipitation sites for the metal impurities. This technique getters impurities away from the device region on the surface, improving device yields. In the PV industry, the stability of the metal precipitates in the bulk appears to hinder external gettering techniques [2,3].

This study focuses on the precipitation behavior of iron in float zone (FZ) and various Cz silicon materials. Iron diffuses more slowly in silicon than Cu or Ni and can be trapped in interstitial sites by quenching. The mobility of iron at room temperature, while low, is still large enough that, within 24 hours, iron has diffused to acceptors such as noron to form Fe-acceptor pairs. These pairs form a trap level at Ev+0.1eV which can be easily measured with deep level transient spectroscopy (DLTS). Iron precipitation has been studied by several researchers. Gilles et. al. [4] precipitated iron at low temperatures and showed that iron precipitated faster in material with higher oxygen precipitate density. Shen et. al. [5,6] observed in Cz and FZ silicon, greater electron beam induced current (EBIC) contrasts of dislocations when slowly cooled rather than quickly cooled in the presence of iron. He concluded that the limiting factor of iron precipitation in this case was the slow diffusion of iron to the dislocations.

This study continues the work of Gilles and Weber [4] by using precipitation kinetics to analyze iron precipitation. Using a better implementation of Ham's law, precipitate site densities are

directly obtained and higher precipitation temperatures are included. Larger number of samples guarantee greater accuracy of the results. The term precipitation is used to describe all aggregation of interstitial iron out of a supersaturated solution.

Procedure

Six types of silicon materials were used in this study as described in Table 1. All samples were boron doped. The FZ doping was $2x10^{15}$ B/cm^3 while the Cz wafers ranged from $4x10^{14}$ to $1x10^{15}$ B/cm^3. The Cz N material was heat treated to dissolve any existing oxygen nuclei, while the other samples were heat treated to form oxygen precipitates in the concentrations listed. The samples were cleaved from the center regions of the 150mm wafers and intentionally contaminated with iron at high temperatures, followed by a quench in ethylene glycol (cooling rate ≈ 1000K/s). The samples were cleaned and then, to allow the iron to precipitate, annealed at various temperatures and times followed by a second quench. More than 40μm of silicon were etched from the surface of the samples before the remaining dissolved iron concentrations were measured by DLTS. The concentrations of remaining iron were then plotted as a function of time and fitted by computer simulations based on Ham's law as discussed below.

Table I

Material	[Oxy precipitates]
FZ	none
Cz N	none
Cz 8	$2x10^8$ cm^{-3}
Cz 9	$2x10^9$ cm^{-3}

Ham's Law

The precipitation rate of an impurity depends on the number of precipitation sites, n, and the effective precipitate radii, r_o. This was described by Ham with the following equation for spherical precipitates for fixed radii and for growing radii after precipitation of over 50% of the solute[7]:

$$C - C_{eq} = (C_o - C_{eq})e^{-t/\tau} \qquad (1)$$

where C_{eq} is the equilibrium concentration at the annealing temperature, Co is the initial interstitial impurity concentration, C is the time dependent concentration and,

$$1/\tau = 3Dnr_o \qquad (2)$$

Here D refers to the temperature dependent diffusivity and $1/\tau$ is the precipitation rate.

The nr_o product can thus be measured by how quickly the supersaturated impurity concentration drops. In previous publications [4], $1/\tau$ was directly derived from the slope of a logarithmic plot of the experimental data points. This is based on the assumption that the precipitate radius does not change during the precipitation process. In fact, the solute precipitation rate increases as the precipitate grows, and does not fit a simple exponential. The slow precipitation rate during the beginning of the precipitation is primarily a result of the small precipitate surface area on to which the solute could be absorbed. Growth of the precipitate makes more surface area available, increasing the precipitation rate. Once more than 50% of the impurities have precipitated, the precipitate radius does not increase significantly, and the precipitation rate approximately follows Eq. (1).

The nucleation site density can be calculated from the conservation of mass, i.e.

$$\Delta C = \frac{4}{3}\pi r_o^3 n\Omega \qquad (3)$$

and Ham's law (Eq. (2)), by,

$$n = \left(\frac{3}{4}\pi \cdot \frac{1}{(3D\tau)^3} \cdot \frac{\Omega}{\Delta C} \right)^{1/2} \quad (4)$$

where ΔC is the drop of interstitial iron concentration, and Ω is the density of iron in the precipitate. Implicit in Eq. (4) is that τ should be obtained from data measured after more than 50% of the solute has precipitated and the precipitation rate is approximately exponential. To fit the whole precipitation curve, the fixed radius approximations, Equations 1 and 2, can be used in an iterative calculation in which the radius, r_o, is continually adjusted as the precipitate grows. In such a manner, even the early precipitation can be modeled and values for n can be obtained.

Computer Simulations

To obtain a more accurate precipitate density, an iterative finite differences computer simulation was used to fit the precipitation data. The following equations, slightly modified from Ham's original formulation, were used in the simulation.

$$\Delta C(\Delta t) = \left[C_{eq}(T) - C_o(t) \right] \left(1 - e^{-\Delta t/\tau} \right) \quad (5)$$

and

$$\Delta C = \frac{4}{3}\pi \left(r_1^3 - r_0^3 \right) n\Omega \quad (6)$$

where $C_{eq}(T)$ is the temperature dependent equilibrium solubility; $C_o(t)$ is the impurity concentrations at the start of the time step, Δt; ΔC is the change in dissolved impurity concentration during the time step Δt; Ω is the volume density of the impurity (iron) in the precipitate (iron silicide); and r_0 and r_1 are the precipitate radii at the beginning and end of the time step, respectively. For $FeSi_2$, the density of iron is roughly 24 Fe/nm^3. Equation (6) is used to determine the incremental change in precipitate radius, $\Delta r = r_1 - r_0$, from changes in concentration, ΔC. It was assumed that all the metal was dissolved in the beginning of the simulation. Small steps in time were simulated. After each step a drop in solute concentration, ΔC, was calculated from Ham's law, and the precipitate radius was increased by an appropriate amount. This approach should yield more accurate results since the radius, and thus nr_o, is incrementally revised as precipitation continues. Numerous simulations were run and the precipitation site density was varied to obtain a fit to the experimental data points as shown in Fig. 1.

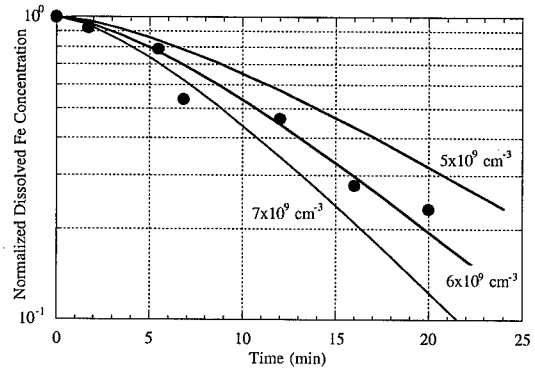


Figure 1: Precipitation rates of iron in Cz with no oxygen precipitates at 650°C. The lines are computer simulations for different iron precipitate site densities.

Results and Discussion

Precipitate site densities were determined from computer simulations as shown in Figure 1. A range of site densities was chosen rather than a single value since variances were observed in the samples with oxygen precipitates. For the temperature range of 235 to 840°C, iron nucleation site densities were measured for the FZ and the Cz 8 materials and are shown in Figure 2.

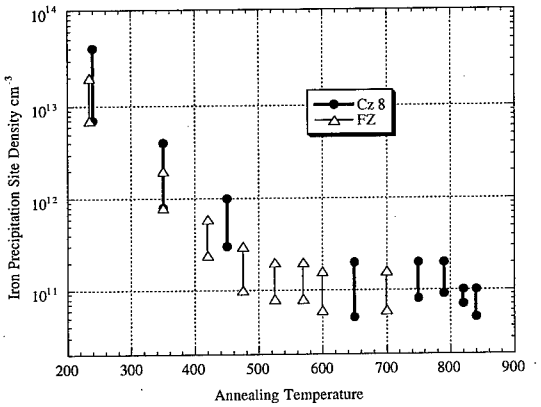


Figure 2: Iron precipitation site densities for various temperatures in FZ and Cz 8 material with approximately $2x10^8$ cm^{-3} oxygen precipitates.

The increase in precipitation site densities at lower temperatures, <500°C, can be understood in terms of nucleation at trapping sites, such as vacancy clusters. Since dissolved iron is detected as FeB pairs by DLTS, iron atoms need only be trapped as clusters or complexes to result in a reduction of dissolved iron. The first step in this process is a small nucleus such as an iron complex. The density of iron occupying such a trap or complex and forming a nuclei, can simply be described as,

$$N_{precip} = N_o \, e^{\Delta E/kT} \qquad (7)$$

where N_{precip} is the concentration of iron precipitates, and N_o is proportional to the dissolved iron concentration and the trap density. Plotting N_{precip} as a function of 1/kT, an effective binding energy of the trap ΔE was estimated to be 0.49±0.14 eV. After this complex/cluster forms, further precipitation can continue as the iron atoms diffuse to these sites. If the concentration of trap sites is similar or greater than the concentration of iron sites, then the precipitation rate is essentially the rate at which iron diffuses to a trap. Since there is no growth in radius of the precipitate, the resulting precipitation curve is a simple exponential as Ham's law would predict. This is observed in samples with high nucleation site densities.

At higher temperatures, in the range of 500°C up to the iron drive-in temperature, a temperature dependence of site density on annealing temperature is difficult to resolve with the present data. The data do show that numerous precipitation sites exist even at high temperatures, indicating that the binding energy of iron to this trap is high and thus they should not be easily dissolved. Lower estimates for this barrier put ΔE >1eV.

A low temperature and a medium temperature annealing at 240°C at 650°C, respectively, were performed on all types of material and the resulting precipitate site densities are shown in Figure 3. Obviously, there is a strong correlation between precipitate site density and oxygen precipitate concentration. This was also observed by Gilles et. al. [4] although he did not explicitly obtain

precipitate site densities. The Cz silicon with no oxygen precipitates showed the lowest precipitate site density. In each type of material, it is observed that the nucleation site density increases as the annealing temperature is reduced below ≈500°C. Thus in each case, the site density at 240°C is greater than at 650°C. Annealing at various temperatures above 500°C yields an approximately constant precipitate site density (see Figure 2).

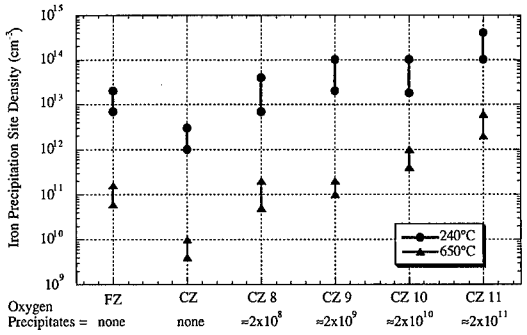


Figure 3: Iron nucleation site densities at 240°C and 650°C for various materials (FZ was annealed at 238°C & 600°C).

Among the different materials, the lowest precipitation site density was in the Cz material with no oxygen precipitates, while the highest site density occurred in the Cz material with $2x10^{11}$ cm^{-3} oxygen precipitates. Such high densities of oxygen precipitates provide large surface areas and high concentrations of associated structural defects, punched out dislocations or stacking faults. In the Cz material with $2x10^{11}$ cm^{-3} oxygen precipitates (smallest precipitates), each precipitate generates approximately ≈15 sites for iron precipitation at 650°C. In the Cz material with $2x10^{8}$ cm^{-3} oxygen precipitates, each precipitate provides ≈400 sites for iron precipitation. The number of iron precipitation sites per oxygen precipitate seems to correlate with the surface area of the oxygen precipitate as shown in Figure 4. Whether iron is precipitating at the silicon/oxide interface is uncertain. Falster et. al. [8] proposed that nickel, which forms a silicon rich silicide of $NiSi_2$, readily nucleates at the silicon/oxide precipitate interface, generates dislocations, and then also precipitates on the dislocations. Cu and Pd, which form metal rich silicides, do not nucleate at silicon/oxide surfaces. It seems likely therefore that iron also nucleates at the silicon/oxide interfaces, resulting in the observed correlation.

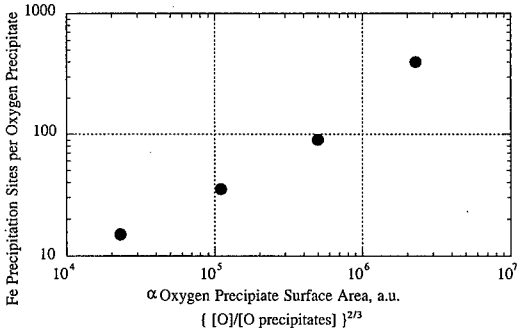


Figure 4: Iron precipitation sites per oxygen precipitate vs oxygen precipitate surface area.

However, if there are no oxygen precipitates present, as in either FZ or Cz with no precipitates, there are still iron nucleation sites present. It is uncertain what defects or impurities are present at levels of $5x10^9$ cm^{-3} (Cz with no precipitates). It has been recently shown from platinum diffusion studies, that in FZ silicon vacancies can exist in concentrations of up to 10^{14} cm^{-3} at high temperatures [9]. After the iron contamination at high temperatures, a quench is used to prevent interstitial iron from precipitating. This quench may also cause these vacancies to cluster, forming vacancy complexes which act as iron nucleation sites. Recent theoretical studies [10] indicate that vacancies can agglomerate to form a ring of six vacancies which is an extremely stable, non-electrically active defect. These could act as nucleation or trapping sites for iron, resulting in the high site densities observed in FZ silicon. The platinum diffusion studies did not detect such high concentrations of vacancies in the Cz materials, which explains the lower site densities detected in this study in the Cz material with no oxygen precipitates.

Conclusions

Iron was precipitated in various silicon materials. A numerical method based on Ham's law was used to obtain precipitation site densities from experimental data. A decrease in iron precipitate densities was observed as precipitation anneal temperatures were increased to approximately 500°C, from which a binding energy of 0.49±0.14 eV was obtained. At temperatures greater than 500°C the iron nucleation site density remains approximately constant even at high temperatures, indicating a high binding energy to defects. Iron precipitate site densities were observed to increase with oxygen precipitate densities and correlated with oxygen precipitate surface energy. FZ silicon was observed to contain greater iron precipitate densities than Cz with no oxygen precipitates. We speculate that vacancy agglomerations are the dominant trapping/nucleation sites in FZ.

Acknowledgments

The authors would like to thank R. Falster for valuable discusions and for supplying the Cz materials. This work was performed under NREL Subcontract No. XD-2-11004-3.

References

1. H.R.Huff, in: "Semiconductor silicon: Concise Encyclopedia of Semiconducting materials and Related Technologies" (ed. S.Mahajan and L.C.Kimerling), Pergamon Press, 1992.
2. S. A. McHugo, H. Hieslmair and E. R. Weber, *Appl. Phys. A* **64**, 1,(1997).
3. H. Hieslmair, S. A. McHugo and E. R. Weber, 1995 NREL PV Review, AIP Conf. Proc. **353**, 519 (1995)
4. D. Gilles, E. R. Weber and S. Hahn, Phys. Rev. Lett. **64**, 196-9,(1990).
5. B. Shen, T. Sekiguchi, R. Zhang, Y. Shi, Y. D. Zheng and K. Sumino, *phys. stat. sol. (a)*, **155**, 321 (1996).
6. B. Shen, T. Sekiguchi, R. Zhang, Y. Shi, H. Shi and K. Yang, *Jpn. J. Appl. Phys.* **35**, 3301 (1996).
7. F. S. Ham, *J. Phys. Chem. Solids* **6**, 335 (1958).
8. R. Falster, Z. Laczik, G. R. Booker, A. R. Bhatti and P. Török, in Defect Engineering in Semiconductor Growth, Processing and Device Technology, San Francisco, CA, USA, Materials Research Society, (1992), p. 945
9. M. Jacob, P. Pichler, H. Ryssel and R. Falster, J. Appl. Phys. **82**, 182 (1997)
10. J. L. Hastings, S. K. Estreicher, P.A. Fedders, "Vacancy Aggregates in Silicon", in this conference

Materials Science Forum Vols. 258-263 (1997) pp. 455-460
© 1997 Trans Tech Publications, Switzerland

The Orthorhombic FeIn Complex in Silicon

Per Tidlund and Mats Kleverman
Solid State Physics, Department of Physics
University of Lund, Box 118, S-221 00 LUND

Keywords: Si, Fe, In, FTIR, Zeeman, and uniaxial stress.

ABSTRACT

The excitation spectrum of the neutral orthorhombic (C_{2v}) FeIn center in silicon has been studied by Zeeman and uniaxial stress Fourier Transmission Infrared Spectroscopy. The electronic structure of the ground and excited state is shown to be similar, i.e., both comprise two nearby Kramers doublets derived from a $^4B_1$ term split by spin-orbit interaction with a $^4B_2$ term. The crystal-field and spin-orbit parameters for the ground state are close to those previously determined for the orthorhombic FeIn center by electron paramagnetic resonance which shows that the same center is studied with both techniques. The electronic parameters for the ground and excited state are almost identical indicating that the final state structure is exclusively determined by the Fe ion. The excitation lines do not split under uniaxial stress which shows that the stress induced energy shifts for the initial and the final states are equal. The Zeeman and stress results thus strongly indicate that the excitation lines are due to internal "d" transitions at the interstitial Fe ion.

INTRODUCTION

The interstitial impurity iron in silicon easily forms pair complexes with the group-III acceptors. The electronic structure of their ground states has mainly been studied by Electron Paramagnetic Resonance (EPR) and is reasonably well understood for all pairs[1]. According to the commonly accepted model for the neutral complexes, the negatively charged group-III acceptor resides on a substitutional site whereas the positively charged Fe impurity occupies a nearby interstitial position. The long-range Coulomb interaction guides the mobile Fe_i^+ ion to the inert group-III acceptor and complexing occurs even at room temperature due to the Fe_i^+ ions high diffusivity at low temperatures. The pairs can be found in two different geometrical configurations with Fe on nearest (trigonal C_{3v}) or next-nearest neighbor (orthorhombic C_{2v}) interstitial position. The FeB center is an exception from this rule since only the trigonal center has been observed so far[1, 2, 3]. The excitation spectra for the FeB and the FeIn pairs in silicon have recently been observed[4, 5]. The excitation spectra for the neutral orthorhombic and trigonal FeIn centers consist of several sharp lines and are denoted the O and T spectrum, respectively. In Fig. 1, typical spectra for the FeIn C_{2v} center measured at T=1.7 K and at 13.1 K are presented. For each temperature, the upper and lower curve shows the measured and calculated spectrum (see further below), respectively. A schematic figure showing the energy-level structure at zero magnetic field is shown in Fig. 3 and our notation for the various transitions is presented. The energy positions for the four transitions (at B=0 T) are indicated by a set of four vertical bars below the calculated spectra. The calculated relative intensity for each transition is also presented and visualized by the height of the bars below the calculated curves.

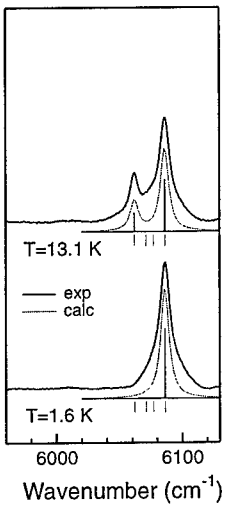


Fig. 1. Transmission spectra (B=0) of iron-doped, originally p-type (In 2 Ωcm) silicon measured at T=1.6 K and T=13.1 K. The experimentally obtained excitation spectra (upper curves) are compared with the calculated ones for each temperature. The possible four transition energies are indicated below each spectrum as well as the calculated relative intensity for each transition.

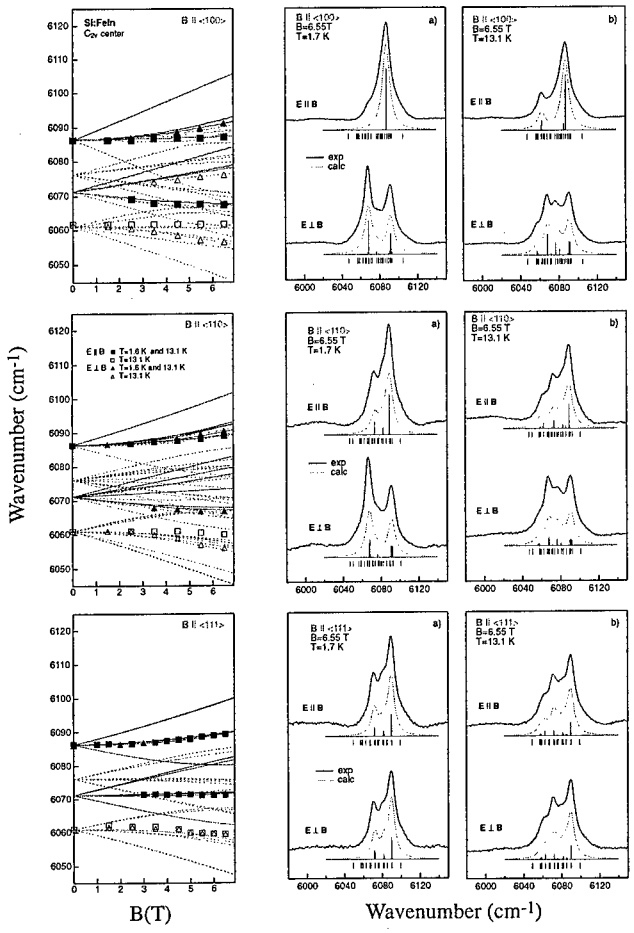


Fig. 2. The Zeeman splitting observed for the excitation spectrum of the orthorhombic FeIn center in silicon with the B-field parallel to <100>, <110>, and <111>. The energy positions for the Zeeman lines detected at T=1.6 and 13.1 K are indicated by full markers and those detected exclusively at T=13.1 K are presented by open markers. The lines are obtained from a calculation using the model described in the text. Solid lines indicate transitions from the lowest Zeeman component in the initial state and dash lines show the expected splitting behavior for transitions from the excited states in the manifold of initial states.

a) and b). The measured and calculated Zeeman excitation spectra for different polarizations. The spectra were measured at B=6.554 T at two different temperatures, T=1.6 and 13.1 K. For each polarization, the upper curve is the measured spectrum and the lower curve is the calculated spectrum. The energy positions for all possible transitions are indicated by vertical markers. Below the calculated intensity curves the relative intensity for each possible transition is indicated, for clarity.

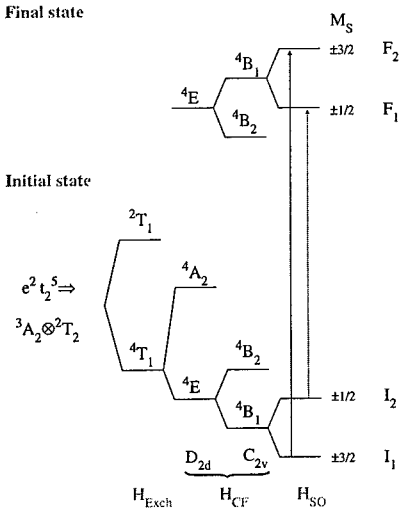


Fig. 3. Schematic picture showing the energy level structure for the initial and final states. See text for details.

At higher temperatures, the line spectrum for the orthorhombic center contains two lines at 6086.2 cm^{-1} and at 6061.7 cm^{-1} and are denoted O_g and O_e, respectively. At lower temperatures, only the O_g line is observed. A comparison between the two spectra measured at the two different temperatures thus reveals a clear thermalization behavior and it may be concluded that the O_g line is due to excitations from the ground state whereas the O_e line is due to transitions from an excited state about 10.5 cm^{-1} above the ground state [2, 5]. Surprisingly, this ground-state splitting is not reflected as the observed energy difference between the O_g and O_e of about 24.5 cm^{-1}. It was therefore previously suggested that the excitations take place from two different initial states to two final states (see Fig. 3) and that only one of the final states could be reached from each of the initial states [5]. Strong selection rules must therefore prevail and an energy splitting between the two final states was estimated to be about 14.0 cm^{-1}.

We will in this paper report results from a detailed Zeeman study on the excitation spectrum of the orthorhombic FeIn center. It will be shown that the ground-state has identical properties as those obtained from previous EPR studies on the orthorhombic FeIn center[2] which unambiguously shows that the same defect is studied in this work. The electronic structure of the final states will be identified and discussed in detail in terms of total spin and orbital symmetry. It will be shown that the strong optical selection rules governing the excitation spectrum are due to the fact that the total spin S and its projection M_S are good quantum numbers for both the initial and final state. A detailed general model will be proposed that gives a perfect agreement between the experimental Zeeman splitting pattern as well as the Zeeman lines polarization properties.

RESULTS AND DISCUSSION

In Fig. 2, the experimentally observed Zeeman splitting of the excitation lines for the orthorhombic FeIn is presented. The full and dashed lines show the calculated Zeeman splitting according to our model that will be discussed below. Data obtained from measurements at two different temperatures are shown and clear thermalization effects are thus observed. Transitions from the ground state are denoted O_g (I_1-F_2) and O_g' (I_1-F_1) and those from the first excited state are denoted O_e (I_2-F_1) and O_e' (I_2-F_2) (see Figs. 1 and 2). The full lines correspond to excitations from the lowest Zeeman state in the ground-state manifold and the dashed lines correspond to transitions from the upper Zeeman component in the ground state as well as all Zeeman components for the first excited initial state I_2. As is readily seen, a good agreement between the experimental points and the calculated energies was obtained. In Figs. 2 a) and b), the observed polarization properties of the Zeeman lines are presented for the magnetic field parallel to the <100> direction (B=6.55 T) and at two different sample temperatures. Below each experimental spectrum, the calculated spectrum is presented as well as all possible transition energies and their corresponding relative intensity. As is readily seen, a perfect agreement between the calculated spectra and the measured ones was obtained which gives additional strong support for our model that will be discussed below. It is interesting to note that out of many possible transitions only a few will have enough intensity to be experimentally observed.

We will here first discuss the established model for the initial state of the neutral FeIn C_{2v} center. The electronic structure for ground-state is mainly derived from the Fe_i^+ ion since In^-, in a full shell configuration, is inert. In this simplified model, the presence by indium therefore only gives rise to a crystal field that perturbs the energy level structure of the Fe_i^+ ion[1]. The starting point for the discussion is the Fe_i^+ $^4T_1$ ground-state term derived mainly from the $t_2^5 e^2$ configuration. The two e electrons combine to the high-spin $^3A_2$ state and exchange coupling with the $^2T_2$ (t_2^5) state results in the Hund's rule ground state term $^4T_1$ as well as in a $^2T_1$ term. The t_2 one-particle orbital has an effective angular momentum l'=1 and all matrix elements of the true angular momentum **l** between the t_2 states is proportional to those for the effective one. It has been shown previously that $g_L \approx -0.3$ which reflects the hybridization between the Fe d orbitals and the Si host states[2]. Similarly, the T_1 many-particle orbital has an effective angular momentum L'=1 and the same constant of proportionality, g_L, with respect to the true angular momentum. In describing the electronic structure of the neutral FeIn C_{2v} center we will start with tetrahedral symmetry, T_d, and discuss the various perturbations, i.e., low symmetry crystal fields and spin-orbit (s-o) interaction according to their strength. The axial field lowers the symmetry to D_{2d} and the $^4T_1$ term splits into a lower ^4E and an upper $^4A_1$ term. The rhombic part of the crystal-field is considerably smaller but splits ^4E into a $^4B_1$ and a $^4B_2$ term with $^4B_1$ at lowest energy. In C_{2v} symmetry, the effective s-o operator $L_z'S_z$ is in the $^4B_1$ and $^4B_2$ basis off-diagonal in B_1 and B_2 but diagonal in M_S. The s-o interaction thus splits each $^4\Gamma$ terms into two doublets with $M_S=\pm 1/2$ and $M_S=\pm 3/2$, respectively. M_S is thus a good quantum number as long as the interaction with the $^4A_1$ term can be neglected. This is indeed the case for the ground state for which the s-o interaction is considerably smaller than the axial field. The s-o interaction mixes B_1 and B_2 but for the two lowest doublets the B_1 character dominates by far over the B_2 character. The states in the ground-state manifold are therefore denoted $\pm 3/2(^4B_1)$, $\pm 1/2(^4B_1)$, $\pm 1/2(^4B_2)$, and $\pm 3/2(^4B_2)$ and the two initial states that takes part in the transitions are $\pm 3/2(^4B_1)$ and $\pm 1/2(^4B_1)$ and are denoted I_1 and I_2 in Fig. 3, respectively.

It is clear from both our previous work[5] and the results in Figs. 1 - 2 that two nearby final states (F_1 and F_2, see Fig. 3) are involved in the optical transitions and that the transitions I_1-F_1 and I_2-F_2 are forbidden. The fact that M_S is a good quantum number in the initial states may facilitate an explanation for the strong selection rules observed. It therefore seems reasonable to assume that M_S in the final states is a good quantum number and that the two final states observed originate from a $^4\Gamma$ term split by the s-o interaction. Employing the same arguments as were used for the initial state, the so-interaction must involve another term $^4\Gamma'$. It is easy to show that only one pair, $^4B_1$ - $^4B_2$, of final state terms fulfills all our requirements. Electric-dipole transitions from B_1 to B_2 are forbidden and the good quantum number M_S ensures that only one of the two $^4B_1$ final state doublets can be reached from each of the two initial states.

The manifold of final states thus shows close similarity with the electronic structure of the initial state. It is therefore reasonable to assume that the $^4B_1$ - $^4B_2$ final state terms are derived from a ^4E term in D_{2d} symmetry split by the orthorhombic crystal field. In analogy with the initial state structure we may ask what term in T_d symmetry gives rise to a ^4E term in D_{2d} symmetry?

The only possibility is that the ^4E term is derived from a $^4T_1$ or a $^4T_2$ term in T_d symmetry. The calculations of the Zeeman splitting and of the polarization rules were carried out by numerically solving the total hamiltonian for different magnetic fields. The various hamiltonian matrices were constructed by employing tensor product using the angular-momentum matrices. In this way, no Clebsch-Gordan coefficients were needed which simplified the construction of the 18 by 18 matrices. The initial state is derived from the $t_2^5e^2$ configuration. The high-spin ground state term is obtained when the two e electrons form a $^3A_2$ spin triplet and exchange coupled to the $^2t_2$ state leading to a $^2T_1$ and a $^4T_1$ term. The exchange parameter J was chosen to be large enough to separate the $^2T_1$ and a $^4T_1$ term and its exact value is of no further interest in this work. δ_{ax} and δ_{rh} are the strength of the axial and orthorhombic crystal fields, respectively, The effective spin-orbit parameter is $\eta=-g_L\xi$ where ξ is expected to be close to the free iron one-electron spin-orbit constant of 345 cm^{-1}. The parameters used in our fitting are presented in Table I.

TABLE I. The parameters used in the calculations and the calculated g-values (g_x, g_y, and g_z, where x,y || <110> and z || <001>, and using a spin-1/2 formalism, see Ref. 2) for the orthorhombic FeIn center. All energies are in cm^{-1}.

State	J	ξ	δ_{ax}	δ_{rh}	g_L	g_x	g_y	g_z
Initial	1900	311.7	1831	95	-0.3			
$\pm3/2(^4B_1)$						0.31	0.33	6.26
$\pm1/2(^4B_1)$						4.26	3.64	2.08
Final	1900	375	1831	-96	-0.3			
$\pm3/2(^4B_1)$						0.16	0.16	5.70
$\pm1/2(^4B_1)$						3.77	4.10	1.88

In constructing the final states we have used the same approach as for the initial states which considerably simplified our calculations. We are basically studying transitions between Zeeman levels of two isolated ^4E terms in D_{2d} symmetry. The further splitting to C_{2v} symmetry and the s-o interaction is uniquely described by only two parameters. We note further that E to E electric-dipole transitions are uniquely defined in D_{2d} symmetry. The direct product $E\otimes E=A_1+A_2+B_1+B_2$ and, since z transforms as B_2 and (x,y) as E, no parameters are needed for the polarization-selection rules. The electric-dipole matrices $\mathbf{D}_x$, $\mathbf{D}_y$, and $\mathbf{D}_z$ could therefore be constructed by, e.g., to considering t_2 to t_2 one-particle hole transitions, i.e., the initial hole configuration is $t_2e^2(^3A_2)$ and the final hole configuration is $t_2'e^2(^3A_2)$. The full hamiltonian containing all terms has been numerically solved and the results are presented in Fig. 2 in terms of Zeeman splitting and relative intensity. The parameters used in the calculations are presented in Table I and the line spectra were calculated by using a lorentzian line shape function with FWHM=9 cm^{-1}. The axial-field, δ_{ax}, parameters as well as the exchange parameters, J, were chosen to be equal for both states and to have the same values as those presented in Ref. 2. The critical parameters for each ^4E term are ξ, δ_{rh}, and g_L, i.e., only six parameters in total are needed to fully describe the experimental results which are surprisingly few compared with those generally needed when a detailed knowledge of the states involved in the transitions is lacking.

The line spectrum for the orthorhombic FeIn center has also been measured for uniaxial stress in the <100>, <110>, and <111> directions. Surprisingly, no splitting of the excitation lines were observed for any direction of stress and only a very small common shift of the lines were observed. This implicates that the stress induced energy shifts of the final and initial states are the same irrespective of the direction of the applied stress. This is at a first glance a very surprising results when considering the relatively low symmetry of the center. However, the stress response of the $^4T_1$ state of the isolated interstitial Fe impurity has previously been studied[6] and no splitting was observed for the J=3/2 and J=5/2 $^4T_1$ levels. This indicates that the t_2 Fe_i one-particle state does not split under stress and that the observed lack of stress splitting for the FeIn center is due to the fact that both the initial and final states are exclusively derived from the perturbed Fe_i ion. It therefore seems possible to rule out that the transitions takes place to shallow levels and to suggest that the FeIn lines are due to internal "d"- transitions at the Fe ion.

CONCLUSIONS

The Zeeman results for the FeIn C_{2v} center in silicon have been fully accounted for by considering electric-dipole transitions between two $^4B_1$ terms spin-orbit split via interaction with a nearby $^4B_2$ term. The initial state is derived from the Fe_i^+ $^4T_1$ ground state term. The lack of any uniaxial-stress induced splitting as well as the observation that both the initial and final states are well described by an almost identical set of electronic parameters strongly suggest that the transitions are intra "d"-level transitions at the interstitial Fe ion.

ACKNOWLEDGMENTS

The authors acknowledge financial support from the Swedish Natural Science Research Foundation, the Board for Industrial and Technical Development and the Swedish Research Council for Engineering Sciences.

REFERENCES

[1] G. W. Ludwig and H. H. Woodbury, in Solid State Physics, edited by F. Seitz and D. Turnbull (Academic Press, New York, 1962), Vol. 13, p 223 and H. H. Woodbury and G. W. Ludwig, Phys. Rev. **117**, 102 (1960)
[2] W. Gehlhoff, P. Emanuelsson, P. Omling, and H. G. Grimmeiss, Phys. Rev. B **47**(12), 12 March 1993
[3] A. Chantre and D. Bois, Phys. Rev. B **31**(12), 7979, 1985
[4] S. Ghatnekar-Nilsson, M. Kleverman, P. Emanuelsson and H. G. Grimmeiss, Semicond. Sci. Technol.**8** (1993) 1857-1861
[5] P. Tidlund, M. Kleverman and H. G. Grimmeiss, Semicond. Sci. Technol. **11** (1996) 748-752
[6] A. Thilderkvist, G. Grossmann, M. Kleverman, and H. G. Grimmeiss, unpublished

Materials Science Forum Vols. 258-263 (1997) pp. 461-466
© 1997 Trans Tech Publications, Switzerland

COPPER IN SILICON: QUANTITATIVE ANALYSIS OF INTERNAL AND PROXIMITY GETTERING

Scott A. McHugo[1], T. Heiser[2], H. Hieslmair[3], C. Flink[3], E.R. Weber[3], S.M. Myers[4] and G.A. Petersen[4]

[1]Lawrence Berkeley National Laboratory, Advanced Light Source, Berkeley, CA 94720 USA
[2]Univ. Louis Pasteur, Lab. PHASE-CNRS, BP20, F67037, Strasbourg Cedex 2 France
[3]Univ. of California at Berkeley, Dept. of Materials Science, Berkeley, CA 94720 USA
[4]Sandia National Laboratories, P.O. Box 5800, Albuquerque, NM 87185-1056 USA

Keywords: copper, silicon, gettering, implantation, oxygen precipitates, transient ion drift

Abstract

The behavior of copper in the presence of a proximity gettering mechanism and a standard internal gettering mechanism in silicon was studied. He implantation-induced cavities in the near surface region were used as a proximity gettering mechanism and oxygen precipitates in the bulk of the material provided internal gettering sites. Moderate levels of copper contamination were introduced by ion implantation such that the copper was not supersaturated during the anneals, thus providing realistic copper contamination/gettering conditions. Copper concentrations at cavities and internal gettering sites were quantitatively measured after the annealings. In this manner, the gettering effectiveness of cavities was measured when in direct competition with internal gettering sites. The cavities were found to be the dominant gettering mechanism with only a small amount of copper gettered at the internal gettering sites. These results reveal the benefits of a segregation-type gettering mechanism for typical contamination conditions.

Introduction

Copper is a prevalent contaminant in silicon with adverse effects on device performance. In spite of this fact, Cu is of particular interest for use as interconnect lines in semiconductor devices because of its low resistivity, however, these lines may act as a source for Cu contamination into the device region. Removal or gettering of Cu contamination out of the device region is highly desired, e.g. specifications for Cu contamination have dropped to 2.5×10^9 atoms/cm^2 [1]. A standard method to remove metal impurities from the near surface/device region is via internal gettering (IG) which utilizes oxygen precipitates in the material bulk [2, 3]. The limitation of IG is that it relies on impurity precipitation at the gettering site as well as impurity diffusion to the site. This creates the contradictory requirement of a low temperature anneal in order to create a supersaturation of the impurity in the silicon matrix leading to precipitation at the IG sites and a high temperature anneal for sufficient diffusion of the impurity. Additionally, contamination is often introduced into the silicon at the annealing temperature such that no supersaturation occurs. To obtain effective gettering under any annealing condition, "proximity" gettering methods located near the device region have been the focus of recent research with a particular interest in mechanisms which do not require an impurity supersaturation. One means to achieve proximity gettering is to use implantation species to getter the metal impurities in a region slightly deeper than the device region. Implantations with C, O, BF_2, N, Ge, Ne, Ar and B have been attempted, however, the gettering mechanisms either require impurity precipitation or are unstable at elevated temperatures [4-8]. A promising method uses cavities formed by He implantation which getter metal impurities on the unsaturated bonds of the cavity walls by chemisorption as well as metal-silicide precipitation when the surrounding silicon matrix becomes supersaturated with the metal impurity [6, 9-12]. The chemisorption mechanism is active without an impurity supersaturation and is stable at high temperatures with a reported binding energy of Cu to the cavity relative to Cu in solution of ≈ 2.2eV [12], above the value for Cu-silicide precipitation, $\approx$1.5eV [13]. From these binding energies, one

would expect less Cu remaining in the silicon matrix when cavities are present than with IG sites after an anneal. Furthermore, considering the cavities form a near continuous plane of sinks near the front surface while IG sites are more dispersed, an even lower impurity concentration would be expected in the device region when cavities are present as opposed to with only IG sites.

In the work presented here, our goal was to determine if the cavities significantly enhance gettering of Cu more than IG sites would getter by themselves. We have monitored Cu behavior in the presence of IG sites and He implantation-induced cavities with the use of secondary ion mass spectroscopy and transient ion drift. Moderate levels of Cu contamination were used such that the Cu was not supersaturated during annealing which provided realistic Cu contamination/gettering behavior. Quantitative measurements of Cu concentrations at both gettering sites were obtained after gettering anneals. Our results clearly demonstrate the advantages of gettering to cavities over IG sites.

Experimental Procedure

Boron doped <100>, 500μm thick CZ silicon with a resistivity of 10 Ω-cm and an initial oxygen concentration of $9x10^{17}/cm^3$ was used. All samples were subjected to a 1100°C, 5 hr anneal to create an ≈10μm denuded zone (DZ). Samples were prepared with and without internal gettering (IG) sites prior to forming the cavity gettering layers. IG sites were formed by a 700°C, 48 hours oxygen precipitate nucleation anneal, followed by a thermal ramp from 700 - 950°C in 50°C increments for 30 minutes each and finally with a 950°C, 8 hours precipitate growth anneal. All anneals were performed in a nitrogen atmosphere. The ramp step allows for oxygen precipitates to have a higher survival probability during the high temperature growth anneal and therefore provide a high concentration of internal gettering sites [14]. Laser Scattering Tomography (LST) measurements of defect densities revealed 10^{10} defects/cm^3 and $7x10^7$ defects/cm^3 for samples with and without the IG formation anneals, respectively. This provides a significant difference in IG site density between the two sample types. The interstitial oxygen (O_i) concentration was monitored with Fourier Transform Infrared Spectroscopy (FTIR) using the new ASTM standard in the as-grown state, following the DZ formation and after the IG formation anneals. No change in O_i was observed after the DZ formation but 10^{17} O_i atoms/cm^3 was precipitated during the IG formation anneal. Based on conservation of mass and the precipitate density measured with LST, a 10^{17} drop in O_i creates precipitates with radii of ≈35nm. To form the cavity gettering sites, He atoms were implanted at 300keV (≈1.35μm deep) with a dose of $1x10^{17}$ atoms/cm^2. $1x10^{14}$ Cu atoms/cm^2 were introduced ≈0.1μm deep on both the front and back sides by a 150keV implantation. The Cu was gettered by annealing the samples at either 700 or 800°C for 6 or 2 hours respectively in a vacuum furnace ($2x10^{-7}$ torr) with a slow cool to room temperature. Past work [9] has shown the cavities form within 30 minutes at 700°C, therefore ensuring the cavities are present and are active gettering sites for the majority of the gettering anneals. Secondary Ion Mass Spectroscopy (SIMS) was utilized to measure the Cu gettered by the cavities and, with the aid of statistical analysis, to roughly estimate the Cu gettered at the IG sites. High purity Float-Zone (FZ) silicon was used as a reference for both of these SIMS measurements. Additionally, the amount of Cu at the IG sites was measured with the use of a rapid thermal anneal with a rapid quench (RTAQ) at 1000°C for 45 seconds and measurements with the transient ion drift (TID) technique [15,16]. The quench rate is approximated as of 1000°C/sec. The RTAQ anneal is designed to dissolve the Cu from its original precipitation site which allows for TID to detect the interstitial Cu (Cu_i). TID exploits the capacitance change induced by the positively charged Cu_i drift in the depletion region of a Schottky barrier. The detection limit of TID is on the order of 10^{12} Cu_i atoms/cm^3 for these experiments. High purity FZ samples were subjected to the same 1000°C-45 sec anneal to act as reference samples. Al evaporation was used to form diodes on all samples. Samples were cleaned prior to the RTAQ and diode formation with VLSI grade piranha ($5:H_2SO_4:1H_2O_2$), HF and high resistivity H_2O.

Results and Discussion

Figure 1 shows SIMS plot of the Cu distribution in the near surface region of a sample with IG sites. The sample has been subjected to a 800°C gettering anneal after He implantation to form cavities at ≈1.35μm and a Cu implantation at ≈0.1μm in order to intentionally contaminate the materials.

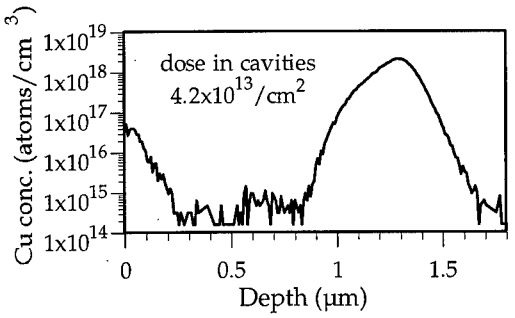


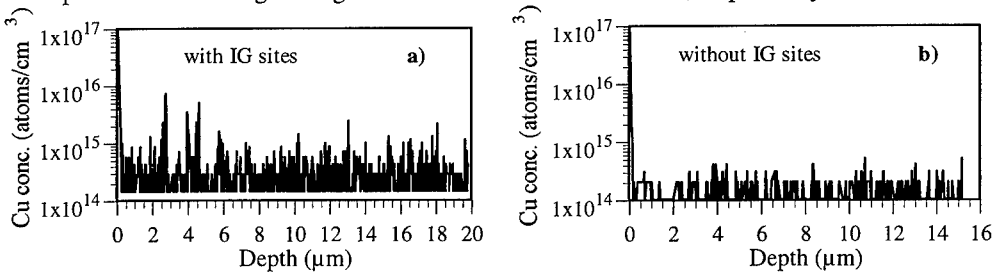
Figure 1: SIMS plots of front surface Cu distribution after a 800°C gettering anneal with IG sites and cavities. The cavity layer is at 1.35μm and the initial Cu implant was at 0.1μm.

Clearly substantial gettering of the Cu has occurred to the cavities. The SIMS results for cavity gettering at 700 and 800°C are summarized in the first column of Table 1. For both temperatures, the amount of Cu gettered to the cavities is hardly influenced by the presence or absence of the IG sites. It should further be noted that the measured amount is far below the level corresponding to saturation of the cavity wall sites, which for our experimental conditions is above 10^{15} atoms/cm^2 [12]. Also included in the table are the amounts of Cu remaining in the front and back near-surface layers where the Cu atoms were initially implanted. SIMS analysis was also performed deep in the bulk of the sample to determine the amount of Cu present at the IG sites. Although the dissolved Cu concentration was expected to be below the sensitivity of

Sample	Cu in cavities (10^{12} cm^{-2})	Cu in front (10^{12} cm^{-2})	Cu in back (10^{12} cm^{-2})	Cu in bulk (10^{12} cm^{-2})
with IG, 700°C	39	3.4	1.4	2-10 (SIMS) 12.5 (TID)
with IG, 800°C	42	0.3	1.8	-
no IG, 700°C	42	3.9	9.6	< DL (SIMS) < DL (TID)
no IG, 800°C	42	0.2	6.9	-

Table 1: Cu doses in the cavities, frontside, backside and bulk after 700 and 800°C anneals. DL = detection limit and - means sample was not measured.

SIMS, it was hoped that extended SIMS profiling would reveal any Cu at IG sites via spikes in the Cu counts at depth intervals where IG sites are present. Figures 2a and 2b show deep SIMS profiles of samples after a 700°C gettering anneal with and without IG sites, respectively. The cavities and a



Figures 2a&b: SIMS plots of Cu deep in the samples following a 700°C gettering anneal a) with and b) without IG sites. The cavities and a ≈150-200μm thickness has been removed prior to measurement.

≈ 150-200μm thickness of the underlying silicon wafer have been removed prior to the SIMS measurements via polishing and etching. Both profiles exhibit noise typical of SIMS data when the concentration of the detected isotope is near or below SIMS sensitivity. However, in the case of the specimen with more IG sites, there are additionally a number of spikes with large amplitudes, suggesting the presence of isolated agglomerations of Cu atoms within the matrix. This raises the possibility that a small fraction of the implanted Cu is gettered to bulk IG sites. A high purity float-zone (FZ) sample with no intentional Cu contamination was also subjected to deep SIMS analysis for comparison. The SIMS profile (not shown here) is similar to Figure 2b, the sample without IG sites.

To quantify the apparent spikes, we evaluated the statistical distributions of the SIMS yields in Figures 2a and 2b as well as the FZ SIMS data (not shown). These results were compared with the Poisson distribution expected for random noise with the same average number of counts per depth interval where counts are proportional to Cu concentration. Our findings are shown in Figures 3a and 3b, where the number of depth intervals yielding a particular number of SIMS counts is plotted versus the number of SIMS counts in the interval, denoted as N. The data from the specimen with

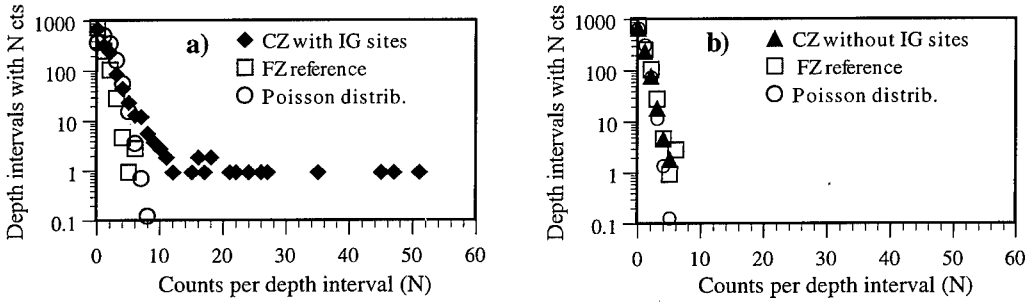


Figure 3a&b: Statistical analysis of data presented in Figure 2 and FZ SIMS data. The Poisson distribution approximates noise. Counts are proportional to Cu concentration. The CZ without IG sites and FZ reference data follows the Poisson distribution of noise.

few IG sites, Figure 3b, conforms well to the calculated Poisson distribution and the reference FZ silicon sample. In contrast, results for the sample with IG sites, Figure 3a, show a pronounced tail extending to large values of N. Moreover, when the number of spikes having amplitudes greater than random noise is divided by the sputtered volume, the resulting volume density is $\approx 2 \times 10^{9}$ cm^{-3}, or less than an order of magnitude smaller than the measured density of IG sites. In our view, this constitutes evidence for gettering of a small fraction of the implanted Cu by the IG sites. The amount of Cu in the spikes (at these IG sites) is $\approx 2\text{-}10 \times 10^{12}$ atoms/cm^2 considering the area and depth probed with SIMS and the thickness of the silicon wafer, 500μm.

The 700°C gettered samples were polished and etched to remove the sputter pit formed by the deep SIMS analysis. Following extensive surface cleaning, the gettered samples were annealed at 1000°C for 45 seconds followed by a rapid quench to dissolve the Cu back into solution. High purity FZ samples were also annealed just prior and just after the gettered samples were annealed in order to check for contamination. This anneal has been used previously to dissolve precipitated Cu completely back into solution [16] and models of dissolution kinetics [17, 18] predict even a 4.4μm Cu_3Si precipitate would dissolve during this 1000°C-45 sec anneal. A precipitate of greater than this size is not expected to be present in the material. Therefore, we anticipate all Cu is dissolved back into solution after this anneal. Following surface cleaning and Al diode formation Transient Ion Drift (TID) measurements were performed on a number of diodes on the FZ reference samples

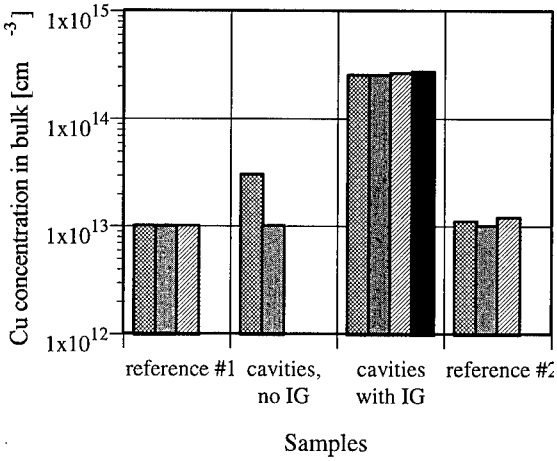


Figure 4: Bulk concentrations of Cu as measured with TID after an RTAQ at 1000°C for 45 sec. Reference samples determine the amount of contamination during the RTAQ.

and on the gettered samples. The results are shown in Figure 4. We see the sample with IG sites contains a significantly higher amount of Cu than the reference samples and the sample with no IG sites. This is consist with the deep SIMS profiling results. The measured concentration of $2.5x10^{14}$ Cu atoms/cm^3 is converted into a Cu dose of $12.5x10^{12}$ Cu atoms/cm^2, by simply considering the silicon samples are 500μm thick. This dose compares well with the dose of $2\text{-}10x10^{12}$ atoms/cm^3 measured with SIMS.

Summing the data in Table 1, we see a significant amount of the original Cu dose ($2x10^{14}$ atoms/cm^2) has been lost during the annealing treatments. This is likely due to Cu evaporation from the silicon at elevated temperatures. Comparable rates of Cu evaporation have been previously observed under similar experimental conditions [12]. Additionally, previous work on Cu solubility in silicon have used vapor transport at temperatures as low as 650°C and anneal times comparable to those used in this study to intentionally contaminate silicon with Cu [19]. Based on these past works, the loss of Cu observed in this work is not a surprising phenomenon.

The information presented above is summarized in Table 1. We see the cavities getter the majority of the Cu regardless of the IG site density. The chemisorption process dominates the gettering action. It should be noted that the $\sqrt{Dt}$ product (where D is the Cu diffusivity and t is the anneal time) is 7700μm and 5700μm for the 700°C-6hr and 800°C-2hr anneal, respectively, which indicates both anneals provide time for significant Cu diffusion. Considering the implanted Cu will rapidly disperse throughout the 500μm thick silicon samples during the gettering treatments, a uniform distribution of $4x10^{15}$ Cu atoms/cm^3 is expected to form throughout the thickness of the material. Also, considering the solubility of Cu in the silicon matrix with respect to a Cu_3Si phase is 10^{16} and $7x10^{16}$ Cu atoms/cm^3 for the 700 and 800°C anneals respectively, the Cu is not supersaturated and no Cu would be expected to getter to the IG sites at the annealing temperature. This is a realistic scenario for Cu contamination since typically only small amounts of Cu are introduced into silicon during integrated circuit processing such that during an annealing the Cu is not supersaturated. However, the slow cool after the anneals allows for gettering of the Cu at the IG sites as it precipitates into Cu_3Si. Conversely, the cavities chemisorb Cu atoms during the anneal and during cooling as well act as a precipitation site for the Cu into the Cu_3Si phase just as the IG sites. Therefore, in these realistic contamination conditions, the cavities are the dominant gettering mechanism. Additionally, considering the close proximity of the cavities to the near surface region as compared to the IG sites and the fact that the cavities form a near continuous sheet of gettering sites while IG sites are more widely dispersed, one would expect the cavities to getter the device region much more effectively with short annealing sequences than the IG sites. Clearly cavity formation is a worthwhile endeavor to ensure efficient gettering of Cu from the device region of silicon integrated circuits.

Conclusions

Gettering of Cu to He implantation-induced cavities and internal gettering sites was quantitatively analyzed for realistic Cu contamination scenarios. Novel SIMS profiling and data analysis and TID measurements allowed for the quantification of Cu at IG sites. The cavities effectively getter Cu in silicon even in the presence of internal gettering sites and the gettering action is dominated by the cavities. These results reveal the chemisorption mechanism of cavity gettering is a highly effective means for proximity gettering of metal impurities.

Acknowledgments

The authors would like to thank Dr. M. Werner and Dr. Kissinger for LST measurements and Dr. F. Kirscht for fascinating discussions. This work was supported by the U.S. D.O.E. under contract No. DE-AC04-94AL85000 and the Director, Office of Basic Energy Research, Materials Science Division, U.S. D.O.E. contract No. DE-AC03-76SF00098.

References

1. *The National Technology Roadmap for Semiconductors* (Semiconductor Industry Assoc., San Jose, CA 1994), p. 110
2. W. K. Tice and T. Y. Tan, *Mat. Res. Soc. Symp. Proc.* **2**, 367-380, 1981.
3. D. Gilles, E. R. Weber and S. K. Hahn, *Phys. Rev. Lett.* **64**, 196, 1990.
4. H. Wong, N. W. Cheung and P. K. Chu, *Appl. Phys. Lett.* **52**, 889-891, 1988.
5. W. Skorupa, R. Kogler, K. Schmalz, P. Gaworzewski, G. Morgenstren and H. Syhre, *Nuc. Instr. and Meth. in Phys. Res. B.* **74**, 70-4, 1993.
6. M. H. F. Overwijk, J. Politiek, R. C. M. d. Kruif and P. C. Zalm, *Nuc. Instr. and Meth. in Phys. Res. B.* **96**, 257-60, 1995.
7. C. J. Barbero, J. W. Corbett, C. Deng and Z. Atzmon, *J. Appl. Phys.* **78**, 3012-3014, 1995.
8. P. A. Stolk, J. L. Benton, D. J. Eaglesham, D. C. Jacobson, J.-Y. Cheng, J. M. Poate, S. M. Myers and T. E. Haynes, *Appl. Phys. Lett.* **68**, 51-3, 1995.
9. S. M. Myers, D. M. Follstaedt, D. M. Bishop and J. W. Medernach in *Proc. Semiconductor Silicon, 7th International Symposium on Silicon Materials Science & Tech.,* edited by H.R. Huff, W. Bergholz and K.Sumino, 1994, pg. 808
10. V. Raineri, A. Battaglia and E. Rimini, *Nuc. Instr. and Meth. in Phys. Res. B.* **96**, 249-252, 1995.
11. J. Wong-Leung, E. Nygren and J. S. Williams, *Appl. Phys. Lett.* **67**, 416-8, 1995.
12. S. M. Myers and D. M. Follstaedt, *J. Appl. Phys.* **79**, 1337-50, 1996.
13. E. R. Weber, *Appl. Phys. A.* **30**, 1, 1983.
14. S. A. McHugo, M. Mizuno, F. G. Kirscht and E. R. Weber, *Appl. Phys. Lett.* **66**, 2840, 1995.
15. T. Heiser and A. Mesli, *Appl. Phys. A.* **57**, 325, 1992.
16. T. Heiser, S. McHugo, H. Hieslmair and E. R. Weber, *Appl. Phys. Lett.* **70**, 3576-3578, 1997.
17. M. J. Whelan, *Metal Science Journal.* **3**, 95, 1969.
18. H. B. Aaron and G. R. Kotler, *Metal. Trans.* **2**, 393, 1971.
19. R. C. Dorward and J. S. Kirkaldy, *Trans. Metall. Soc.* **242**, 2055, 1968.

Materials Science Forum Vols. 258-263 (1997) pp. 467-472
© 1997 Trans Tech Publications, Switzerland

A STUDY OF THE COPPER-PAIR RELATED CENTERS IN SILICON

A.A.Istratov[1], T.Heiser[2], H.Hieslmair, C.Flink, J.Krüger, E.R.Weber

Department of Materials Science, University of California, Berkeley, CA 94720-1760, USA
[1]on leave from the Institute of Physics of St.-Petersburg State University, 198904 Russia
[2]on leave from University Louis Pasteur, Laboratoire PHASE-CNRS, F67037 Strasbourg, France

Keywords: copper, silicon, DLTS.

Abstract.

The dissociation of CuCu-related centers in p-type silicon is studied as a function of temperature just after copper contamination with subsequent quench when a significant concentration of copper remains at interstitial site, and after a long storage time. The binding energy of Cu-pair related centers is determined to be 1.02±0.07 eV. Some conclusions on the mechanism of copper precipitation are made. It is suggested that the potential barrier for copper precipitation of 0.55 eV is due to the coulombic repulsion between the interstitial copper atoms and the positively charged copper precipitates.

Introduction.

It is well known that copper in silicon precipitates almost completely during cooling from high temperatures. However, a small fraction of copper can remain in an electrically or optically active state. A variety of copper-related deep energy levels were reported in literature. Since no correlation of these defects to defined defect structure was established and since their concentrations were very small (usually below 0.1% of the copper concentration), it could not be excluded that several of these defects were due to other impurities, introduced into the sample during the heat treatment. According to Graff [1], only four centers showed reproducible results, though even their nature was not certain. One of these centers introduced a deep level at E_V+0.1 eV. Recently, Erzgräber and Schmalz [2] established a quantitative correlation between the amplitude of the DLTS peak, corresponding to this center, and the amplitude of a photoluminescence line at 1.015 eV, previously identified [3] as a copper-related center from observed isotope shift. Since the photoluminescence emission intensity depended quadratically on copper concentration, J.Weber *et al* [3] suggested copper pairs as a model for this defect. The capture kinetics of this center was discussed in Ref.4.

In this paper, the kinetics of dissociation of Cu-pair related centers were studied at different temperatures. The time dependence of the concentration of CuCu-related centers in the presence of high concentrations of interstitial copper was monitored. The goal of this experiment was to understand if the Cu-pair related centers can be formed at room temperature. For this purpose we used the experimental procedure, recently applied for the evaluation of the recombination activity and electron capture cross-section of interstitial copper [5]. The procedure is based on the fact that high concentrations of interstitial copper (up to the doping level) [6] can be kept in p-type silicon for several hours at room temperature after a fast quench. This experimental procedure can be used to measure the electrical activity of interstitial copper and its interaction with other types of defects.

Experimental procedure.

In our experiments, copper was diffused in float zone boron-doped p-Si samples at 600°C for 30 minutes. This relatively low diffusion temperature made cross-contamination by other transition metals very unlikely and ensured that the concentration of copper was below the doping level ($2 \cdot 10^{15}$ cm^{-3}). Almost all copper, dissolved at the diffusion temperature, was kept in interstitial state by the rapid quench in ethylene glycol. To prevent copper precipitation after the quench, the samples were kept in liquid nitrogen until the beginning of measurements except for the time required for the chemical etching of the sample and evaporation of Schottky diodes.

The dependence of the concentration of Cu-pair related centers as a function of anneal time was studied as follows: The sample was kept in the DLTS holder at a stabilized annealing temperature for a certain amount of time (from several minutes to several hours), after which it was cooled down to 35 K with an average cooling rate of 30 K/min. A DLTS spectrum of the CuCu peak and capacitance-voltage characteristic at T=70 K were measured. Finally, the sample was heated up to the annealing temperature with a heating rate of 10 K/min and the whole procedure was repeated several times.

Furthermore, since copper is believed to be a single donor, the apparent decrease of the effective concentration of shallow acceptors could be determined by the capacitance-voltage measurements, by the Hall effect or by TID [19], giving the density of interstitial copper donors. In this study, capacitance-voltage characteristics were used to determine the concentration of copper donors.

Precipitation of the interstitial copper.

The decays of copper concentration were fitted by exponentials. The measurements were done in the temperature range between 270 and 333 K. The dependence of the decay time constant, plotted as a function of temperature in the Arrhenius coordinates, gave the activation energy of copper precipitation of 0.55±0.05 eV. This value was derived from the linear regression $\ln(\tau)=-12.12+0.55/kT$. (Fig.1).

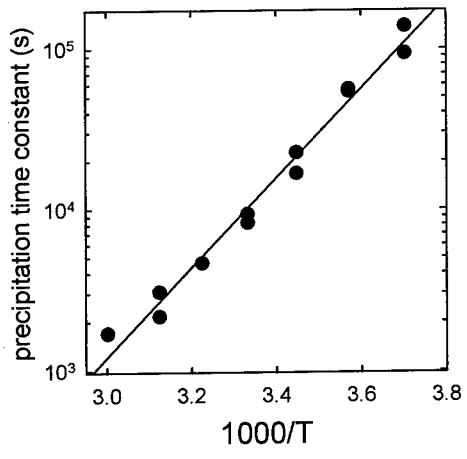


Fig.1 Arrhenius plot for the agglomeration of the interstitial copper.

The meaning of the activation energy of 0.55 eV is the potential barrier which interstitial copper has to overcome to precipitate. A certain activation energy for precipitation should necessarily exist since precipitation includes diffusion of metal atoms towards sinks. For example, the activation energy of iron precipitation was found to be 0.70±0.03 eV [7], which was in a good agreement with the migration enthalpy for the diffusion of interstitial Fe (0.68 eV). On the contrary to iron, the precipitation energy of copper (0.55±0.05 eV) is higher than its diffusion enthalpy (0.43 eV as determined at high temperatures, and 0.39 eV after the correction on copper-boron pairing [8]). This implies that the precipitation of copper is limited by the overcoming of a potential barrier for the precipitation rather than by a diffusion process. This barrier may be the energy required for the rebonding process, necessary for the introduction of one more copper atom into copper silicide.

However, since the value of 0.55 eV is very close to the repulsive Coulomb energy of two unit charges at a range of about a lattice constant (compare to the binding energy of a donor-acceptor pair, see below), it is also possible that the barrier is caused by the repulsion between positively charged nuclei or precipitates and interstitial copper atoms.

This conclusion is confirmed by the studies of electrical properties of copper-silicide precipitates [9]. DLTS measurements made on n-type silicon after the quench, revealed an unusually wide DLTS peak. Variations of the DLTS rate window and the filling pulse length showed that this was a single peak due to one extended defect, forming a band-like state in the upper half of the bandgap. Numerical simulations, based on the model of band-like states in the bandgap, revealed that the defect should be neutral, when it is almost completely (up to 80-90%) filled by electrons. The position of the defect band depended on the cooling rate. For the fast cooling rates, comparable with the ones used in this work, the band was estimated to be approximately between E_c-0.15 eV and E_c-0.40 eV. In p-type silicon, where the Fermi level lies close to the valence band, the precipitate-related band will be not occupied. The corresponding positive charge of precipitates might represent the potential barrier for copper precipitation.

In this model the potential barrier for the precipitation, existing in p-type silicon, should disappear in strongly doped n-Si, where the defect band will be below the Fermi level. This explains, why in p-type silicon significant concentrations of copper remain interstitially dissolved (at least for several hours), and why it is impossible in n-type. Moreover, this explains why the maximum concentration of interstitially quenched copper is close to the boron concentration [6]. Since copper is a donor, a boron-doped sample retains p-type conductivity as long as the concentration of interstitial copper remains below the boron doping level. As soon as copper concentration exceeds that of the boron, the sample becomes n-type, which causes a change of the charge state of the precipitates, eliminating the precipitation barrier and greatly accelerates the precipitation. It is easy to calculate, that if the activation energy of the precipitation process decreases from 0.55 eV to the diffusion-limited value 0.39 eV, the precipitation rate at room temperature would increase in $\exp((0.55\text{-}0.39)/kT)\approx 570$ times. The "lifetime" of interstitial copper, quenched at interstitial sites in n-Si, would be about 20 seconds compared to four hours in p-Si. The influence of the charge state of copper precipitates on the precipitation kinetics confirms the hypothesis recently suggested in Ref.6 that the position of the Fermi level during cooling down may have an effect on the precipitation process.

Studies of the Cu-pair related centers immediately after the quench.

The amplitude of the Cu-pair related DLTS peak $2\Delta C/C$, measured immediately after the quench, decreased by a factor of two during the first hours. This apparent decrease was mainly due to the precipitation of interstitial copper and resulting increase of the concentration of non-compensated shallow acceptors N_A-N_D. The concentration N_D is the concentration of positively charged donors due to interstitial copper. However, the increase of N_A-N_D alone could not explain the decrease of $2\Delta C(t)/C(t)$. The density of traps, determined by $N_T=(2\Delta C/C)\times(N_A\text{-}N_D)$ also revealed a decrease by 20 to 30% of the initial amplitude. This residual decrease was due to the incomplete flattening of bands during the filling pulse, which caused a certain time-dependent change of the zero-bias capacitance value. Since the position of CuCu-related center was close to that of the Fermi level, there was no need to consider the λ-point effect [10]. The correct density of traps taking into consideration the incomplete filling of the traps in the space-charge region was determined from the expression

$$N_T = (2\Delta C / C)\cdot(N_A - N_D)\cdot(1 - C^2(V_{bias}) / C^2(V_{pulse}))^{-1} \qquad (1)$$

where V_{pulse} is the bias voltage on the sample during the filling pulse, N_A-N_D is the concentration of non-compensated acceptors, determined from the CV-measurements. The usage of this formula showed that within the uncertainty range of the measurements there was no time dependence of N_T at the temperatures below 60^0C. Thus, the Cu-pair related centers can not be formed at room temperature even in the presence of 10^{15} cm^{-3} of interstitial copper. This implies that either a large amount of energy is required for the formation of a bond between two copper atoms, or, as it will be discussed below, a substitutional copper atom is necessary for the formation of the pair. Since the concentration of substitutional copper can not be high (otherwise it would have been detected by DLTS), it is possible that all available substitutional copper atoms are already paired with interstitial ones.

Dissociation of CuCu-related center at elevated temperatures

The dissociation of the CuCu-related defects was studied in the temperature range 60-140^{0}C. The dependence of the dissociation rate on temperature was fitted in the Arrhenius plot by a linear dependence $\ln(\tau) = -22.64 + 1.02/kT$ (Fig.2). The activation energies of dissociation was determined to be 1.02±0.07 eV taking into account the uncertainties of data points.

It is interesting to compare the position of data points for the dissociation of Cu-pairs related centers with the data of Aboelfotoh *et al* [11]. In that paper, an effect of compensation of boron in the near-surface region was detected. Copper was introduced into the silicon using an unusual technique of copper diffusion from copper Schottky diodes at room or slightly elevated temperatures [11]. The compensation of shallow boron was explained by copper-boron pairing. The activation energy of reactivation of passivated boron of 0.89 eV, reported in Ref.11, was substantially different from our data. It predicted the decay time of about two years at room temperature. All our results, obtained on various samples by CV, TID and Hall effect gave reproducible time constants in the range of hours, which unambiguously shows that the compensating effect in the Ref.11 was due to other defects than interstitial copper. Hydrogen, which also can passivate boron, can be excluded since the activation energy of reactivation of H-compensated boron would be much higher than it was reported by Aboelfotoh (1.68±0.1 eV, according to Ref.12).

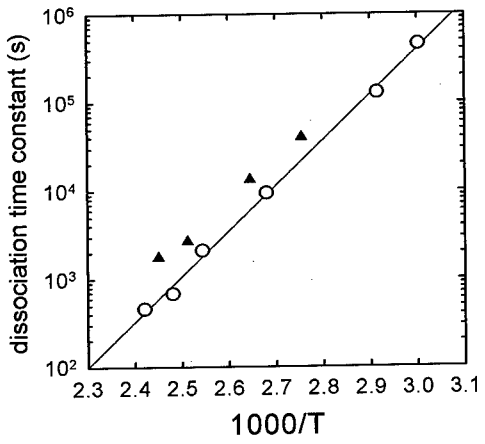


Fig.2. Arrhenius plot for the dissociation of CuCu pairs-related center (open circles). Triangles are the data from Ref.[11], discussed in the text.

Though the energy of 0.89 eV, determined by Aboelfotoh (filled triangles on Fig.2), is somewhat different from our 1.02 eV, the position of the data points on the Arrhenius plot is very close to the position of data points for the CuCu-related pairs dissociation, which suggests that both energies match within the uncertainty range.

This may indicate that the centers, which compensated boron in Ref.11 were Cu-pair related centers. In this case, they should be positively charged at room temperature and become doubly positively charged below 50 K after the capture of a hole. This double donor nature contradicts to the conclusions of J.Weber [3]. Another possibility would be that a very similar potential barrier

prevents unstable copper-precipitates, formed during the fast quench, from forming more energy favorable configuration of the precipitates. This follows from the studies of the processes of structural realignment of copper-precipitates, formed in the bulk of silicon, after the diffusion of copper and fast quench [13]. The change of the precipitate structure manifests itself by noticeable change of the DLTS peak shape and happens approximately at the same temperatures and on a similar time scale as the dissociation of CuCu-related centers. The analysis of the change of the DLTS peak shape indicates that the positive charge of the precipitates decrease as their configuration changes [14]. This may imply the decrease of the compensating effect of agglomerations of copper and may explain the "dissociation" of positively charged centers observedin Ref.11.

Unlike nickel silicide or iron silicide, which have the formula $MeSi_2$, copper silicide is believed to have the chemical formula Cu_3Si. This implies that any type of growth or dissociation of copper precipitates would involve the formation or dissociation of CuCu pairs or incomplete atomic cells Cu_2Si as an intermediate step for the formation or dissociation of Cu_3Si. The value of 1.02 eV can then be considered as a characteristic energy for one type of bonding between copper atoms and as a lower estimate for the energy, required for the dissolution of copper precipitates. Indeed, since the interstitial copper disappears from the silicon lattice in spite of the precipitation barrier, it should be bound in precipitates more strongly than 0.55 eV. The values of above 1 eV for the dissociation of clusters of transition metals was expected from the gettering studies and studies of iron precipitation kinetics. McHugo et al [15] suggested that the microdefects, which decrease substantially the efficiency of multicrystalline solar cells, are clusters of transition metals. These clusters are stable to gettering due to potential barriers for the dissolution. Hieslmair *et al* [16] estimated the binding energy of iron at precipitation sites, which were detected in concentration about 10^{10} cm^{-3} in both FZ and CZ silicon and were stable below 850^0C, of more than 1 eV.

Discussion

A generally assumed model of Cu-pair related center is that it is a pair consisting of a substitutional and an interstitial copper atoms. Since the substitutional copper is believed to be a triple acceptor, and the interstitial copper is a donor, the most straightforward model for the Cu-pair related defect would be that of a donor-acceptor pair. This type of pairing is quite common for transition metals in silicon. For example, complexes of iron with Al, Ga, In are donor-acceptor pairs [8-10]. The binding energy of such a pair should be 0.55 eV for the orientation <111> and 0.48 eV for the orientation <100>. Frequently, the concentration of more stable <111>-oriented pairs exceed significantly the concentration of <100>-oriented ones.

The <111> axis orientation of the donor-acceptor pair is consistent with the orientation, determined from uniaxial stress and Zeeman data by J.Weber *et al* [3] for the Cu-pair related defect. However, the binding energy of Cu-pair related center is almost twice as high as the energy of a donor-acceptor pair, provided the both components are singly charged. The binding energy of 1.02 eV would fit into the model of a donor-acceptor pair only if it is formed by a doubly negatively charged substitutional copper, i.e. the pair has the formula $Cu_s^{-2}Cu_i^{+}$. Donor-acceptor pairs, where one of the components is doubly charged, has also been reported (see for example Ref.20)

J.Weber [3] concluded, comparing the spectroscopic localization and thermal ionization energies of bound exciton, that the CuCu-center is an isoelectronic center. The donor nature of this center, frequently mentioned in the papers, which followed Ref.3, does not seem to be consistent with the dissociation energy of the Cu-pair related center. The only model which does not contradict Ref.3, is that of a single acceptor with the change of the charge state 0/- upon the capture/emission of a hole.

Conclusions

The concentration of Cu-pair related centers was measured as a function of time and temperature during and after the precipitation of interstitial copper. It was found that high concentrations of interstitial copper (10^{15} cm^{-3}) do not lead to the formation of new Cu-pair related centers. This favors the model of a pair of a substitutional and interstitial copper atoms, where the density of defects is limited by the concentration of available substitutional atoms. However, since the binding energy of Cu-pair related center was found to be 1.02±0.07 eV, the model of a donor-acceptor pair would imply that this center should be a single acceptor. A commonly accepted model of a single donor can thus be ruled out.

The barrier for the precipitation of interstitial copper is evaluated. Evidence is provided that this barrier (0.55±0.05 eV) can be due to coulomb repulsion between positively charged copper precipitates and interstitial copper. This implies that the precipitation rate of interstitial copper should depend on the Fermi level position and explains the role of shallow acceptors in keeping high concentrations of copper in interstitial state in p-Si for several hours after the quench.

Acknowledgements.

This work was supported by NREL. Helpful discussions with H.Hedemann and W.Schröter are acknowledged.

References.

1. K.Graff, "Metal impurities in silicon-device fabrication" (Springer, Berlin, 1995), p.86.
2. H.B.Erzgräber, K.Schmalz, J.Appl.Phys. **78**, 4066 (1995).
3. J.Weber, H.Bauch, R.Sauer, Phys.Rev. **B25**, 7688 (1982).
4. S.Koveshnikov, Y.Pan, H.Mollenkopf, Electrochem.Soc.Proc., 96-13, 473 (1996).
5. A.A.Istratov, C.Flink, H.Hieslmair, T.Heiser, E.R.Weber, to be published.
6. T.Heiser, S.McHugo, H.Hieslmair, E.R.Weber, Appl.Phys.Lett., **70**, 3576 (1997).
7. D.Gilles, E.R.Weber, S.Hahn, Phys.Rev.Lett. **64**, 196 (1990).
8. A.Mesli, T.Heiser, E.Mulheim, Mater.Sci.Engin. **B 25**, 141 (1994).
9. A.A.Istratov, H.Hedemann, M.Seibt, W.Schröter, to be presented at "Semiconductor Silicon-98".
10. Y.Zohta, M.O.Watanabe, J.Appl.Phys.**53**, 1809 (1982).
11. M.O.Aboelfotoh, B.G.Svensson, Phys.Rev.B **44**, 12742 (1991).
12. A.Majumdar, S.Balasubramanian, V.Venkataraman, N.Balasubramanian, J.Appl.Phys. **82**, 192 (1997).
13. A.Sattler, W.Schröter *et al*, unpublished.
14 H.Hedemann, Ph.D.thesis, Göttingen, 1995.
15. S.A.McHugo, H.Hieslmair, E.R.Weber, Appl.Physics A **64**, 127 (1997).
16. H.Hielmair, A.Istratov, C.Flink, S.McHugo, E.R.Weber, this conference
17. A.Chantre, D.Bois, Phys.Rev. B **31**, 7979 (1985).
18. H.Feichtinger, J.Ostwald, R.Czaputa, P.Vogl, K.Wünstel, in the proceedings of the ICDS-13 (the Metallurgical Soc. Of AIME, Warrendale, Pennsylvania 1984), p.855.
19. T.Heiser, A.Mesli, Appl.Phys. A **57**, 325 (1993).
20. H.E.Altink, T.Gregorkiewicz, C.A.J.Ammerlaan, IN: Defect Engineering in Semiconductor Growth, Processing and Device Technology Symposium, San Francisco, CA, USA, (Mater. Res. Soc 1992) p. 525-36.

Materials Science Forum Vols. 258-263 (1997) pp. 473-478
© 1997 Trans Tech Publications, Switzerland

THE PHOTOLUMINESCENCE OF Pt-IMPLANTED SILICON

E. Alves*, J. Bollmann#, M. Deicher%, M.C.Carmo$, M.O.Henry%&, M.H.A.Knopf%, J.P.Leitão$, R.Magerle% and C.J.McDonagh&

***Centro de Física Nuclear, Universidade de Lisboa, 1699 Lisboa, Portugal**
#Humboldt Universitaet Berlin, Invalidenstrasse 110, D-10115 Berlin, Germany
%Fakultaet Physik, Universitaet Konstanz, D-78434 Konstanz, Germany
$Departamento de Física, Universidade de Aveiro, 3810 Aveiro, Portugal
&School of Physical Sciences, Dublin City University, Dublin 9, Ireland

Keywords: silicon, photoluminescence, Si:Pt, stress.

Abstract. Photoluminescence measurements on Pt-implanted n-type FZ silicon samples show that three vibronic bands are produced, with principal zero-phonon lines at $\sim$ 1026, 884 and 777 meV. The thermal binding energies are 34.6, 5.2 and 11.2 meV, respectively. Uniaxial stress data show that all centres are axial. None of the spectra can be identified with known transitions on the Pt donor or acceptor centres, and they do not correspond to any previously published PL or absorption spectra. Evidence for the involvement of iron and lithium in some of the centres is presented.

Introduction

Several recent studies have shown that platinum readily participates with light impurities hydrogen and lithium in the formation of complex defects in silicon. The defects reported to date have been observed in IR and EPR[1]. In all of these cases, the platinum was introduced using diffusion[1, 2, 3, 4]. We are currently involved in experiments using radioactive isotopes of Pt (and other elements) which are introduced by implantation, and in this paper we report the results of photoluminescence(PL) studies of silicon implanted with stable Pt isotopes. We find that, within the spectral range covered by our detector, the spectra consist of three distinct vibronic bands. Although we have not proven that the defects reported here correspond to any of those previously observed using other techniques, we describe indirect evidence for the involvement of Li and Fe in some of the defects.

Experimental details

Samples were prepared from float-zone (001) n-type silicon wafers of room temperature resistivity in the range $1 - 10\,\Omega \cdot$ cm. The implantation energies were in the range 60 to 200 keV, and doses from 10^{11} to $10^{13}\,\mathrm{cm}^{-2}$ were used. The standard annealing procedure was to seal the samples in a helium gas ambient (at a pressure of 0.5 atmosphere at room temperature). The ampoules were heated at 900 C for 10 minutes and rapidly submerged in water. PL measurements were made using argon ion laser excitiation (typically 100 mW at 514.5 nm) and either Fourier transform or dispersive spectrometers fitted with North Coast germanium detectors.

Results

A representative broad-range PL spectrum is shown in Figure 1. In addition to band edge features at $\sim$ 1090 meV and above, three prominent vibronic spectra are observed at lower energies. The relative intensities of the spectra vary between samples, showing that three distinct defects are involved. We label the spectra using the energy of the lowest energy sharp line in each spectrum. The 777 meV centre, first observed in Ag-implanted silicon by Nazare et al[5], was subsequently shown to be Pt related by the use of radioactive isotopes[6]. The 884 meV and 1026 meV centres have not been reported previously, to our knowledge. For all three centres, the sidebands contain some local in-band resonance character, the extent of which varies for the three centres. Sharp local mode phonons with energies greater than that of the maximum silicon phonon energy have not been observed in any of the spectra. More detailed information for each of the centres is provided in Figure 2, where PL spectra at several different temperatures are shown. Fine structure is observed in all three cases, and thermalisation measurements show that transitions occur from two or more excited states to a single ground state in each of the three centres. The details of the excited state splittings, the value of the local phonon energies (and the strength, S, of the coupling), and the thermal binding energies (E_a) are given in Table 1 for all three spectra.

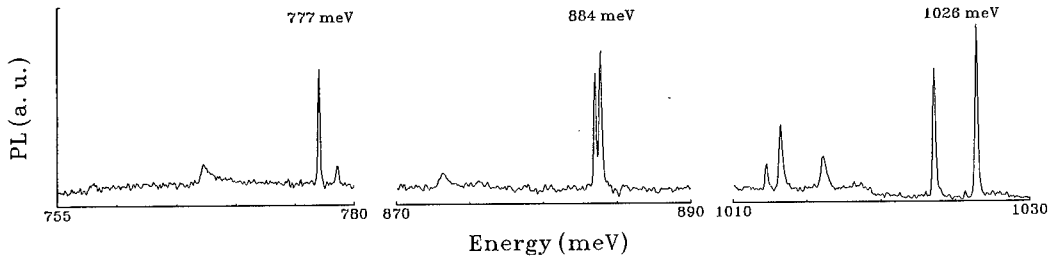


Fig. 1. Photoluminescence from Si:Pt at 7.6 K.

Centre	L_0^0	$\Gamma(L_0^0)$	L_0^1	L_0^2	L_1^0	$\Gamma(L_1^0)$	L_1^1	L_1^2	L_2^0	$\Gamma(L_2^0)$
(meV)	(meV)	(meV)	(meV)	(meV)	(meV)	(meV)	(meV)	(meV)	(meV)	(meV)
777	777.17	0.22	767.59	758.04	778.70	0.33	769.18	759.61		
884	883.51	0.2			883.88	0.23				
1026	1023.6	0.22			1026.4	0.23			1030.4	0.25

Centre	E_a	S_1	S_2	W_1/W_0	W_2/W_0
(meV)	(meV)				
777	11.2	0.6	1.1	4	
884	5.2			4	
1026	34.6			83	86

Table 1. Compilation of the transitions observed for the centers 777, 884 and 1026 meV. In the notation each line is labeled by L_i^j, where i describe the excited state and j the number of phonons involved; the linewidth at half height is described by Γ; S_m is the Huang–Rhys factor for the line m; W_n is the probability of transition from the excited state n.

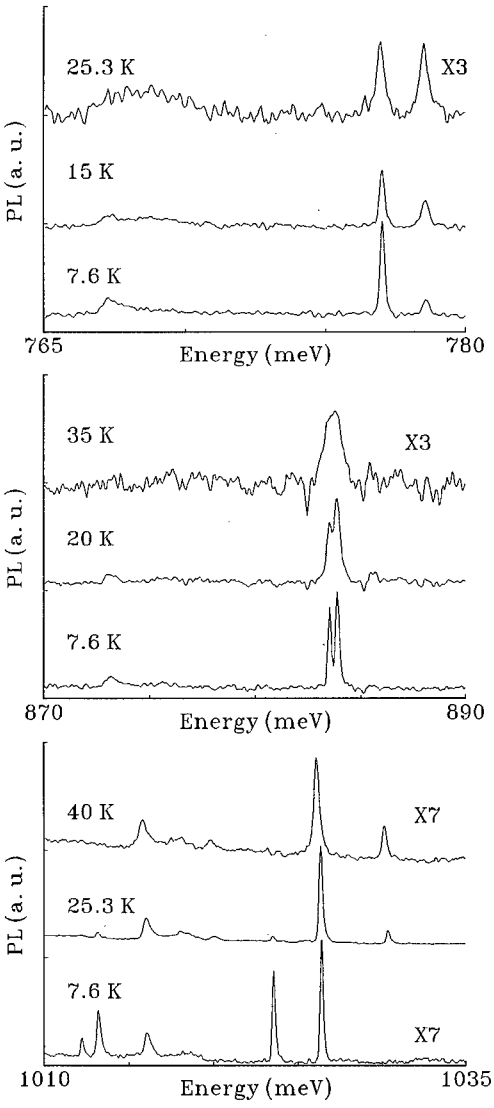


Fig. 2. Photoluminescence of the three centers observed in CZ Si:Pt measured at difierent temperatures.

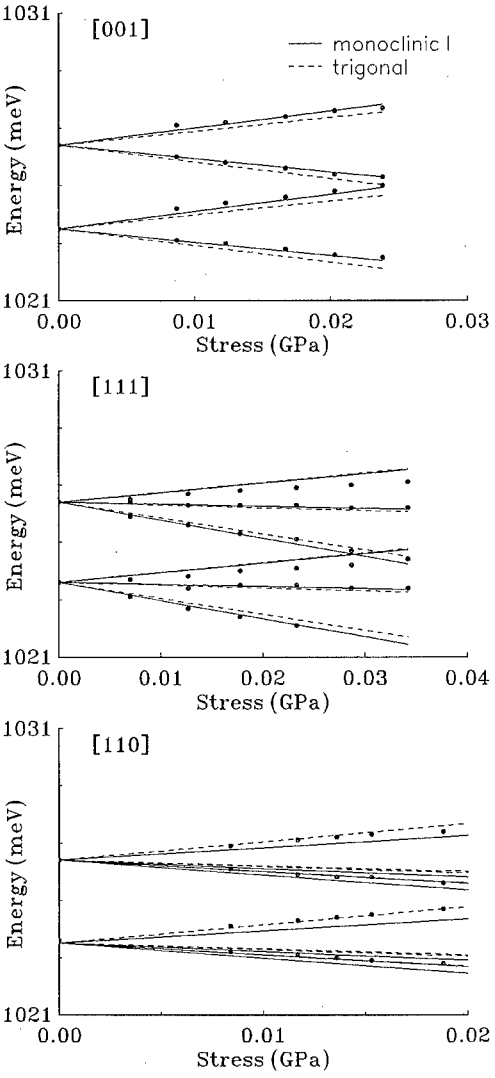


Fig. 3. Splitting of the 1026.4 and 1023.5 meV transitions under uniaxial stress. The lines represent the best fitting to the experimental points (dots).

Uniaxial stress measurements were made on all three centres, and the results are summarised in the fan diagrams of Figure 3. As shown in this figure the data can be fitted well for two cases: monoclinicI (A $\leftrightarrow$ A or B $\leftrightarrow$ B transitions) and trigonal (A $\leftrightarrow$ E transitions). The best parameters are indicated in Table 2. In both cases the intensity of the lines shows strong dicroism even at low stress values, as well as evidence for higher energy line states. For the 884 meV and 777 meV centres, the uniaxial stress data are incomplete. However, available data indicate that the centres are axial in nature.

Monoclinic I				Trigonal			
a_1	a_2	a_3	a_4	A_1	A_2	B	C
59.6	-52.5	-40.8	102.4	-4.9	-25.4	26.5	16.5

Table 2. Uniaxial stress parameters for the fitting shown in the Figure 3 using the notation of local coordinates for the monoclinic I and of Huges and Runciman[7] for trigonal symmetry. The units are meVGPa^{-1}.

Discussion

The energy levels produced by isolated Pt impurities in silicon are well documented in the literature. Several charge states of the impurity can be observed, and analogies to Au impurities are commonly invoked in describing the nature of the Pt levels[1]. In addition to the isolated impurities, quite a few complex defects involving one or more Pt atom, sometimes in conjunction with other impurities, have been cited as the origin of EPR, IR and DLTS signatures[8]. It is apparent that Pt impurities in silicon play a large role due to its strong tendency to form both Pt clusters and complexes with other impurities, namely Li[1] and H[9]. We now consider the results of our PL measurements in the light of the known properties of Pt-related centres.

The 1026 meV centre: The PL spectra reveal three excited electronic states for this centre, with transition rates into the ground state being in the ratio 1:83:86 approximately, and with separations between the levels of 2.8 and 4.0 meV. We now consider the position of the defect ground state, as deduced from the spectral and thermal information summarised in Table 1. For this centre, the thermal ionisation energy is 34.6 meV. Therefore, from the spectral position the ground state is $\sim$ 95meV from one of the band edges.

We next consider the details of the line shape of the zero-phonon lines. Figure 4 shows the lines on an enlarged energy scale, and it is evident that the lines are asymmetric. Furthermore, we can reproduce the observed line shape by a superpositioning of three lines in the ratio of the naturally occurring silicon isotopes. Thirdly, we have found that introducing Li into the ampoule when annealing the Pt-implanted samples enhances the production of this defect, although the defect can be produced without this intentional co–doping with Li. We note that the Pt-Li centre reported in EPR by[10] shows a strong silicon isotope effect also. The stress results show that the stress response to hydrostatic stress (parameter A_1 for trigonal symmetry) is -4.9 meV/GPa. This value is $\sim$ 33% of the hydrostatic shift for the silicon band edge (-15meV/GPa) showing that the centre is considerably harder to deform than the silicon lattice. This is consitent with a large defect envolving a few atoms.

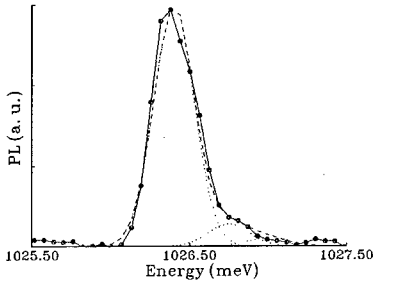


Fig. 4. Structure of the zero phono line at 1026.4 meV. The fitting (short dash curve) with theoretical curves (dots) in the ratio of the naturally occurring silicon isotopes is shown.

The 884 meV centre: In this case we have to date recorded only outline information. We detected two lines, very close together, and existing uniaxial stress data show that the centre is axial. A surprising feature of the temperature dependence data is the observation of a thermal deactivation energy of only $\sim$ 5.2 meV for the PL. This low value could be due either to the existence of a non–radiative excited state ($\sim$ 5.2 meV higher in energy) or to destabilisation of

the defect over a $\sim 5.2\,\mathrm{meV}$ barrier.

The 777 meV centre: The PL spectra for this centre reveals two electronic excited states separated by 1.7 meV and with transition rates from the upper level being a factor of four greater than from the lower level. Coupling to the local mode phonon is slightly stronger for the upper level, too, with the Huang-Rhys parameter values being 1.1 and 0.6, respectively. The data in Table 1 show that the thermal deactivation energy for the luminescence is only 11.2 meV, compared to 34.6 meV for the 1026meV centre. To date, this centre has been observed with greatest intensity in n-type samples known to have some Fe contamination, but it is not yet possible to confirm that Fe is essential for the formation of the centres. We find that when Au–Fe centres (which produce a PL band at 735 meV[11]) created using radioactive Au decay to Pt–Fe, only the 777 meV centre has a concurrent increase in the PL intensity. However, we cannot exclude the possibility that the 777meV centres are the daughter of some other Au parent centre.

In p-type samples we find that the 777 meV centres produced via the decay of Au to Pt are highly unstable at room temperature, annealing out completely within a few hours, similar to the annealing behaviour of the 735 meV Au-Fe centres which we have observed for p-type material. We cannot pursue the parallels between the two PL centres fully, as the data on the 777 meV centre are not yet complete, but we note that one key difference is the occurrence of three lines for the 735 meV centre compared to two for the 777 meV case. The presence of a sizeable spin–orbit coupling has been found to account for the splitting between the two lowest energy lines in the Au-Fe case[11]. The absence of a comparably strong spin-orbit interaction in the case of Pt–Fe would result in there being only two lines, as observed in the 777 meV case. It should be noted that an important aspect of current controversy regarding Au and Pt in Si is that spin–orbit effects are predicted to be considerably more important for Au than for Pt[12]. If the 777 meV centre can be verified to be the Pt analogue of the Au–Fe 735 meV centre, then the first experimental evidence to support that contention would be established.

Acknowledgements:

We wish to acknowledge the support of the Irish Science and Technology Agency (Forbairt). J. P. Leitão has a grant from the European Prodep programme.

References

1. P. Alteheld, S. Greulich–Weber, J.–M. Spaeth, H. Weihrich, H. Overhof and M. Höhne, Phys. Rev. B **52**, 4998(1995).
2. G. Armeles, J. Barrau, M. Brousseau and J. P. Noguier, Phys. Rev. B **33**, 1243(1986).
3. F. G. Anderson, F. S. Ham and G. D. Watkins, Phys. Rev. B **45**, 3287(1992).
4. P. Omling, M. Kleverman, P. Emanuelsson, J. Olajos and H. G. Grimmeiss, Solid State Commun. **65**, 557(1988).
5. M. H. Nazaré, M. C. Carmo and A. J. Duarte, Mat. Sci. Eng. B **4**, 273(1989).
6. M. O. Henry, S. E. Daly, C. A. Frehill, E. McGlynn, C. McDonagh, E. Alves, J. C. Soares and D. Forkel, Proc. Int. Conf. Phys. Semicond. (Berlin), 1996.
7. A. E. Huges and W. A. Runciman, Proc. Phys. Soc. **90**, 827(1967)
8. Y. K. Kwon, T. Ishikawa, H. Kuwano, J. Appl. Phys. **61**, 1055(1987).
9. P. M. Williams, G. D. Watkins, S. Uftring and M. Stavola in "Paper at ICDS" ed. H. Heinrich and W. Jantsch(Gmunden: Trans Tech Publications) pp. 891(1994).

10. P. Alteheld, S. Greulich–Weber, J.–M. Spaeth, H. Overhof and M. Höhne in "Papers at ICDS" ed. H. Heinrich and W. Jantsch(Gmunden: Trans Tech Publications) pp. 891(1994).

11. M. C. Carmo, M. I. Calão, G. Davies and E. C. Lightowlers in "Papers at ICDS" ed. G. Ferensi(Zurich: Trans Tech Publications) pp. 1497 (1989).

12. G. D. Watkins, M. Kleverman, A. Thilderkvist and H. G. Grimmeiss, Phys. Rev. Lett. **67**, 1149(1992).

Materials Science Forum Vols. 258-263 (1997) pp. 479-484
© 1997 Trans Tech Publications, Switzerland

IDENTIFICATION OF THE Si:Au AND Si:Pt $1S_{3/2}(\Gamma_8)+\Gamma$ PHONON-ASSISTED FANO RESONANCE

M. Kleverman, J. Olajos, and P. Tidlund
Solid State Physics, University of Lund
Box 118, S-221 00 Lund, Sweden

Keywords: Fano resonance, shallow acceptor, hole states, Si:Au, and Si:Pt

Abstract. The acceptor spectra of the Au and Pt centers in silicon have been studied by Fourier transform infrared spectroscopy including uniaxial-stress. A line, previously assigned to the 2p' Coulombic line, is identified as the $1S_{3/2}(\Gamma_8)$ phonon-assisted Fano resonance involving the Γ optical phonon. The deformation potentials b and d for the Au and Pt $1S_{3/2}(\Gamma_8)$ state are in good agreement with those for the B acceptor. Stress-induced preferential alignment effects are revealed and the doublet structure is due to the crystal-field split $1S_{3/2}(\Gamma_8)$ shallow acceptor state.

I. Introduction.

The excitation spectrum of the Pt and the Au isolated substitutional impurities in silicon are well known [1-3]. Both defects have similar electronic structure [4-6]. Shallow acceptors in silicon have two sets of excited states. The first set is found in the band gap and are denoted as the $P_{3/2}$ series and are mainly derived from the upper $P_{3/2}$ valence band. A second set is derived from the $P_{1/2}$ split-off band and transitions to p-like excited hole states, $nP_{1/2}$, denoted 2p', 3p',... , have been observed for the shallow group-III acceptors.

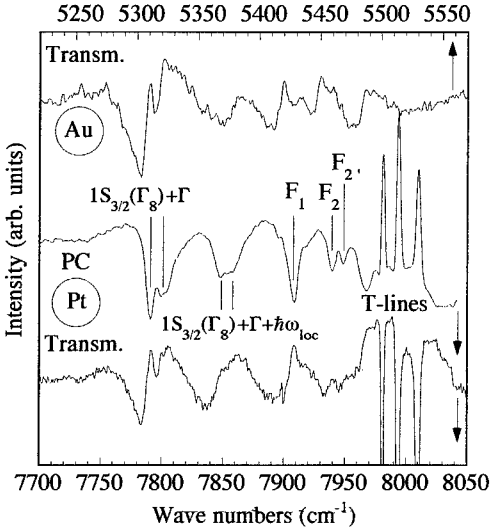


Fig. 1 Au (transmission) and Pt (transmission and PC) spectra showing the structures in valence band continuum. (See text for details).

The high-energy continuum part of the Au and the Pt acceptor spectra is presented in Fig. 1. Both the transmission and the photoconductivity (PC) spectra are shown for Pt whereas only the transmission spectrum for Au is reproduced in Fig. 1. F_1, F_2 and F_2' denotes phonon-assisted Fano resonances (PAFR), i.e., transitions to pseudo-discrete hole-phonon states that are resonant with the valence-band continuum. They consist [2,3] of the lowest $P_{3/2}$

acceptor states plus a Γ phonon (519 cm^{-1}). As is readily seen, the PAFR line shape varies considerably when observed in absorption compared to that for PC which is characteristic to PAFRs [7].

A doublet structure, labeled $1S_{3/2}(\Gamma_8)+\Gamma$ in Fig. 1, was observed for both defects close to the energy position expected for the 2p' line which previously lead us to tentatively assigned it as the 2p' line for the two centers. Also a second feature is observed labeled $1S_{3/2}(\Gamma_8)+\Gamma+\hbar\omega_{loc}$ in Fig. 1 and is a phonon replica of the $1S_{3/2}(\Gamma_8)+\Gamma$ line involving a Pt local phonon with an energy of about 58 cm^{-1} [3].

The negatively charged platinum center Pt has orthorhombic I symmetry [5] (C_{2v}) and a tetragonal (D_{2d}) (or lower) symmetry has been assigned to the neutral Au center [6], Au^0. However, the $2P_{1/2}$ state is a Kramers doublet and thus for the doublet structure. The excitation spectra are schematically described by $A^0+\hbar\nu \rightarrow A^-+h^+$, where A^0 and A^- indicate the neutral and negatively charged center, respectively, and h^+ indicates the hole in an excited state. We have so far only considered the excited hole but the A^- final core states may have an energy-level structure of two nearby states. If both core states can be reached in the transition to the $2P_{1/2}$ state a doublet structure are then expected to be observed even though the hole is excited to an orbital singlet. This explanation improbable since the very same doublet structure would then be expected to be observed for all lines, e.g., for the $P_{3/2}$ lines.

It will be shown that the doublet is due to transitions to the $1S_{3/2}(\Gamma_8)$ Coulomb state plus a Γ phonon coupled to the $P_{3/2}$ valence-band continuum, i.e., a phonon-assisted Fano resonance. The doublet line shape is due to the crystal-field split $1S_{3/2}(\Gamma_8)$ discrete state. Reorientations effects are observed in agreement with previous results [8,9].

II. Experimental details.

The samples were lapped, polished, and etched ($HF+H_20$) and Pt and Au diffused samples were prepared by sputtering Au or Pt onto 14 Ωcm p-type (boron) floating-zone silicon. The Pt samples were heat treated at 1260 °C for 1-7 days and the Au samples for 16h. All samples were quenched to room temperature in ethylene glycol. For the PC samples Ohmic contacts were prepared by rubbing Ga-Al onto parts of the surfaces. All spectra were obtained with a BOMEM DA3.02 Fourier transform infrared spectrometer (FTIR). The sample temperature was in all cases about 10 K.

III. Results and discussion

For both centers, the stress splitting of the $1S_{3/2}(\Gamma_8)+\Gamma$ lines have been studied by both PC and transmission measurements. The results obtained from the two different techniques are, within experimental errors, identical but as is seen in Fig. 1, the energy positions of the spectral features, e.g., the minima are not observed at the same energy positions when viewed in PC and transmission. These observations are in agreement with previous results [7].

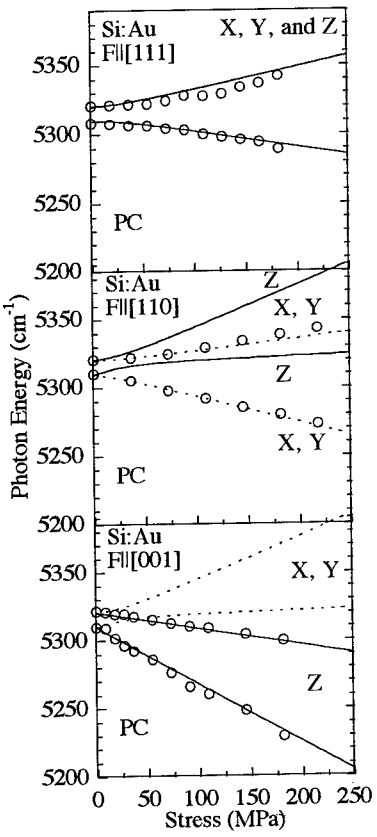


Fig. 2 The uniaxial-stress splitting of the $1S_{3/2}(\Gamma_8)+\Gamma$ Au line for F||[001], [110], and [111]. The spectra have been measured by photoconductivity.

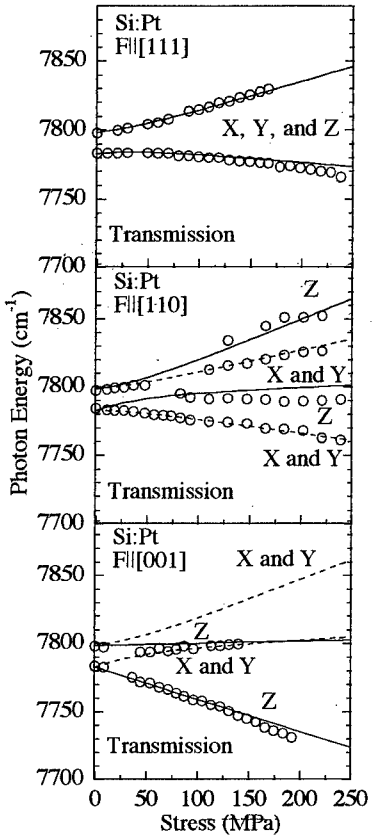


Fig. 3 The uniaxial-stress splitting of the $1S_{3/2}(\Gamma_8)+\Gamma$ Pt line for F||[001], [110], and [111]. The spectra have been measured by transmission.

Orientation	F||[001]	F||[110]	F||[111]
Z	A_1	A_2	$\frac{1}{2}(A_1+2A_2)$
X and Y	A_2	$\frac{1}{2}(A_1+A_2)$	$\frac{1}{2}(A_1+2A_2)$

TABLE I. The splitting due to orientational degeneracy for a D_{2d} center.

In Fig. 2 and 3, the uniaxial-stress results for the Au and Pt $1S_{3/2}(\Gamma_8)+\Gamma$ lines are presented, respectively. The lines show our calculated splitting behavior (see further below). In spite of some difference between the two spectra, the overall stress response is similar for the two centers. As is seen in

Figs. 2 -3, the splitting expected for centers orientated differently with respect to the stress axis have been indicated by X, Y, and Z. The X, Y, and Z centers are defined by their C_2 axis orientated the [100], [010], and [001] directions, respectively. An excitation

line at a tetragonal center is expected to split into 0, 2, and 2 components for stress in the [111], [110], and [001] directions, respectively. This splitting of the orientational degeneracy [10] is presented in Table I. The splitting of an electronic degenerate state may show up as an additional pattern superimposed onto the orientational splitting pattern.

We model the stress splitting by assuming that the transitions originate from a Kramers doublet to a Γ_8 state split by the D_{2d} crystal field although it is well known that the Pt center has C_{2v} symmetry but an dominating D_{2d} distortion. The stress-hamiltonian matrix $\mathbf{H}_{Stress}$ becomes [11]

$$\mathbf{H}_{Stress} = b\left(\varepsilon_{xx}\left(\mathbf{J}_x^2 - \frac{1}{3}J^2\right) + \varepsilon_{yy}\left(\mathbf{J}_y^2 - \frac{1}{3}J^2\right) + \varepsilon_{zz}\left(\mathbf{J}_z^2 - \frac{1}{3}J^2\right)\right) + \frac{2d}{\sqrt{3}}\left(\varepsilon_{xy}\mathbf{V}_{xy} + \varepsilon_{yz}\mathbf{V}_{yz} + \varepsilon_{zx}\mathbf{V}_{zx}\right) \quad (1)$$

$$\mathbf{V}_{xy} = \frac{1}{2}\left\{\mathbf{J}_x\mathbf{J}_y + \mathbf{J}_y\mathbf{J}_x\right\},\ \mathbf{V}_{yz} = \frac{1}{2}\left\{\mathbf{J}_y\mathbf{J}_z + \mathbf{J}_z\mathbf{J}_y\right\},\ \text{and}\ \mathbf{V}_{zx} = \frac{1}{2}\left\{\mathbf{J}_z\mathbf{J}_x + \mathbf{J}_x\mathbf{J}_z\right\}.$$

Note that the hydrostatic shift is excluded in eq. 1 but will be included via the parameters A_1 and A_2. ε_{ij} are components of the strain tensor and $\mathbf{J}_i$ (i=x, y, and z) are the angular-momentum matrices for a an atomic J=3/2 state derived from a s=1/2 p-state. The values used for the compliance tensor components[12] are s_{11}=7.617· 10^{-6}, s_{12}=-2.127· 10^{-6}, and s_{44}=1.246· 10^{-5} MPa^{-1}. The parameters b and d are deformation potentials and the stress is defined to be negative for compressional stress. The zero-stress splitting of the Γ_8 state in the D_{2d} crystal field is modeled by effective operators $\mathbf{H}_X$, $\mathbf{H}_Y$, and $\mathbf{H}_Z$, for X, Y, and Z orientated centers, respectively.

$$\mathbf{H}_X = S\cdot\left(2\mathbf{J}_x^2 - \mathbf{J}_y^2 - \mathbf{J}_z^2\right),\ \mathbf{H}_Y = S\cdot\left(2\mathbf{J}_y^2 - \mathbf{J}_z^2 - \mathbf{J}_x^2\right),\ \text{and}\ \mathbf{H}_Z = S\cdot\left(2\mathbf{J}_z^2 - \mathbf{J}_x^2 - \mathbf{J}_y^2\right) \quad (2)$$

where S is the strength of the distortion and determines the zero-stress splitting for the Γ_8 state. The results are presented in Fig. 2 and 3 and the parameters used are presented in Table II.

By taking both the electronic and orientational degeneracies into account we expect to observe 4, 4, and 2 lines for stress in the [001], [110], and [111] directions, respectively. However, only two lines are detected for all three stress directions for the Au center. In the case of Pt the expected number of lines was observed for [110] and [111] directions whereas only two lines are detected for [001] stress. It has been shown that the Pt and Au centers [8,9] preferentially aligns along the stress axis for compressional stress. In equilibrium, the centers are randomly distributed among the three different orientations whereas, e.g., for stress in the [001] direction, X and Y centers change their orientation and, accordingly, the number of Z centers increases. For stress in the [110] direction, X and Y centers are preferred and the number of Z centers decreases. Since all centers have the same angle to the stress axis for [111] stress no alignment occurs in

this case. As is seen in Fig. 2, a complete preferential stress alignment is observed for the Au center. For the Pt center, a complete alignment is observed for [001] stress whereas all four line components are observed for [110] stress. It should be noted that a third component has been observed for the Au center for [001] stress when the sample was subjected to inhomogenous stress.

The deformation potentials b and d for the boron acceptor $1S_{3/2}(\Gamma_8)$ ground state [13] are presented in Table II. As is readily seen the values for the deformation potentials b and d for the Au and Pt $1S_{3/2}(\Gamma_8)+\Gamma$ are very close to those for boron which strongly suggests that the $1S_{3/2}(\Gamma_8)$ state indeed is involved in doublet line.

The experimental results thus strongly indicate that the Au and Pt doublet line is the $1S_{3/2}(\Gamma_8)+\Gamma$ phonon-assisted Fano resonance. This identification thus enables a simple explanation for the differences in observed line shape when viewed in PC and transmission as well as for the doublet structure. The energy position for the Au and Pt $1S_{3/2}(\Gamma_8)$ pure electronic state is determined by subtracting the Γ phonon energy from the experimental energy positions. The energy positions in this way determined are 4796 and 7278 cm^{-1} for the Au and Pt center, respectively, where we have used the mean value for each doublet. In spite of several attempts no excitation lines have been observed at these energies. In the case of, e.g. the chalcogen double donors in silicon similar observations have been made [7].

TABLE II. The parameters used in the stress splitting calculations. The deformation potentials b and d for the boron $1S_{3/2}(\Gamma_8)$ ground state[13] is presented for comparison. See text for details.

Center	b (eV)	d (eV)	A_1 (cm^{-1}/MPa)	A_2 (cm^{-1}/MPa)	S (cm^{-1})
Au	-1.9	-4.9	-0.27	0.17	1.8
Pt	-1.6	-4.9	-0.11	0.17	2.6
B	-1.61	-4.5	-	-	-

The binding energies for the Au and Pt acceptors have been deduced in previous optical studies [2,3] and are about 5021.0 cm^{-1} (622.6 meV) and 7511.1 cm^{-1} (931.3 meV), respectively. The $1S_{3/2}(\Gamma_8)$ binding energy becomes 225 cm^{-1} (27.9 meV) and 233.1 cm^{-1} (28.9 meV) for Au and Pt, respectively. These energies are considerably smaller than the binding energies found for the group-III acceptors in silicon. An important difference between deep and shallow centers is that the ground state has very different origin. For true shallow centers, the acceptor ground state is the $1S_{3/2}$ (Γ_8) Coulomb state which possibly is perturbed by central-cell and screening effects whereas for deep centers the ground state is bound by the localized potential. The deep localized state

may give rise to a repulsive potential due to orthogonalization effects as have been observed for the interstitial Li donor [15] and for the Pt T-lines [16] in silicon. Such effects may be the cause for the decreased binding energy observed for the $1S_{3/2}$ state.

IV. Conclusions.

The Pt and Au doublet lines previously identified as the 2p' lines have been identified as transitions to the $1S_{3/2}(\Gamma_8)+\Gamma$ phonon-assisted Fano resonance. The doublet structure is due to a crystal-field splitting due to lower that tetrahedral symmetry of both centers.

Acknowledgments.

The authors acknowledge financial support from the Swedish Natural Science Research Foundation (NFR) and the Swedish Research Council for Engineering Sciences (TFR).

References.

1. G. Armelles, J. Barrau, M. Brosseau, B. Pajot, and C. Naud, Solid State Commun. **56**, 303 (1985)
2 M. Kleverman, J. Olajos, and H. G. Grimmeiss, Phys. Rev. **B35**, 4093 (1987)
3. M. Kleverman, J. Olajos, and H. G. Grimmeiss, Phys. Rev. **B37**, 2613 (1988)
4. J. W. Petersen and J. Nielsen, Appl. Phys. Lett. **56**, 1122 (1990)
5. H. H. Woodbury and G. W. Ludwig, Phys. Rev. **126**, 466 (1962)
6. G. D. Watkins, M. Kleverman, A. Thilderkvist, and H. G. Grimmeiss Phys. Rev. Lett. **67**, 1149 (1991)
7. E. Janzén , G. Grossmann, R. Stedman, and H. G. Grimmeiss, Phys. Rev. **B31**, 8000 (1985)
8. R. F. Milligan, F. G. Anderson, and G. D. Watkins, Phys. Rev. **B29**, 2819 (1974)
9. M. Kleverman, A. Thilderkvist, and G. D. Watkins, unpublished
10. A. A. Kaplyanskii, Optics Spectrosc., **16**, 329 (1964)
11. E. P. Kartheuser, S. Rodriquez, and P. Fisher, phys. stat. sol. (b), **64**, 11 (1974)
12. J. J. Hall, Phys. Rev. **161**, 756 (1967)
13. H. R. Chandrasekhar, P. Fisher, A. K. Ramdas, and S. Rodriquez Phys. Rev. **B8**, 3836 (1973)
14. M. Kleverman, A. Thilderkvist, G. Grossmann, and H. G. Grimmeiss, Proc. 16th Int. Conf. Defects in Semicond., Bethlehem 1991, Mater. Sci. Forum, Vol. 83-87, (1992) p. 125
15. H. Nara and A. Morita, J. Phys. Soc. Jpn., **23**, 831 (1967)
16. J. Olajos, M. Kleverman, and H. G. Grimmeiss, Phys. Rev. **B40**, 6196 (1989)

Materials Science Forum Vols. 258-263 (1997) pp. 485-490
© 1997 Trans Tech Publications, Switzerland

SILVER-RELATED DONOR DEFECT IN SILICON

Meng-Xia Zhu, Gordon Davies, M Zafar Iqbal*, E C Lightowlers
Department of Physics, King's College London, Strand, London WC2R 2LS, UK
*** Permanent address: Semiconductor Physics Laboratory, Department of Physics, Quaid-i-Azam University, Islambad, Pakistan**

Keywords: silicon, silver, photoluminescence, Zeeman effect, uniaxial stress.

Abstract. We report new data on the 6282 cm^{-1} photoluminescence band of a silver-related defect in silicon. We show that the main structure of the luminescence bandshape is caused by the vibronic interaction between the excited states of the centre, so that at low temperatures the phonon sideband originates from a forbidden zero-phonon line. The excited states are derived from a tightly bound hole and a weakly bound electron. The electron can be treated as moving in an effective T_d symmetry with parameters directly related to the conduction band minima. The hole establishes the symmetry of the optical centre as C_{1h}.

1. Introduction

Silver in silicon has attracted much attention in the last few years. This is due to its interesting physical properties as well as its role in silicon processing. It has been reported that silver in silicon can produce several centres [1,2]. The investigation of Olajos et al [3] identified that one of those defects, which produces the 6282 cm^{-1} photoluminescence (PL) system is a deep donor centre, and is possibly related to an isolated substitutional silver (Ag_s) atom. The sharp lines have been described as due to the transitions from the split effective-mass-like electronic states near the conduction band to the ground state. Further investigation of this centre [4-8] has shown that the dominant 3 zero-phonon lines of its PL, line "A" at 6282.3 cm^{-1}, "B" at 6289.9 cm^{-1} and "C" at 6326.2 cm^{-1} were transitions to the same ground state, and were associated with spin-triplet and singlet-singlet transitions. The phonons replicas with quanta of ~ 47 cm^{-1} and 117 cm^{-1} were believed to be phonon-sidebands of the A, B and C zero-phonon (ZP) lines. There is disagreement about the symmetry of this centre[3,6,8]. In spite of the optical studies of this centre, there are only a few works about the diffusion and heat treatment published so far [9,10]. To clarify some of the remaining problems we report new measurements here. We show that the phonon sidebands derive from a forbidden state through vibronic interactions with higher excited states, and that the effects of uniaxial stress perturbations can easily treated in an independent particle approximation, with the hole moving in the C_{1h} symmetry of the centre.

2. Sample preparation and experimental method

The centre was produced from either 1000 Ω n-type float-zone (FZ) silicon, with an oxygen concentration of less than 10^{14} cm^{-3} and carbon about 5×10^{15} cm^{-3}, or from 1000 Ω n-type WASO silicon, with oxygen less than 10^{15} cm^{-3} and carbon about 5×10^{15} cm^{-3}. The material was first gettered to drive out Cu atoms. It was then HF/HNO_3 etched, RCA cleaned, and HF dipped before Ag was evaporated on one side. The slices were heated at 1100°C for 20 hours in a quartz tube in flowing Ar gas and cooled down in the tube . The surface was etched to remove about 70μm. Optical measurements were carried out using either a Boman DA3 Fourier transform spectrometer or a Nicolet 60SX Fourier transform spectrometer fitted with North Coast Ge diode detectors. The samples were excited by a 594 nm Ar^+ laser operated at a constant power of about 400 mw. Uniaxial stress measurements were carried out at temperatures from 4.2 K up to 20 K and with stresses up to 600 MPa.

3. Structure of the vibronic sideband

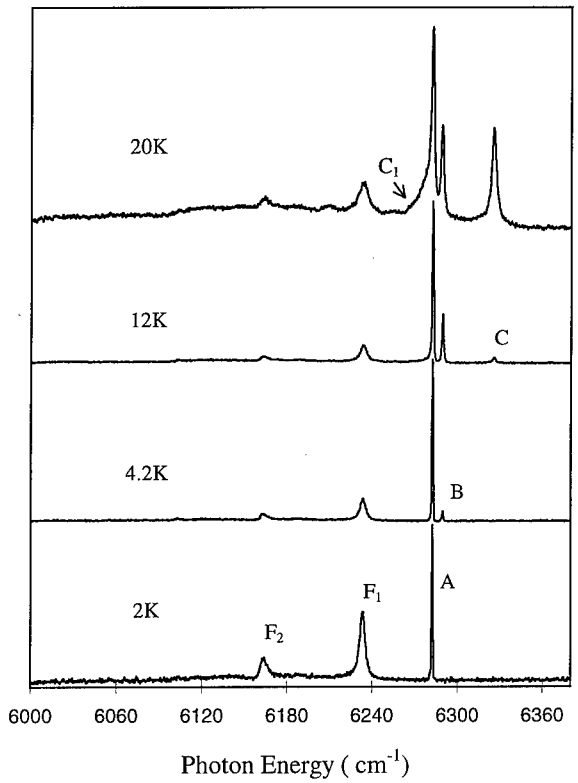


Figure 1. Photoluminescence spectra for silver-related donor centre in silicon. At very low temperature, kT << $\hbar\omega$, zero-phonon line A weakens relative to F_1 and F_2 on cooling from 4.2K to 2K.

Figure 1 shows typical photoluminescence spectra from our Ag-doped Si samples at 2, 4.2, 12 and 15 K. The zero-phonon lines labelled A, B and C are known to originate in three excited states of the centre which are able to come to thermal equilibrium with each other [6]. At 2 K a very weak line F is resolved, at 6280 cm^{-1}, 2 cm^{-1} below A. The phonon sidebands labelled F_1 and F_2 correspond to phonons of quanta $\hbar\omega = 47$ cm^{-1} and 117 cm^{-1}. Comparing the spectra at 2, 4.2 and 12K, it is clear that the B line does not produce an obvious contribution to the sideband, and that C_1 is the C-associated one-phonon line. We note that even at very low temperatures, kT << $\hbar\omega$, the observed zero-phonon line A *weakens* relative to the one-phonon sidebands on cooling from 4.2 to 2 K. This behaviour shows that F_1 and F_2 are not conventional phonon sidebands. Figure 2 establishes that the phonon sidebands in fact originate from the electronic state F. Here we plot the intensity of the phonon sideband F_1 to the intensity of the A zero-phonon line. The ratio follows an Arrhennius behaviour with an activation energy of 2.1 cm^{-1}, equal to the optical separation of F and A. Similarly, the ratio of F_1 to C has an activation energy equal to the splitting of F and C. Sideband F_2 follows the same behaviour: the vibronic sidebands originate through a vibronic coupling of F with the higher excited states. Coupling of the excited states through a term which is linear in the displacement of the phonon makes the one phonon transitions allowed, even though the F zero-phonon transition is still forbidden. This type of vibronic coupling is unusual in silicon, and appears to have been reported previously only for an FeB centre [11].

As a check on the data in Fig. 2 we note that the ratios extrapolated to infinite temperature are $I_C/I_{F1} = 45.1$ and $I_A/I_{F1} = 2.1$, resulting in the ratio $I_C/I_A = 22$, which is close to the value of 28 reported in [7].

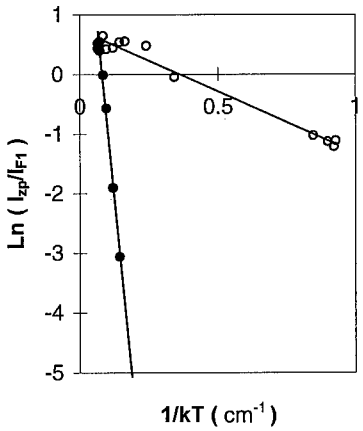


Figure 2. Variation of the intensities of line A (circles) and C (dots) relative to F1 with temperature. Lines are the least-square fits.

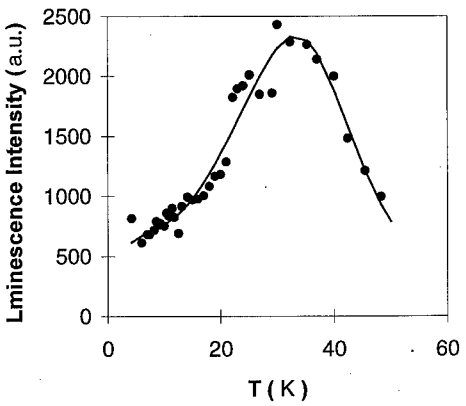


Figure 3. Absolute intensity of the total luminescence from the band as a function of temperature.

Figure 3 shows the temperature dependence of the total luminescence from the band. The intensity can be described by

$$I(T)\approx I(0)\frac{1+\frac{P_A g_A}{P_F g_F}\exp(-\Delta E_A/kT)+\frac{P_B g_B}{P_F g_F}\exp(-\Delta E_B/kT)+\frac{P_C g_C}{P_F g_F}\exp(-\Delta E_C/kT)}{\{(1+\frac{g_A}{g_F}\exp(-\Delta E_A/kT)+\frac{g_B}{g_F}\exp(-\Delta E_B/kT)+\frac{g_C}{g_F}\exp(-\Delta E_C/kT)\}\{1+gT^{3/2}\exp(-\Delta E_T/kT)\}}.$$

Here P_i/P_F is the ratio of the transition probabilities for all luminescence originating in states i and F, E_i is the energy of i above F, and g_i is the degeneracy of the ith state. With increasing T the total intensity increases as the state C becomes populated, from which, as we have seen, transitions are strongly allowed. At higher T, the intensity decreases by thermal dissociation of the excited state. The line is calculated with a thermal dissociation energy of E_T = 25 meV, much less than the spectroscopic binding energy of 385.3 meV. E_T is comparable with the ionisation energies in Si of an effective mass electron or hole orbitting one charge at the centre. The implication is that if we regard the excited state as a bound exciton, there is one tightly bound charge and one weakly bound charge at a neutral centre.

4. External fields.

The effects of uniaxial stresses on the energies of the zero-phonon lines are shown in Fig. 4. We will discuss these results using the independent-particle approximation, where the orbital motions of the two particles in the bound exciton are treated separately. We will confirm the suggestion [3] that it is the electron which is the weakly bound particle by examining the effects of uniaxial stresses. The electron can be regarded as moving in an effective tetrahedral symmetry, and only the tightly-bound hole experiences the true symmetry of the optical centre. If the orbital motion of the tightly-trapped hole is completely quenched by the strong axial bonding to the centre, the angular momentum of the hole is limited to its spin. The spin-spin interaction between hole and electron

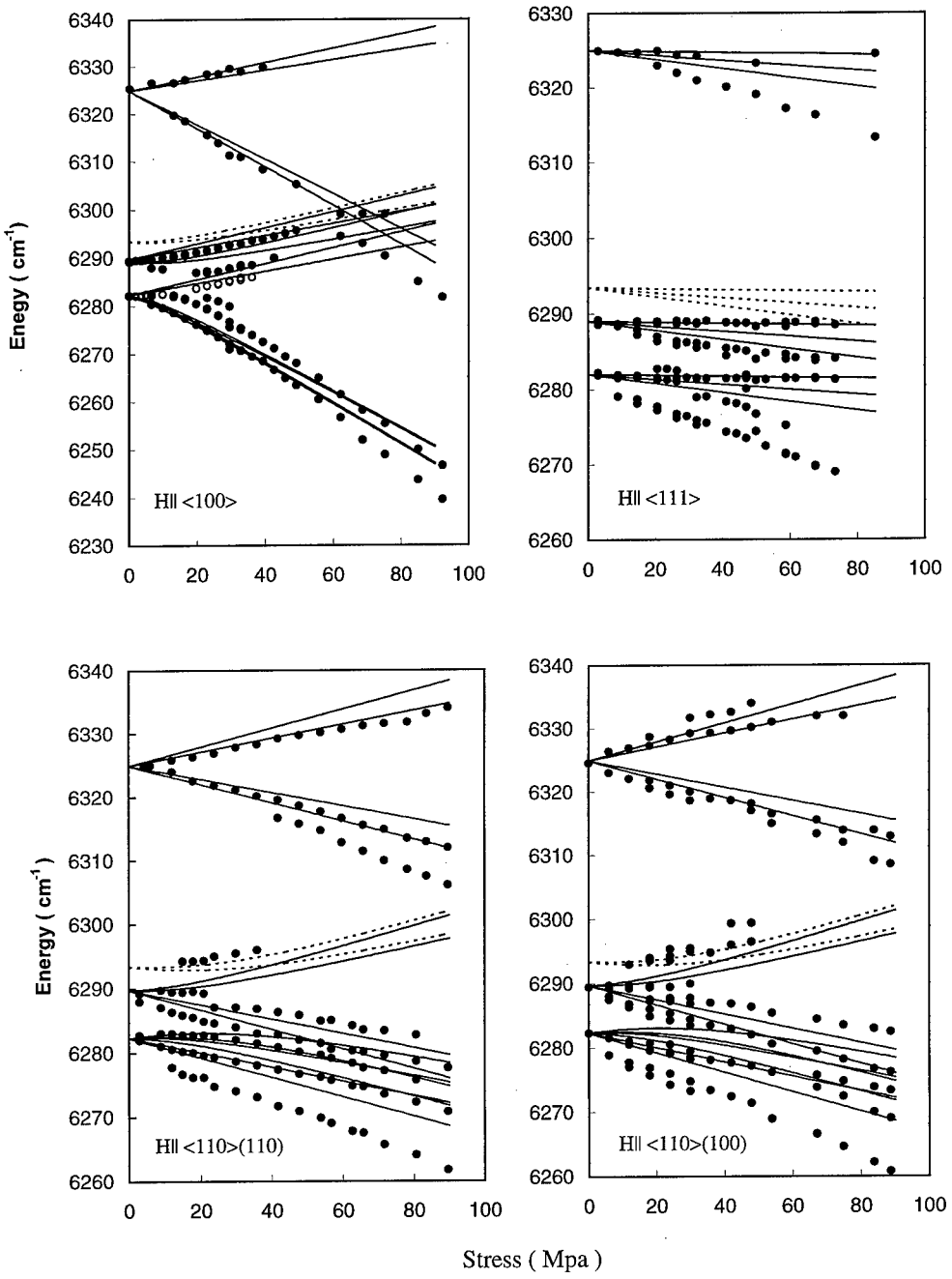


Fig. 4 Stress dependence of the ZP lines for stress along the principal crystal directions. Lines are represent the fits based on an independent particle approximation: the hole movies in the a C_{1h} symmetry, and the electron experiences a T_d symmetry.

produces singlet and triplet spin states. An effective-mass electron has an orbital state built up from the six-fold degenerate valleys of the conduction band [12]. The degeneracy is lifted by the valley-

orbital interaction, producing a singlet A, doublet E and triplet T_2 state in T_d symmetry. Spin-orbit interaction splits the triplet T_2 state further into three states with J=0, 1 and 2. The ground state is taken to be a "vacuum" state and so is a singlet spin state. Triplet to singlet transitions are expected to be weak, which gives, in our case, the allowed singlet-singlet transition line C and triplet-singlet forbidden lines A, B and F. Within the $^3T_2$ states, the spin-orbital Hamiltonian can be written as [13]

$$H_{SO} = \lambda (\boldsymbol{L} . \boldsymbol{S})$$

as in a ^3P term of an atom, where λ is the spin-orbital coupling parameter. Here we assume that A and B line are the J=1 and 2 of T_2 states. The best fitting of experimental data gives λ=-3.72 cm^{-1}. The tightly-bound hole moves in the lower symmetry of the optical centre. The fit to the data establishes this as C_{1h}. In this low symmetry, the hole will be perturbed by those stresses which transform as the A_1 representation of the point group C_{1h} of the centre. These stresses are

$$V=A_1\sigma_{zz}+A_2(\sigma_{xx}+\sigma_{yy})+2A_3\sigma_{xy}+4A_4(\sigma_{yz}-\sigma_{xz})$$

in the standard notation introduced by Kaplyanskii [14]. The fit to the data, allowing also for the behaviour of the electron as described in the next paragraph, gives A1 = 0.06, A2 = 0.02, A3 = 0, A4 = $\pm$0.02 cm^{-1}/MPa.

For the loosely bound electron we are working in T_d symmetry, and the potential produced by stress in a centre of T_d symmetry can be written in terms of the combinations of stress-tensor components which transform as the A_1, E and T_2 irreducible representations of the T_d point group :

$$V=A_1(\sigma_{xx}+\sigma_{yy}+\sigma_{zz})+A_\theta(2\sigma_{zz}-\sigma_{xx}-\sigma_{yy})+A_\varepsilon\sqrt{3}(\sigma_{xx}-\sigma_{yy})+A_xA_{yz}+A_y\sigma_{xz}+A_z\sigma_{xy}$$

where σ_{ij} are stress tensor components, and the A_1 are electronic operators. The effect of V on the conduction-band states is then known, as, e.g. in [15]. For brevity we note only that the effect of V on the T_2 states can be written as

V	T_{2x}	T_{2y}	T_{2z}
T_{2x}	$C(-\sigma_\theta+\sqrt{3}\sigma_\varepsilon)$	0	0
T_{2y}	0	$-C(\sigma_\theta+\sqrt{3}\sigma_\varepsilon)$	0
T_{2z}	0	0	$2C\sigma_\theta$

where the $C = x/2$, and x is the "valley strain" of the crystal. The extension to include all the A_1 and E valley orbit states is given in [15]. Considering the spin-orbital interaction, λ=-3.72 cm^{-1}, among the m states, the best fit to the experimental data gives C=0.09 cm^{-1}/MPa. This value coincides with that derived (C=0.087 cm^{-1}/MPa) by Thonke et al [15] for the effective mass electron orbitting the "C" centre.

6. Summary

Almost forbidden transitions from the level F have been shown to be the origin of the phonon sidebands of the centre, as a result of vibronic coupling to the higher excited states of the centre. The main splittings under stress can be explained using an independent-particle model in which the hole is bound in the C_{1h} symmetry of the centre and the electron orbits in states derived from the lowest conduction band, and effectively moves in T_d symmetry. The excited state multiplet structure can be derived from the conduction-band valley-orbit states plus the effect of spin-orbital

interaction λ=-3.72 cm^{-1} of the $^3T_2$ states of the electron-hole system. An extension of the calculation is needed to explain the splitting of F.

7. Acknowledgments
MXZ thanks the Overseas Research Studentship award and the K C Wong Education Foundation for financial support. This work was supported by the Engineering and Physical Sciences Research Council.

References
1. A.Fazzio, M.J.Caldas and Alex Zunger, Phys. Rev., **B32**(2), 924 (1985)
2. N.T.Son, V.E.Kustov, T.Gregorkiewicz, and C.A.J.Ammerlaan, Phys. Rev, **B46**(8), 4544(1992)
3. J.Olajos, M.Kleverman, and G.Grimmeiss, Phys. Rev., **B38**(15), 10633 (1988)
4. M.Kleverman, J.Olajos, B.Bech Nielsen, and G.Grimmeiss, Physica. Scripta, **T25**, 134 (1989)
5. J.H.Svensson, B.Monemar, and E.Janzén, Phys. Rev. Letts., **65**(14), 1796 (1990)
6. M Zafar Iqbal, G.Davies, E.C.Lightowlers, Mat. Sci. Forum, **143-147**, 773 (1994)
7. N.T.Son, M.Singh, J.Dalfors, B.Monemar, and E.Janzén, Phys. Rev., **B49**(24), 17428 (1994)
8. M.Singh, W.M. Chen, B.Monemar, and E.Janzén, Solid state Communications, **93**(5), 415 (1995)
9. F.Rollert, N.A.Stolwijk, and H.Mehrer, J. Phys, **D20**, 1148 (1987)
10. Ali Alkbar, M.Zafar Iqbal, and N Babar, J Appl. Phys. **77**(7), 3315 (1995)
11. G.Davies, Phys. Rep, **3&4**, 83 (1989), and references there.
12. F.Seitz and P.Turnbull, Solid State Physics, **5**, Academic Press, Inc., New York, (1957)
13. F.S. Ham, Phys. Rev., **138**(6A), A1727 (1965)
14. A.A.Kaplyanskii, Optics and Spectroscopy, **16**, 329 (1964)
15. K.Thonke, A.Hangleiter, J.Wagner, and R.Sauer, J Phys., **C18**, L795 (1985)

Materials Science Forum Vols. 258-263 (1997) pp. 491-496
© 1997 Trans Tech Publications, Switzerland

ISOLATED SUBSTITUTIONAL SILVER AND SILVER-INDUCED DEFECTS IN SILICON: AN ELECTRON PARAMAGNETIC RESONANCE INVESTIGATION

P.N. Hai[1,2], T. Gregorkiewicz[1], C.A.J. Ammerlaan[1] and D.T. Don[2]

[1]Van der Waals–Zeeman Institute, University of Amsterdam, Valckenierstraat 65-67, NL-1018 XE Amsterdam, The Netherlands

[2]Faculty of Physics, National University of Hanoi, 90 Nguyen Trai Street, Hanoi, Vietnam

Keywords: silver, silicon, electron paramagnetic resonance, hyperfine interaction.

Abstract Two new electron paramagnetic resonance spectra in silicon doped with silver in a water vapor atmosphere are reported. The observed centers, labeled Si-NL56 and Si-NL57, show a symmetry lower than cubic and an effective electron spin S=1/2. Based on studies with enriched silver isotopes and analysis of the observed two-fold hyperfine splitting, the participation of one silver atom is established for two centers. The Si-NL56 center of the orthorhombic-I symmetry is identified as an isolated substitutional silver atom, and its electronic structure is shown to conform to the vacancy model. Due to the presence of an additional hyperfine interaction with a nuclear spin I=5/2 the Si-NL57 spectrum of the trigonal symmetry is assigned to a complex of silver with another impurity introduced during the diffusion process. Taking into account the sample preparation procedure, the Si-NL57 center is attributed to an Al_s-Ag_i pair in a negative charge state. This observation also indicates the diffusion enhancement of aluminum in silicon treated in the water vapor atmosphere.

Introduction

Silver receives considerable interest as a deep-level dopant in silicon. This is due to its interesting role in silicon processing. From a more fundamental point of view, the Ag dopant constitutes a particularly interesting case of a transition element with a complete d^{10} electron shell, and is directly comparable to such centers as Au and Pt whose electronic structure is intensively investigated.

Some information on electrical and optical properties of the silver impurity in silicon has been established in the past. Electrical measurements [1] revealed its amphoteric character. Using optical spectroscopies Olajos *et al.* [2] investigated the excitation spectra of electronic excited states in Ag-doped silicon and identified those as arising from the deep state of the, probably substitutional, Ag donor. However, the microscopic structure of the Ag-induced centers, which is often revealed by means of electron paramagnetic resonance (EPR) spectroscopy, is not clear. In EPR measurements on Ag-doped silicon [3,4] a number of Ag-related centers has been found. One of the spectra, Si-NL42, has been attributed to a single Ag atom in a neutral charge state on a tetrahedral, probably interstitial, site. The issue of the existence of the isolated substitutional silver center in silicon, as postulated from optical and electrical studies, remains therefore open.

In this contribution we present results of an EPR investigation of silicon samples doped with silver in water vapor environment; the high temperature annealing in water vapor was shown to be an effective manner to hydrogenate silicon [5]. In the frame of the study two new EPR spectra have been detected. While their generation was evidently related to the presence of the (heavy) water vapor, no evidence of a direct hydrogen involvement in the microscopic structure of these centers has been found.

Experimental procedures

The samples used in this study were made from B- and P-doped, dislocation-free, float-zone silicon crystals with a room-temperature resistivity in the range of 1000 Ωcm. The dimensions of samples were typically $1\times1\times15$ mm^3 with the length along the $[0\bar{1}1]$ crystal direction. The samples were diffused with silver. In this procedure small amounts of natural high-purity silver (99.999%) or monoisotopically enriched (but not high-purity) silver ^{107}Ag (99.5%) or ^{109}Ag (99.4%) were deposited on both sides of the sample by scratching. The crystals were then sealed in quartz ampoules

containing argon atmosphere and a few milligrams of water. The diffusion treatment was performed in a tube furnace at a temperature of 1250 °C for a duration of several hours, and then abruptly terminated by quenching to room temperature.

The EPR measurements were performed with a superheterodyne spectrometer operating in the microwave frequency of about 22.9 GHz (K band), tuned to dispersion. The sample was mounted with the $[0\bar{1}1]$ crystal direction perpendicular to the plane of the rotation of the magnetic field. Most measurements were taken at liquid-helium temperature.

Experimental results and discussion

Following the quenching several new spectra were observed. Figures 1(a) and (b) show typical EPR spectra recorded for ^{107}Ag- and ^{109}Ag-doped samples, respectively. An anisotropic spectrum, labeled Si-NL56, reproducible for doping with natural or monoisotopically enriched silver, consists of two groups of intense EPR lines corresponding to a two-fold hyperfine (hf) splitting. In addition to this signal, another anisotropic spectrum, labeled Si-NL57, was also detected in samples for which monoisotopically enriched silver was used as a dopant source. These two spectra have different angular and temperature dependencies: the Si-NL56 spectrum remains unchanged whereas the other one vanishes when measuring at temperature of 8 K or higher, as depicted in Figs. 1(c) and (d). These facts indicate that these spectra belong to different centers.

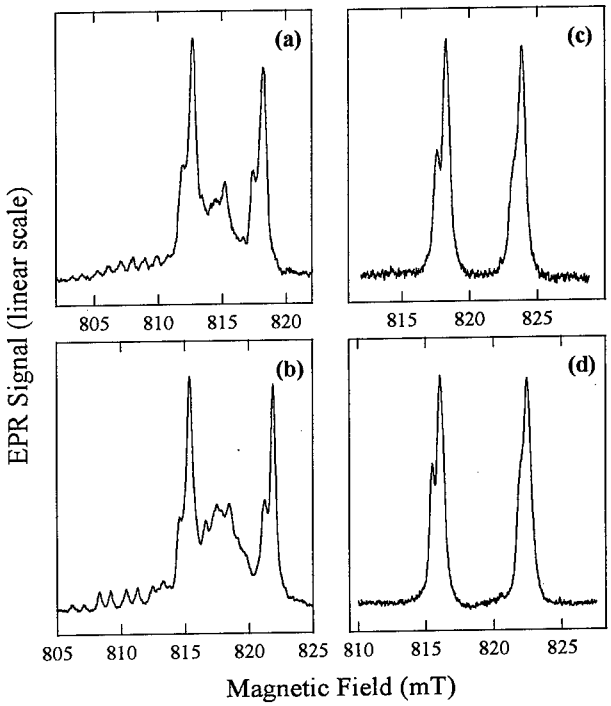


Fig. 1: *Anisotropic EPR spectra observed at an angle of approximately 2.5° away from the* [011] *direction in the* $(0\bar{1}1)$ *plane at temperature T=4.2 K for a sample doped with* (**a**) ^{107}*Ag (microwave frequency* ν*=22.7838 GHz) and* (**b**) ^{109}*Ag* (ν*=22.8697 GHz) silver isotope. The EPR spectra recorded 32° away from the* [011] *at T=8 K for samples doped with* (**c**) ^{107}*Ag* (ν*=22.9412 GHz) and* (**d**) ^{109}*Ag* (ν*=22.8935 GHz).*

A. Si-NL56 center

Taking into account the fact that the anisotropic spectrum could only be produced when diffusing Ag in the water vapor ambient at high temperature, we consider Ag or/and H as the possible candidate(s) responsible for the two-fold splitting. To examine the role of Ag and H in the defect structure, two

additional sets of different samples were prepared: the first set of samples was doped with natural (high-purity) or monoisotopically enriched silver in the atmosphere of Ar gas only; the second set was heated without Ag in the ambient of water vapor. The heat-treatment parameters were kept identical in both cases. No Si-NL56 EPR spectrum for the two sets of samples was detected. From these observations we conclude that both Ag and H are needed in the formation process of this center. Another set of samples was prepared with the use of Ag and heavy water vapor (D_2O, with nuclear spin I=1 for deuterium). No differences between samples doped with Ag in the atmosphere of water and heavy water vapor have been found. This leaves Ag as the prominent candidate for the explanation of the hf structure. A similar sample doped with the enriched silver isotope ^{109}Ag was prepared. The Si-NL56 spectrum could be detected again with the distinct difference in the hf splitting, as shown in Fig. 1(b). The ratio between the splittings observed in the experiment is equal to 0.87, and perfectly matches the ratio of the nuclear magnetic moments of the two isotopes [6]. On the basis of these isotope effects on the spectra we conclude that the anisotropic Si-NL56 center involves a single Ag atom. While H is not observed as a structural component of the Si-NL56 center, it takes part in its formation process. If further confirmed, this would be the first observation of the H-related enhancement of diffusion for a transition metal impurity in silicon.

The spectrum could be fitted with the spin Hamiltonian

$$\mathcal{H}_S = \mu_B \vec{B} \cdot \mathrm{g} \cdot \vec{S} + \vec{S} \cdot \mathrm{A} \cdot \vec{I}, \qquad (1)$$

where **g** and **A** represent the Zeeman splitting and the hf interaction tensors, respectively, with the electron spin S=1/2 and nuclear spin I=1/2. Full angular dependence of the spectrum, showing the orthorhombic-I (C_{2v}) symmetry , was obtained when rotating the external magnetic field in the $(0\bar{1}1)$ crystal plane, with the result as given in Fig. 2. The results of the computer fit for the Si-NL56 center, are summarized in Table 1.

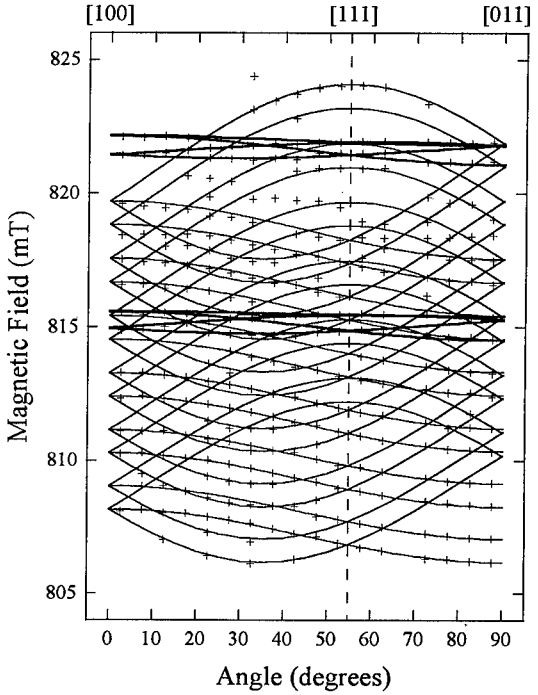


Fig. 2: *Angular dependence of the Si-NL56 and Si-NL57 spectra measured in the ^{109}Ag-doped sample. The bold and thin solid lines represent a fit to the experimental points (+) according to equation (1) for spectrum Si-NL56 and equation (2) for Si-NL57, respectively. The microwave frequency is ν=22.8697 GHz*

Cu, Ag and Au atoms have similar free-atom electronic configurations in vacuum (n-1)d^{10}ns^1 (n=4, 5 and 6, respectively). The same applies to Pt in the negative charge state Pt^-, which is isoelectronic to Au^0. Therefore the similar kind of symmetry in the isolated sites could be expected for all of them. In fact several experimental results were shown to support the idea. The EPR data for the isolated substitutional platinum Pt_s^- [7] revealed the C_{2v} symmetry. Also for Au in silicon a C_{2v}

spectrum (Si-NL50 [8]) has been reported, although its relation to an isolated neutral gold atom is under dispute and requires further confirmation. In the IR absorption measurements for Ag-doped

Table 1: *Spin-Hamiltonian parameters of the Si-NL56 center. Respective values for the oxygen-vacancy defect are also given for comparison. The hf components are given in MHz.*

Center	Tensor	Principal values			Ref.
		$\parallel [100]$	$\parallel [011]$	$\parallel [0\bar{1}1]$	
Si-NL56	g	1.9954	1.9960	1.9980	This
(^{107}Ag)	A	160.0	155.5	159.4	work
(^{109}Ag)	A	184.3	179.2	183.7	
Si:OV$^-$	g	2.0033	2.0025	2.0093	[12]
(^{17}O)	A	4.363	−0.997	5.593	

silicon [2] the observation of four lines for the $1s(E+T_2)$ multiplet indicates that the center has C_{2v} symmetry (or lower). Based on the vacancy model [9] this spectrum was then postulated to arise from a neutral substitutional silver dopant. From these findings, it seems reasonable to conclude that the common trend for the symmetry of these impurities in the isolated substitutional site in silicon is the orthorhombic-I. Following the observation of the isotope effects, we concluded on the participation of a single Ag atom in the structure of the C_{2v} Si-NL56 center reported here. At the same time the isotope effects on the spectra do not support the possibility that the center consists of a pair of Ag and H atoms. Also a pair of Ag and an impurity with zero nuclear magnetic moment seems improbable, although such a possibility cannot be ruled out experimentally. Therefore we suggest that the Si-NL56 spectrum of the C_{2v} symmetry arises from an isolated substitutional Ag atom. With the current findings the microscopic picture of an isolated Ag impurity in silicon becomes complete. It bears also a close similarity to the behavior of nickel in silicon: the isolated interstitial nickel Ni_i^+ in the high-symmetry site [10] and the isolated substitutional nickel Ni_s^- of the C_{2v} symmetry [11].

The Si-NL56 spectrum, with the orthorhombic-I symmetry, the electron spin S=1/2, the principal g values close to the spin-only value g_e=2.00232, and the nearly [011] axial hf interaction, (i.e. similar to the case for the isolated vacancy V^- in silicon [12]), is in good agreement with the vacancy model proposed by Watkins [9]. Following this model, the substitutional Ag atom in its neutral charge state has a completely filled $4d$ shell accommodating 10 electrons ($4d^{10}$). The unpaired $5s$ electron, responsible for the paramagnetism of the center, occupies the b_1 orbital of the vacancy t_2 gap manifold state, which is split due to a Jahn-Teller distortion. Applying the treatment proposed by Anderson *et al.* [13] with the anisotropic term of the hf interaction P=−176.4 MHz for a ^{107}Ag $4d$ orbital [14], we find that the experimental value of $A_{[0\bar{1}1]}-(A_{[100]}+A_{[011]})/2$=+1.65 MHz corresponds to the $N^2\approx$1.2% percentage of d character in the orbital. This value is in good agreement with the spin density value of 2.8% for $4d$ orbital on the Ag atom found alternatively in the numerical analysis of the experimental hf interaction based on the conventional one-electron linear-combination of atomic-orbitals (LCAO) approximation. Such a localization value is reasonable within the vacancy model.

B. Si-NL57 center

The trigonal symmetry of this center is evident from its angular dependence in the $(0\bar{1}1)$ crystal plane depicted in Fig. 2. The observed spectrum is not very well resolved, and overlaps partially with the Si-NL56. It contains six groups of EPR lines consistent with the six-fold hf splitting due to an interaction of an effective electron spin S=1/2 with a nuclear spin I=5/2 with an abundance of 100%. Further two-fold splitting within a line group can be explained by the hf interaction with a nuclear spin I=1/2 with an abundance of 100%. This spectral structure indicates a complex consisting of two different impurity atoms. Using the isotope effects, the two-fold hf splitting could be explained by Ag since the ratio of the doublet splittings observed for the samples doped with enriched ^{107}Ag and ^{109}Ag is consistent with the ratio of the nuclear magnetic moments of the two isotopes, and the identical spectra are obtained regardless of whether water or heavy water vapor atmosphere is used.

We therefore conclude to the involvement of one Ag atom in the defect structure of this center. With the nuclear spin I=5/2, the other component of the complex has to be considered as a contaminant introduced by diffusion. One can note that the Si-NL57 spectrum was not present in samples doped with high-purity natural silver. There are several elements with I=5/2 and a 100% natural abundance: ^{27}Al, ^{55}Mn, ^{127}I, ^{141}Pr, Re (with two isotopes having roughly identical nuclear magnetic moments). Out of these, I, Pr and Re can be excluded as rare contaminants of silicon. Several samples were prepared under the same conditions and with a very small amount of Mn. The Si-NL57 spectrum could not be observed in such cases. In this way Mn has been ruled out as a possible constituent of the Si-NL57 center. On the other hand, the Si-NL57 spectrum could be readily seen in samples prepared under the same conditions and co-doped with natural high-purity Ag (99.999%) and Al. We note further that the isotopically enriched Ag used in our experiments was indicated to have a considerable Al contamination. In view of the above facts we assume that Al is involved in the defect composition and propose to assign the Si-NL57 spectrum to an Al-Ag pair.

The experimental data could be fitted using the spin Hamiltonian

$$\mathcal{H}_S = \mu_B \vec{B} \cdot \mathrm{g} \cdot \vec{S} + \vec{S} \cdot \mathrm{A}_{Al} \cdot \vec{I}_{Al} + \vec{S} \cdot \mathrm{A}_{Ag} \cdot \vec{I}_{Ag}, \qquad (2)$$

where $\mathbf{g}$, $\mathbf{A}_{Al}$ and $\mathbf{A}_{Ag}$ represent the Zeeman splitting tensor and the hf interaction tensors for Al and Ag, respectively, with the effective electron spin S=1/2. The results of the computer fit are listed in Table 2. Applying the LCAO treatment to analyze the experimentally determined hf interaction components, the spin densities $\eta^2\alpha^2$ and $\eta^2\beta^2$ in the 3s and 3p orbitals on the Al atom are then determined as 1.6% and 0.8%, respectively. For the Ag atom only the isotropic part of the hf interaction is detected resulting in the spin density $\eta^2\alpha^2$ in the 5s orbital of 1.6%.

Based on the observed hf interactions we propose to identify the Si-NL57 center as an Al-Ag pair. Obviously, the trigonal symmetry of the pair requires two atoms located along ⟨111⟩, possibly on the nearest-neighbor sites. In nonirradiated silicon, Al is known to occupy substitutional sites and acts as a shallow acceptor, spin S=0. Therefore the observed electron spin S=1/2 of the Si-NL57 center has to arise from the Ag component. From the analysis of the experimental results, one can see that the hf interaction with the Ag atom is isotropic and, as such, results from the localization of the unpaired spin predominantly in the 5s orbital. This situation corresponds to the $4d^{10}5s^1$ electronic configuration of a Ag atom, in which a 5s electron gives rise to the electron spin S=1/2. As discussed for the Si-NL56 spectrum, both Ag_i^0 and Ag_s^0 isolated silver centers have the required electronic configuration. However, in view of the results obtained for the Si-NL56 center and the general trend of (n-1)d^{10}ns^1 type impurities outlined earlier, a neutral Ag atom on a substitutional site is likely to undergo a tetragonal Jahn-Teller and a weaker trigonal distortion, so that the overall symmetry of the hypothetical Al_s^--Ag_s^0 pair would be C_{2v}, or lower. Since the observed symmetry of the Si-NL57 center is trigonal, the Al_s^--Ag_s^0 pair is not a good candidate for the microscopic model of this defect. On the other hand, the Al_s^--Ag_i^0 pair will be trigonal and therefore in agreement with the experimental findings. Based on this reasoning, we attribute the Si-NL57 spectrum to the Al_s^--Ag_i^0 pair in the negative charge state.

Table 2: *Spin-Hamiltonian parameters of the center Si-NL57. The hf components are given in MHz.*

Element	^{107}Ag	^{109}Ag	^{27}Al
$g_\parallel$		1.9971	
$g_\perp$		2.0127	
$A_\parallel$	21.4	24.7	61.4
$A_\perp$	21.4	24.7	59.2

Since the Si-NL57 spectrum was only observed for the samples doped with isotopically enriched Ag which was contaminated with Al, and not when natural Ag of high purity (99.999%) was used, we conclude that Al ions were introduced into silicon during the heat treatment. At first sight such a conclusion appears unlikely since Al is known to be a very slow diffusant in silicon. We point out, however, that in this case the diffusion process of Al could be influenced by three additional factors: i) a simultaneous presence of Ag, which is known to create vacancies [10], and therefore promotes the substitutional diffusion mechanism; ii) the oxidation of the sample surface, which took place in water vapor atmosphere at 1250 °C temperature, and which also enhances the diffusion [15]; iii) the presence of H atoms which could affect the activation energy for diffusion. In any case, a low concentration of aluminum contamination is consistent with the low intensity of the Si-NL57 spectrum observed in this study.

Conclusions

The isolated substitutional silver atom in silicon has been identified and analyzed by the EPR technique. The experimental data could be satisfactorily explained within the vacancy model. The other new EPR spectrum reported here is associated with the $Al_s^- - Ag_i^0$ pair. In the process of sample preparation for the current study also the hydrogen-enhanced diffusion of Al and Ag in silicon has been observed.

Acknowledgements

One of us (P.N.H) acknowledges the Faculty of Mathematics, Informatics, Physics and Astronomy, University of Amsterdam for the study fellowship in the Van der Waals–Zeeman Institute.

References

1. N. Baber, H.G. Grimmeiss, M. Kleverman, P. Omling and M.Z. Iqbal, J. Appl. Phys **62**, 2853 (1987) and references therein.
2. J. Olajos, M. Kleverman and H.G. Grimmeiss, Phys. Rev. B **38**, 10633 (1988).
3. N.T. Son, V.E. Kustov, T. Gregorkiewicz and C.A.J. Ammerlaan, Phys. Rev. B **46**, 4544 (1992).
4. N.T. Son, T. Gregorkiewicz and C.A.J. Ammerlaan, J. Appl. Phys. **73**, 1797 (1993).
5. M. Höhne, U. Juda, Yu.V. Martynov, T. Gregorkiewicz, C.A.J. Ammerlaan and L.S. Vlasenko, Phys. Rev. B **49**, 13423 (1994).
6. G.H. Fuller, J. Phys. Chem. Ref. Data **5**, 835 (1976).
7. H.H Woodbury and G.W. Ludwig, Phys. Rev. **126**, 466 (1962).
8. N.T. Son, T. Gregorkiewicz and C.A.J. Ammerlaan, Phys. Rev. Lett. **69**, 3185 (1992).
9. G.D. Watkins, Physica **117B & 118B**, 9 (1983).
10. G.W. Ludwig and H.H. Woodbury, in *Solid State Physics*, edited by F. Seitz and D. Turnbull (Academic Press, New York, 1962), Vol. **13**, 223.
11. L.S. Vlasenko, N.T. Son, A.B. van Oosten, C.A.J. Ammerlaan, A.A Lebedev, E.S. Taptygov and V.A. Khramtsov, Solid State Commun. **73**, 393 (1990).
12. M. Sprenger, S.H. Muller, E.G. Sieverts and C.A.J. Ammerlaan, Phys. Rev. B **35**, 1566 (1987).
13. F.G. Anderson, F.S. Ham and G.D. Watkins, Phys. Rev. B **45**, 3287 (1992).
14. A.K. Koh and D.J. Miller, At. Data Nucl. Data Tables **33**, 235 (1985).
15. S. Mizuo and H. Higuchi, Jpn. J. Appl. Phys. **21**, 56 (1982).

Materials Science Forum Vols. 258-263 (1997) pp. 497-502
© 1997 Trans Tech Publications, Switzerland

PSEUDO OR DEEP DONOR EXCITATION SPECTRA IN SILICON

Mats Kleverman
Solid State Physics, University of Lund
Box 118, S-221 00 LUND, Sweden

Keywords: pseudo donors, shallow donors, deep donors

Abstract The often used pseudo-donor model for luminescence and excitation spectra in semiconductors will be discussed in some detail. The model has been applied to excitons bound at, e.g., isoelectronic centers but also to excitation spectra of deep levels. It will be argued that the pseudo-donor model is applicable only to bound excitons for which the binding is weak. For more strongly bound excitons as for deep centers *"there is no point in using the term bound exciton, since one has simply an excited state of the defect"* [1]. It will be argued that the particular spectral features observed for deep "pseudo-donors" are well accounted for by considering the "molecular" gap state of deep donors in addition to the shallow-donor states.

Discussion

The energy structure of shallow donors is known for many semiconductors and is well described by the effective-mass-theory, EMT. The electronic structure of a neutral donor in cubic semiconductor with the conduction band minimum at the Γ point is simply that for atomic hydrogen although the energy scale is reduced due to the static dielectric constant and the effective mass. The lowest state is 1s and since it is the ground state transitions to, e.g., 2p, 3p, and etc. may be observed.

Silicon has six equivalent conduction minima in the <100> directions. All shallow donor states are therefore at least six-fold degenerate and in tetrahedral symmetry, valley-orbit interaction and central-cell effects split the six-fold degenerate 1s state to $1s(A_1)$, $1s(T_2)$, and 1s(E) being 1-, 3- and 2-fold degenerate, respectively (Fig. 1). For shallow donors for which no bound states exists in the band gap except the Coulombic states, the $1s(A_1)$ state is usually the ground state since it is the only 1s state that has a non-vanishing amplitude at the origin and, accordingly, is most strongly affected by the attractive localized impurity potential. The $1s(T_2)$ and the 1s(E) states have energies close to the 1s EMT energy. Electric-dipole transitions are symmetry allowed from $1s(A_1)$ to $1s(T_2)$ but this transition is usually not observed for true shallow centers since it is forbidden in the EMT approximation. The 1s energy level structure is nevertheless well known for shallow donors since the energy positions of $1s(T_2)$ and 1s(E) have been

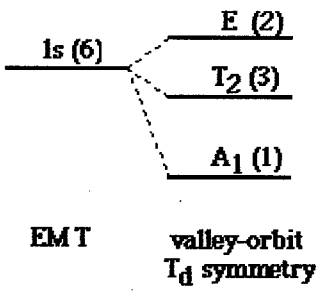


Fig. 1 Multivalley splitting of 1s donor states in silicon for tetrahedral symmetry.

established, e.g., by thermal population studies.

Transitions to states in the 1s manifold have been observed for many deep donors in silicon. In the case of the chalcogen double donors S, Se, and Te in Si transitions to the 1s(T_2) state have been observed. Their ground states (A_1 symmetry) are not EMT like and this symmetry allowed but EMT-forbidden transition becomes visible. The presence of the 1s(E) state has been confirmed by observing the corresponding phonon-assisted Fano resonance [2] and by uniaxial stress studies [3]. Another example is the T-line spectrum in platinum doped silicon [4]. The uniaxial stress splitting pattern and the Zeeman spectra were perfectly accounted for by considering all six 1s states, 1s(A_1), 1s(T_2), and 1s(E). The excitation spectrum of Ag in silicon is also dominated by transitions to states in the 1s manifold [5]. This spectrum is presented in Fig. 2 and is more complex since many-particle effects is observed. However, uniaxial stress measurements have revealed that all six 1s state are found in an energy region close to the 1s EMT position. The excitation spectrum of the low symmetry C-line defect [6,7] and 615 meV defect [8] both show transitions to all six states but for the latter, the lowest 1s state is found 165 meV below the 1s EMT value. The C-line photo-current spectrum is presented in Fig. 3

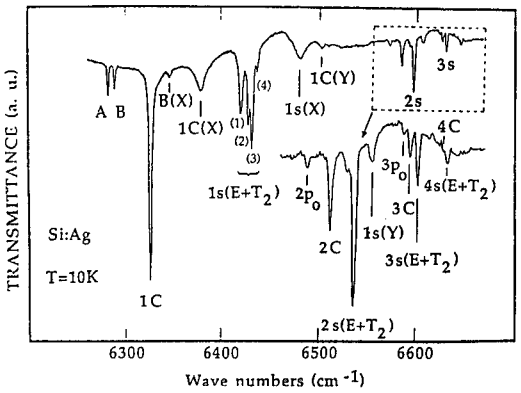


Fig. 2 The excitation spectrum of the Ag donor. Transitions to s states dominate the spectrum.

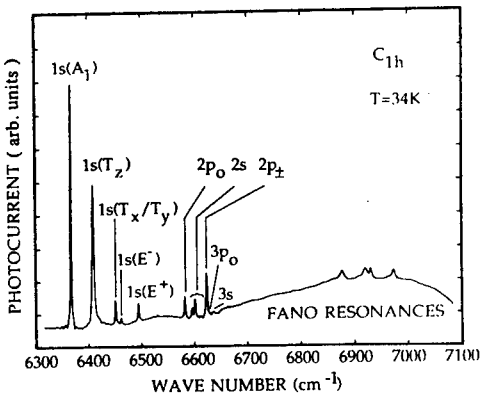


Fig. 3 The photocurrent spectrum for the C line donor.

The model of bound excitons stems from work around 1960 [9,10]. It has clearly been demonstrated experimentally that the energy spectrum of bound excitons at neutral or isoelectronic centers can show close similarity with shallow-donor spectra. The excitonic spectrum is then termed a pseudo-donor spectrum. The name indicates that the center is not a true donor. The cause behind the transformation from an ordinary exciton spectrum to a donor like spectrum is due to the fact that when the hole is more strongly bound the localization of the hole increases. As the localization of the hole increases the potential felt by the delocalized electron becomes more like a potential

from a point charge, i.e., Coulombic like. Accordingly, the energy spectrum becomes shallow-donor like when the hole is localized with one important distinction; the ground state is not the 1s state but the one when the hole and electron have recombined. This difference has been used as a fingerprint for a pseudo-donor, i.e., when transitions to the 1s state are observed in, e.g., an excitation spectrum, the center is termed a pseudo donor and when it is missing the center is simply an ordinary donor [8]. Employing this fingerprint, shallow donors and the chalcogens are donors whereas the Ag, Pt T-line, C-line, and the 615 meV centers are pseudo-donors. It should be noted, however, that transitions to the $1s(A_1)$ state are not symmetry allowed for the chalcogen T_d centers and no $1s(A_1)$ absorption line would be observed even if the $1s(A_1)$ shallow-like state exists.

In the original bound-exciton model it is assumed that the defect still is neutral and the hole is bound by the local defect potential and the local defect induced strain field [11]. From several work on donor-like spectra in silicon a hole binding energy up to about 0.5 eV has been inferred. Its difficult to understand that the defect still can be considered as neutral and that no strong interactions between the localized hole and the defect states occur. The potential felt by an electron in excited shallow donor states has two parts, the long range Coulomb potential and a localized potential. According to the bound-exciton model the localized potential should be hole-attractive [12] whereas a strong local electron-attractive potential has been inferred from several "pseudo-donor" spectra [8]. In order to account for this discrepancy, the hole was considered to be so localized that it was associated with the deep defect ground state canceling the electron repulsive part leading to a net electron attractive potential [8]. It therefore seems very attractive to abandon the pseudo-donor model based on the bound exciton concept as a whole and instead consider the shallow-donor like excitation spectrum as being due to excitation of an electron from a deep ground state to shallow-donor states.

There exists a good basic understanding on the ground-state properties of deep defects in silicon. Different schemes are applicable for different classes of defects. A simple approach for substitutional impurities is to first consider the electronic structure of the Si vacancy. The four vacancy sp^3 hybrids transform as a_1 and t_2, being 1- and 3-fold degenerate. The a_1 state is found in the valence band and the t_2 state is found in the band gap. When inserting the defect into the vacancy, the defect valence states interact with the vacancy orbitals and bonding and antibonding states are formed according to a LCAO molecular model [13,14]. This model well accounts for the electronic structure of the transition-metal impurities at the end of the rows in the periodic table. The d-states split in the tetrahedral crystal field into an e and t_2 orbital, denoted de and dt_2 for clarity. Interaction between the vacancy t_2 and impurity dt_2 states gives rise bonding and antibonding states [14]. For the heavier impurities, the antibonding t_2 state is found in the gap and by occupying it with the electrons available the many-particle defect ground state is formed. This gap state will be termed a molecular state since its electronic properties is determined by the energy positions of the non-interacting vacancy and impurity orbitals and the matrix elements describing the interaction between the two sets of orbitals in the view of LCAO.

A similar scheme can be set up for the substitutional sp-bonded impurities, e.g., the chalcogens and the group-V donors. The impurity s and p states interact with the vacancy a_1 and t_2 orbitals, respectively. For the group-V donors the antibonding and bonding states are found as resonances in conduction and valence band, respectively whereas for the chalcogens an antibonding a_1 state is pulled down from the conduction band and appears as a bound state in the gap. As above we will consider this state as a molecular state mainly due to interaction between the impurity s and vacancy a_1 orbitals. When the a_1 state appears as a resonance in the conduction band the group-V and the chalcogens are shallow single and double donors, with one and two electrons occupying the lowest Coulombic 1s state, respectively. What will happen if we move the a_1 molecular state from the conduction band into the bandgap? This is schematically shown in Fig. 4 employing matrix elements describing the interaction between the localized a_1 state and the hydrogenic states. The matrix elements are proportional to the overlap between a very localized a_1 state (delta function) and hydrogenic s-states. As is readily seen in Fig. 4, avoiding crossing behavior is observed, as expected, and when the localized a_1 state is well below the Coulombic states the resulting electronic structure is simply that of a localized ground state and a perfect ladder of Coulombic states. Similar behavior is expected for a t_2 gap state described above for substitutional transition metals but only hydrogenic states of t_2 symmetry will interact with the this state.

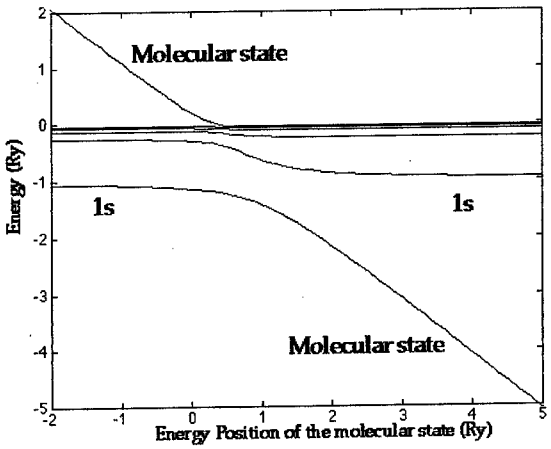


Fig. 4 Schematic picture showing the interaction between a localized state and hydrogenic states as the localized state is pulled down from the continuum.

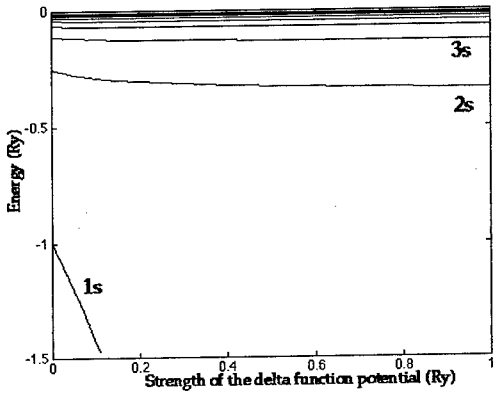


Fig. 5 Schematic picture showing the effect upon the hydrogenic states as the strength of a delta function potential is increased.

We have not yet found any reason why, e.g., the 1s(A_1) state should be missing in the manifold of 1s EMT states. For an electron-attractive localized potential as discussed in conjunction with pseudo-donors above all ns(A_1) states will in general increase their binding energy and the 1s(A_1) state in particular. For a weak potential, first-order perturbation theory is sufficient to calculate the energy shifts and they are expected to scale as the probability to find the electron at the origin. However, there will also be matrix elements coupling the various ns(A_1) states that become important when the strength of the potential increases. In order to understand how the ladder of states for a hydrogenic system are affected by a localized potential a simple model was employed considering a delta-function hydrogenic s states. The result is presented in Fig. 5. As the strength of the localized potential increases a bound state is pulled down from the continuum and avoided crossings with the Coulombic states appears. The behavior is that expected for a central-shift of the shallow-donor states. The localization of the lowest state increases drastically well below the 1s position. In the case of sp-bonded deep donors, the localized state will ultimately interact with the a_1 molecular gap state. Even though it seems physically improbable that an avoided crossing between the molecular state and the central-cell shifted "1s" state can occur it will nevertheless only lead to an inverted level ordering, i.e., the central-cell shifted "1s" state becomes the ground state and the molecular state an excited state of the defect. No states have disappeared but the level ordering has been altered.

The discussion above strongly indicates that all six s states should exist for all deep donors in silicon although some with drastically changed character, e.g., localization. Its interesting to speculate that this also can be the case for the chalcogen double donors in silicon. Electric-dipole transitions from the deep ground state to the 1s(A_1) state is strictly forbidden and will never be observed. Attempts to occupy this state by optical excitation (and its spin-triplet version) and have failed.

The observation of singlet-triplet states [15,16] for many bound exciton lines in silicon has been taken as an indication favoring the pseudo-donor model [8]. Singlet-triplet states naturally follow from the deep donor model since for all neutral donor centers with integer spin both the excited electron in a shallow donor state and the remaining core state has spin 1/2 and series of spin singlet and triplet excited states will exist. The chalcogen double donors have both spin singlet and triplet states but so far no attempts have been made to explain their electronic structure employing a pseudo-donor model. Furthermore, of all the defect centers listed above (except the chalcogens) only the Ag spectrum indicates the presence of spin-triplet states.

Conclusions

It has been shown that all spectral features that has been considered to be specific for pseudo-donors naturally follows from the well known "molecular" properties of deep donor ground states

Acknowledgments.

The authors acknowledge financial support from the Swedish Natural Science

Research Foundation (NFR) and the Swedish Research Council for Engineering Sciences (TFR).

References

1. W. Hayes and A. M. Stoneham in *Defects and Defect Processesing in Nonmetallic Solids*, John Wiley & Sons. 1985, p. 273
2. E. Janzén, G. Grossmann, R. Stedman, and H. G. Grimmeiss, Phys. Rev. **B31**, 8000 (1985)
3. K. Berman, G. Grossmann, H. G. Grimmeiss, M. Stavola, C. Holm, and P. Wagner, Phys. Rev. **B37**, 10738 (1988) and references therein.
4. J. Olajos, M. Kleverman, and H. G. Grimmeiss, Phys. Rev. **B40**, 6196 (1989)
5. J. Olajos, M. Kleverman, and H. G. Grimmeiss, Phys. Rev. **B38**, 10633 (1988)
6. K. Thonke, A. Hangleiter, J. Wagner, and R. Sauer, J. Phys. C **18**, L795, (1985)
7. M. Kleverman, J.-O. Fornell, J. Olajos, H. G. Grimmeiss, and J. L. Lindström, Phys. Rev. **B37**, 10199 (1988)
8. J. H. Svensson, B. Monemar, and E. Janzén, Phys. Rev. Lett. **65**, 1796 (1990)
9. M. Lampert, Phys. Rev. Lett. **1**, 450 (1958)
10. J. R. Haynes, Phys. Rev. Lett. **4**, 361 (1961)
11. B. Monemar, U. Lindefelt and W. M. Chen, Physica **146 B&C**, 256 (1987)
12. J. J. Hopfield, D. G. Thomas, R. T. Lynch, Phys. Rev. Lett. **17**, 312 (1966)
13. L. A. Hemstress, Phys. Rev. **B15**, 834 (1977)
14. G. D. Watkins, Physica **117B** & **118B**, 9 (1983)
15. B. Monemar, CRC Crit. Rev. Solid State Matter Sci. **15**, 111 (1988)
16. G. Davies, Phys. Rep. **176**, 83 (1989)

Materials Science Forum Vols. 258-263 (1997) pp. 503-508
© 1997 Trans Tech Publications, Switzerland

VACANCIES AND INTERSTITIAL ATOMS IN e⁻-IRRADIATED SILICON

H. Zillgen and P. Ehrhart
IFF, Forschungszentrum Jülich GmbH, D 52425 Jülich, Germany

Keywords: Silicon, Vacancies, interstitial atoms, Frenkel pairs, electron irradiation

Abstract. Differently doped Si-wafers were irradiated with 2.5MeV electrons and subsequently investigated by X-ray diffraction methods. We show that a large fraction of the induced defects is stabilized in the form of close Frenkel pairs which are characterized by the nearly perfect cancellation of the long-range displacement fields of the interstitial atom and the vacancy. We discuss the absolute size of these displacements as well as the introduction rate of the defects, which is of the order of $\Sigma = 1\text{cm}^{-1}$. By comparing weakly doped Cz-Si or FZ-Si and degenerate p-type Si(B) and n-type Si(As) we show that the results are independent of the oxygen content of the samples and of the position of the Fermi level. We discuss the difference of the observed high defect introduction rates to the results of electrical and EPR investigations and discuss the consequences for the understanding of the defect production in Si and for the assumption of an athermal migration of interstitial atoms. In addition we compare the defect patterns observed after 4K irradiation to those observed after annealing at room-temperature and after room temperature irradiations.

1. Introduction.

Point defects in Si have been investigated in great detail [1] and as the thermal equilibrium concentrations of the intrinsic point defects, i.e. vacancies and interstitial atoms, are very low most information has been obtained from low temperature electron irradiation experiments. Nevertheless, there are many open questions or speculative models for the details of the defect behavior. Although electron irradiations produces Frenkel pairs (FPs) in a reproducible manner, the defect introduction rates observed e.g. by electron paramagnetic resonance (EPR) are generally quite low as compared to calculations using a threshold energy for defect production of 20-40eV [2]. For typical electron energies of $E_e \approx 1.5\text{MeV}$ introduction rates of $\Sigma \approx 1\text{cm}^{-1}$ are expected, whereas the highest introduction rate observed by EPR at low temperatures amounts to $\Sigma = 0.03\text{cm}^{-1}$ in p-type Si. For n-type and intrinsic Si the values are at least an order of magnitude lower. The low introduction rate has been explained by an athermal, ionization- induced mobility of the interstitial atoms which yields a direct recombination of most of the Frenkel pairs. Defects seem only to survive if the interstitial atom escapes direct recombination and arrives at another trap (e.g. a dopant atom) and forms a stable complex. Especially the reactions of interstitial atoms with group-III dopant atoms in p-type Si have been investigated in detail by EPR techniques [1]. As no clear evidence for the presence of undisturbed interstitial atoms or FPs has been found so far, the EPR results gave strong support for the assumption of an athermal interstitial mobility; nevertheless the evidence for athermal migration must be considered to be an indirect conclusions and therefore alternative formation mechanisms for these complexes cannot be excluded [3].

As most of these spectroscopic studies are limited to low defect concentrations or irradiation doses ($\Phi t \leq 10^{17} e^-/\text{cm}^2$), we started X-ray diffraction investigations which yield information on defect structures especially for high irradiation doses. Such high dose irradiations offer the advantage that the intrinsic defects reactions are dominant and the interaction with electrically inactive impurities like O or C is negligible. We have reported first results on lightly doped Si at the preceding conference [4], and demonstrated that a high concentration of Frenkel pairs can be frozen in at 4K for this material. This observation is in complete contrast to the expectation of the evolution of the defect pattern assuming highly mobile interstitial atoms, as we would expect either a saturation of the defect concentration at the concentration of the doping atoms ($\approx 10^{16}\ \text{cm}^{-3}$,model of saturable

traps), or the beginning of cluster growth at the corresponding dose (unsaturable traps). In the present paper we concentrate on the extension of the investigation on heavily doped Si in order to check for a possible dependence of the defect properties on the position of the Fermi level and to arrive at more general conclusions.

2. Experimental.

The experimental investigations were started with slightly doped p-type samples ($3\cdot10^{15}$ B cm^{-3}), and Cz-Si as well as FZ-Si wafers were used in order to check for a possible influence of oxygen on the defect reactions. In order to investigate the possible influence of the position of the Fermi level on defect production and defect mobility we used degenerate p-type Si ($2\cdot10^{19}$ B cm^{-3}) and n-type Si ($2\cdot10^{19}$ As cm^{-3}) wafers. The irradiations were performed with 2.5 MeV electrons at the Jülich irradiation facility [5] using current densities between 5 and 10μA/cm^2. The samples were cooled in a stream of liquid He at 4.7K or in He gas during the room temperature (RT) irradiation.

The investigations of the diffuse scattering X-ray intensity and of the change of the lattice parameter were performed with $CuK_{\alpha 1}$ radiation at a measuring temperature of 6K (for details see e.g. ref.6).The theory necessary to deduce the information contained in the measured diffuse scattering cross section, S, is well documented[7], and we will use the so-called Huang Diffuse Scattering (HDS) which is observed for small deviations, **q**, of the scattering vector, **k**, from a reciprocal lattice vector, **G**. The scattering cross section of the HDS is given by: $S_H(\mathbf{k}) = c\, f^2\, |\mathbf{G}\, \mathbf{s}(\mathbf{q})|^2$; $\mathbf{s}(\mathbf{q})$ is the Fourier transform of the displacement field of an isolated defect, c is the defect concentration, and f is the atomic scattering factor. Expressing the strength of the displacement field $\mathbf{s}(\mathbf{r})$ by the relaxation volume V^{rel} of the defect we obtain:

$$S_H \sim c\,(V^{rel})^2\, G^2/q^2 \qquad (1)$$

S_H yields the product $c(V^{rel})^2$, and by combination with measurements of the change of the lattice parameter, $\Delta a/a \sim c\, V^{rel}/3$, the two unknown numbers c and V^{rel} can both be determined. As we are considering FPs, the experiment yields, however, only average values from contributions of interstitials and vacancies:

$$S_H \sim c\,((V_i^{rel})^2 + (V_v^{rel})^2) \quad \text{and} \quad \Delta a/a \sim c\,(V_i^{rel} + V_v^{rel}) \qquad (2)$$

These equations show that defects with the opposite sign of V^{rel} can cancel in $\Delta a/a$, however, the diffuse scattering S_H adds up.

3. Defects after 4K irradiation.

The slightly boron doped samples have a very high resistivity at 4K and it is well known that the charge carriers are removed after very low irradiation doses. We can therefore consider these samples to be highly ohmic Si over the range of high doses investigated here. The degenerate samples allow for in situ measurements of the electrical resistivity. For the n-type samples the carrier removal rate is small ($\eta = 0.1 cm^{-1}$) and the samples remained highly conductive even after irradiation doses of $2\cdot10^{19}$ e^-/cm^2 [8] whereas the p-type samples ($\eta \approx 2 cm^{-1}$) became highly ohmic and finally converted to n-type conductivity at this highest dose [8,9].

Fig.1 shows the distribution of the defect-induced HDS close to different Bragg reflections for the degenerate Si samples. We observe a similar distribution of the intensity as well as similar values for the absolute intensity values as for the undoped samples [4,8]: a decrease of $S_H q^2$ at small values of q, which characteristically indicates deviations from a random distribution of defects. Combined with additional features of the distribution of the scattering intensity, e.g. the angular distribution of the intensity around the Bragg peak, and especially the asymmetry of the intensity for ±q [8, and ref.6 for the example of InP], we can conclude that there is a dominant contribution of close FPs with a typical distance of 1-2 lattice constants present after irradiation (Fig.2).

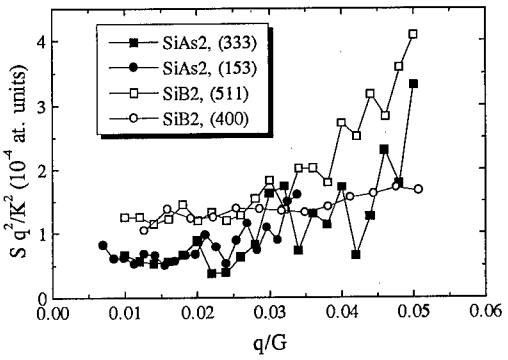


Fig.1: Symmetrical part of the HDS scattering cross section plotted as a function of the distance, q, of the scattering vector, k, from different Bragg reflections. Data are shown for degenerate Si(B) and Si(As) after an irradiation dose of 1.7 10^{19} e^-/cm^2.

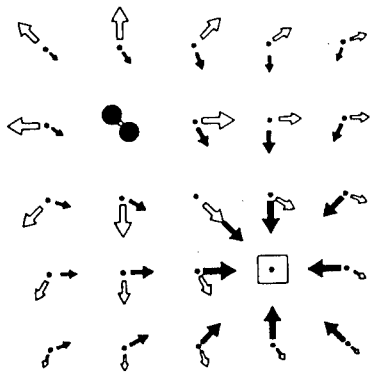


Fig.2: Schematic view of the configuration of a close FP, which can explain the intensity distribution shown in fig.1. The opposite displacements around the interstitial atom and the vacancy add up in the region between the defects and cancel at large distances.

In contrast to the increase of S_H we observe no systematic change of the lattice parameter: $\Delta a/a \leq (0.5 \pm 0.5)\times10^{-5}$ in agreement with earlier results for the undoped samples[4,8]. From eq.2 we conclude therefore that the displacement fields of interstitials and vacancies must nearly compensate, i.e. $V_i^{rel} = -V_v^{rel}$. For this condition eq.2 allows no further separation of c and $(V^{rel})^2 = (V_i^{rel})^2 = (V_v^{rel})^2$, and we have to make assumptions about either V^{rel} or the defect concentration which, after normalization by the irradiation dose, Φt, yields the introduction rate $\Sigma = c/(\Omega\Phi t)$, ($\Omega$ = atomic volume). If we assume a reasonable value for $V_v^{rel} = -0.5\Omega$ we obtain an introduction rate $\Sigma \approx 1 cm^{-1}$, which corresponds to an average displacement threshold of 40 eV for Si. The given values should be considered as a maximum for $|V^{rel}|$ and a minimum for Σ (see refs.[8,6] for details).

The observation of more than 10^{19} FPs/cm^3 and the similarity of the results for the Cz and FZ wafers clearly show that these defects are intrinsic and not stabilized by impurities. The quantitative results for the n-type Si agree exactly with those of the slightly doped samples (see fig.4 below), whereas the boron doped Si shows a somewhat higher scattering intensity (fig.1). As the distribution of the scattering intensity is very similar, we suppose that there is the same defect structure in all samples and only the introduction rate of the stable intrinsic FPs is higher in p-type Si. This conclusion is supported by the missing change of the lattice parameter in all types of samples. As the boron atoms yield a decrease of the lattice parameter for the unirradiated samples, we might expect a compensation of this effect along with the reaction of mobile irradiation defects with these boron atoms; this effect is, however, only observed during annealing to RT (section 4).

The linear increase of the defect concentration with no indication of saturation behavior up to doses of $2\cdot10^{19}$ e^-/cm^2 (fig.4) might simply be explained by the continuous production of immobile FPs. This observation is in contrast to the electrical measurements which indicate very small carrier removal rates for n-type Si and demonstrates that the electrically deduced carrier removal rate may reflect only a small percentage of the irradiation-induced defects especially in n-type Si. Therefore one of the main arguments for the assumption of an athermal interstitial migration is no longer valid.

Nevertheless, the present results cannot exclude this interstitial mobility, which explains the production of the interstitial group-III dopants[1] most straightforwardly, if we allow for special defect interaction potentials [8]. Assuming that the interstitials can escape from their vacancy by athermal migration, they can form other complexes, however, as soon as all extrinsic traps are

saturated the vacancies necessarily become the dominant traps and retrap mobile interstitials[6,8]. This means that there must be a binding energy for the FP as well as a recombination barrier for the FP. In addition these results indicate that the dissociation and recombination probability of the FPs as well as the interaction of the athermally migrating interstitial atoms with oxygen, As, and B are different during athermal migration at 4K and during thermally activated migration at higher temperatures as discussed below. Such behavior can be explained by a Coulomb repulsion in the 'excited' charge state.

4. Defects after RT annealing and after RT irradiations.

During irradiation at elevated temperatures we expect a thermally activated defect mobility in addition to the possible athermal interstitial mobility. Presently available data indicate very similar values for the activation energy for vacancy migration (H^M_v varying, dependent on the charge state, between 0.18 and 0.45 eV) and interstitial migration (H^M_i smaller than 0.57eV [1]) and do not allow a discrimination by selecting different irradiation temperatures. We used room temperature irradiations and both defects must be considered as possibly mobile[1].

Fig.3 shows examples of the changes of the distribution of the scattered intensity S_H as compared to the result of a 4K irradiation and of a subsequent annealing at RT. For the lightly doped Cz-Si we observe that during annealing up to RT about 50% of the intensity is lost and that the scattering distribution no longer indicates close pairs. After RT irradiations we observe a very similar intensity distribution as after annealing up to RT; hence the close FPs recombine by thermally activated jumps. Whereas there is no important difference between Cz- and FZ-Si for the 4K irradiations and for the annealing at RT, the RT- damage rate for FZ-Si is lower by more than a factor of three than that of the Cz-Si. This behavior indicates that impurities are necessary to stabilize the defects at RT. Although this explanation seems straightforward in a qualitative sense, the observed defect concentrations for the Cz-Si are only lower by a factor of two as compared to the 4K irradiations and consequently still much higher than the number of traps. In order to explain the build-up of these high densities of small defects we might speculate about a kind of catalytic reaction of the oxygen: e.g. the formation of di-interstitials close to oxygen sites and later on the possibly ionization-assisted detrapping of interstitial oxygen[8].

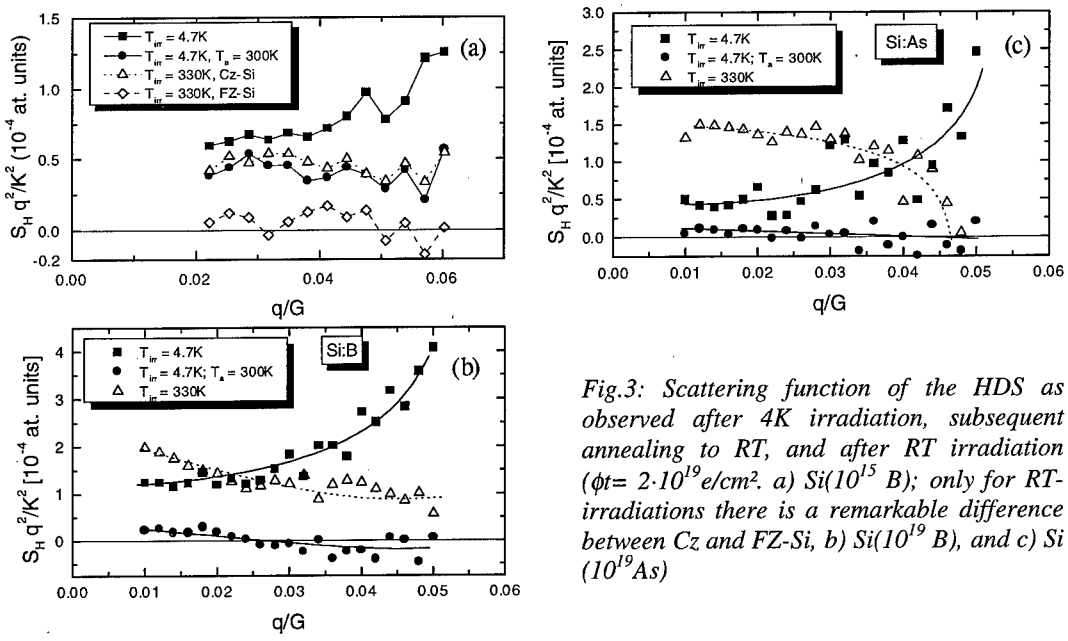


Fig.3: Scattering function of the HDS as observed after 4K irradiation, subsequent annealing to RT, and after RT irradiation (ϕt= 2·10^{19}e/cm². a) Si(10^{15} B); only for RT-irradiations there is a remarkable difference between Cz and FZ-Si, b) Si(10^{19} B), and c) Si (10^{19}As)

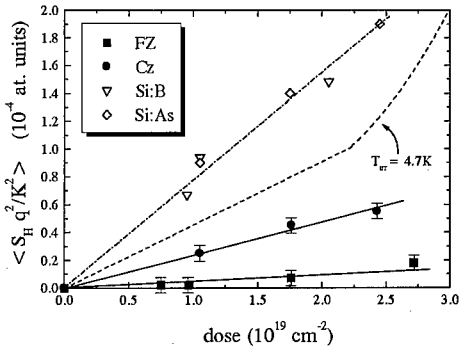


Fig.4: Dose dependence of the average of the HDS for RT-irradiated Si. Differently doped samples are indicated by different symbols.

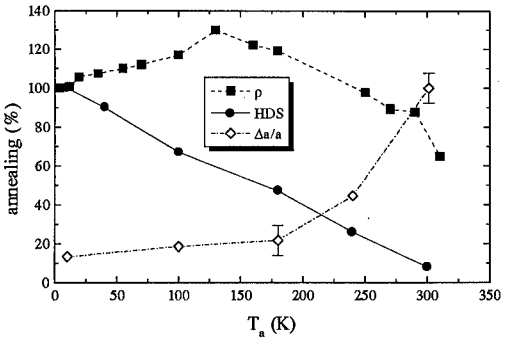


Fig.5: Low temperature annealing of the electrical resistivity, of the HDS-intensity and of the lattice parameter of degenerate Si(B) irradiated with $2 \cdot 10^{19}$ e$^-$/cm^2 at 4K. The lattice parameter change is normalized at its largest value after annealing at RT.

The curves for the degenerate samples differ remarkably from those of the undoped samples. For Si(As) we observe a strong annealing for the 4K-irradiated samples, which compares to the annealing of undoped samples at lower irradiation doses[8]. This faster annealing might be explained by the temporary trapping of the mobile defect by the dopants which keeps the defects in high dilution and thus enhances the recombination if the antidefect becomes mobile too. In contrast to this we observe after RT irradiation the characteristics of the scattering from defect clusters with a rather sharp size distribution, a good indication of a q^{-2} decay at small q-values and a sharp decay (q^{-4}) at larger q values. The transition at q/G = 0.04 yields a small cluster radius of 5Å. We assume that these clusters are of the interstitial type as vacancies are supposed to be effectively trapped at As dopants [1,10]. This defect dopant interaction at RT is also supported by the much higher carrier removal rate observed [8].

The B-doped samples show qualitatively a similar behavior (fig.3c), however, the scattering intensity after RT-irradiation indicates a broader distribution of defect sizes. This formation of defect clusters in the doped samples also yields an increase of the total diffuse scattering cross section, which contributes to the high values of S_H shown in Figs.3,4. The annealing behavior is shown in Fig.5 in more detail. We observe a strong annealing of the HDS and only small changes of the electrical resistivity, which agrees well with the similarity of the carrier removal rates at 4K and RT [9]. Most remarkably we observe an increase of the lattice parameter along with the annealing of the HDS and a similar increase is also observed during RT-irradiation. This observation indicates that interstitial atoms escaping from close pair recombination react with B-atoms essentially only at temperatures above ≈200K.

Comparing the observations after 4K and after RT irradiations we observe some general trends which can straightforwardly be explained without the assumption of an athermal migration at 4K. (i) At 4K immobile close FPs are frozen in and these FPs recombine during subsequent annealing up to RT to a large part. During RT irradiation these defects can recombine immediately, however, the escape probability may be different. (ii) For the RT irradiations we observe a strong dependence of the damage rate on the sample purity (Figs.3,4). Qualitatively this increased diffuse intensity for the doped samples is expected due to the increased number of traps. However, the quantitative details are puzzling: e.g. there is increased cluster growth for the degenerate samples although there are more doping atoms than defects. We tentatively attribute this enhanced cluster growth to the much shorter screening length of the Coulomb repulsion between defects of the same kind.

If we allow for an athermal mobility at 4K the observed differences between the two irradiation temperatures indicate different defect interactions for the different jump modes: during athermal migration the interstitials seem to surpass the recombination threshold only rarely, but with additional thermal activation the probabilities for recombination or escape become comparable. Such differences in the escape probabilities between thermally activated reactions and ionization-assisted reactions might be explained by a Coulomb repulsion in the 'excited ' charge state [8].

5. Summary and Conclusions.

We have shown that in Si a high concentration of intrinsic FPs can be frozen in which is quite independent of the sample purity and the position of the Fermi level. Some basic defect properties may be summarized:

(i) The XRD results show that the displacement fields of interstitial atoms and vacancies in Si cancel nearly exactly i.e.: $V_i^{rel} = - V_v^{rel} \approx 0.5$ at. volumes.

(ii) The total introduction rate is in the order of $\Sigma = 1 cm^{-1}$ for 2.5MeV electrons and corresponds to an effective threshold energy for the defect production of $\approx$ 40eV. This high introduction rate indicates that many electrical methods observe only a small percentage of the defects introduced at low temperatures. Hence, one of the arguments for a high athermal mobility of the interstitial atom in silicon is no longer valid. However, the present results cannot directly exclude athermal migration and we discussed some assumptions on the defect interaction which seem necessary to allow for an athermal migration during 4K irradiation.

(iii) Thermally activated defect reactions up to room temperature are dominated by the recombination of FPs, however, the escape probability seems to depend on the type and concentration of the available extrinsic and/or intrinsic traps.

(iv) During RT irradiations defects survive essentially due to trapping reactions at solute atoms and we observe large differences between FZ- and Cz-Si. The observed defect agglomeration in the highly doped Si indicates the importance of screening the Coulomb repulsion during clustering reactions of similar defects in degenerate samples.

Acknowledgements. We thank Prof. W. Schilling for many helpful discussions and we gratefully acknowledge technical assistance from W. Bergs and U. Dedek and support from Dr. F. Dworschak and B. Schmitz during the irradiations. We thank Prof. V. V. Emtsev for the highly doped samples .

References.

1. G.D. Watkins, in Electronic Structure and Properties of Semiconductors (W.Schroeter ed., Vol.4 of Materials Science and Technology ,VCH, Weinheim 1992) p.105
2. J.W. Corbett and J.C. Bourgoin in Point Defects in Solids,Vol.2 (J.H. Crawford and L.M. Slifkin eds, Plenum Press, 1975) p.1
3. V.A.J.van Lint, T.M. Flanagan, R.E. Leadon, J.A. Naber, and V.C. Rogers, in Mechanisms of Radiation Effects in Electronic Materials (Wiley, NY, 1980) pp.290
4. St. Bausch, H. Zillgen, and P. Ehrhart, Mat.Sci.For.196/201,(1995) 1141
5. J. Hemmerich, W. Sassin, and W. Schilling, Z.Angew. Phys.,**29** (1970) 205.
6. K. Karsten and P. Ehrhart, Phys.Rev. **B51** (1995) 10508
7. P.H. Dederichs, J.Phys. **F3** (1973) 471
8. P. Ehrhart and H. Zillgen , to be published in MRS Symp.Proc. Vol.**469** (1997)
9. V.V. Emtsev, U. Dedek, P. Ehrhart, P.D. Kervalishvili, M.A. Margaryan, D.S. Poloskin, and H. Zillgen this conf.
10. J.W. Corbett,J.C. Bourgoin, L.J. Chang, J.C. Corelli, Y.H. Lee, P.M. Mooney, C. Weigel, Inst, Phys. Conf. Ser. **31** (1977) 1

Materials Science Forum Vols. 258-263 (1997) pp. 509-514
© 1997 Trans Tech Publications, Switzerland

VACANCY AGGREGATES IN SILICON

J.L. Hastings, S.K. Estreicher, and P.A. Fedders[1]
Physics Department, Texas Tech University, Lubbock, TX 79409, USA
[1]Physics Department, Washington University, St.Louis MO 63130, USA

Keywords: vacancies, silicon, ring-hexavacancy, molecular-dynamics

Abstract. We have calculated the lowest-energy configurations, stability, and electronic structures of vacancy aggregates (V_n) containing up to n=7 vacancies. The calculations were done using first-principles tight-binding molecular-dynamics simulations (in periodic supercells) and at (and near) the *ab-initio* Hartree-Fock level (in molecular clusters). The results show that the reaction $V_{n-1} + V_1 \rightarrow V_n$ is exothermic at least up to n=7. The most stable aggregate, by far, is the ring-hexavacancy (V_6) which has remarkable properties. In contrast to the other V_n's, it is not vacancy-like: It has no deep level in the gap and its dipole moment is extremely small. It is sufficiently stable to survive high-temperature annealing. V_6 is a small trigonal void which is likely to be a gettering center and is a plausible nucleus for a range of extended defects.

I. Introduction.

Vacancies and self-interstitials are the two basic intrinsic defects in silicon.[1-3] Vacancies are better understood than self-interstitials.[3] The isolated vacancy and a number of complexes containing vacancies have been observed experimentally and studied theoretically. In particular, the neutral monovacancy distorts from tetrahedral to tetragonal symmetry, and reconstructs by forming two long bonds (see [4] and refs. therein). Reconstruction (rebonding) takes place in other clusters of vacancies as well. How efficiently the crystal reconstructs around such a defect affects its stability and electronic properties.

While the equilibrium concentration of vacancies in Si is low,[5] above-equilibrium concentrations are (believed to be) generated during a variety of processes such as ion implantation, electron or neutron irradiation, ion-beam milling, wet and dry etching,[6] laser annealing, deposition of Al back contacts, or exposure to various plasmas.

Vacancies are rapid diffusers, with activation energies[3] of 0.45 eV for V^0, 0.32 eV for V^{++}, and 0.18 eV for V^{--}. A recent molecular dynamics (MD) study[7] shows that at high temperatures, V^0 hops in very short times. Vacancies interact with impurities and with each other. Divacancies diffuse[8] above $\sim 250\ ^\circ C$ with an activation energy of about 1.3 eV. Positron annihilation spectroscopy[9,10] shows that a wide range of vacancy aggregates exist in irradiated silicon.

In the present paper,[11] we report the results of theoretical studies of (neutral) vacancy aggregates (up to 7) in Si. The methodology is discussed in Sec. II, the results in Sec. III, and Sec. IV contains a summary and speculations.

II. Methodology.

Two approaches were used: Density-functional-based MD simulations, and Hartree-Fock (HF) theory. The configurations, energetics, and electronic structures calculated at both levels have been compared and the results below are (at least qualitatively) independent of the methodology used and the way the host crystal is described.

The MD simulations were performed with the first-principles tight-binding method of Sankey *et al.*[12,13]. The host crystal is represented by periodic supercells with $64 - n$ atoms, where $n = 1, \ldots, 7$ is the number of vacancies. Most calculations were done with the Harris energy functional, but a few self-consistent runs were performed to confirm the key results. The time step was fixed at $2\,fs$.

The HF calculations were done with the approximate *ab-initio* HF method of partial retention of diatomic differential overlap (PRDDO/M).[14] It uses minimal basis sets and provides approximate energetics and electronic structures, but predicts reliable geometries. We used the PRDDO/M geometries for single-point *ab-initio* HF[15] calculations, with Hay-Wadt pseudopotentials[16] and split-valence polarized basis sets. All the HF calculations were done in H-saturated molecular clusters containing $38 - n$ host atoms.[17]

We first used MD simulations to find the configurations of aggregates of n-vacancies, V_n, with $n = 1, \cdots, 6$. We removed symmetrically inequivalent sets of n atoms from the supercell and quenched. The simulated quenching procedure forces the convergence toward a local minimum of the potential energy and guarantees that all the lattice relaxations and distortions are included. The results allow a comparison of the relaxed structures and energies of inequivalent V_n complexes.

Then, the lowest-energy structures of the V_n's were re-optimized using gradient techniques with the PRDDO/M method. Because of the large number of degrees of freedom, only the nearest-neighbors (NNs) to the various vacancy aggregates were allowed to relax, but with no symmetry constraints. These geometries were used as inputs for the *ab-initio* HF calculations.

III. Results.

The formation energy of the vacancy at the MD level is 4.15 eV, close to that of other authors.[18-20] The reconstruction and properties of V_1 were discussed elsewhere.[4,7]

The lowest-energy configurations of the V_n's, with $n = 1, \ldots, 6$ correspond to Si atoms successively removed from a hexagonal ring in the crystal. Figure 1 shows the energy gained by adding V_1 to the most stable aggregate V_{n-1}. This energy difference $\Delta E_n = \{E_n + E_0\} - \{E_{n-1} + E_1\}$ is minus the dissociation energy of V_n into $V_{n-1} + V_1$. The open circle is minus the experimental binding energy[8] of the divacancy. We obtained V_7 by removing a Si atom adjacent to the lowest-energy configuration of V_6 and quenching. The various inequivalent ways of doing this lead to similar energies.

The MD calculations predict the following dissociation energies. $V_2 \rightarrow V_1 + V_1$ costs 1.69 eV and $V_3 \rightarrow V_2 + V_1$ costs 2.08 eV. $V_4 \rightarrow V_3 + V_1$ and $V_4 \rightarrow V_2 + V_2$ cost 1.92 and 2.31 eV, respectively. $V_5 \rightarrow V_4 + V_1$ and $V_5 \rightarrow V_3 + V_2$ cost 3.05 and 3.28 eV, respectively. $V_6 \rightarrow V_5 + V_1$, $V_6 \rightarrow V_4 + V_2$, and $V_6 \rightarrow V_3 + V_3$ cost 3.76, 5.12, and 4.96 eV, respectively. Finally, $V_7 \rightarrow V_6 + V_1$ costs only about 1.3 eV. Thus, up to n=6, the lowest dissociation energy of V_n increases with n and occurs for the dissociation $V_n \rightarrow V_{n-1} + V_1$. However, the dissociation energy of V_7 is less than that of V_2.

While V_4 and V_5 have metastable configurations close in energy to the stable one, the configurations of V_6 which are not the ring are much higher in energy (the lowest one is 0.87 eV above the ring). High-temperature MD runs suggest that the metastable states of V_6 quickly collapse into the ring configuration. We believe that hexavacancies other than the ring are not realized in appreciable concentrations. V_6 is a trigonal ellipsoid-shaped void, with diameter 7.8 Å (internuclear distance across the defect) and height 4.4 Å (distance between the planes of NNs to V_6 perpendicular to the trigonal axis).

The plot of ΔE_n shows that V_6 is by far the most stable of the small vacancy aggregates. This result confirms a prediction by Chadi and Chang[21] (see also Ref. [22]).

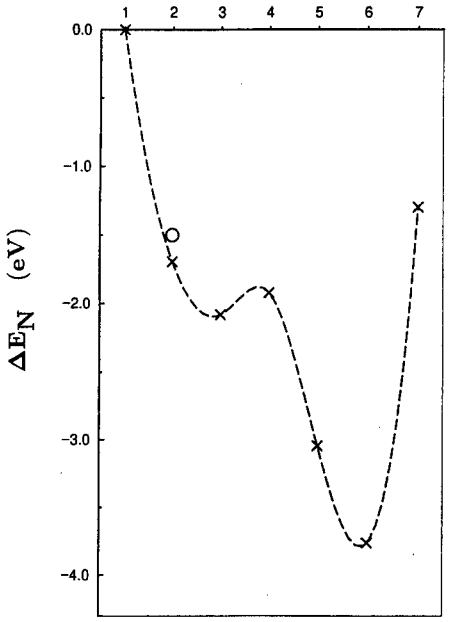


FIGURE 1: Energy gained by adding V_1 to the lowest-energy V_{n-1} calculated at the MD level. The circle shows the dissociation energy of the divacancy.[1]

V_6 is very stable because the crystal reconstructs almost perfectly around it. As a result, the dangling-bond-like features normally associated with vacancies are lacking. This is visible when plotting the energy eigenvalues of the various aggregates. We are well aware of the dangers associated with predicting energy levels in the gap on the basis of either HF or DF calculations. However, comparisons and trends are meaningful, especially when qualitatively identical features are predicted by different methodologies.

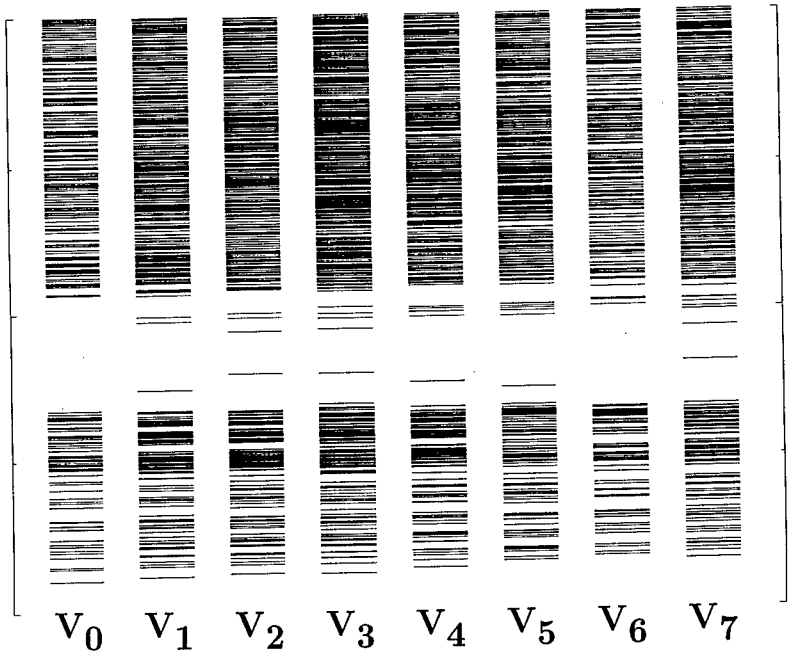


FIGURE 2: Energy eigenvalues near the gap calculated at the *ab-initio* HF level for the perfect cluster (V_0) and the most stable V_n aggregates.

Figure 2 shows the energy eigenvalues calculated at the *ab-initio* HF level. While the $V_{n\neq 6}$ all have deep levels in the gap, V_6 has none, and shows only some band-tailing (unoccupied levels) from the conduction band into the gap. The details depend of course on the methodology and the basis set. In particular, the band tailing is more pronounced in the MD than the HF eigenvalues. However, both methods agree that V_6 is not vacancy-like and should not be an efficient electron-hole recombination center. It should not be visible by DLTS or produce sharp photoluminescence (PL) lines.

The dipole moments (in a.u.'s) of the V_n's calculated at the HF level are as follows: 0.00 when no vacancy is present, 0.09 for V_1, 0.22 for V_2, 3.03 for V_3, 0.19 for V_4, 0.26 for V_5, 0.01 for V_6, and 1.67 for V_7. The dipole moment associated with V_6 is exceedingly small. The intensity of the signal in infra-red absorption spectroscopy (FTIR) depends on how much the dipole moment varies[23] rather than on its absolute magnitude. Since small oscillations of V_6 should not affect the reconstruction, we expect the dipole moment to remain small. V_6 should be essentially invisible to FTIR spectroscopy.

Note that there could be Raman-active modes, visible if they are not degenerate with host atom vibrations and if high-enough concentrations of V_6 can be generated. We did not investigate the vibrational modes of V_6 at this time. We estimate that much larger supercells will have to be used in order to obtain reliable vibrational properties. Such studies are being planned at this time.

IV. Discussion.

Our key results can be summarized as follows. Vacancies in Si attract each other and form aggregates. Up to n=7, the most stable one is the ring-hexavacancy, V_6, which should survive any high-temperature treatment. This defect is not vacancy-like: it has no deep levels in the gap and should not be an electron-hole recombination center. Further, it should be invisible to DLTS and FTIR, and produce no sharp PL feature. However, it could be Raman-active.

V_6 is a large, trigonal, planar void in the crystal. It should be a gettering center for a range of impurities (such as H, O, or transition metals). Further, it could be the nucleus or precursor to a range of extended defects.

There is no direct experimental evidence for the existence of V_6. However, there is experimental evidence that invisible defects remain in processed samples after high temperature anneals, and the properties of a sample often depend on its history. A few examples follow.

Neutron-transmutation doping results in extensive radiation damage. This damage becomes electrically and optically invisible following $850 - 1,000\,^{\circ}C$ anneals. However, if the annealed material is exposed to atomic H, shallow donors appear.[24] V_6 should survive the anneal, and could be activated by H. The properties of $\{V_6, H_n\}$ complexes are under investigation.

The low-energy implantation of noble-gas (NG) ions into Si, followed by a brief anneal around $250\,^{\circ}C$, gives rise to characteristic PL bands.[25] These defects have recently been assigned[26] to $\{NG, V_2\}$ complexes. Further anneals at $450\,^{\circ}C$ lead to the disappearance of the sharp spectra, which are replaced by a broad PL, independent of the NG. A possible explanation is that the complex binds more vacancies leading to the formation of $\{NG, V_6\}$ complexes. The free volume in V_6 is sufficiently larger than the atomic radius of the impurity that a NG-independent broad PL could result.

The exposure of crystalline Si to a remote H (or D) plasma may result in the formation of huge, disk-shaped defects known as platelets.[27-29] They are trigonal and planar. They appear to have a nucleation and a growth stage.[28] A defect such as V_6, which itself is trigonal and planar, is a plausible nucleus or precursor for platelets.

The V_6 defect resembles small prismatic dislocations such as those nucleated by vacancy condensation.[30] Although it is not clear how one goes from an isolated V_6 to an extended structure, the MD calculations show that V_6 could trap more vacancies.

Raman studies[31] of ion-implanted Si have shown that an unidentified line near 90 cm^{-1} intensifies as the implantation dose increases. The properties of the spectrum are consistent with this line being caused by a defect cluster with a size of the order of 10 Å.

Note that we do not claim that V_6 is related to all these observations. However, we do suggest that it combines the properties needed to explain the experimental data. V_6 may well be a fundament, long-overlooked, defect in Si.

Acknowledgements: The work of SKE is supported in part by the grant D-1126 from the R.A. Welch foundation and the contract RAD-7-17652-01 from the National Renewable Energy Laboratory. The work of PAF is supported in part by the NSF grant under the grant DMR 93-05344.

References.

1. J.W. Corbett, in *Electron Radiation Damage in Semiconductors and Metals* (Academic, New York, 1966).
2. G.D. Watkins, in *Defects and their Structure in Non-Metallic Solids*, edited by B. Henderson and A.E. Hughes (Plenum, New York, 1976).
3. G.D. Watkins, in *Deep Centers in Semiconductors*, edited by S.T. Pantelides (Gordon and Breach, New York, 1986).
4. M.A. Roberson and S.K. Estreicher, Phys. Rev. B **49**, 17040 (1994).
5. M. Jacob, P. Pichler, H. Ryssel, and R. Falster, J. Appl. Phys. (in print).
6. J.W. Corbett, J.L. Lindström, and S.J. Pearton, MRS Proc. **104**, 229 (1988).
7. Y.K. Park, S.K. Estreicher, C.W. Myles, and P.A. Fedders, Phys. Rev. B **52**, 1718 (1995).
8. G.D. Watkins and J.W. Corbett, Phys. Rev **138**, A543 (1965).
9. P. Mascher, S. Dannefaer, and D. Kerr, Phys. Rev. B **40**, 11764 (1989).
10. M. Saito and A. Oshiyama, Phys. Rev. B **53**, 7810 (1996).
11. S.K. Estreicher, J.L. Hastings, and P.A. Fedders, Appl. Phys. Lett. **70**, 432 (1997) and J.L. Hastings, S.K. Estreicher, and P.A. Fedders, Phys. Rev. B (in print).
12. O.F. Sankey and D.J. Niklewski, Phys. Rev. B **40**, 3979 (1989).
13. O.F. Sankey, D.J. Niklewski, D.A. Drabold, and J.D. Dow, Phys. Rev. B **41**, 12750 (1990).
14. A. Derecskei-Kovacs and D.S. Marynick, Int. J. Quant. Chem. **58**, 193 (1996); A. Derecskei-Kovacs, D.E. Woon, and D.S. Marynick, Int. J. Quant. Chem. **61**, 67 (1997).
15. M.W. Schmidt, K.K. Baldridge, J.A. Boatz, S.T. Elbert, M.S. Gordon, J.H. Jensen, S. Koseki, K.A. Nguyen, S. Su, T.L. Windus, M. Dupuis, and J.A. Montgomery, Jr., J. Comp. Chem. **14**, 1349 (1993).
16. W.R. Wadt and P.J. Hay, J. Chem. Phys. **82**, 284 (1985).
17. For details, see S.K. Estreicher, Mat. Sci. Engr. R **14**, 319 (1995).

18. G.D. Watkins and J.W. Corbett, Phys. Rev. **134**, A1359 (1964).

19. S. Dannefaer, P. Mascher, and D. Kerr, Phys. Rev. Lett. **56**, 2195 (1986).

20. J.H. Nelson, private communication.

21. D.J. Chadi and K.J. Chang, Phys. Rev. B **38**, 1523 (1988).

22. A. Oshiyama, M. Saito, and O. Sugino, Appl. Surf. Sci. **85**, 239 (1995).

23. R. Jones, private communication.

24. J. Hartung and J. Weber, Phys. Rev. B **48**, 14161 (1993), and J. Appl. Phys. **77**, 118 (1995).

25. G. Davies, Phys. Rep. **176**, 83 (1989).

26. S.K. Estreicher, J. Weber, A. Derecskei-Kovacs, and D.S. Marynick, Phys. Rev. B **55**, 5037 (1997).

27. N.M. Johnson, F.A. Ponce, R.A. Street, and R.J. Nemanich, Phys. Rev. B **35**, 4166 (1987).

28. N.M. Johnson, C. Herring, C. Doland, J. Walker, G. Anderson, and F. Ponce, Mater. Sci. Forum **83-87**, 33 (1992).

29. B.L. Sopori, K. Jones, and X.J. Deng, Appl. Phys. Lett. **61**, 2560 (1992).

30. J.P. Hirth and J. Lothe, *Theory of Dislocations* (Krieger, Malabar, 1992), p.614.

31. L.P. Avakyants, E.D. Obrastsova, and V.S. Gorelik, J. Molec. Struct. **219**, 141 (1990).

Materials Science Forum Vols. 258-263 (1997) pp. 515-520
© 1997 Trans Tech Publications, Switzerland

IDENTIFICATION OF VH IN SILICON BY EPR

P. Johannesen[1], J. R. Byberg[2], B. Bech Nielsen[1], P. Stallinga[1], and K. Bonde Nielsen[1]
[1] Institute of Physics and Astronomy, University of Aarhus, DK-8000 Århus C, Denmark.
[2] Institute of Chemistry, University of Aarhus, DK-8000 Århus C, Denmark.

Keywords: Silicon, vacancies, hydrogen, dangling bonds, EPR, point defects, electronic properties.

Abstract
Floatzone grown silicon crystals have been implanted with protons or deuterons. Electron Paramagnetic Resonance (EPR) spectra show the presence of a strongly temperature dependent signal in addition to the well-known S1 signal. The temperature dependent signal displays monoclinic-I symmetry below 65 K and trigonal symmetry above 110 K. The g- and ^{29}Si hyperfine tensors are characteristic of defects with the unpaired electron confined mostly to a dangling bond orbital in a vacancy-type defect. The signal shows splittings arising from the hyperfine interaction with a single proton. On this basis, and from the close similarity with the familiar VP^0 signal (the E-center), we conclude that the signal originates from VH^0, the neutral charge state of the silicon monovacancy containing a single hydrogen atom.

Introduction

The continued search for the detailed structures of hydrogen-related point defects in crystalline silicon is essential to our understanding of how hydrogen modifies the electronic and optical properties of silicon. Furthermore, experimentally determined structures of such defects constitute an excellent testing ground for *ab initio* calculations. Although the properties of hydrogen in silicon have been intensively studied during the past decade [1], few defect structures involving hydrogen have been established [2, 3, 4, 5]. The present work offers the identification of a fundamental hydrogen-related point defect in silicon, the existence of which has been expected for more than a decade.

In molecular compounds, such as SiH_4, hydrogen and silicon form strong covalent bonds. Therefore, any defect that may form such bonds constitutes a deep trap for hydrogen. The monovacancy is such a structure. Bech Nielsen *et al.* [5] found direct evidence of this in a study of the local vibrational modes of point defects in proton-implanted silicon by FTIR (Fourier Transform InfraRed) spectroscopy. They identified the Si-H stretch modes of VH_2, VH_3 and VH_4, that is, monovacancies binding two, three and four hydrogen atoms, respectively. Thus the existence of vacancy-hydrogen complexes in silicon has been established, but the electronic properties of these defects remain to be determined experimentally. Furthermore, VH, the simplest member of this series of defects, has not yet been identified.

The expected structure of VH^0, the EPR-active neutral charge state of VH, may be deduced from a simple LCAO picture: Introducing a vacancy in the silicon lattice creates four free sp^3 hybridized silicon orbitals, one of which forms a strong covalent bond with the hydrogen atom. The one-electron energies of the bonding and antibonding combinations of the silicon orbital and the hydrogen 1s orbital lie well below the top of the valence band and well above the edge of the conduction band, respectively. This is due to the large ionization potential of hydrogen and to the strong overlap of the two orbitals. The presence of the hydrogen atom changes the symmetry of the unrelaxed vacancy from T_d to C_{3v}. The remaining three silicon orbitals form a bonding combination belonging to the symmetric representation A with energy well below the top of the valence band and a pair of degenerate combinations belonging to the representation E with energy within the band gap.

In the neutral charge state of VH the E level is singly occupied leading to a Jahn-Teller distortion from C_{3v} to C_{1h} symmetry. Hence two of the silicon orbitals are expected to combine, forming a reconstructed bond, while the remaining silicon orbital is left as a singly occupied dangling bond that contains most of the unpaired electron spin density. According to this description, VH^0 should have monoclinic-I symmetry with the dangling bond and the Si-H bond pointing almost in ⟨111⟩ directions in a {110} mirror plane. This structure, depicted in Fig. 1, is consistent with the results of *ab initio* calculations [6, 7].

Since the structure sketched above corresponds closely to that of VP^0 (the E-center) [8], in which a substitutional phosphorus atom is located next to a monovacancy, it may be expected that the electronic properties of VH^0 resemble those of VP^0.

In this paper we report the identification of VH^0 in proton-implanted silicon. The observed properties, including the electron spin distribution, the hydrogen hyperfine interaction and a thermally activated change of the effective symmetry, all corroborate the model of VH^0 and testify to the close similarity with VP^0.

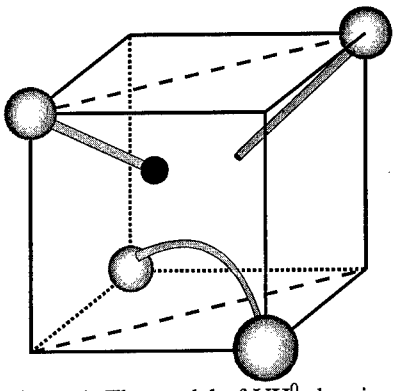


Figure 1. The model of VH^0 showing the vacancy in the center, the Si-H bond and the dangling bond in the {110} mirror plane, and the reconstructed bond perpendicular to the plane.

Experimental

The samples were n-type (resistivity: 600 Ωcm) silicon crystals grown by the floatzone technique. The concentration of phosphorus was ~9×10^{12} cm^{-3}, while the concentration of other impurities, mainly oxygen and carbon, was below 3×10^{16} cm^{-3}. Slabs measuring 1×3×4 mm^3 were cut with the large faces perpendicular to a {110} plane. After polishing, both large faces were implanted with protons (or deuterons) at 56 (or 38) successive energies in the range from 5.3 to 10.5 MeV (or 5.0 to 10.6 MeV). The dose implanted at each energy was calculated to ensure a uniform distribution of hydrogen throughout the sample corresponding to a concentration of ~4×10^{17} cm^{-3}. During the implantation, the sample temperature was kept below 120 K. The samples were subsequently warmed to room temperature and etched in nitric and hydrofluoric acid to remove surface defects that might be EPR active.

The experimental setup consists of a Bruker ESP300E spectrometer operating in absorption mode at X band (~9 GHz) and Q band (~34 GHz). EPR spectra were recorded at 5° intervals in the $(1\bar{1}0)$ plane. The static magnetic field $\mathbf{B_0}$ was monitored with a resolution of 1 μT with a Bruker ER-035 NMR gaussmeter. Resolution enhancement by third harmonic detection [9, 10] was employed: The magnetic field was modulated at 33 kHz with a small admixture of 100 kHz, and the EPR signal was lock-in detected at 100 kHz. By adjusting the amplitudes of the 33 and 100 kHz modulations correctly, a decrease in linewidth of ~30 % could be obtained without introducing spurious lines. The sample was placed in a liquid helium cryostat allowing its temperature to be controlled in the range from 10 K to 300 K. Isochronal (20 minutes) annealing of the samples was done in steps of 15°C with a controlled flow of heated nitrogen gas.

Results

In addition to the S1 signal, previously observed in EPR spectra of proton-implanted silicon crystals [11], our EPR spectra contain a new, strongly temperature dependent signal which we label vh^0, anticipating the identification with the VH^0 defect made below. The spectrum of the deuterium implanted sample Si:D recorded with $\mathbf{B_0} \parallel [111]$ at different measurement temperatures is shown in

Fig. 2. At the microwave power employed, the S1 signal becomes partially saturated below 85 K, which makes it possible to separate out the vh^0 signal. At 45 K, vh^0 consists of the three lines *A*, *B* and *C* (line *A* almost coincide with one of the lines of S1). As the temperature is raised, *A* and *B* begin to broaden and finally disappear at 85 K, while *C* persists. Above 110 K a new line *AB* emerges at a position dividing the distance from *A* to *B* in the ratio 1:2. It attains a maximum in intensity (and a minimum in linewidth) at 145 K. At higher temperatures both *C* and *AB* broaden, becoming undetectable at room temperature. An isochronal annealing study confirmed that *A*, *B*, *C* and *AB* originate from the same defect, which anneals out at ~480 K.

Spin-Hamiltonian terms		VH^0	VP^0
$\underline{\mathbf{g}}$ (± 0.0001)	X	2.0090	2.0096
	Y	2.0114	2.0112
	Z	2.0006	2.0005
	θ	32.4°	32°
$\underline{\mathbf{A}}(^{29}Si)$ (MHz) (± 1 MHz)	X	-275	-295
	Y	-275	-295
	Z	-435	-450
	θ	35.3°	35.3°
$\underline{\mathbf{A}}^{\mathbf{H}}$ (MHz) (± 0.3 MHz)	X	-3.3	
	Y	-4.6	
	Z	8.5	
	θ	8°	

Table I. The spin Hamiltonian parameters for vh^0 at 45 K and for VP^0 [8]. The principal axis Y is parallel to the $[1\bar{1}0]$ axis, while X and Z span the $(1\bar{1}0)$ plane, Z making the angle θ with the [110] axis. The quoted uncertainties pertain to vh^0.

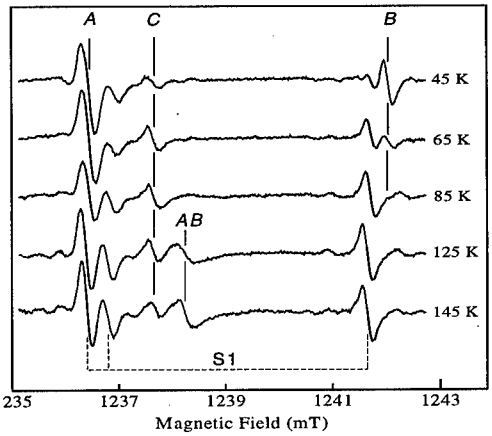


Figure 2. Spectra of Si:D recorded at different sample temperatures with $\mathbf{B_0}$ along [111] and at 34.778 GHz. The lines *A*, *B*, *C* and *AB* belong to the signal vh^0.

The temperature dependence of vh^0 in the region 45-145 K suggests that the corresponding defect undergoes a thermally induced symmetry change. This is confirmed by the angular variation of vh^0 in the $(1\bar{1}0)$ plane for Si:D, which is shown in Fig. 3: The g tensor shows monoclinic-I symmetry at 45 K (open circles) and trigonal symmetry at 145 K (filled circles).

Direct evidence of the incorporation of hydrogen in the defect responsible for vh^0 is obtained by a comparison of the spectra of Si:H and Si:D: Fig. 4 shows corresponding spectra recorded at 45 K with $\mathbf{B_0} \parallel [110]$; the four lines belonging to vh^0 in Si:D are labelled by *D* through *G*. The lines *D* and *G* appear as doublets in Si:H, whereas the lines *E* and *F* appear at the same positions in Si:D and Si:H. The doublet splittings in Si:H reveal the involvement of a single hydrogen atom in the defect, while the absence of resolved splittings of *E* and *F* indicates that the hyperfine interaction is strongly anisotropic. The spectra may be represented in terms of the spin Hamiltonian

$$H_{spin} = \beta\, \mathbf{S}\underline{\mathbf{g}}\mathbf{B}_0 - g_p\beta_n\, \mathbf{I}\cdot\mathbf{B}_0 + \mathbf{S}\underline{\mathbf{A}}^{\mathbf{H}}\mathbf{I}$$

where g_p is the g value of the proton, and β and β_n are the Bohr- and nuclear magneton, respectively. The principal values of $\underline{\mathbf{g}}$ and $\underline{\mathbf{A}}^{\mathbf{H}}$, describing the hyperfine interaction with the hydrogen nucleus, are listed in Table I, and simulations of the signals for $\mathbf{B_0} \parallel [110]$ calculated from these parameters are shown in Fig. 4 as dashed curves. The nuclear Zeeman energy of the proton at the magnetic fields employed is much larger than the proton hyperfine interaction, implying that the splittings observed *between* the principal directions of $\underline{\mathbf{A}}^{\mathbf{H}}$ depend strongly on the relative signs of the principal values. Hence these signs could be determined unambigously. The deuteron hyperfine

splittings calculated from the observed proton splittings are smaller than the linewidth for all orientations of $\mathbf{B_0}$ in accordance with the absence of resolved splittings in the signal observed in Si:D.

In the spectra recorded below 65 K of both Si:D and Si:H, we observe a pair of weak satellites belonging to each of the main lines. The relative intensitiy of each pair of satellites is ~2 %, and the splitting between a pair of satellites is independent of the microwave frequency. We therefore ascribe these satellites to the hyperfine interaction with the ^{29}Si nucleus of *one* nearby silicon atom. The corresponding hyperfine tensor has trigonal symmetry (Table I). Hyperfine interactions with other silicon nuclei in the vicinity of the defect were not resolved.

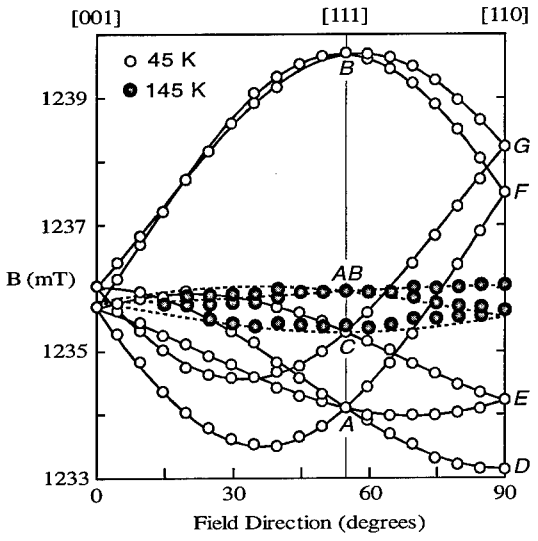


Figure 3. The angular dependence of vh^0 in the $(1\bar{1}0)$ plane at 34.710 GHz for Si:D. The open and filled circles indicate measurements at 45 K and 145 K, respectively. The solid curves are calculated from the g tensor in Table I, and the dashed curves are calculated from the motional average of this tensor (see text). Labels at B_0 || [111] refer to Fig. 2, while labels at B_0 || [110] refer to Fig. 4.

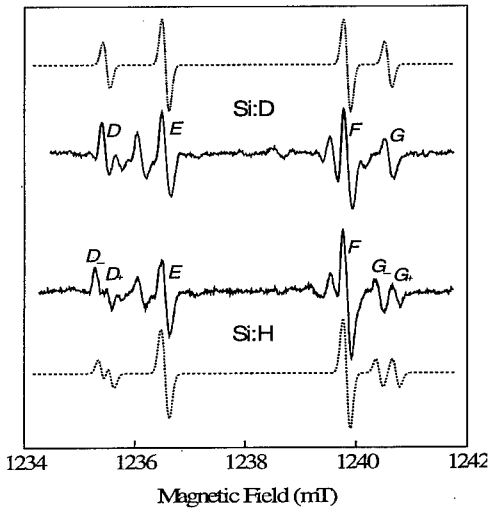


Figure 4. Spectra (solid curves) of Si:D and Si:H recorded at 45 K and 34.777 GHz with $\mathbf{B_0}$ along [110]. The labelled lines belong to vh^0. The dashed curves represent simulations based on the parameters in Table I.

Analysis and discussion

The g tensor representing the low temperature form of vh^0 has monoclinic-I symmetry and is nearly axial ($g_X \approx g_Y$) with its unique axis Z deviating only 3° from the [111] axis (Table I). According to the classification scheme of Lee and Corbett [12], such a g tensor is typical for centers in which the unpaired electron is largely confined to a dangling bond orbital in a vacancy-type defect. A simple LCAO analysis of the observed hyperfine interaction with a single ^{29}Si nucleus suggests that 54 % of the electron spin is located on the silicon atom in an orbital with 13 % s-character and 87 % p-character. These values are typical for dangling bonds around vacancies [12]. From Table I it can be seen that $\underline{\mathbf{g}}$ and $\underline{\mathbf{A}}(^{29}Si)$ of vh^0 closely resemble the corresponding parameters of VP^0. This indicates that the structure and distribution of electronic spin of the defect associated with the vh^0 signal are very similar to those of VP^0.

Combining this result with the observation of a hyperfine interaction with one proton, we may conclude that the defect consists of one or several vacancies binding a single hydrogen atom. The number of vacancies involved may be inferred from the magnitude of the proton hyperfine interaction: We note that the isotropic hyperfine constant $a = {}^1/_3 (A_X + A_Y + A_Z)$ is only 0.2 MHz (Table I) indicating a negligible spin density at the proton. We may therefore ascribe the observed anisotropic hyperfine splitting to the dipolar interaction of the proton spin with the electron spin confined essentially to the dangling bond orbital. Within the point dipole approximation, the distance R between the proton and the silicon atom carrying the dangling bond may be estimated from the expression $b = g_e\beta\, g_p\beta_n\, R^{-3}$ with $b = {}^1/_6(2A_Z - A_X - A_Y) = 4.1$ MHz (Table I). The result is R = 2.7 Å, in excellent agreement with the value of 2.8 Å calculated from the unrelaxed geometry of VH^0 with the 1.5 Å Si-H bond pointing exactly in a ⟨111⟩ direction. A similar calculation for the unrelaxed geometry of the divacancy binding a single hydrogen atom (V_2H^0) yields R = 4.7 Å. These values strongly indicate that vh^0 originates from VH^0 rather than from V_2H^0. Scaling R with the ratio of the lattice constants of diamond and silicon yields R = 1.8 Å for VH^0 in diamond, in accordance with the value of 1.9 Å derived for the H1 defect in diamond [13], the structure of which is believed to resemble that of VH^0.

The identification of the defect responsible for vh^0 with the neutral charge state of the silicon monovacancy containing a single hydrogen atom gains additional support from the observed transition from monoclinic-I to trigonal symmetry. This transition is very similar to that described by Watkins and Corbett for the E-center (VP^0) [8]. It may be explained as the result of a thermally induced reorientation of the VH^0 defect among three equivalent orientations that have the hydrogen atom bound to the same silicon atom. The 12 equivalent orientations of VH^0 can be grouped in four sets each associated with a particular ⟨111⟩ axis, so that the members of a given set are interrelated through C_3 orientations around the ⟨111⟩ axis belonging to the set. Considering the special case of $\mathbf{B_0} \parallel [111]$ as in Fig. 2, it is obvious that the set belonging to the [111] axis gives rise to a single line, the position of which is unaffected by the reorientation process. This line is *C* in Fig. 2. The other three sets all contribute to both line *A* and line *B*, which means that a defect reorienting at a frequency ν among the configurations within one of these sets contributes alternatingly to *A* and *B*. This switching adds a dynamic component $\Delta\omega$ to the "static" linewidth $\Delta\omega_0$ of *A* and *B* and, since ν increases when the temperature is raised, *A* and *B* become broadened. At some temperature, ν exceeds the spectral separation ω_{A-B} between *A* and *B* causing *A* and *B* to disappear while a single line *AB* emerges at a position that is the weighted average of the original positions of *A* and *B*. This phenomenon is known as motional narrowing [14]. In the notation of Watkins and Corbett, the relationships between $\Delta\omega$ and the lifetime τ of the reorientation process are

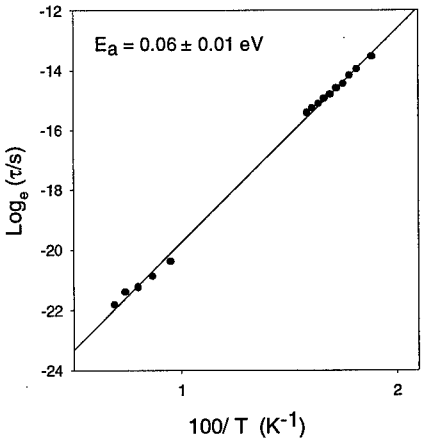


Figure 5. The temperature dependence of the lifetime τ showing that the reorientation has an activation energy of 0.06 eV.

$$\Delta\omega_A = \frac{p_A}{\tau}, \quad \Delta\omega_B = \frac{p_B}{\tau} \quad \text{and} \quad \Delta\omega_{AB} = \frac{\tau}{4}\left[1-(p_A - p_B)^2\right]\omega_{A-B}^2$$

where p_A and p_B are the relative propabilities for finding the defect in a configuration contributing to line *A* and *B*, respectively ($p_A = {}^2/_3$ and $p_B = {}^1/_3$). Assuming that the lineshape is a convolution of a Lorentzian and a Gaussian [8], $\Delta\omega$ can be estimated as $\Delta\omega = \frac{1}{2}\left(\Delta\omega_t - \Delta\omega_0 + \sqrt{\Delta\omega_t^2 - \Delta\omega_0^2}\right)$,

where $\Delta\omega_t$ is the total linewidth. From these expressions, we have estimated τ for different temperatures in the regions of broadening of *B* and narrowing of *AB*. In Fig. 5 the logarithm of τ is plotted versus T^{-1}. The simple temperature dependence $\tau = \tau_\infty \exp(E_a / kT)$ corroborates the assignment of both broadening and narrowing to a single reorientation process with an activation energy of E_a = (0.06 ± 0.01) eV. This value is exactly the same as that derived by Watkins and Corbett for VP^0 [8], which indicates that the reorientation processes in VH^0 and VP^0 are very similar.

The trigonal angular dependence of the EPR signal calculated from the g tensor measured at 45 K and the reorientation model is included in Fig. 3 as dashed curves. Noting that the linewidth is ~0.25 mT at 145 K, the agreement with the data is very good. Thus, the thermally induced symmetry change strongly corroborates our identification of the defect.

Conclusions

VH^0 is present in proton-implanted high-resistivity silicon at temperatures below 450 K. Its electronic properties are determined almost completely by the silicon dangling bond. The defect shows monoclinic-I symmetry as expected from theory, and it reorients with an activation energy of only 0.06 eV among three equivalent configurations with the hydrogen atom bound to the same silicon atom. The electronic properties of VH^0 and VP^0 are very similar, indicating that the Si-H fragment of VH^0 may be regarded as a "pseudo atom" acting like a group-V impurity.

Acknowledgements

This work was supported by the Danish National Research Foundation through Aarhus Center for Advanced Physics (ACAP).

References

[1] S.J. Pearton, J.W. Corbett, and M. Stavola, *Hydrogen in Crystalline Semiconductors*, Springer-Verlag, Berlin (1992).
[2] K. Bergman, M. Stavola, S.J. Pearton, and T. Hayes, Phys. Rev. B **38**, 9643 (1988).
[3] Yu.V. Gorelkinskii and N.N. Nevinnyi, Physica B **170**, 155 (1991).
[4] J.D. Holbech, B. Bech Nielsen, R. Jones, P. Sitch, and S. Öberg, Phys. Rev. Lett. **71**, 875 (1993).
[5] B. Bech Nielsen, L. Hoffmann, and M. Budde, Mater. Sci. Eng. B **36**, 259 (1996).
[6] P. Deák, L.C. Snyder, M. Heinrich, C.R. Ortiz, and J.W. Corbett, Physica B **170**, 253 (1991).
[7] M.A. Roberson and S.K. Estreicher, Phys. Rev. B **49**, 17040 (1994).
[8] G.D. Watkins and J.W. Corbett, Phys. Rev. **134**, A1359 (1964).
[9] S.H. Glarum, Rev. Sci. Instrum. **36**, 771 (1965).
[10] L.C. Allen, J. Chem. Phys. **40,** 3135 (1964).
[11] H. Lütgemeier and K. Schnitzke, Phys. Lett. A **25**, 232 (1967).
[12] Y.H. Lee and J.W. Corbett, Phys. Rev. B **8**, 2810 (1973).
[13] X. Zhou, G.D. Watkins, K.M. McNamara Rutledge, R.P. Messmer, and S. Chawla, Phys. Rev. B **54**, 7881 (1996).
[14] H.S. Gutowsky and A. Saika, J. Chem. Phys. **21**, 1688 (1953).

Materials Science Forum Vols. 258-263 (1997) pp. 521-526
© 1997 Trans Tech Publications, Switzerland

NOVEL LUMINESCENT CENTRES IN CADMIUM DOPED SILICON

C.A. Frehill, M.O. Henry, E. McGlynn, S.E. Daly[#], M. Deicher[&], R. Magerle[&], K.G. McGuigan[$], A. Safanov[*] and E.C. Lightowlers[*]
School of Physical Sciences, Dublin City University, Glasnevin, Dublin 9, Ireland
[#]School of Physics, Dublin Institute of Technology, Kevin Street, Dublin 2, Ireland
[&]Fakultät Physik, Universität Konstanz, D-78434 Konstanz, Germany
[$]Department of Physics, RCSI, St. Stephen's Green, Dublin 2, Ireland
***Department of Physics, Kings College London, Strand, London WC2R 2LS, UK**

Keywords : Silicon, Photoluminescence, Si:Cd

Abstract
Samples of silicon doped with cadmium are found to produce a series of unusual and complex luminescence spectra. For the lowest energy group (minimum energy zero-phonon line at 1058.2 ±0.1 meV) transitions occur from an excited state manifold of five levels spread over 4.3 meV into a single ground state. Another group of lines (with the minimum energy zero-phonon line at 1066.8 ±0.1 meV) is broadly similar to the 1058 meV group, except that there are not less than eight lines within a range of only 2.4 meV, and both the ground and excited states are manifolds of several levels. For the third group (lowest energy zero-phonon line at 1083.3 ±0.1 meV) thermalisation data clearly show that both the excited and ground states are manifolds of three levels each, with very strong selection rules governing the transitions. Co-doping with lithium and annealing the samples in the temperature range 50-450°C following a quench from high temperatures substantially enhances the intensities.

Introduction

In a previous study [1] of silicon implanted with the radioactive isotope ^{111}In (which decays to ^{111}Cd with a 2.8 day half-life) three new photoluminescence (PL) systems appeared in the samples over a period of weeks, at a rate unconnected with the ^{111}In half-life. The Si:^{111}In had been subjected to a high temperature anneal at ~1100^{0}C followed by a quench to room temperature. It was concluded that these systems were due to the ^{111} Cd daughter forming defect complexes (possibly with other impurities) through a slow diffusion process as the samples were stored at room temperature. In order to verify the origin of these PL systems, high-resolution measurements have been performed on Cd-implanted and Cd-diffused float zone (FZ) and Czochralski (CZ) silicon annealed at ~1100^{0}C followed by a quench to room temperature. The three systems have been observed, group I centered at 1060.6 meV, group II at 1068 meV and group III centered at 1079 meV.

Experimental

A large number of Si:Cd samples were produced by cadmium implantation into high resistivity FZ and CZ material of both conductivity types. The typical ion implantation energy and dose were 200 keV and 1x10^{14} ions cm^{-2}, respectively. Samples were also prepared by diffusion from Cd vapour, as described below. The implanted samples were RCA cleaned before all heat treatments and were placed in a quartz tube which was heated to ~1100^{0}C for 10 sec and quenched to room temperature in a 4:6 water:isopropanol mixture. Subsequent annealing treatments were carried out in an RCA-cleaned quartz tube for a duration of 30 min and for temperatures up to 450^{0}C. The production of the three defects depends upon the cooling rate during the rapid quench to room temperature, which can be affected by the sample dimensions. By placing a pellet of lithium metal in the quartz tube during the high temperature anneal the intensities of the three defects increases. The stress samples were prepared by diffusion. Samples were cut into rectangular parallelepipeds, with the sample long

axis parallel to one of the crystal axes <001>, <111> and <110>. A cadmium pellet was placed together with the samples in a quartz ampoule at 0.5 atm of helium and heated to 1100^0C for 2h. The diffused samples were then annealed in an ampoule containing a lithium pellet and heated to 850^0C for 5 min at 0.5 atm of helium. To achieve a rapid quench to room temperature the ampoules were plunged into water. For the isotope substitution studies, ^{106}Cd and ^{116}Cd were used, implanted either separately into different wafers or together for dual implant studies. The luminescence was excited using the 514 nm line of an argon-ion laser and the excitation power was typically ~100 mW (unfocussed) on the sample face. Details of the apparatus used for recording the PL measurements and producing the uniaxial stresses are described elsewhere [2,3].

Results

A PL spectrum of cadmium-implanted FZ silicon quenched to room temperature following a 10sec anneal at 1100^0C and subsequently annealed to 100^0C for 30 min is shown in Fig. 1. Three independent groups of lines, which we label group I, group II and group III, are observed, for which the relative intensities depend upon the annealing treatment. All three groups are multi-line spectra, with low energy in-band phonon modes clearly observed for groups I and III. High resolution spectra of the three systems at a series of temperatures were recorded as illustrated in Fig. 2. For group I transitions occur from five excited state levels to a single ground state. An energy level diagram for group I is given in Fig. 3(a). The total group I intensity initially grows to a maximum at 15 K, then decreases with increasing temperature and becomes undetectable at temperatures >40 K. The group I zero phonon lines (ZPL) couple to an in-band local mode phonon of energy ~ 7.8 meV. The Huang-Rhys factor is estimated to be ~ 0.6 from the ratio of the integrated intensities of the zero phonon lines and the first phonon sideband.

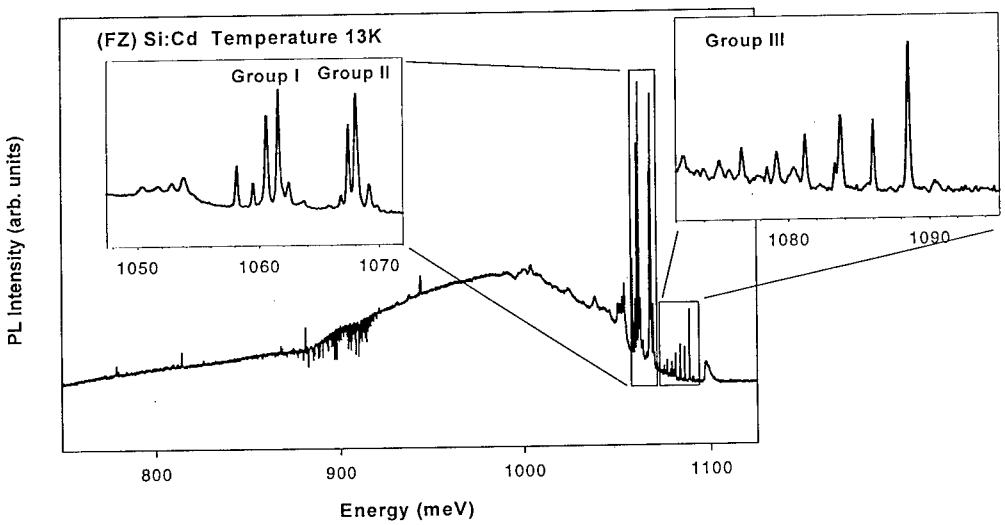


Figure 1 PL spectrum of cadmium-implanted silicon showing positions of Groups I, II and III

The group II spectra revealed eight lines within a range of 2.4 meV. At the highest resolutions employed, there was considerable overlap of different components within this group of lines, and as a result the energy level diagram deduced, shown in Fig. 3(b), is somewhat uncertain. However it appears that there are sublevels within the both the ground and excited states for this group of lines.

The total group II intensity grows to a maximum at ~5.5 K and the PL disappears at temperatures >30 K. For this group, the local mode phonon (7.2meV) is observed clearly only in the 4.2K spectrum – at higher temperatures the sideband is obscured by the additional group I lines which appear in the spectrum.

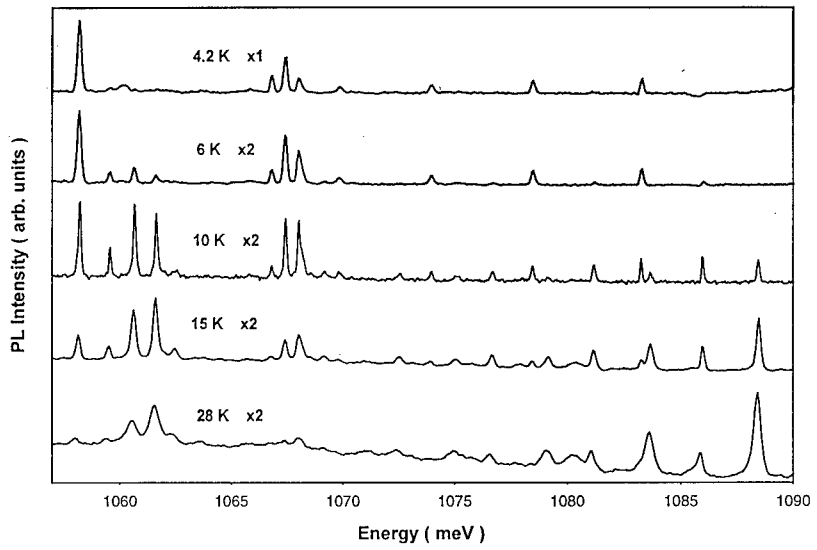


Figure 2 Photoluminescence spectra of Si:Cd as a function of temperature

The third group of lines is a complicated system with three ZPLs at 1083.3, 1078.5 and 1074 meV, each with a series of sidebands involving an in-band local mode of energy 4.8 meV. At 4.2 K only the lowest energy ZPL and its sidebands are observed. At higher temperatures the other two ZPL appear along with their sidebands. The separations of the ZPL are close to the phonon energy, which accounts for the complexity seen in the spectrum. The overlapping lines were deconvolved to Gaussian fits and an energy level diagram is shown in Fig. 3(c). In this case, the quality of the thermalisation data is very high, and there is no doubt about the splittings. The Huang-Rhys factor for the 4.8 meV local mode is calculated to be ~1.2 using data from the first three phonon sidebands. The total group III intensity initially grows to a maximum at ~22 K and then decreases with increasing temperature until it disappears at temperatures >40 K. The calculated infinite temperature intensity ratios for the lines within each group are given in Fig. 3. It is immediately obvious that strong selection rules are in operation for these centres.

Unambiguous evidence of the involvement of cadmium in the three systems was established using isotope substitution experiments. A positive shift of ≤ 0.1 meV is observed in the ZPLs of all three spectra resulting from an isotopic change from ^{106}Cd and ^{116}Cd. In the case of group III, a shift of 0.3 meV (in near exact agreement with that calculated for an inverse square-root dependence on the mass of the Cd atom) is observed for the phonon replica at 1079 meV, and is illustrated in Fig. 4. In order to determine the role of lithium in the defect complexes isotope substitution of ^{6}Li and ^{7}Li will be performed in the near future.

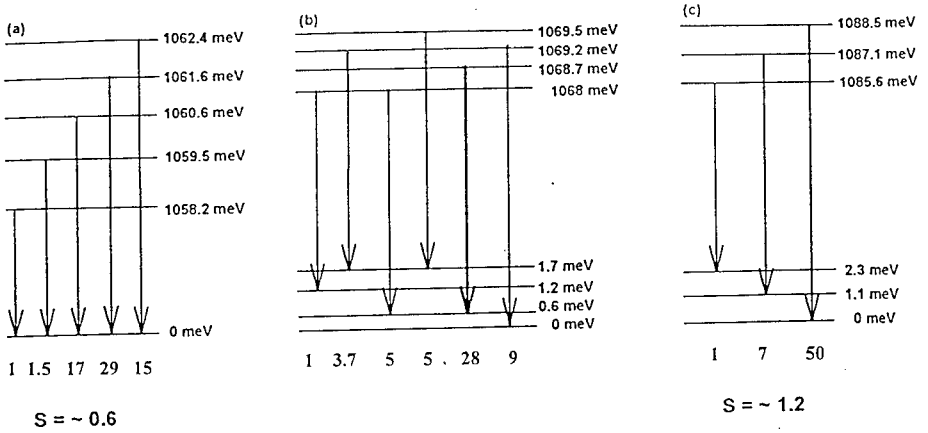


Figure 3: Energy level diagrams for (a) Group I, (b) Group II and (c) Group III. There are three components within the group II line at 1068.1meV. The numbers beneath the arrows show the approximate infinite temperature intensity ratios. The S values are the Huang-Rhys parameters for the dominant local phonon mode.

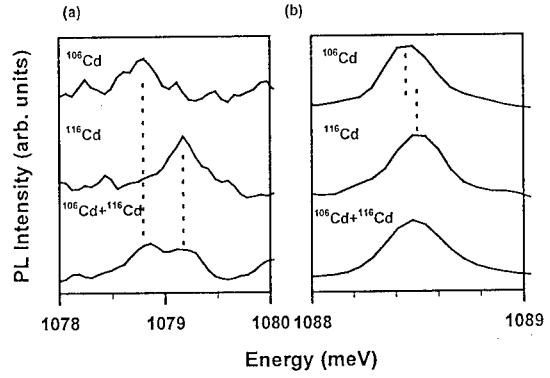


Figure 4: Isotope shift of (a) Group III 1079 meV phonon replica and (b) Group III 1088.5meV ZPL

Uniaxial stress measurements were performed to determine the symmetry of the defects associated with each of the three zero phonon line spectra. Unequivocal identifications are difficult for all groups due to the complexity of the spectra, and the measurements were hampered also by poor signal levels for groups I and III in the oriented samples. Consequently, there is as yet no definite identification of the defect symmetries for these PL systems. From the available data, and applying the theories of Kaplyanskii [4] and the shift rate equations calculated by Mohammad *et al* [5], the group II lowest energy line appears to originate at a defect of rhombic I (C_{2v}) symmetry. Although good agreement is obtained for the <001> and <111> stress directions, as indicated in table 1, this is not so for the <110> data. Further experiments are required in order to clarify this problem. The data available for group I indicate that the centre may be trigonal, but for group III we do not yet have any reliable results.

Stress Direction	Theoretical Shift Rate Expression	Measured Shift Rate (meV GPa^{-1})	Best Fit Shift Rate (meV GPa^{-1})	Measured Intensity	Expected Intensity
<001>	A_1	-56	-56.0	0.46	0.33
	A_2	19	19.0	1	1
<111>	$(A_1+2A_2-2A_3)/3$	-21	-21.0	0.75	0.6
	$(A_1+2A_2+2A_3)/3$	9.8	9.0	1	1
<110>	$(A_1+A_2)/2$	-34	-18.5	1	1
	(A_2+A_3)	-22	-3.5	~0.1	0.33
	(A_2-A_3)		41.5		0

Table 1. Uniaxial stress results for the group II lowest energy line. Fit parameter values (in units of meV GPa^{-1}: $A_1 = -56.0$, $A_2 = 19.0$, and $A_3 = -22.5$. Intensity values are normalised so that the most intense component for each stress direction has an intensity of 1. The expected intensity values are based on the experimental geometry used.

Discussion

The Cd isotope substitution data show that Cd is present in all three centres. For Group III, where the local mode is clearly resolved, the shift is in near exact agreement with the $m^{-½}$ mass dependence expected for vibration of the Cd atom with respect to a static lattice. In addition to Cd, we find that the presence of Li in the samples results in a substantial increase in the PL intensities, especially for groups I and II, although isotope substitution evidence has not yet been obtained to confirm that Li is incorporated in the defects. Zn-Li complexes were reported for Ge [6] in early electrical transport measurements, and it is very likely that similar complexes involving Cd-Li are the origin of the PL spectra we have observed. The annealing data show some interdependence in the PL intensities for the groups, and it is probable that the main difference between the centres lies in the number and lattice locations of the Li atoms. The observation of the PL in samples not deliberately doped with Li is attributed to out-diffusion of Li from the quartz during the high temperature anneal.

On the basis of detailed temperature dependence measurements, energy level diagrams deduced for the three centres are shown in Fig. 3. For group I a single electronic ground state is observed, with strong selection rules governing the transitions from a manifold of five excited state levels. For group III, the data clearly require that both the ground and excited states contain more than one level, and once again there are strong selection rules in operation. In the case of group II, there is a complex fine structure with overlapping lines observed at the highest resolutions employed. Here, too, the data indicate the occurrence of a manifold of levels in both ground and excited states, but the uncertainties in the intensity measurements make the deduction of the energy level structure somewhat imprecise in comparison to the case of group III. It is possible that more than one defect (or defect configuration) contributes to the group II lines, so we regard the energy level diagram as tentative for this group of lines. Taken as a whole, the spectra show that the defect energy level structures are unusual for silicon both in their fine structure and selection rules.

The uniaxial stress measurements suggest that the group II transitions originate in defects of C_{2v} symmetry. A general trend in the group II data is for the lines to diverge into two groups which separate under <001> and <110> stresses at roughly the same rate as the conduction band minima, indicative of donor character in the defect. In particular, the response to <001> stress shows a splitting of ~ 75 meV/Gpa, in near exact agreement with that of the conduction band minima [7]. As stated above, only limited stress data are available for groups I and III.

To fully describe the luminescence transitions, and especially to explain the pronounced selection rules, it is essential that Zeeman measurements be performed so that a full description in terms of orbital and spin quantum numbers can be given. In the absence of such information, we can provide at best an outline of how the spectra can be accounted for. The uniaxial stress data point towards donor character for group II at least, and the small binding energies require that the excited states are shallow for all three groups. For the ground states, we have the unusual situation of several closely spaced levels for groups II and III. We have not detected the momentum-conserving phonon replicas, nor two-electron or two-hole satellites, which characterise neutral donor and acceptor bound exciton recombination. Rather, we find broad multiphonon sidebands involving phonons

from the full spectrum of lattice modes, with a cut-off in the one phonon sideband at the energy of the O^{Γ} phonon. These factors indicate that the PL involves at least one strongly localised particle and is not due to the recombination of band-edge electrons and holes at simple donor or acceptor centres. For vibronic PL centres in Si, generally, luminescence has been attributed to electron-hole recombination, with the singlet ground state (which is usually observed) being the bare defect. It may turn out to be the case that the group I center is another example of such centres. For group II and III, this picture is not adequate and we must look for an alternative description of the luminescence process. There are exceptions to the general observation that the final state of luminescence transitions for vibronic centres in Si is a bare defect. A notable example is the case of the Au donor. Here, the ground state is paramagnetic, and the luminescence and absorption can be explained using the vacancy model proposed by Watkins [8]. The essence of this model is that the 5d shell of the Au impurity atom is deep in the valence band and that the 6s electron occupies one of the vacancy orbitals, with the result that the electrical and optical properties of Si:Au can be modelled, in a first approximation, as those of the silicon vacancy in the appropriate charge state. There is no reason *a priori* to reject a vacancy model approach to the analysis of impurity centres such as isolated Cd and complexes of Cd with other impurities. The first requirement – that the d-shell lies well below the valence band maximum - is satisfied. Accordingly, we can expect the 5s electrons to occupy the vacancy orbitals, as for the 6s electron in the case of Au. We suspect that this approach is likely to provide the necessary variety of energy level fine structure, produced by the impurity electrons occupying states derived from the vacancy t_2 orbitals, and selection rules to explain the complex spectra we have described above. As a final comment, we note a recent study of Fe-In centres involving split ground and excited states, for which absorption spectra have been attributed to intra-d-shell transitions on the Fe atom [9]. We doubt that this applies in the present case, except perhaps for the group III lines, which may involve (in addition to Cd) an impurity other than Li.

Acknowledgements:
This work is being supported by Forbairt, the Irish Science and Technology Agency. M.O.Henry wishes to acknowledge the hospitality of the University of Konstanz and Kings College London, where some of the experiments were performed.

References:

1. S.E. Daly, MO Henry, K. Freitag and R. Vianden, J. Phys.: Condensed Matter **6**, L643 (1994).
2. K. G. McGuigan, M. O. Henry, E.C. Lightowlers and M. H. Nazare, Mater. Res. Soc. Symp. Proc. **163**, 299-302 (1990).
3. C. O'Morain, K. G. McGuigan, M. O. Henry and J. D. Campion, Meas. Sci. Technol. **3**, 337-339 (1992).
4. A. A. Kaplyanskii, Opt. Spectros. **16**, 329-337 (1964).
5. K. Mohammed, G. Davies and A. T. Collins, J. Phys. C: Solid State Phys. **15**, 2779-2788 (1982).
6. F. J. Morin and H. Reiss, Phys. Rev. **105**, 384-389 (1957).
7. J.C. Merle, M. Capizzi and P. Fiorini, Phys. Rev. B **17**, 4821-4834 (1978).
8. F.G. Anderson, F.S. Ham, and G.D. Watkins, Phys. Rev. B **45**, 3287-3302 (1992).
9. P. Tidlund, M. Kleverman and H. G. Grimmeiss, Semi. Sci. Technol. **11**, 748-752(1996).

Materials Science Forum Vols. 258-263 (1997) pp. 527-534
© 1997 Trans Tech Publications, Switzerland

DEFECT CLUSTERS IN SILICON: IMPACT ON THE PERFORMANCE OF LARGE-AREA DEVICES

Bhushan L. Sopori

National Renewable Energy Laboratory, 1617 Cole Boulevard, Golden, CO 80401, U. S. A.

Key words: defect clusters, dislocations, solar cells

ABSTRACT Defect clusters, consisting of agglomerations of dislocations, stacking faults and grain boundaries in an otherwise low defect density wafer, are caused by thermal stresses during the crystal growth. Defect clusters are ideal sites for impurity precipitation. A phenomenological approach to calculate the characteristics of a device with extended defects shows that a defect cluster can produce extensive shunting. Finally, a network model is used to show that clustering of defects can cause significantly more degradation in the device performance compared to a situation if the total number of defects are uniformly distributed over the entire device.

INTRODUCTION

Silicon solar cells use low-cost substrates grown by modified CZ, casting, and ribbon growth techniques. Each of these growth processes uses low-quality feedstock that contains significantly higher concentrations of impurities than the semiconductor grade feedstock. In addition, the crystal growth is carried out at much higher rates and under conditions that compromise the material purity to minimize the substrate cost. Because of the thermal stresses resulting from high growth rates, these substrates contain high densities of defects. Because the grain sizes are very large, typically in the cm range, the dominant defect is the intragrain dislocation density [1]. Recent improvements in the crystal growth conditions have reduced the average density of dislocations, with concomitant improvements in the device performance. These improvements have yielded ingots in which the majority of the substrate area is defect-free. However, clusters of defects are observed in some parts of the substrate. These defect clusters can have a profound influence on the device characteristics because they act as "sinks" for current that dissipate power internally within the device. Indeed, the performance of the high-efficiency, large-area solar cells is limited primarily by the defect clusters. This paper briefly describes the nature of the defect clusters in the photovoltaic (PV) silicon substrates and explains how these defects control the device performance.

NATURE OF DEFECT CLUSTERS

Defect clusters are localized defects consisting of agglomerations of dislocations, stacking faults and (in some cases) grain boundaries, in an otherwise very low defect density wafer. Figure 1a is a dislocation map of a commercial 4-in x 4-in wafer from a cast ingot, taken with PVSCAN5000[2]. It shows that the majority of the wafer has a low dislocation density, with the average dislocation density $<10^5/cm^2$. However, some defect clusters are seen as localized regions of high ($>10^6/cm^2$) defect densities. Figure 1b is a magnified view of a very large defect cluster whose location on the wafer is identified in Figure 1a. A different behavior of defect generation is observed in ribbon substrates. In ribbon substrates, the dislocation density is highly orientation dependent; the grains with (110) surface and <112> growth direction show zero dislocation density. Other grain orientations may be heavily decorated with defect clusters. Figure 2a is a photograph of a defect etched sample showing etch pit configurations in a region with a series of defect clusters. The defect cluster is the entire conglomeration of dislocation networks and stacking faults gathered in the vicinity of grain boundaries. Figure 2b is a higher magnification view of the region, showing that the defect cluster consists of a series of long, intertwined dislocation loops. Because these loops and networks are high-energy

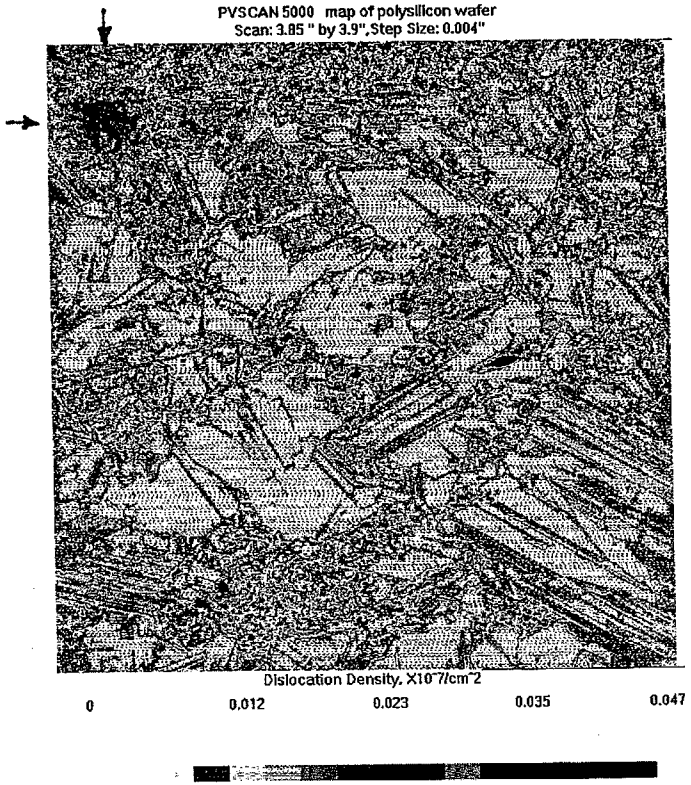


Figure 1a. A PVSCAN map of dislocation density in a comercial PV Si wafer. A large defect cluster is identified by the arrows.

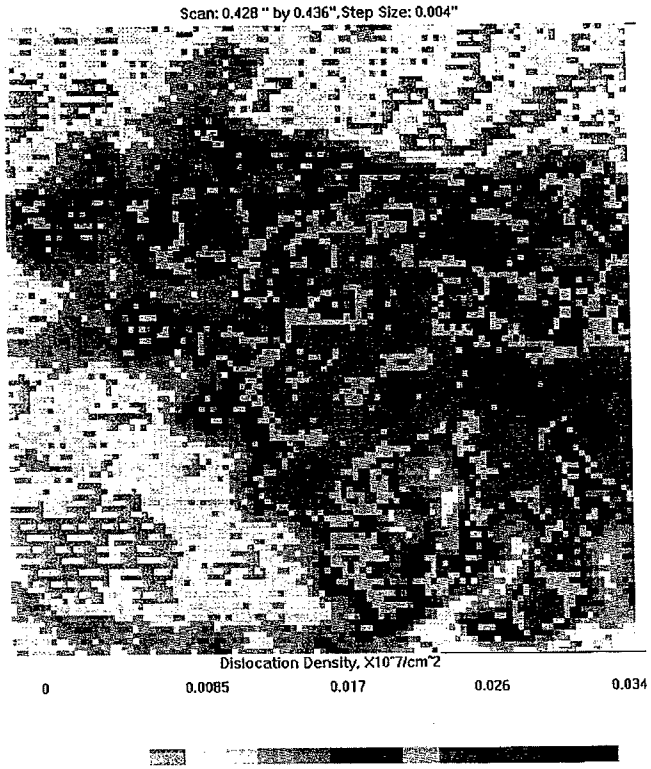


Figure 1b. A magnified image of the selected defect cluster indentified in Figure 1a.

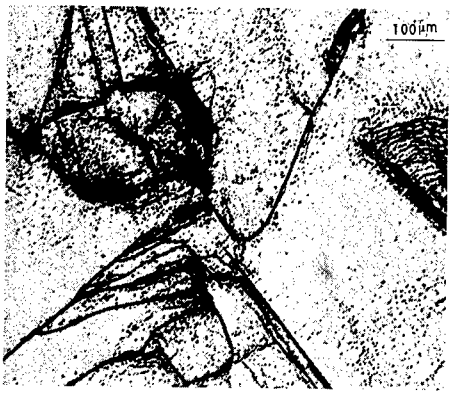


Figure 2a. Photograph of a defect etched sample showing agglomeration of dislocations at a defect cluster

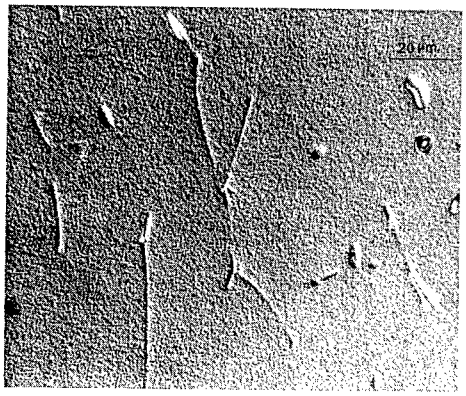


Figure 2b. A magnified view of dislocations in a defect cluster showing tracks of network inter-connection between dislocations.

defect configurations, they are thermally unstable and can change during device processing. Furthermore, the defect clusters are efficient nucleation sites that become decorated with impurity precipitates during crystal growth. This propensity for impurity decoration of a defect cluster has a strong bearing on how it affects the device performance.

INFLUENCE OF DEFECT CLUSTERS ON THE DEVICE PERFORMANCE

Defect clusters can influence the device performance in a number of ways. A defect cluster is a site of very high recombination for minority carriers, leading to a reduction in the minority carrier lifetime in the base region. In addition, as described in this paper, because it propagates through the entire thickness of the substrate, it is a "filamentary" junction shunt. Figure 3 illustrates the dominant roles of a defect cluster in the base and the depletion regions. The shunting effect is further enhanced by the impurity decoration during the crystal growth. Unfortunately, the gettering and passivation processes, typically used in solar cell fabrication to ameliorate the effects of impurities and defects, do not work well in the regions of defects clusters.

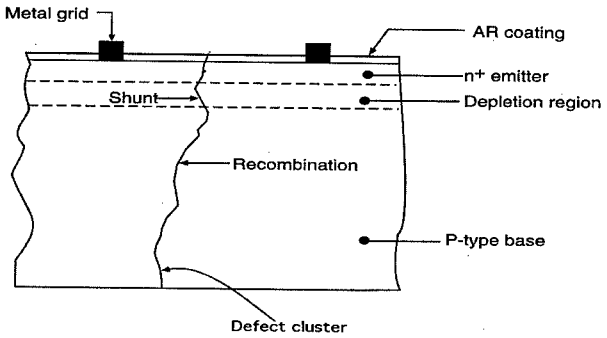


Figure 3. Illustration of a defect cluster as a recombination "filament" through different regions of a device; each region is characterized by specific voltage dependencies of the recombination.

To determine the influence of defect clusters on the total large-area cell performance, we need to determine:

1. the characteristics of the cells in regions with no defect clusters
2. the characteristics of cells in the defected region, and
3. a method of combining a distributed device.

It is straightforward to describe the current-voltage characteristics of a standard N/P junction device. Here we describe a phenomenological approach of extending the N/P junction device formalism to include local defects. Next, we describe a network model that combines the spatial distributions of solar cells to get the terminal characteristics of the entire cell.

In an N/P junction device the recombination, arising from various segments of a defect, can have different voltage dependencies. These effects can be incorporated into an electronic device model by considering the total current to be a superposition of the photogenerated current (which is a short circuit condition with no voltage dependence) and the dark current. Thus, for a solar cell we can write the total current density as:

$J = J_{ph} - J_{dark}(V)$, where J_{ph} and $J_{dark}(V)$ are the photogenerated and the dark current densities, respectively. The dark current can be expressed in a standard form as:

$$J_{dark}(V) = J_{01} \exp\{(eV/kT)-1\} + J_{02} \{ \exp(eV/2kT) - 1\}$$

The saturation currents J_{01} and J_{02} can be written as:

$$J_{01} \cong e\cdot[D_n/ \tau_n]^{1/2} \cdot n_i^2/N_a$$
$$J_{02} \cong (eW/2) \cdot N_s \cdot\sigma\cdot v_{th}\cdot n_i$$

Here, we have assumed a p-type base with a dopant concentration N_a. n_i is the intrinsic carrier concentration, τ_n and D_n are the minority carrier lifetime and diffusion coefficient respectively. N_s, σ, v_{th}, and W represent the interface state density, carrier capture cross section, the thermal velocity, and the depletion width, respectively. The photocurrent can be written as, $J_{ph} = L_{eff}\cdot\phi$, where ϕ is the number of photons transmitted into the device, and L_{eff} is the effective minority carrier diffusion length. The above equations describe an "undefected" cell.

Cell performance of the defected region

It is well known that defects act as sites of high carrier recombination, lowering the local minority carrier lifetime in the bulk of the material. The recombination associated with a defect depends on the nature of the defect as well as on the location of the defect within the device. It is instructive to examine how the characteristics of the small cell, fabricated on a defect cluster, differ from that of a small cell fabricated on an undefected region.

An electronic model for a defect cluster can be similar to that of an energy band model used in the treatment of dislocations[3-5]. A relationship between τ and dislocation density can be determined by considering surface state density along the length of the defect. One can apply Poisson's equation to determine the surface recombination velocity at the edge of the space charge region (r = w). The effective surface recombination velocity, S(w), can be expressed as:

$$S(w) \propto S(0) \exp\cdot(eV_d/kT) = N_s \cdot\sigma\cdot v_{th}\cdot(E_{fn} - E_{fp})\cdot\exp(eV_d/kT)$$

where E_{fn} and E_{fp} are the quasi Fermi levels and V_d is the diffusion potential under illumination. Following the arguments similar to those of references [3-5], we can write an expression for

the effective volume concentration (N_r) of recombination centers in terms of the density of dislocations (N_d) in the defect cluster, as:

$$N_r \propto N_d^{1/2} \cdot N_s \cdot N_T \cdot (E_{fn} - E_{fp}) \cdot \exp(eV_d/kT)$$

Here N_T is the number of traps per unit length of the dislocation. From expression in the above equation, the minority carrier lifetime (which is a function of N_d) for the defected region can be written as:

$$\tau(N_d) \propto \exp(-eV_d/kT) \,/\, \{ N_s \cdot \sigma \cdot v_{th} \cdot N_d^{1/2} \cdot N_T \cdot (E_{fn} - E_{fp}) \}$$

This can be expressed in terms of the commonly used parameter, diffusion length, as:

$$L(N_d) = [D \cdot \tau\,(N_d)]^{1/2} \propto [D \cdot \exp(-eV_d/kT)/\{N_s \cdot \sigma \cdot v_{th} \cdot N_d^{1/2} \cdot N_T \cdot (E_{fn} - E_{fp})\}]^{1/2}$$

From the above equation we see that within a defect cluster the effective diffusion length, $L(N_d)$, is inversely proportional to $(N_d)^{1/4}$. Furthermore, it depends on the resistivity through V_d. Qualitatively, in most cases, V_d increases with decrease in the resistivity, implying that an increase in the resistivity should lead to a decrease in $\tau(N_d)$.

It is instructive to compare the above predicted dependence of diffusion length on N_d with measured values. Figure 4 shows the measured diffusion length as a function of dislocation density for three different resistivities of the substrate. It can be seen that for high dislocation density, in the range that corresponds to formation of a defect cluster, the diffusion length is somewhat independent of the number of dislocations in the cluster. Furthermore, the diffusion length decreases with a decrease in resistivity. These results are in agreement with our model, as represented by the above equations.

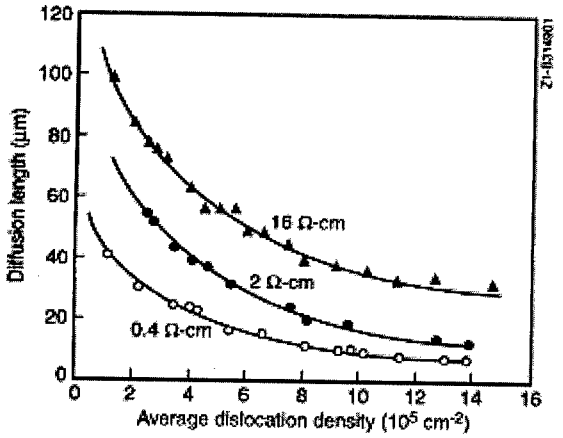


Figure 4. Measured dependencies of the minority carrier diffusion length on the dislocation density for substrates of three different resistivities. In the range of cluster formation, the diffusion length is nearly independent of the dislocation density.

Thus, we can infer from the above equations that a defect cluster is a region of low diffusion length with an electric field similar to that of a depletion region. In principle, one can calculate the corresponding J_{01} and J_{02} required for determining the characteristics of a "defected" cell. Unfortunately, all the parameters needed to calculate J_{01} and J_{20} are not known in detail. In

addition, their values depend strongly on impurities in the substrate, its thermal history, as well as on the process conditions for cell fabrication. We are performing experiments that will lead to deconvolution of such dependencies. In the mean time, one can use the experimental data to obtain the dependencies of J_{01} and J_{02} on N_d; this can be obtained directly from specially fabricated devices[6].

Network model for total cell characteristics

Figure 5 shows schematically the network model that we use to describe the large-area cell. The device is divided into an array of diodes; each diode is small enough to assume a uniform distribution of defects[7,8]. Each node in the matrix depicts a local cell, connected to other cells by a resistor representing the series resistance. The series resistance arises from a number of sources that include the sheet resistivity of the junction in an N/P device. Each local region, having a known defect density, is described by a dark current given by :

$$I_{dark} = I_{01} \{ \exp(eV/kT)-1 \} + I_{02} \{ \exp(eV/2kT)-1 \} + I_{01} \{ \exp(eVn)-1 \}$$

The last term in the above equation is added to represent tunneling current that occurs in heavily defected regions due to hopping mechanism. Hence, a local cell element (n,m) in the matrix is represented by a current source comprised of I_{01nm}, and I_{02nm}, and a corresponding light-induced current density $J_{ph,nm}$. One can represent

$$I_{01nm} = I_{01} F_{nm} \cdot \{\exp(ev/kT)-1\}, \text{ and}$$
$$I_{02nm} = I_{02} F'_{nm} \cdot \{\exp(ev/2kT)-1\},$$

where I_{01} and I_{02} represent dark currents in the "defect-free" device element. F_{nm}, and F'_{nm} are the factors representing the ratio of dark current normalized by the "defect-free" current, for each component. A finite element computer code, written in Microsoft Excel, is used to analyze the network[6.7].

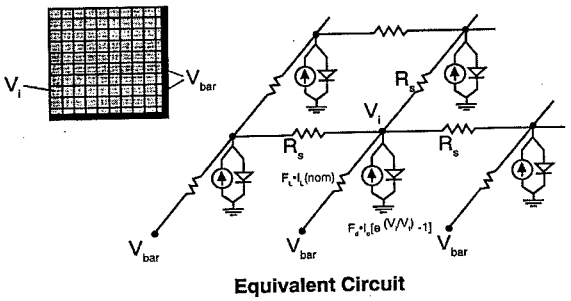


Figure 5. A schematic of the network model for calculating characteristics of a non-uniform junction device.

We consider an example of a cell in which 20% of the device area is covered by defect clusters, and 80% area is defect-free. The parameters for the defect-free region are:

$$J_{ph} = 0.035 \text{ A/cm}^2,\ J_{01} = 3.6 \times 10^{-9} \text{ A/cm}^2,\ J_{02} = 4.5 \times 10^{-13} \text{ A/cm}^2$$

The parameters for the "defected" cell are:

J_{ph}= 0.021 A/cm^2 , J_{01}= 7.2 x 10^{-8} A/cm^2 , J_{02}= 9 x 10^{-12} A/cm^2

Figure 6 shows the calculated I-V characteristics of these two cells. Their cell parameters are: {V_{oc}= 650 mV, J_{sc}= 35 mA/cm2, FF= 81.19}for defect-free and {V_{oc}= 615 mV, J_{sc}=32.7 mA/cm^2, FF= 77.63} for defected cells, respectively. It is seen that all the parameters of the "defected" cell are lower than for the "defect-free" cell. However, the major reduction is in the V_{oc}. It should be pointed out that in an "undefected" cell, a reduction of 30 mV would be accompanied by a large reduction in J_{sc} in accordance with the cell equation. Thus, we see that defect clusters produce a disproportionate reduction in the device voltage, thereby acting as shunts.

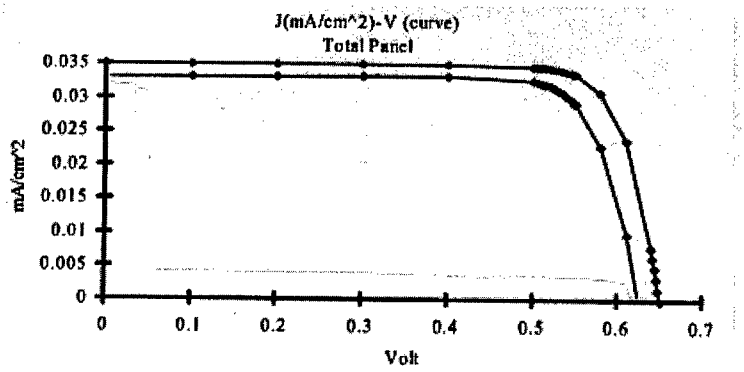


Figure 6. Calculated I-V characteristics of two devices - the upper and the lower curves correspond to the defect-free and the 12% -area defected cells, respectively.

We now discuss another feature from our calculations - we present results of calculations that demonstrate the effect of changing the spatial distribution of defects. Figure 7 shows schematically various distributions. Figure 7a shows a uniform cell of a material quality that yields 17.6% cell efficiency with the cell parameters of {V_{oc} = 650 mV, J_{sc} = 34.9 mA/cm^2, FF=77.6}. Figure 7b illustrates an extreme case in which the entire cell consists of uniformly distributed defect clusters. The calculated values of the cell parameters are: {V_{oc} = 565 mV, J_{sc} = 26.2 mA/cm2, FF=75}. Figures 7c and 7d show cells with 20% area covered by defect clusters but in the configuration of a "T" and a "bar" respectively. The calculated parameters are: {V_{oc} = 615 mV, J_{sc} = 33.2 mA/cm2, FF=75.91 }, and {V_{oc} = 615 mV, J_{sc} = 33.2 mA/cm2, FF=77.38 }, respectively. It is seen that the "T" configuration of defects has a lesser effect on the cell performance compared to the "bar" configuration. Now we calculate cell parameters for a configuration where total number of defects corresponding to the configurations c and d, are uniformly distributed within the entire cell (Figure 7e). The calculated values are: {V_{oc} = 650 mV, J_{sc} = 32.5 mA/cm2, FF=77.58}, with an efficiency of 16.4%. Clearly, as seen from Figure 7e, the effect of defect clustering is significantly more severe even though the same number of defects are participating in the carrier transport.

We have used our modeling to investigate the distribution of local voltages and currents for any given terminal voltage. These results have shown that defect clusters can act as current "sinks" for certain operating conditions of the device. This is a direct result of shunting produced by the defect clusters. The degree of shunting depends on the size and the nature of the defect cluster. As the degree of shunting increases, the terminal voltages at which the "sinks" appear is lower, producing internal dissipation at lower voltages. Therefore, it is important to minimize the effect of defect clusters to obtain a high efficiency solar cell.

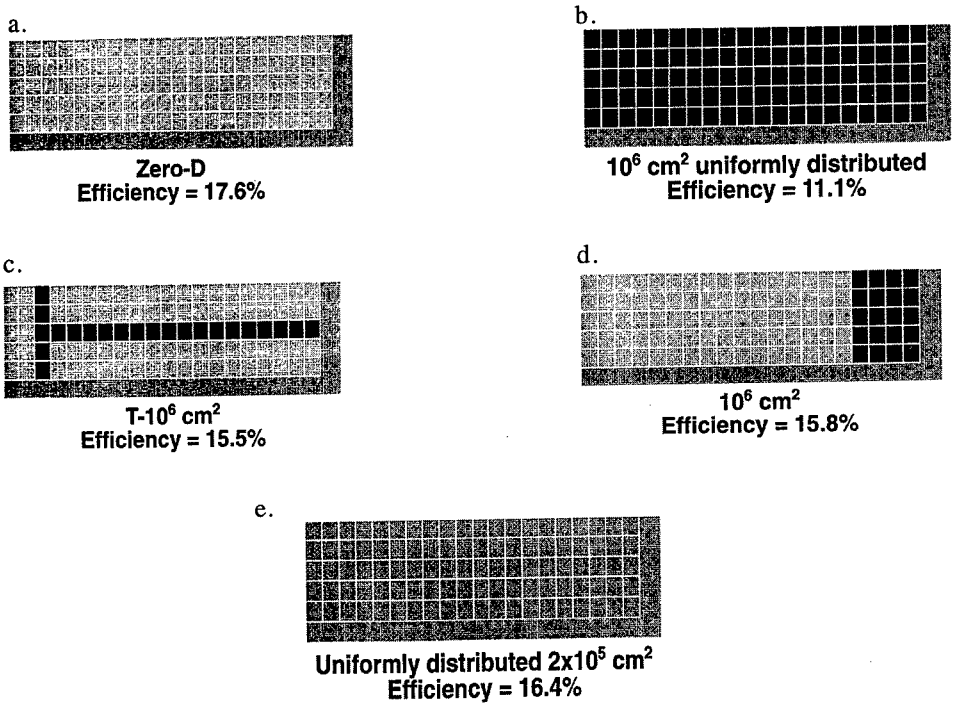


Figure 7. Illustrations of various distributions of defects and their influence on the solar cell efficiency.

ACKNOWLEDGMENT

This work was supported by the US Department of Energy under the contract No. DE-AC02-83CH10093.

REFERENCES

1. B. L. Sopori, Solar Cells, 1,237(1980).
2. PVSCAN5000 is a commercial instrument available from Labsphere for analysis of defects in semiconductor substrates.
3. S. M. Sze, Physics of Semiconductor Devices, John Wiley, New York, 1981.
4. Howard C. Card and Edward S. Yang, IEEE Trans. ED -24, 397(1977).
5. Jerry G. Fossum and Fredrik A. Lindholm, IEEE Trans. ED-27, 692(1980).
6. B. L. Sopori, Appl. Phys. Lett., 53, 1780(1988).
7. B. L. Sopori and R. Murphy, " A Model for an Inhomogeneous Solar Cell," Procd. PVSEC, 1995.
8. R. Murphy, B. L. Sopori, and D. Rose, MRS Procd., 378, 749(1995).

Materials Science Forum Vols. 258-263 (1997) pp. 535-540
© 1997 Trans Tech Publications, Switzerland

MODELING OF SELF-INTERSTITIAL CLUSTERS AND THEIR FORMATION MECHANISM IN Si

S. Takeda, N. Arai and J. Yamasaki[1]

Department of Physics, Graduate School of Science
Osaka University, 1-16 Machikane-yama, Toyonaka, Osaka 560, Japan

[1]Graduate School of Engineering Science
Osaka University, 1-16 Machikane-yama, Toyonaka, Osaka 560, Japan

Keywords : silicon, self-interstitials, clustering, total energy calculation

Abstract. We discuss the possible structures of self-interstitial clusters and their formation mechanism in Si. We find that a single [100] split interstitial generates the dilatation in lattice on (100), while the compression appears above and below it along [100]. Therefore, whenever the compression side of an interstitial locates in the dilatation side of another interstitial, the elastic energy may be reduced. In addition, the rebonding reduces the energy further. We compute the energies of a single interstitial and the clusters which consist of two to five interstitials. It is suggested that the clustering of four interstitials occurs in succession and then the fully reconstructed I4 cluster forms. The I4 cluster is four-coordinated, and the corresponding defect localized state inside the minimum band gap is occupied by two electrons in the ground state. Thus, self-interstitials in the form of the cluster are virtually impossible to detect by standard experimental techniques.

Introduction.

It is well known that a self-interstitial in Si has never been identified in a convincing manner in contrast to lattice vacancies. However, the primary point defects are believed to exist by many researchers, since, for instance, transmission electron microscopy (TEM) has yielded substantial data about the very extended clusters of self-interstitials such as the {111} and {113} defects. Therefore, a fundamental issue about the primary defects is whether they are agglomerated or isolated in crystal. A recent theoretical study showed that four additional atoms in perfect crystal can be accommodated fully as the reconstructed structure without dangling bonds and it is more favorable than four isolated interstitials in terms of energy. In this communication, we discuss the possible cluster structures of self-interstitials and their formation mechanism based on static energy computations. Our discussion implies that the primary defects, created as the Frenkel partner of the lattice vacancy during ion-implantation and electron irradiation, migrate in crystal and agglomerate whenever the energy is gained appreciably. From the computations, we suggest that a self-interstitial acts as an attractive center of other self-interstitials and this could be an origin of the clustering of self-interstitials.

Computational procedure.

We assumed a supercell which consists of 4x4x4 cubic unit cells of perfect crystal (512 Si atoms) with one to five interstitials inserted as an initial structure. With this relatively large super cell, we take account of the clustering of several self-interstitials. The energies of the supercell were computed with the lattice relaxation procedure using the Stillinger and Weber (SW) potential [1], since we think that sufficiently accurate dynamic computations based on an electronic theory have not yet been available for handling the large super cell. We assumed the initial configuration of a self-interstitial to be the split <100> interstitial configuration [2] in this work.

Relaxed structure of a split <100> interstitial.
Figure 1 shows the atomic configuration of a split [100] interstitial determined by the lattice relaxation procedure. The formation energy of the interstitial is estimated to be 5.28 eV. For looking at the additional atom as well as its nearby atoms, the surrounding perfect crystal is removed in Fig. 1. Here, the bonds whose length is reduced from the ideal value by over 0.5% are represented by the dark lines, while the bonds stretched by over 0.3 % , the gray lines. The less distorted bonds whose length distortion ranges from -0.5 to +0.3 % are not shown in Fig. 1. It is found that the bond distortion nearby the split [100] interstitial is anisotropic: The compression side appears above and below it along [100] , and the dilatation side extends on (100). The dilatation field on (100) extends anisotropicaly along the [011] and [01T] directions. Hence, one may be aware of the possibility of the clustering of self-interstitials, since the gain of elastic energy is expected whenever the compression side of an interstitial extends in the dilatation side of another interstitial and vice versa.

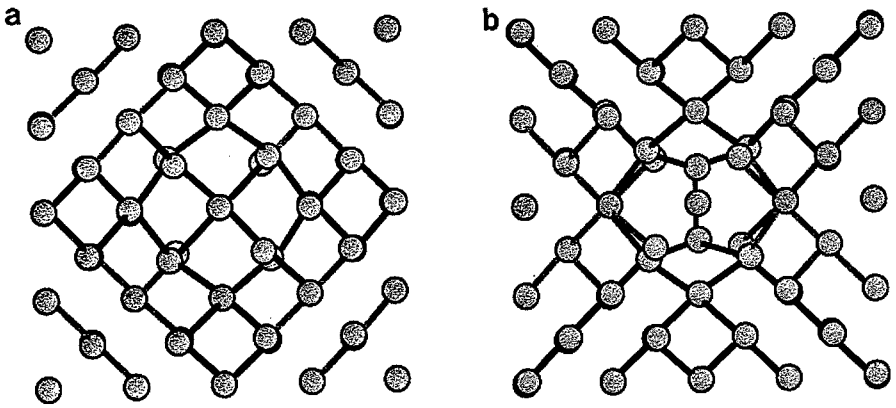


Fig. 1 Relaxed configuration of a split [100] self-interstitial in Si, viewed along [100] in (a) and [010] in (b).

Cluster of four self-interstitials, I4 .
A model was recently proposed for a reconstructed cluster of self-interstitials. This is not a isolated Si cluster [3] but the cluster in crystalline in Si. It consists of four self-interstitials and is constructed by five and seven-membered atomic rings without dangling bonds. The relaxed structure obtained after the lattice relaxation procedure is viewed along [100] and [011] (Fig. 2). It is well known that a structure constituted only by four coordinated Si atoms with relatively small bond distortions yields no active energy states in the band gap . Actually, an electronic calculation based on the semi-empirical tight binding theory has clarified [4] that a defect localized state inside the minimum band gap is occupied by two electrons in the ground state, and the cluster exhibits no active energy level like reconstructed grain boundaries and dislocations in Si [5]. The formation energy per self-interstitial, E_f of the cluster is smaller than that of an isolated self-interstitial (Table 1). Therefore, we theorize that, once self-interstitials form the cluster, it is stable and undetectable by any conventional electronic and spectroscopic techniques. Possibly, this corresponds to the experimental results that a single self-interstitial has never been identified.

The cluster structure was formally connected with four split [100] self-interstitials which appear on the (100) plane, mutually the second or fourth nearest neighbor distance apart. This hypothetical concerted formation process interprets well the complex bond topology of I4. The actual procedure for deriving the cluster model has been illustrated elsewhere [6].

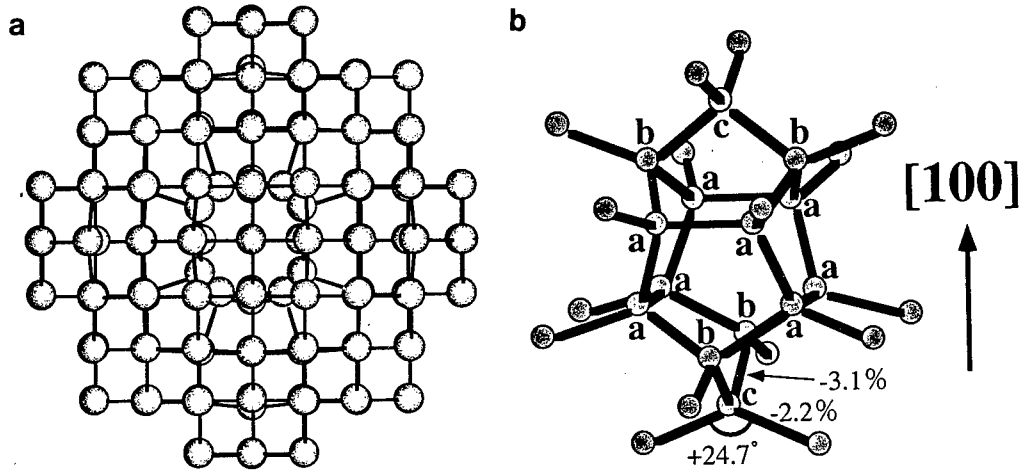


Fig. 2 Self-interstitial cluster, I4 after the lattice relaxation procedure. Viewed along the (a) [100] and (b) [011] directions.

Planar cluster of self-interstitials on {100}.

An experimental data somewhat related to the cluster was obtained in germanium. When germanium is implanted by D^+ (deuteron) at the certain temperature range, the clusters of Ge self-interstitials come out on {100}. An analysis of high resolution TEM images revealed that the lattice reconstruction occurs on {100} involving only Ge self-interstitials. The planar structure is regarded as a two-dimensional extension of I4, or the periodic arrangement of I4s on the {100} plane. So, the {100} defect also bounds on perfect crystal without dangling bonds.

Comparing the formation energy per self-interstitial of the {100} defect with that of the {113} defect [7] (Table 1), the {100} defect structure is sufficiently stable once it is formed. The energies of the several related line structures such as a single line up and a doubled line ups of I4s along <110> are tabulated in Table 1. These results suggest that the more extended structures become more favorable in terms of energy. The similar discussion was made about the extension of the {113} defects along the <332> direction: The planar defect is extended along <332> by the successive formation of the line interstitial defect (LID) structures elongated along <110>. More precisely speaking, a short LID nucleates next to the fully grown LID which constitutes the edge of the existing {113} defect, and that the growth of the LID along <110> gives rise to the extension of the {113} defect along <332> by the single LID width. According to this picture, we think that it is unnecessary to break the bonds in order to trigger off the growth of {113} defects, since a LID leaves the dangling bonds at its ends. In contrast to the {113} defects, the {100} defect needs the energy to break the bonds for its growth. The extended {100} defect has been found only when the sample is irradiated by deuteron, therefore indicating that some interactions between hydrogens and self-interstitials [8] occur and the cluster is extended on {100}.

Interstitial structures	bond distortion length (%) min.	max.	angle (degree) min.	max.	Formation energy per self-interstitial (eV)
{100}	-1.4	2.5	-14.0	17.4	0.74
Double lines	-2.8	2.7	-21.2	17.5	1.37
Single line	-3.8	2.3	-21.8	18.5	1.75
I 4	-5.0	1.5	-22.2	22.8	2.10
{113}	-1.7	2.2	-21.1	22.0	0.85
LID	-2.9	2.1	-19.0	18.9	1.60
split <100> interstitial					5.28

Table 1 Formation energies and bond distortions of the clusters of self-interstitials in Si

Formation energy of a pair of self-interstitials.

A natural question arises about the formation mechanism of the I4 cluster. As shown above, a self-interstitial gives rise to the anisotropic lattice distortion in the short range. Therefore, we first perform the energy computations of all the possible ways of the pair configurations of split <100> self-interstitials up to the ninth nearest neighbor distance apart [10]. Figure 3 depicts the coordinate system which describes a pair of self-interstitials. In our static computations, one split <100> self-interstitial is located at the origin designated by 0, and we assume the other one located at one of the nth (n=1 to 9) nearest neighbor sites designated by the numbers. The direction of the split is designated by x, y or z.

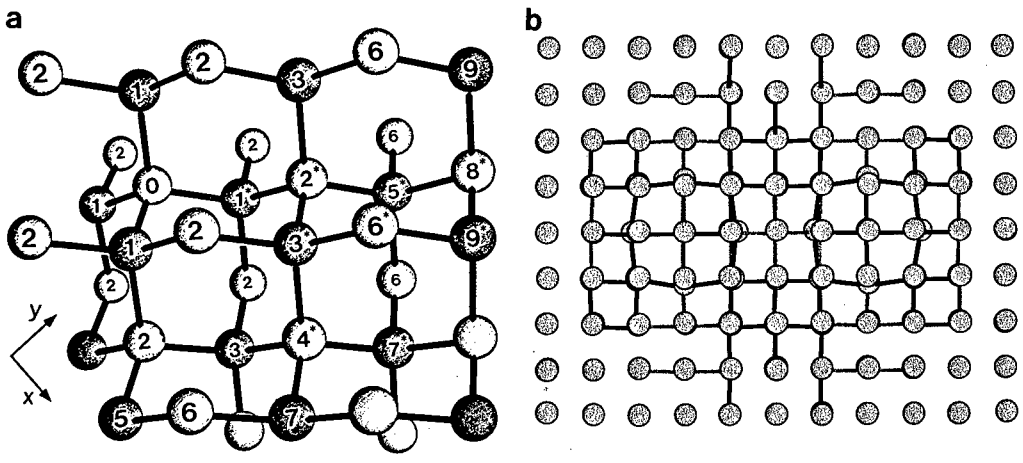


Fig. 3 Formation of a pair of self-interstitials. (a) The sites where the self-interstitials are located are marked by the numbers with asterisks. (b) A pair of split <100> interstitials with the eighth nearest neighbor distance apart (after lattice relaxation).

The formation energies of the pairs are summarized in Fig. 4. Comparing the average formation energy of the *n*th nearest neighbor pairs with that of a self-interstitial, i. e. 5.28 eV, the trend is found that the energy more decreases in the closer pairs. The abrupt decreases of energy at the fifth and eighth nearest neighbor pairs can be interpreted in a simple way: The elastic energy, in particular estimated by the SW potential, depends on not the distance of the two atoms but the distortion of the bonds midway between the atoms. For instance, the numbers of bonds which bridge the atom at the fifth nearest neighbor site and at the origin are three in the shortest path (Fig. 3(a)), and therefore, the fifth nearest neighbor pair may be regarded as the closer pair than the fourth nearest neighbor pairs (Fig. 3(a)).

In Fig. 4, we find that the energy much decreases at the fifth nearest neighbor zz pair (E_f=2.94eV) and the second nearest neighbor xz (or its equivalent) pair (E_f=2.91eV). Clearly, in these pairs, the compression side of an interstitial locates at the dilatation side of the other. Of course, we cannot discuss the electronic interactions among atoms in this potential and the low formation energy of the close pairs, in particular the first nearest neighbor pairs, should be taken as suggestions. However, to our knowledge, much less have been studied about the self-interstitial clustering in terms of energy, and therefore our data presented here provides the useful information about the clustering.

Suppose that self-interstitials migrate switching the two interstitialcy sites, i.e. the split-<100> and the bond-centered configurations [9]. We find that only a few geometrical paths are available for an interstitial migrating toward the other located at the origin; for instance, 9 -> 6 -> 3 -> 2 -> 1 and 7 -> 6 -> 5 -> 2 -> 1 in Fig. 3(a). The second nearest neighbor pair may be quasi-stable in the first path, and the fifth nearest neighbor pair, in the second path. The fifth nearest neighbor pairs are nearly located on the {113} plane, the habit plane of the extended interstitial defects and the second nearest neighbor pairs are connected with the I4 cluster. We skip over the discussions about the {113} defects, since it is suggested that the nucleation of the {113} defects is caused by impurities.

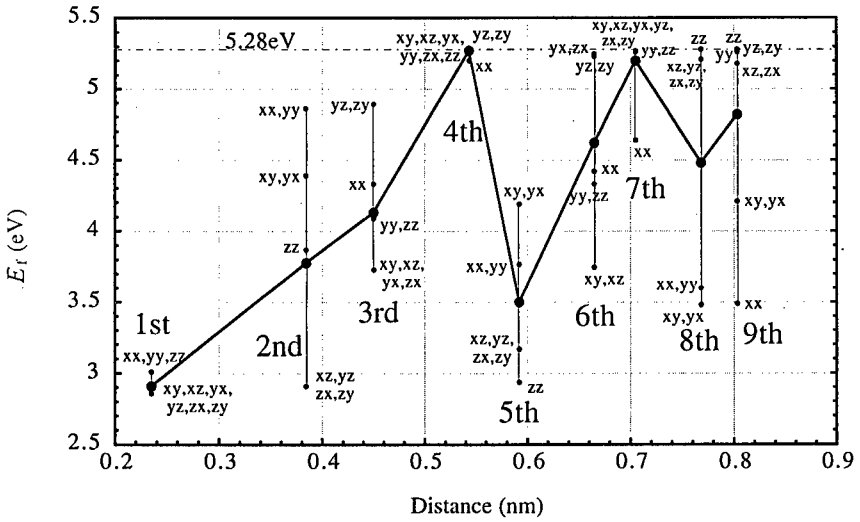


Fig. 4 Formation energies of the pairs (per self-interstitial). The first letter represents the direction of the split at the origin, and the second one, that of the other site (Fig. 3). The bold line shows the averaged formation energies of the *n*th neighbor pairs

Formation of clusters of three, four and five self-interstitials.
Systematic computations of several interstitials located in the supercell are difficult to achieve. So we compute the energy of the supercell which includes the third interstitial in addition to one of the second nearest neighbor pairs; 1) the xz pair of the lowest energy and 2) the zz pair of a medium energy (Fig. 4), the latter of which also gains over 1.3eV on the formation of the pair.

When the third interstitial stays away from the interstitial pair further than about $2a$ (a; the lattice parameter) , the formation energy is close to the value of the infinite separation, i.e., E_f^{∞}(tripple) = {2 x E_f (pair) + E_f (single)}. It is found that, in most cases, the energy reduces as the separation decreases. In the xz pair, the energy is gradually reduced upto 0.67 eV from E_f^{∞} (tripple) = 3.70 eV, in which the third interstitial locates the second nearest neighbor site of the split z interstital. Assuming the zz pair, we find that the third interstitial nearby the pair causes much reduction of the formation energy. The minimum formation energy, 3.01 eV is obtained for the cluster, which consists of the three split z interstitials mutually the second and fourth nearest neighbor distance apart and is regarded as a precursor of the I4 cluster. Hence, we suggest that the clustering progresses in succession whenever the initially formed pairs retain the sufficient life times.

When the fourth interstitial is located at the second nearest neighbor sites of the triple interstitial cluster of the lowest energy, then the rebonding takes place during the lattice relaxation procedure and the I4 cluster comes out. In addition, we have confirmed that at least five different configurations with the fourth interstitial turn out to be the I4 cluster after the lattice relaxation procedure. We add an additional self-interstitial to the I4 cluster without finding significant energy gains: The gain in the formation energy is smaller than 0.5 eV, and occasionally the addition gives rise to the energy increase. Therefore, only when the sufficient accumulation of the primary defects is achieved like by intense electron irradiation and ion-implantation, further agglomeration may occur and the more extended planar structures are formed. As mentioned above, it is more reasonable to conclude that hydrogen acts an important role in extending the cluster by the bond-breaks and rebonding involving self-interstitials.

In conclusion, we have discussed that the possible cluster structures of Si self-interstitials and their formation mechanism. We suggest the possibility of the clustering which provides an useful insight into the various phenomena related to the primary defect at the atomic level.

Acknowledgment.
The authors very thank Dr. Kohyama for his providing a computer program of energy calculations based on the SW potential.

References
[1] F. H. Stillinger and T. A. Weber, Phy. Rev. **B31** (1985) 5262.
[2] G. D. Watkins, R. P. Messmer, S. Weigel, D. Peak and J. W. Corbett, Phys. Rev. Lett., **27** (1971) 1573.
[3] for instance, M. Menon and K. R. Subbaswamy, Phys. Rev. **B47** (1993) 12754.
[4] N. Arai, S. Takeda and M. Kohyama, Phys. Rev. Lett. **78** (1997) 4265.
[5] J. R. Chelikowsky, Phys. Rev. Lett. **49**, 1569 (1982).
[6] S. Takeda, to appear in Proc. Int. Conf. *Microscopy of Semiconducting Materials* (Oxford), 1997.
[7] M. Kohyama and S. Takeda, Phys. Rev. **B46** (1992)12305.
[8] C. G. Van de Walle and J. Neugebauer, Phys. Rev. **B52** (1995) R14320.
[9] L. C. Kimerling , Inst. Conf. Ser. No. **46** (1979) p.56.
[10] in preparation for publication.

Materials Science Forum Vols. 258-263 (1997) pp. 541-546
© 1997 Trans Tech Publications, Switzerland

SELF-INTERSTITIALS IN IRRADIATED SILICON

B.N.Mukashev, Kh.A.Abdullin and Yu.V.Gorelkinskii
Physical-Technical Institute of the Ministry of Science - Academy of Science of the Republic Kazakstan, 480082, Almaty 82, KAZAKSTAN

Keywords : silicon, defects, self-interstitial, impurity interstitials, athermal diffusion.

Abstract. Deep level transient spectroscopy (DLTS) studies of floating zone (FZ) and Czochralskii grown (Cz) silicon irradiated at 77 K with electrons, protons and α-particles as well as the electron paramagnetic resonance (EPR) studies of proton irradiated silicon are reported. Behavior of the silicon self-interstitial was explored by monitoring known impurity interstitial centers (C_i , Al_i , $(Si\text{-}O)_i$) and intrinsic defects. A reduction of the self-interstitial mobility under conditions of proton or α-particle irradiation was observed as against the electron irradiation. It is concluded that this limited mobility results from the lower injection level under proton or α-particles irradiation conditions, and self-interstitials may be stable up to room temperature at the equilibrium state.

Introduction

It is known that the silicon self-interstitial has not been observed experimentally and its structure, properties and diffusion behavior were still not established. In p-type silicon, irradiated by one or a few MeV energy electrons, the self-interstitial is unstable and migrates even at temperatures ≤ 4.2 K until it is trapped by impurities [1]. The diffusion of Si_i is more likely to be athermal recombination-enhanced motion than an equilibrium process. The properties of created interstitial impurities have been studied in detail, their appearance are the result of interactions with self-interstitials through the replacement mechanism [1,2]. In n-type silicon, the emergence of interstitial trapped configuration C_i was observed at ~140 K [3]. Why the self-interstitial has a low mobility in n-type silicon is not understood. The state of self-interstitial, isolated or trapped, is also still a question.

A new possibility to explore the self-interstitial properties emerges when proton and α-particle irradiation are used. As reported recently [4], the low temperature diffusion rate of the self-interstitial is reduced and concentrations of impurity interstitial centers after 77 K irradiation of both p- and n-type silicon are insignificant in contrast to electron irradiation. The emergence of known impurity interstitials upon subsequent thermal anneal may be used as a monitor of the self-interstitial migration and trapping [3]. This paper is concerned with observation of impurity interstitial as well as recently detected self-interstitial-related defects in silicon irradiated at 77 K with protons and α-particles.

Impurity interstitials

The migration, trapping and release of the self-interstitial was studied by monitoring of interstitial defects C_i , Al_i and $(Si\text{-}O)_i$.

Carbon Interstitial. It is well known the carbon atom can trap the silicon self-interstitial and is injected from substitutional sites to interstitial ones. As a result, an <100>-split configuration is created [1,5]. The defect C_i has two levels in the bandgap : the single acceptor (-/0) level at E_c-0.1 eV and the single donor (0/+) level at E_V+0.29 eV [6]. The donor level is observed immediately following 77 K electron irradiation of p-type silicon [4], indicating that most self-interstitials undergo long range diffusion and are trapped by carbon atoms. When 30 MeV proton or 4.5 MeV α-particle irradiation is carried out at the temperature 77 K, the E_C-0.1 eV and E_V+29 eV level concentrations are negligibly small. Instead of the C_i center, a new defect $E1=E_C$-0.39 eV is detected in p-type silicon. In n-type silicon the C_i centers appear upon thermal anneals at ~160-180 K, as in the case of electron irradiation [3]. In p-type silicon the C_i centers appear and E1 centers disappear partially upon thermal anneals at

~260-280 K in FZ-Si samples as well as in Cz-Si ones. An important points is that the thermal anneal is not a critical requirement to observe the interstitial carbon. The C_i centers appear and the E1 disappear completely upon injection annealing at 77 K (Fig. 1).

Aluminum Interstitial. Interstitial aluminum atom appears as a result of interaction of substitutional Al_S and self-interstitial through the replacement mechanism [1,2]. The Al_i is placed in T_d interstitial site [1,2,7] and the known EPR spectrum Si-G18 corresponds to charge state (2+) of the defect. A DLTS level E_V+0.18 eV has been identified as arising from the second donor state (+/++) [8,9].

The DLTS level E_V+0.18 eV and Si-G18 spectrum are not observed immediately following 77 K proton or α-particle irradiation, but appear upon thermal annealing at 260-300 K [10,11], much as the C_i appears. The Al_i centers appear also at temperatures 77-250 K under injection condition (Fig. 2), and the introduction rate of Al_i is approximately 100 times larger than that of C_i. Indeed, in spite of the fact that the concentration of Al in the samples is 20 times smaller than that of carbon, the amplitude of the Al_i state is 5 times larger than that of C_i (Fig. 2). We have concluded that the Si_i atom is a positively charged particle in p-type silicon and attracted to negatively charged substitutional Al impurity. The EPR study [11] showed that the Si-G18 spectrum growth coincides with the Si-AA12 spectrum disappearance (Fig. 3).

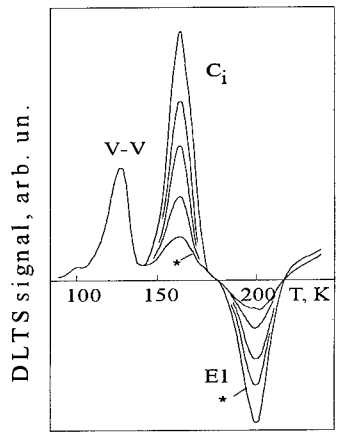


Fig. 1. DLTS spectra of the p-FZ-Si(B) sample α-irradiated at ~250 K The spectra were observed under low level injection conditions.

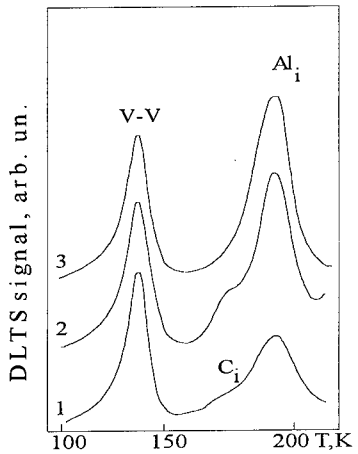


Fig. 2. DLTS spectra of α-irradiated p-FZ-Si(Al): 1 - "as irradiated", 2 - after injection annealing at ~250 K, 3 - after the heat treatment at 300 K.

Oxygen-related interstitial complex. The oxygen interstitial atom O_i can also be a trap for self-interstitial. The infra-red localized modes have been observed in irradiated silicon and assigned to $(Si-O)_i$ defect [12,13]. Harris and Watkins demonstrated that in silicon irradiated at low temperature the self-interstitials are trapped of by oxygen and re-released upon thermal annealing at ~245 K [3]. Consequently, the interaction Si_i and O_i atoms is reversible in contrast to the other impurities (C, Al, B):

$$Si_i + O_i \underset{\text{~245 K anneal}}{\overset{\text{under 80 K irradiation}}{\rightleftharpoons}} (Si\text{-}O)_i \qquad (1)$$

Our EPR results [11] are in agreement with this conclusion. It has been discovered that a metastable complex (MC) is formed in Cz-Si under proton irradiation conditions at ~80 K. The EPR spectra A18, AA13 and AA14 are associated with tree paramagnetic states of the MC. Thermal stability of MC and oxygen-related interstitial traps [3] is the same. To provide strong evidence that oxygen is involved in

MC structure, we performed the test experiment proposed for the first time by Trombetta and Watkins [14]. An "as-grown" sample was subjected to a <110> stress of 250 MPa at 450^{0}C in order to align the isolated interstitial oxygen atoms [15]. Then the sample was irradiated at ~80 K to form radiation defect. It was found that the resulting population of A18 and AA13 defects has a <111> alignment of the same sense as for the <111> oriented oxygen interstitial [11]. This fact implies that interstitial oxygen is involved in MC structure and in addition the O_i atom retains its <111> bond-centered isolated configuration upon trapping of some mobile defect when the MC is formed. This sort of mobility at 80 K indicates that the defect may be either a vacancy or self-interstitial only. The identification of MC as interstitial complex $(Si\text{-}O)_i$ is confirmed by hyperfine structure of the A18 and AA13 spectra [11].

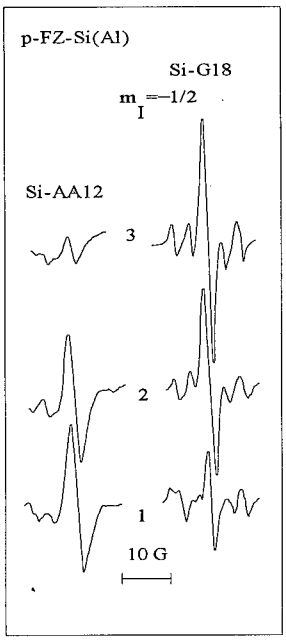


Fig. 3. Si-AA12 and Si-G18 EPR spectra at 77 K in FZ-Si(Al) sample irradiated with protons at ~80 K and annealed at 260 K (1) , 330 K (2) and 355 K (3) for 5 min, ν=37.15 GHz.

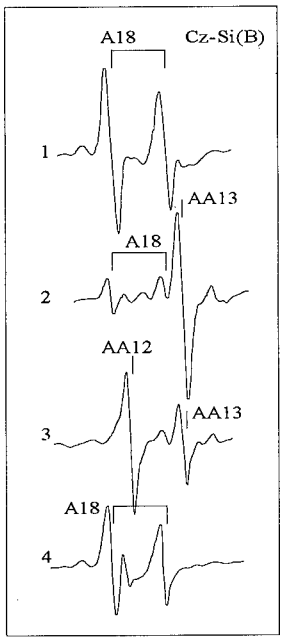


Fig. 4. EPR spectra in Cz-Si irradiated with protons at ~80 K : 1 - "as-irradiated", 2 - annealed at 200 K (A18→AA13 transition), 3 - annealed at 230 K (AA13→AA12 transition), 4 - after illumination at 77 K with bandgap light (AA12→A18 transition).

The MC concentration observed after 80 K irradiation is not changed until 220-250 K when it begins to disappear. The annealing kinetics have a large pre-exponential factor, ~$2x10^{12}$ sec^{-1}. Consequently, the annealing of MC proceeds without long-range migration and the disappearance of the complex could result from the separation of the Si_i and O_i . When the MC disappears a new intrinsic AA12 defect appears correspondingly (Fig. 4). The conversion from MC (A18, AA13) to AA12 is reversible. The AA12 spectrum disappears under the prolonged bandgap light illumination at 77 K and the MC is produced again (Fig. 4, curve 4). A correlation between annealing temperature of a sample in the range from 230 K until 300 K and efficient recovery of the $(Si\text{-}O)_i$ complex is observed: the lower the annealing temperature the more easily the AA12 defect converts to MC under 77 K photoinjection. Obviously the high temperature of annealing leads to considerable separation of the Si_i and O_i and it is more difficult for the Si_i to be re-trapped by the O_i atom.

The properties of MC (temperature of annealing, reversible conversion to intrinsic defect and deep level position for AA14 state) agree closely with the properties of the oxygen-related DLTS defect E_V+0.13 eV [4].The E_V+0.13 eV defect was detected in p-type Cz-Si and absent in FZ-Si. Originally the

E_V+0.13 eV level has been identified as arising from the acceptor level of vacancy [10], but a more detailed study of the annealing kinetics [4] showed that the E_V+0.13 eV level belongs to a new interstitial defect. The concentration of the E_V+0.13 eV defects and C_i centers is increased when the E1=E_C-0.39 eV defects are annealed under injection at 77 K. Under prolonged injection annealing the E_V+0.13 eV defect disappears also. The defect disappears upon thermal anneals at ~250 K or at ~160 K when the diode is held under reverse bias or under zero bias conditions correspondingly. At the same time as the E_V+0.13 eV disappears the E1 defect re-appears. This procedure can be repeated until all the E1 and E_V+0.13 eV defects have converted into C_i centers. There is a linear relationship between C_i rise and E_V+0.13 eV defect disappearance [4]. It was concluded that the E_V+0.13 eV defect may be identified as $(Si\text{-}O)_i$ complex and reversible transitions corresponds to eq. (1).

Self-interstitial-related defects

As noted above, the appearance of impurity interstitials C_i and Al_i is accompanied by disappearance of E1=E_C-0.39 eV DLTS level and AA12 EPR defect.

The E1 states are observed in all Cz and FZ samples irrespective of the kind of acceptor impurities after proton or α-particle irradiation of p-type silicon at 77 K. Therefore these states do not include impurity atoms and should arise from an intrinsic complex. The amplitude of E1 appears to drop slowly until ~330-350 K when it begins to disappear rapidly and the defect is annealed out at ~350 K for 10 min.

At 77 K the E1 defect may be annealed by minority carrier injection. The amplitude and the rate of annealing of E1 defect depends on the minority carrier injection level as well as on the concentration of carbon and oxygen impurities. The rate of E1 injection annealing is the same over the temperature range 77-280 K. Strong correlation between injection annealing of E1 and increasing the concentration of C_i in FZ-Si (Fig. 1) or concentration of C_i and E_V+0.13 eV in Cz-Si samples is observed. In Al-doped silicon the annealing of E1 is simultaneous with the growth of C_i and Al_i (Fig. 2). Additional studies of injection annealing of E1 defect at 77 K shows that it is completely annealed during (1-10) min under the density of current (5-0.5) A/cm^2, respectively.

The band E1 can be seen clearly in the spectra of the thermally stimulated capacitance (TSCAP). An injection pulse was applied to the sample at 77 K before the recording of the spectrum in order to detect the level E1 by the TSCAP method. A single injection pulse of length 0.1 μs was sufficient to saturate the TSCAP signal from level E1. This result means that the cross section for trapping of electrons by the defect is many times the cross section for trapping of holes, i.e., the center is positively charged.

Irradiation at 77 K of FZ samples introduced a new intense EPR signal labeled Si-AA12 [11]. We have resolved the hyperfine structure (hfs) due to a ^{29}Si at one equivalent site with a value of A-tensor ~45.5 MHz. Unresolved hfs (~9.5 MHz) due to a ^{29}Si at 4-6 equivalent sites are also observed and the axis of this hfs is along <111>. The charge state of the defect giving rise to the AA12 spectrum does not appear to be stable at ~160 K annealing and a burst of bandgap light is required to generate the spectrum at 77 K. The kinetics of the recharging process gives the energy level position of AA12 about 0.4 eV. The AA12 defect is annealed at 280-350 K and Si-G18 in FZ-Si(Al) (Fig. 3) or Si-G12 (C_i) spectrum [5] in Cz-Si(B) grows. The features of hfs and annealing kinetics allow the AA12 spectrum to be attributed to an interstitial related defect. The AA12 was observed also in irradiated high purity Si. Therefore it has to be an intrinsic defect.

We did not observe the AA12 in Cz-Si immediately after irradiation. The AA12 defect appears only after annealing of MC at ~250 K. It is very important to note that the AA12 spectrum disappears under prolonged bandgap light illumination at 77 K and the MC is produced again (Fig. 4). However, after thermal annealing of the AA12 at 330-350 K the MC don't generate again under illumination at 77 K.

Therefore, the presence of AA12 is necessary for generation of MC. One may conclude that MC involves the AA12 defect and an oxygen atom.

It has been shown that the AA12 spectrum and the E1=E_c-0.39 eV DLTS states have very similar properties [16] and may be related to the same defect. Correlation of properties of the B configuration of MC and H7=E_V+0.13 eV DLTS defect is also observed [11,16]. The observed correlation is additional evidence of the interstitial nature of the defects.

Anihilation of Si_i-V pairs

There are great differences between the spectra of samples irradiated at 77 K by electrons or protons and α-particles [4]. The relative amplitude of V(E_V+0.13 eV) and C_i(E_V+0.29 eV) bands are remarkably smaller in samples irradiated by protons and α-particles. At the same time, heavy particle bombardment greatly increased the concentration of defects H4 and introduced some unidentified states. The H4 states are observed in all samples irrespective of the kind of acceptor impurities in both Cz and FZ crystals. Band H4 has a half-width >20K, which is significantly greater than the half-width of the isolated line in the DLTS spectra (~10 degree at 100 K) recorded with the help of the third-order filter. The low-temperature decay of H4 overlaps with the V band, while the high-temperature decay overlaps with the V-V band (E_V+0.21 eV), indicating a spreading of the energy spectrum of the levels which form the H4 band. The energy corresponding to the maximum of H4 is E_V+0.20 eV and the corresponding trapping cross section is $\sigma_4=1.6\times10^{-13}cm^2$. Band H4 has complex annealing kinetics. The linearity of the curves (A_o-A) versus the time in the early stages means that the annealing process is of second order $A(t)=A_o/(1+t/\tau)$. The temperature dependence of τ can be approximated by a curve $\tau^{-1} = \tau_o^{-1} \exp(-E_{a1}/kT)$, where $\tau_0\sim10^{-15}$ sec and $E_{a1}=0.47\pm0.05$ eV. A second-order process is observed until the relative number of H4 defects which have been annealed out is 60-80%, thereafter, the annealing slows down. Since the plot becomes linear in coordinates $\phi=(A_o-A)/A_o$ versus $t^{-1/2}$, the annealing process is approximately of third order. Determining the activation energy by the procedure of [17] we find $E_{a2}=0.48\pm0.05$ eV. Additionally the H4 defects were annealed at 77 K under conditions of minority carrier injection. The annealing of the H4 band is accompanied by an increase in the amplitudes of V(H1) and V-V(H2). During a subsequent heating, the amplitude of V-V continues to rise, possibly because other defect, not distinguished by the DLTS method, are annealed out.

The H4 defects thus have several properties which would be expected of Frenkel's pairs. The large width of H4 band is evidence that it is formed by a set of defects which have approximately the same properties but have a spread of energies. The injection annealing may mean that an intrinsic interstitial atom is involved in the H4 defect structure. The increase in the amplitude of the V(E_V+0.13 eV) band may mean that vacancies are liberated when H4 is annealed out. The H4 defect annealing kinetics is similar to that which would be expected for Frenkel's pairs [17-19]. Therefore we suppose that H4 defects consist from core containing one, two or more lattice vacancies and there must be a pair of vacancy and self-interstitial atom at the periphery, some of which are removed a considerable distance from the core.

Discussion

Experimental results show that self-interstitials have a lower mobility under proton and α-particle irradiation conditions than under electron irradiation. When the impurity concentration is about of $\sim10^{18}$ cm^{-3} as in case of oxygen impurity, most of the self-interstitials are trapped immediately after 77 K irradiation. But if the impurity concentration is about 10^{16} cm^{-3} (the typical value for carbon or shallow impurities), the concentration of known impurity interstitial defects is negligibly low after 77 K irradiation. In this case the limited mobility of self-interstitial may be a consequence of the low injection level under proton and α-particle irradiation conditions. As a result, the self-interstitial-related defects E1 and AA12 are observed.

The E1 DLTS level and AA12 EPR spectrum may even be suggested to arise from the isolated self-interstitial. Indeed, among the intrinsic defects in silicon only two defects have been found to exhibit enhanced migration under low-temperature (<77 K) irradiation or minority-carrier injection conditions: the well-investigated silicon vacancy [1,2,20] and eluded self-interstitial [1-3]. Observation of injection-enhanced annealing of the E1 (AA12) with trapping by the carbon, aluminum or oxygen impurities implies that either the enhanced migration of a simple defect or a disintegration of the complex defect and emission of the self-interstitial takes place.

If the E1 is a complex defect, it must consist from a core (X) and trapped self-interstitial: $E1=X+Si_i$. The disappearance of the $X+Si_i$ complex could result from the separation of the components, in a one-step process, and the annealing kinetics of the complex and a large pre-exponential factor would be expected. This fact is inconsistent with the E1 annealing behavior and the broad temperature region in which the E1 (AA12) disappears. Long range migration is more suitable to explain the E1 annealing. It may be suggested that the E1 becomes mobile as soon as it changes charge state. This re-charge can be induced by temperature, background irradiation or charged carriers released from another deep levels. In n-p-junction the re-charge of the E1 may be produced by leakage current. The ability of the E1 (AA12) to migrate implies that the defect is a simple defect and may even be the isolated self-interstitial. Further research should be aimed at clarifying the structure of this defect.

References

1. G.D.Watkins, Material Science Forum, **143-147**, 9 (1994); in *Radiation Damage in Semiconductors*, ed. P.Baruch (Dunod, Paris, 1964) p. 97.
2. G.D.Watkins, MRS Spring 1997, to be published.
3. R.D.Harris and G.D.Watkins, in *13th Int.Conf.Defects in Semiconductors* , (Warrendale, PA, 1985) p. 799.
4. Kh.A.Abdullin and B.N.Mukashev, Semicond. **28**, 1012 (1994) [Fiz. Techn. Poluprov. **28**, 1831 (1994)].
5. G.D.Watkins and K.L.Brower. Phys. Rev. Lett. **36**, 1329 (1976).
6. L.C.Kimerling, P.Blood, W.M.Gibson, Inst. Phys. Conf. Ser. **46**, 273 (1978).
7. K.L.Brower. Phys. Rev. B. **1**, 1908 (1970).
8. L.C.Kimerling, Inst. Phys. Conf. Ser. **31** , 221 (1977).
9. J.R.Troxell, A.P.Chatterjee, G.D.Watkins and L.C.Kimerling, Phys. Rev. B **19**, 5336 (1979).
10. Kh.A.Abdullin, B.N.Mukashev , M.F.Tamendarov and T.B.Tashenov. Phys. Lett. **166A**, 40 (1992).
11. Kh.A.Abdullin, B.N.Mukashev and Yu.V.Gorelkinskii, Semicond. Sci. Technol. **11**, 1696 (1996).
12. A.Brelot, J.Charlemagne, Rad. Effects, **8**, 161 (1971).
13. A.Brelot, Inst. Phys. Conf. Ser. **31**, 191 (1973).
14. J.M.Trombetta and G.D.Watkins, Appl. Phys. Lett. **51**, 1103 (1987).
15. J.W.Corbett, R.S.McDonald and G.D.Watkins, J.Phys.Chem. Solids, **25**, 873 (1964).
16. B.N.Mukashev, Kh.A.Abdullin and Yu.V.Gorelkinskii, in *Shallow-Level Centers in Semicond.*, eds. C.A.J.Ammerlaan and B.Pajot (Amsterdam, World Scientific, 1996) p.447.
17. J.Bourgoin and M.Lannoo, Point Defects in Semiconductors .II Experimental Aspects (Springer-Verlag, Berlin Heidelberg New York, 1983).
18. T.R.Waite, Phys. Rev. **107**, 463 (1957).
19. D.Peak and J.W.Corbett, Phys. Rev. B. **5**, 1226 (1972).
20. G.D.Watkins, J.R.Troxell, A.P.Chatterjii, Inst. Phys. Conf. Ser. **46**, 16 (1978).

Materials Science Forum Vols. 258-263 (1997) pp. 547-552
© 1997 Trans Tech Publications, Switzerland

HIGH RESOLUTION EELS STUDY OF EXTENDED DEFECTS IN SILICON

H. Kohno[1], N. Arai[1], T. Mabuchi[1], M. Hirata[1], S. Takeda[1], M. Kohyama[2], M. Terauchi[3], and M. Tanaka[3]

[1]Department of Physics, Graduate School of Science, Osaka University 1-16 Machikaneyama, Toyonaka, Osaka 560, JAPAN

[2]Department of Material Physics, Osaka National Research Institute, 1-8-31 Midorigaoka, Ikeda, Osaka 563, JAPAN

[3]Research Institute for Scientific Measurements, Tohoku University, 2-1-1 Katahira Aoba-ku, Sendai 980, JAPAN

Keywords: EELS, extended defect, interband transition, JDOS, *ab initio*, tight binding

Abstract. The electronic structure of the {113} extended defect in electron-irradiated silicon is investigated by high-resolution transmission electron energy-loss spectroscopy (HR-EELS) combined with the tight-binding and *ab initio* calculations. We have found that the peak in the imaginary part of the dielectric function, ε_2 in the defect-rich region shifts at 2~2.5 eV. We attribute this result to the nonvertical interband transition between the defect-localized states at the band edges. The detection of the extended defect in semiconductor in ε_2, has been demonstrated for the first time in this study.

Introduction.

High resolution electron energy-loss spectroscopy (HR-EELS) is a powerful means of studying the optical and electronic properties at the nano-scale region [1]. The energy loss near edge structure (ELNES) in the core-loss spectrum is sensitive to only the projected (partial) density of the unoccupied states (conduction band in the case of semiconductor and insulator) [2, 3] and the analysis of ELNES has been performed by many groups. Meanwhile the low-loss spectrum may provide the information on the change in the valence and the conduction bands through the interband transition. However, the low-loss spectroscopy of defect structures is still a developing method due to the experimental difficulty. In this study, we have applied the high energy resolution energy-loss spectroscopy to the study of the electronic structure of the defects which can not be detectable by the ordinary means such as electron paramagnetic resonance (EPR) and optical absorption because of the inactivity and smallness in absolute number.

We have performed EELS measurements of the well-known {113} extended defect in silicon and have calculated its electronic structure to explain the experimental data. The {113} defect is the typical extended defect introduced by the aggregation of supersaturated self-interstitials in electron-irradiated or annealed silicon and germanium. The high-resolution TEM observations elucidated its atomic configuration which is a sequence of two kinds of structural units [4,5] called *I* and *O* units [6]. An *I* unit contains a self-interstitial atom chain along the <110> direction and seven-membered rings, and an *O* unit contains an eight-membered ring and no interstitial atom. The {113} defect also contains five-membered rings. Figure 1 shows the charge distribution of the *IIOI* model calculated by the *ab initio* method [7]. The recent electronic computations of the extended defects based on the atomic structure data have shown that the reconstructed extended defects yield the defect-localized states (DLS) near the valence- and conduction- band edges and inside the valence band [8].

Experimental.

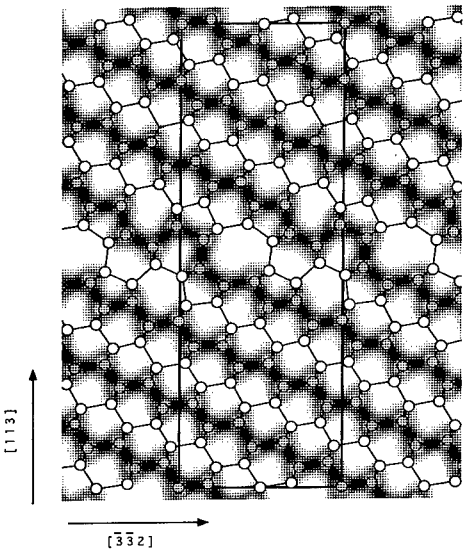


Fig. 1: The charge distribution of the |*IO*| model calculated by *ab initio* method.

Disk of 3 mm in diameter and 0.27 mm in thick was prepared from P doped Cz-Si (110) wafer by ultrasonic drill. The center of disk was mechanically thinned using dimpling machine and chemically perforated in a mixed solution of $HF:HNO_3$=5:32. Carbon (99.99% in purity) was evaporated on one side of the disk in vacuum of 10^{-6} torr in order to promote the nucleation of the defects. The sample was then irradiated by 2 MeV electrons with a dose of 10^{22} electrons/cm^2 at 425 °C in a 2 MeV high voltage electron microscope. The flux was about 10^{20} electrons/cm^2·s. After the electron irradiation, both side of the disk were etched carefully by Ar ions with an accelerating voltage of 3 kV to locate the produced defects in a thinner part with a thickness of about 10 nm. The sample was examined using 200 keV microscopes, JEM2000EX and JEM2010 before the EELS measurements.

EELS measurements were performed using a specially developed high-resolution EELS microscope which is equipped with a thermal-type field emission gun as an electron source and the double-focus Wien filters as a monochromator and an analyzer [9]. The energy resolution was 0.1 eV and the incident electron energy was 60 keV in this experiments. Imaging system of the EELS microscope is based on a JEM1200EX transmission electron microscope. The energy dispersive spectra of electrons transmitted through the sample were obtained using the parallel-recording system with a charge-coupled device (CCD) detector. The collection semiangle was 2.5 mrad which corresponds to the momentum transfer of 2.9/nm. The electron probe was 180 nm in diameter.

Results and discussion.

Figure 2-a shows the loss-functions from the defect region and the perfect region. The intense zero-loss peak was subtracted from the observed EELS spectrum and the Fourier-log deconvolution method leaded to the single-scattering distribution (SSD) of energy loss spectrum. Then, the SSD was normalized and the loss-function, $\mathrm{Im}[-1/\varepsilon]$ was deduced using the refractive index, n = 3.35 for silicon. The loss function of defect region around 3~4.5 eV is intenser than that of perfect region. Imaginary parts of the dielectric functions were obtained through Kramers-Kronig analysis. Two peaks are clearly observed at 2~2.5 eV and about 4.5 eV.

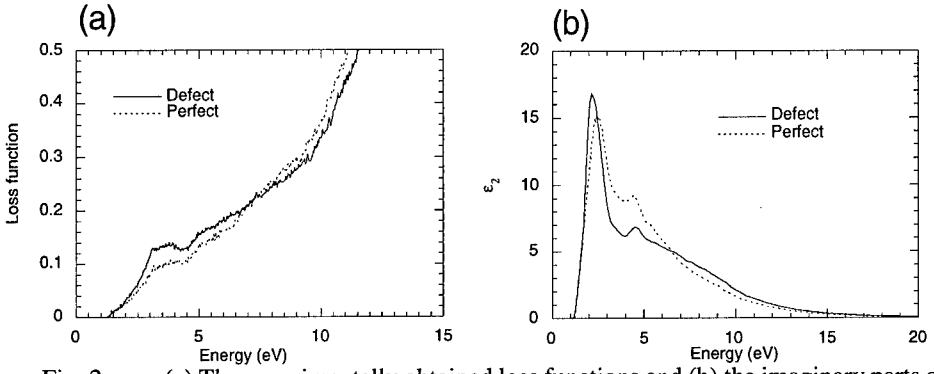


Fig. 2: (a) The experimentally obtained loss functions and (b) the imaginary parts of dielectric functions obtained through Kramers-Krong analysis. Energy resolution is 0.1 eV.

Applying the transferable semi-empirical tight-binding method [10, 11], we calculated the relaxed atomic configurations, the band structures and the joint density of states (JDOS) for both the perfect and the defect structures.

JDOS, $J(E)$ is given by the following equation,

$$J(E)=\sum_{\boldsymbol{k}}\sum_{i,j}\delta\left[E_i^{\mathrm{c}}(\boldsymbol{k})-E_j^{\mathrm{v}}(\boldsymbol{k})-E\right],$$

where $E_i^{\mathrm{c}}(\boldsymbol{k})$ and $E_j^{\mathrm{v}}(\boldsymbol{k})$ represent the energy of the i-th conduction band and the j-th valence band at the particular $\boldsymbol{k}$-point. For the defect structure, the weighted JDOS, $J'(E)$ was calculated using the equation,

$$J'(E)=\sum_{\boldsymbol{k}}\sum_{i,j}P_i^{\mathrm{c}}(\boldsymbol{k})P_j^{\mathrm{v}}(\boldsymbol{k})\delta\left[E_i^{\mathrm{c}}(\boldsymbol{k})-E_j^{\mathrm{v}}(\boldsymbol{k})-E\right].$$

Herein $P_i^{\mathrm{v}}(\boldsymbol{k})$ is the localization factor which describes the probability that the j-th valence band state is at the core area of the defect structures. That goes for $P_i^{\mathrm{c}}(\boldsymbol{k})$, too.

It is well known that the method well reproduces the structure of the valence band and the shape of the dispersion of the lower part of the conduction band. However, the width of the band gap is poorly estimated as 2.2 eV. The defect structures of both |*IO*| and |*IIO*| models were examined by the super-cell method. The numbers of atoms in an unit cell were 90 and 136 for the |*IO*| and |*IIO*| models, respectively. Super-cells of perfect crystal which are almost equivalent to the |*IO*| and |*IIO*| models were also examined as reference. JDOS was calculated at the 12 special $\boldsymbol{k}$-points. Thirty and forty six atoms in an unit cell were defined as core region of the defect for |*IO*| and |*IIO*| model, respectively. The calculated JDOS and DOS were convoluted by the gaussian function with a width of 0.1 eV or 0.2 eV.

Ab initio calculation of the |*IO*| model was performed based on the density functional theory. We adopted the TM-type pseudopotential [12] and the plain-wave basis with a energy-truncation of 35 Ry. The atomic configuration was determined by the lattice relaxation procedure using the two special $\boldsymbol{k}$-point, and then the electronic structure was calculated. The atomic configurations determined by the tight-binding and *ab initio* methods were almost the same. The minimum band gap was underestimated as about 0.5 eV, while the structures of both the valence and conduction bands were well

reproduced by the method. The defect structure of the *IOI* model was examined by the super-cell method. The calculations of the JDOS were performed at six special $\boldsymbol{k}$-points in the Brillouin zone of the supercell.

The imaginary part of the dielectric function, ε_2 of perfect crystalline silicon was calculated using the following expression [13, 14] for the vertical interband transitions,

$$\mathrm{Im}\,\varepsilon_{\alpha\alpha}(\omega)=\frac{8\pi^2e^2\hbar^2}{V}\sum_{c,v}\sum_{\boldsymbol{k}}\frac{\left|\left\langle c\boldsymbol{k}\left|\frac{\hbar k_\alpha}{m}\right|v\boldsymbol{k}\right\rangle\right|^2}{\left[E_c(\boldsymbol{k})-E_v(\boldsymbol{k})\right]^2}\delta\left[E_c(\boldsymbol{k})-E_v(\boldsymbol{k})-\hbar\omega\right].$$

We also calculated the ε_2 of perfect crystalline silicon for nonvertical interband transitions.

It could be reasonable to identify the first peak to the direct nonvertical interband transitions between the parallel bands from Γ-point and L-point because the vertical gap of crystalline silicon is near 3 eV. However, no structure appears in the corresponding region of the JDOS calculated by the tight-binding method (at about 3~3.5 eV in Fig. 3-a,b) and *ab initio* method (at about 1.5~2 eV in Fig. 3-c). The imaginary part of the dielectric functions were calculated for both vertical and nonvertical interband transitions for perfect crystalline silicon by the *ab initio* method and shown in Fig. 4. Likewise, no structure appears. The second peak (4.5 eV) of the experimental data can be reproduced in ε_2 calculated by the *ab initio* method (4.2 + 0.6 = 4.8 eV).

The experimentally obtained ε_2 of the defect region differs from that of the perfect region in following two points. First, the first peak is shifted to lower energy side. Second, it has a broad swelling around 5 ~ 10 eV. JDOS calculated by tight-binding method shows the increase of the JDOS from 2 to 5 eV

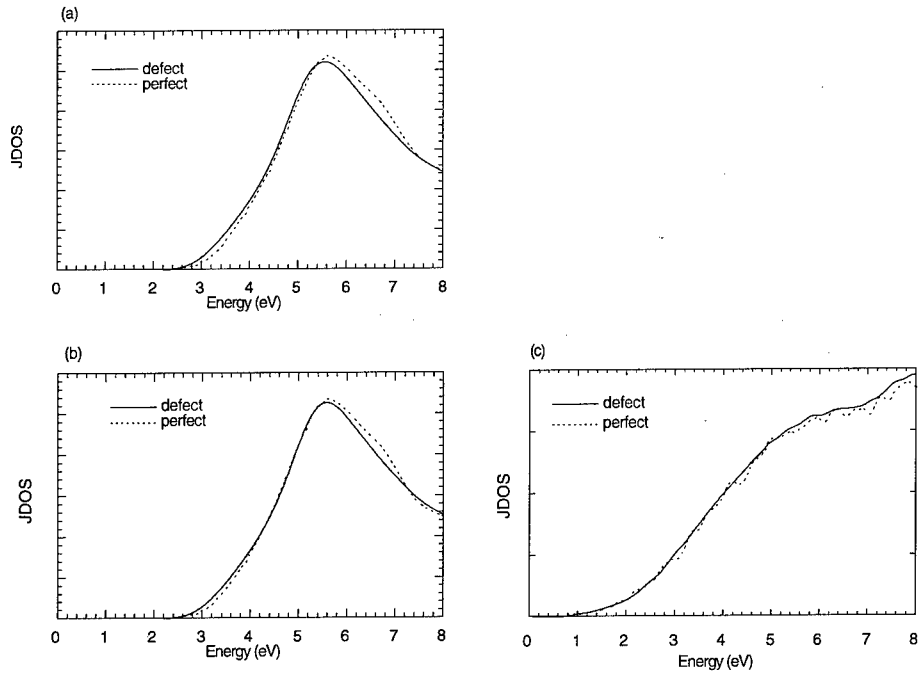


Fig. 3: Joint density of states calculated using the tight-binding method for both (a) the *IOI* and (b) *IIOI* model, and (c) by the *ab initio* method for the defect structures of the *IOI* model compared with that for the defect-free structure.

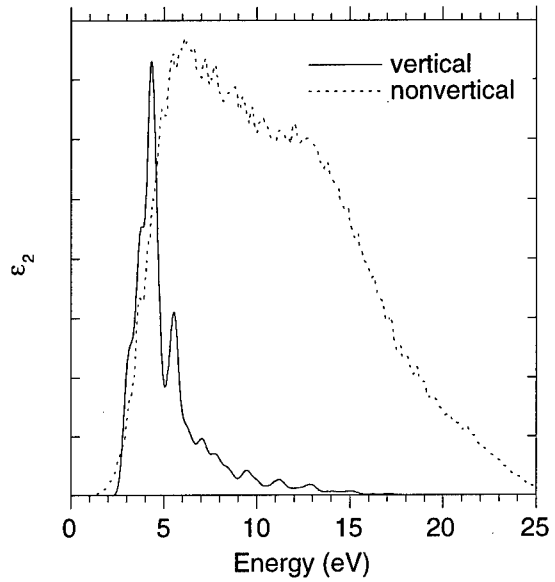


Fig. 4: Theoretically calculated imaginary part of dielectric function of perfect crystalline silicon by the *ab initio* method for vertical transitions and nonvertical transitions.

(Fig. 3-a,b). However, JDOS's calculated for the *IOI* model by the *ab initio* method have little difference (Fig. 3-c). The result of the *ab initio* calculation should be reliable because this method also well reproduces the conduction band in addition to the valence band. The JDOS should not be sufficient to analyze the shape of the specific peak because it reproduces no peak, while it is useful only for the discussion of the rough feature of a whole spectrum.

It is reported that the defect-localized states (DLS) exist at the band edges [8]. Transitions between DLS in valence band and DLS in conduction band should be emphasized because of the overlap of their wave functions in the real space. However, as mentioned above, the first peak in the experimentally obtained ε_2 can not be explained fully by our theoretical calculations. Nonvertical transitions between DLS's at the top of valence band and the bottom of conduction band is a tentative explanation of the enhancement of this peak. The origin of the second feature is not drawn yet. Concerned about the peak at about 4.5 eV, which should be identified to the vertical transitions between the top of the valence band and the bottom of the conduction band, no shift was observed between two spectra. This is consistent with the JDOS calculated by the *ab initio* method.

Summary.

The electronic structure of silicon containing the {113} extended defects was studied by the high-resolution transmission EELS and the theoretical calculations. The change of ε_2 was detected for the first time in this study. The tentative identification of the change of ε_2 of defect structure is the nonvertical transitions between DLS's at the band edges. The calculated JDOS is so broad and no peak due to the van Hove singularity is produced. It seems that JDOS is not adequate for the detail analysis of a specific peak in the case of silicon.

References.

1. R. F. Egerton, Electron-energy loss spectroscopy in the electron microscope, (1986) Plenum Press, New York.
2. X. Weng, P. Rez and O. F. Sankey, Phys. Rev. **B40**, 5694 (1989).
3. X. Weng, P. Rez and P. E. Batson, Solid State Commun. **74**, 1013 (1990).
4. S. Takeda, Jpn. J. Appl. Phys. **30**, L639 (1991).
5. S. Takeda, M. Kohyama and K. Ibe, Philos. Mag. **A70**, 287 (1994).
6. M. Kohyama and S. Takeda, Phys. Rev. **B46**, 12305 (1992).
7. M. Kohyama *et al.*, in preparation.
8. M. Kohyama and S. Takeda, Phys. Rev. **B51**, 13111 (1995).
9. M. Terauchi, R. Kuzuo, F. Satoh, M. Tanaka, K. Tsuno and J. Ohyama, Microsc. Microanal. Microstruct. **2**, 351 (1991).
10. S. Sawada, Vacuum **41**, 612 (1990).
11. M. Kohyama, J. Phys. Condens. Mater **3**, 2193 (1991).
12. M. T. Yin and M. L. Cohen, Phys. Rev. B26, 5668 (1982).
13. B. Adolph, V. I. Gavrilenko, K. Tenelsen, F. Bechstedt and R. Del Sole, Phys. Rev. **B53**, 9797 (1996).
14. B. Adolph, K. Tenelsen, V. I. Gavrilenko and F. Bechstedt, Phys. Rev. **B55**, 1422 (1997).

Materials Science Forum Vols. 258-263 (1997) pp. 553-558
© 1997 Trans Tech Publications, Switzerland

ELECTRON IRRADIATION EFFECTS IN SILICON THIN FOILS UNDER ULTRA-HIGH VACUUM ENVIRONMENT

S. Takeda, K. Koto[1], M. Hirata, T. Kuno, S. Iijima[2] and T. Ichihashi[2]

Department of Physics, Graduate School of Science,
Osaka University, 1-16 Machikane-yama, Toyonaka, Osaka 560, Japan
[1]Graduate School of Engineering Science,
Osaka University, 1-16 Machikane-yama, Toyonaka, Osaka 560, Japan
[2]Fundamental Research Laboratory, NEC, Miyuki-cho, Tsukuba, Ibaraki, Japan.

Keywords: silicon, nanometer sized-structures, UHV, TEM, electron irradiation, surface

Abstract. Silicon thin foils are irradiated by electrons in an ultra-high vacuum (UHV) environment (1.0×10^{-7} Pa). We have found that electron irradiation yields the novel nanometer-sized structures on an electron exit surface; an array of holes 2 to 3 nm in diameter and several nm deep. The irradiation temperature is needed to be below 300℃. The holes are formed regardless of the surfaces, i.e. {111} and {110} and of the type of specimens, CZ and FZ. We have also studied the effect of impurities on the formation of electron-irradiation-induced defects. It is found that the nucleation and growth of the {113} defects are promoted after the O_2 gas is injected in a UHV specimen chamber.

Introduction.

Electron irradiation has been utilized in the studies of defects in semiconductors. Even though the precise knowledge is accumulated about the defects created inside crystal by electron irradiation, much less has been described about the contribution of surfaces to the electron-irradiation-induced phenomena. In particular, the surfaces of silicon are usually covered with oxide or contaminated under a conventional vacuum environment, and thus the effects of electron irradiation in silicon have never been entirely examined. We have applied the ultra high vacuum (UHV) transmission electron microscopy (TEM) to this subject. We present our finding of the novel phenomenon in nanometer dimension involving point defects on surfaces. We also show that the impurities on surfaces affect the electron-irradiation-induced phenomena: The O_2 gas is introduced in the UHV chamber during electron irradiation, and the nucleation and growth of the {113} defects are pursued by *in-situ* UHV-TEM.

Experimental Procedures.

Discs of Si, 3mm of diameter were mechanically prepared using an ultrasonic drill. The center of a disc was dimpled and then etched in the mixed solution of HNO_3 and HF. The specimens are non-doped FZ {111} and CZ{110} Si. The disc was heated in a pre-treatment chamber of a UHV-TEM (Jeol JEM2000FXV)[1] by illumination of infrared light at about 1200℃ for several minutes. The heating process provided the thermally etched flat terraces on both sides of the disc and consequently a number of parallel-sided thin slabs of 10 to several 100 nm in thick were created. The base pressure in the UHV-TEM was estimated to be 1.0×10^{-7} Pa. The electron energy for irradiation, E_r was 141, 160 and 200keV. The electron flux in irradiation was equal to 3.5×10^{21} e cm^{-2} s^{-1} . The specimen temperature during irradiation, T_r was set at 200, 300, 400 and 500℃ . While O_2 flowed in the specimen chamber in order to modify surfaces of a specimen, the estimated pressure was kept to be 5.0×10^{-5} Pa. The thicknesses of the observed slabs were measured by convergent beam electron diffraction technique using a conventional TEM (Jeol JEM2010) after the UHV-TEM observations. The thicknesses in the following observations ranged from 30 to 50nm, and no change was yet found in experimental results depending on the thickness.

Surface control of Si specimens in UHV-TEM.
Figure 1 shows a bright-field UHV-TEM image of a slab before electron irradiation. Clearly, the slab exhibits the transmission electron diffraction spots from the clean surface of Si 7x7 (111). The surface reconstruction cannot be observed in a conventional TEM.

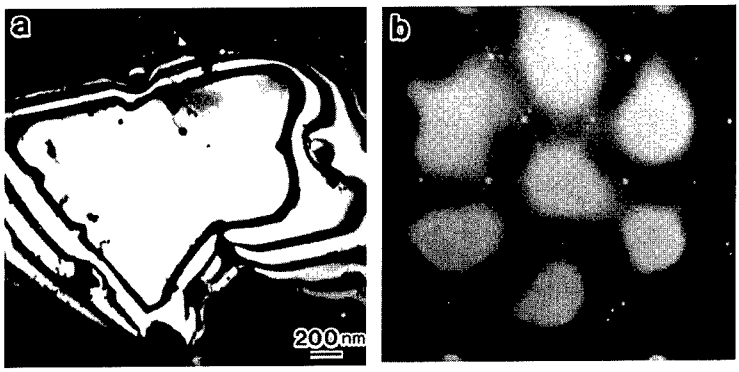


Fig. 1 (a) TEM image of a slab and (b) the transmission electron diffraction pattern from the slab, observed before electron irradiation.

Formation of nanoholes.
We have found that nanometer-sized holes are formed on Si surface by electron irradiation in UHV environment. Figure 2 depicts the nanoholes. The contrast of the nanoholes varies with the focus condition of the TEM objective lens. The bright rings (Fig. 2 (a)) are observable at an under-focussed condition (about 300nm), while the same rings appear to be dark (Fig. 2(b)) at an over-focussed condition (about 300nm). The variation arises from the Fresnel diffraction effect, and accordingly we are assured that hollow spaces are created either inside the thin foil or at the surfaces. Furthermore, a stereo TEM microscopy observation clarifies that the ring-contrasts locate near or at the electron exit surface. Figure 3 shows the post-irradiation observation, using conventional TEM. The area, irradiated with the electron beam along <110>, was observed in three other directions. Clearly, the ring-contrasts observed along <110> in Fig. 3(a) are

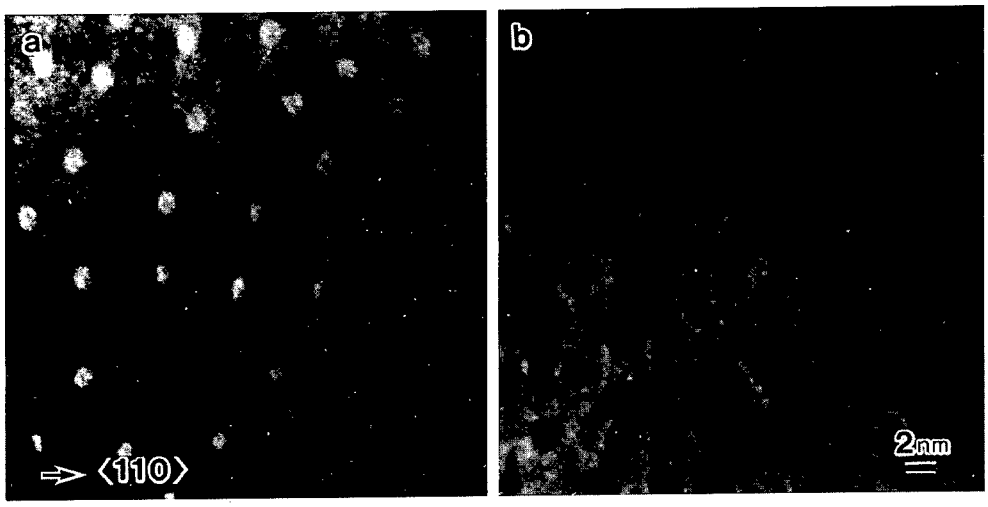


Fig. 2 Nanoholes with grooves on a Si surface (*E*r=141keV, *T*r=200℃, CZ-Si (110)). The image in (a) was taken at the under-focused condition, and the image in (b) , at the over-focused condition.

slightly elongated in the oblique views (Fig. 3(b), (c), (d)). These geometrical analyses have led to a conclusion that the holes of 2 to 3 nm in diameter and 5 to 10 nm deep are created on the electron exit surface.

The array of nanoholes is created by not the focused electron beam, which has been utilized for the fabrication of nanometer-sized structures [2], but the uniform intensity electron beam. The beam covers the area of about 100nm in diameter during electron irradiation. At the early stage, the fuzzy spot-contrasts appear in the irradiated area, and then the contrasts are gradually enhanced with the increase of irradiation time. The spots are linked by the fainter band-like contrasts. The locations and sizes of these contrasts are kept unchanged during irradiation. Figure 4 depicts a UHV high-resolution (HR)- TEM image of an area after electron irradiation. The holes are separated by 6 nm in average and the holes exhibit the facets of {111} and {100} which are parallel to the direction of the electron beam.

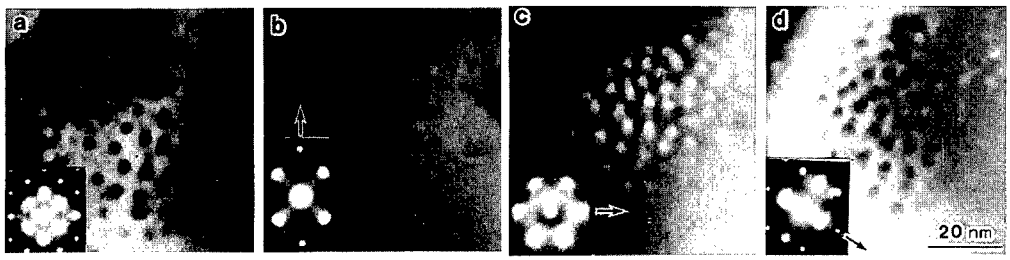


Fig. 3 Bright field TEM images of the same irradiated area, observed with different incident beam directions (Er=200keV, Tr= 200℃ , CZ-Si (110)). Observation along the irradiation direction, <110> in (a). Tilting the specimen around the rotation axes marked by the arrows, the same area is observed along the <100> in (b), <111> in (c) and <112> in (d).

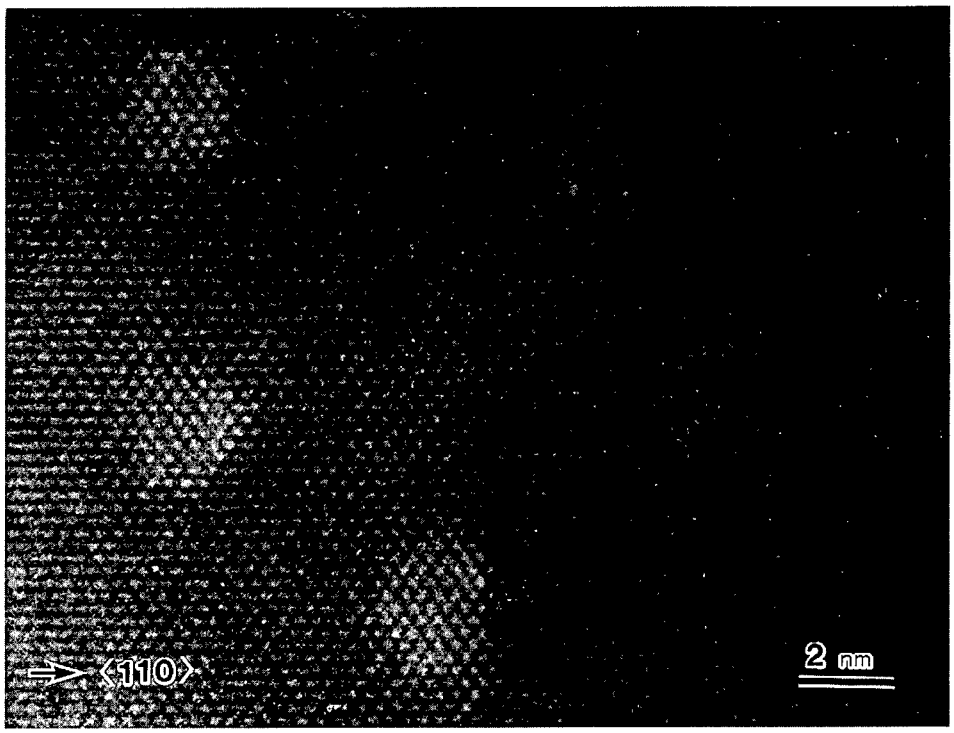


Fig. 4 Nanoholes observed by UHV-HRTEM (Er= 200keV, Tr=200℃, CZ Si (110)).

We summarize the experimental condition that the phenomenon can be observed [3]. First, the array of the nanoholes forms only in UHV environment. After we observed the formation of the nanoholes, the O_2 gas was injected in the UHV specimen chamber and the irradiation proceeded on a different area in the same specimen. We found that the generation of the holes was very suppressed. The pressure at the specimen during the flow of O_2 was comparable to that in a conventional TEM, i.e. 5.0×10^{-5} Pa. Then, we interrupted the flow of O_2 , and the irradiation commenced on another area in the same specimen under the restored pressure better than 5×10^{-7} Pa. The holes were created again. Second, the array is formed by irradiation of electrons whose energy ranges from 141 to 200keV. Apparently, the phenomenon is irrelevant to the Frenkel pairs created inside crystal by electron irradiation. When the specimens were irradiated by electrons whose energy exceeds the threshold energy of the Frenkel pairs (160 and 200keV), the nanoholes were created as well as the numerous {113} planar interstitial defects inside crystal. Due to the restriction on the accelerating voltages of electrons in the UHV-TEM, we have not yet determined the threshold energy of the nanohole formation. Third, the irradiation temperature is needed to be below 300° C. Figure 5 summarizes the size distribution of the holes depending on various experimental conditions. As shown in Fig. 5(a) and (b), the formation of the nanoholes is almost suppressed at 300° C. Actually, we have never observed the holes above 400° C. Lastly, the holes are generated regardless of the surfaces, i. e. {111} and {110} and the content of oxygen, i. e. FZ and CZ (Fig. 5(a) and (c)).

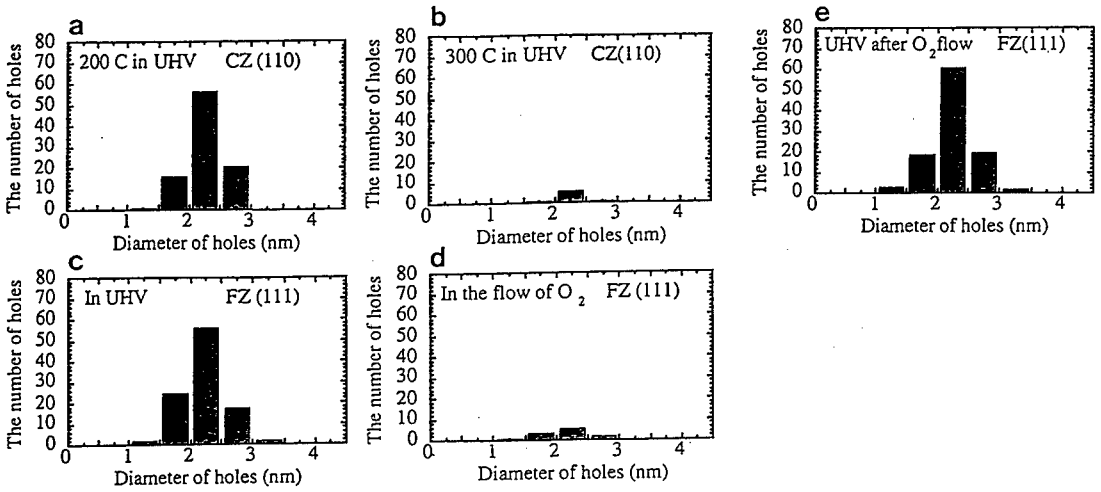


Fig. 5 Size distribution of nanoholes depending on various experimental conditions. The specimens received the same dose, i. e. 3.1×10^{24} cm^{-2} .

We discuss the generation mechanism of the holes [3]. It is natural to assume that a large number of vacancies are accumulated near and at the electron-exit surface due to sputtering of atoms [4]. Considering the distribution of vacancies and atoms on a surface, we connect a two dimensional Ising model to the surface system. According to the picture, surface vacancies form clusters at lower temperatures, while at higher temperatures the random distribution of surface vacancies is expected. This interprets the temperature dependence of the nanohole formation (Fig. 5). Below the critical temperature, we expect a spinodal instability in the system, with which a morphology of vacancy clusters evolves in time. The micro-structures driven by the spinodal decomposition and the related instability can be observable in several metallic alloys. A computation based on the Monte-Carlo simulation reproduce the qualitatively similar patterns of the holes. Hence, we suggest that the spacial pattern of the holes is attributed to "spinodal decomposition" involving the accumulated surface vacancies in the steady state under the uniform intensity electron irradiation. The flow of O_2 (Fig. 5(b)) gives rise to the oxygen absorbed surface, and thus prevents the surface vacancies migrating freely. Consequently, the formation of the patterns is interrupted.

The subsequent irradiation in UHV induces further sputtering to expose the surfaces of lower energy as the walls of a hole. Once the initial morphology is set up, the holes may be deepened under irradiation, since the surface vacancies must flow preferentially from the higher surface to the lower (or bottom) surfaces of the holes along the wall of the holes. The formation of grooves may be caused by the preferential sputtering at the surface steps.

Effects of O_2 on the {113} defect formation.

It is well known that electron irradiation introduces the {113} planar defect in Si and Ge. A question has still remained about the nucleation and growth rates of the defects. Several authors have argued that impurities such as carbon, oxygen etc. affect the rates [5, 6]. Even though the nature of the defects has been identified to be of self-interstitial type [7], no conclusive data has been presented about the effect of impurities. The most serious defect in the previous studies arises from the uncontrolled surfaces of a thin crystal, and therefore the unintentional contamination was probably involved.

In UHV environment, on the other hand, we provide the silicon thin slabs whose surface structures are well controlled as shown in Fig. 1. Electron (200keV) irradiation was performed on the slabs at 400 and 500℃. Numerous {113} defects were created by electron irradiation in UHV environment (Fig. 6(a)). The number of defects increases continuously with the increase of irradiation time. After the first irradiation was terminated, the O_2 gas was injected and flowed in the specimen chamber. The irradiation under the flow of O_2 was performed on another area on the same slab. This procedure ensures that the specimen temperature and thickness, which may affect greatly the nucleation and growth of the defects, were kept nearly constant in the experiment. Just after O_2 was injected, the nucleation of the observable defects by TEM was extremely promoted. The number of the defects was counted and shown in Fig. 6. The similar experimental procedure was repeated on other discs, which possess the slabs of different thickness and crystal bent, and it is found that the nucleation of the defects was always promoted under the flow of O_2 as summarized in Fig. 6 (b) [8]. After the promoted defect nucleation was observed, we terminated the flow of O_2 and proceeded irradiation again in UHV environment. The promoted nucleation was not suppressed promptly in contrast to the nanohole formation on the surface as described above. Therefore, the result indicates that oxygen affects the nucleation and growth of the {113} defects, which may be thermally diffused and impinged by accelerated electrons from the surface into a thin crystal.

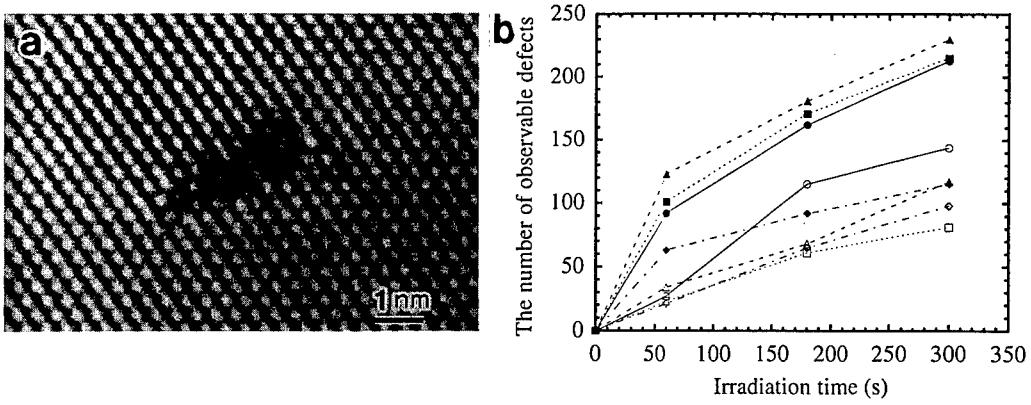


Fig. 6 (a) UHV-HRTEM image of a {113} defect. (b) Promoted nucleation of the {113} defects under the flow of O_2. The data from five samples are compiled. The open marks represent the data in UHV and the closed marks, under the flow of O_2. All the data were taken from the {111} samples, except the {110} sample marked by the lozenge.

It is well known that electron irradiation in Si introduces an oxygen-vacancy pair (A-center) [9]. The enhanced formation of the centers by the additional oxygen may disturb the mutual annihilation of Frenkel pairs further, and interstitials are more accumulated in a thin foil. Consequently, their agglomeration is promoted. Alternatively, the agglomeration of self-interstitial begins after the specific core structures, involving impurities such as oxygen, are formed. The incubation period was accordingly interpreted. These arguments were based on the data comparison between CZ and FZ silicon, between doped and undoped silicon and between the furnace annealing in O_2 ambient and in vacuum. The intentional contamination of impurities has been attempted not on clean surfaces but on uncontrolled oxidized surfaces. In this work, we have demonstrated that the UHV-TEM is a useful means of describing the effects of impurities on the growth and development of the extended defects.

Conclusion.

We have applied UHV-TEM to the studies of electron irradiation effects in silicon thin foil. We have found that the array of the nanoholes is formed on the electron exit surface by the electron irradiation in UHV environment. The nanoholes may be utilized for the future microelectronic works. We have also observed *in situ* the effect of impurities on the formation of electron-irradiation-induced defects.

References.

[1] E. Bengu, R. Plass, L. D. Marks, T. Ichihashi, P. M. Ajayan and S. Iijima, Phys. Rev. Lett. **77** (1996) 4226.
[2] for instance, G. S. Chen, C. B. Boothroyd and C. J. Humphreys, Appl. Phys. Lett. **62**, 1949 (1993) .
[3] S. Takeda, K. Koto, S. Iijima and T. Ichihashi, submitted (1997).
[4] D. Cherns, Surface Science **90**, 336 (1979).
[5] M. Hasebe, R. Oshima and F. E. Fujita, Jpn. J. Appl. Phys, **25** (1986) 159.
[6] M. Reiche, J. Reichel and W. Nitzshe, phys. stat. sol. a**107**, 851 (1988).
[7] S. Takeda, Jpn. J. Appl. Phys. **30**, L639 (1991)
[8] K. Koto, S. Takeda, T. Ichihashi and S.Iijima, to be published in Appl. Phys. Lett. (1997).
[9] G. D. Watkins and J. W. Corbett, Phys. Rev. **121** (1961) 1001.

Materials Science Forum Vols. 258-263 (1997) pp. 559-564
© 1997 Trans Tech Publications, Switzerland

APPLICATION OF SPIN DEPENDENT RECOMBINATION FOR INVESTIGATION OF POINT DEFECTS IN IRRADIATED SILICON

M.M.Afanasjev[1], R.Laiho[2], L.S.Vlasenko[1] and M.P.Vlasenko[1]
[1] A.F.Ioffe Physico-Technical Institute, 194021 St.-Petersburg, Russia
[2] Wihuri Physical Laboratory University of Turku, FIN-20014 Turku, Finland

Keywords: silicon, point defects, spin dependent recombination, electron paramagnetic resonance.

Abstract. A high sensitive method for detection of the magnetic resonance, based on spin dependent change of the microwave photoconductivity, was applied for investigation of radiation defects at low concentration in silicon. Temperature induced change of symmetry of carbon related centers at low temperatures (4-30 K) and new spectra originating from an electron pair center with a small exchange constant were studied in pure float-zoned silicon. In oxygen rich silicon irradiated at high temperatures (360-420 °C) a new spectrum similar to that of an oxygen+vacancy complex was found.

Introduction

Investigations of spin dependent recombination (SDR) in irradiated silicon [1-4] show that the main channel of the SDR is the recombination through the excited triplet states of radiation defects. Magnetic resonance in the excited triplet states leads to the change of the recombination rate of the photoexcited carriers and, consequently, to the change of photoconductivity of samples. Resonance induced variation of photoconductivity is usually detected by ordinary electrical methods using electrical contacts and by a contact free method based on absorption of the electrical component of microwave field by photoexcited carriers. Sensitivity of the contact free method allows to detect electron paramagnetic resonance (EPR) spectra of the recombination centers at concentrations four orders lower than the concentration needed for usual EPR method. Using this method EPR spectra of the excited triplet states of a carbon related center [1,4], a phosphorus+vacancy complex [2], and a divacancy [3] have been found. It has been shown [5] that SDR induced change of photoconductivity takes place not only at the magnetic resonance conditions but at the specific points of the magnetic level structure like the anticrossing points of magnetic sublevels of triplet states and gives additional information about parameters and structure of the recombination centers. It is expected that SDR based methods will be useful for investigation of point defects in semiconductors when the usual EPR methods are not applicable.
In the present paper we report results of the investigations of the SDR-EPR spectra of paramagnetic recombination centers at low concentration when the defects are produced by low dose irradiation and by irradiation at high temperatures.

Experimental

The samples were prepared from crystalline wafers of float-zoned (FZ) n-type (300 Ω·cm) and crucible grown oxygen rich p-type (10 Ω·cm) silicon. The samples were irradiated by 1MeV electrons with doses varied from $5 \cdot 10^{16}$ to $2 \cdot 10^{17}$ cm^{-2}. Irradiation was made at room temperature and at higher temperatures within the range of 150 - 420 °C.
Spectra of the SDR induced change of the microwave photoconductivity of samples were detected in the temperature range of 4 - 300 K by a X-band EPR spectrometer with microwave power below 400 mW. The samples were illuminated by a 100 W halogen tungsten lamp. The change of photoconductivity at the magnetic fields corresponding to EPR transitions and to the crossing of magnetic sublevels of paramagnetic recombination centers was detected as a variation of the Q-factor of the cavity.

The second derivative signals were recorded over a wide magnetic field scan range using modulation frequencies of 100 KHz and 100 Hz. This allows to reduce the strong background originating from the magnetoresistance and cyclotron resonance lines.

Results and Discussion

Temperature transformation of the symmetry of the C_s -Si_I - C_S complex in silicon.

It was found that Substitutional Carbon - Interstitial Silicon - Substitutional Carbon (C_S - Si_I - C_S) complex gives the main contribution to the SDR process in irradiated FZ silicon. A strong SDR-EPR spectrum with trigonal symmetry (Si-PT1) of the excited triplet state of this defects is observed in a wide temperature range of 20 - 120 K. At low temperatures (4 - 10 K) SDR-EPR spectrum of monoclinic symmetry was found. These spectra are shown in Fig.1(a,b). When the temperature increases from 4 K to 30 K the spectrum of monoclinic symmetry decreases gradually and the trigonal spectrum increases.

Two carbon atoms in the (C_S - Si_I - C_S) - complex occupy neighboring substitutional positions on <111> axis. Silicon atom (Si_I) is localized on the C - C bond with a displacement from <111> axis so that the defects have monoclinic symmetry at low temperatures. This model has been deduced from the optically detected magnetic resonance (ODMR) spectrum of monoclinic symmetry detected at temperatures T < 30 K [7,8]. The ODMR spectrum and spectrum detected by SDR induced change of microwave photoconductivity, shown in Fig.1(a), are described by the spin Hamiltonian with the same parameters. At higher temperatures the thermally activated motion of a Si_I atom around the <111> axis leads to transformation of the symmetry of the defect from monoclinic to trigonal. This transformation has been observed by the ODMR method [7]. It has been supposed [8] that trigonal Si-PT1 spectrum is a transformed ODMR spectrum of the monoclinic symmetry.

Simultaneous detection of both monoclinic and trigonal SDR-EPR spectra and investigations of their intensity and symmetry transformations in the temperature range of 4-30 K allow us to confirm this supposition and to determine the activation energy E_a of the motion of the Si_I atom around the <111> axis.

The energy E_a can be determined in two ways. The first one is based on determination of the temperature T_a at which the lines of the averaged trigonal spectrum appear between the lines of the low symmetry spectrum separated by ΔB (see. Fig.1(a)). This takes place when the motional

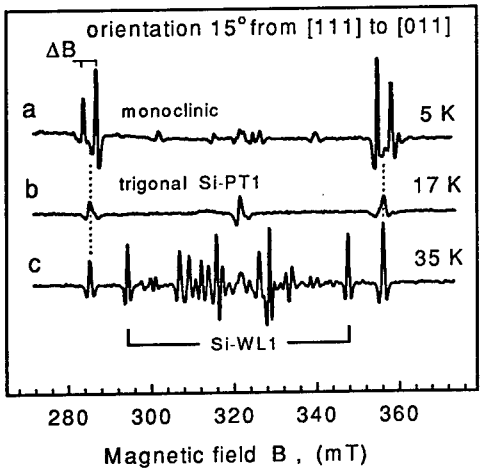


Fig.1 SDR-EPR spectra detected in electron irradiated FZ silicon at different temperatures.

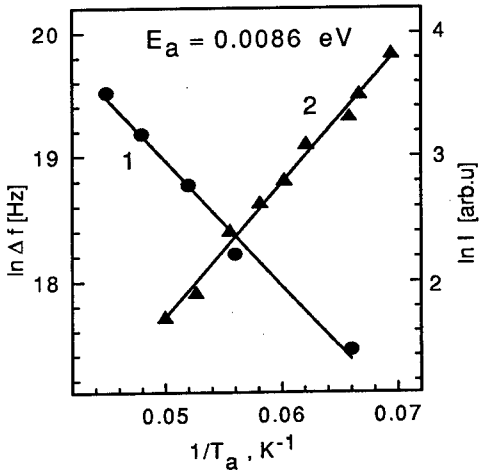


Fig.2 Arrhenius plots of ln(Δf) (curve 1) and ln(I) (curve 2) vs $1/T_a$.

frequency $f_m = f_o \exp(E_a/kT)$ is comparable with a frequency $\Delta f = g\,\beta\,\Delta B / h$ which depends on the angle between the magnetic field **B** and the <111> crystal axis (g is the g-factor, β - Bohr magneton, and h - Plank's constant). The temperature T_a can be found for different orientations of the crystal in the magnetic field, and consequently for different Δf. The Arrhenius plot of ln(Δf) vs $1/T_a$, shown in Fig.2 (curve 1), gives the slope of the straight line corresponding to $E_a = (0.0086 \pm 0.0004)$ eV.
Using the second method we find the activation energy from the temperature dependence of the amplitude (I) of the lines of the monoclinic spectrum. The plot of ln (I) vs 1/T shown by curve 2 in Fig.2 gives the same activation energy within the error limits.
Several new SDR-EPR spectra were found in the same samples at higher temperatures. One of them, labeled Si-WL1, is shown in Fig.1(c). This spectrum has a monoclinic symmetry and is observed in a narrow temperature range of 30-50 K. Other spectra are observed at T > 50 K and they could be described separately. Here we discuss the spectrum, labeled Si-WL2, which is detected in a wide temperature range up to room temperature.

Two electron exchange interaction detected by SDR.
The lines of the spectrum Si-WL2 detected by SDR induced change of microwave photoconductivity in different ranges of the magnetic field B (at the same microwave frequency of 9.028 GHz) are shown in Fig.3 (b,c,d,). The lines (c) originate from the EPR transitions and are observed at the magnetic field B around 322 mT corresponding to the g-factor about 2. Angular dependencies of the positions of the lines (c) are shown in Fig.4(a) (dots). The lines shown in Fig.3(d) were found at the magnetic field approximately twice higher than the field for the lines (c). Angular dependencies of these high field lines (see Fig.4(b)) exhibit a trigonal symmetry.
Two significant features of high field lines were found. First, the positions of these lines *do not depend* on microwave frequency. The second important feature is the strong *temperature dependence* of the position of this high field spectrum in the magnetic field whereas their symmetry and the fine structure splitting do not depend on temperature. Within the temperature range 4 - 30 K this spectrum is observed around B ≈ 615 mT. At room temperature it is shifted to B ≈ 440 mT.

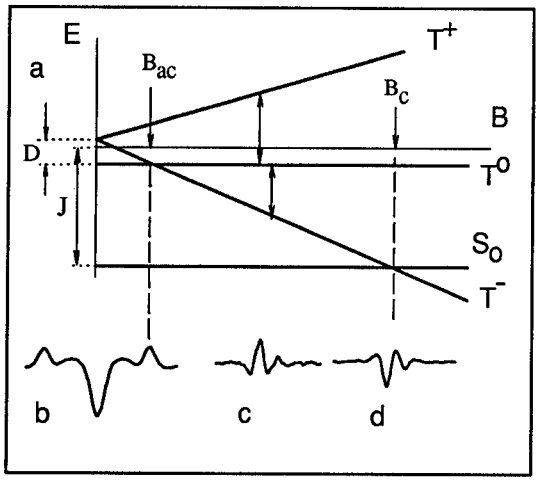


Fig.3 Energy levels for a two electron system in a magnetic field (a) and SDR lines (b,c,d) detected in electron irradiated FZ silicon for B || <111> and T = 125 K.

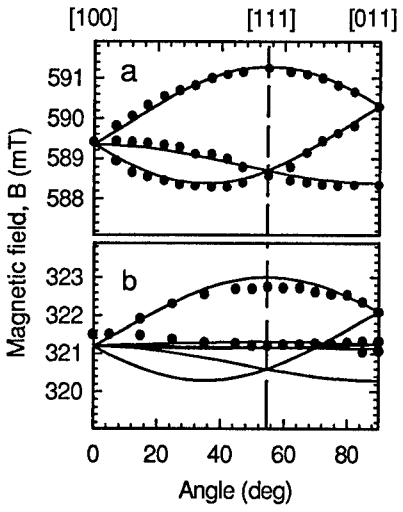


Fig.4 Angular dependences of the high field spectrum (a) and spectrum corresponding to the SDR-EPR transitions (b) at T = 125 K.

This allows us to conclude that the high field SDR spectrum does not originate from the EPR induced transitions between magnetic levels of the paramagnetic recombination center but rather from specific points of the magnetic level structure, similar to the lines observed earlier [1,5] at the anticrossing points of the magnetic levels of triplet centers. We can suppose that the detected spectra originate from defects containing two electrons with a weak exchange interaction comparable with the Zeeman energy.

To describe the angular dependences of the observed SDR spectra we shell consider a simple model of defect including two interacting identical electrons localized on points of trigonal symmetry in the silicon lattice. The Hamiltonian taking into account the Zeeman interaction between the applied magnetic field **B** and the electron spins $\mathbf{S_1}$ and $\mathbf{S_2}$, the isotropic exchange interaction, $J\,\mathbf{S_1}\,\mathbf{S_2}$, and the anisotropic dipole-dipole interaction, $\mathbf{S_1}\,\mathbf{D}\,\mathbf{S_2}$, where **D** is a symmetric traceless tensor, can be written in the form

$$H = \mu_B\,\mathbf{B}\,\mathbf{g_1}\mathbf{S_1} + \mu_B\,\mathbf{B}\,\mathbf{g_2}\,\mathbf{S_2} + J\,\mathbf{S_1}\,\mathbf{S_2} + \mathbf{S_1}\,\mathbf{D}\,\mathbf{S_2}\,. \qquad (1)$$

We assume that the **g**-tensors of the electrons are identical ($\mathbf{g_1} = \mathbf{g_2} = \mathbf{g}$) and have trigonal symmetry defined by the components $g_{\parallel}$ and $g_{\perp}$. The **D**-tensor is also assumed to be trigonal and defined by one parameter D.

The energy levels corresponding to the Hamiltonian (1) are shown in Fig.3(a). The anticrossing of the T^0 and T^- levels may be expected in a magnetic field B_{AC}. Indeed, two lines were observed symmetrically around B = 0 at $B_{AC} \cong \pm 0.85$ mT for the orientation of $B \parallel <111>$ (see Fig.3(b)). With increasing the angle between **B** and <111> axis they disappeared gradually. Such angular dependence is specific for the change of photoconductivity due to anticrossing of levels [1,5]. From the value of B_{AC} the parameter $D \cong \pm 23.8$ MHz could be determined.

Angular dependencies of both spectra shown in Fig.4 by solid lines were calculated from the Hamiltonian (1) with the parameters $g_{\parallel} = 2.0027 \pm 0.0002$, $g_{\perp} = 2.0117 \pm 0.0002$, J(T=125 K) = 16570 MHz, and D = 23.8 MHz. The best fit with the experimental data in Fig.4 requires the same sign of J and D. If we suppose that J > 0, corresponding to the ground singlet state, the D constant must be positive. Because all lines of the SDR induced change of microwave photoconductivity are observed in the same temperature region up to room temperature and their angular dependences are well described by the same parameters of the spin Hamiltonian we can conclude that they arise from the same defect.

It should be noted that lines corresponding to EPR transitions (see Fig.3(c)) show strong angular dependence of the intensity, so that not all orientations of the defects could be observed. This is a common feature of the spectra detected by the SDR method [1-4].

The signs of the anticrossing line (see Fig.3(b)) at $B = B_{AC}$ and the lines of EPR induced transitions (Fig.3(c)) are the same and corresponds to decrease of microwave photoconductivity whereas the line at B = 0 and the lines corresponding to crossing of the levels S_0 and T^- at $B = B_C$ have the opposite sign. This difference is likely to be related to mechanisms of SDR through the excited triplet states and should be investigated in details separately.

New SDR-EPR spectrum in crucible grown silicon irradiated at high temperature.

In crucible grown silicon crystals oxygen atoms play an important role in creation of defects under irradiation. Detailed EPR investigations of the oxygen related defects [10,12] show that at room temperature irradiation only simplest complexes of oxygen atoms O and vacancies V, such as (O+V) and ($O+V_2$), are formed. Heat treatment of the irradiated samples leads to decay of these defects and produces new defects of more complex structure, (O_2+V_2), ($O+V_3$), (O_2+V_3), (O_3+V_3) [12]. These investigations have been performed on silicon irradiated by 2-MeV electrons with doses of 10^{18} - 10^{19} cm^{-2} when the concentration of radiation defects is sufficient for detection by the conventional EPR method. At lower doses of irradiation the concentration of radiation defects in annealed samples is too small to be detected by the usual EPR method. Irradiation at high temperatures when annealing of the simplest complexes takes place can also lead to the formation of new types of defects.

We applied SDR-EPR method for detection of paramagnetic recombination centers in oxygen rich silicon irradiated by 1 MeV electrons with the dose about $2 \cdot 10^{17}$ cm^{-2} at temperatures between 150 - 420 °C.

After irradiation of the samples in the temperature range of 150 - 350 °C the usual EPR spectrum Si-SL1 [10] of the excited triplet state of the oxygen+vacancy complex (A-center) is observed. When the temperature increases from 350 °C to 400 °C the intensity of this spectrum decreases to zero and a new spectrum, labeled Si-WL3, appears. These spectra are shown in Fig.5. The Si-WL3 spectrum is similar to Si-SL1 spectrum. They have the same orthorhombic symmetry and close values of the **g**- and **D**-tensors as summarized in Table 1.

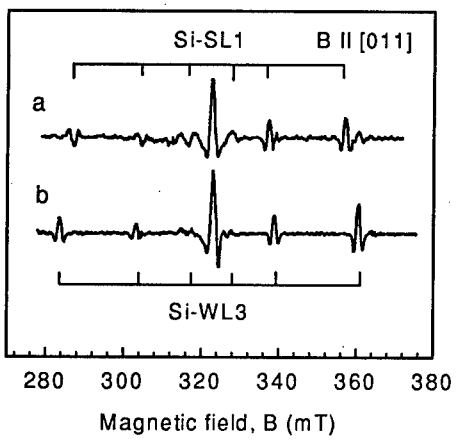


Fig. 5 EPR spectra detected in crucible grown silicon after irradiation by 1 MeV electrons at 360 °C (a) and 420 °C (b).

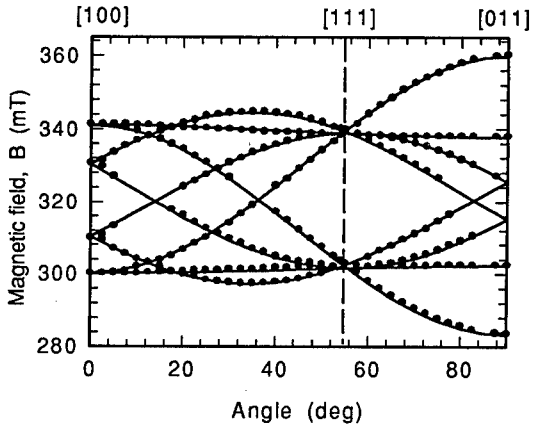


Fig. 6 Angular dependence of Si-WL3 spectrum.

Table 1. Comparison of the parameters of Si-SL1 and Si-WL3 spectra.

Spectrum	Principal axes	g-tensor	D-tensor (in MHz)
Si-SL1	[100]	$g_1 = 2.0075$	$D_1 = \mp 526$
	[011]	$g_2 = 2.0057$	$D_2 = \pm 988$
	[$0\bar{1}1$]	$g_3 = 2.0102$	$D_3 = \mp 462$
Si-WL3	[100]	$g_1 = 2.0075$	$D_1 = \mp 577$
	[011]	$g_2 = 2.0040$	$D_2 = \pm 1078$
	[$0\bar{1}1$]	$g_3 = 2.0100$	$D_3 = \mp 501$

The intensity of the Si-WL3 spectrum is too low to detect the ^{29}Si hyperfine structure and to compare with the hyperfine structure of the Si-SL1 spectrum. Perhaps the future investigations of the SDR-EPR spectra in silicon irradiated with different doses at high temperatures will allow us to increase the intensity of detected spectra and to determine the structure of the defects responsible for the spectrum Si-WL3.

The similarity of the Si-SL1 and Si-WL3 spectra allows us to suppose that both spectra originate

from the A-centers. The spectrum Si-SL1 originates from the usual A-center in regular silicon lattice. A stress in the neighbourhood of the A-center can change the EPR parameters and increase the annealing temperature of the centers. So, we can suppose that Si-WL3 spectrum originates from A-centers formed in regions of silicon crystal with additional stress, for example, near the dislocations, impurity atoms, or near the surface of the crystal. The investigations of stress effects due to Ge atoms on the g-and D parameters of the Si-SL1 EPR spectrum in Si_{1-x} - Ge_x solid solutions were performed in Ref.13. It was shown that additional stress decreases the components of g-tensor and increases the components of D-tensor. The maximal variations of g- and D- components was found for orientation of the magnetic field $B \,||< 011 >$ [13]. The parameters summarized in Tab.1 are in agreement with the results obtained in [13].

Summary and Acknowledgments

Two SDR-EPR spectra of the excited triplet state of a carbon-silicon-carbon complex were detected in irradiated pure FZ silicon crystals. They indicate transformation of the complex symmetry from monoclinic to trigonal due to thermally activated motion of an interstitial silicon atom around the <111> axis in the temperature range of 10-30 K. The activation energy of this motion, $E_a \approx 0.0086$ eV was determined. The new spin-1 spectrum of monoclinic symmetry, labeled Si-WL1, was observed in a narrow temperature range of 30 - 50 K.
SDR-EPR spectrum Si-WL2 was found in the same samples in a wide temperature range up to room temperature. This spectrum was attributed to a defect including two electrons characterized by exchange energy comparable with the Zeeman energy. Crossing of the ground singlet state and the excited triplet state level with spin projection $S_Z = -1$ was detected for the first time by the SDR method in silicon. Strong temperature dependence of the positions of the crossing lines was found.
In crucible grown silicon irradiated at high temperatures (300 - 420 °C) a new spin-1 SDR-EPR spectrum Si-WL3 was detected. This spectrum can be described by g- and D-tensors with the orthorhombic symmetry and components close to those of the Si-SL1 spectrum of the excited triplet state of oxygen+vacancy complex.
We thank Dr.V.N.Lomasov for irradiation of the samples. This work was supported by the Wihuri Foundation and partly by the Russian Science Foundation under Grant No 97-02-18062.

References

1. L.S.Vlasenko, M.P.Vlasenko, V.N.Lomasov, and V.A.Khramtsov, Sov. Phys. JETP **64**, 612 (1986).
2. V.A.Khramtsov, V.N.Lomasov, Ya.Ya.Pilkevich, M.P.Vlasenko, and L.S.Vlasenko, Phys. Stat. Sol. (a) **109**, 127 (1988).
3. M.P.Vlasenko and L.S.Vlasenko, Sov. Phys. Solid State **33**, 1326 (1991).
4. L.S.Vlasenko, Yu.V.Martynov, T.Gregorkiewicz, and C.A.J.Ammerlaan, Phys. Rev. B **52**, 1144 (1995).
5. L.S.Vlasenko and V.A.Khramtsov, Sov. Phys. JETP Lett. **42**, 38 (1985).
6. K.M.Lee, K.P.O'Donnell, J.Weber, B.C.Cavenett, and G.D.Watkins, Phys. Rev. Lett. **48**, 37 (1982).
7. K.P.O'Donnell, K.M.Lee, and G.D.Watkins, Physica **116 B**, 258 (1983).
8. G.D.Watkins (private communication).
9. G.D.Watkins, Phys. Rev. **155**, 802 (1967).
10. K.L.Brower, Phys. Rev. B **4**, 1968 (1971).
11. W.Jung and G.S.Newell, Phys. Rev. **132**, 648 (1963).
12. Y.-H.Lee and J.Corbett, Phys. Rev. B **13**, 2653 (1976).
13. A.A.Bugai, I.A.Kravtsova, V.M.Maksimenko, B.D.Shanina, and V.I.Shakhovtsov, Phys. Stat. Sol. (b) **151**, 159 (1989).

Materials Science Forum Vols. 258-263 (1997) pp. 565-570
© 1997 Trans Tech Publications, Switzerland

ELECTRICAL AND OPTICAL CHARACTERISATION OF DEFECTS INDUCED IN EPITAXIALLY GROWN n-Si DURING 1 keV NOBLE GAS ION BOMBARDMENT

P.N.K. Deenapanray, F.D. Auret, G. Myburg, W.E. Meyer and S.A. Goodman
Department of Physics, University of Pretoria, Pretoria 0002, South Africa

Keywords : photoluminescence, DLTS, C- and O-related defects, noble gas ion bombardment.

Abstract. The modification in the G-line (969.5 meV) and the C-line (789.4 meV) PL intensities were studied as a function of the fluence, energy and the mass of the bombarding ions (He, Ne, Ar and Kr). The intensities of the luminescent lines induced by 1 keV Ne bombardment were found to decrease with increasing dose, after reaching a maximum at about $1x10^{12}$ ions/cm^2. Considerable reductions in the intensities of the G- and C-lines were also recorded during bombardment using heavier noble gas ions. The incident ion energy at which the PL intensities of the spectral lines reached their maximum values were found to be dependent on the ion mass and fluence, and hence, on the nuclear energy deposited. The decrease in PL intensities of the G-line and C-line is explained in terms of the introduction of increased amounts of non-radiative recombination centres with increasing incident ion dose and mass.

Introduction

Low-energy noble gas ions are commonly used, for instance during ion beam etching (IBE), reactive ion etching (RIE) and sputter deposition. During these processes energetic ions create defects in the near-surface region of the exposed semiconductor. These defects can significantly alter the optical, electrical and structural properties of the material. The creation of a class of optically active noble gas (NG) related defects involving the intrinsic I_1 defect was previously reported after ion implantation and IBE using NG ions[1,2]. Besides two characteristic luminescent lines termed G (969.5 meV) and C (789.4 meV) are observed in silicon containing carbon and oxygen after dry etching using CF_4 reactive ion etching (RIE) [3] and IBE [2]. It is known that oxygen and carbon impurities play an important role in the creation of defects responsible for the G- and C-lines [4,5]. Furthermore, several studies have shown that the magnitude of G-line luminescence can be used as an accurate measure of the carbon content in Si crystals [2,6]. The G-line luminescence is attributed to an interstitial silicon atom Si_i located between two adjacent substitutional carbon atoms (C_s-Si_i-C_s) [7], while the C-line luminescence is caused by complexes composed of an interstitial carbon atom C_i and an interstitial oxygen atom O_i (C_i-O_i) [2]. The 969.5 meV PL defect has been identified with the EPR-detected G11 centre [8], whereas the 789.4 meV defect was identified as the EPR G15 centre [9].

The concentration and type of defects formed during irradiation depend on the fluence, energy and species of ions. Moreover, impurity-defect complexes are produced through the interaction between defects and impurities. It is, therefore, important to study the dependences of ion mass, dose and energy on the luminescent lines by noble gas ion implantation. In the present study, we investigated the effect of fluence, mass and energy of bombarding noble gas ions on the intensities of the G- and C-lines luminescence. The electrical properties of the low energy bombardment-induced defects have also been studied by deep level transient spectroscopy (DLTS).

Experimental procedure

Samples used were epitaxially grown (111) oriented Si layers on n^+-substrates and doped with $5x10^{15}$ cm^{-3} phosphorous. The epitaxial side of the samples were bombarded with 1 keV noble gas ions (He, Ne, Ar, Kr) at doses ranging from $1x10^{10}$ to $1x10^{15}$ ions/cm^2 using an ion gun. Photoluminescence measurements were carried out using the 514 nm line of an argon-ion laser, a 0.64 μm infra red monochromator (resolution 1.4 Å), a cooled germanium detector and conventional

lock-in amplifier technique. Samples were mounted in a closed cycle helium-cooled cryostat and the temperature could be varied between 11 K and 90 K. Circular Pd Schottky contacts of 0.77 mm diameter and 100 nm thickness were resistively deposited on the bombarded samples through a metal contact mask for DLTS analyses. The energy levels, E_T, and apparent capture cross-sections, σ_a, associated with the defects were determined from DLTS Arrhenius plots of $\log(e/T^2)$ vs $1/T$, where e is the emission rate at a temperature T. For control purposes, PL and DLTS measurements were taken using unirradiated Si samples.

Results and discussion

A. Dose dependence

Figure 1 shows the G-line and the C-line intensities after 1 keV Ne ion bombardment as a function of fluence from $5x10^{10}$ to $1x10^{14}$ ions/cm^2. It is found that the intensity of optically active defects increased with increasing Ne ion dose, and decreased after reaching a maximum at a fluence of $1x10^{12}$ ions/cm^2. A saturation in the intensity of the defects is expected at higher doses since the number of defects is limited by the concentration of carbon and oxygen atoms originally present in the Si crystals. We attribute the reduction in the PL intensities of the G- and C-lines for higher doses to the formation of non-radiative recombination centres with either discrete levels related to VO- and VP-pairs, divacancies, higher-order vacancy clusters or continuous levels related to extended defects in the band gap. Furthermore, complexes composed of vacancies and neon atoms [10,11] could also increase the number of optically inactive recombination centres for bombardment doses larger than $1x10^{12}$ ions/cm^2. The higher concentrations of defects at higher doses are due to the higher densities of collision cascades, and hence higher rates of nuclear energy deposition by the bombarding ions.

Now the presence of discrete and continuous levels in 1 keV Ne-bombarded Si is demonstrated. The electrically active defects introduced by He- and Ar-ion bombardment are discussed in the next section. Figure 2 shows the DLTS spectra obtained for n-Si after 1 keV Ne ion bombardments at doses ranging from $1x10^{12}$ and $1x10^{14}$ cm^{-2}. The VO-centre has an energy level at E_c - 0.183 eV and is labelled ENe183. In the nomenclature used, "E" denotes an electron trap, "Ne" implies the defect

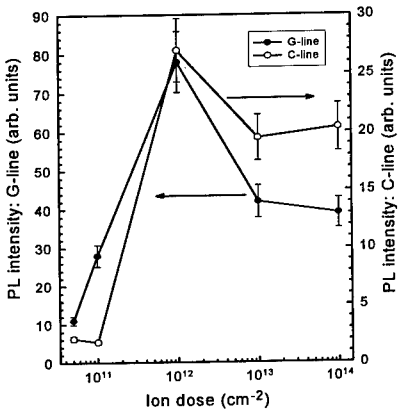


Fig. 1 Plot of PL intensities of the G- and C-line as a function of incident ion dose during 1 keV Ne ion bombardment of n-Si. Sample temperature was fixed at 11 K for the PL measurements.

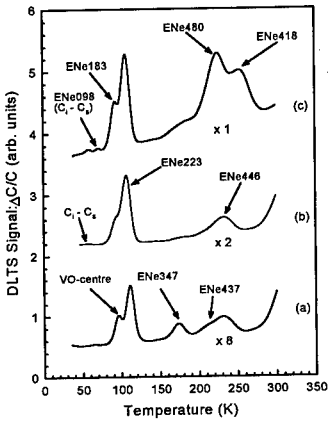


Fig. 2 DLTS spectra of 1 keV Ne-ion bombarded n-Si to fluences of: (a) $1x10^{12}$ cm^{-2}, (b)$1x10^{13}$ cm^{-2} and (c) $1x10^{14}$ cm^{-2}. All curves were recorded at a lock-in amplifier frequency of 46 Hz (decay time constant of 9.23 ms), V_r = 1 V and V_p = 1.4 V.

is introduced by Ne ions and the number gives the position of the level below the conduction band

in meV. The second charge state of the divacancy, $V_2^{-/0}$, could be observed in very low concentrations after removing the VP-centre (ENe437) by annealing at 180 °C for 30 min. The non-detection of the first charge state of the divacancy, $V_2^{=/-}$, may be attributed to the presence of stress fields in the highly perturbed region probed by DLTS [12]. The following comments can be made about the spectra to validate our discussion: Firstly, the intensities of the defect peaks (i.e., concentrations of defects) are found to increase with increasing ion dose. Secondly, a new prominent defect at E_c - 0.48 eV can be observed during bombardment at $1x10^{14}$ ions/cm^2. This defect, being close to the mid-bandgap position, could indeed be an efficient recombination centre [13]. Finally, it is clear from Fig. 2 that the baseline "skewing" of the DLTS spectra increases with increasing ion dose. The baseline "skewing" phenomenon has previously been observed in 5.4 MeV electron-irradiated GaAs and has been speculated to be due to the presence of extended defects [14]. Furthermore, the baseline "skewing" is accompanied by the broadening of some of the DLTS defect peaks such as ENe347 and those observed in the temperature range 200-280 K when the bombarding ion dose is increased. The peak broadening phenomenon is also indicative of the presence of extended defects [15].

The non-radiative defects result in an increased amount of existing or new recombination paths such that the recombination of electrons and holes between the levels responsible for the G- and C-lines is decreased. Consequently, the luminescence from the G-line and C-line defects is reduced when the irradiation dose exceeds the critical level of $1x10^{12}$ ions/cm^2.

B. Dependence on incident ion mass

Figure 3 shows the variation in the PL intensities of the G- and C-lines after 1 keV He, Ne, Ar and Kr ion bombardments. The nuclear energy deposited to recoils by each incident ion is also depicted in Fig. 3. All the low energy irradiation were done at a dose of $1x10^{12}$ ions/cm^2. The intensities of the two spectral lines were observed to decay almost exponentially with the mass of the bombarding ions. This mass dependence of the PL intensities is explained by considering the energy deposited by the different noble gas ions as they penetrate the Si lattice. Nuclear stopping is the dominant mechanism for energy transfer to the target during 1 keV He, Ne, Ar and Kr ion bombardments. As the mass of the incident ion is increased, the cross section for elastic collision is also increased. This results in a higher density of recoil atoms being produced and consequently a higher rate of energy deposition. For instance, TRIM [16] simulations reveal that the nuclear energy loss to the Si lattice increases with incident ion mass as shown in Fig. 3. Since the energy deposited by a 1 keV He ion is well above the critical value of the energy (~1 eV/Å) required for non-linear effects such as energy spikes [17] - one mechanism of forming extended defects - the amount of damage introduced to the Si lattice is expected to increase drastically with the mass of bombarding ions. The lowering in the PL intensities of the G- and C-lines can thus be explained by the introduction of increased amounts of non-radiative recombination centres with increasing incident ion mass. Since the energy deposited per unit length (eV/Å) of the incident ions

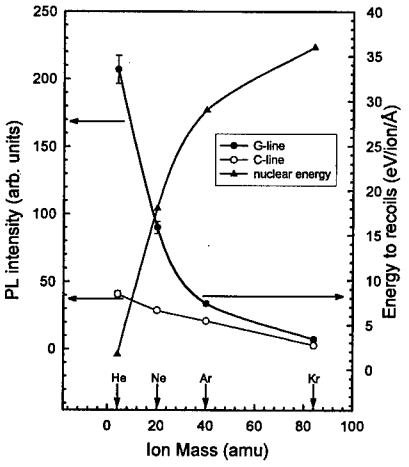


Fig. 3 Variation of PL intensities of the G- and C-lines as a function of bombarding ion mass. PL measurements were done on 1 keV He-, Ne-, Ar- and Kr-ion bombarded epitaxially grown n-Si to a dose of $1x10^{12}$ cm^{-2}. The nuclear energy deposited to recoils by the ions, as calculated from TRIM simulations, is also shown.

is much higher than the threshold for spike formation throughout their entire range, it is highly probable that non-radiative centres are produced in large concentrations during 1 keV bombardments using the noble gas ions.

DLTS measurements have shown that 1 keV He and Ne ion bombardment of Si at a dose of $1x10^{12}$ ions/cm^2 introduced the same set of defects [18]. However, the concentration of the defects were found to be relatively higher during Ne ion irradiation. On the other hand, a more complex set of defects was created in the same material during Ar [18] and Kr ion bombardments. We have also observed that, except for the VO- and VP-centres, the low energy defects created during noble gas ion irradiation are different from the primary defects introduced during high energy (MeV) electron and alpha-particle irradiation of the same wafer [19,20]. The presence of the first charge state, $V_2^{=/-}$, of the divacancy could not be observed in our low energy ion bombarded samples. However, annealing studies at 180 °C for 30 minutes have revealed the presence of the second charge state, $V_2^{-/0}$, of the divacancy produced by 1 keV noble gas ion bombardments, but in very low concentrations. We argue that $V_2^{=/-}$ could not be detected because of the presence of stress fields due to regions of high defect densities in our bombarded samples [12]. Furthermore, the low concentrations of $V_2^{-/0}$ in our samples could mean that vacancy clusters (larger than the divacancy) are predominantly formed during 1 keV noble gas ion bombardments. Low energy noble gas ion bombardment of epitaxially grown n-Si is found to introduce a class of defects similar to ENe223 (Fig. 2), the DLTS signal intensities of which increase with the mass of the bombarding ion. Based on isochronal annealing studies of both low energy noble gas ion and alpha-particle irradiated n-Si, and on epitaxial Si layers containing different O and C contents, we have proposed have that this class of defect is caused either by vacancy clusters larger than the V_2 but smaller than the hexavacancy (not electrically active) or the incorporation of the noble gas atoms into V_2 or higher-order vacancy clusters [21]. Thus our DLTS results agree with the TRIM simulation results presented above and can be used to confirm the propositions made to explain the reduction in PL intensities of the G- and C-lines with increasing bombarding ion mass. We have also noted significant baseline "skewing" of our DLTS spectra together with DLTS peak broadening during analysis of samples exposed to the heavier noble gas ions.

C. Dependence on ion energy

Figure 4 shows the PL intensities of the G- and C-lines as a function of incident ion energy for He ions at fluences of $1x10^{10}$ to $1x10^{12}$ ions/cm^2. It is observed from Fig. 4 that the PL intensities of the G- and C-lines initially increase to maximum values and thereafter decrease. Figure 4 also suggests that the maxima are dose dependent. We explain our results by considering the energy dependence of the electronic and nuclear stopping of He ions in the Si crystal. In addition, we have considered the range of He ions with different bombarding energies together with the excitation depth of our Ar-ion laser. For any implanted ion, the nuclear stopping component of energy loss decreases as the energy of the ion is increased, whereas its electronic energy deposition increases [22]. The projected range and energy loss to recoils for He ions, as calculated from TRIM, in the energy range 1-150 keV are shown in Fig. 5.

For a given noble gas species the number of optically active defects increases with ion dose from a minimum as the energy of the incident ion is increased. It can be deduced from Fig. 5 that a 150 keV He ion will create much less energetic recoil atoms in the first 100 Å below the semiconductor surface compared to a 1 keV He ion. However, as the 150 keV ion loses energy and slows down as it penetrates further into the Si lattice, its nuclear stopping increases. As a result, the ion produces increasingly more energetic recoil atoms and, thus, introduces increasingly more damage in the semiconductor as it continues to slow down over its range of approximately 8200 Å. TRIM simulations also show that spike formation could occur when the energy of the ion is slightly less than 150 keV. Thompson and Walker [23] have shown that non-linear effects, such as the overlapping of individual collision cascades to produce higher density ones, can occur in ion

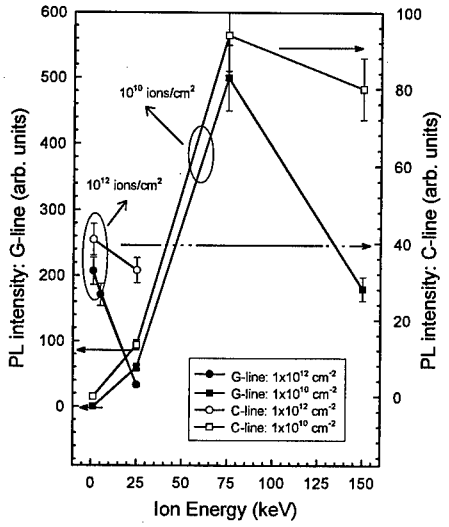


Fig.4 Influence of incident ion energy on the PL intensities of the G- and C-lines by He-ion bombardment of n-Si to doses of 1x10^{10} cm^{-2} and 1x10^{12} cm^{-2}.

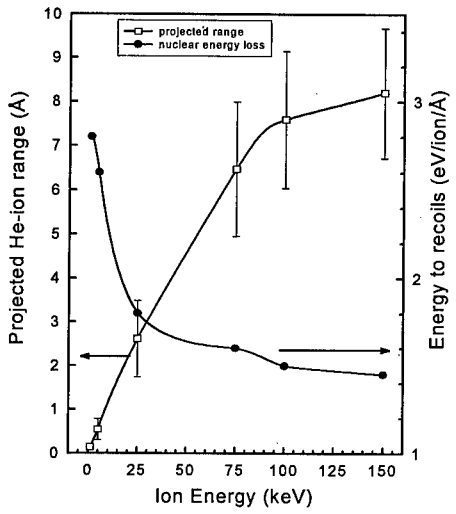


Fig. 5 TRIM simulations of projected range and nuclear energy deposited of He ions in Si for energies ranging from 1 keV to 150 keV. The error bars assigned to the projected ion range correspond to the longitudinal straggling.

bombarded Si when the average deposited energy density is as small as 0.1 eV/atom. The integral sum of defects distributed over the penetration depth of ~ $\lambda/2$ = 2570 Å of the Ar-ion laser will, therefore, be larger for the 150 keV ion than for the 1 keV ion. Consequently, the Ar-ion laser "sees" more non-radiative recombination centres when PL measurements are taken on a sample bombarded with 150 keV He ions.

For all implantation doses or noble gas ion that were used, we found that the number of optically active defects increases from a minimum as the energy of the incident ion is increased. The intensities of the two transitions start to decrease at specific ion energies, which are dose dependent, when the number of non-radiative recombination centres as discussed above provide alternative recombination paths to those responsible for the G- and C-spectral lines. For instance, the energy corresponding to maximum intensities of the G- and C-lines for a dose of 1x10^{10} He$^+$/cm^2 is about 75 keV (Fig. 4), after which the sum total of defects increases, causing a reduction in PL intensities. Since nuclear energy deposition increases with increasing bombarding ion dose, the temperature corresponding to the maximum PL intensities of the two lines is lower for an irradiation dose of 1x10^{12} He$^+$/cm^2 compared to 1x10^{10} He$^+$/cm^2. This dose dependence of the maximum is translated into a shift in the intensity curves in Fig. 4 to the left for the higher ion dose.

Conclusion

We have investigated the influence of noble gas ion species as well as their fluence and energy on the G-line and C-line luminescence in epitaxially grown n-Si. DLTS measurements of the electrical properties of the defects induced by 1 keV noble gas ion bombardment of the same material are also reported. Bombardments using 1 keV Ne ions in the dose range 1x10^{10} cm^{-2} to 1x10^{15} cm^{-2} have shown that the PL intensities of the G- and C-line luminescence increase to reach their maximum values at 1x10^{12} cm^{-2} and, thereafter, decrease with ion fluence. We have attributed the reduction in intensities beyond 1x10^{12} Ne$^+$cm^{-2} to be due to the introduction of higher concentrations of non-radiative recombination centres, which provide alternative recombination paths to those responsible for the G- and C-transitions. DLTS results have indeed shown that higher concentrations of defects are introduced when the ion fluence is increased for a particular noble gas species. A prominent new electron trap at E_c - 0.48 eV, which being close to the mid-bandgap position could well be an

efficient recombination centre, has been detected in $1x10^{15}$ $Ne^{+}cm^{-2}$ bombarded material. Furthermore, the baseline "skewing" and peak broadening phenomena observed in our DLTS spectra may suggest that extended defects, with a continuous distribution of deep levels in the bandgap, are introduced in our samples at irradiation doses higher than $1x10^{12}$ cm^{-2}. The PL intensities of the G- and C-lines were found to decrease almost exponentially with incident ion mass for 1 keV bombardments at $1x10^{12}$ cm^{-2}. The increasingly higher nuclear stopping component of energy deposited by the incident ions with higher mass results in larger amounts of damage to be created in the Si lattice. Consequently, the introduction of non-radiative recombination centres is increased resulting in a decrease in PL intensities of the luminescent lines. We have also observed an increase in the intensities of the prominent electrically active electron traps with increasing bombarding ion mass. Finally, we have demonstrated that the incident ion energy at which the PL intensities reach their maximum values is dose dependent. We have explained the observed trends qualitatively by considering the integral sum of defects produced over the excitation depth of the Ar-ion laser used in our PL experiments.

References

1. N. Burger, K. Thonke, R. Sauer and G. Pensl, Phys. Rev. Lett. **52**, 1645 (1984).
2. J. Weber and M. Singh, Appl. Phys. Lett. **49**, 1617 (1986).
3. R.J. Davis, H.-U. Habermeier and J. Weber, Appl. Phys. Lett. **47**, 1295 (1985).
4. J. Weber, R. J. Davis, H.-U. Habermeier, W. D. Sawyer and M. Singh, Appl. Phys. A **41**, 175 (1986).
5. W.D.Sawyer, J. Weber, G. Nabert, J. Schmalzlin and H.-U. Habermeier, J. Appl. Phys. **68**, 6179 (1990).
6. M. Nakamura, E. Kitamura, Y. Misawa, T. Suzuki, S. Nagai and H. Sunaga, J. Electrochem. Soc. **141**, 3576 (1994).
7. M. T. Assom, J. L. Benton, R, Sauer and L. C. Kimerling, Appl. Phys. Lett. **51**, 256 (1987).
8. K.L. Brower, Phys. Rev. B **9**, 2607 (1974).
9. G.D. Watkins, in *Radiation Damage in Semiconductors*, edited by P. Baruch (Dunod, Paris, 1965).
10. A.V. Mudryi, A.L. Puschkarchuk and A.G. Ul'yashin, Sov. Phys. Semicond. **19**, 225 (1985).
11. S.K. Estreicher, J. Weber, A. Derecskei-Kovacs and D.S. Marynick, Phys. Rev. B **55**, 5037 (1997).
12. B.G. Svensson, B. Mohadjeri, A. Allen, J.H. Svensson and J.W. Corbett, Phys. Rev. B **43**, 2292 (1991).
13. S.M. Sze, Physics of Semiconductor Devices (Wiley, New York, 1981), p. 37.
14. F.D. Auret, S.A. Goodman, R.M. Erasmus, W.E. Meyer and G. Myburg, Nucl. Inst. and Meth. B **106**, 323 (1995).
15. W. Schröter, J. Kronewitz,U. Gnauert, F. Riedel and M. Seibt, Phys. Rev. B **52**, 13 726 (1995).
16. J.F. Ziegler, J.P. Biersack and U. Littmark, "*The Stopping and Range of Ions in Solids*", vol. 1, ed. J.F. Ziegler (Pergamon Press, New York, 1985).
17. P. Sigmund, Appl. Phys. Lett. **25**, 164 (1974).
18. P.N.K. Deenapanray, N.E. Perret, F.D. Auret, G. Myburg and J.B. Malherbe, 1996 Conference on Optoelectronic and Microelectronic Materials and Devices Proceedings, (Ed. C. Jagadish) IEEE, Piscataway, NJ (USA) 1997.
19. S.D. Brotherton and P. Bradley, J. Appl. Phys. **53**, 5720 (1982).
20. J.R. Troxell, Solid-State Electronics **26**, 539 (1983).
21. P.N.K. Deenapanray, F.D. Auret, G. Myburg , J.B. Malherbe and M.C. Ridgway, unpublished.
22. J.A. Davies, MRS Bulletin **26** (June 1992).
23. D.A. Thompson and R.S. Walker, Rad. Effects **36**, 91 (1978).

Materials Science Forum Vols. 258-263 (1997) pp. 571-574
© 1997 Trans Tech Publications, Switzerland

FANO RESONANCE IN A VIBRONIC SIDEBAND IN SILICON

Joanne Gower, Gordon Davies and E.C. Lightowlers
Physics Department, King's College London, Strand, London WC2R 2LS, U.K.

Keywords: Fano resonance, silicon, uniaxial stress

Abstract. We report here the existence of a novel Fano resonance in a luminescence band. The luminescence band has its zero phonon line at 991 meV and a vibronic continuum produced by coupling to a broad spectrum of lattice modes. The resonance is observed at 980 meV, in the part of the vibronic band involving low energy acoustic modes. We show here that the centre possesses trigonal symmetry, that the zero-phonon line is an E to A transition, and that the energy of the Fano resonance is pinned to only some components of the stress split zero-phonon line. Furthermore we show that the lineshape of the resonance can be modulated by uniaxial stresses along the 110 axis.

Introduction.

Fano resonances occur when a discrete state interacts with a continuum. In silicon Fano resonances are especially well known for the chalcogen donors [1], where the discrete state is an electronic state plus a well defined phonon, and the continuum is the electronic ionisation continuum. Here we report the presence of a novel Fano resonance in the vibronic sideband of the 991 meV defect (described by Pankove in [2]) in silicon. The resonance was of sufficient intensity to allow us to examine the effects of uniaxial stress perturbations on both the zero phonon transition and the resonance. These indicate that the centre possesses trigonal symmetry and that the resonance follows a similar behaviour to the zero phonon line, except intriguingly the lineshape of the resonance can be modulated by uniaxial stresses along the 110 axis.

Experimental.

The samples used in this study were mainly Czochralski (CZ) silicon with high concentrations of both carbon and oxygen, typically [C] ~ 2 x 10^{17} cm^{-3} and [O] ~ 10^{18} cm^{-3}. Samples were saturated with 1.5 x 10^{16} cm^{-3} H or D by heating in flowing gas for 30 minutes at 1300°C and rapidly cooling in silicone oil [3]. The samples were electron irradiated with a total flux of 2 x 10^{17} cm^{-3} 2 MeV electrons and then annealed for 30 minutes at a temperature ≥ 500 °C. Photoluminescence measurements were carried out on either a Nicolet 60SX or a Bomem DA3 Fourier transform spectrometer fitted with a North Coast cooled Ge diode detector with excitation by a 514 nm Ar^+ laser. Uniaxial stress measurements were made employing stresses of up to 0.16 GPa using 12 x 2 x 2 mm^3 X-ray oriented samples.

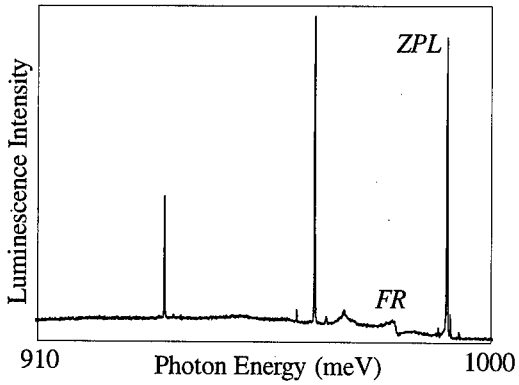


Figure 1. Typical spectrum of the 991 meV centre, the zero phonon line is marked ZPL and the resonance FR.

Figure 1 shows a typical spectrum, the centre has a zero phonon transition at 991 meV and is labelled ZPL. The resonance (FR) can very clearly be seen in the vibronic band.

Because of the considerable size of the resonance it was possible to use uniaxial stress perturbations to study the resonance as well as the zero-phonon line itself. The zero phonon line split into 2, 3 and 4 components when stress was applied along the (001), (111) and (110) directions respectively, significant thermalisation effects between the split components led to the assignment of trigonal symmetry to the centre and an E - A transition for the zero-phonon line. Figure 2 shows the stress fittings, the points are experimental data and the lines are the calculated fit using linear splitting coefficients [4]. Where $A_1 = 6.9$, $A_2 = -4.7$, $B = 9.2$ and $C = -10.0$ meV/GPa.

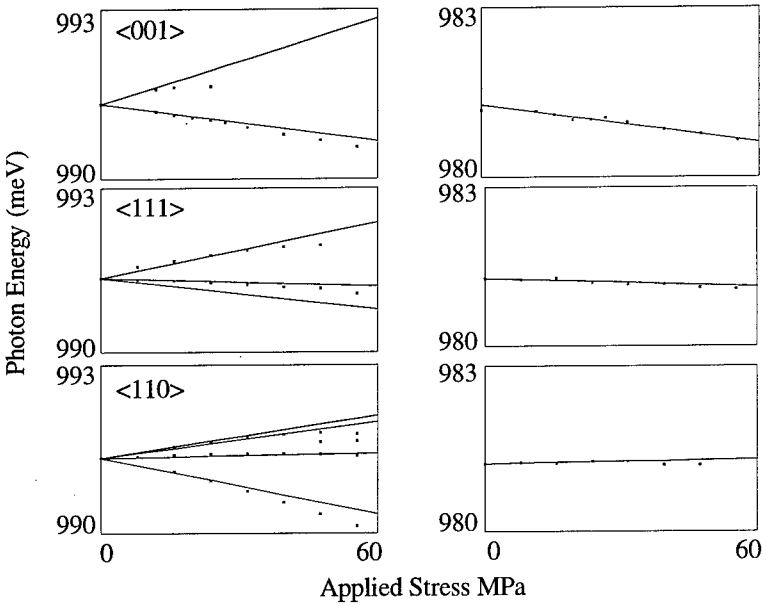


Figure 2. Energy of the 991 meV centre and Fano resonance as a function of applied stress. Points are experimental values, lines are calculated as described in the text. Left column is the stress dependence of the zero phonon transition while the right column is the resonance.

The energy shift of the resonance can be modelled using a single split component from the centre. These correspond to the $A_1 - 2B$, $A_1 + 2A_2$, and $A_1 + A_2 + C + B$ states in the (001), (111) and (110) directions. In the (111) direction this component corresponds to the orientationally degenerate state rather than the electronically degenerate states. The (110) uniaxial stress direction shows a modulation of the lineshape as the magnitude of the stress is increased (Fig. 3). It is interesting to note that this perturbation is also the only one that shifts the resonance to higher energy. Magnetic field perturbations (not discussed here) were also carried out, again shifting the resonance to lower energies and producing no lineshape modulation.

Discussion.

Often a Fano resonance is observed when a previously forbidden transition mixes with a continuum [1]. Exactly the same parameters used for the fitting of the uniaxial stress results can also be used to fit the shift of the resonance, implying that the discrete state is a feature of the 991 meV band rather than a separate centre. The phonon sidebands are expected to follow the zero-phonon line very closely under stress so that the continuum relative to the zero-phonon line is expected to be unchanged. Nevertheless changes in the fano lineshape are clearly occurring (Fig. 3) implying that the continuum and the discrete state (both components of the 991 meV band) are reacting differently to the 110 compression.

To describe the lineshape of the resonance we use the notation developed by Fano in [5], we describe a Hamiltonian, H, with matrix elements given by :-

$$\langle \varphi | H | \varphi \rangle = E_{\varphi}\,,\ \langle \psi_{E'} | H | \varphi \rangle = V_{E'}\,,\ \langle \psi_{E'} | H | \psi_{E} \rangle = E'\,\delta(E'-E')$$

where φ represents the discrete state and ψ_E the unperturbed continuum.

Fano's analysis leads to an expression for the lineshape L(E) of the resonance in terms of the transition probability between the initial state I and the modified continuum eigenstates Ψ_E, and I and the unperturbed continuum ψ_E (T is the transition operator):-

$$L(E) = \frac{\left|\langle \Psi_E | T | I \rangle\right|^2}{\left|\langle \psi_E | T | I \rangle\right|^2} = \frac{(q+\varepsilon)^2}{1+\varepsilon^2}$$

$\varepsilon = \dfrac{E - E_{\varphi} - F}{1/2\Gamma}$ is dependent on the energy , and width of the resonance, with $\Gamma=2\pi|V_E|^2$ indicating the spectral width of the discrete state φ. q is a parameter dependant on Φ the modified discrete state with $\dfrac{1}{2}\pi q^2 = \dfrac{\left|\langle \Phi | T | I \rangle\right|^2}{\left|\langle \psi_E | T | I \rangle\right|^2 \Gamma}$ being the ratio of the probabilities of transitions to the modified discrete state and an unperturbed continuum of band width Γ.

Figure 3 shows the modulation of the resonance lineshape as the applied stress is increased. The baseline shown in the left hand column has been subtracted and the resulting lineshape fitted. The lineshape is then shown in the right hand column. The difficulty in accurately determining the baseline and effects of broadening make results arising from this fitting ambiguous at least, but the change in the lineshape is obvious.

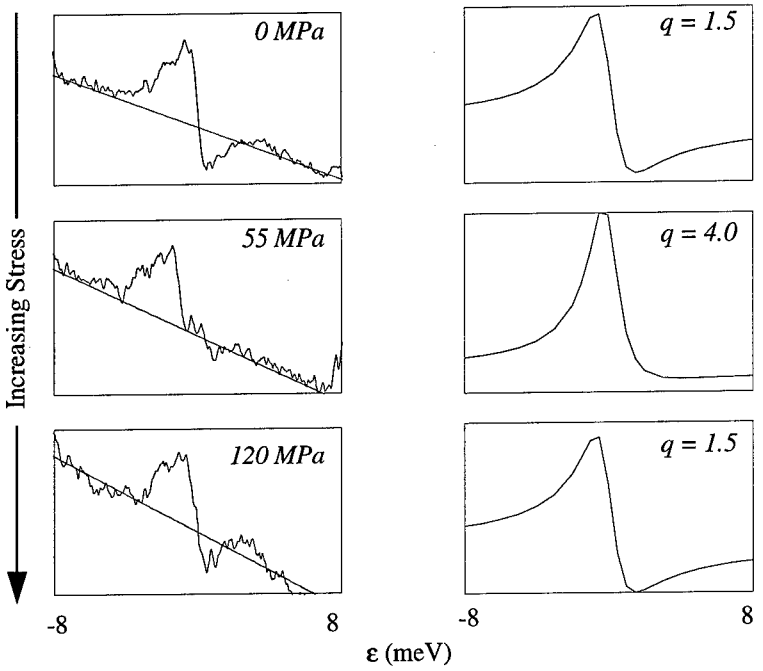


Figure 3 Modulation of the Fano resonance with increasing stress.

Conclusions

We have uniquely observed a Fano resonance in the vibronic band of a deep centre in silicon. We have shown that the centre possesses trigonal symmetry and that the resonance follows a similar shift pattern to the zero phonon transition when uniaxial stress is applied. We have also observed a modulation in lineshape of the resonance when uniaxial stress is applied along the 110 axis. A more in depth analysis of the defect centre and the origin of the resonance are needed to understand this modulation fully.

Acknowledgements

This work was supported by the EPSRC, and Joanne Gower thanks EPSRC for the provision of a research studentship.

References

[1] E. Janzén et al, Phys. Rev. B P8000, Vol 31, No 12 (1985)
[2] J.I. Pankove and C.P. Wu, Appl. Phys. Lett. P937, Vol 35, No 12 (1979)
[3] M. J. Binns et al, Semicond. Sci. Technol. P1908, 8 (1993)
[4] A.E. Hughes and W.A. Runciman, Proc. Phys. Soc. P827, Vol 90 (1967)
[5] U. Fano, Phys. Rev. P1866, Vol 124, No 6 (1961)

Materials Science Forum Vols. 258-263 (1997) pp. 575-580
© 1997 Trans Tech Publications, Switzerland

FRENKEL PAIRS AND IMPURITY-DEFECT INTERACTIONS IN p-TYPE SILICON IRRADIATED WITH FAST ELECTRONS AND GAMMA-RAYS AT LOW TEMPERATURES

V.V. Emtsev, U. Dedek[1], P. Ehrhart[1], P.D. Kervalishvili[2], M.A. Margaryan, D.S. Poloskin, and H. Zillgen[1]
Ioffe Physicotechnical Institute, 194021 St.Petersburg, RUSSIA
[1]Institut für Festkörperforschung, Forschungszentrum Jülich GmbH, D-52425 Jülich, GERMANY
[2]Institute for Stable Isotopes, 380000 Tbilisi, GEORGIA

Keywords: silicon, shallow acceptors, irradiation, electrical measurements

Abstract. Investigations of defect production and annealing in moderately and heavily doped p-Si subjected to low-temperature electron irradiation at 2.5 MeV have been made. Removal rates of charge carriers were found to be about 2 cm^{-1} over the doping range studied. Recovery of the charge carrier concentration is not significant after annealing at room temperature. Substantial annealing of defects responsible for carrier removal takes place at temperatures higher than 600 K. However, recovery of the hole mobility displays puzzling behaviour. Data on removal rates of charge carriers in lightly doped p-Si subjected to low-temperature gamma-irradiation suggest that electronic excitation conditions during irradiation can strongly affect defect formation processes.

Introduction

Fast electron irradiation of Si at cryogenic temperatures is widely used as a tool for production of intrinsic defects. In most studies of defects in Si, lightly and moderately doped materials with impurity concentrations less than $10^{17}cm^{-3}$ have been treated. Until recently, radiation effects in degenerate Si were remaining in the shade. To our knowledge, there are several papers [1-3] (see also a few references therein] devoted to this question in the past. However, investigations of defect interactions in degenerate Si in the presence of impurity traps of one kind may highlight some important features of the defect behaviour. Actually, the recent X-ray measurements on lightly and heavily doped Si after low-temperature electron irradiation and annealing [4,5] revealed new facts relating to the fate of Frenkel pairs and formation of defect clusters. The present work is aimed at investigating the electrical properties of moderately and heavily doped p-Si after electron irradiation at cryogenic temperatures and subsequent annealing. We also report some data on removal rates of charge carriers in lightly doped p-Si under low and high excitation conditions during gamma-irradiation at 78 K. It has been known that electronic excitation can exert strong effects on many properties of defects in Si, among them thermal stability, activation energies for diffusion and so on; see for instance [6,7]. This question is of particular interest for lightly doped materials with impurity concentrations less than $1 \cdot 10^{17}$ cm^{-3}, as the excitation conditions during electron irradiation at $T \leq 20$ K can be low or high, depending upon irradiation temperature, electron energies, beam current etc. For the present gamma-ray irradiation we can realize low excitation conditions for B and Ga *vs* high, excitation conditions for In due to the different ionization energies of these dopants.

Experimental

Czochralski-grown Si with B, Ga, and In impurities were used. For low-temperature electron irradiation the samples were cut from heavily doped Si:B (about $6 \cdot 10^{18}cm^{-3}$, and $3 \cdot 10^{19}cm^{-3}$). Besides, some moderately doped samples of Si:B and Si:Ga (about $8 \cdot 10^{17}cm^{-3}$) were also investigated. For low-temperature gamma-irradiation the samples were cut from lightly doped Si:B, Si:Ga, and Si:In and the impurity concentrations were about $1 \cdot 10^{15}cm^{-3}$.

Electron irradiation experiments were conducted at the low-temperature irradiation facility in Jülich [8]. The current densities of 2.5 MeV electrons were in the range of 1 $\mu A/cm^2$ to 15 μA / cm^2. In the

course of irradiation at T=4.7 K the samples were immersed in a stream of liquid helium. Conductivity and Hall effect measurements were taken *in situ* at T=4.2 K by means of the Van der Pauw technique.

Gamma-irradiation experiments were conducted at a ^{60}Co gamma-ray facility. The dose rate was $3\cdot10^{12}cm^{-2}\cdot s^{-1}$. The samples were placed in a container for gamma-irradiation at T=78 K. After irradiation the container was transferred at T= 78 K into another cryostat for electrical measurements over the temperature range of 20 K to 300 K. All measurements were carried out in the dark. Finally, we would like to recall that under ^{60}Co gamma-irradiation Frenkel pairs are produced in Si mostly by the Compton electrons whose average energy is about 0.6 MeV [9].

Results and Discussion

Defect production under electron irradiation at T=4.7 K

For the samples Si:B we used, the hole concentration before irradiation was in the range of $2\cdot10^{19}$ cm^{-3} to $3\cdot10^{19}$ cm^{-3}. The hole mobility at room temperature was close to 50 $cm^2/(V\cdot s)$. This value agrees well with the literature data available; see for instance [10].

At the beginning of irradiation the conductivity varies directly with dose; see curve 1 in Fig. 1. At doses larger than $\Phi=6\cdot10^{18}cm^{-2}$, there are pronounced departures from linearity due to increasing compensation of the acceptor states of boron. It is widely believed that small conductivity changes over a linear region can be converted into concentration changes for estimating removal rates if the charge carrier mobility remains unaffected by radiation-induced defects. At first sight, the latter assumption seems to be valid, as the hole mobility in degenerate Si:B turned out to be nearly constant, within 4 per cent, over the doping range of $2\cdot10^{19}cm^{-3}$ to $4\cdot10^{19}cm^{-3}$ [10]. In doing so, one can evaluate a removal rate of (4.5±0.5) cm^{-1} which is in line with those reported previously [11]. Moreover, Figure 2 provides conclusive evidence that this rate η is independent of current density. However, the Hall effect data clearly show that the actual rate is smaller by a factor of two; cf curves 1 and 2 in Fig.1. This difference in η stems from the marked changes in the hole mobility upon irradiation; see curve 3 in Fig. 1. It means that the radiation-induced defects are more effective in the charge carrier scattering than ionized substitutional boron atoms B_s^-.

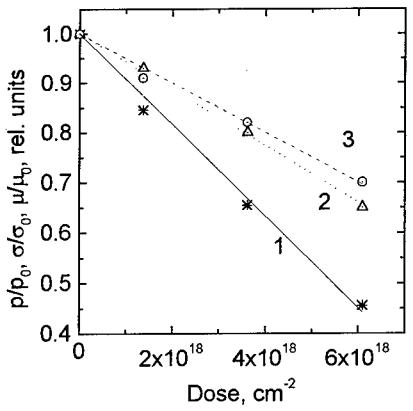


Fig. 1. Relative changes in conductivity (curve 1), charge carrier concentration (curve 2) and mobility (curve 3) *vs* dose for degenerate Si:B subjected to electron irradiation at T= 4.7 K.

Two questions are important for our understanding of what is going on under irradiation: how to estimate the production rate of Frenkel pairs and what kind of defects may be responsible for the strong scattering? Let us proceed from the Watkins model of defect production in moderately doped p-Si [12]. Frenkel pairs produced as primary defects during electron irradiation are believed to be unstable, since self-interstitials Si_i, most likely positively charged, are claimed to be mobile even at T≤ 20 K, at least under electronic excitation conditions. The mobile self-interstitials can be trapped at substitutional boron atoms giving rise to a bound interstitial configuration, or shorter B_i. The appearance of spatially separated isolated vacancies V^{2+} and interstitial boron atoms B_i^+ was evidenced by EPR in their metastable charge states V^+ and B_i^0 under illumination[12]. Assuming this model for the electrically active defects, we can convert the observed removal rate into the production rate of Frenkel pairs being about 0.5 cm^{-1}. By comparison, the production rate quoted in [12] for 1.5 MeV electron irradiation is about 0.03 cm^{-1}. However, the expected value for electron irradiation at 2.5 MeV is in the range of 1 cm^{-1} to 2 cm^{-1} assuming that the threshold energy for

atomic displacement in Si lies in the interval of 40 eV to 20 eV. It should be noted that the production rate of Frenkel pairs close to the expected one has been obtained very recently in [5] using the data of X-ray measurements on the same Si:B irradiated at T=4.7 K. It is felt that only a fraction of the Frenkel pairs produced can be separated under irradiation. Among the defects considered, vacancies V^{2+} and close (not separated) Frenkel pairs may be responsible for the strong scattering of charge carriers in degenerate Si:B subjected to electron irradiation. Another interesting observation is that the removal rates of charge carriers in Si:B turned out to be nearly the same in the doping range of $6\cdot10^{18}$cm^{-3} to $3\cdot10^{19}$ cm^{-3}. Moreover, this range may be expanded down to about $8\cdot10^{17}$cm^{-3} if one takes a look at moderately doped Si:B and Si: Ga. For p-Si with impurity concentrations less than $1\cdot10^{18}$cm^{-3}, it is impossible to take electrical measurements at T=4.2 K. However, one can estimate removal rates relying on the data obtained after low-temperature irradiation and subsequent annealing at room temperature, as the recovery fraction at T≤ 300 K is less than 20 per cent; see below.

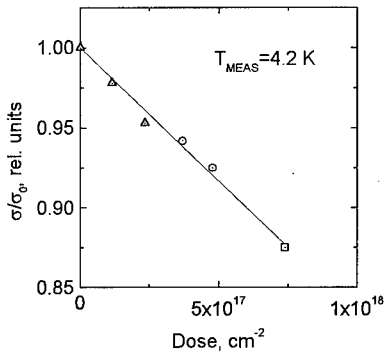


Fig. 2. Relative changes in conductivity *vs* dose for degenerate Si:B subjected to low-temperature electron irradiation at different current densities of the electron beam. Current density: 7 μA/cm^2 (triangles), 15 μA/cm^2 (circles), 1 μA/cm^2 (squares).

Defect annealing after electron irradiation at T= 4.7 K

Annealing of radiation-induced defects in the Si doped with boron displays two stages upon warming-up to room temperature, at T≈ 200 K and T≈ 300 K. As an illustration, Figure 3 shows the annealing curves for two degenerate samples of Si:B irradiated with 1 MeV taken from [11] and 2.5 MeV electrons. In all cases there are relatively small changes in conductivity after the annealing at room temperature, not exceeding 20 per cent. Interestingly, we observed no recovery in the case of Si:Ga at T≤ 300 K.

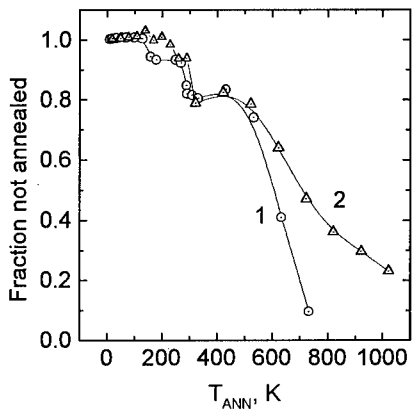


Fig. 3. Annealing of defects in degenerate Si:B after electron irradiation at 4.7 K. Electron energy: 1 MeV, curve 1; 2.5 MeV, curve 2. Dose: $\Phi=6\cdot10^{18}$cm^{-2}, curve 1; $\Phi=2\cdot10^{18}$cm^{-2}, curve 2.

Referring to the Watkins model [12] we think that the observed changes do not reflect the main annealing processes taking place at the above stages. Actually, one couldn't expect substantial recovery of the charge carrier concentration taking into account that the vacancies V^{2+} which are mobile at T≈ 200 K [12] should be trapped at B_s^-, whereas the interstitial boron atoms B_i^+ which are mobile at T≈ 300 K [13] could pair with B_s^-. The latter complex $[B_s^-B_i^+]$ is reportedly stable at least up to T≈ 700 K [14]. Evidently, both reactions result in additional loss of the acceptor states of substitutional boron atoms. Besides, the complex $[VB_s]$ may be positively charged in p-Si [15]. Therefore, this way of annealing couldn't release holes into the valence band. It is felt that the observed recovery at the above stages is a side effect due to trapping of V^{2+} and B_i^+ at other sinks like oxygen, divacancies etc.

Let us now discuss the annealing process above room temperature. For all the irradiated samples, pronounced recovery of the charge carrier concentration starts at T≈ 600 K. It is instructive to follow the annealing behaviour of degenerate Si:B for which prolonged electron irradiation at T= 4.7 K

results in concentrations of Frenkel pairs close to the initial concentration of boron. Similar samples have been investigated in [4,5] by means of X-ray measurements on the lattice spacing as well as the Huang Diffuse Scattering. The data obtained for degenerate Si:B after heavy irradiation at T= 4.7 K and subsequent annealing at room temperature point to the fact that the low-temperature defects responsible for strong changes of the Huang Diffuse Scattering die out at T≈ 300 K, whereas some structural modifications of boron-related complexes lead to a pronounced increase in the lattice spacing. The latter is consistent with the data on thermal instability of both boron-related defects B_i and $[VB_s]$ at room temperature [13,15], so one has to deal with other boron-related complexes formed at T≈ 300 K, e g $[B_s^- B_i^+]$ pairs.

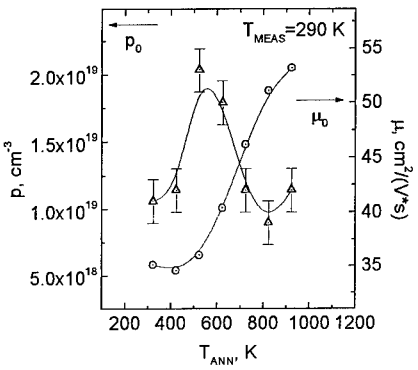


Fig. 4. High-temperature annealing of degenerate Si:B after electron irradiation at 4.7 K. Dose: Φ=1.8·10^{19}cm^{-2}. Concentration of charge carriers, circles; mobility of charge carriers, triangles. Initial concentration and mobility of charge carriers are also shown.

The electrical data obtained on heavily irradiated samples revealed some peculiar features of the defect annealing above room temperature; see Fig. 4. Just after the electron irradiation the samples displayed very low conductivity at T= 4.2 K. In the course of annealing at T≤ 300 K the hole concentration increased by about 20 percent. As is seen from Fig. 4, with increasing temperature the hole mobility appears to be completely restored at T≈ 500 K, whereas the charge carrier concentration shows little changes. In stark contrast, at elevated temperatures the charge carrier concentration gradually recovers against the background of decreasing mobility. It should be pointed out that qualitatively similar changes in the hole concentration and mobility are also observed for the same Si:B irradiated at much smaller doses (Φ≈2·10^{18}cm^{-2}). This puzzling behaviour of defects upon annealing calls for further investigation.

Defect production under gamma-irradiation at T= 78 K

For lightly doped Si:B, Si:Ga, and Si:In, complete electrical measurements (conductivity and Hall effect) were taken over the temperature range of 15 K to 300 K. Analysis of these data with the help of relevant electroneutrality equations [16] makes it possible to evaluate the concentrations of shallow acceptors, N_A, and compensating donors, N_D, in a separate way; see for instance [17]. The initial concentrations of group-III acceptors were about 1·10^{15}cm^{-3}. The compensation ratio K= N_D / N_A was very low for all samples, not exceeding a few per cent. The ionization energies of group-III acceptor states found for the initial materials (45 meV, 73 meV and 153 meV for B, Ga, and In, respectively) agree well with the literature data; see for instance [10].

The concentrations of oxygen and carbon in the lightly doped p-Si are much higher than the concentration of shallow acceptors, at least by an order-of-magnitude. Because of this interactions of group-III impurity atoms with intrinsic defects are expected to be suppressed and compensation effects due to radiation-induced donors become most important. By way of illustration, Fig. 5 and Fig. 6 depict the hole concentration *vs* temperature for two samples of Si:Ga and Si:In before and after gamma-irradiation at T= 78 K. After irradiation the electrical measurements could be conducted up to T= 150 K, as the first annealing stage is centered at T≈ 180 K. The data obtained make it possible to trace all changes in the compensation ratio. In all cases the compensation progressively increases with increasing dose; see Fig. 7. However, the rate of compensation for Si:In turned out to be larger by a factor of seven than those for Si:B and Si:Ga. Based on these data one can evaluate the corresponding production rates of radiation-induced donors being about 7·10^{-4} cm^{-1} *vs* 1·10^{-4} cm^{-1} for Si:In *vs* Si:B and Si:Ga. This striking difference in the production rates is thought to be due to different excitation conditions under irradiation which, in turn, may change the fraction of Frenkel pairs subjected to separation (and as a consequence may also change the electrical properties); for

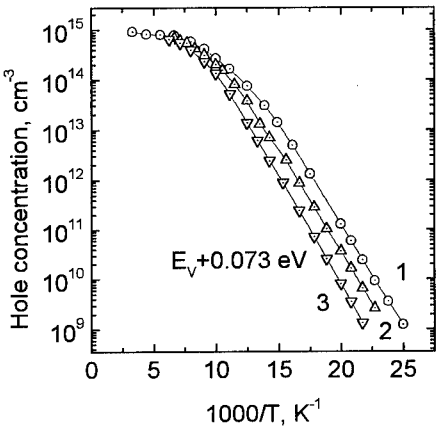


Fig. 5. Charge carrier concentration *vs* temperature for Si:Ga before and after gamma-irradiation at 78 K. Dose: Φ=0, curve 1; Φ=1.1·10^{18}cm^{-2}, curve 2; Φ=2·10^{18}cm^{-2}, curve 3. Points, experimental; curves, calculated.

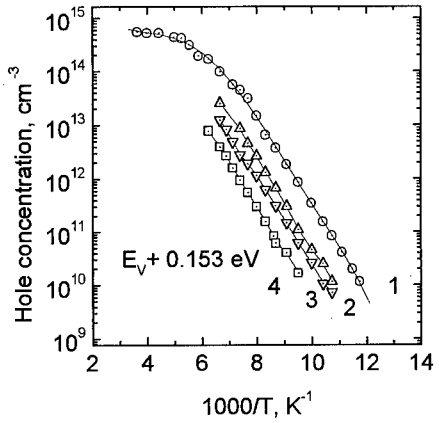


Fig. 6. Charge carrier concentration *vs* temperature for Si:In before and after gamma-irradiation at 78 K. Dose: Φ=0, curve 1; Φ=3.4·10^{17}cm^{-2}, curve 2; Φ=4.8·10^{17}cm^{-2}, curve 3, Φ=4.8·10^{17}cm^{-2}, curve 4. Points, experimental; curves, calculated.

^{60}Co gamma-rays the calculated production rate of Frenkel pairs equals 1.3·10^{-3} cm^{-1} [9] assuming that the threshold energy is about 40 eV.

Let us examine the relation between the equilibrium concentration of holes at the irradiation temperature, p_0, and the concentration of excess charge carriers, Δp (Δn), due to ionization of Si by gamma-rays in more detail. As seen from Fig. 5 and Fig. 6, p_0 is of order of 10^{13}cm^{-3} and 10^{9}cm^{-3} for the Si:Ga and Si:In, respectively. For the Si:B, it is even higher than that in the Si:Ga because the ionization energy of boron is smaller. Measurements of the photocurrent generated by gamma-rays in the Si:In at T= 78 K allows us to estimate Δp (Δn) being in the range of 10^{11}cm^{-3} to 10^{12}cm^{-3}. Evidently, the defect formation in the Si:B and Si:Ga takes place under low excitation conditions, p_0 >> Δp (Δn). By contrast, the excitation conditions for the Si:In are opposite, Δp (Δn) >> p_0. In addition, it might be important to point out that with increasing irradiation temperature to T≈ 300 K the excitation conditions are getting similar for all the samples and the removal rates show no significant difference any longer, being ~ 5·10^{-5} cm^{-1}.

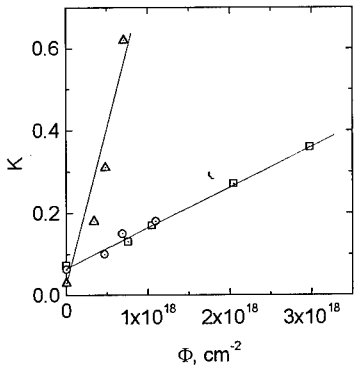


Fig. 7. Compensation ratio N_D/N_A *vs* dose for Si:B (squares), Si:Ga (circles), and Si:In (triangles) subjected to gamma-irradiation at 78 K.

Conclusions

First of all, the present study of defect production in moderately and heavily doped p-Si due to 2.5 MeV electron irradiation at T= 4.7 K provides insight into the properties of defects making their appearance at this low temperature. The removal rate of charge carriers turned out to be nearly constant, about 2 cm^{-1}, over a wide range of impurity concentrations. Strong changes in the hole mobility after irradiation point to the fact that the defects formed during low-temperature irradiation are very effective scattering centers. Analysis of the relevant information on defect production in Si at cryogenic temperatures allows us to conclude that a large fraction of Frenkel pairs is not subjected to separation. Most likely, these frozen-in primary defects are responsible for marked changes in the

Huang Diffuse Scattering of X-rays. They may also be responsible for the observed scattering of holes. The charge carrier concentration and mobility are recovered in different ways upon annealing above room temperature. The mobility was found to be sensitive to defect transformations. The role of electronic excitation in the defect production for lightly doped p-Si under gamma-irradiation has been evidenced. Switching the excitation conditions from low to high one can strongly modify the formation rate of electrically active defects.

A plausible model of the defect production should be based on the concept of Frenkel pairs. Tightly bound pairs (close Frenkel pairs) seem to show no electrical activity related to some energy states in the bandgap. Their presence in Si after low-temperature irradiation can be detected by some specific techniques sensitive to disturbance of the lattice, e g measurements of the Huang Diffuse Scattering and the lattice spacing. Loosely bound Frenkel pairs with a larger distance between the constituent defects introduce energy levels into the bandgap and can be separated under appropriate conditions. The separation process should depend on charge states of the defects which, in turn, are dependent on electronic excitation under irradiation. The self-interstitials in these loosely bound pairs can be mobile at cryogenic temperature, at least under irradiation. If separated they interact with impurities and can be traced in this way. In such a situation, the disappearance of the characteristic X-ray scattering at $T \leq 300$ K may be attributed to the annealing of close Frenkel pairs.

Acknowledgements

One author (V.V.E.) is deeply indebted to the Deutsche Forschungsgemeinschaft (DFG) for financial support of his visit to Germany. The work was partly supported by the Deutscher Akademischer Austauschdienst (DAAD).

References

1. L.L. Sivo and E.E. Klontz, Phys.Rev. **178**, 1264 (1969).
2. J.F. Angress, A.R. Goodwin, and S.D. Smith, Proc. R. Soc. A **64** (1965).
3. A.R. Bean, S.R. Morrison, R.C. Newman, and R.S. Smith, J. Phys. C **5**, 379 (1972).
4. St. Bausch, H. Zillgen, and P. Ehrhart in *Mater.Sci.Forum*, Vols **196-201**, eds M. Suezawa and H. Katayama-Yoshida (Switzerland-Germany-UK-USA: Trans Tech Publications) pp. 1141-1146 (1995).
5. P. Ehrhart and H. Zillgen in *MRS Symp.Proc.*, Vol. **469**, eds S. Coffa, T. Diaz de la Rubia, C.S. Rafferty, and P.A. Stolk (Pittsburgh, Pennsylvania: MRS) (1997), in print.
6. L.C. Kimerling in *Defects and Radiation Effects in Semiconductors, 1978*, Conf. Ser. No 46 (Bristol and London: The Institute of Physics) , pp. 56-73 (1971).
7. J.R. Troxell, A.P. Jatterjee, G.D. Watkins, and L.C. Kimerling, Phys. Rev. B **19**, 5336 (1979).
8. J. Hemmerich, W. Sassin, and W. Schilling, Z.Angew.Phys.**29**, 1 (1970).
9. O.S. Oen and D.K. Holmes, J. Appl. Phys. **30**, 1289 (1959).
10. *Semiconductor Parameters*, Vol. **1**, eds M. Levishtein, S. Rumyantsev, and M. Shur (Singapore-New Jersey-London-Hong Kong) (1996).
11. P. Ehrhart, V.V. Emtsev, D.S. Poloskin, and H. Zillgen in *Mater.Sci.Forum*, Vols **196-201**, eds M. Suezawa and H. Katayama-Yoshida (Switzerland-Germany-UK-USA: Trans Tech Publications), pp.151-156 (1995).
12. G.D. Watkins in *Lattice Defects in Semiconductors, 1974*, Conf. Ser. No 23 (London and Bristol: The Institute of Physics), pp. 1-22 (1975).
13. J.R. Troxell and G.D. Watkins, Phys. Rev. B **22**, 921 (1980).
14. L.C. Kimerling, M.T. Asom, J.L. Benton, P.J. Drevinsky, and C.E. Caefer in Mater.Sci.Forum, Vols **38-41**,ed. G. Ferenczi (Switzerland-Germany-UK-USA: Trans Tech Publications) pp.141-150 (1989).
15. G.D. Watkins , Phys. Rev. B **13**, 2511 (1976).
16. J.S.Blakemore, *Semiconductor Statistics* (New York: Pergamon Press) (1962).
17. K. Geim, G. Pensl, and M. Schulz, Appl. Phys. (Springer) A **27**, 71 (1982).

Materials Science Forum Vols. 258-263 (1997) pp. 581-586
© 1997 Trans Tech Publications, Switzerland

IMPURITY-VACANCY COMPLEXES FORMED BY ELECTRON IRRADIATION OF CZOCHRALSKI SILICON

V. Avalos and S. Dannefaer
Department of Physics
University of Winnipeg
Winnipeg, MB, Canada R3B 2E9

Keywords: Silicon, irradiation damage, positron annihilation

Abstract.

A positron annihilation study of electron irradiated Cz-Si has been conducted on eight samples ranging from heavily doped n-type to heavily doped p-type. The influence from dopants was investigated as well as that arising from oxygen by comparison with undoped float-zone silicon. High dopant concentrations ($\geq 5 \times 10^{17}/cm^3$), either P or Sb, cause a high introduction rate of P·V_2 or Sb·V complexes in the order of 1 cm^{-1}. Oxygen modestly increases the introduction rate of free divacancies by a factor of 2.

Introduction.

Irradiation of silicon leads to the formation of vacancies and interstitials. At room temperature these fundamental defects are highly mobile and many will recombine but some will remain by forming complexes with impurities such as dopants or oxygen. Divacancies may also be formed by migrating monovacancies as well as directly by the irradiation and they are immobile at room temperature. Numerous studies have been conducted to elucidate the character of complexes, but the majority deals with vacancy associated complexes (divacancies[1,2], P·monovacancy[3], B·monovacancy[4,5] and O·multivacancy[6]) whereas only one form of pure interstitials (the di-interstitial[7]) and one form of carbon-interstitial complex[8] have been reported on.

In this work we have employed positron annihilation (and in a few cases Fourier transform infrared spectroscopy) to investigate vacancies formed by electron irradiation, taking advantage of the fact that highly doped materials can also be investigated by positron annihilation. The aim is mainly to assess the influence from doping on vacancy production by comparing results for variously doped samples irradiated under identical conditions. We have employed positron lifetime spectroscopy which is forceful in distinguishing between different vacancy sizes. One main finding from this work is that dopants at high concentrations enhance significantly the concentration of vacancies by reducing recombination with interstitials and that dopant-vacancy complexes dominate in such materials.

Experimental.

a: Samples

The samples were cut from Czochralski-grown wafers (Cz-Si) doped as listed in Table I.

Table I. Sample Characteristics. For easy identification of dopant concentration the number in the sample codes reflects the impurity concentration.

Sample code	Dopant & Type	Impurities/cm^3	Resistivity Ω-cm
P4	P(n)	5×10^{18}	0.01
P3	P(n)	5×10^{17}	0.1-0.2
P2	P(n)	5×10^{16}	1-2
P1	P(n)	2×10^{16}	3
Sb4	Sb(n)	1×10^{18}	0.01
B4	B(p)	5×10^{18}	0.01
B3	B(p)	5×10^{17}	0.1
B0	B(p)	4×10^{14}	100
Fz	none		~2000

The letter(s) in the codes for each sample signifies the dopant type while the number indicates, on a scale 0–4, increasing dopant concentrations. These codes will be used in figures displaying the results. The samples were in the form of bars of dimensions 4 × 0.5 × 30 mm^3 and were irradiated along the long axis with 10 MeV electrons using a pulsed beam (240 pulses/s each of 3 ms duration) with an average current density of 4.5μA/cm^2. The dose at the beam-facing end of the samples was 1.2×10^{18}e$^-$/cm^2. The samples were irradiated simultaneously and were cooled by water at 8°C and were spaced by 1/2 mm to allow for free water flow. After irradiation the samples were stored at −18°C until commencement of the positron measurements.

b: Positron Annihilation

When vacancies trap positrons their lifetime is increased relative to the bulk value (i.e. that for non-trapped positrons) due to the smaller average electron density which is what makes possible the observation of vacancies by means of positron annihilation. The trapping rate of the positrons is proportional to the vacancy concentration according to

$$\kappa = \mu \cdot C_V, \tag{1}$$

where μ is the absolute specific trapping rate (ns^{-1}cm^3) and C_V is the vacancy concentration (cm^{-3}). The absolute trapping rate is strongly temperature dependent for negatively charged vacancies (large at low temperatures) while essentially temperature independent for neutral vacancies. For positively charged vacancies (or complexes) the specific trapping rate is estimated to be 1/10 (or less) of that for neutral defects (due to coulomb repulsion) and increases with temperature; these are very helpful features in assessing the charge state of free vacancies (or vacancy-impurity complexes).

Results.

All the unirradiated samples showed a small contribution from grown-in vacancy clusters giving a trapping rate of only ~ 0.1 ns^{-1}. The lifetime was 400-450 ps.

Lifetime results for the n type irradiated samples are shown in Fig. 1.

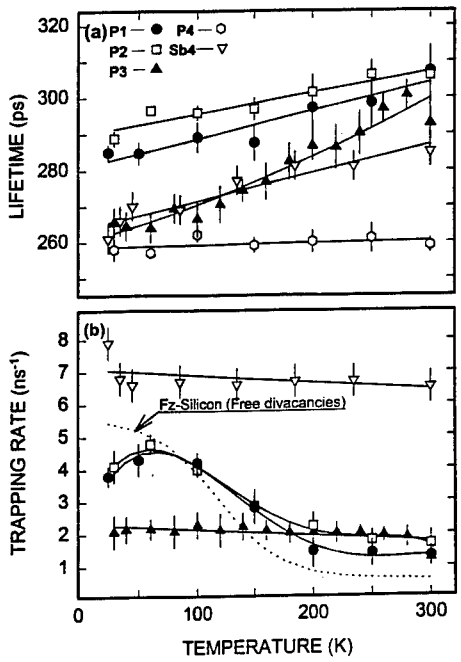


Fig. 1. Irradiation-produced positron lifetimes and trapping rates for n type materials as a function of sample temperature. The sample codes are those listed in Table I. The broken curve in panel (b) is for Fz-Si, From Ref. 9. The trapping rate for the P4 was too high to be calculable.

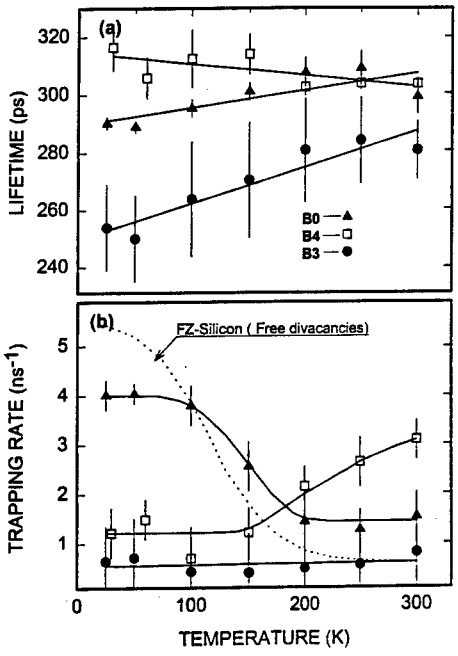


Fig. 2. Irradiation-produced positron lifetimes and trapping rates for p type materials. In panel (b) the broken curve shows the results for Fz-Si (Ref. 9).

These samples were cut from the front end of the bars (and hence irradiated with 10 MeV electrons to the dose of $1.2 \times 10^{18}/\text{cm}^2$). In this figure as well as in Fig. 2 we show, for the sake of brevity, only the important irradiation-produced lifetime τ and its associated trapping rate.

The samples show quite different temperature dependencies. For the two lightly P doped samples (P1 and P2) τ increases little with temperature while κ decreases strongly which are characteristics very similar to those observed in electron irradiated oxygen-free undoped Si (Fz-Si), where they were shown to arise from trapping by negatively charged divacancies[9].

For the P3 sample τ increases with temperature whereas the trapping rate is essentially constant (at 2 ns^{-1}). The lifetimes cover the range between monovacancies ($\sim$270 ps) and divacancies ($\simeq$300 ps).

For the highly P doped P4 sample, τ is constant (at 260 ± 3 ps), but the trapping rate cannot be calculated because of its high value. However, from other positron measurements (Doppler broadening) we can estimate a trapping rate of about 45 ns^{-1}.

Turning to the results for the p type material, Fig. 2 depicts lifetime results for the boron doped materials.

The data for the lightly doped sample (BO) are very similar to those for the lightly doped P1 and P2 samples (and the Fz-Si sample). The medium doped B3 sample has a small trapping rate (0.7 ns^{-1}), which makes the determination of the lifetime rather uncertain. The highly doped B4 sample is unique in showing a trapping rate which *increases* with temperature above 150 K.

Discussion.

The temperature dependence of the trapping rates as well as the lifetime values for the P1, P2 and BO samples are similar to that for undoped Fz-Si for which reason we ascribe the trapping arising from free negatively charged divacancies. The difference observed between the trapping rates for the Cz-Si and the Fz-Si is probably caused by A centers which at low temperatures causes a change in the Fermi level so that some of the divacancies become neutral. The presence of oxygen increases the concentration of divacancies by a factor of $\simeq$2 above 200 K which indicates that interstitials can be trapped by oxygen or oxygen clusters. The doping concentrations in the P1, P2 and BO samples have no detectable influence on the positron data, but the highly doped P3 and Sb4 samples show completely different responses.

The trapping rates are temperature independent but the lifetime varies between 265 and 295 ps.

Thus we conclude that free divacancy formation is significantly suppressed in these samples being replaced by P (or Sb) divacancy complexes. The variation in lifetime suggests that these complexes either have temperature dependent configurations or that the positron "favours" at low temperature only one of the vacancies in the complex. The introduction rate in P3 of these complexes corresponds to $\simeq$ 0.4 cm^{-1}; for the Sb doped sample the introduction rate is $\simeq$ 1 cm^{-1}.

For the P4 sample only a monovacancy response could be found. This is explained by noting that the high P concentration relative to the introduced amount of vacancies will cause trapping by only monovacancies. A maximum introduction rate of 4 cm^{-1} can be estimated in this case.

The positron data for the B3 sample indicate trapping by neutral divacancies (the neutral state was verified by optical measurements). The introduction rate was $\sim$ 0.08 cm^{-1}. For the B4 sample it is important first to note that due to the large B concentration the holes will screen charged states of vacancies or complexes. The constant trapping rate up to 150 K is thus

explained to arise from screened positively charged free divacancies, and the increase above that temperature is interpreted to arise from thermally activated trapping by $B \cdot V_2$ complexes. A similar effect was observed in InP[10] where the thermal activation was suggested to arise from a difference in the complex coordiantion as caused by the presence or not of the positron at the complex.

Conclusion.

Positron annihilation experiments have shown that $P \cdot V_2$ and $B \cdot V_2$ complexes are formed in electron irradiated Cz-Si. For high doping concentrations the introduction rates for the various complexes can be as large as 1–4 cm^{-1}.

References.

1. G.D. Watkins and J.W. Corbett. Phys. Rev. 138A, 543 (1965).
2. J.W. Corbett and G.D. Watkins. Phys. Rev. 138A, 555 (1965).
3. E.G. Sieverts, S.H. Muller and C.A.J. Ammerlaan. Solid St. Commun. **28**, 221 (1978).
4. G.D. Watkins. Phys. Rev. B**13**, 2511 (1976).
5. M. Sprenger, R. van Kemp, E.G. Sieverts and C.A.J. Ammerlaan. Phys. Rev. B**35**, 1582 (1987).
6. Young-Hoon Lee and J.W. Corbett. Phys. Rev. B**13**, 2653 (1976).
7. Young-Hoon Lee, N.N. Gerasimenko and J.W. Corbett. Phys. Rev. B**14**, 4506 (1976).
8. H.J. Stein. Radiation Effects **22**, 169 (1974).
9. V. Avalos and S. Dannefaer. Phys. Rev. B**54**, 1724 (1996).
10. T. Bretagnon, S. Dannefaer and D. Kerr. J. Appl. Phys. **81**, 3446 (1997).

Materials Science Forum Vols. 258-263 (1997) pp. 587-592
© 1997 Trans Tech Publications, Switzerland

LUMINESCENCE CENTERS IN HIGH-ENERGY ION-IMPLANTED SILICON

Koichi Terashima, Taeko Ikarashi, Masahito Watanabe[1], and Tomohisa Kitano[2]

Silicon Systems Research Laboratories, NEC Corporation,
34 Miyukigaoka, Tsukuba 305, JAPAN
[1]Fundamental Research Laboratories, NEC Corporation,
34 Miyukigaoka, Tsukuba 305, JAPAN
[2]ULSI Device Development Laboratories, NEC Corporation,
1120 Shimokuzawa, Sagamihara 229, JAPAN

Keywords: photoluminescence, silicon, ion implantation, Cu contamination, point defect

Abstract. We have observed luminescence lines at 0.992 eV and at 1.097 eV in Si implanted with 300 keV B^+ or 700 keV P^+ to a dose of $2x10^{13}$ cm^{-2}. These lines appear after thermal annealing in both the B-implanted and the P-implanted samples. The formation of the 0.992 eV center is strongly affected by the annealing atmosphere and the Cu contamination while that of the 1.097 eV center is not affected. The 0.992 eV line appears only after annealing in vacuum. If there is no Cu contamination in the vacuum, this line appears after annealing at 500 - 600℃. However, if there is Cu contamination in the vacuum, it appears over a wider annealing range of 300 - 600℃. The 1.097 eV line is observed in the samples annealed at 300 - 400℃ and depends on neither the annealing atmosphere nor the Cu contamination. We believe these lines are due to the different types of point defect clusters. The annealing behavior of the PL spectra suggests a strong correlation between the 0.992 eV center and the I1 center.

Introduction

In recent Si ULSI technologies, high-energy (several hundred keV) ion implantation has been used in the device fabrication processes [1]. During the ion implantation and the following thermal annealing, various defects are induced in Si substrates and these defects might interact with other defects and impurities. One of the most important problems is the interaction with transition-metals because the damaged layer induced by the ion implantation may act as a gettering site for metallic impurities [2]. However, fundamental properties of these process-induced defects, especially their interaction with other defects and impurities, are not well understood.

Photoluminescence (PL) is a powerful method for investigating defects in semiconductors and various PL lines such as I1 - I4 lines have been found in the ion-implanted Si [3]. These lines have been reported to be due to defects such as vacancy clusters induced by radiation damage and thermal annealing [3-6]. However, the origins of the PL lines are still controversial and the detailed nature of the defects has not yet been clarified.

In this study, we have investigated the defects in Si induced by ion implantation and thermal annealing by using a PL technique. We have focused especially on the effects of the annealing atmosphere and Cu contamination on the PL spectra.

Experiments

The substrates used in this work were (100) Czochralski-grown Si wafers with a resistivity of 10-20 Ωcm doped with B. Samples were implanted at room temperature with 300 keV B^+ ions or 700 keV P^+ ions to a dose of $2x10^{13}$ cm^{-2}. The depth profile of the implanted impurities was measured by secondary ion mass spectroscopy (SIMS). The theoretical projected range of the implanted impurities is about 0.8 μm for both cases and agrees well with the results of the SIMS measurement. Samples were cut from the wafer and annealed in a furnace at 200 - 700℃ for 60 minutes in vacuum or in a N_2 atmosphere. In the case of annealing in vacuum, samples were put in a sealed quartz ampoule (~$1x10^{-5}$ Torr) and Cu contamination was carried out by putting a small Cu wire in the ampoule with the samples.

PL spectra were measured at liquid-He temperature. Samples were excited by the 488 nm line of an Ar ion laser. The emission from the samples was analyzed with a 50 cm single monochromator with a 600 groove/mm grating blazed at 1 μm and was detected with a cooled Ge detector. The spectral bandpass was kept at 1.2 nm.

Results and discussion

PL spectra of the samples implanted with B and annealed at 300℃ for 60 minutes are shown in Fig. 1 for the different annealing conditions. Almost identical PL spectra are observed for the samples annealed in the N_2 atmosphere and in vacuum. However, the PL spectrum of the sample annealed in vacuum with Cu is a little different from the others. In these PL spectra, sharp lines labelled B^{TO} are the emission due to bound exciton and bound multiple exciton complexes (BMECs) and the broad line labelled EHD^{TO} is the emission due to electron-hole droplet (EHD) [7-9]. The superscript TO indicates the transition assisted by the transverse optical (TO) phonon. Sharp lines labelled I1 and I3 and a small peak labelled I2 are observed in all cases. The I2 line is very weak in intensity and overlaps with the EHD^{TO} line. These I1 - I3 lines have been reported to originate from radiation damage [3-6]. Small lines on the lower energy side of the I1 line and the I3 line are phonon structures of these lines. The I2 line and the I3 line do not depend on the annealing conditions, nor does the emission due to bound exciton, BMEC, or EHD. However, the I1 line becomes weak in intensity when the samples is annealed in vacuum with Cu.

Besides those lines, PL lines at 0.992 eV and at 1.097 eV can be seen in Fig. 1. We have not observed these lines in the samples annealed under the same conditions without ion implantation. As these lines appear only in the ion implanted samples, we believe these lines are due to defects induced by the ion implantation and the subsequent thermal annealing. The PL line at 0.992 eV appears only in the samples annealed in vacuum with Cu while the PL line at 1.097 eV appears in all the spectra in Fig. 1. The energy position of the 1.097 eV line coincides with that of the PL line due to free exciton [7]. However, we have observed that the 1.097 eV line is relatively strong in intensity and can be distinguished from the free exciton line in the high-resolution measurement at 10 K. A similar PL line at 1.0966 eV has been reported by Henry et al. [10] in In-implanted Si. We will discuss the difference between the reported line and the line observed in this work below. On the other hand, the PL line at 0.992 eV has not been previously reported to the best of our knowledge.

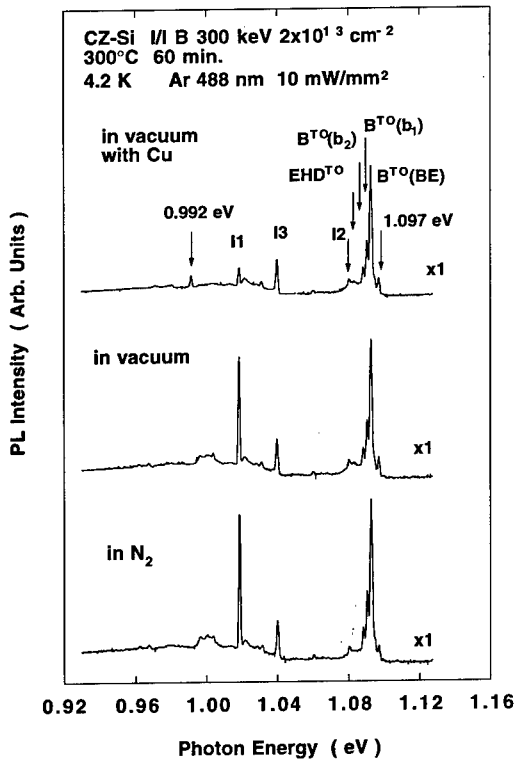


Fig. 1. PL spectra of Si implanted with 300 keV B^+ to a dose of $2x10^{13}$ cm^{-2} and annealed at 300℃ under various conditions.

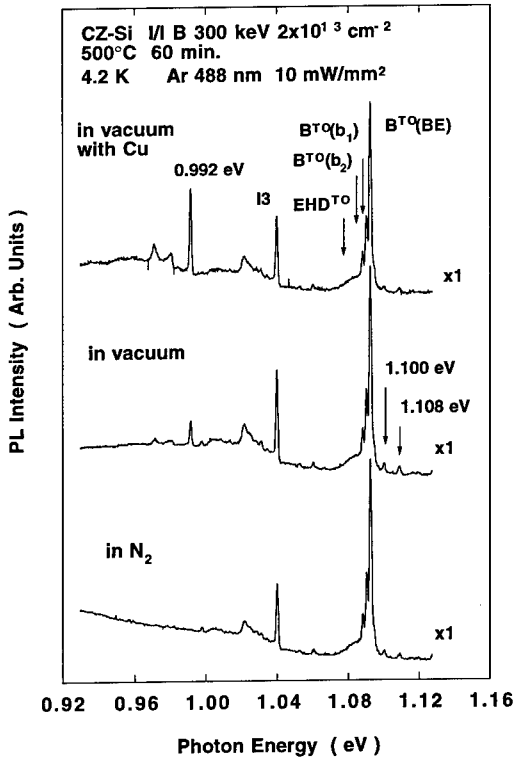


Fig. 2. PL spectra of Si implanted with 300 keV B^+ to a dose of $2x10^{13}$ cm^{-2} and annealed at 500℃ under various conditions.

Similar spectra have been observed in the samples implanted with B and annealed at 500℃ as shown in Fig. 2. In this case, however, the I1, I2, and 1.097 eV lines disappear and the 0.992 eV line is observed also in the case of annealing in vacuum without Cu. In Fig. 2, the intensity of the 0.992 eV line is much stronger than that in Fig. 1 and small peaks can be clearly seen on the lower energy side of this line. Similar small peaks on the lower energy side have been reported for the I1 and I3 lines [5, 6] and they are considered to be phonon structures. Davies et al. [6] has reported that the structures on the lower energy side of the I1 line are well explained by the model of the vibronic transition. The energy separation and the spectral shape of the small lines near the 0.992 eV line resemble those of the phonon structures of the I1 line. In the PL spectra measured in this work, the 0.992 eV line is always followed by the small peaks. Therefore, we consider that the small peaks on the lower energy side are the phonon structures of the 0.992 eV line. In Fig. 2, there are also small peaks at 1.100 eV and 1.108 eV. These small peaks are the same as the series of lines observed by Nakayama et al. [11] in CZ-Si annealed at 500℃.

PL intensities of the observed lines relative to the intensity of the bound exciton line (B^{TO}(BE) in Figs. 1 and 2) are plotted as a function of annealing temperature in Fig. 3 for various annealing conditions. For the I2 and I3 lines, the annealing behavior is almost the same as that reported in the past [3] and does not depend on the annealing conditions. In the cases of annealing in N_2 and in vacuum without Cu, the I1 line shows the same annealing behavior as previously reported [3]. However, the intensity of the I1 line becomes weak after annealing at 300℃ in vacuum with Cu.

As can be seen from Fig. 3, the 1.097 eV line appears at the annealing temperature of 300 - 400℃ and depends on neither the annealing atmosphere nor the Cu contamination. Thus Cu atoms are not related to the luminescence center of the 1.097 eV line. As mentioned above, Henry et al. [10] reported a PL line at 1.0966 eV in In-implanted Si and this line might be the same line observed in this work. However, they observed the 1.0966 eV line in samples annealed at 500 - 700℃. In our experiment, the 1.097 eV line disappears after annealing above 500℃. Therefore, we consider the 1.097 eV line observed in this work to be due to a different origin from the 1.0966 eV line.

On the other hand, the annealing behavior of the 0.992 eV line is strongly affected by the annealing conditions. In the case of annealing in the N_2 atmosphere, this line does not appear. The 0.992 eV line is observed after annealing at 500℃ in vacuum and after annealing at 300 - 500℃ in vacuum with Cu. This indicates that the Cu atom plays an important role in the appearance of the 0.992 eV line, as does the annealing temperature and the annealing atmosphere. However, the defect responsible for the 0.992 eV line does not contain a Cu atom itself because the line also appears in the samples annealed in vacuum without Cu.

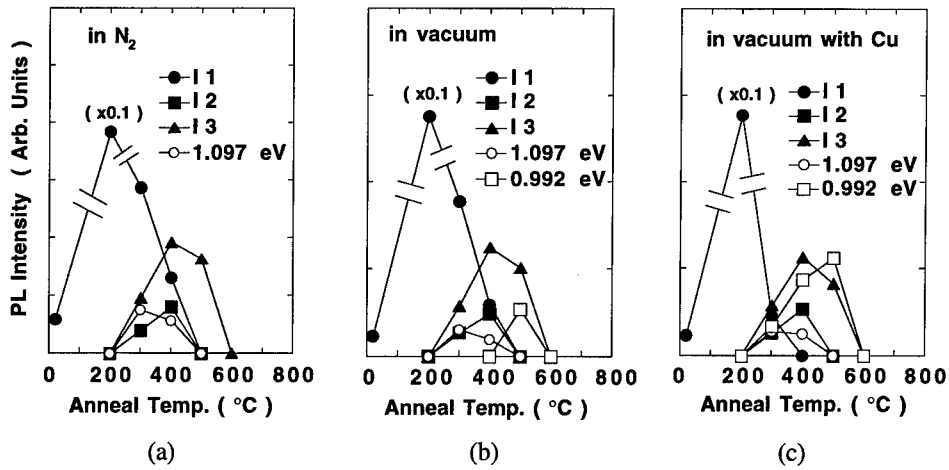


Fig. 3. PL intensity of the observed lines relative to the intensity of the bound exciton line in Si implanted with 300 keV B^+ to a dose of $2x10^{13}$ cm^{-2} as a function of annealing temperature for various annealing conditions: (a) in a N_2 atmosphere, (b) in vacuum without Cu, and (c) in vacuum with Cu. The original intensity of the I1 line at the annealing temperature of 300℃ is magnified by a factor of 0.1.

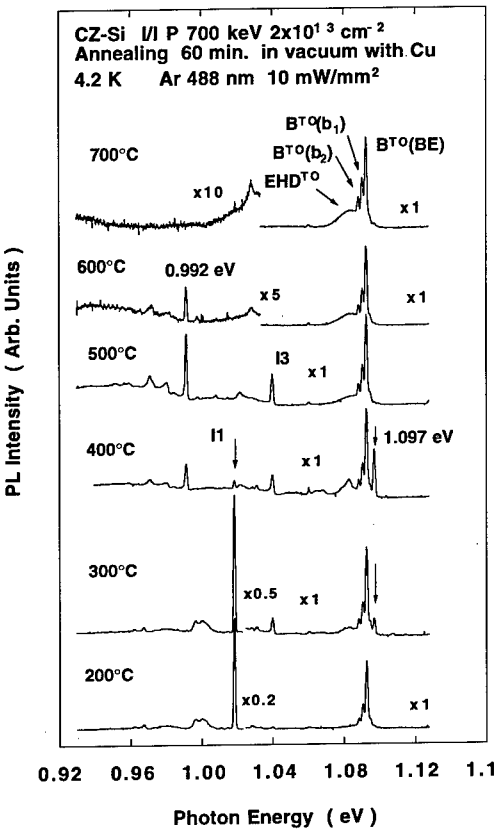


Fig. 4. PL spectra of Si implanted with 700 keV P^+ to a dose of $2x10^{13}$ cm^{-2} and annealed at 200 - 700℃ in vacuum with Cu for 60 minutes. The notation "x5" indicates that the original intensity is magnified by a factor of 5.

We obtained similar results for the P-implanted samples. PL spectra of Si implanted with P and annealed at 200 - 700℃ in vacuum with Cu for 60 minutes are shown in Fig. 4. The 0.992 eV line and the 1.097 eV line are also observed in the PL spectra of the P-implanted samples, but the I2 line is not observed. The luminescence center of the I2 line has been reported to contain B atoms because the I2 line appears only in B-implanted samples and shows the fine structures due to the B isotope effect [4]. However, the 0.992 eV line and the 1.097 eV line are observed in both the B-implanted and the P-implanted samples. Thus the luminescence centers of these lines contain neither B atoms nor P atoms. In Fig. 4, in contrast to the case of the B-implanted samples (Fig. 1), the 0.992 eV line does not appear and the I1 line is relatively strong in intensity at the annealing temperature of 300℃.

The PL intensity of the observed lines relative to the intensity of the bound exciton line (B^{TO}(BE) in Fig. 4) in the P-implanted samples are plotted as a function of annealing temperature in Fig. 5. The annealing behavior of the PL lines in the P-implanted samples is a little different from that in the B-implanted samples. Comparing the P-implanted case with the B-implanted case, the 1.097 eV line is observed at the annealing temperature of 300 - 400℃ in both cases. However, the relative intensity of the 1.097 eV line is stronger at the annealing temperature of 400℃ in the P-implanted samples than in the B-implanted samples. On the other hand, the 0.992 eV line appears after annealing at 600℃ in vacuum without Cu and appears over the annealing range of 400 - 600℃ in vacuum with Cu. The annealing temperature at which the 0.992 eV line appears in the P-implanted samples shifts to a higher temperature range. The intensity of the I1 line does not decrease after annealing at 300℃ in vacuum with Cu in contrast to the case of the B-implanted samples. In our experiment, the uncertainty of the annealing temperature was ±5℃ and the annealing temperature could be verified by the annealing behavior of the other PL lines such as the I3 line. At present, we consider the differences in the annealing behavior of the 0.992 eV line and the 1.097 eV line between the B-implanted samples and the P-implanted samples to be due to the difference in the amount of damage induced by the ion implantation. In this experiment, B^+ and P^+ were implanted at 300 keV and 700 keV, respectively, because we used samples with the same projected range of implanted impurities. Due to the larger mass of P^+ and the higher implantation energy, more defects were induced in the P-implanted samples than in the B-implanted samples.

Now, we will discuss the origins of the 0.992 eV line and the 1.097 eV line. These lines are only observed after the ion implantation and the thermal annealing, thus the defects induced by these processes must be the luminescence centers of the observed lines. The most probable defects induced by the ion implantation and the thermal annealing are point defects and their clusters such as divacancies. The I1 - I4 lines observed in the ion-implanted Si have been reported to be due to point defect clusters [3-6]. We consider the 0.992 eV line and the 1.097 eV line to also be due to the point defect clusters induced by the ion implantation and thermal annealing.

The 0.992 eV line appears only in the case of annealing in vacuum. When the sample is annealed in a N_2 atmosphere, this line does not appear. This could be attributed to nitrogen combining with the

0.992 eV center. However, the equilibrium solid solubility of nitrogen is low in Si and little nitrogen is introduced in Si from the ambient at such low temperatures as used in this work. In vacuum, though, some atoms such as impurities in the interstitial site are more likely to diffuse out of Si and a new defect may be formed. As a result of the diffusion of such atoms, point defect clusters may be rearranged and the 0.992 eV center may be formed. The observed effect of the Cu contamination suggests that Cu atoms strongly enhance the formation of the 0.992 eV center. If we assume that the 0.992 eV center is formed by the diffusion of atoms into vacuum, Cu atoms would enhance this diffusion.

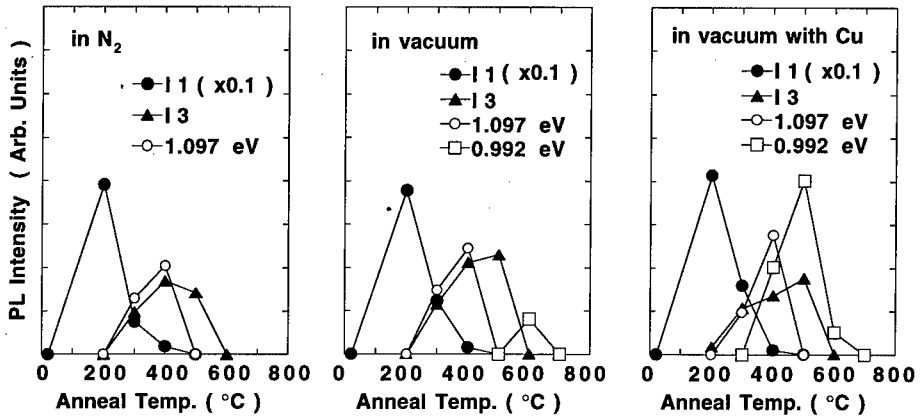


Fig. 5. PL intensity of the observed lines relative to the intensity of the bound exciton line in Si implanted with 700 keV P^+ to a dose of $2x10^{13}$ cm^{-2} as a function of annealing temperature for various annealing conditions: (a) in a N_2 atmosphere, (b) in vacuum without Cu, and (c) in vacuum with Cu. The original intensity of the I1 line is magnified by a factor of 0.1 in all the cases.

Note that the intensity of the I1 line becomes weak at the annealing temperature where the 0.992 eV line appears as shown in Fig. 3. This suggests that the 0.992 eV line is related to the I1 line. The origin of the I1 line is still controversial. The assignment of the I1 line varies from vacancy clusters to interstitials. Estreicher et al. [12] have reported recently that the I1 line is due to the neutral divacancy. The 0.992 eV center and the I1 center might have a similar structure and the I1 center might be transformed into the 0.992 eV center. This idea is supported by the fact that the I1 line and the 0.992 eV line have similar phonon structures.

On the other hand, the 1.097 eV line depends on neither the annealing atmosphere nor the Cu contamination, so the structure and the formation mechanism of the 1.097 eV center must be very different from those of the 0.992 eV center. We have not yet obtained enough data to determine the origins of the 0.992 eV and 1.097 eV lines, but we tentatively attribute these lines to different types of point defect clusters.

As mentioned above, the 0.992 eV center and the 1.097 eV center contain neither B atoms nor P atoms. The defects do not contain Cu atoms although the Cu contamination strongly affects the annealing behavior of the 0.992 eV line. At present, we believe the 0.992 eV and 1.097 eV centers are clusters of vacancies and/or Si interstitials. We have not yet investigated the dependence of the PL spectra on the C or O concentration, and it is possible that these defects contain C and/or O atoms. Defects containing C or O atoms in Si have been widely studied by various methods including PL measurement, and PL lines have been assigned to the defect complexes containing C and O atoms [13, 14]. However, PL lines similar to the lines observed in this work have not been reported in those studies. The dependence of the PL spectra on the C and O concentrations should be examined in future work.

Conclusions

We have measured the PL spectra of Si implanted with 300 keV B^+ or 700 keV P^+ to a dose of $2x10^{13}$ cm^{-2} and observed luminescence lines at 0.992 eV and at 1.097 eV. These lines appear after thermal annealing in both the B-implanted and the P-implanted samples and the centers of these luminescence lines contain neither B atoms nor P atoms. The centers do not contain Cu atoms, although the Cu contamination strongly affects the annealing behavior of the 0.992 eV line. The 0.992 eV line appears only after annealing in vacuum, while the 1.097 eV line depends on neither the annealing atmosphere nor the Cu contamination. The structure and the formation mechanism of the 1.097 eV center are very different from those of the 0.992 eV center. We consider these lines to be due to the different types of point defect clusters. The annealing behavior of the PL spectra suggests a strong correlation between the 0.992 eV center and the I1 center.

Acknowledgements

We are grateful to Kazuko Ikeda, Takashi Mizutani, and Haruhiko Ono for their helpful discussions, especially concerning the defects in ion-implanted Si, and also for their great encouragement.

References

1. J. F. Ziegler, Nucl. Instrum. & Methods **B 6**, 270 (1985).
2. H. Wong, N. W. Cheung, and P. K. Chu, Appl. Phys: Lett. **52**, 889 (1985).
3. C. G. Kirkpatrick, J. R. Noonan, and B. G. Streetman, Radiat. Eff. **30**, 97 (1976).
4. K. Thonke, J. Weber, J. Wagner, and R. Sauer, Physica **116B**, 252 (1983).
5. Z. Ciechanowska, G. Davies, and E. C. Lightowlers, Solid State Commun. **49**, 427 (1984).
6. G. Davies, E. C. Lightowlers, and Z. E. Ciechanowska, J. Phys. C: Solid State Phys. **20**, 191 (1987).
7. P. J. Dean, J. R. Haynes, and W. F. Flood, Phys. Rev. **161**, 711 (1967).
8. K. Kosai and M. Gershenzon, Phys. Rev. **B 9**, 723 (1974).
9. A. S. Kaminskii, Ya. E. Pokrovskii, and N. V. Alkeev, Zh. Eskp. Teor. Fiz. **59**, 1937 (1970) [Sov. Phys. JETP **32**, 1048 (1971)].
10. M. O. Henry, T. B. Kehoe, M. H. Nazare, K. Freitag, and R. Vianden, Appl. Surf. Sci. **63**, 232 (1993).
11. H. Nakayama, T. Nishino, and Y. Hamakawa, Appl. Phys. Lett. **38**, 623 (1981).
12. S. K. Estreicher, J. Weber, A. Derecskei-Kovacs, and D. S. Marynick, Phys. Rev. **B55**, 5037 (1997).
13. J. M. Trombetta and G. D. Watkins, Appl. Phys. Lett. **51**, 1103 (1987).
14. W. Kürner, R. Sauer, A. Doren, and K. Thonke, Phys. Rev. **B39**, 13327 (1989).

Materials Science Forum Vols. 258-263 (1997) pp. 593-598
© 1997 Trans Tech Publications, Switzerland

PERFORMANCE DEGRADATION OF MICROCRYSTALLINE SILICON-BASED p-i-n DETECTORS UPON He^4 IRRADIATION

R. Schwarz[1], M. Vieira[2], F. Maçarico[2], S. Koynov[3], S. Cardoso[4], J.C. Soares[5]

[1] Physics Department, Instituto Superior Técnico, 1096 Lisboa, Portugal
[2] ISEL, Instituto Superior de Engenharia de Lisboa, 1900 Lisboa, Portugal
[3] CL-SENES, Bulgarian Academy of Sciences, 1784 Sofia, Bulgaria
[4] INESC, Instituto de Engenharia de Sistemas e Computadores, 1000 Lisboa, Portugal
[5] ITN, Instituto Tecnologico e Nuclear, 2685 Sacavém, Portugal

Keywords: Radiation damage, microcrystalline silicon, infrared detector

Abstract. Microcrystalline silicon p-i-n structures show a good responsivity in the visible and near infrared spectral region. We have used a 1.6 MeV He^4 beam to study the -degradation of the spectral response and the changes in the current-voltage characteristics of such detectors. All the layers in the detector structure were deposited by high-rate plasma-enhanced chemical vapor deposition. Under a fluence of $3x10^{15}$ cm^{-2} the short circuit current decreased by about a factor of 3. The decrease of bulk material recombination life time is evidenced by the shift of the peak energy of the spectral response to short wavelengths. The degradation effect is compared to reports on amorphous and monocrystalline silicon detectors.

Introduction.

Radiation effects in semiconductors are not only of interest for understanding defect creation mechanisms - which mainly occur through inelastic collisions with electrons or elastic collisions with atomic nuclei via Rutherford scattering - but also for very pratical purposes like the estimate of soar cell life time for space applications. The incoming particles suffer energy loss either through ionization or through direct atomic displacement, so-called knock-on collisions. Standard materials like crystalline silicon (Si) and gallium arsenide (GaAs) were extensively studied in the 60's and 70's by groups at NASA and JPL [1,2]. In particular, using 1 MeV electrons the degradation of the short-circuit current I_{sc} in silicon pn junctions was proven to follow a linear dependence on the particle fluence ϕ [3]. This originates from the following linear increase of the recombination rate (τ is the recombination life time):

$$1/\tau = 1/\tau_0 + K_\tau \phi \qquad (1)$$

where K_τ is the damage coefficient for the given type of semiconductor unter test.

One report stated that the damage coefficient might by considerably smaller in amorphous silicon (a-SI:H) films and devices when compared to pure crystalline silicon (c-Si) material. However, a later study showed that the degradation mechanism does not follow the simple linear behaviour of eq. (1), which seems to be a natural manifestation of the disorder present in these films [4].

In this study we use entirely microcrystalline silicon (μc-Si:H) structures. The layers were deposited by a cyclic chemical vapor deposition method, the so-called closed-chamber CVD [5] that ensures a high deposition rates of 1-2 Å/s at low substrate temperatures. Thin entirely μc-Si:H p-i-n structures result in photodiodes with an enhanced sensitivity to the near infrared region. Details of the optoelectronic characterization is described elsewhere [6], however, we recall that the optical band gap lies at 1.7 - 1.8 eV similar to a-Si:H. It will therefore be one of our goals to compare degradation in those three manifestations of silicon materials.

Ion bombardment.

For degradation of the microcrystalline detector structures we exposed the samples to a 1.6 MeV He^4 beam focussed to about 2 mm diameter. The fluences ranged from 10^{12} to $3x10^{15}$ cm^{-2}. The total areal thickness of the samples was 0.3 mg/cm^2. We expect a homogenous profile of newly created defects since the energy loss is only 0.5 $MeV/mg/cm^2$ [7]. The helium beam was entering the samples through a thin Cr contact layer deposited on top of the n-type μc-Si:H layer as indicated in Fig. 1.

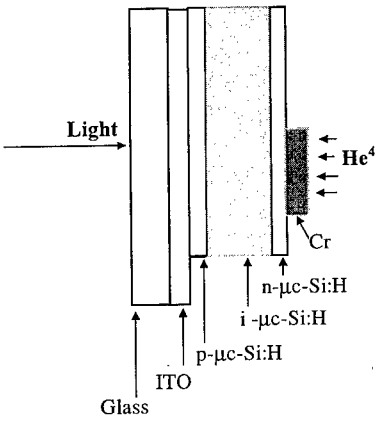


Fig. 1:
Layout of the μc-Si:H p-i-n detector. The He^4 beams enters through the top metal contact and the light beam through the glass substrate

After degradation the short circuit current I_{sc} and open-circuit voltage V_{oc} of the detectors were measured under 2 mW HeNe laser light (633 nm). The spectral response was taken with a halogen lamp and a 25 cm focal length monochromator between 400 and 1000 nm.

Changes in the spectral response.

First, we consider the changes in the spectral response curves taken at different levels of irradiation (see Fig. 2). Apart from the overall decrease one can observe a shift of the energy of maximum response towards the blue spectral region when the fluence increases. The spectra show interference fringes reflecting the film thickness.

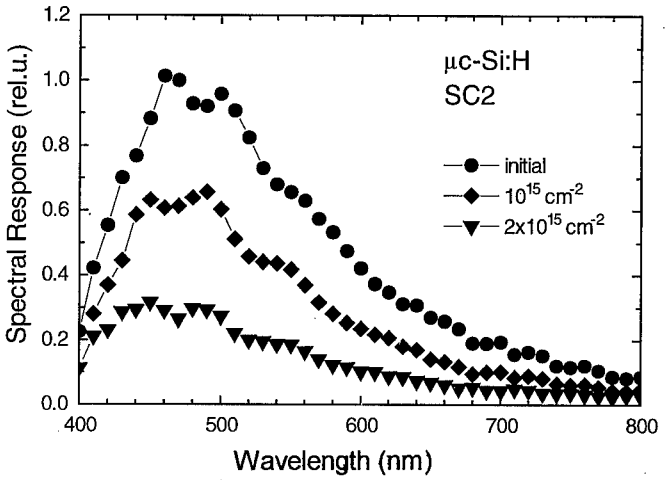


Fig. 2:
Spectral response curves for two levels of degradation. The non-degraded case serves as a reference level.

Fig. 3 shows the normalized change of spectral response after the highest irradiation level considered. The overall result is a decrease by about 75 % of the response in the red until near infrared region and, second, a much smaller degradation in the blue spectral region.

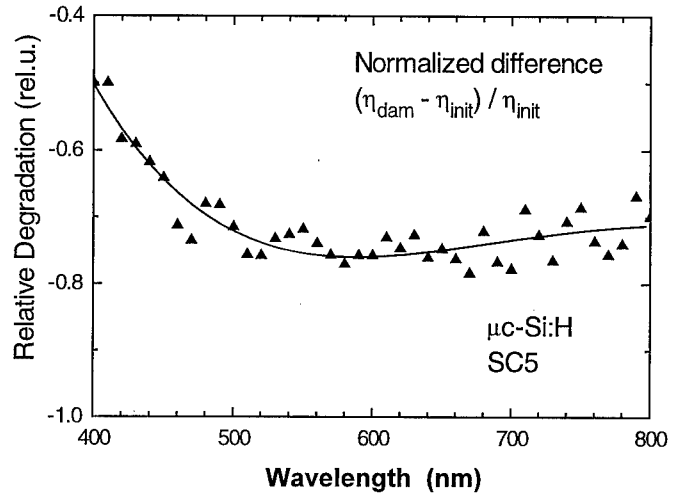


Fig. 3:
Changes in the spectral response indicating a 75 % loss of responsivitiy in the visible and near infrared region and a much lower degradation in the blue region

Short-cirucuit current degradation.

From measurements under red laser illumination (about 60 mW/cm^2) we found that the open-circuit voltage V_{oc}, which showed initial values of 400 mV, decreased by about 90 mV. The decrease in short-circuit current is much stronger, it decreased by a factor of 3 down from the initial value of about 8 mA/cm^2.

Fig. 4 shows the normalized short-circuit current values upon different levels of helium irradiation. The large fluctuations are the result of a series of different sources of error,

either during degradation or during the subsequent optoelectronic characterisation. However, there is a clear difference of the degradation behaviour also shown in Fig. 4 for experiments on a-Si:H Schottky barrier detectors [4] and c-Si solar cells (dotted line) [3]. It is important to note that in all three cases the type of incident particle was different; 12 MeV protons were used for the first study, and 1 MeV electrons in the case of c-Si. It is known, as a rule of thumb, that 1 MeV electrons create 3000 times less damage than 10 MeV protons, so the relatively early onset of degradation in the amorphous and microcrystalline detectors is expected.

Discussion.

Similar to the case of degradation of a-Si:H detectors the shift of the spectral response to the blue region in the microcrystalline samples indicates that the internal electric field is screened after charged defects have been created. So photogenerated carriers from the center region of the p-i-n structure, especially holes, will mostly be lost by recombination before they can be collected at the contacts. Blue light with its small absorption length will create holes the near front p-contact. Electrons can more easily cross the device due to their larger mobility-lifetime product. It would be helpful to check this reasoning with numerical simulation programs that were developed in recent years [8,9].

The slight difference in absolute degradation values between a-Si:H and μc-Si:H solar cells might be due to differences in the stopping power of 10 MeV protons and 1.6 MeV He, and in a different initial level of defect density.

There is, however, a significant difference from the linear degradation hypothesis of eq. (1). An adequate mathematical description should take two effects into account, defect creation and, once a large enough number of defects is created, defect annealing. The following ansatz reflects this argument:

$$\delta N_d = c\ \phi^m - K_{ann}\, N_d\, \delta\phi^m \qquad (2)$$

That we have to choose an exponent m smaller than 1 is suggested not only from the overall result for the normalized short-circuit current reduction, but mainly from the knowledge that microcrystalline silicon does behave in many respects similar to amorphous silicon. It can actually be considered of a mixed material where the main tissue is made of small silicon crystallites which are embedded in an amorphous matrix. From this material it is well known that degradation by any type of irradiation - light, electrons, ions - does indeed follows a power law due to its inherent disorder. In addition, a certain degree of metastability is observed in the electrical properties of amorphous films and can be monitored by the amount of defect density present. The interesting aspect of metastability, however, is not further discussed here.
The annealing term is only seen when the defect density reaches saturation. In the experiments described here this point is far from being reached. So we can consider the simpler case without annealing which leads to the simple relation:

$$I_{sc}/I_{sc,0} = N_0 / (N_0 + c\ \phi^m) \qquad (3)$$

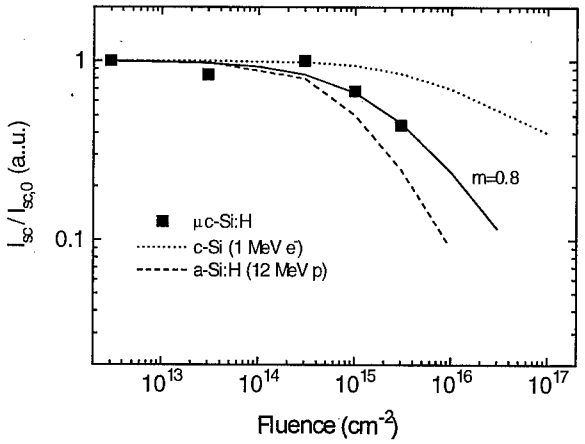


Fig. 4:
Normalized short-circuit current degradation for the microcrystalline p-i-n detector and comparison with literature data on amorphous and crystalline silicon detectors

A reasonable fit within the possibilities of the limited amount of data available is obtained with the exponent $m = 0.8$, very near to results obtained in a-Si:H ($m = 0.62$)

Also, there is a minimum fluence ϕ_0 of about 10^{14} cm^{-2} that is necessary before the samples show any degradation. This is obviously a reflection of the initial non-zero defect density present in the non-degraded microcrystalline films.

An interesting question is whether radiation-induced defects are created homogeneously within the microcrystalline films or whether the detector structure is more sensitive to degradation of its interfaces. There has been a long debate in the literature on this topic as far as degradation of amorphous silicon solar cells under strong illumination is concerned. We suggest, that due to the long penetration depth, and presuming a fairly balanced initial state of interface and bulk quality, that the degradation is acting homogeneously throughout the detector. It would be challenging to test this conclusion in future with numerical simulation programs.

Conclusion.

We have monitored the performance degradation of microcrystalline silicon p-i-n detectors upon irradiation with 1.6 MeV helium ions. As reported in the case of amorphous silicon based cells, the degradation is best seen in the normalized short-circuit current and follows a power law behaviour with an exponent of 0.8. We suspect that the magnitude of this exponent will vary with the degree of disorder present in the microcrystalline films. This type of experiments are quite advantageous for the study of ion-induced effects in detector structures, since a 15 min run with He ions can replace the need to test solar cells in a three year space mission.

Acknowledgement: We want to thank M. Fernandes for assistance during experiments. In particular we want to thank the crew running the Sacavém facility for their kind support. This work was financed in part by the Portuguese Ministry of Science and Technology through project PRAXIS/PCEX/P/FIS/7/96.

References.

1. G.W. Simon, J.M. Denney, and R.G. Downing, Phys. Rev. **129** (1963) 2454.
2. J.J Wysocki, IEEE Trans. on Nucl. Sc. (1963) 80.
3. H.Y. Tada, J.R. Carter, B.E. Anspaugh, R.G. Downing, JPL Publication 82-96, Nov. 1982..
4. R. Schwarz, J. Kolodzey, S. Aljishi, S. Wagner, Proc. of 18th IEEE Photovolt. Spec. Conf., Las Vegas, October 1985, p. 903.
5. S. Koynov, R. Schwarz, T. Fischer, S. Grebner, and H. Muender, Jpn. J. Appl. Phys. **33** (1994) 4534
6. R. Krankenhagen, M. Schmidt, W. Henrion, I. Sieber, S. Koynov, S. Grebner, and R. Schwarz, Solid State Phenomena **47** (1995) 607
7. J.F. Ziegler, *Stopping Cross Sections for Energetic Ions in all Elements* (Pergamon, Oxford, 1980).
8. W. Kopetzky and R. Schwarz, Appl. Phys. Lett. **62** (1993) 2959
9. A. Fantoni, M. Vieira, J. Cruz, R. Martins, and R. Schwarz, Proc. 13th ECPV Conf., Nice, October 1995.

Materials Science Forum Vols. 258-263 (1997) pp. 599-604
© 1997 Trans Tech Publications, Switzerland

PERSISTENT EXCITED CONDUCTIVITY INDUCED BY PROTON IRRADIATION IN a-Si:H

H. Amekura,[1,2] N. Kishimoto[1] and K. Kono[1]

[1]**National Research Institute for Metals (*NRIM*), 3-13 Sakura, Tsukuba, Ibaraki, 305, Japan**

[2]**Institut für Schicht- und Ionentechnik, Forschungszentrum Jülich, D-52425, Jülich, Germany**

Keywords: radiation induced conductivity, a-Si:H, radiation damage, PEC, Staebler-Wronski effect

Abstract. Radiation induced conductivity (RIC) of a-Si:H has been studied under 17 MeV proton irradiation. Electric conductivity increases during the proton irradiation, and the conductivity enhancement remains, to some degree, even after stopping the irradiation. At $T \leqq 400$ K, the protons cause the persistent excited conductivity (PEC). The PEC continues longer at the lower temperatures. At $T = 200$K, the PEC sustains itself over 30 hours, after the irradiation for 2 min. Simultaneously with occurrence of the PEC, a hump around $E = 1.9$ eV appears in the photoconductivity spectrum. The PEC disappears after annealing above $T = 450$ K.

Introduction

Hydrogenated amorphous Si (a-Si:H) has been widely used for solar cells and optical sensors, etc., since hydrogen passivation of dangling bonds has succeeded in a high quantum efficiency. However, a-Si:H is subjected to the so-called Staebler-Wronski (SW) effect [1], ie.,strong light illumination deteriorates both photo- and dark conductivity. The SW effect is basically explained in terms of defect formation due to electronic excitation.

Recently, it has been proposed [2] that a-Si:H is potentially applicable for devices under strong radiation fields, e.g., in spacecrafts, accelerators and nuclear reactors. As for photoconductivity(PC), a-Si:H showed higher radiation performance than crystalline Si (c-Si)[2], which was tentatively ascribed to structural flexibility of the amorphous structure. High-energy ions ($E > 1$ MeV/amu), as injected into a solid, deposit most of the incident energy via electronic excitation. Only a small amount of the energy is partitioned to atomic displacements. Accordingly, SW-like effects could be also induced by high-energy ions.

In this point of view, radiation-induced conductivity (RIC) of a-Si:H by 17 MeV protons has been studied. The RIC slowly increases during the irradiation, and shows extremely slow decay after terminating the irradiation. This behavior is entirely different from the conventional SW effect, and we call this RIC as persistent excited conductivity (PEC).

Experimental

Specimens of 1 - 2 μm thickness were fabricated by glow-discharge onto silica substrates (fused quartz) at 500 K. The ohmic electrodes were made by Al films pre-deposited onto the substrates. Spin density of as-grown specimens, measured by ESR, was $3 \cdot 10^{16}$ cm^{-3}, which confirmed the good quality. Just before the measurement, the specimens were annealed at $T = 450$K, to maximize the photoresponse.

Experimental setups were similar to those described in Ref.[3]. A 17 MeV proton beam from the NRIM cyclotron was used for irradiation. For PC measurements, a halogen lamp via a monochromator was employed as an excitation source.
According to TRIM code[4], the projectile range calculated is 1.7 mm in Si, which is much larger than thickness of the specimen. Since all the incident protons pass through, the specimens are free from hydrogen implantation. The TRIM calculation indicates that electronic excitation and damage generation are uniform along the depth. Specimen temperatures under the irradiation were well controlled, within 0.2K[5] even under the irradiation.

Results

Electric conductivity σ, induced by visible light (2.1 eV) and protons (17 MeV), is shown in Fig.1. In the case of the light (ie., photoconductivity), the σ steeply increases in the beginning of the irradiation, and subsequently keeps a high value during the irradiation. After terminating the irradiation, the σ instantly returns to the value before the irradiation. It was confirmed that light irradiation of much stronger intensity caused the typical SW effect.
In the case of the proton, the σ shows a steep rise, followed by a gradual rise during the irradiation. After stopping the irradiation, the σ decays but maintains a 2 - 3 orders higher value than the unirradiated one. This enhanced dark-conductivity lasts for hours, decaying very sluggishly, and is named as persistent excited conductivity (PEC). It was verified that this phenomenon was not due to the substrate but inherent in a-Si:H, since no PEC occurred in the bare silica substrate without a-Si:H.
Before the irradiation, the I-V characteristics were not sufficiently ohmic, due to the low σ. However, the characteristics became ohmic, under the light and after the proton irradiation.
After the proton irradiation, the visible light was repeatedly irradiated. The quick response of the photocurrent was reversible, while the dark-conductivity (PEC) was higher than the unirradiated. The increment of σ was the same as that before the proton irradiation. The photocurrent response was quick enough to be separate from the PEC.

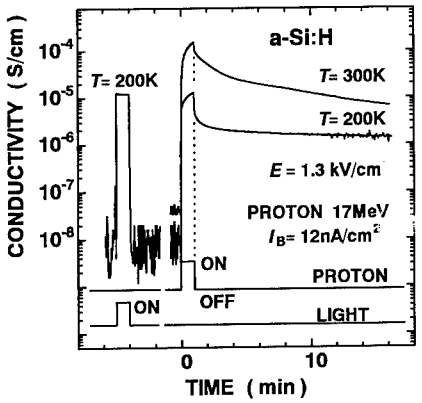


Fig.1 Electric conductivity due to visible light and 17MeV proton irradiations. Irradiation time is both 1 min.

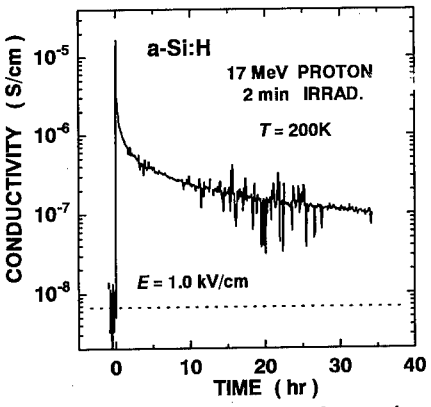


Fig.2 Electric conductivity, on a longer time scale, due to 17 MeV proton irradiation of 2 min.

The PEC continues longer at the lower temperatures. Time evolution of conductivity at T= 200K is shown in Fig.2. The PEC sustains itself over 30 hours, after the proton irradiation for 2min. Temperature dependence of the PEC is shown in Fig.3. The PEC decays faster with increasing the temperature, and disappears at T = 450 K. It is noted that the dangling bonds of a-Si:H are annealed out in a similar temperature region [1]. The PEC decay does not follow a single exponential function. The decay curves are likely to fit with a stretched exponential function [6], ie.,

$$\sigma(t) = \sigma_0 \exp\{-(t/\tau)^p\}, \qquad (1)$$

where the time-constant τ and the exponent p depend on temperature. In the best-fit conditions, the p disperses between 0.2 and 0.6, and the τ steadily decreases with increasing T. The curves at the lower temperatures are well fitted with Eq.(1), while they somewhat deviate at T ≧ 300K.

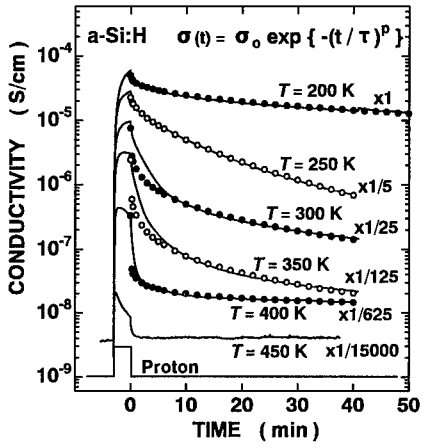


Fig.3 Temperature dependence of the PEC decay. Circles are the fitting of the stretched exponential decays.

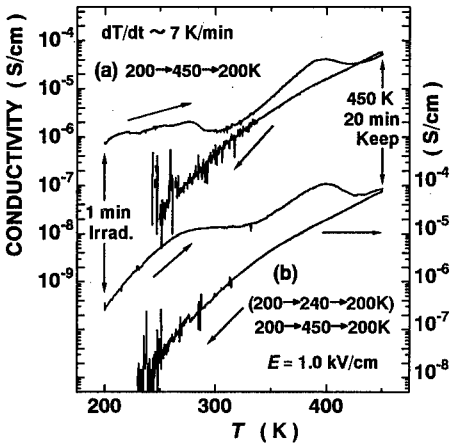


Fig.4 Conductivity evolution under a constant heating rate, after the proton irradiation at 200K. After the annealing at 450K, the temperature is decreased at the same rate.

Isochronal annealing was attempted, but the results were scattered, sensitively depending on annealing time and temperature-ramp rate. It is probably due to a variety of recovery temperatures for defects in the amorphous structure. To roughly evaluate the recovery behavior, an alternative method using a constant ramp rate was conducted.

Results shown in Fig.4 are conductivity evolutions, obtained in the following sequence. The specimen, irradiated at 200 K for 1 min, was heated with a constant rate 7 K/min, up to 450K. Then the specimen was retained at 450 K for 20 min until the PEC annihilated. After the 450K-annealing, the specimen was cooled down at the same constant rate. Since the curve after the 450K-annealing does not include the PEC, approaching to the curve indicates recovery. There are recovery stages around 300K and 420K. Another wide stage exists around 200 - 250 K. (see curve(a).) In the case of curve (b), the specimen was once annealed to 240K after the irradiation. By means of this pre-annealing, the recovery stage at 200 - 250K (curve (a)) vanishes, as seen in the curve (b).

As shown in Fig.3, the decay curves above 300K deviate from the stretched exponential. The deviation

may result from the partial annealing of various defects, e.g., reduction in disorder [6]. A conductivity response to longer irradiation is shown in Fig.5. The σ increases and saturates for the initial 10 min, and then tends to steadily decrease. The latter decrease is attributable to formation of deep defect levels via the atomic displacement or a SW-like effect.

Figure 6 shows PC spectra before and after the proton irradiation, and a spectrum after the annealing. It is again noted the photocurrent response is quick, even in co-existence with the PEC. After the irradiation, the PC increased only by a factor of 2, though the dark-conductivity increased about 3 orders. By the 450K annealing, the PC decreased to the value before the irradiation. To compare the relative shapes, the spectra were normalized at the values at E = 2.2 eV (shown by an arrow). A shoulder around E = 1.9 eV is enhanced by the irradiation, and decreases after the annealing. In Fig.6, the normalized curves of 3 min and 38 min after the irradiation coincide with each other, but magnitude for 3 min is larger than that for 38 min.

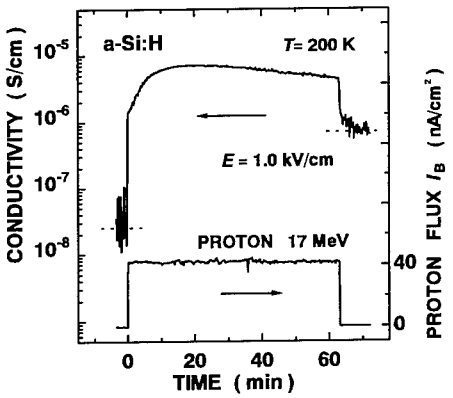


Fig.5 Electric conductivity for a longer time irradiation of the proton. The proton flux is also given. The flux is 2-3 times higher than the other measurements, to quickly obtain the decrease in RIC. .

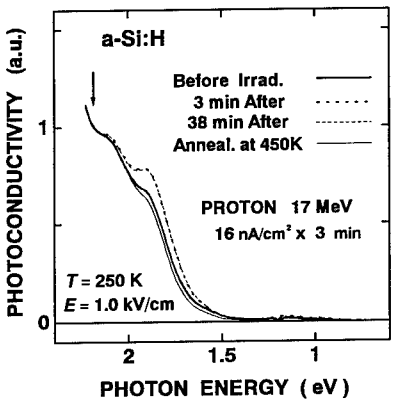


Fig.6 Photoconductivity spectra before and after the proton irradiation, and at 3 and 38 min past. The spectrum annealed at 450K is also given. All the spectra are normalized at the values at 2.2 eV. (indicated by an arrow).

Discussion

Similarity between RIC and PC in c-Si.

It is important in understanding the mechanisms to compare the RIC results of a-Si:H with those of crystalline Si (c-Si). Evolution of the RIC in c-Si has been studied by using 17 MeV protons[7,8]. In c-Si, the RIC-response to the proton irradiation is quick and reversible, except for the long-term degradation. The time response and the fluence dependence in c-Si are qualitatively similar between the RIC and the photoconductivity (PC). While non-doped c-Si easily degrades with the irradiation[3], the RIC and PC in doped c-Si gradually decrease with accumulating the defects[7]. As well as the PC, the quick response of RIC is therefore regarded as being induced by electron-hole generation, due to the band-to-band transition. In c-Si, the entire proton effects are described roughly with two separate processes, i.e., electronic excitation for a short period and defect production for a long term. The electronic excitation occasionally affects atomic displacements, e.g., a shift of the defect annealing stage

by electronic excitation [9]. In comparison with a-Si:H, the electronic excitation, however, does not greatly affect the overall atomic arrangement. It is probably because of the lattice rigidity of c-Si, as will be discussed later.

Contrast of RIC between a-Si:H and c-Si.

In contrast, RIC of a-Si:H shows quite different behaviors from that of c-Si. The RIC-response to the protons is sluggish in a-Si:H and the most striking is the PEC, lasting long after stopping the proton irradiation. These slow processes imply metastable structural changes indicating atomic movements. It is noted that collisional effects are basically the same between amorphous and crystalline Si, since displacement energy E_d (minimum energy to displace an atom) of covalent network should be close to each other. The E_d of a-Si:H could be slightly smaller than that of c-Si (15.8eV[10]), since the so-called weak-bonds partially exist. Consequently, the different evolution of RIC is ascribed to different electronic processes and/or to being amorphous. In other words, the proton effects in a-Si:H are not separately described with the electronic excitation and the atomic displacement. It is speculated for a-Si:H that the large electronic excitation by protons causes metastable atomic displacements, because of localization of the electronic states and flexibility of the amorphous structure.

Mechanism of RIC and PEC in a-Si:H.

To understand mechanisms of the PEC, the PC spectra are informative. As seen in Fig.6, the spectral shape around the band edge changes before and after the irradiation, also depending on the annealing condition. A shoulder (hump) emerges at E= 1.9 eV, somewhat larger than the energy-gap, and vanishes after annealing at 450K. There are two options to interpret the shoulder in the PC spectra. One is an effect associated with interference fringe of the film. The other is a change in density-of-states due to defect levels. In the former case, the irradiation generates a material phase or states of different refractive index, and the phase annihilates by the annealing. However, the former is less likely, because the energy position of the shoulder does not shift. The change in density-of-states is consistent with the spectra and the other results.

Although the rapid component of RIC in a-Si:H is due to electron-hole generation (Fig.1), origins of the slow components and the extremely slow PEC are not known. The candidate mechanisms are (1) spurious effects due to beam heating, (2) RIC of silica substrate, (3) Persistent photoconductivity (PPC) which is observed in GaAlAs system[11], (4) nuclear-transmutation doping of shallow unstable isotopes by protons, (5) reverse SW effects, (6) beam-annealing of deep defect levels, (7) beam-induced phase transformation (including recrystallization), and (8) radiation-induced defects with shallow levels.

However, only the last two cases, (7) and (8), agree with the experimental results, and the others are excluded as follows: The long-time decay over 30 hours eliminates the case (1). Since the PEC does not occur in the silica substrate without a-Si:H, the case (2) is excluded. Since the PEC is not caused by photoexcitation, the (3) is denied. The PPC is a strange but fairly common phenomenon[6], observed in many semiconductors. The PEC is quite different from the PPC and is inherent in ion irradiation. From the strong temperature dependence of the PEC, the (4) is denied. No nuclear transmutations have such a strong temperature dependence. Also, cross-sections of the relevant reactions are too small. Since the normal SW effect is observed under photoexcitation in our specimens, the (5) is denied. Neither the (6) is likely, because defects must be generated coincidently with the decay.

As for the phase transformation (7), nuclear-energy deposition would not yield the bulk transformation because the point-defect density ($10^{-8} \sim 10^{-6}$ dpa) for the present is too low. However, electronic excitation may cause a significant effect. It is known for a-SiO_2 that electronic-energy deposition of an ion beam induces a high-density phase with different refractive index. The proton beam may induce a

high-mobility phase with different refractive index in a-Si:H, via electronic excitation. This case (7) is not very probable, since experimental evidence is yet not obtained as discussed above(Fig.6) and the metastability of PEC (Figs.2 and 3) may not be given by the transformation. In any case, the possibility of (7) cannot be decisively excluded.

Finally, the case (8) explains appearance of the shoulder in the PC spectra, as near-band-edge levels. This is also consistent with the quick PC response, even in coexistence with the PEC. Consequently, the promising mechanism of the slow RIC and PEC is production and the metastable recovery of shallow levels near the band-edge.

As shown in Fig.4, there occur two distinct (300K and 420K) and one broad (200- 250K) recovery stages. It has been reported [1] that the dangling bonds (DB) are annealed out above T= 420K. Since the DB's are believed to act as deep levels, other type of defects are responsible for those recovery stages. Since shallow defect levels by particle irradiation have not been reported in a-Si:H, the shallow levels are possibly due to cascade defects, generated by high-energy ion irradiation. This is the reason why the PEC has not been observed under electron irradiation[12], where low-energy electrons generate dangling bonds or small defects as deep centers.

Another possible origin of the shallow levels may be interfacial defects between a-Si:H and the substrate, though it is not clear why the PEC has not been observed under electronic irradiation. Further investigation of the RIC- and PEC-mechanisms is underway.

Summary

Radiation induced conductivity (RIC) of a-Si:H has been studied under 17 MeV proton irradiation. At $T \leqq 400$ K, RIC with very long lifetimes is observed. After terminating the irradiation, the conductivity decays but keeps a 2 - 3 orders higher value than the unirradiated one. This persistent excited conductivity (PEC) continues longer at the lower temperatures. At T = 200K, the PEC sustains itself over 30 hours after the irradiation for 2 min. The PEC disappears after annealing at T = 450 K. The origin of the PEC may be shallow defect levels which are generated by high-energy proton irradiation.

References

1. D.L.Staebler and C.R.Wronski, Appl.Phys.Lett. **31**, 292 (1977).
2. N.Kishimoto, H.Amekura, K.Kono and T.Saito, Proc.MRS Fall Mtg., Dec. 1996.
3. H.Amekura, N.Kishimoto and T.Saito, J. Appl.Phys. **77**, 4984(1995).
4. J.F.Ziegler, J.P.Biersack and U.Littmark, *The Stopping and Range of Ions in Solids*, (Pergamon Press, New York, 1985) Chap.8.
5. H.Amekura, N.Kishimoto, K.Kono and T.Saito, Trans. Mat.Res.Soc. Jpn. **20**, 347 (1996).
6. D.Redfield and R.H.Bube, *Photoinduced defects in Semiconductors*, (Cambridge Univ.Press, 1996).
7. N.Kishimoto, H.Amekura, K.Kono and T.Saito, J.Nucl.Mater. **233-237**, 1244 (1996).
8. H.Amekura, N.Kishimoto, K.Kono and T.Saito, Trans. Mat.Res.Soc. Jpn. **20**, 343 (1996).
9. H.Amekura, N.Kishimoto, K.Kono and T.Saito, Mat.Sci.Forum, **196-201**, 1159 (1995).
10. J.A. Van Vechten , Inst.Phys.Conf.Ser.No.31, 441 (1977).
11. R. J. Nelson, Appl.Phys.Lett. **31**, 351 (1977).
12. A.Scholz and B.Schroder, J.Non-cryst. Solids, **137&138**, 259 (1991).

Materials Science Forum Vols. 258-263 (1997) pp. 605-610
© 1997 Trans Tech Publications, Switzerland

PHOTOLUMINESCENCE CENTERS ASSOCIATED WITH NOBLE-GAS IMPURITIES IN SILICON

Stefan K. Estreicher and Joerg Weber[1]
Physics Department, Texas Tech University, Lubbock, TX 79409, USA
[1]Max-Planck Institute–FKF, 70569 Stuttgart, Germany

Keywords: noble-gas impurities, silicon, photoluminescence, vacancies, theory

Abstract. The implantation of noble-gas (NG) ions into Si followed by an anneal results in the formation of defects observed by photoluminescence (PL). The defects grow at the expense of the PL band at 1018 meV. This paper discusses the results of calculations which involve the NG atom and vacancies. The results explain many of the observed features of the NG-related centers and imply that the 1018 meV band is associated with the neutral divacancy. Theory suggests that Xe should be covalently bound in a divacancy and behave differently from the other NG complexes.

I. Introduction.

Noble-gas (NG) elements are commonly used in semiconductor processing. They provide inert atmospheres for crystal growth and thermal anneals. NG ions are used in dry etching, ion beam milling,[1] sputtering, or the formation of thin amorphous films on crystalline surfaces. Implantation followed by thermal anneals is carried out to create 'bubbles',[2] which are efficient gettering centers.[3] NG ion implantation results in the formation of dislocation loops, microtwins,[2,4] and the appearance of photoluminescence (PL) centers.[5]

In the early 1980's, it was noticed[6,7] that NG-related defects in Si give rise to sharp PL peaks. NG ions are implanted with energies of several keV's. A $\sim 250\,^{\circ}C$ anneal results[1,5] in the formation of deep-level defects which give rise to rich PL spectra. The zero-phonon lines are closely related to the 1018 meV (or 'I_1' or 'W') line and grow at its expense. They are at 1012 (He), 1014 (Ne), 1009 (Ar), 1004 (Kr), and 1001 (Xe) meV.

The 1018 meV line appears after an anneal of Si samples exposed to neutron irradiation, ion implantation, thermal laser anneals, or other damage-inducing treatments, and is caused by an intrinsic defect. The line has C_{3v} symmetry.[8] It has been tentatively associated with the 'A3' center[9] (believed to be a trigonal tetravacancy) and with the trigonal di-intersticialcy.[10] The NG-related PL lines have the following features.[5-7]

1. Piezospectroscopic studies show that they correspond to defects with trigonal symmetry, except Xe which is associated with a tetragonal defect.
2. The thermal stability of the complex is $\sim 450\,^{\circ}C$ (only $\sim 300\,^{\circ}C$ for He). After this anneal, the bands disappear and are replaced by a broad and NG-independent PL band.
3. The occurrence of TA phonon modes in the spectrum shows a coupling of these modes to the NG lines. Tkachev *et al.* suggested[6] that NG-Si covalent bonds are formed. However, an empirical model[5,11] provides a simpler explanation involving only strain effects.
4. Sharp zero-phonon transitions and low-energy satellites are observed. The rich vibrational spectrum suggests a complex defect. Some modes shift with the NG isotope while others do not. The zero-phonon line shifts toward lower energies (relative to the 1018 meV line) and the smallest shift occurs for Ne.

5. The splitting of the NG-related PL lines under uniaxial stress is non-linear and NG-dependent. Varying the stress at constant temperature shows that the intensity ratios vary much less than would be expected from the reorientation of four trigonal centers.
6. The energy threshold[1,12,13] required to create the NG-related PL centers is consistent with a defect containing at most 4 vacancies.
7. According to standard implantation theory, the NG ions should penetrate only a few dozen Å's. Instead, they are observed[1,14] at depths of $\sim 1\,\mu m$. The enhanced diffusion occurs *during* the initial exposure, not the subsequent anneal.
8. It is unclear whether the defect responsible for the PL forms during the implantation and becomes PL active after the anneal, or is created during the anneal.

Details about the properties of NG elements and a review of earlier theoretical work are in Ref. [15]. The early theoretical work used Extended Hückel theory and ignored lattice relaxations and distortions.

II. Methodology.
We performed geometry optimizations in C_1 symmetry for interstitial He, Ne, Ar, and Kr as well as for each interacting with vacancies. Our goal is to obtain the general features of the various defect centers. We plan to perform higher-level calculations on selected defect structures when these become computationally tractable.

The present results were obtained with the approximate *ab-initio* Hartree-Fock (HF) method of partial retention of diatomic differential overlap (PRDDO/M).[16] Its results are comparable to minimal basis set *ab-initio* HF ones, but the calculations are substantially faster. This allows us to perform a large number of geometry optimizations that would require prohibitive amounts of CPU time at the *ab-initio* level. The Si crystal is approximated by H-saturated clusters[17] with 14 host atoms for the *ab-initio* calculations and 44 host atoms for the PRDDO/M ones.

In the case of interstitial NG impurities, for which small clusters can be used, we also performed *ab-initio* HF calculations with Hay-Wadt (HW) core potentials.[18] For Si atoms, a polarized split-valence (SV*)basis set was used, with a SV basis set for the H saturators. The NG atoms were treated at the all-electron level with an SV* basis set.

PRDDO/M is self-consistent and contains no semiempirical parameters. It can handle at a uniform level of theory the elements in the first four rows of the Periodic Table. It uses a minimal basis set of Slater orbitals, to which we added a set of 3*d*'s for the nearest-neighbors (NNs) to the vacancy or divacancy. The method provides reliable geometries but approximate energetics and electronic structures. The energy differences are larger than the *ab-initio* ones. The comparison of PRDDO/M and *ab-initio* HF results for interstitial NG impurities shows that both methods predict the same (qualitative) behavior.

III. Results.
NG interstitials: Interstitial NG impurities are at the tetrahedral interstitial (T) site. There is very little perturbation to the energy eigenvalues relative to the perfect cluster in the case of He and Ne, which minimally perturb the host crystal (less than 1% lattice relaxation). Ar, Kr, or Xe result in increasingly large lattice relaxations around the T site and some band-tailing occurs.

The saddle point for the diffusion is at the hexagonal interstitial (H) site. The activation energies for diffusion calculated at the *ab-initio* HF level are 1.38 eV for He (experiment:[19] 1.27 eV), 2.03 eV for Ne, 3.51 eV for Ar, 3.88 eV for Kr, and 3.93 eV for Xe. The PRDDO/M

values are larger (see below).

Since interstitial NG impurities have T_d symmetry and no deep levels in the gap, they cannot be the centers causing the PL. Since their activation energies for diffusion are very high, they cannot by themselves diffuse rapidly.

NG-vacancy interactions: The monovacancy (V_1)in Si is a fast diffuser.[20,21] The expected reaction between an interstitial atom and V_1 consists in the interstitial becoming substitutional. The case of NGs is different because the promotion energy from the ground to the lowest-energy open-shell configuration is very large and a NG atom will not bind to the host atom. Inside V_1, a NG not only disrupts the rebonding, but is strongly repelled by the electron density in the reconstructed bonds. Geometry optimizations for a NG *inside* result in energies substantially higher than *outside* V_1, near the T site. Even in the best configuration, the $\{NG, V_1\}$ pair is much higher in energy than the isolated interstitial NG far away from V_1. The NG-V_1 repulsion energy is compared to the activation energy E_a for diffusion of the *interstitial* NG in Fig. 1.

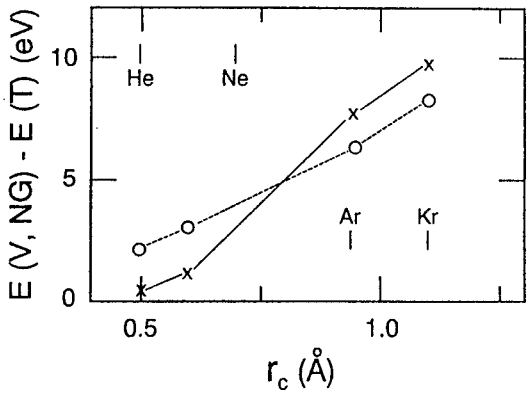


FIGURE 1: The dashed line is the activation energy of the interstitial NG and the solid line the NG-vacancy repulsion, both calculated at the PRDDO/M level.

The NG-V_1 repulsion is less than E_a for He and Ne, and more for Ar and Kr. However, the difference between the two curves is small. This suggests an unusual vacancy-enhanced diffusion mechanism. If an energetic flux of V_1's comes from the surface as could occur during the etching,[22] the vacancies would repel the NG interstitials with enough energy to help them overcome the barrier.

Noble-gas–divacancy complexes: The lowest-energy structure of the neutral V_2 in Si calculated at the PRDDO/M level is shown in Fig. 2. The configuration was obtained in the (44-2) Si atoms cluster by gradient optimization of its six NNs in C_1 symmetry. The three Si atoms above and below the center of V_2 rearrange themselves: one of them forms a 'strong' bond with its two NNs and the other two form one 'weak' bond with each other and each makes a bond 'across' V_2. The overlap population in each of these reconstructed bonds is positive, indicating a bonding interaction. Note that the bond strengths are not known or predicted! The words 'strong' and 'weak' refer only to the degree of bonding.[23]

Since there are three identical configurations, the symmetry will be trigonal on the average provided that the activation energy for reorientation is small. A few hundredths of an eV are quoted for such a reorientation in Ref. [24].

V_2 diffuses around 250 $^{\circ}C$ with an activation energy of 1.3 eV.[24] Geometry optimizations show that an interstitial NG (even Kr) is easily 'swallowed' by V_2 with a substantial gain in

energy (no activation energy is involved). The energy difference between an NG interstitial far from an isolated V_2 and the NG inside V_2 shows that NG atoms are remarkably stable in V_2. Almost 80% of the energy needed to insert a free NG into the T site in Si is recovered by putting it into V_2.

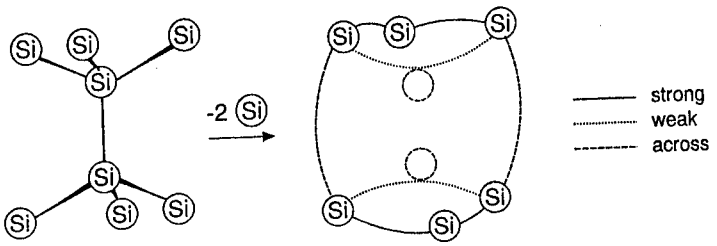


FIGURE 2: Schematic representation of the lowest-energy configuration of the neutral divacancy. The dashed circles show the lattice sites of the missing Si atoms.

The NG weakly perturbs the reconstruction of V_2 (Table I). The covalent character of the bonds is reduced, but there is no configurational change. The NG pushes its six NNs away from it by a small amount and remains almost on center. This suggests that a reorientation between three equivalent configurations around the same trigonal axis can still occur.

	Divacancy	He	Ne	Ar	Kr
			displacement (Å)		
each NN (avg.)	0.00	0.05	0.07	0.23	0.27
NG (off center)	–	0.07	0.09	0.11	0.06
			degree of bonding/overlap population		
strong bond	0.49/0.20	0.48/0.18	0.46/0.16	0.41/0.09	0.40/0.08
weak bond	0.07/0.04	0.07/0.04	0.06/0.03	0.07/0.01	0.03/0.01
across bond	0.18/0.02	0.19/0.01	0.20/0.01	0.16/0.00	0.14/0.00
			Mulliken charge ($\|e\|$)		
each NN (avg.)	−0.11	−0.12	−0.13	−0.14	−0.16
NG	–	+0.01	+0.08	+0.22	+0.29

TABLE I: Divacancy-NG complexes. First row: average displacement of the 6 NNs caused by the NG. Second row: displacement of the NG off the center of V_2. Third to fifth rows: degree of bonding/overlap population for the various bonds (Fig. 2). Sixth row: average Mulliken charge on the 6 NNs. Seventh row: Mulliken charge on the NG.

The change in Mulliken charges shows that the six NNs capture increasing amounts of electron density from the NG. The charge on each of the Si NNs varies from -0.11 to -0.16 while that on the NG changes from $+0.01$ to $+0.29$, as one goes from He to Kr. The ionization enthalpies decrease from He to Kr, making it easier for the reconstructed bonds to grab charge from the NG. This trend should continue with Xe. An extrapolation of the He–Kr trends shows that its charge should be around 0.5. This is enough for Xe to form a covalent bond. For example, the charges calculated at the HF level for KrF_2 and XeF_2 are 0.4 and 0.5, respectively. Table I shows that, Kr in $\{Kr, V_2\}$ is not sufficiently polarized to form a covalent bond, but Xe should be. High-level calculations will be needed to confirm this.

V_2 and each of the $\{NG, V_2\}$ complexes have six levels in the gap, three of which are doubly occupied. The positions of these levels shift with the NG. While the calculated eigenvalues are qualitative at best, the trends and shifts for $\{NG, V_2\}$ relative to V_2 are more meaningful. We calculated the energy differences between the eigenvalues then the shifts of these differences relative to V_2. All the shifts are toward lower energies. Some of them are almost independent

of the NG, others vary monotonically with the size of the NG, but two of the shifts have a trend identical to that of the zero-phonon line discussed by Davies *et al.*[11]

Larger vacancy aggregates: We have calculated[25] the formation energies and stable configurations of vacancy aggregates up to the V_7. Since experiment[1,13,14] shows that the NG-related defects contain 4 vacancies or less, our calculations cover all the possible vacancy clusters. In the lowest-energy configuration, only V_2 and V_6 can have trigonal symmetry. As the observed PL lines correspond to a trigonal defect, we rule out V_3, V_4, and V_5.

V_6 consist of a missing hexagonal ring.[25] It reconstructs very efficiently, has no deep levels in the gap, and therefore cannot produce sharp PL features. However, a broad PL spectrum could be associated with it. The stability of V_6 could explain the irreversible disappearance of the NG-related PL lines after high-temperature anneals. The large gain in energy resulting from the formation of $\{NG, V_2\}$ complexes makes it nearly impossible that it dissociates. Instead, more vacancies could cluster around it until the $\{NG, V_6\}$ centers forms.

IV. Discussion.

If the NG-related PL centers involve only one NG and vacancies, our calculations imply the following. *(1)* The NG-related PL centers are due to the formation of $\{NG, V_2\}$ complexes. The calculated features agree at least qualitatively with the observed properties of the centers. *(2)* The enhanced diffusion of NG impurities could be caused by the strong NG-V_1 repulsion if the etching results in a flux of vacancies diffusing into the bulk. *(3)* The PL centers are created during the anneal which follows the implant, as mobile V_2's 'swallow' NG interstitials. *(4)* $\{NG, V_n\}$ complexes with n=3, 4, or 5 should not be trigonal. *(5)* The broad-band PL which follows high-temperature anneals could be due to the formation of $\{NG, V_6\}$ complexes.

Although the features of our model are consistent with many experimental features, there exist discrepancies[26] between the reported properties of the divacancy and the model presented here for the NG-related PL.

The divacancy was studied in great detail by many experimental techniques (EPR, IR, and DLTS). The symmetry of the EPR-active charge states V_2^+ and V_2^- is C_{2h}. There is also evidence for the same symmetry lowering in the V_2^0 state.[27] A motional averaging between the equivalent Jahn-Teller distorted sites around a specific $< 111 >$ direction is detected only at higher temperatures. However, the splitting of the W-line and the NG-related lines (except Xe) in a uniaxial stress field exhibits trigonal symmetry. Although the stress data[11,28] are complicated by strong interactions of excited states and small stress splittings, the discrepancy between the divacancy splitting and the splitting of the NG lines is obvious. The only way to reconcile the differences is to assume a higher symmetry of the optical excited state compared to the ground state, which should have the symmetry deduced from the EPR measurements.

The divacancy is generated directly at room temperature irradiation in contrast to the W line and the NG-related lines which require annealing. However, we note that there is an early report that the W-line is also weakly detectable directly after room-temperature irradiation).[29] Further, the divacancy and the W-line anneal out in the same temperature regime. Further PL and DLTS experiments on the annealing of the divacancy and W-line in the *same* samples are needed.

Acknowledgements: We are thankful to G.D. Watkins for pointing out some inconsistencies in the NG defect model. The work of SKE is supported in part by the grant D-1126 from the R.A. Welch foundation and the contract RAD-7-17652-01 from the National Renewable Energy Laboratory. SKE is thankful to Professor Queisser and his group at the Max-Planck Institute in Stuttgart (FKF) for their hospitality.

References.

1. For a recent review, see J. Weber, Physica B **170**, 201 (1991).
2. K. Wittmaack and W. Wuch, Appl. Phys. Lett. **32**, 532 (1978).
3. S.M. Myers, D.M. Follstaedt, H.J. Stein, and W.R. Wampler, Phys. Rev. B **45**, 3914 (1992); H.J. Stein, S.M. Myers, and D.M. Follstaedt, J. Appl. Phys. **73**, 2755 (1993).
4. P. Revesz, M. Wittmer, J. Roth, and J.W. Mayer, J. Appl. Phys. **49**, 5199 (1978).
5. G. Davies, Phys. Rep. **176**, 83 (1989).
6. V.D. Tkachev, A.V. Mudryi, and N.S. Minaev, Phys. Stat. Sol. (a) **81**, 313 (1984).
7. N. Bürger, K. Thonke, R. Sauer, and G. Pensl, Phys. Rev. Lett. **52**, 1645 (1984).
8. N.S. Minaev, A.V. Mudryi, and V.D. Tkachev, Phys. Stat. Sol. (b) **108**, K89 (1981).
9. Y.H. Lee and J.W. Corbett, Phys. Rev. B **9**, 4351 (1974).
10. J.W. Corbett, J.C. Bourgoin, and C. Weigel, IOP Conf. Ser. **16**, 1 (1973).
11. G. Davies, E.C. Lightowlers, and Z.E. Ciechanowska, J. Phys. C **20**, 191 (1987).
12. W.D. Sawyer, J. Weber, G. Nabert, J. Schmälzlin, and H.-U. Habermeiser, J. Appl. Phys. **68**, 6179 (1990).
13. W.D. Sawyer and J. Weber, MRS Proc. **176**, 197 (1987).
14. J. Weber and W.D. Sawyer in *Defect Control in Semiconductors*, ed. K. Sumino (Elsevier, 1990), p.513.
15. S.K. Estreicher, J. Weber, A. Derecskei-Kovacs, and D.S. Marynick, Phys. Rev. **55**, 5037 (1997).
16. A. Derecskei-Kovacs and D.S. Marynick, Int. J. Quant. Chem. **58**, 193 (1996), A. Derecskei-Kovacs, D.E. Woon, and D.S. Marynick, Int. J. Quant. Chem. **61**, 67 (1997).
17. S.K. Estreicher, Mat. Sci. Engr. Reports **14**, 319 (1995).
18. P.J. Hay and W.R. Wadt, J. Chem. Phys. **82**, 270 (1985).
19. A. Van Wieringen and N. Warmholtz, Physica **22**, 849 (1956).
20. G.D. Watkins in *Deep Centers in Semiconductors*, ed. S.T. Pantelides (Gordon and Breach, New York, 1986), p. 147.
21. Y.K. Park, S.K. Estreicher, C.W. Myles, and P.A. Fedders, Phys. Rev. B **52**, 1718 (1995).
22. J.W. Corbett, J.L. Lindström, and S.J. Pearton, MRS Proc. **104**, 229 (1988).
23. D.R. Armstrong, P.G. Perkins, and J.J.P. Stewart, J. Chem. Soc. Dalton Trans. 1973, p. 838.
24. J.W. Corbett in *Electron Radiation Damage in Semiconductors and Metals* (Academic, New York, 1966).
25. S.K. Estreicher, J.L. Hastings, and P.A. Fedders, Appl. Phys. Lett. **70**, 432 (1997); J.L. Hastings, S.K. Estreicher, and P.A. Fedders, Phys. Rev. B (in print) and this conference.
26. G.D. Watkins, private communication.
27. G.D. Watkins and J.W. Corbett, Phys. Rev. **138**, A543 (1965).
28. N. Bürger, E. Irion, A. Teschner, K. Thonke, and R. Sauer, Phys. Rev. B **35**, 3804 (1987).
29. C.G. Kirkpatrick, J.R. Noonan, and B.G. Streetman, Rad. Eff. **30**, 97 (1976).

Materials Science Forum Vols. 258-263 (1997) pp. 611-616
© 1997 Trans Tech Publications, Switzerland

IMPLANTATION OF REACTIVE AND UNREACTIVE IONS IN SILICON

J.R. Brucato(1), G.A. Baratta(2), G. Compagnini(3), G. Strazzulla(2)

(1) Osservatorio Astronomico di Capodimonte, Napoli, Italy
(2) Osservatorio Astrofisico di Catania, Citta' Universitaria. I-95125 Catania, Italy
(3) Dipartimento di Chimica dell'Universita', Catania, Italy

Keywords: silicon, implantation, infrared

Abstract. We present the results of a series of experiments, performed in our laboratory, on the implantation of reactive (H, C, N, O) and unreactive (He, Ar) ions into silicon. In particular we investigated the formation of chemical bonds between the projectile and the target atoms searching for the appearance of characteristic IR bands. When the impinging ions are reactive (H, C, N, O) they form bonds with the Si atoms in the target that are evidenced by IR spectroscopy. The astrophysical relevance of the results is also discussed.

Introduction

Ion implantation of reactive species into amorphous or crystalline matrices has been used to investigate the formation of stable (silicon oxide, nitride, carbide,..) surface thin films or buried layers[1-3] in order to use them in several fields such as microelectronics, wear and optical coatings. This is because the method allows to vary with good accuracy and reproducibility the concentration of the reactive species into the implanted target[4,5]. In the case of incoming reactive ions both chemical and radiation damage effects are produced. For this reason the obtained results must be compared with those found after implantation of unreactive noble gas ions. Vibrational spectroscopy has to be considered a usefull technique in investigating these systems because it is able (using either Raman scattering or infrared absorption) to give information on the state and bonding configuration of the foreign species inside the solid and on the formation and evolution of disorder due to radiation damage effects[5,6]. For instance, the detection and characterization of both homonuclear (Si-Si, C,...) and etheronuclear (Si-C, Si-N,.....) stretching signals in a-$Si_{1-x}C_x$, a-$Si_{1-x}N_x$ and a-$Si_{1-x}O_x$ samples can give a complete view of the bonding arrangement of the investigated matrix and allows to separate topological and compositional disorders.

Astrophysicists are interested in studying implantation of reactive ions in materials as well. In space there are in fact many places, including interstellar dust and planetary objects, where energetic (keV-MeV) particles impinge on solid surfaces made of refractory (carbonaceus and/or silicates) materials and/or frozen ices[7]. Implantation experiments are, in particular, very important for application to objects in the Solar System (planetary surfaces, comets, asteroids, etc.) continuosly irradiated by some ion populations (flare and solar wind ions, magnetospheric particles, cosmic rays, etc.). Most of the incoming ions (H, C, N, O) are in fact reactive and could produce, in the irradiated layers, new species that include the projectile. This implies the possibility to detect, on planetary surfaces, molecular species not necessarily native of that object but formed by implantation of incoming reactive ions.

Here we present results of a series of experiments, performed in our laboratory, on the implantation of about 1 keV/amu reactive (H, C, N, O) and unreactive (He, Ar) ions into silicon used as a

reference material. The results furnish an extimation of the absorbances of the newly formed absorption bands that could be used for astrophysical applications.

Experimental apparatus

We used "in situ" FTIR spectroscopy in the 400-4400 cm^{-1} (25-2.27 microns) range. The experimental apparatus has been already described [7]: it is essentially constituted by a scattering chamber faced through IR-transparent windows, to an FTIR spectrophotometer. Vacuum is better than 10^{-7} mbar. The targets are silicon (111) single crystals (600 microns thick) mounted onto a cold finger (10-300 K). Ions have been obtained from a 30 keV ion implanter.

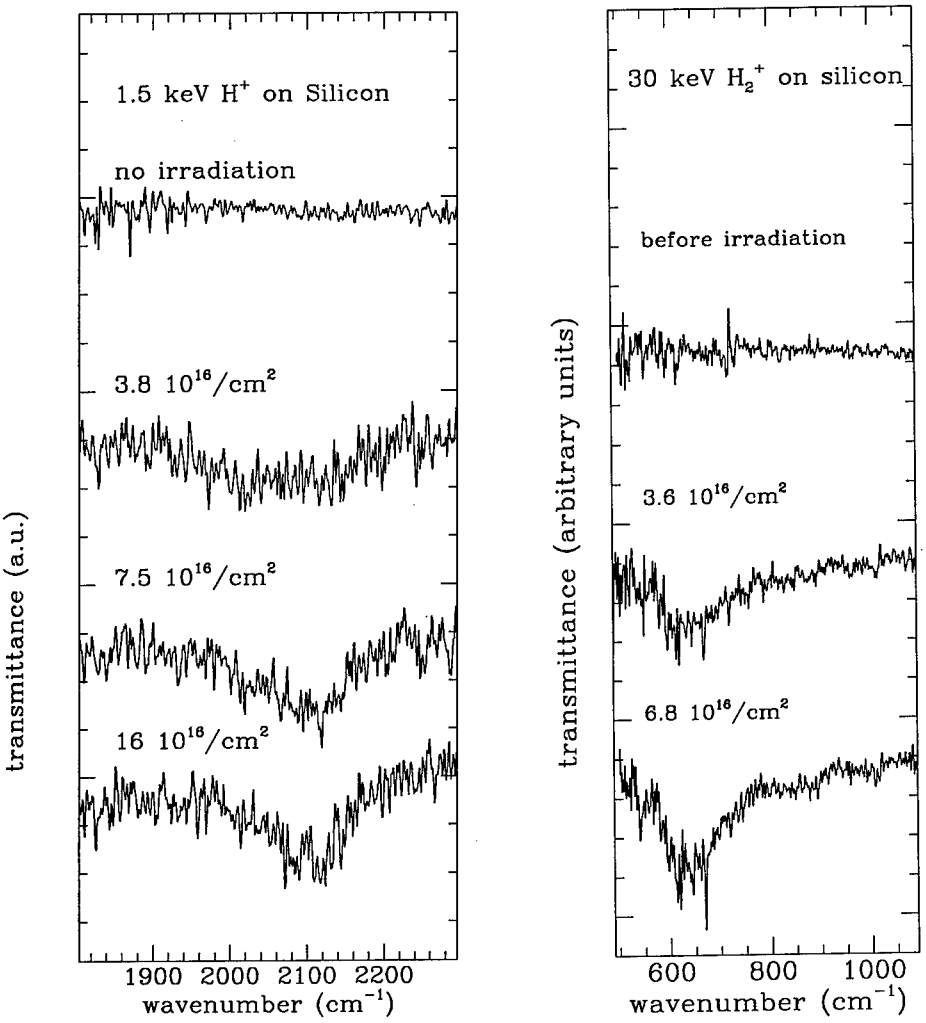


Figure 1. IR spectra in the 1800-2300 cm^{-1} (Si-H stretching, left panel) and in the 500-1100 cm^{-1} (SiH wagging, right panel) obtained after irradiation, at different fluences, of crystalline silicon with 1.5 keV H^+ and 30 keV H_2^+ ions respectively.

Experimental results

1.5-30 keV H^+ or H_2^+ ion beamss have been implanted into silicon crystals at fluences between 10^{16} and 5 10^{17} protons cm^{-2}. In Figure 1 some IR spectra in the 1800-2300 cm^{-1} (Si-H stretching) and in the 500-1100 cm^{-1} (SiH wagging) are presented. We have measured the variation of the integrated band due to the Si-H stretch as a function of the ion fluence and temperature (Figure 2). It is clear a linear relationship between the area of the band and ion fluence. For the lowest ion energy (3 keV H_2^+) saturation is observed at fluences greater than about 6 10^{16} protons cm^{-2}. This result is in agreement with theoretical calculations we performed by using TRIM code (the TRansport of Ions in Matter) explained in detail in [8]. Implants have been done at room temperature, the target has then been cooled down to 10 K and spectra taken at different temperatures. The results indicate an increase in the absorbance of the stretching band as shown in Figure 2.

Some spectra obtained after implantation of N and O ions are shown in Figure 3 (left and central panel respectively). In the right panel we show the spectra obtained after implantation of H, C, N, O and Ar.

The new bands we observe after irradiation with reactive ions are due to the formation of chemical species (Si-H bonds, silicon carbide and nitride). Of course defects have been produced in the crystalline structure of silicon as well. Anyway IR technique is not able in quantify this effect. We are planing to use "in situ" Raman spectroscopy to study the details of the ion induced radiation damage and crystal-amorphous transition.

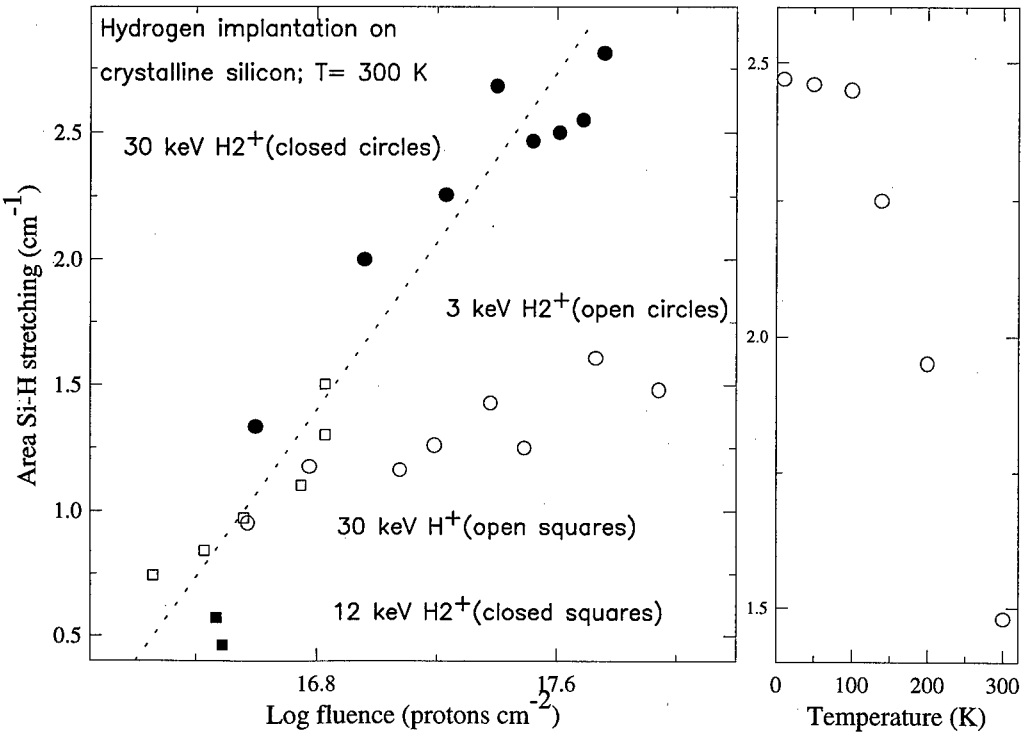


Figure 2. The integrated band strength due to the Si-H stretch is reported, for several ion energies, as a function of the ion fluence (left panel) and temperature (right panel).

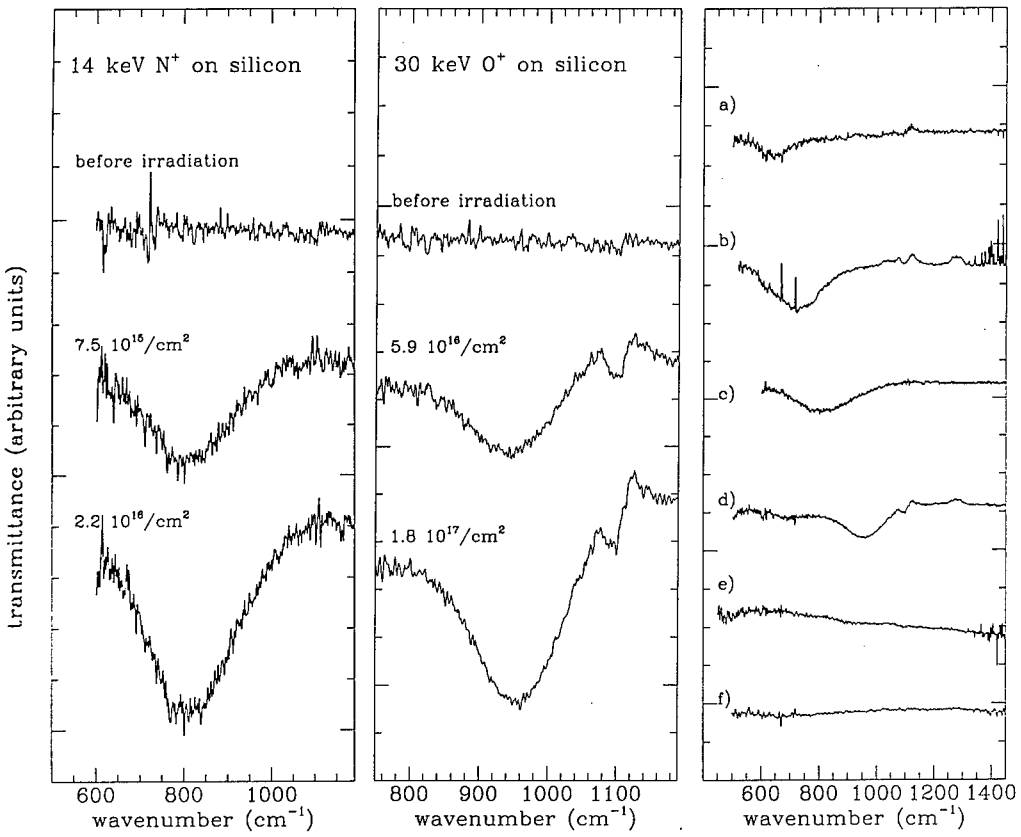


Figure 3. IR spectra obtained after irradiation of crystalline silicon with 14 keV N^+ (left panel) and O^+ (central panel). In the right panel the spectra have been obtained after implantation of:
(a) 7.5 10^{16} H^+ (30 keV)/cm^2; (b) 1.1 10^{17} C^+ (30 keV)/cm^2;
(c) 2.2 10^{16} N^+ (14 keV)/cm^2; (d) 1.7 10^{17} O^+ (30 keV)/cm^2;
(e) 1.5 10^{16} Ar^+ (100 keV)/cm^2; (f) 1.5 10^{16} Ar^{++} (60 keV)/cm^2.

Discussion

The ion population in the interplanetary medium is essentially due to solar wind and flare ions. Solar wind ions are produced by plasma expansion whose velocity, at a distance of few solar radii, becomes supersonic, of the order of 400 km/sec (i.e. ions have energies of about 1 keV/amu). At 1 Astronomical Unit (1AU = 1.495 10^{11} m) the wind has a density of the order of 5 protons cm^{-3}, corresponding to a flux of about 2 10^8 protons cm^{-2} sec^{-1}. The flux varies as the inverse of the square of the distance from the Sun. Thus, for example, at a distance of the order of 3 AU the number of protons impinging on an hypothetical asteroidal surface is of the order of 10^{17} cm^{-2} in only 100 yrs. Such a high flux is expected to produce a number of effects such as sputtering [9] and ion implantation. It has been suggested that a clear test of proton implantation could be the observability of the Si-H stretching band on the surfaces of atmosphearless planetary objects [10, 11]. Although such a possibility has been questioned by our group [12] on the

basis of some results obtained by ion implantation in amorphous silicates, the possibility exists to detect some IR features due to implantation of reactive ions on both amorphous and crystalline silicates (these latter recently detected by ISO, Infrared Space Observatory, satellite in cometary dust). The results we have presented here would permit to quantitatively measure the number of implanted ions and then the time to which those objects have been exposed to cosmic radiation.

References

1. G.K. Celler, P.L.F. Hemment, K. West and J.M.Gibson, Appl.Phys.Lett. 48 (1986) 532.
2. H.J. Stein, J.Electochem.Soc. 132 (1985) 668.
3. G. Compagnini and L. Calcagno, Mat.Sci.and Eng. R13 (1994) 193.
4. J. Bullot and M.P. Schmidt, Physica Status Solidi, 143 (1987) 345.
5. G. Compagnini, L. Calcagno, G. Foti and G.A. Baratta, J.Mater.Res. 11 (1996) 2269.
6. P.I. Rovira and F. Alvarez, Phys.Rev. B55 (1997) 4426 .
7. G. Strazzulla, J.R. Brucato, M.E. Palumbo and M.A. Satorre, NIM B116 (1996) 289.
8. J.F. Ziegler, J.P. Biersack and U. Littmark, The stopping and range of ions in solids, Pergamon Press, New York (1985)
9. W. Hage, A. Hallbrucker and E. Mayer, J.Am.Chem.Soc. 115 (1993) 8427.
10. J.A. Nuth, M.H. Moore and T. Tanabh, Icarus 98 (1992) 207.
11. M.H. Moore and T. Tanabh and J.A. Nuth, Astrophys. J. Lett. 373 (1991) L31.
12. A. Buemi, G. Cimino, G. Leto and G. Strazzulla, Icarus 108 (1994) 169.

Materials Science Forum Vols. 258-263 (1997) pp. 617-622
© 1997 Trans Tech Publications, Switzerland

PHOTOLUMINESCENCE VIBRATIONAL SPECTROSCOPY OF DEFECTS CONTAINING THE LIGHT IMPURITIES CARBON AND OXYGEN IN SILICON

E. C. Lightowlers and A. N. Safonov
Physics Department, King's College London, Strand, London WC2R 2LS, United Kingdom

Keywords: silicon, carbon, oxygen, photoluminescence, vibrational modes

Abstract. A brief report is made on the carbon and oxygen isotope structures of the local vibrational modes of the C-line and G-line luminescence systems created by radiation damage of Czochralski silicon with a high carbon concentration, together with a first time investigation of the local mode structures of the F-line and H-line luminescence systems created by subsequent annealing at 350 and 450°C. A preliminary analysis shows that there is no carbon-carbon or carbon-oxygen bonding in any of these centres, and only very minor dynamic interaction between the different carbon and oxygen atoms exists. The presence of similar and, in some cases, almost identical local modes for the different centres suggests that parts of defect structures responsible for G- and C-line, F- and H-line and some other luminescence systems have similar atomic configurations. It is suggested that the F-line centre is created by the capture of a mobile version of the G-line centre by the C-line centre, and that the subsequent capturing of extra oxygen atom gives rise to the H-line centre.

Introduction

Photoluminescence (PL) spectra of deep level centres in silicon generally have a sharp zero-phonon line, together with a broad side band of phonon-assisted transitions at lower energies associated with perturbed lattice modes. When the defect contains light impurities such as hydrogen, carbon and oxygen, its spectrum can also have relatively sharp structures at lower energies due to phonon-assisted transitions involving local vibrational modes with energies greater than the highest energy lattice mode. The local mode satellites are commonly between 10 and 100 times weaker than the zero-phonon line, and often lie outside the spectral range of the high sensitivity Ge detector generally employed for PL measurements on silicon, which explains the difficulties of their investigation for many luminescence system. However, they contain important information concerning the atomic composition of the defect and can enable the structure to be identified. One of the examples for this is the di-carbon hydrogen centre responsible for the T-line, whose microscopic structure has been identified recently as a result of *ab-initio* cluster calculations of local vibrational modes combined with uniaxial stress and magnetic field perturbation measurements on the zero-phonon luminescence line [1].

Spectroscopic identification of defect vibronic properties has been long established as one of the most effective methods for characterising impurity centres. The main technique extensively used for this purpose is mid-infrared absorption spectroscopy, which has proved to be particularly effective for the investigation of electrically inactive centres. Unfortunately, many oxygen and carbon related local modes lie within the two-phonon lattice absorption bands which makes them difficult to observe in absorption spectra other than at quite high concentrations. Therefore, in some cases PL spectroscopy is a more appropriate method for their investigation. In addition, it provides several advantages associated with PL technique, including a more effective way for identifying the different modes belonging to the same centre and for establishing the symmetry of the defect from uniaxial stress and magnetic field perturbation measurements on the zero-phonon line.

In this paper a brief report is made of some recent investigations of the local vibrational modes associated with several major luminescence centres created in Czochralski (CZ) silicon by radiation damage and by subsequent thermal treatment. Two of these systems, C-line (0.7896 eV) and G-line

(0.9694 eV), created in as-irradiated silicon, have been heavily investigated previously [2] and are well established now to be associated with centres containing one carbon and one oxygen atom, and two carbon atoms, respectively. The local mode features of two other systems, F-line (0.9499 eV) and H-line (0.9256 eV), created by subsequent thermal treatment, which have not been investigated previously in any detail, will also be reported. No structural analysis has been carried out at this stage. However, these preliminary results clearly show that, during the thermal treatment of irradiated CZ material in the temperature range 200-450^{o}C, the annealing of the original di-carbon and carbon-oxygen centres results in formation of more stable carbon-oxygen complexes containing more than three impurity atoms.

Experimental

The material used in these investigations was CZ silicon with [O] ~ 1 x 10^{18} cm^{-3} and [C] between 1 and 2 x 10^{17} cm^{-3}, with either normal isotope ratios or with ^{13}C : ^{12}C ~ 5 : 1 or ~ 1 : 1. The material with ^{18}O : ^{16}O ~ 2 : 1 or ~ 1 : 1 was created by heating float zone (FZ) silicon, with [C] between 1 and 2 x 10^{17} cm^{-3}, in water vapour with 95% ^{18}O at 1300^{o}C for either 2 or 4 days. Deliberate hydrogen incorporation at ~ 1.5 x 10^{16} cm^{-3} was carried out by heating in flowing hydrogen gas at 1300^{o}C for 30 minutes, followed by rapid cooling either by dropping the sample in silicone oil or the quartz tube was withdrawn from the furnace and thrust in water in ~ 2 seconds with the hydrogen gas flowing. The samples were then irradiated with either 2 or 4 x 10^{17} cm^{-2} 2 MeV electrons. The subsequent thermal treatments were carried out in air.

All the spectra reported here were obtained using a Nicolet 60SX Fourier transform spectrometer modified for PL measurements. A North Coast cooled Ge diode detector was used for measurements at energies > 0.7 eV, and a Cincinnati Electronics cooled InSb diode detector, fitted with a 2800 nm short wavelength pass cold filter, for measurements below 0.7 eV. All the spectra were recorded with the samples immersed in liquid helium at 4.2 K, excited by a 514 nm Ar^{+} laser with power typically 400 mW. Recording times varied from ~ 15 minutes for a standard zero-phonon line spectrum to ~ 8 hours for recording local modes at energies < 0.7 eV. The resolutions employed were either 0.5, 1.0 or 2.0 cm^{-1}.

Results and discussion

Figure 1 shows some PL spectra extracted from a detailed isochronal annealing study of electron irradiated high carbon containing CZ silicon, with (a-c) and without (d-f) deliberate hydrogen incorporation. With no thermal treatment (a,d), the only centres created in the both types of the material are those responsible for the C-line and G-line luminescence systems. Radiation damage creates silicon interstitials which remove carbon atoms from their substitutional sites, and then mobile carbon can create carbon-oxygen and carbon-carbon centres which are responsible, respectively, for the C-line and G-line luminescence systems. Models have been proposed for both of these centres [3-5], based to some extent on local vibrational mode data. Clearly, the presence of hydrogen has little effect on the spectra from as-irradiated silicon, but plays an important role in the formation of luminescence centres during subsequent thermal treatments at T > 300^{o}C. The G-line centre is destroyed in less than 30 minutes at 250^{o}C and the F-line and P-line (0.7671 eV) begin to appear along with some other weaker systems which have not been labelled or investigated, but the C-line is not destroyed at this temperature. With a 30 minute anneal at 350^{o}C (b,e), the C-, F- and P-lines are the major systems present, together with the M-line (0.7608 eV) and another not labelled system in hydrogenated material. Both the C-line and the F-line are rapidly destroyed at temperatures > 400^{o}C, and with a 30 minute anneal at 450^{o}C (c,f) the H-line and P-line systems are dominant in material without deliberate hydrogen incorporation, and the T-line and I-line (0.9650 eV) systems are dominant in hydrogenated material. As stated earlier, the T-line has recently been investigated in detail [1], and recent investigations of the M-line [6] and the I-line [7] systems are reported at this conference. In this paper we will concentrate on the creation and the properties of the F-line and H-line centres and compare their characteristics with those of the G-line and C-line centres.

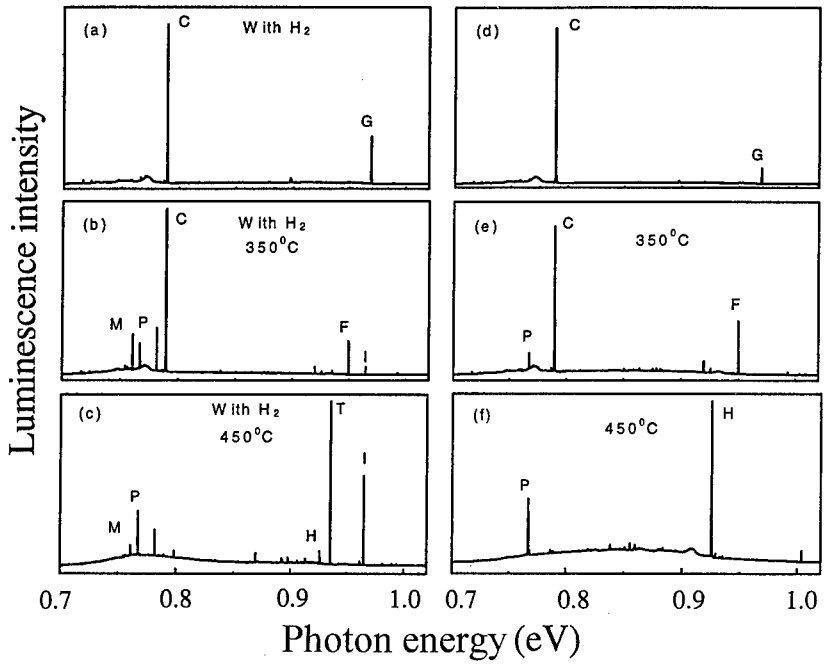


Fig.1. Photoluminescence spectra obtained from CZ silicon with [C] ~ $1x10^{17}$ cm^{-3}, either (a-c) with deliberate hydrogen incorporation of ~ 1.5×10^{16} cm^{-3}, or (d-f) no deliberate hydrogen incorporation, irradiated with $2x\ 10^{17}$ cm^{-2} 2MeV electrons, (a,d) with no further treatment, or subsequently annealed for 30 min. at either (b,e) 350°C or (c,f) 450°C.

Figure 2 shows the major features in the local mode structure of the C-line luminescence system obtained from material with either ^{18}O : ^{16}O ~ 2 : 1 (a,b) or ^{13}C : ^{12}C ~ 5 : 1 (c,d). This structure was investigated several times in the 1980's [8-10], and the labelling employed is that used in the last report [10] in which 14 local mode features were identified. However, careful examination shows that the many of them correspond to different combinations of four basic local modes. Both of the major features L_1 and L_2 show a small oxygen isotope splitting, which can be seen more clearly at higher resolution, but no carbon isotope splitting [8]. Silicon isotope structure can also be observed in these features [8] which are clearly associated with the vibration of a silicon atom close to the oxygen atom but remote from the carbon atom in the centre. The broader feature at lower energy labelled with an asterisk has a large oxygen isotope splitting. The local mode frequency is 741.4 cm^{-1} (91.92 meV) for ^{16}O and 709.1 cm^{-1} (87.92 meV) for ^{18}O, and the ratio of 1.046 is fairly close to $(18/16)^{0.5}$ =1.061 expected for a pure oxygen vibrational mode. In the lower energy region, the feature labelled L_4 coincides almost exactly with $2L_2$ and has similar oxygen isotope structure as L_2. The feature L_5 is very close to the sum of L_2 and the feature labelled with an asterisk, and shows the same oxygen isotope structure as the latter. L_3 coincides almost exactly with $L_1 + L_2$, but the shape and size shown in Fig. 2a would appear to be inconsistent with this interpretation. However, in material with ^{13}C : ^{12}C ~ 5 : 1 (Fig. 2c), a new feature appears at higher energy which we have labelled ^{13}C, and the L_3 feature is closer to what would be expected for the sum of $L_1 + L_2$. It is clear from these data that there is a carbon vibrational mode which for ^{12}C we have labelled ^{12}C and which coincides with $L_3 = L_1 + L_2$ for ^{16}O. The local mode frequencies are 1116 cm^{-1} (138.4 meV) for ^{12}C and 1079 cm^{-1} (133.8 meV) for ^{13}C, and the ratio 1.034 is fairly close to $(13/12)^{0.5}$ =1.041 expected for a pure carbon vibrational mode. This has removed some of the confusion in the earlier work [10] and is consistent with the results of mid-infrared absorption measurements. We have to note the presence of the oxygen mode (741.4 cm-1), which is of particular interest since two other

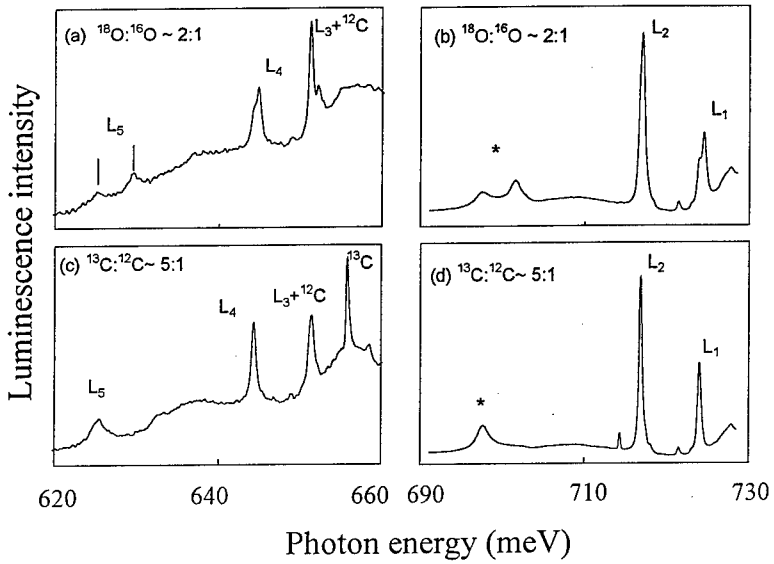


Fig. 2. Photoluminescence spectra showing the local mode structure of the C-line, obtained from material with (a,b) ^{18}O : ^{16}O ~ 2:1 and (c,d) ^{13}C : ^{12}C ~ 5:1.

systems with zero-phonon lines at 0.9198 eV and 0.9499 eV (F), to be discussed below, have similar modes suggesting that all three centres contain an oxygen atom in the same configuration.

We will now turn briefly to the G-line luminescence system. There is a very strong local mode feature labelled S [11] with a frequency of 579.5 cm^{-1} (71.85meV) for ^{12}C and 564.4 cm^{-1} (69.97 meV) for ^{13}C. A very much weaker system was also identified at higher energy [11], labelled W, with a frequency of 543.1 cm^{-1} (67.34 meV) for ^{12}C and 532.2 cm^{-1} (65.98 meV) for ^{13}C. We have recently noticed that the weak feature at lower energy labelled S + A [11], with A being the sharp peak on the lattice acoustic mode, has a frequency of 731.1 cm^{-1} (90.64 meV) for ^{12}C and 709.4 cm^{-1} for ^{13}C, the isotope shift of 21.7 cm^{-1} being different from 15.1 cm^{-1} for the S feature. This is clearly a third carbon vibrational mode of the G-line centre which, similar to the two other modes, has a ^{12}C / ^{13}C frequency ratio close to that expected for an isolated carbon-silicon pair vibration. The presence of three carbon vibrational modes, showing only very small coupling between the carbon atoms, does not appear to be consistent with the proposed model for the G-line centre [5]. However this problem requires a special consideration and will be discussed in more detail elsewhere.

The zero-phonon line at 0.9499 eV, created by annealing radiation damaged CZ silicon at temperatures in the range 250 to 400^{o}C, was reported in 1977 [12] but was called the G-line rather than the F-line. Because the zero-phonon line at 0.9694 eV had also been labelled as the G-line and was heavily investigated, the line at 0.9499 eV was relabelled as the F-line in reference 13. In spite of the fact that this is the major new system created by annealing radiation damaged CZ silicon at temperatures < 400^{o}C, rather than at 450^{o}C so commonly used, no investigations appear to have been made or reported. Actually, another system with zero-phonon line at 0.9198 eV is always created along with the F-line and can be seen in Fig. 1b and 1e. Some other systems appear and disappear in the temperature range 200-300^{o}C in which the G-line is slowly or quickly destroyed and the F-line begins to be created. We will concentrate here on the F-line.

The major local mode features in the F-line luminescence system are shown in Fig. 3 for material with (a) no isotope substitution, (b) ^{13}C : ^{12}C ~ 1 : 1 and (c) ^{18}O : ^{16}O ~ 1 : 1. Those clearly identified are labelled L_1 to L_6. In the range of materials investigated so far, the first relatively sharp feature below L_1 always appears to have the same ratio to L_1, but the second one varies from sample to sample. Some of the structure below the L_6 is associated with the zero-phonon line at 0.9198 eV

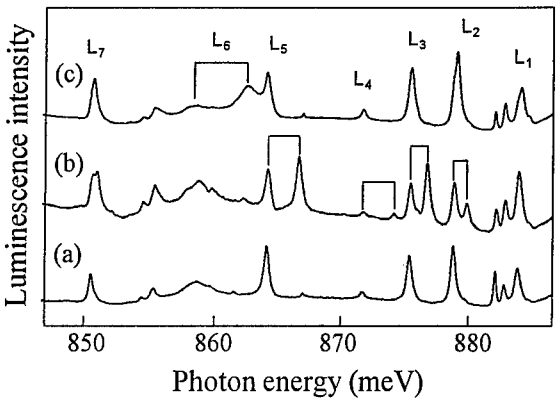


Fig. 3. Photoluminescence spectra showing the local mode structure of the F-line,obtained from material with (a) no isotope substitution, (b) ^{13}C : ^{12}C ~ 1:1 and (c) ^{18}O : ^{16}O ~ 1:1.

which is always created with the F-line. L_1 with frequency 532.6 cm^{-1} (66.03 meV) has no carbon isotope splitting but is broadened in ^{18}O doped material. The features L_2, L_3, L_4 and L_5 with ^{12}C frequencies of 572.9 cm^{-1} (71.03 meV), 600.5 cm^{-1} (74.45 meV), 630.4 cm^{-1} (78.16 meV) and 691.5 cm^{-1} (85.74 meV), respectively, correspond to carbon vibrations. All of them have quite large carbon isotope splittings with ^{12}C / ^{13}C frequency ratios of 1.013, 1.018, 1.031 and 1.030, respectively. Similar to the modes of the G-line centre, they give no indication of any carbon-carbon bonding. Note, also, that the frequencies of these modes all lie in the same region as those observed for the G-line. The broad feature L_6 has ^{16}O and ^{18}O frequencies of 735 cm^{-1} (91.1 meV) and 704 cm^{-1} (87.3 meV) and is clearly associated with an oxygen vibration. As we noted above, the energy and isotope shift of this mode are very close to those observed for the C-line oxygen mode. The characteristics of the L_2-L_6 modes suggest that the F-line centre could be a combination of the C-line and G-line centres, i.e.. it contains one oxygen and at least three carbon atoms with no direct coupling between them. This also possibly suggests that the centre responsible for the G-line does not break up but changes its configuration and becomes mobile and can be captured by a C-line centre. Otherwise it is difficult to imagine why it could not be created during the irradiation without subsequent thermal treatment, though this could be due to a formation barrier. As a final point with reference to Fig.3, it is interesting to note that the relative intensities of the ^{12}C and ^{13}C components is different for the different modes, particularly for the lowest energy mode L_2. This is also the case for the G-line system and the H-line system which will be considered next.

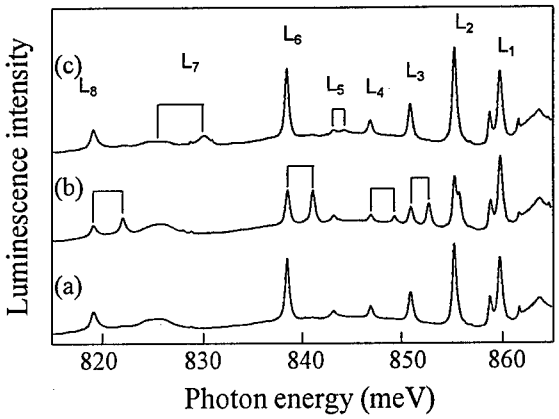


Fig. 4. Photoluminescence spectra showing the local mode structure of the H-line, obtained from material with (a) no isotope substitution, (b) ^{13}C : ^{12}C ~ 1:1 and (c) ^{18}O : ^{16}O ~ 1:1.

The H-line luminescence system is dominant in radiation damaged high carbon containing CZ silicon, with no deliberate hydrogen incorporation, annealed at 450°C. The P-line tends to be more dominant at lower carbon concentrations, and the T-line and I-line when hydrogen has been incorporated (Fig.1). The major features in the local mode structure of the H-line are shown in Fig. 4, obtained from material with (a) no isotope substitution, (b) ^{13}C : $^{12}C \sim 1 : 1$ and (c) ^{18}O : $^{16}O \sim 1 : 1$. There is negligible interference from features related to other centres in these spectra. L_1 with a frequency of 531.4 cm^{-1} (65.89 meV) shows no isotope shift or splitting. This is also the case for the two smaller features close to L_1 which have been found with the same ratios to L_1 in all the material investigated. These are probably also local modes of the H-line. L_2 with a ^{12}C frequency of 567.6 cm^{-1} (70.37 meV) has a small carbon isotope splitting of ~ 3.5 cm^{-1} and a negligible oxygen isotope shift. L_3, L_4, L_6 and L_8 with ^{12}C frequencies of 602.8 cm^{-1} (74.74 meV), 635.3 cm^{-1} (78.77 meV), 702.8 cm^{-1} (87.14 meV) and 858.7 cm^{-1} (106.46 meV), respectively, all have large carbon isotope splittings with ^{12}C / ^{13}C frequency ratios of 1.024, 1.032, 1.030 and 1.028, respectively. A comparison of the spectra in Fig.3 and Fig.4 shows a striking resemblance between the structures of carbon related modes of the H-line centre (L_2, L_3, L_4, L_6) and those of the F-line centre (L_2-L_5). On the other hand, the F- and H-line systems have different structures of the oxygen modes. The latter has clearly two oxygen modes. L_5 has an ^{16}O frequency of 665.5 cm^{-1} (82.51 meV) and an ^{18}O frequency of 656.5 cm^{-1} (81.40 meV). L_7 has an ^{16}O frequency of 808 cm^{-1} (100.2 meV) and an ^{18}O frequency of 770 cm^{-1} (86.8 meV). Neither of them are close to those observed for the F-line and C-line luminescence systems. Taking into account that the formation of H-line centre takes place at T> 400°C when oxygen interstitials becomes mobile, it is possible that the H-line centre is created due to the capturing of an extra oxygen atom by the F-line centre. This could account for the difference between the vibronic spectra of the two systems.

The interactions between the major contaminants in silicon, oxygen, carbon and hydrogen, during thermal treatment or after radiation damage, which mimics several device fabrication processes, and subsequent thermal treatment, are still not clear. We consider that more detailed photoluminescence isochronal and isothermal annealing studies, combined with theoretical analysis of local vibrational modes, could lead to a better understanding of these process.

Acknowledgement

This work was funded by the Engineering and Physical Sciences Research Council (UK).

References

1. A.N. Safonov, E.C. Lightowlers, G. Davies, P. Leary, R. Jones and S. Öberg, Phys.Rev. Letters **77**, 4812 (1996).
2. G. Davies and R.C. Newman, *Handbook on Semiconductors* Vol.3. Ed. S.Mahajan (North Holland, Amsterdam, 1994) p.1557.
3. J. Trombetta and G.D. Watkins, Appl. Phys. Lett. **51**, 1102 (1987).
4. R. Jones and S. Öberg, Phys. Rev. Letters **68**, 86 (1992).
5. L.W. Song, X.D. Zhan, B.W. Benson and G.D. Watkins, Phys. Rev. B **42**, 5765 (1990).
6. A.N. Safonov and E.C. Lightowlers, this conference.
7. J. E. Gower, G. Davies, E. C. Lightowlers and A. N. Safonov, this conference.
8. G. Davies, E.C. Lightowlers, R. Woolley, R.C. Newman and A.S. Oates, J. Phys. C : Solid State Phys. **17**, L499 (1984).
9. K.Thonke, G.D. Watkins and R. Sauer, Solid State Commun. **51**, 127 (1984).
10. W. Kürner, R. Sauer, A. Dörnen, and K. Thonke, Phys. Rev. B **39**, 13327 (1989).
11. G. Davies, E.C. Lightowlers and M. do Carmo, J. Phys. C : Solid State Phys. **16**, 5503 (1983).
12. V.D. Tkachev and A.V. Mudryi, Inst. Phys. Conf. Ser. No. 31, 231 (1977).
13. G. Davies, Physics Reports **176**, 83 (1989).

Materials Science Forum Vols. 258-263 (1997) pp. 623-628
© 1997 Trans Tech Publications, Switzerland

RAMAN SCATTERING MEASUREMENTS IN NEUTRON-IRRADIATED SILICON

M. Coeck[1,2], C. Laermans[2], R. Provoost[3], R.E. Silverans[3]

[1]SCK•CEN, Dept. BR2, Boeretang 200, 2400 Mol, Belgium
[2]Laboratorium voor Halfgeleiderfysica, Katholieke Universiteit Leuven, Celestijnenlaan 200D, 3001 Leuven, Belgium
[3]Laboratorium voor Vaste-stoffysica en Magnetisme, Katholieke Universiteit Leuven, Celestijnenlaan 200D, 3001 Leuven, Belgium

Keywords : neutron-irradiation, silicon, radiation damage, Raman scattering

Abstract. Raman spectroscopy measurements were carried out on silicon single crystals which were irradiated with a fast-neutron dose of 1.7 and 3.2×10^{21} n/cm^2 (E > 0.1 MeV). This irradiation gives rise to large regions of structural damage in the material. We report on the appearance of a Raman band at 483 cm^{-1}, indicating the introduction of an amorphous fraction due to the fast-neutron irradiation. At lower Raman frequencies we also observed a feature reminiscent of the so-called boson peak, which is a typical characteristic for amorphous solids.

Introduction.

Neutron transmutation doping (NTD) of silicon is one of the well-known methods to produce high-quality n-type silicon. This technique is based on the capture of a thermal neutron (E < 0.5 eV) by a Si^{30} isotope. This leads to the production of phosphorus according to the following reaction : $^{30}Si\,(n,\gamma)\,^{31}Si \rightarrow {}^{31}P + \beta^-$. The two advantages which make NTD silicon a frequently used product in the semiconductor industry are that the doping of the material is very homogeneous and that the target resistivity of the material can be controlled via the irradiation dose. Unfortunately, not only phosphorus elements are formed during the irradiation, but also a lot of irradiation damage is introduced in the material. This damage drastically increases the target resistivity and for industrial uses, it is removed by annealing the crystal up to temperatures of 800 °C.

Based upon energy deposition, it is clear that contribution to the displacement damage is primarily made by fast neutrons (E > 0.1 MeV), which always accompany the thermal ones, and less by the gamma and beta recoil mechanisms resulting from the doping reaction. The high-energy collisions lead to a cascade process, resulting in large regions of displaced atoms, which may be amorphous. In general, these regions are considered to be spherical, with a radius of the order of 100 Å [1, 2], where a center of vacancies is embedded in a region of interstitials. Since they are uncharged, the damaging neutrons are unaffected by the electrical field around the atomic nuclei and hence they can travel large distances through the silicon. Therefore, the resulting structural damage is not restricted to the surface but distributed uniformly throughout the whole crystal. This was also confirmed by measurements performed by Chandrasekhar et. al. [3]. The density of the cascades depends on the irradiation dose. According to Schröder et. al. [4], a detectable amount of amorphous regions is already introduced from a fast-neutron dose of 4×10^{20} n/cm^2.

We are interested in the study of the disorder induced in silicon by means of the fast neutrons. Herefore we use single-crystalline silicon which is irradiated with various high fast-neutron doses (of the order of 10^{21} n/cm^2). The underlying idea of this approach is that we can vary the amount of disorder by changing the fast-neutron irradiation dose. But since the amount of damage that is introduced not only depends on the irradiation dose but also on several irradiation conditions such as the temperature of the silicon during the irradiation, a quantification of this irradiation damage is not straightforward. A lot of techniques are available for this purpose. One of the techniques that monitors the introduction of disorder is Raman scattering. Because it can simultaniously detect a remaining crystalline structure, Raman spectroscopy gives a direct verification of the fact that a disordered lattice is amorphous.

Here we will present the results obtained from Raman spectroscopy experiments on single-crystalline silicon which was partly amorphized by means of fast-neutron irradiation. The intensity of the peak observed around 480 cm^{-1} will be discussed in view of the calculations of the percentage of amorphous areas present in the samples. We also report on a feature which arises at very low Raman frequencies. We will give evidence for the idea that this peak can be considered as a Boson peak, which is a typical feature in amorphous solids.

Experimental details.

Measurements were carried out on a single-crystalline CZ silicon sample, further labelled as Si-0, and on two similar samples after an irradiation with fast neutrons. The samples are cylindrically shaped and their symmetry axis lies along the crystallographic [100] direction. The irradiations were carried out at the BR2 reactor of the Belgian Nuclear Research Center (SCK•CEN). The effective irradiation time to obtain fast-neutron doses (E > 0.1 MeV) of 1.7×10^{21} n/cm^2 (sample labelled Si-2) and 3.2×10^{21} n/cm^2 (sample Si-4) is resp. 42 and 78 days. The samples were positioned inside a fuel element of the core of the reactor. They were loaded into an aluminum irradiation capsule filled with helium gas to reduce the temperature increase due to the γ-heating under irradiation. A good thermal contact between the irradiation capsule and the primary cooling water was also provided. Nevertheless, the calculated maximum temperature in the center of the silicon during the irradiation was 150 °C.

The Raman spectra were obtained at 295 K using a DILOR XY triple spectrometer equipped with a LN cooled CCD detector. The excitation was provided by the 514.5 nm line of an Ar^+ laser. The polarisation and the propagation of the incident and scattered light were performed in an $x\,(^{y}_{z},y)\,x$ geometry, with x, y and z indicating the principal axis of the crystals. The propagation of the excitation and the backscattered light are along the [100] direction. The Raman spectra are the sum of a polarized (incident and scattered light parallel to the [010] direction) and a depolarized (incident light parallel to the [001] direction and the scattered light along the [010] direction) Raman spectrum.

Results and discussion.

Amorphization due to neutron irradiation.

The Raman spectra for the unirradiated (Si-0) and the irradiated samples (Si-2 and Si-4) are shown in Fig. 1. All spectra are background subtracted and normalized on the intensity of the crystalline silicon phonon mode at 520 cm^{-1}.

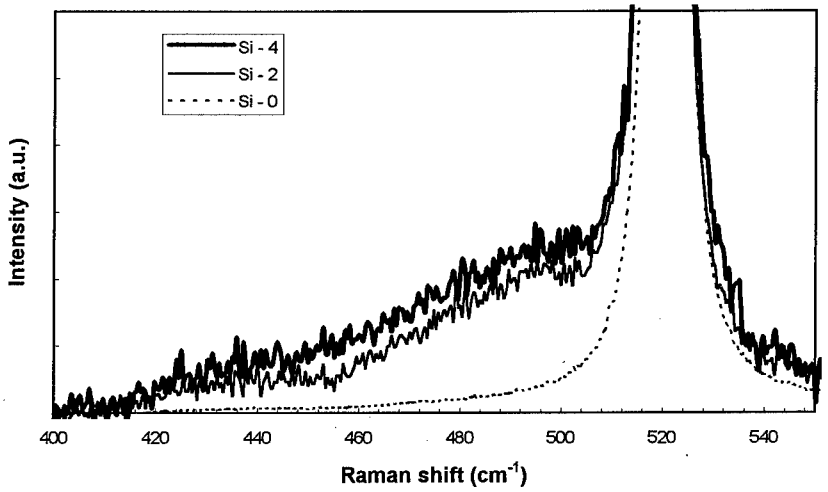


Fig. 1 : Raman spectra for the crystalline Si-0 and the neutron-irradiated Si-2 and Si-4

The influence of the irradiation is clearly visible in the Raman spectra of Si-2 and Si-4 : besides the intensity decrease of the crystalline mode, the appearance of a broad band with a maximum at 483 cm^{-1} announces the presence of amorphous regions in the irradiated samples. The intensity of this mode is slightly higher in Si-4 than in Si-2. This indicates that due to higher irradiation doses, the amorphous part in the sample increases. An estimation of the ratio between the amorphous and the crystalline parts of the samples can be obtained from the ratio of the areas under the crystalline and the amorphous Raman band, taking into account the fact that the scattering efficiency of amorphous silicon is ten times larger than that of crystalline silicon [5]. From the ratio between the integrated intensities of the amorphous and crystalline Raman modes, we calculated the values for the amorphous portion in Si-2 and Si-4 to be resp. 3.7 % and 4.1 %. These values are of the same order as those reported by Schröder et. al. [4]. However, one has to take into account that the obtained values are an underestimation due to different absorption coefficients of crystalline and amorphous silicon. Brodsky et. al. [5] reported that the ratio of the absorption coefficients of pure crystalline and pure amorphous silicon is about 30. In neutron-irradiated silicon however, the penetration of the laserlight will be blocked on his way through the sample due to the homogeneous distributed amorphous regions.
It is also striking that although the irradiation dose is roughly doubled, the amorphous portion in the Si-4 sample is only slightly increased. This is probably the result of the high temperature of the silicon during the irradiation.

Boson peak.
Figure 2.a shows the Raman scattering in the low-frequency region, measured for Si-4 at 295 K. It shows a peak at 114 cm^{-1}. In this frequency range the unirradiated silicon single crystal does not show any scattering intensity. It is well known that in the low-frequency Raman spectrum of amorphous solids a broad band universal characteristic exists. It is the so called boson peak for which a generally accepted theory still does not exist. Martin en Brenig [6] put forward a model to explain this peak in glasses and more recently an explanation has been given in the framework of the soft potential model (SPM) [7, 8]. The presence of a boson peak in amorphous hydrogenated silicon has been put forward ealier by Ivanda et. al. [9] but Zwick and Carles [10] seem to disagree about the interpretation.

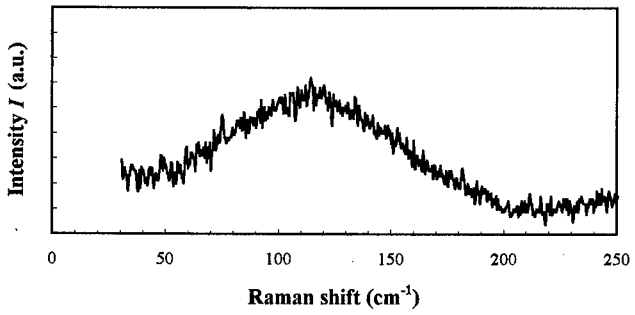


Fig. 2.a : Part of Raman spectra for Si-4 at 295 K.

In this last paragraph we will discuss our results concerning the peak observed at 114 cm^{-1} in more detail. We will give indications for the idea that this peak can be considered as the boson peak and a comparison will be made with results obtained in a-SiO_2 .

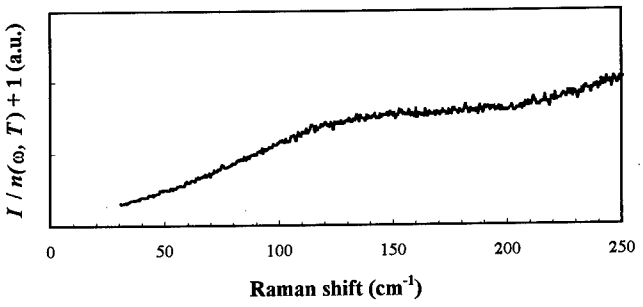


Fig. 2.b : Plot of $I / (n(\omega, T) + 1)$ as a function of ω.

As already mentioned above, there is proof of the presence of an amorphous part in our samples. Additional evidence is given in Fig. 2.b which shows a plot of the scattering intensity I devided by $n(\omega, T) + 1$, where $n(\omega, T)$ is the Bose factor, as a function of ω. It is clear that no maximum is observed anymore. Moreover, it can be seen that $I / (n(\omega, T) + 1)$ is approximately constant above 114 cm^{-1} . Since $\frac{I}{n(\omega,T)+1} = \frac{C(\omega)g(\omega)}{\omega}$, where $C(\omega)$ is the coupling constant and $g(\omega)$ is the vibrational density of states, this behavior indicates that the product $C(\omega)g(\omega)$ is linear in ω above 114 cm^{-1}. Similar observations have already been made in several other materials [11] and it is believed that this is a universal behavior for frequencies above the boson peak.

The idea that the observed peak at 114 cm^{-1} is a boson peak is also confirmed by Raman measurements obtained at 77 K. This spectrum also show a peak at 114 cm^{-1}, but the intensity is less than that of the peak observed at 295 K. Furthermore, if the reduced spectrum at 295 K is multiplied by the Bose factor at 77 K, a similar curve as the measured spectrum at 77 K is obtained.

According to the SPM the position of the maximum of the boson peak is related to the typical parameters W and C as follows : $\omega_d \sim W\ C^{-1/3}$. W represents the characteristic energy in the SPM and C is related to the interaction between quasilocal harmonic oscillators responsible for the boson peak. To investigate whether the position of the peak in question is meaningful in order to be a boson peak, we make a comparison with a-SiO_2 where the boson peak is detected at 52 cm^{-1}. From the theoretical expression for W used in the SPM [8] we find that W is approximately equal for a-SiO_2 and Si-4. We have performed ultrasonic velocity variation measurements on Si-4 [12] from which we can derive $C = 5 \times 10^{-6}$. Using C of amorphous quartz to be 3.1×10^{-4} [13] and taking into account that Si-4 is at least 4.1 % amorphous, the ratio for a-SiO_2 and Si-4 of ω_d and W $C^{-1/3}$ are in agreement. This indicates that the position of the boson peak at 114 cm^{-1} is meaningful.

From the five indications mentioned above, it can be concluded that our results support the existence of a boson peak in the partly amorphous Si-4 sample at 114 cm^{-1}.

Acknowledgements.

The authors thank D.A. Parshin for helpful discussions. They also thank J.Vermunt and B.Ponsard of the SCK•CEN for performing the neutron irradiations and calculations.

References.

[1] R. Truell, Phys. Rev. **116**, 890 (1959).

[2] M. Bertolotti, Radiation Effects in Semiconductors, ed. F. L. Vook (Plenum Press, New York, 1967), p. 311.

[3] M. Chandrasekhar, H.R. Chandrasekhar and J.M. Meese, Sol. State Comm. **38**, 1113 (1981).

[4] B. Schröder, H. Wild and E. Minninger, J. of Nucl. Mat. **108 & 109**, 685 (1982).

[5] M.H. Brodsky, M. Cardona and J.J. Cuomo, Phys. Rev. B **16**, 3556 (1977).

[6] A.J. Martin and W. Brenig, Phys. Stat. Solidi B **64**, 163 (1974).
[7] V.L. Gurevich, D.A. Parshin, J. Pelous, H.R. Schober, Phys. Rev. B **48**, 16318 (1993).
[8] D.A. Parshin, Phys. Solid State **36**, 991 (1994).
[9] M. Ivanda, K. Furic, O. Gamulin and D. Gracin, J. Non Cryst. Sol. **137-138**, 103 (1991).
[10] A. Zwick and R. Carles, Phys. Rev. B **48**, 6024 (1993).
[11] F. Terki, C. Levelut, M. Boisier and J. Pelous, Phys. Rev. B **53**, 2411 (1996) and references herein.
[12] M. Coeck and C. Laermans, to be published.
[13] Arup K. Raychaudhuri and S. Hunklinger, Z. Phys. B **57**, 113 (1984).

Materials Science Forum Vols. 258-263 (1997) pp. 629-634
© 1997 Trans Tech Publications, Switzerland

RECOMBINATION CENTERS IN ELECTRON IRRADIATED Si AND GaAs.

J.C. Bourgoin[1], M. Zazoui[2] and M. A. Zaidi[3]

[1]Groupe de Physique des Solides, Université Paris 7, C.N.R.S., Tour 23, 2 place Jussieu, 75251 Paris Cedex 05, France

[2]Laboratoire d'Opto-Electronique, Faculté des Sciences & Techniques, Université Hassan II, blvd. Hassan II, B.P. n° 146, Mohammedia, Maroc

[3]Laboratoire des Semiconducteurs, Faculté des Sciences de Monastir, Route de Kairouan, 5000 Monastir, Tunisia.

Keywords : *Solar cells, recombination centers, lifetime, Si, GaAs, space degradation.*

ABSTRACT – Using the current-voltage characteristics of an abrupt Si n^+p junction, we show how the minority carrier lifetime, the capture cross sections for electrons and holes, and the energy level of the corresponding recombination center can be determined independently, thus allowing to characterize completely this center. This technique is illustrated by studying the main recombination center in p-type Czochralski grown Si and epitaxial n-type doped GaAs layers. It is then applied to characterize the recombination centers introduced by electron irradiation at various temperatures in Si and GaAs solar cells. In electron irradiated Si cells, we find that the main recombination center introduced by irradiation at 90 K is the vacancy. It becomes the divacancy for higher irradiation temperatures. In irradiated GaAs the recombination center, presumably associated with the As vacancy, does not change with the temperature of irradiation in the range 80 – 300 K.

I. INTRODUCTION

Although they play an important role in many electronic and opto-electronic devices, recombination centers have not yet been correctly characterized specially on the point of view of their ability to trap electrons and holes. Usually, one measures the associated lifetime τ, combination of the cross sections σ_n and σ_p for electron and hole trapping. One of these cross sections can be measured when the recombination center plays the role of a majority or minority carrier trap. But, no general technique exists allowing to measure both σ_n and σ_p, and thus to deduce τ. This can only be realized in particular cases [1,2].

The aim of this communication is to present such a technique, based on the analysis of the current-voltage characteristics of a diode. We shall apply it to the case of Si and GaAs. Indeed, although the defects in these materials have been extensively studied, the native recombination centers, to which these materials owe their lifetime, have not been detected. In the case of irradiated materials, many defects are detected but it has not yet been possible to determine which one is responsible for the change in the lifetime.

The study is performed using solar cells because the lifetimes in the materials used for solar cells are the purest, i.e. exhibit the longest lifetimes, then measured easily. As a result the study of irradiated cells is directly useful for the knowledge of solar space degradation, still unknown in the case of deep space missions (low temperature and low illumination).

II. PRINCIPLE OF THE TECHNIQUE

It consists to analyze the voltage and temperature dependences of the d.c. current of a p-n junction under direct and reverse biases. The current obeys the celebrated Schottky equation :

$$J = J_s \left(\exp\left(\frac{qV}{kT}\right) - 1\right) \tag{1}$$

where the saturation current J_s is directly related to the minority carrier lifetime. For a $p^+ - n$ junction, when the n side contains N_D dopants (the case of a GaAs solar cell, the opposite case for a Si cell), J_s reduces to :

$$J_s = q\left(\frac{D_p}{\tau_p}\right)\left(\frac{n_i^2}{N_D}\right) \tag{2}$$

where n_i is the intrinsic carrier concentration, and D_p and τ_p the diffusion constant and the lifetime, respectively, of the minority (holes) carriers. Hence, τ_p and its temperature dependence can be extracted from $J_s(T)$.

In practice, these ideal characteristics are valid only in limited voltage and temperature ranges. In other ranges, generation and/or recombination of carriers in the depleted region can dominate. The corresponding currents are :

$$J = \int_0^W qUdx \tag{3}$$

where W is the width of the space charge region. These currents provide information on the rates of generation (U_e) or recombination (U_r) of electrons and holes from the recombination centers, i.e. on the capture cross sections σ_n and σ_p.

Under reverse bias, because the free electron (n) and hole (p) concentrations are low ($pn \ll n_i^2$), the dominant process is emission, with the rate of generation given by :

$$U_g = \frac{\sigma_n\ \sigma_p\ v\ N_t\ n_i}{\left[\sigma_n \exp\left(\frac{E_t - E_i}{kT}\right) + \sigma_p \exp\left(\frac{E_i - E_t}{kT}\right)\right]} \tag{4}$$

where N_t is the concentration of recombination centers associated with an energy level at E_t, E_i is the intrinsic Fermi level and v the thermal velocity of the carriers.

Under forward bias the major process in the depletion region is capture, and the corresponding recombination current is given by relation (3) where U becomes :

$$U_r = \frac{\sigma_n\ \sigma_p\ v\ N_t\ n_i^2\left(\exp\frac{qV}{kT} - 1\right)}{\sigma_n\left[n + n_i \exp\left(\frac{E_i - E_t}{kT}\right)\right] + \sigma_p\left[p + ni\ \exp\left(\frac{E_i - E_t}{kT}\right)\right]} \tag{5}$$

Hence, the determination of the diffusion, generation and recombination currents provide three equations allowing to determine independently σ_n, σ_p, E_t, N_t, when one of these parameters has

been determined by another technique. For instance, Deep Level Transient Spectroscopy (DLTS) can provide N_t and E_t when the recombination center is placed in a situation where it behaves as a trap.

We shall illustrate this analysis to provide information on the native recombination centers in Si and GaAs materials used for the fabrication of solar cells. We shall also extend this analysis to the case of electron irradiated cells.

III. NATIVE RECOMBINATION CENTERS

We illustrate the determination of the characteristics of recombination center in the case of unirradiated Si cells. The studied cells are n^+p structures made on a Czochralski grown p-type material having a nominal resistivity of 10 Ω·cm. Capacitance voltage measurement indicates a doping concentration $N_A = 1.3 \times 10^{15}$ cm^{-3}. In this material the defect responsible for the lifetime has been detected and characterized by DLTS [2]. Its associated energy level is located at 474 meV above the conduction band and its concentration is 2×10^{13} cm^{-3}.

The diffusion current is recognized in the range 0.4 – 0.7 V by the linear variation of ln J versus V for $V \gg kT$. The value of log J(0) provides immediately τ by application of relation (2). This is illustrated in Figure 1 for J–V characteristics performed at room temperature ($D = 30$ cm^2 s^{-1}, $n_i = 1.45 \times 10^{10}$ cm^{-3}), giving $\tau = 45$ µs a value which is verified by direct lifetime measurement [2]. In the bias range 0.1 – 0.4 V, the slope of ln J(V) is half that in the higher range and the current is dominated by recombination. Since the energy level of the defect is at midgap, expression (5) can be simplified for $V > kT/q$ and gives, once integrated over the space charge region :

$$J_r = q \frac{W}{2} \sigma_a v N_t n_i \exp\left(\frac{qV}{2kT}\right) \quad (6)$$

where

$$\sigma_a^{-1} = \sigma_n^{-1} + \sigma_p^{-1} \quad (7)$$

The data of Figure 2, corresponding to the same situation than Figure 1, give : $\sigma_a v N_t = 10^6$ s^{-1}, i.e. $\sigma_a \simeq 5 \times 10^{-14}$ cm^2.

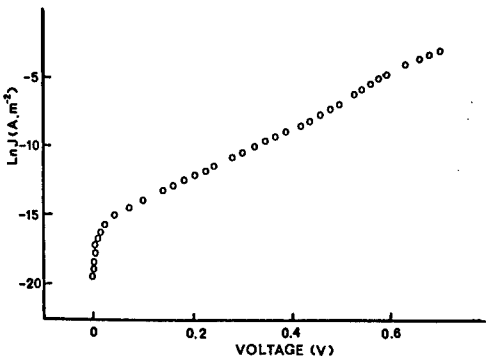


Fig. 1 – Forward current-voltage characteristics of a Si solar cell monitored at 300 K.

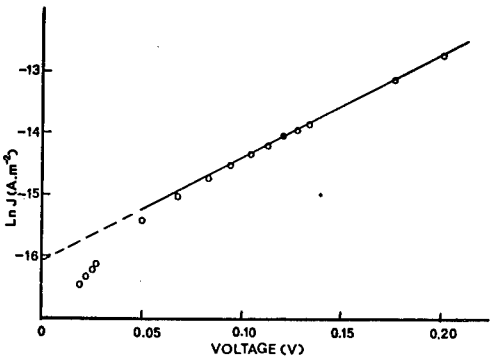


Fig. 2 – Range of the characteristics of Fig. 1 corresponding to the recombination regime.

From σ_a and τ, it becomes, in principle, possible to deduce both σ_n and σ_p. Indeed, under low injection conditions (assuming the electron and hole velocities are equal) :

$$\tau = \frac{1}{v N_t} \left[\frac{\alpha}{\sigma_p} + \frac{\beta}{\sigma_n}\right] \tag{8}$$

where α and β are two coefficients :

$$\alpha = (n + n')/(n + p) \qquad \text{and} \qquad \beta = (p + p')/(n + p) \tag{9}$$

where n' and p' are the electron and hole concentrations that would exist if the Fermi level was located on the defect level ($\beta \simeq 1$, $\alpha \simeq 0.23$). The results show that $\sigma_n \simeq 10^{-14}$ cm^2 while σ_p is too large to be correctly evaluated. Then, minority carrier recombination is limited by electron trapping.

Under reverse bias the current is limited by carrier generation which can be rewritten :

$$J_q = q\, n_i\, w\, \tau_g^{-1} \tag{10}$$

where

$$\tau_g = n_i/U_g. \tag{11}$$

This regime can be recognized by the linear dependence of J with (see Fig. 3) the width of the space charge region :

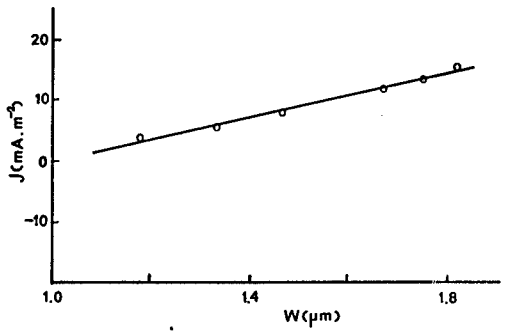


Fig. 3 – Variation of the current versus the width of the space charge regime in the generation regime under reverse bias, measured at 300 K.

$$W = \left[\frac{2\,\varepsilon\,(V + V_{bi})}{q\,N_A}\right]^{1/2} \tag{12}$$

where V_{bi} is the built-in voltage of the junction (0.66 V at room temperature). In the case considered here, τ_g reduces to :

$$\tau_g^{-1} = \sigma_p\, \sigma_n\, v\, N_t\, (\sigma_n + \sigma_p)^{-1} \tag{13}$$

i.e.

$$\tau_g^{-1} = \sigma_a\, v\, N_t. \tag{14}$$

Consequently, the generation regime provides in this case the same information as the recombination regime.

The same analysis has been performed on GaAs solar cells made of a $p^+ - n$ structure grown by MOCVD on n^+ GaAs substrates. It is then found that the effective recombination center exhibits an energy level located at 0.7 – 0.8 eV from the conduction band and cross section $\sigma_n = 4.4 \times 10^{-16}$ cm^{-2} and $\sigma_p = 3.8 \times 10^{-16}$ cm^{-2} at room temperature. These results, as well as the temperature dependence of σ_n (see Figure 4), demonstrate that the recombination center is the defect associated with the As antisite labelled EL2.

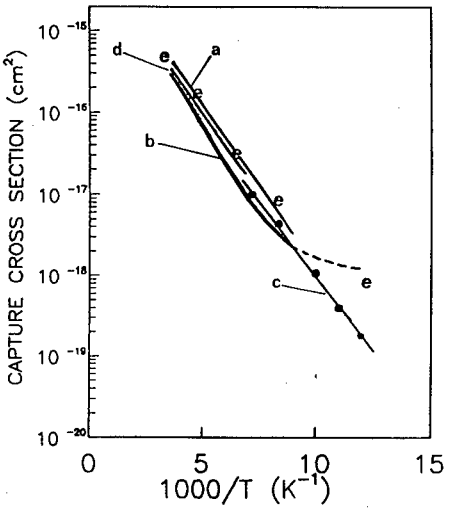


Fig. 4 – Temperature dependence of the capture cross section on the EL2 defect in GaAs. The e signs are our data. The lines correspond to data reported in refs. 3 (a), 4 (b), 5 (c) and 6 (d).

IV. RECOMBINATION CENTERS IN IRRADIATED CELLS

The same analysis has been performed on Si and GaAs cells irradiated at various temperatures with 1 MeV electrons. The fluences (typically between 10^{15} and 10^{16} cm^{-2}) have been chosen to insure that the recombination centers created by irradiation dominate over the native ones.

The results are simple to describe in the case of GaAs because the lifetime does not vary with the temperature of irradiation. This is in agreement with DLTS observation which shows that the nature and concentration of the created defects are temperature independent [7]. The data are consistent with the characteristics of the defect labelled E5 which is located at 0.96 eV below the conduction band [7]. The capture cross section for holes is found to be very large (~ 10^{-9} cm^{-2}) compared to that for electron (10^{-12} cm^{-2}).

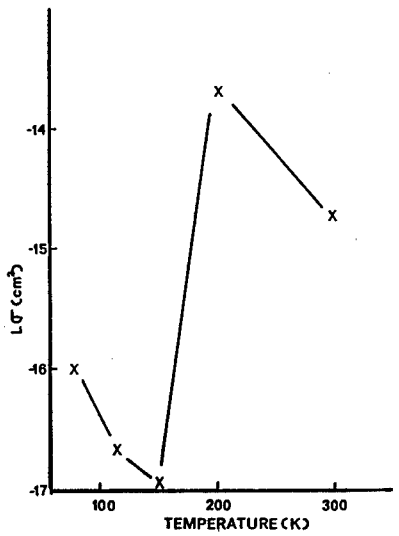


Fig. 5 – Variation of the logarithm of the minority carrier cross section for the recombination center introduced in Si cells. versus the temperature of irradiation.

In Si the situation is more complicated because the nature and concentration of the created defects are temperature dependent [8]. As shown in Figure 5, three different temperature ranges can be distinguished, which are in agreement with DLTS

observation [8]. Below 100 K the created defect is the isolated vacancy, and its associated cross section is $\sim 10^{-16}$ to 10^{-17} cm^2. Above 110 K, the vacancy becomes mobile and other defects are created. In the third range, it is known that the divacancy dominates since the material is lightly doped. Because this defect possesses several energy level in the gap, the measured electron cross section ($\sim 10^{-15}$ cm^2) should be ascribed to this defect.

V. SUMMARY AND CONCLUSION

We have proposed a simple technique to determine both the minority and majority carrier cross sections of recombination centers. The technique has been illustrated in case of Si and GaAs on the native recombination centers as well as those created by electron irradiation.

ACKNOWLEDGMENTS

This work has been performed on Si cells provided by G. Strobl (Angewandte Solar Energy, Heilbronn, Germany) and C. Flores (CISE, Milano, Italy).

REFERENCES

1. M.A. Zaidi, H. Maaref and J.C. Bourgoin, Appl. Phys. Lett. **61**, 2452 (1992).
2. M. Zazoui, M.A. Zaidi, J.C. Bourgoin and G. Strobl, J. Appl. Phys. **74**, 3944 (1993).
3. A. Mircea, A. Mitonneau, J. Hallais and M. Jaros, Phys. Rev. B **16**, 3665 (1977).
4. D.V. Lang and C.H. Henry, Phys. Rev. Lett. **35**, 1525 (1975).
5. T. Neffati and J.C. Bourgoin, *unpublished.*
6. T. Matsumoto, P.K. Bhattacharya and M.J. Ludowise, Appl. Phys. Lett. **41**, 662 (1982).

Materials Science Forum Vols. 258-263 (1997) pp. 635-640
© 1997 Trans Tech Publications, Switzerland

STUDY OF A Li- AND C-RELATED CENTER FORMED AT HIGH ANNEALING TEMPERATURES IN NEUTRON-IRRADIATED FZ SILICON DOPED WITH Li.

F. Rodriguez[1], G. Davies and E.C. Lightowlers
Physics Department. King's College London, Strand, London WC2R 2LS, UK.
[1]On Sabbatical leave from the University of Cantabria (Spain)

Keywords: Si; Li; Uniaxial stress spectroscopy; Isotopes; Bound excitons; Photoluminescece

Abstract. This work investigates the formation and structure of a new photoluminescent deep center in irradiated FZ C- and Li-doped silicon created upon annealing during the last steps of the radiation damage release. Uniaxial stress measurements reveal that the associated defect has monoclinic I symmetry with only small departures from the trigonal symmetry. The isotope structure exhibited by the zero-phonon line at 879.3 meV indicates that the center involves one Li atom. The isotope shift, ΔE_{isot}= 0.18 meV, is similar, per atom, to that observed for the Q center (Li_4-V) in silicon. The intensity dependence of the zero-phonon line with [C] suggests that carbon is also involved in this center.

Introduction

Due to its high mobility lithium is an important impurity in silicon that can passivate many defects giving rise to different Li associated complexes [1-5]. Although a great number of Li centers have been reported for many years in the literature [2-10] the structural characterisation for most of them still remains unknown. The reasons for this lack of structural information lie in the difficulties of obtaining suitable crystals doped with different isotopes and in understanding the chemical processes involved in the formation of the centers. Neutron or electron irradiation and subsequent annealing is an effective way to create defects in silicon [9-11]. The four-Li associated vacancy, Li_4-V, observed by photoluminescence (PL) at 1045 meV (the "Q" center) or the C- related four-Li center at 1082 meV (S center) are examples of this behaviour [8-10]. In both cases the isotope structure of the corresponding zero-phonon line (ZPL) was crucial for revealing the four-Li atom structure of these centers. Similar procedures employing Si with mixed H and D led to the identification of different radiation induced centers involving several hydrogen atoms [12].
In this work we investigate a new Li center observed by PL at 879.3 meV. The interest for studying this new deep center is twofold. Firstly, the center is formed at high annealing temperatures (550-600 °C) in Li-doped silicon enriched with C during the last steps of the radiation damage release, the corresponding ZPL dominating the low temperature PL spectrum. Secondly, the center appears to be passivated upon prolonged annealing at room temperature as is evidenced through the continuous decay of PL intensity at 879.3 meV with time.

Experimental

Three series of Li-doped silicon crystals have been employed in this work. Czochralski (CZ) 30 Ωcm p-type carbon-lean Si, Float zone (FZ) 60 Ωcm n-type oxygen-lean Si with [C] = $1.6x10^{17}$ cm^{-3} and FZ 1000 Ωcm oxygen- and carbon-lean Si doped with [Li] in the 10^{14} to 10^{17} Li cm^{-3} concentration range. For uniaxial stress measurements we used four single crystals of 2x2x18 mm^3 oriented along <100>, <111> and two along <110> for exploring the PL polarisation along <110> and along the two orthogonal <1-10> and <001> directions. The isotope structure was investigated with different ^6Li:^7Li ratios using the same Li-doped Si crystals employed elsewhere [9]. The crystals were neutron irradiated with a dose of $1x10^{17}$ cm^{-2} and then annealed during 30-60 minutes at 550-600 °C. Photoluminescence spectra were obtained using Nicolet 60XS or Bomem DA3 Fourier Transform spectrometers fitted with North Coast Ge diode detectors. Most of the experiments were done with samples immersed in liquid helium at 4.2 K, except for stress experiments and temperature

dependence studies that were performed in an Oxford helium flow cryostat. The excitation was accomplished by a 514 nm Argon laser.

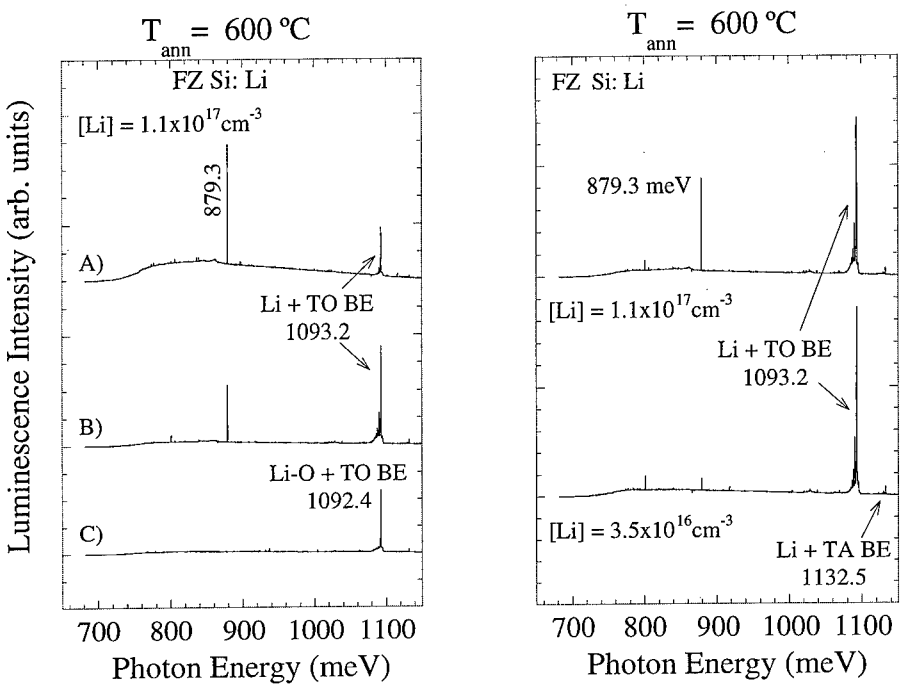


Figure 1. (left): PL spectra at 4.2 K corresponding to A) FZ oxygen-lean Si with [C] = $1.6x10^{17}$ cm^{-3}, B) FZ carbon- and oxygen-lean Si and C) CZ carbon-lean Si doped with [Li] = $1.1x10^{17}$ cm^{-3}, neutron irradiated with a dose of $1x10^{17}$ cm^{-2} and annealed at 600 °C for 30 minutes.
(Right): Dependence of the PL spectrum of FZ carbon- and oxygen-lean Si on [Li].

Results and discussion

Center formation

Figure 1 shows the PL spectra at 4.2 K from neutron irradiated FZ Si with [C] = $5x10^{15}$ and $1.6x10^{17}$ cm^{-3} and from CZ carbon-lean Si doped with [Li] = $1.1x10^{17}$ cm^{-3}. The spectra were obtained after isochronal annealing of 30 minutes at 600 °C. As expected for these high annealing temperatures the spectra from FZ Si consist only of two main lines at 879.3 and 1093.2 meV. The latter is an intense feature associated with the emission from an exciton bound to a Li donor with the creation of one TO phonon [13]. This emission is also accompanied by weak multiexciton lines. Bound exciton luminescence with the emission of one TA phonon is also observable as a minor peak of the PL spectrum at 1132.5 meV. This big difference between the emission intensity for TO and TA is usually found for shallow BE-related luminescence where the vibronic coupling is dominated by silicon TO modes [10, 13, 14]. Moreover this Li emission is the unique feature observed in the PL spectrum either from non-irradiated Li-doped FZ- Si crystals or from irradiated crystals annealed above about 650 °C. Annealing at these temperatures appears to completely remove the effects of radiation damage. The ZPL at 879.3 meV observed in the FZ Si crystals (Fig. 1) shows its maximum intensity in the carbon-enriched crystal. The presence of oxygen inhibits the formation of this defect, as it is reflected in the PL spectrum of the CZ Si (Fig. 1; C) and from C- enriched FZ Si doped with oxygen (not shown here). In CZ Si, we only observe PL associated with Li bound excitons, shifted (by the oxygen content) to 1092.4 meV. This result together with the intensity

dependence of the 879.3 meV ZPL on [Li] shown on the right side of Fig. 1 strongly suggest that the optical center involves Li and C. As we show below, there is one optical-active Li atom associated with the center. An interesting feature concerning this line is the progressive decrease of PL intensity observed upon annealing at room temperature. Figure 1 (A) shows the zero-phonon intensity obtained just after annealing at 600 °C; a decrease by about 1/3 occurs after 12 hours of room temperature annealing, and the same reduction occurs after fifteen minutes for annealing at 100 °C. This annealing-induced reduction of ZPL intensity could be due to the passivation by Li of the center responsible for the 879.3 meV line. In such a case the resultant defects that would involve at least two Li atoms, are evidently not able to produce luminescence in the spectral range explored. It must be pointed out that the 879.3 meV PL discussed here is not related to PL at 878 meV produced by the "W" found by Johnson et al. [11] upon annealing at 100 °C. The reported annealing temperature for this defect (300 °C) supports this view.

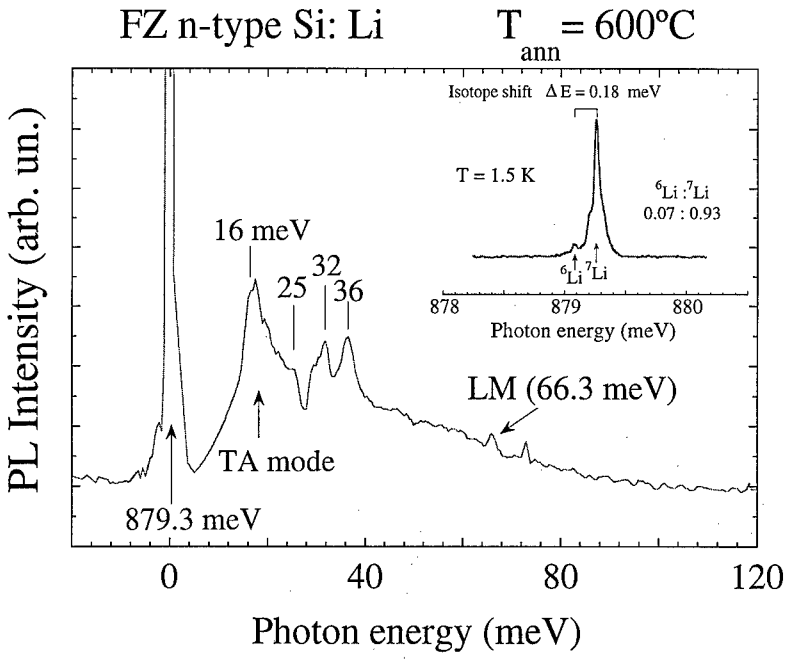


Figure 2. Phonon spectrum of the 879.3 meV line at 18 K. Resolution: 1.2 meV.
Inset: High resolution spectrum of the ZPL at 1.5 K. The same spectrum is obtained at 4.2 K. The isotope structure is indicated. Resolution: 0.012 meV.

Phonon side band and isotope structure

Figure 2 shows the phonon side band associated with the ZPL at 879.3 meV. A detailed account for this spectrum will be reported later, but it can be seen that the phonon couplings are dominated by resonant phonons having vibrational energies close to the acoustical transverse mode energy in pure Si. The one-phonon spectrum consists mainly of phonons at 16 meV. The temperature dependence of the spectrum in the 4.2 - 70 K range allows us to identify the peak at 66.3 meV as a local mode (LM) of this center. The neighbouring peak placed toward low energy at 806.2 meV corresponds to a different defect, as shown by sample statistics.

The temperature dependence of the ZPL intensity plus the phonon side band increases by a factor 3 from 5 to 30 K. Above this temperature it decreases following a characteristic thermal dissociation behaviour with an activation energy of 35±5 meV. This is the value expected in Si when one effective mass particle orbits one opposite charge, suggesting that one of the exciton particles is

highly localised to the defect while the other is bound to the coulomb field created by the first. The inset shows a high resolution spectrum of the ZPL. Two structured components can be seen at 879.07 meV (a weak component) and at 879.25 meV (a strong component). The measured integrated intensity for these components 0.07:0.93, is very similar to the natural isotope abundance of ^{6}Li:^{7}Li, suggesting that the ZPL is perturbed by the effects of one Li atom. This result is confirmed by the ZPL value of 879.1 meV obtained in ^{6}Li-doped FZ Si. For an isotope ratio of 0.53:0.47 the components could not be resolved spectroscopically but the envelope peaks, as expected now, at 879.15 meV. The centre therefore contains at least one Li atom. The isotopic shift, $\Delta E = E(^7Li) - E(^6Li) = 0.18$ meV, is similar, per active Li atom, to that observed for the Q center (Li_4-V) in silicon [9]. The presence of C can be inferred from the dependence of the ZPL intensity on the C concentration in the two FZ Si crystals investigated.

Efforts to form this center in mixed ^{12}C and ^{13}C-doped FZ Si for isotope analysis were unsuccessful due to incorporation of oxygen from quartz during the in-diffusion of ^{13}C (carried out with methane at 1300 °C for 7 days). The presence of oxygen in the crystal was revealed by a prominent C line (879.6 meV) observed in PL whose intensity was an order of magnitude higher than the G line intensity in a FZ Si with [C] = 1.6×10^{17} cm^{-3}. This unintentional doping with oxygen inhibited the formation of the center being investigated here and therefore no conclusive result about its carbon structure could be obtained from isotope experiments.

Uniaxial stress measurements.

Figure 3 plots the stress data performed upon this center along the three high symmetry directions of Si. The ZPL splitting is illustrated as well. Two facts must be underlined: i) there is a linear dependence of the ZPL shifts with the stress, and there is no evidence of any stress induced coupling of excited states. ii) The observed orientational splitting indicates that the center has monoclinic I symmetry. The experimental shift rates and the calculated least square fit values with the corresponding A_i parameters (i=1 to 4) for a monoclinic I center are collected in Table I, using Kaplyanski notation [15]. Moreover the polarisation analysis of the intensities of all the stress-split components indicates that the electric dipole is not directed along the principal <110> axis of the monoclinic I center but it lies on the perpendicular (110) plane [16].

A simpler view of the splitting pattern of Fig. 3 is to note that it is similar to that expected for a transition between non-degenerate orbital states in a center of trigonal symmetry (no splitting along <100> and two split components along <111> and <110>), implying that the stress data can be described in terms of small perturbations of a center of trigonal symmetry.

The stress behaviour can also be explained on the basis of a descendent symmetry scheme as follows. We can think of an s $\rightarrow$ p electric dipole allowed transition with T_d symmetry. In a trigonal symmetry the p states split ($T_2 \rightarrow A_1+E$) and a non-degenerate state $(p_x+p_y+p_z)/\sqrt{3}$ is created directed along <111>. If we take a combination $\Psi = \alpha (p_x - p_y) + \beta p_z$ with $2\alpha^2 + \beta^2 = 1$, we have a state with a dipole moment at an angle $\cos^{-1}(\beta)$ to the <100> axis and perpendicular to <110>. Transforming the crystal coordinate x, y, z axes to the conventional trigonal axes is possible to calculate easy the stress perturbation $\langle\Psi\ V\ \Psi\rangle$, where V is the general stress operator, corresponding a singlet to singlet transition in monoclinic symmetry as

$V = A\,S + 2C/3\,S' + B\,(S_\theta + S_\varepsilon)$.

Here $S = S_{xx}+S_{yy}+S_{zz}$, $S' = S_{xy}+S_{yz}+S_{xz}$, $S_\theta = 2S_{zz}-S_{xx}-S_{yy}$ and $S_\varepsilon = (S_{xx}-S_{yy})\sqrt{3}$ are combinations of the stress tensor components. The stress parameters A and B describe the changes in energy of the p_z state for unit hydrostatic stress S and a unit S_θ stress, respectively, and C is defined through CS_{xy} being the coupling for the p_x and p_y states by a unit S_{xy} stress. After some arithmetic the matrix element can be expressed as Eq. (1)

$$\langle\Psi\ V\ \Psi\rangle = [A-2B(\alpha^2 - \beta^2)]\,S_{zz} + [A+B(\alpha^2 - \beta^2)]\,(S_{xx}+S_{yy}) - 2\,\alpha^2\,C\,S_{xy} + 2\alpha\beta\,C\,(S_{xz} - S_{yz}) \qquad (1)$$

In the case of trigonal symmetry with dipole along <1-1-1> (this condition is required for the electric dipole to be in the (110) plane) the trigonal stress parameters are then $A_1^t = A$ and $A_2^t = -C/3$.

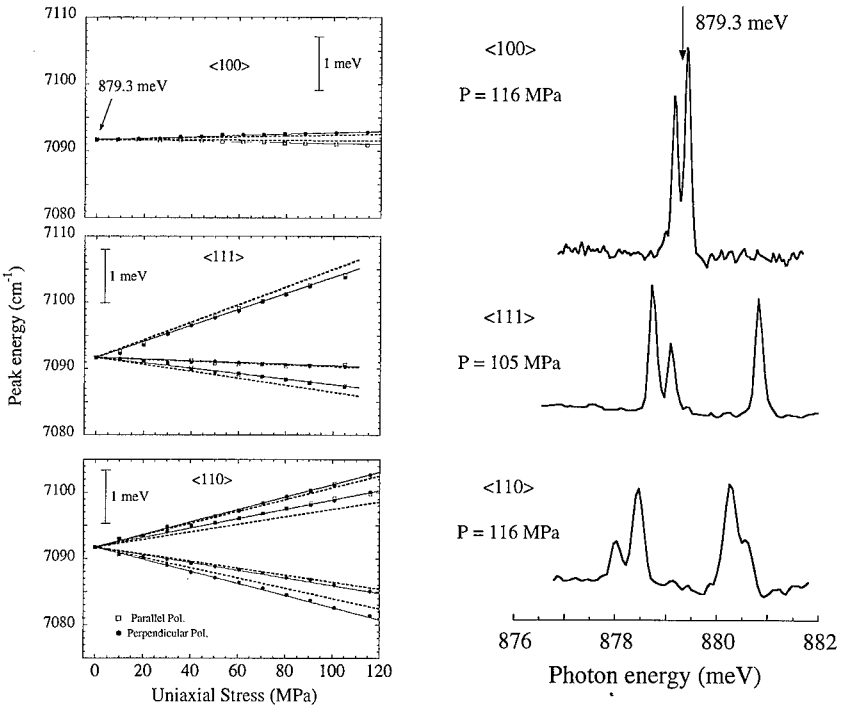


Figure 3. (Right): Uniaxial stress spectra at T = 8 K of the 879.3 meV line. The stress is directed along high symmetry directions (unpolarised spectra). (Left): Line energy shift versus stress plots. Straight lines represent the experimental shift rate (full line) and the calculated one (dashed line). Energy shifts are given in cm^{-1} and stress in MPa (See Table I).

In terms of monoclinic I notation, the stress parameters are given by

$A_1^m = A\text{-}2B(\alpha^2 - \beta^2)$; $A_2^m = A+B(\alpha^2 - \beta^2)$; $A_3^m = -\alpha^2 C$; $A_4^m = \alpha\beta C$ (2)

Note that for trigonal symmetry with electric dipole along <1-1-1> ($\alpha = -\beta = 1/\sqrt{3}$), and so $A_1^m = A_2^m = A_1^t$ and $A_3^m = A_4^m = A_2^t$

With this model we can explain the present stress data from a perturbed trigonal center taking A= 3.9 cm^{-1}/GPa and C= 203 cm^{-1}/GPa, or $A_1^t = 3.9$ and $A_2^t = 67.7$ cm^{-1}/GPa, which predict shift rates of 3.9 along <100>; 139 and -41 along <111>; and 72 and -63 along <110>, all in cm^{-1}/GPa units. These shifts approximate to the gross splittings (Table I). Taking the stress parameters obtained by fitting for the monoclinic I symmetry (Table I) we can estimate the α and β coefficients of the wavefunction from Eqs. (1 and 2): $\alpha^2 = A_3^m/(3\,A_2^t)$ and $\alpha\beta = A_4^m/(3\,A_2^t)$

From Table I, we obtain B = 11.5 cm^{-1}/GPa, $\alpha = 0.64$ and $\beta = 0.41$ which implies that the dipole is at an angle $\theta = \cos^{-1}\beta = 65.8°$ with <001>. Considering the trigonal angle of 54.7°, the dipole is making an angle of 10° with the C_3 axis which emphasises the quasi-trigonal symmetry of this center. The α and β values provide also the best fit to the observed polarisation intensities thus confirming the present interpretation.

In conclusion the present analysis indicates that the center is monoclinic I (quasi-trigonal) with the electric dipole within the (110) plane and at 10° from <111>. Based on this fact, the high annealing temperatures required to form the center, the need for C in the lattice, and the evidence for (at least) one Li atom, a possible model for this center is a carbon radiation damage involving a Li atom, perhaps as an analogue of the hydrogen-carbon centers like the T center [17-19]. If so, one can anticipate a family of Li-related centers parallel to the H-related centers; however, more research is needed to substantiate this suggestion.

Table I. Stress data for the 879.3 meV line. The experimental shift rates and the calculated ones (in parenthesis) from least-square fitting to the theoretical expressions for monoclinic I symmetry given in the second column are in cm^{-1}/GPa units.
Fit parameters: A_1= -1.6; A_2= 6.6; A_3= -83.7; A_4= 55.0 (cm^{-1}/GPa);
(See text) A= 3.9; B = 11.5; C= 203 (cm^{-1}/GPa); $\alpha = 0.64$ and $\beta = 0.41$

Direction stress	Theoretical expressions	Experimental (calculated) shift rates (cm^{-1}/GPa)
<100>	$a = A_1$	-6.5 (-1.6)
	$b = A_2$	10 (6.6)
<111>	$c2 = (A_1+2A_2-2A_3+4A_4)/3$	121 (133)
	$c1 = (A_1+2A_2-2A_3-4A_4)/3$	-14 (-14)
	$d = (A_1+2A_2+2A_3)/3$	-41 (-52)
<110>	$f = A_2 - A_3$	95 (90)
	$e2 = (A_1+A_2+2A_4)/2$	72 (58)
	$e1 = (A_1+A_2-2A_4)/2$	-55 (-53)
	$g = A_2 + A_3$	-89 (-77)

Acknowledgements
Thanks are due to Dr A. Safonov for fruitful discussions. One of us (FR) is indebted to the DGICYT (Grant Ref. PR95-282) for financial support. FR also thanks the Solid State Group at King´s College for the hospitality and friendship extended to him during his Sabbatical. This work was financed by the Engineering and Physical Science Research Council.

References

1. E. Ö. Sveinbjörnsson, S. Kristjansson and H.P. Gislason, J. Appl. Phys. 77, 3146 (1995)
2. H.P. Gislason, S. Kristjansson and E. Ö. Sveinbjörnsson, Mat. Sci. Forum 196, 695 (1995)
3. L.T. Canham, PhD Thesis, University of London (1983)
4. U. Wahl, M. Restle, C. Ronning, H. Hofsäss and S.G. Jahn, Phys. Rev. B 50, 2176 (1994)
5. T.K. Kwok, J. Lumin. 65, 327 (1995)
6. P. Alteheld, S. Greulich-Weber, J.M. Spaeth, H. Weihrich, H. Overhof and M. Hohne, Phys. Rev. B 52, 4998 (1995)
7. H. Weihrich, H. Overhof, P. Alteheld, S. Greulich-Weber and J.M. Spaeth, Phys. Rev. B 52, 5007 (1995)
8. G. Davies, L.T. Canham and E.C. Lightowlers, J. Phys. C: Solid State Phys. 17, L173 (1984)
9. E.C. Lightowlers, L.T. Canham, G. Davies, M.L.W. Thewalt and S.P. Watkins, Phys. Rev. B 29, 4517 (1984)
10. G. Davies, Phys. Rep. 176, 83 (1989) and references therein
11. E.S. Johnson, W.D. Compton, J.R. Noonan and B.G. Streetman, J. Appl. Phys. 44, 5411 (1973)
12. A.N. Safonov and E.C. Lightowlers, Adv. Techn. 36, 251 (1996)
13. M.L.W. Thewalt, Solid State Comm. 28, 361 (1978)
14. M.O. Henry and E.C. Lightowlers, J. Phys. C 13, 2215 (1980)
15. A.A. Kaplyanskii, Opt. Spectrosc. 16, 329 (1964)
16. G. Davies, E.C. Lightowlers, M. Stavola, K. Bergman and B. Svensson, Phys.Rev. B 35, 2755 (1987)
17. E. Irion, K. Thonke and R. Sauer, J. Phys. C 18, 5069 (1985)
18. A.N. Safonov, E.C. Lightowlers, G. Davies, P. Leary, R. Jones and S. Öberg, Phys. Rev. Lett. **77**, 4812 (1996)
19. A.N. Safonov, E.C. Lightowlers and G. Davies, Mat. Sci. Forum 196, 909 (1995)

Materials Science Forum Vols. 258-263 (1997) pp. 641-646
© 1997 Trans Tech Publications, Switzerland

THE INFLUENCE OF ACCUMULATED DEFECTS ON THE LATERAL SPREAD OF IMPLANTED IONS

S.T.Nakagawa, Dept. Appl. Physics, Okayama Univ. of Science, 700 Okayama, Japan

keywords : high-fluence implantation, nanoscale-device, dynamical relaxation

Abstract. We aim at describing the influence of high-fluence(Φ) ion implantation on the three dimensional range distribution. When increasing the Φ there is a forced redistribution of ion ranges caused by the sputtering and the local swelling in the target. We examine the high-Φ effects using a Monte-Carlo simulation code called TRIDYN, an extended version of TRIM, to analyze the composition change in a one dimensional amorphous target. In this paper we will examine a case of B implanted into Si, with the fluence from Φ=10^{13} to Φ=10^{16} ions·cm^{-2} with an incident energy(E_0) range from 1 to 200 keV. The results will be summarized as two types of quantities; the *critical fluence*, Φ_c, beyond which the non-linear effect emerges significantly and the *extrapolation factors*. Φ_c is determined by the maximum fraction of B into Si depending on the level of the E_0. The relation of Φ_c with respect to the E_0 is expressed by an algebraic function. The extrapolation factors are to be multiplied by the projected range, R_p, and the longitudinal range straggling, ΔR_p. Most importantly the extrapolation factor on the lateral range straggling, ΔR_L, is obtained by means of a correlation between ΔR_p and ΔR_L even from the result of one dimensional calculation like TRIM.

1. Introduction

When simulating the three-dimensional distribution of stopped ions or dopants, we often conventionally adopt the generally accepted low-fluence, Φ, approximation [1]. Our assumption for a low-Φ approximation means that if a target can be regarded as not having any accumulated defects, the dopant concentration is proportional to Φ. However, the density of 2×10^{20} As atoms (cm^{-3}) is actually observed at 100keV implantation with Φ=10^{15} ions·cm^{-2} at a depth of 0.05 μm in Si [2]. The implantation implies that the number of total Frenkel pairs (FKP) produced can be comparable with the atomic density of the host target. Recently the measurements of accumulated defects has been developed, by means of coupling the thermo-wave and PAD techniques [3]. However, when considering the precision of range profiling required, computer simulation is invaluable, thus a low-Φ approximation should be considered as an evaluation technique as well.

The high-Φ effects create changes with the surface sputtering or surface deposition, swelling, and radiation enhanced diffusion (RED), leading to the redistribution of implanted ions. One change concerns the surface shift due to low-energy ions with less than several keV. In this energy regime. the surface deposition and the sputtering compete to shift the surface position into opposite directions. Both effects are enhanced by increasing Φ. Another changes occur in the bulk. The swelling happens when the host material cannot further locally accommodate more impurity ions in a small volume inside the bulk, because of not being able to retain too high strain energy. In addition to the swelling, RED also introduces a change. It was confirmed to occur when the impurity concentration is increased, e.g. P and B in Si [4]. The increase of the diffusion constant is interpreted by the reduction of the defect formation energy, E_f, due to the accumulated defects. There is a test to evaluate the diffusion constant of RED by analyzing the three dimensional range profiles formed by heavily doped Hg^+ ions in Ni [5]. In order to take into account the effect of the accumulated defects during sequential ion bombardment, we employ a simulation code called TRIDYN(ver.4) [6] created by Möller and Eckstein. It is an extended version of TRIM, used for analyzing the composition change with high-Φ implantation. Note that TRIDYN only evaluates the longitudinal dimension for the amorphous target and ignores the RED in principle.

First the limiting Φ_c, under which the low-Φ approximation is probable, is determined. The high-Φ influence is evaluated in terms of range moments; the mean projected range, R_p and the longitudinal range straggling, ΔR_p. Second the extrapolation factors are defined so as to obtain R_p and ΔR_p. under high-Φ condition from those calculated under low-Φ approximation. Finally the similar extrapolation factor to be multiplied on the ΔR_L is defined, by means of a correlation between ΔR_p and ΔR_L.

2. The limit of low fluence approximation

The maximum fraction of impurity species, F_{max}, varies even against the same target. The higher the E_f, the lower the F_{max}. Even with abundant Φ as much as possible, the maximum concentration observed decreases in the order of As, P, and B [7], which order is interpreted by means of E_f.

When exceeding the threshold F_{max} by chance, the medium must relax and the redistribution of impurity ions occurs. In TRIDYN, an assumption is introduced, i.e., each atom keeps its fixed volume which is defined when those atoms cohere into an elemental solid, according to Littmark and Hoffer [6]. Then if the areal density of impurity exceeds the limit determined by F_{max}, the excessive density in a slab causes the increase in the thickness of the slab involved, during sequential ion bombardment. This treatment is called "*dynamical relaxation*".

In our TRIDYN simulation the nuclear stopping power, S_n, was determined by the Kr-C potential and we selected the local electronic stopping power, S_e, following the Oen-Robinson model [8]. This framework of velocity proportional S_e is well suited for B into Si with the incident energy regime of E_0 <2MeV. The sputtering occurs when the recoil atom has an energy higher than the surface binding energy U(=4.65eV), to leave the surface. A FPK is produced by receiving a higher energy than the displacement energy E_d(=13eV), according to the Seitz-Köhler model [9]. However, the possibility of a defect formation due to S_e is excluded in this version of TRIDYN. For the value of U, the mean value of the binding between B-B and Si-Si is used [10]. For the value of E_d, the same value is used for Si-origin and B-origin FKP. The maximum fraction F_{max} is determined from experimental data. The highest density observed was 8×10^{20}atoms·cm^{-3} at 10keV B into Si (100) with $\Phi=3\times10^{15}$ions·cm^{-2} [11] or 6×10^{20}atoms·cm^{-3} at 120keV B into Si(111) with $\Phi=1\times10^{16}$ ions·cm^{-2} [12]. Thus we determined the optimal value of F_{max} for B into Si to be 0.01, which value is independent of E_0. Although the E_f differs with the types of defects, we hypothesize that there is no significant difference between amorphous and crystalline Si, as far as F_{max} is concerned.

The Fig.1 shows the B fraction in Si as a function of depth scaled by R_p, for two typical cases showing nearly saturated B concentration. One is the case of E_0=2keV(by open circles) and another E_0=200keV(by filled circles), with $\Phi=1\times10^{15}$ and 1×10^{16} ions·cm^{-2}, respectively. The critical fluence, Φ_c, yielding F_{max} = 0.01 increases monotonously with E_0, as is shown in Fig.2. If exceeded Φ_c the non-linear effect following the impurity's saturation should be counted. Consider the volume V_d enclosing the stopped ions in the bulk. The higher the E_0 the larger the V_d whose space expands towards the deeper site. Hence with increasing E_0 the larger Φ is required to reach the F_{max}, at a site having the maximum B fraction. However, on the other hand, the relative importance of S_e to the whole energy loss process increases with E_0. This preference suppresses the number of stopped ions beneath the surface and decreases the V_d relatively. The two competing trends are shown in Fig.1 as a convex curve even below E_0=200keV. The latter trend is consistent with the ordinary expectation that an almost isolated doping layer is produced at a deep site, for the case of high-energy implantation. Note that the maximum B density observed [11,12] are produced with a fluence of $\Phi > \Phi_c$.

We theorize the curve drawn in Fig.2 so as to define the boarder line Φ_c, beyond which the low-Φ approximation fails evidently. The relation is expressed by an following algebraic function of E_0,

$$\Phi_c = \alpha\left(\beta E_0 + \gamma\sqrt{E_0} + 1\right)^{\lambda}, \qquad (1)$$

where four coefficients are $\alpha=10^7$, β=-840.7, γ=25930, λ=1.750, for the present case of B into silicon in an energy range of $1 \le E_0 \le 200$keV.

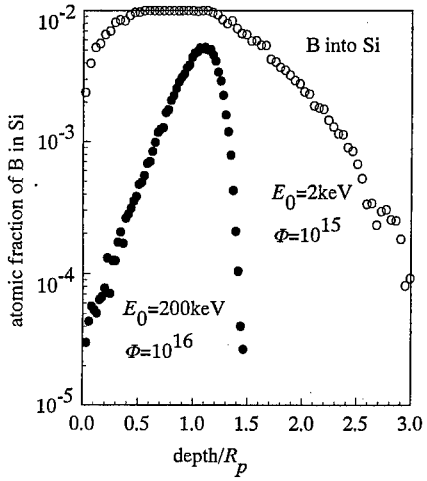


Fig.1 The almost saturated B density in Si, created at 2keV B with $\Phi=10^{15}$ ions·cm^{-2} and 200keV B with $\Phi=10^{16}$ ions·cm^{-2}, where the maximum fraction of B is set to be F_{max}=0.01.

In order to touch the Φ-dependence on ion ranges, a low value Φ should be higher than the lowest Φ where a statistical average of ranges can be taken. In this regard, the value of $\alpha(=10^7)$ may be too small as the lowest fluence from which non-linear effect emerges notably at the extreme of E_0=0.

The total numbers of FKP associated with B implantation are shown by plots in Fig.3. Open and filled symbols are used to distinguish origins due to Si and B, respectively. With Φ=10^{13} implantation (triangles), we can ignore the influence of accumulated defects, as far as in the energy range beyond 1keV. With reminding the result in Fig.2, the B saturation is associated with a large number of Si-origin FKP, which is as high as N_0(4.978×10^{22} atoms·cm^{-3}) indicated by a horizontal hair line. While provided 200keV B, there is still a room for accommodating further defects.

As Φ increases, the number of FKP of Si-origin is proportional to Φ. The accumulated B ions in the target also increases with Φ proportionally, thus the number of FKP of B-origin increases in proportion to Φ^2. These relation explain the relative height among these eight curves.

Consider the following case. If the F_{max} is settled at a much higher value, *e.g.* 0.4 as is taken for D in C, the longitudinal range straggling, ΔR_p, decreases with Φ. This value of F_{max} =0.4 corresponds to that if five of tetrahedral interstitial sites of crystalline Si were occupied by B. A higher S_n results due to B-B collision than that of B-Si collision. The corresponding gamma factors are (B-B: γ=1, B-Si: γ =0.082). Therefore if the region around the R_p is already occupied by excessive B ions, the next B ion should experience a higher S_n due to excessive B concentration, which suppresses the ion range. In fact as Φ increases, the S_n-profile as a function of depth becomes sharper and higher. On the other hand, the S_e decreases in relation to the excessive B concentration is predicted by Bragg's Rule [13]. Such a concentration could not occur actually because the swelling precedes before this stage.

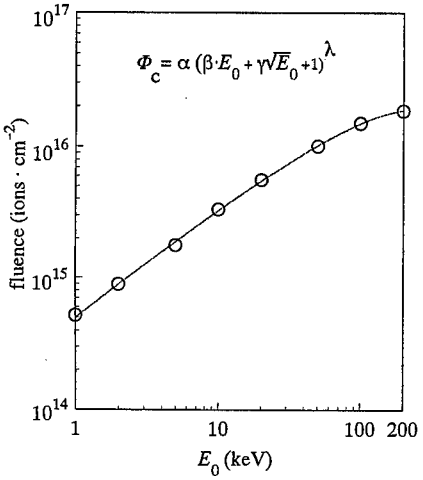


Fig.2 Critical fluence Φ_c yielding F_{max} in Si as the function of E_0. The curve indicates the boarder line below which the low-Φ approximation is allowable.

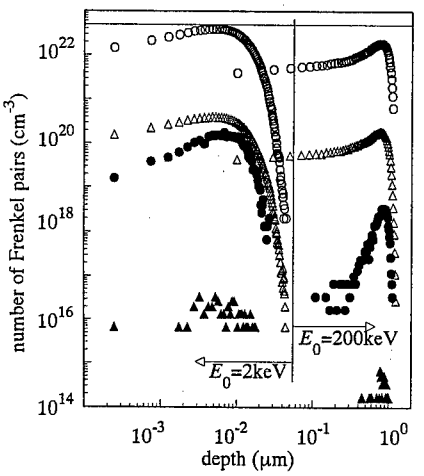


Fig.3 The accumulated Frenkel pairs for 2keV B with Φ=10^{13} (triangles) and Φ=10^{15}(circles), and 200keV B with Φ=10^{13} and Φ=10^{15}. Open and filled symbols denote Si-origin and B-origin Frenkel pairs, respectively. The horizontal hair line shows the atomic density of Si target.

3. The high-fluence effects and the extrapolation factor

E_0 (keV)	1	2	5	10	20	50	100	200
Calc.	0.6461	0.7471	0.7452	0.6285	0.4569	0.2462	0.1368	0.06998
Simul.	0.255	0.305	0.306	0.272	0.209	0.113	0.046	0.011

Table I The amount of the surface recession (Å) of Si caused by B ions with Φ=10^{15} ions·cm^{-2}. The notation "Calc." and "Simul." mean the results due to empirical formula [14] and the present simulation, respectively. The fluence dependence on the R_p and the ΔR_p of longitudinal range distribution, by means of the ratios to those calculated assuming without accumulated defects.

In accordance with the ion implantation, the sputtering and the deposition shift the surface in opposite directions, then the depth distribution of stopped ions is changed mathematically.
The lower the E_0 the more the deposition takes place. For example, the surface position shifts only towards the vacuum for Cs ions into Si with E_0 << 1keV [10]. Table I summarizes the degree of surface recession Δx of Si bombarded with Φ=10^{15} B ions·cm^{-2} as a function of E_0 ("Simul."), in comparison with the calculated values from the sputtering yield, Y, using an empirical formula [14] ("Calc."). Here $\Delta x = Y\Phi/N_0$ is used. Using B ions with E_0 >1 keV, the surface shift is always leaded by the sputtering, although the surface deposition seems to begin to counteract the surface recession at E_0<5keV. The surface recession is stronger than surface deposition, however, the net shift is negligible as is compared with the values of R_p and ΔR_p. Hence the swelling seems to be the major key to determine the redistribution of ion ranges. So we can predict that $\Delta R_p = \langle (z-R_p)^2 \rangle^{1/2}$ will increase significantly due to swelling. The change to be occurred in $R_p = \langle z \rangle$ cannot be predicted simply.
The Fig.4 summarizes the Φ–effect on R_p and ΔR_p of B ions implanted into Si, in terms of ratios to those obtained by neglecting the accumulated defects. The lower the incident energy, the deviation due to the higher Φ becomes more pronounced. For the case of Φ <10^{15}ions·cm^{-2}, there appeared to be no significant difference in both R_p and ΔR_p from those respectively obtained in the low-Φ cases. Thus far we supposed the non-linear effect emerges gradually, by judging from the number of FKP in Fig.2. Nevertheless, this Fig.4 reveals that high-Φ effects appear so critically when E_0 exceeds a certain critical value, E_c, as if certain synergistic non-linearity in the ion concentra-tion profiles takes places. The value E_c should be given by converting Eq.(1) as $E_c = E(\Phi_c)$. The ratios depart abruptly from unity when E_0 is reduced to a smaller value than E_c. Each set of curves seem almost parallel to each other and the difference among them is solely in the value of E_c. Then the function describing such a synergistic behavior would be arranged by means of the Heviside function $H(E_c-E)$. Terms are; a negative power function of (E_c-E) and an exponential term to include certain physical continuity. Ratios are arranged, for all the cases with different E_0 and Φ, in terms of E_c (Φ) determined by Eq.(1)

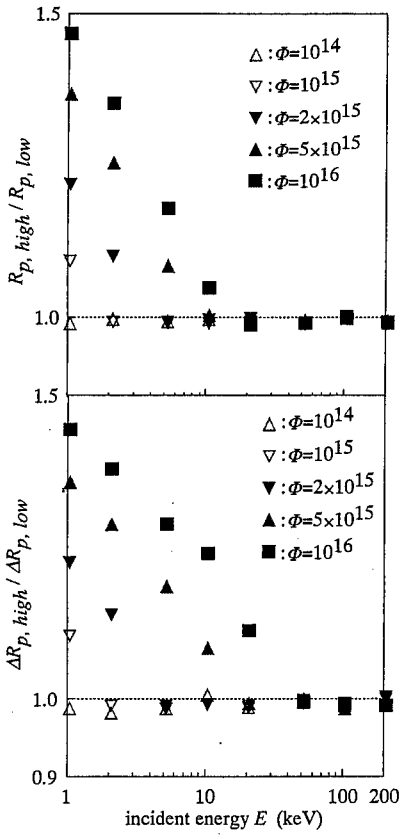


Fig. 4 The fluence dependence on the R_p and the ΔR_p of longitudinal range distribution, by means of the ratios to those calculated values assuming without accumulated defects.

$$\frac{R_{p,high}}{R_{p,low}} = 1 + \xi(E_c - E)^{\lambda} \cdot H(E_c - E) + \eta \exp(-\mu(E - E_c)), \quad (2\text{–}1)$$

$$\frac{\Delta R_{p,high}}{\Delta R_{p,low}} = 1 + \xi'(E_c - E)^{\lambda'} \cdot H(E_c - E) + \eta' \exp(-\mu'(E - E_c)), \quad (2\text{–}2)$$

where the indices of *high* and *low* mean to include the non-linear effect and exclude it, respectively. The common parameters (ξ, η, λ, μ, ξ', η', λ', μ') are determined by the non-linear least square analysis.The two equations give the extrapolation factors for the respective range moments. That is

for the longitudinal ranges, we can predict R_p and ΔR_p under high-Φ, once calculated those values under the low-Φ approximation.
We will further intend to derive the similar extrapolation factor for the lateral range straggling, ΔR_L ($=<(x^2+y^2)>^{1/2}$). The investigation into which directions the excessive ions diffuse has not yet been complete. However we hypotheses that when an excessive ion enters in the last stage after having dissipated almost of E_0 with the lost memory of incident direction, the direction of diffusion would be isotropic. Therefore the ratio of the lateral to longitudinal straggling may be kept even under the high-Φ condition. If this is realistic,

$$\frac{\Delta R_{L,high}}{\Delta R_{p,high}} \cong \frac{\Delta R_{L,low}}{\Delta R_{p,low}} \quad , or \quad \Delta R_{L,high} \cong \Delta R_{L,low} \cdot \left(\frac{\Delta R_{p,high}}{\Delta R_{p,low}} \right). \quad (3)$$

Then by means of the same extrapolation factor of Eq.(2-2), we can evaluate the $\Delta R_{L,high}$, if we had already calculated $\Delta R_{L,low}$ from the three dimensional ion range calculation under low-Φ condition. Otherwise, for other calculations supposing one-dimensional target like TRIM, we can estimate $\Delta R_{L,high}$ from $\Delta R_{p,high}$ indirectly, as will be discussed in the next section.

4. Correlation between lateral and longitudinal straggling

Furukawa et al. [15] supposed an ellipsoid of revolution of which the lengths of two axes are determined by the ΔR_L and ΔR_p. The eccentricity or the ratio of ΔR_L to ΔR_p was known to depend on the mass ratio of ion to target atom, with the aid of semi Monte-Carlo simulation. As a result $\Delta R_L > \Delta R_p$ for light ions and $\Delta R_L < \Delta R_p$ for heavy ions. By further including the energy dependence of the eccentricity, Fink et al. [16] generally arranged the correlation between ΔR_L and ΔR_p, via a comparison using the TRIM calculation. It was established under the low-Φ approximation, by introducing the universal straggling $\sigma_{long,gen}$ in the LSS unit

$$\frac{\Delta R_{L,high}}{\Delta R_{p,high}} \cong \frac{\Delta R_{L,low}}{\Delta R_{p,low}} = a \cdot \sigma_{long,gen}{}^{b} \quad or \quad \Delta R_{L,high} \cong \Delta R_{p,high} \; a \cdot \sigma_{long,gen}{}^{b} . \quad (4)$$

The set of two coefficients, a and b in Eq.(4), are different for the three energy regimes; low, intermediate, and high E_0. These cases are classified as follows,

$$\begin{aligned} &a = 0.47, b = -0.03 \quad for \; \sigma_{long,gen} < 0.05, \\ &a = 1.23, b = 0.26 \quad for \; 0.05 < \sigma_{long,gen} < 7, \\ &a = 2.34, b = -0.08 \quad for \; 7 < \sigma_{long,gen} . \end{aligned} \quad (5)$$

The smaller the $\sigma_{long,gen}$ the more dominant the S_n (low E_0) is. The larger the $\sigma_{long,gen}$ the more dominant the S_e (high E_0) is. The second case in Eq.(5) corresponds to the intermediate energy regime, where S_n and S_e are competing against each other. This energy regime which corresponds to 30Å< ΔR_p < 3000Å fully covers the range of 1< E_0 < 200keV, as is shown in Table II. Therefore we can fix a=1.23 and b=0.26 in this study. The definition of $\sigma_{long,gen}$ is,

$$\sigma_{long,gen} = \Delta R_p \frac{4\pi N_0 a_{12}{}^2 M_1 M_2}{(M_1 + M_2)^2} , \quad (6)$$

where M_1 and M_2 are the mass of the ion and the target atom, respectively. The screening length a_{12} is coincident with that defined for the BZ potential [17] which was used to determine the two parameters a and b. It is

$$a_{12} = \frac{0.8854\ a_B}{Z_1^{.23} + Z_2^{.23}} \quad . \quad (7)$$

E_0(keV)		1	2	5	10	20	50	100	200
$\Phi=10^{13}$	R_p	651.6	113.4	252.2	483.2	954.2	2369	4547	8393
	ΔR_p	39.01	65.35	135.6	237.9	423.2	839.5	1302	1811
$\Phi=10^{16}$	R_p	95.49	151.5	292.4	504.9	948.0	2362	4562	8386
	ΔR_p	56.13	89.27	171.9	290.2	466.5	8395	1300	1802

Table II The range moments(Å) of B into Si at energies from 1 to 200keV.

5. Conclusions

Our final purpose was to define the high-fluence (Φ) effect on the lateral spread. The high-fluence effect mainly discussed here are the swelling and the sputtering or deposition in some case, which bring the redistribution of the stopped ions in solids. By means of a Monte-Carlo simulation code called TRIDYN the composition change and the dynamical relaxation was analyzed in the case of B implanted into Si. The amount of the surface recession due to sputtering negligible. The limiting Φ above which non-linear effect became undeniable was determined as a function of the incident energy(E_0). The swelling is supposed to take place at $\Phi > \Phi_c$, where the linearity of ion concentration with respect to Φ fails. We extracted two of extrapolation factors as the function of E_0. They derive the projected range(R_p) and the longitudinal range straggling(ΔR_p) under high-Φ, respectively, from those values calculated under the low-Φ approximation. For the lateral spread, we can derive the lateral range straggling(ΔR_L) using the same extrapolation factor for ΔR_p. If the low-Φ calculation is done for one dimensional target like TRIM, we can still obtain ΔR_L under high-Φ by adopting a correlation between ΔR_p and ΔR_L.

Acknowledgments

The author expresses thanks to Dr. W.Eckstein of Max-Plank in Garching for invaluable comments, to Dr. D.Fink of Hahn-Meitner-Institut in Berlin for encouraging discussions and preprint prior to submission, to Prof. L.Thomé of CNRS in Orsay for sharp discussions, to Prof. H.Saito of Okayama Univ. of Science for valuable discussions, and to Mr. D.Neill for careful reading of the manuscript.

6. References

[1] S. T. Nakagawa, "**Semiconductors and Semimetals**," vol.45(Academic Press, Boston, 1997), pp.55-84.
[2] E. Rimini, "**Ion implantation: Basics to device fabrication**," (Kluwer Academic Publishers, Boston, 1995).
[3] M.I.Current, L.Larson, W.A.Keenan, and C.B.Yarling, "**Handbook of Ion Implantation Technology**, " ed. by J.F.Ziegler, (Elsevier, Amsterdam, 1992), pp.647-674.
[4] N.D.Thái, J.Appl.Physics **41**, 2859 (1970).
[5] D.Fink, et al. to be published (1997).
[6] W. Eckstein, "**Computer Simulation of Ion-Solid interactions**," (Springer-Verlag, Berlin, 1991).
[7] F.A.Trumbore, Bell Sys. Tech. J. **39**, 205 (1960).
[8] O.S.Oen and M.T.Robinson, Nucl. Instrum.Meth. **132,** 647-653 (1976).
[9] F.Seitz and J.S.Köhler, "Displacement of Atoms during irradiation" in "**Solid State Physics**," vol.2, (Academic Press, New York, 1956), pp. 305-448.
[10] W.Eckstein, M.Hou, and V.I.Shulga, Nucl.Instrum.Meth. B**119**, 477 (1996).
[11] M.I.Current, et. al, "**Adv.Mat.'93, IV, Laser and Ion Beam Modification of Materials**,"(I.Yamada et al. eds.), (Elsevier, Amsterdam, 1994), pp.401-406.
[12] H.Ryssel, K.Müller, K.Haberger, R.Henkelmann, and F.Jahnel, Appl.Phys. **22**, 35 (1980).
[13] W.Eckstein, private communication.
[14] N.Matsunami et al., Atomic Data and Nuclear Data Tables **31,** 1 (1984).
[15] S.Furukawa, H.Matsumura, Appl.Phys.Lett. **22**, 97 (1977).
[16] D.Fink and M.Müller, Surface and Coating Technology **51,** 352 (1992).
[17] J.F.Ziegler, J.P.Biersack, and U.Littmark, "**Stopping and Ranges of ions in Solids**," vol.**1**.

Materials Science Forum Vols. 258-263 (1997) pp. 647-652
© 1997 Trans Tech Publications, Switzerland

STRUCTURAL CHANGE AND RELAXATION PROCESSES OF TETRAHEDRAL POINT DEFECTS

El-Maghraby Mohamed* and Yuzo Shinozuka
Department of Applied Science, Faculty of Engineering,
Yamaguchi University, Tokiwadai 2557, Ube 755, Japan

Keywords: point defects, structural change, metastability, electron correlation, defect reaction.

Abstract. We have performed a comprehensive theoretical study on the structural change and relaxation processes of a tetrahedral (T_d) four-site model, which is the most conceivable simple model for various point defects in covalent semiconductors. The stable electronic and atomic configurations are calculated exactly for the electronic ground and excited states for possible electron occupation n (=0~8). Stable structures are shown to be either T_d, C_{3v}, C_{2v} or C_s depending on the electron number, the electron spin and the strengths of the electron-electron interaction and the electron-lattice interaction. With the obtained phase diagrams we discuss the structural changes and relaxation processes of the defect induced by an intra-defect excitation (n=constant, ground$\rightarrow$ excited) or a carrier trapping ($n \rightarrow n \pm 1$).

Introduction.

Most of electronic and atomic processes in semiconductors, and hence their physical properties, are affected by point defects (vacancies, substitutional and interstitial impurities). Recently, large lattice relaxation phenomena have attracted much attention such as the negative-U effect and the off-center instability found at several substitutional impurities in covalent semiconductors. For instance, a localized electronic excitation induces a bond breaking and some times shows a bistability (sp^3-sp^2), found at EL2-center in GaAs and DX-center in AlGaAs [1 - 3]. These are local "*structural change induced by electronic excitation*" that strongly related to the photo-induced phase transition [4].

The common structure of covalent semiconductors (e.g., IV, III-V, II-VI) is the four fold coordination. Then the tetrahedral symmetry is very important because it is the most popular structure of point defects in covalent materials. Several point defects, which originally possess a T_d symmetry, show symmetry breaking structural instability to D_{2d}, C_{3v}, and C_{2v}. Examples are vacancy [5, 6] and nitrogen substitutional impurity [7] in silicon. Various electronic-atomic processes including structural changes could be fully understood only if we investigate the local and global stability of the ground and excited states of the system. The most simplest model to discuss this would be the *T-U-S* model. The model consists of several interacting electrons in a deformable lattice and was first applied to a two-site two-electron system [8]. Studies covering the adiabatic competition between these interactions have been done on various systems, for example, the 4-site 4-electron ring-shape system [9], one dimensional half-filled system [10] and two-site hetero system [11]. No such studies have done on the T_d system although of its importance and reality. In this paper we study the

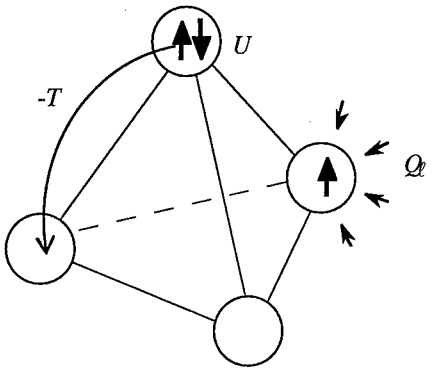


Fig. 1. The *T-U-S* model for a four-site tetrahedral system.

stable structures and relaxation processes of a tetrahedral (T_d) four-site *T-U-S* model. The obtained results are applied to explain the structural changes and relaxation processes of various point defects in covalent semiconductors.

T-U-S Model.

Let us introduce a four-site model which has a tetrahedral symmetry. This system is characterized by the electronic transfer energy, $-T$, describing the quantum hopping from site to site, the on-site (short range) Coulomb repulsion energy, U, between two electrons, the lattice relaxation energy, S, due to the short range interaction of an electron with the lattice mode, Q_ℓ, at the site ℓ (=1~4) and the number n (=0~8) of the occupied electrons (Fig. 1). The site ℓ represents either atomic or molecular orbital: four dangling bonds for a vacancy case; four bonding (or antibonding) orbitals for a substitutional impurity.

Treating the system adiabatically, the Hamiltonian is given by

$$H = -T\sum_{\ell}\sum_{\ell'}\sum_{\sigma} a^{+}_{\ell\sigma}a_{\ell'\sigma} + U\sum_{\ell} n_{\ell+}n_{\ell-} + \tfrac{1}{2}\sum_{\ell} Q_\ell^2 - c\sum_{\ell}(n_{\ell+}+n_{\ell-})Q_\ell. \qquad (1)$$

Here, $a^{+}_{\ell\sigma}$ ($a_{\ell\sigma}$) is the creation (annihilation) operator of an electron with spin σ (+ (up), - (down)) at the site ℓ=1, 2, 3, 4 and $n_{\ell\sigma} \equiv a^{+}_{\ell\sigma}a_{\ell\sigma}$. The site energy at ℓ is assumed to change linearly with the lattice distortion Q_ℓ around the site with c the lattice-coupling constant. The lattice relaxation energy for a single electron occupancy at a site is $c^2/2 \equiv S/2$, and that for double occupancy is $2S$.

The present Hamiltonian commutes with the number of electrons n and the total spin S_σ. Then they are constants of motion. Diagonalizing the Hamiltonian matrix for each subspace one obtains the electronic energies of both the ground and excited states.

We calculate the adiabatic potential $W(Q)$ of the lowest state $|\Psi\rangle = \sum_\alpha c_\alpha \prod a^{+}_{\ell\sigma}|0\rangle$ of the Hamiltonian of n=0 (8), 1 (7), 2 (6), 3 (5), and 4 electrons as a function of Q_ℓ's. Here $|0\rangle$ is the vacuum state. Applying the Feynman-Hellmann theorem; the lattice distortion at the stable configuration is shown to be proportional to the local electron density as $\overline{Q}_\ell = \langle n_{\ell+} + n_{\ell-}\rangle c$ and then the sum rule holds, $\sum_\ell \overline{Q}_\ell = nc$.

The system has the electron-hole symmetry: the character of the ground (excited) state of n electrons corresponds to that of the 8-n electrons.
In the rigid lattice (Q_ℓ=0) and if the electron-electron interaction is neglected (U=0), one electron eigen states in the present T_d system are one a_1 state with an eigen energy -3T and three t_2 states with T. In a deformable lattice ($Q_\ell \neq 0$) and if the electron-electron interaction is switched on ($U \neq 0$), however, eigenstates of n electrons become complicated and structural changes may take place lowering the symmetry, as will be shown in the next section.

Results.

Hereafter we show the calculated results classified in the electron number n and the total spin S_σ. It should be first stated that in the present system the minimum energy of high spin S_σ states are always higher than that of low spin states.

1. n=0 (8): There is only one possible state (S_σ =0), where $\overline{Q}_1 = \overline{Q}_2 = \overline{Q}_3 = \overline{Q}_4 = 0$ (or 2c) and then it has the T_d symmetry.

2. n =1 (7): There are 8 electronic states (4×2 spin doublet S_σ=1/2). The stable state is either symmetric **F** (an electron is delocalized, where $\overline{Q}_1 = \overline{Q}_2 = \overline{Q}_3 = \overline{Q}_4$, T_d symmetry) or asymmetric **S** (an electron is self trapped such that $\overline{Q}_1 > \overline{Q}_2 = \overline{Q}_3 = \overline{Q}_4$, $C_{3v}(1)$). It changes from **F** to **S** as a first-order transition at S/T=6. When S/T >8 the **F** state becomes unstable. The excited states in the rigid lattice ($Q_\ell = 0$) are triply-degenerate and always show the Jahn-Teller distortion ($\overline{Q}_1 = \overline{Q}_2 > \overline{Q}_3 = \overline{Q}_4$, C_{2v}).

3. n =2 (6): There are 28 electronic states, which are classified into 6×3 spin triplet states (S_σ=1) and 10×1 spin singlet states (S_σ=0).

(a) Singlet states. Figure 2 (a) shows the stable configurations of these states. When T is large enough the symmetric state (T_d) is stable, where two electrons have equal amplitudes at every four sites. With increasing U and/or S, structural changes take place. If $U \sim S >> T$, the charge transfer state (C_{3v} (1')) becomes stable, where two electrons are shallowly localized around one site (such that $\overline{Q}_1 > \overline{Q}_2 = \overline{Q}_3 = \overline{Q}_4$). If $S > U >> T$, the charge transfer state ($C_{3v}(1)$) becomes stable, where two electrons are deeply localized at one site (such that $\overline{Q}_1 >> \overline{Q}_2 = \overline{Q}_3 = \overline{Q}_4$).
When $U > S >> T$, two electrons are localized at different sites repelling each other such that ($\overline{Q}_1 = \overline{Q}_2 > \overline{Q}_3 = \overline{Q}_4$, C_{2v}). In the limit $U >> S$, T, the transition from T_d to C_{2v} occurs at S/T=6.097 as a second-order. For the small limit of T, C_{2v} state (two electrons occupy separately two of four sites) is stable for $U > S$ and $C_{3v}(1)$ (double occupation at one site) is stable for $U < S$. The transition between C_{2v} and $C_{3v}(1)$ is of the first-order type. When U=0 (on the T-S side), the $C_{3v}(1)$ state becomes stable for $S > 3T$, while the T_d state becomes unstable for $S > 4T$. The values of the parameters at the critical points are: at O, S/T =4.972, U/T=3.514; at O', S/T=6.250, U/T=6.000, and at Q, S/T=6.098, U/T=9.040.

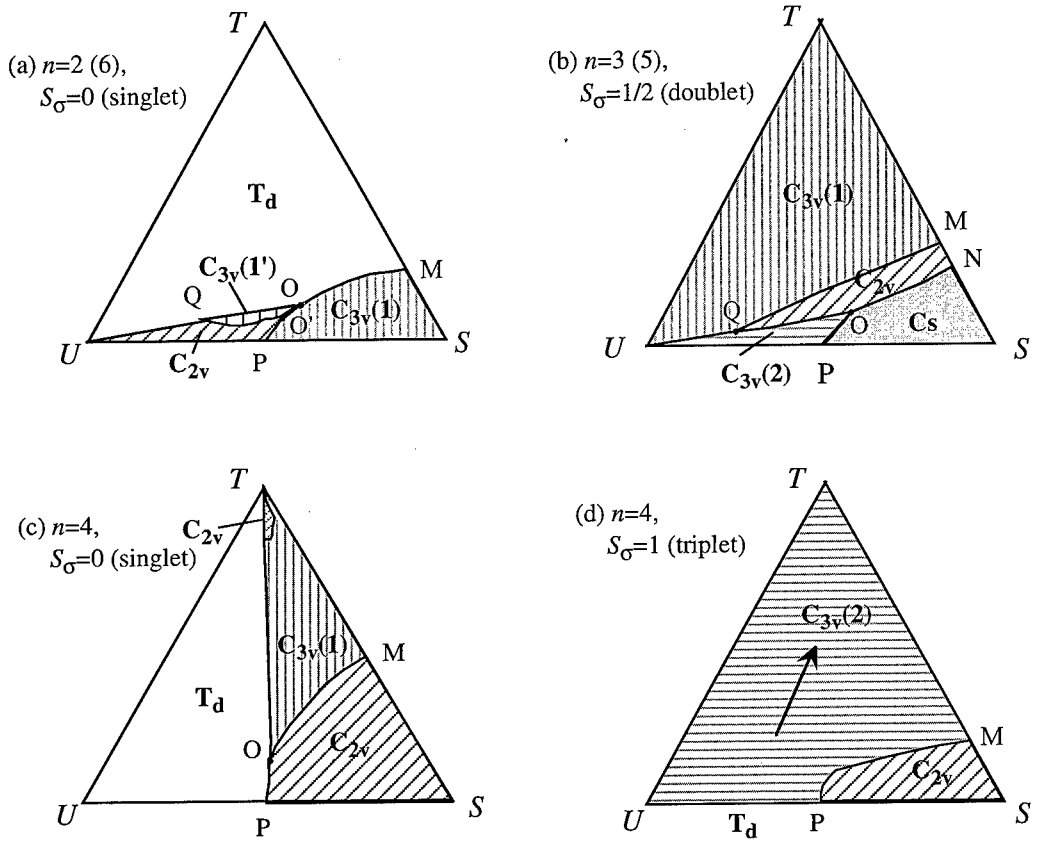


Fig. 2. Phase diagrams for different electron occupations of the 4-site tetrahedral *T-U-S* model. The coordinates of (*T*, *U* , *S*) at any point in the triangle are proportional to the lengths of the perpendiculars from that point to the *US*, *ST*, and *TU* side respectively.

(b) Triplet states. They always show an asymmetric distortion, such that $\overline{Q}_1 = \overline{Q}_2 > \overline{Q}_3 = \overline{Q}_4$ (C_{2v}) except for S=0.

4. n =3 (5): There are 56 electronic states, which are classified into 4×4 quartet states with S_σ =3/2 and 20×2 doublet states with S_σ =1/2.

(a) Doublet states. Symmetric T_d state ($\overline{Q}_1 = \overline{Q}_2 = \overline{Q}_3 = \overline{Q}_4$) is not stable for any parameter sets, as shown in Fig. 2 (b). When T=0, three electrons occupy three sites or two sites depending upon whether $U<S$ or $U<S$. For large T the stable structure is $C_{3v}(1)$ with $\overline{Q}_1 > \overline{Q}_2 = \overline{Q}_3 = \overline{Q}_4$. As S increases it changes from $C_{3v}(1)$ to C_{2v} ($\overline{Q}_1 = \overline{Q}_2 > \overline{Q}_3 = \overline{Q}_4$) as a first-order transition. Further increase of S causes a second-order transition from C_{2v} to C_s ($\overline{Q}_1 > \overline{Q}_2 > \overline{Q}_3 = \overline{Q}_4$). The transition point on the *T-S* side is given by S/T=2.109 at M, and by S/T=2.859 at N. If $U>S>>T$, three electrons are separately localized at three sites, $C_{3v}(2)$, such that $\overline{Q}_1 = \overline{Q}_2 = \overline{Q}_3 > \overline{Q}_4$. The values of the critical parameters are, S/T=4.882, U/T=4.128 at O, and S/T=3.762, U/T=15.667 at Q.

(b) Quartet states. In the rigid lattice, the ground state is triply degenerate with an eigen energy $-T$, which does not depend on U. In a deformable lattice, it always shows an asymmetric (J-T) distortion, such that $\overline{Q}_1 = \overline{Q}_2 = \overline{Q}_3 > \overline{Q}_4$ ($C_{3v}(2)$) except for S=0.

5. n =4: This is a so-called half filled case with 70 electronic states, which are classified into 5×1 spin quintet (S_σ=2), 15×3 spin triplet (S_σ=1), and 20×1 spin singlet (S_σ=0).

(a) Singlet states. The stable configurations are shown in Fig. 2(c). There are three kinds of stable states; T_d state with $\overline{Q}_1 = \overline{Q}_2 = \overline{Q}_3 = \overline{Q}_4$ is dominant for $U>S$, $C_{3v}(1)$ state with $\overline{Q}_1 > \overline{Q}_2 = \overline{Q}_3 = \overline{Q}_4$ for $T>S>U$, and C_{2v} with $\overline{Q}_1 = \overline{Q}_2 > \overline{Q}_3 = \overline{Q}_4$ for $T>U>S$. In a narrow region of $T>>U\sim S$, C_{2v} is found to be lower than $C_{3v}(1)$. Transitions between these phases occur as a first-order ones. The parameters for critical points are: at P, $U=S$; at M, S/T=1.005; at O, U/T =4.000 and S/T=4.244. In the atomic limit (T=0), four sites are singly occupied (T_d) when $U>S$, or two sites are doubly occupied (C_{2v}) when $U<S$.

(b) Triplet states. The stable configurations are shown in Fig. 2 (d). There are two kinds of stable structure; $C_{3v}(2)$ state with $\overline{Q}_1 = \overline{Q}_2 = \overline{Q}_3 > \overline{Q}_4$ and C_{2v} state with $\overline{Q}_1 > \overline{Q}_2 = \overline{Q}_3 > \overline{Q}_4$. Only in the atomic limit (T=0), tetrahedral (T_d) structure is stable for $U>S$. Increasing of the electron-lattice coupling distorts the symmetry and the stable structure is $C_{3v}(2)$. When $S>U>>T$, C_{2v} structure is stable which corresponds to a state in the atomic limit where one site is occupied by up and down spin electrons and two sites are singly occupied. The transition between $C_{3v}(2)$ and C_{2v} is a first-order one. At the critical point M, S/T=4.537.

(c) Quintet states. S_σ=2. This is a trivial case; the system is always in its symmetric state ($\overline{Q}_1 = \overline{Q}_2 = \overline{Q}_3 = \overline{Q}_4$, T_d) and the lowest adiabatic potential is given by $W_1(\overline{Q})$=-2S.

Summary and Discussion.

The stable structures of the tetrahedral four-site system have been calculated exactly in the adiabatic approximation for the whole range of the T, U, and S parameters. Stable structures are shown to be either T_d, $C_{3v}(1)$, $C_{3v}(2)$, C_{2v} or C_s depending on the electron number, the electron spin and the strengths of the electron-electron interaction and the electron-lattice interaction.

Let us briefly discuss the relaxation processes in the present T_d system. We must differentiate between two processes: one induced by an intra-system excitation without change in the number of occupied electrons, and the other induced by the change in the electron number, for example the system is embedded in a host semiconductor and captures an electron or a hole. In the first case, transitions between two electronic states of constant n take place. Excited states are rather instable [8] since they contain large amplitude for the charge transfer electronic states. In the second case, if we start with the half filled case (n=4), the stable structure for singlet is either T_d, $C_{3v}(1)$ or C_{2v} depending upon the relative values of T, U, and S (Fig. 2 (c)). Captures of an electron or a hole results in a structural change, some typical examples are listed in Table 1. The vacancy (V) in Si is shown to have different stable structures depending on the charge state [5, 6]: D_{2d} for V^0 and V^+, C_{2v} for V^-, and T_d for V^{++}. Since V^0 corresponds to n=4 in the present model, V in Si may fall into the fifth case

Table 1. Typical examples of stable structures of different electron occupation for the lowest spin state.

parameters	n =4	n=3, 5	n=2, 6	n=1, 7	n=0, 8
U/T=1, S/T=0.5	T_d	$C_{3v}(1)$	T_d	T_d	T_d
U/T=10, S/T=8	T_d	$C_{3v}(2)$	C_{2v}	$C_{3v}(1)$	T_d
U/T=1, S/T=8	C_{2v}	C_s	$C_{3v}(1)$	$C_{3v}(1)$	T_d
U/T=0.4, S/T=0.8	$C_{3v}(1)$	$C_{3v}(1)$	T_d	T_d	T_d
U/T=4, S/T=2.4	C_{2v}	C_{2v}	T_d	T_d	T_d

(U/T=4, S/T=2.4) in Table 1. However, in the present work we have assumed the diagonal type electron-lattice interaction, then D_{2d} type structure is not appeared. The effect of the off-diagonal type interaction is now under study.

Finally, we hope that the present work would reveals the basic physics of the structural change of various tetrahedral point defects in covalent semiconductors.

Acknowledgments.

The present work is supported by the Proposal-Based Advanced Industrial Technology R&D Program of NEDO Japan and Grant-in-Aid by the Japanese Ministry of Education, Science and Culture. One of the authors, El-Maghraby M., would like to thank the Japanese Ministry of Education, Science and Culture for kindly supporting his stay in Japan.

* On leave from Physics Department, Faculty of Science, Assiut University, Assiut 71516, Egypt.

References.

[1] Y. Shinozuka, *"Relaxations of Excited States and Photo-Induced Structural Phase Transitions"*, Proc. 19th Taniguchi Symposium (Springer, 1997) ed. K. Nasu, 229.

[2] J. Dabrowiski and M. Scheffler, Phys. Rev. Lett. **60**, 2183 (1988).

[3] D. J. Chadi and K. J. Chang, Phys. Rev. Lett. **60**, 2187 (1988).

[4] K. Nasu (ed.), *"Relaxations of Excited States and Photo-Induced Structural Phase Transitions"*, Proc. 19th Taniguchi Symposium (Springer, 1997).

[5] G. D. Watkins, Proc. Defects in Semiconductors 1972, 228; Physica **117B&118B**, 9 (1983).

[6] M. Sprenger, S. Muller, E. Sieverts and C. Ammerlaan, Phys. Rev. B**35**, 1566 (1987).

[7] K. L. Brower, Phys. Rev. B**26**, 6040 (1982).

[8] Y. Toyozawa, J. Phys. Soc. Jpn. **51**, 1861 (1981).

[9] J. Takimoto and Y. Toyozawa, J. Phys. Soc. Jpn. **52**, 4331 (1983).

[10] K. Nasu and Y. Toyozawa, J. Phys. Soc. Jpn. **51**, 2098, (1982); **51**, 3111 (1982).

[11] Y. Shinozuka and El-Maghraby M., Proc. of EXCON-96 (Dresden Univ. Press, 1996) 335.

Materials Science Forum Vols. 258-263 (1997) pp. 653-658
© 1997 Trans Tech Publications, Switzerland

THE JAHN–TELLER EFFECT AND THE STRUCTURE OF MONOVACANCIES IN Si, SiC AND C

A. Zywietz, J. Furthmüller and F. Bechstedt

Institut für Festkörpertheorie und Theoretische Optik,
FSU Jena, Max–Wien–Platz 1, D-07743 Jena, Germany.
Ph. +49-3641-636683 Fax +49-3641-635182

Keywords: Vacancies, Jahn–Teller effect, Si, SiC, C, First–principles calculations

Abstract. We present *first–principles* plane–wave supercell calculations for the neutral monovacancy in Si and diamond and neutral and charged monovacancies in cubic SiC using extremely soft non-normconserving Vanderbilt pseudopotentials. The occurrence and symmetry of a Jahn–Teller distortion are studied. For the case of Si the results are very sensitive with respect to numerical details such as supercell size, supercell shape and **k**–sampling. Sufficiently converged results for Si require a 128(127)–atom cell. For SiC a 64(63)–atom cell is sufficient. The convergence behaviour can be explained in terms of the finite dispersion of the defect bands. A tight–binding description of the electronic vacancy–vacancy interaction allows to extract the vacancy energy levels and the Jahn–Teller splittings from the calculated bands. With rising supercell size we find a tendency for the stabilization of the D_{2d} symmetry in the case of Si. For cubic SiC we find also a pronounced Jahn–Teller distortion for the C–site vacancy which is energetically preferable over the Si–site vacancy. Furthermore, C–site vacancies in SiC are found to act as donors. The Si–site vacancy shows practically no Jahn–Teller effect. This can be explained in terms of the different overlaps of the dangling–bond orbitals at the atoms neighbouring the vacancy. In diamond the Jahn–Teller effect is also strongly suppressed. This might be related to the extreme hardness of diamond.

Introduction

Native defects such as vacancies strongly influence the electrical and optical properties of semiconductors. The monovacancy in Si induces deep levels in the fundamental gap and plays a major role in atomic diffusion and aggregation[1, 2, 3]. In SiC the presence of vacancies strongly limits the doping efficiency of acceptors[4, 5]. Apart from the technological relevance, vacancies in semiconductors exhibit interesting physics of their own. The introduction of a vacancy in a cubic diamond or zinc–blende structure possessing T_d symmetry leads to four dangling bonds at the neighbouring atoms giving rise to a ("s–like") non–degenerate a_1 state and a ("p–like") triply degenerate t_2 state in the fundamental gap. Since the t_2 state is only partially occupied a vacancy with full T_d symmetry would lead to a *degenerate ground state*. One has to expect that this degeneracy should cause a symmetry–lowering Jahn–Teller distortion of the surrounding atomic geometry resulting in a splitting of the t_2 level and in an energy gain via the band–structure energy contribution. In order to obtain a non–degenerate ground state the t_2 level must at least split into a non–degenerate and a doubly degenerate state (neutral and positively charged vacancies). Possible symmetries leading to such a splitting are C_{3v} and D_{2d}. In order to understand the formation and the effect of native defects in various semiconductors crystallizing in the diamond or zinc–blende structure we performed *first–principles* studies of the atomic and electronic structure of monovacancies in Si, cubic (zinc–blende) SiC and diamond.

Method

Our calculations are performed within the framework of density functional theory in the local density approximation. The Perdew–Zunger parametrization of the exchange–correlation energy per electron is taken into account. We use extremely soft Vanderbilt pseudopotentials[6] in a plane–wave basis corresponding to a kinetic energy cutoff of 180 eV for Si and SiC. For diamond we have to use a kinetic energy cutoff of 270 eV. Explicitely we use the Vienna Ab–initio Simulation Package (VASP)[7, 8]. The atomic coordinates are optimized according to the calculated Hellmann–Feynman forces using a conjugate–gradient technique. The relaxation of the electronic degrees of freedom is done by a band–by–band residual minimization method. The resulting Kohn–Sham eigenvalues are used to interprete the bulk band structure and the defect bands. The defect bands are fitted to a simple tight–binding model for interacting vacancies assuming nearest–neighbour interactions only. From the fitted thight–binding parameters we can extract the "true" defect levels for the limiting case of non–interacting vacancies. The defect structures are modelled by means of repeated supercells of different size and shape. Most calculations are done in a simple cubic 63–atom cell, for Si also a face–centered cubic 127–atom cell is used. Some tests for other cells (face–centered cubic 15-atom cell and 53–atom cell) have been performed too. However, the smaller cells turn out to be of insufficient size. The **k**–sampling is performed using different sets of **k**–points. We check **k**–point sets according to the suggestions of Baldereschi (B)[9], Chadi and Cohen (CC)[10] and Monkhorst and Pack (MP)[11]. On the analogy of the procedure of Baldereschi for constructing the special mean–value point we construct a new set of two special points which we might call "two Baldereschi points" (2 B). Furthermore, we check also the sampling using only the Γ–point.

Results

Neutral monovacancy in Si

In Table 1 we have summarized the formation energy for a neutral monovacany in Si for three different supercell sizes and a variety of **k**–point samplings in dependence on the local symmetry. Apart from the Γ–only sampling and smaller supercells the absolute value of the formation

Table 1. Formation enerygy (in eV) of the neutral monovacancy in Si calculated for several supercells, point–group symmetries and **k**–point samplings.

N_{atom}	**k**–point set	T_d	D_{2d}	C_{3v}
127	2 CC	3.615	3.372	3.590
	1 B	3.606	3.679	3.614
	2 B	3.586	3.568	3.587
	Γ–point	3.292	3.086	3.292
	MP (2x2x2)	3.573	3.570	3.573
63	2 B	3.556	3.551	3.559
	MP (2x2x2)	3.376	3.376	3.377
	MP (3x3x3)	3.566	3.566	3.567
53	1 B	3.462	3.443	3.467
	2 B	3.416	3.415	3.417
	MP (2x2x2)	3.040	3.041	3.041
	MP (3x3x3)	3.313	3.313	3.313

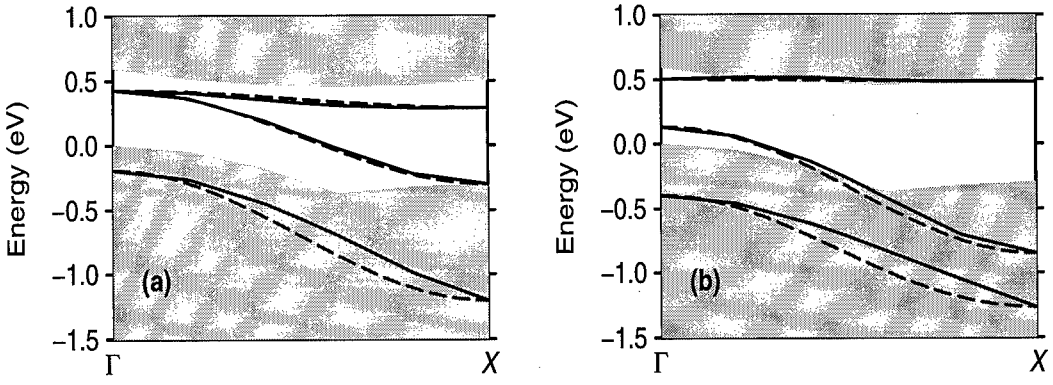
energy ranging from 3.0 ... 3.6 eV is not too sensitive on the numerical details. We observe a

tendency towards the larger values for increasing supercell size. The larger values agree quite well with the experimental value of the formation energy of 3.6 ± 0.2 eV[12, 13]. For the smaller cells the influence of the local symmetry on the formation energy is almost negligible and the deviations of the atomic displacements from T_d symmetry remain small. Only for the largest 127–atom cell we find a pronounced Jahn–Teller effect except for the Γ–only sampling. Here we find significant deviations of the atomic displacements from T_d. A D_{2d} symmetry is energetically favoured by several 0.01 or 0.001 eV depending on the **k**–point sampling. The corresponding atomic geometry is related to a pairing of Si atoms neighbouring the vacancies, i.e., the formation of (weak) bonds between these Si atoms. A D_{2d} symmetry is in agreement with findings of low temperature experiments[2] and other recent *first–prinicples* studies[14, 15]. However, there are other recent calculations[16] predicting the C_{3v} symmetry to be most stable. We believe that this result is an artifact of the used **k**–point sampling and the 63–atom cell, as also pointed out by other authors[15].

Serious problems are related to the strong dispersion of the defect bands. For the smaller cells the band dispersion is as large as or larger than the fundamental gap of Si (our calculated value is E_{gap}=0.47 eV) and we find already an overlap between the defect bands and the bulk conduction band. Hence, smaller cells and certain **k**–point samplings can lead to an unphysical occupation of the lowest conduction band states. This unphysical band occupation can result in a wrong symmetry of the ground state or it can even completely suppress the Jahn–Teller distortion. These problems occur even in a 63–atom cell. Only for a 127–atom cell we can conclude that the ordering of the vacancy bands and the lowest conduction bands is correct.

The huge dispersion of the defect bands makes it also difficult to extract the "true" defect states in the limit of (approximately) isolated vacancies. Hence, we are not aware of any study discussing the *electronic structure* of the monovacany in Si. The band dispersion results from the rather strong vacancy–vacancy interactions in our artifical vacancy–superlattice. We attack the problem of extracting the "true" defect levels via a simple tight–binding model assuming only nearest–neighbour vacancy–vacancy interactions. For a hypothetical T_d symmetry we find

Fig. 1. Defect band structure of the monovacancy in Si for a 127–atom cell. The shaded region denotes the projected bulk bands. The solid lines are the calculated defect bands, the dashed lines denote the bands obtained from our tight–binding fit. Left panel (a): T_d symmetry, right panel (b): D_{2d} symmetry.



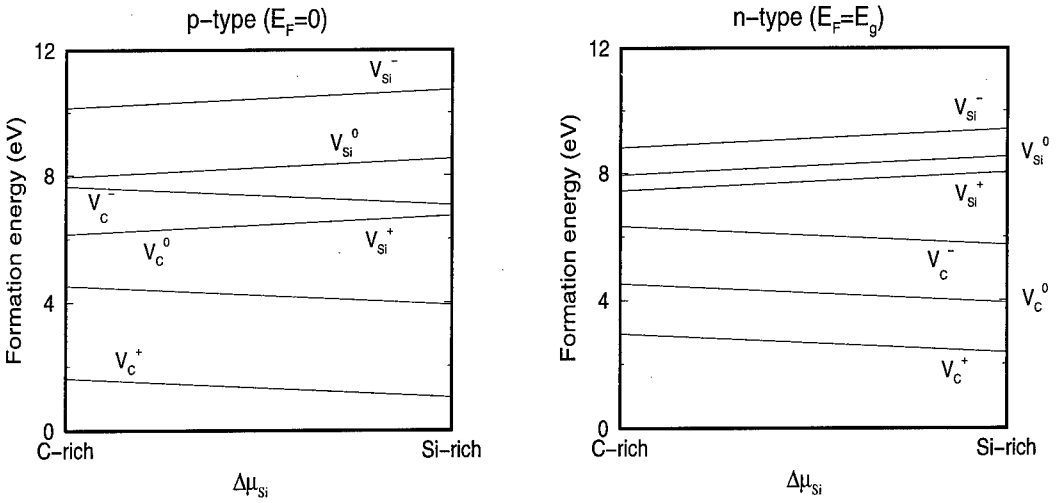
the a_1 state deep in the valence band at about 1 eV below the valence band maximum (VBM), the t_2 level is found in the lower part of the fundamental gap at an energy of about 0.38 E_{gap} (0.18 eV) above the VBM. The Jahn–Teller splitting found for the 127–atom cell resulting in a twofold degenerate e state and a non–degenerate b_2 state amounts to about 1.15 E_{gap} (0.54 eV). The occupied b_2 level is pushed towards the VBM. Explicitely we find that it is even pushed

below the VBM by about 0.23 eV. The unoccupied e level occurs in a midgap position at about 0.66 E_{gap} (0.31 eV) above the VBM. Fig. 1 shows the band structure along the Γ–X line for a 127–atom cell.

Monovacancies in SiC

In the case of cubic SiC we have not only studied neutral but also charged monovacancies. Furthermore, since SiC is a two–component compound we have to distinguish between Si–site and C–site vacancies and we have to discuss the formation energy in dependence on the preparation conditions, i.e., the chemical potentials of the constituents. In addition, the treatment of charged vacancies requires also a discussion of the formation energies in dependence on the position of the Fermi level (p–type or n–type). Fig. 2 shows according phase diagrams for the formation energies of neutral and singly charged Si–site and C–site vacancies. The results

Fig. 2. Formation energies of monovacancies in SiC for different charge states and sites as a function of the Si chemical potential for two positions of the Fermi level in the fundamental gap. Left panel: p–type SiC, right panel: n–type SiC.



shown in Fig. 2 correspond to a calculation with a 63–atom cell. In contrast to Si we do not find such critical convergence problems with the supercell size. This is related to the much larger fundamental gap in SiC, i.e., although the dispersion of the defect bands is also rather large in SiC this causes no unphysical occupations of the wrong states such as bulk conduction bands.

In all cases we find that C–site vacancies are significantly more favourable than Si–site vacancies. Furthermore, we find only a pronounced Jahn–Teller effect for the C–site vacancy leading again to D_{2d} symmetry. For the Si–site vacancy the geometry remains approximately in a T_d configuration. These findings are related to the different overlaps of the dangling bonds at the atoms neighbouring the vacancy. Around a C–site vacancy we have Si atoms, i.e., a similar situation as in Si. But in contrast to Si the Si–Si distance is now even smaller due to the smaller lattice constant of SiC and there is a very strong interaction between the Si dangling bonds. The small Si–Si distance leads already to such a strong overlap that one finds an outward relaxation of the Si atoms whereas in Si one finds an inward relaxation of the atoms neighbouring the vacancy. For the C–dangling bonds around a Si–site vacancy, however, the situation is

dramatically different. Since the SiC lattice constant is much larger than that of diamond the C–C distance is so large that the extremly localized C dangling bonds possess almost no overlap. This suppresses almost completely any Jahn–Teller effect because a significant Jahn–Teller splitting could only be achieved if the C–atoms come rather close together. However, this would require a huge displacement and, hence, cost a huge amount of elastic energy. Furthermore, these findings explain the energetical preference of the C–site vacancy because the strong Si dangling bond overlap implies always some weak Si–Si bonding leading to an energetically more favourable situation than for the isolated non–interacting dangling bonds found around Si–site vacancies.

Interesting results are found when discussing the formation energy as a function of the charge state and the position of the Fermi level in the gap. For p–type SiC there is a very pronounced preference for the positively charged C–site vacancy and even for an undoped or n–type material there is a certain preference for the positively charged vacancy. This has an important consequence: C–site vacancies act like a donor, i.e., like a n–dopant. Hence, in p–doped material we have to expect a strong compensation of the introduced acceptors, i.e., the vacancies release electrons and these electrons are captured by the acceptors. This explains clearly the experimental findings that vacancies in SiC critically limit the doping efficiencies of acceptors[4, 5].

Neutral monovacancy in diamond

In the case of diamond we obtain a formation energy of 6.97 eV for T_d symmetry. We do not find any Jahn–Teller effect, i.e., within our numerical accuracy the atomic geometry relaxes always towards a T_d symmetry. The distortion of the atomic geometry around the vacancy corresponds to an outward breathing relaxation of the C atoms. We suspect that the Jahn–Teller effect is strongly suppressed in diamond because any significant distortion of the atomic geometry would cost too much elastic energy due to the extreme hardness of diamond.

Summary

We presented a *first–principle* study of the energetics, Jahn–Teller effect and electronic structure of monovacancies in Si, SiC and diamond. We have carefully checked the dependence of the results on the numerical details such as supercell size, supercell shape and **k**–point sampling. For the case of Si we find a D_{2d} symmetry to be most favourable. From a simple tight–binding model of interacting vacancies we extracted the "true" defect levels. We find the occupied levels slightly below the VBM and the unoccupied levels in a midgap position. In the case of SiC we always find an energetical preferrence for the C–site vacancy and only the C–site vacancy shows a pronounced Jahn–Teller effect but not the Si–site vacancy. This can be explained in terms of the different overlaps between the dangling bonds at the atoms neighbouring the vacancy. We find that the C–site vacancies in SiC act as a donor. Consequently, this must lead to a significant limitation of the doping efficiency for acceptors what explains according experimental findings. For diamond we find that the atomic geometry remains in a T_d symmetry. This might be related to the competition between the band structure energy gain and the costs in elastic energy.

Acknowledgement

This work was supported by the Deutsche Forschungsgemeinschaft, SFB 196.

References

[1] Watkins, G.D., Troxell, J.R. and Chaterjee, A.P., in *Defects and Radiation Effects in Semiconductors 1987*, IOP Conf. Ser. No. 146, The Institute of Physics, Bristol, p. 16 (1987).

[2] Watkins, G.D. and Troxell, J.R., Phys. Rev. Lett. **44**, 593 (1980); Troxell, J.R. and Watkins, D., Phys. Rev. B **22**, 921 (1980).

[3] Watkins, G.D., in *Deep Centers in Semiconductors*, ed. S. T. Pantelidis, Gordon and Breach, Philadelphia, p. 177 (1992).

[4] Kim, H.J. and Davis, R.F., J. Electrochem. Soc. **133**, 2350 (1986).

[5] Yamanaka, M., Daimon, H., Sakuma, E., Misawa, S. and Yoshida, S., J. Appl. Phys. **61**, 599 (1986).

[6] Vanderbilt, D., Phys. Rev. B **41**, 7892 (1990).

[7] Kresse, G. and Hafner, J., Phys. Rev. B **47**, RC558 (1993).

[8] Kresse, G. and Furthmüller, J., Comput. Mat. Sci. **6**, 15 (1996); Phys. Rev. B **54**, 11169 (1996).

[9] Baldereschi, A., Phys. Rev. B **7**, 5212 (1973).

[10] Chadi, D.J. and Cohen, M.L., Phys. Rev B **8**, 5747 (1973).

[11] Monkhorst, H.J. and Pack, J.D., Phys. Rev. B **13**, 5188 (1976).

[12] Watkins, G.D. and Corbett, J.W., Phys. Rev. **134**, A1359 (1964).

[13] Dannefaer, S., Mascher, P. and Kerr, D., Phys. Rev. Lett. **56**, 2195 (1986).

[14] Blöchl, P.E., Smargiassi, E., Car, R., Laks D.B., Andreoni, W. and Pantelidis, S.T., Phys. Rev. Lett. **70**, 2435 (1993).

[15] Mercer, J.L., Nelson, J.S., Wright, A.F. and Stechel, E.B., J. Phys.: Condensed Matter (submitted).

[16] Virkkunen, R., Alato, M., Puska, M.J. and Nieminen, R.J., Comput. Mat. Sci. **1**, 151 (1993).

Materials Science Forum Vols. 258-263 (1997) pp. 659-664
© 1997 Trans Tech Publications, Switzerland

TRANSIENT LATTICE VIBRATION INDUCED BY SUCCESSIVE CARRIER CAPTURES AT A DEEP-LEVEL DEFECT AND THE EFFECT ON DEFECT REACTIONS

Yuzo SHINOZUKA and Tetsuya KARATSU
Department of Applied Science, Faculty of Engineering,
Yamaguchi University, Tokiwadai 2557, Ube 755, Japan

Keywords: deep-level, multiphonon recombination, lattice relaxation, defect reaction.

Abstract. We study theoretically the dynamics of the transient lattice vibrations induced by successive carrier captures by a deep-level defect. The time evolution of the normal phonon modes $\{q_k(t)\}$ and the interaction mode $Q_1(t)$ are calculated classically. After each carrier capture, $Q(t)$ shows a damping oscillation in a period $\sim 2\pi/\Delta\omega$, where $\Delta\omega$ is the width of the phonon frequency distribution. The carrier captures and the transient lattice vibration are shown to be highly correlated processes (capture enhanced capture), which depend on the carrier densities, n_e and n_h, the capture cross sections, σ_e and σ_h, the activation energies, E_{act}^e and E_{act}^h, and $\Delta\omega$. If several pairs of electrons and holes are captured within a short period $\sim 2\pi/\Delta\omega$, the amplitude of the vibration of $Q_1(t)$ increases remarkably, and then it may overcome the potential barrier for a defect reaction. More than the band gap energy E_g can be used for this phonon kick mechanism.

Introduction.

The nonradiative multiphonon recombination in semiconductors takes place as successive captures of an electron and a hole by a deep-level defect. After an electron (hole) capture, the lattice relaxation takes place and an electronic energy equal to the thermal depth E_{th}^e (E_{th}^h) of an electron (hole) is converted to phonon energies. The whole process of nonradiative multiphonon recombination can be described consistently only by using a proper configuration coordinate diagram with many electron representation [1]. It has been suggested that the transient vibration induced by a carrier capture enhances a following capture of the opposite carrier [1, 2]. These coherent captures are considered as a key mechanism for recombination enhanced defect reactions, which are observed in many semiconductor optical devices [3]. The purpose of the present paper is to study theoretically the dynamics of the transient lattice vibration induced by *successive* carrier captures by a deep-level defect and its effect on the defect reaction.

Vibronic Hamiltonian

Let us first study the lattice vibrations around a deep-level defect in a semiconductor. The normal modes of the lattice are denoted by q_k and their conjugate momentums p_k with an angular frequency ω_k. The suffix k runs over the mode and the wave number for the bulk mode, and over localized modes if any. Without loss of generality we assume that the equilibrium positions of lattice modes are $q_k=0$ when the defect is neutral (D^0) and $q_k=\bar{q}_k$ when the defect is occupied by an electron (D^-). The vibronic Hamiltonian of the system for

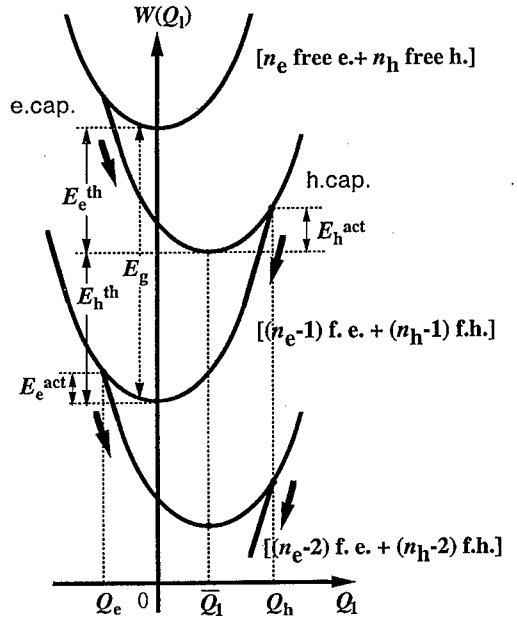


Fig. 1. The configuration coordinate model for a deep-level defect with many carriers.

D^0 with n_e free electrons in the conduction band and n_h free holes in the valence band is written as

$$H_{n_e,n_h} = \frac{1}{2}\sum_k (p_k^2 + \omega_k^2 q_k^2) + n_e E_g. \tag{1}$$

The origin of the total energy is measured from that for D^0 with $n_h - n_e$ free holes (no electron), and E_g is the band gap energy. After an electron has captured, the vibronic Hamiltonian for D^- is written as

$$H_{n_e-1,n_h} = \frac{1}{2}\sum_k [p_k^2 + \omega_k^2 (q_k - \bar{q}_k)^2] + n_e E_g - E_{th}^e. \tag{2}$$

Here, E_{th}^e presents the thermal depth of a bound electron. The quantity $E_{th}^h = E_g - E_{th}^e$ presents the thermal depth of a bound hole as if a hole is bound in D^0.

The bulk modes of lattice vibrations in solids are usually classified into the acoustic mode (ac) and the optical mode (op). If we assume the deformation potential type electron-lattice interaction for the acoustic mode and the Fröhrich type interaction for the optical mode, the lattice shift $\bar{q}_k$ is given by

$$\bar{q}_k^{ac} = \frac{E_d}{u^2 k}\left(\frac{2}{NM}\right)^{\frac{1}{2}} \exp\left(-\frac{a^2k^2}{8\pi}\right) \quad \text{for ac,} \tag{3}$$

$$\bar{q}_k^{op} = \frac{1}{k}\left(\frac{8\pi e^2}{V\varepsilon\omega_{op}^2}\right)^{\frac{1}{2}} \exp\left(-\frac{a^2k^2}{8\pi}\right) \quad \text{for op.} \tag{4}$$

for a localized electron whose wave function is a gaussian $\exp(-\pi r^2/a^2)$ with a radius a.

Let us introduce an orthogonal transformation from $\{\omega_k q_k\}$ to $\{Q_l\}$, in which the interaction mode Q_1 is taken as

$$Q_1 = \frac{1}{\overline{Q}_1}\sum_k \omega_k^2 \overline{q}_k q_k . \tag{5}$$

Then the corresponding adiabatic potentials for H_{n_e,n_h} and H_{n_e-1,n_h} are respectively given by

$$W_{n_e,n_h}(Q_l) = \frac{1}{2}\sum_k Q_l^2 + n_e E_g, \tag{6}$$

$$W_{n_e-1,n_h}(Q_l) = \frac{1}{2}\sum_k Q_l^2 - \overline{Q}_1 Q_1 + n_e E_g - E_{th}^e + E_{LR}. \tag{7}$$

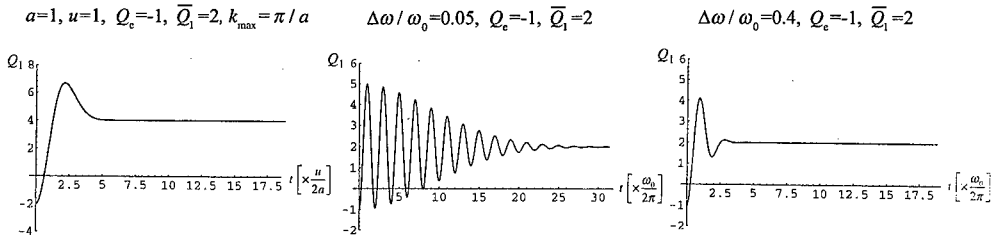
Here $E_{LR} = \frac{1}{2}\sum_k \omega_k^2 \overline{q}_k^2 = \frac{1}{2}\overline{Q}_1^2$ is the lattice relaxation energy. Thus the effect of the electron-lattice interaction has put into the interaction mode Q_1 only.

Transient lattice vibrations

In this section we study the transient lattice vibration classically which is induced by a single capture by a defect D^0. Before the capture the lattice q_k vibrates around each equilibrium q_k=0 and is sometimes activated to distort $Q_1 = Q_e$, at which a nonradiative electron capture can takes place. If we assume the minimum activation energy for each mode q_k so as to reach $Q_1 = Q_e$ [2], the time dependence of the interaction mode after the capture, which has occurred at t=0, is given by,

$$Q_1(t) = \frac{1}{\overline{Q}_1}\sum_k \omega_k^2 \overline{q}_k^2 \left[1 - \left(\frac{Q_e}{\overline{Q}_1} + 1\right)\cos\omega_k t\right]. \tag{8}$$

It should be noted here that all the normal modes $q_k(t)$ vibrate *harmonically*: no damping and no energy dissipation. Since the interaction mode Q_1 is a linear combination of many normal modes q_k with different frequencies ω_k, $Q_1(t)$ shows a damping oscillation. Figure 2 (a) shows a typical example of $Q_1(t)$ for the interaction with the acoustic modes. It is damped very quickly because the acoustic modes have a very wide ω_k distribution ($0 \sim uk_{max} = \pi u/d$). For the interaction with the optical mode, on the other hand, $Q_1(t)$ vibrates harmonically with ω_{op} and show no damping. Figure 2 (b) shows results on a model where $\overline{q}_k$=constant and the frequency distribution is a gaussian centered at ω_0 with a width $\Delta\omega$. It shows a damping oscillation which lasts in a period $\tau \sim 2\pi/\Delta\omega$. As can be seen in Fig. 2 (b) it represents both limits, ac and op. If $\Delta\omega$ is rather small, the transient lattice vibration lasts rather long and it



(a) acoustic phonon. (b) gauss distribution of ω_k.

Fig. 2 Transient vibration of the interaction mode $Q_1(t)$ after a carrier capture.

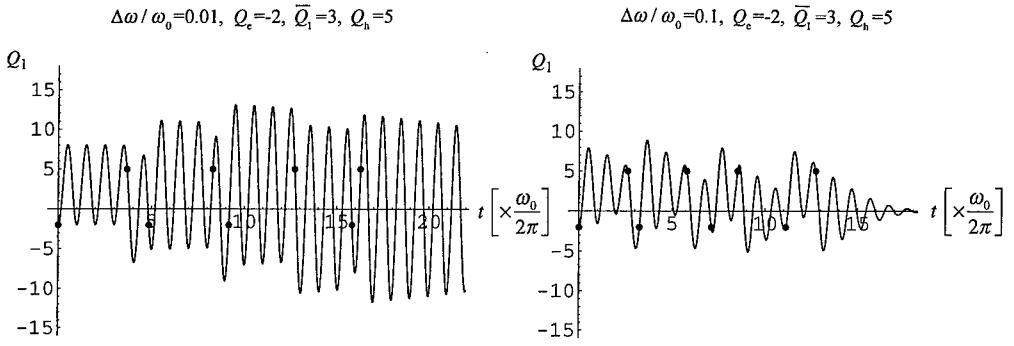


Fig. 3 Time evolution of $Q_l(t)$ during a series of captures.

then can enhance a following capture of the opposite carrier. In the next section we simulate the dynamics of the transient vibration and a series of captures, using the gauss distribution model.

Coherent recombination and transient lattice vibration

If the host semiconductor is a p-type, the defect is stationary occupied by a majority hole (D^0). A capture of a minority electron occurs by a thermally activated process ($Q_l \rightarrow Q_e$, with the activation energy E_{act}^e; the capture cross section is $\sigma^e = \sigma_\infty^e \exp(-E_{act}^e / k_B T)$), which is followed by a transient lattice vibration of Q_l around $\overline{Q}_l$. If a hole is captured during the transient lattice vibration, the activation energy E_{act}^h is not necessary ($\sigma^h = \sigma_\infty^h$, cf. Dexter-Krick-Russel mechanism for the F-center in alkalihalides [4]). Once a hole is captured, it again induces a transient lattice vibration around Q_l=0, which activates the second electron capture, and so on.

Let us simulate the dynamics of the transient vibration and a series of captures. We use following assumptions:

1) Each normal mode q_k vibrates around either q_k=0 or $q_k = \overline{q}_k$ depending on the charge of the defect (D^0 or D^-).
2) The time dependence of $Q_l(t)$ is determined by $\{q_k(t)\}$ through the equation (5).
3) The first electron capture takes place by a thermal activation $Q_l \rightarrow Q_e$.
3) If the motion of the interaction mode, $Q_l(t)$, crosses the point Q_e (Q_h) of the adiabatic potentials, there arise a large probability P_e (P_h) per time to capture an electron (hole) nonradiatively.
4) If the motion $Q_l(t)$ has been damped out before a carrier capture takes place, the coherence in successive captures is quitted. The next capture is again thermally activated process.

Figure 3 shows typical examples of the simulation for the time evolution of $Q_l(t)$ with parameters $P_e/\omega_0 \sim P_h/\omega_0 \sim 0.05$. Small black circles indicate a time when a carrier capture takes place. If the conditions, $P_e\tau > 1$ and $P_h\tau > 1$, are satisfied, coherent captures can take

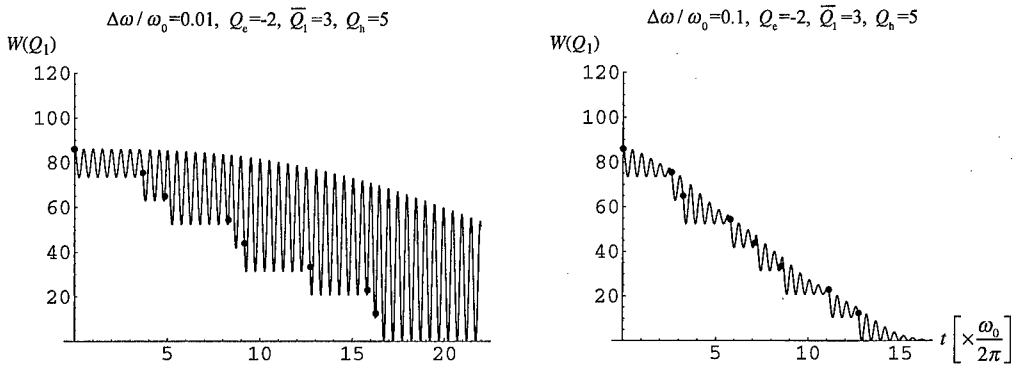


Fig. 4 Time evolution of the adiabatic potential $W(Q_l)$ during a series of captures.

place. Figure 4 shows the time evolution of the adiabatic potential $W(Q_l)$. It is readily seen that if $P_e\tau<1$ the vibronic energy, i.e. the kinetic energy of the vibration of Q_l, is dissipated constantly. On the other hand, if $P_e\tau>1$ the energy dissipation is weak and the vibronic energy of Q_l increases, which enhances following carrier capture processes.

Summary and discussion

We have studied the transient lattice vibration induced by a successive carrier captures and the effect on following captures. After each capture, $Q_l(t)$ shows a damping oscillation around $Q_l= 0$ or $\overline{Q_l}$ in a period $\sim 2\pi/\Delta\omega$, where $\Delta\omega$ is the width of the phonon frequency distribution. The carrier captures and the transient lattice vibration are highly correlated processes (capture enhanced capture), which depend on the carrier densities n_e and n_h, the capture cross sections σ_e and σ_h, the activation energies E_{act}^{e} and E_{act}^{h}, and the frequency distribution $\Delta\omega$ of phonons.

Let us discuss the athermal capture process. We have assumed that an electron (hole) can be athermally captured just when $Q_l(t)$ crosses Q_e (Q_h), the intersection of two adiabatic potentials. The capture rate P_i is related as $P_i= n_i\, v_T^i\, \sigma_\infty^i$, where n is the carrier density, v_T the thermal velocity and σ the capture cross section, which has a form $\sigma = \sigma_\infty \exp(-E_{act}/k_BT)$ for the nonradiative multiphonon process. If the transient vibration enables $Q_l(t)$ to cross Q_e (Q_h), the capture rate is given by $P_e= n_e\, v_T^e\, \sigma_\infty^e$. In the *adiabatic* limit it is theoretically shown that $P_e\sim\omega_0/2\pi$ [2]. Then the condition for the coherent captures turns out to be $P_e\tau\sim P_h\tau\sim\omega_0/\Delta\omega>1$. The details depend on the parameters: Q_e, Q_h, $\overline{Q_l}$, ...

If several pairs of electrons and holes are captured within a short period $\sim 2\pi/\Delta\omega$, the amplitude of the interaction mode $Q_l(t)$ increases remarkably, and it may overcome the potential barrier for a defect reaction [3]. More than the band gap energy $E_g=E_{th}^{e}+E_{th}^{h}$ can be used for this phonon kick mechanism.

When we apply the present results to recombination enhanced defect reactions [3, 5-8], we should mind that there are many situations depending on the variety of charged states of a defect, the magnitude of E_{th}^{e} and E_{th}^{h}, the relation between the relaxation mode Q_l and the

reaction coordinate Q_R, the magnitude of capture cross sections, and so on. If the relaxation mode Q_l is a symmetric mode such as a breathing mode, Q_l is then orthogonal to Q_R which is a symmetry breaking mode by definition. Then the symmetrical relaxation process does not affect defect reactions.

If the symmetry breaking relaxation takes place by the charge change of a defect, the point is which corresponds to the asymmetrical configuration, Q_l=0 or $\overline{Q}_l$? If the reaction coordinate Q_R is almost parallel to Q_l, a defect reaction occurs by the structural instability mechanism induced by a minority electron capture [8]. If E_{th}^{e} is large and $Q_l // Q_R$ but there is a potential barrier, the phonon kick mechanism takes place with the aid of E_{th}^{e} induced by an electron capture. If E_{th}^{h} is large and $Q_l // -Q_R$, the phonon kick mechanism takes place by a hole capture which has been enhanced by an electron capture. If a majority carrier capture occurs very quickly within the local transient vibration, the band gap energy $E_g=E_{th}^{e}+E_{th}^{h}$ can be used for exciting a defect reaction. This could be the most effective path to the defect reaction and nothing but so called the recombination enhanced mechanism.

In an n-type semiconductors, defect reactions can be discussed in a similar way as above, starting from $Q_l=\overline{Q}$ and D^0+e+h. In contrast to a p-type, the first capture of a minority hole by a neutral center D_i^0 is not accelerated by the Coulomb attraction while the second electron capture by D_i^+ is accelerated.

We have assumed that the initial defect has D^0 and D^+ charged states. If it has D^- and D^0, the above discussion can be also valid with respective replacements $D^0 \rightarrow D^-$ and $D^+ \rightarrow D^0$. As we have shown, either in n-type and p-type, the capture of a majority carrier always enhanced by a minority carrier capture, and *vice versa*. But only a hole capture is accelerated by the Coulomb attraction of D^-.

Acknowledgments

The present work is supported by the Proposal-Based Advanced Industrial Technology R&D Program of NEDO Japan and by Grand-in-Aid by the Japanese Ministry of Education, Science and Culture.

References.

[1] Y. Shinozuka: J. Phys. Soc. Jpn. **51** (1982) 2852 ; Jpn. J. Appl. Phys. **32** (1993) 4560 .

[2] H. Sumi: Phys. Rev. B**29** (1985) 4616, J. Phys. C**17** (1984) 6071.

[3] O. Ueda, "*Reliability and degradation of III-V optical devices*" (Artech House Publishers, Boston-London, 1996).

[4] D. L. Dexter, C. C. Klick, and G. A. Russel, Phys. Rev. **100** (1956) 603.

[5] M. K. Sheinkman, JETP Lett. **38** (1983) 330, and M. K. Sheinkman and L. C. Kimerling, "*Defect Control in Semiconductors*", ed. K. Sumino (North-Holland, 1990) p. 97.

[6] J. D. Weeks, J. C. Tully, and L. C. Kimerling, Phys. Rev. B**12**, 3286 (1975).

[7] Y. Shinozuka, Proc. 19th Taniguchi Symposium, "*Relaxations of Excited States and Photo-Induced Structural Phase Transitions*" (Springer, 1997) ed. by K. Nasu, p. 229.

[8] Y. Shinozuka, Proc. MRS 1996 Fall Meeting **442**, "*Defects in Electronic Materials* II", ed. J. Michel, T. Kennedy, K. Wada and K. Thonke, p. 225.

Materials Science Forum Vols. 258-263 (1997) pp. 665-670
© 1997 Trans Tech Publications, Switzerland

CHARACTERISATION OF RECOMBINATION CENTRES IN SOLAR CELLS BY DLTS

Tomas Markvart
Department of Engineering Materials
University of Southampton
Southampton SO16 1BJ, U.K.

Key words: DLTS, recombination centres, solar cells

Abstract. This paper reports a further development of the Recombination DLTS technique which, by combining the majority and minority carrier injection, allows deep levels to be filled by both types of carriers in a controlled manner and thus provides a convenient technique for the detection and characterisation of recombination centres. Using a theoretical description of this technique to determine the minority carrier capture cross sections of majority carrier traps observed by DLTS, this paper presents a detailed account of how the obtained defect parameters can be used to describe the effect of defects on solar cell performance. It is shown that an excellent agreement is obtained with the observed solar cell data.

1. Introduction

Characterisation of recombination centres plays an important part in the manufacture and operation of semiconductor solar cells. Although much progress has been made in the understanding of defects in semiconductors in general, the understanding of defect responsible for electron-hole recombination is less complete. This paper reports on a further development of Recombination DLTS (RDLTS) which has made it possible to observe and characterise a deep level associated with recombination activity [1,2].

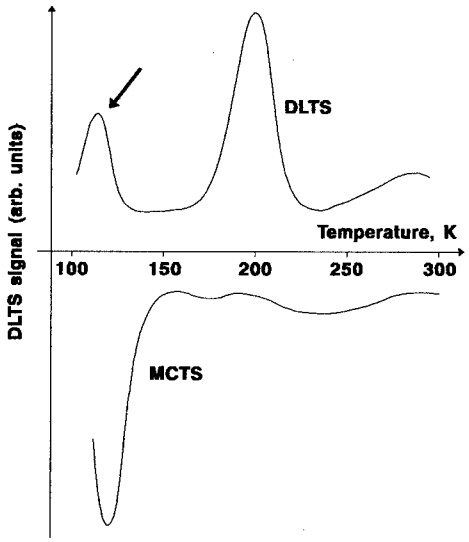


Figure 1 Typical DLTS and MCTS spectra of electron-irradiated p-type CZ silicon

This technique relies on the simultaneous injection of electrons and holes in a controlled manner - majority carriers by an electrical pulse, minority carriers by illumination. The principles of RDLTS are summarized in Figs. 1 and 2. Figure 1 shows typical DLTS and MCTS spectra of electron-irradiated p-type Czochralski silicon where the electrical and optical pulse are applied in separation. Focusing on the divacancy peak (shown by arrow in Fig. 1), Fig. 2 shows the effect of minority carrier injection on the amplitude of this peak: as the illumination intensity increases, the amplitude is reduced, indicating filling of the deep level by electrons. This demonstrates that both electrons and holes are captured by the defect as one would expect for

a recombination centre. It is significant that other peaks in the DLTS spectrum are not affected by similar illumination.

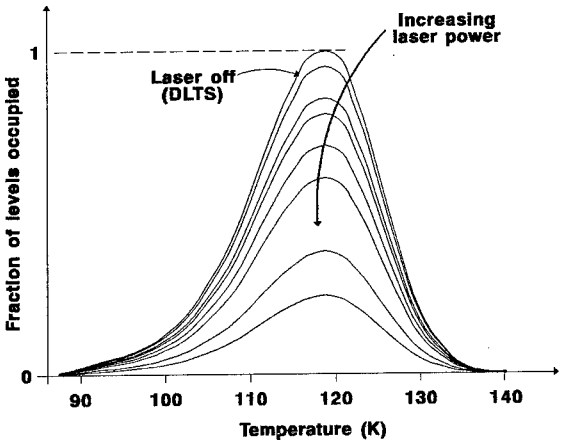


Figure 2 Effect of superimposing laser light on the DLTS peak of the divacancy

These results, as well as the analysis in this work refer to samples fabricated from crystalline silicon solar cells (Fig. 3) irradiated to 1E15 e/cm^2 by 1 MeV electrons. Since the top diffused n^+ layer is highly doped, the DLTS monitors defects in the p-type base. The shallow junction depth (fraction of a micron) ensures that almost all of the electron-hole pairs are generated also in the base, i.e. within the same part of the device as observed by the DLTS. Further details of the samples and experimental procedure can be found in [1,2].

This paper gives a further analysis of the RDLTS results by combining two theoretical developments. Firstly, results of RDLTS theory are presented (Sec. 2) which makes it possible to obtain an accurate value of the minority-carrier (i.e., electron) capture cross section of the divacancy, alongside the hole capture cross section available from conventional DLTS. Secondly, using a detailed model of the solar cell (Sec. 3), this capture cross section is used in Sec. 4 to determine the effect of this defect on solar cell performance.

2. Analysis of RDLTS data

To analyse the RDLTS spectra, the fraction of traps occupied can be plotted as a function of the photogenerated current density injected into the samples by the laser beam which was measured in a separate experiment (Fig. 3). Since most of the electron-hole pairs are generated in the base of cell which also contributes to the DLTS signal, the photogenerated current is an accurate measure of the minority carrier density in this region, and this allows an accurate determination of the minority-carrier (electron) capture cross section [3]. Using the known value of the hole capture cross section

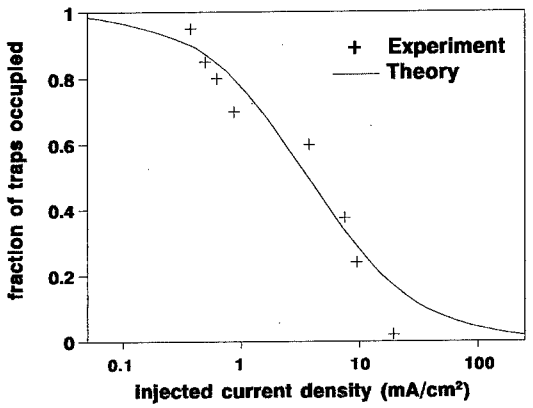


Figure 3 The deep-level occupation as a function of the photogenerated current injected by laser illumination

[4], the following results are obtained:

$$\sigma_p = 3\times10^{-16}\ cm^2$$
$$\sigma_n = 8\times10^{-12}\ cm^2 \qquad (1)$$

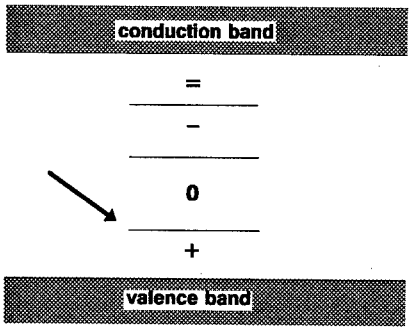


Figure 4 The energy levels of the divacancy and the associated charge states

The electron capture cross section (1) agrees with a previous result [2] which was obtained by a less rigorous analysis. The difference in magnitudes of the two capture cross sections is striking but not unusual. It can be understood from a more detailed picture (known from a wealth of other experimental evidence) of the charge states of the divacancy (Fig. 4). The lowest level (shown by arrow) is the one observed in this experiment. It is seen that when this level is about to capture a hole, the defect is neutral but before it captures an electron, the defect is positively charged. Hence the much larger observed capture cross section for electrons than holes, with sizes that are in keeping with other charged or neutral defects.

3. Brief solar cell theory [5]

A conventional solar cells represents a planar diode structure (Fig. 4). Incident light generates current carriers which move towards the junction where they are separated and produce useful power output. The I-V characteristic of an ideal solar cell is described by the equation

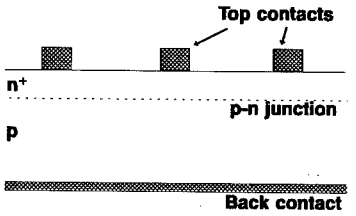


Figure 5 Cross section of solar cells under study

$$I = I_o\left\{\exp\left(\frac{qV}{kT}\right) - 1\right\} - I_l \qquad (2)$$

which differs from the diode equation only by the presence of the light-generated current I_l. In Eq. (2), e (>0) is the electron charge, k is the Boltzmann constant, T is the absolute temperature, and I_o is the dark saturation current.

The power output of the solar cell can be described by two principal parameters, the open-circuit voltage V_{oc} and the short-circuit current I_{sc} which are given by:

$$I_{sc} = -I_l$$
$$V_{oc} = \frac{kT}{q}\log\left(1 + \frac{I_l}{I_o}\right) \qquad (3)$$

The light-generated current I_l is determined principally by the minority-carrier transport, and depends crucially on the minority-carrier lifetime τ. In terms of the diffusion length $L = \sqrt{D\tau}$, where D is the minority-carrier diffusion constant one can broadly say that only carriers which are generated within the distance L of the junction are collected; the rest is lost by recombination. It is the lifetime τ (or, equivalently, the diffusion length L) which is the principal quantity of concern when the cell is subjected to the particle radiation in space.

The dark saturation current which enters the expression for the open-circuit voltage can be estimated by the expression

$$I_o \alpha \frac{1}{N_d \sqrt{\tau}} \tag{4}$$

where the dopant concentration N_d and lifetime τ refer to the lightly doped side of the junction.

This argument implies that the short-circuit current will degrade most under irradiation, and degradation of the open-circuit voltage will be less pronounced. This follows from the logarithmic dependence (4), and is observed for the majority of solar cells.

The behaviour of L upon irradiation can be described by the equation

$$\frac{1}{L^2} = \frac{1}{L_o^2} + K\phi \tag{5}$$

where L_o is the diffusion length in the unirradiated cell, ϕ is the particle fluence (integrated flux), and K is a (dimensionless) damage constant characteristic for the material and the type of irradiation. In terms of the microscopic constants, K is given by

$$K = \frac{\sigma v_{th} r}{D} \tag{6}$$

where v_{th} is the thermal velocity of minority carriers, and σ and r are the minority-carrier capture cross section and defect introduction rate, respectively. The damage constant K generally depends on the type of dopant, and a different damage constant should therefore be introduced for each region of the cell.

The reduction of the diffusion length describes usually the most significant part of the damage, but changes in other parameters on irradiation sometimes also need to be considered. The dark current I_o in Eq. (4) may increase as a result of compensation by the radiation-induced defects. This, however, occurs usually at particle fluences orders of magnitude higher than that which degrades τ or L. Another source of degradation are defects created in the depletion region which increase the so-called recombination current which was not included in (1). Similarly, an increase of the defect concentration at the interfaces between different regions of the cell, as well as at the external surfaces, may reduce the solar-cell output in certain circumstances.

4. Effect of divacancy on the solar cell operation

Using the theory outline in the previous section, the capture cross section determined in Sec. 2 can now be used to determine the effect of the electron irradiation on the solar cell performance. It is known [5] that the spectral response of the solar cell (i.e., the short circuit current under monochromatic illumination as a function of wavelength) is a sensitive indicator of the minority-carrier lifetime in the base of the cell which can be used for independent verification of the DLTS data.

Using the capture cross-sections (1), one obtains the following value of the damage constant in the base of the solar cell:

$$K = 3.7\times10^{-11} \qquad (7)$$

When this value of the damage constant is fed into the solar-cell model, the resulting spectral response is shown in Fig. 6. In this plot, the theoretical fit to the measured data for an unirradiated cell was used to obtain the diffusion length L_o. The degradation of the diffusion length was then calculated using Eq. (5) which was, in turn, the used to calculate the spectral response of the irradiated cell. It is seen that the agreement with the measured data is excellent.

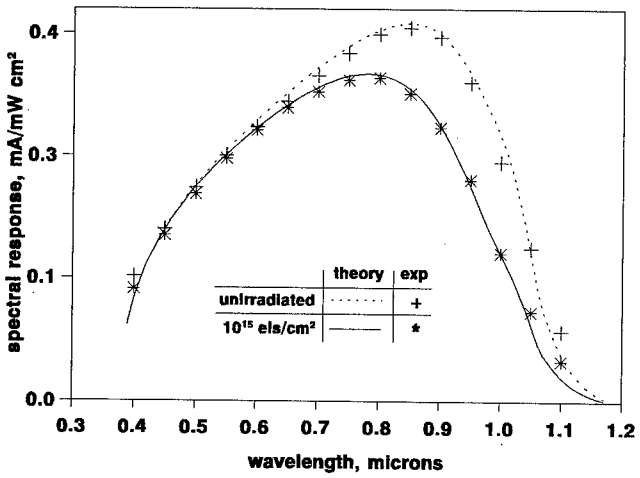


Figure 6 Comparison of the experimental and calculated spectral response for a solar cell before and after irradiation.

Using the equations of Sec. 3, other solar cell parameters can also be obtained, with a similarly good agreement with experimental data.

5. Conclusion

It was shown by using the Recombination DLTS data for the divacancy in silicon in a solar cell model that a very good agreement is obtained with the measured spectral response of the solar-cell. This result give perhaps the strongest evidence to-date for the divacancy as the dominant recombination centre in electron irradiated p-type silicon. It also shows, on the example of the solar cell, that Recombination DLTS can provide accurate quantitative data which can be used to predict the performance of semiconductor devices.

Acknowledgement

The author is grateful to the Royal Academy of Engineering and the Engineering and Physical Sciences Research Council for support through a Clean Technology Fellowship.

References

1. T. Markvart, D.P. Parton, J.W. Peters and A.F.W. Willoughby, DLTS of recombination centres in semiconductors, Materials Science Forum **143-147**, 143 (1994).
2. D.P. Parton and T. Markvart, Recombination centres in solar cells: DLTS study, Proc. 12th European Solar Energy Conf. (1994), p. 520.
3. T. Markvart, to be published
4. See, for example, P.M. Mooney, J.L. Cheng, M. Suli, J.D. Gerson and J.W. Corbett, Defect energy levels in boron-doped silicon irradiated with 1-MeV electrons, Phys. Rev. **B15** 3836 (1977).
5. T. Markvart, Radiation damage in solar cells: a review, Journal of Materials Science: Materials in Electronics **1** 1 (1990)

Materials Science Forum Vols. 258-263 (1997) pp. 671-676
© 1997 Trans Tech Publications, Switzerland

DEFECT-ENGINEERING RAD-HARD DETECTORS FOR THE CERN LHC

B. MacEvoy[1], K. Gill[2] and G. Hall[1]
[1]Blackett Laboratory, Imperial College, London SW7 2BZ, UK
[2]PPE Division, CERN, CH-1211 Geneva 23, Switzerland

Keywords: silicon, radiation, particle detectors, defect-engineering, divacancies

Abstract. Silicon particle detectors will be used extensively in experiments at the CERN Large Hadron Collider, where high radiation levels will cause significant atomic displacement damage. After irradiation, such detectors exhibit changes in the effective doping concentration of the substrate material which represent the limiting factor to long-term operation in a particle physics environment. A model has been developed to estimate the evolution of defect concentrations and to predict the electrical behaviour of irradiated devices using Shockley-Read-Hall semiconductor statistics. Discrepancies between the model calculations and experimental data, and other observed phenomena, suggest that a non-SRH mechanism may be responsible for a large fraction of the measured changes in detector properties. The proposed mechanism is the direct transfer of charge between the clustered divacancy (V_2) defects formed by hadronic irradiation. This leads to a large enhancement in both V_2 acceptor state occupancy and carrier generation rate. The consequences of this mechanism for the prospects of defect-engineering rad-hard devices are discussed.

1. Introduction

It is planned to use silicon detectors for many applications at the CERN Large Hadron Collider (LHC), which will commence operation around the year 2005. This accelerator will collide counter-circulating beams of protons at a centre-of-mass energy of 14 TeV and a rate of 40 MHz. The high interaction rate is essential to accumulate sufficient numbers of the rare events from which new physics discoveries are expected, but means that inner detector layers will be exposed to unprecedented fluences of penetrating charged particles. In the course of their operational lifetime, it is anticipated that microstrip layers will receive an ionising dose of ~10 Mrad coupled with a hadron fluence equivalent to ~10^{14} cm^{-2} 1 MeV neutrons [1].

The detectors used in particle physics are basically diodes, consisting of p-type strips ion-implanted on a high resistivity (~5 kΩ.cm) n-type float-zone substrate [2]. This choice of material allows full depletion at moderate bias voltages (< 200 V) and minimises the leakage current. About 150 m^2 of silicon detectors will be used in the LHC experiments - or ~100,000 four-inch wafers. This is a large amount of silicon for the high energy physics community, but only a small fraction of the silicon produced by wafer manufacturers for the semiconductor industry world-wide. Consequently, radiation effects in float-zone particle detectors have been somewhat neglected and it is only recently that significant progress has been made in understanding their microscopic origins.

2. Radiation effects in detectors

The principal obstacle to long-term operation at the LHC arises from bulk damage due to atomic displacements in the substrate material. The main effects are briefly summarised below.

2.1. Leakage current changes

Detector leakage currents increase significantly during irradiation. The current is described in terms of J_v, which is the leakage current per unit volume. It is well established that the increase in J_v is directly proportional to particle fluence:

$$\Delta J_v = \alpha \Phi \tag{1}$$

The proportionality constant, α, is known as the "damage constant" and has the value (5-10)×10^{-17} A.cm^{-1} for high energy hadrons [3]. The current is sensitive to temperature and can be reduced considerably by modest cooling. The dependence is usually parameterised as:

$$J_v \propto T^2 e^{-E_a/kT} \tag{2}$$

with E_a = (0.62±0.03) eV [4].

2.2. Effective doping changes

In an unirradiated device, the space-charge results from shallow dopants in the silicon, usually phosphorus and boron. Photoluminescence studies indicate that the level of compensation by boron contamination is typically very low. It is found that n-type detectors become progressively less n-type with increasing hadron fluence until they invert to effectively p-type at around 2×10^{13} n.cm^{-2} and then continue to become more p-type beyond this point, apparently without limit. Typical results are shown in Fig. 1 [3]. In practice, detectors still work beyond the inversion fluence because the junction moves from the p^+ strips to the n^+ back-plane contact.

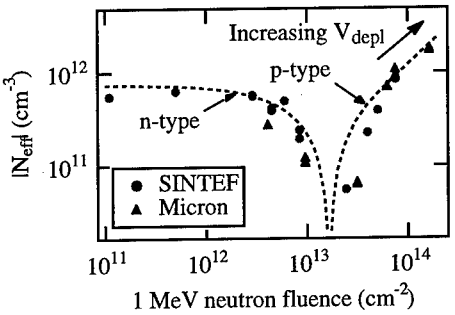


Fig. 1. Evolution of N_{eff} with neutron fluence for n-type detectors from two manufacturers [3].

The effective doping concentration, N_{eff}, can be inferred from the voltage required to obtain full depletion, V_{depl}:

$$N_{eff} = \frac{2\varepsilon_0\varepsilon_{Si}}{ed^2} V_{depl} \tag{3}$$

where d is the diode thickness. After high particle fluences, N_{eff} can be such that the depletion voltage exceeds the breakdown voltage of the device and efficient operation is no longer possible. This effect represents the limiting factor for long-term operation at future experiments.

3. Defect kinetics model

A detailed understanding of radiation effects can be achieved by numerical calculations of the evolution of complex defects formed during irradiation. A 1 MeV neutron can transfer up to 130 keV to the primary knock-on atom (PKA). An atom with this energy can produce a cascade of many interactions, some of which produce energetic secondary recoils. Simulations have shown that a tree-like displacement cascade is usually created with two or three "terminal clusters" of linear dimensions ~50 Å [5]. These clusters contain a high density of self-interstitial (I) and vacancy (V) Frenkel pairs. At the centre of the cluster, I-V recombination is initially the dominant process and most (> 90%) of the Frenkel defects are annihilated in a very short time. Some vacancies combine to form divacancies (V_2), and possibly larger multi-vacancy complexes. Those interstitials and vacancies which escape recombination diffuse away from the damaged region until they reach a surface or are trapped at other defects and impurities, particularly oxygen and carbon.

These trapping events may be thought of in terms of quasi-chemical "reactions". Reaction rates are controlled by the concentrations of trapping sites and their relative capture radii. Davies et al. have explained the optical absorption spectra of electron-irradiated silicon by using a small number of reactions [6]. A kinetics model, based on this work but suitably modified, has been used to predict the evolution of defects during the irradiation of detector material. The reactions used in the model are shown in Table 1 [4,7]. The reactions in list A only have a significant chance of occurring during a PKA cascade, whereas the diffusion reactions in list B take place away from the cluster region.

This modelling approach can be applied equally well to the case of gamma irradiation, for example with ^{60}Co photons. Here, the bulk damage arises primarily as a result of the interaction between Compton electrons and the host atoms. The scattered electrons typically have energies of only a few hundred keV [8], which is insufficient to displace more than one or two silicon atoms from their

lattice sites. Consequently, there are no terminal clusters and the damage profile consists of point defects distributed uniformly throughout the crystal bulk.

List A - primary reactions (in the PKA cluster)

I reactions	V reactions	C_i reactions
$I + V \rightarrow Si$	$V + V \rightarrow V_2$	.....

List B - diffusion reactions (outside the cluster)

I reactions	V reactions	C_i reactions
$I + C_s \rightarrow C_i$	$V + V \rightarrow V_2$	$C_i + C_s \rightarrow CC$
$I + CC \rightarrow CCI$	$V + V_2 \rightarrow V_3$	$C_i + O \rightarrow CO$
$I + CCI \rightarrow CCII$	$V + O \rightarrow VO$	
$I + CO \rightarrow COI$	$V + VO \rightarrow V_2O$	
$I + COI \rightarrow COII$	$V + P \rightarrow VP$	
$I + VO \rightarrow O$		
$I + V_2 \rightarrow V$		
$I + VP \rightarrow P$		

Table 1. Kinetics model reaction scheme [4,7].

In order to make quantitative calculations, the oxygen, carbon and phosphorus concentrations ([O], $[C_s]$ and [P]) and introduction rates, η, of I, V and V_2 are required. It is well established that [O] and $[C_s]$ in detector material are typically a few$\times 10^{15}$ cm^{-3}. The exact value of [P] depends upon the resistivity of the material and is normally ~10^{12} cm^{-3}. Introduction rates of I, V and V_2 have been calculated from DLTS measurements. Although there is some controversy between the various groups working in this field, reasonable estimates are $\eta_I = 1.26\times10^{-3}$ cm^{-1}, $\eta_V = 1.2\times10^{-3}$ cm^{-1}, $\eta_{V2} = 2.8\times10^{-5}$ cm^{-1} for ^{60}Co photons and $\eta_I = 11.5$ cm^{-1}, $\eta_V = 2.1$ cm^{-1}, $\eta_{V2} = 4.7$ cm^{-1} for 1 MeV neutrons [9,10]. Figure 2 shows how various defect species are predicted to evolve as a function of ^{60}Co gamma dose and 1 MeV neutron fluence. Uncertainties in the predicted concentrations are at the level of ~40% and arise mainly from errors in the introduction rates and ratios of capture radii.

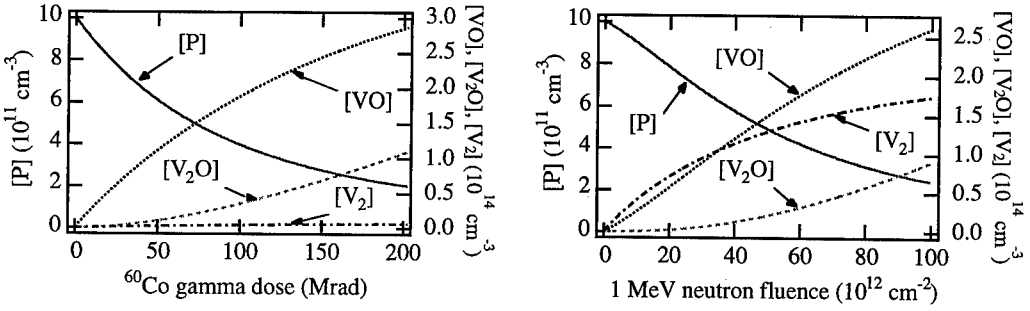


Fig. 2. Model predictions for evolution of various defect concentrations with ^{60}Co gamma dose and 1 MeV neutron fluence.

4. Modelling data from gamma-irradiated devices

Using the defect concentrations from the kinetics model, it is reasonably straightforward to predict the experimental observables, N_{eff} and ΔJ_v, from first principles on the basis of Shockley-Read-Hall (SRH) theory [10]. By solving the Poisson and current continuity equations in conjunction with SRH statistics, the occupancy of each trap can be derived. The effective doping concentration may then be calculated from:

$$N_{eff} = \sum_D (1 - f_D)[D] - \sum_A f_A[A] + p - n \qquad (4)$$

by summing over the donors D and acceptors A. Note that N_{eff} is defined here as being positive for n-type material. Similarly, the increase in leakage current may be calculated by summing the generation rates, G, at each defect:

$$\Delta J_v = e \sum_{A,D} G \tag{5}$$

The states included in the calculation of N_{eff} and ΔJ_v are listed in Table 2 [10]. It is assumed that the capture cross-sections of each defect for electrons and holes, σ_n and σ_p, are equal.

Defect identity	Energy (eV)	Type	Charge states
VO	E_c-0.17	Acceptor	(0/-)
V_2O	E_c-0.50	Acceptor	(0/-)
V_2	E_v+0.20	Donor	(+/0)
	E_c-0.41	(First) Acceptor	(0/-)
	E_c-0.23	(Second) Acceptor	(-/=)
VP	E_c-0.45	Acceptor	(0/-)
CO	E_v+0.36	Donor	(+/0)
CC	E_c-0.17	Acceptor	(0/-)

Table 2. Defect states considered in the modelling procedure [10].

The predictions of the model are compared with experimental data from gamma-irradiated devices in Fig. 3. According to the model, the changes in N_{eff} are dominated by the creation of V_2O defects and the removal of the phosphorus dopant via the process V + P → VP. E_{V2O} is not precisely known (E_c-0.50±0.05 eV [11]) and, within the uncertainty interval, the model results vary significantly. Excellent agreement with the data was obtained for E_{V2O} = E_c-0.515 eV. Due to the proximity of the defect to mid-gap, the concentration of V_2O also determines the magnitude of the leakage current; again, the agreement with the experimental data is remarkably good.

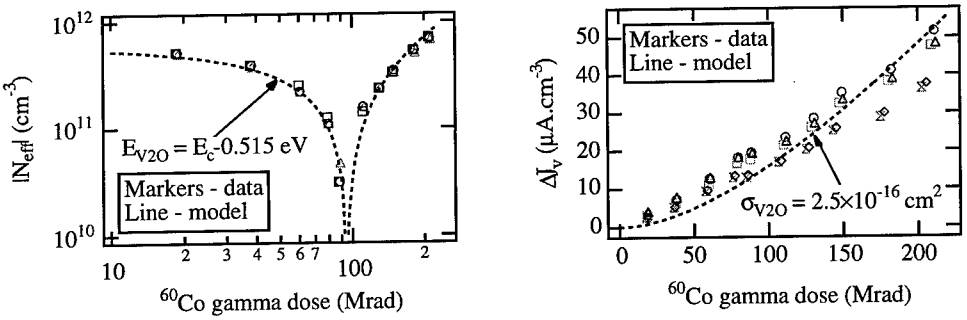


Fig. 3. Comparison between model predictions and experimental data for N_{eff} and ΔJ_v as a function of ^{60}Co gamma dose.

5. Modelling data from neutron-irradiated devices - V_2 charge exchange

Similar calculations have been used to predict the evolution of doping concentration and leakage current for neutron irradiation. The results are shown in Fig. 4.

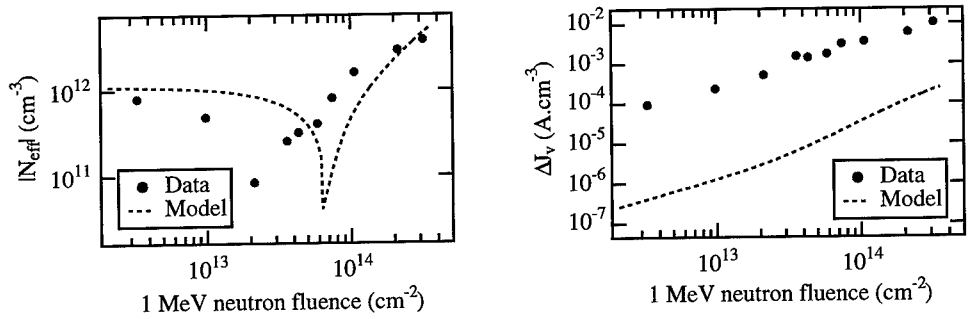


Fig. 4. Comparison between model predictions and experimental data for N_{eff} and ΔJ_v as a function of 1 MeV neutron fluence.

Values of E_{V2O} = E_c-0.515 eV and σ_{V2O} = 2.5×10^{-16} cm^2 were used since these had given excellent agreement with the gamma data. The dominant contribution to N_{eff} is again made by the V_2O complex, although the agreement with the data is poor. More seriously, the leakage current is consistently underestimated by around two orders of magnitude.

Considering firstly the changes in N_{eff}, in principle a substantial improvement in radiation tolerance can be achieved by suppressing production of the V_2O complex. More detailed investigations with the kinetics model have demonstrated that an increase in the initial oxygen concentration leads to a substantial reduction in V_2O production [7]. This is because the oxygen impurity getters the vacancies produced during irradiation and suppresses the channel V + VO → V_2O. These predictions have prompted workers to investigate oxygenated material as a solution to the problem of radiation hardness. Recent results from diodes fabricated on epitaxial material, where the oxygen concentration is known to be considerably greater than in standard float-zone detectors, are very promising and appear to bear out the model predictions (see, for example, Ref. [9]).

Although these results represent considerable progress in our understanding of radiation effects, and, indeed, towards the defect-engineering of rad-hard devices, it is evident from Fig. 4 that the picture is not yet complete. A careful consideration of the possible errors in the model [10] suggests that the apparent failure in the prediction of electrical characteristics after neutron irradiation is a real effect that does have a physical origin. A further acceptor-like contribution to N_{eff} is clearly required to bring the model into agreement with the data, while the enormous underestimate of the leakage current is inexplicable within the framework of SRH theory.

The obvious difference between ^{60}Co photon damage, where the model is successful, and fast neutron damage, where it is not, is the production of dense defect clusters in the case of the latter. Simple calculations indicate that the local divacancy density in these clusters may be as high as ~10^{20} cm^{-3} [10]. Since the extent of the bonding distortion caused by an isolated divacancy is ~10 Å, it is possible that **direct** carrier transitions occur between some of the clustered divacancies. These transitions invalidate the SRH calculation, which assumes that the only communication between defects is the indirect statistical link via the occupation of the bands.

There is compelling experimental evidence in the literature for inter-defect charge exchange (see, for example, Ref. [12]). More recently, enhanced diode currents have been attributed to this mechanism [13], although the reported case is for communication between non-identical defects where reactions of the type $X^0Y^- \Leftrightarrow X^-Y^0$ can enhance the occupation of the state with the higher emission rate. Reactions of the type $X^0X^- \Leftrightarrow X^-X^0$ cannot have the same consequence. However, the divacancy is unusual in that it has four charge states which give rise to three energy levels in the forbidden gap (Table 2). The + and = states have very high emission rates. In a high resistivity diode under reverse bias, the neutral state of the divacancy is strongly favoured. Thus the V_2 contribution to the leakage current can be enhanced if the charge exchange reaction $V_2^0V_2^0 \Rightarrow V_2^+V_2^-$ occurs. This mechanism will also increase the number of V_2^- states, which make an acceptor-like contribution to N_{eff}.

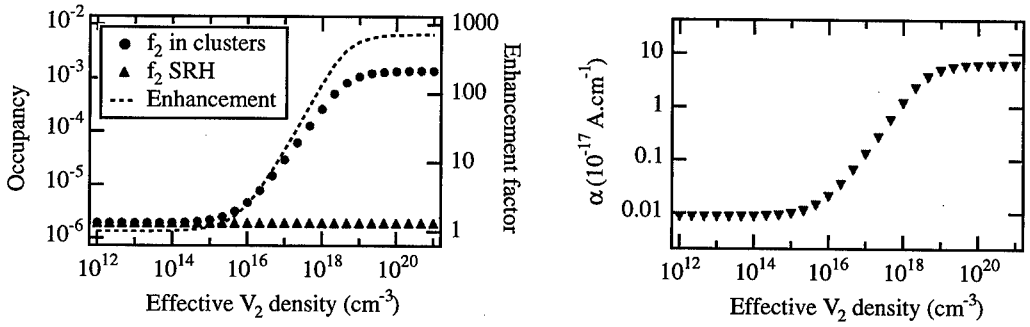


Fig. 5. Consequences of inter-defect charge exchange for V_2 first acceptor occupancy (f_2) and damage constant (α).

By writing general expressions for the rates of emission and capture between any two divacancy states, it is possible to solve for the occupancy of each state as a function of V_2 density within the clusters. This is necessary because the fraction of V_2 defects that are actually close enough to

exchange charge is not known. Results are shown above in Fig. 5; full details of the calculation may be found in Ref. [10]. The reaction $V_2^0V_2^0 \Rightarrow V_2^+V_2^-$ dominates, leading to a significant enhancement in the occupancy of the first acceptor state (denoted f_2) over the value predicted by the SRH calculation. For an effective density of 10^{19} cm^{-3}, the contribution of the filled acceptors to N_{eff} at a fluence of 5×10^{13} n.cm^{-2} is $\sim2\times10^{11}$ cm^{-3}, which is quite significant. The predicted value of the damage constant, α, is $\sim5\times10^{-17}$ A.cm^{-1}, in close agreement with what is actually observed. Moreover, the predicted temperature dependence of the current corresponds to $E_a = (0.59\pm0.01)$ eV, which compares favourably with the measured value of $E_a = (0.62\pm0.03)$ eV (Eq. (2)).

6. Summary and discussion

A numerical model has been used to investigate the evolution of complex defects in detector material during ^{60}Co gamma and fast neutron irradiation. The defect concentrations from the model have been combined with SRH semiconductor statistics to predict observed quantities such as effective doping concentration and leakage current. In the case of gamma irradiation, the model predictions are in good agreement with the experimental data. According to the model, the changes in N_{eff} and leakage current are dominated by the creation of V_2O defects. In the case of neutron damage, the agreement with the data is poor. It has been shown that these discrepancies may be explained by the non-SRH mechanism of inter-defect charge transfer between divacancy states in the dense terminal clusters formed by heavy particle irradiation. The charge exchange reaction $V_2^0V_2^0 \Rightarrow V_2^+V_2^-$ leads to a large increase in carrier generation rate and a significant enhancement in the number of V_2^- states.

The calculations presented here suggest that detectors would be extremely radiation-hard from the point of view of both leakage current and changes in N_{eff} if V_2 production could be suppressed. This requires very high impurity concentrations to ensure that gettering centres are distributed on a similar scale to the PKA cascade. Isoelectronic elements such as germanium (Ge) and tin (Sn) appear to be suitable candidates. However, float-zone devices with Ge levels of ~0.1% are no more radiation tolerant than standard detectors [14]. It is possible that a higher impurity fraction of germanium is required. Doping with tin is known to suppress V_2 production in Czochralski material [15]. Unfortunately, there are technological problems associated with processing such material and no working devices have yet been produced. Nevertheless, research in this field is very active (see, for example, Ref. [16]), and it is hoped that it will be possible to demonstrate truly rad-hard detectors for use at the LHC within the time remaining.

Acknowledgements

Valuable discussions with Professor G. Davies, Dr. S. Watts and Dr. J. Matheson are gratefully acknowledged. We also acknowledge the financial support of the UK Particle Physics and Astronomy Research Council.

References

[1] CMS Collaboration, CERN/LHCC 94-38 (1994).
[2] G. Hall, Rep. Prog. Phys. **57**, 481 (1994).
[3] S. Sotthibandhu, PhD thesis, Rutherford Appleton Laboratory RALT-025 (1994).
[4] B. C. MacEvoy, PhD thesis, Rutherford Appleton Laboratory RAL-TH-97-003 (1997).
[5] G. P. Mueller et al., IEEE Trans. Nucl. Sci. **29**, 1493 (1982).
[6] G. Davies et al., Semicond. Sci. Technol. **2**, 524 (1987).
[7] B. C. MacEvoy, Nucl. Instr. and Meth. A **388**, 365 (1997).
[8] G. Summers et al., IEEE Trans. Nucl. Sci. **40**, 1372 (1993).
[9] S. J. Watts, Nucl. Instr. and Meth. A **386**, 149 (1997).
[10] K. Gill et al., J. Appl. Phys. **82**, 126 (1997).
[11] Y. H. Lee et al., Radiat. Eff. **29**, 7 (1976).
[12] W. Chen et al., Phys. Rev. Lett. **67**, 914 (1991).
[13] A. Schenk and U. Krumbein, J. Appl. Phys. **78**, 3185 (1995).
[14] S. J. Bates et al., CERN/ECP 95-18 (1995).
[15] B. G. Svensson et al., J. Appl. Phys. **72**, 5616 (1992).
[16] ROSE Collaboration, CERN/LHCC 96-23 (1996).

Materials Science Forum

ISSN 0255-5476

As of January 1992 combined with Crystal Properties and Preparation

Editors, Editorial and Advisory Board

see front inside cover

Scope

Materials Science Forum specializes in the rapid publication of international conference proceedings in every area of Materials Science, Solid State Physics and Chemistry. This permits such proceedings to be conveniently referenced, abstracted and read. It also guarantees that the proceedings are available in major libraries within two to three months of the close of the conference.

Materials Science Forum also publishes, on a regular basis, collections of research and review papers on topics of current interest. Abstracted in all of the major abstract media, and available in practically all of the major libraries which service materials research communities, *Materials Science Forum* offers both very rapid publication (within two months of acceptance of the manuscript) and high visibility.

Internet

The table of contents of each volume is available on the World Wide Web at http://www.ttp.ch/perdcs/msf.htm.

Preview Service

Trans Tech Publications' Preview Service offers automatic delivery of tables of contents via e-mail - several weeks before the actual release of the respective publication. This service is free of charge. For more information, please visit our home page or send an e-mail to preview@ttp.ch containing simply the word *help* as the message body.

Subscription Information

Materials Science Forum is published in 30 volumes per year. In 1997, volumes 233-262 are scheduled to be published. The subscription rate is CHF 99.50 per volume (CHF 2985.00 per year).

Standing orders

Standing Orders are available for the following topical areas of interest: Pt. A: Electronic and Electro-optic Materials; Pt. B: Metal Physics; Pt. C: Ceramic Materials and Glasses; Pt. D: Ionic Materials, Oxides; Pt. E: Corrosion and Oxidation; Pt. F: Surfaces, Interfaces and Thin Films; Pt. G: Crystal Growth and Crystal Structures.

Standing orders for one or more of these sections may be placed: the topics are not meant to be exclusive, i.e. a given volume can be assigned to two or more of these sections. Should a title be assigned to more than one section, the subscriber will receive the respective title only once. The price per volume is CHF 99.50.

Trans Tech Publications Ltd
Brandrain 6 • CH-8707 Uetikon-Zuerich • Switzerland
Fax +41 (1) 922 10 33 • e-mail: ttp@ttp.ch
http://www.ttp.ch